

PROCEEDINGS OF SPIE



SPIE—The International Society for Optical Engineering

Laser Applications in Microelectronic and Optoelectronic Manufacturing V

Henry Helvajian
Koji Sugioka
Malcolm C. Gower
Jan J. Dubowski
Chairs/Editors

DISTRIBUTION STATEMENT A
Approved for Public Release
Distribution Unlimited

24–26 January 2000
San Jose, USA

Sponsored by
AFOSR—U.S. Air Force Office of Scientific Research
SPIE—The International Society for Optical Engineering



Volume 3933

DTIC QUALITY INSPECTED 4

20001019 017

REPORT DOCUMENTATION PAGE				Form Approved OMB No. 0704-0188	
<small>Public reporting burden for this collection of information is estimated to average 1 hour per response, including the time for reviewing instructions, searching data sources, gathering and maintaining the data needed, and completing and reviewing the collection of information. Send comments regarding this burden estimate or any other aspect of this collection of information, including suggestions for reducing this burden to Washington Headquarters Service, Directorate for Information Operations and Reports, 1215 Jefferson Davis Highway, Suite 1204, Arlington, VA 22202-4302, and to the Office of Management and Budget, Paperwork Reduction Project (0704-0188) Washington, DC 20503.</small> PLEASE DO NOT RETURN YOUR FORM TO THE ABOVE ADDRESS.					
1. REPORT DATE (DD-MM-YYYY) 08-06-2000		2. REPORT DATE Final Technical Report		3. DATES COVERED (From - To) 15-01-2000 to 14-07-2000	
4. TITLE AND SUBTITLE Laser Applications in Microelectronic and Optoelectronic Manufacturing V				5a. CONTRACT NUMBER	
				5b. GRANT NUMBER F49620-00-1-0135	
				5c. PROGRAM ELEMENT NUMBER	
6. AUTHOR(S) Helvajian, Henry Sugioka, Koji Dubowski, Jan J. Gower, Malcom C.				5d. PROJECT NUMBER	
				5e. TASK NUMBER	
				5f. WORK UNIT NUMBER	
7. PERFORMING ORGANIZATION NAME(S) AND ADDRESS(ES) Society of Photo-Optical Instrumentation Engineers (SPIE) PO Box 10 Bellingham, WA 98227-0010				8. PERFORMING ORGANIZATION REPORT NUMBER Volume 3933	
9. SPONSORING/MONITORING AGENCY NAME(S) AND ADDRESS(ES) Air Force Office of Scientific Research 801 N. Randolph St. Room 732 Arlington, VA 22203-1977				10. SPONSOR/MONITOR'S ACRONYM(S) AFOSR/NE	
				11. SPONSORING/MONITORING AGENCY REPORT NUMBER	
12. DISTRIBUTION AVAILABILITY STATEMENT Approved for Public Release					
13. SUPPLEMENTARY NOTES ISBN 0-8194-3550-3					
14. ABSTRACT This proceedings contains papers on the following topics: fundamental processes of laser material interaction phenomenon, laser material processing techniques, pulsed-laser deposition, and laser microengineering. The latter topic was added to LAMOM V and reflects the strong growth in the application of lasers to micromachining, 3D fabrication, and microtexturing operations.					
15. SUBJECT TERMS Laser, Microelectronic, Optoelectronic					
16. SECURITY CLASSIFICATION OF:			17. LIMITATION OF ABSTRACT SAR	18. NUMBER OF PAGES 514	19a. NAME OF RESPONSIBLE PERSON Marshall Weathersby
a. REPORT Non-classified	b. ABSTRACT	c. THIS PAGE			19b. TELEPHONE NUMBER (Include area code) (360)676-3290



PROCEEDINGS OF SPIE
SPIE—The International Society for Optical Engineering

Laser Applications in Microelectronic and Optoelectronic Manufacturing V

Henry Helvajian
Koji Sugioka
Malcolm C. Gower
Jan J. Dubowski
Chairs/Editors

DISTRIBUTION STATEMENT A
Approved for Public Release
Distribution Unlimited

24–26 January 2000
San Jose, USA

Sponsored by
AFOSR—U.S. Air Force Office of Scientific Research
SPIE—The International Society for Optical Engineering

Published by
SPIE—The International Society for Optical Engineering



20001019 017

Volume 3933

SPIE is an international technical society dedicated to advancing engineering and scientific applications of optical , photonic, imaging, electronic, and optoelectronic technologies.



The papers appearing in this book compose the proceedings of the technical conference cited on the cover and title page of this volume. They reflect the authors' opinions and are published as presented, in the interests of timely dissemination. Their inclusion in this publication does not necessarily constitute endorsement by the editors or by SPIE. Papers were selected by the conference program committee to be presented in oral or poster format, and were subject to review by volume editors or program committees.

Please use the following format to cite material from this book:

Author(s), "Title of paper," in *Laser Applications in Microelectronic and Optoelectronic Manufacturing V*, Henry Helvajian, Koji Sugioka, Malcolm C. Gower, Jan J. Dubowski, Editors, Proceedings of SPIE Vol. 3933, page numbers (2000).

ISSN 0277-786X
ISBN 0-8194-3550-3

Published by
SPIE—The International Society for Optical Engineering
P.O. Box 10, Bellingham, Washington 98227-0010 USA
Telephone 1 360/676-3290 (Pacific Time) • Fax 1 360/647-1445
<http://www.spie.org/>

Copyright ©2000, The Society of Photo-Optical Instrumentation Engineers.

Copying of material in this book for internal or personal use, or for the internal or personal use of specific clients, beyond the fair use provisions granted by the U.S. Copyright Law is authorized by SPIE subject to payment of copying fees. The Transactional Reporting Service base fee for this volume is \$15.00 per article (or portion thereof), which should be paid directly to the Copyright Clearance Center (CCC), 222 Rosewood Drive, Danvers, MA 01923 USA. Payment may also be made electronically through CCC Online at <http://www.directory.net/copyright/>. Other copying for republication, resale, advertising or promotion, or any form of systematic or multiple reproduction of any material in this book is prohibited except with permission in writing from the publisher. The CCC fee code is 0277-786X/00/\$15.00.

Printed in the United States of America.

Contents

- ix *Conference Committee*
- xi *Introduction*

SESSION 1 FUNDAMENTAL PROCESSES I

- 2 **Investigations of laser desorption from modified surfaces of ionic single crystals (Invited Paper) [3933-01]**
C. Bandis, M. L. Dawes, Y. Kawaguchi, S. C. Langford, J. T. Dickinson, Washington State Univ. (USA)
- 14 **Dynamical Stark effect in small quantum dots [3933-04]**
J. T. Andrews, P. Sen, Shree G S Institute of Technology & Science (India)

SESSION 2 FUNDAMENTAL PROCESSES II

- 26 **Explosive femtosecond ablation from ionic crystals (Invited Paper) [3933-05]**
J. Reif, M. Henyk, D. Wolfframm, Brandenburgische Technische Univ. Cottbus (Germany)
- 34 **Interaction of shock electromagnetic waves with transparent materials: classical approach [3933-06]**
A. S. Gruzdeva, V. E. Gruzdev, S. I. Vavilov State Optical Institute (Russia)
- 46 **Analysis of laser ablation process in semiconductor due to ultrashort-pulsed laser with molecular dynamics simulation [3933-08]**
K. Watanabe, Y. Ishizaka, E. Ohmura, I. Miyamoto, Osaka Univ. (Japan)

SESSION 3 LASERS AND TECHNIQUES I

- 58 **Laser technologies for manufacturing of advanced materials and devices (Invited Paper) [3933-09]**
J. J. Dubowski, National Research Council (Canada)
- 62 **Nonlinear optical characterization of silicon wafers: in-situ detection of stacking faults and external stress [3933-10]**
J. Reif, T. Schneider, R. Schmid, D. Wolfframm, Brandenburgische Technische Univ. Cottbus (Germany)
- 69 **Influences of hydrogen in precursor Si films on excimer laser crystallization [3933-11]**
M. Takahashi, M. Saitoh, K. Suzuki, K. Ogata, Hitachi, Ltd. (Japan)
- 77 **Laser chemical process for clean applications of semiconductor manufacturing [3933-12]**
D. Yogev, M. Y. Engel, S. Zeid, I. Barzilay, B. Livshits, ORAMIR Semiconductor Equipment Ltd. (Israel)

SESSION 4 LASERS AND TECHNIQUES II

- 90 **Present status and future aspects of high-power diode laser materials processing under the view of a German national research project (Invited Paper) [3933-13]**
F. G. Bachmann, Rofin-Sinar Laser GmbH (Germany)
- 105 **Direct writing of electronic materials using a new laser-assisted transfer/annealing technique [3933-14]**
A. Piqué, J. Fitz-Gerald, D. B. Chrisey, Naval Research Lab. (USA); R. C. Y. Auyeung, H. D. Wu, SFA, Inc. (USA); S. Lakeou, SFA, Inc. (USA) and Univ. of the District of Columbia (USA); R. A. McGill, Naval Research Lab. (USA)
- 113 **Stress measurements in silicon microstructures [3933-17]**
S. Amimoto, D. J. Chang, A. D. Birkitt, The Aerospace Corp. (USA)

SESSION 5 PULSED LASER DEPOSITION I

- 124 **Pulsed-laser deposition of electronic oxides: superconductor and semiconductor applications (Invited Paper) [3933-18]**
D. P. Norton, C. Park, Y. E. Lee, J. D. Budai, M. F. Chisholm, D. T. Verebelyi, D. K. Christen, D. M. Kroeger, Oak Ridge National Lab. (USA)
- 131 **Optical and electronic properties of amorphous WO₃ thin film irradiated by laser in air [3933-19]**
H. Qiu, Y. F. Lu, National Univ. of Singapore
- 140 **Effect of film thickness on the properties of indium tin oxide thin film grown by pulsed-laser deposition for organic light-emitting diodes [3933-21]**
H. Kim, George Washington Univ. (USA); J. S. Horwitz, A. Piqué, G. P. Kushto, Z. H. Kafafi, Naval Research Lab. (USA); C. M. Gilmore, George Washington Univ. (USA); D. B. Chrisey, Naval Research Lab. (USA)

SESSION 6 PULSED LASER DEPOSITION II

- 152 **Developments of laser processing technologies in the Japanese MITI project (Invited Paper) [3933-22]**
T. Yoshida, Matsushita Research Institute Tokyo, Inc. (Japan); T. Sato, Y. Yoshida, K. Matsuno, RIPE—R&D Institute for Photonics Engineering (Japan)
- 166 **TiN growth by hybrid radical beam-PLD for Si barrier metal [3933-23]**
K. Obata, RIKEN—The Institute of Physical and Chemical Research (Japan) and Science Univ. of Tokyo (Japan); K. Sugioka, RIKEN—The Institute of Physical and Chemical Research (Japan); K. Toyoda, Science Univ. of Tokyo (Japan); H. Takai, Tokyo Denki Univ. (Japan); K. Midorikawa, RIKEN—The Institute of Physical and Chemical Research (Japan)
- 174 **Laser ablation of solid films at a cryogenic temperature [3933-24]**
H. Niino, T. Sato, A. Yabe, National Institute of Materials and Chemical Research (Japan)
- 182 **Pulsed-laser deposition of AlN thin films [3933-25]**
Y. F. Lu, Z. M. Ren, H. Q. Ni, Y. W. Goh, B. A. Cheong, S. K. Chow, J. P. Wang, T. C. Chong, National Univ. of Singapore

SESSION 7 PULSED LASER DEPOSITION III

- 192 **Production of photoluminescent Si-based nanostructures by laser ablation: effects of ablation and postdeposition conditions** [3933-27]
A. V. Kabashin, M. Charbonneau-Lefort, M. Meunier, École Polytechnique de Montréal (Canada); R. Leonelli, Univ. de Montréal (Canada)
- 200 **Pulsed-laser deposition growth of SBN and correlation study of structure and optical properties** [3933-28]
F. E. Fernández, Y. González, H. Liu, E. Rodríguez, V. Rodríguez, W. Jia, Univ. of Puerto Rico/ Mayagüez
- 207 **Electric signal diagnostics of plasma dynamics at an early stage of laser ablation** [3933-29]
M. H. Hong, Y. F. Lu, A. Foong, National Univ. of Singapore

SESSION 8 LASERS AND TECHNIQUES III

- 218 **KrF-excimer-laser-induced ohmic metallization of ZnO substrate** [3933-31]
T. Akane, K. Sugioka, K. Midorikawa, RIKEN—The Institute of Physical and Chemical Research (Japan)
- 225 **Achievements in near-field investigations in Russia (IFMO SPb)** [3933-32]
V. P. Veiko, N. B. Voznesensky, T. V. Ivanova, St. Petersburg State Institute of Fine Mechanics and Optics (Russia)
- 237 **Scribing blue LED wafer using laser-induced plasma-assisted ablation with a Q-switched Nd:YAG laser** [3933-34]
J.-M. Lee, LGIS Research & Development Ctr. (Korea); J.-H. Jang, T.-K. Yoo, LG Corporate Institute of Technology (Korea)

SESSION 9 LASER MICROENGINEERING I

- 246 **Microfabrication by femtosecond laser irradiation (Invited Paper)** [3933-35]
H. Misawa, H.-B. Sun, S. Juodkazis, M. Watanabe, S. Matsuo, Univ. of Tokushima (Japan)
- 261 **Laser micromachining: new developments and applications** [3933-36]
N. H. Rizvi, D. K. Milne, P. T. Rumsby, M. C. Gower, Exitech Ltd. (UK)
- 272 **Excimer lamp stereolithography** [3933-37]
S. Satoh, T. Tanaka, S. Ihara, C. Yamabe, Saga Univ. (Japan)
- 280 **Femtosecond pulse laser machining of InP wafers** [3933-68]
J. M. Wrobel, Univ. of Missouri/Kansas City (USA); J. Bonse, J. Krüger, W. Kautek, Federal Institute for Materials Research and Testing (Germany)

SESSION 10 LASER MICROENGINEERING II

- 290 **Custom specific fabrication of integrated optical devices by excimer laser ablation of polymers (Invited Paper)** [3933-39]
T. Klotzbücher, M. Popp, T. Braune, J. Haase, A. Gaudron, I. Smaglinski, T. Paatzsch, H.-D. Bauer, W. Ehrfeld, Institut für Mikrotechnik Mainz GmbH (Germany)

- 299 **Laser-based microscale bending for microelectronics fabrication [3933-40]**
X. Xu, Purdue Univ. (USA)
- 309 **Fabrication of microgrooves with excimer laser ablation techniques for plastic optical fiber array alignment purposes [3933-41]**
K. Naessens, A. Van Hove, T. Coosemans, S. Verstuyft, Univ. Gent/IMEC (Belgium);
H. Ottevaere, Vrije Univ. Brussel (Belgium); L. Vanwassenhove, P. Van Daele, R. G. Baets,
Univ. Gent/IMEC (Belgium)
- 316 **Spectroscopic investigation of SiO₂ surfaces of optical materials for high-power lasers [3933-42]**
S. G. Demos, L. M. Sheehan, M. R. Kozlowski, Lawrence Livermore National Lab. (USA)

SESSION 11 LASER MICROENGINEERING III

- 322 **Excimer laser micromachining for fabrication of diamond diffractive optical elements (Invited Paper) [3933-43]**
V. I. Konov, V. V. Kononenko, S. M. Pimenov, A. M. Prokhorov, General Physics Institute (Russia); V. S. Pavelyev, V. A. Soifer, Image Processing Systems Institute (Russia); P. F. Muys, E. Vandamme, Laser Power Europe N.V. (Belgium)
- 332 **Microprocessing of glass materials by laser-induced plasma-assisted ablation using nanosecond pulsed lasers [3933-44]**
J. Zhang, K. Sugioka, K. Midorikawa, RIKEN—The Institute of Physical and Chemical Research (Japan)
- 338 **Novel technique for high-quality microstructuring with excimer lasers [3933-45]**
S. Roth, M. Geiger, Univ. of Erlangen-Nuremberg (Germany)
- 347 **Micromachining by laser ablation of liquid: superheated liquid and phase explosion [3933-46]**
J. Wang, H. Niino, A. Yabe, National Institute of Materials and Chemical Research (Japan)

SESSION 12 LASER MICROENGINEERING IV

- 356 **Analysis of excimer laser patterning process of Cu thin film [3933-47]**
T. Sano, I. Miyamoto, H. Hayashi, H. Ochi, Osaka Univ. (Japan)
- 365 **High-accuracy microdrilling of steel with solid state UV laser at a rate of 10 mm/sec [3933-67]**
S. V. Govorkov, E. V. Slobodtchikov, A. O. Wiessner, D. Basting, Lambda Physik, Inc. (USA)
- 371 **Laser beam joining of optical fibers in silicon V-grooves [3933-49]**
S. Kaufmann, Bavarian Laser Ctr. (Germany); A. Otto, Univ. of Erlangen-Nuremberg (Germany);
G. Luz, Alcatel Corporate Research Ctr. (Germany)
- 379 **CO₂ laser drilling of printed wiring boards and development of in-process monitoring system [3933-50]**
T. Nakayama, T. Sano, I. Miyamoto, Osaka Univ. (Japan); K. Tanaka, Y. Uchida, Matsushita Electric Works, Ltd. (Japan)

SESSION 13 POSTER SESSION

- 388 **Laser-induced temperature-rise measurement by infrared imaging [3933-15]**
J. Gu, S.-Tam, Y.-L. Lam, Nanyang Technological Univ. (Singapore); Q. Zheng, X. Wei,
Huazhong Univ. of Science and Technology (China)
- 396 **New infrared stereolithography: control of the parameters of the localized curing
thermosensitive materials [3933-38]**
M. A. F. Scarpato, A. L. J. Munhoz, G. Marinho, D. S. Salles, State Univ. of Campinas (Brazil);
S. D. Allen, Florida State Univ. (USA)
- 404 **Pulsed x-ray emission by laser-plasma-triggered electron beam [3933-52]**
Y. Nagumo, S. Hayashi, Shimadzu Corp. (Japan); T. Yagi, T. Matsumura, S. Yamazaki,
Tokai Univ. (Japan); K. Honda, I. Kojima, National Institute of Materials and Chemical
Research (Japan)
- 412 **Light scattering by rough dielectric surface [3933-53]**
V. E. Gruzdev, A. S. Gruzdeva, S. I. Vavilov State Optical Institute (Russia)
- 425 **Capacitive discharge excilamps [3933-54]**
E. A. Sosnin, M. V. Erofeev, A. N. Panchenko, M. I. Lomaev, V. S. Skakun, D. V. Shitz,
V. F. Tarasenko, High Current Electronics Institute (Russia)
- 432 **Optimization of nanosecond UV laser illumination for semiconductor materials (Si, HgCdTe,
InSb) [3933-55]**
A. R. Novoselov, A. G. Klimenko, E. V. Fedosenko, A. E. Plotnikov, Institute of Semiconductor
Physics (Russia)
- 438 **Reprography method of nondestructive testing of micro-cracks inside the wall of a pinhole
micromanufactured by laser [3933-56]**
C. Zhou, W. Yu, J. Sun, Yantai Univ. (China); H. Chen, Xi'an Medical Univ. (China)
- 445 **Model predicting the microhole profiles of laser drilling processes in carbon fiber composites
[3933-57]**
F. F. Wu, R. D. Pilkington, Salford Univ. (UK)
- 457 **Microscopic observation of laser-induced forward transfer process by two-dimensional laser-
induced fluorescence technique [3933-58]**
Y. Nakata, T. Okada, M. Maeda, Kyushu Univ. (Japan)
- 469 **Ion-source-assisted pulsed-laser deposition of carbon nitride thin films [3933-59]**
Z. F. He, Y. F. Lu, Z. H. Mai, Z. M. Ren, National Univ. of Singapore
- 478 **Pulsed-laser deposition of hydrogenated amorphous carbon films from a polymeric target
[3933-60]**
S. M. Huang, Y. F. Lu, National Univ. of Singapore; Z. Sun, Nanyang Technological Univ.
(Singapore)
- 487 **Preparation of polyperinaphthalenic organic semiconductor thin films by excimer laser
ablation and application to anode electrodes for ultrathin rechargeable lithium ion batteries
[3933-61]**
S. Nishio, S. Kuriki, Y. Tsujine, A. Matsuzaki, H. Sato, Mi'e Univ. (Japan); N. Ando, Y. Hato,
Kanebo Ltd. (Japan); K. Tanaka, Kyoto Univ. (Japan)

- 496 **Novel thin-film deposition method and system with IR-FEL [3933-63]**
M. Yasumoto, N. Umesaki, Osaka National Research Institute (Japan); T. Tomimasu, A. Ishizu,
K. Awazu, Free Electron Laser Research Institute (Japan)
- 502 **Structure and properties of porous PZT ceramics synthesized by selective laser sintering
method [3933-64]**
E. Yu. Tarasova, G. V. Kryukova, A. L. Petrov, I. V. Shyshkovsky, P. N. Lebedev Physical
Institute (Russia)
- 505 **Selectively deposited copper on laser-treated polyimide using electroless plating [3933-65]**
G. Zhao, Nanyang Technological Univ. (Singapore), Gintic Institute of Manufacturing
Technology (Singapore), and Anhui Institute of Optics and Fine Mechanics (China);
H. M. Phillips, H. Zheng, Gintic Institute of Manufacturing Technology (Singapore); S.-C. Tam,
Nanyang Technological Univ. (Singapore); W. Liu, G. Wen, Z. Gong, Anhui Institute of Optics
and Fine Mechanics (China); Y.-L. Lam, Nanyang Technological Univ. (Singapore)
- 511 *Addendum*
- 512 *Author Index*

Conference Committee

Conference Chairs

Henry Helvajian, The Aerospace Corporation (USA)
Koji Sugioka, RIKEN—The Institute of Physical and Chemical Research (Japan)
Malcolm C. Gower, Exitech Ltd. (UK)
Jan J. Dubowski, National Research Council (Canada)

Program Committee

Carmen N. Afonso, Instituto de Optica (Spain)
David Ashkenasi, Max-Born-Institut (Germany)
Steven R. J. Brueck, University of New Mexico (USA)
H. Frederick Dylla, Thomas Jefferson National Accelerator Facility (USA)
Yong Feng Lu, National University of Singapore
Félix E. Fernández, University of Puerto Rico/Mayagüez
Richard F. Haglund, Jr., Vanderbilt University (USA)
Peter R. Herman, University of Toronto (Canada)
Wayne P. Hess, Pacific Northwest National Laboratory (USA)
Ernst W. Kreutz, Technical University of Aachen (Germany)
Boris S. Luk'yanchuk, General Physics Institute (Russia)
Vladimir I. Merkulov, Oak Ridge National Laboratory (USA)
Michel Meunier, École Polytechnique de Montréal (Canada)
Kiyotaka Miura, Japan Science and Technology Corporation
Lukas Novotny, Pacific Northwest National Laboratory (USA)
Mary O'Neill, University of Hull (UK)
Daniel V. Palanker, Stanford University (USA)
Alberto Piqué, Naval Research Laboratory (USA)
Gouri Radhakrishnan, The Aerospace Corporation (USA)
Katsumi Tanimura, Nagoya University (Japan)
Frank Traeger, University of Kassel (Germany)
Kunihiko Washio, NEC Corporation (Japan)
Takashi Yabe, Tokyo Institute of Technology (Japan)
Takehito Yoshida, Matsushita Research Institute Tokyo, Inc. (Japan)

Session Chairs

- 1 Fundamental Processes I
David P. Taylor, The Aerospace Corporation (USA)
- 2 Fundamental Processes II
Richard F. Haglund, Jr., Vanderbilt University (USA)
- 3 Lasers and Techniques I
Malcolm C. Gower, Exitech Ltd. (UK)

- 4 Lasers and Techniques II
Jan J. Dubowski, National Research Council (Canada)
- 5 Pulsed Laser Deposition I
Koji Sugioka, RIKEN—The Institute of Physical and Chemical Research (Japan)
- 6 Pulsed Laser Deposition II
James S. Horwitz, Naval Research Laboratory (USA)
- 7 Pulsed Laser Deposition III
David P. Norton, Oak Ridge National Laboratory (USA)
- 8 Lasers and Techniques III
Andrew C. Tam, IBM Almaden Research Center (USA)
- 9 Laser Microengineering I
Henry Helvajian, The Aerospace Corporation (USA)
- 10 Laser Microengineering II
Vitali I. Konov, General Physics Institute (Russia)
- 11 Laser Microengineering III
Richard F. Haglund, Jr., Vanderbilt University (USA)
- 12 Laser Microengineering IV
Peter D. Fuqua, The Aerospace Corporation (USA)

Introduction

The laser is currently in its fourth decade of development and is emerging as the tool of choice for material processing in the 21st century. Laser processing is by nature an environmentally "clean" and in-situ processing approach. It has a very large dynamic range of processing size from a scale that can exceed the wavelength of light to dimensions measured in many square meters. It has also been shown to process a variety of materials, from delicate matter of biological origin to diamond, the hardest material known. Therefore, one can defend the notion that the laser, as a material processing tool, has advanced to a relatively mature stage to merit an annual review of its applicability to various material processing tasks. The Laser Applications in Microelectronics and Optoelectronics Manufacturing (LAMOM) conference series is an attempt to provide a common forum for both scientific and engineering exchange to address aspects of processing materials with lasers. The LAMOM conference series was established in 1995 (see *Proceedings of SPIE* Volumes 2403, 2703, 2991, 3274, and 3618) and held in San Jose, California, as part of the SPIE Photonics West international symposium.

This volume presents the proceedings from the fifth in the LAMOM series (LAMOM V). The conference was held during a three-day period (January 24–26, 2000) and comprised 12 oral sessions plus a poster session. These sessions included papers on fundamental processes of laser material interaction phenomenon, laser material processing techniques, pulsed-laser deposition, and laser microengineering. The latter topic was added to LAMOM V and reflects the strong growth in the application of lasers to micromachining, 3D fabrication, and microtexturing operations. More than 60 oral and poster presentations were delivered with strong representation from Asia, Europe, and North America.

We thank the members of the program committee, the invited speakers, and all of the participants for making LAMOM V so successful. We also extend our thanks to the SPIE technical personnel for helping in the organization of this meeting.

Finally, we respectfully acknowledge the U.S. Air Force Office of Scientific Research (Dr. Howard Schlossberg, in particular) for the continued financial support provided to this conference series.

**Henry Helvajian
Koji Sugioka
Malcolm C. Gower
Jan J. Dubowski**

SESSION 1

Fundamental Processes I

Investigations of laser desorption from modified surfaces of ionic single crystals

C. Bandis, M. L. Dawes, Y. Kawaguchi*, S. C. Langford, J. T. Dickinson**

Surface Dynamics Laboratory, Department of Physics, Washington State University,
Pullman, WA 99164-2814

ABSTRACT

Wide band gap insulators irradiated with UV and/or IR pulsed lasers have been shown to yield neutrals, photoinduced electrons, and energetic positive ions suggesting occupied electronic defect states in the band gap. We explore the consequences of applying a variety of stimuli, which can generate defects on single crystal surfaces of inorganic ionic crystals. The stimuli include electron beam irradiation, a second laser beam, mechanical treatment, and thermal treatment. Our experiments on a wide variety of ionic crystals find that a common theme evolves where these stimuli generate sites that strongly interact with the probing laser beam. Such interactions lead to dramatic decrease in the laser intensities needed for ejection of ions, neutrals, as well as eventual plume formation, and result in increased vulnerability of the materials to the laser radiation.

Keywords: Laser desorption, ablation, ion emission, photoemission, plume formation, defects, photoelectronic, photothermal lattice relaxation, polarization.

1. INTRODUCTION

The combination of laser ablation/desorption with mass and/or optical spectroscopies is often used for chemical analysis and characterization of a wide variety of materials.¹ However, reliable quantitative analysis requires detailed understanding of the laser photodecomposition and desorption mechanisms, since they can often affect the sample composition and resulting signals.² In addition, laser surface modification, etching, and machining also require an understanding of the details of laser materials interactions. For that reason, both the electron and ion emission properties are of great interest since they play an important role in the onset of plasma formation^{3, 4} and the large scale removal of material. Thus, considerable research has been devoted on how nanosecond laser pulses with sub-bandgap wavelengths interact with ionic insulators in order to generate the multitude of interactions necessary for the photoemission of electrons, the photodesorption of energetic positive ions, as well as the desorption of neutral atoms and molecules.

In most cases involving nanosecond pulse lengths, multiphoton processes and heating by inverse bremsstrahlung do not dominate, particularly at lower laser intensities whereas the role of defects is by far more important. For single crystal ionic oxyanion (e.g., NO_3^- , SO_4^{2-} , PO_4^{3-} , CO_3^{2-}) containing materials, those defects associated with the anion often serve as electron traps which provide binding sites for desorbing species with binding energies considerably smaller than those associated with bulk interatomic bonds. Furthermore, such defects can create energy levels accessible with sub-bandgap energy photons. Thus, any perturbation of the crystal by radiation, mechanical stress, or by thermal excitation that can form such centers will potentially increase the vulnerability of the surface to laser irradiation.

In order to create and study such modified ionic crystal surfaces with increased vulnerability to laser irradiation, we utilized the combination of two or more stimuli (e.g., electron beam and laser beam or two laser beams). It is the purpose of this paper to present evidence of the synergistic influence of these combined stimuli showing dramatic changes in the laser induced ion emission, and to discuss the mechanisms responsible for these dramatic changes. Although, we performed such experiments on a wide variety of ionic crystals, including alkali halides, MgO , CaCO_3 etc., in this paper we will limit our discussion to two materials containing oxyanions, sodium nitrate (NaNO_3) and brushite ($\text{CaHPO}_4 \cdot 2\text{H}_2\text{O}$). The interest for

* Permanent address: Chugoku National Industrial Research Institute, Kure, Hiroshima 737-0197, Japan

** Electronic mail: jtd@wsu.edu

sodium nitrate comes from it being a model for materials found in the environment and in nuclear wastes, while the interest for brushite comes from its potential applications in dentistry, medical implants, and in prosthetic devices.

2. EXPERIMENT

Our experiments were performed on NaNO_3 (99.0% pure) melt and solution grown single crystals, cleaved in air into ~2-mm thick slices, and then mounted into a vacuum chamber with pressure of 1×10^{-9} Torr. Sodium nitrate forms a molecular-ionic crystal with hexagonal unit cell and the same structure as calcite. The cleavage plane of NaNO_3 is along the $10\bar{1}4$ direction in the hexagonal unit cell, which intersects the c-axis at an angle of $43^\circ 49'$. Single crystals of brushite ($\text{CaHPO}_4 \cdot 2\text{H}_2\text{O}$ --a monoclinic structure) were grown by diffusion from aqueous solutions of $\text{Ca}(\text{NO}_3)_2$ and $\text{NH}_4(\text{H}_2\text{PO}_4)$ adjusted to a pH of 2-4 with nitric acid. The resulting plate-like crystals displayed broad (010) surfaces and were transparent in the visible region. Because of the layered structure of brushite (the waters of hydration form alternating layers with the CaHPO_4 layers), the crystals cleave easily along the (010) planes. Sample irradiation was performed with both Lambda Physik excimer lasers (pulse width of 30 ns at 248 nm, KrF) and a Continuum SureLight II Nd:YAG laser with pulse width of 10 ns at 1064 nm. The intensity of the incident IR (1064 nm) radiation was varied using a CVI continuously variable beamsplitter positioned just before the focusing optics, while the intensity of the UV (248 nm) radiation was varied with a variable attenuator (MICROLAS Lasersystem GmbH).

Energetic electrons were provided by a Varian Model 981-2455 Auger electron gun operated at electron energies from 1 to 3 keV and current densities from 30 to $600 \mu\text{A}/\text{cm}^2$. The total electron currents were determined by directing the beam onto a positively biased copper plate and measuring the current to the plate with an electrometer.

The emitted particles were detected with a Quadrupole Mass Spectrometer (QMS) mounted with its axis along the sample surface normal. Mass resolution was better than ± 1 amu/e. The QMS mass filter was typically tuned to a specific mass/charge ratio and the output detected as a function of time. Neutral particles were ionized by electron impact (70 eV electrons) in the QMS ionizer. The resulting ions were drawn into the mass filter section, mass selected, and detected with a Channeltron Electron Multiplier (CEM) (10^4 gain). When high sensitivity was more important than good time response, the CEM output was amplified with a fast electrometer, digitized, and averaged over 20-200 successive pulses with a LeCroy 9450 digital oscilloscope. Improved time response could be obtained with some loss in sensitivity by eliminating the electrometer and pulse counting the CEM output. The CEM signal was amplified by an Ortec Model 579 fast filter amplifier (rise time 5 ns), then discriminated and counted by either an EG&G Model 914P Multiple-Channel Scaler or a Lecroy LC584AXL, 1GHz digital oscilloscope and a peak finding routine. The pulse counted signal was summed over 50-200 laser pulses with a typical time resolution of 500 ns.

3. RESULTS AND DISCUSSION

3.1. Study of the brushite single crystals

The waters of hydration in $\text{CaHPO}_4 \cdot 2\text{H}_2\text{O}$ introduce an entirely unique set of complications regarding the way lasers interact with this ionic solid.⁵ The layers of water contained in this structure are parallel to the cleavage surface and can readily diffuse to the surface. Thus, upon introduction to vacuum we see large quantities of water outgassing from the crystal at room temperature. Nevertheless, both the as grown and cleaved surfaces show Ca^+ ion emission when irradiated at 248 nm. Experiments on heated, abraded and electron-irradiated surfaces demonstrate that the observed Ca^+ ion emission strongly depends on the surface treatment and therefore the defect concentration in the surface.

3.1.1. Effects of Treatments of Brushite

Fig. 1 shows on a log scale the intensities of the Ca^+ ions at one laser fluence ($1.3 \text{ J}/\text{cm}^2$) for a variety of brushite surfaces including e-beam irradiated, cleaved (after extensive heating), abraded, as grown, and as cleaved. Note the substantial increase accompanying the first three treatments over the other surfaces. Treating surfaces in such a way is known to create defect rich surfaces and, therefore, the strong effect of such treatments on the ion emission intensity demonstrates that defects play a major role in the emission process. Although the detailed understanding of the type of defects involved in the observed emissions is far from being complete, the strong increase in the particle emissions shows

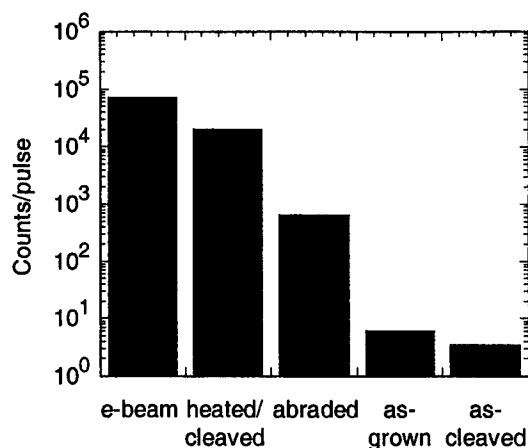


Fig. 1. Ca⁺ yields observed at 1.3 J/cm² from treated (electron irradiated, heated and then cleaved, and abraded) as well as untreated (as-grown and cleaved) CaHPO₄ · 2H₂O single crystals.

that abrading, heating and irradiating with electrons the brushite surfaces results in increased vulnerability of the surface to the laser radiation. Abrasion and mechanical damage has also been shown to generate significant increases in emissions from MgO,⁶ NaNO₃, and CaCO₃.⁷

As we have previously reported, the fluence dependence of laser desorption of positive ions is a highly non-linear process.^{8, 9} For a variety of treated brushite surfaces we show this on a log-log plot in Fig. 2. The steepest portions of these curves correspond to power law of order 8. Although tempting to attribute these nonlinearities to multiphoton absorption, we have repeatedly argued that a *multiple single-photon* process (a sequence of excitations) is easier to justify. In this model, the final launching of the ion occurs when a nearby electron trap is being emptied leading to the Coulomb repulsion necessary to push the ion away.

In Fig. 3 we show the time of flight histograms for as grown, abraded, and e-beam irradiated brushite surfaces. The time-of-flight (TOF) curves were fit to Gaussian energy distributions as follows:

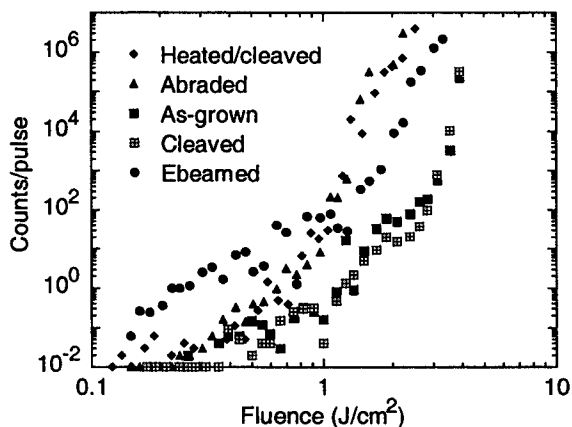


Fig. 2. Ca⁺ emission as a function of fluence for treated (heated/cleaved, abraded, and electron irradiated) and untreated (as-grown and cleaved) brushite samples. The emission intensity of the untreated surfaces is always lower than the emission from the defect rich treated surfaces.

$$I(t) = \frac{Amd^2}{t^3} \exp\left(-\left(E - \frac{md^2}{2t^2}\right)^2 / 2\sigma^2\right) \quad (1)$$

where d is the distance between the sample surface and the CEM, 28 cm; m is the mass of the ion; t is the flight time of the ion; E is the mean kinetic energy; σ is the standard deviation of the kinetic energy, and A is a constant. Typical ion energies obtained from such fits are 4-7 eV, as shown in Fig. 3. We have recently demonstrated¹⁰ that by taking into account the binding energy of the adion, which is usually of the order of few tenths of an eV, and treating the crystal as a collection of fixed point charges, one can successfully predict the energy of the emitted ions from a wide variety of ionic crystals, assuming ionization of an electron trap nearby an ion sitting atop the surface. We estimate that for brushite, distances on the order of a lattice spacing require 1 to 2 charges at the defect site in order to explain most of the ion kinetic energies measured.

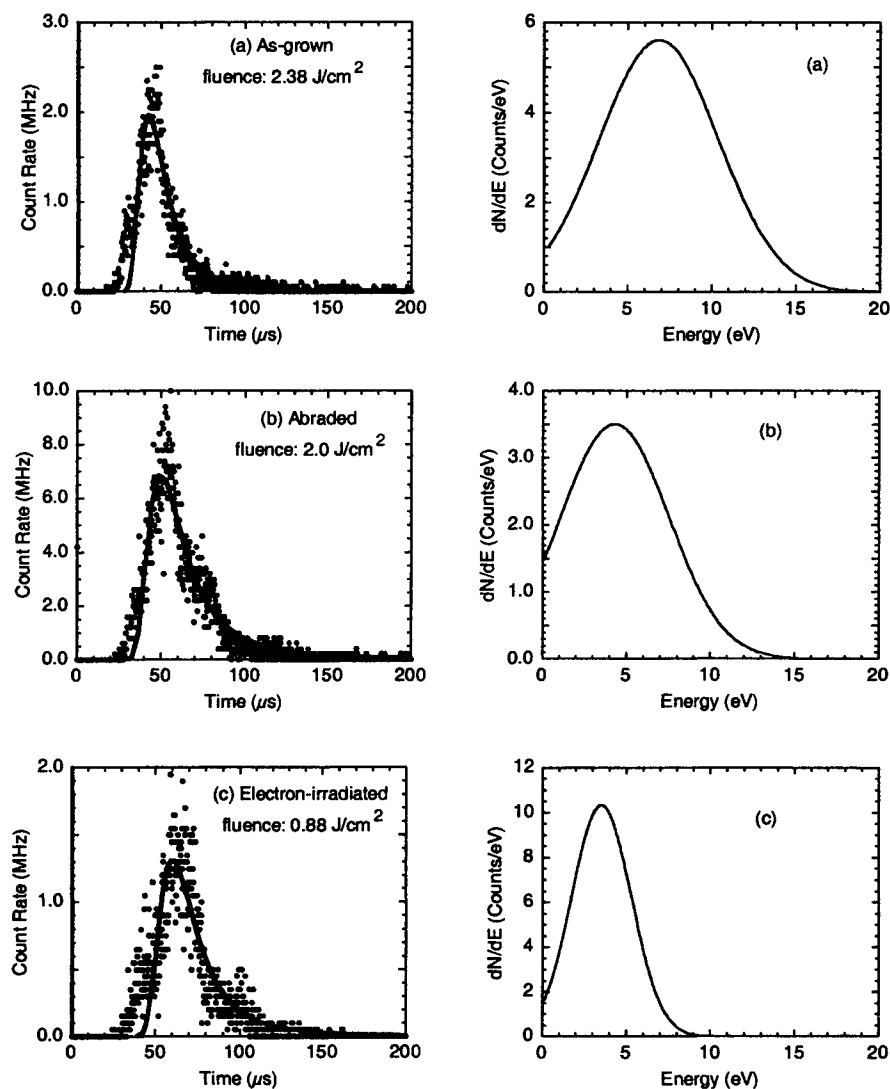


Fig. 3. Ca^+ ion TOF from as-grown (a), abraded (b) and electron irradiated (c) brushite surfaces. The ion energy distributions are calculated from the fits of the TOF histograms. Typical peak ion energies range from 4-7 eV with the treated surfaces exhibiting slightly lower ion kinetic energies.

3.1.2. Characterization of treated brushite

The nature of these defects in brushite is very uncertain, particularly when one sees the surfaces that are generated by these treatments (heat, abrasion and electron irradiation). Fig. 4 shows SEM photographs of portions of each of the following: (a) as-grown, (b) cleaved (c) abraded, (d) heated (and then cleaved), and (e) the e-beam irradiated surfaces. The as-grown surface (a) appears smooth, but on the micron scale it is rough. The cleaved surface (b) appears much smoother but exhibits highly defined cleavage steps. The abraded surface (c) is fragmented with areas of high particle density. The heated (d) and electron irradiated (e) micrographs show delaminated regions where small plate-like crystals have grown below the

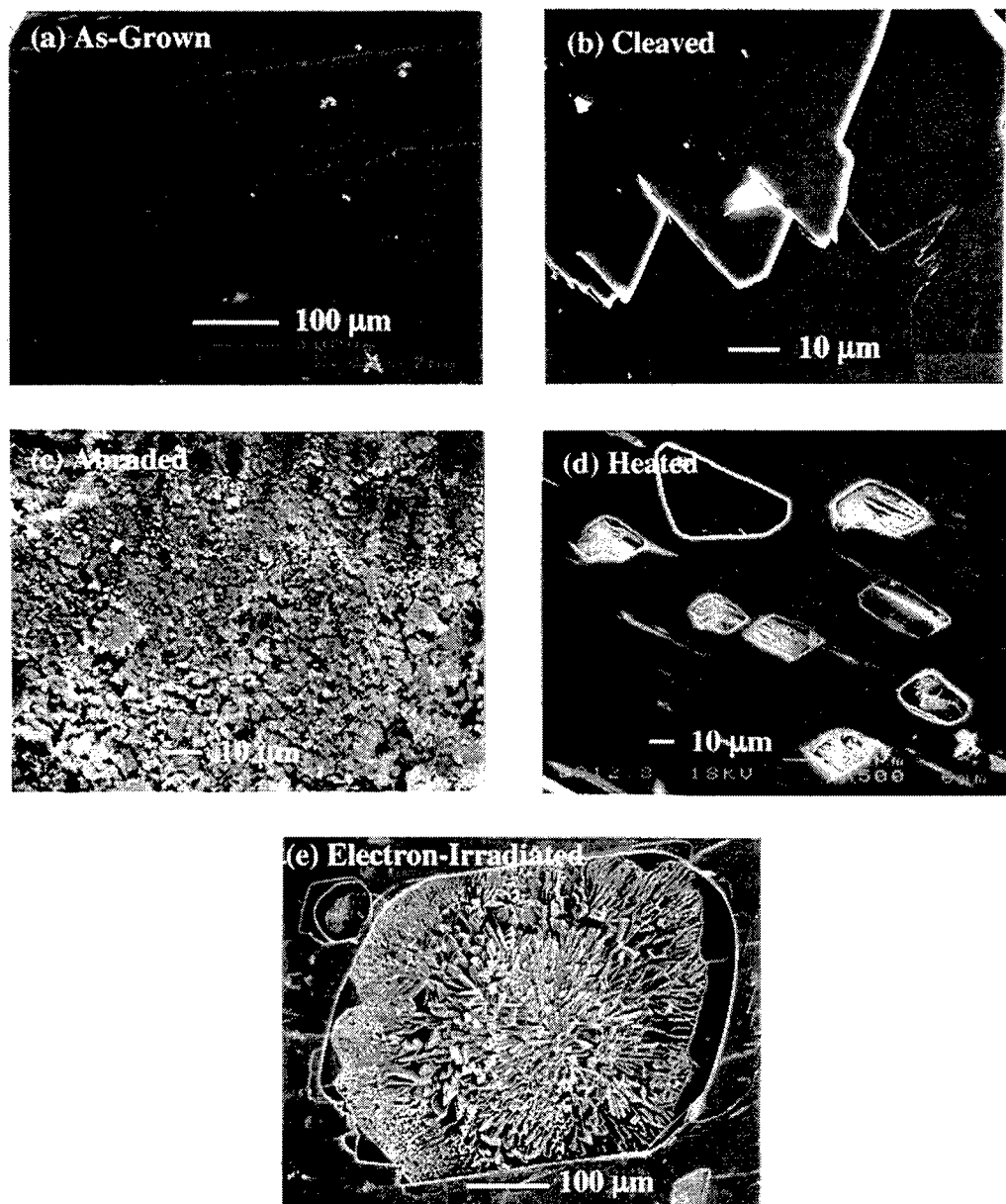


Fig. 4. SEM images of untreated: as-grown (a) and cleaved (b), as well as treated: abraded (c), heated (d), and electron irradiated (e) brushite surfaces.

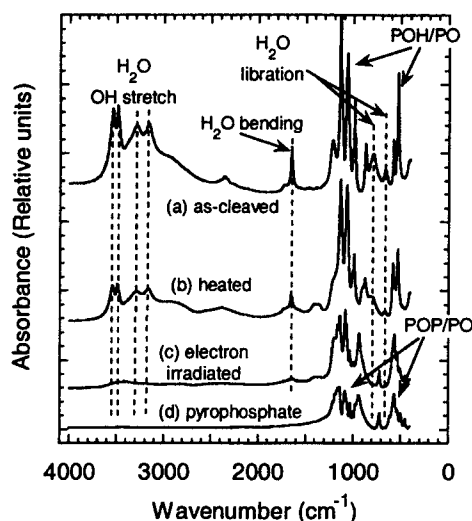


Fig. 5. Infrared absorption spectra of brushite samples before and after surface treatment. The H₂O and POH peaks are greatly reduced with treatment, and the POP modes become clearly visible in the electron-irradiated surface (compare with the spectrum (d) from pyrophosphate, Ca₂P₂O₇)

surface. These subsurface crystallites have recrystallized in the voids remaining after brushite is dehydrated.

The surface treatments in addition to the surface morphology change in many cases the chemical composition of our brushite samples. Such chemical changes in the case of brushite are most of the time due to the loss of the water and subsequent recrystallization. In order to study such chemical changes we performed both infrared absorption and X-ray photoelectron experiments with the former testing the bulk chemical composition, and the later being more surface sensitive. The infrared absorption spectra of as-grown, heated, and electron irradiated material are shown in Fig. 5. The two nonequivalent water molecules can be seen in the two O-H stretch doublets of water on the as-grown spectrum. The more tightly bound water (bound to both Ca²⁺ and H⁺) is found at the lower frequency (~3200 cm⁻¹), and the less tightly bound (bound to Ca²⁺) at the higher frequency (~3500 cm⁻¹). The in-plane bending mode of the water molecule is the sharp peak near 1600 cm⁻¹. In the region below 1600 cm⁻¹, the P-O and P-O-H stretching and bending modes, and the water rocking and wagging modes are found. These absorption peaks are characteristic of brushite.¹¹ One expects ten IR active modes for the orthophosphate ion (HPO₄²⁻) and three IR active modes for the water molecules. Both the heated and electron irradiated samples show weaker water related absorption. Brushite begins to lose its waters of hydration at temperatures above 80 °C and the hydrogen phosphate oxyanion (HPO₄²⁻) decomposes into P₂O₇⁴⁻ at temperatures above 250 °C.¹² The electron irradiated sample shows five IR active P-O-P stretching and bending modes. The water doublets, the sharp peak near 1600 cm⁻¹, the O-H, and P-O-H modes of HPO₄²⁻ have essentially been eliminated in the electron irradiated sample, consistent with HPO₄²⁻ decomposition to P₂O₇⁴⁻. When we compare the infrared absorption spectrum of an electron irradiated crystal with that of a calcium pyrophosphate (Ca₂P₂O₇) crystal, Fig. 5(d), we find that both samples show the same peaks, verifying that the material is γ-pyrophosphate, the lowest temperature phase of pyrophosphate.

In addition to the infrared absorption spectra, we performed X-ray photoelectron spectroscopy (XPS) experiments, the results of which are shown in Fig. 6. Untreated, cleaved brushite samples (Fig. 6a) showed two types of oxygen atoms, the protonated oxygen (O-H) at the higher binding energy of ~531.5 eV and the three equivalent oxygen atoms linked to the phosphorus (P-O) at the lower binding energy of ~529.9 eV. Consistent with our observations in the infrared absorption spectra, when samples were heated or electron irradiated the protonated oxygen significantly decreased in atomic concentration. Furthermore, although the binding energy of phosphorus peaks (~132-134 eV) did not significantly change, analysis of the integrated intensity of the calcium and phosphorus peaks finds that in most cases for both heated and electron irradiated surfaces the ratios of Ca to P are close to one. This is consistent with both monetite (CaHPO₄) and pyrophosphate (Ca₂P₂O₇) being present in the nearby surface region (Fig. 6b). The only exception was observed on the rough areas of electron irradiated surfaces (Fig. 4e) which showed atomic concentration ratios Ca/P=1.58, and O/P=4.2, both consistent with tricalcium phosphate, Ca₃(PO₄)₂ (Fig. 6c). The above results lead us to conclude that the treated surfaces can be a mixture of recrystallized brushite (monoclinic) and/or CaHPO₄ (monetite -- a triclinic crystal structure), as well as pyrophosphate

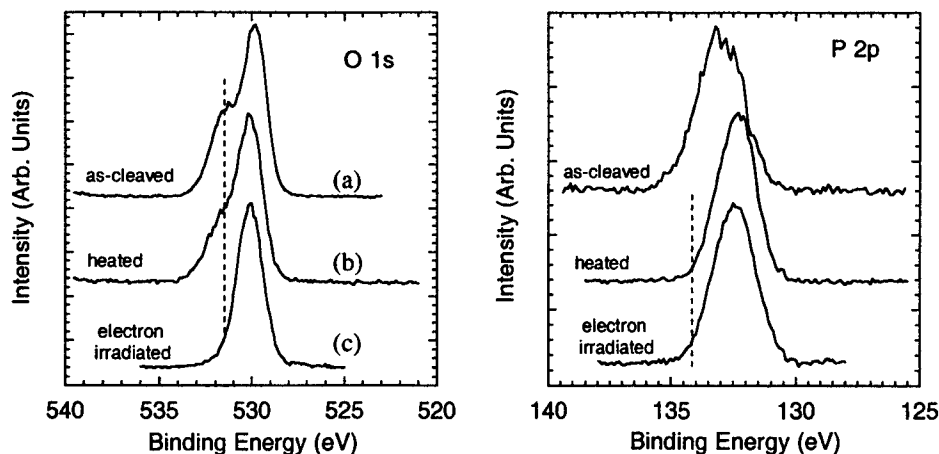


Fig. 6. XPS spectra from as cleaved, heated, and electron irradiated brushite surfaces. Consistent with the infrared absorption data the intensity of the peak at 531.5 eV due to OH is significantly lower in the spectra from the treated surfaces.

($\text{Ca}_2\text{P}_2\text{O}_7$ -- known to undergo three polymorphic transformations) and tricalcium phosphate, $\text{Ca}_3(\text{PO}_4)_2$. Since these new structures are growing and recrystallizing rapidly at a complex solid liquid interface, high densities of point defects are expected.

To summarize this complex situation, treatments like the ones previously discussed result in modifications of the crystal morphology, composition, and defect concentrations that lead to extraordinary changes in the laser desorption of positive ions from brushite. Heating generally results in a "pop-corn" effect, in which large voids are generated inside the crystal due to expansion of water. The cavities or pods so produced form incubators for recrystallization, resulting in the growth of tiny platelets. Electron beaming which is done for long times (many minutes) heats the crystal, but also reduces the crystal via electron stimulated desorption. The major product during electron beam irradiation (other than water!) is O_2 and PO. In the case of the heated sample, these cavities are exposed when we cleave through the heated surface. For the e-beam irradiated surfaces, the tops to these cavities often spontaneously pop off, revealing the underlying structures. Obviously, hitting this surface with a laser can also eject many additional tops, thereby exposing the cavities. From our spectroscopy results, these surfaces are no longer brushite but highly dehydrated often oxygen deficient material.

3.2. Studies of single crystal NaNO_3 at $\lambda=1064$ nm

The absorption spectra of NaNO_3 show major bands at 6.4 eV due to $\pi \rightarrow \pi^*$ transitions within the nitrate anion, and at ~10.5 eV as well as ~12.1 eV due to electron transfer into the sodium cationic states.¹³ Because sodium nitrate is a wide band gap insulating crystal, one might not expect emission of several eV positive ions from NaNO_3 surfaces upon irradiation with low energy photons ($h\nu=1.16$ eV; $\lambda=1064$ nm). Surprisingly, we do observe Na^+ emission accompanying nanosecond laser pulses at 1064 nm with fluences below the single pulse damage threshold from single crystal NaNO_3 surfaces. The fluence dependence of the ion yield is highly nonlinear and the emitted ions exhibit kinetic energies up to 5 eV. In addition to positive ions, laser induced electron emission with characteristics similar to those of the ions is also observed, suggesting that both ion and electron emission probes are mechanistically linked. Both the fluence dependence and the ion energy distributions can be understood by modifying a previously presented model^{9, 14} involving electrostatic ejection of adions siting atop electron traps photoionized by a multiple single photon mechanism. Evidence for the role of defects during the observed ion emission are provided by two beam experiments, one beam (UV KrF excimer laser, $\lambda=248$ nm) is used to generate defects, and the second beam (near-IR laser, $\lambda=1064$ nm) is used to desorb ions. Exposure of the sodium nitrate surfaces to UV laser radiation significantly increases the ion emission due to near-IR laser radiation. Finally, for comparison we will briefly discuss how the ion emission due to UV excimer laser radiation is being affected by the prolonged exposure of the surface to the laser radiation itself as well as the exposure of the NaNO_3 surfaces to an electron

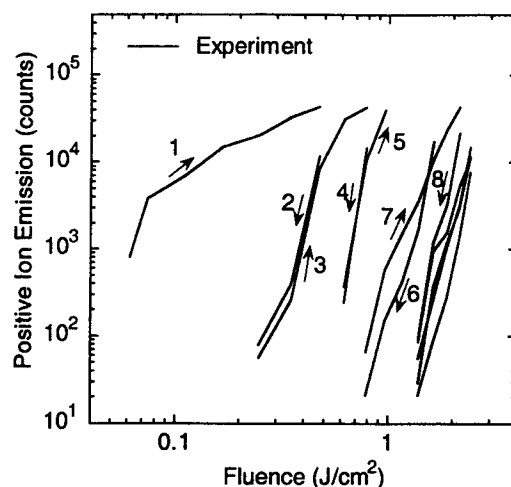


Fig. 7. Fluence dependence of Na^+ ion yield as we expose for first time an as-cleaved NaNO_3 surface to 1064 nm laser radiation and successively increase and decrease the fluence of the incident light. The fluence dependence is nonlinear and the ion yield depletes with increasing number of laser pulses. The arrows indicate the direction the fluence was varied and the numbers the order the data were collected.

beam. Detailed studies of the surface treatment (cleavage, abrasion, exposure to energetic electrons or photons) effects on the ion and neutral emissions under UV (248 nm) laser irradiation from NaNO_3 have been previously presented.^{4, 7, 15, 16}

3.2.1. Effects of Treatments of NaNO_3

Optical transmission measurements show no detectable absorption features in the vicinity of 1064 nm on as-cleaved, melt grown NaNO_3 . However, exposure of these surfaces in vacuum to 1064 nm laser radiation at fluences below the single pulse damage threshold ($\sim 4 \text{ J/cm}^2$) resulted in both electron and Na^+ ion emission. No emission of any other ions or neutrals during near-IR laser irradiation at those fluences is observed. In contrast, irradiation at 248 nm with fluence below the damage threshold at this wavelength yields, in addition to electrons and Na^+ ions, emission of both neutrals and molecular ions (typically NO , O_2 , Na_2O^+).^{4, 14, 15}

As we irradiate for the first time the surface of an as-cleaved NaNO_3 sample with 1064 nm radiation and slowly increase the fluence, we obtain the Na^+ ion emission fluence dependence shown on the upper left-hand side (lowest fluence response) in Fig. 7. The arrows indicate the direction the fluence was varied and the numbers indicate the order the data sets were collected. As we repeatedly and sequentially increase and decrease the fluence of the incident light, significant depletion of the ion emission is observed. Furthermore, as it can be seen in Fig. 7, with exception of the first curve (labeled 1), which shows an approximately linear initial response, the ion yield vs. fluence curves rapidly become highly nonlinear. When fitted with power law functions, the powers that best describe the experimental fluence dependence of the ion yield are typically between 6 and 10 indicating that multiple photon processes are responsible for the observed emission. The observed decrease of the ion emission intensity with increasing number of laser pulses implies that the emission originates from specific defect sites, which are being depleted with repeated laser pulses. Depletion of the defect sites by slowly increasing the fluence of the incident radiation "hardens" the surface, i.e., higher and higher laser fluences are required for Na^+ emission to be observed. In addition to Na^+ ions, electron emission (not shown here) is also observed upon irradiation of the as cleaved NaNO_3 surfaces with IR laser radiation (1064 nm).¹⁷ The fluence dependence of the emitted ions and electrons can be understood assuming electrostatic ejection of adions sitting atop electron traps photoionized by a multiple single photon mechanism by taking into account the depletion of the emission sites.¹⁷

Motivated by the fact that all experimental evidence suggest that the observed ion emission originates from rapidly depleting defect sites with Na^+ ions associated with them, and trying to verify that, we performed two beam experiments in an effort to restore the depleted ion emission. In Fig. 8 we show the fluence dependence of the ion emission due to near-IR laser irradiation from a NaNO_3 surface after it has been depleted (curves 1, 2). In the same figure (curves 3, 4), we plot the

ion emission due to near-IR laser irradiation, where before each near-IR pulse the surface is exposed to one UV (248 nm) laser pulse with fluence of $\sim 130 \text{ mJ/cm}^2$. We emphasize that the Na^+ intensities plotted here are those generated by the near-IR laser pulses, not by the UV laser. As can be seen, exposure of the depleted NaNO_3 surfaces to 248 nm excimer laser radiation results in a significant increase of the Na^+ ion emission. A similar enhancement is obtained by multiple pulses of UV followed by probing with the near-IR laser. Previous studies found that upon 248 nm excimer laser irradiation significant radiolysis of the NaNO_3 surfaces occurs resulting in emission of both ions and neutrals, as well as a defect rich, sodium rich surface.^{14, 15, 18} Therefore, such UV induced sensitization of the surface, which implies an increase in sorbed Na^+ ions associated with nearby electron traps, is consistent and offers additional evidence for the validity of the emission mechanism proposed in the previous subsections.

The effects of the laser radiation itself on the energy distributions of the emitted ions are shown in Fig. 9 where we

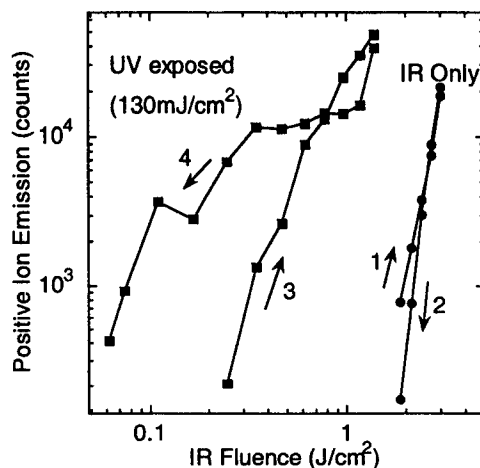


Fig. 8. Two beam experiment. Fluence dependence of the Na^+ ion emission from NaNO_3 due to IR (1064 nm) laser irradiation, while before each IR laser pulse we exposed the sample to one UV (248 nm) laser pulse. The arrows indicate the direction the IR fluence was varied and the numbers the order the data were collected. Exposure to UV laser radiation significantly increases the depleted ion emission due to IR laser irradiation.

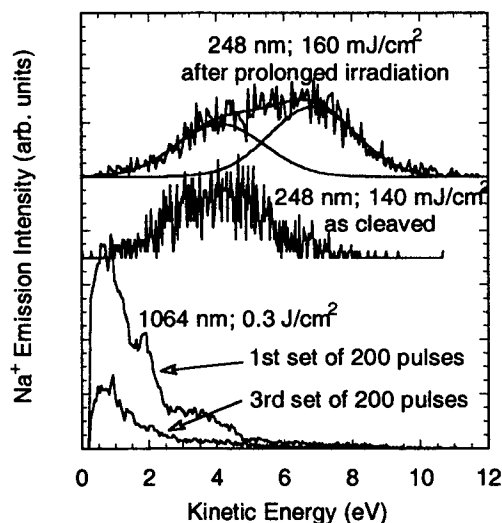


Fig. 9. Na^+ ion energy distributions from NaNO_3 due to IR (1064 nm) laser radiation and due to UV (248 nm) excimer laser radiation showing the effects of the laser radiation itself. Consistent with our simple electrostatic ion ejection model, the feature at $\sim 4 \text{ eV}$ appears in both UV and IR distributions.

plot for comparison the energy distributions due to both IR (1064 nm) and UV (248 nm) laser radiation. Assuming electrostatic ejection of the ion after ionization of the defect below, the energy of the emitted ions would be approximately equal to the electrostatic repulsive energy minus the binding (Madelung) energy, BE , of the specific site. Ionization of such defect results in an ion kinetic energy $KE=4.1$ eV ($KE = \frac{e^2}{r} - BE$, $r=3.24$ Å, $BE=0.3$ eV), which is in reasonable agreement with the 4 eV feature that we observe in both UV and IR distributions. Within this model, the emission of the slower ions can be understood assuming that it originates from sites where either the distance between the ionized defect and the adion is larger or the binding energy of the adion is higher (i.e. cleavage steps). The higher energy (7-8 eV) feature, which is observed only in ion distributions due to UV laser irradiation after prolonged irradiation demonstrates the effects of the UV radiation itself. Those energies can also be understood within the same model, assuming that the emission originates from doubly charged defect sites.¹⁴ Such sites, compared to singly charged defect sites, would require higher excitation photon energies to be doubly ionized, and therefore the absence of significant ion emission due to IR laser irradiation with energies above 5 eV is consistent with the proposed mechanism and assignments. The existence of doubly charged defects in a singly charged lattice will be demonstrated in section 3.2.2.

In addition to surface modifications due to the laser radiation itself, we also studied the effects of electron irradiation on NaNO_3 surfaces. Fig. 10 shows the fluence dependence of the ion emission from both as cleaved and electron irradiated NaNO_3 surfaces due to UV (248 nm) excimer laser radiation. Similar to the brushite treated surfaces the ion emission intensity is greatly enhanced upon exposure of the surface to the electron beam. The energies of the emitted ions are ~ 7 eV or higher⁴ demonstrating the presence of doubly charged defect sites as well as the presence of larger clusters of defects.

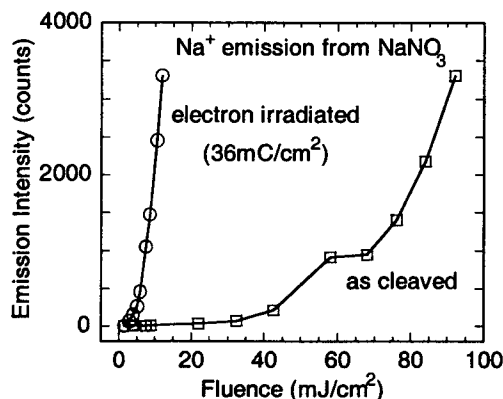


Fig. 10. Influence of electron beam irradiation on cleaved NaNO_3 single crystal. Exposure of the surface to electrons increases significantly the emission of Na^+ ions.

3.2.2. Characterization of treated NaNO_3

The XPS core level spectra from cleaved, melt grown NaNO_3 single crystals before irradiation are shown in Fig. 11, along with the spectra from cleaved, melt grown single crystal sodium nitrite (NaNO_2). The only other element, not shown in Fig. 11, which we were able to observe, was carbon, typically with atomic concentration less than 5 %. Although, the surfaces under investigation are hygroscopic, no evidence of water contamination were observed neither in the XPS nor in the UPS spectra (not shown here¹⁸), which leads us to conclude that the water contamination was relatively low and below our detection limit.

The XPS spectra after exposure of the NaNO_3 crystal to 248-nm excimer laser radiation are also shown in Fig. 11 ($\text{NaNO}_3/\text{laser}$). Comparison with the spectra from the cleaved sodium nitrate and nitrite demonstrates the nitrite formation due to exposure to the excimer laser radiation. Furthermore, an oxygen peak with binding energy 531 eV, which due to its energy position cannot be attributed to nitrite, also appears. This feature is consistent with being due to sodium peroxide

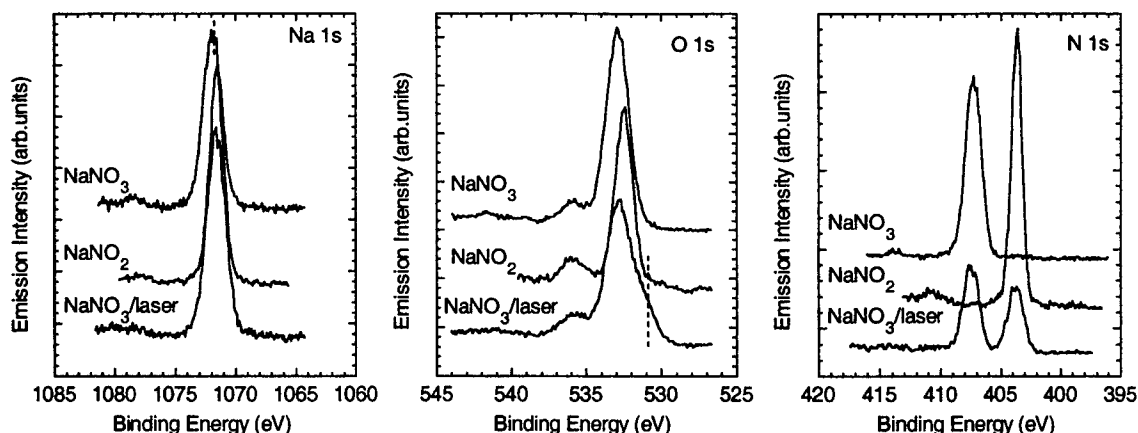


Fig. 11. XPS core level spectra of as-cleaved melt grown sodium nitrate (NaNO_3), as cleaved melt grown sodium nitrite (NaNO_2), and cleaved NaNO_3 after UV excimer laser irradiation ($\text{NaNO}_3/\text{laser}$). Exposure of the as cleaved NaNO_3 surfaces to both x-rays and UV laser radiation results in decomposition with sodium nitrite and sodium peroxide being the main products left on the surface.

(Na_2O_2).^{18, 19} The only other possibility is that the 531 eV peak is due to OH^- . However, such an assignment is hard to justify if we take into account that no significant water contamination was observed on the as-cleaved surfaces. The feature with binding energy 536 eV is the Na (KL_1L_{23}) Auger peak structure. Finally, we would like to mention that the Na 1s shift due to formation of sodium peroxide is expected to be only few tenths of an eV²⁰ and that is why it is not observable in Fig. 11. Sodium nitrate surfaces with much higher peroxide and oxide concentrations (not shown here) definitely show an increase of the FWHM of the Na 1s peak.

These results are also consistent with recent studies^{14, 15, 21, 22} of the neutral emissions due to UV laser radiation. Upon irradiation $\pi \rightarrow \pi^*$ transitions occur, which result in decomposition of the nitrate NO_3^{*-} to either $\text{NO}(\text{g}) + \text{O}_2^-(\text{s})$ or $\text{NO}_2^{*-} + \text{O}(\text{g})$ with the possibility of further decomposition to $\text{NO}(\text{g}) + \text{O}^-(\text{s})$, where (g) and (s) denote gas and surface species, respectively. The surface oxygen then can lead to the emission of O_2 and the formation of oxide and peroxide species (doubly charged defects) on the surface. We note that emission of neutral O_2 , Na_2O^+ as well as Na_2O_2^+ has been observed during laser irradiation providing further evidence for those assignments.¹⁵ Both oxides and peroxides can be thought of as doubly charged defects in the near surface region. Thus, they can lead to laser desorption of Na^+ ions with kinetic energies of $\sim 6\text{--}8$ eV from NaNO_3 surfaces due to low fluence 248 nm light, as previously discussed. In agreement with our observations such ion emissions are more likely to be observed from surfaces which have been previously exposed to either higher fluence 248 nm excimer laser radiation or to electron beams and, therefore, exhibit higher concentrations of sodium oxides and peroxides.^{18, 23}

CONCLUSION

We have presented examples of the way a variety of surface treatments, such as heating, abrasion, and exposure to electron beams, can modify the sensitivity of ionic crystals to sub-bandgap radiation from pulsed lasers. The creation of defects by one stimulus can form absorption centers appropriate for the second stimulus (the 248 nm or 1064 nm laser light), as well as efficient sites for the launching of adions and neutral atom/molecule desorption. Such interactions lead to dramatic decrease in the laser intensities needed for ejection of ions, neutrals, as well as eventual plume formation, and result in increased vulnerability of the material to the laser radiation. These effects also reveal themselves in other less complex materials such as MgO and NaCl. The implications for modification, chemical analysis, and laser ablation of materials, include finding methods of controlling the interaction, localizing the coupling of the laser to the surface to allow, for

example, localized etching of the surface, and providing quantitative tools for increasing our understanding of laser-materials interactions.

ACKNOWLEDGEMENTS

We thank David Ermer, Vanderbilt University, J.-J. Shin, National Taiwan University, Wayne Hess and Tom Orlando of Pacific Northwest Laboratory for their assistance and helpful discussions. This work was supported by the Department of Energy under Contract DE-FG03-99ER14864 and an Equipment Grant from the National Science Foundation, DMR-9503304.

REFERENCES

- 1 L. J. Radziemski and D. A. Cremers, *Laser Induced Plasmas and Applications* (Marcel Dekker, New York, 1989), p. pp. 295.
- 2 J. C. Miller, *Laser Ablation: Principles and Applications* (Springer-Verlag, Berlin, 1994).
- 3 D. R. Ermer, S. C. Langford, and J. T. Dickinson, *J. Appl. Phys.* **81**, 1495 (1997).
- 4 J. J. Shin, D. R. Ermer, S. C. Langford, and J. T. Dickinson, *Appl. Phys. A* **64**, 7 (1997).
- 5 M. Dawes, S. C. Langford, and J. T. Dickinson, *Appl. Surf. Sci.* **127-129**, 81 (1998).
- 6 R. L. Webb, L. C. Jensen, S. C. Langford, and J. T. Dickinson, *J. Appl. Phys.* **74**, 2323 (1993).
- 7 J. J. Shin, M.-W. Kim, and J. T. Dickinson, *J. Appl. Phys.* **80**, 7065 (1996).
- 8 J. T. Dickinson, S. C. Langford, J. J. Shin, and D. L. Doering, *Phys. Rev. Lett.* **73**, 2630 (1994).
- 9 J. T. Dickinson, in *Experimental Methods in Physical Sciences*, edited by J. C. Miller and R. F. Haglund (Academic Press, 1998), Vol. 30, p. 139.
- 10 C. Bandis, S. C. Langford, and J. T. Dickinson, *Appl. Phys. Lett.* **76**, 421 (2000).
- 11 I. Petrov, B. Soptrajanov, N. Fuson, and J. R. Lawson, *Spectrochim. Acta A* **23**, 2637 (1967).
- 12 A. T. Zdukos and T. K. Vaimakis, *Zh. Neorgan. Khim.* **30**, 1983 (1985).
- 13 H. Yamashita and R. Kato, *J. Phys. Soc. Jpn.* **29**, 1557 (1970).
- 14 D. R. Ermer, J.-J. Shin, S. C. Langford, K. W. Hipps, and J. T. Dickinson, *J. Appl. Phys.* **80**, 6452 (1996).
- 15 R. L. Webb, S. C. Langford, and J. T. Dickinson, *Nucl. Instrum. Meth. Phys. Res. B* **103**, 297 (1995).
- 16 J. T. Dickinson, J.-J. Shin, and S. C. Langford, *Appl. Surf. Sci.* **96-98**, 326 (1996).
- 17 C. Bandis, S. C. Langford, J. T. Dickinson, D. R. Ermer, and N. Itoh, *J. Appl. Phys.* **87**, 1522 (2000).
- 18 C. Bandis, L. Scudiero, S. C. Langford, and J. T. Dickinson, *Surf. Sci.* **442**, 413 (1999).
- 19 S. Aduru, S. Contarini, and J. W. Rabalais, *J. Phys. Chem.* **90**, 1683 (1986).
- 20 *Handbook of X-ray Photoelectron Spectroscopy* (Perkin-Elmer Corp., Eden Prairie, 1992).
- 21 W. P. Hess, K. A. H. German, R. A. Bradley, and M. I. McCarthy, *Appl. Surf. Sci.* **96-98**, 321 (1996).
- 22 K. Knutsen and T. M. Orlando, *Phys. Rev. B* **55**, 13246 (1997).
- 23 J.-J. Shin, S. C. Langford, J. T. Dickinson, and Y. Wu, *Nucl. Instrum. Meth. Phys. Res. B* **103**, 284 (1995).

Dynamical Stark effect in small quantum dots

J. Thomas Andrews^a and Pratima Sen^b

Department of Applied Physics

Shri G S Institute of Technology & Science, Indore 452003. India

ABSTRACT

Using time dependent perturbation technique, Stark shift and self-energy correction in semiconductor quantum dot are studied. The analytical results are obtained by incorporating the important excitonic and biexcitonic effects. The numerical estimations are made for potentially important II-VI semiconductor quantum dot CdS of size smaller than the bulk exciton Bohr radius. The demonstration of analytical and numerical results predicts a red shift of $\Delta E/3$ with ΔE being the biexciton binding energy. The Stark shift and self energy correction are found to have higher amplitudes at high excitation intensities due to the presence of biexcitons.

Keywords: quantum dot, AC Stark effect, self energy correction, excitons, biexcitons

1. INTRODUCTION

Recent advances in the fabrication technology of nanostructures have made the possibility of realization of semiconductor quantum dots of dimensions even smaller than the bulk exciton Bohr radius.¹ The three dimensional electronic confinement in such quantum boxes enhances the optical nonlinearities significant for the fabrication of improved electronic and optoelectronic devices.²⁻⁴ The study of optical properties of these small quantum dots are important in predicting the utilization of these materials for fast optoelectronics devices such as quantum dot array lasers, modulators, memory devices, etc. Recently developed technology of fabrication of self-organized quantum dots attracts the experimentalists, because of the well controlled growth parameters favorable for the manufacturing of fast quantumoptoelectronic devices.⁵⁻⁸

The dynamical (AC) Stark effect arises due to the dynamic coupling of electronic states with the fast oscillating quasiresonant electromagnetic field leading to the shifting of energy levels. After its first demonstration,⁹ it has been studied widely in atomic, molecular and semiconductor systems.¹⁰ Lindberg and Koch have correlated the transient oscillations in the pump-probe spectroscopy to the DSE (Dynamic Stark Effect) in two-dimensional quantum well structures.¹¹ In the present article, we have made an attempt to study analytically the DSE in small quantum dots and obtained the numerical estimations for the potentially important quantum dot structures such as CdS. In QD arrays, the presence of many QDs of different sizes, induces an inhomogeneous broadening. Such broadening can be incorporated by assuming that the particles have a size distribution around a mean value of dot radius (R_o). The recent experimental observations suggest that a Gaussian distribution of dot sizes fits very well in semiconductor quantum dots.¹²

2. THEORETICAL FORMULATIONS

The semiclassical wave equation technique, has been used to study the dynamical Stark effect in small quantum dots (QDs). In a semiconductor QD, the confinement induced exciton binding energy increases rapidly when its geometrical size R becomes smaller than the bulk exciton Bohr radius a_B .¹³ Such QDs are classified as belonging to the strong confinement regime (SCR). The interaction of a photon with the zero-dimensional semiconductor quantum dot creates one electron-pair (well known as exciton). At high excitation intensities, the density of photoinduced excitons becomes large enough to enhance the probability of formation of quasi-excitonic molecules known as biexcitons. The co-existence of excitons and biexcitons in the QD introduces a three-level energy structure viz., vacuum ($|0\rangle$), exciton

Further author information:

^aPresent address: Department of Applied Physics, Birla Institute of Technology, Mesra, Ranchi 835 215. India

Fax No.: 091-651-535522; E-mail: josthoand@rediff.com

^bFax No. 091-731-432540, E-mail: pratima.sen@hotmail.com

$\langle |e\rangle \rangle$ and biexciton ($|b\rangle$) states of electron-hole pairs. Accordingly, we have defined the total wave function of the QD as

$$|\Psi\rangle = C_o e^{-i\omega_o t} |0\rangle + \sum_{n=e,b} C_n e^{-i\omega_n t} |n\rangle \quad (1)$$

with $C_{o(e,b)}$ and $\hbar\omega_{o(e,b)}$ being the probability amplitude and energy of the vacuum (exciton and biexciton) state, respectively. The interaction of resonant photons with the QD creates one electron-hole pair (1EHP) states. The band gap energy of such excitonic states will be modified due to the presence of three dimensional electronic confinement in QDs. The corrected band-gap energy of 1EHP state is found to be¹⁴

$$\hbar\omega_{oe} = \hbar\omega_g + E_R \left(\alpha_{nl} \frac{a_B}{R} \right)^2. \quad (2)$$

Here, E_R is the exciton Rydberg energy, α_{nl} is the n th root of the l th order Bessel function. a_B and R are the bulk exciton Bohr radius and the radius of the quantum dot, respectively. At high excitation intensities, the density of excitons becomes large enough to create exciton molecule also termed as biexcitons. The energy of such biexcitons are reduced by the Coulombic binding energy between the two electron-hole pairs. Accordingly, the energy of the biexciton will be slightly less than twice the energy of the exciton and defined as¹⁵

$$\hbar\omega_{ob} = 2\hbar\omega_{oe} - \Delta E \quad (3)$$

with ΔE being the binding energy of the biexciton. The pump frequencies which in resonance with the excitonic state will show off resonance to biexciton transitions by a factor of $\Delta E/\hbar$. We assume that the pump is allowed to shine the QD for times $t \geq 0$. The total Hamiltonian representing the QD, radiation and their interaction are represented by

$$H = H_o + H_I \quad (4)$$

where H_o is the unperturbed Hamiltonian. The dipole type interaction Hamiltonian is defined as $H_I = -\hat{\mu} \cdot \vec{E}$ with $\vec{E} [= \vec{E}_o \exp(i\omega t) + c.c.]$ being the time varying amplitude of the electromagnetic field of frequency ω and constant amplitude \vec{E}_o . $\hat{\mu}$ is the transition dipole moment operator. In a centrosymmetric system, the diagonal elements of $\hat{\mu}$ vanishes while the off-diagonal elements remain finite. Also for near resonant transitions, one can assume $|\mu_{jj'}| = |\mu_{j'j}|$. For a small quantum dot of dimensions smaller than the bulk exciton Bohr radius the dipole elements for exciton and biexciton states are defined as¹³

$$\langle e | \hat{\mu} | 0 \rangle = \mu_{oe} \int \phi(r_e, r) dr \quad (5)$$

$$\langle b | \hat{\mu} | e \rangle = -\sqrt{2}\mu_{oe} \int \int \int \phi(r_e, r, r_h, r)^* \phi(r_e, r_h) dr_e dr_h. \quad (6)$$

where $\mu_{oe} = [e|\hat{p}_{oe}|/(m_o\omega_{oe})]$, is the transition dipole moment with m_o being the free electron rest mass. $\phi(r_e, r)$ and $\phi(r_e, r, r_h, r)$ are the exciton and biexciton wave functions, respectively related to the single particle wave function $\phi(r)$ as

$$\phi(r_e, r) = \phi(r_e)\phi(r) \text{ and } \phi(r_e, r, r_h, r) = \phi(r_e)\phi(r)\phi(r_h)\phi(r)$$

with

$$\phi(r) = \sqrt{\frac{2a_B^3}{R^3}} \frac{j_l(\alpha_{nl}r/R)}{j_{l+1}(\alpha_{nl})}.$$

Here, a_B and R are the bulk exciton Bohr radius and the radius of the quantum dot.

The equation of motion of the probability amplitudes C_o , C_e and C_b may be obtained by using the Schrodinger's time dependent perturbation equation as

$$i\hbar \frac{\partial}{\partial t} \Psi = H \Psi. \quad (7)$$

Usage of (1)-(7), yields the probability amplitudes as

$$\begin{aligned} \dot{C}_o &= i \sum_e C_e \Omega_{oe} e^{i\Delta_{oe}t} \\ \dot{C}_e &= iC_o \Omega_{oe} e^{-i\Delta_{oe}t} + C_b \Omega_{eb} e^{i\Delta_{eb}t} - \gamma_e C_e \\ \dot{C}_b &= iC_e \Omega_{eb} e^{-i\Delta_{eb}t} - \gamma_b C_b. \end{aligned} \quad (8)$$

In obtaining the above set of coupled equations, we have used the identity $\langle j|H_o|j'\rangle = \hbar\omega_j\delta_{jj'}$, since we are interested in centrosymmetric systems only. Also, we have ignored the two-photon transitions such as $|0\rangle$ to $|b\rangle$, and vice-versa. In (8) we have defined the Rabi frequency as $\Omega_{jj'} = \mu_{jj'}E_o/2\hbar$ and the detuning parameter $\Delta_{jj'} = \omega - \omega_{jj'}$. In order to solve the coupled equations (8) we have defined

$$\begin{aligned} C_o &= A_o e^{i\Omega t}, \\ C_e &= A_e e^{i(\Omega - \Delta_{oe})t}, \\ C_b &= A_b e^{i(\Omega - \Delta_{ob})t}. \end{aligned} \quad (9)$$

Here, $A_i (i = o, e, b)$ is a time independent dimensionless parameter and Ω is the unknown parameter having the dimension of frequency. Substitution of (9) in (8) and after simplification we find a cubic equation in Ω as

$$\Omega^3 + x_2\Omega^2 + x_1^2\Omega + x_0^3 = 0 \quad (10)$$

with $x_0^3 = \Omega_{oe}^2\beta$, $x_1^2 = \alpha\beta - \Omega_{oe}^2 - \Omega_{eb}^2$, $x_2 = -(\alpha + \beta)$, $\alpha = \Delta_{oe} + i\gamma_e$ and $\beta = \Delta_{ob} + i\gamma_b$. At low excitation intensities, the biexcitons are hardly created and hence the parameters Ω_{eb} and β signatured by the biexciton states vanishes. For such cases the cubic equation (10) reduces to a standard quadratic equation obtainable for a two-level system.¹⁶ In the presence of excitons and biexcitons the solutions of the cubic equation (10) are found to be¹⁷

$$\Omega_1 = \frac{A^2 - B^2}{A} - \frac{x_2}{3} \quad (11)$$

$$\Omega_{2,3} = -\frac{A^2 - B^2}{2A} - \frac{x_2}{3} \pm \frac{\sqrt{3}i}{2} \frac{A^2 + B^2}{A} \quad (12)$$

with

$$A = \left[\frac{x_1^2 x_2}{6} - \frac{x_0^3}{2} - \frac{x_2^3}{27} + \frac{\sqrt{3}}{18} \sqrt{4x_1^6 - x_1^4 x_2^2 - 18x_1^2 x_2 x_0^3 + 27x_0^6 + 4x_0^3 x_2^3} \right]^{1/3} \quad (13)$$

and

$$B = \frac{x_1^2}{3} - \frac{x_2^2}{9} \quad (14)$$

The three solutions $\Omega_{1,2,3}$ obtained for the unknown frequency Ω may be interpreted to be the oscillation frequencies corresponding to the vacuum to exciton and exciton to biexciton, transitions. In order to confirm this interpretation, we have obtained the Rabi frequency in the absence of biexcitonic contribution. In the absence of biexcitons the three-level structure of excitons and biexcitons reduce to a simple two-level structure of excitons. Accordingly, following the same standard technique used earlier for the biexcitons we obtained the two solutions for the unknown frequency Ω . In order to differentiate it with the solutions for a two-level system, we represent it as μ_1 and μ_2 and found to be^{16,18}

$$\mu_{1,2} = \frac{\Delta_e + i\gamma_e}{2} \pm \frac{[(\Delta_e + i\gamma_e)^2 + 4\Omega_{oe}^2]^{1/2}}{2}. \quad (15)$$

In the absence of biexcitons the analytical reduction of 12 from 15 becomes tedious due to the cumbersome mathematics involved in the calculation. However, a satisfactory numerical comparison has been made by applying arbitrary values for Δ_{oe} , γ_e and Ω_{oe} in both (12) and (15). The numerical estimations are demonstrated in Figures 1 and 2. In Figure 1, we have obtained the real and imaginary parts of the solutions $\Omega_{1,2,3}$ in the absence of biexcitons (i.e. by making $\Omega_{eb} = 0$ and $\beta = 0$). The inset of the Figures 1A and 1B shows the corresponding variation of $\mu_{1,2}$. It is evident from the figures that the nature of Ω_1 (Ω_2) matches exactly with the standard solutions μ_1 (μ_2). However, in the absence of biexcitons the third solutions Ω_3 reduces to a negligible value much smaller than γ_e . Which leads one to the conclusion that the third solution explicitly corresponds to the oscillations signatured by the biexciton transitions.

In the presence of both excitons and biexcitons, an important conclusion can be drawn from Figure 2, where we have demonstrated the variation of the three solutions as a function of normalized detuning parameter (Δ_{oe}/γ_e). It is interesting to note from the figure that in the presence of both excitons as well as biexcitons, the behavior of Ω_1 and Ω_3 resembles μ_1 and μ_2 , respectively. However, the nature of Ω_2 changes drastically for positive detuning which could not be observed earlier in Figure 1A. Which leads one to the conclusion that the Ω_2 contains the terms common

for both excitons and biexcitons. Also, Ω_3 becomes finite for negative detuning confirms the earlier conclusion of explicit dependency on biexcitonic states. Accordingly, we have employed Ω_2 for the study of Stark shift and self energy correction in small quantum dots.

Following the standard technique Ω_2 has been utilized to calculate the Stark shift and broadening. For nearly sharp resonant frequencies and moderate excitation intensities of the pump we have simplified Ω_2 by assuming $\Delta_{oe}^2 \gg \Omega_{oe}^2 \gg \gamma_e^2$ and $\Delta_{eb}^2 \gg \Omega_{eb}^2 \gg \gamma_b^2$ and find

$$\Omega_{SS} = -\frac{1}{2} \frac{x_1^2}{\alpha + \beta} (1 + u) \quad (16)$$

where the dimensionless parameter u is defined as

$$u = \frac{9}{x_2^3} \left[\frac{x_1^2 x_2}{6} + \frac{x_0^3}{2} + \frac{\sqrt{3}}{18} \sqrt{4x_1^6 - x_1^4 x_2^2 - 18x_1^2 x_2 x_0^3 + 27x_0^3 + 4x_2^3 x_0^3} \right].$$

The real part of (16) corresponds to the Stark shift (Ω_{ST}) while the imaginary part (Ω_{SE}) corresponds to the self energy correction. The generalized expression obtained in (16) incorporates both exciton and biexciton contributions. However, to understand the qualitative behavior of biexcitons on Stark effect, we have reduced (16) in the absence of biexcitons by ignoring the biexciton contribution ($\beta = 0$ and $\Omega_{eb} = 0$) as

$$\Omega_{SS0} = \frac{1}{2} \frac{\Omega_{oe}^2}{\Delta_{oe} + i\gamma_e}. \quad (17)$$

The subscript 0 as introduced in (17) represents the absence of biexcitons. The expression obtained in the absence of biexcitonic effect shows a good agreement with the standard expression obtainable for a TLS,¹⁹ except the summation which corresponds to different excitonic states. The comparison of (16) and (17), shows that in the presence of biexcitons the dimensionless parameter u plays an important role. At low excitation intensities u can be reduced to $u \approx \alpha\beta/(\alpha + \beta)^2$. From the definition of α and β , it is evident that the magnitude of u will oscillate between ± 1 , for below to above resonance values of pump frequencies. However, a change in nature will be imminent when the sign of u changes from positive to negative and vice versa.

The well known AC Stark shift in the absence of biexcitons obtainable from (17) shows resonances at $\omega = \omega_{oe}$. Hence the stark shift will show discrete excitonic peaks corresponding to different excitonic transitions. Quite interestingly, the same is not true for biexcitonic transitions where the resonance occurs for $\omega = \omega_{oe} - \Delta E/3$. This suggests that due to the presence of biexcitons the peaks may shift by a magnitude of $\Delta E/3$. Hence the measure of this shift may unveil the mechanism responsible for the red shift observed in the absorption/emission spectra of small quantum dots.²⁰

3. RESULTS AND DISCUSSIONS

The theoretical calculations discussed above are developed for a single quantum dot of dimensions smaller than the Bulk exciton Bohr radius. However, in realistic applications such as lasers and detectors, QD arrays are preferred over a single QD (SQD). In a QD array the variation in the size of different QDs introduces an inhomogeneous distribution to the absorption/emission spectra. Hence, these QD arrays are also termed as inhomogeneously distributed quantum dots (IQD). The inhomogeneous distribution can be incorporated by assuming that the particles have a Gaussian size distribution $F(R)$ around a mean value $\Delta R (= xR_0)$ with x being the percentage variation in the Gaussian width. The Stark shift for an IQD is defined as

$$\Omega_{St|av} = \int_0^{a_B} F(R) \Omega_{St|R} dR. \quad (18)$$

The present model has been applied to a realistic system of quantum dots of CdS duly irradiated by a near resonant laser.

In Figure 3, we have studied the AC Stark shift and self energy correction as a function of detuning parameter in the presence and absence of biexcitonic effect. The Curve *a* is obtained in the absence of biexcitons while the Curve *b* is obtained in the presence of both excitons and biexcitons. The curves show resonances at 3.331eV and

3.322eV respectively, corresponding to a red shift of 9meV. For a SQD of size $0.6a_B$, the exciton energy is found to be 3.33eV, which agrees well with the observed value of resonance at 3.331eV. This magnitude of red shift exactly matches with the expected value of $\Delta E/3 = 9.1\text{meV}$. This leads to the conclusion that the red shift in SS and SEC has its origin in the creation of biexcitons. Further, one can notice an interesting phenomena from the same figure that, in the presence of biexcitons self energy correction shows a change in its sign from positive to negative around the shoulders which may be related to the experimentally observed gain spectra in the quantum dots of CdS and GaAs.

The nature of dependence of SS and SEC with the electric field intensity of the electromagnetic field has been demonstrated in Figures 4A and 4B, respectively. The Curves *a* and *b* are obtained in the presence and absence of biexcitonic effects, respectively. It is evident that both SS and SEC increases consistently with the intensity. However, the curves obtained in the presence of biexcitons shows a larger change than the curves obtained in the absence of such effects. The reason for the higher contribution may be attributed to the high density of excitons at large excitation intensities. The same has been demonstrated more clearly in the inset of the figures. Quite interestingly, at low excitation intensities, the biexcitons are hardly created, hence one can expect a reduction of gain and a reduced shift as evident from Figure 4.

4. CONCLUSIONS

To conclude, Stark shift and self energy correction are studied analytically. The numerical estimations have been made for small quantum dot sample of CdS. The major results noted from the analytical and numerical estimations are;

- At high excitation intensities the creation of biexcitons shifts the absorption spectra by a factor $\Delta E/\hbar$,
- The Stark shift and self energy correction are enhanced at high excitation intensities. However, the shift arising due to the biexcitons is much larger than the shift observed for excitons,
- At low excitation intensities the Stark shift obtained in the absence of biexcitons dominate over the one obtained in the presence of biexcitons.

ACKNOWLEDGMENTS

The authors are thankful to Prof. Pranay K. Sen for fruitful discussions. One of the author (JTA) thank Prof. P. K. Barhai for constant encouragement. The authors are also thankful to Department of Atomic Energy, Mumbai, and University Grants Commission, New Delhi (PS) for financial support.

REFERENCES

1. R. C. Ahsoori, "Electrons in artificial atoms," *Nature* **379**, pp. 413–419, 1996.
2. L. Brus, "Zero-dimensional "excitons" in semiconductor clusters," *IEEE, J. Quantum Electron.* **22**, pp. 1909–1914, 1986.
3. D. S. Chemla and D. A. B. Miller *Opt. Letter* **11**, p. 522, 1986.
4. H. Sakaki *Jpn. J. Appl. Phys.* **28**, p. L314, 1989.
5. J. Y. Marzin, J. M. Gerald, A. Izrael, D. Barrier, and G. Bastard, "Photoluminescence of single InAs quantum dots obtained by self-organized growth on gaas," *Phys. Rev. Lett.* **73**, p. 716, 1994.
6. G. M. Ribeiro, G. Leonard, and P. M. Petroff *Appl. Phys. Lett.* **66**, p. 1676, 1995.
7. M. Grundman, J. Christen, N. N. Lendenstov, J. Bohrer, D. Bimberg, S. S. Ruvimov, P. Werner, U. Gosele, J. Heydenreich, V. M. Ustinov, A. Y. Egorov, A. E. Zhukov, P. S. Kopev, and Z. H. Alfereov *Phys. Rev. Lett.* **74**, p. 4043, 1995.
8. K. Chang and J. B. Xia, "Asymmetric stark shifts of exciton in InAs/GaAs pyramidal quantum dots," *Solid State Commun.* **104**, pp. 351–354, 1997.
9. S. H. Autler and C. H. Townes *Phys. Rev.* **100**, p. 703, 1955.
10. J. T. Andrews, P. Sen, and P. K. Sen, "Effect of magnetic field on Rabi oscillations in III-V semiconductors," *Nonlinear Optics* **12**, pp. 327–337, 1995.

11. M. Lindberg and S. W. Koch, "Transient oscillations and dynamic Stark effect in semiconductors," *Phys. Rev. B* **38**, pp. 7607-7614, 1988.
12. J. Butty, Y. Z. Hu, N. Peyghambarian, Y. H. Kao, and J. D. Mackenzie, "Quasicontinuous gain in sol-gel derived CdS quantum dots," *Appl. Phys. Lett.* **67**, pp. 2672-2674, 1995.
13. Y. Z. Hu, M. Lindberg, and S. W. Koch, "Theory of optically excited intrinsic semiconductor quantum dots," *Phys. Rev. B* **42**, p. 1713, 1990.
14. L. Banyai and S. W. Koch, *Semiconductor Quantum Dots*, vol. II, World Scientific, Singapore, 1993.
15. W. Y. Wu, J. N. Schuan, T. Y. Hsu, and U. Efron *Appl. Phys. Lett.* **51**, p. 710, 1987.
16. M. S. III, M. O. Scully, and J. W. E. Lamb, *Laser Physics*, Addison-Wesley, Massachusetts, 1974.
17. M. Abramowitz and I. Stegun, *Handbook of Mathematical Functions with Formulas*, pp. 295-330. Dover, New York, 1965.
18. P. Sen and J. T. Andrews, "Rabi oscillations in III-V semiconductors," *Solid State Commun.* **90**, pp. 117-120, 1995.
19. R. Zimmermann, "The dynamical Stark effect of excitons," in *Festkorperprobleme / Adv. in Solid State Physics*, U. Rossler, ed., vol. 30, pp. 295-320, Vieweg, Braunschweig, 1990.
20. J. Butty, N. Peyghambarian, Y. H. Kao, and J. D. Mackenzie, "Room temperature optical gain in sol-gel derived CdS quantum dots," *Appl. Phys. Lett.* **69**, pp. 3224-3226, 1996.

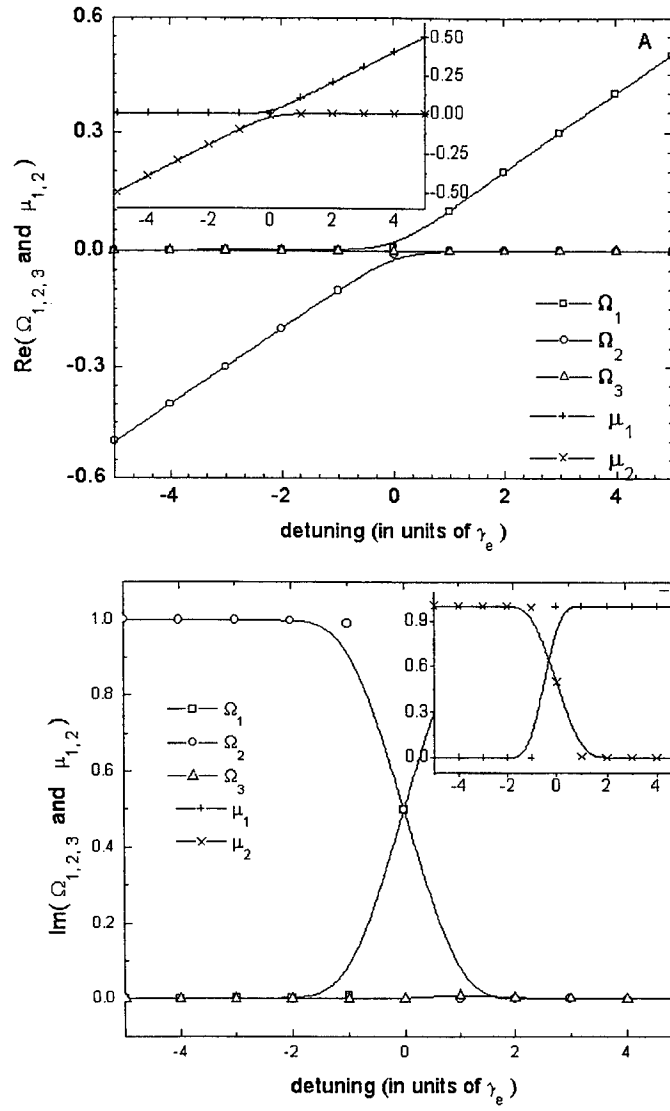


Figure 1. The numerical estimation real and imaginary parts of the solutions $\Omega_{1,2,3}$ (three-level system) and $\mu_{1,2}$ (two-level system) for arbitrary values of Δ_{oe} , γ_e and Ω_{oe} . The results are obtained in the absence of biexcitons

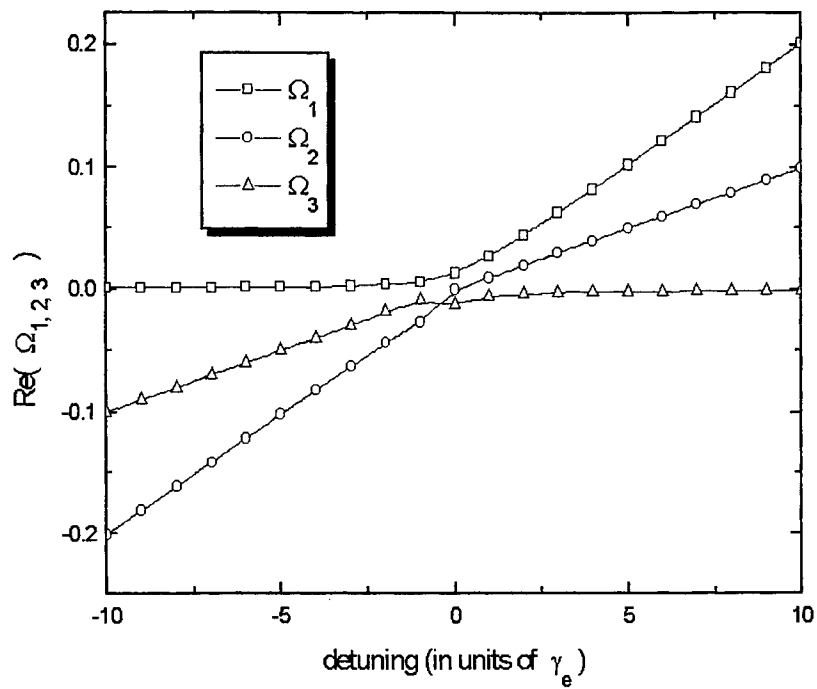


Figure 2. The dependence of normalized detuning parameter on $\Omega_{1,2,3}$ in the presence of excitons and biexcitons.

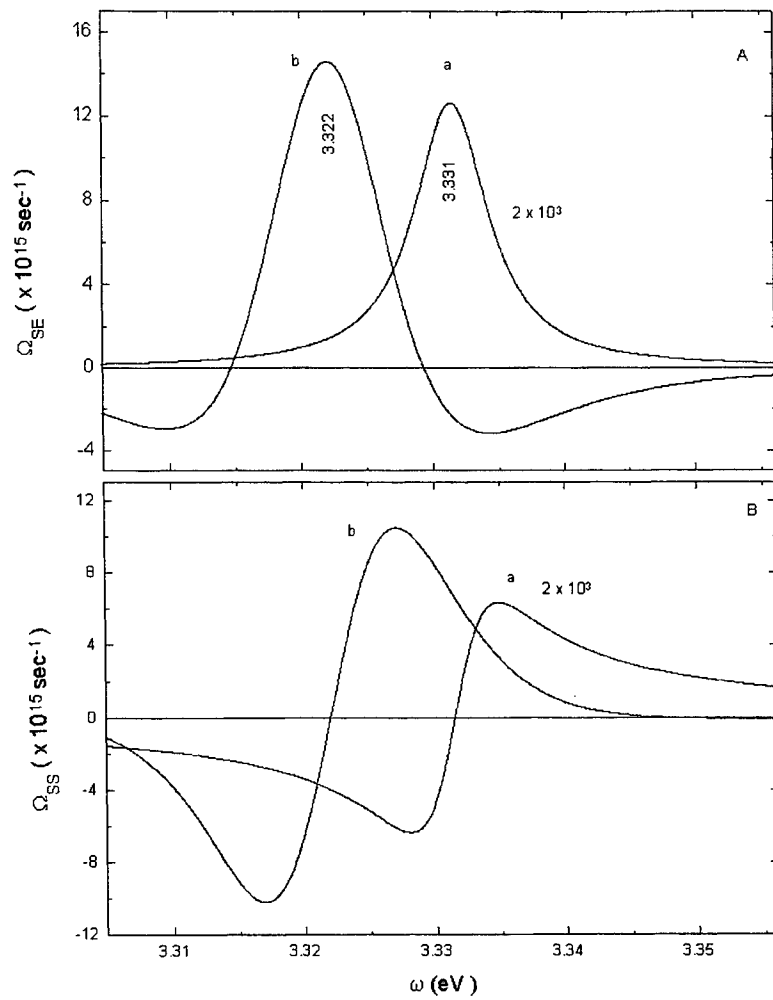


Figure 3. Dependence of Stark shift and self energy correction on wavelength in a single quantum dot of CdS. The Curve *a* is obtained in the absence of biexcitons and the Curve *b* is obtained in the presence of excitons and biexcitons.

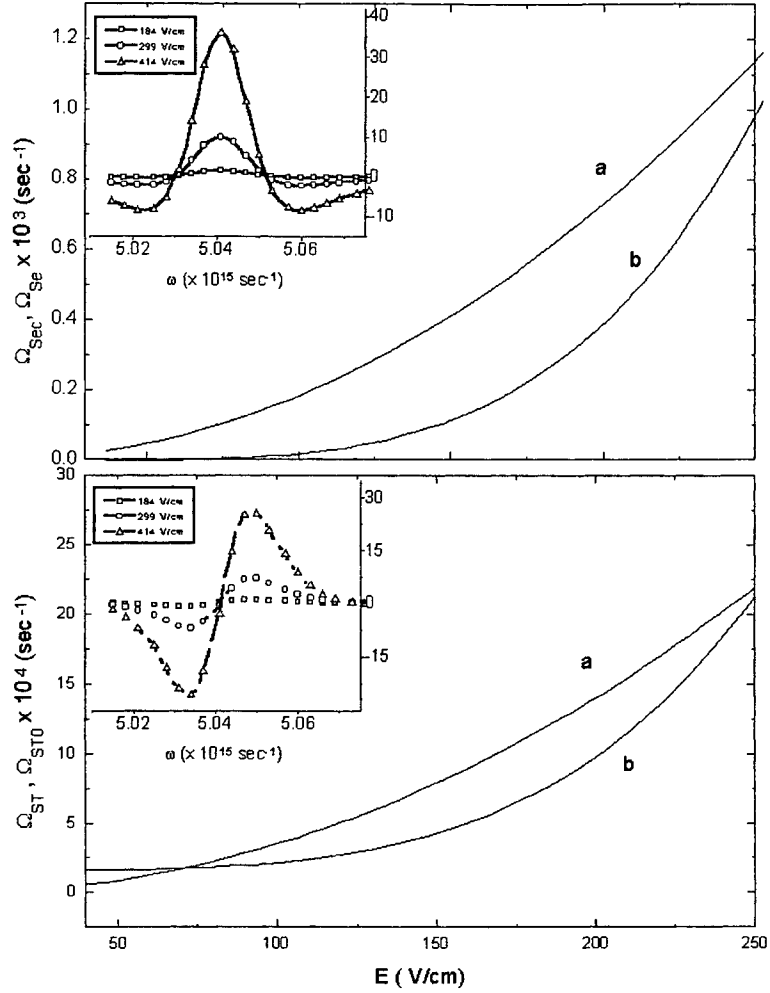


Figure 4. Stark shift and self energy correction in a single quantum dot of CdS at different intensities. The Curve *a* is obtained in the absence of biexcitons and the Curve *b* is obtained in the presence of excitons and biexcitons. The inset shows the variation for different intensities and pump wavelengths.

SESSION 2

Fundamental Processes II

Explosive Femtosecond Ablation from Ionic Crystals

Juergen Reif*, Matthias Henyk, Dirk Wolfframm

LS Experimentalphysik II; Brandenburgische Technische Universitaet Cottbus
Universitaetsplatz 3-4; 03044 Cottbus, Germany

ABSTRACT

Femtosecond laser ablation of positive ions from transparent ionic crystals is studied by time-of-flight mass spectrometry. We find an explosive emission of positive ions. The ion yield dependence on the laser fluence is highly nonlinear. The material is emitted in characteristic bursts, depending chaotically on the number of laser pulses hitting the sample. The mean kinetic energy of the positive ions is on the order of 100 eV while their temperature is only around 1 eV (10^4 K), very similar to supersonic expansion of a molecular jet. The last observation is independent of the ion species, indicating that all ions were born at the same instant and kicked out of the material simultaneously with identical kinetic energy. Negative ions, on the contrary, appear considerably later (about 0.5 μ s) and are much slower. All ablation is preceded by effective electron emission. We suggest that the laser generates a high-density plasma. The resulting electrons may possibly escape, due to the short pulse duration, without being disturbed by the build-up of a space charge zone. Subsequently, positive ions are expelled by Coulomb explosion of the unstable surface. Negative ions may be produced much later from the hot sample or by secondary processes.

Keywords: Laser ablation, femtosecond pulses, Coulomb explosion, ionic crystals, time-of-flight spectroscopy

1. INTRODUCTION

The phenomenon of massive particle emission from solid materials upon irradiation with intense laser pulses has been known for a long time¹⁻⁵. A number of possible mechanisms has been proposed for being at the origin of this laser desorption and ablation²⁻⁵. But only with the advent of lasers with pulse duration significantly below one picosecond, it has become feasible to study the dynamics of the fundamental interactions and processes⁶⁻⁸. Thus far, it is widely assumed that noticeable ablation always is the result of a plasma, generated by the laser at the surface of the target^{9,10}. The microscopic processes, however, leading to particle emission are not undisputed, yet. One model predicts the formation of an electrostatically unstable surface which then decays via Coulomb explosion¹¹. The other model assumes superheating of the target with subsequent phase explosion¹². Respective experiments were mostly centered on the ablation from sapphire as a model substance¹³⁻¹⁵. Those investigations exhibited two regimes of the interaction: the first one – at low laser intensity or for the first tens of laser shots – where the ablation cross-section is relatively low, but increases from shot to shot. This may be called the 'gentle etch' or incubation regime. The second one, called 'strong etch' regime, is observed at high laser intensity after a few incubating shots. It is characterized by a mean, steady ablation, superimposed by strong bursts of material which depend stochastically on the number of laser pulses.

In the present contribution, we report on experiments which might help to a better understanding to the microscopic processes in femtosecond laser ablation from sapphire. In these experiments both aspects are addressed, the mechanism of incubation as well as that of explosive particle emission. First, we will sketch the layout of our experiments, then we will present our results, followed, finally, by a comparison with the different models for the interaction.

2. EXPERIMENT

All studies were conducted in a high vacuum chamber at 4×10^{-7} mbar, connected to a time-of-flight spectrometer (Fig. 1).

* Correspondence: Email: reif@tu-cottbus.de; WWW: <http://www.physik.tu-cottbus.de/physik/xp2/>;
Telephone: +49 355 69 3185; Fax: +49 355 69 3985

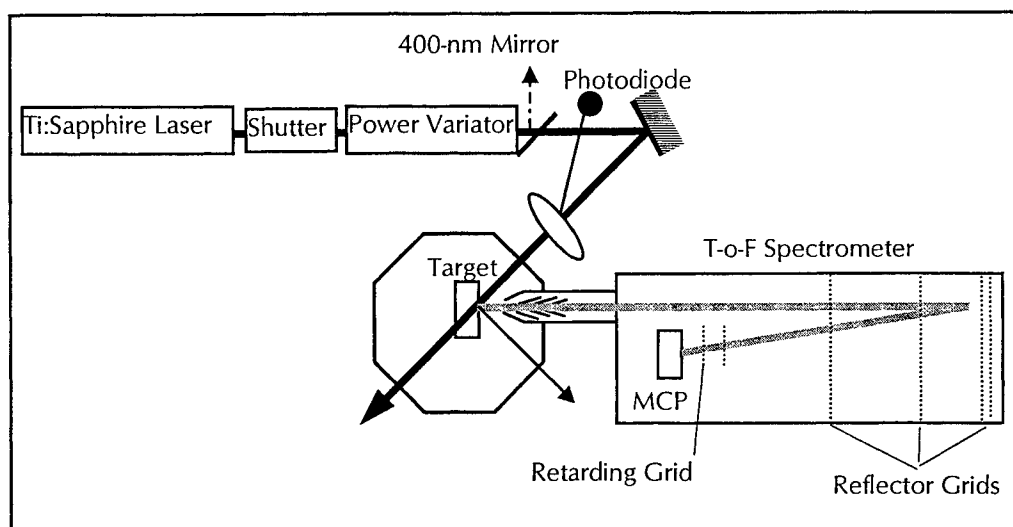


Figure 1: Experimental Setup. The continuous sequence (1 kHz) of femtosecond pulses from the Ti:Sapphire laser may be sliced by a mechanical shutter into pulse trains of 500 pulses each, separated by dark periods of 500 ms. A 400-nm mirror serves to block any second harmonic of the fundamental Ti:Sapphire light, generated at optical components along the beam path. The laser intensity is monitored by a photodiode, fed by an idle reflection. The charged particles are analyzed by a reflectron-type time-of-flight spectrometer. An additional retarding potential in front of the MCP detector allows to obtain information about the absolute kinetic energy of the particles. The output from the MCP is further processed by a gated integrator, a digital converter and then stored in a computer which controls the complete experiment (not shown in the figure for simplicity).

The linearly polarized output from an amplified Ti:Sapphire laser (λ : 800 nm; τ : 120 fsec; repetition rate: 1 kHz) was focused by an $f = 500$ mm lens onto a 0.03 mm^2 spot at the target. The incident fluence could be varied by a combination of a half-wave plate and a thin-film polarizer between 0.5 J/cm^2 and 2.7 J/cm^2 , the maximum being well below the single-shot damage threshold for Al_2O_3 at 3.0 J/cm^2 quoted in the literature¹⁶. As targets we used polished slides of, mainly, single crystalline Al_2O_3 and, for comparison, NaCl. We investigated, by means of a reflectron-type time-of flight spectrometer¹⁷, the emission of charged particles from these samples (electrons, positive and negative ions). Thus far, no evidence for the emission of neutral particles was found, in contrast to experiments with longer pulses¹⁸.

We investigated the dependence of all emissions on the fluence of the incident light. In most cases, we averaged the signals over several hundred pulses. By means of the T-o-F spectrometer, we analyzed the species of emitted ions as well as their kinetic-energy distributions. In order to obtain an absolute calibration of kinetic energy, we could introduce a retarding potential in front of our detector to determine the cutoff energy.

3. RESULTS

All our experiments were conducted in the previously described 'strong etch' regime¹³⁻¹⁵, i.e. on materials which after a preceding incubation show a strong response to the incident radiation. In this regime, the ion emission is characterized by a stable average rate, consisting of stochastically alternating pulses with high and with low yield. Thus, sampling over 500 pulses for each data point leads stable, reliable, and reproducible results.

3.1. Mass Spectra of Emitted Ions

From both types of samples, Al_2O_3 and NaCl, we observed the emission of both positive and negative ions. The positive ions represented all fragments, i.e. Al^+ , O^+ , Al_2O^+ , AlO^+ , and Al_2O_2^+ , resp. Na^+ . The negative ion spectra were less rich and consisted of O^- , AlO^- , AlO_2^- , Al_2O_2^- , and Al_2O_3^- , resp. Cl^- and NaCl^- . These spectra are displayed in Figs. 2, 3.

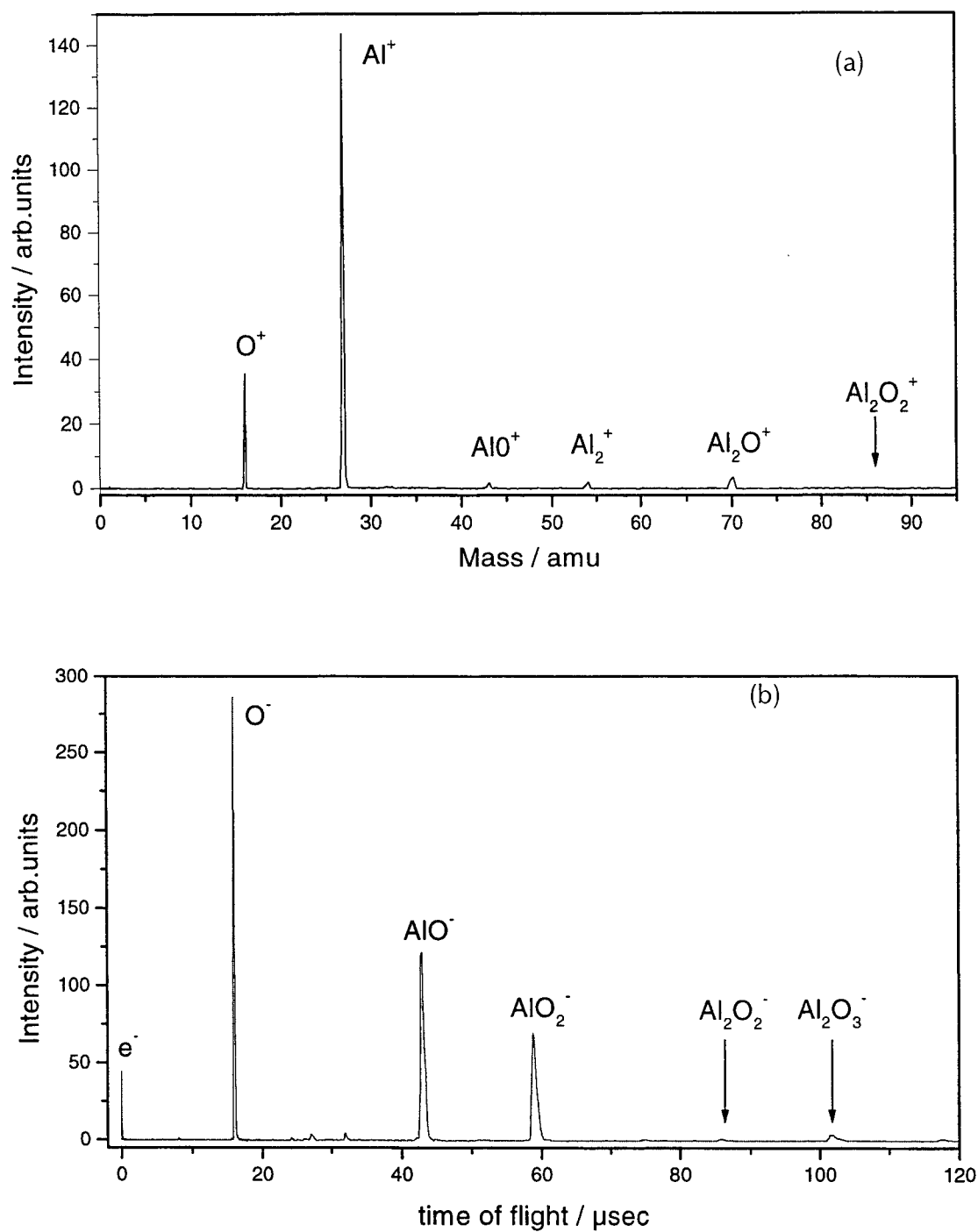


Figure 2: Mass spectra of (a) positive and (b) negative ions, emitted from Al_2O_3 upon irradiation with 120-fs laser pulses.

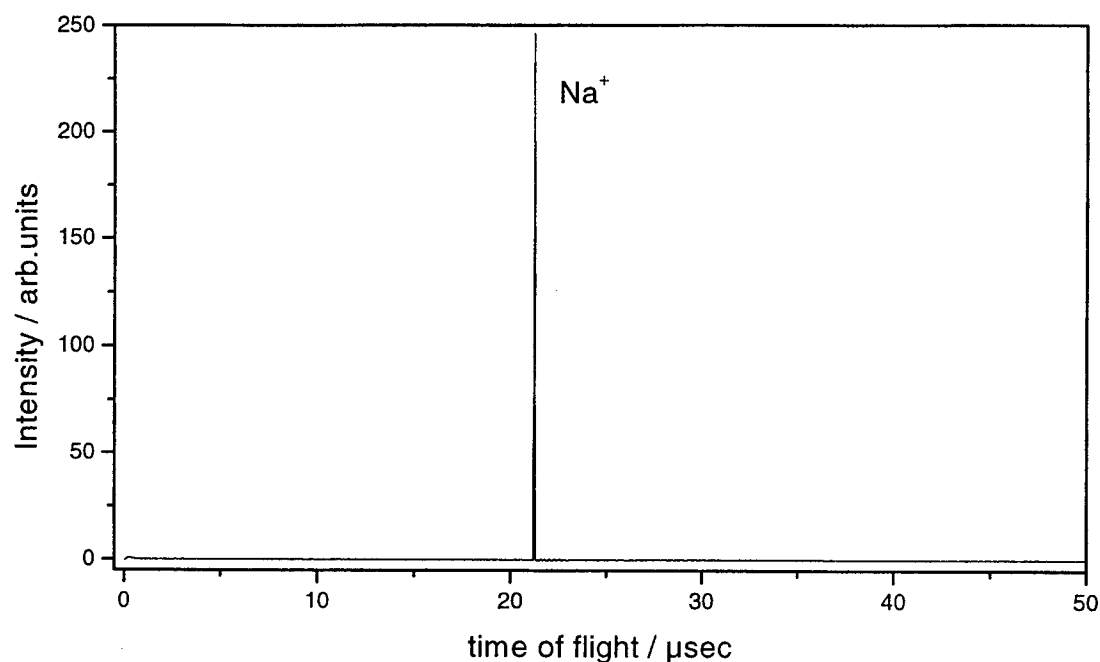


Figure 3: Mass spectrum of positive ions, emitted from NaCl upon irradiation with 120-fs laser pulses.

3.2. Fluence Dependence of Ion Emission

The dependence of the ion emission yield on the incident laser fluence F is highly nonlinear. From the ratio between the materials' bandgap (≈ 9 eV) to the photon energy (1.55 eV) one might expect six-photon coupling between radiation and material, resulting in an F^6 dependence. In fact, however, the slopes in a log-log representation of emission yield vs. F are so steep (> 20) that the assumption of a classical multiphoton process does not appear reasonable. However, we find kind of a threshold behavior slightly above the threshold for white light generation¹⁹. This is shown in Fig. 4.

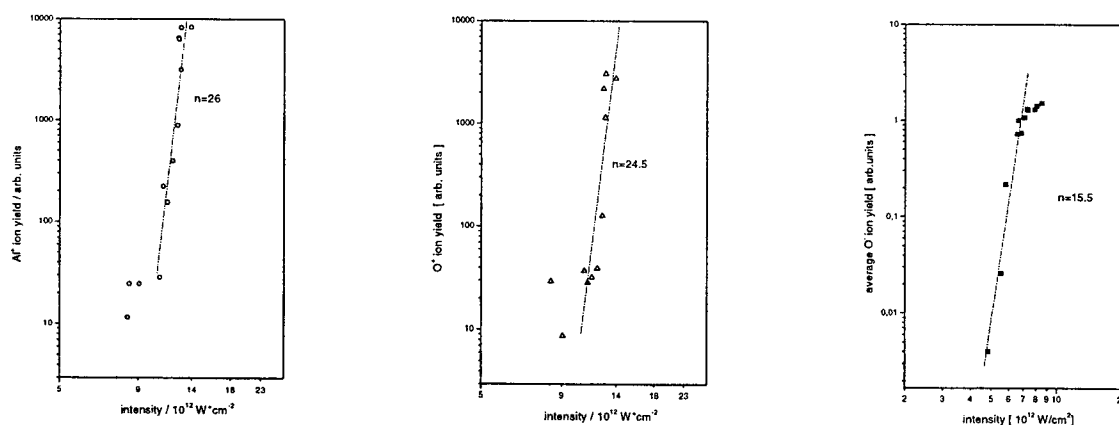


Figure 4: Typical ion yield as a function of incident laser fluence for Al_2O_3

3.3. Ion kinetic Energy

The kinetic energy of the ablated ions was measured in two ways: In order to absolutely determine the birth energy, a retarding grid was introduced in front of the detector, and we measured the voltage necessary to block the ion flux. In Fig. 5(a), the ion yield for Al^+ is plotted vs. the birth energy (= retarding – accelerating voltage) as a typical example. From the slope this "transmission" curve, we can derive a distribution of the ion velocities, assuming, like in a seeded atomic beam, a flow velocity u superimposed by a thermal distribution of relative velocities v :

$$f(v) = cv^2 \exp\left(-\frac{m(v-u)^2}{2kT_u}\right) \quad (1)$$

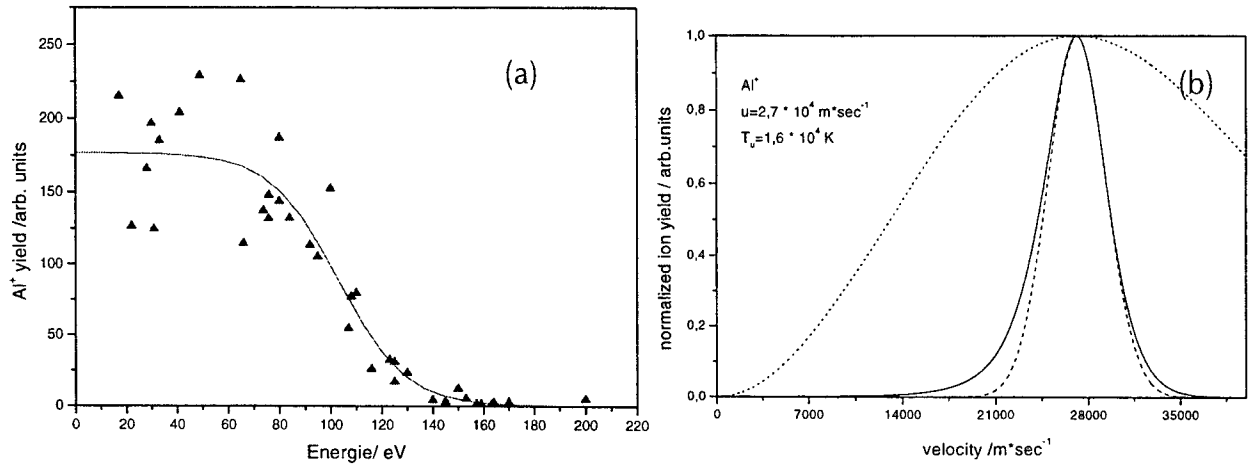


Figure 5: (a) Ion transmission through retarding grid as a function of birth energy; (b) ion velocity distribution derived from the data in panel (a), assuming a flow velocity u superimposed to a thermal velocity distribution $f(v)$.

Alternatively, we exploited the potential of our T-o-F spectrometer to obtain a more detailed information about the actual relative ion velocities. These are shown in Fig. 6 for Al^+ and for Na^+ , as typical examples. Note the important contribution of slow ions from NaCl. To explain the late arrival of the negative ions, it is not sufficient to assume much lower kinetic energy. We rather have to take into account, in fact, a delayed emission.

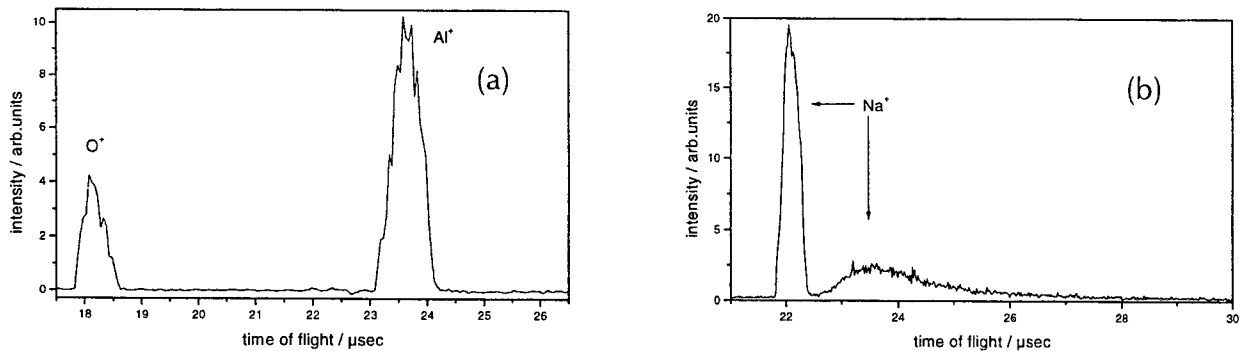


Figure 6: T-o-F spectra (drifting condition) of emitted ions: (a) Al^+ and O^+ , (b) Na^+ .

As can be seen from Fig. 7, all positive ions have identical kinetic energy, pointing to a common source.

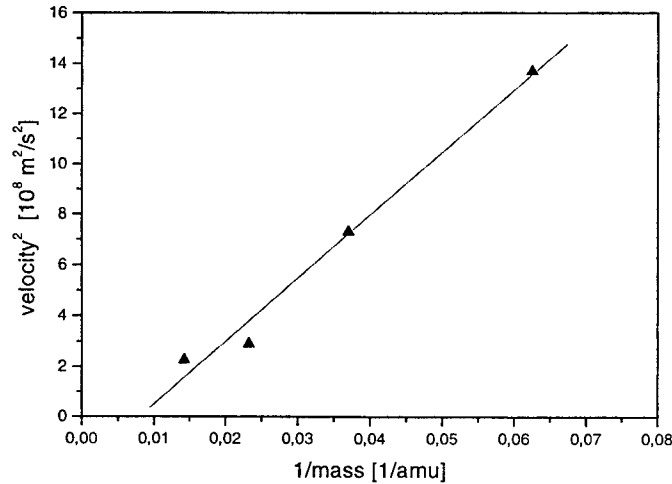


Figure 7: Plot of velocity squared vs. reciprocal of ion mass. The straight line indicates constant kinetic energy.

From both types of experiments, we find that a large fraction of positive ions are emitted with a kinetic energy of the order of 100 eV. At the same time, their temperature, i.e. the width of the energy distribution, corresponds to only 1 eV. In addition to these fast ions, we also find a second group of ions having only about thermal velocities. From Al_2O_3 the amount of these slower ions is negligible in comparison to the fast ones. From NaCl, however, the total number of slow ions is significantly larger than that of the fast ones.

3.4. Electron Emission

All ion ablation is preceded by strong electron emission. Unfortunately, our experiment does not allow, so far, the T-o-F analysis of the electron kinetic energy. We can, however, determine the fluence dependence of the electron yield, as is demonstrated in Fig. 8 for sapphire.

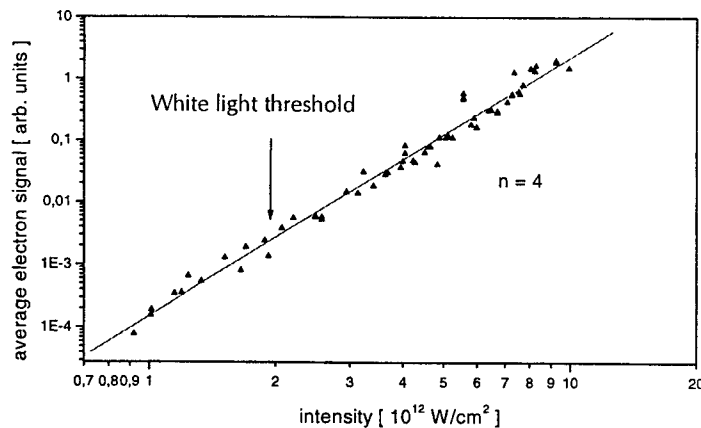


Figure 8: Fluence dependence of the electron yield from Al_2O_3 (log-log plot). Marked is the threshold for white light generation, which is close to that for the detectable ablation of ions.

Obviously, we find a very pronounced F^4 -dependence over several orders of magnitude. This clearly points to four-photon coupling of the incident light, involving an excitonic state as an intermediate¹⁹.

DISCUSSION

Resuming the experimental results, we find for the incubated material:

- Substantial emission of electrons
- Emission of positive ions with very high kinetic energy (100 eV)
- Sample temperature of about 1 eV (10^4 K)
- Delayed emission of slow negative ions.

From these observations, we try to develop the following model of what may happen during the ablation process. Before ablation successfully can occur, the system must be incubated, as was demonstrated earlier¹³⁻¹⁷, presumably via the creation of defect states. Whereas for Al_2O_3 these states appear to be long-lived, they decay rapidly in NaCl ²⁰.

Our very stable electron emission indicates, that for *sapphire*, this defect state is the exciton at about 6 eV¹⁹. This intermediate state helps the absorption of photons, but does not immediately lead to the emission of ion. More likely, we assume that the strong loss of electrons due to the irradiation leads to a charging of the sample surface. Because of the short duration of our laser pulses, all ionized electrons are able to escape the vicinity of the surface before any space charge can build up and shield the sample. As can be seen from Fig. 8, the number of detected electron beyond the ablation threshold of $\approx 9 \times 10^{12} \text{ W/cm}^2$ is very high, close to saturation of our detector at $\approx 15 \times 10^{12} \text{ W/cm}^2$. This indicates that the actual number of electrons emitted before ion emission is of the order of 10^4 to 10^5 . Assuming that only the central 10% of our irradiated spot really contribute to the emission, and assuming an interaction depth of about one atomic layer, this leads to an electron density of roughly 10^{18} cm^{-3} , corresponding to usual plasma densities. The corresponding ions remaining after the charge separation, but still being in close vicinity to the electrons, represent a substantial positive charging of the interaction volume of the order of 10^{-14} C . As a consequence of this charge, Coulomb explosion of the surface sets in and thrives out the positive ions. Whereas the electron-ion plasma represents a temperature of grossly 10^4 K , the Coulomb repulsion should then be responsible for the high kinetic ion energy detected in our experiments.

The emission of negative ion occurs considerably later, with the ions being much slower. There, we suggest that they are emitted thermally after the positive ions have left the sample.

From NaCl , we also observe fast ions at about 100 eV. In addition, however, about the same rate of slow ions (10 eV) is emitted. Up to date, we cannot yet explain the different behavior, also observed for other features of the emission^{20,21}.

ACKNOWLEDGEMENTS

We gratefully acknowledge the skilled technical assistance by Juergen Bertram. We thank Rainer Schmid, Thomas Schneider and Christian Weickhardt for fruitful discussions.

REFERENCES

- 1• R. F. Haglund, R. Kelly in: *Math. Fys. Medd. Dan. Vid. Selsk* **43**-Fundamental processes in Sputtering of Atoms and Molecules ed. by P. Sigmund, (Copenhagen, 1992)
- 2• J. C. Miller (Ed.), *Laser Ablation-Principles and Applications*, Springer (1994)
- 3• R.F. Haglund Jr., *Appl. Surf. Sci.* **96-98**, **1** (1996)
- 4• N. Georgiev, N. Itoh, *J. Phys.: Condens. Matter* **2**, 10021 (1990)
- 5• N. Bloembergen, *Appl. Opt.* **12**, 661, (1973)
- 6• G. Petit, P. Daguzan, S. Guizard, P. Martin, *Appl. Surf. Sci.* **109/110**, 36 (1997)
- 7• N. Itoh in: *Interfaces under laser irradiation* ed. by L. D. Laude, D. Bäuerle and M. Wautelet, NATO ASI Ser. **134**, 219 (1987)

- 8• P. Townsend, J. Olivares, *Appl. Surf. Sci.* **109/110**, 275 (1997)
- 9• R. W. Dreyfus in: Laser ablation of electronic Materials ed. by E. Fogarassy and S. Lazare, Elsevier, (1992)
- 10• C. R. Phipps, T. P. Turner, R. F. Harrison, G. W. York, W. Z. Osborne, G. K. Anderson, X. F. Corlis, L. C. Haynes, H. S. Steele, K. C. Spicochi, *J. Appl. Phys.* **64**, 1083 (1988)
- 11• Hai-Ping Cheng, J. D. Gillasp, *Phys. Rev. B* **55**, 2628 (1997)
- 12• R. Kelly, A. Miotello, *Nucl. Instr. Meth. Phys. Res. B* **122**, 374 (1997)
- 13• H. Varel, M. Wähmer, A. Rosenfeld, D. Ashkenasi, E.E.B. Campbell, *Appl. Surf. Sci.* **127-129**, 128 (1998)
- 14• R.W. Dreyfus, R. Kelly, R.E. Walkup, *Appl. Phys. Lett.* **49**, 1478 (1986)
- 15• J.E. Rothenberg, R. Kelly, *Nucl. Instr. Meth. Phys. Res. B* **1**, 291 (1984)
- 16• D. Ashkenasi, A. Rosenfeld, H. Varel, M. Wähmer, E.E.B. Campbell, *Appl. Surf. Sci.* **120**, 65 (1997)
- 17• M. Henyk, R. Mitzner, D. Wolfframm, J. Reif, *Appl. Surf. Sci.*, in press
- 18• O.M. Efimov, K.Gabel, S.V. Garnov, L.B. Glebov, S. Grantham, M. Richardson, M.J. Soileau, *J. Opt. Soc. Am B* **15**, 193 (1998)
- 19• J.T. Dickinson, D.R. Ermer, J.-J. Shin, S.C. Langford, *Appl. Surf. Sci.* **127-129**, 7-20 (1998)
- 20• M. Henyk, D. Wolfframm, J. Reif, *NIM B*, in press
- 21• M. Henyk, D. Wolfframm, J. Reif, *Appl. Phys. A*, in press

Interaction of shock electromagnetic waves with transparent materials: classical approach

Anastasia S. Gruzdeva⁺, Vitali E. Gruzdev⁺
State Research Center «S.I. Vavilov State Optical Institute»
Birzhevaya Liniya 12, St. Petersburg, 199034, Russia

ABSTRACT

There is discussed a theoretical model of initiating of laser-induced damage and ablation of transparent materials by femtosecond pulses based on properties of shock electromagnetic wave (SHEW). Advantages of this model are increased efficiency of SHEW-induced ionization and possibility of effective straight action of SHEW front on ions at crystal-lattice points. It is presented simplified description of SHEW-induced processes within approach of classical mechanics and electrodynamics: atoms are described as dipoles with certain ionization energy interacting with SHEW in potential well formed by crystal lattice. There are considered possibilities of laser-induced ionization by higher harmonics appearing during SHEW formation and point-defect formation and delocalization of ions at crystal points by SHEW. Obtained results and predictions are compared with experimental data and shown to be capable of explaining many observed regulations of femtosecond laser interactions with transparent media.

Key words: femtosecond laser ablation, femtosecond laser-induced damages, transparent materials, shock electromagnetic waves, laser-induced ionization, laser-induced desorption

1. INTRODUCTION

This paper is devoted to theoretical consideration of one of topics in a large field of femtosecond laser-matter interactions - femtosecond laser interactions with wide band-gap transparent materials. This problem is of great fundamental and applied meaning and for this reason intensity of investigations in that direction is still very high [1, 2]. In particular, some possibilities and perspectives in application of femtosecond lasers to material processing do not meet analogies among laser systems with larger pulse duration (picosecond and nanosecond) [2, 3]. One of serious problems slowing down progress of femtosecond laser technology is that mechanisms of femtosecond laser-matter interactions are still not clear in spite of intensive experimental and theoretical investigations carried out worldwide. Observed regularities of femtosecond laser ablation and damage show traditional thermal models of ablation and damage not to be valid for femtosecond pulse duration. On the other hand, developing of theoretical models for femtosecond laser-induced non-equilibrium processes in transparent materials is rather complicated and only few models have appeared recently [1, 4, 5]. Till now, there are no answers to some important questions, for example, there is no estimation of damage threshold and its dependence on radiation and material parameters which corresponds to experimental data at least qualitatively.

To our mind, one of important points of femtosecond laser interactions is influence of nonlinear optical phenomena on character of laser-induced processes. For example, one-photon absorption is much more effective than multi-photon absorption. Due to that, generation of higher harmonics (HH) can change ionization rate sufficiently because absorption of HH of suitable photon energy $h\nu > E_g$ dominates multiphoton absorption in case of effective generation of HH. For this reason we consider the problem of mechanisms of femtosecond laser interaction with transparent materials once more. Key point of presented model is nonlinear electrodynamical process of formation of shock electromagnetic wave (SHEW) in the vicinity of focal area. Formation of SHEW is connected with distortions of laser-cycle profile due to laser-induced nonlinear modulation of refraction resulting in "falling down" of top part of the profile onto the region where electric-field strength is about zero [15, 16, 18, 19] followed by appearing of field disruption. That phenomenon can appear near leading edge of femtosecond pulse and results in generation of higher harmonics (HH) and formation of abrupt SHEW front where space variations of electric-field strength are very large [15, 16]. As it is shown below, those specific features of SHEW make it very suitable for initiating of laser-induced damage and desorption by femtosecond pulses.

As it was mentioned in [15, 16] the problem of SHEW formation, propagation and interaction with transparent materials is

⁺ Phone: 7-81272-246-22, fax 7-81272-246-22, e-mail: gru@mailbox.alkor.ru

self-consistent and very complicated because many factors influencing SHEW propagation should be taken into account. That general problem can be reduced to two practically independent problems: formation and propagation of few first field disruptions (no more than 10 periods of laser radiation) considered in [15, 16], and interaction of SHEW with material that is to be considered in this paper. Material properties are taken to be constant and influence of their SHEW-induced variations on SHEW propagation are neglected in the framework of the first problem. Results of solving of that problem are SHEW profile and regularities of its unperturbed propagation. They are used to consider SHEW interaction with materials, thus, SHEW profile is assumed to be constant and independent of induced changes in material (increasing of absorption due to ionization, formation of point defects and so on) for the second problem. Thus, we assume influence of laser-induced modification of material properties on SHEW propagation to be so small as to be neglected throughout this paper. This results in breaking of energy conservation law [15, 16]: energy transferred from SHEW to electrons (ionization and absorption by electrons) and crystal lattice (formation of point defects) is not taken into account within this approximation. Thus, some energy appears in material and leads to its modification while nothing disappears from SHEW. On the other hand, neglecting of energy dissipation at SHEW front results in formation of non-steady SHEW. Two points should be mentioned in this connection: 1) the energy dissipating from SHEW to material is assumed to be small enough at leading part of laser pulse not to influence sufficiently on SHEW propagation; 2) presented consideration is the first approximation to exact solution while calculated absorption rate will be used to estimate energy dissipation in further approximations.

In order to develop general concept of SHEW interaction with transparent materials we start with brief review of experimental data on femtosecond laser-matter interactions and consider previously developed theoretical models. Then we describe general approach to the problem, propose approximate description of SHEW front and develop classical model of SHEW interaction with single charges (free electrons), uncharged (atoms) and charged dipoles (ions) in potential wells. Results of theoretical analysis include thresholds of SHEW-induced ionization and moving of dipoles away from their potential wells, i.e., delocalization of crystal points and formation of point defects.

2. REVIEW OF EXPERIMENTAL FACTS

Experimental investigations of femtosecond laser-matter interactions have been carried out in many laboratories worldwide. Being out of any intention to present full review of experimental results, we consider briefly only some typical data and results obtained by several investigation teams but we have included results on both nonlinear femtosecond-pulse propagation and on laser-induced damage and ablation. Our aim is to sketch general situation and experimental regularities in femtosecond interactions.

All mentioned below results are concerned with processes induced by femtosecond laser pulses in transparent wide band-gap materials. *Characteristic parameters of laser radiation* are as follows:

- pulse duration $\tau_p = 900 \text{ fs} - 10 \text{ fs}$ [6 - 14];
 - laser wavelength in vacuum $\lambda_0 = 10.6 \mu\text{m} - \text{IR}$ [13] - $1.06 \mu\text{m}$ [3] - $0.8 \mu\text{m}$ [7, 8] - $0.6 \mu\text{m}$ [6];
 - energy of laser quantum $h\nu$ 0.117 eV - 1.17 eV - 1.55 eV - 2.07 eV ;
- | | | | |
|-----------|-------------------------|-------------|---|
| ↓ | ↓ | ↓ | ↓ |
| FE lasers | Nd ³⁺ :glass | Ti:sapphire | |
- type of laser
 - intensity of laser radiation at focal plane $I_{TH} = 10^{13} - 10^{14} \text{ W/cm}^2$ [6 - 14];
 - focal spot radius $r_F = 1 \mu\text{m} - 10^2 \mu\text{m}$ [6 - 14], what allows estimating of beam path s in nonlinear material along which nonlinear interaction is the most effective: $s \cong 2z_c = \pi r_F^2 / \lambda = (10 - 3 \cdot 10^4) \lambda$, typical value of s is $(10 - 100) \lambda$;
 - repetition rate (for multi-pulse damage and ablation) from 10 Hz to 10^9 Hz (pulse trains [11, 13]).

It should be emphasized that some parameters of radiation are often not mentioned in scientific publications, in particular, light polarization, space and time profile of the pulse and some others. That makes difficult both control of experimental situation and comparison of experimental data with theoretical results.

Materials used in experiments are wide band-gap semiconductors and dielectrics which typical band gap is 3 or more times larger than radiation quantum: $E_g \geq 3h\nu$. Nonlinear coefficient of refraction is about $n_2 \cong 10^{-16} \text{ cm}^2/\text{W}$. Linear constant part of refractive index n_0 varies between 1.45 and 3 for most of considered materials. Many of investigated materials are isotropic, for example, fused silica, glasses of various types. Looking through papers with experimental data [6-14], one finds that fused silica is the most often used material for femtosecond laser-induced damage and ablation. Its parameters are as follows: $E_g = 7.5 \text{ eV}$ [23], $n_0 = 1.45$, $n_2 = 2 \cdot 10^{-16} \text{ cm}^2/\text{W}$. Thus, ionization of fused silica by main harmonic radiation can be observed only for nonlinear absorption varying from 7-photon ($\lambda_0 = 1.06 \mu\text{m}$) to 4-photon ($\lambda_0 =$

0.6 μm) absorption.

Typical regularities of femtosecond-pulse propagation and interaction with transparent materials are as follows:

1. Very high damage and ablation threshold ($10^{13} - 10^{14} \text{ W/cm}^2$) [6 - 8]. Such thresholds are observed practically for all tested materials and they vary little from one material to other. Thus, laser-induced variations of refraction at threshold laser fluence are about $\Delta n_{NL} = n_2 I_{TH} \cong 0.1 - 0.005$. It is useful to remind that much smaller nonlinear variations of refractive index about 10^{-4} result in such strong nonlinear phenomena as self-focusing and higher harmonic generation.
2. Super-continuum generation [9] during propagation of femtosecond laser pulses in transparent materials. Spectrum analysis shows appearing of many Stokes and anti-Stokes peaks near central laser line in spectrum of generated white light. Important point is that anti-Stokes wing of the spectrum of generated white light is about an order of magnitude longer than Stokes wing [27]. White-light generation is observed only for materials which band gap exceeding certain threshold value showing threshold band-gap dependence [27].
3. Thresholds of self-focusing and white-light generation are similar with very good accuracy [23]. The thresholds are so similar that white-light generation is used to detect presence of self-focusing [14]. This points at that white-light generation starts only after laser intensity exceeds certain threshold level and self-focusing helps to increase the intensity upto that level.
4. Most femtosecond interactions as well as propagation of femtosecond pulses are accompanied by generation of higher harmonics. In case of isotropic materials the harmonics are odd and can be of very high order (21-st – 27-th harmonics observed in [10]).
5. Detection of laser-induced damage is connected with one of important problems – what process should be taken as a signal of damage onset. Correct investigations [12] shows that bulk laser-induced femtosecond damage of transparent solids consists of several stages, each with its characteristic threshold. Formation of plasma comes before irreversible changes take place and threshold of plasma formation is the lowest among all other thresholds. Next process is formation of invisible single-shot and multi-shot damage which threshold is higher than that of plasma formation. This type of damage results from appearing of color centers and their disappearing after heating shows that. Appearing of visible laser-induced damage and irreversible fall of transparency have the highest threshold that is about 10 times higher than that for plasma formation.
6. Dependence of damage morphology on wavelength [13] is one more characteristic feature of laser ablation and damage. If laser wavelength is far from absorption bands then it is observed nonthermal damage for low repetition rates [12, 14] when irradiated material changes its structure from crystalline to amorphous and even voids can appear in focal area. For high repetition rates it is observed thermomechanical fracture [1, 11] for laser wavelength far from absorption bands. Clear melting is observed in case when laser wavelength is within absorption band (electronic or vibrational) [1, 11].
7. One of the most interesting features of femtosecond damage and ablation is practical absence of thermal damage around ablated crater for low repetition rates and single shots [3, 7, 8, 12, 14]. This clearly shows absence of heating sufficient for damage and ablation by evaporation. Size of damaged or ablated site is determined by focusing system only and coincides with laser-spot size. It can be decreased down to one micrometer or less [12, 14] what is important for technological applications.
8. Thermal damage around ablated sites is observed for multi-pulse ablation at high repetition rates [1, 8, 11]. Its morphology depends on laser wavelength as it was explained above and can result from thermomechanical fracturing or melting followed by evaporation. In any case ablated or damaged area is much larger than laser-spot size.
9. Dependence of damage threshold on pulse duration has not been studied reliably so far. Well-known results from [5] and [25] are in contradiction: it was observed decreasing of damage threshold with decreasing of pulse duration τ_p for pulse duration less than 10 ps scaling as $\tau_p^{1/2}$ in [5] while damage threshold increased as τ_p^{-1} with decreasing of pulse duration according to data from [25]. This contradiction has not got any interpretation till now.

The most important and characteristic features of femtosecond interactions leading to problems in building their theory are 1) small pulse duration excluding classical thermal mechanisms of laser-induced heating and damage resulting from phase explosion; 2) high radiation intensity which can result in a variety of nonlinear optical processes accompanying laser action on transparent materials and changing its character.

3. THEORETICAL MODELS OF FEMTOSECOND LASER-MATTER INTERACTIONS

The problem is that most theoretical models developed within last 5 years do not take into account mentioned nonlinear optical phenomena. They are based on the simplest model of radiation – plane harmonic wave which is not valid for high-

power femtosecond pulses at least because of HH generation. Among the models the most widely referred to is model proposed by Stuart et al [5]. Its basic idea is formation of electron plasma resulting from multiphoton and/or avalanche ionization. It is widely accepted that multiphoton ionization comes first to give seed electrons for developing of avalanche and can even dominate in solids while avalanche ionization seems dominating in water and biological tissue [4, 12, 14, 17]. Further processes within this model are absorption of radiation by free electrons leading to heating up of the plasma, energy transfer from heated plasma to phonons resulting in local heating of material, its melting and evaporation. Energy absorption by electrons accompanied by laser-induced generation of hot nonequilibrium plasma is described by kinetic equations and equations of energy balance while heating and energy transfer from hot electrons to crystal lattice is described by two-temperature model [5, 17]. The processes following heating of ionic lattice, in particular, motion of plasma away from surface, are described by hydrodynamic equations [17, 18]. Proposed in [5] model was later verified with numerical calculations of energy transfer from electrons to phonons [4] based on Boltzmann's kinetic equation including terms accounting for multiphoton and avalanche ionization. One of serious drawbacks is the problem of multiphoton absorption and ionization. As one can see from experimental data, an electron must absorb from 4 to 7 photons to get to conduction band from valence band. Such high-order absorption has very small probability and can hardly take place in real situations. Taking into account presence of HH shows that multiphoton ionization gives so few free electrons as to be easily neglected as compared to ionization by HH (section 4.1). Developing of electron avalanche is hardly possible too [12, 14] because its characteristic time is about 1 — 10 picoseconds.

Other models are based on detailed concept of energy transfer from laser-induced excitations (both electronic and vibrational) [1, 4, 11]. They take into account energy transfer through slow and fast pathways [1] leading to both heating followed by thermal ablation and nuclear motion (desorption, formation of vacancies, interstitials). That can result in particle and defect diffusion (non-thermal ablation) [1].

Considering vibrational and electronic excitations, ionization and plasma formation, most investigators do not take into account nonlinear optical processes, in particular, generation of higher harmonics that take place before absorption process and can change sufficiently all following processes of energy transfer from radiation to matter. For this reasons we base proposed model on certain nonlinear electrodynamic processes and pay much attention to consideration of their role in initiating of femtosecond laser-induced damage and ablation.

4. INTERACTION OF SHEW WITH TRANSPARENT MATERIALS

4.1. Basic idea

As it follows from experimental results, initial stages of femtosecond laser-matter interactions should be managed by fast mechanisms with very small *inertia* because typical pulse duration is less than time of energy transfer from electrons to phonons. The mechanisms must be rather universal, without strong dependence on wavelength if the latter is within transparent band and must act for pulse duration from several hundreds of femtoseconds to few tens of femtoseconds. The mechanism must describe both effective ionization taking place before irreversible changes of material properties and non-thermal laser-induced damage of transparent materials. The most promising candidate for being that fast mechanism is a nonlinear electrodynamic process that must result in both effective ionization and straight action on crystal lattice.

We suppose shock electromagnetic wave to be the most suitable nonlinear electrodynamic process for being fast mechanism of initiating of femtosecond damage and desorption. There are two reasons for that connected with *main features of SHEW* [15, 16, 19, 20]:

- generation of higher harmonics (odd harmonics in isotropic medium) – can result in effective ionization;
- formation of abrupt shock front (can result in straight action on crystal lattice).

The first reason for considering SHEW as the most suitable candidate is possibility of effective one-photon ionization within SHEW model by HH. Really, laser-induced ionization goes through generation of higher harmonics and single-photon absorption in a pathway shown below in Fig. 1. Let compare density of SHEW-induced free electrons with density of electrons appearing due to multiphoton ionization.

In the first approximation speed of electron generation dn/dt (ionization rate) can be described by a constant G which depends on material and radiation parameters rather than on electron density [21]:

$$\frac{dn}{dt} = G, \quad (1)$$

where $G \propto \alpha I / h\nu$, α is absorption coefficient dependent on laser intensity I in case of multiphoton absorption:

$$\alpha_{N\text{-photon}} = n' \cdot \sigma_N \cdot I^{N-1}, \quad (2)$$

where n' is density of absorbing particles. According to estimations and numerical results [15, 16, 19, 20] intensity of higher harmonics I_{HH} can reach about 10% of radiation intensity I_0 at initial laser wavelength. On the other hand, cross-section for one-photon absorption $\sigma_{1\text{-photon}}$ is about 10^{-16} cm^2 [22] what gives absorption $\alpha_{1\text{-photon}} \cong 10^6 \text{ cm}^{-1}$. Ionization rates, produced by multiphoton absorption and higher harmonic of the same order as absorption, can be estimated for example, for two-photon absorption [22, 23] which is the most effective among other types of multi-photon absorption: $\alpha_{2\text{-photon}} = \delta_2 I n = \beta I$ where $\delta_2 \cong 10^{-50} 1/(\text{cm}^2 \text{ s})$ [22] and $\beta = 10^{-8} \text{ cm/W}$ [23]. Thus, for speed of free-electron generation at laser irradiance 10^{13} W/cm^2 one obtains [21]

$$\frac{G_{2\text{-photon}}}{G_{2\text{-harmonic}}} = \frac{\alpha_{2\text{-photon}} I_0}{\alpha_{1\text{-photon}} I_{2\text{-harmonic}}} = \frac{\beta I_0}{\alpha_{1\text{-photon}} 0.1 I_0} \cong 0.1 \quad (3)$$

Similar estimations for 3-photon absorption gives $G_{3\text{-photon}} / G_{3\text{-harmonic}} \cong 0.01$. Thus, in presence of SHEW in isotropic dielectric the lowest order odd harmonic along produces 100 times more free electrons than 3-photon ionization, i.e., multiphoton ionization gives about 1% or less of total amount of free electrons. Ratio of ionization speeds decreases with increasing of order of harmonics and multiphoton absorption because probability of multiphoton absorption decreases fast while absorption of HH increases. Thus, ionization by SHEW due to generation of HH is much more effective than multiphoton ionization widely accepted in theoretical models [4, 5].

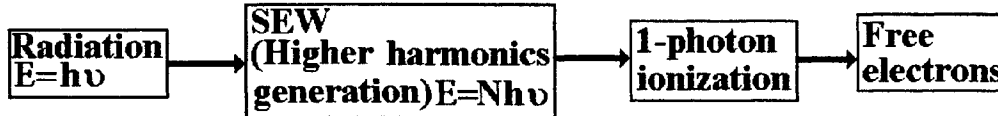


Fig. 1. Sketch of ionization process in the framework of SHEW model: energy of initial photons $E=h\nu$ is N -times increased by generation of higher harmonics of N -th order. Then free electrons appear due to single-photon ionization by large-energy photons of higher harmonics.

The second reason for consideration of SHEW as the most suitable candidate for femtosecond interactions is possibility of effective straight action on atoms and ions on crystal lattice. Rough estimation can be obtained in the following way. Interaction of electric field of strength E with a dipole d results in a mechanical force F

$$\vec{F} = \vec{\nabla}(\vec{E} \cdot \vec{d}) \quad (4)$$

that is determined by spatial derivations of electric-field strength. Considering plane harmonic wave of amplitude E_{PHW} resulting in a force F_{PHW} and a SHEW resulting in a force F_{SHEW} one can see that $F_{SHEW} \gg F_{PHW}$ even for $E_{SHEW} = E_{PHW}$, because

$$\frac{F_{SHEW}}{F_{PHW}} = \frac{(\partial E / \partial x)_{SHEW}}{(\partial E / \partial x)_{PHW}} \gg 1 \quad (5)$$

near SHEW front. Thus, energy of field-dipole interaction stays the same for both waves if their amplitudes are equal while power of interaction is much more for SHEW than for harmonic wave. This can result in specific processes considered in Section 4.2.

To conclude, we depict general picture of femtosecond laser-matter interactions with participating of SHEW. Processes taking place at single-shot as well as at few first shots of low-rate multi-shot interactions are dominated by SHEW interaction with transparent materials. That is connected with effective ionization and damage of crystal lattice (delocalization of crystal points, formation of point defects, i.e., vacancies) through straight action of electric field near SHEW front if amplitude of input wave exceeds threshold of SHEW formation [15, 16]. Important point is that ionization takes place before damage because formation of even weak SHEW is accompanied by generation of HH. That phase turns into the next phase of femtosecond interactions dominated by nonequilibrium processes of relaxation, non-diffusion and diffusion motion of SHEW-generated electron plasma and defects, in particular, delocalization of crystal points and even ablation from surface if laser fluence is high enough. After-heating can be neglected in most practical cases of single-shot and low-repetition rate multi-shot damage because electrons transfer absorbed energy into bulk faster than it is transferred to phonons in the vicinity of focal spot [24].

Multiple-pulse action is accompanied by incubation of SHEW-induced defects resulting in increasing of absorption at main harmonic wavelength and higher-harmonics wavelengths. Thus, in case of multi-shot femtosecond action with high repetition rate it is possible to distinguish fast mechanisms acting during few first shots and slow mechanisms connected with incubation of laser-induced defects and after-heating produced through absorption by the defects that dominates in formation of ablation crater. This idea is supported by observed morphology of ablation craters formed by multi-pulse radiation at high repetition rates [1, 11]. In this paper we concentrate on fast SHEW-induced processes that can dominate for single-shot damage and ablation or for few first shots of multi-shot ablation at low repetition rates. As it is shown below, presented model has good qualitative agreement with many experimental regularities of femtosecond laser-matter interactions.

4.2. Description of SHEW

Detailed investigation of SHEW formation and propagation is out of aims of presented in this paper model. We use below results of our investigations obtained in the framework of the model of SHEW propagation in unperturbed dielectric [15, 16]. Throughout this paper we consider propagation of linearly polarized plane homogeneous wave in direction x with electric-field vector along y -axis. Propagation of high-power plane wave is accompanied by formation of field disruptions on optical cycle [15, 16] referred to as shock electromagnetic waves (SHEW). Several initial stages of SHEW formation are depicted in Fig. 2.

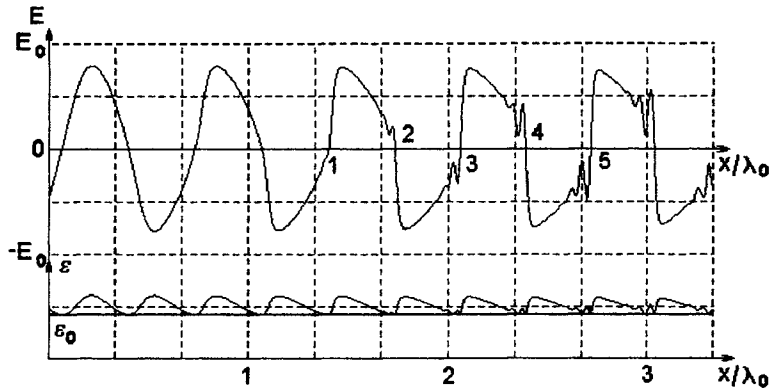


Fig. 2. Formation of SHEW in fused silica (results of FDTD modeling from [15, 16]). 1 – appearing of field disruption, 2 – the disruption turns into abrupt SHEW front, 3, 4, 5 – developing of high-frequency vibrations near SHEW front. Lower part of this figure depicts field-induced variations of dielectric function.

As one can see in Fig. 2, abrupt SHEW front can be approximated by linear dependence on space coordinate for early steps of SHEW propagation while the rest of laser-radiation period looks like unperturbed or lightly perturbed part of sine. In the first approximation we can neglect field distortions near SHEW front appearing during SHEW propagation and take into account other important SHEW feature – becoming of its front more sharper with developing of SHEW. Bearing this in mind, we use below the following approximate description of SHEW (Fig. 3). SHEW front is approximated by linear dependence, and front depth Δ varies from $0.1\lambda_0/n_0$ (weak SHEW describing initial stages of its formation) to $0.01\lambda_0/n_0$ (strong SHEW at late stages of its formation). Other part of wave profile is approximated by a part of sine dependence.

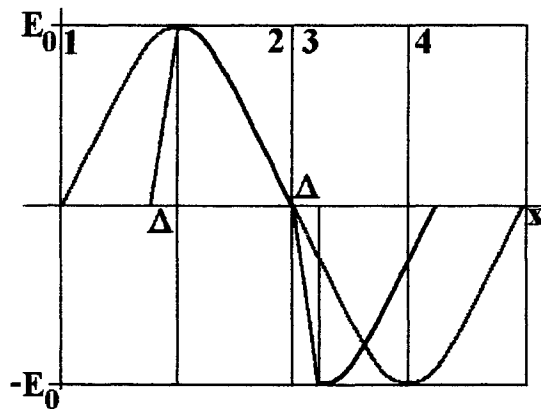


Fig. 3. Approximate description of SHEW for investigation of interactions between SHEW front and transparent material with positive nonlinear coefficient of refractive index (focusing nonlinearity). SHEW is shown by black line while one cycle of harmonic wave is shown by grey line. SHEW fronts of depth Δ appear within the second and the third quarters of initial laser wavelength and are described by linear function. The fronts are considered to move with speed V of SHEW given by (7). Harmonic wave of initial laser frequency is shown with grey for comparison.

General feature of SHEW is decreasing of effective laser period due to formation of SHEW and generation of HH. Accepting proposed above model of SHEW, we use the following description of electromagnetic field:

$$\begin{aligned} 1. E(x, t) &= R \cdot (x - V \cdot t), \quad R = \frac{\partial E}{\partial x}; \\ 2, 3. E(x, t) &= E_0 \cdot \sin(kx - \omega \cdot t); \\ 4. E(x, t) &= R \cdot (x - \lambda_{SEW} - V \cdot t) \end{aligned} \quad (6)$$

This hybrid wave is assumed to move without distortions at speed of SHEW that depends on value of electric-field strength E and electric induction D before SHEW front E_1, D_1 and behind it E_2, D_2 :

$$V = \frac{c_0 \cdot (E_2 - E_1)}{\mu_0 \cdot (D_2 - D_1)} \quad (7)$$

One more important feature of SHEW to be taken into account is threshold of its formation [15, 16] estimated by simple formula

$$E_{th} \approx \sqrt{\frac{n_0}{n_2} \left(\exp \left\{ \frac{\delta x}{l_D} \right\} - 1 \right)}, \quad (8)$$

where δx is length of wave profile that collapses during wave overturning and formation of abrupt SHEW front, l_D is length of path in nonlinear transparent medium passed by one optical cycle upto the moment of SHEW front formation. It is obvious, that $\delta x \leq \lambda/4$ while l_D depends on focusing system and can reach several tens of λ for typical focusing systems [15, 16]. For example, considering strong SHEW which front appears due to mashing of a quarter of optical cycle, one obtains $I_{th} \approx 6 \cdot 10^{13} \text{ W/cm}^2$ for $\delta x = \lambda/4$, $l_D = 30 \lambda$, $n_0 = 1.45$, $n_2 = 2 \cdot 10^{-16} \text{ cm}^2/\text{W}$ (corresponds to fused silica). Thus, strong SHEW can appear at laser irradiance close to damage and ablation threshold.

At last, we should mention one more important property of SHEW which is incubation of its action on a dipole. Really, as one can see from Fig. 2 and (4), SHEW front always acts in the same direction in contrary to action of harmonic wave. That happens due to breaking of symmetry of harmonic waves resulting from formation of SHEW front (Fig. 3). Moreover, interaction of SHEW front with a dipole can be especially effective because a sine part of deformed optical cycle forms a dipole, which reaches its maximum value before it begins to interact with SHEW front. Thus, mechanical force (4) reaches its maximum value due to "pre-action" of sine part of optical cycle moving before SHEW front.

4.3 Classical description of SHEW action on dielectric

In general case the problem of SHEW interaction with transparent materials is very complicated and it should be attacked within quantum-mechanical approach. In spite of that we start consideration of this problem with classical model when electric field of laser radiation is described by classical electrodynamics (that is quite correct for high-power radiation) and motion of structural units of crystal is described by equations of classical mechanics. Advantages of that approach are quite clear:

- 1) obtaining of simple model and equations that can be integrated;
- 2) developing of clear intuitive insight into the problem of SHEW-matter interactions;
- 3) possibility of comparison with similar results for plane harmonic waves [for example, 1, 26].

Developing of quantum-mechanical approach for considered problem is the next natural step to be done by the authors. Nevertheless, we touch some quantum-mechanical effects playing important role in SHEW interaction with solids in final section of this paper.

Structural units of ionic crystal that interact with SHEW are as follows:

- | | |
|--|----------------|
| <ul style="list-style-type: none"> • ionic pair, which composes basis of lattice • single ion • neutral atom* | } dipoles |
| <hr/> <ul style="list-style-type: none"> • single ion* • free electron* | |
| | single charges |

Among them asters denote structural units that should be considered as defects in ideal crystal lattice. Interaction of a single ion with SHEW is considered within two models – model of charged dipole and model of single charge – to compare two types of SHEW action on the ion.

In the simplest model of SHEW interaction with crystal lattice and defects there should be taken into account the following factors: 1) action of SHEW electric field described by force $F_{SHEW}=qE$ for each single charge; 2) bonding force appearing due to particle motion in a potential well $U(x)$ and described by force $F_U=-\nabla U$; 3) damping due to energy transfer to surrounding particles described by damping force $F_D=m\gamma dr/dt$ where γ is damping constant. Considering motion of single charge $q=Ne$ consisting of N units of electron charge e , we use the following equation:

$$m \cdot \frac{d^2 \mathbf{r}}{dt^2} = N \cdot e \cdot \mathbf{E} - m \cdot \gamma \cdot \frac{d\mathbf{r}}{dt} - \nabla U \quad (9)$$

where $\mathbf{r}=(x, y, z)$. In case of single free charge (free electron) the latter term in right-hand part of (9) disappears.

Motion of a dipole consisting of two particles with masses m_1 and m_2 with charges of $q=Ne$ should be described by a couple of equations similar to (9) written for each charge forming the dipole. Those equations can be transformed into system of other two equations. The first of them describes motion of mass center of the dipole

$$M \frac{d^2 \mathbf{R}}{dt^2} = N \cdot e \cdot (\mathbf{d}, \nabla) \cdot \mathbf{E} - M \cdot \gamma \cdot \frac{d\mathbf{R}}{dt} - \nabla U, \quad (10)$$

and the second one describes motion of the charges with respect to each other, i.e., variations of dipole momentum:

$$m_{1,2} \frac{d^2 \mathbf{d}_{1,2}}{dt^2} = -m_{1,2} \omega_0^2 \mathbf{d}_{1,2} - m_{1,2} \gamma \cdot \frac{d\mathbf{d}_{1,2}}{dt} + Ne \mathbf{E}, \quad (11)$$

where d is dipole length. Equations (9) - (11) do not include terms describing action of magnetic field that is very small as compared to F_{SHEW} for particle speeds much below speed of light.

Bearing in mind geometry of plane wave (electric-field vector is along y -coordinate axis while the wave moves along x -coordinate axis), one can separate vector equations (9) - (11) and reduce them to simpler form. For example, single free charge moves in y -direction under action of electric field of SHEW according to equation

$$m \cdot \frac{d^2 y}{dt^2} = N \cdot e \cdot E - m \cdot \gamma \cdot \frac{dy}{dt} \quad (12)$$

while its motion in x -direction is managed by damping force only:

$$m \cdot \frac{d^2 x}{dt^2} = -m \cdot \gamma \cdot \frac{dx}{dt} \quad (13)$$

Thus, single charges move in y -direction under action of SHEW. Similar transformation can be done for equations (10) - (11). Then separated equations can be integrated in quadratures for accepted model of SHEW (6). As a result one obtains speed of motion in a certain direction, and kinetic energy transferred from SHEW wave of amplitude E_0 to the particles can be found. In the first approximation damping can be neglected because duration of SHEW-front action is much less than usual value of $1/\gamma$. Then one can obtain the following expressions for energy transferred from single SHEW front to

- single free charge $q=Ne$:
$$W^+ = \frac{1}{8} \frac{N^2 e^2 E_0^2 \Delta^2}{m V^2} \quad (14)$$

- ion $q=Ne$ in potential well (bonded single charge):
$$W^+ = \frac{N^2 d_0^2 e^2 R^2}{2 m_i \omega_0^2} \left(\sin^2 \left(\frac{\Delta \cdot \omega_0}{V} \right) - \frac{\omega_0 \Delta^2}{2 V d_0} \right)^2 \quad (15)$$

- dipole with momentum $p=d_0(Ne)$:
$$W^+ = \frac{1}{2} \frac{d_0^2 (Ne)^2}{M \omega_0^2} R^2 \sin^2 \left(\frac{\Delta \cdot \omega_0}{V} \right) \quad (16)$$

Obtained expressions (14) - (16) can be used for

- 1) calculating of absorption of SHEW energy due to its transfer to various structure particles of crystal lattice;
- 2) calculation of SHEW amplitude required for moving particles away from their potential wells.

In order to calculate energy dissipation near SHEW front one should add energy of absorbed HH to the energy (14) - (16)

transferred to various types of particles in dielectric.

Moving away an electron from its potential well means ionization by SHEW and formation of color center. As one can see from (15) at $N=1$, SHEW can produce ionization (referred to as straight SHEW-induced ionization) even if all HH have so small photon energy that cannot ionize the material. Moving of a dipole away from its well means laser-induced delocalization of crystal points and formation of point defect like a vacancy or interstitial. SHEW-induced delocalization of crystal points at surface of material is desorption or ablation [1]. As one can see from (14) – (16), all those processes depend on depth of SHEW front Δ . One interesting conclusions from (14) – (16) is that SHEW-induced straight ionization and moving a single ion away from its potential well is more effective than moving away an atom because energy transferred from single SHEW front to the ion is about an order of magnitude higher than energy transferred to an atom. For pure theoretical interest we estimate below also threshold of straight ionization.

5. RESULTS OF THEORETICAL ANALYSIS

Equations (14) – (16) allow calculating of threshold amplitude of SHEW for corresponding processes in the following way. One should assume kinetic energy of a particle to be equal to depth of potential well U_0 for ions at crystal lattice (threshold of laser-induced delocalization) and U_0^e for electron in valence band. That means we calculate intensity of laser field at which kinetic energy transferred from single SHEW front is close to maximum potential energy of bonded particle. The depth of potential well for electron is about band gap, i.e., 7.5 eV for fused silica. Potential well depth for ion at crystal lattice can be estimated as follows. To melt a piece of dielectric with mass m consisting of $N=N_A m/M$ particles (M is molecular weight, $N_A=6.022 \cdot 10^{23}$ 1/mol – Avogadro number), one should transfer to it the following amount of energy:

$$Q = \int_{T_0}^{T_{melt}} m \cdot C(T) \cdot dt$$

where T_{melt} is melting temperature, C is heat capacity per kg. Energy transferred to single particle during melting is given by $\delta Q = Q/N$. Considering 1 m³ of fused silica (density $\rho = 2.2 \cdot 10^3$ kg/m³, $C(293 \text{ K})=890$ J/(kg K), $C(873 \text{ K})=1000$ J/(kg K), $C(1473 \text{ K})=1140$ J/(kg K), $T_{melt}=1480$ K, $M=60.1$ kg/kmol) one can obtain estimation of potential well depth: $U \approx \delta Q = 0.8$ eV.

Using obtained equations and data, one obtains the following estimations for SHEW amplitudes:

1) threshold of removing of an ion (N -charged dipole) or electron from potential well

$$E_0^* = \frac{\Delta \cdot \sqrt{2m_e(U_0^e - W_0^e)}}{Ne \left| \frac{d_0}{\omega_0} \sin\left(\frac{\Delta \cdot \omega_0}{V}\right) - \frac{\Delta^2}{2V} \right|} \quad (17)$$

2) threshold of removing of neutral dipole from potential well

$$E_0^{**} = \frac{\Delta \cdot \omega_0 \sqrt{2M(U_0 - W_0)}}{ed_0 \left| \sin\left(\frac{\Delta \cdot \omega_0}{V}\right) \right|} \quad (18)$$

where W_0 and W_0^e are initial kinetic energies of corresponding particles in absence of SHEW.

One of the most interesting result following from (17) and (18) is that for rather weak SHEW (front depth $\Delta \approx 0.1\lambda$) ionization takes place before delocalization of ions and the latter always take place before neutral dipoles are moved away from their potential wells. But there is an area of SHEW parameters within which removing of dipole from potential well occurs at lower amplitude of electric-field strength than ion delocalization:

$$\frac{E_0^{**}}{E_0^*} = \frac{N \sqrt{M(U_0 - W_0)}}{\sqrt{m_e(U_0^e - W_0^e)}} \left| 1 - \frac{\Delta}{2d_0} \right| \quad E_0^{**} \ll E_0^* \text{ when } \Delta \approx 2d_0, \quad (19)$$

where dipole size d_0 is about atom size $2a \approx 1\text{Å}$.

Other interesting result is tend of ionization and atom delocalization thresholds to certain limits with decreasing of SHEW

front depth:

$$E_{LIM}^* = \frac{V \sqrt{2m_e(U_0^e - W_0^e)}}{Ned_0} \quad (20)$$

$$E_{LIM}^{**} = \frac{V \cdot \sqrt{2M(U_0 - W_0)}}{Ned_0} \quad (21)$$

Among SHEW parameters only SHEW speed influences on the limiting values of the thresholds. Their ratio is constant and $E_{LIM}^{**}/E_{LIM}^* = (M/m_e)^{0.5} \approx 60$ for fused silica and most glasses.

Using (17) – (18) one can obtain estimations of ionization, ion and atom delocalization thresholds to be produced by single front of weak and strong SHEW (Table 1). Parameters used for estimations are as follows: $N=1$, $e=1.6 \cdot 10^{-19}$ Coulombs, $d_0=10^{-10}$ m, $\omega_0=10^{14}$ Hz, $m_e=9.1 \cdot 10^{-31}$ kg, $M=1.6 \cdot 10^{-26}$ kg, depth of dipole's and ion's potential wells $U_0=1$ eV, ionization potential $U_0^e=8$ eV. Initial kinetic energies of both ion and dipole are assumed to be zero. As one can see from Table 1, those thresholds are much higher than interatomic electric-field strength that points out at limited applicability of classical description to consideration of SHEW-induced processes.

Table 1. Estimations of ionization and delocalization thresholds for weak and strong SHEW

Threshold of ionization and ion delocalization	Threshold of removing of a dipole from potential well
<i>for weak SHEW ($\Delta \approx 0.1\lambda$)</i>	<i>for weak SHEW ($\Delta \approx 0.1\lambda$)</i>
$I_{TH} = 10^{17}$ W/cm ² ($E_{TH} = 3 \cdot 10^9$ V/cm)	$I_{TH} = 10^{19}$ W/cm ² ($E_{TH} = 3 \cdot 10^{10}$ V/cm)
<i>for strong SHEW ($\Delta \approx 0.01\lambda$)</i>	<i>for strong SHEW ($\Delta \approx 0.01\lambda$)</i>
$I_{TH} = 10^{13}$ W/cm ² ($E_{TH} = 3 \cdot 10^7$ V/cm)	$I_{TH} = 10^{15}$ W/cm ² ($E_{TH} = 3 \cdot 10^8$ V/cm)

6. DISCUSSION AND CONCLUSIONS

Formation and propagation of SHEW presents a complicated self-consistent problem because SHEW propagates in a medium with parameters changed by the SHEW. As it was proposed in [15, 16], that problem can be reduced to two independent problems – propagation of SHEW in a medium with unperturbed properties and interaction of unperturbed SHEW with dielectric where it propagates. The first problem is considered in [15, 16] while the second problem is considered in this paper. Thus, all obtained results can describe only early steps of SHEW propagation and interaction with solids when SHEW-induced variations of optical parameters are so small as to be neglected without.

It is also evident limited applicability of classical approach to description of SHEW interaction with transparent solids. That has resulted in extremely large estimations of ionization and delocalization thresholds obtained within classical description (Table 1). One should also take into account mentioned above incubation effect for action of SHEW on dipoles. Thus, if 10 laser cycles (the largest number of optical cycles where SHEW can appear according to used approximation [16]) can pass through a dipole, then the latter accumulates energy from all of them. Then thresholds estimated in Table 1 decreases by factor of 10 but they still stay high. Correct consideration should be based on quantum-mechanical approach. One of sufficient quantum effects to be taken into account for more correct description of SHEW interaction with matter is tunneling effect: SHEW can give some initial energy to a dipole that can then tunnel from its original potential well and form lattice defect. Such defects can, in turn, change depth of potential wells in their vicinity resulting in decreasing of delocalization threshold and formation of positive feedback. They also can contribute to linear absorption at basic wavelength and higher harmonics.

Nevertheless, presented approach has several advantages that were mentioned above. The most important of them is intuitive insight into considered problem. On the other hand, classical consideration allows constructing Hamiltonian function that will be substituted by Hamiltonian operator in quantum mechanical approach. One of important aims of presented classical approach is verification of influence of various terms from Hamiltonian on particle motion under action of SHEW.

In spite of limited applicability of obtained results and evident drawbacks of classical approach to investigation of SHEW interactions with matter one can derive several qualitative results that can be true in the framework of quantum-mechanical approach. The first of them is that nonlinear electrodynamical process of SHEW formation and propagation can play important and even key role in damaging and ablation of transparent materials by femtosecond laser. As compared to traditional models, SHEW model give increased efficiency of ionization by higher harmonics generated during SHEW formation. It should be also mentioned that presented model describes formation of localized electronic and vibrational excitations [1] induced by SHEW.

Second, straight action of SHEW front on crystal lattice can result in moving away of atoms and ions from their potential wells, i.e., delocalization and desorption if SHEW acts near the surface. Thresholds of delocalization are usually higher than ionization thresholds except the case of very strong SHEW when front depth is comparable to atomic size. In the limiting case of ideal SHEW with $\Delta \rightarrow 0$ ionization and delocalization thresholds become independent on front depth and their ratio tends to constant level.

Important conclusion is also that SHEW model is in good qualitative agreement with many peculiarities of femtosecond laser-matter interactions (Section 2). Really, very high thresholds of femtosecond damage and ablation are very close to obtained estimation of threshold for SHEW formation (8) what makes proposed model very promising for study of femtosecond laser-induced processes at high laser fluences. Picture of generation of super-continuum becomes more natural when one takes into account generation of higher harmonics characteristic of SHEW formation. This process can also be a model for description of generation of higher harmonics of very high order (21 – 27 in UV and X-ray ranges) observed during femtosecond interactions [10, 16].

Sequence of laser-induced processes during femtosecond damage [12] is also in good agreement with proposed picture of SHEW formation. Really, at early stage of SHEW propagation SHEW front is large and the SHEW is weak, thus, ionization by higher harmonics is much more efficient than delocalization. Increasing of laser fluence results in appearing of string SHEW that can ionize atoms and ions as well as move single atoms and ions away from their positions in crystal lattice. That results on formation of point defects that are not visible. Further increasing of laser fluence makes SHEW so “strong” that density of damaged lattice points becomes large and damaged site becomes visible. Changes of SHEW-induced material structure can vary from appearing of voids (strong SHEW moves away all ions and atoms) to transition from crystal to amorphous structure [12]. Presented model is also in good agreement with absence of thermal damage around ablated and damaged sites because SHEW-induced damage of crystal lattice is very fast process and energy transfer to heat is rather small. Description of thermal effects accompanying multi-shot damage and ablation at high repetition rates is out of aim of this work and will be considered by the authors in other their paper.

7. REFERENCES

1. R.F.Haglund, Jr., “Mechanisms of Laser-Induced Desorption and Ablation”, in *Laser Ablation and Desorption*, eds. J.C.Miller and R.F.Haglund, Jr. (Boston, Academic Press, 1998), pp. 15-138.
2. R.F.Haglund, Jr., “The Future of Laser Ablation”, in *Laser Ablation and Desorption*, eds. J.C.Miller and R.F.Haglund, Jr. (Boston, Academic Press, 1998), pp. 625-640.
3. T.V.Kononenko, V.I.Konov, S.V.Garnov, R.Danielius, A.Piskarskas, G.Tamoshauskas, F.Dausinger, “Comparative study of material ablation by femtosecond and pico/nanosecond laser pulses”, *Quantum Electronics*, v. 28, N 2, pp. 167-172, 1999.
4. B.Rethfeld, A.Kaiser, M.Vicanek, and G.Simon, “Irradiation of solids with subpicosecond laser pulses: excitation and relaxation dynamics of electrons and phonons”, in *High-Power Laser Ablation*, Proc. SPIE, v. 3343, pp. 388-399, 1998.
5. B.C.Stuart, M.D.Feit, S.Herman, A.M.Rubenchik, B.W.Shore, and M.D.Perry, “Nanosecond-to-femtosecond laser-induced breakdown in dielectrics”, *Phys. Rev. B*, v. 53, pp. 1749-1761, 1996.
6. D.von der Linde, H.Schuler, “Breakdown threshold and plasma formation in femtosecond laser-solid interaction”, *JOSA B*, v. 13, N 1, pp. 216-222, 1996.
7. D.Ashkenasi, A.Rosenfeld, H.Varel, M.Wahmer, E.E.B.Campbell, “Laser processing of sapphire with picosecond and sub-picosecond pulses”, *Appl. Surface Science*, v. 120, pp. 65-80, 1997.
8. E.E.B.Campbell, D.Ashkenasi, and A.Rosenfeld, “Ultra-short-Pulse Laser Irradiation and Ablation of Dielectrics”, in *Lasers in Materials*, edited by R.P.Agarwal (Trans Tech Publ., 1998), Ch. 5.
9. R.L.Fork, C.V.Shank, et al, *Opt. Letters*, v. 8, N 1, p. 1, 1983.

10. A.Bouhal, R.Evans, G.Grillon, A.Mysyrowicz, P.Breger, P.Agostini, R.C.Constantinescu, H.G.Muller, D. von der Linde, "Cross-correlation measurement of femtosecond noncollinear high-order harmonics", *JOSA*, v. 14, N 4, pp. 950-956, 1997.
11. R.F.Haglund Jr., R.Cramer, D.R.Ermer, M.R.Papantonakis, H.K.Park, and O.Yavas, "Vibrational Excitation and Relaxation Processes in Insulators Initiated by Ultrashort, Mid-Infrared Laser Pulses", in *Laser Applications in Microelectronic and Optoelectronic Manufacturing IV*, Proc. of SPIE, v. 3618, 1999 (to appear).
12. C.B.Schaffer, E.N.Glezer, N.Nishimura, and E.Mazur, "Ultrafast laser induced microexplosions: explosive dynamics and sub-micrometer structures", in *Commercial Applications of Ultrafast Lasers*, Proc. SPIE, v. 3269, pp. 36-45, 1998.
13. H.K.Park, R.F.Haglund Jr., "Laser Ablation and Desorption from Calcite from Ultraviolet to Mid-Infrared Wavelengths", *Appl. Phys. A*, v. 64, pp. 431-438, 1997.
14. C.B.Schaffer, A.Brodeur, N.Nishimura, and E.Mazur, "Laser-induced microexplosions in transparent materials: microstructuring with nanojoules", Proc. SPIE, v. 3616, 1999, to appear.
15. V.E.Gruzdev, A.S.Gruzdeva, "Formation and propagation of shock electromagnetic waves in transparent solids", in *High-Power Laser Ablation II*, Proc. SPIE, v. 3885, 2000, to appear.
16. V.E.Gruzdev, A.S.Gruzdeva, "Formation of shock electromagnetic waves during femtosecond pulse propagation in transparent solids", in *Optical Pulse and Beam Propagation II*, Proc. SPIE, v. 3927, 2000, to appear.
17. A.A.Oraevsky, L.B.Da Silva, A.M.Rubenchik, M.D.Feit, M.E.Glinsky, M.D.Perry, B.M.Mammini, W.Small, IV, B.C.Stuart, "Plasma Mediated Ablation of Biological Tissues with Nanosecond-to-Femtosecond Laser Pulses: Relative Role of Linear and Nonlinear Absorption", *IEEE J. of Selected Topics in Quantum Electronics*, v. 2, pp.801-809, 1996.
18. A.M.Rubenchik, M.D.Feit, M.D.Perry, J.T.Larsen, "Numerical simulation of ultra-short laser pulse energy deposition and bulk transport for material processing", *Appl. Surf. Science*, v. , 1998.
19. A.M.Beliantsev, et al, *Sov. Phys. - JETP*, v. 35, 1965, p. 677
20. G.B.Whiteham, *Proc. Roy. Soc., Ser. A*, v. 283, 1965, p. 238
21. S.A.Akhmanov, V.I.Emelyanov, N.I.Koroteev, V.N.Seminogov, "Action of high-power laser radiation on surface of metals and semiconductors: nonlinear optical effects and nonlinear optical diagnostics", *Sov. Phys. - Uspehi Phisicheskikh Nauk*, v. 147, N 4, pp.675-745, 1985 (in Russian).
22. A.D.Twarowski, *Chem. Phys. Lett.*, v. 20, N 2, pp. 253-258 and 259-264, 1977.
23. E.W.Van Stryland, M.Sheik-Bahae, A.A.Said, D.J.Hagan, and M.J.Soileau, "Characterization of nonlinear optical materials", in *Laser-Induced Damage in Optical Materials: 1993*, Proc. SPIE, v. 2114, pp. 444-468, 1994.
24. M.N.Libenson, private communications.
25. D.Du, X.Liu, G.Korn, J.Squier, and G.Mourou, *Appl. Phys. Lett.*, v. 64, p. 3071, 1994.
26. E.Mazur, "Interaction of Ultrashort Laser Pulses with Solids", in *Spectroscopy and Dynamics of Collective Excitations in Solids*, ed. B.Di Bartolo, Plenum, NATO ASI series, 1996.
27. A.Brodeur, S.L.Chin, "Band-Gap Dependence of the Ultrafast White-Light Continuum", *Phys. Rev. Lett.*, v. 80, N 20, pp. 4406-4409, 1998.

Analysis of Laser Ablation Process in Semiconductor Due to Ultrashort Pulsed Laser with Molecular Dynamics Simulation

Koji WATANABE, Yuri Ishizaka, Etsuji OHMURA and Isamu MIYAMOTO

Department of Manufacturing Science, Graduate School of Engineering, Osaka University
2-1, Yamada-Oka, Suita, Osaka 565-0871, Japan

ABSTRACT

Rapid fusion and evaporation phenomena of silicon with ultrafast laser irradiation were simulated using the three-dimensional molecular dynamics. Surface structure dependence of laser shock phenomena, fusion and evaporation process was examined for the Si (100) and Si (111) surface structures. It was shown that the crystal orientation influences the propagation velocity of shock wave and that heat conduction but laser absorption in the material, that is, absorption coefficient affects the fusion depth when the pulse width is subpicosecond.

Keywords : Ultrafast laser, Laser ablation, Silicon, Molecular dynamics, Fusion, Evaporation, Crystal orientation

1. INTRODUCTION

Silicon (Si) is usually used for electronic components and is also useful as a material of micromachine. Therefore microfabrication of Si becomes more and more important. On the other hand, ultrafast lasers whose pulse width is picosecond or subpicosecond have been developed in recent years, and are expected as a tool of microfabrication. It is difficult to elucidate experimentally various process phenomena in the microfabrication with such an ultrafast laser. Over the years, Ohmura et al. [1-3] have carried out two dimensional molecular dynamics simulation, and have been making the ablation phenomena of metal and Si with ultrafast laser irradiation clear.

By the way, it has been reported that etching rate and surface roughness depend on the surface structure in the anisotropic etching of Si [4,5] and cutting force also depends on the crystal orientation in the cutting of Si [6]. In this study, the surface structure dependence of ablation phenomena of Si with ultrafast laser was studied by the three-dimensional molecular dynamics method using the three-body potential proposed by Stillinger-Weber [7]. Simulations were carried out with laser beam of uniform intensity distribution and Gaussian beam. In the former simulation, laser shock phenomena in Si (100) and Si (111) surface structures were compared. Then both surface structure dependence and pulse width dependence of fusion depth were examined. In evaporation process, the amount of removal atoms and scattering velocity of evaporated atoms were analyzed quantitatively. In the simulation with Gaussian beam, we investigated fusion process, evaporation process and the deposition process around the hole.

2. SIMULATION METHOD

Single crystal Si has a diamond structure with covalent bonds. The ideal diamond structure has regular tetrahedral

structure. Therefore, three- or many-body potentials must be considered for Si. Stillinger-Weber potential is one of such potentials, which is given by

$$\phi_i = \sum_{j \neq i} v_2(r_{ij}) + \sum_{\substack{j \neq i \\ k \neq i, j}} v_3(r_i, r_j, r_k) \quad (1)$$

where r_{ij} is the distance between two atoms i and j , r_i , r_j and r_k are the position vectors of atoms i , j and k , respectively. The function v_2 , which is given by Eq. (2), is a pair potential, and the function v_3 , which is given by Eq. (3), is a triplet potential.

$$v_2(r_{ij}) = \epsilon f_2(r_{ij}/\sigma) \quad (2)$$

$$v_3(r_i, r_j, r_k) = \epsilon f_3(r_i/\sigma, r_j/\sigma, r_k/\sigma) \quad (3)$$

where ϵ indicates the strength of bond and σ indicates the size of atom. The function f_2 , which depends only on scalar distance between each atom, is given by Eq. (4) and the function f_3 , which depends on full translational and rotational symmetry in addition to the scalar distance, is given by Eq. (5).

$$f_2(x_{ij}) = \begin{cases} A(B/x_{ij}^p - 1/x_{ij}^q) \exp[1/(x_{ij} - a)], & x_{ij} < a \\ 0, & x_{ij} \geq a \end{cases} \quad (4)$$

$$f_3(x_i, x_j, x_k) = h(x_{ij}, x_{ik}, \theta_{jik}) + h(x_{ji}, x_{jk}, \theta_{ijk}) + h(x_{ki}, x_{kj}, \theta_{ikj}) \quad (5)$$

where θ_{jik} is the angle between two vectors $x_j - x_i$ and $x_k - x_i$. The function h is given by Eq. (6).

$$h(x_{ij}, x_{ik}, \theta_{jik}) = \lambda \exp[\gamma(x_{ij} - a)^{-1} + \gamma(x_{ik} - a)^{-1}] \left(\cos \theta_{jik} + \frac{1}{3} \right)^2. \quad (6)$$

The parameter concerning Si is indicated as follows:

$$\begin{aligned} \epsilon &= 2.1672 \text{ eV}, \sigma = 0.20951 \text{ nm}, A = 7.04955677, B = 0.6022245584, \\ p &= 4, q = 0, a = 1.8, \lambda = 1.2 \end{aligned}$$

In the case of the simulation with laser beam of uniform intensity distribution, periodic boundary condition is given to the side surface and natural boundary condition is given to the bottom surface. Assuming 200 atoms per layer parallel to the surface, we take 240 layers in the depth direction, yielding an atomic configuration of a total of 48000 atoms as the Si (100) surface structure. For the Si (111) surface structure, 240 atoms per layer, 210 layers, and a total of 50400 atoms are arranged. In the case of the simulation with Gaussian beam, natural boundary condition is given to the interior surface. Assuming 800 atoms per layer parallel to the surface, we take 120 layers in the depth direction, yielding an atomic configuration of a total of 96000 atoms as the Si (100) surface structure. For the Si (111) surface structure, 896 atoms per layer, 108 layers, and a total of 96768 atoms are arranged.

Two-dimensional model which Ohmura et al. [1-3] have proposed is expanded into the present three-dimensional model, that is, the configuration method of the initial atomic-array model, laser absorption model of crystal and

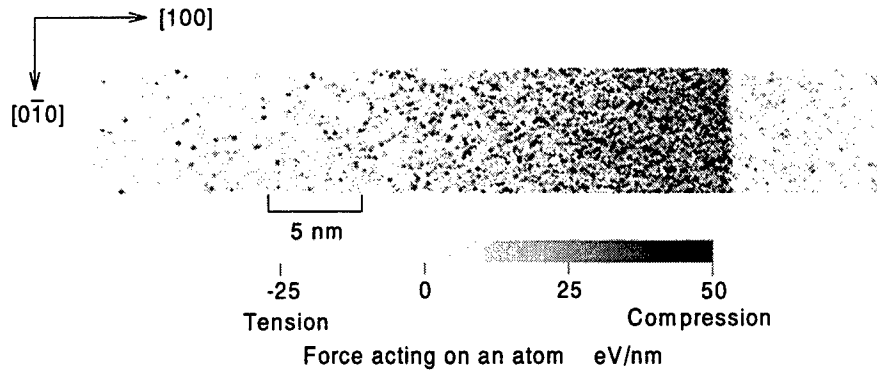


Fig.1 Stress state of Si atoms during laser irradiation, which is shown by a gray scale (laser power 50 GW/cm², pulse width 1 ps, time 2.5 ps).
Left end of the scale corresponds to the position of the initial surface

estimation method of microscopic stress state of atoms are also applied here. It is postulated that the laser beam is the fourth harmonics of Nd:YAG laser whose wave length is 266 nm. Absorption coefficient of Si for the fourth harmonics of Nd:YAG laser is 2.09×10^8 1/m [8].

3 RESULTS AND DISCUSSION

3.1 Propagation of shock wave

When the uniform intensity laser beam of power density 50 GW/cm² and pulse width 1 ps is irradiated to the Si (100) surface, the microscopic stress state of Si atoms in the depth direction at the time 2.5ps is shown in **Figure 1**. The gray scale shows the force acting on an atom. Compressed field occurs in the material due to the laser shock. **Figure 2** shows the relationship between the force acting on an atom and the depth from the initial surface in Figure 1, where compression and tensile force are positive and negative, respectively. Force acting on an atom is plotted every 0.5 nm depth after calculating the average value of each section. Shock wave is generated and its peak intensity

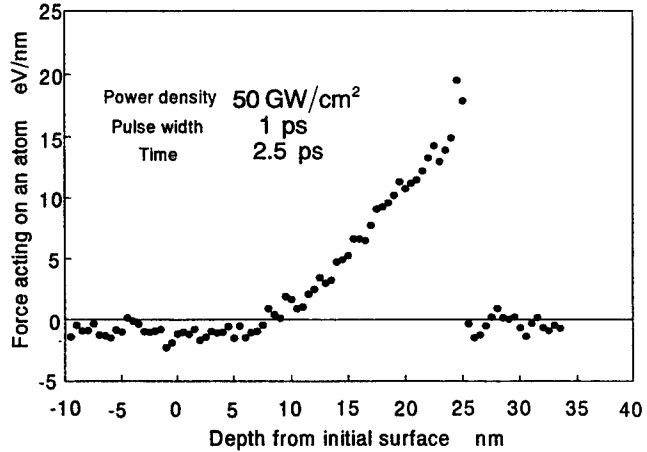


Fig. 2 Thermal shock wave in Fig. 1

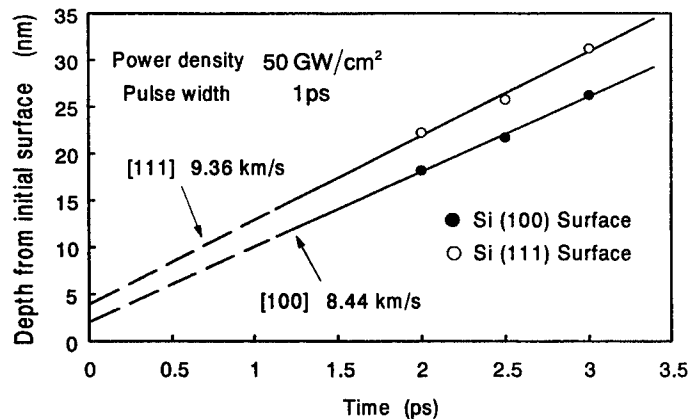


Figure 3 Transition with time of the peak intensity of shock wave

position is at the neighborhood of depth 25 nm. We call this position peak intensity position. The area where the number density of atoms becomes high due to thermal expansion is stressed compressively, therefore the wave front of shock wave at this time is steep and waveform of the shock wave is almost a right triangle.

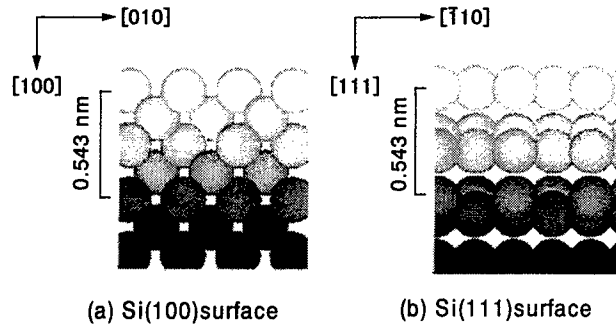


Figure 4 Atomic configurations in the Si (100) and (111).

An example of transition with time of the peak intensity position of the shock wave is shown in **Figure 3**, when the laser of power density 50 GW/cm² and pulse width 1 ps is irradiated to the Si (100) and Si (111) surfaces. The vertical axis shows the peak intensity position that is evaluated by the depth from the initial surface and the horizontal axis shows the time after the laser irradiation starts. Each gradient of these lines is the elastic wave velocity of each gradient, which are 8.44 km/s in the Si [100] direction and 9.36 km/s in the Si [111] direction and these are given by elastic theory. It is found that the propagation velocity of shock wave agrees well with the velocity of elastic wave in Si and its velocity to [111] direction is faster than that to [100] direction. This fact is very important to understand the fusion and evaporation phenomena. **Figure 4** shows the atomic configurations in the Si (111) and Si (100) surface structures. The atomic configuration in the Si (111) surface structure has the layer structure to [111] direction that is depth direction. This layer structure is the reason why the lattice vibration, therefore the elastic wave or the shock wave, travels to Si [111] direction much faster than to Si [100] direction. This also means that the thermal conductivity to Si [111] direction is larger than that to Si [100] direction.

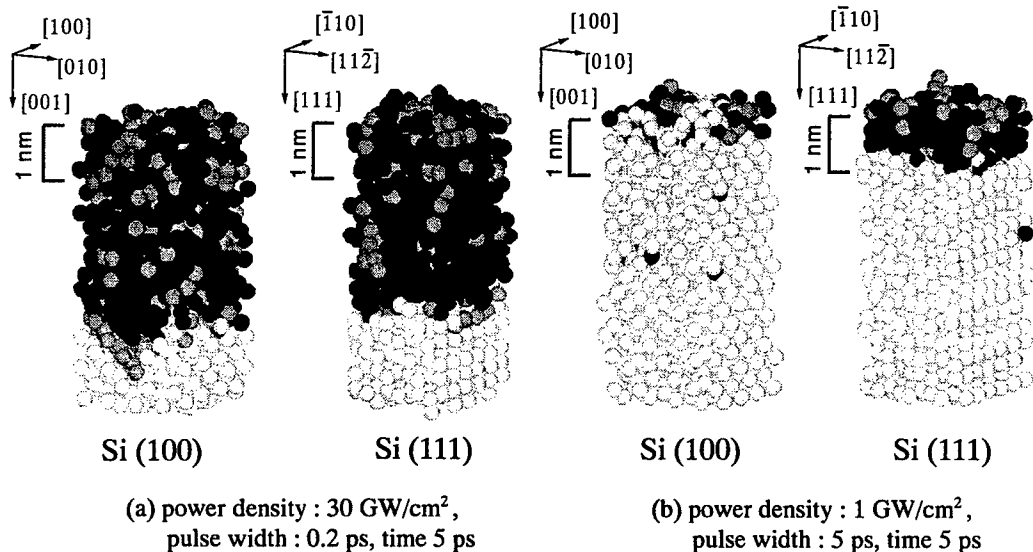


Figure 5 Surface structure and pulse width dependence of fusion phenomena.

3.2 Fusion phenomena

Uniform intensity laser beam of power density 30 GW/cm^2 , pulse width 0.2 ps and power density 1 GW/cm^2 , pulse width 5 ps are irradiated to the Si (100) surface and Si (111) surface. Their fusion processes are shown in **Figure 5**. In order to evaluate the fusion depth, we propose a method to discriminate fused atoms. A white sphere shows an atom whose adjacent atoms are not different from the initial configuration, therefore the number of the adjacent atoms is still four. A gray sphere shows an atom whose number of the adjacent atoms is still four but at least one of them is different from the initial configuration. A black sphere shows an atom whose number of the adjacent atoms is not four, as a consequence, we define black spheres the fused or evaporated atoms.

In Figure 5 (a), the fusion depth does not depend on the surface structure, therefore it can be understood that laser absorption in the material, that is, absorption coefficient becomes predominant when pulse width is as short as 0.2 ps . On the other hand, we can see from Figure 5 (b) that the fusion depth to Si [111] direction becomes larger than that to Si [100] direction when the pulse width is 5 ps . These phenomena can be explained by the fact that the thermal conductivity to Si [111] direction is larger than that to Si [100] direction as above mentioned, and the influence of heat conduction becomes larger than that of laser absorption in the material when the pulse width becomes large.

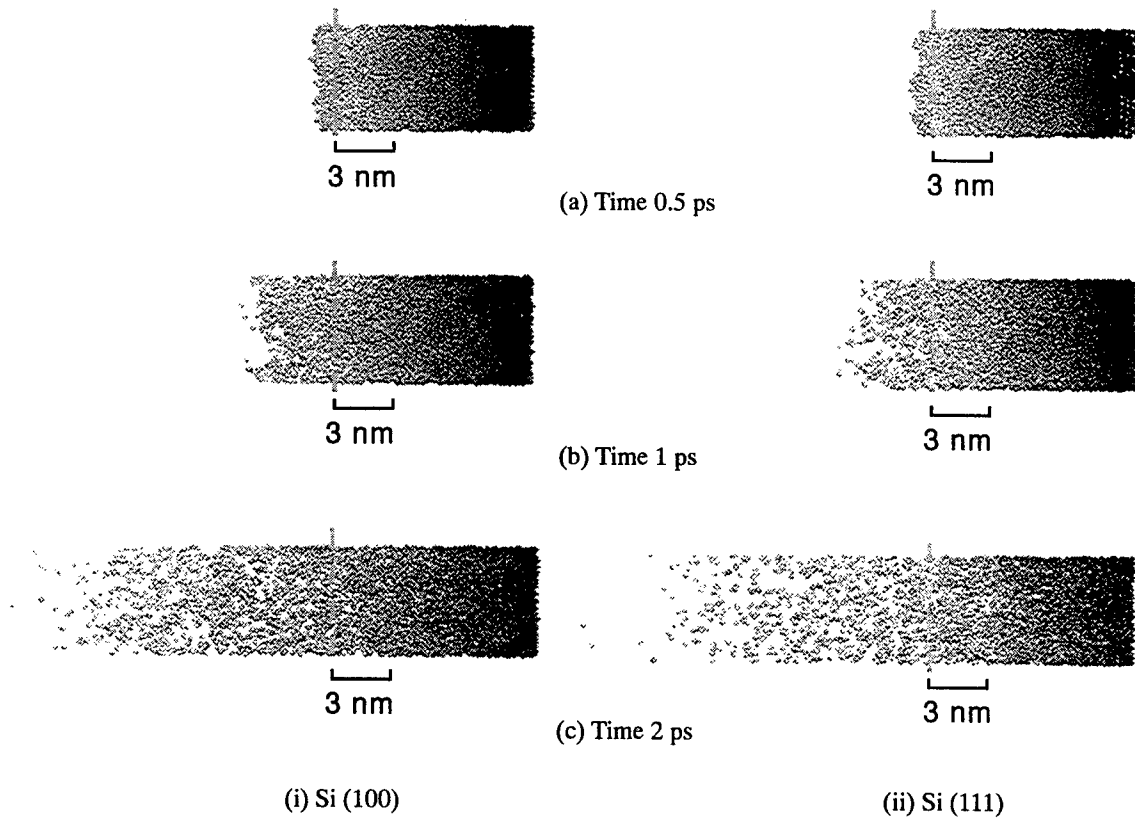


Figure 6 Comparison of evaporation phenomena between Si (100) and (111).
(laser power density : 50 GW/cm^2 , pulse width : 1 ps)

3.3 Evaporation process and velocity of evaporation atoms

Snapshots of evaporation process of Si are shown in **Figure 6**, where uniform intensity laser beam of power density 50 GW/cm² is irradiated to the Si (100) surface and Si (111) surface for 1 ps. A gray scale corresponds to the layer number in the direction in the initial atomic configuration. At 0.5 ps during laser irradiation, little evaporation occurs from both Si (100) surface and Si (111) surface (see **Figure 6 (a)**) and evaporation almost starts after stopping the laser irradiation at the time 1 ps (**Figure 6 (b)** and **Figure 6 (c)**).

Rosenfeld et al. [9] estimated the

evaporation start time of dielectric with laser beam of pulse width 0.12 ps, pulse energy about 50 mJ and wave length 800 nm by measuring the scattering intensity of probe laser. They reported that the delay time of evaporation depends on the material and it is 3 ps for amorphous and crystalline quarts, 12 ps for sapphire and 20 ps for MgO, for example, that is, there is delay time of ps order usually. The material in our simulation is different from them but our results are at least consistent with their results. **Figure 6** also shows that the evaporation from Si (100) surface is more remarkable than that from Si (111) surface. Namba et al. [10] experimentally investigated the removal rates from Si (100) and Si (111) surface structures with a pulsed ultraviolet laser of maximum fluence 0.95 J/cm² and repetition rate 3 Hz. They reported that the removal rate were 4.1×10^{-2} nm/pulse and 3.2×10^{-2} nm/pulse for Si (100) surface and Si (111) surface, respectively. Our simulation result does not also contradict their result.

Figure 7 shows the number of evaporated atoms from Si (100) surface and Si (111) surface, when the pulse width is 0.1 ps, 1 ps and 5 ps under the constant laser fluence 50 mJ/cm². When the pulse width is 1 ps and 5 ps, the number of evaporated atoms from Si (100) surface is about two times of that from Si (111) surface. On the other hand, the number of evaporated atoms from Si (100) surface is almost the same as one from Si (111) surface when the pulse width is as short as 0.1 ps. As the case of fusion depth explanation, when the pulse width is as short as 0.1 ps, the influence of laser absorption, which depends on the absorption coefficient, becomes predominant, therefore the remarkable difference between the surface structure does not appear in the number of evaporated atoms. However, when the pulse width is 1 ps and 5 ps, the number of evaporated atoms from Si (111) surface becomes smaller than that from Si (100) surface, because the heat conduction to the interior in the Si (111) surface structure is larger than that in the Si (100) surface structure as mentioned above.

Figure 8 shows the relationship between the velocity in the height direction of Si atoms in both the evaporated particles and the substrate and the depth from the initial surface in **Figure 6**. The instantaneous velocity distribution of

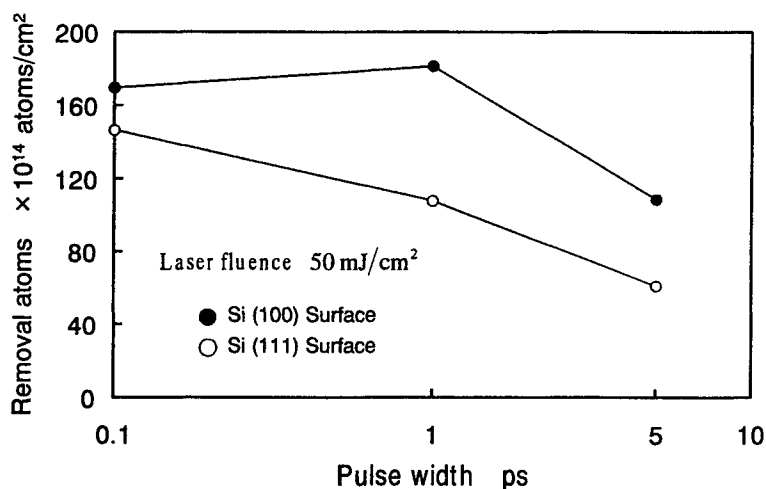
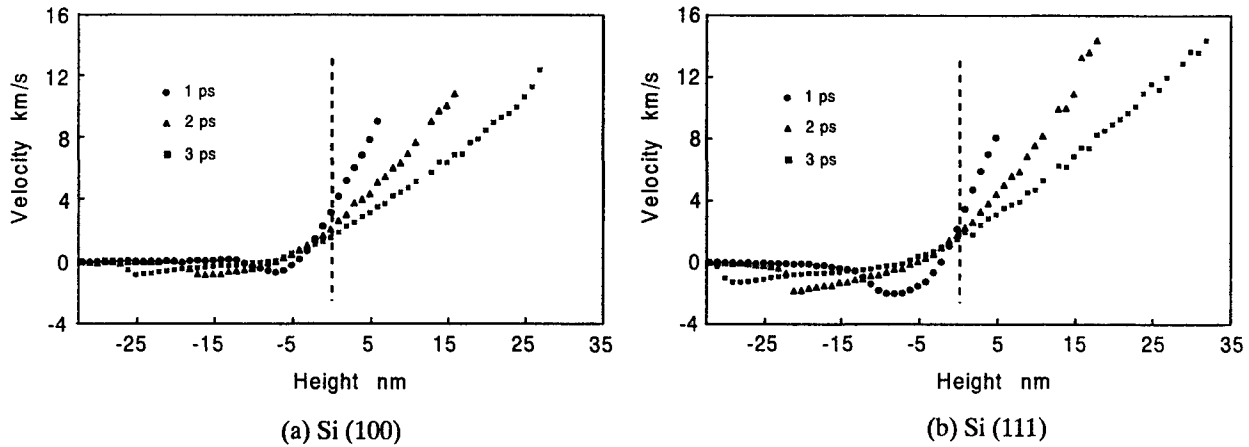


Figure 7 Effect of pulse width and crystal orientation on removal rate.



evaporated atoms is in proportion to the height from the surface, because evaporated atoms with higher velocity fly away

Figure 8 Velocity distribution of evaporated atoms and atoms in the substrate.
(Laser power density : 50 GW/cm², pulse width : 1 ps)

to the higher level. On the other hand, we can see the velocity distribution in the substrate, which has the peak value, and its peak position propagates in the depth direction with time. This phenomenon corresponds to the propagation of the laser shock wave caused by the evaporation recoil pressure (see 3.1).

3.4 Laser ablation process

Snapshots of ablation process of Si with Gaussian beam whose diameter is about 6 nm are shown in **Figure 9**, where the average power density is 100 GW/cm² and pulse width is 0.1 ps. The beam diameter is defined at which the intensity diminishes from its central value by a factor of e^2 . The atom configurations are shown by the three kinds of spheres in the same manner as in Figure 5. The surface rises due to thermal expansion induced by laser absorption at first (see Figure 9 (a)). Then atoms scatter in pieces forming into relatively fine clusters (Figure 9 (b)). Fusing atoms flow out from the molten pool and deposit around the hole (Figure 9 (c)). Evaporation from Si (100) surface occurs early comparing with Si (111) surface. This reason can be explained by the fact that the potential energy of an atom in Si (111) surface, which is -3.22 eV, is lower than that of an atom in Si (100) surface, -2.92 eV, therefore, Si (111) surface is more stable than Si (100) surface.

Figure 10 shows the snapshots of fusion process of Si with Gaussian beam, when the average power density is 5 GW/cm² and pulse width is 1 ps. Disarray in the crystal occurs at the depth 3 - 5 nm during laser irradiation (see Figure 10 (a)), but disappears at the time 1.5 ps (Figure 10 (b)). This phenomenon means the recover of the crystal structure. The fusion depth of the Si (111) surface structure is larger than that of Si (100) surface structure (Figure 10 (c)), as the pulse width is relatively long, as shown in Figure 5 (b).

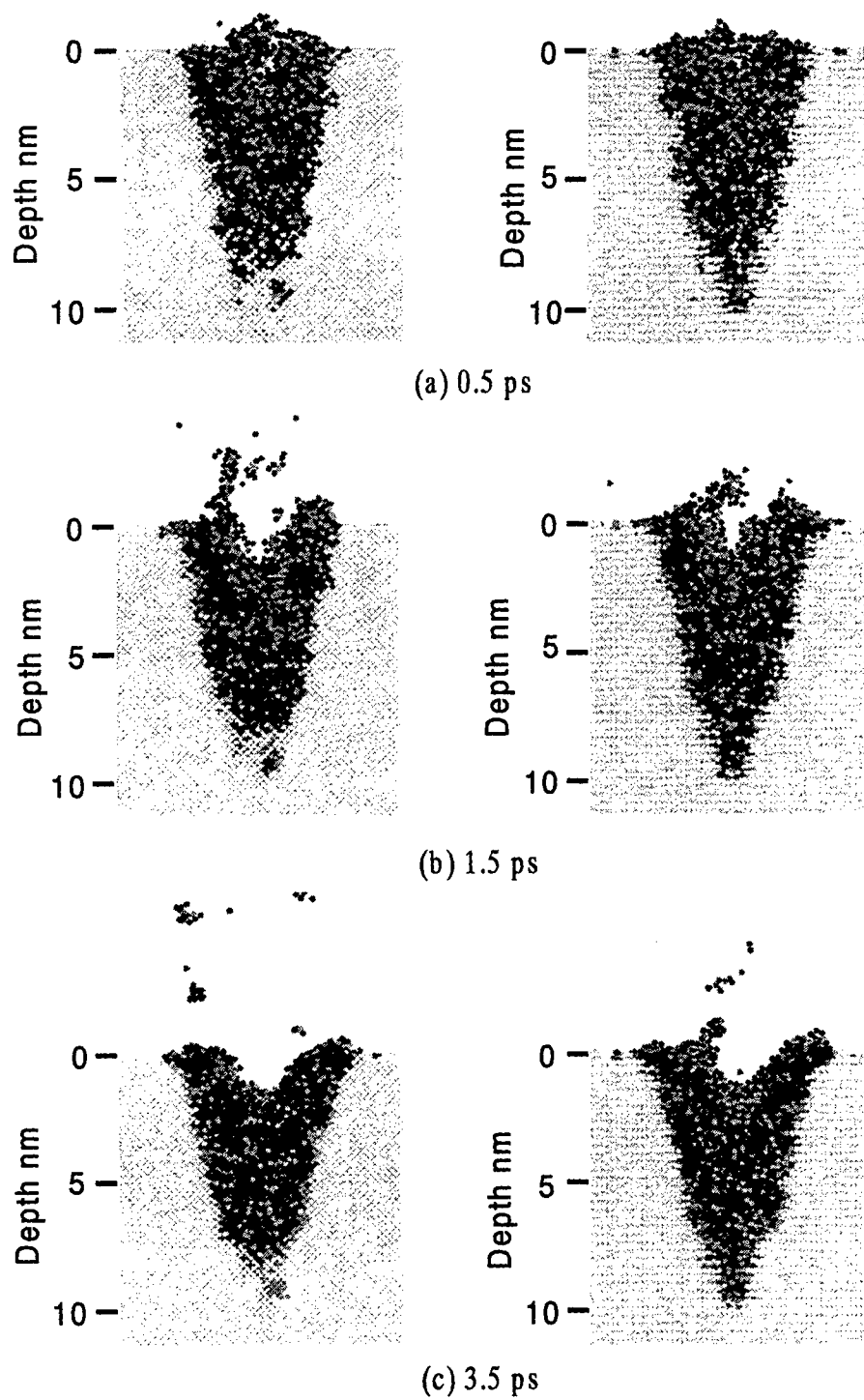


Figure 9 Comparison of ablation process between Si (100) and Si (111).
(Laser power density : $100\text{GW}/\text{cm}^2$, pulse width : 0.1 ps)

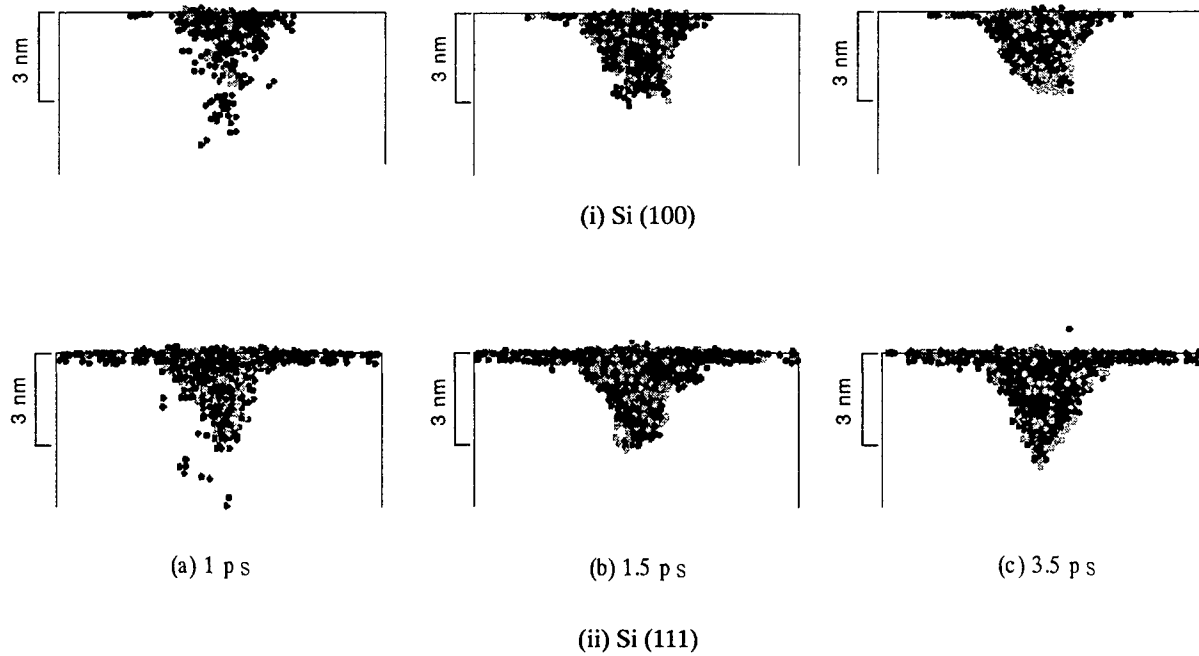


Figure 10 Comparison of fusion phenomena between Si (100) and Si (111).
(Laser power density : 5 GW/cm², pulse width : 1 ps)

4. CONCLUSION

The surface structure and pulse width dependence of ablation phenomena of Si with ultrafast laser was studied by the three-dimensional molecular dynamics method using the Stillinger-Weber potential. Main conclusions obtained are summarized as follows:

- (1) The propagation velocity of the laser induced shock wave agree well with the velocity of elastic wave in each direction, and laser induced shock wave propagates to Si [111] direction faster than to Si [100] direction.
- (2) When the pulse width is subpicosecond, laser absorption in the material is predominant, while heat transfer by lattice vibration becomes predominant in fusion and evaporation phenomena when the pulse width is more than ps order.
- (3) Instantaneous velocity distribution of evaporated atoms is in proportion to the height from the initial surface. The velocity distribution in the substrate has a peak value, and its peak position propagates in the depth direction with time. This phenomenon corresponds to the propagation of the laser shock wave caused by the evaporation recoil pressure (see (1)).
- (4) In ablation process, the surface rises due to thermal expansion induced by laser absorption at first. Then particles scatter in pieces forming into relatively fine cluster. Fusing atoms flow out from the molten pool and deposit around the hole.

ACKNOWLEDGEMENTS

This study was supported by Grants-in-Aid of Scientific Research from the Ministry of Education, Science and Culture of Japan in 1997, 1998 and 1999.

REFERENCES

- [1] E. Ohmura and I. Fukumoto: J. High Temp. Soc. **20** (1984) 228.
- [2] E. Ohmura and I. Fukumoto: Int. J. JSPE **30** (1996) 128.
- [3] E. Ohmura, I. Fukumoto and I. Miyamoto: Int. J. JSPE **32** (1998) 248.
- [4] C. Ju and P.J. Hesketh: Thin Solid Films **215** (1992) 58.
- [5] P.J. Hesketh, C. Ju, S. Gowda, E. Zanolari and S. Danyluk: J. Electrochem. Soc. **140** (1993) 1080.
- [6] E.Brinksmeier, W. Preuss, O.Riemer and R. Malz: Proc. ASPE Spring Top. Meet. Silicon Mach. (1998) 55.
- [7] F.H.Stillingner and T.A. Weber: Phys.Rev. **B31** (1985) 5262.
- [8] E.D. Palik ed.: "Handbook of Optical Constants of Solids" (Academic Press, London, 1985).
- [9] A. Rosenfeld, D. Ashkenasi, H. Varel, M. Wahmer and E.E.B. Campbell: Appl. Surf. Sci., **127-129** (1998) 76.
- [10] Y.Namba, L. He: Int. J. JSPE **32** (1998) 13.

SESSION 3

Lasers and Techniques I

Laser technologies for manufacturing of advanced materials and devices

J.J. Dubowski

Institute for Microstructural Sciences, National Research Council of Canada, Ottawa, Ontario K1A 0R6, Canada

ABSTRACT

As demand is growing for devices capable of performing new and increased numbers of operations within an ever shrinking physical volume the laser has become an increasingly important tool helping to overcome the limitations of conventional microfabrication technologies. In addition to "classical" applications of lasers such as via hole drilling, trimming or pulsed laser deposition of thin films, there have been new developments of laser-based technologies for the fabrication of advanced micro- and nano-devices. Of particular interest for optoelectronic and photonic applications is the potential of the laser for the fabrication of integrated and monolithically integrated photonic devices and circuits.

Keywords: Laser microstructuring, laser etching, laser ablation, laser annealing, quantum well intermixing, photonic integrated devices

1. INTRODUCTION

The constantly growing demand of reduced size devices capable of performing new and increased numbers of operations has created strong research in the area of new materials and new materials processing technologies. Historically, the microelectronic industry was the main driving force behind this trend. Recent developments in fiber optics, wireless communications and multimedia applications have been possible due to the emergence of new technologies for manufacturing of advanced optoelectronic and photonic devices. Those developments have often taken advantage of unique features that lasers offer in device manufacturing – a consequence of tremendous progress in both laser technology and our understanding of the fundamental processes involved in laser-matter interaction.

2. LASERS AS MANUFACTURING TOOLS

Advancements in **UV laser beam technology**, mostly represented by the development of excimer lasers that took place between 1970 and 1980, and the development of **high-harmonic high-power IR lasers** (e.g., Nd:YAG at 355 and 266 nm) observed from the beginning of 1990s, have resulted in a rapid increase in the use of various laser-based technologies for manufacturing. Fabrication of thin films and precision structuring of materials are the most spectacular examples of applications that have been influenced by these developments. The advantages of the use of lasers for these applications include:

- a) flexibility, i.e., the ease with which a laser-based process can be switched from one material to another
- b) clean vaporization (only the target material is heated)
- c) direct deposition of complex materials (three and more elements in the target)
- d) possibility of forming exotic heterostructures, such as ferroelectric and high-temperature superconductors
- e) patterning of materials by direct ablation
- f) possibility of low-damage 3D shaping of materials using a reactive (dry) etching approach

Short-pulse ($\tau < 10$ ps) laser processing of materials is a rapidly growing activity due to its potential in precision micromachining. The significant progress observed in this area over the recent 5-6 years has been achieved due to key developments concerning fs-pulse lasers. However, fs-pulse laser technology is at the moment relatively expensive and it remains to be demonstrated where it could compete with other laser-based

technologies for large-scale production of advanced materials and devices, or where unique features of this technology would justify the high costs of its implementation.

Non-contact processing of materials that can be carried out with any laser-based technology is an attractive feature from the process control viewpoint since it makes it possible to carry out *in-situ* monitoring with variety of tools.

3. APPLICATIONS OF LASERS FOR DEVICE FABRICATION

Numerous high- and medium-power lasers have made a significant contribution to the development of advanced manufacturing technologies. Today, some of the most developed applications that involve lasers as tool in the manufacturing process of microelectronic and optoelectronic devices are:

- Precision ablation/micropatterning (via hole drilling for printed circuit boards, resistor/capacitor trimming, wire stripping, ink jet nozzle fabrication)
- Marking, scribing (semiconductor and non-semiconductor wafers, solar panels)
- Sub- μm photolithography (248 nm, 193 nm, 157 nm)
- Annealing
 - excimer (a-Si for flat panel displays)
 - non-excimer (quantum well/dot intermixing for integrated photonics)
- Thin film deposition
 - Pulsed laser deposition (high-Tc superconductors)
 - Laser-CVD, laser-CBE (selective area growth)
- Selective doping of semiconductors (GILD)
- Surface processing (planarization, computer hard disks texturing)
- Microwelding (ceramics, glass)
- 3D microstructures (prototyping, Laser-LIGA, MEMS)
- Surface cleaning (sub- μm debris removal)
- Etching (low-damage structuring)

Many of these applications have been discussed at conferences on Laser Applications in Microelectronic and Optoelectronic Manufacturing over the past 5 years [1-5]. Lasers, in addition to offering novel solutions, often become tools of choice because their application leads to cost-effective solutions. As an illustration, the cost of mechanically drilling 200 μm diameter holes during the manufacture of printed circuit boards is about \$2 per 10^3 holes and it increases dramatically, to almost \$18 for 100 μm diameter holes. This compares with \$0.4 and \$0.9 per 10^3 holes for 100 and 200 μm diameter holes, respectively, when laser drilling is applied [6].

4. LASER TECHNOLOGIES FOR NEW MATERIALS AND DEVICES

Pulsed laser deposition (PLD) is one of the most successful laser technologies that has contributed significantly to the development of new materials and devices. It is a leading approach in fabricating thin films of oxides and, especially, high-temperature superconductors. Numerous proceedings from symposia, conferences and books on this topic were published between 1990 and 1999 and they give a wide-ranging overview of the progress and status in this field [7-12]. It is interesting to note that PLD offers extremely high deposition rates, as well as the ability to control deposition rates at a monolayer level, or less, per pulse. Thus, in addition to manufacturing capabilities, PLD is an important tool in the investigation of growth mechanisms of thin films and formation of material systems that are not attainable with conventional methods of film deposition, e.g., [13].

Laser-assisted dry etching (LDE) is an example of laser-based technology that has drawn steadily growing attention. One of the most attractive features of LDE is that it is a direct patterning process, which means that structuring of materials can be achieved without the use of photoresist. In addition, the laser pulse energy (fluence) required for etching in a reactive atmosphere of gasses such as Cl_2 or HBr is much smaller than that normally required during direct laser ablation [14]. Consequently, LDE leads to reduced-damage or damage-free patterning of materials, which is one of the most desirable features in processing of optical components and semiconductor micro- and nano-devices. Complicated patterns are typically achieved by projecting conventional masks made of metallic thin films (e.g., Cr on glass) or a stack of dielectric films. More advanced applications, where utilization of the beam is an important issue, can be realized with phase-shift or diffractive masks designed specifically for a particular application. If fast processing is not critical, the patterning or 3D shaping (laser carving) can be carried with a tightly focused laser beam. The LDE process has the potential of offering cost-effective solutions in the manufacturing of some microelectronic and optoelectronic devices, especially if the microfabrication process does not require lateral resolution better than $\sim 1 \mu\text{m}$. Examples of successful implementation of the LDE technology for device fabrication include patterning of $\text{InAlAs}/\text{InGaAs}$ high-electron-mobility transistors [15] and $\text{GaAs}/\text{AlGaAs}$ multiple quantum well circular ring lasers [16].

Laser-induced quantum well intermixing (Laser-QWI) is a relatively new technology investigated for the fabrication of monolithically integrated photonic devices (MIPD).

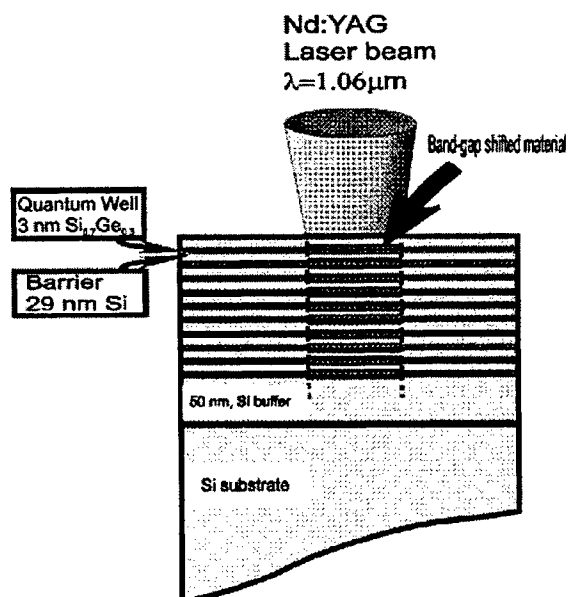


FIG. 1. Schematic illustration of the concept of laser-induced quantum well intermixing for writing of monolithically integrated photonic devices [19].

Individual photonic devices such as semiconductor lasers, waveguides, optical switches and amplifiers require different material architecture, which is realized either with dedicated growth runs or with different bulk materials. An MIPD structure can be fabricated if regions of material with different band-gaps are formed within same wafer. Typically, this can be achieved by implementing growth-related techniques such as molecular beam epitaxy (MBE), chemical beam epitaxy (CBE) or metal-organic vapor phase epitaxy (MOVPE). Two the most popular approaches involve growth/etch/re-growth and growth on patterned substrates. However, it is important to realize that the advanced epitaxial growth is highly complex and any new step such as re-growing on a partially etched wafer adds even more complexity to that process. The controlled intermixing between the barrier and quantum well material – a process referred to as quantum well intermixing (QWI) is a post-growth process that makes possible the fabrication of material with regions of different band-gap materials. The possibility of using lasers to achieve QWI has been investigated in recent years [17-19]. The method of laser-induced QWI (laser-

QWI), which is schematically illustrated in Fig. 1, has the potential for rapid fabrication of novel microstructures (prototyping) due to the flexibility in matching laser parameters required for efficient processing of a particular microstructure. It has been demonstrated that laser-QWI can be successfully used for selective area band-gap tuning (in excess of 140 meV) in $\text{Si}/\text{Si}_{1-x}\text{Ge}_x$ QW microstructures [19]. Application of this technology to III-V material systems, such as $\text{InGaAs}/\text{InGaAsP}$ QWs, offers the possibility of fabricating QWI material with continuously changing band-gap along one direction. This feature may find application in the fabrication of broad-spectrum light emitting diodes. A multicolor array of telecommunication lasers, operating between 1.4 and 1.5 μm , is an example of probably the most advanced MIPD device fabricated thus far by laser-QWI [20].

5. CONCLUSION

Laser-based technologies play a constantly increasing role in the manufacturing process of advanced microelectronic and optoelectronic devices. The key features that drive these trends are: a) the precision in micro-scale machining of variety of materials, b) the uniqueness of the process which allows new solutions, c) compatibility with the many characterization techniques due to the non-contact character of processing with lasers. Micro-hole drilling and trimming of resistors and capacitors demonstrate the most successful applications of laser technologies in microelectronics. Advanced optoelectronic and photonic devices require both a manufacturing precision applied to the variety of materials and processing that could help realizing a device integration concept. Especially demanding in this respect is the concept of a monolithic integration of photonic devices. This challenging area has been addressed with limited success by conventional microfabrication techniques and, consequently, it has become one of the most attractive experimental topics in the investigation of new laser-based technologies for manufacturing of advanced devices. The results indicate that this approach has the potential for the writing of photonic materials - where "writing" signifies the geometrical microshaping as well as 3D modification of the material properties. A multicolor array of telecommunication lasers, operating between 1.4 and 1.5 μm , is an example of probably the most advanced monolithically integrated photonic device fabricated thus far with a laser-based technology.

REFERENCES

1. *Laser-induced Thin Film Processing*, Editor: J.J. Dubowski, Proc. SPIE **2403** (1995).
2. *Lasers as Tools for Manufacturing of Durable Goods and Microelectronics*, Editors: J.J. Dubowski, J. Mazumder, L.R. Migliore, C.S. Roychoudhuri, R.D. Schaeffer, Proc. SPIE **2703** (1996).
3. *Laser Applications in Microelectronic and Optoelectronic Manufacturing-II*, Editor: J.J. Dubowski, Proc SPIE **2991** (1997).
4. *Laser Applications in Microelectronic and Optoelectronic Manufacturing-III*, Editors: J.J. Dubowski, P.E. Dyer, Proc SPIE **3274** (1998).
5. *Laser Applications in Microelectronic and Optoelectronic Manufacturing-IV*, Editors: J.J. Dubowski, H. Helvajian, E.W. Kreutz, K. Sugioka, Proc SPIE **3618** (1999).
6. G. Forest, Laser Focus World, June 1997, p. 105.
7. *Laser Ablation for Materials Synthesis*, Editors: D.C. Paine and J.C. Bravman, MRS Proc. Vol. **191** (1990).
8. *Laser Ablation in Materials Processing: Fundamentals and Applications*, Editors: B. Braren, J.J. Dubowski and D.P. Norton, MRS Proc. Vol. **285** (1993).
9. *Pulsed Laser Deposition of Thin Films*, Editors: D.B. Chrisey, G.H. Hubler, John Wiley & Sons, Inc., New York, 1994.
10. *Advanced Laser Processing of Materials: Fundamentals and Applications*, Editors: R. Singh, D. Norton, L. Laude, J. Narayan, J. Cheung, MRS Proc. Vol. **397** (1996).
11. *Laser Ablation*, Proc. 4th International Conf. on Laser Ablation, Editors: R.E. Russo, D.B. Geohegan, R.F. Haglund, Jr., K. Murakami, Appl. Surf. Sci. **127-129** (1998).
12. *Laser Ablation*, Proc. 5th International Conf. on Laser Ablation, Editors: J.S. Horwitz, H.-U. Krebs, K. Murakami, M. Stuke, Appl. Phys. A69 [Suppl.], **S45-S48** (1999).
13. M. Kanai, T. Kawai and S. Kawai, MRS Proc. Vol. **285**, 257-262 (1993).
14. M. Prasad, H. Ruda and J.J. Dubowski, J. Vac. Sci. Technol. **B 15(6)**, 2046-2051 (1997).
15. H. Takazawa, S. Takatani, K. Higuchi and M. Kudo, Jpn. J. Appl. Phys. Vol. **35**, 6544-6548 (1996).
16. C.H. Tsai, J.H. Lee, H.J. Chiang, C.C. Yang, M.C. Shih, B.C. Chen, T.J. Chuang and Y. Chang, IEEE Photonics Technol. Lett. Vol. **10(6)**, 751-753 (1998).
17. J.H. Marsh, A.C. Bryce, R.M. De La Rue, C.J. McLean, A. McKee and G. Lullo, Appl. Surf. Sci. **106**, 326-334 (1996).
18. J.J. Dubowski, S. Charbonneau, P.J. Poole, A.P. Roth, C. Lacelle and M. Buchanan, Proc. SPIE **3274**, 53-59 (1998).
19. J.J. Dubowski, N. Rowell, G.C. Aers, H. Lafontaine and D.C. Houghton, Appl. Phys. Lett. **74(14)**, 1948-1950 (1999).
20. J.J. Dubowski, G. Marshall, Y. Feng, P.J. Poole, C. Lacelle, J.E. Haysom, S. Charbonneau and M. Buchanan, Proc. SPIE **3618**, 191-197 (1999).

Nonlinear optical characterization of silicon wafers: in-situ detection of stacking faults and of external stress

Juergen Reif^{a*}, Thomas Schneider^a, Rainer Schmid^b, Dirk Wolfframm^a

^aLS Experimentalphysik II, ^bLS Physikalische Chemie und Analytik;
Brandenburgische Technische Universitaet Cottbus; Universitaetsplatz 3-4; 03044 Cottbus, Germany

ABSTRACT

Femtosecond second harmonic generation from the surface of as-grown 6-inch silicon wafers is used as a tool for in-situ characterization. Czochralski-grown crystals are not homogeneous over their cross section. A central zone of vacancy-rich and an outer zone of interstitial-rich crystal are separated by a ring of stacking faults. Gate oxide layers grown on such substrate show different quality in their dielectric properties, making it desirable to locate these zones before producing different devices. Exploiting the symmetry sensitivity of surface SHG, we use a particular two-pulse arrangement, similar to a conventional pump-probe setup, to obtain a non-destructive, in-situ information about the location of the three different crystal zones. Further, we demonstrate the potential of surface SHG to monitor external stress, exerted on the sample for instance by improper mounting, providing a tool for on-line optimization of process parameters. Finally, the applicability of the technique for on-line analysis and control during the growth of different types of gate dielectrics is discussed.

Keywords: Femtosecond laser, silicon wafers, structural defects, in-situ characterization, on-line control

1. INTRODUCTION

Ever increasing integration in semiconductor devices is accompanied with an increase at the same pace of the demands concerning the quality of the substrate wafer, the gate oxide layers, and the metallic contacts. A typical problem, encountered in this context, is the observation that Czochralski-grown silicon wafers are not uniform across their diameter¹. This translates into a non-uniform quality of gate oxide grown on this type of wafers. Two concentric regions are found with markedly different breakdown stability of the oxide. These regions, the width of which depends on the growth speed, are separated by a ring, grossly ten percent of the wafer diameter wide, where practically no useable oxide can be grown at all (for more details see refs. in [1]). An accepted explanation for the different oxidation behavior of the three zones postulates different compositions during growth¹. According to this picture, the inner zone consists of vacancy-rich silicon crystal, the outer zone is oversaturated interstitial-rich. In the separating ring, no long-range regular crystalline structure is developed, as can be seen from the fact that additional oxidation reveals an agglomeration of stacking faults (cf. Fig. 1).

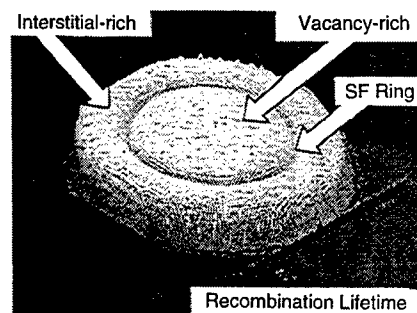


Figure 1: Carrier recombination lifetime³, revealing the three zones in a wafer of Czochralski-grown silicon

* Correspondence: Email: reif@tu-cottbus.de; WWW: <http://www.physik.tu-cottbus.de/physik/xp2/>;
Telephone +49 355 69 3185; Fax: +49 355 69 3985

Up to present, several methods have been developed^{1,2} to analyze this situation, all of which lack, however, from the problem that the analyzed wafer is no longer usable for device fabrication. Most desirable are methods for preselecting appropriate substrates. As shown in Fig. 1, the investigation of the carrier recombination lifetime by microwave spectroscopy³ might be helpful. It is, however, tedious and not really suited for *in-situ* or *on-line* control. Bearing mind that the symmetry of the three crystal regions should differ in a distinguished way, it appears promising to devise a spatially resolved check of the crystal symmetry to probe the wafer quality or, at least, to determine the position of the separating ring. Unfortunately, conventional tests of crystal symmetry such as X-ray diffraction are, again, not very well adapted to rapid *in-situ* control of larger wafers. This is a genuine field for optical techniques, which are *per se* non-destructive and *in-situ*-applicable wherever light has access. However, there are only very few cases where conventional optics yields information about crystal symmetry properties, such as dichroism or birefringence. The reason for this lack of sensitivity lies in the fact that in most cases the optical susceptibility (i.e., in principle, the dielectric constant) is only a scalar, relating input and output optical fields linearly to each other.

In nonlinear optics, however, such as second harmonic generation (SHG), the output optical field is the result of more than one input field. Consequently, the nonlinear susceptibility χ^{NL} is highly symmetry sensitive, since it has tensor character, as is shown in Eq. 1:

$$E_j^{out}(\omega') = \chi_{jkl}^{NL}(\omega' = \omega_1 + \omega_2) E_k^{in}(\omega_1) E_l^{in}(\omega_2) \quad (1)$$

Usually, this second order susceptibility vanishes under inversion symmetry⁴. At the surface of a cubic crystal, however, this symmetry is broken, and the nonlinear optical process becomes allowed. This matches well with the fact that, for visible light, we can only use reflection signals, anyway, and it may yield, in an easy way, the required information on the crystal symmetry⁵⁻⁸. This symmetry sensitivity is not restricted to the detection of intrinsic symmetry variations. Also, disturbances due to external conditions, like stress on the wafer, are reflected by the technique.

In the present contribution, we demonstrate the sensitivity of surface SHG. We report on both, the discrimination between the three growth zones on a 6-inch wafer as well as the detection of reversible stress in the sample, exerted by the mounting procedure. This enables a reliable *in-situ* and *on-line* control before further processing.

2. EXPERIMENTAL

In our experiment, we apply the SHG technique to check the as-grown 6-inch silicon wafer in (100) orientation, presented already in Fig. 1. It is well known⁷, that the reflected SH-intensity strongly depends on the azimuthal orientation of the surface with respect to the light polarizations. E.g., Tom *et al.*⁷ and Aksipetrov *et al.*⁸ found a four-fold symmetry for the silicon (100) surface when they rotated their sample about the surface normal, relative to the light polarizations. We want to exploit this symmetry information. Therefore, we first analyzed our sample by checking the azimuthal anisotropy. The corresponding experimental set-up is shown schematically in Fig. 2:

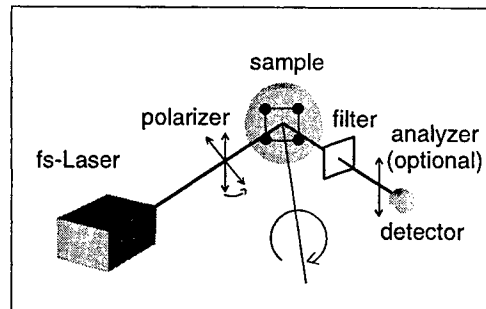


Figure 2: Experimental set-up: The linearly polarized output of a femtosecond laser is directed under 45°-incidence to the surface of a silicon (100) wafer. The reflected second harmonic light is detected by a photomultiplier. To obtain the SHG azimuthal dependence, the sample is rotated about its normal.

In order to not over charge the sample thermally, we use a femtosecond Titanium:Sapphire laser (wavelength: 800 nm, pulse duration: 100 fs, maximal energy: 1 mJ/pulse, repetition rate: 1 kHz) as the source for our experiments. The short pulse duration allows to obtain the high intensity required for the nonlinear process at reasonably low pulse energy. Earlier investigations⁹ showed, that absorption under these conditions does not play a significant role. The linearly polarized laser output hits the wafer surface under 45° incidence, and the specularly reflected second harmonic is detected after eliminating the fundamental by appropriate filtering with a dielectric mirror. By rotation of the sample about its normal, we detect the dependence of the second harmonic on the azimuthal orientation. A typical result for *p*-polarized excitation is shown as a polar-plot in Fig. 3 (bold line):

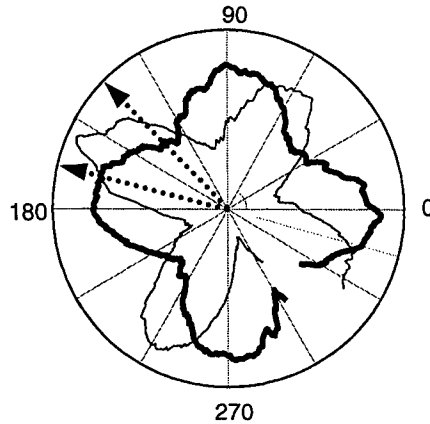


Figure 3: Polar plot of the azimuthal dependence of second harmonic generation on a silicon wafer in (100) orientation; the bold trace is for *p*-polarized excitation, the excitation for the light trace is rotated by 60°. Both curves are normalized to the maximum signal. The dotted arrows indicate the respective crystal orientations (135°, 170°) for taking the scans along the wafer diameter, described below.

When the polarization of the exciting laser is rotated away from the *p*-direction, the azimuthal pattern appears to be rotated by the same amount (see Fig. 3). Thus, for a given orientation of the crystal, we obtain a certain ratio $R = S_{60}/S_p$ between the signals for *p*- and for 60°-excitation, which is determined by the crystal symmetry. The idea of our experiment to check the homogeneity of the crystal over its cross-section is now the following: we measure the ratio *R* as a function of the position of the interaction spot along the wafer diameter. Any change in this ratio is, then, the indication of a change in symmetry. The respective experimental arrangement is sketched in Fig. 4:

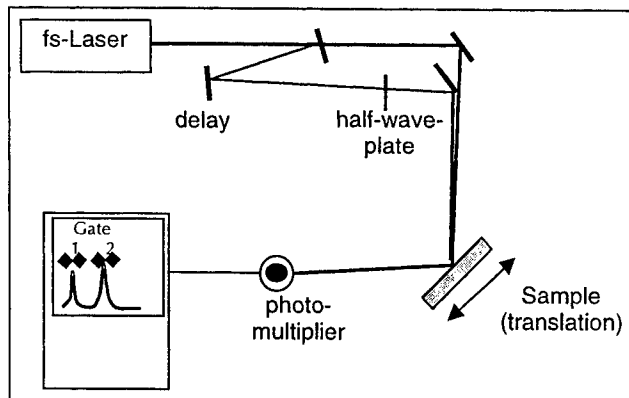


Figure 4: The output of the femtosecond laser is split into two beams, one of which is delayed and rotated in polarization, before both beams are recombined at the sample. The reflected second harmonic light is polarization analyzed and then detected. The temporally separated signals from both exciting beams are further processed, to obtain their ratio. The sample may be scanned by translation along its diameter

In this case, the output of our laser is split into two beams, one of which is delayed with respect to the other. Further, one of the beams is p -polarized, the other one is polarized at 60° . Both beams hit the same spot on the sample, which can be scanned by stepwise translation along its radius (100 steps of 0.75 mm each). The reflected second harmonic is separated from the fundamental. It is detected by a photomultiplier, yielding two temporally separated signal peaks for the two input beams, respectively. These signal peaks are recorded by two gated integrators, followed by a personal computer.

3. WAFER HOMOGENEITY

The result is given in Fig. 5 for two different azimuthal orientations of the wafer (135° and 170° , cf. dotted arrows in Fig. 3). For both scans, the signals for p -polarization (bold trace) and 60° -polarization (light trace) are normalized to the signal at the outer rim of the wafer, indicated by the dashed arrows. The vertical dotted line represents the position where the data of Fig. 3 were taken.

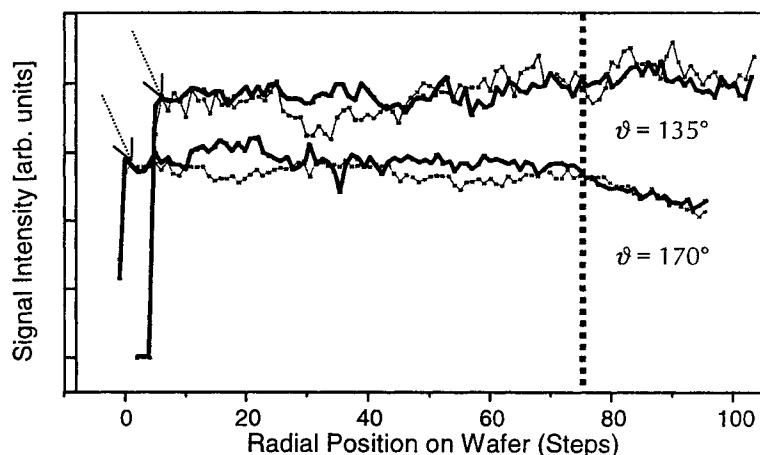


Figure 5: Stepwise scan from the outer rim (step 0) to the center of the wafer (step 100). For two azimuthal orientations of the wafer, the SHG signal is recorded for both p -polarization (bold trace) and 60° -polarization (light trace) of the input. The dashed arrows indicate the normalization points, the dotted line gives the position where the data of Fig. 3 were taken. The offset between the data at 135° and at 170° is due to the fact that because of the off-center rotation axis only one set was taken on an exact radial line.

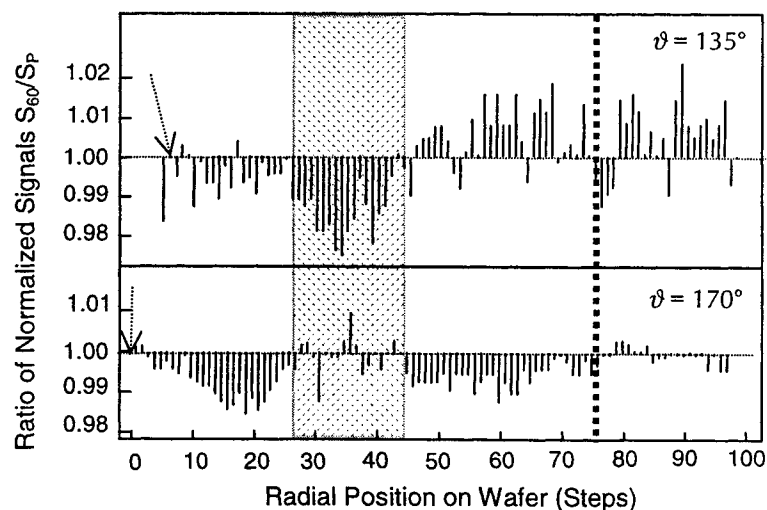


Figure 6: Ratio of the normalized SHG signals from Fig. 5 as a function of radial position on the wafer. The shaded area highlights a zone of markedly different symmetry, which may be attributed to the stacking fault ring (Fig. 1).

The ratio of the normalized signals for the two input polarizations is displayed for both azimuthal orientations in Fig. 6. Both traces show a characteristic structure of three zones, the first one for the outer 26 steps (corresponding to 19.5 mm), the next from step 27 to step 43 (12 mm wide), and finally from step 44 to step 100 at the center of the wafer (42 mm). According to the result of Fig. 1, this corresponds to a central area with a diameter of 84 mm, a 12 mm wide ring of different symmetry, highlighted by the shaded area in Fig. 6, and an outer ring of 19.5 mm width. Further, the comparison between both traces indicates, that also the inner zone and the outer ring are different in symmetry.

This result has to be compared with an analysis of the carrier-recombination-lifetime measurement of Fig. 1. In Fig. 7, we show an enlarged section of these data, together with a ruler divided in units corresponding to ten steps of our scans presented above.

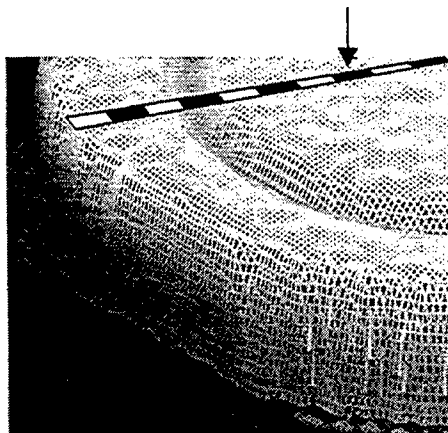


Figure 7: Enlarged sector of Fig. 1. The superimposed ruler is divided in units corresponding each to 10 steps of Fig. 5, 6. The arrow indicates the spot where the azimuthal dependence (Fig. 3) was measured.

Obviously, the position and the width of the stacking fault ring correlates well with the highlighted range of deviating symmetry in Fig. 6. This makes us confident that we, indeed, are able to distinguish the three different ranges of the wafer cross-section. The optical measurement can be conducted *in-situ* under practically any environment and for any size of the wafer.

4. EXTERNAL STRESS

For the monitoring of external stress, we modified the experimental setup of Fig. 2 by introducing an additional polarizer (in *s*-direction) in the detection path, serving as an analyzer of the SHG polarization. Though it dramatically reduces the total signal intensity by about three orders of magnitude, this helps to be much more sensitive to the anisotropic part of the azimuthal dependence⁷. When we exercise uniaxial external stress on the sample, a new symmetry axis is introduced to our azimuthal dependence. This translates into an additional *m*-symmetry superimposed to that of the (100)-wafer as is shown in Fig. 8 (a). Note that the pattern exhibits much larger contrast than Fig. 3. This is due to the fact that for the detection of *s*-polarized SHG the isotropic contribution from oscillations perpendicular to the surface vanishes¹¹. When the direction of the external stress is changed, this corresponds to an associated change in the symmetry of the azimuthal pattern as shown in Fig. 8 (b). At this point, it is not yet clear which of two reasons yields the main contribution to our observation: either, the stress results in deformation of the sample surface, or it leads to a noticeable deformation of the bond length and thus of the binding potential in one direction. The first situation means that upon rotation the signal beam may geometrically wander around the detector, with a corresponding change in detection efficiency. In the second case, the susceptibility tensor would actually change, and the change in azimuthal pattern has an intrinsic reason. To date, we tend to favor the second possibility, in particular because of the high contrast and regularity in our azimuthal patterns. The difference in the results of Fig. 8 (a), (b) as well as the symmetry reported in Fig. 3 allow to rule out the problem of a vicinal cut of the inspected wafer. However, our technique would be able to also detect such a situation.

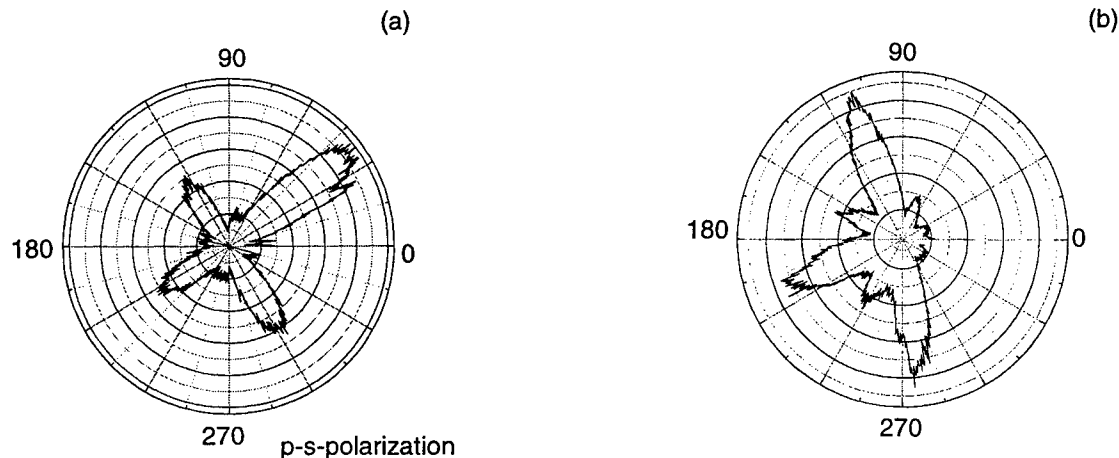


Figure 8: Polar plot of the s -polarized SHG yield for p -polarized input. Panels (a) and (b) represent two situations of different external stress.

5. CONCLUSION

We demonstrated the potential of femtosecond second harmonic generation to characterize the quality of as-grown silicon wafers. Our purely optical technique exhibits the same inhomogeneities for the cross-section of Czochralski-grown ingots as were observed by other techniques. We found excellent quantitative agreement with the result of carrier recombination lifetime measurements. We also showed the possibility to monitor external stress due to incorrect mounting of the wafer. This could have implications for process control applications.

Because of the very weak thermal load of the sample due to the low energy of our ultra-short pulses, the technique is essentially non-destructive. Being purely optical, it is readily applicable wherever light has access and may, therefore, be used for *in-situ* and *on-line* control of wafer quality as well as for simple preselection before processing.

ACKNOWLEDGEMENTS

We thank H. Richter, IHP Frankfurt/Oder, for bringing this subject to our attention and for providing us with the sample wafer. We gratefully acknowledge skilled technical assistance by J. Bertram.

REFERENCES

1. D. Zemke, P. Gerlach, W. Zulehner, K. Jacobs; *J. Crystal Growth* **139** (1994) 37
2. G. Kissinger, G. Morgenstern, T. Grabolla, H. Richter, J. Vanhellmont, U. Lambert, D. Gräf; *Electrochem. Soc. Proc.* (1998/9) in print
3. H. Richter *et al.*, private communication
4. In more detail, this statement is only true if only electric-dipole (i.e. local) light-matter interaction is considered. For non-local interaction, e.g. electric quadrupole or magnetic dipole, this symmetry condition is lifted off (cf. [5]). This has been observed, in particular, for silicon (100)⁷.
5. For an introduction see: Y.R. Shen; *Annu. Rev. Mater. Sci.* **86** (1986) 69
6. J.C. Zink, J. Reif, E. Matthias; *Phys. Rev. Lett.* **68** (1992) 3595
7. H.W.K. Tom, T.F. Heinz, Y.R. Shen; *Phys. Rev. Lett.* **51** (1983) 1983

8. O.A. Aksipetrov, I.M. Baranova, Yu.A. Il'inskiĭ; *Sov. Phys. JETP* **64**, 167 (1986)
9. Y.-S. Lee, M.C. Downer; *Opt. Lett.* **23**, 918 (1998)
10. I.e., the exciting light oscillates perpendicular to the plane of incidence and parallel to the sample surface.
11. J. Reif, P. Tepper, E. Matthias, E. Westin, A. Rosén; *Appl. Phys. B* **46**, 131 (1988)

Influences of hydrogen in precursor Si films to excimer laser crystallization

Michiko Takahashi ^a, Masakazu Saitoh ^a, Kenkichi Suzuki^{*a}, and Kiyoshi Ogata ^b

^aDisplays, Hitachi, Ltd., 3300 Hayano, Mobara, Chiba 297-8622 JAPAN

^bProduction Engineering Research Laboratory, Hitachi, Ltd.,
292 Yoshida-cho, Totsuka-ku, Yokohama 244-0817 JAPAN

ABSTRACT

The excimer laser crystallization (ELC) is a key technology of the low temperature polycrystalline silicon (LTP) thin film transistor (TFT) processes. The precursor Si for ELC is amorphous Si (a-Si) film, and hydrogen in the film has to be eliminated down to a certain concentration to prevent explosive evolution of hydrogen gas when excimer laser is irradiated. Hydrogen has been concerned only with respect to the effect for practical applications. This paper points out another aspect of hydrogen effect. There is correlation between the bonding environments of precursors and polycrystalline Si (p-Si) structures produced through ELC process. The effect becomes explicit under 0.8 at. % of hydrogen contents, and are clearly manifested in differences in (111) lattice spacings of p-Si films. Variations of microscopic structure of the precursors are provided by three kinds of deposition methods, and dehydrogenation conditions. This paper also shows that transient boiling behaviours by the excimer laser discriminate prominently the differences among precursors. Although relationships between the behaviour and microscopic structures are not clear, it gives an efficient measure for the bonding environment. It is also shown that the contents of p-Si is typically $10^{18}/\text{cm}^3$ after multishot ELC process., and effusion of the hydrogen at one shot is rather small. This may leads to the infereneces that hydrogen influence profoundly ELC process, and also contributes to preserve characteristic structure of the precursors.

Keywords: Excimer laser crystallization, Hydrogen, Amorphous silicon, Polycrystalline silicon, Ablation, Ebullition, XRD

1. INTRODUCTION

The TFT-LCD(thin film transistor type liquid crystal display) technology is now prevailed by a-Si type TFT in mass-production. Recently the p-Si type TFT has been developed ¹ and quite a few manufacturers have launched the mass production ². A merit of p-Si over a-Si is that it is possible to integrate peripheral circuitries, which leads to reduction of the display cost and versatility of display designs. However due to low cost glass substrate for LCD, the whole process should be at low temperature, hopefully lower than 450°C. On the other hand, the p-Si TFT is fundamentally SOI device, and it should be manufactured according to the principles of Si processes. The essence of Si processes consist of high quality Si-substrate, thermal oxidation, and various thermal annealing processes, in short, characterized by high temperature. The primary difficulty of p-Si TFT is attributed to the confinement that the comparable performance to Si LSI should be realized at low temperature processes.

The LTP-TFT processes start from deposition of a-Si film on a glass substrate. The film is then melted by excimer laser irradiation, and recrystallized to polycrystalline through rapid quenching. The gate oxide is a deposited film which is necessarily of degraded quality than thermal oxide. The two layers and a metal gate are essential constitutions of LTP-TFT, and the subsequent processes are not so much different from the conventional Si processes except they should be at low temperature. Among the processes, the ELC ³ of a-Si is a key technology of LTP-TFT,

*Correspondence: e-mail: suzuki-kenkichi@mobara.hitachi.co.jp, TEL: +81-475-26-3932, FAX: +81-475-26-3990

as the p-Si film is just correspondent to Si substrate. Moreover ELC process is essentially a high temperature crystallization as the p-Si process which has a possibility to realize same quality to crystalline Si, and there have been very many R & D to improve the crystallinity⁴.

This paper is concerned with interrelationships between the microstructure of precursor and the structure of p-Si. The precursor Si films are dehydrogenated before ELC down to a few at. %, so as to prevent explosive evolution of hydrogen gas. Except the effect, there have not been paid any attentions to the influences of hydrogen for the crystallization process. It might be due to well established experimental fact in the case of crystalline Si that almost all hydrogen are evolved out by annealing at more than 400°C⁵. In the case of ELC, it may be implicitly accepted that hydrogen is not effective, as the process includes high temperature liquid phase. However, detailed observations of SEM micrographs have revealed subtle but appreciable differences in p-Si grain structures according to the starting precursors and dehydrogenation conditions. This implies that the bonding environments of the precursors might influence microscopic structures of p-Si even through ELC process. In the next section, more apparent experimental evidence than SEM pictures is shown that there is an correlation between precursor and p-Si lattice spacing. The bonding structures of the precursors are considered to be varied by deposition methods⁶ and dehydrogenation conditions. In the third section, a novel method making use of laser ebullition⁷ is introduced to characterize the bonding environments. The bonding environment means Si networks modified by Si-H bonding structures, and the differences among the precursors are profoundly related to hydrogen. The final section is devoted to the discussions concerning the influence of hydrogen to ELC process and possibility of the structural correlation between precursor and p-Si.

2. HYDROGEN CONCENTRATION AND MORPHOLOGY OF ELC POLY-SILICON

Four kinds of Si precursor films were prepared to elucidate the influences of hydrogen to ELC process; (1) as-deposited a-Si films by LP-CVD (low pressure chemical vapour deposition) at 550°C substrate temperature (Ts), (2) micro-crystalline Si film (μ -Si) sputtered in high vacuum⁸, (3) as-deposited a-Si films by PE-CVD (plasma enhanced CVD) of monosilane at Ts=380°C, (4) PE-CVD a-Si films furnace-annealed at 400~600°C for 5~180 min. All the films are 50 nm thick on 6" quartz substrates.

The hydrogen concentrations were measured both by SIMS (secondary ion mass spectroscopy) and APIMS-TDS (atmospheric pressure ionization mass spectroscopy-thermal desorption spectroscopy). The latter data are shown in Fig.1. The spectra are typical, as the films with higher hydrogen concentration have two peaks⁹. The peak at the lower temperature is assigned to SiH₂ or (SiH₂)_n bonds, and the peak at the higher temperature to SiH bonding usually. The first peak is also associated to instability of a-Si:H structure. For ablation-free film, it is necessary to dehydrogenate

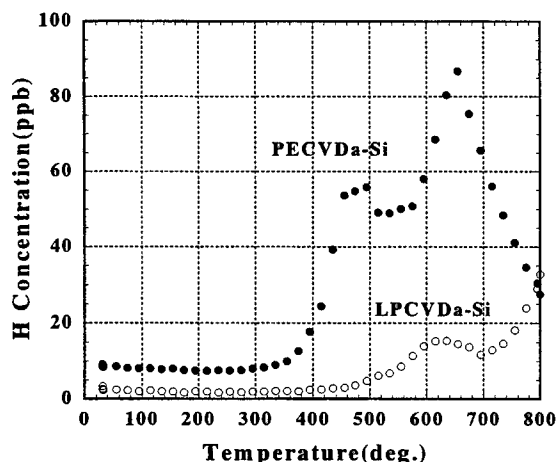


Fig. 1
APIMS-TDS Spectra

Solid circles: as-deposited PE-CVD film
Open circle: as-deposited LP-CVD film
The film thickness is 50 nm on quartz substrate. Temperature rising rate of TDS is 20°C/min.

until to obtain a single peak spectrum at higher temperature. The TDS spectra are convenient to observe qualitatively Si-H structures, however they give only rough estimates of hydrogen concentration. There are large discrepancies from SIMS data as shown in Table 1. The problem is whether there is an optimum hydrogen concentration of precursor Si film to obtain high quality p-Si film. This is practically very important as it is relating the manufacturing equipments for deposition of a-Si and dehydrogenation.

Table 1 Hydrogen concentration measured by SIMS and APIMS-TDS

As-deposited samples are of; (a) PVD, (b) LP-CVD, (c) PE-CVD, and (d) is an annealed sample of (c) at 450°C for 5 min.

	(a)	(b)	(c)	(d)
SIMS	0.05	0.1	4.4	1.2
TDS	1.0	0.9	8.1	3.7

The performance of p-Si TFT is better for the larger sized grain, and thus the grain size is primary characteristics to be determined. It is dependent upon the fluence and the shot number. Concerning the effects of the fluence, there are three regions of grain growth according to irradiation fluence. Initial stage is the region of vertical growth, where the grain size remains to be small. It increases sharply at the subsequent lateral growth region, and then abruptly enter into microcrystalline region. The critical fluence of microcrystallization is approximately 400 mJ/cm² for 50 nm LP-CVD film. It is reasonable to dehydrogenate down to the concentration where the ablation does not occur during these crystallization regions.

ELC was carried out using a 308 nm excimer laser in vacuum at room temperature. The irradiation area is 150 x 0.3 mm², and the beam is scanned along the short axis of the slit pattern. The illumination overlap is 96.7 %. The PE-CVD samples, as-deposited and annealed at 450°C for 5 min. were ablated when they were irradiated at 280 mJ/cm². The PE-CVD samples annealed at 450°C for 30 min. were on the verge of ablation, although the hydrogen concentration is not much different from that of the samples annealed at 450°C for 60 min. From the data the critical hydrogen concentration is near to 1 at.%, and dehydrogenation should be less than the value. Contrary to the critical behaviour of ablation threshold, fluence versus grain size relationships are irrespective to the deposition and annealing condition if the hydrogen concentration is under the critical value, as shown in Fig.2. There is a prominent feature in p-Si grain of μ -Si. Almost all grains have a twin boundary inside the grain, however few boundary is observed inside of the grain started from μ -Si. This may be an evidence that grain growth is influenced by a microscopic morphology of the precursor.

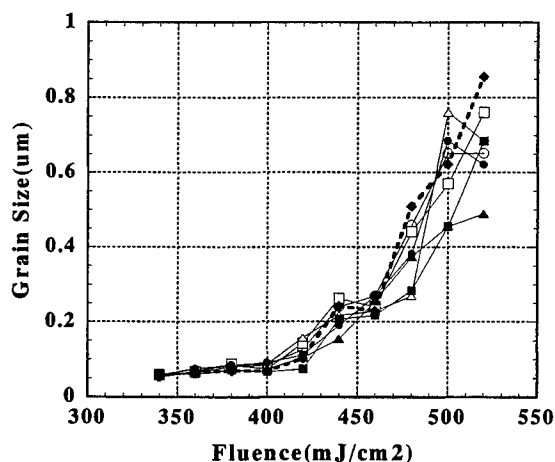


Fig. 2
Relationship between fluence and grain size
of PE-CVD films with various annealing
conditions;

450°C 5 min.(○), 450°C 30 min.(□)
450°C 60 min.(△), 550°C 5 min.(●)
550°C 30 min.(■), 550°C 60 min.(▲)
600°C 60 min.(◆).

Except the above prominent feature, SEM micrographs only exhibit subtle differences of the grain surfaces among the samples, and we need more distinct and quantitative relationship between p-Si crystallinity and the bonding environments of the precursor a-Si films. According to XRD (X-ray diffraction) measurements, p-Si films shows two

peaks; distinct (111) and a slight (220). The peak height and width of (111) line are a measure of the crystallinity. Comparing to usual analyses of Raman peak of 521 cm^{-1} , the XRD is advantageous as it gives lattice constants and crystalline directions at the same time. Figure 3 shows the relationship between lattice distances and fluence for various kinds of films. The LP-CVD p-Si film is denser than that of microcrystalline precursor although the hydrogen concentration of LP-CVD is a little larger than that of microcrystals. Another interesting feature is that the lattice spacing of p-Si from PE-CVD are not much different in spite of different hydrogen concentrations. The data suggest that some microscopic structures inherent to the deposition method are preserved and influence the crystallinity of p-Si even through the ELC process.

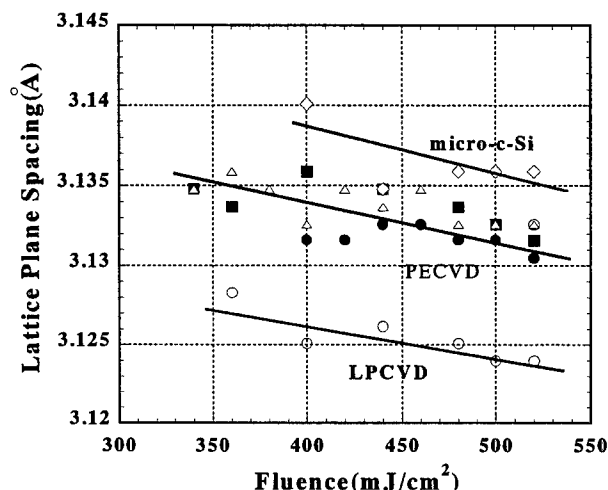


Fig. 3
Relationship between ELC fluence and spacing of (111) lattice planes.

The precursor films are of ;
as-deposited LP-CVD(\circ), PVD(\diamond)
annealed PE-CVD at 450°C 5 min.(\bullet),
450°C 30 min.(\blacksquare), 450°C 60 min.(\triangle).

3. NOVEL CHARACTERIZATION METHOD OF THE PRECURSOR FILM

The crystallinity of p-Si can be specified by XRD and Raman spectroscopy, however it is rather difficult to define amorphous structure quantitatively relevant to p-Si through ELC process. IR and Raman spectroscopy give in principle useful information as to the local bonding structures of Si-H¹⁰. However, the precursor film of TFT is typically 50 nm thick on the buffer layer on the glass substrates. Thus it is very difficult to measure quantitative IR and Raman spectra especially at low hydrogen concentration.

Instead of the conventional spectroscopy, we propose a new method to estimate an average bonding strength making use of pre-ablation phenomenon. When a precursor film is irradiated by excimer laser with higher fluence than the crystallization, it is melted and boiled. The creation of the bubble at boiling is manifested by completely circular pin-holes left after irradiation as shown in Fig. 4. This is clearly an hole produced by bursting of the bubble. The diameter

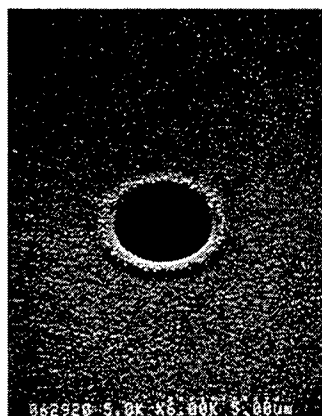
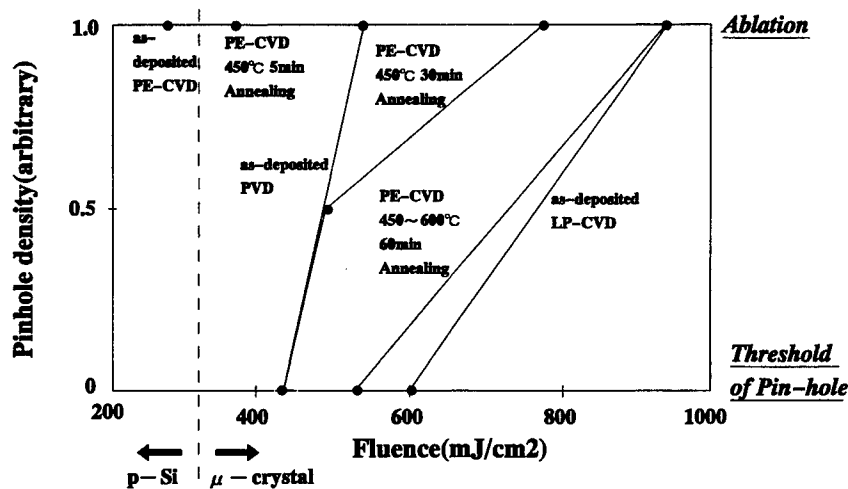


Fig.4
SEM picture of a pin-hole created by bursting of a bubble formed in the boiling Si film by excimer laser heating.

changes from 5 to 20 μ m according to fluence. The number of the pinholes increases when fluence is increased, and finally merged and ablated. The feature is depicted in Fig.5, where the abscissa indicates fluence in mJ/cm^2 and the ordinate represents semi-quantitatively the density of the pin-hole. The density is normalized to 1 when the whole area is covered by the pin-holes, that is, ablation or evaporation occurs. Zero corresponds to appearance of a single pin-hole. The density versus fluence is delineated by a straight line, and named as a pre-ablation line for convenience. The line corresponding to as-deposited LP-CVD((a) in the figure) is far separated from that of μ -Si ((b)) toward higher fluence, although the hydrogen contents of LP-CVD is larger than that of μ -Si. On the other hand, the pre-ablation line of the annealed PE-CVD (450°C, 30 min.) is coincident with that of μ -Si, notwithstanding that PE-CVD film contains more than 20 times hydrogen than μ -Si. An as-deposited PE-CVD film is ablated within the fluence region of crystallization.

Fig. 5 Pre-ablation behaviours of the precursors.



The pre-ablation is mainly ebullition, and it is a phenomenon of evaporation from inside of the liquid Si. The vapour is produced by breaking Si-Si bond and Si-H bond, and thus the fluence of onset of a bubble formation is inferred to reflect an average strength of the local bonding. The strength might be influenced by hydrogen concentration, and in Fig.6, the relationships between hydrogen contents and pre-ablation are depicted. There seems to be a critical hydrogen concentration, 0.8 at.%, where effects of hydrogen is expected to change.

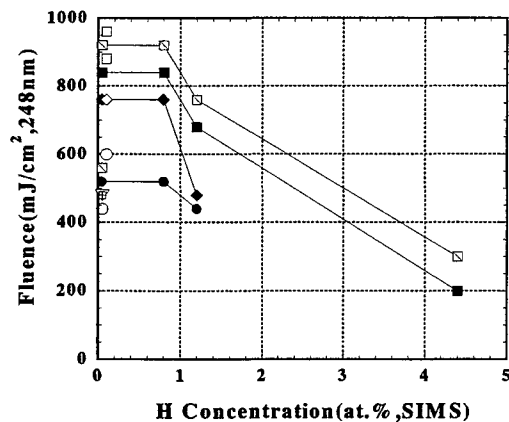


Fig. 6 Relationship between pre-ablation behaviours and hydrogen concentration of PE-CVD precursors.

Threshold fluence of a single pinhole(●), ablation threshold(■), and 50% ablation(□).

It is difficult to estimate correctly the heat consumed for fusion and evaporation in ELC process, where the most of the heat is lost by thermal conduction. Here we try to estimate roughly the thermal budget in the process. The melting point of the precursor a-Si is approximately 1,200°C, and the corresponding excimer fluence is less than 250 mJ/cm², and confined within small region less than 50 mJ/cm². The fluence corresponding to the boiling point is assumed the point at creation of a single bubble, then the boiling point varies in wide range according to the precursor. The fluence difference between onset of boiling and ablation indicates the heat required to evaporate whole film thickness, that is, a product of the mass and the latent heat. The density does not change appreciably among the precursors in the case of low hydrogen concentration¹¹, the difference is due to the latent heat. Both the boiling point and the latent heat is related to the strength of bonds, we expect a linear relationship between both the quantities. As shown in Fig.7, the linear relationship is apparent for PE-CVD films. The bonding strength increases as the hydrogen concentration is reduced. Concerning LP-CVD and PVD films, we have only as-deposited films with low hydrogen concentration. In the Figure Both the points are separated far from the line of PE-CVD, which indicates differences in bonding structures among the films, especially related to different contribution of hydrogen to the bonding structures.

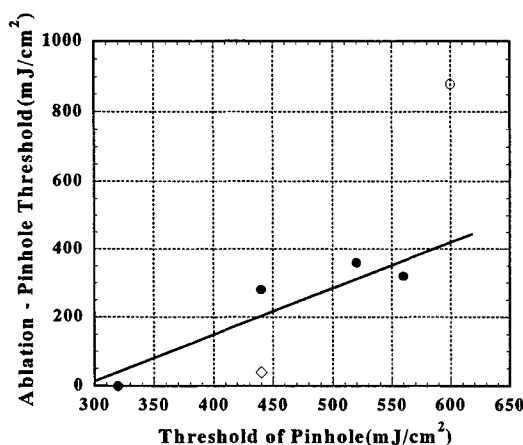


Fig. 7
Correlation between a single pin-hole threshold, and difference between total ablation and single pin-hole threshold.

● : PE-CVD
◇ : PVD
○ : LP-CVD

4.DISCUSSIONS

XRD measurements show the spacing of (111) lattice plane of p-Si is different according to the deposition method. This may suggest that some bonding structures of the precursor Si films influence ELC process. In other words, some microscopic structures of the precursor are preserved through the recrystallization process. There are huge pile of the investigations concerning microscopic structures of a-Si:H¹², and it is well known that the parameters characterizing SRO(short range order) are just nearest neighbor atomic distance and bonding angle, and these quantities are only slightly different from single crystalline Si, establishing the tetrahedral bonding structure. The bond angle varies about 10 %, but far less for the nearest neighbor atomic distance. Generally the structural characteristics of a-Si:H is described by network coordination which are originated mainly from the fluctuation of the bonding angles and Si-H bonds. The IRO(intermediate range order) is also influenced by deposition method and conditions. These information of a-Si structure have been mainly concerned with device grade a-Si:H, which includes typically 10 at.% hydrogen. On the other hand, the precursor a-Si film should include less than 1 at.% hydrogen, and this is achieved by the deposition methods and conditions different from those for a-Si:H and dehydrogenation starting from the conventional a-Si:H. It is inferred that microscopic topology of the precursor with less hydrogen concentration is different from that of a-Si:H only with respect to the spatial distribution of hydrogen, and thus IRO or LRO, but not so much as to SRO. We are concerned with possibility of preservation a part of SRO through ELC process.

The precursor Si film is heated by excimer laser with 25 ns pulse width and kept liquid phase during 0 to 50 ns according to the fluence. Such time duration would be enough to establish thermal equilibrium, that is, enough to randomize the bonding structure, if the temperature distribution is uniform. At cooling the melt is recrystallized. The recrystallization is a dynamic process of rearrangement of Si atoms at the liquid -solid interface¹³. The velocity of the

interface proceeding toward the liquid phase is approximately 2 m/s for 50 nm thickness film¹⁴, and whole crystallization finish within 50 ns cooling time duration. Although ELC is such a non-equilibrium and non-uniform thermal process, it is generally accepted that a grain of polycrystal by ELC includes only slight defects as there is no time to grow them due to high quenching rate, and each grain is considered to be very near to the single crystal. Actually in the conventional experiments of crystalline Si, the defects is quenched with the rate of 10^5 K/s, and it is far less than the rate in LA process, 10^{10} K/s.

The crystallinity of p-Si is usually evaluated by FWHM (full width of half maximum) of 520 cm^{-1} Raman spectrum. Even for small grain size, it indicates rather good quality irrespective of the starting precursors. The Raman data are however rough estimate of the crystallinity, as almost all data show less than 1 cm^{-1} variation with 0.1 cm^{-1} resolution at best. More precise evidence of high crystal quality is spin density measurements by ESR, which show completely amorphous-like isotropic signals¹⁵. This is explained by the fact that the dangling bonds are concentrated mainly at the grain boundary region, and far less inside of a grain. The lattice spacing also reflects the stress field of the crystal. For ELC p-Si, it is reported that there are no stress field at the grain boundaries¹⁶, although TEM pictures of cross section of p-Si films show close contact of crystallites without any intermediate region. There are dangling bonds at the boundary, and it is expected the electronic trap levels are much reduced by hydrogen termination. The high crystalline quality of the grains and the effect of termination of the dangling bonds at the boundaries are evidenced by high performance of the p-Si TFT. We fabricated TFT devices through a standard LTP-TFT process. With final hydrogenation process, we could get TFTs with field effect mobility of over $300\text{ cm}^2/\text{Vs}$ for $0.4\text{ }\mu\text{m}$ average grain size.

The microscopic structures characterizing each precursor Si film are mainly due to various Si-H bondings. In the excimer laser fusion process, the bonds are dissociated, and hydrogen atoms and ions diffuse inside of the film and evolved out of the surface. Actually a precursor, PE-CVD a-Si film annealed at 450°C for 30 min. has initially 0.8 at.% of hydrogen, and the amount is reduced down to $0.02\sim 0.04$ at.% through ELC process. This means about 95% of hydrogen contents are released out of the film. The remaining hydrogen concentration is approximately 10^{18} atoms/ cm^3 , and still nearly three order higher magnitude than that of the limit of solid solution of c-Si, 5×10^{15} atoms/ cm^3 . It should be noted that the amount is resulted after 30 shots irradiations of excimer laser per a site. If we postulate a constant rate for evolution of hydrogen, only 10% of existing amount is released at each shot. This means large part of hydrogen remains inside of the film during one ELC process.

The diffusivity of the hydrogen atoms have been measured over only limited temperature range, and is not known for higher temperature near the melting point and liquid Si. We roughly estimate the diffusion velocity to be 1 m/s around the temperature, extrapolating the experimental result of Van Wieringen and Warmoltz¹⁷. This value is nearly same order of magnitude to liquid-solid interface velocity. With the diffusivity, almost all hydrogen are evolved out during 50 ns, which is approximately high temperature duration through ELC process. To explain the small effusion rate, it is reasonable to assume that slight fraction of the hydrogen are dissociated during temperature rising by excimer irradiation, and the solubility of hydrogen in liquid Si is high. Accordingly rearrangement of atoms at l-s interface includes partly Si-H bonds. The effusion rate of hydrogen may be actually higher at the beginning of the multishot irradiation, and gradually decrease. This process may leave the strongest bonding structures which is inherent to the deposition method.

CONCLUSIONS

The explicit evidence for structural correlation between precursor a-Si and ELC p-Si was shown in the XRD data of (111) lattice spacing. The average bonding strength of a precursor is well characterized by pre-ablation behaviours. The microscopic structure of the precursor is determined by various Si-H bonds, and the correlation infers possibility of preservation a part of the bond structure through ELC process, and a new aspect for the crystallization mechanism.

ACKNOWLEDGEMENTS

The authors wish to thank Dr. Hatano of Hitachi Central Res. Lab. and Prof. K. Murakami of Tsukuba Univ. for valuable discussions as to hydrogen effects to Si and ELC mechanisms, and gratefully acknowledge a continuing supports and encouragement of Mr. K. Kinugawa and Mr. H. Kawakami of Displays, Hitachi, Ltd.

REFERENCES

1. H.Kuriyama, et al, Jpn. J. Appl. Phys. **30** pp3700-3703 (1991)
2. Y. Matsueda, et al, SID 98 Digest pp879-882
3. T.Sameshima, S.Usui, and M.Sekiya, IEEE Electr. Devices, **EDL-7** pp 276-278 (1986)
4. J.S. Im and R.S. Sposili, MRS Bulletin **vol. 21** pp 39-48 (1996), K. Ishikawa, M. Ozawa, C.H. Oh, and M. Matsumura, Jpn. J. Appl. Phys. **37** pp731-736 (1998)
5. J.I. Pankove and N.M. Johnson, *Hydrogen in Semiconductors*, Academic Press Inc, Boston,1991
6. R.A. Street, *Hydrogenated amorphous silicon*, Cambridge University Press, New York, 1991 pp 18-34
7. Max Jacob, *Heat Transfer*, John Wiley & Sons, New York, 1956 vol.1 pp614-634
8. E. Demaray, SID 99 Digest p853 (1999)
9. D.K. Biegelsen, R.A. Street, C.C. Tsai, and J.C. Knights, Phys. Rev. **B20** pp 4839-4846 (1979)
10. M.H. Brodsky, Manuel Cardona, and J.J. Cuomo, Phys. Rev. **B16** pp 3556-3571 (1977), G. Lucovsky, R.J. Nemanich, and J.C. Knights, Phys. Rev. **B19** pp 2064-2073 (1979)
11. Z. Remes, M. Vanecek, A.M.Mahan, and R.S. Crandall, Phys. Rev. **B56** R12 pp 710-713 (1997)
12. M.H. Brodsky, *Properties of Amorphous Silicon*, emis data review aeries #1, INSPEC, 1985 § 2.1-2.6, R.A. Street, *Hydrogenated amorphous silicon*, Cambridge university Press, New york, 1991 pp44-61, C.G.Van de Walle, J. Non-Cryst. Solids, **227-230** pp111-119 (1998)
13. R.F. Wood, and G.A. Geist, Phys. Rev. **B34** pp2606-2620 (1986)
14. M. Hatano, S. Moon, M. Lee, K. Suzuki, and C.P. Grigoropoulos, J. Appl. Phys. **87** pp36-43 (2000)
15. G. Kawachi, private communications
16. K. Kitahara, A. Moritani, A. Hara, and M. Okabe, Jpn. J. Appl. Phys. **38** pp L1312-L1314 (1999)
17. A. Van Wieringen, and N. Warmoltz, Physica **22** pp849-865 (1956)

Laser Chemical Process for Clean Applications in Semiconductor Manufacturing.

David Yogeve, Michael Engel, Shaik Zeid, Izhak Barzilay and Boris Livshits

ORAMIR Semiconductor Equipment LTD. P.O.B 306, Yokneam 20692, ISRAEL.

Email: d_yogev@oramir.com

ABSTRACT

Cleaning applications in the semiconductor manufacturing industry are tougher to meet as the device dimensions decrease. The uniqueness of Oramir-Laser-Chemical process relies on the mutual combination and effectiveness of laser particle removal mechanisms and laser induced photo-thermal-chemical reaction in the mixture of O_2 / O_3 / NF_3 gases. The process involves ozone blast wave, photo decomposition of O_3 into O radicals, photo-thermal decomposition of NF_3 into fluorine radicals, thermal effects and thin liquid-chemistry ablation enhanced particle removal. Recent results on Bare Si wafers, photo masks, EUV masks and scalpel masks show substantial removal efficiency, up to 100% for certain applications.

Keywords: Laser cleaning, Bare Si, Photo masks, EUV / Scalpel masks.

1. INTRODUCTION

Particle contamination is a constant problem faced by the microelectronics industry with increasing impact on device yield. With each new device generation, the cleaning requirements become tougher and the number of cleaning steps increases. A "killer defect" is less than half the size of the device CD (critical dimension) which means that for 0.25 micron technology, one have to remove particles less than 0.12 micron. For 0.18 micron technology, the cleaning process has to be efficient for particles less than 0.1 micron. Since the density of contaminants increases rapidly with diminishing size, every wafer processing step becomes a source of contamination.

Not just that particles density increases for small submicron particles, their removal becomes harder because of the nature of adhesion forces as compared to removal forces¹. The main physical adhesion forces operates between submicron particles and the substrate are van der waals force, capillary force and electrostatic force. Although the relative amount of those forces depends on the nature and chemical composition of both, particle and substrate surface, they are proportional to the particle diameter. However, mechanical-type removal forces are proportional to particle cross section, e.g. it is harder to deliver the necessary force to over come adhesion forces for smaller particles.

In addition to the fundamental aspects described above, traditional wet (chemical solutions) cleaning techniques which include: ultrasonic / megasonics, and / or brush scrubbing, face the risk of becoming a contaminate source and add particles onto the surface. The reason is based on the critical requirements for the cleanliness of the liquid solutions as well as for immersion bath and brushes.

Laser cleaning is one of the promising dry cleaning techniques which may replace wet cleans in the near future. There are number of groups which report on variety of pulsed laser clean applications¹⁻⁹. One main approach is based on "dry laser clean" to lift the particle from the surface, while the second dominant approach uses a simultaneous deposition of thin liquid layer and laser radiation. In this approach, the laser radiation leads to explosive evaporation of the liquid which eject the particles. This technique is known as "steam laser clean".

The uniqueness of Oramir Laser Chemical Process is based on the ability to combine dry / steam laser clean approaches with additional of photo chemical / mechanical reactions in the mixture of O_2 / O_3 / NF_3 process gases. In this article we will report on our recent results on bare Si wafers, photo masks, EUV and SCALPEL masks.

2. EXPERIMENTAL

Oramir Laser Chemical Process is described elsewhere¹⁰. Briefly, the UV photons generated by a KrF excimer laser (248 nm) are introduced to a closed process chamber via a quartz window. For reactive clean process, oxygen is passed through silent electric discharges (gas excitor) and supplied to the process chamber as a mixture of O₂ and ozone (O₃). In addition, we can feed, simultaneously, a small amount of NF₃ to mix with the O₂ / O₃. The exothermic photo dissociation of ozone into oxygen radicals induces thermal dissociation of the halogen process gas into halogen atoms (in this example, F atoms). The substrate is simultaneously irradiated by the excimer laser and exposed, locally, to the reactive gas mixture under the laser spot. Vacuum and gas system which control the flow, pressure and temperature can be used for deposition of thin liquid layers on the substrate surface for "steam laser clean". Once the particles are lifted off the surface, they are carried away by a laminar flow of the O₂ process gas.

a Experimental Setup

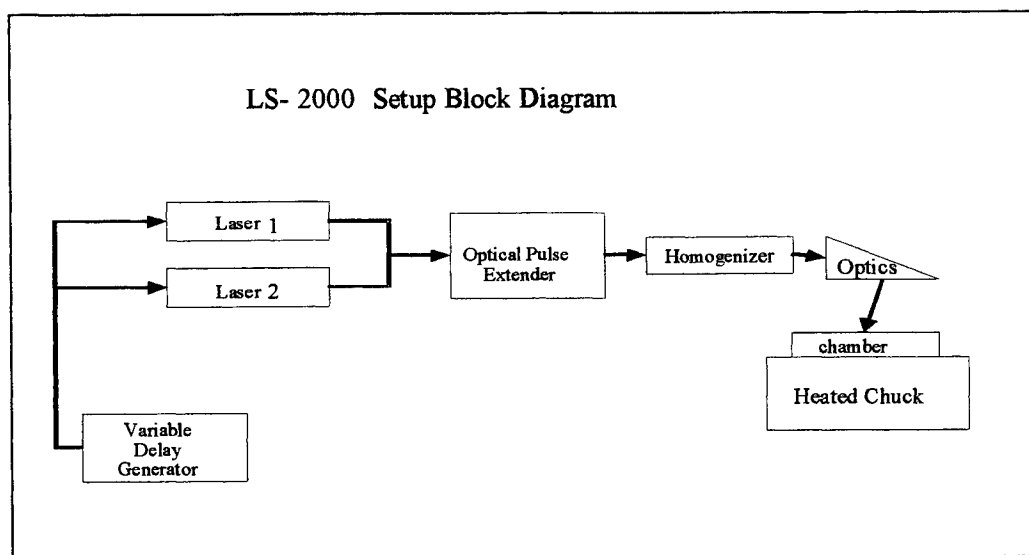
All clean applications are performed in our development lab and by Oramir LS-2000 machine.

The LS-2000 machine

The LS-2000 machine is the current state of the art machine for Excimer laser processing of semiconductor materials. The machine consists of:

- two synchronized Excimer lasers each capable of producing 400 mJ pulses at rates up to 200Hz,
- electronic system for pulse delay control between the two lasers,
- proprietary optical pulse extender that allows to extend each of the laser pulses two or three folds,
- optical homogenizer system that produces a rectangular uniform laser spot
- an optical scanning system that allows scanning of an area of 200x200 mm with different scanning schemes and different fluence levels (determined by the spot size)
- a chamber that allows processing of wafers/samples in a controlled atmosphere with capability of uniformly heating the wafer/samples up to 250°C
- vacuum and gas system which controls the temperature, flow and the pressure of the process gases and liquids
- Built in beam profiler and energy probe allow in- situ measurement of the beam parameters.

A block diagram and general layout of the LS-2000 is given below (figures 1 and 2).



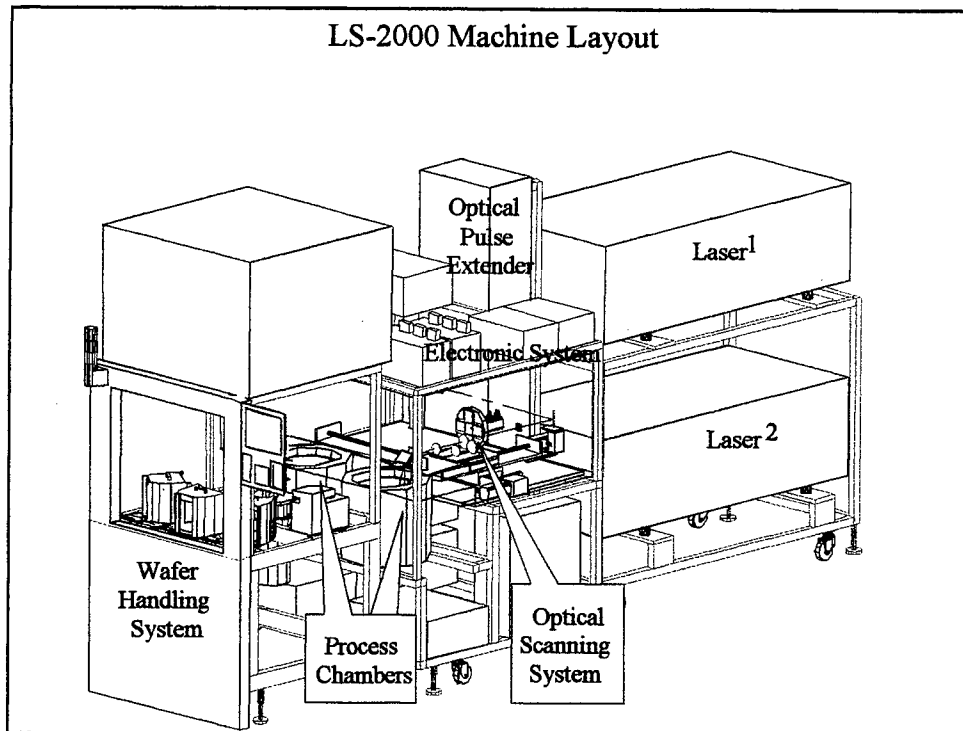


Figure 2: General layout of the LS-2000 machine

Pulse duration

A major “dry laser” cleans mechanism is based on a fast photo-thermal expansion of the substrate under the laser irradiation due to strong absorbance and fast heating. Particle ejection is due to the sudden expansion (in time scale of the pulse duration) which results in a very high velocity and acceleration¹. Cleaning (ejection) efficiency is directly proportional to laser fluence and $\sim 1/\tau^2$ to pulse duration. Although high cleaning efficiency is the major task, we have to avoid any damage to the substrate. By varying and controlling the laser pulse duration we can keep the heat evaluation in the substrate (device) below damage threshold.

The temporal distribution of the composite pulse arriving to the specimen can be varied in three ways:

a. Pulse Delay:

This is a delay that is introduced between the two laser pulses. This is achieved by electronically changing the delay time between the trigger time of the two lasers. This is possible by using the synchronization system of the two lasers.

b. Optical Pulse Extension:

Optical pulse extension is achieved by splitting a laser pulse into two or three parts and introducing delay between the parts by different path lengths that each part goes through.

c. Composite Pulse Extension:

Composite pulse extension is the combination of an “active” delay between the two lasers and optical pulse extension of each of the laser pulses. This composite mode allows achieving complex temporal behavior of the composite pulse intensity.

The effect of each of the pulse extension mechanism is shown, schematically, in figure 3.

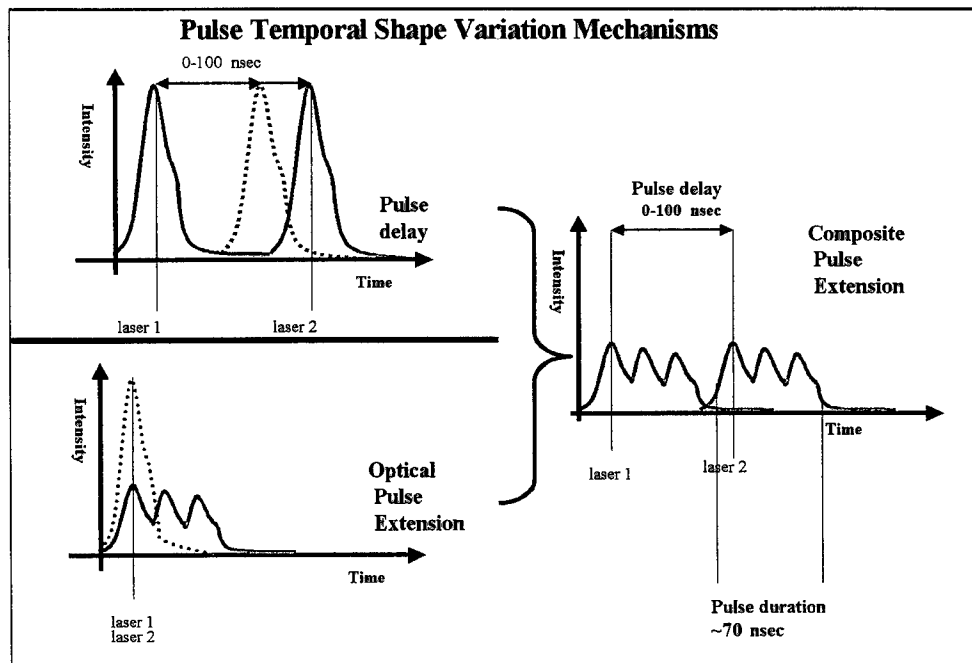
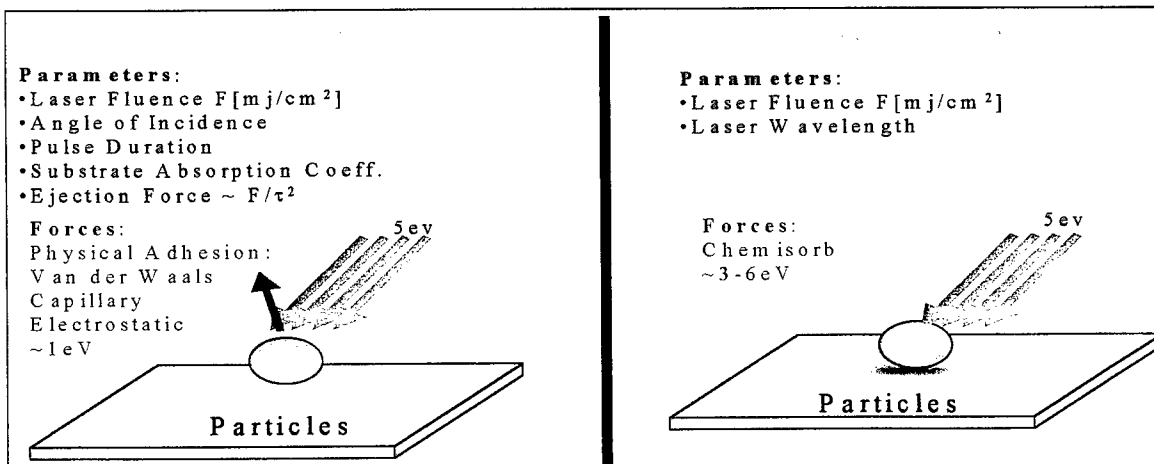


Figure 3: Pulse extension and delay mechanism for changing the temporal intensity distribution.

3. THEORY

The fundamental and practical aspects of adhesion (physical) forces between submicron particles and substrate surface, as well as dry / steam laser cleans mechanisms, are well documented¹⁻⁹.

In the following figures (figure 4) we will present the versatility and arsenal of cleaning processes that relates to Oramir's laser technology.



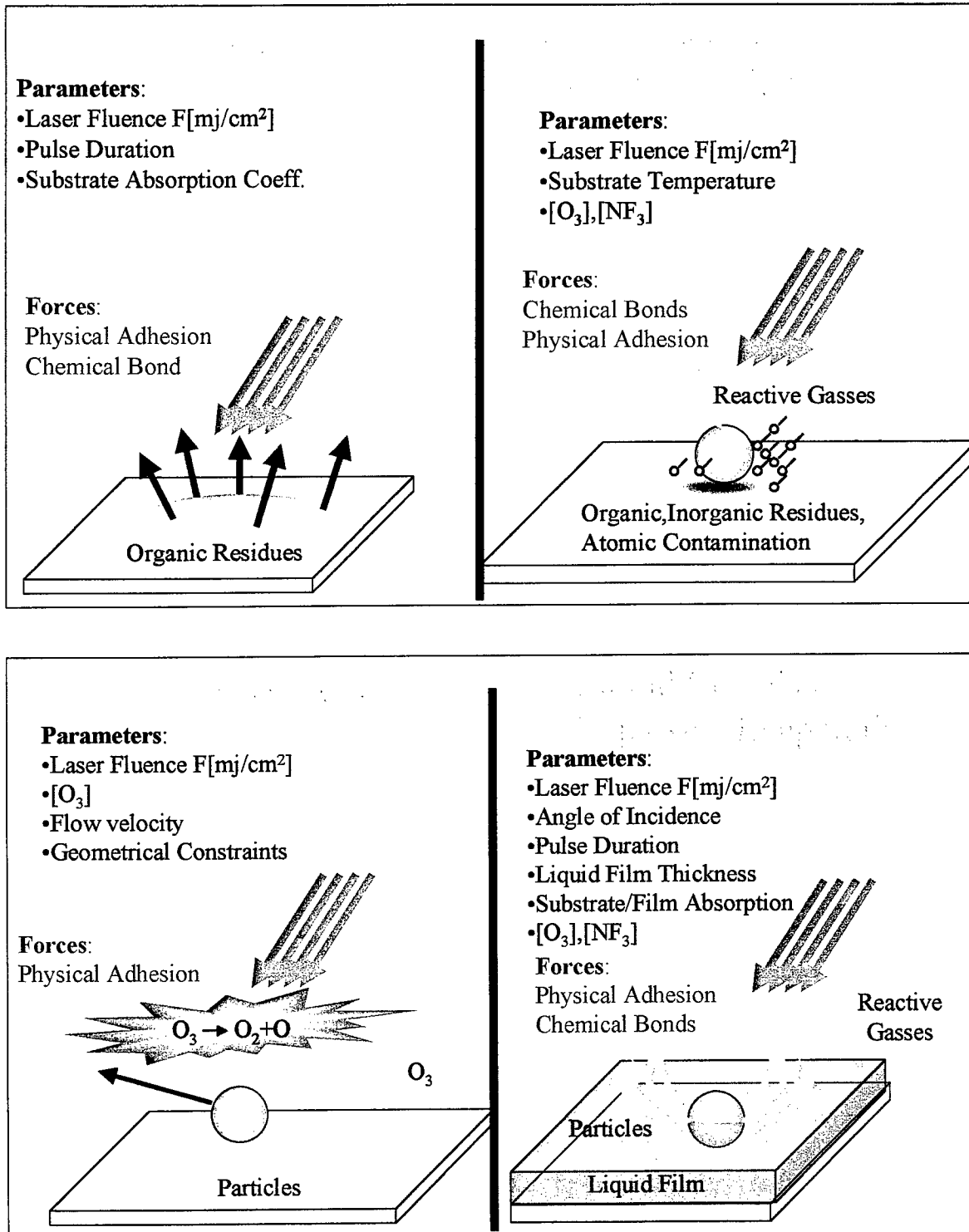


Figure 4: Contamination removal mechanisms

The added values of Oramir processes are:

- The exothermic photo decomposition of O_3 into O radicals induces chemical etching of organic particles. Also, the heat generation due to the exothermic reaction facilitates the chemical reactions on the substrate and in the gas phase with the laser-ablation products. The oxidizing of the ablation residues (combustion), prevents massive re-deposition on the substrate.
- The process chamber contains ozone which absorbs the laser UV radiation and decomposes in an exothermic reaction to atomic oxygen and oxygen molecule. The fast exothermic reaction of oxygen atoms with ozone molecules causes an instant gas heating and a successive thermal explosion, producing shock wave, "ozone blast". Depending on experimental parameters, this blast is able to shift and detach particles from the surface.
- The photo and thermal decomposition of process gases into atomic oxygen and atomic fluorine results in a highly reactive atmosphere which can etch inorganic contaminants and undercut chemical bonds between particle and surface.
- The introduction of water vapors into the process chamber and reaction with F radicals (from NF_3 process gas) creates trace amounts of HF acid which undercuts the chemical bonds. One major advantage of this in situ HF formation, relies on the fact that we don't need a special, costly, system as compared to standard HF systems.

4. RESULTS

1. Bare Si wafers.

Figure 5 bellow shows the results of "dry" laser clean process on the LS-2000 tool.

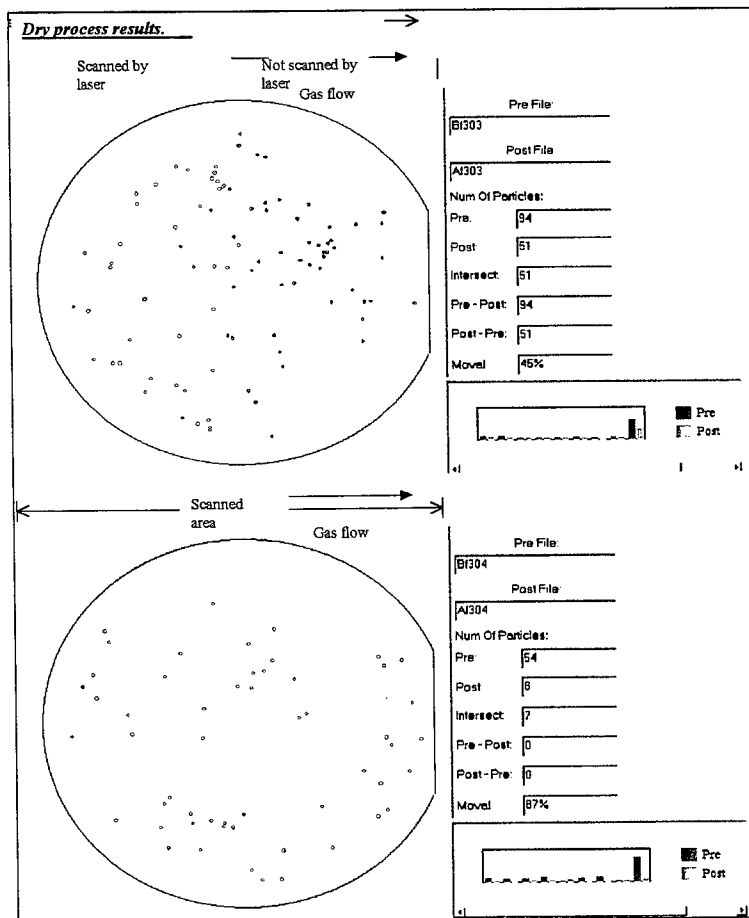


Figure 5:
"dry" laser clean process on the
LS-2000 tool.

Each one of the two wafer maps in figure 5 is a superposition of two Tencor maps. The first map taken before the clean process and is referred as “pre” measurement, and the second map is referred as “post” process measurement. Figure 5 shows the superposition of the two maps. The red circles marks are for the “pre” measurements while the blue dots represent “post” measurements. The 150 mm bare Si wafer in figure 5 contained, pre process, 94 air-born particles (> 0.24 micron). In first stage (upper part of figure 5) we scanned and exposed only the left half of the wafer to laser radiation. We didn’t operate any reactive chemistry during the laser process beside constant laminar flow of O_2 . As the result of a laser process almost all particles were removed from the left half of the wafer (3 blue dots remained). In addition, one can note that there is no re deposition of particles which removed from the left side onto the right side of the wafer. The right side of the wafer contained just “blue dots” inside “red circles”. An addition of blue dots outside of red circle, would reflect re deposition. After the ejection of particles by the laser pulses, the laminar flow carried them out of the wafer surface. This type of efficient removal is hard to achieve in “open” chamber systems. The bottom of figure 5 shows full wafer scans by the laser. 54 pre-process particles were measured and 8 particles left on the surface after process. It is important to mention that 7 particles out of the 8, left after the clean process, remained in the original location (dots inside circles) which clearly indicates that the re deposition didn’t occur.

The results of “steam” laser clean appear in figure 6. Over 98% of air-born particles (> 0.24 micron) were removed.

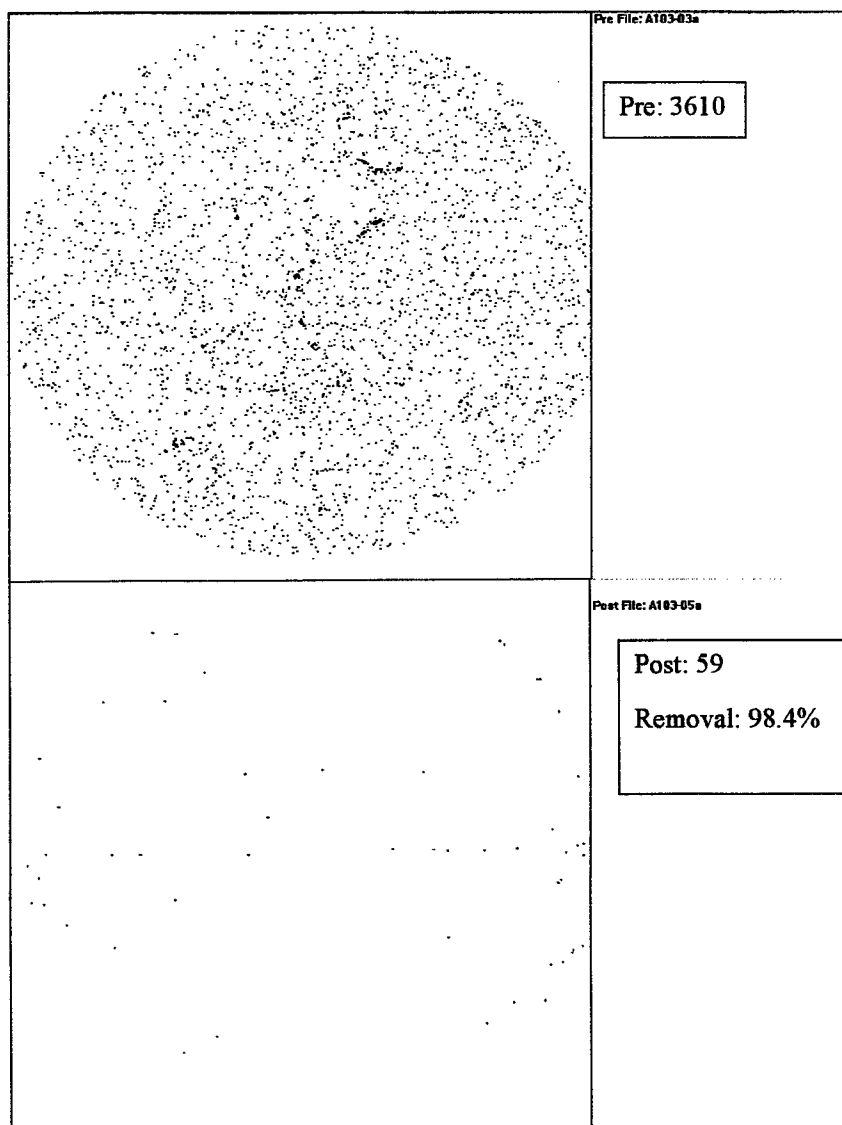


Figure 6:
“steam” laser clean process.

In addition to the above results, we developed a laser-chemical process for the final clean step during the manufacturing of bare Si wafers. The wafers contained less than 10 particles per wafer (> 0.125 micron) in average, mostly in-organic in nature. Those particles were left after several wet cleaning steps during manufacturing and may have chemical bonds to the surface beside the physical adhesion forces. By the combined effect of laser radiation and reactive atmosphere we were able to remove up to 100% of the particles ("optimize" recipe removed 100% of particles from 8 wafers in a 24 wafers lot. On the other wafers the removal was better than 90%).

One major cleaning task relates to the risk of possible damage or change in surface properties. We compared surface properties of "post" laser clean wafers with control wafers (from the same lot). The results are:

- AFM measurements: Ra roughness of 0.109 nm for control wafer versus Ra roughness of 0.131 nm for the post process wafer.
- Reflectivity measurements: 0.4178 mean reflectivity (range: 400 nm to 800 nm) for control wafer versus 0.4315 mean reflectivity for the post process wafer.
- Contact angle:

Measurement point	Angle (degree) Control wafer	Angle (degree) Processed wafer
Anti flat	20 – 22	22 - 24
Flat	17 – 19	18 – 20
Right	17 – 19	22 – 24
Left	16 - 18	18 –20

The results show that the post process wafer retains hydrophilic surface.

To summarize, all measurements show that after the cleaning process, the wafer retains its basic properties.

2. Photomask.

Device technology movement from critical dimension of 0.25 micron to current 0.18 micron and future 0.15 / 0.13 micron increases the requirements from mask manufactures (mask shops). By year 2001, industry will need masks with zero defects above 0.25 micron. Mask shops feel that they need dry cleaning to adequately meet 2001 needs.

At Oramir we performed feasibility studies for the removal of several different types of defects: broken pellicle and adhesive residues (the adhesive material between the pellicle and quartz); particle removal from "clear" (quartz) and "opaque" areas. Although particles from opaque area are not printed on the photo resist during lithography steps, they may migrate into clear areas and cause the same wafer defects as clear area defects.

The two main project goals were: particle removal for the final last pre-pellicle clean step and pellicle / adhesive removal in case of re-pelliclizing process.

Figure 7 shows the results of adhesive removal process. The upper area contains a stripe from a previous laser-removal experiment. One can see that the adhesive was removed but some traces of the adhesive and particles remained in the same positions. The basic assumption regarding the clean process was that the process consists of evaporation / ablation of the adhesive and transport of the residues by the process gasses.

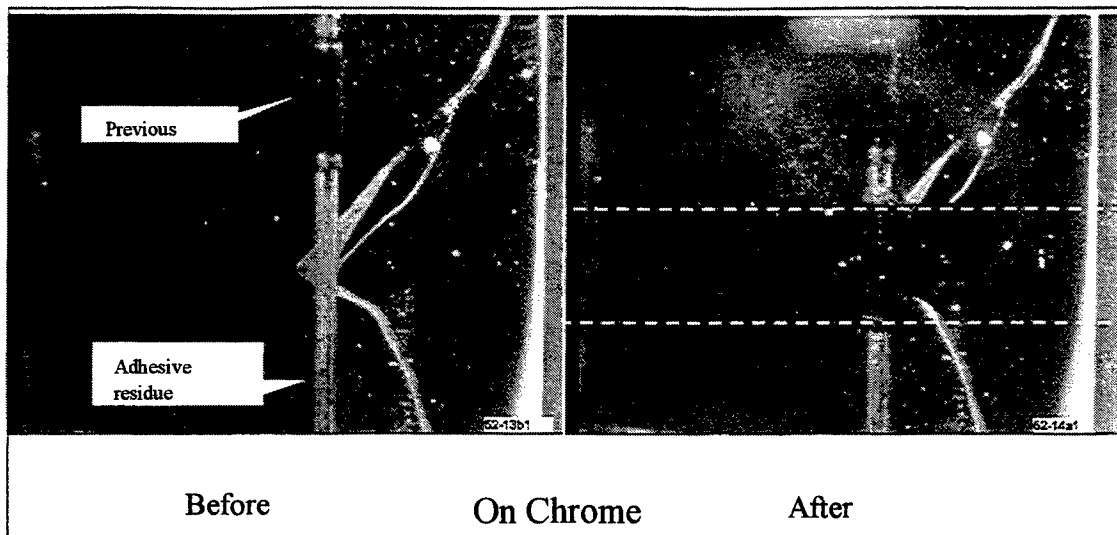


Figure 7: Adhesive residue removal.

Figure 8 shows the results of pellicle residue removal. Since in this mask, most of the area was covered with chrome, the test demonstrated pellicle residue removal from chrome areas. Later tests were conducted to demonstrate removal capability from patterned areas.

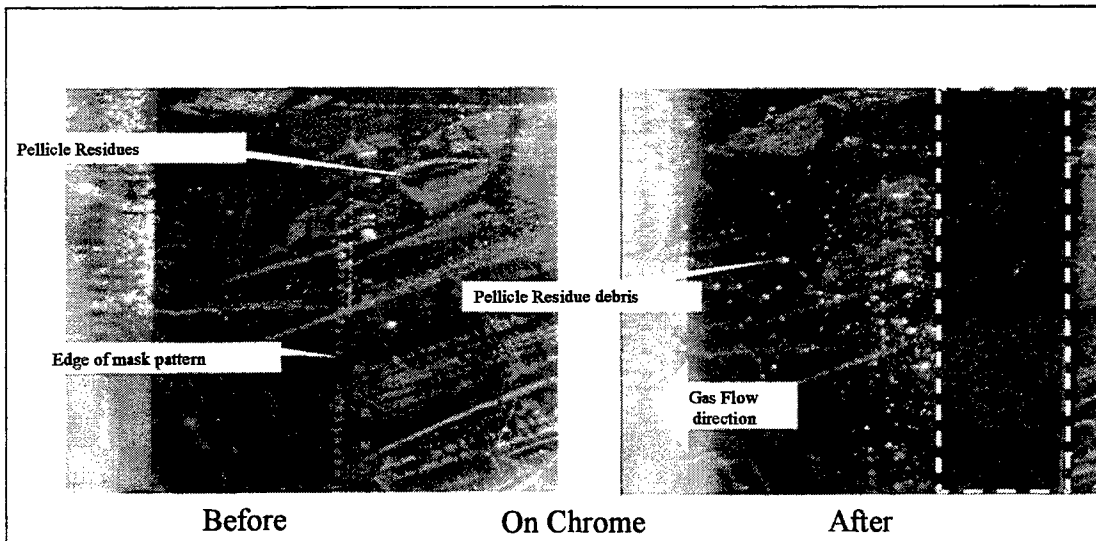


Figure 8: Pellicle residue removal.

Figure 9 demonstrates particle removal process. The part with the brighter background is the pattern region and the darker part (on the right of each image) is the chrome area on the margin of the mask. The area between the two dotted lines is the stripe that was scanned by the laser. This area shows much less particles compared to its status before the laser scan.

To summarize, it is clear to us that these results demonstrate the feasibility of mask cleaning by laser photochemical processes, but still don't meet, yet, the final industry requirements.

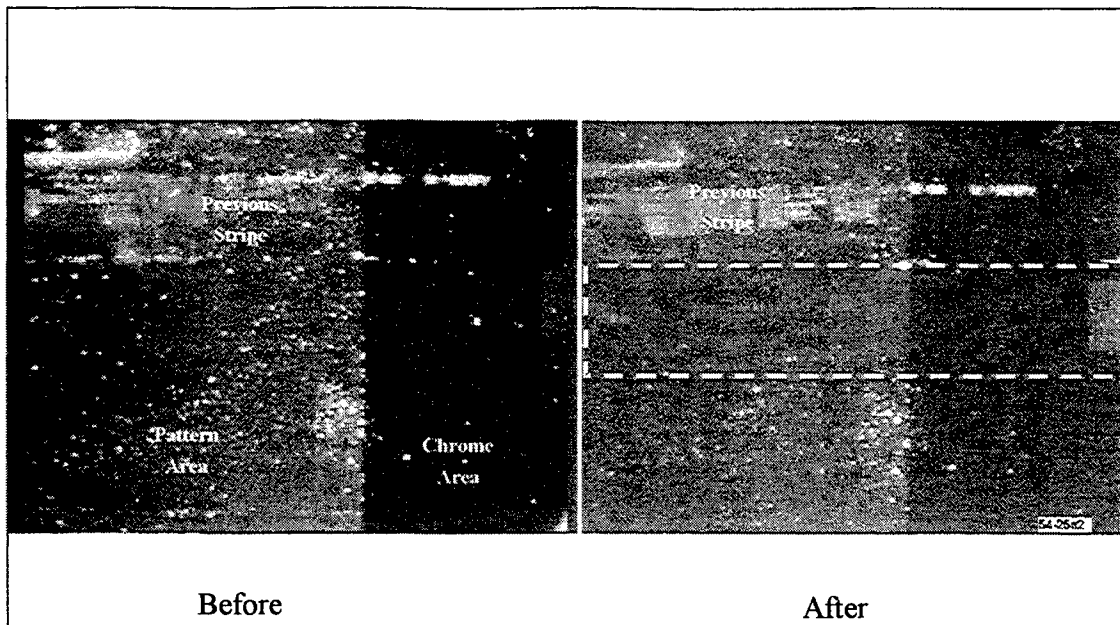


Figure 9: particle removal.

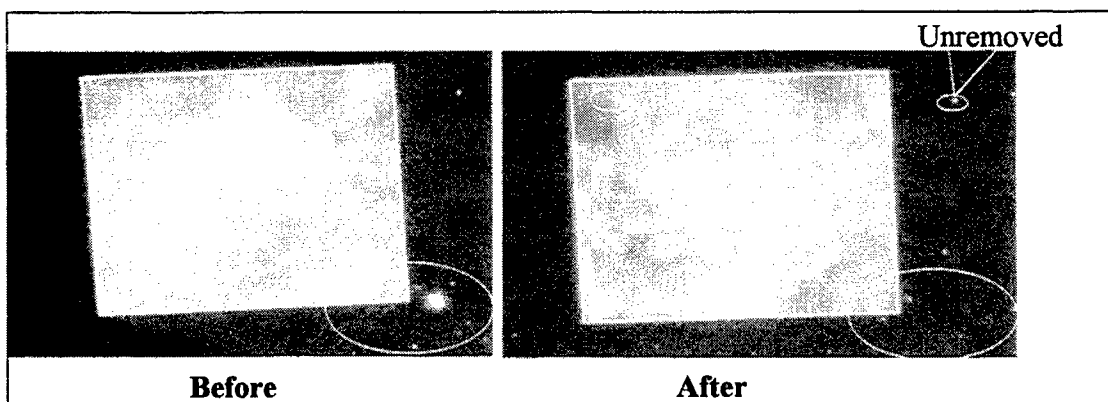
3. EUV / Scalpel masks.

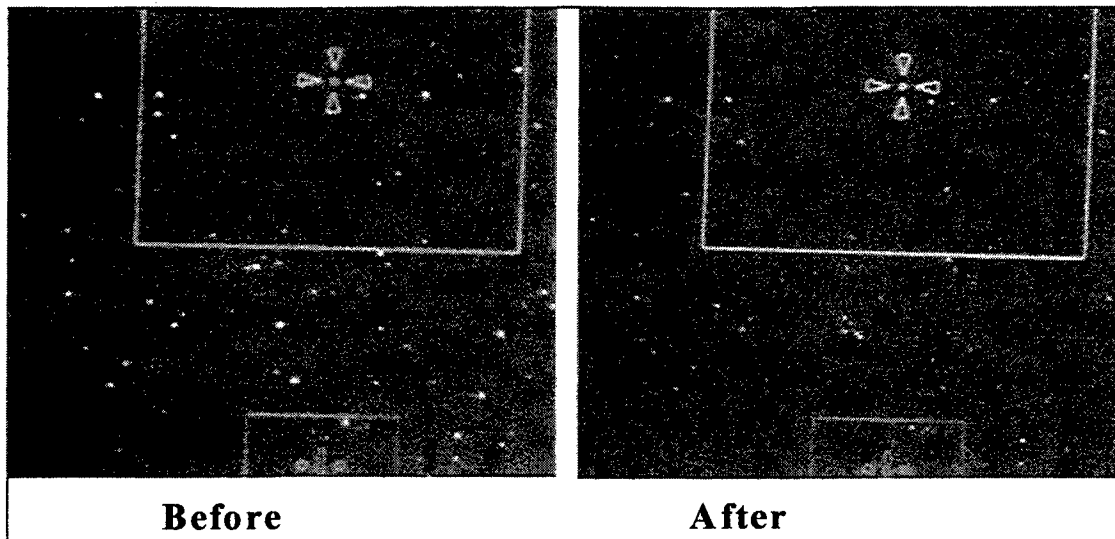
Optical photolithography has been used by chip makers for three decades, but it is finally running out of steam. The industry is developing advanced technologies to replace the optical process. Two major candidates for the “next generation lithography” are: EUV (Extreme Ultraviolet lithography) and the Scalpel electron-beam lithography. Both techniques claim to be able to create circuit features down to 50 nm and even below.

Obviously, there are many challenges regarding next generation lithography. Developers have to face new cleaning requirements with regards to minimum particle size, as well as to the delicate nature of the manufacturing process, particle type and mask material. For example, scalpel membrane thickness is less than one micron, which reject almost any mechanical cleaning treatments.

For EUV mask clean we performed the laser photochemical process. We were unable to check and verify particle removal efficiency by Tencor because of no repeating structure (pattern) on the surface. Dark field optical microscopy showed some reduction in the amount of particles without any damage to the pattern. We still have to optimize cleaning efficiency and measurement sensitivity.

Figures 10 and 11 show particles removal from Scalpel SiN blank membrane and from Scalpel patterned membrane.





Figures 10 and 11: particles removal from Scalpel SiN blank membrane (upper) and from patterned membrane.

Particles were inspected, pre and post cleaning process, by optical microscope linked to a video CCD camera / PC with frame grabber (dark field mode). As for feasibility test, we can note reduction of particles number on top of SiN blank membrane and patterned membrane.

5. SUMMARY

Industry faces show stoppers in cleaning processes during the fabrication of advanced device generation as well as next generation lithography masks. Conventional cleaning techniques will be shortly unable to meet industry requirements. There is also a demand to reduce the amount of chemical and water consumption and to develop an environmentally friendly processes.

There are few groups which work on the application of laser technique for contaminates / particles removal processes and gained several success but with limited adoption capabilities. The uniqueness of Oramir Laser Chemical process relies on the option to combine laser particle removal mechanisms with reactive chemistry. The reactive chemistry can overcome chemical adhesion forces besides the physical ones.

6. REFERENCES

1. A. C. Tam, W. P. Leung, W. Zapka and W. Ziemlich, "Laser-cleaning techniques for removal of surface particulates," *J. Appl. Phys.* 71(7), pp. 3515-3523, 1992.
2. W. Zapka, A. C. Tam, G. Ayers and W. Ziemlich, "Liquid film enhanced laser cleaning," *Microelectronic Engineering* 17, pp. 473-478, 1992.
3. A. C. Tam, W. P. Leung and W. Zapka, in *Particles on Surfaces*, pp. 405-418, Marcel Dekker, Inc. 1995.
4. G. Vereecke, E. Rohr and M. M. Heyns, "Evaluation of a dry laser cleaning process," *44th Annual Technical Meeting Inst. Env. Sci. Technol.*, Phoenix, 1998.
5. Y. F. Lu, Y. Zhang, Y. H. Wan and W. D. Song, "Laser cleaning of silicon surface with deposition of different liquid films," *Applied Surface Science* 138-139, pp. 140-144, (1999).

6. Y. F. Lu, W. D. Song, C. K. Tee, D. S. H. Chan and T. S. Low, "Wavelength effects in the laser cleaning process," *Jpn. J. Appl. Phys.* 37, pp. 840-844, 1998.
7. S. J. Lee, K. Imen and S. D. Allen, "CO₂ laser assisted particle removal threshold measurements," *Appl. Phys. Lett.* 61 (19), pp. 2314-2316, 1992.
8. S. J. Lee, K. Imen and S. D. Allen, "Shock wave analysis of laser assisted particle removal," *J. Appl. Phys.* 74 (12), pp. 7044-7047, 1993.
9. O. Yavas, A. Schilling, J. Bischof, J. Boneberg and P. Leiderer, "Study of nucleation processes during laser cleaning of surfaces," *Laser Physics* 7 (2), pp. 343-348, 1997.
10. B. Livshits, O. Tehar-Zahav, E. Iskevitch and M. Genut, "Laser, dry and plasmaless, photoresist removal," *SolidState Technology*, July 1997.

SESSION 4

Lasers and Techniques II

Present status and future aspects of high power diode laser materials processing under the view of the German national research project

Friedrich G. Bachmann*

MDS Project Management
ROFIN-SINAR Laser GmbH
Galileo-Galilei-Strasse 10
D-55129 Mainz / Germany

ABSTRACT

High power diode lasers from a few Watts up to several Kilowatts have entered industrial manufacturing environment for materials processing applications. The technology has proven to show unique features, e.g. high efficiency, small size, low energy consumption and high reliability. In the first part of this paper a short description of state-of-the-art high power diode laser technology and applications is provided and the benefits and restrictions of this laser technology will be evaluated.

For large scale penetration into the manufacturing market, the restrictions, especially the rather poor beam quality of high power diode lasers compared to conventional lasers have to be overcome. Also, the specialties of the high power diode lasers, i.e. their modular structure and their extremely small size have to be translated into laser manufacturing technology.

The further improvement of high power diode lasers as well as the development of new diode laser specific manufacturing technologies are the essential topics of a National German Minister Priority Project entitled "Modular Diode Laser Beam Tools" (MDS): 22 Partners from industry and institutions, 4 semiconductor experts, 5 laser manufacturers and 14 applicants are working together in frame of this project to work out and transfer a joint strategy and system technology to the benefits of the future of high power diode laser technology. The goals, the structure and the work of this project will be described in the second part of this paper.

Keywords: diode lasers, high power lasers, materials processing, laser applications,

1. INTRODUCTION

The last year of the millennium, year 1999, has been named "The Year of the Diode Laser" for the laser community recently [1]!

This statement is based on the extremely rapid development of this technology in the last few years, especially in 1999: When first laser action in homojunction GaAs or GaAsP diodes at cryogenic temperatures has been demonstrated in 1962 [2,3,4] or a few years later, when cw lasing has been shown at room temperature in AlGaAs/GaAs double-heterostructure in 1970 [5,6], certainly no one had the vision, that these lasers could ever play an important role in materials processing. Even after the lifetime could be considerably improved by the successful investigation of the crystalline structures and the understanding of the phenomena at the laser facet and, thus, the detailed understanding of the failure mechanisms [7], which finally led to the acceptance of semiconductor lasers in the communication, computer and consumer electronics technology in the mid 80s, the picture, that diode lasers are not well suited for materials processing did certainly not change. However, it was recognized, that one key technology for the power increase of semiconductor lasers is efficient active cooling of the

* Correspondence: E-mail: f_bachmann@compuserve.com; telephone +49 (0)6131 9226-28; fax +49 (0)6131 9226-57

semiconductor elements and special micro-channel coolers have been developed [8]. At this time, the major interest for high power semiconductor lasers was to apply them as a pumping source for solid-state lasers. In the early 1990s development of multi-stripe arrays [9], Cu-based micro-channel coolers [10], investigation of mounting and stacking technology [9] and studies of micro-optical components [11] have been started; besides the semiconductor technology, which is especially essential for achieving high power over an acceptable lifetime, cooling, mounting and beam forming are the key elements for today's high power diode lasers, which must be mastered for the successful implementation of these lasers for materials processing in an industrial environment. In the mid 1990s direct diode laser applications have been published for the first time [12]. In 1999 major breakthroughs in diode laser technology and applications have been achieved: lifetimes of laser bars are now far beyond 10000 hours [13], diode laser power up to above 2 kW can be delivered through an optical fiber [14] and power densities, which are sufficient for deep penetration welding [15] could be obtained from standard industrial diode laser sources. Diode lasers stepped into the industrial manufacturing floors in 1999 and are now accepted as an industrial tool. Thus, indeed, in the laser materials processing world 1999 was the year of the diode lasers. Nevertheless, the development seems still to be at its beginning and high power diode lasers look into an extremely bright future.

2. THE TECHNOLOGY OF HIGH POWER DIODE LASERS

2.1. Semiconductor integration, mounting and stacking technology

From a traditional diode laser element typically only a few milliwatts can be extracted from a pn-transition (fig. 1/1); to increase the power, several single elements are integrated into one semiconductor element, which has a size of about $10000 \times 600 \times 115 \mu\text{m}$ (fig. 1/2). This unit is called a "laser bar". The special shape of the light generation area leads to special light emitting characteristics, which shows a high divergence in the direction of the pn-transition ("fast axis"), and a lower divergence, but a wide emitting "stripe" in the other ("slow axis"). Even if these laser bars show electrical to optical efficiencies of up to over 50%, considerable amount of heat must be removed if power is increased further. Therefore, the laser bar must be mounted onto a special water-cooled heat sink, which allows to use the laser at currents up to 50 A, i.e. to create laser power up to 40 or 50W (fig. 1/3). The fast axis is collimated by cylindrical micro-lenses to get parallel light (fig. 1/4); these units can be stacked on top of each other, so that finally up to 1 kW can be reached from such a unit (fig. 1/5 & 1/6).

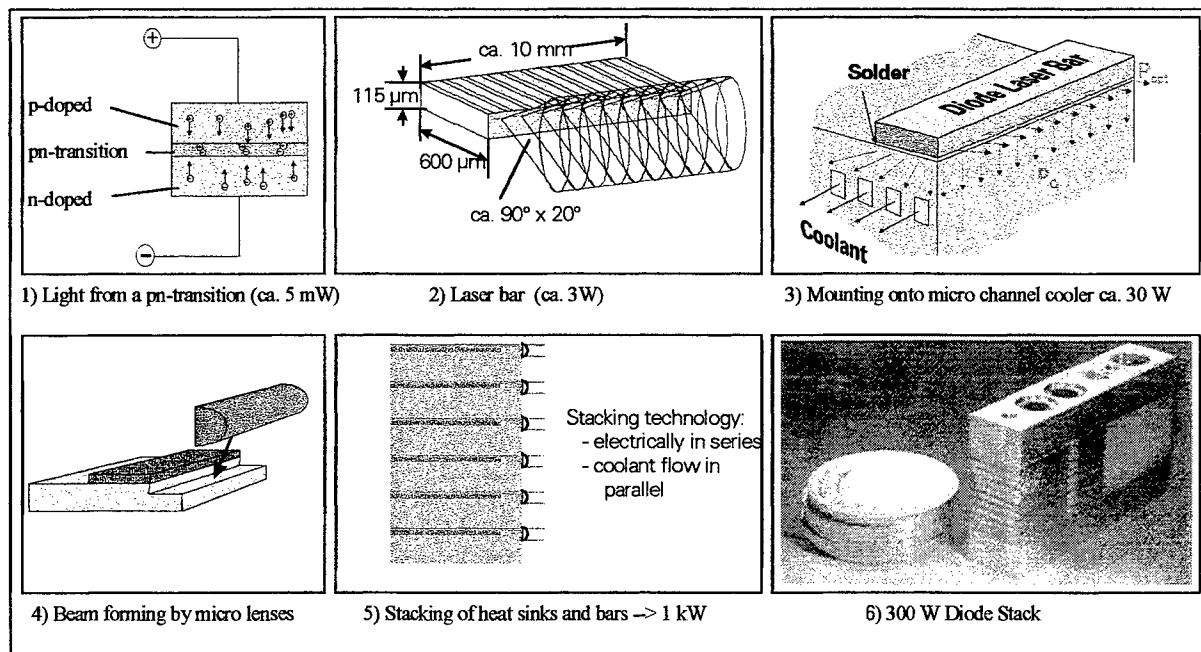


Fig. 1: The way from the diode chip to the high power diode laser

2.2 Beam rearrangement, combination and forming

For improvement of the beam quality and matching of the different divergences, sophisticated beam rearrangement concepts and systems are applied, e.g. step mirror [16] or a beam tilt unit [17, 18]. Those special optical elements cut the wide beam of the diode laser bar into smaller pieces and re-arrange them on top of each other (fig. 2/1), so that the width and divergence are reduced in one direction at the expense of the other, where width and divergence are increased. For increase of power with a theoretically constant beam quality, two or even three of such stacks can be combined by stripe mirrors (fig. 2/2) to fill in the aperture; single or combined stacks can be further directed onto the same optical path by polarization coupling (fig. 2/3) or wavelength coupling (fig. 2/4), so that up to 5 or 6 kW laser power can be delivered from a laser head, which is typically no greater in size than a shoe box. Finally in some cases the beam has to be compressed in the stacking dimension, so that it can be fed through a focussing lens system with an acceptable diameter and then focussed onto the work piece, as shown schematically in the sketch in fig. 2/5. Typical high power diode laser systems with (right) or without (left) optical fiber are presented in fig. 2/6.

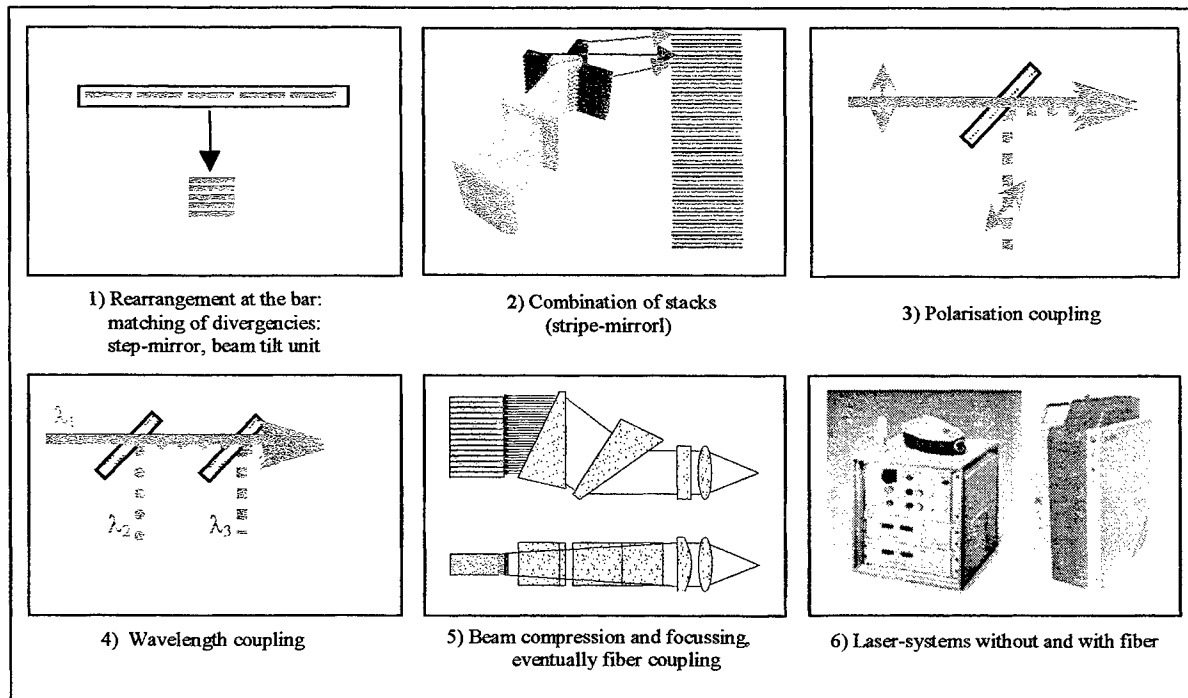


Fig. 2: Beam rearrangement, combination and forming

2.3 Beam quality of high power diode lasers

In diode lasers, high power is generated by incoherent coupling of several individual laser sources under the use of reflective and diffractive optics, as described in section 2.1 and 2.2. Because of the different beam qualities of the single laser bar and the stacking of the laser bars to increase the total power, the focal area of standard high power diode lasers is rectangular (as long as no fiber coupling is used). Thus, it is not surprising, that the beam quality of high power diode lasers is not (yet) as good as the one of the conventional CO₂ and Nd:YAG lasers. Fig. 3 shows a comparison of the beam-parameter-product of CO₂, Nd:YAG and diode lasers¹ versus the output power. In the diode laser area, the values for commercial products - as far as they are known to the author - are shown; the bottom line seems to be a limit for the state of the art diode lasers; such a limit has been predicted under certain parameters in 1997 [19].

¹ The beam parameter product of diode lasers is taken as the geometric average of the two axes: $BPP = \sqrt{BPP_x \times BPP_y}$; focal dimensions are set at $1/e^2$

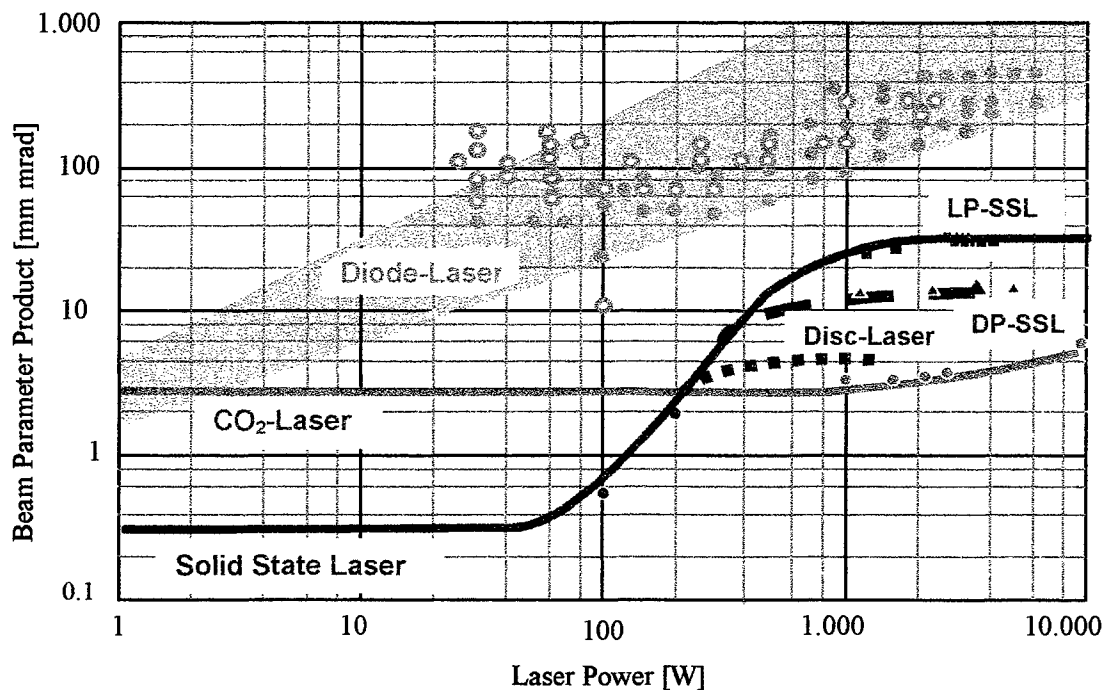


Fig. 3: Beam quality (Beam-Parameter-Product) vs. power for different lasers: CO₂, solid-state and diode lasers
Dots represent state-of-the art high power diode lasers: filled = standard optics; open: fiber coupling
(LP-SSL = Lamp pumped solid state; DP-SSL = Diode pumped solid state)

3. APPLICATIONS OF HIGH POWER DIODE LASERS

As a consequence of the rather poor beam quality traditional laser applications such as cutting and high speed deep penetration welding are not yet available as a market for high power diode lasers (even if deep penetration welding has been demonstrated recently [15]- see section 5.4.3.1). However, as we can easily see from fig. 4, where typical requirements for power and beam quality are presented as well as today's high power diode laser beam quality limit shown in fig.3, there are still applications with a high potential available for the high power diode lasers: In fact, some of these applications have been demonstrated years ago with Nd:YAG or CO₂ lasers, but could not penetrate into the industrial manufacturing for technological or - mainly - cost reasons. The investment costs of today's high power diode laser systems are in the range or even below those of CO₂ lasers and, thus, already considerably less than Nd:YAG lasers; the running costs are much less than those of conventional lasers because of their high efficiency (typically the wall plug efficiency is in the range or even above 30%) and since they are almost service free over the lifetime of the diodes. Considerable reduction of the running costs is expected with the increase of lifetime of the diode laser bars, since simple cost calculations show, that besides the depreciation, the replacement of the diodes creates the lion's share of the running costs. Last but not least, the small size of not only the laser head, but - based on the high electrical to optical efficiency - also of the power supply and the chiller, make them a very attractive tool for many of these applications, where beam quality of the conventional laser is simply not necessary.

Almost all of the applications mentioned in fig. 4 above the diode laser limit line have not only been proven to be feasible with the diode lasers, but also to be much more cost effective, sometimes also more process effective [21, 22]. This means, that there is an advantage for the diode laser in many cases and actually most of the applications are already introduced into industrial manufacturing [18], especially surface hardening [23] as well as soldering [24] and polymer welding [25, 26].

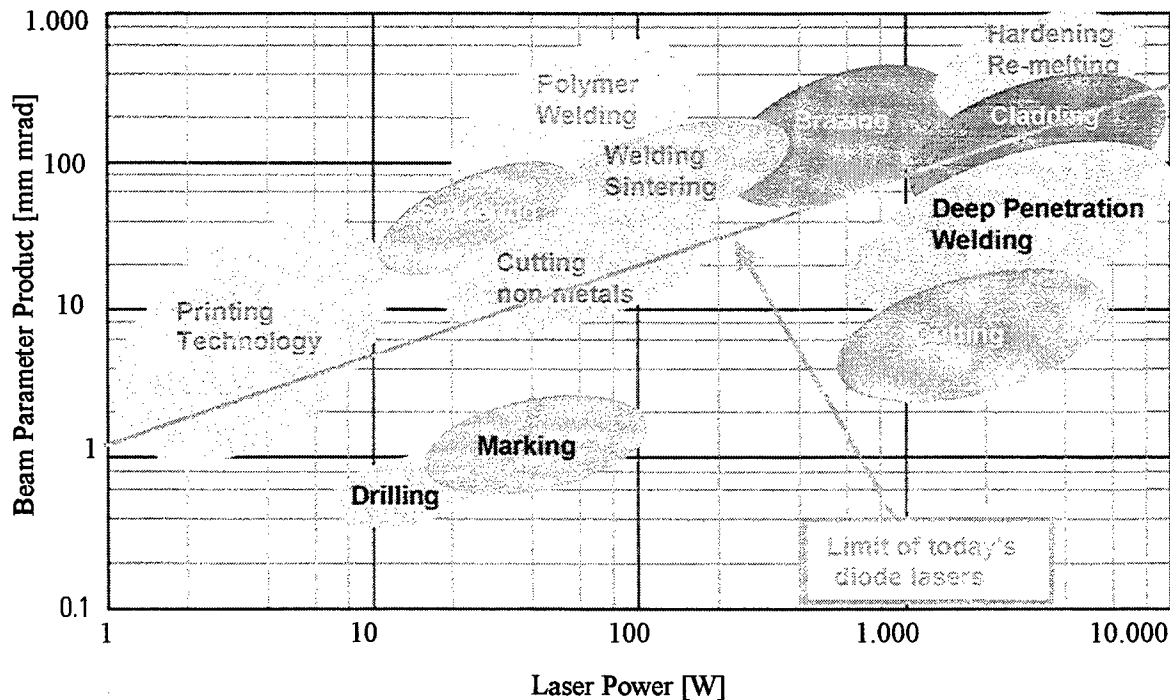


Fig. 4: Beam parameter field for the materials processing with lasers (after [20])
(based on focal number $F/\# = 4$)

4. FUTURE ASPECTS OF HIGH POWER DIODE LASERS

From the statements made so far it is very evident, that one of the main topics for the research and development in this technology will be the improvement of the beam quality of the high power diode lasers. Here we have to take into account the complex technology of beam forming and beam combination in high power diode lasers, especially the accuracy, which is necessary for the mounting of the laser bars onto the heat sink as well as for the manufacturing and the alignment of the beam forming and combination optics. Even if it is proven by the lasers on the marketplace, that this technology can be mastered well, it is obvious that not only power increase of the individual bars, but also improvement of their beam quality is essential for either to get also better beam quality in high power diode lasers or to reduce the expenditure to reach high power at lower beam quality. Last but not least, concepts for coherent coupling are investigated for the improvement of the beam quality [27].

On the first glance, the fact, that high power diode lasers consist of many individual lasers may appear as an disadvantage, which is of course true, if only high beam quality at high power i.e. high brightness is considered; we are used to think that way about lasers, influenced by our traditional laser applications. However, there comes also an attractive chance for a totally new concept of laser processing from this situation: the individual bars can be mounted in a way, which is adapted to the process resp. to the work piece, which allows "parallel processing" with high throughput. A sketch of an application of this modular arrangement of lasers is given in fig. 5 [26]; certainly, this way lasers can form large areas, long lines, or to some extent any shape. If we think a little further in this concept, and if we take into account, that not only the geometrical setup can be adjusted, but also the individual elements can be individually controlled, the dream of a fast controllable individual intensity profile of a laser beam may become true; this would open unsuspected possibilities for laser surface treatment.

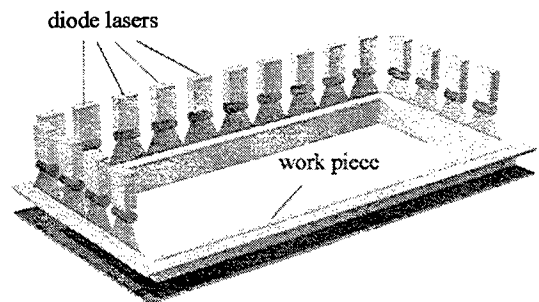


Fig. 5: sketch of simultaneous welding of polymers [26]

Also, very often considerable cost reduction is forecasted for high power diode lasers in the next future: the price per Watt to be paid for naked diode laser bars has been reduced by one order of magnitude every five years since the beginning in 1975 and is now in the range of about 10 \$/W [28]; the forecast for year 2005 is 1 \$/W [28]. Since the fabrication of diode laser bars is a wafer based batch process in expensive machines, this is of course a consequence of the manufacturing volume and the improvement of yield and can be easily understood. For the high power diode laser systems, as they are described above in §2 of this paper, such a dramatic price reduction cannot realistically be expected: even if mounting technology will be simplified, even if micro-optical element manufacturing will be automated and mounting and alignment procedure will be simplified as well, supporting units as e.g. power supplies, control units and chillers are still necessary and not expected to follow "order of magnitude price drops" even at considerable production numbers. Today's high power diode laser system investment costs (in \$/W) are roughly in the range of CO₂ lasers; we expect a reduction to 60 or 50% within the next five or ten years.

Of course, high power diode lasers have a considerable advantage over all the conventional lasers because of their high efficiency, their simple, almost service free operation, their small size and their flexibility. Thus, research projects, as the one described here in this paper, focus on the improvement of beam quality, the elongation of diode life, the improvement and simplification of optical beam combination and forming concepts and especially on the matching of the special novel laser source "high power diode laser" with the application needs in the industry.

5. THE MINISTER PRIORITY PROJECT "MODULARE DIODENLASER STRAHLWERKZEUGE"

The German title of the project "Modulare Diodenlaser-Strahlwerkzeuge (MDS)", means "modular diode laser beam tools"; the target of the project is the development of novel diode laser based laser systems and the application of those laser systems in the production technology. The concept of the high power diode lasers is new and not yet established world wide. With the introduction of high power diode lasers, the laser processing technology will experience a similar fundamental leap as could be observed in electronics with the transition from electronic tubes to semiconductor technology. The project investigates the scientific and technological basis for the diode laser and laser systems technology and generates the fundamental knowledge for the application of these laser systems; these laser systems represent a new generation of lasers, based on the unique features of the diode lasers: their small size, high efficiency and modularity. It is expected, that this technology will be a revolution in manufacturing technology and will enhance the number of laser processes in industrial manufacturing lines considerably world wide. The project is funded from the "Bundesministerium für Bildung und Forschung (BMBF)"².

5.1 Genesis of the project

In the first half of year 1997 a competition for project ideas under the title "Innovative Products on the Basis of Novel Technologies" was launched from the BMBF. Every German institution or company could participate with a project idea, which should be explained to an independent jury of high ranked experts from industry, science, economy and politics in a 10-page description. 271 proposals have been sent in at the deadline on Sept. 30, 1997; 15 out of these 271 proposals have been selected for further elaboration in the second round. The "MDS" passed this hurdle. Complete project plans had now to be put together including exact project description of the entire project as well as the work packages of the individual partners. Not only scientific, technical and financial issues had to be covered in this second proposal, but also economic, social and environmental aspects had to be illuminated. Exploitation plans had to be added. Furthermore, structure and controlling of the entire project as well as a draft cooperation contract was to be explained in detail. Finally, this second proposal was presented to the jury at February 28, 1998. 5 out of the 15 finalists have finally been recommended to the BMBF for funding from the jury and MDS was among the winners. After minor revisions in the project plan, in the cooperation contract and in the finance plan, the project could finally start on July 1st, 1998 with the agreements from the ministry to each partner.

5.2 Structure of the project

The theme gains its importance especially by the fact that there will not only new semiconductor chips and laser beam sources developed, but also the wide usability of the new technology must be demonstrated in several selected applications and, thus, numerous applications and processes will be opened up step by step. Consequently, the over all target of the

² German Ministry of Education and Research

project is to establish the scientific and technological basis for the novel modular diode laser beam tools by concentrated and carefully matched co-operation between the partners in three groups,

- chip technology
- laser and systems technology and
- applications and production technology,

and to open the application related potential of this beam sources to the full. At the beginning of the technology chain, new semiconductor chips will be developed and manufactured to provide an output power and a beam quality, which are above state of the art technology by a factor of 2 to 5. These new chips will be assembled by the partners of the laser technology group to high power laser systems. For this task techniques for micro-optic beam forming and beam combination have to be developed, which are about ten times as powerful as those which are in use today. It is the task of the partners at the end of the chain, i.e. the application technology, to further develop the present knowledge about the laser as a tool, so that the specific advantages of the novel diode laser beam tools will be applied in manufacturing processes with considerably increased quality and with economic efficiency.

5.3 Partners and organizational scheme

According to the structure, which was shortly explained in the previous paragraph, the organization is split in to three groups - chip technology (CT), laser- and systems technology (LG) and applications and processing technology (AP) with the following partners:

Chip technology:	Ferdinand-Braun-Institut für Höchstfrequenztechnik, Berlin Fraunhofer-Institut für Angewandte Festkörperphysik (IAF), Freiburg Infineon Technologies AG, München Osram Opto Semiconductor, Regensburg
Laser and system technology:	Fraunhofer-Institut für Lasertechnik (ILT), Aachen DILAS Diodenlaser GmbH, Mainz Haas Lasertechnik, Schramberg JenOptik Laserdiode GmbH, Jena Rofin-Sinar Laser GmbH, Hamburg
Applications and process technology:	Robert Bosch GmbH, Stuttgart Bremer Institut für Angewandte Strahltechnik, Bremen DaimlerChrysler AG, Stuttgart Fraunhofer-Institut für Lasertechnik (ILT), Aachen Fraunhofer-Institut für Produktionstechnologie (IPT), Aachen Fraunhofer-Institut für Werkstoff- und Strahltechnik (IWS), Dresden KUKA Schweiss-Anlagen GmbH, Augsburg LBBZ-NRW GmbH, Aachen Marquardt GmbH, Rietheim-Weilheim Mikromat Werkzeugmaschinen GmbH & Co. KG, Dresden C.Stiefelmayer KG, Denkendorf Thyssen Hüller-Hille GmbH, Werk Hessap, Taunusstein Thyssen Lasertechnik GmbH, Aachen

The structure of the work in the project is shown in the organizational plan (fig. 6). The network of economic enterprises and scientific institutions, which has been developed and established in Germany over the last 10 years in the field of industrial materials processing with lasers and in recent years also in the field of high power diode lasers, shall be used and further developed in frame of the project, aimed onto the development of the novel, modular diode laser beam sources.

In the field of "chip technology" Osram Opto Semiconductor Corporation, the former Siemens Opto Semiconductor group is together with Infineon Technologies, the former Siemens Semiconductor division, a reliable vendor of high quality laser bar material, which is the basis for the following tasks in frame of the system development. The science group is represented by

the Fraunhofer-Institut für angewandte Festkörpertechnologie (IAF) and the Ferdinand-Braun Institut für Höchstfrequenztechnik (FBH), which have already contributed to the still continuing fundamental investigations in the project "High Power Diode Lasers and Diode Pumped Solid State Lasers", which is also funded from the Bundesministerium für Bildung und Forschung (BMBF).

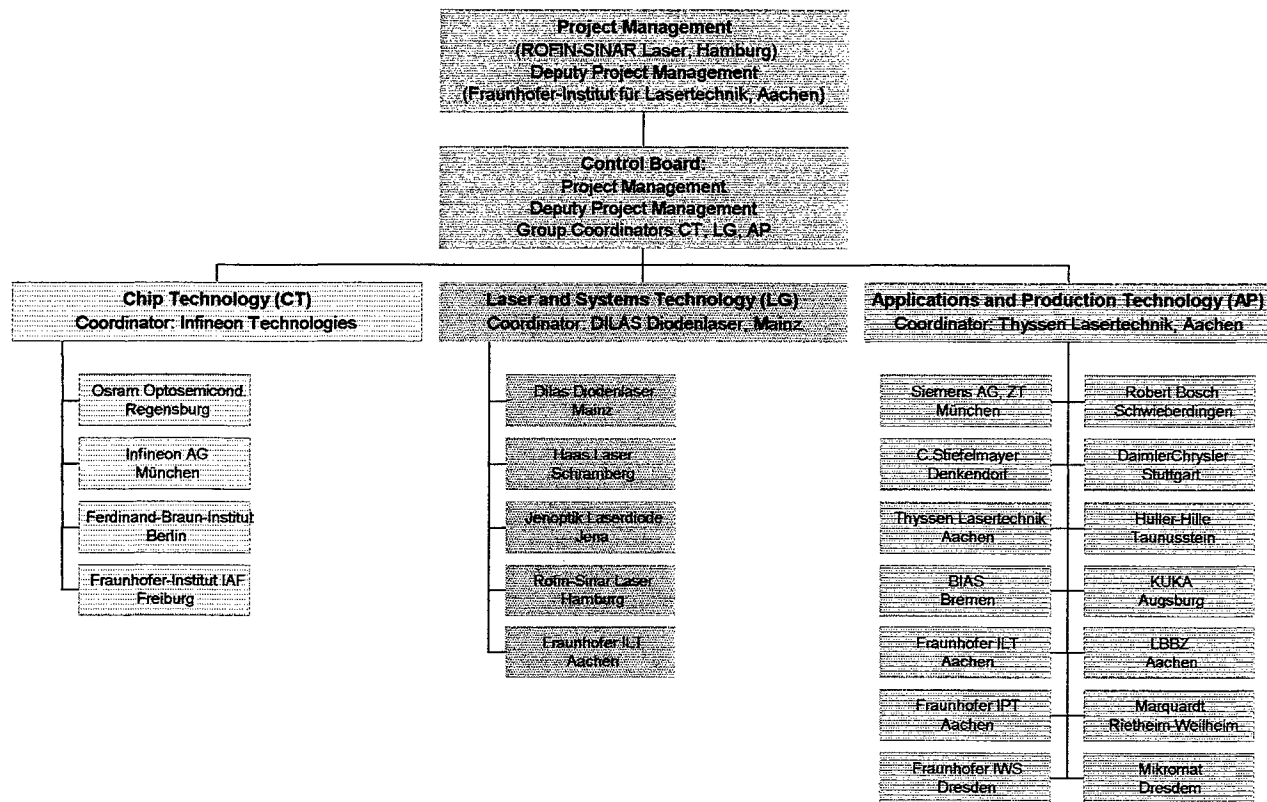


Fig. 6: Organizational scheme of the project

In the next link in the technology chain, "laser system technology", Jenoptik Laserdiode and Dilas Diodenlaser have qualified world wide as vendors for mounted semiconductor bar material and possess the potential to develop, manufacture and sell diode laser modules and systems of highest quality and power in a world wide market; they will be assisted scientifically by the Fraunhofer Institut für Lasertechnik. Haas Lasertechnik and Rofin-Sinar Laser are well established manufacturers of conventional laser sources for materials processing and have access to the world wide market and to industrial manufacturing technology.

In the area of applications and process technology partners of several branches are represented. The combination of laser devices with handling systems and robots resp. the integration of diode lasers into machine tools and facilities is performed by the partners Thyssen Hüller-Hille, Mikromat, Stiefelmayer and KUKA. The applications of diode lasers in the automotive industry will be investigated by the automotive manufacturer DaimlerChrysler and Robert Bosch. The use of diode lasers for the manufacturing of electrical components is the goal of basic investigations at Siemens Corp. And Bosch, the joining of polymers is the work of Siemens and Marquardt Corp.. The tasks of the steel industry are introduced by Thyssen Laser Technik, acting for several partners in the Thyssen-Krupp-Concern. LBBZ GmbH represents the sector of laser job shops and technology transfer into small and mid-sized enterprises.

The work of the industrial partners will be assisted scientifically by the Fraunhofer Institute für Lasertechnik (ILT), the Fraunhofer Institut für Produktionstechnik (IPT), the Fraunhofer Institut für Werkstoff- und Strahltechnik (IWS) and the Bremer Institut für angewandte Strahltechnik (BIAS), which contribute with their broad fundamental knowledge in the area of laser technology, production technology and materials science.

5.4 Technological plan

As explained above, the project is vertically structured in that sense, that each group is dependent from the success of the one above: The "Chip Technology" group delivers the bars for the integration in systems, which is to be performed in the "Laser- and Systems" group; these systems are matched with the requirements of the applicants in the "Application and Production Technology" group.

5.4.1 Chip Technology

Naturally, at the beginning of the technology chain the semiconductor technology is located. Diode laser bars with output power and beam quality, which are both a factor of 2 to 5 above today's values are required for the future systems. At the same time, of course, degradation behavior, i.e. life time has to be improved and costs have to be maintained or even reduced further.

The semiconductor development is planned to be performed in three steps with increased technological difficulty. The optimal values of focal intensities are directly linked to the beam quality of the laser bar. Each new generation of bars, which is represented by "band 1" to "band 3" in fig. 7 leads to an improved system generation for a special application (see 5.4.3). In band 1 and 2 conventional "wide area emitter" diode laser bars will be further optimized in terms of output power, beam quality, available wavelengths (for λ -coupling), lifetime etc., and especially be matched to the requirements of optimized micro-optical devices, which are essential for efficient coupling. In band 3 new types of emitters with a considerable improvement in beam quality, e.g. tapered laser arrays, shall be available for the integration into high power diode laser systems.

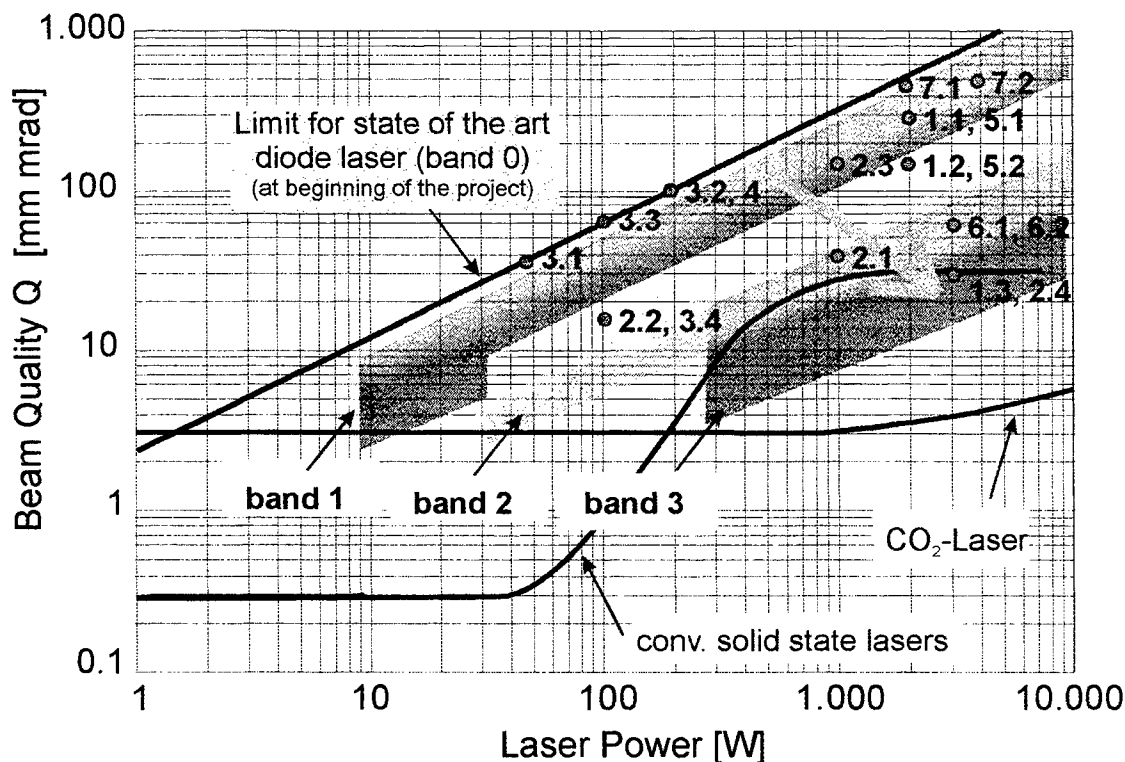


Fig. 7: Development of chip technology is performed in three steps, which leads to three "bands", where systems can be realized ("band 0" represents the situation at the beginning of the project). The dots represent laser systems, which are used for certain applications (see § 5.4.3)

The realization of these semiconductor elements in the three bands will be performed almost sequentially, i.e. the performance of these bar generations determines the timeframe of the project. On the other hand this procedure assures the step by step approach to the goals of the project and a wide knowledge base already during the time of the project.

5.4.2 Laser- and systems technology

The introduction of the high power diode lasers faces the traditional laser manufacturer with a technology change, the transfer from a mechanical and electrical engineering based technology to semiconductor oriented micro-system technology as represented in fig. 8. The heart of the laser, which has been a gas tube or a solid state rod so far is replaced by the pn-junction in a GaAs-semiconductor crystal, the resonator mirrors are replaced by the facet of the crystal, huge heat exchangers are eliminated by micro-channel coolers, beam forming optics are now in a millimeter range and the mounting of lasers takes now place with micro-manipulators and in clean rooms.

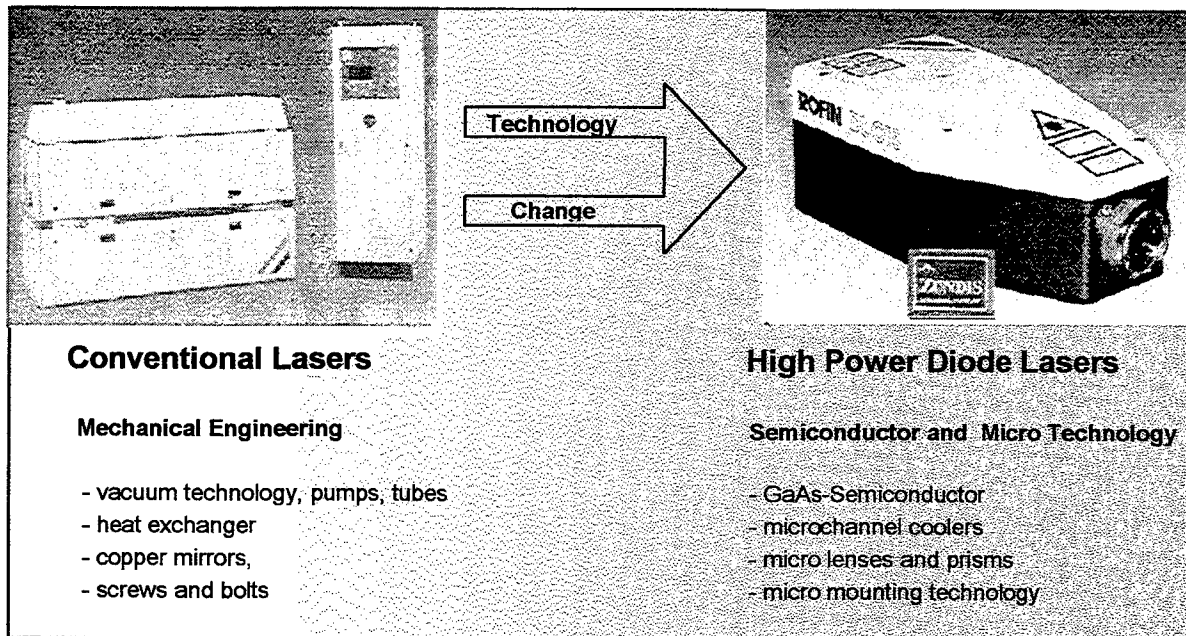
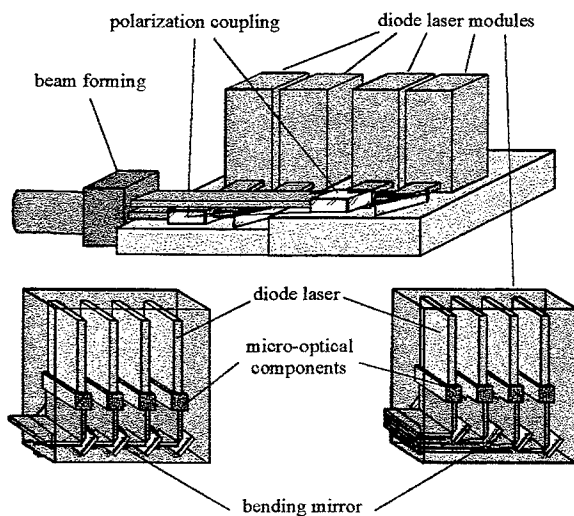


Fig. 8: Technological change in the laser system manufacturing industry



The partners in the laser- and systems group will further process the diode laser bars, developed and manufactured from the chip technology group; the bars will be mounted onto micro channel heat sinks, coupled with micro-optical components and assembled to high power diode laser systems, which are suitable for materials processing applications. New mounting technologies, novel beam forming and combining techniques must meet the 10-fold increase of performance of the laser bars.

Fig. 9: Sketch of components and assembly of a modular high power diode laser device [29]; the bottom shows two different assemblies of diode lasers into a module, the top represents the coupling of modules.

Flexibility must, nevertheless, be maintained or even increased at the same time: one of the essential differences of high power diode lasers and conventional lasers is the modular structure, which allows totally new approaches to the laser materials processing (see §4). It is another goal of the project to set the fundamental technologies or concepts for modular, but standardized base modules, which can provide the basis for beam sources, which are ideally adapted to the requirements of the process. The sketch in fig. 9 [29] may explain the idea.

Characterization and standardization of diode laser beams and development and qualification of measuring tools is another important topic, which is covered in frame of this work package.

5.4.3 Applications and process technology

In frame of the work of the chip technology group and the laser and systems group, which have been described above, laser systems are generated, which are tailored according to the requirements of the planned applications. The applications are divided in seven work packages:

1. Joining of sheet metals: sheet metals, car- and airplane structures
2. Cutting technology: coil materials and metal foils
3. Micro-joining in electrical technique and electronics: soldering of IC's on PCB's, micro welding
4. Polymer joining technology
5. Repair and Generation: on-site use for large components, large motor axles, turbines
6. Integration of diode lasers in machine tools
7. Hardening: deep drawing and injection molding tools, automotive components

Systems have been defined in the definition phase of the project regarding power, beam quality and shape. The systems specification (without the special beam shape) can be found in fig. 7, represented by the dots: 1.1, 1.2, 1.3 represent systems used for working package 1, joining of sheet metals; 2.1 through 2.4 systems used in working package 2, cutting, and so on.

5.4.3.1 Joining technology

Of course one of the most attractive goals of the joining technology must be to perform deep penetration welding; this has actually already been demonstrated in frame of the project recently as shown in fig.10 [15]. This demonstration is of course a break through for the diode lasers, since such a result was not expected at such an early stage of the project, but nevertheless working distance and speed must be considerably increased for acceptance in manufacturing, i.e. improved beam quality is mandatory, which is a major goal of the project. Deep penetration welding at processing parameters, which are comparable with today's state-of-the-art values is planned to be performed with system 1.3 (see fig. 7). Furthermore, an idea which is based on the possibility of an extremely compact design could well be the integration of the light source directly into the welding device. To some extent, this would allow a welding device, which is adapted to the welding geometry - again a demonstration of the modularity of high power diode laser beam tools. Brazing and laser assisted hybrid joining processes will also be investigated.

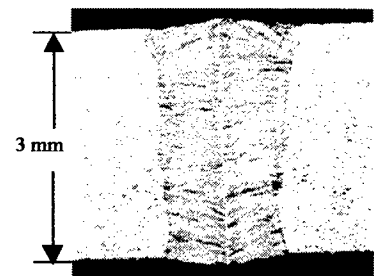


Fig. 10: deep penetration welding with diode laser [15]; 2.5 kW, $f = 50$ mm, $v = 0.7$ m/min, (ROFIN DL025S)

5.4.3.2 Cutting technology

The idea of cutting with diode laser represents in an impressive way, how the modularity and the line shaped beam geometry of the diode laser can be turned into an advantage: fig. 11 shows the sketch of an optical eccentric cutter for the separation of thin sheet metal from a coil into plates [29]: the linear assembly of diode laser modules forms an "optical knife", which moves for a short while with the running metal sheet and melts it through. This assembly allows a contactless and wear-free cross cutting of thin metal sheets. First experiments on 0.5 mm thick stainless steel foils have proven the viability of the concept: separation could be performed with 300 W line shaped laser within 200 ms even if beam quality was still rather poor [30]. Of course, besides this setup qualification of diode lasers for more conventional cutting methods is also target of the program.

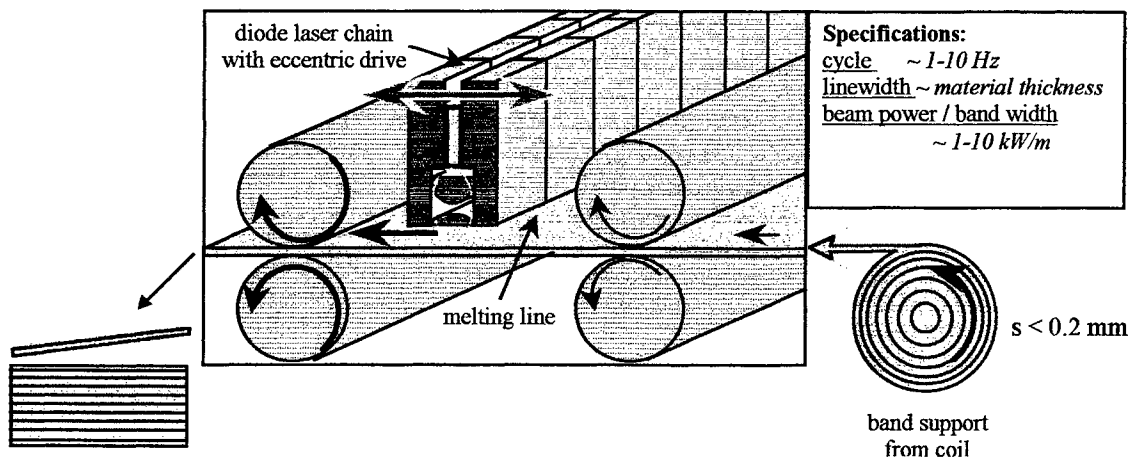


Fig. 11: sketch of an eccentric cutter using a linear assembly of high power diode lasers

5.4.3.3 Micro joining technology

Micro joining technology includes welding of miniaturized parts as well as soldering. For this applications of course rather low power devices are sufficient; however, special care must be taken for the homogeneity and for the controllability of the laser power. The increasing miniaturization of the microelectronic components requires well controlled spatial and temporal control of the laser source. The integration of the energy source diode laser into miniaturized clamping tools as well as the integration of miniaturized temperature and positioning control devices is the challenge of this task. For high speed simultaneous micro welding individually addressable emitters or emitter groups are desirable - again a demonstration of the advantage of the modular design.

5.4.3.4 Polymer joining technology

Even if polymer welding with diode lasers is already established in manufacturing [25], for most polymer parts high hurdles have to be overcome for the acceptance of diode laser welding: sequential welding, which is most commonly used at the moment, is in many cases too slow to replace conventional ultrasonic welding, vibration welding, hot element welding or gluing. This could be overcome, if simultaneous polymer welding (see fig. 5) would be applied; the most essential problem today is, that - as can be seen from the sketch in fig. 5 - so far only straight lines can be properly matched with the diode lasers. Concepts to solve this problem are one target of this working package. Improvement of basic understanding of polymer welding, optimization of weld seam geometry and processing parameters (pressure, temperature etc.), development of optimized design rules as well as on-line process control are other topics of this task.

5.4.3.5 Generation and repair

Deposition of metallic layers by laser radiation, either from wire or powder are well known; however practical use is rather rarely reported with the use of conventional lasers. High power diode laser provide several advantages for this technology: not only, that the process efficiency has been proven to be higher by more than a factor of two [21, 22], but also that the small size and high efficiency of the laser source itself gives the chance for a mobile deposition station, which can be used at the factory for repair of heavy parts in production machines or at the location, where heavy motor components must be repaired by layer deposition, e.g. in ships. This will provide a new extremely cost effective tool for repair of components. Also, for coating of parts which suffer from wear, e.g. motor components or turbine blades, with special wear resistant layers the diode laser may bring the process into cost efficient area by its high efficiency and low costs. The process fundamentals, the deposition heads eventually with integrated diode laser source and the process control are the goals of this task of the project.

5.4.3.6 Integration of diode lasers into machine tools

Laser assisted turning and milling of hard titanium and nickel alloys, which leads to a reduction of the necessary working forces resp. to a reduction of the wear of the machining tool has been investigated with CO₂ and NdYAG lasers several years ago [31]. Recently, also diode lasers have been successfully used in a turning machine for the machining of hard and brittle materials, e.g. silicon nitride ceramics [32]. A modular setup with diode lasers provides the possibility to adapt the geometry of the focus to the machining geometry and the optimization of the intensity profile. Fig 12 shows a sketch of the integration of diode lasers in a hexapod milling machine: The diode array, which is located around the milling tool and heating the work piece in front of it, can be switched dependent from the milling direction.

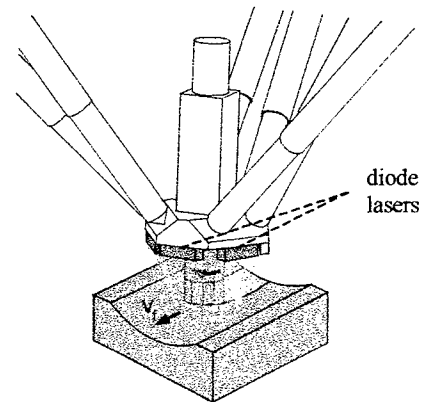


Fig. 12: sketch of diode laser integration into a hexapod milling machine [29]

Diode lasers are also attractive for hardening (see 5.4.3.7); the machine tool integrated diode lasers as described above, may not only provide the possibility for laser assisted machining, but also gives the possibility to do laser hardening in the machine tool right after the machining process, which saves valuable time, since mounting and transfer times can be considerable reduced.

5.4.3.7 Hardening

High power diode lasers are especially well suited for surface hardening because of their beam shape and their wavelength, as has been proven recently by introduction into manufacturing [18, 23]. However, so far the modular concept is not yet applied, neither for control of beam shape or intensity distribution nor for a geometric setup, which is adapted to the work piece, as schematically shown in fig. 13. This type of simultaneous hardening will provide an extremely high throughput and thus open a market for hardening of high volume parts. The idea behind the control of intensity distribution and beam shape is, to generate a segmented laser beam by use of separately controlled diode laser units, which are combined to the hardening beam, with e.g. a rectangular shape. An on-line control unit with spatial resolution controls the temperature at the surface of the work piece and keeps the temperature profile in a desired, preset shape by individual power setting of the individual diodes. With this method reliable laser hardening even of complex shaped parts will be possible.

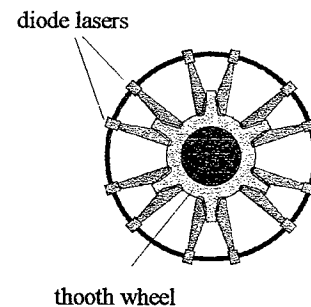


Fig. 13: sketch of simultaneous hardening with diode laser [29]

5.5 Economic importance and finance

The impact of the developments in the frame of the project to the market and the employment in Germany will be discussed in three different categories.

The world market for industrial laser sources and systems has grown over the last ten years almost continuously with two digit rates and has reached a volume of 2.4 Bio. US\$ in 1997. German manufacturers hold a considerable share of 30 to 40 %. If the targets of the project will be achieved, we proceed from the assumption that the market for industrial lasers and systems will grow importantly and the market share of German manufacturers will be increased.

For the economic position of Germany it is even more important, that by use of the new manufacturing tools considerable progress of productivity in branches of industry with central importance for the position of the production site Germany can be initiated. Especially car manufacturing and metal processing industry will be strengthened, which have an overall economic productivity of 330 Bio. US\$, which is equivalent to about 1/6 of the overall productivity in Germany.

A further aspect of the political and social importance of the project results from the image of Germany as a location, at which highly innovative capital goods are developed, manufactured and applied. In all three aspects, German laser technology and the network of industry and science have gained over the last fifteen years an outstanding international reputation and world wide importance, which will be consolidated or even extended by the new diode laser tools. With the

project the reputation of Germany as a "world centre for laser manufacturing technology" will be improved and an important contribution for the global positioning of Germany as a location for high technology will be accomplished.

The project has a budget of about 78 Mio. DM, which is funded from the German Ministry of Education and Research (BMBF) by 46.7 %. The budget is spent to about 50% for the investigation of applications resp. the adaptation of applications to the special features and benefits of the high power diode lasers; the other half is split to about 50% each for the semiconductor development and the systems integration technology. The duration of the project, which has been started at July 1st, 1998 will be 5 years.

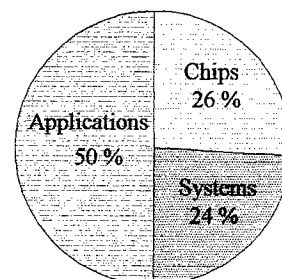


Fig. 14: share of the budget (ca. 78 Mio. DM)

6 SUMMARY AND CONCLUSION

High power diode lasers have entered the materials processing market recently and are already used in the industrial manufacturing. They are attractive energy sources, since they are reliable, energy and cost efficient, small in size and easy to handle. Their potential, however, lies in their special features, which is so far often considered as a limitation, if they are compared with conventional high brightness laser sources. To rise this potential is the goal of the ambitious German National Research Project "Modular Diode Laser Beam Tools".

7 ACKNOWLEDGEMENT

I would like to thank all participants of the MDS project for their work and contributions in frame of the project and especially the deputy coordinator of the project Dr. Peter Loosen of the Fraunhofer-Institut für Laser Technik in Aachen for providing material for this article. My further thanks are to be addressed to the Bundesministerium für Bildung und Forschung (BMBF) for continuous support of the project and to the Verein Deutscher Ingenieure - Technologiezentrum (VDI-TZ) for comprehensive and extensive assistance and controlling.

REFERENCES

- [1] E.Beyer, *Euro Laser* 12/99, p.3 (1999)
- [2] R.N.Hall, G.E.Fenner, J.D.Kingsley, T.J.Soltys, R.O.Carlson, *Phys. Rev. Lett.* 9, 366 (1962)
- [3] M.I.Nathan, W.P.Dumke, G.Burns, F.H.Dill jr., G.Lasher, *Appl. Phys. Lett.* 1, 63 (1962)
- [4] T.M.Quist, R.H.Rediker, R.J.Keyes, W.E.Krag, B.Lax, A.L.Whorter, H.J.Ziegler, *Appl. Phys. Lett.* 1, 91 (1962)
- [5] I.Hayashi, M.B.Panish, P.W.Foy, S.Sumski, *Appl. Phys. Lett.* 17, 109 (1970)
- [6] Zh.I.Alferov, V.M.Andreev, D.Z.Garbuzov, Yu.V.Zhilyaev, E.P.Morozov, E.I.Portnoi, V.G.Trofim, *Fiz. Tekh. Poluprovodn.* 4, 1826 (1970) resp. *Sov. Phys. Semicond.* 4, 1573 (1971)
- [7] M.Fukuda, "Reliability and degradation of semiconductor lasers and LEDs", Artech House Inc., ISBN 0-89006-465-2 (1991)
- [8] B.D.Tuckerman, "Heat-transfer microstructures for integrated circuits", Thesis, Stanford University, 1984
- [9] L.Bernier, *Electronica*, Nov 11, p21 (1992)
- [10] V.Krause, H.G.Treusch, P.Loosen, SPIE-Conf. OE/LASE 94, Los Angeles 1994
- [11] J.Biesenbach, P.Loosen, H.G.Treusch, V.Krause, A.Köstlers, S.Zamel, W.Hilgers, *Proc. SPIE*, 2263, 154 (1994)
- [12] P.Loosen, H.G.Treusch, C.R.Haas, U.Gardenier, *Proc. SPIE*, 2382, 78 (1995)
- [13] C.Hanke, L.Korte, B.Acklin, J.Luft, S.Grötsch, G.Herrmann, Z.Spika, M.Marchiano, B.De Odorico, J.Wilhelmi, *Photonics West* 1999
- [14] Data sheet ROFIN DF022, see also <http://www.rofin.com>
- [15] D.Petring, *LaserOpto* 31, (5), 6 (1999)
- [16] Patent No. DE 44 38 368 C2, Fraunhofer-Institut für Lasertechnik, Aachen, Germany
- [17] Patent No. DE 195 00 513 C1, Dilas Diodenlaser GmbH, Mainz, Germany
- [18] F.Bachmann, *Proc. SPIE* Vol. 3888 (1999), to be published
- [19] E.Beyer, G.Herziger, P.Loosen, R.Poprawe in *Strahltechnik* Vol. 10, (1997) BIAS Verlag, ISBN: 3-9805011-4-0
- [20] P.Loosen, Fraunhofer-Institut für Lasertechnik, Aachen, Germany
- [21] S.Novotny, A.Richter, E.Beyer, *Proc. ICALEO '98*, Orlando 16.-19.11.1998, LIA Vol. 85 (1999), 68-74

- [22] A.Richter S.Novotny, T.Naumann, E.Beyer, *Laser Opto* 31, 3, 63 (1999)
- [23] B.Schürmann, F.Bachmann, *Laser-Praxis* (2000), to be published
- [24] N.N., *Laser* 5, 24 (1998)
- [25] H.Pütz, H.G.Treusch, D.Hänsch, *Maschinenmarkt* 105, 17, 38 (1999)
- [26] H.Pütz, Aachener Kolloquium für Lasertechnik, Aachen, Germany, 24./25.Juni 1998
- [27] U.Brauch, P.Loosen, H.Opower, in "High Power Diode Laser and Advanced All Solid State Laser Systems", Chap. 8, ed. by R.Diehl, Springer Verlag, Berlin (2000), to be published
- [28] SDL Corp., USA, "Advanced High Power Lasers and Applications Conference", Osaka, Nov 1-5, 1999
- [29] P.Loosen, Presentation of MDS-Project, March 1998
- [30] D.Petring, personal communication
- [31] W.König, A.Zaboklicki, *VDI-Z* 135, 6, 34 (1993)
- [32] M.Weck, S.Kasperowski, *Production Engineering* 6, 1 (1997)

Direct Writing of Electronic Materials Using a New Laser Assisted Transfer/Annealing Technique

A. Piqué^{a*}, J. Fitz-Gerald, D.B. Chrisey^a, R.C.Y. Auyeung^b, H. D. Wu^b, S. Lakeou^{b,c} and R.A. McGill^a

^aNaval Research Laboratory, Washington, DC 20375

^bSFA, Inc. Largo, MD 20774

^cUniv. of the District of Columbia, Washington, DC 20008

ABSTRACT

MAPLE direct write is a new laser-based direct write technique which combines the basic approach employed in laser induced forward transfer with the unique advantages of matrix assisted pulsed laser evaporation. The technique utilizes a laser transparent donor substrate with one side coated with a matrix consisting of the electronic material to be transferred mixed with an organic binder or vehicle. As with LIFT, the laser is focussed through the transparent substrate onto the matrix coating. When a laser pulse strikes the coating, the matrix is transferred to an acceptor substrate placed parallel to the donor surface. *Ex situ* thermal or laser treatments can be used to decompose the matrix and anneal the transferred material, thus forming structures with the desired electronic properties. MAPLE DW is a maskless deposition process designed to operate in air and at room temperature that allows for the generation of complex patterns with micron scale linewidths. The various structures produced by MAPLE DW were characterized using 3-D surface profilometry, scanning electron microscopy and optical microscopy. The electrical resistivity of the silver metal lines made by MAPLE DW was measured using an impedance analyzer. Patterns with $\text{Zn}_2\text{SiO}_4\text{:Mn}$ powders were fabricated over the surface of a dragon fly wing without damaging it. An overview of the key elements of the MAPLE DW process including our current understanding of the material transfer mechanism and its potential as a rapid prototyping technique will be discussed.

Keywords: Matrix Assisted Pulsed Laser Evaporation, MAPLE Direct Write, Laser Induced Forward Transfer, LIFT, direct write of metals, direct write of phosphors.

1. INTRODUCTION

The use of electronic systems has become an integral part of our lives. There is an ever increasing demand to develop electronic assemblies that are smaller, lighter, cheaper and more versatile. Passive electronic components such as capacitors, resistors, inductors, and metal interconnects are some of the building blocks of these assemblies. Until now, limited progress in miniaturization of electronic components has been achieved with the use of surface mounted components. Surface mount technologies are not practical for applications where the customization or modification of an existing system is required. From a design standpoint, surface mount technologies are inherently rigid, and are not compatible with Just In Time Manufacturing (JITM) methods. What is required are techniques, materials, and tools to build passive circuit elements on any type of substrate or surface required for the fabrication of complete working electronic assemblies. Such a capability would create new opportunities in the way electronic systems are currently designed, manufactured and implemented. The development of rapid prototyping techniques for the fabrication of electronic devices is only recent. They offer the capability to deposit or pattern the different types of materials that make an electronic device without the use of masks or patterns and, as such, they are known as direct write processes. For example, using direct write processes it is possible to quickly fabricate prototype circuit designs, test and compare their operation with the modeling

* Correspondence: Email: pique@nrl.navy.mil; Telephone: (202) 767 5653; Fax: (202) 767 5301

data and adjust the design or modeling parameters accordingly. These steps could be executed in an iterative fashion for maximum optimization in a fraction of the time required by traditional manufacturing techniques. Direct write processes are the key enabling technology for the above scenario to become a reality. As Figure 1 schematically shows, the essential link in the development chain that goes from concept to working prototype device or system is the direct write tool or machine. Direct write techniques are not intended to compete with current photolithographic circuit design and fabrication, but rather for the development of new capabilities required by next generation electronic systems.

Over the past decade, various laser-based direct write techniques have been developed for depositing different types of materials. Laser induced forward transfer (LIFT) has shown the ability to direct write metals for interconnects and for mask repair and also simple dielectric materials such as metal oxides^{1,2}. LIFT is a technique that employs a focused pulsed laser beam to vaporize a thin film from a laser transparent donor substrate in air and at room temperature³. The material then condenses onto an acceptor substrate placed in close proximity (25-75 μm) to the donor substrate. The area coated per laser pulse depends on the size of the laser spot striking the film as well as the gap between both substrates. However, because LIFT causes among other things the vaporization of the material being transferred, it is not useful for direct writing of complex multicomponent metal oxides, polymers, organics and composite materials.

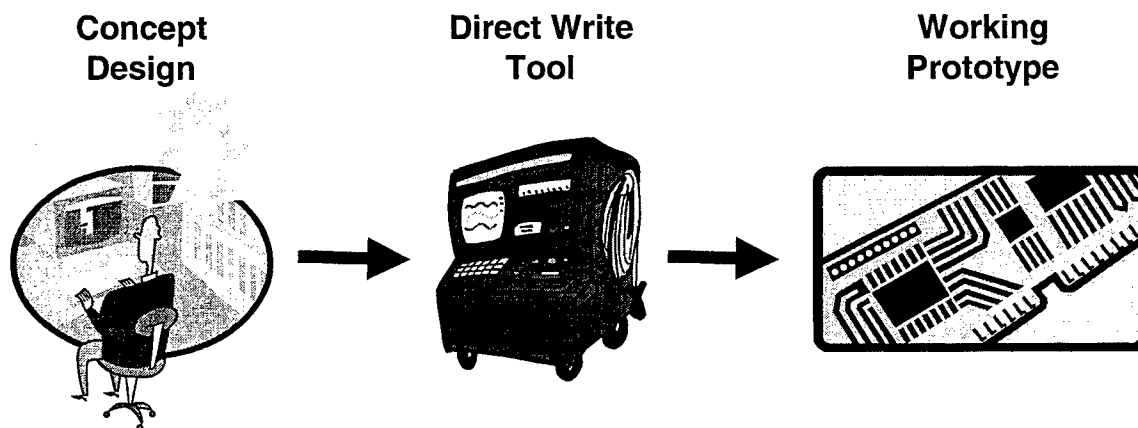


Figure 1. Elements for a rapid prototyping process. The enabling technology is the direct write tool.

In this paper, a novel laser transfer technique similar in implementation to LIFT is described. The technique evolved from the combination of LIFT with a laser-based vacuum deposition technique for transferring organic and polymeric materials called matrix assisted pulsed laser evaporation (MAPLE)⁴. Specific examples of the MAPLE process are described elsewhere^{5,6}. Briefly, MAPLE utilizes a frozen target made from a dilute solution of the organic material to be deposited and a volatile solvent. When the laser pulse strikes the surface of the target, the solvent is vaporized and pumped away, while the organic material is released and collected over a substrate placed opposite to the target, thus forming a highly uniform thin film with minimal organic degradation. The combination of the mechanistic aspects of MAPLE with LIFT's laser transfer process using a matrix coated ribbon resulted in MAPLE Direct Write or MAPLE DW^{7,8}. Because MAPLE DW utilizes a beam delivery optics and imaging similar to a laser micromachining system, it can be used to perform several distinct operations. The process can be both additive as in LIFT and MAPLE DW, and also subtractive as in laser micromachining. Furthermore, the laser can be used to perform *in situ* material processing operations such as annealing and pretreatment of surfaces.

2. MAPLE DW

The interaction of lasers with materials can result in a wide range of effects that depend on the properties of the laser, the material, and the ambient environment. As a function of beam energy and wavelength, these effects can range from simple

photothermal heating to photolytic chemical reactions and to ablation and plasma formation. Furthermore, by carefully choosing the laser wavelength and fluence it is possible to limit the interaction of the laser with a given material system to a certain depth as well as discriminate among the different types of materials present. The only constraint to the spatial resolution of these processes is given by the diffraction limit of the laser wavelength in use. It is clear then that laser based direct write processes offer many advantages such as the ability to process, anneal or modify the material being direct written *in situ* and at room temperature with resolutions down to the micrometer range.

MAPLE DW is a process in which material is transferred from a support or "ribbon" to a substrate by the irradiation of a laser pulse, as shown in the insert in Figure 2. To date, various UV laser wavelengths have been tested, in particular 248, 308 and 355 nm. Other fundamental wavelengths from UV-VIS to IR could be used with advantageous effects depending

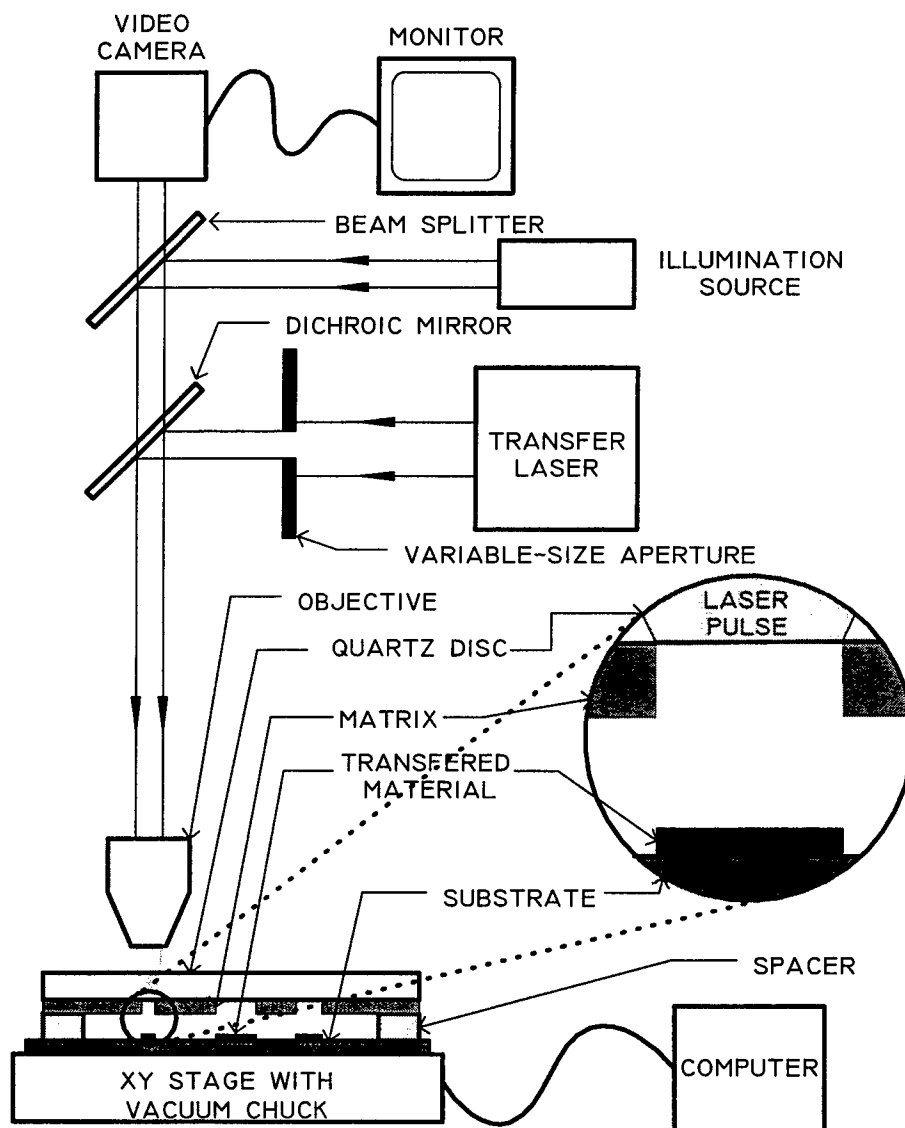


Figure 2. Schematic diagram illustrating the basic components of a MAPLE DW system. The insert shows a close-up of the region where the material transfer takes place.

of the material system or the type of direct write application. The "ribbon" is composed of a laser transparent support, a solvent matrix incorporating binders, vehicles and other ingredients, and the material to be deposited. The various components can either be dissolved or dispersed within the matrix. The support typically does not participate in the transfer of material, although it could be made part of the matrix. The matrix material can take many forms as can the material to be deposited. The matrix material can be prepared in the form of a homogenous mixture or as a dispersion of the material to be deposited. It can also be made in the form of a layered structure with the laser-absorbing layer on the support substrate first, followed by a layer of the material to be deposited, but other distributions are possible. The matrix material binds the material to be deposited to the support substrate. It also preferentially absorbs the laser radiation and desorbs the material to be deposited from the support, and can assist in the adhesion of the deposited layer. Ideally, the matrix material should evaporate or decompose into a volatile material, and be carried away by a purge gas, leaving no residue. Furthermore, unlike other laser-based direct write processes, MAPLE DW is a pyrolytic technique with respect to the matrix material, but not with respect to the materials that are to be deposited. This has been confirmed by post-deposition analysis of the transferred materials which have shown no changes in their functionality before and after the transfer process⁹. The material to be deposited can consist of nanophase powders up to micron size particulates, single crystallites, metal-organic or sol-gel precursors and polymer composites. Since the electronic, mechanical, and thermal properties of the materials to be deposited often differ with respect to bulk or single crystals, there is a great deal of complexity in designing the material to be deposited so as to achieve good adherence to the substrate or previous layers, near 100% theoretical densities and bulk-like properties.

The ribbons required by MAPLE DW can be prepared using different techniques, such as spin or spray coating, electrophoresis, screen printing and doctor blading depending on the type of matrix being used. The coating formed must be uniform across the surface of the ribbon support in order to minimize transfer variations. Depending on the type of matrix, the thickness of the coating can vary from 2 to 20 microns. Once transferred, the material can be thermally or laser annealed if required. The annealing process can take place *ex situ* by placing the substrate in a furnace or by irradiating it with a second laser after all the material has been transferred. For *in situ* annealing, a second laser beam sharing the optical path of the transfer laser is required. *In situ* annealing offers the possibility for processing only the transferred material, without affecting the substrate or any adjacent layers. In this work only *ex situ* annealing experiments were conducted. Annealing might be necessary in order to remove any matrix residue left after the transfer, to improve the electrical and mechanical properties of the transferred materials, or to transform or decompose the transferred materials. An ideal example of the effect of annealing in the case of the transfer of powders is shown schematically in Figure 3, where the powders are fused together into a denser and bulk-like structure after the annealing step.

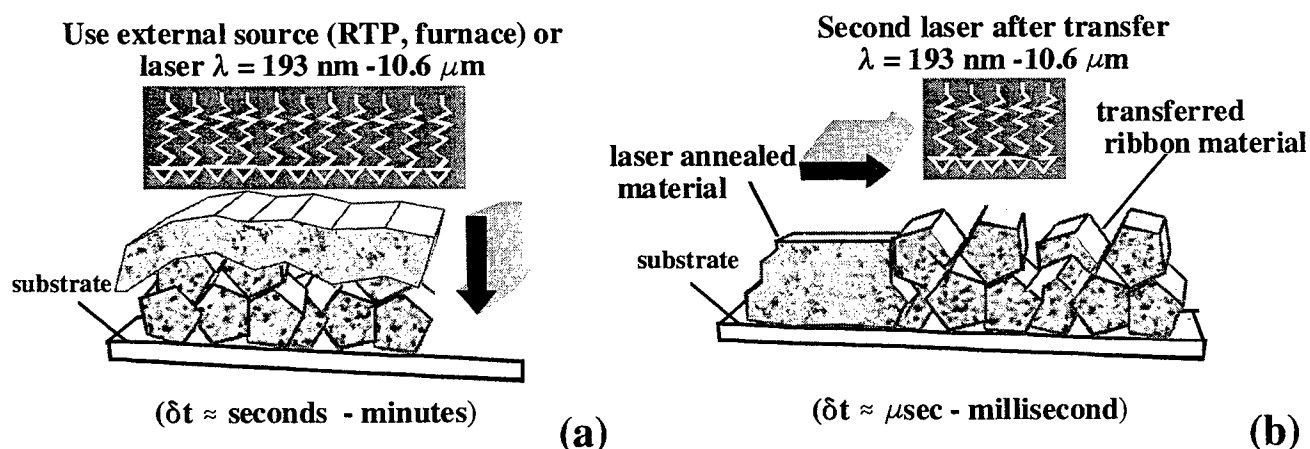


Figure 3. Schematic showing the effect of annealing on powders after being deposited by MAPLE DW. (a) Ex situ annealing using thermal or laser treatments, (b) in situ annealing using a second laser with the same optical path as the transfer laser.

3. RESULTS AND DISCUSSION

Fused silica discs, double side polished, 5.0 cm in diameter, with thickness' ranging between 2 to 6 mm were used as ribbon supports. The coated side of the ribbons was kept at a distance of 25 μm from the substrate with a spacer. Both the substrate and the ribbon were held in place using a vacuum chuck over the X-Y substrate translation stage, as shown in Figure 2. The laser pulse was directed through a variable-size circular aperture and then through a 10x objective lens. By changing the aperture size, beam spots with diameters ranging from 10 to 200 μm were generated. The laser fluence (0.1 – 2.5 J/cm²) was estimated by averaging the total energy of the incident beam over the irradiated area.

The transfer of metal powders was evaluated using silver ribbons (5 to 15 μm thick) made by doctor blading silver pastes. The silver pastes were supplied by Superior Micropowders, Inc.¹⁰. The pastes consisted of spherical silver powders with a bimodal size distribution centered around 1 micron mixed with an organic vehicle. The bimodal distribution improves the packing density of the powders on the ribbon so as to maximize the transfer yield. Silver lines up to 1 cm long and 300 μm wide were deposited on glass, alumina and polyimide substrates. Depending on the number of passes, the thickness of the lines varied from 10 to 50 μm . Figure 4 shows a 3-D profilometer image of one such line deposited on a glass substrate. Using a furnace, an *ex situ* anneal step (250 °C for 15 minutes) was performed on these lines after transfer. The conductivity of the lines was evaluated at 1 MHz using a HP4284A LCR meter. The lines exhibited resistivities 10 to 25 times higher than that of bulk silver ($\rho_{\text{Ag}} = 1.62 \times 10^{-6} \Omega \text{ cm}$). The adhesion of the silver to glass substrates was also evaluated after the transfer and anneal steps using scotch tape tests. They passed the tape tests without any sign of damage. SEM analysis of the lines before and after the tape tests did not reveal any change to their morphology. Furthermore, no changes in their resistivity were measured.

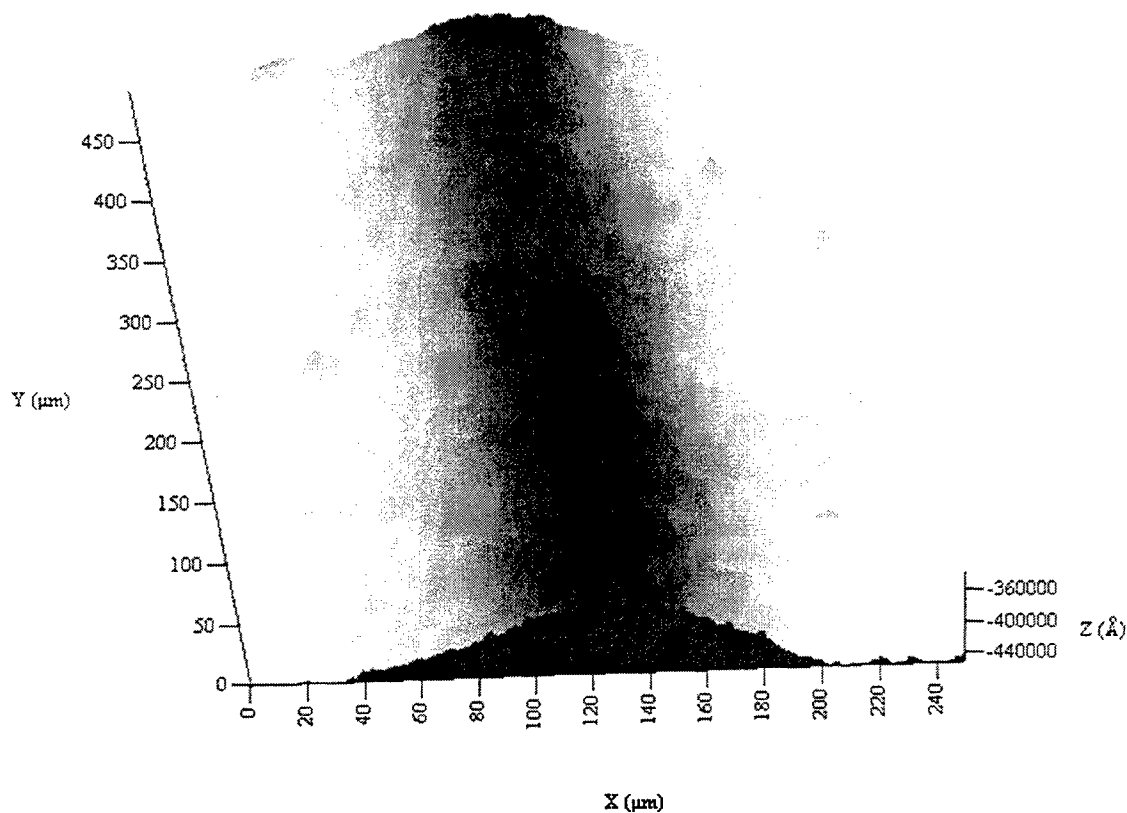


Figure 4. 3-D Surface profile image of a silver line deposited on a glass substrate by MAPLE DW.

The thermal annealing of the silver lines only improves the conductivity to about 10 times that of bulk. The temperature at which the thermal annealing experiments were conducted was high enough to remove any matrix residue from the transferred silver powders, but too low to cause the transferred powders to sinter. This could have been achieved at higher annealing temperatures which were not compatible with some of the substrates used in this work, such as polyimide. Instead laser annealing was used. The advantage of laser vs. furnace anneal is that it minimizes the heating of the substrate while processing only the transferred materials requiring annealing. Laser annealing is then a better choice for working with substrates and materials that melt or decompose at elevated temperatures.

For the *ex situ* laser annealing experiments, the 1064 nm emission from an Nd:YAG laser operating in a free running mode (non Q-switched) was used, in order to obtain pulses about 50 μsec long. Portions of several silver lines were laser annealed at various power levels. For low laser powers, no changes in the structure of the lines were observed. For very high laser power levels, the annealed sections of the line melted completely and once solidified tended to delaminate from the substrate. The best results were obtained for intermediate power levels in the neighborhood of 25 W/cm^2 using a $250 \mu\text{m}$ spot size. After 40 passes, dramatic changes in the morphology of the silver lines could be observed under the optical microscope and with an SEM, as the images in Figure 5 illustrate. Prior to the laser anneal, the silver lines were essentially formed by an agglomeration of the transferred silver powders, but after the laser anneal, the powders fused together to form a continuous bulk-like structure (at least on the surface of the line). It is not clear what fraction of the line's cross section was transformed by the laser anneal. SEM cross sectional analysis of these lines will be performed in the near future in order to determine what percentage of the line was sintered by the laser annealing. Because only discrete portions of the silver lines were laser annealed, their electrical conductivity was not measured. The use of an *in situ* laser annealing step instead, should result in further optimization of the properties of the transferred material, since it would allow for the anneal to take place right after each spot transfer. Optimal performance should be obtained by adjusting the thickness of the transferred material per laser shot to the penetration depth of the laser anneal pulse that follows. In this way each deposited layer would be 100% annealed.

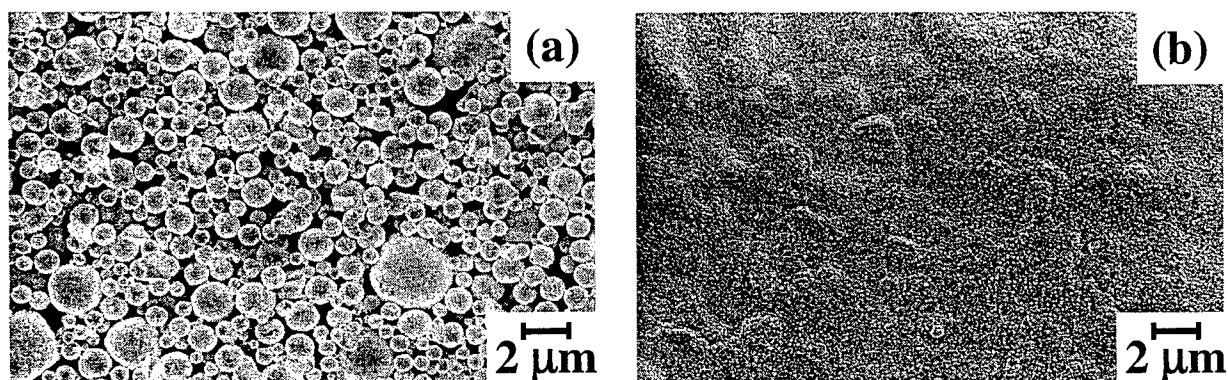


Figure 5. SEM micrographs of silver deposited on a glass substrate by MAPLE DW. (a) Surface morphology after transfer, showing the powder. (b) Same region after *ex situ* 1.06 μm laser anneal.

The MAPLE DW process has also been used successfully for depositing phosphor materials. Using ribbons consisting of a gold-coated fused silica disk, which was then eletrophoretically coated with various types of oxide phosphor powders, the direct write of these powders has been demonstrated over a variety of substrates. The phosphor ribbons were typically 10 μm thick. Using ribbons made from two different color phosphors, 6×6 arrays have been demonstrated. Cathodoluminescence measurements of the deposited materials confirm that the laser process does not affect the phosphor performance. These results have been described elsewhere⁹. In this work, a ribbon containing $\text{Zn}_2\text{SiO}_4\text{:Mn}$ powders, which luminesces primarily in the green was used to demonstrate the ability of MAPLE DW to deposit materials over any type of substrate, even over the surface of a dragonfly wing. As the optical micrographs from Figure 6 show, the letters NRL were formed by MAPLE DW of the phosphor powder over the wing without damage. Furthermore, the fact that the properties of

the phosphor had not been affected by the transfer was demonstrated by the luminescence of the powders when stimulated by a ultraviolet lamp at 254 nm.

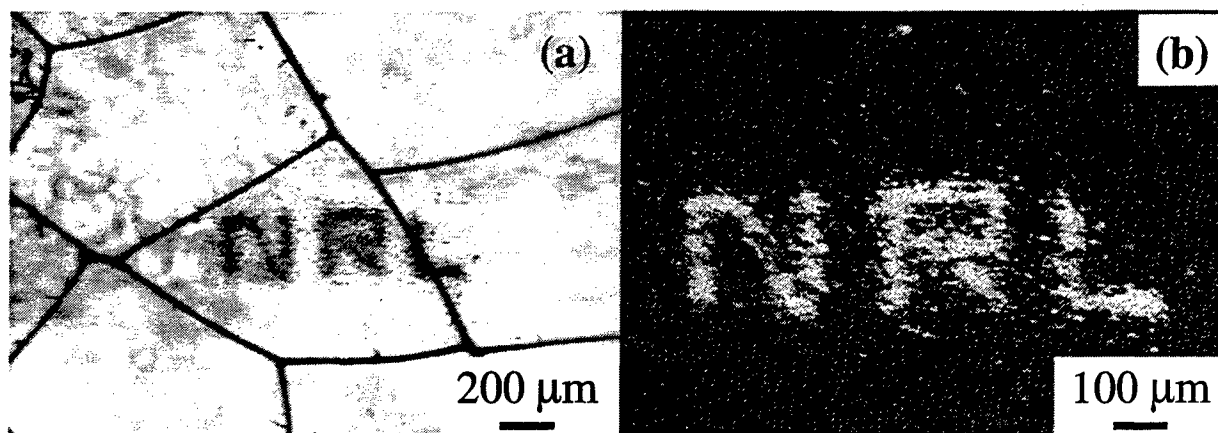


Figure 6. Optical micrograph of $\text{Zn}_2\text{SiO}_4\text{:Mn}$ deposited by MAPLE DW onto a dragon fly wing. Notice that the wing was not damaged during the direct write process. (b) Stimulated emission (green) from the powders when excited with a UV lamp (254 nm).

4. SUMMARY

The efficacy of a novel laser driven direct write technique, MAPLE DW, has been demonstrated. This technique allows for the direct writing of numerous types of materials, such as metals and phosphors over glass, silicon, alumina and polyimide substrates. Silver metal lines with fair conductivities and good adhesion were demonstrated after *ex situ* thermal annealing. *In situ* laser annealing of the deposited silver powders resulted in the sintering of at least the surface of the silver lines. Phosphor powders were directly written with MAPLE DW on the surface of an insect's wing without damaging the wing, while preserving the phosphor's luminescence. The above are some examples of the potential applications of the MAPLE DW technique. MAPLE DW offers many advantages when compared with existing direct write techniques including the ability to operate in air and at room temperature. Since MAPLE DW is compatible with CAD/CAM processes, 3D-structures can be generated in a fast and reproducible fashion. With this technique multilayer structures of different materials can be fabricated with accurate thickness control and spatial resolutions down to the micron scale can be achieved. Overall, MAPLE DW is a very powerful direct write technique with great potential for the rapid prototyping of electronic components.

5. ACKNOWLEDGEMENTS

This work was supported by the Office of Naval Research and DARPA, through the DARPA-MICE program. We would like to thank Toivo Kodas and Paolina Atanassova from Superior Micropowders, for providing the silver powders used in this work. The authors would also like to thank Mike Duignan and Russell Chung for all their assistance.

6. REFERENCES

1. J. Bohandy, B.F. Kim, and F.J. Adrian, J. Appl. Phys. **60**, 1538 (1986).
2. J. Bohandy, B.F. Kim, F.J. Adrian and A.N. Jette, J. Appl. Phys. **63**, 1558 (1988).
3. F.J. Adrian, J. Bohandy, B.F. Kim, A.N. Jette, and P. Thompson, J. Vac. Sci. Technol. B **5**, 1490 (1987).
4. R.A. McGill, R. Chung, D.B. Chrisey, P.C. Dorsey, P. Matthews, A. Piqué, T.E. Mlsna, and J.L. Stepnowski, IEEE Trans. On Ultrasonics, Ferroelectrics and Frequency Control, **45**, 1370 (1998).
5. A. Piqué, R.C.Y. Auyeung, R.A. McGill, D.B. Chrisey, J.H. Callahan, and T.E. Mlsna, *Advances in Laser Ablation of Materials*, MRS Proceedings, **526**, p. 375, 1998.
6. A. Piqué, D.B. Chrisey, B.J. Spargo, M.A. Bucaro, R.W. Vachet, J.H. Callahan, R.A. McGill, D. Leonhardt, and T.E. Mlsna, *Advances in Laser Ablation of Materials*, MRS Proceedings, **526**, p. 421, 1998.
7. A. Piqué, D.B. Chrisey, R.C.Y. Auyeung, S. Lakeou, R. Chung, R.A. McGill, P.K. Wu, M. Duignan, J. Fitz-Gerald, and H. D. Wu, SPIE Proceedings, **3618**, p. 330, 1999.
8. A. Piqué, D.B. Chrisey, R.C.Y. Auyeung, J. Fitz-Gerald, H.F. Wu, R.A. McGill, S. Lakeou, P.K. Wu, V. Nguyen and M. Duignan, Appl. Phys. A, (Sept. 1999), to be published.
9. J. Fitz-Gerald, A. Piqué, D.B. Chrisey, P.D. Rack, M. Zeleznik, R.C.Y. Auyeung and S. Lakeou, Appl. Phys. Lett. (Nov. 1999), to be published.
10. Superior MicroPowders Inc., Albuquerque, New Mexico 87109; (505) 342 1492.

Stress Measurements in Silicon Microstructures

Sherwin T. Amimoto^a, Dick J. Chang^b, and Andra D. Birkitt

Propulsion Science and Experimental Mechanics Department, M5-753,

The Aerospace Corporation

P.O. Box 92957, El Segundo, CA 90245

ABSTRACT

Raman spectroscopy is used as a non-contact probe of stress with high spatial resolution in micro-machined silicon structures. The motivation for this work is that reliability or cycle life can be substantially increased by understanding the origin of stress including residual stress. Excessive stresses induced by workmanship shortcomings or design constraints may be addressed by Raman measurements. In microelectronics, stress is known to play a significant role in interconnects which limits reliability, life, and ultimately cost of many circuits. We wish to demonstrate the utility of Raman spectroscopy as a tool for the development and design of silicon microstructures.

The equations for a general two-dimensional stress field are discussed. Calibration studies using macro-mechanical fixtures for single crystal silicon specimens under two-dimensional stress field are presented. Our measurements show good agreement with the theoretical values and thus validate the approach taken. Stress maps of conventionally fabricated test structures, laser machined, and polysilicon structures are presented.

Keywords: Raman spectroscopy, stress, stress field, micro-machined silicon

1. INTRODUCTION

High stress levels play a significant role in determining the life, the reliability, and the failure modes of micromachined and microelectronic devices. High stresses due to CTE mismatch and discontinuities have lead to failures in interconnects and metallizations due to stress migration and electromigration effects. Stress in films may also cause adhesion failure between film layers. Fatigue life may be considerably shortened by the presence of localized high stress in critical regions. Structural designs, workmanship, and manufacturing methods including laser machining also play a role in determining stress. We have proposed Raman spectroscopy as a non-contact method for measuring highly localized stresses at the surface of silicon structures to understand the effects of macro- and micro-material property variations, design, and defects as they influence stress concentrations. Raman spectroscopy has excellent spatial resolution of 1 μm and is well suited to probing nanostructures used in MEMS devices. The stress measurement is based on the relative frequency shift of the Raman spectra when the crystal lattice is strained. Stresses as small as 8.7 MPa (1.25 ksi) may be detected.

This paper presents the Raman secular equation for cubic crystal systems and discusses the general, two-dimensional surface stress field effects on Raman frequency shifts and polarization. Raman stress measurements of single-crystal silicon test structures undergoing 4-point bend loading are used to validate the theory. These are the first measurements reported for single crystal silicon undergoing tensile stress. Residual stress measurements in polysilicon cantilever beams and preliminary stress maps in laser machined test structures using the REVISE process are also reported.

2. THE RAMAN EQUATIONS FOR CUBIC SYSTEMS

The Raman dynamic equations for optical modes in a cubic crystal were used to derive the stress dependent frequency shift relationships. The two-dimensional stress field is appropriate to a surface whereby stress perpendicular to the surface is absent. Consider a general two-dimensional stress field τ_{11} , τ_{22} , and τ_{12} where τ_{11} and τ_{22} are normal stresses and τ_{12} is the shear stress with respect to a Cartesian coordinate system with axes 1, 2, and 3. Further, let the 1, 2, and 3 axes coincide

with the principal axes of the cubic crystal material with axis 3 normal to the surface. Let the three stress components be related by the parameters α and β as follows:

$$\tau = \tau_{11}, \tau_{22} = \alpha \tau, \text{ and } \tau_{12} = \beta \tau \quad (1)$$

The following three roots (frequency shifts) may be derived:

$$\begin{aligned} \Delta\Omega_1 &= (\tau/4\omega_0)\{p(1+\alpha)(S_{11} + S_{12}) + q(1+\alpha)(S_{11} + 3S_{12}) + [(1-\alpha)^2(S_{11} - S_{12})^2(p-q)^2 \\ &\quad + 4(rS_{44}\beta)^2]^{1/2}\}, \\ \Delta\Omega_2 &= (\tau/4\omega_0)\{p(1+\alpha)(S_{11} + S_{12}) + q(1+\alpha)(S_{11} + 3S_{12}) - [(1-\alpha)^2(S_{11} - S_{12})^2(p-q)^2 \\ &\quad + 4(rS_{44}\beta)^2]^{1/2}\}, \\ \Delta\Omega_3 &= (\tau/2\omega_0)\{p(1+\alpha)S_{12} + q(1+\alpha)(S_{11} + S_{12})\} \end{aligned} \quad (2)$$

where S_{ij} are elements of the compliance matrix that relates stress to strain; p , q , and r are calibration constants; and ω_0 is the reference frequency of unstressed silicon, 520 cm^{-1} . It is interesting to note that the root $\Delta\Omega_3$ is independent of the shear stress whereas the other two roots, $\Delta\Omega_1$ and $\Delta\Omega_2$ will show a splitting relative to each other that is shear and biaxial stress dependent. The values of $p/\omega_0^2 = -1.85$, $q/\omega_0^2 = -2.31$, $r/\omega_0^2 = -0.71$, $S_{11} = 7.68 \times 10^{-12} \text{ Pa}^{-1}$, $S_{12} = -2.14 \times 10^{-12} \text{ Pa}^{-1}$, and $S_{44} = 12.7 \times 10^{-12} \text{ Pa}^{-1}$ were used for single crystal silicon¹. For polycrystalline silicon² the values are $p/\omega_0^2 = -1.40$, $q/\omega_0^2 = -2.00$, $r/\omega_0^2 = -0.67$, $S_{11} = 7.73 \times 10^{-12} \text{ Pa}^{-1}$, $S_{12} = -2.15 \times 10^{-12} \text{ Pa}^{-1}$, and $S_{44} = 12.7 \times 10^{-12} \text{ Pa}^{-1}$.

2.1 Transition Dipole Moments and Selection Rules

The three frequency shifts associated with the stress field are not necessarily observable simultaneously at a specific orientation. Their detectability depends on the combination of the polarization of the incident light and the scattered light. For cubic crystals such as silicon, the Raman tensors in the 1, 2, and 3 directions are respectively

$$R_1 = \begin{bmatrix} 0 & 0 & 0 \\ 0 & 0 & d \\ 0 & d & 0 \end{bmatrix}, \quad R_2 = \begin{bmatrix} 0 & 0 & d \\ 0 & 0 & 0 \\ d & 0 & 0 \end{bmatrix}, \quad R_3 = \begin{bmatrix} 0 & d & 0 \\ d & 0 & 0 \\ 0 & 0 & 0 \end{bmatrix}$$

The Raman tensors corresponding to the three Eigenvectors under the above two-dimensional stress field are

$$\bar{R}_1 = \frac{1}{\sqrt{1+\Delta_1^2}} \begin{bmatrix} 0 & 0 & \Delta_1 d \\ 0 & 0 & d \\ \Delta_1 d & d & 0 \end{bmatrix}, \quad \bar{R}_2 = \frac{1}{\sqrt{1+\Delta_2^2}} \begin{bmatrix} 0 & 0 & d \\ 0 & 0 & \Delta_2 d \\ d & \Delta_2 d & 0 \end{bmatrix}, \quad \bar{R}_3 = \begin{bmatrix} 0 & d & 0 \\ d & 0 & 0 \\ 0 & 0 & 0 \end{bmatrix}$$

Selection rules were examined by evaluating the dipole moment for the strain-induced Eigenvectors for the following polarizations of incident and scattered light. Let \mathbf{e}_i and \mathbf{e}_s be the incident and scattered light with polarizations of:

$$\mathbf{e}_i^j = \begin{bmatrix} l_{i1}^j \\ l_{i2}^j \\ l_{i3}^j \end{bmatrix}, \quad \mathbf{e}_s^j = \begin{bmatrix} l_{s1}^j \\ l_{s2}^j \\ l_{s3}^j \end{bmatrix} \quad (3)$$

where l_{km}^j are directional cosines and $(l_{k1}^j)^2 + (l_{k2}^j)^2 + (l_{k3}^j)^2 = 1 \quad k = i, s$.

The superscript j labels the three roots in (2). The scattering intensity of the Raman signal is defined as $C \sum |\mathbf{e}_i^j \bar{\mathbf{R}}_j \mathbf{e}_s^j|^2$ where C is a scalar constant. The results summarized below show the amplitude strength of the observed frequency shift for each solution in (2).

$$e_i^1 \bar{R} e_s^1 = l_{i3}^1 (l_{s1}^1 \Delta_1 + l_{s2}^1) d / \sqrt{1 + \Delta_1^2}, \quad (4a)$$

$$e_i^2 \bar{R} e_s^2 = l_{i3}^2 (l_{s1}^2 + l_{s2}^2 \Delta_2) d / \sqrt{1 + \Delta_2^2}, \quad (4b)$$

$$e_i^3 \bar{R} e_s^3 = (l_{i2}^3 l_{s1}^3 + l_{i1}^3 l_{s2}^3) d. \quad (4c)$$

where

$$\Delta_1 = \frac{(1 - \alpha)(S_{11} - S_{12})(p - q)/2 - D}{rS_{44}\beta}, \quad \Delta_2 = \frac{rS_{44}\beta}{(1 - \alpha)(S_{11} - S_{12})(p - q)/2 + D},$$

$$D = \frac{1}{2} \sqrt{(1 - \alpha)^2 (S_{11} - S_{12})^2 (p - q)^2 + 4(rS_{44}\beta)^2}.$$

A strategy to uniquely identify the transitions from <001> single crystal silicon can be developed from the selection rules. It is seen from Eqn. (4) that for cases corresponding to backscatter from a <001> surface, only longitudinal phonons can be observed since it is only (4c) which remains non-zero for polarizations in the x-y plane. When the polarization angles of incident light and the scattered light complement each other in backscatter from the <001> surface, the amplitude (4c) is maximized. When the incident and scattered polarizations are parallel and the polarization vectors are aligned with either the x or y axis in the backscatter configuration, all amplitudes becomes zero. The (4c) term is non-zero for all other polarization orientations. Hence its behavior can be used to determine the crystallographic orientation of the cubic crystal³.

In order to observe the effects of shear as expressed by $\Delta\Omega_1$ and $\Delta\Omega_2$, the sample must be tilted to allow a non-zero projection along the z-axis. In this tilted configuration, if the polarizations of the incident and scattered light are parallel, then the longitudinal phonon transition (4c), can be nulled to enable observation of only the first two roots. In general as observed in the backward direction to the tilted incident beam, one will detect the sum of the transition intensities of 4(a) and 4(b). If the frequency difference between $\Delta\Omega_{(q=1)}$ and $\Delta\Omega_{(q=2)}$ is sufficiently large compared to the linewidth, then it will be very easy to identify each transition by a rotation of the polarization vector around the incident axis. One or the other transition intensity will go to zero at an angle determined by Δ_1 . In general, the ease of identifying the transitions and shifts is dependent on how much biaxial- and shear-stress is present. The separation of the peak positions of $\Delta\Omega_1$ and $\Delta\Omega_2$ is equal to $2D$ where D is defined above. In principle, if there is knowledge of the frequency shifts of all three transitions and the polarization angle at which either $\Delta\Omega_1$ or $\Delta\Omega_2$ becomes, then it is possible to derive the values of τ , α , and β .

3. EXPERIMENTAL

In the Raman stress experimental setup, a monochromatic light or laser shines on the surface of a specimen through a microscope. The specimen sits on a translation stage whose motion is controlled through a micrometer. The Raman scattered light is analyzed with a spectrometer. When the specimen is unstressed, the spectrometer measures a reference spectrum whose center position is that of the unstressed sample. When the specimen is placed in a stressed state, the spectrum will show a frequency shift which varies linearly with the applied stress. The measurements were conducted using an argon ion laser with a wavelength of 488 nm. The diameter of the laser spot is typically 1 to 2 μm with an estimated penetration depth for the incident light of 0.6 μm . The Raman spectra were least squares fitted with a Lorentzian profile to determine the center frequency shift.

The specimens that were used in the experimental tests included both calibration and MEMS specimens. The calibration specimen was in a strip configuration. The strip specimen was either clamped or simply supported at its two end regions depending on the holding fixture used. The specimens had a clear central span L and were loaded with two rollers that are located symmetrically with respect to the center of the specimen. Loads in the samples were induced by turning the set screw located at the center of the supported strip. The magnitude of the load setting was recorded from the load cell. The maximum surface stress of the sample between the central supports is:

$$\sigma_s = 3Pb^2/(Lwt^2) \quad (5)$$

for the clamped sample and for the simply supported sample is:

$$\sigma_s = 3Pb/(wt^2) \quad (6)$$

where P is the total load measured by the load cell, b and L are the dimension shown in Fig. 1, and w and t are the width and thickness respectively, of the strip.

Strip samples of <001> single crystal silicon were fabricated from 3 inch diameter standard n-type single crystal silicon wafers for use in either fixture. The sample dimensions were 12.7-mm (0.500 in.) in width and 0.394-mm (0.0155 in.) in thickness. They consist of two types such that a unidirectional stress could be applied either in the (110) or (100) directions.

The calculated results for single crystal silicon using (2) relate the Raman shifts in units of cm^{-1} to stress σ in units of Pascals as follows:

For applied uniaxial stress along the (100) direction, $\tau = \sigma_s = \sigma$, $\alpha = 0$ and $\beta = 0$: $\Delta\Omega_3 = -2.3 \times 10^{-9} \sigma_s$.

For applied uniaxial stress along the (110) direction, $\tau = \sigma_s/2 = \sigma/2$, $\alpha = 1$ and $\beta = 1$: $\Delta\Omega_3 = -2.3 \times 10^{-9} \sigma_s$.

The calculated results for polysilicon using (2) relates the Raman shifts in units of cm^{-1} to stress τ in units of Pascals as follows:

For "internal" uniaxial stress, $\alpha = 0$ and $\beta = 0$: $\Delta\Omega_3 = -2.12 \times 10^{-9} \tau$.

For "internal" equal biaxial stress without shear, $\alpha = 1$ and $\beta = 0$: $\Delta\Omega_3 = -4.24 \times 10^{-9} \tau$.

The term "internal" refers to stress components in the same direction as the crystal axis. The latter case may correspond to stress caused by a mismatch in the coefficient of thermal expansion between two adjacent layers.

The MEMS specimen is a cantilever beam fabricated by the MUMPS process⁴. Its nominal dimensions are 200 μm long, 20 μm wide, and 2 μm thick. It simulates an electrical relay. Since polysilicon is partially conductive, an insulating oxidation layer was deposited between the cantilever and the ground to allow application of a voltage that induces an electrostatic force to the cantilever. When the voltage increases to a critical value, the cantilever beam will collapse onto the ground. The deformation induced by the voltage will generate bending stresses in the beam with maximum values at the clamped end. Fig. 2 shows a photograph of a set of three cantilever beams.

Simple test structures were fabricated from <100> single crystal silicon using a REVISE⁵ laser machining work station. The process uses thermal heating by a laser to enhance chemical etch rates in an atmosphere of chlorine gas. Resolution of 2 μm is possible when the laser beam is focussed. Square shaped trenches were fabricated by raster scanning the laser spot at a power of a few watts with the 514.5 and 488.0-nm wavelengths from a Ar ion laser.

4. RESULTS AND DISCUSSION

Figure 3 depicts the Raman spectra of wafer cut from an annealed single crystal silicon boule. The average center frequency shift measured at random locations on the wafer is $520.28 \pm 0.06\text{-cm}^{-1}$ at room temperature. This uncertainty should correspond only to a uniaxial stress with no shear component with a value of $\pm 26\text{-MPa}$ (or $\pm 3.8\text{-ksi}$). The estimated error in the determination of the fitted line position is 0.02-cm^{-1} or 8.7-Mpa (1.25-ksi). Measurements were also taken on an annealed polysilicon layer deposited on a SiO_2 layer on top of a single-crystal silicon substrate in Fig. 4. These measurements showed a spatial variability of $\pm 68.3\text{-MPa}$ (9.8-ksi) which is well in excess of the residual stress of the uncoated substrate, indicating that the coating has increased the residual stress. This finding is consistent with the earlier work of Miura⁶.

Raman frequency measurements for <001> single crystal silicon strip with (100) applied unidirectional stress are presented in Fig. 5. The measured slope is $2.86 \pm 0.27 \times 10^{-9}\text{-cm}^{-1}/\text{Pa}$. The theoretical slope is $2.3 \times 10^{-9}\text{-cm}^{-1}/\text{Pa}$. The Raman frequency measurements with (110) applied unidirectional stress are presented in Fig. 6. This sample and its stress orientation correspond to the equal biaxial case discussed above. The measured slope is $2.07 \pm 0.14 \times 10^{-9}\text{-cm}^{-1}/\text{Pa}$ compared to the expected value of $2.3 \times 10^{-9}\text{-cm}^{-1}/\text{Pa}$. The agreement for both types of samples is within 20% of theory and is within the 2-sigma error bounds of the data. While these data provide the necessary calibration and confirmation of the theoretical and experimental approach taken in this paper further refinements of the measurements and reduction of experimental uncertainties are in progress.

In Fig. 7, a preliminary residual stress map for a polysilicon cantilever beam is presented for the critical region of the beam near the support. Locations of the measurements are indicated in the figure. Large compressive stresses were observed despite

the factor of 2 uncertainty which arises from whether the stress is uniaxial or biaxial. The measurements were taken near a discontinuity in layered films of dissimilar thermal expansion coefficients. Further study is required to resolve the stress into its many components for this geometry. In the near future, stress from flexing the cantilever beam will be compared to the model predictions. To date, many investigators have assumed that only equal biaxial stresses are present for polysilicon. This assumption needs to be validated through further investigation.

Preliminary stress profiles in terms of frequency shifts near the edge of a 0.20-mm square, 28- μm deep trench fabricated using the REVISE laser-enhanced (thermal) Chlorine etch are shown in Fig. 8. The laser has a spot size of 2- μm and power of a few watts. While some variation on the order of a few tenths of a cm^{-1} occurs due to residual stress and processing defects in the substrate, the fabrication of the trench has caused large stresses. Relative to the outside to the inside of the trench, a large negative shift of 1.9- cm^{-1} is observed. This indicates that the floor of the trench has less compressive stress (more tensile). Assuming this is due only to a uniaxial stress, the stress difference is 830-MPa. The magnitude of this stress is sufficiently large to cause significant concern for the mechanical reliability of parts using this fabricated trench. In addition at the outer and inner edges of the trench wall, sharp stress gradients can be observed causing additional concern. The origin of the stresses may be due to stress concentration caused by the discontinuity of the edge of the trench or to heating by the laser to cause compressive yielding. Further experiments are required to identify the mechanism responsible.

In summary, we have demonstrated analytically that the two-dimensional surface stresses normal to the $\langle 001 \rangle$ plane of a cubic crystal have a unique relationship with the Raman frequency shifts. In other words, for a cubic crystal whose spring constants p , q , r are known, once the Raman frequency shifts and polarization characteristics are measured, then the associated surface stress components can be determined. We have also demonstrated that the measured Raman frequency shifts for single crystal silicon under uni-directional tensile stress in both (110) and (100) agree with analytical predictions. With this validation in hand, Raman spectra can be used to address the role of stress for reliability assessments and failure mechanisms in MEMS and microelectronics. The use of this Raman stress diagnostics will lead to improved lifetimes, the identification of defects, and improved fabrication for future silicon devices. In this work, high stress levels have been observed in simple single and poly-crystalline samples that raise concern for deleterious effects for these types of structures.

ACKNOWLEDGMENTS

This work was performed under the support of Mission Oriented Investigation and Experimentation project funded by Air Force Space and Missile Systems Center (AFSMC) and a grant funded by the Directorate of Aerospace and Materials Sciences of the Air Force Office of Scientific Research (AFOSR).

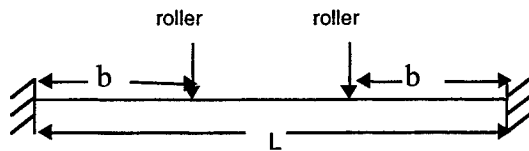


Figure 1. Schematics of a strip specimen in a fixture for either a clamped or simply supported end. The values of $b = 0.75$ inch (1.91-cm) and $L = 2.25$ inch (5.72-cm) were used.

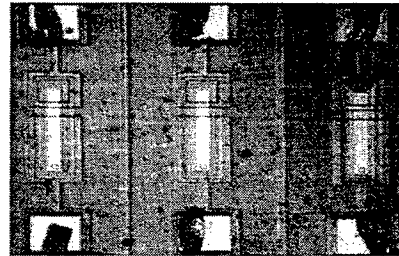


Figure 2. Photograph of MEMS cantilever beams. (Middle portion is the cantilever, top and bottom square structures are pads).

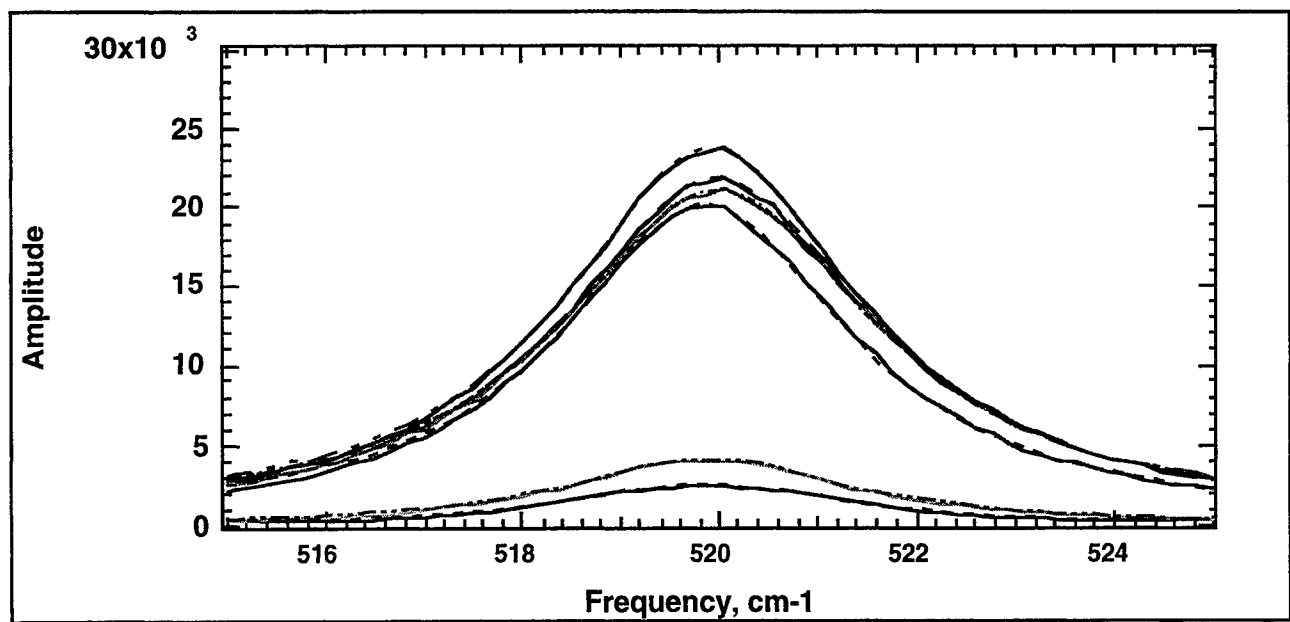


Figure 3. Raman spectra for unstressed, single-crystal Si.

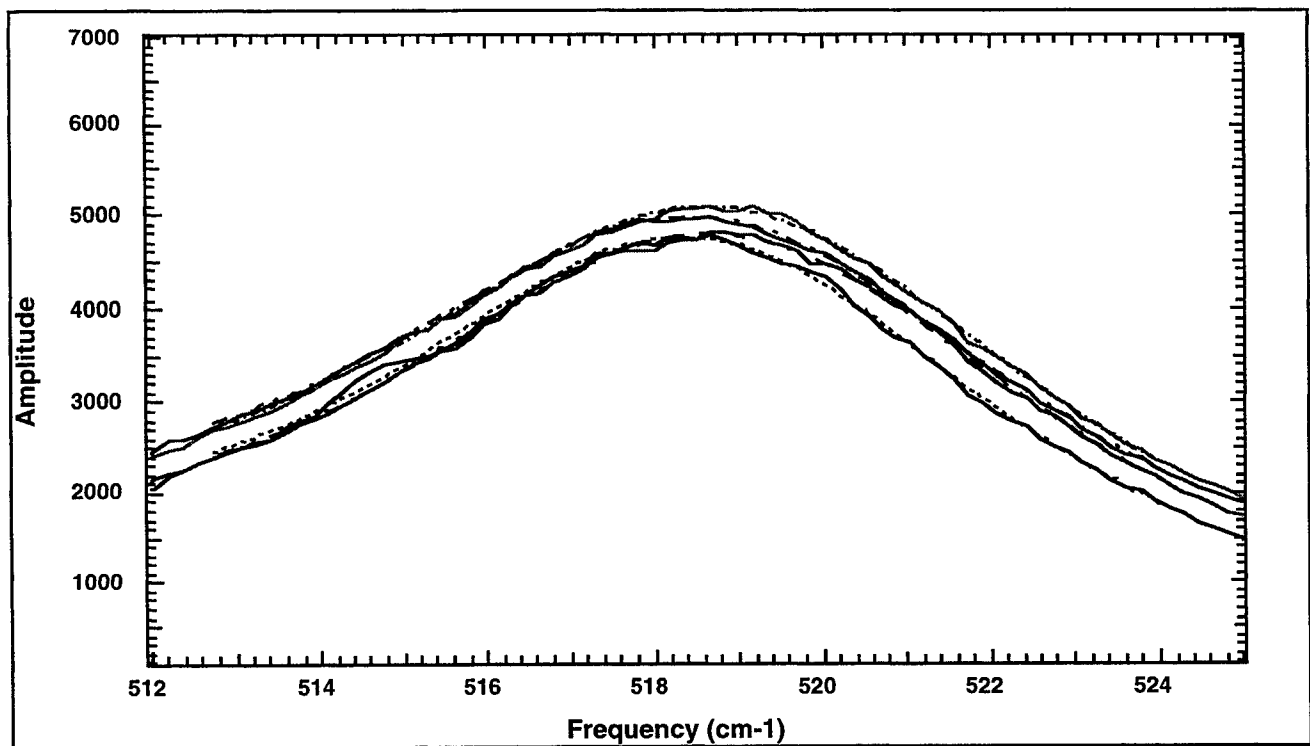


Figure 4. Raman spectra for polysilicon deposited on SiO₂ on single crystal Si substrate.

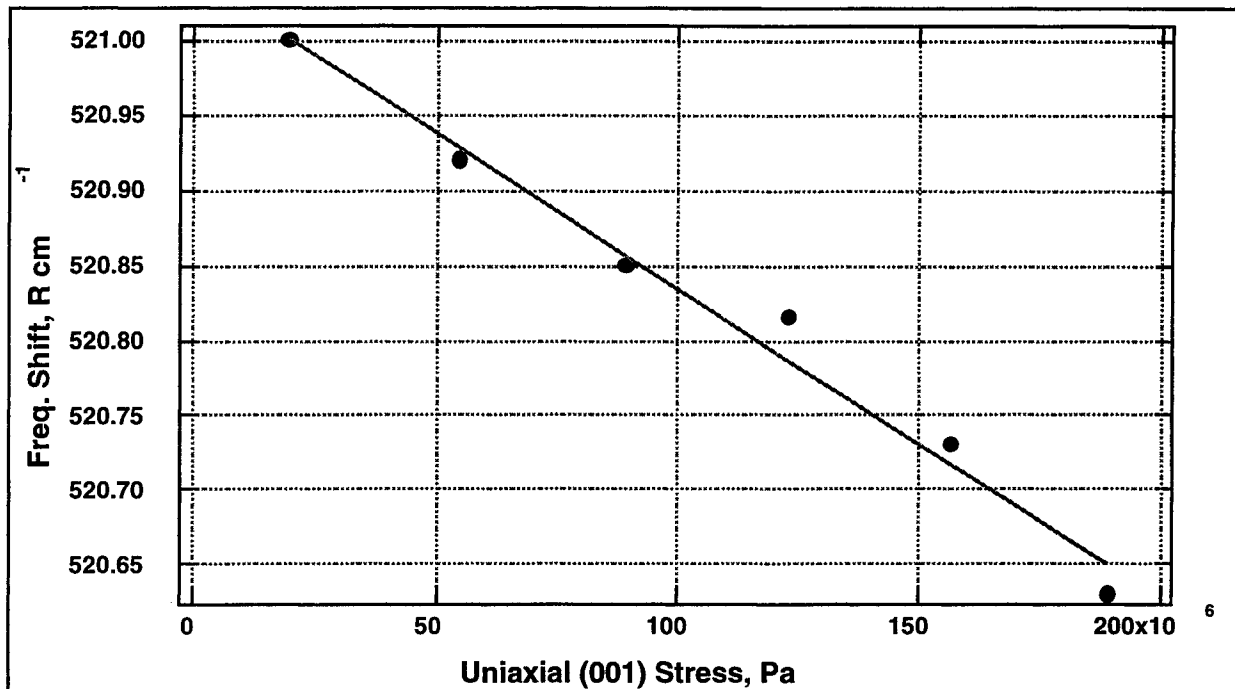


Figure 5. Frequency shift as a function of external uniaxial applied stress in the (100) direction. The sample is a strip of <001> single crystal silicon. The fitted line has a slope of $-2.07 \times 10^{-9} \text{ cm}^{-1}/\text{Pa}$ with an error of 0.14×10^{-9} . The theoretical value is $2.30 \times 10^{-9} \text{ cm}^{-1}/\text{Pa}$.

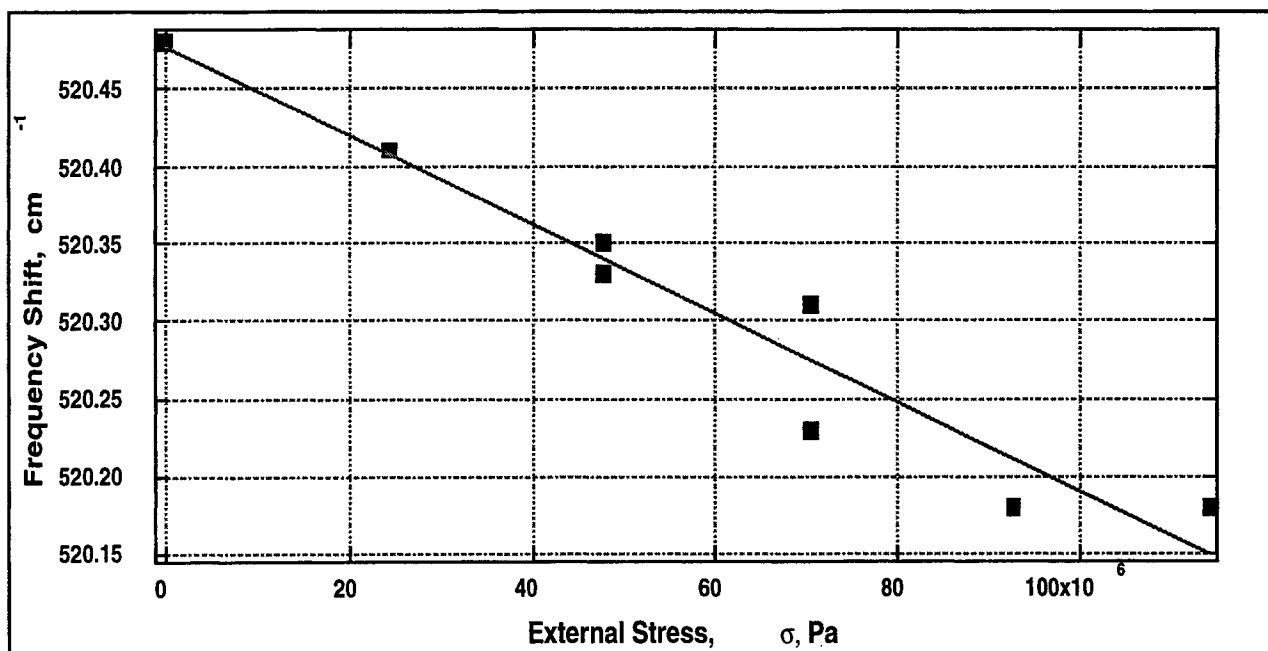


Figure 6. Frequency shift as a function of applied external uniaxial stress in the (110) direction. The sample is a strip of <001> single crystal silicon. The fitted line has a slope of $-2.86 \times 10^{-9} \text{ cm}^{-1}/\text{Pa}$ with an error of 0.27×10^{-9} . The theoretical value is $2.30 \times 10^{-9} \text{ cm}^{-1}/\text{Pa}$.

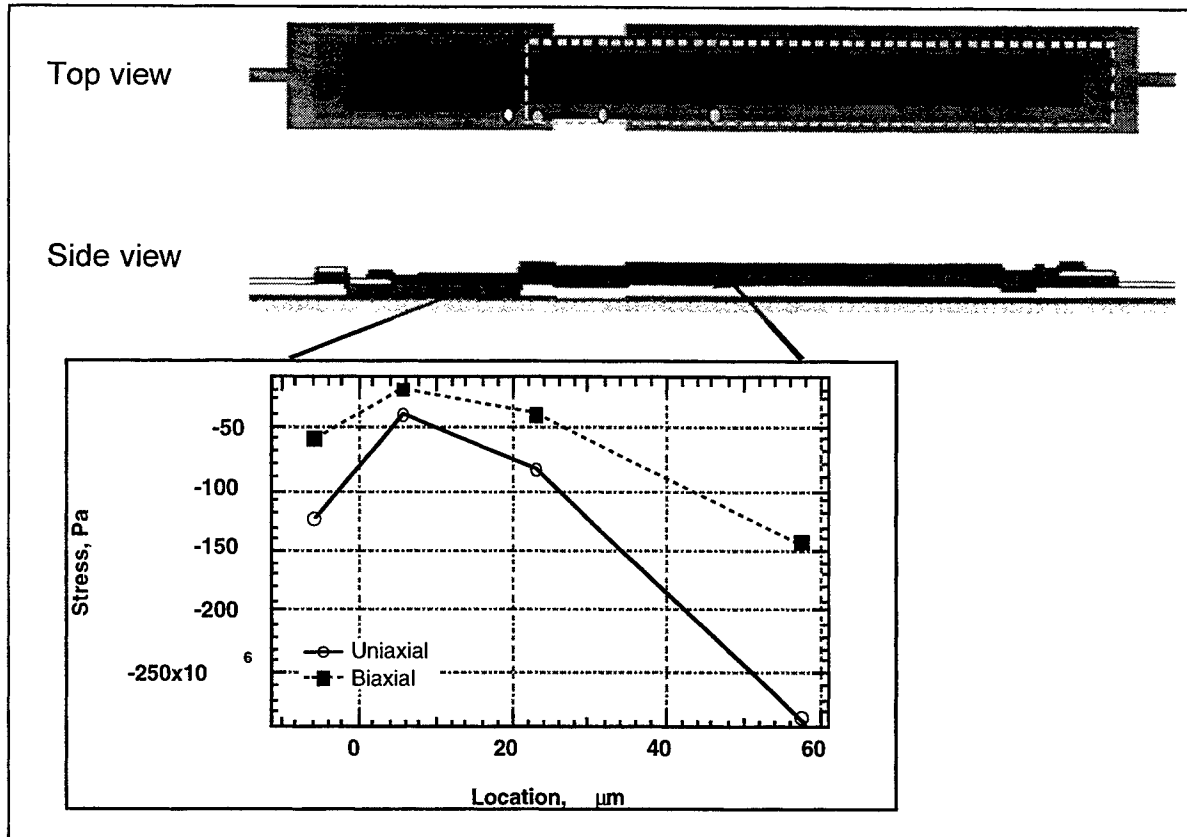


Figure 7. Stress map of a 20 x 200 μm polysilicon (dashed lines) cantilever beam. The stress measurement locations correspond to the locations near the lower edge of the top view of the cantilever beam.

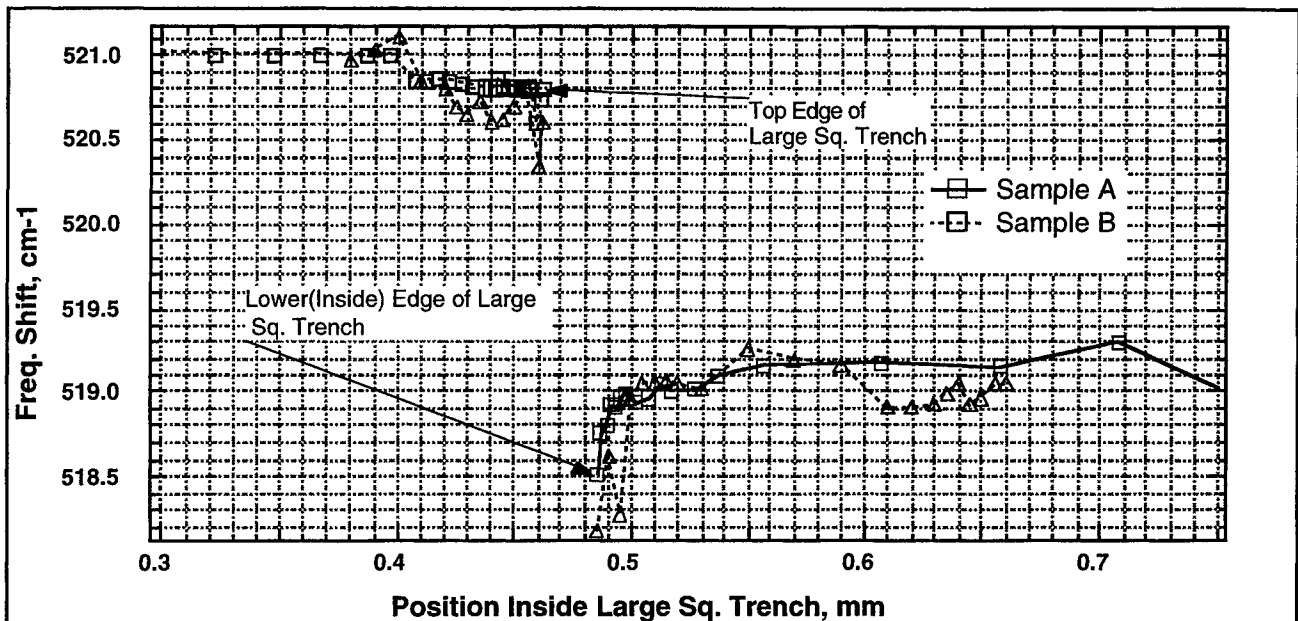


Figure 8. Stress profiles near the edges of two sample specimens of a 0.20-mm square trench. Lower values of the frequency shift indicate a relative more tensile stress inside the trench relative to the outside stress on the lefthand side of the profile. Measurements were not taken along the sloping edges of the trench. The estimated depth of the trench is 28-micron.

REFERENCES

- ¹ E. Anastassakis, A. Cantarero, and M. Cardona, "Piezo-Raman measurements and anharmonic parameters in silicon and diamond", *Phys. Rev. B* **41**, pp. 7529-7535, 1990 and E. Anastassakis, A. Pinczuk, E. Bernstein, F. H. Pollak, and M. Cardona, "Effect of static uniaxial stress on the Raman spectrum of silicon", *Sol. State Comm.* **8**, pp. 133-138, 1970.
- ² E. Anastassakis and E. Liarokapis, "Polycrystalline Si under strain: Elastic and lattice-dynamical consideration", *J. Appl. Phys.* **62**, pp. 3346-3352, 1987.
- ³ G. Kolb, Th. Salbert, and G. Arstreiter, "Raman-microprobe study of stress and crystal orientation in laser crystallized silicon", *J. Appl. Phys.* **69**, pp. 3387-3389, 1991.
- ⁴ MUMPS or Multi-User MEMS Processes at the MEMS Technology Application Center, MCNC, 3021 Cornwallis Rd, Research Triangle Park, NC 27709.
- ⁵ This process is described in T. M. Bloomstein and D. J. Erhlich, "Stereo laser micromachining of silicon", *J. Vac. Sci. Technol. B*, 2671(1992)
- ⁶ H. Miura, H. Sakata, and S. Sakata, "Residual stress measurement of Si substrates after thermal oxidation using microscopic Raman spectroscopy", pp. 1301-1306, Proceedings of the 9th International Conference on Experimental Mechanics, 20-24 August 1990, Copenhagen, Denmark.

^aE-mail: sherwin.t.amimoto@aero.org, ph. (310)-336-7660

^bE-mail: dick.j.chang@aero.org, ph (310)-336-5808

SESSION 5

Pulsed Laser Deposition I

Pulsed-laser deposition of electronic oxides: superconductor and semiconductor applications

D. P. Norton^a, C. Park^a, Y. E. Lee^a, J. D. Budai^a, M. F. Chisholm^a, D. T. Verebelyi^a, D. K. Christen^a, and D. M. Kroeger^b

^aSolid State Division, Oak Ridge National Laboratory, Oak Ridge, TN 37831-6056

^bMetals and Ceramic Division, Oak Ridge National Laboratory

ABSTRACT

Over the past decade, pulsed-laser deposition (PLD) has proven to be one of the most versatile and effective methods for obtaining high-quality electronic oxide thin-film materials. Much of this success can be attributed to its initial use in depositing high temperature superconducting materials. However, pulsed-laser deposition is now a leading research tool in the development of various electronic oxide thin-film technologies. In this paper, recent progress in the deposition of oxide materials on dissimilar materials for both superconductor and semiconductor applications is discussed. Recent developments in the synthesis of superconducting wires via epitaxial growth of superconducting oxides on biaxially textured metal tapes is described. In addition, efforts to integrate high-k dielectric oxides on semiconductor surfaces using pulsed-laser deposition are highlighted.

Keywords: Pulsed-laser deposition, electronic oxides, superconductor, dielectric, dissimilar epitaxy, epitaxial growth

1. INTRODUCTION

In the epitaxial growth of oxide materials, pulsed laser deposition continues to excel as a highly effective method for obtaining high-quality crystalline films. One of the more interesting materials challenges in electronic oxides is that of dissimilar epitaxy on non-oxide substrates. The synthesis and properties of crystalline ionic oxide films on metallic or covalent substrates is important for many applications, as single crystal oxides are rarely the substrate of choice. Two examples involving dissimilar oxide epitaxy are described in this paper: superconducting films on metals for coated conductors and dielectrics on semiconductors for MOSFET devices.

2. SUPERCONDUCTING OXIDES ON METAL TAPES FOR CONDUCTORS

Significant effort to develop a high temperature superconducting (HTS) wire or tape has focused on the epitaxial growth of superconducting films on biaxially textured metals.^{1,2} This approach, illustrated in Fig. 1, is dependent on the heteroepitaxial growth of oxide buffer layer films on metal surfaces. In order to realize an HTS film possessing a high critical current on a biaxially textured metal substrate, the buffer layer architecture must satisfy a set of rather stringent requirements. The buffer layer construct must be chemically compatible with both the metal and superconductor. It must be mechanically robust so as to prevent microcrack formation at the HTS/buffer layer interface. It must also be epitaxial relative to the biaxially textured metal with a singular (001) orientation. The latter requirement is particularly challenging as the epitaxy of metal oxides on metal surfaces is determined not only by the relative lattice match

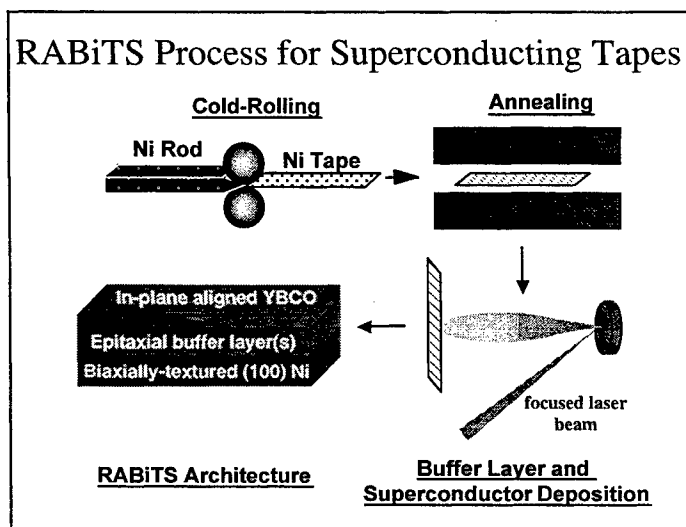


Figure 1 Schematic of Rolling Assisted Biaxially Textured Substrate (RABiTS) approach to coated conductor development.

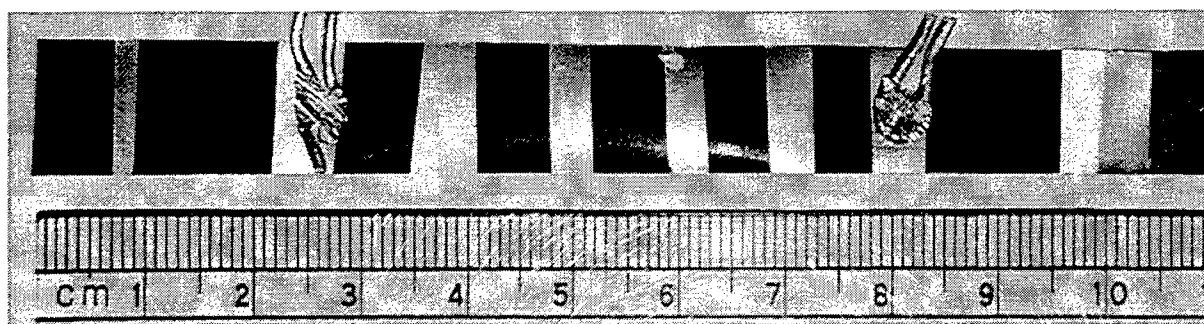


Figure 2 Photograph of 10 cm long YBCO/CeO₂/YSZ/CeO₂/Ni tape

between film and substrate, but by possible roles of a native oxide layer and/or intermetallic phases formed during film nucleation.

Previous efforts have satisfied these requirements with multilayer combinations of various oxide buffer layers. Superconducting films with critical current densities in excess of 1 MA/cm² at 77 K have been achieved for epitaxial YBa₂Cu₃O₇ films on rolled-textured Ni substrates with the use of certain epitaxial buffer-layer constructs.³ For example, PLD has been used to nucleate an epitaxial (001)-oriented CeO₂ layer on a biaxially textured (001) Ni surface.⁴ A tendency for the CeO₂ layer to crack due to differences in thermal expansion coefficients of the oxide film and metal tape requires an additional epitaxial yttria-stabilized zirconia (YSZ) buffer layer on the CeO₂ in order to achieve crack-free superconducting films.¹ In this case, the superior mechanical properties of the YSZ layer circumvent the cracking problem, and enable the formation of superconducting films with high critical currents. A 10 cm long YBCO/CeO₂YSZ/CeO₂/Ni superconductivity tape is shown in Fig. 2.

Though effective in forming a high current superconducting tape, the use of a multilayer buffer architecture introduces significant complexity to the fabrication process. Ideally, one would prefer to use a single buffer layer. One of the most attractive materials for a single buffer layer that is mechanically robust and chemically inert is YSZ.⁵⁻⁷ Unfortunately, previous efforts to grow epitaxial YSZ films with a single (001) orientation directly on rolled-textured (001) Ni tapes have been unsuccessful, with a mixture of (100) and (111) orientation realized. We have recently investigated the nucleation and growth of epitaxial (001) YSZ on the (001) Ni surface using pulsed-laser deposition. Nucleation on an oxide-free (001) biaxially-textured Ni surface yields a mixed (111) and (001)-oriented film. However, (001)-oriented epitaxy is achieved by nucleating the YSZ film on a surface that is apparently oxygen terminated. Exposing the surface to conditions where significant NiO forms results in the nucleation of polycrystalline material. Using the (001)-oriented YSZ as a template, a YBa₂Cu₃O₇/YSZ/biaxially-textured Ni structure with a high J_c is realized.

The substrates used in this study were biaxially-textured (001) Ni tapes (50 μm thick) produced by cold-rolling and annealing.⁸ The starting purity of the Ni tape was 99.99%. For texture development, the cold-rolled metal tape was enclosed in a tantalum envelope and annealed in vacuum with a base pressure of 2×10^{-6} Torr at 800-1000 °C for 60 minutes. The tantalum envelope serves as a local oxygen getter during the anneal. The degree of in-plane and out-of-plane texture for the substrates as determined by x-ray diffraction (XRD) rocking curves was approximately 8°. After annealing, the Ni tape was stored in air until mounted on a heater block using Ag paint and loaded into an o-ring sealed vacuum chamber for pulsed-laser deposition. Note that exposure to air almost immediately oxidizes the nickel surface. A 10 mol.% yttria-stabilized ZrO₂ ceramic target was used to deposit the YSZ film. A KrF excimer laser beam was incident on the rotating target surface at an angle of 45°. The laser energy density was 2.6 J/cm² with a deposition rate of 0.25 nm/sec. The target-to-substrate distance was 7 cm. The base pressure of the growth chamber was 10^{-6} Torr, assumed to consist primarily of water vapor. The YSZ nucleation experiments were performed in the temperature range of 600-800°C.

For the experiments reported here, an initial nucleation layer (~5 nm) of YSZ was deposited under various conditions, followed by the additional epitaxial growth of a 200 nm thick YSZ film with $P(O_2) = 10^{-4}$ Torr. The relatively thick epitaxial film grown on the nucleated template layer effectively reflects the crystalline orientation of the nucleated layer. Three

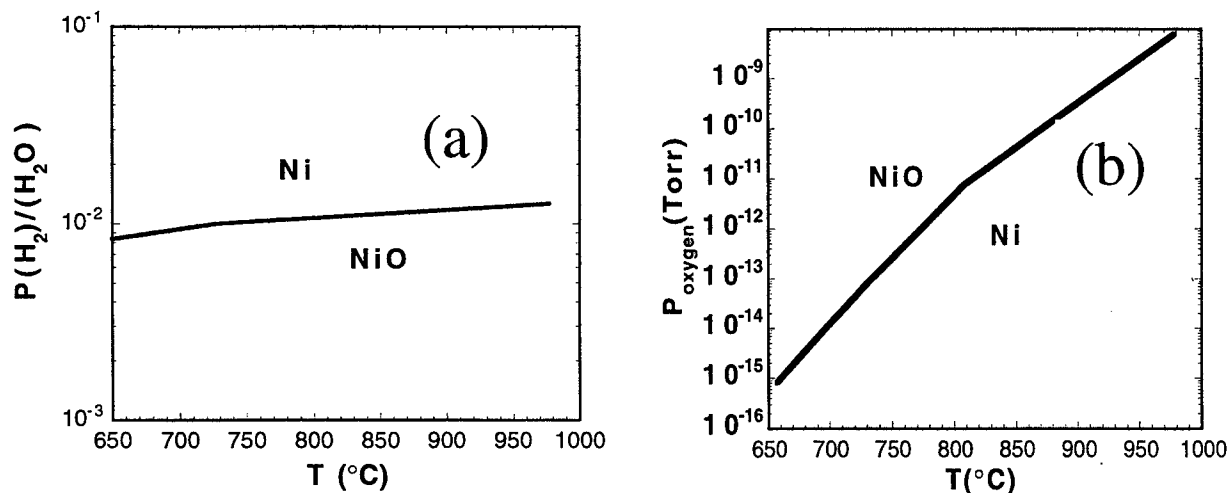


Figure 3 NiO stability curves in the presence of hydrogen (a) and oxygen (b).

ambient conditions were considered during nucleation. First, nucleation was carried out on an oxide-free surface by introducing sufficient hydrogen partial pressure (up to 200 mTorr 4% H_2 / 96% Ar mixture) so as to reduce any NiO on the Ni surface as determined from the thermodynamics of NiO reduction (case A). Figure 3a) shows the stability curve for NiO in the presence of hydrogen and water vapor.⁹ For $P(H_2)/P(H_2O) > 10^{-2}$ at $T > 600^\circ\text{C}$, NiO will be reduced, yielding an oxide-free surface. Second, nucleation was performed under base pressure conditions (case B). For a vacuum system with a base pressure of $\sim 10^{-6}$ Torr, the residual oxygen pressure will be at least 10^{-8} Torr. Using Ellingham diagrams for binary oxides, the equilibrium oxygen partial pressure for NiO heated to 600-800°C should be in the range of 10^{-16} to 10^{-11} Torr as illustrated in Fig. 3b.⁹ Under the above conditions, oxygen termination of the surface would be expected. Lastly, nucleation was carried out in an oxygen partial pressure of 5×10^{-6} Torr or greater (case C). Under these conditions, significant NiO coverage of the Ni surface is expected.

For nucleation of YSZ in the presence of sufficient hydrogen to yield an oxide-free nickel surface (case A), polycrystalline films with mixed orientation were realized. This differs from the case for CeO_2 , where (001) epitaxy is achieved via nucleation on an oxide-free nickel surface.¹ One possible explanation for this difference in CeO_2 and YSZ nucleation resides in the different cation chemistry. Ce can exist in either +4 or +3 valence, while Zr is a monovalent +4. Within the cubic fluorite structure, CeO_{2-x} can accommodate significant oxygen deficiency, while YSZ can not for a given cation composition. The excess Zr may react with the nickel surface forming intermetallic compounds that interfere with (001) epitaxy. Additional work needs to be performed to address this issue.

In contrast to nucleation in the presence of hydrogen, nucleation of YSZ at a base pressure of 10^{-6} Torr (case B) results in a singular (001) epitaxial relationship. X-ray diffraction θ - 2θ scans along the surface normal for an epitaxial (001) YSZ film that was nucleated on the Ni (001) substrate at 800°C in a background pressure of 2×10^{-6} Torr with no intentional oxygen or hydrogen flow shows that the film is essentially 100% (001) oriented with an intensity ratio of the (111) to (200) peaks less than 0.01. ω -scans and ϕ -scans of the YSZ peaks indicate that the film is in-plane aligned and epitaxial with respect to the biaxially textured Ni substrate. The in-plane and out-of-plane mosaic spread for the film is slightly smaller than that measured for the substrate. Similar results were obtained for films deposited at temperatures as low as 600°C . For the case where an oxygen partial pressure greater than 5×10^{-6} Torr is introduced during either substrate heating or film nucleation (case C), a significant or dominant YSZ (111) oriented component was evident in the x-ray diffraction data. An oxygen partial pressure of 10^{-5} Torr or greater during nucleation yields nearly 100% (111)-oriented YSZ.

With the epitaxial growth of high-quality YSZ on biaxially textured nickel, a single buffer layer architecture for the growth of $\text{YBa}_2\text{Cu}_3\text{O}_7$ becomes possible. A 0.25 nm thick $\text{YBa}_2\text{Cu}_3\text{O}_7$ film was deposited on the 250 nm YSZ layer at a deposition temperature of 750°C and oxygen pressure of 200 mTorr. A θ - 2θ XRD scan along the surface normal for the $\text{YBa}_2\text{Cu}_3\text{O}_7$ / YSZ / Ni structure shows only c-axis oriented $\text{YBa}_2\text{Cu}_3\text{O}_7$, with the intensity ratio of the YSZ (111) to (200) peaks less than 0.02. X-ray diffraction ω -scans and ϕ -scans for the YSZ and $\text{YBa}_2\text{Cu}_3\text{O}_7$ peaks show that the layers are in-plane aligned and epitaxial with respect to the biaxially textured Ni substrate. The in-plane and out-of-plane mosaic spreads for the

YBa₂Cu₃O₇ and YSZ layers are similar to that measured for the metal tape. Scanning electron microscopy images of the (001) YSZ/Ni films show no evidence for microcracking in the YSZ layer. The critical current density at 77 K for the YBa₂Cu₃O₇ film was as high as 1 MA/cm², which is the highest reported value for any epitaxial YBa₂Cu₃O₇ film on biaxially-textured metal substrate with a single buffer layer separating the superconductor from the biaxially textured metal substrate.

3. HIGH-K DIELECTRICS ON SEMICONDUCTORS FOR MOSFET DEVICES

Another interesting case of dissimilar epitaxy involving oxides is the growth on semiconductors. Metal/oxide/semiconductor (MOS) structures are key elements in microelectronic applications.^{10,11} Various semiconductor materials would be attractive for MOS-type device applications given a method to form well-defined oxide/semiconductor interfaces suitable for functional structures. For example, Ge and SiGe alloys are attractive semiconductor materials for electronic applications, possessing higher carrier mobilities and thermal conductivities than that of silicon. Germanium possesses a simple cubic crystal structure with $\mu_n = 3900$ cm²/V-sec, $\mu_p = 1800$ cm²/V-sec, and a thermal conductivity of 0.6 W/cm-K. Unfortunately, the native germanium oxides are not suitable for MOS-type device structures.^{12,13} The formation of stable metal oxides on Ge could prove instrumental in the development of Ge and/or SiGe alloy integrated circuits. For applications involving sensors, photovoltaics, and optoelectronics, the formation of well-defined metal oxide/semiconductor interfaces for semiconductor materials other than silicon is vital to current and future device architectures. In many cases, one would prefer to have a well-defined metal oxide/semiconductor structure devoid of any native oxide at the interface, as the presence of native oxide at the interface limits the performance of these structures. This has been demonstrated for the case of silicon, in which molecular beam epitaxy was used to grow a crystalline oxide as a monolithic, commensurate structure on silicon.[5] In addition, a method to form oxides that are epitaxial on semiconductors would enable the integration of various epitaxial oxide materials and device structures with semiconductor electronics by providing a crystalline oxide template for additional epitaxial oxide film growth.

We have recently explored the epitaxial growth and properties of CeO₂ on (001) Ge using pulsed-laser deposition. Hydrogen is introduced as a background gas during the film nucleation in order to eliminate the native GeO₂ on the Ge surface and achieve epitaxy.^{1,15} The use of hydrogen greatly relaxes vacuum requirements needed for the formation of a GeO₂-free surface. Using this approach, (001)-oriented CeO₂ thin films were obtained on the (001) Ge surface. The resulting metal oxide/semiconductor interface is atomically abrupt, with no apparent native oxide present at the semiconductor /metal oxide interface. These results differ from that observed for CeO₂ on (001) Si, where the film is (110)-oriented with significant SiO₂ formation at the film/substrate interface.¹⁶⁻¹⁸

The deposition of (001) epitaxial cerium oxide on single crystal Ge (001) was performed by pulsed-laser deposition using a KrF excimer laser. Single crystal (001) Ge substrates were cleaned by successive rinsing in trichloroethylene, acetone, and methanol, followed by rinsing in deionized water. The native oxide was then removed by a 30 sec dipping in a 1:10 HF:H₂O solution. The substrate was blown dry with dry nitrogen and mounted on the heater platen using silver paint. The sample was loaded into the vacuum chamber for pulsed-laser deposition of the oxide film. The chamber was evacuated to an initial base pressure that ranged from 5×10^{-6} Torr to 2×10^{-9} Torr. The mounted Ge substrate was annealed in vacuum at 350°C for 2-12 hrs in order to decompose the organic binder in the silver paint. Prior to heating, the ablation target was in situ cleaned by laser ablation with a shutter between the substrates and ablation target.

In order to minimize or eliminate any native germanium oxide on the substrate surface prior to growth, hydrogen gas was introduced into the chamber to a sufficient pressure such that the ratio of hydrogen to water vapor partial pressure $P(\text{H}_2) / (P(\text{H}_2\text{O}))$ was approximately at or above the GeO₂ stability curve at the anticipated oxide film growth temperature as shown in Fig. 4. This curve was derived from Ellingham diagrams for oxide materials.^{9,19} The oxide stability line can be estimated from the temperature-dependent Gibbs free energy of the chosen native oxide when compared to the H₂O/H₂ equilibrium behavior. Depending on the anticipated metal oxide deposition temperature, the GeO₂ instability criterion translates into a value of $P(\text{H}_2)/P(\text{H}_2\text{O}) > 0.04$, preferably greater than 1.0. As a practical matter, the base pressure of the vacuum systems consists mostly of H₂O.

For the experiments reported here, a flow of 4% H₂ / 96% Ar was introduced into the chamber with the H₂/Ar pressure ranging from 10^{-5} to 10^{-1} Torr, depending on the base pressure. For example, an H₂/Ar pressure of 0.1 Torr yields a hydrogen partial pressure of 4×10^{-3} Torr, and a value of $P(\text{H}_2)/P(\text{H}_2\text{O})$ of 8×10^2 for a base pressure of 5×10^{-6} Torr. The substrate was then heated to the growth temperature in the 4% H₂ / 96% Ar background. As the substrate is heated, the hydrogen reduces

any GeO_2 that resides or forms on the substrate surface, resulting in the gas-phase etching of the native oxide. The final growth temperature must be consistent with the requirement that the conditions (temperature, water vapor partial pressure, hydrogen partial pressure) be above the GeO_2 stability line where the formation of GeO_2 is thermodynamically unfavored. Under these conditions, a metal oxide material that is stable for the chosen temperature/water vapor/hydrogen conditions can be deposited onto the heated substrate by means of pulsed-laser deposition. This oxide material should be thermodynamically stable in contact with Ge.²⁰ Cerium oxide satisfies this criterion.

After heating to the selected growth temperature, a CeO_2 film was deposited on the Ge surface. The KrF excimer laser energy density was $\sim 1.5 \text{ J/cm}^2$ with a laser repetition rate of 1 Hz. These conditions yielded a deposition rate of $\sim 0.1 \text{ nm/laser pulse}$ when using a pressed and sintered CeO_2 ablation target.

Both the metal cation and oxygen atoms are provided by laser ablation as short, discrete pulses. Between the laser pulses, the metal oxide / semiconductor system can relax to the conditions that thermodynamically favor instability of the native oxides. After the initial film nucleation, additional CeO_2 could be deposited on the initial oxide film template using deposition conditions that do not necessarily coincide with the requirements of GeO_2 thermodynamic instability as outlined for the template oxide layer, thus allowing the CeO_2 stoichiometry to be controlled. After film growth, the germanium substrate was typically cooled in vacuum.

Figure 5 shows x-ray diffraction data for a 50 nm thick CeO_2 film on (001) Ge grown at 750°C . The CeO_2 film was deposited with $P(\text{H}_2) = 4 \times 10^{-7} \text{ Torr}$ and a base pressure $= 2 \times 10^{-9} \text{ Torr}$. Approximately 5 nm was deposited in the presence of hydrogen. The remaining 45 nm of CeO_2 was deposited with no hydrogen flow. Note that for temperatures greater than

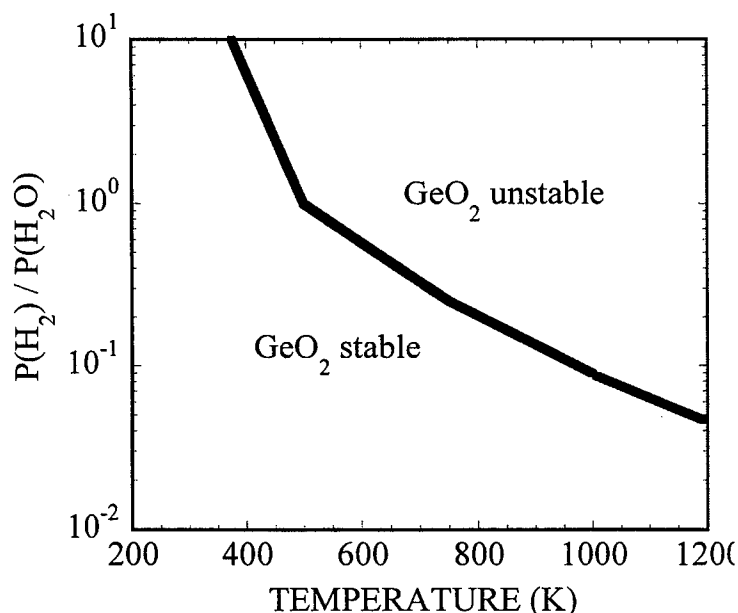


Figure 4. Plot showing GeO_2 stability line with respect to the ratio of hydrogen gas to water vapor. The conditions for which GeO_2 is unstable are explicitly denoted.

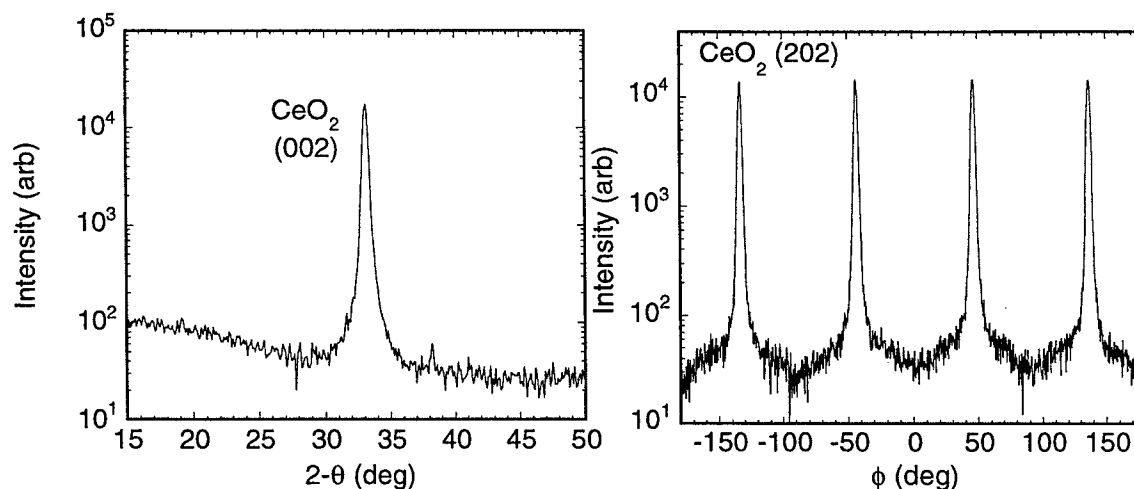


Figure 5 X-ray diffraction 2- θ and ϕ -scans of CeO_2 on (001) Ge.

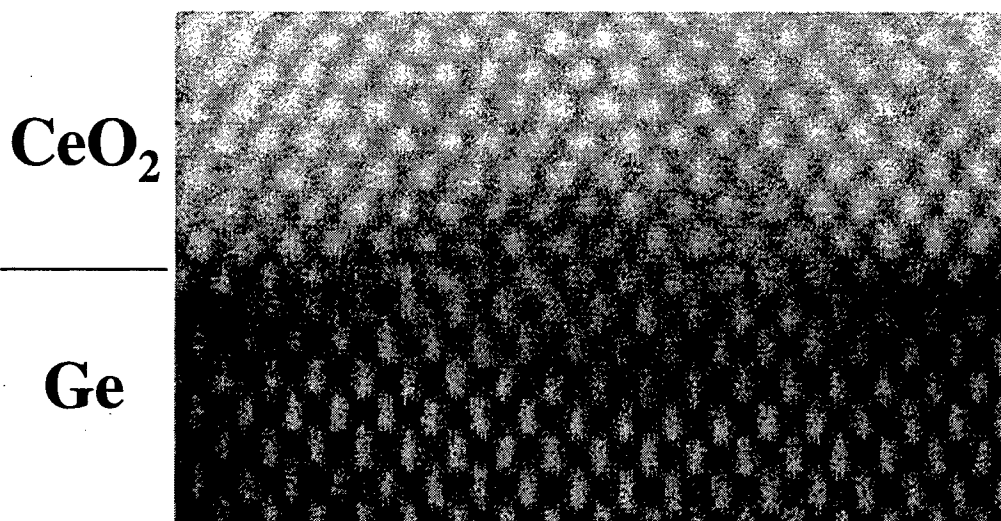


Figure 6 Z-contrast STEM image of epitaxial CeO₂/Ge interface.

550°C, only the (001) orientation is observed. In-plane XRD scans confirm that the CeO₂ films are in-plane aligned. Note that some broadening in 2θ is observed at the lower growth temperature, indicating that strain is present in the film.

In addition to x-ray diffraction, the properties of the CeO₂ / Ge interface were investigated using high-resolution scanning transmission electron microscopy (STEM). Cross-section images reveal that CeO₂ films deposited at 750°C possess a 3D island-like morphology that is faceted, with extended defects (pinholes) extending to the substrate at some of the faceted boundaries. Disruption of the CeO₂/Ge interface in the form of etched holes or amorphous material was evident in the proximity of these defects. Between the defects, the CeO₂/Ge interface is atomically abrupt and free of GeO₂. At slightly lower temperatures, faceting is significantly diminished. Figure 6 shows a cross-section Z-contrast STEM image of a CeO₂ film that was grown at 650°C. The absence of an amorphous native oxide layer at the interface differs from that observed for CeO₂ films on Si, where significant SiO₂ is observed at the film/substrate interface. The fact that GeO₂ is thermodynamically less stable than SiO₂ suggests that the formation of GeO₂ at the interface should be less likely.

4. CONCLUSIONS

In conclusion, we have investigated the heteroepitaxial growth of oxides on dissimilar substrates using pulsed-laser deposition. In the nucleation of epitaxial YSZ directly on biaxially-textured (001) Ni tapes using pulsed-laser deposition, the orientation of YSZ depends on the initial state of the substrate, with (001) epitaxy possible by nucleation on an oxygen-terminated metal surface. The epitaxial (001) YSZ layer grown on the Ni (001) surface can be used as a single buffer layer for a high temperature superconducting coated conductor architecture, yielding superconducting YBa₂Cu₃O₇ films with high critical current densities. In addition, the growth of (001) epitaxial CeO₂ on a (001) Ge surface using pulsed-laser deposition in a hydrogen ambient has been realized. By using hydrogen to eliminate GeO₂ from the surface during film nucleation, a CeO₂ / Ge interface that is essentially free of GeO₂ can be formed. The use of hydrogen to promote the epitaxial growth of oxides on semiconductor surfaces should be applicable not only to CeO₂ on Ge by PLD, but to other material systems and physical vapor deposition techniques.

ACKNOWLEDGMENTS

This research was sponsored by the Office of Sciences and the Office of Power Technology, U.S. Department of Energy under contract No. DE-AC05-96OR22464 with Lockheed Martin Energy Research Corp.

REFERENCES:

1. D. P. Norton, A. Goyal, J. D. Budai, D. K. Christen, D. M. Kroeger, E. D. Specht, Q. He, B. Saffian, M. Paranthaman, C. E. Klabunde, D. F. Lee, B. C. Sales, and F. A. List, *Science* **274**, 755 (1996); A. Goyal, D. P. Norton, J. D. Budai, M. Paranthaman, E. D. Specht, D. M. Kroeger, D. K. Christen, Q. He, B. Saffian, F. A. List, D. F. Lee, P. M. Martin, C. E. Klabunde, E. Hartfield, and V. K. Sikka, *Appl. Phys. Lett.* **69**, 1795 (1996).
2. M. Paranthaman, D. F. Lee, A. Goyal, E. D. Specht, P. M. Martin, X. Cui, J. E. Mathis, R. Feenstra, D. K. Christen, and D. M. Kroeger, *Supercond. Sci. & Tech.* **12**, 319 (1999).
3. C. Park, D. P. Norton, D. F. Lee, J. D. Budai, D. K. Christen, D. Verebelyi, R. Feenstra, A. Goyal, M. Paranthaman, and D. M. Kroeger, *Appl. Phys. Lett.* **73**, 1904 (1998).
4. D. P. Norton, C. Park, B. Saffian, J. D. Budai, A. Goyal, D. K. Christen, D. M. Kroeger, D. Lee, Q. He, and M. Paranthaman, *Materials Research Society Symp. Proc. Vol. 474*, (Materials Research Society, Pittsburg, 1997), pp. 401-406.
5. P. Spielbuchler and G. Gritzner, *J. Mater. Sci. Lett.* **11**, 1426 (1992).
6. G. N. Morscher, P. Pirouz, and A. H. Heuer, *J. Am. Ceram. Soc.* **74**, 491 (1991).
7. S. Maschio, O. Sbaizero, and S. Meriani, *J. Euro. Ceram. Soc.* **9**, 127 (1992).
8. H. Makita, S. Hanada, and O. Izumi, *Acta Metall.* **36**, 403 (1988).
9. T. B. Reed, "Free Energy of Formation of Binary Compounds," (MIT Press, Cambridge, MA, 1971).
10. S. K. Ghandhi, "VLSI Fabrication Principles: Silicon and Gallium Arsenide," John Wiley & Sons, New York, 1983.
11. E. H. Nicollian and J. R. Brews, "MOS (Metal Oxide Semiconductors) Physics and Technology," John Wiley & Sons, New York, 1982.
12. K. M. Horn, E. Chason, J. Y. Tsao, J. A. Floro, S. T. Picraux, *Surface Science* **320**, 174-184 (1994).
13. L. Surnev and M. Tikhov, *Surface Science* **123**, 505-518 (1982).
14. R. A. McKee, F. J. Walker, and M. F. Chisholm, *Phys. Rev. Lett.* **81**, 3014 (1998).
15. M. Paranthaman, A. Goyal, F. A. List, E. D. Specht, D. F. Lee, P. M. Martin, Q. He, D. K. Christen, D. P. Norton, J. D. Budai, and D. M. Kroeger, *Physica C* **275**, 266 (1997).
16. S. H. Jang, D. Jung, and Y. Roh, *J. Vac. Sci. Technol. B* **16**, 1098 (1998).
17. H. Koinuma, J. Nagata, T. Tsukahara, S. Gonda, and M. Yoshimoto, *Appl. Phys. Lett.* **58**, 2027 (1991).
18. T. Inoue, T. Ohsuna, L. Luo, X. D. Wu, C. J. Maggiore, Y. Yamamoto, Y. Sakurai, and J. H. Chang, *Appl. Phys. Lett.* **59**, 3604 (1991).
19. P. W. Atkins, "Physical Chemistry", (Oxford University Press, Oxford, 1982)
20. K. J. Hubbard and D. G. Schlom, *J. Mater. Res.* **11**, 2757-2776 (1996).

*Correspondence: Email: ntn@ornl.gov, Telephone: 865 574 5965; FAX: 865 576 3676

Optical and electronic properties of amorphous WO_3 thin film irradiated by laser in air

H. Qiu^a and Y.F. Lu

Laser Microprocessing Laboratory,

Department of Electrical Engineering and Data Storage Institute, National University of Singapore,

10 Kent Ridge Crescent, Singapore 119260

ABSTRACT

To study the potential in optical recording, the laser induced chromism of amorphous WO_3 thin films has been investigated. The original film can be colored from grey to purple by one pulse of the KrF excimer laser at 248 nm and bleached to dark grey by one pulse of Nd-YAG laser at 1.06 μm in air. Spectroscopy measurements were applied to study the films at the three alternate states: original, colored and bleached. The changes of refractive index (n) and extinction coefficient (k) from colored states to bleached states, could be measured by ellipsometry spectroscopy that showed increasing and decreasing tendency, respectively in luminous range at colored state. X-ray photoelectron spectroscopy (XPS) was used to study the chemical states. With some W^{5+} ions existed in the original films by pulsed laser deposition, more lower states ions, such as the W^{3+} ions were produced along with decreasing W^{6+} states in films colored by KrF excimer. Laser bleaching was accompanied with decreasing of W^{5+} , W^{3+} states and increasing of W^{6+} states in films. The purple color was thought due to the polaron transition between W^{3+} states and W^{4+} states or, W^{5+} states and W^{4+} states. Scanning tunneling spectroscopy (STS) showed that the colored films had more characteristics of n type semiconductor after coloring. We attribute the coloring and bleaching process to photochemical activation and photothermal oxidation, respectively. Raman spectroscopy showed slight crystallization after coloration in films. From temperature field calculation, the crystallization is suggested most likely caused by ion intercalation instead of thermal crystallization. The color states in films are very stable after long-time exposure in air, as well as in oxygen..

Keywords: Polaron transition, Photochromism, Photon-mode, Thermal-oxidation, Band bending

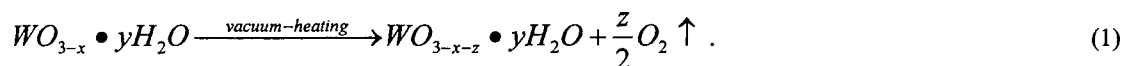
1. INTRODUCTION

Optical recording has demonstrated its advantages by memory density, capacity, switching speed and thermal stability. Recently, magneto-optical recording and phase-change optical recording play a major role in rewritable optical recording in which the laser is used for either heating the medium to Curie temperature in MO writing process or causing phase change (crystalline or amorphous) in the latter writing process. However, the memory density is restricted by the diffraction limit of the laser beam.¹ One possible solution is to utilize the photon-sensitive medium, such as photochromic medium whose properties change with the light wavelength, phase, polarity and others.² Multiple storage layers and near field recording techniques provide more potential for the future.

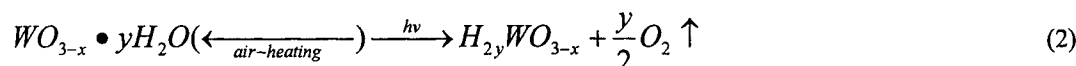
Tungsten oxide (WO_3), a transition metal oxide, has been widely studied for its outstanding electrochromic property that an absorption band is formed by electrochemical reaction.^{3,4} The photochromic property that an identical absorption band is formed upon UV light irradiation was found by Deb⁵ in the first time, and has been extensively investigated further.^{6,7,8} "Double charge injection model" for the electrochromism and the "polaron model" for the photochromism are widely accepted. In the former model the color in films is attributed to bronze phase formation, while in the later one the color is attributed to small polaron transitions between the two nonequivalent sites of tungsten (W^{5+} , W^{6+} and/or W^{5+} , W^{4+}).^{8,9} The

* Correspondence: Email address: engp7726@nus.edu.sg

coloration efficiency is low and the state is unstable if the surface is exposed to oxygen gas or even air.³ Recently, Bechinger et al.¹⁰ have succeeded in shifting the photochromic sensitivity band of WO₃ from UV to visible by a cadmium sulfide interlayer beneath WO₃ film for easy availability of compact laser diodes. Zhao et al.¹¹ used a XeCl excimer laser ($\lambda = 308$ nm, $\tau = 36$ ns, $E = 100$ mJ/cm²) instead of the UV light to irradiate the WO₃ sintered pellet. Stable blue color is obtained after melting happened on the surface. The process was attributed to thermochromism which has been described by Goulding:¹²



The larger the x and z are, the less transparent of the film is after being heated in vacuum. Goulding also showed that UV-colored films of amorphous WO₃ could be bleached by heating in oxygen, which was described as:



The hydrogen for the formation of hydrogen-tungsten bronze (H_{2y}WO_{3-x}) originates from the photolysis of water absorbed in the film. The film becomes darker along with the increasing of y. However, the formation of the bronze phase has encountered some conflicting experimental results.⁸ Moreover, bleaching by heating the medium in oxygen gas or electrochemical reactions impedes the development of erasable optical storage devices.

To investigate the potential in optical storage, we demonstrated in this study that the color formed on WO₃ films by excimer laser irradiation ($\lambda = 248$ nm, $\tau = 23$ ns) could be erased by irradiation of Nd-YAG laser ($\lambda = 1064$ nm, $\tau = 7$ ns) in air. The writing is believed due to photon stimulation. Small polaron model was proposed to explain our results. Various measurements were applied. Ellipsometry spectroscopy and XPS have been used to investigate the chromism of WO₃ by achieving accurate optical properties and composition.^{13,14} Raman spectroscopy was also used to analyze the structure and composition transformation.^{15,16} Furthermore, STS was also employed to study the surface states in the coloring and bleaching process.

2. EXPERIMENTAL DERAIS

WO₃ films were deposited by pulsed laser deposition on silicon wafer (n type, <100> orientation) substrate. A KrF excimer laser ($\lambda = 248$ nm, $\tau = 23$ ns) was used for ablation of a sintered polycrystalline, stoichiometric WO₃ target (99.9%). A laser fluence of 2 J/cm² and a repetition frequency of 10 Hz were set to attain a smooth surface and a high deposition rate of 1 nm/s. A substrate temperature was varied in the range of 25~800 °C. The films were deposited in a vacuum pressure of 2×10^{-5} Torr or in an O₂ pressure of 60 mTorr. In order to gain high coloring efficiency, amorphous WO₃ films were deposited at a substrate temperature of 150 °C. Thickness of the WO₃ films was 1.5 μ m.

Photochromic effect of the WO₃ thin films was realized by irradiation of the same excimer laser at 248nm. The films were placed under the laser spot with an area of 5mm \times 5mm and an energy density of 0.1 J/cm². The Nd-YAG laser ($\lambda = 1064$ nm, $\tau = 7$ ns) was chosen to bleach the colored films through a homogenizer with a focused spot of 2 mm \times 5 mm size and an energy density of 0.4 J/cm². STM/STS measurements were performed with an Autoprobe CP, Park Scientific instrument. The images were taken with a sample bias of -2 V and a tunneling current of 0.1 nA in air. The system was operated in constant current mode. The tunneling I - V spectra were taken with the setting of the tip bias of -1 V and tunneling current of 1 nA (before disabling the feedback) for the film samples. The surface composition and electronic properties of the samples were studied by analyzing the tungsten (W 4f) XPS core levels. The curve fitting and deconvolution were performed. Ellipsometry measurements were made with UVISSEL spectroscopic phase modulated ellipsometer for all the films. The structure of films was investigated by Raman spectroscopy performed at room temperature with a Renishaw double monochromator using the 514.5 nm excitation line of an argon laser. Incident power level of 20 mw and spot of about 4um in diameter were found not to perturb the measurements here. The resolution of the Ramanscope was about 1.5 cm⁻¹.

3. RESULTS AND DISCUSSION:

3.1. Examination by microscopy and ellipsometry spectroscopy

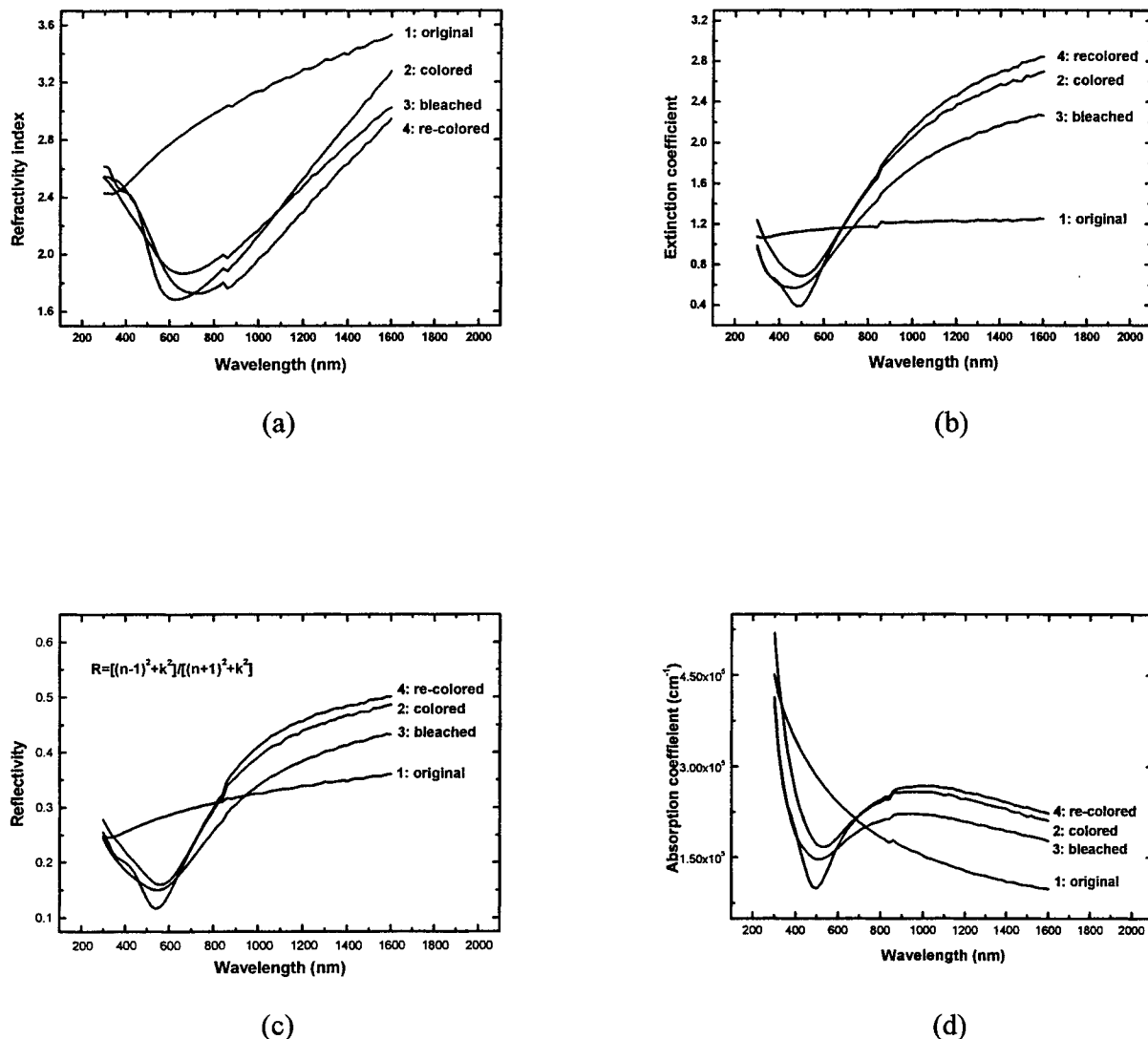


Figure 1. Refractive index n (a), Extinction coefficient k (b), reflectivity R (c), and absorption α (d); optical spectra of as-deposited (1), colored (2), bleached (3) and re-colored (4) tungsten oxide films.

The as-deposited films are not completely stoichiometric since they are in grey color instead of transparent and can be concluded from the XPS spectra. The surface became purple color upon one pulse of excimer laser irradiation ($\lambda = 248$ nm). The purple was completely bleached to dark grey after one pulse of Nd-YAG laser ($\lambda = 1064$ nm). The ellipsometric measurements were carried out for four states of WO_3 films: as-deposited, colored, bleached and re-colored. The changed refractive index n and extinction coefficient k values are shown in Figs. 1(a) and 1(b), respectively. Since the refractive index is high compared to the conventional one, which is usually around 2.1 in the mid-visible wavelength, the fresh deposited films show denser structure. A decline in n value after one pulse of excimer laser irradiation at 248 nm could be an indication of porous structure development, which actually are nanocrystalline air-tungsten oxide composites manifested by our Raman spectroscopy and STM investigations. Then one pulse of Nd-YAG laser irradiation at 1064 nm could "erase" the purple color to the dark grey. All the above films are not transparent.

We calculated the absorption α and reflectivity R of the films by $\alpha=4\pi\kappa/\lambda$ and $R = [(n^2-1)+k^2] / [(n^2+1)+k^2]$, respectively at normal incidence, since k is too large to be ignored. In Figs 1(c) and 1(d), it is observed that reflectivity and absorption change up to 20% and 28% respectively in visible and near-infrared range at the first coloration. Both states are very stable in air or even in oxygen, in contrast to the easily self-bleached tungsten oxide films colored by UV light.³

3.2. X-ray photoelectron spectroscopy

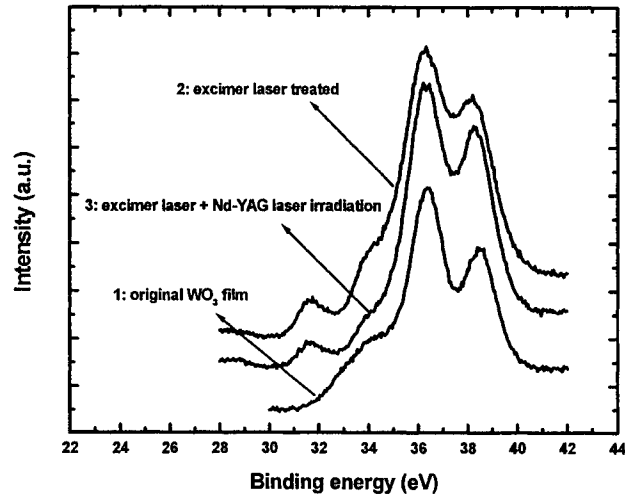


Figure 2. W 4f core level XPS spectra of tungsten oxide films: (1) as-deposited at 2×10^{-5} Torr, 150 °C; (2) irradiated by excimer laser; (3) irradiated by excimer laser and Nd-YAG laser consecutively.

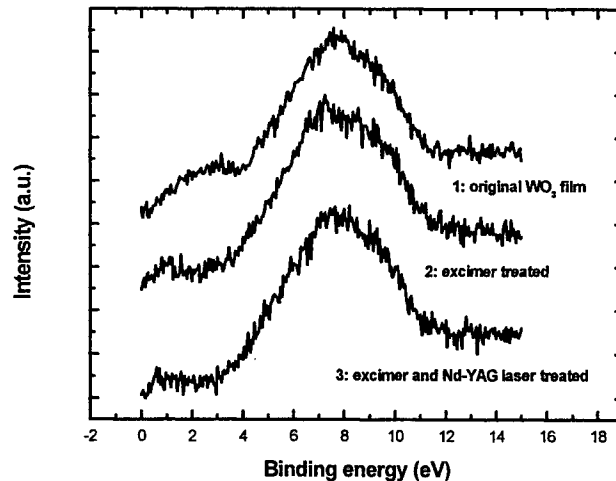


Figure 3. Valence XPS spectra of tungsten oxide films: (1) as-deposited at 2×10^{-5} Torr, 150 °C; (2) irradiated by excimer laser; (3) irradiated by excimer laser and Nd-YAG laser consecutively.

The W 4f XPS spectra for films in the three different colors are shown in Fig 2. Films were deposited at 150 °C and found to be stable when exposed to oxygen at atmospheric pressure. In Fig. 2, W components are present in the as-deposited film: an obvious shoulder at 34.1 eV is believed to be correlated to the W^{5+} states which were thought as color centers; and the main doublet peaks located at 36.3 and 38.5 eV are believed to be correlated to the W^{6+} states.¹⁷ The freshly-deposited amorphous tungsten oxide films were not transparent due to W^{5+} states, which were probably formed in the deposition process by oxygen reduction on the target surface as a result of excimer laser irradiation, as reported by Zhao.¹¹ After films were irradiated by excimer laser in air, a new peak appeared at 31.9 eV which was associated with the W^{4+} states while the shoulder for W^{5+} states decreased and the valley of doublet for W^{6+} states obliterated. Due to excimer laser irradiation, water molecules absorbed in the films were decomposed into protons, H-O bonds and highly reactive oxygen atoms by photolysis. Some protons will combine with some O^{2-} from the WO_3 to form water so that oxygen deficiency appears in WO_3 . W^{4+} states are produced and ions of higher state are decreased with the help of electron charges in films. The purple color formed in excimer laser irradiation is due to the polaron transitions between W^{3+} states and W^{4+} states, or W^{5+} states and W^{4+} states. When films were irradiated by Nd-YAG laser in air afterwards, the valley of the doublet for W^{6+} states becomes clear again. W^{4+} , W^{5+} states were reduced and W^{6+} states were increased. This is an oxidation by utilizing the oxygen in air, similar to heating in air. Oxygen deficiency in the films was partially restored.

Figure 3 illustrates the effect of occupation of the W 5d state on the valence band structure of the XPS spectra. The main feature between 4 eV and 12 eV was generally attributed to O2p dominated valence band. For spectrum (1), a broad peak was located around 3 eV below Fermi level at the original state, which is probably associated with W^{5+} ion pairs held together by σ bonding.¹⁷ After excimer laser irradiation it was reduced to a peak located at 1 eV below Fermi level indicating a larger metallic density of states at E_F , as shown in spectrum (2). O2p peak also slightly downshifted and shrank. Clearly the oxygen reduction was so significant that W^{4+} states were produced in the film while W^{5+} , W^{6+} states decreased. In spectrum 3, after Nd-YAG laser irradiation, oxygen was partially restored that the occupied W 5d state nearly disappeared and the O2p broad peak was also upshifted.

3.3. Scanning tunneling spectroscopy

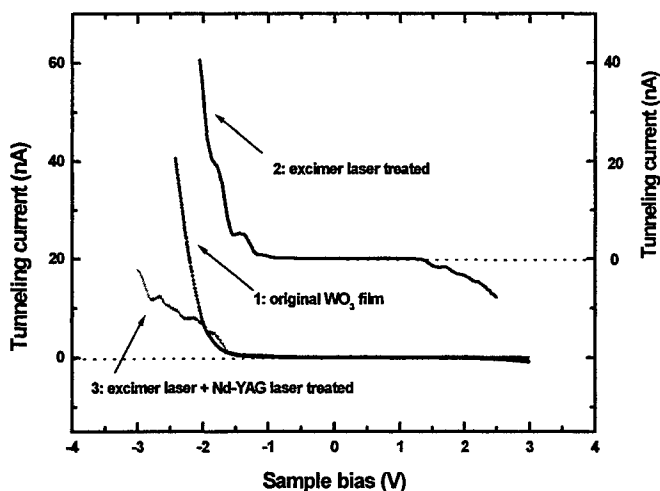


Figure 4. Tunneling I-V characteristics taken at room temperature in air on tungsten oxide films: as-deposited at 2×10^{-5} Torr, 150°C; (2) irradiated by excimer laser; (3) irradiated by excimer laser and Nd-YAG laser consecutively.

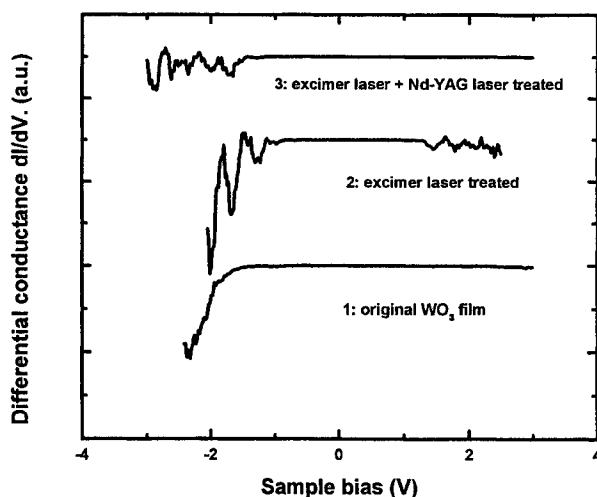


Figure 5. Differential conductance dI/dV vs V curves taken at room temperature in air on tungsten oxide films: (1) as-deposited at 2×10^{-5} Torr, 150°C ; (2) irradiated by excimer laser; (3) irradiated by excimer laser and Nd-YAG laser consecutively.

Slightly non-stoichiometric WO_3 is n-type semiconductors whose Fermi energy level is pinned close to the bottom of the conduction band by donor states associated with oxygen deficiency. Figs. 4 and 5 present three tunneling $I - V$ characteristics and differential conductance dI/dV vs. V of as-deposited amorphous film, film after excimer laser irradiation only and film after excimer laser plus Nd-YAG laser irradiation, respectively. In Fig. 5, the three tunneling $I - V$ curves show different characteristics. Generally, at a positive sample bias most of the electrons from the tip is tunneling into the empty W 5d states in the conduction band. At a negative sample bias, the tunneling is from the filled states of sample, O 2p and W 5d, to the empty tip states. Crystalline WO_3 as a semiconductor shows a valence band dominated by O 2p states and a conduction band dominated by W 5d states. However, for amorphous WO_3 hybridization is substantial between these bands.⁷ Therefore, at negative sample bias, the electrons to the tip is more likely tunneled from the hybridization states of both the occupied 5d states and filled O 2p states near the Fermi level of WO_3 . In Fig. 4, the curve for as-deposited film shows significant tunneling current in negative-bias range which is ascribed to both O 2p and W 5d states. While in the positive bias range the nearly null current should be attributed to a Schottky barrier behavior and subsurface properties formed by absence of surface states and Fermi level pinning.¹⁸ Tunneling of electrons from the tip to the sample can occur when the Fermi level position of the tip coincides with the empty W 5d conduction states. The voltage at which current appears corresponds to the conduction band minimum. Similarly, when the sample bias is negative, tunneling of electrons from sample to tip can occur only when the position of the tip Fermi level gets shifted below the filled W 5d states or O 2p valence states. Actually, the amorphous film is deposited and then cooled down in UHV, it is reasonable to assume an oxygen deficient surface termination and occupied 5d states, which is also manifested by W^{5+} states in the W 4f core level spectra of XPS in our previous analysis. Therefore, it is easier for n-type, non-stoichiometric WO_3 to have a higher tunneling current at low negative bias which has filled states for tunneling as low as in conduction band. In the positive bias, the tip Fermi level does not exceed the conduction band minimum of the sample surface and is situated in the band gap so that the tunneling is lower. Considering that Pt has a higher Fermi energy level than WO_3 , we propose an energy band diagram for Pt tip - vacuum - (n - type) WO_3 semiconductor tunnel structure at zero bias displayed in Fig. 6. In addition, conduction between tip and semiconductor electrodes involves thermionic emissions of electrons over the barrier followed by tunneling of electrons through the vacuum barrier to the metal tip. An increasing of negative sample bias decreases the band bending, lowering the barrier and enhancing electron emission, while an increasing of positive bias will increase the band bending and barrier.

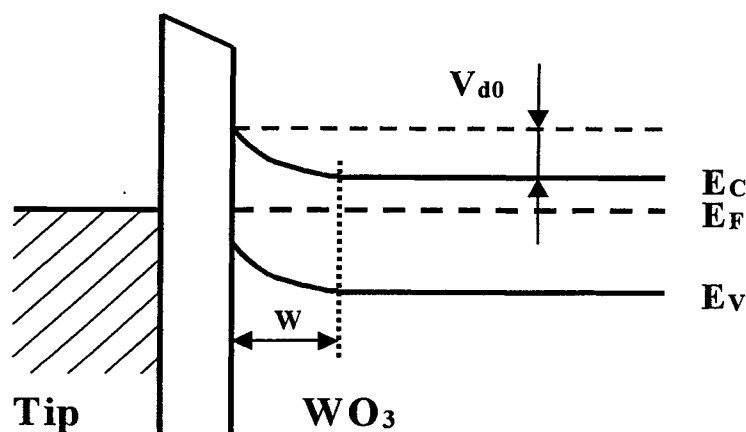


Figure 6. Energy band diagram of a planar MIS Schottky interface, Shown with zero applied voltage. V_{d0} is the zero – bias band bending; W is depletion width.

After film treated by excimer laser, the tunneling curve shows an increased tunneling current in both negative and positive bias. In this case, more W 5d occupied states are produced as manifested in our XPS analysis and partial oxygen loss happens. In lower negative bias, tunneling to the tip is mostly from the increased W 5d occupied states rather than from filled O 2p valence states. It is because a band gap energy about 3 eV needs to be overwhelmed for the latter except at larger bias. A.I.Gavrilyuk¹⁹ claimed that upon injection of hydrogen ions or in UV-light photochromism, the presence of oxygen vacancies raised the Fermi level. Therefore, Fermi level can reach the conduction band edge in a lower positive bias and higher current is obtained. “negative differential resistance” (NDR), which is more evident in Fig. 5, are attributed to the high density of surface states after laser irradiation, such as the increased occupied W 5d states. Over a particular range of bias, the decrease in the density of states near the Fermi energy can overwhelm the increase in the voltage dependent tunneling transmission probability, resulting in a net decrease in tunneling current.

The tunneling current at negative bias decreased again when Nd-YAG laser applied. In this stage, the oxygen vacancies are reduced and Fermi level was lowered by thermal oxidation. Occupied W 5d states are also decreased. An even lower tunneling current in the high negative bias in Fig. 4 indicates that the overall hybridization states of both the occupied 5d and filled O 2p states are reduced compared to the original film. A slight higher tunneling current in the lower negative bias than that of the original film in Fig. 4, may mean that W 5d occupied states in this stage are more than that in original state due to existence of W^{4+} states, although nearly all of W^{5+} states were transformed to W^{6+} states. NDR still existed, possibly due to existence of the W^{4+} states.

3.4. Raman spectroscopy

Figure 7 shows the Raman spectra before coloration, after coloration and after bleaching. The broad band near 220 cm^{-1} and 800 cm^{-1} indicates their amorphous character of the as-deposited films. After laser coloration, two broad peaks appeared, indicating slightly crystallization. The one with center located in low frequency range could be deconvoluted into peaks at 200 cm^{-1} and at 283 cm^{-1} , while the other in high frequency range could be deconvoluted into three peaks, located at 690 , 820 and 950 cm^{-1} , respectively. The peaks at 820 and 690 cm^{-1} corresponds to $\nu(\text{O-W-O})$ stretching mode and peaks between 200 to 283 cm^{-1} corresponds to $\delta(\text{O-W})$, $\delta(\text{O-O})$ bending mode. The 950 cm^{-1} mode was the well-known W=O stretching mode of terminal oxygen and generally existed on film surface.¹⁵ It was caused by the O^{2-} from decomposition of water in films. In fig. 6, curves 1, 2 and 3 displays similar peaks located at 690 , 820 and 950 cm^{-1} in changing trends as well as magnitudes, indicating that new W-O bonds and W=O bonds are formed with slight changes on W-O-W bond length and bond angle.

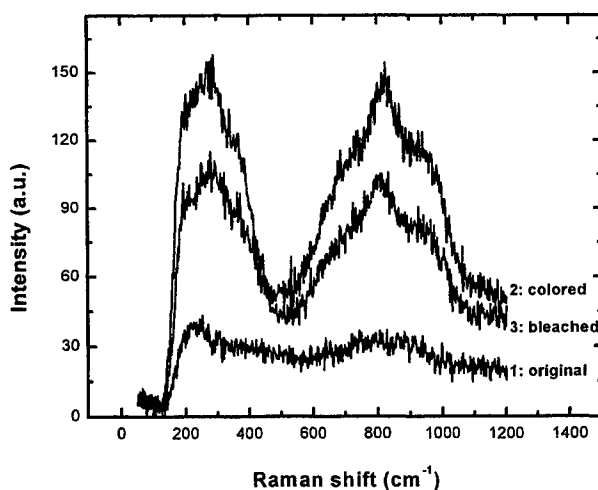


Figure 7. Raman spectra of tungsten oxide as-deposited amorphous (1), colored (2) and bleached (3) films deposited at 2×10^{-5} Torr at substrate temperature 150 °C.

Non-reversible cycling-induced crystallization of tungsten oxide films has been reported by P Delichere^{15,20} that happened in an electrochromic device attributed to ion accumulations. In this study, the temperature field was calculated by SLIM software. Absorption coefficients at 1064 and 248 nm for the respective films could be obtained by $\alpha = 4\pi\kappa / \lambda$, as 2.5×10^5 and $7 \times 10^5 \text{ cm}^{-1}$ respectively. Other thermal property constants could be referred to the paper given by Zhao et al.⁹ The highest temperatures were 1656 K for coloring and 1643 K for bleaching. Both are lower than the melting point of 1746 K for tungsten oxide. Therefore, the possibility of melting-solidification could be ruled out in laser coloring and bleaching cycling.

4. CONCLUSIONS

The amorphous WO_3 thin film can be photonically colored by excimer laser ($\lambda = 248 \text{ nm}$) irradiation in air while the colored films can be thermally bleached in air by Nd-YAG laser ($\lambda = 1.06 \mu\text{m}$) irradiation. Thermal oxidation may exist in laser coloring process which competes with photo coloring effect simultaneously when high fluence is used. Repetitive laser coloring of the amorphous WO_3 thin film is applicable. Changes up to 20% in reflectivity and 28% in absorption are obtained between the colored and original states in visible and near-infrared range. Better results could be anticipated if less W^{5+} states existed in original films or coloring proceeded in vacuum. The purple color formed in excimer laser irradiation is due to the polaron transitions between W^{3+} states and W^{4+} states, or W^{5+} states and W^{4+} states.

ACKNOWLEDGEMENTS

The authors would like to thank Mr. Y. W. Goh, Ms. H. L. Koh, and B. A. Cheng for their technical support, Mr. Y. X. Jie for the help in XPS measurements, Mr. Z. H. Mai for the help in STM/STS measurements.

REFERENCES

1. M. Hamano and M. Irie, "Rewritable near-field optical recording on Photochromic thin films", *Jpn. J. Appl. Phys.* **35**, pp. 1764 – 1768, 1996.
2. M. Irie, ed. "Photo-reactive Materials for ultrahigh Density Optical Memory", (1994).
3. C. G. Geanqvist, "Handbook of Inorganic electrochromic materials", (1995).

4. P. M. S. Monk, "Electrochromism, fundamentals and applications", (1993).
5. S. K. Deb; Phil. Mag. **27**, pp 801 – 805, 1973.
6. Y. Shigesato, "Photochromic properties of amorphous WO₃ films", Jpn. J. Appl. Phys. **30**(7), pp 1457 – 1462, 1991.
7. C. Bechinger, "On the fundamental role of oxygen for the photochromic effect of WO₃", J. Appl. Phys. **74**(7), pp 4527 – 4533, 1993.
8. J. G. Zhang, "Chromic mechanism in amorphous WO₃ films", J. Electrochem. Soc., **144**(6), pp 2022 – 2026, 1997.
9. O. F. Schirmer, J. Phys. (paris), Colloq. **6**, pp 479 – 483, 1980.
10. C. Bechinger, E. wieth, and P. Leidener, "Photochromic coloration of WO₃ with visible light", Appl. Phys. Lett. **68**, pp 2834 – 2836, 1996.
11. Y. Zhao, "Laser-induced coloration of WO₃", Appl. Phys. Lett. **71**(16), pp 2227 – 2229, 1997.
12. M. R. Goulding, "A comparison of thermo- and photo-chromic behaviour", Solid State Communications", **46**(6), pp 451 – 453, 1983.
13. E. Pascual, "Infrared and UV-visible ellipsometric study of WO₃ electrochromic thin films", Thin Solid films, **313-314**, pp 682 – 685, 1998.
14. T. H. Fleisch and G. J. Mains, "An XPS study of the UV reduction and photochromism of MoO₃ and WO₃", J. Chem. Phys. **76**(2), pp 780 – 786, 1982.
15. T. Wadayama, H. Wako and A. Hatta, "Electrobleaching of WO₃ as Probed by Raman Scattering", Materials Transactions, JIM, **37**(9), pp 1486 – 1489, 1996.
16. P. Delichere P. Falaras M. Froment A. H. L. Goff and B. Agius, "In the origin and coloured states", Thin solid films, **161**, pp 35-46, 1988.
17. R. A. Dixon, J. J. Williams, D. Morris, J. Rebane, F. H. Jones, R. G. Egdell, S. W. Downes, "Electronic states at oxygen deficient WO₃ (001) surfaces: a study by resonant photoemission", Surface Science **399**, 199 – 211, 1998.
18. W. J. Kaiser, L. D. Bell, M. H. Hecht, and F. J. Grunthaner, "Scanning tunneling microscopy characterization of the geometric and electronic structure of hydrogen-terminated silicon surfaces", J.Vac.Sci.Technol. A **6**(2), pp 519 – 522, 1988.
19. A. I. Gavriluk, "Photochromism in WO₃ thin films", Electrochimica Acta, **44**, pp 3027 – 3037, 1999.
20. M. Pham Thi and G. Velasco, "Raman Study of WO₃ thin films", Solid State Ionics, **14**, pp 217 – 200, 1984.

Effect of Film thickness on the Properties of Indium Tin Oxide Thin Film Grown by Pulsed Laser Deposition for Organic Light-emitting Diodes

H. Kim^{*b}, J. S. Horwitz^a, A. Piqué^a, G. Kushto^a, Z. H. Kafafi^a, C. M. Gilmore^b, and D. B. Chrisey^a

^aNaval Research Laboratory, 4555 Overlook Ave, SW, Washington DC 20375

^bSchool of Engineering and Applied Science, George Washington University, Washington DC 20052

ABSTRACT

Transparent conducting indium tin oxide (ITO) thin films were grown by pulsed laser deposition (PLD) on glass substrates. The structural, electrical and optical properties of these films were investigated as a function of film thickness (300 - 8700 Å). Films were deposited using a KrF excimer laser (248nm, 30 ns FWHM) at a fluence of 2 J/cm², at substrate temperature of 300 °C and 10 mTorr of oxygen pressure. For ITO films (500 - 4000 Å thickness) deposited at 300 °C in 10 mTorr of oxygen pressure, the resistivity of $2 - 4 \times 10^{-4} \Omega\text{-cm}$ was observed and the average transmission in the visible range (400 - 700 nm) was about 85 - 90 %. The Hall mobility and carrier density for ITO films (500 - 4000 Å thickness) were observed to be in the range of 24 - 27 cm²/V-s and $5 - 9 \times 10^{20} \text{ cm}^{-3}$, respectively. We have used the ITO thin films, deposited by PLD on silica substrates, as the anode contact in organic light emitting devices and studied the effect of ITO film thickness on the device performance. The optimum thickness of the ITO anode for the maximum device efficiency was observed to be about 500-1000 Å. The device showed an external quantum efficiency of about 0.8 % at 100 A/m².

Keywords: pulsed laser deposition (PLD), indium tin oxide (ITO), and organic light emitting diodes (OLEDs)

1. INTRODUCTION

Indium tin oxide (ITO) thin films are used extensively in the optoelectronic industry because they combine both unique transparent and conducting properties. ITO thin films are characterized as highly degenerate n-type semiconductors with a c-type rare earth oxide structure¹ (also called cubic bixbyte structure) which has low electrical resistivity of $2 \sim 4 \times 10^{-4} \Omega\text{-cm}^1$. The degeneracy is due to both oxygen vacancies and substitutional tin dopants created during film deposition. The carrier concentration of high conductivity ITO films is in the range of $10^{20} \sim 10^{21} / \text{cm}^3$.¹ Furthermore, ITO is a wide band gap semiconductor (3.5 ~ 4.3 eV)² which shows high transmission in the visible and near-IR regions of spectrum. Due to these unique properties, ITO has been used in a wide range of applications including solar cells, heat-reflecting mirrors, anti-reflection coatings, gas sensors, and flat panel displays.¹ Since ITO films have shown good efficiency for hole injection into organic materials, they have also been widely utilized as the anode contact in the organic light-emitting diodes (OLEDs).^{2,3}

There are several deposition techniques which have been used to grow ITO thin films including magnetron sputtering^{4,6}, chemical vapor deposition (CVD)^{7,8}, spray pyrolysis^{9,10} and pulsed laser deposition (PLD)^{2,11}. In comparison with other techniques, PLD provides several advantages. The composition of the films grown by PLD is quite close to that of the target, even for multicomponent targets. PLD films crystallize at lower substrate temperatures due to the high kinetic energies (> 1eV) of the atoms and ionized species in the laser-produced plasma [12]. Also, the surface of the films grown by PLD can be very smooth [2]. ITO films, grown by PLD, have been used as the anode contact in organic light emitting diodes (OLEDs) [2,11],

In this paper, we report a study of the structural, electrical and optical properties of ITO films deposited by PLD on glass substrates, without a post-annealing treatment, as a function of film thickness. We used these ITO films as the anode contact in the OLEDs and studied the effect of ITO film thickness on the device performance.

*Corresponding author: Email: hskim@ccf.nrl.navy.mil

2. EXPERIMENT

ITO films were grown on glass substrates using PLD, as shown in Figure 1. A KrF excimer laser (Lambda Physics LPX 305, 248 nm and pulse duration of 30 ns) was operated at a pulse rate of 10 Hz and the laser beam quality was improved by passing it through a spatial filter. The laser beam was focused through a 50-cm focal length lens onto a rotating target at a 45° angle of incidence. The energy density of the laser beam at the target surface was maintained at 2 J/cm². The target-to-substrate distance was 4.7 cm. The laser beam was rastered across the surface of the target with a computer-controlled mirror while the target was rotated. The geometry of this PLD system produced uniform films over 1.5 cm x 1.5 cm substrate area with a thickness variation of less than 10 %.

The target was a 2" diameter by 0.25" thick sintered oxide ceramic disk (98 wt% ZnO and 2 wt% Al₂O₃, 99.99 % purity) supplied by Target Materials, Inc., USA. The substrates were cleaned in an ultrasonic cleaner for 10 minutes with acetone and then methanol. All substrates were blown dry with dry nitrogen gas before they were introduced into the deposition system. The deposition chamber was initially evacuated to 1×10^{-5} Torr and during deposition, oxygen background gas was introduced into the chamber to maintain the desired pressure and its pressure (0.1 to 100 mTorr). The substrate was attached with a stainless steel mask to a substrate holder, which was heated by two quartz lamps. The growth temperature was held constant at 300 °C during deposition using a temperature controller with input from a thermocouple imbedded in the center of the stainless steel substrate holder. After deposition, for films deposited at elevated temperature, the films were cooled to room temperature at the same oxygen pressure used for film growth.

The film thickness was measured by a stylus profilometer [Tencor Alpha-Step 250]. The sheet resistance (R_s) measurements were performed using a four-point probe. By assuming that the thickness of the films was uniform, the film bulk resistivity ρ was determined using the simple relation $\rho = R_s t$, where t is the film thickness. All sheet resistance and resistivity values were determined as the average of 3 measurements for each film. Hall mobility and carrier density measurements were made using the Van der Pauw method¹³ at room temperature with a field strength of 5 kG. The optical transmission and reflectance measurements were made using a UV-visible-near infrared (IR) spectrophotometer (200-3200 nm) [Perkin-Elmer Lambda 9]. X-ray diffraction (XRD) [Rigaku rotating anode X-ray generator with Cu K α radiation] was used to characterize the crystal structure of the films. From an analysis of the diffraction pattern, we determined the lattice parameter, preferred orientation and grain size. The grain size (t) is determined using the Scherr formula; $t = 0.9 \lambda / (B \cos \theta)$, where λ is the x-ray wavelength, B is the corrected peak width and θ is the Bragg diffraction angle.¹⁴ X-ray photoelectron spectroscopy (XPS) [VG Scientific, 220I] was used to analyze the film composition.

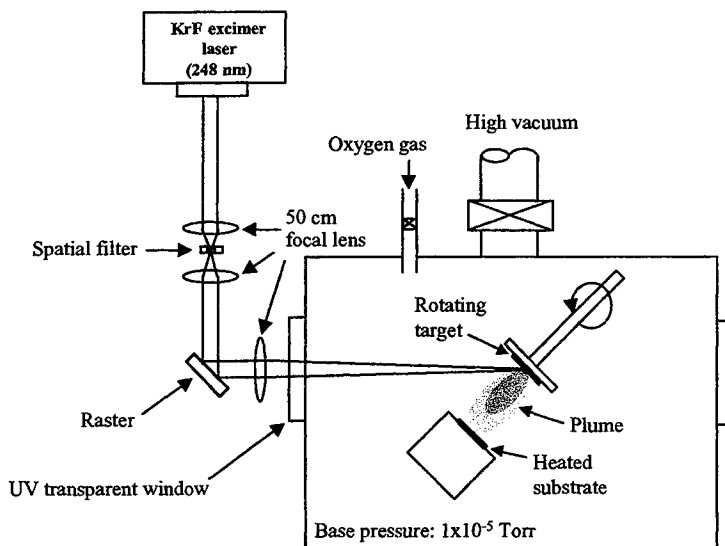


Figure 1: A schematic diagram of the pulsed laser deposition system

3. RESULTS AND DISCUSSION

3.1 Effect of oxygen pressure on the deposition rate

As shown in Figure 2, the oxygen deposition pressure has a strong effect on the deposition rate. The deposition rate decreased from 0.85 to 0.40 Å/pulse with increasing oxygen deposition pressure from 1 to 100 mTorr. This is due to a reduction of the kinetic energy of the ejected particles, which are collided with the oxygen molecules. At high oxygen deposition pressure, the number of ejected species arriving at the substrate is reduced due to an increase in the collisions between the ejected species and oxygen molecules. The strong dependence of the deposition rate on the oxygen deposition pressure has been previously observed for the films grown by PLD.^{12,15}

3.2 Effect of film thickness on the structural properties

The crystalline structure of the ITO films was affected by film thickness. Figure 3 shows X-ray θ -2 θ scans as a function of film thickness for ITO films grown at 300 °C and 10 mTorr of oxygen. It is found that the intensity of the (222) reflection increased and the width of the (222) peak decreased with increasing the film thickness, indicating that the crystallinity of the film was improved and the grain size of the films increased with increasing film thickness. In thin films, it is generally observed that the grain size increases with increasing film thickness^{16,17}. Table I shows the calculated grain size and lattice parameters of the ITO films with different film thickness. ITO films were observed to be polycrystalline and showed a similar crystal structure to that of undoped In₂O₃. However, the lattice parameter, calculated from the XRD patterns for the ITO films, was in the range from 10.197±0.0067 to 10.232±0.0082 Å, which is normally larger than the JCPDS value¹⁸ of 10.118 Å for the In₂O₃ powder. This increase in lattice constants of the ITO films can be explained by the substitutional incorporation of Sn⁴⁺ ions into In³⁺ sites and/or the incorporation of Sn ions in the interstitial positions. This increase in lattice parameters may be also related to oxygen deficiency and strain effect due to thermal expansion coefficient mismatch between the film ($7.2 \times 10^{-6}/^{\circ}\text{C}$)¹⁹ and glass substrate ($4.6 \times 10^{-6}/^{\circ}\text{C}$).

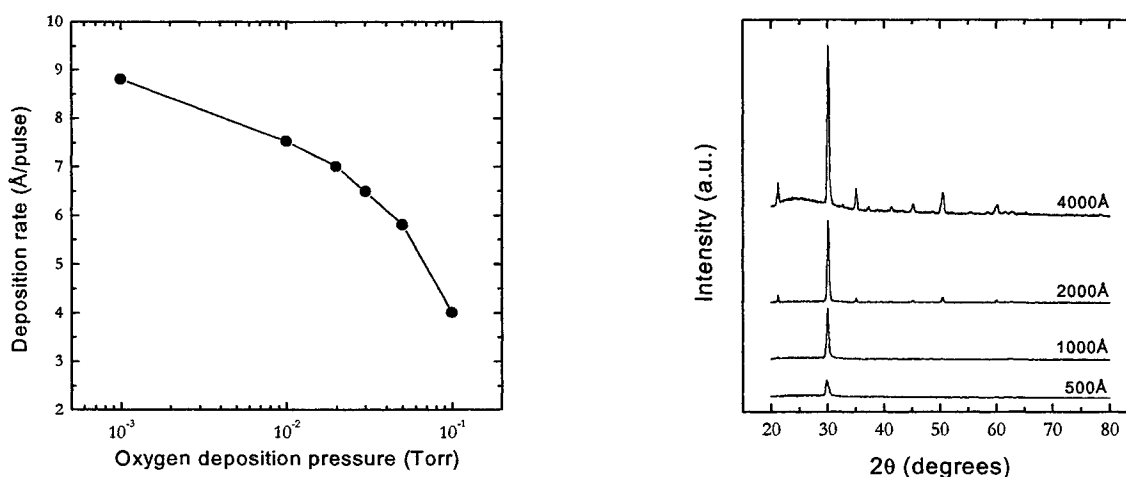


Figure 2: Effect of oxygen deposition pressure on the deposition rate for the ITO films deposited at 300 °C. Each film was deposited at the same deposition conditions except the oxygen deposition pressure: 10 Hz, 2 J/cm², and 2500 shots.

Figure 3: X-ray θ -2 θ scans for ITO films as a function of the film thickness. All films were deposited on glass at 300 °C and 10 mTorr of oxygen.

3.3 Effect of film thickness on the electrical properties

Figure 4 shows the effect of the film thickness on the resistivity (ρ) and sheet resistance (R_s), and carrier density (N) and Hall mobility (μ) of the ITO films. All the films showed here were grown from the 5 wt% SnO₂-doped In₂O₃ target at the deposition temperature of 300 °C and the oxygen pressure of 10 mTorr. The film thickness is directly proportional to the

Table I. Variation of calculated grain size and lattice parameter for the ITO films grown with different film thickness. All films were deposited at 300°C and 10 mTorr of oxygen using the target with 5 wt% of SnO₂.

Film thickness (Å)	Grain size (Å)	Lattice parameter (Å)
500	140	10.2319±0.0082
1000	170	10.2256±0.0079
2000	200	10.2104±0.0071
4000	260	10.1968±0.0067

number of laser shots with an average deposition rate of ~ 0.7 Å/shot. As seen in Figure 4(a), the resistivity of the ITO films initially decreases with an increase in the film thickness up to 2000 Å and remains almost constant with further increases in the film thickness up to 8700 Å. It is also observed from Figure 4(a) that the sheet resistance decreases rapidly with increasing the film thickness from 500 Å to 2000 Å and slightly decreases with further increases in the film thickness up to 8700 Å. In Figure 4(b), the carrier density increases with an increase in the film thickness up to 2000 Å and then remains almost constant with further increases in the film thickness up to 8700 Å. It is also seen in Figure 4(b) that the Hall mobility increases with increasing film thickness. XRD measurements indicate that the thicker films are more crystalline and have larger grains than the thinner films have; the 500 Å thick film has an average grain size of ~ 140 Å and the 4000 Å thick film has an average grain size of ~ 260 Å. The larger grain size can lead to a decrease in the density of grain boundaries, which are traps for free carriers and barriers for carrier transport in the film. Hence, the larger grain size can cause a decrease in grain boundary scattering, which leads to an increase in the conductivity. Thus, the initial decrease in resistivity is due to an increase in both carrier density and carrier mobility of the films, which are a consequence of the improved film crystallinity. For thicker films (>3000 Å), the resistivity remains constant because both carrier density and carrier mobility become independent of film thickness.

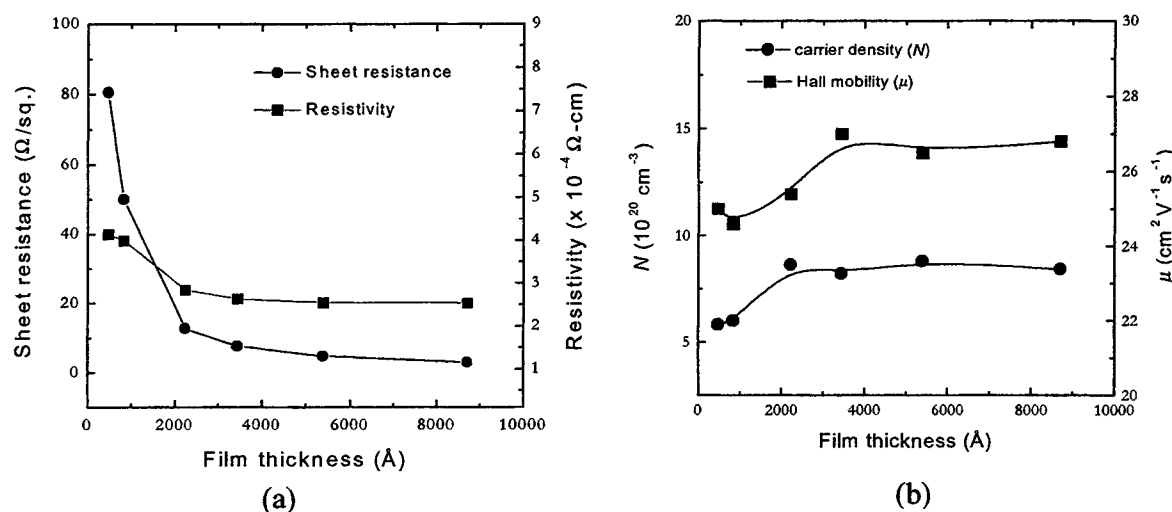


Figure 4: Effect of the film thickness on (a) the sheet resistance (R_s) and resistivity (ρ), and (b) carrier density (N) and Hall mobility (μ) of the ITO films deposited at 300 °C and 10 mTorr of oxygen.

3.4 Effect of film thickness on the optical properties

The optical transmittance (T) and reflectance (R) measurements were performed using a UV-VIS-NIR spectrophotometer (Perkin-Elmer-Lambda 9) in a double-beam configuration. Figure 5(a) shows the variation of optical transmittance (T) and

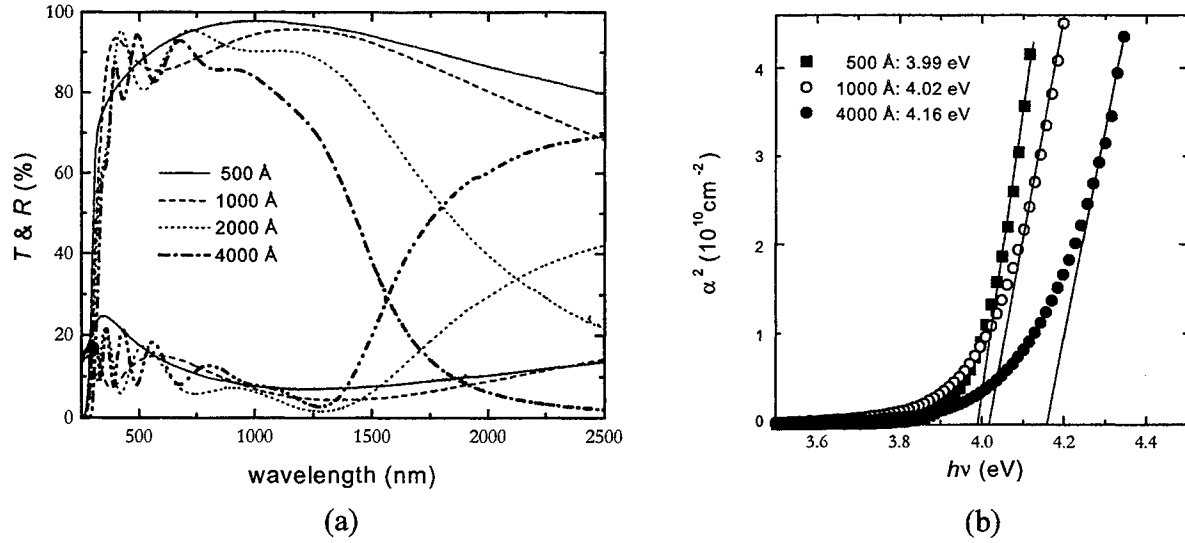


Figure 5: (a) Optical transmittance (T) and reflectance (R) spectra, and (b) dependence of photon energy on α^2 as a function of the film thickness. All films were deposited on glass at 300 °C and 10 mTorr of oxygen.

reflectance (R) as a function of the film thickness for ITO films deposited at 300 °C and 10 mTorr of oxygen. It is observed from Figure 5(a) that the optical transmittance in the visible range (400 – 700 nm) slightly increases with decreasing film thickness. Although the transmission is slightly reduced, the increase in reflectance is significant. The reflectance in the near infrared region increases from 20 % to 80 % with an increase in the film thickness from 500 Å to 4000 Å. As the film thickness increases, variation in the transmission as a function of wavelength is due to interference phenomena.

The transmittance and reflectance data were used to calculate absorption coefficients of the films at different wavelengths. The absorption coefficient, α , is given by the relation:

$$\alpha = \frac{1}{t} \ln \left(\frac{1-R}{T} \right) \quad (1)$$

where t is the film thickness. The absorption coefficient data were used to determine energy gap, E_g , using the relation²⁰:

$$\alpha = A(h\nu - E_g)^{1/2} \quad (2)$$

where A is constant, h is the plank's constant and ν is the frequency. The values of the direct optical band-gap (E_g), $E_g = E_0 + \Delta E$ where E_0 is the intrinsic energy gap and ΔE is the energy shift, were determined by extrapolations of the linear regions of the plots of the α^2 versus $h\nu$ to zero absorption ($\alpha h\nu = 0$). The ΔE is called the Burstein-Moss (B-M) shift^{21,22} and is the increase in the Fermi level in the conduction band. The relationship between the energy shift (ΔE) and the carrier concentration (N) is given by

$$\Delta E_g^{BM} = \frac{\hbar^2}{2m^*} (3\pi^2 N)^{2/3}, \quad (3)$$

where \hbar is the reduced Plank's constant ($=h/2\pi$) and m^* is the reduced effective mass of the electron carriers. Figure 5(b) shows the variation of the direct band-gap as a function of the film thickness for the ITO films deposited at 300 °C and 10 mTorr of oxygen. The value of E_g is observed to increase from 3.99 eV to 4.16 eV with an increase of the thickness from 500 Å to 4000 Å. This increase in band-gap is due to increase in free electron concentration in the films evidenced in Figure 4(b). This shift of the band-gap with the change in the carrier concentration can be explained by the B-M shift^{21,22}; the absorption edge shifts toward higher energy with an increase in the carrier density.

The plasma wavelength (or cut-off wavelength), λ_p , is defined at Transmittance = Reflectance where the dielectric-like visible transmittance equals to the metallic-like IR reflectance. Figure 5(a) also shows that the plasma wavelength edge shifts towards shorter wavelengths with growing the film thickness up to 4000 Å. The decrease in the plasma wavelength is also related to the increased carrier concentration in the films (see Figure 4(b)). Thus, the plasma wavelength can easily be controlled by changing the carrier density: The higher the carrier density, the lower is the value of λ_p . This result is in good agreement with the Drude's theory.^{1,23} The plasma wavelength of ~1550 nm was observed for the 4000 Å thick ITO film in Figure 5(a).

3.5 Conduction mechanisms

For polycrystalline TCO films, conduction can be explained on the basis of four different scattering mechanisms: ionized impurity scattering, neutral impurity scattering, grain boundary scattering, and lattice vibration scattering. The total mobility (μ) of the carriers can be written as

$$\frac{1}{\mu} = \frac{1}{\mu_i} + \frac{1}{\mu_n} + \frac{1}{\mu_g} + \frac{1}{\mu_l} \quad (4)$$

where μ_i , μ_n , μ_g and μ_l are mobilities corresponding ionized impurity scattering, neutral impurity scattering, grain boundary scattering, and lattice vibration scattering, respectively. Since the values of μ_n and μ_l for degenerate ITO films are estimated to be much larger than the others, these two terms can be neglected in equation (1).²⁴

In order to analyze the temperature dependence of the electrical properties, the Hall effect measurements were performed at temperatures ranging from 4 K to 300 K. Figure 6(a) shows the resistivity (ρ), carrier density (N) and Hall mobility (μ) as a function of temperature for a 2000 Å thick ITO film grown at 300 °C and 10 mTorr of oxygen. The resistivity, the carrier density and the Hall mobility are observed to remain almost constant as the temperature is increased from 4 K to 300 K. This result is a typical behavior of highly doped semiconductors. In general, the grain boundary scattering mechanism is considered as the dominant scattering mechanism in polycrystalline films, whose grain size is smaller than the mean free path of carriers [1]. However, for the ITO films grown by PLD, the grain size was observed to be much larger than the calculated mean free path. The average grain size calculated from the XRD data for the film used in Figure 6(a) was ~200 Å. The mean free path (ℓ) of the charge carriers for the same film was calculated to be ~58 Å by the relation:¹

$$\ell = \left(\frac{h}{2e} \right) \left(\frac{3N}{\pi} \right)^{1/3} \mu \quad (5)$$

where h is the Plank constant, e is the carrier charge, N is the carrier concentration and μ is the mobility. Hence, the contribution of the grain boundary scattering mechanism may not be dominant in this film.

According to the Petritz model²⁵, the mobility due to the grain boundary scattering can be written as

$$\mu_g = \mu_0 T^{-1/2} \exp\left(\frac{-eE_b}{kT}\right) \quad (6)$$

and

$$\mu_0 = \left(\frac{ed}{(2\pi m^* k)^{1/2}} \right) \quad (7)$$

where E_b is the potential barrier between the grain boundaries, k is the Boltzmann's constant, T is the temperature (in Kelvin) and d is the grain size. In these equations, the value μ_g is a function of the grain boundary potential barrier (E_b) and the grain size (ℓ). The value E_b was obtained from the slope of a plot of $\mu T^{1/2}$ versus T^{-1} (see Figure 6(b)) for the ITO films grown by PLD at 300°C and 10 mTorr of oxygen. The observed value from the curve is $E_b \cong 0.007$ eV. The grain size of the ITO films was estimated from XRD data to be $d \cong 12 - 30$ nm. Using $E_b \cong 0.007$ eV, $d \cong 20$ nm and $m^* = 0.3 m$,¹⁵ the grain boundary scattering mobility (μ_g) is estimated to be ~282 cm²V⁻¹sec⁻¹ at 300 K.

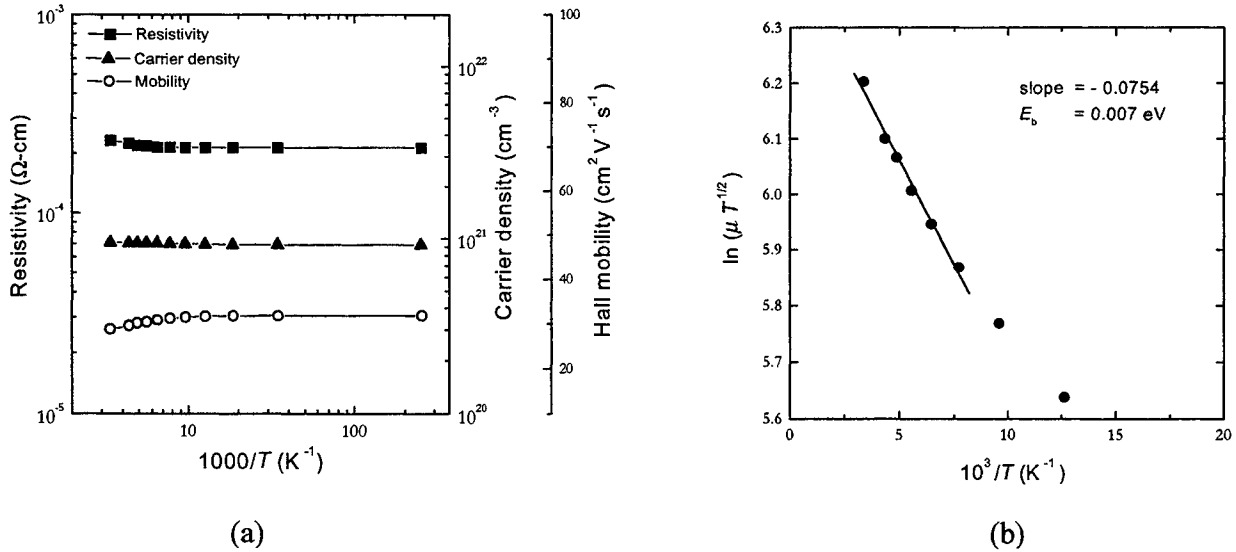


Figure 6: (a) Variations of carrier density, Hall mobility and resistivity as a function of reciprocal temperature and (b) plot of $\mu T^{1/2}$ versus $10^3/T$ for the ITO films (2000 Å) grown at 300 °C and 10 mTorr of oxygen.

In the case of highly doped semiconductors in which the carriers are degenerate, the mobility due to the ionized impurity scattering is simplified by Johnson and Lark-Horovitz²⁶ as follows:

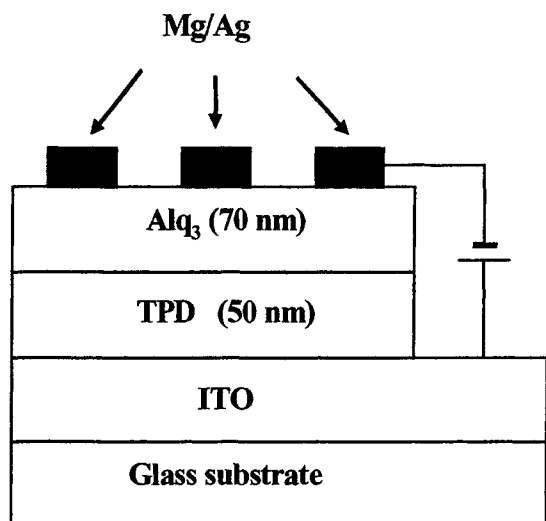
$$\mu_i = \frac{4e}{h} \left(\frac{3}{\pi} \right)^{1/3} N_{id}^{-2/3} = 9.816 \times 10^{14} N_{id}^{-2/3} \text{ (cm}^2 \text{ V}^{-1} \text{ sec}^{-1} \text{)} . \quad (8)$$

In this equation, the mobility due to the ionized impurity scattering can be calculated based on the ionized impurity concentration (N_{id}). Assuming that the ionized impurity concentration (N_{id}) is equal to the average carrier concentration ($N \cong 5 \times 10^{20} \text{ /cm}^3$) observed by Hall effect measurements, the ionized impurity scattering mobility (μ_i) is estimated to be $\sim 15 \text{ cm}^2 \text{ V}^{-1} \text{ sec}^{-1}$.

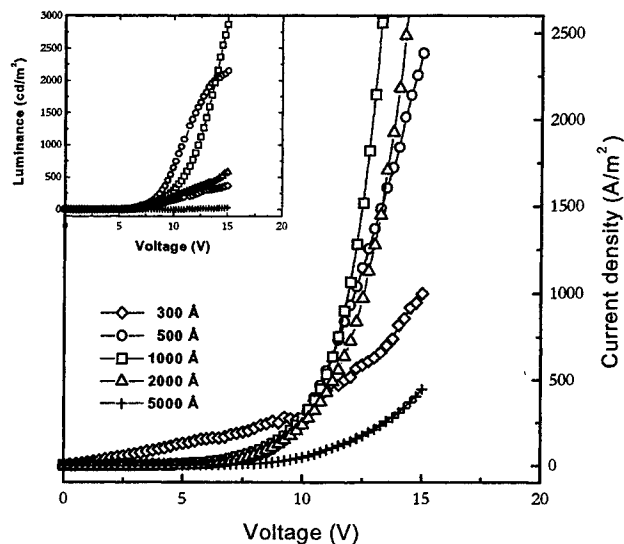
Substituting $\mu_i \cong 15 \text{ cm}^2 \text{ V}^{-1} \text{ sec}^{-1}$ and $\mu_g \cong 282 \text{ cm}^2 \text{ V}^{-1} \text{ sec}^{-1}$ into equation (4), the total mobility will be $\mu \cong 14 \text{ cm}^2 \text{ V}^{-1} \text{ sec}^{-1}$ at 300 °K, which is close to the ionized impurity scattering mobility ($\mu_i \cong 15 \text{ cm}^2 \text{ V}^{-1} \text{ sec}^{-1}$). Therefore, it is concluded that the overall mobility is governed mainly by the ionized impurity scattering mobility. It should be noted that this estimation is made with the assumption of $T = 300 \text{ °K}$ and $m^* = 0.3 m_o$. However, the overall mobility may be changed by varying temperature (T) and electron effective mass (m^*) because μ_g depend on the temperature (T) and the electron effective mass (m^*) depends on the carrier concentration (N) of the films.

3.6 Device performance with ITO anode

We have used the ITO thin films, deposited by PLD on fused silica (SiO_2) substrates, as an anode contact in OLEDs and measured the device performance. Figure 7(a) illustrates the schematic structure of an OLED used in this research. The device structure is made of a hole transport layer (HTL, $\sim 500 \text{ Å}$) of N, N'-diphenyl-N, N-bis (3-methylphenyl)1,1'-diphenyl-4,4'-diamine (TPD), and an electron transport/emitting layer (ETL/EML, $\sim 700 \text{ Å}$) of tris (8-hydroxyquinolinolato) aluminum (III) (Alq_3). The cathode contact deposited on top of the ETL is an alloy of Mg:Ag (ratio = 12:1 and a thickness of 2000 Å). Details of fabrication are described elsewhere.²⁷ The active area of the device is $\sim 2 \text{ mm} \times 2 \text{ mm}$. The current density-voltage-luminance (J-V-L) data were taken (in N_2 atmosphere) using a Keithley 238 current/voltage source and a luminance meter (Minolta LS-110).



(a)



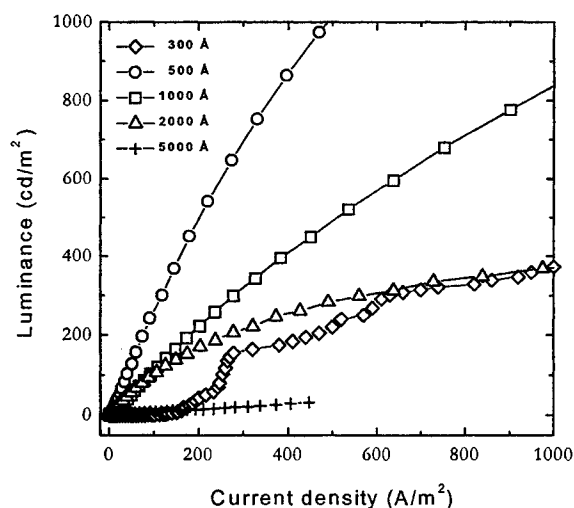
(b)

Figure 7: (a) A schematic structure of an organic light-emitting device (OLED); (b) Current density-voltage-luminance (J-V-L) characteristics of the heterostructure devices with different ITO film thicknesses. ITO films, deposited at 300 °C and 10 mTorr of oxygen, were used in these devices.

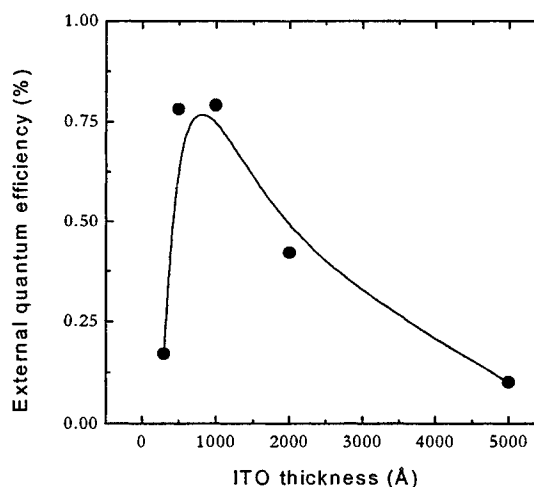
Figure 7(b) shows the characteristics of the forward biased current density (J)-voltage (V) output for the OLEDs as a function of ITO thickness. The J-V characteristics of the (ITO/TPD/Alq₃/MgAg) diode show a typical diode behavior, with the current and luminance power output observed only in the forward bias. It is observed from Figure 7(b) that the current density depends strongly on the ITO film thickness. The voltage, required to obtain about 100 A/m² of current density, was found to increase from 4.2 V to 11.2 V with an increase in the ITO film thickness from 300 Å to 5000 Å. For the devices with 500 - 2000 Å thick ITO films, the current density of ~100 A/m² was obtained at ~8 V of voltage. In the high voltage regions (>10 V), the current density for both 300 Å and 5000 Å thick ITO films increases much slower than those for the 500 Å, 1000 Å, 2000 Å thick ITO films. The visible light emission greater than 1000 cd/m² is observed only for the 500 Å and 1000 Å thick ITO films. Figure 8(a) shows the luminance - current density (L - J) characteristics of the devices used in Figure 7(b). The luminance output is linearly proportional to the current density, in agreement with what is measured with a reference device fabricated with a commercial ITO film (supplied by Planar America). Figure 8(b) shows the variation of the external quantum efficiency as a function of the ITO film thickness for the (ITO/TPD/Alq₃/MgAg) devices. The external quantum efficiency was calculated at 100 A/m². The EL efficiency increases up to 0.8 % with increasing the ITO thickness to 500 Å, remains constant between 500 Å and 1000 Å, and then gradually decreases up to 5000 Å. Therefore, it is suggested that the optimum thickness of the ITO anode for high efficiency of OLEDs is about 500-1000 Å.

4. SUMMARY

Indium tin oxide (ITO) thin films have been deposited by PLD on glass substrates. The structural, electrical and optical properties of these films were investigated as a function of film thickness. ITO films, deposited on glass at 300 °C, were polycrystalline and showed a similar crystal structure to that of undoped In₂O₃. However, the lattice parameter, calculated from the XRD patterns for the ITO films, is normally larger than that of the In₂O₃ powder. For ITO films (500 - 4000 Å thickness) deposited at 300 °C in 10 mTorr of oxygen pressure, the resistivity of $2 - 4 \times 10^{-4} \Omega\text{-cm}$ was observed and the average transmission in the visible range (400 - 700 nm) was about 85 - 90 %. The Hall mobility and carrier density for ITO films (500 - 4000 Å thickness) were observed to be in the range of 24 - 27 cm²/V-s and $5 - 9 \times 10^{20} \text{ cm}^{-3}$, respectively. Since there is a high density of ionized impurity centers in the ITO films due to oxygen vacancies and/or Sn dopants, the ionized impurity scattering is considered as dominant scattering mechanism for the conduction of the films. The grain boundary scattering is not dominant in this case because the estimated mean free path of the charge carriers is much smaller than the



(a)



(b)

Figure 8: (a) Luminance-current density (L-J) characteristics and (b) external quantum efficiency as function of ITO film thickness for the same devices with Figure 7.

grain size of the ITO films. We have used the ITO thin films, deposited by PLD on fused silica substrates, as the anode contact in organic light emitting devices and studied the effect of ITO film thickness on the device performance. The optimum thickness of the ITO anode for the maximum device efficiency was obtained to be about 500-1000 Å. The device with the optimum thickness of ITO anode showed an external quantum efficiency of about 0.8 % at 100 A/m².

ACKNOWLEDGMENTS

This work was financially supported by Office of Naval Research (ONR). We would like to thank Dr. Eric Jackson for his help relating Hall effect measurements.

REFERENCES

1. H. L. Hartnagel, A. L. Dawar, A. K. Jain and C. Jagadish, *Semiconducting Transparent Thin Films*, Institute of Physics Publishing, Bristol and Philadelphia, 1995.
2. H. Kim, A. Piqué, J. S. Horwitz, H. Mattoussi, H. Murata, Z. H. Kafafi and D. B. Chrisey, "Indium tin oxide thin films for organic light-emitting devices," *Appl. Phys. Lett.* **74**, pp.3444-3446, 1999.
3. C. W. Tang and S. A. Van Slyke, "Organic electroluminescent diodes," *Appl. Phys. Lett.* **51**, pp.913-915, 1987.
4. M. Buchanan, J. B. Webb, and D. F. Williams, "Preparation of conducting and transparent thin films of tin-doped indium oxide by magnetron sputtering," *Appl. Phys. Lett.* **37**, pp.213-215 1980.
5. R. P. Howson and H. A. Jafar, "Reactive sputtering with an unbalanced magnetron," *J. Vac. Sci. Technol. A* **10**, pp.1784-1790, 1992.
6. T. Karasawa, Y. Miyata, "Electrical and optical properties of indium tin oxide thin films deposited on unheated substrates by d.c. reactive sputtering," *Thin Solid Films* **223**, pp. 135-139, 1993.
7. T. Maruyama and K. Fukui, "Indium tin oxide thin films prepared by chemical vapor deposition," *Thin Solid Films* **203**, pp.297-302, 1991.
8. T. Maruyama and K. Fukui, "Indium-tin oxide thin films prepared by chemical vapor deposition," *J. Appl. Phys.* **70**, pp.3848-3851, 1991.

9. V. Vasu and A. Subrahmanyam, "Reaction Kinetics of the formation of indium tin oxide films grown by spray pyrolysis," *Thin Solid Films* **193/194**, pp.696-703, 1990.
10. S. Kulaszewicz, W. Jarmoc and K. Turowska, "Electrical and optical properties of thin $\text{In}_2\text{O}_3\text{:Sn}$ and $\text{SnO}_2\text{:Sb-In}_2\text{O}_3\text{:Sn}$ films obtained by the hydrolysis method," *Thin Solid Films* **112**, pp.313-316, 1984.
11. H. Kim, C. M. Gilmore, A. Piqué, J. S. Horwitz, H. Mattoussi, H. Murata, Z. H. Kafafi and D. B. Chrisey, "Electrical, optical and structural properties of indium tin oxide thin films for organic light-emitting devices," *J. Appl. Phys.* **86**, pp. 6451-6461, 1999.
12. D. B. Chrisey and G. K. Hubler, *Pulsed Laser Deposition of Thin Films*, Wiley, New York, 1994.
13. D. K. Schroder, *Semiconductor Material and Device Characterization*, John Wiley & Sons, New York, 1990.
14. B. D. Cullity, *Elements of X-ray Diffraction*, 2nd ed. (Addison-Wesley, Reading, MA, 1978).
15. I. Hamberg and C. G. Granqvist, "Evaporated Sn-doped In_2O_3 films: Basic optical properties and applications to energy-efficient windows," *J. Appl. Phys.* **60**, pp. R123-R159, 1986.
16. Y. Sadaoka, T. A. Jones, W. Gopel, S. Kimura and N. Honda, "Effect of NO_2 in air on the electrical conductance of In_2O_3 films with and without added ZnO prepared by R.F. sputtering," *J Mater. Sci.* **25**, 2632 (1990).
17. E. Bertran, J. L. Morenza and M Varela, "Indium thin films on metal-coated substrates," *Thin Solid Films* **129**, 103 (1985).
18. JCPDS Card No. 06-0416.
19. W.-F. Wu and B.-S. Chiou, "Mechanical properties of r.f. magnetron sputtered indium tin oxide films," *Thin Solid Films* **293**, pp.244-250, 1997.
20. J. Tauc, R. Grigorovici and A. Vancu, "Optical properties and electrical structure of amorphous germanium," *Phys. Stat. Sol.* **15**, pp.627-637, 1966.
21. E. Burstein, "Anomalous optical absorption limit in InSb," *Phys. Rev.* **93**, pp.632-633, 1954.
22. T. S. Moss, *Proc. Phys. Soc. London, Sect. B* **67**, pp.775, 1954.
23. J. L. Vossen, "Transparent conducting films," *Phys. Thin Films* **9**, pp.1-71, 1977.
24. H. Kim, D.Sc. Dissertation in Materials Science, School of Engineering and Applied Science, George Washington University, (2000).
25. R. L. Petritz, "Theory of photoconductivity in semiconductor films," *Phys. Rev.* **104**, 1508 (1956).
26. V. A. Johnson and K. Lark-Horovitz, "Transition from classical to quantum statistics in germanium semiconductors at low temperature," *Phys. Rev.* **71**, pp.374-375, 1947.
27. H. Murata, C. D. Merritt and Z. H. Kafafi, "Emission mechanism in rubrene-doped molecular organic light-emitting diodes: direct carrier recombination at luminescent centers," *J. Sel. Topics in Quant. Elec.* **4**(1), pp.119-124, 1998.

SESSION 6

Pulsed Laser Deposition II

Developments of Laser Processing Technologies in Japanese MITI Project

Takehito YOSHIDA, Toshio SATO*, Yoshiaki YOSHIDA*, and Ken-ichi MATSUNO*

Matsushita Research Institute Tokyo, Inc., Higashimita, Tama-ku, Kawasaki 214-8501, Japan

*RIPE: R&D Institute for Photonics Engineering, Atago, Minato-ku, Tokyo 105-0002, Japan

ABSTRACT

The "Advanced Photon Processing and Measurement Technologies" project was started in Aug. 1997 as part of the Industrial Science and Technology Frontier Program of the Agency of Industrial Science and Technology (AIST), the Ministry of International Trade and Industry (MITI) in Japan. Thirteen private companies, one university, and four national research institutes are developing new technologies using high-quality photon beams, in the three technology fields: "Photon-applied processing technology", "Photon-applied measurement technology", and "Photon generation technology". Recent topics in the "Photon generation technology" field are 3.3 kW output power from LD-pumped all-solid-state Nd:YAG lasers of both rod-type and slab-type, and 20 W UV output power via CLBO crystals. There are various topics also in the other two technologies. In "Photon-applied processing technology" field, high speed (1 m/min) defects-free welding properties have been confirmed for 10 mm thick stainless steel, by using a 8.5 kW iodine laser and nitrogen assist gas. Furthermore, we have developed integrated process systems of pulsed laser ablation in helium background gas, size classification using a differential mobility analyzer, and deposition onto a substrate, for the purpose of synthesizing for semiconductor and refractory metal nanoparticles size-controlled accurately. Consequently, we have deposited the size-controlled nanoparticles (silicon and tungsten) onto substrates with sharp size distributions in geometrical standard deviation: 1.2.

Keywords: Solid-state laser, LD pumping, UV-output laser, Fiber laser, Laser welding, Pulsed laser ablation, Inert background gas evaporation, Nanoparticles, Functional materials, Differential mobility analyzer

1. INTRODUCTION

Applications of laser beams have been expanding in manufacturing industries in all over the world. These have already been the important tools for promoting the manufacturing industries. The laser beams are widely applied to material processing in the manufacturing industries, from macroscopic processing such as drilling, cutting and welding in the fields of mechanical and electric industries to microscopic processing such as recent photo-lithography and laser annealing for semiconductor and liquid crystal devices. The features of the laser material processing are spatially and/or temporarily localized interaction without mechanical contacts and higher degree of freedom, in comparison with the conventional mechanical processing. Recently, since the material processing and measuring technologies are going to the spatial regions from micrometer order to nanometer, the laser beams should be treated as "photons" for the high quality processing. Therefore, it is mandatory to construct photon processing systems where high quality photon generation units are highly combined with material processing and/or accurate measuring units.

However, the high-power and high-quality photon generation technology with high-efficiency and low-cost is not established enough, at the present stage. In addition, high-quality photon application technologies of the material processing and measuring should also be facilitated into the next stage. Especially in the future manufacturing industries, it is necessary to consider environmental compatibilities in terms of energy saving, resource saving (recyclability) and pollution free.

In this paper, we are focusing on the "Photon-applied processing technology" field. In "Macroscopic processing technology" theme, we are developing laser hybrid process and in-process monitoring technology to realize a highly reliable laser welding system. In "Microscopic processing technology" theme, we are developing formation technology for nanocrystallites of high quality and homogeneous size, for synthesis into new quantum functional devices. Recently, we have developed integrated process systems for formation of semiconductor and refractory metal nanoparticles by pulsed laser excitation, size classification by means of nanoparticle mobility, and deposition onto substrates. This integrated process systems can be applied to the clean physical vapor synthesis for near future quantum functional devices.

2. OUTLINE OF THE “ADVANCED PHOTON PROCESSING AND MEASUREMENT TECHNOLOGIES” PROJECT

From the above viewpoints, The Agency of Industrial Science and Technology (AIST) started the above mentioned 5 year project in the framework of the Industrial Science and Technology Frontier Program of the Ministry of International Trade and Industry (MITI). Its aim was to develop technologies for not only generating high-power, high-quality photon beams (lasers) of high efficiency and low cost but also the advanced material processing and measurement technologies.

2.1 R&D themes and their goals

This project sets the three technical fields, “photon-applied processing technology”, “photon-applied measurement technology” and “photon generation technology”, and selects six themes as its priority R&D subjects. They are “macroscopic processing technology” and “microscopic processing technology” in the field of photon-applied processing technology, “*in-situ* status measurement technology” and “nondestructive composition measurement technology” in the field of photon-applied measurement technology, “high-power all-solid-state laser technology” and “tightly-focusing all-solid-state laser technology” in the field of photon generation technology.

Table 1 Details and Goals of “Advanced Photon Processing and Measurement Technologies” R&D

Field	Theme	R&D Details	Goals to be Achieved
Photon-applied processing technology	Macroscopic processing technology	Development of highly reliable laser welding technology by applying the in-line process monitoring and feed forward control of welding phenomena.	Establishment of technology for laser welding of 30 mm thick steel plates or 20 mm aluminum alloy plates at a rate higher than 1 m/min, providing high aspect ratio and equivalent or better strength than the base material.
	Microscopic processing technology	Development of microstructure fabrication technology with new quantum level functions by fabricating, integrating and depositing ultra-fine particles with high purity and uniform particle size and structure.	Fabrication of high-purity ultra-fine particles with sizes from 1 to 50 nm and geometric standard deviation of particle size distribution (σ_g) below 1.2, establishment of technology for fabricating functional microstructures with quantum level functions using these ultra-fine particles.
Photon-applied measurement technology	<i>In-situ</i> status measurement technology	Development of high-sensitivity <i>in-situ</i> measurement technology of gas/particle components / concentrations and object shapes/temperatures by utilizing photons from the IR to vacuum UV regions.	Establishment of technology for measuring gas concentration with 1 ppb or better sensitivity using light source wavelength scanning absorption spectroscopy in the IR region, and technology for measuring element contents of 30 nm or finer particles with emission spectroscopy up to the UV region. Establishment of technology for measuring object shapes with 10nm or better sensitivity (at measuring distance of about 0.5 m) using wavefront-controllable interference technology, and technology for measuring internal temperatures from normal temperature to 1000°C with 1°C sensitivity.
	Nondestructive composition measurement technology	Development of nondestructive measurement technology for highly accurate observation of the composition and status in the proximity of object surfaces and defects inside objects using a compact source of photons with high intensity and short wavelengths.	For solid surface proximity measurements, establishment of technology for detecting impurities with 30 nm or better spatial resolution using opto-electronic spectrometry, technology for detecting impurities in μm level micro region with 1 ppb or better detection sensitivity using short wavelength photo detection, and technology for measuring internal defects of solids with 1 μm or better spatial resolution.
Photon generation technology	High-power all-solid-state laser technology	Development of an all-solid-state laser technology pumped by laser diodes with high-power, high-efficiency oscillation, for use as machining tools.	Establishment of laser generation technology of high-power, all-solid-state laser devices with laser head volumes below 0.05 m ³ , average power of more than 10 kW and oscillation efficiency of more than 20%.
	Tightly-focusing all-solid-state laser technology	Development of tightly-focusing, all-solid-state laser technology with excellent handling for use as precision and high-accuracy processing tools.	Establishment of a laser generation technology of compact, all-solid-state laser devices with beam convergence on the processing target of less than 50 μm , average power of more than 1 kW and oscillation efficiency of more than 20%.

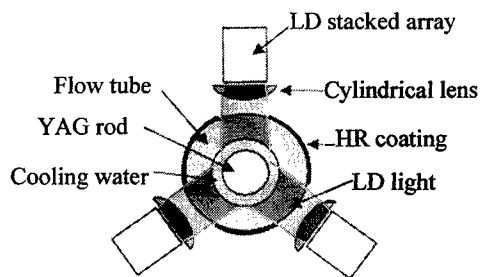


Fig. 1. Schematic view of LD pumped module of rod-type all-solid-state laser.

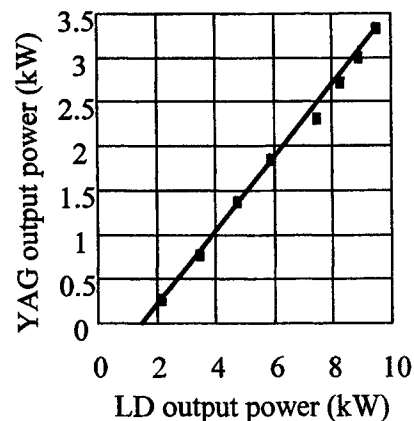


Fig. 2. Output characteristics of 3k W rod-type all-solid-state laser.

Table 1 shows the details and goals of the 6 R&D themes. Each theme has quantifiable goals, which are fairly high when seen from the perspective of the current technological levels. There are several problems needing to be cleared up in order to achieve these goals in the projected 5 year period and outstanding ideas and exceptional efforts will be required.

2.2 Research system and budget

The R&D Institute for Photonics Engineering (RIPE) was established on August 1, 1997 as the organization to promote the project in the private industry sector. The R&D of the project is conducted by accepting assignments from the New Energy and Industrial Technology Development Organization (NEDO), and re-assigning to the 13 private companies and 1 university forming the members of the RIPE. With some research subjects allotted to four research institutes under the AIST, MITI, and joint research with many universities, the present R&D project is based on cooperation between industry, universities and governmental institutions. The research period is to be 5 years until the end of FY2001 and the total budget (initial appropriation) for the 5 years is 7 billion yen.

3. PROGRESS AND ACHIEVED RESULTS

The themes have been making smooth progress and we have already obtained prominent results. In this paper, we describe the recent progress about "Photon generation technology" and "photon-applied processing technology". Especially in the theme of "microscopic processing technology" in the technical field of "photon-applied processing technology", we carry out a relatively detail explanation.

3.1 High-power all-solid-state laser technology ¹⁾

The goal to be achieved in "High-power all-solid-state laser technology" is the establishment of laser generation technology of high-power, all-solid-state laser devices with laser head volumes below 0.05 m³, average power of more than 10 kW and oscillation efficiency of more than 20%. Two kinds of high-power, high-efficiency laser are being developed using rod-type and slab-type laser oscillation media made of YAG crystal which are pumped by the stacks of laser diodes (LD) peripherally arranged. At present, in both types the performance of the 3 kW class lasers developed to date are being improved and the development of 10 kW class lasers have commenced.

3.1.1 The rod-type laser

Toshiba Corp. is developing the rod-type Nd:YAG laser pumped by LD ^{2,3)}. It is necessary to achieve high density pumping in the pumping module for the high power operation of the LD pumped Nd:YAG laser.

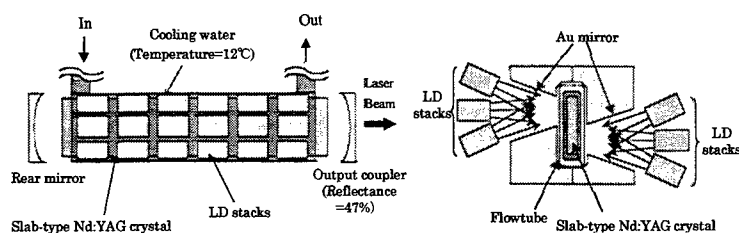


Fig. 3. Configuration of 3 kW slab-type all-solid-state laser.

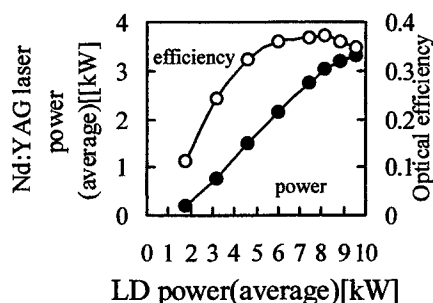


Fig. 4. Output characteristics of 3 kW slab-type all-solid-state laser.

The schematic view of the laser head using LD stacked-arrays is shown in Fig. 1. The laser rod is mounted inside a flow-tube. The optical pump source consists of nine LD stacked-arrays with an output power of up to 240 W each at an average input current of 25 A. The pump radiation from the LD stacked-arrays is imaged into the laser rod by collimating cylindrical lenses. A maximum output power of about 1 kW is achieved at the pump power of about 2.1 kW, in the one head resonator. The resonator composed of four heads in 940 mm length had 50% of output coupling. The input-output characteristics are shown in Fig. 2. This indicates that laser power of 3.3 kW was obtained at pumping power level of 9.4 kW. This proves the possibility of high power laser operation with multi-head resonator design.

3.1.2 The slab-type laser

Fanuc Ltd. is developing the slab-type Nd:YAG laser^{4,5)}. They chose one-sided pumping method which is superior to conventional two-sided pumping method as obtaining high efficiency (Fig. 3).

Figure 4 shows the output characteristics of 3 kW class slab-type all-solid-state laser. The average output power of 3.3 kW and the peak output power of 13 kW were obtained with the optical-optical efficiency of 35% and the electrical-optical efficiency of 13% when LD pump power was 9.5 kW.

3.2 Tightly-focusing all-solid-state laser technology¹⁾

The goal to be achieved in "Tightly-focusing all-solid-state laser technology" is the establishment of laser generation technology of compact, all-solid-state laser devices with beam convergence on the processing target of less than 50μm in diameter, average power of more than 1 kW and oscillation efficiency of more than 20%. Two kinds of lasers are being developed. One is the fiber laser, and the other is the high-brightness and high-repetition-rate UV all-solid-state laser with CLBO(CsLiB₆O₁₀) crystals invented in Japan.

3.2.1 Fiber laser

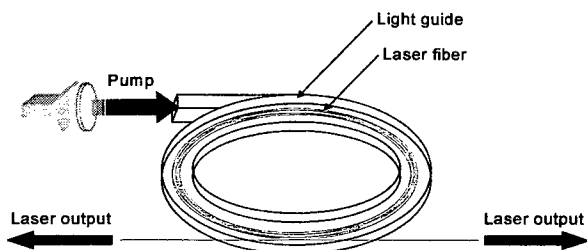


Fig. 5. First implementation of the fiber embedded structure laser concept: "Fiber embedded tube laser".

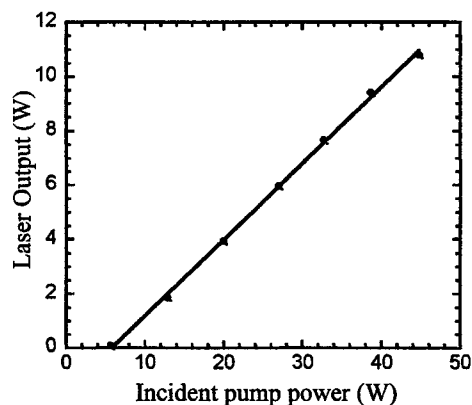


Fig. 6. Fiber laser characteristics for the setup shown in Figure 5. The laser output corresponds to the sum of the output powers at both ends.

An original "structure type" fiber laser based on the unique idea of winding the laser fiber into a disk or cylindrical shaped structure and pumping it from the LD located on the surroundings is being developed by HOYA Corp.⁶⁻⁹⁾. The concept of this fiber laser is invented by Prof. K. Ueda (University of Electro-Communications). **Figure 5** shows their first implementation of the concept. They coiled about 100 m-long Nd³⁺ doped silica fiber into a ring 10 cm in diameter and set it into a structure using a resin. **Figure 6** shows the output characteristics of the ring type fiber laser. For a pump power of 44 W from the LD, the fiber laser output reached 10.8 W, an optical-optical slope efficiency of 28% were achieved.

In this theme, a new type high-power/high-intensity LD with higher average power per array for the fiber laser is also developed by Hamamatsu Photonics K.K.^{10,11)}. Novel InGaAsP high power diode modules with high conversion efficiency, tight focus ability for pumping optical fiber laser, and longer lifetimes are investigated. They have adopted Al free InGaAsP as an active layer material. Cooling method and LD bar assembly process are carefully studied to realize such high performance LDs. They have developed a "FUNRYU" water cooled heat sink to efficiently cool the LDs and a new assembling system to reliably fabricate LD arrays. Hamamatsu Photonics K.K. achieved a CW output power over 20 W and QCW operation output over 80 W.

3.2.2 High-brightness and high-rep-rate UV all-solid-state laser with CLBO crystal

Mitsubishi Electric Corp. is developing the high-brightness and high-repetition-rate pulsed laser with good beam quality^{12,13)}. They propose the HIPER (High-Brightness Polarization-dependence Erased Resonator) cavity configuration to obtain a high power with a high quality beam. This technology compensates for the beam quality degradation caused by thermally induced defocusing in the rod.

At present, they propose a new diode-pumping configuration CIDER (Close-coupled Internal Diffusive Exciting Reflector) to achieve high-efficiency and uniform pumping distribution in a small solid-state crystal. The Nd:YAG rod is pumped in a diffusive cavity by a stacked diode-bars. The transferred diode beams are recycled in the cavity to generate uniform pumping distribution in the Nd:YAG rod. **Figure 7** shows the laser output characteristics of one pumping cavity. The maximum peak power of 2.7 kW and average power of 270 W are obtained with the electrical-optical efficiency of 18%.

For 4th harmonic generation of Nd:YAG laser beam, CLBO crystal is being grown by Osaka University with a new method¹⁴⁾. Fabrication technology of CLBO crystal is being developed by Kogakugiken Co., Ltd. Their CLBO crystal is strong against ultraviolet beams. In Mitsubishi Electric Corp., 20 W 266 nm UV power is generated using its CLBO crystal¹⁵⁾. **Figure 8** shows the schematic drawing of the high-power ultraviolet all-solid-state laser, and its output characteristics.

3.3 Macroscopic processing technology: Highly reliable laser welding technology

High-power laser beams are very attractive tools for material processing in heavy industries, especially in thick material welding. As well known, CO₂ lasers have widely been used for the high-power thick material processing. However, it is necessary to improve the beam quality, the efficiency and the degree of operating freedom and so on, for the future thick material processing where accuracy, reliability and low cost operation will become more important. Near infrared region lasers: Nd:YAG lasers and COIL (Chemical Oxygen Iodine Lasers) of 10 kW class are very suitable for the future trend,

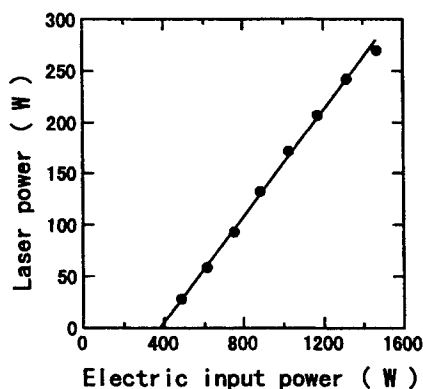


Fig. 7. Lasing performance of one cavity

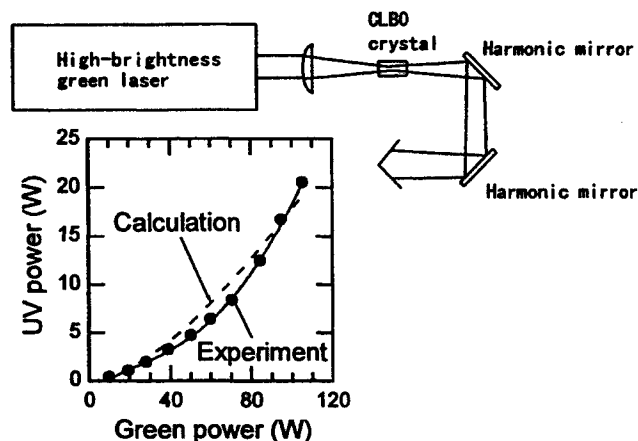


Fig. 8. High power UV beam generation by using CLBO crystals.

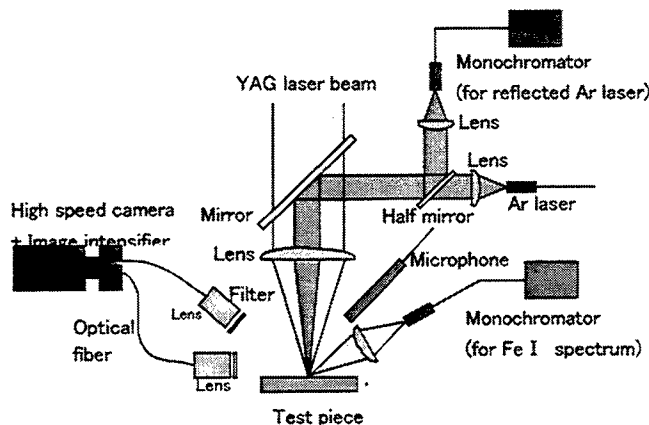


Fig. 9. Schematic arrangement of keyhole monitoring.

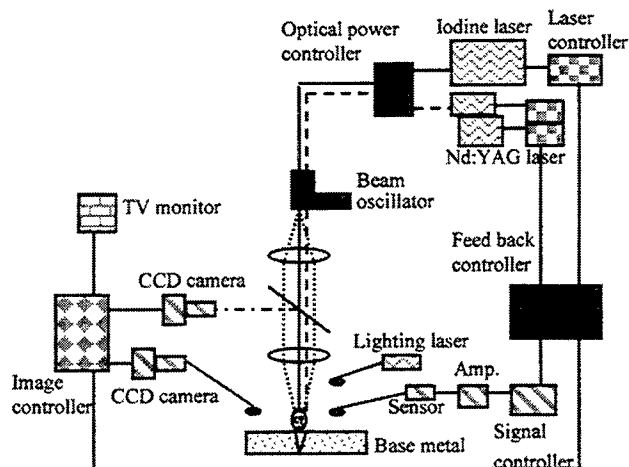


Fig. 10. High performance welding system.

because these have many advantages in comparison with the CO₂ lasers as follows: 1) high transmission via flexible optical fibers, 2) tight-focusing properties, 3) high absorption at metal surface, 4) weak interaction with plasma plume. From above reasons, we have introduced the near infrared region high-power lasers: the COIL (wavelength: 1315 nm) and the Nd:YAG lasers (wavelength: 1064 nm). In this section, we describe the research results of Kawasaki Heavy Industries Ltd., on defect free thick material welding using the COIL.

3.3.1 Phenomena of laser welding process

Laser welding phenomena where laser beams have interactions with plasma and molten pool are possible to be observed by high speed cameras and x-ray high speed video cameras which are possible to observe the inside of molten metal. Plasma formation from the keyhole and molten pool was observed simultaneously and propagation of defect like porosity could be evaluated. By using assist gas of nitrogen, defect free welding of stainless steel could be observed by a video camera. One of the effects of nitrogen gas is gradual change for the surface tension of molten pool, so that the flow of molten pool is smooth and defect free welding can be obtained. However, we can not verify its mechanism yet.

A short time pulse modulation of laser power was effective to remove welding defects like porosity. Optimum pulse conditions of used laser power can be obtained experimentally. Continuous laser power makes spiking at the top of the deep penetration, and makes the porosity at the same time. It is considered that optimum impinging laser power and pulse modulation change this spiking phenomenon, so that porosity free welding can be obtained¹⁶⁾.

3.3.2 Evaluation of monitoring factor

In-process monitoring systems are required at the industrial laser welding process. Monitoring factor which shows the welding results exactly will be fixed in order to apply new technology in industrial manufacturing. For the thin material up to 3 mm, it is sometimes welded by laser with the plasma monitoring sensor^{17,18)}. However for the thick material, monitoring the intensity of plasma plume is difficult to assure the results of welding joints. There are some kind of relationship between welding defects and keyhole dynamic motions, so that monitoring sensors for keyhole were investigated. Figure 9 shows the arrangement of the keyhole monitoring equipment which can measure the size of a keyhole directly¹⁹⁾.

3.3.3 High performance welding process for thick plate

Figure 10 shows the system concept for high performance welding process. In-process monitoring sensors which measure the dynamic keyhole conditions are arranged on the optical system. Laser conditions are controlled by the personal computer which dispose the signal of keyhole monitoring sensor and the data of the welding conditions selected from the data base. Welding conditions are always monitored by CCD camera and recorded by video deck^{20,21)}.







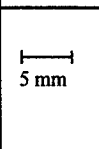
		Welding Speed (m/min)			
		0.50	0.75	1.00	1.50
Shielding Gas	He				
	Ar				
	N ₂	Laser power: 8.5 kW Delivery optics: mirror Focal length: 200 mm Nozzle diameter: 8 mm Gas flow rate: 20 l/min			

Fig. 11. Welding characteristics of iodine laser.

Figure 11 shows the welding characteristics of the iodine laser welding. Three different types assist gas(N₂, Ar, He) were used. Penetration depths were approximately equal and shapes of transverse cross sections were same, but defect formation was different. The wavelength of the iodine laser and Nd:YAG are 1315 nm and 1064 nm, respectively. Furthermore, the interaction between the near infrared lasers and plasma plumes were weak, comparing to CO₂ lasers. Defect free welding was obtained by using nitrogen gas.

Figure 12 shows the transverse welding cross section of 10 mm thick stainless steel type 304. Welding condition is 8.5 kW of the iodine laser power and 1m/min of welding speed. Full penetration and defects-free welding can be obtained up to 10 mm thick by using nitrogen assist gas.



Fig. 12. Cross section of full penetration.

3.4 Microscopic processing technology:

Well-controlled ultrafine particle formation and its application to quantum functional structures

Nanometer-sized fine particles which exhibit properties and functions that are not evident when they are in the bulk state are labeled “ultrafine particles”. For example, with respect to light emitting properties, it is well known that group IV semiconductors can emit strong visible light at room temperature once their size is reduced on the order of less than ten nanometers, even though they emit almost no light in the bulk state because they are indirect transition semiconductors²². Furthermore, it has confirmed that the emission wavelength can be controlled as a function of their size, in a limited wavelength region²²). However, the development of ultrafine particles into advanced functional devices has been difficult because they have a large percentage of surface-exposed atoms (nearly 40% when the diameter is 5 nm), and are extremely sensitive to impurities and/or damage.

Laser processing is a typical cold-walled processing which excites only beam focused areas, can enables a clean and damage-free ambient, and is thus highly suitable for ultrafine particle synthesis. In particular, pulsed laser ablation (PLA) can be used to synthesize refractory and/or compound materials^{23,24)}, and has excellent features, notably from the viewpoints of safety and compatibility with the environment.

It is obvious that silicon (Si) is the main material in the present electronic industry. In this project, Matsushita Research Institute Tokyo, Inc. (MRIT) is attempting to realize visible light emitting properties of Si^{25,26)}, by synthesizing the Si into nanometer-sized ultrafine particles using the PLA in inert background gas (PLA-IBG)^{27,28)}. Furthermore, MRIT is trying to fabricate structure-controlled quantum functional devices, whose functions (eg. emitting wavelength) can be determined by controlling the particle size, surface structure, and dispersion structure.

On the other hand, focusing on refractory metals, for example tungsten (W) or molybdenum (Mo), these refractory metals are expected as high-migration-resistant conductive materials on semiconductor integrated circuits and multi-layered

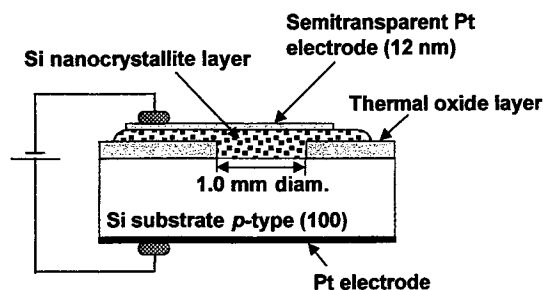


Fig. 13. Light emitting device of Si nanocrystallite active layer.

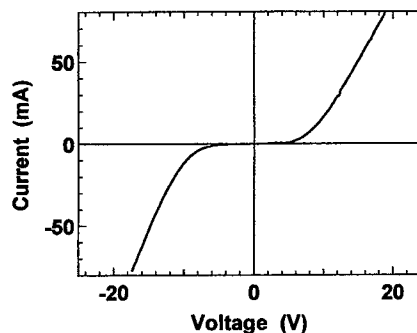


Fig. 14. Current-voltage (I - V) characteristics.

printed substrates. In addition, some refractory metal (eg. tantalum:Ta) oxides can be high dielectric materials. Nanometer-sizing of the refractory materials can achieve low temperature sintering on thermally unstable substrates. For these reasons, Vacuum Metallurgical Co. Ltd. is developing synthesis methods for ultrafine particles of the refractory metals, using pulsed laser evaporation in inert background gas, in this project.

3.4.1 Semiconductor ultrafine particles

In this section, first, we fabricate visible light emitting devices whose active layers are Si nanocrystallites prepared by the PLA-IBG²⁹⁾. Excitation beam is a second harmonic Q-switched (pulsed) Nd:YAG laser. The Q-switched Nd:YAG laser can tune the pulse width in a nanosecond region. Next, for accurate size controlling of Si nanocrystallites, we develop an integrated process system for the formation of nanoparticles by PLA-IBG, size classification using a low pressure operating differential mobility analyzer (LP-DMA), and deposition onto substrates.

Light emitting devices of silicon nanocrystallite active layers:

Figure 13 shows the cross-sectional structure of the light emitting diodes (LEDs) of the Si nanocrystallite active layers. Substrates were (100) oriented p -type Si wafers with a resistivity of $0.02 \Omega \cdot \text{cm}$. Thermal oxide layers were formed with a thickness of 300 nm for the isolation dielectrics. Electrically active regions of 1.0 mm diameter were defined by removing the thermal oxide layer. The Si nanocrystallite layers were deposited using PLA-IBG where second harmonic Nd:YAG laser beams (wavelength: 532 nm) excite the single crystalline Si target (p -type (100)). The thickness of the deposited active layers was approximately 200 nm. The PLA-IBG conditions were as follows: pulse energy: 10 mJ, pulse width: 42 ns, He gas pressure: 3.75 Torr. These were optimized conditions for synthesizing the Si nanocrystallites, by varying the pulse width of the excitation laser for droplet/debris suppression and He background gas pressure for the optical quantum confinement effect appearance^{30,31)}.

Thermal annealing was carried out at 825 °C for 10 min in N_2 gas. In order to form contacts with the Si nanocrystallite layers, semitransparent platinum (Pt) films of 12 nm thickness were deposited. Finally, wiring contacts were performed using silver paste. We evaluated the current-voltage (I - V) characteristics and light emitting properties in the case of direct current excitation.

Weak rectifying behavior was observed in the I - V characteristics of the LED (Fig. 14). The external series resistance was estimated to be about 100 Ω . The onset of the emission was at a forward bias of 5.0 V and current density of 35 mA/cm^2 . Oxygen inclusion during the thermal annealing led to strong rectifying behavior²⁹⁾. The rectifying behavior appears to be caused by the surface oxide of the Si nanocrystallites.

Furthermore, the integrated light emitting intensity (I_{EL}) shows an abrupt nonlinear dependence on the forward current j : $I_{\text{EL}} \sim j^m$, $m=1.8-2.2$ (Fig. 15). This dependence is different from that of the usual minority-carrier-injection-type LEDs. We have observed the visible spectrum of the LED at room temperature. Figure 16 shows the spectrum measured at the dissipation power of 1.6 W. The spectrum is composed of Gaussian waveforms of a main unit peaked at 1.7 eV, and sub-units peaked at 2.1 eV and 2.25 eV. We observed a tendency of the peak height of the sub-unit 2.1 eV to increase with increasing temperature of oxidation treatment for the Si nanocrystallite active layers. This result suggests that sub-unit 2.1 eV is originated from the surface oxide layers. The light emission in Fig. 16 seemed orange under naked eye observation.

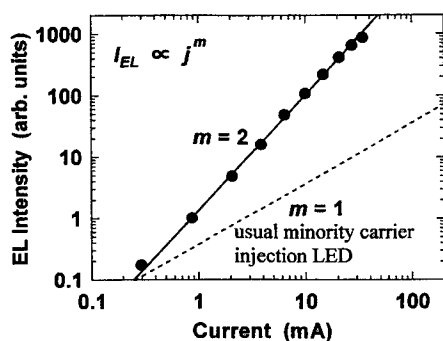


Fig. 15. Integrated EL Intensity as a function of injection current.

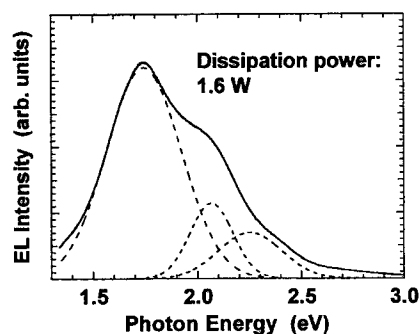


Fig. 16. EL spectrum.

One possible mechanism of this emission is impact ionization by hot electron tunneling through the surface oxide layers and the subsequent radiative recombination. The nonlinearity is attributed to the dependence of the impact ionization quantum efficiency on acceleration energies of the tunneling hot electrons³²⁾.

Deposition processing for monodispersed silicon nanoparticles:

It is necessary to control nanoparticle size as a typical “structural parameter” more accurately, for advancing the controllability for the wavelength and the efficiency of the light emitting devices with the Si nanocrystallite active layers. In this study, we have constructed a nanoparticle deposition process with sharp size distributions called a “monodisperse system”, by size classification for the nanoparticle systems prepared by the PLA-IBG. Following points are requisites for an integrated process system in which the classification and deposition units are combined into the formation unit of the PLA-IBG, for synthesizing the Si nanocrystallite active layers of light emitting devices.

1. Cleanliness associated with active regions in semiconductor devices
2. Sufficient yield of the classified nanoparticles for device fabrication processing
3. Operating pressure compatible with the PLA-IBG: 3-5 Torr
4. Mean diameter controllability: 2-15 nm, geometrical standard deviation: 1.2

For the above requirements, we adopted a low pressure operating differential mobility analyzer (LP-DMA)^{33,34)} as the main component. The LP-DMA classification unit is combined with the PLA-IBG formation unit and a nozzle effusing deposition unit, as an ultrahigh-vacuum integrated process system. A schematic diagram and a photograph of the novel

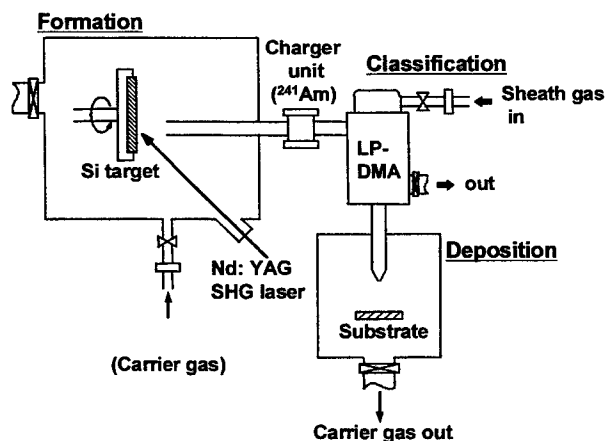


Fig. 17. Schematic diagram of nanoparticle formation-classification-deposition integrated process system.

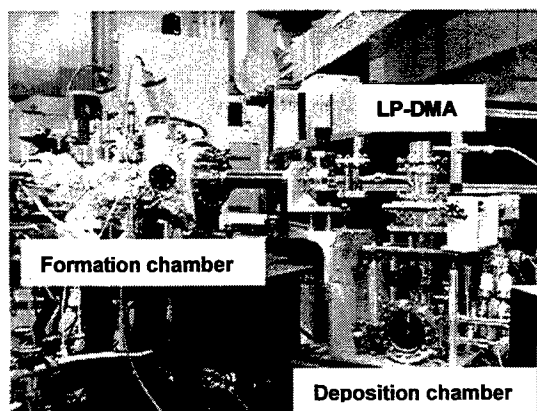


Fig. 18. Photograph of nanoparticle formation-classification-deposition integrated process system.

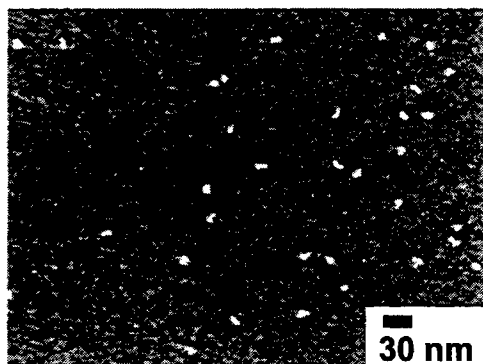


Fig. 19. Scanning electron microscope image of Si nanoparticles deposited by the integrated process system.

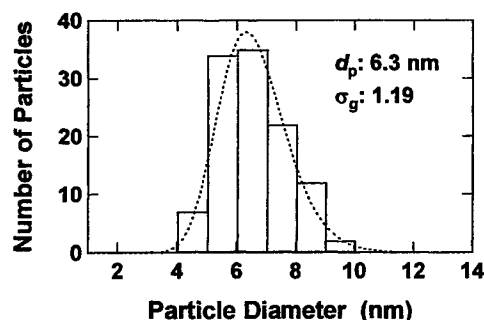


Fig. 20. Size histogram of Si nanoparticles deposited by the integrated process system.

nanoparticle formation-classification-deposition integrated process system are shown in Fig. 17 and Fig. 18, respectively. The Si nanoparticles formed by the PLA-IBG were transferred by differential pressure from the formation chamber, with a carrier gas (formation background He gas). The Si nanoparticles were introduced into the LP-DMA, via a charging process by a radio isotope (^{214}Am). Here, we briefly explain the classification mechanism in the LP-DMA. In the classification region in the LP-DMA, the charged Si nanoparticles through an inlet slit are carried downward with uniform velocity, by a laminar flow of a sheath gas (He), and are deflected in the horizontal direction by the uniformly applied electrostatic field. The charged Si nanoparticles move along each locus determined by their own electrical mobilities. As the electrical mobility is approximately a function of particle cross-section, the charged Si nanoparticles can be classified through an outlet slit. The classified Si nanoparticles were transferred to the deposition chamber by a differential pressure. In the deposition chamber, the Si nanoparticles were effused through a nozzle, and were deposited on substrates. Bias voltages can be applied to the substrates to increase the collection yields for the charged Si nanoparticles. Fixing the electrostatic intensity in the classification region, we can deposit the monodispersed Si nanoparticles which can compose quantum dot type functional structures. On the other hand, when we sweep the electrostatic field, it is possible to perform real-time monitoring for the size distribution of the Si nanoparticles in formation fields.

DMA's were originally developed for analysis of aerosols in the atmosphere. In the operation pressure range from atmospheric pressure to 70 Torr, it was confirmed that fine particles ranging from submicron to two nanometers in size can be classified³³⁾. It is necessary to reduce the operating pressure by one order because the background gas pressure of the PLA-IBG is less than 5.0 Torr, for the Si nanoparticle formation with optical quantum confinement effect appearance³⁴⁾. In general, the classification resolution of the DMA degrades with decreasing operating pressure. Therefore, we made efforts to conserve the resolution in geometrical designing, with increasing evacuation conductance for the carrier and sheath gases³⁴⁾.

Figure 19 shows a scanning electron microscope image of the classified Si nanoparticles deposited on a Si substrate by the integrated process system. We observe well-dispersed nanometer-sized Si nanoparticles on the Si substrate. Processing conditions for the results shown in Fig. 19 were as follows: He gas pressure in the formation chamber: 10 Torr, He gas pressure in the deposition chamber: 8.8 Torr, carrier gas flow: 1.0 SLM, sheath gas flow: 5.0 SLM, voltage applied to the LP-DMA: 15.0 V, and substrate bias: 70.0 V. The diameter of the classified Si nanoparticles under the above conditions is theoretically estimated to be 5 nm.

Figure 20 shows the size histogram of Si nanoparticles formed under the conditions shown in Fig. 19. Assuming the histogram to be the log-normal distribution, we extracted that the geometrical mean size d_p is 6.3 nm, and the geometrical standard deviation σ_g is 1.2. We have successfully deposited the classified Si nanoparticles onto a substrate with sharp size distribution, called a monodisperse system.

3.4.2 Refractory metal ultrafine particles^{35,36)}

There have been few systematic studies for formation of refractory metal ultrafine particles, because it is very difficult to get enough quantity of the refractory metal ultrafine particles by conventional heating methods³⁷⁾. In this section, first, we describe an effective synthesizing method of tungsten ultrafine particles, by using two synchronized-pulsed Nd:YAG laser excitation in inert background gas. Their pulse width is in a millisecond region. Next, size distribution of the tungsten

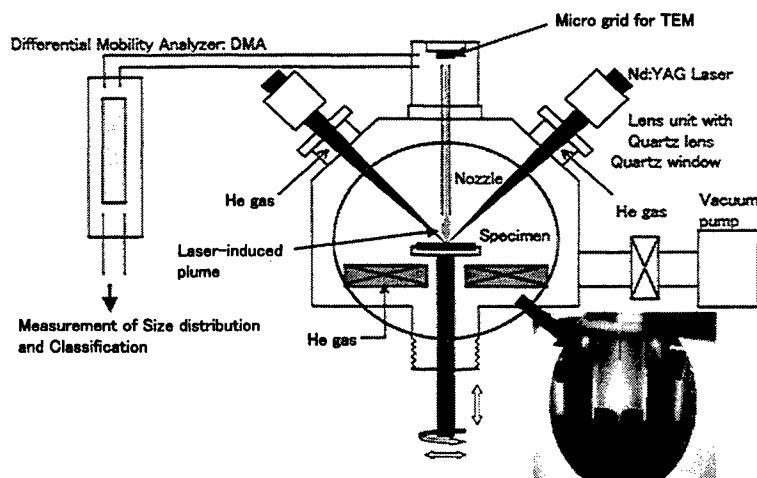


Fig. 21. Schematic diagram of the experimental apparatus.

ultrafine particles in their formation fields are characterized real-timely, by using a LP-DMA. Furthermore, size-classified ultrafine particles are deposited on substrate.

Formation process for tungsten ultrafine particles:

A schematic diagram of the experimental apparatus is illustrated in Fig. 21. The two laser beams were symmetrically irradiated to the tungsten target from about 45° upper positions. The generated particles are ejected mostly in the vertical direction from the target surface, pass through a nozzle and out of the chamber.

Two different types of lasers, the main laser (max. power: 10 J/pulse, wavelength: 1064 nm, pulse width: 0.2 ms) and an assisting laser (max. power: 150 J/pulse, wavelength: 1064 nm, pulse width: 10 ms), were used to synthesize the tungsten ultrafine particles. The main pulsed laser was irradiated to the sample, 9 ms after the assisting laser pulse irradiation. The conditions of the laser irradiation were 10 J/pulse (fluence: 51 J/cm²) for the main laser power (E_m), and 46.5 - 132 J/pulse (fluence: 2.4×10^2 - 6.7×10^2 J/cm²) for the assisting laser power (E_a).

High purity helium gas (99.9999 mass%) was introduced into the chamber at a pressure of 1.3 - 67 kPa after the chamber had been evacuated to 7×10^{-5} Pa. The target was a high purity tungsten disk (99.9999 mass%) with polished surface. The tungsten disks were cleaned in acetone and petroleum benzene using a supersonic wave cleaner.

Results of tungsten ultrafine particle formation:

Figure 22 shows TEM micrographs of tungsten ultrafine particles synthesized with $E_a = 46.5$ J/pulse at pressures from 6.7 kPa to 67 kPa. We can observe an agglomeration of the primary particles generated at 40 kPa. Under higher pressure, the amount of synthesized particles decreased due to the cooling effect of the specimen by the high thermal conductivity of the He gas. The size of the primary particles is about several nm in diameter for each pressure.

Figure 23 shows TEM micrographs of tungsten ultrafine particles synthesized with $E_a = 132$ J/pulse at different pressures. The agglomeration of the primary particles is observed for all conditions, with round particles formed at 40 kPa. This indicates that the size distribution and shape of the generated ultrafine particles are controllable by selecting a suitable combination of pressure and laser power conditions. However, the primary particles of several nm in diameter are also observed for each experimental condition.

Size distribution measurement and classification for tungsten ultrafine particles:

Figure 24 shows the particle size distribution measured by LP-DMA. The particles were obtained with $E_a = 100$ J/pulse, at 2.0 - 40 kPa. The peak of distribution corresponding to the mean diameter of the particles shifts from several nm to the tens of nm with increasing ambient pressure. In addition, the distribution profile changed from a narrow distribution to a broad peak distribution. Because the suspended time of the ultrafine particles in the laser-induced plume increases with

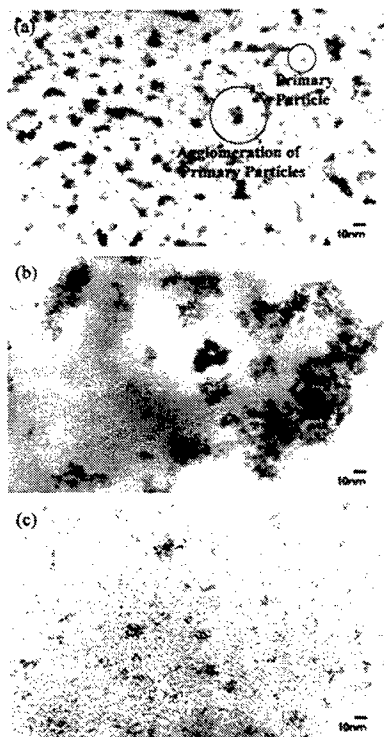


Fig. 22. TEM images of tungsten ultrafine particles under different pressures (main laser power: 10 J/pulse, assist laser power: 46.5 J/pulse). (a) 6.7 kPa, (b) 40 kPa, (c) 67 kPa.

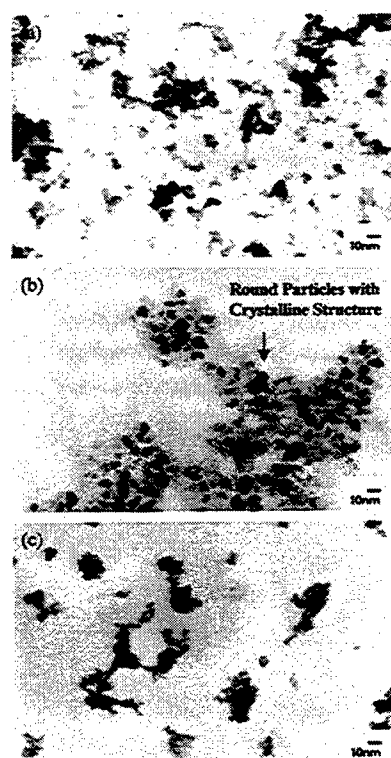


Fig. 23. TEM images of tungsten ultrafine particles under different pressures (main laser power: 10 J/pulse, assist laser power: 132 J/pulse). (a) 6.7 kPa, (b) 40 kPa, (c) 67 kPa.

pressure, the time available for particle growth and agglomeration of the ultrafine particles also increases. These results are in good agreement with the TEM observations.

Figure 25 shows TEM microphotographs of 20 nm-size particles classified by LP-DMA with $E_a=132$ J/pulse, at 13 kPa. Compared with these figures, the objective size of the particles, 20 nm, was obtained. The shape of these 20 nm-classified particles is also in good agreement with both figures. Therefore, we can conclude that DMA can be used as a classification apparatus for ultrafine particles; the DMA can classify without changing the shape of the particles.

4. CONCLUSION

The laser technology covers a very wide range, is ambitious and has the potential to radically change industry and social life in the 21st century. Although the "Advanced Photon Processing and Measurement Technologies" project is developing technologies in only limited areas, it has already led to world's first or world leading research results one after another.

The RIPE is presently surveying the laser processing technologies inside and outside Japan. It is expected that the progress in laser processing technology and the consequent construction of databases can bring about innovative advancements in the fields where the lasers have already been introduced. New kinds of developments in the laser-related fields will also be enabled, thereby leading to the creation of new industries and the further advancement of existing industries.

For the outline of the "Advanced Photon Processing and Measurement Technologies" project and activities of the RIPE, please also visit our web site at <http://www.ripe.mstc.or.jp>.

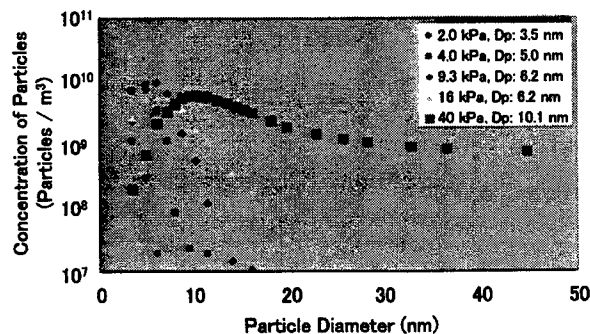


Fig. 24. Measurement of size distribution by LP-DMA.

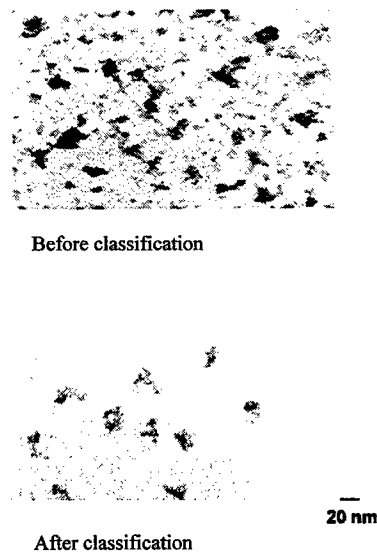


Fig. 25. Before/after classification of tungsten ultrafine particles by LP-DMA.

ACKNOWLEDGEMENTS

Developments for the integrated process system using the LP-DMA have been carried out by collaboration with H. Shimura and his colleagues of Mechanical Engineering Laboratory (AIST). The defect free thick material welding has developed in collaborations with Joining and Welding Research Institute, Osaka University on the modeling for welding mechanism, with Shikoku National Industrial Research Institute (AIST) on the hybrid welding, and with Applied Laser Engineering Research Institute on the *in-situ* monitoring technology. The authors would like to express their appreciation to above collaborators.

REFERENCES

1. K. Matsuno and T. Satoh, *SPIE Advanced High-Power Lasers and Applications*, (Osaka, 1999) 3889-17.
2. A. Takada, Y. Akiyama, T. Takase, H. Yuasa, and A. Ono, *OSA Advanced Solid-State Lasers*, (Boston, 1999) MB18.
3. Y. Akiyama, T. Takase, A. Takada, H. Yuasa, and A. Ono, *OSA Technical Digest of Conference on Lasers and Electro-Optics*, (Baltimore, 1999) CMF-5.
4. M. Sato, S. Naito, H. Machida, N. Iehisa, and N. Karube, *OSA Advanced Solid-State Lasers*, (Boston, 1999) MA2.
5. M. Sato, S. Naito, N. Iehisa, and N. Karube, *SPIE Photonics China '98*, (Beijing, 1998) 3550-76.
6. A. Liu and K. Ueda, *Optics Commun.* **132**, (1996) 511.
7. K. Ueda, *OYO BUTURI* **67**, (1998) 513.
8. K. Ueda, *Optonews*, (no. 2, 1997) 28.
9. K. Ueda, H. Sekiguchi, Y. Matsuoka, H. Miyajima, and H. Kan, *OSA CLEO/Pacific Rim '99*, (Seoul, 1999) WJ3.
10. H. Kan, T. Kanazaki, H. Miyajima, M. Miyamoto, and T. Hiruma, *O plus E* **21**, (1999) 173.
11. H. Miyajima *et al.*, *46th The Japan Society of Applied Physics Extended Abstracts*, (Noda, 1999) 29p-F-1.
12. K. Yasui, S. Konno, T. Kojima, and S. Fujikawa, *The Review of Laser Engineering* **27**, (1999) 469.
13. K. Kojima and K. Yasui, *Appl. Opt.* **36**, (1997) 4981.
14. I. Yamada, M. Yoshimura, Y. Mori, T. Sasaki *et al.*, *OSA CLEO/Pacific Rim '99* (Seoul, 1999) P2.72.

15. T. Kojima, K. Yasui, Y. Mori, T. Sasaki, M. Tanaka, Y. Okada *et.al.*, *OSA Advanced Solid-State Lasers* (Boston, 1999) PD.
16. N. Seto *et al.*, *Abstracts of The National Meeting of Japanese Welding Society* **63**, (1998) 220.
17. M. Mori, *Welding Technique*, **45** (1997) 92.
18. T. Ishide *et al.* *Proceedings of 27th Laser Materials Processing Conf.*, (1992) 123.
19. K. Kamimuki *et al.*, *Abstracts of The National Meeting of Japanese Welding Society* **64**, (1999) 44.
20. K. Yasuda, *Proceedings of the 1st Symposium on Photon Processing and Measurement Technologies*, (1998) 16.
21. T. Nakabayashi *et al.*, *Abstracts of The National Meeting of Japanese Welding Society* **64**, (1999) 90.
22. For example, as a recent review book, D. Lockwood: *Light Emission in Silicon from Physics to Devices* (Academic Press, 1998).
23. D. H. Lowndes, D. B. Geohegan, A. A. Puretzky, D. P. Norton, and C. M. Rouleau, *Science* **273**, (1996) 898.
24. Y. Yamada, N. Suzuki, T. Makino, and T. Yoshida, *J. Vac. Sci. & Technol. A* **18**, (2000) 83.
25. Y. Yamada, T. Orii, I. Umezu, S. Takeyama, and T. Yoshida, *Jpn. J. Appl. Phys.* **35**, (1996) 1361.
26. T. Makimura, Y. Kunii, and K. Murakami, *Jpn. J. Appl. Phys.* **35**, (1996) 4780.
27. T. Yoshida, S. Takeyama, Y. Yamada, and K. Mutoh, *Appl. Phys. Lett.* **68**, (1996) 1772.
28. D. B. Geohegan, A. A. Puretzky, G. Duscher, and S. Pennycook, *Appl. Phys. Lett.* **72**, (1998) 2987.
29. T. Yoshida, Y. Yamada, and T. Orii, *J. Appl. Phys.* **83**, (1998) 5427.
30. T. Yoshida, Y. Yamada, N. Suzuki, T. Makino, T. Orii, and S. Onari, *Proc. SPIE* vol. **3618** (San Jose, 1999) 465.
31. N. Suzuki, T. Makino, Y. Yamada, and T. Yoshida, to be published in *Appl. Phys. Lett.* **76**, (2000).
32. C. Chang, C. Hu, and R. W. Brodersen, *J. Appl. Phys.* **57**, (1985) 302.
33. T. Seto, T. Nakamoto, K. Okuyama, M. Adachi, Y. Kuga, and K. Takeuchi, *J. Aerosol Sci.* **28**, (1997) 193.
34. T. Makino, N. Suzuki, Y. Yamada, T. Yoshida, T. Seto, and N. Aya, *Appl. Phys. A*, (in press, 1999).
35. Y. Kawakami, T. Seto, E. Ozawa, *J. Japan Inst. Metals* **63**, (1999) 1101.
36. Y. Kawakami, T. Seto and E. Ozawa, *Appl. Phys. A*, (in press, 1999).
37. A. Matsunawa, S. Katayama, *Proc. of ICALEO '85*, (1985) 205.

TiN growth by hybrid radical beam-PLD for Si barrier metal

Kotaro Obata^{*A,B}, Koji Sugioka^A, Koichi Toyoda^B, Hiroshi Takai^C, and Katsumi Midorikawa^A.

^ARIKEN (The Institute of Physical and Chemical Research),
Hirosawa 2-1, Wako, Saitama 351-0198, Japan.

^BScience Univ. of Tokyo, Yamazaki 2641, Noda, Chiba 278-8510, Japan

^CTokyo Denki Univ., 2-2 Kanda-Nishiki-cho, Chiyoda-ku, Tokyo 101-8457, Japan

ABSTRACT

Combination of PLD and nitrogen radical beam has grown high quality TiN films on Si substrate without silicidation at the interface between TiN thin film and Si substrate even at growth temperature more than 700 °C. Additionally, X-ray photoelectron spectroscopy (XPS) revealed that this method achieved synthesis of almost stoichiometric TiN films. Diffusion barrier characteristics of the grown film were examined by deposition of Al thin films of about 400 nm thick on the TiN grown films, followed by post-thermal treatment at 500 °C for 30 minutes. Scanning electron microscopy (SEM) observation and Rutherford backscattering spectroscopy (RBS) analysis revealed that sharp interfaces between Al and TiN were maintained after the thermal treatment, indicating excellent property of the TiN films as Si barrier metal.

Keywords: PLD, Radical beam, Nitrogen radical, Barrier metal, TiN, Nitride, Thin film.

1. INTRODUCTION

TiN thin films are of great use for electronic and mechanical industry due to their excellent properties of high hardness, high melting point, good electric conductivity, and good diffusion barrier [1-4]. For instance, TiN thin film is expected to be used as barrier metal in Si very large-scale integrated circuits (VLSI) which suppresses inter-diffusion during device fabrication processes and electromigration during device operation [1]. Crystallinity of the TiN film is one of the most important issues for the barrier property. The polycrystalline film is usually composed of columnar structures with grain boundaries normal to the substrate. In this structure, the grain boundaries enhance thermal diffusion, resulting in degradation of ability for barrier metal. TiN thin films have been so far grown by various kinds of methods such as physical vapor deposition (PVD) and chemical vapor deposition (CVD) [5-7]. CVD has the potential to exhibit excellent step coverage; however, TiN films grown by CVD have a problem of contamination such as organic matters. Thus, it is not suitable for integrated circuits (IC) processing. The pulsed laser deposition (PLD) using an excimer laser, which is classified into PVD, is very attractive for growth of TiN as well as other nitride thin films [8-12]. The most simple way for TiN growth by PLD is the use of a TiN target, but high-purity TiN target are not available (typically 99.5%). Moreover, the grown films become Ti-rich when the growth is carried out in a vacuum. For the growth of high quality TiN thin film with little contaminations, it is necessary to use high-purity target. For this purpose, a high-purity Ti target which is commercially available, was ablated in N₂ gas ambient. But the grown films showed more Ti-rich than the case of TiN target. Furthermore, it is important to supply sufficient nitrogen during the growth to obtain stoichiometric films [13-14]. In this paper, to overcome these problems we demonstrate growth of high-quality TiN thin film on Si(100) substrate by hybrid nitrogen radical beam-PLD using high-purity titanium (Ti:99.99%) metal target and nitrogen radical beam. Additionally, diffusion barrier characteristics of the grown film were examined.

2. EXPERIMENTAL PROCEDURE

Schematic illustration of hybrid radical-beam PLD system used in this study is shown in Fig. 1. The TiN thin films were grown on Si(100) substrates using a high purity metal Ti target (purity: 99.99%) and nitrogen radical beam gun. Nitrogen radical was generated by radio frequency (RF) excitation in the radical beam gun. The surfaces of the samples were terminated with hydrogen by dipping in 10% HF acid solution after ultrasonic cleaning in organic solutions. Then, the

*Correspondence: E-mail: kobata@postman.riken.go.jp

Si substrate was placed parallel to the Ti target at a distance of 40 mm in a vacuum chamber. The Ti target was ablated by a KrF excimer laser (wavelength: 248 nm, pulse duration: 34 ns, repetition rate: 5 Hz) with an incident angle of 45°. The laser beam was spatially homogenized by using a couple of fly's eye lenses to reduce the number of particles incorporated into the films as well as to improve crystallinity [12]. Homogenized beam was projected to the target through an aperture (9.0×9.0 mm²) and fused quartz lenses. The spatial uniformity of laser beam at this target was more than 95%. The irradiated area on the Ti target was formed to be 4.1 mm² (1.7×2.4 mm²). Film thickness of grown films for each fluence was set to be constant (about 150 nm) by controlling growth time. The RF power of radical beam was varied from 0 (N₂ gas ambient) to 550 W, here larger RF power generates larger amount of nitrogen radicals. The substrate temperature during the growth was varied from room temperature (RT) to 900 °C. The chamber was evacuated down below 5×10⁻⁷ torr using a turbomolecular pump before the growth. After evacuation, the pressure was kept at 8.0×10⁻⁴ torr by filling high purity nitrogen gas (above 99.998%). Nitrogen radical was continuously introduced to Si surface during the growth. Diffusion barrier characteristics were examined by deposition of Al thin films of about 400 nm thick on the grown TiN films by RF sputtering, followed by post-thermal treatment at 500 °C for 30 min. The orientation and crystallinity of TiN thin films were evaluated by X-ray diffraction (XRD: Cu K α radiation). Chemical binding energy as well as N/Ti ratio of the grown films was X-ray photoelectron spectroscopy (XPS). Surface morphology of the grown films was observed by atomic force microscopy (AFM). Cross-sectional structures of the prepared sample were examined by Rutherford backscattering spectroscopy (RBS) and scanning electron microscopy (SEM).

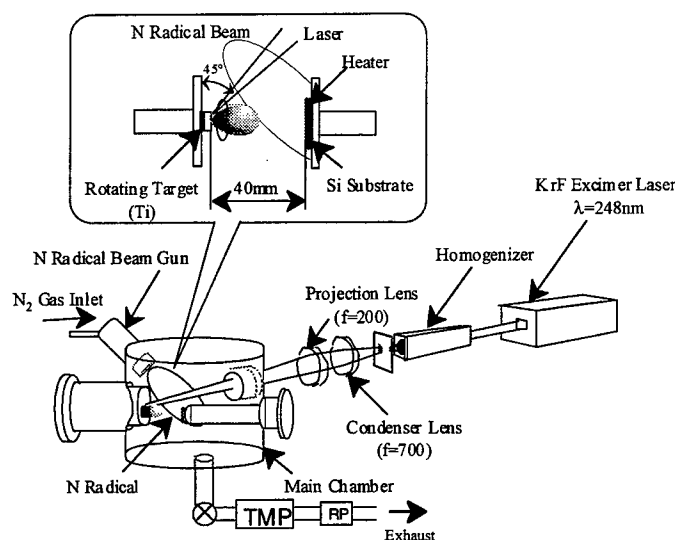


Figure 1. Schematic illustration of experimental setup for TiN growth by hybrid radical beam-PLD.

3. RESULTS AND DISCUSSION

Every sample prepared under different conditions (laser fluence, RF power of nitrogen radical beam, and growth temperature) shows gold color. Figure 2(a) shows XRD patterns of TiN thin films grown on Si(100) substrate with nitrogen radical as a function of the growth temperatures. The orientation and crystallinity are sensitive to growth temperature, laser fluence and RF power of nitrogen radical beam. During the growth, laser fluence and RF power of nitrogen radical beam are kept at an optimum condition of 550 W of RF power and 2.5 J/cm² of laser fluence in this experimental setup [13]. X-ray diffraction (XRD) pattern indicates TiN thin film at RT has no crystallinity. However at a growth temperature above 300 °C, sharp peak near 42.59° which corresponds to the TiN(200) orientation appears and intensities are drastically enhanced with increasing the growth temperature. Therefore, the grown film has preferred orientation of TiN(200) being parallel to the Si(100) substrate. Narayan et. al. suggested that four unit cells of TiN matched with three unit cells of Si with about 4.0% misfit [8]. Thus, this preferred orientation was determined by Si(100) substrate. For comparison, XRD patterns of TiN thin films grown on Si(100) substrate in nitrogen gas ambient (N₂) are shown in Fig. 2(b). The peaks at TiN(200) are much smaller than those for the radical beam samples even at 900 °C, and peaks corresponding to titanium oxides are observed for some of the samples. Moreover, at the temperature beyond 700 °C, peaks corresponding to titanium silicide (TiSi₂) were

observed. Thus, it deduced that silicidation between TiN film and Si substrate takes place during the growth in N_2 gas ambient at the higher temperature.

The rocking curve of XRD gives information about the crystallinity of the thin films. Figure 3 shows FWHM values of the rocking curve of TiN(200) for the sample used in Fig. 2(a). The FWHM monotonously decreases with increasing growth temperature and almost saturated at more than 700 °C. A minimum value as small as 0.998° was obtained at growth temperature of 700 °C.

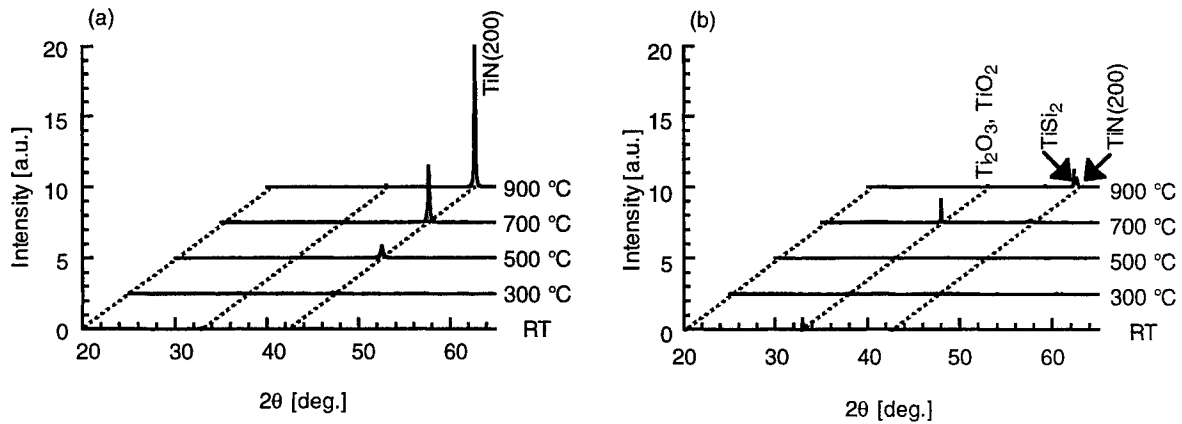


Figure 2. Dependence of XRD spectra of TiN grown films on substrate temperature (a)with nitrogen radical and (b)in N_2 gas ambient.

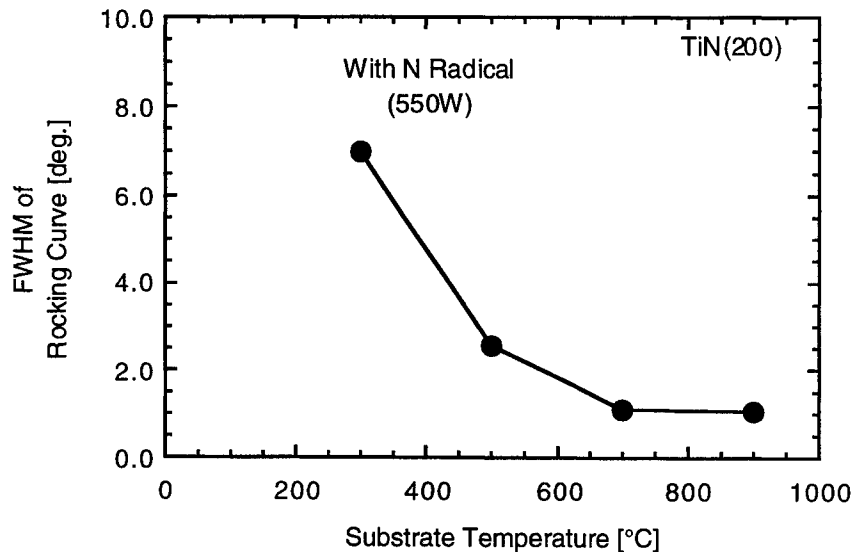


Figure 3. Dependence of rocking curve values of the diffraction peak at TiN(200) on substrate temperature.

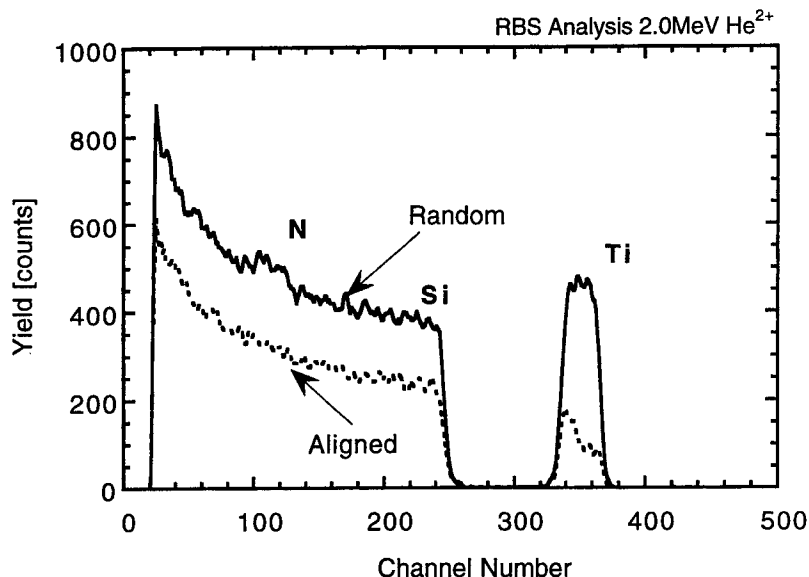


Figure 4. Random (solid line) and aligned (dashed line) RBS spectra of the grown TiN film with nitrogen radical.

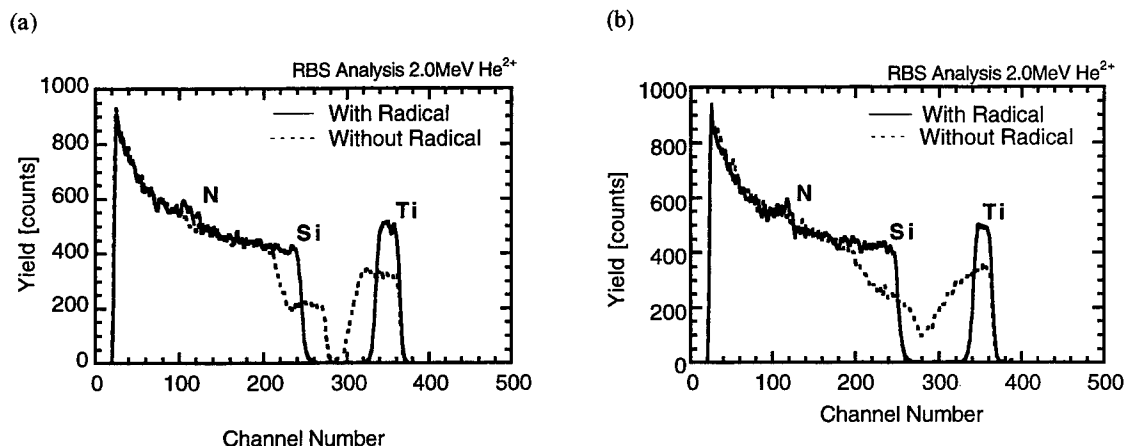


Figure 5. RBS spectra of TiN films grown with nitrogen radical and N_2 gas ambient at (a) 700 °C and (b) 900 °C.

Crystallinity of the grown film was also evaluated by RBS. Figure 4 shows random (solid line) and aligned (dashed line) RBS spectra of the sample prepared by nitrogen radical at the optimum condition, i.e., 2.5 J/cm² of laser fluence, 550 W of RF power of radical beam, and 700 °C of growth temperature. χ_{min} of nitrogen radical sample, which is defined as the average ratio of aligned yield to random yield at 10 channel numbers just behind surface peak of Ti aligned spectrum, is estimated to be 19.6%. This value is corresponded to that of epitaxially grown film published value for TiN thin films grown on Si [8]. Higher yield of Ti spectrum at deeper region and Si spectrum may be due to scattering by disordering at the interface ascribing lattice mismatch.

RBS random spectra of sample grown at 700 and 900 °C in nitrogen radical (solid line) and N_2 gas ambient (dashed line) were shown in Fig. 5. The films grown in nitrogen radical show sharp interface without inter-diffusion during the growth even at the high temperature beyond 700 °C. On the other hand, the films grown in N_2 gas ambient show obvious inter-diffusion of Ti and Si across the interface. This inter-diffusion formed TiN observed in Fig. 2(b).

Surface morphology of the grown films was observed by AFM. Figure 6 (a) and (b) show AFM images of TiN film grown in nitrogen radical at RT and 700 °C, respectively. AFM images indicate that the films grown in nitrogen radical maintain very smooth surface even at 700 °C. In the meanwhile, those of TiN films grown in N₂ gas ambient at RT and 700 °C are shown in Fig. 6 (c) and (d). The RT sample seems to be almost same as nitrogen radical sample. However surface roughness increases with increasing the growth temperature. It is deduced that silicidation at interface between the TiN film and Si substrate induces this significant roughness.

The chemical binding energy and N/Ti ratio of the grown TiN film were analyzed by XPS. Figure 7 shows the XPS spectra of Ti2p and N1s core level from TiN thin films grown at 900 °C with nitrogen radical and N₂ gas ambient. To remove the surface contamination layer, short Ar⁺ etching was carried out before the XPS analysis. The chemical binding energy of Ti2p_{3/2}, and N1s for both samples are shifted to 254.8 eV and 396.8 eV, respectively. These chemical shifts mean formation of the chemical bond of TiN. From these spectra, N/Ti ratio of the films grown in nitrogen radical and in N₂ gas ambient were estimated to be 0.97 and 0.84, respectively. In this quantitative estimation, commercial TiN target with N/Ti ratio of 0.95 was used for control. Thus, nitrogen radical beam-PLD achieves synthesis of almost stoichiometric TiN film.

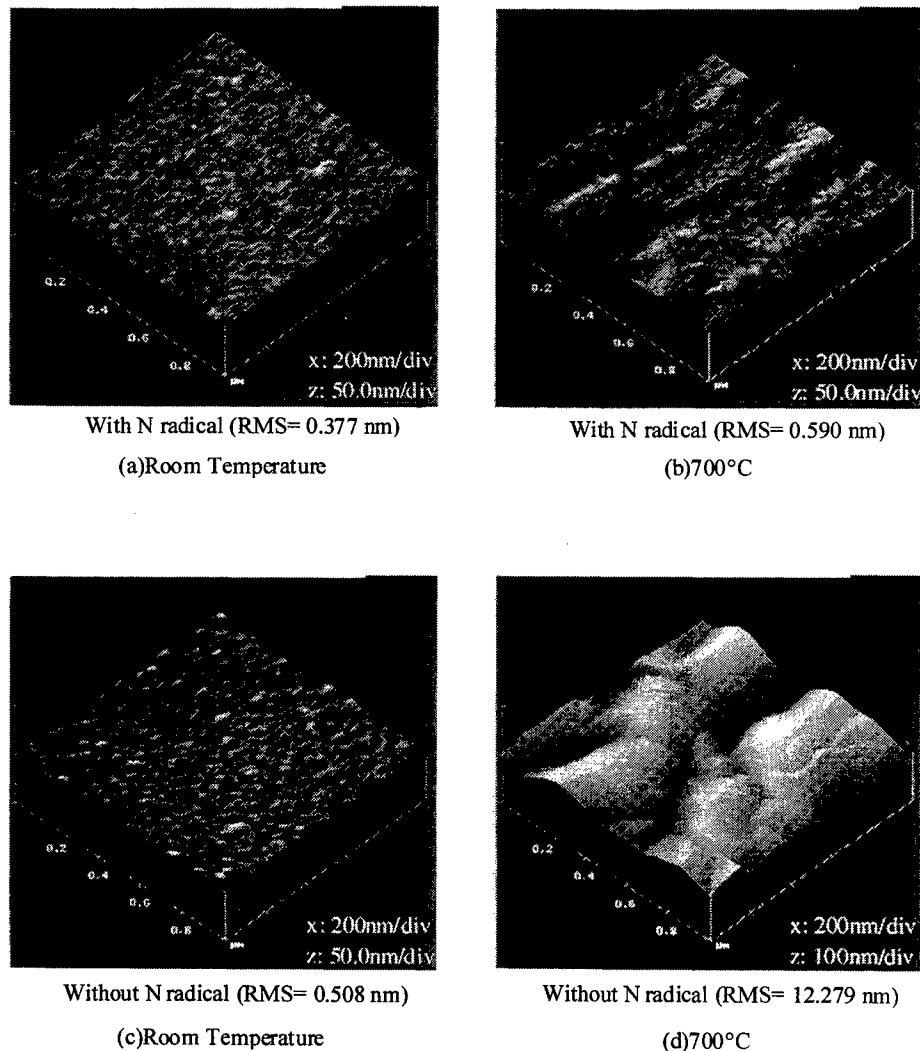


Figure 6. AFM images of TiN films grown with nitrogen radical ((a) RT and (b) 700 °C) and N₂ gas ambient at ((c) RT and (d) 700 °C).

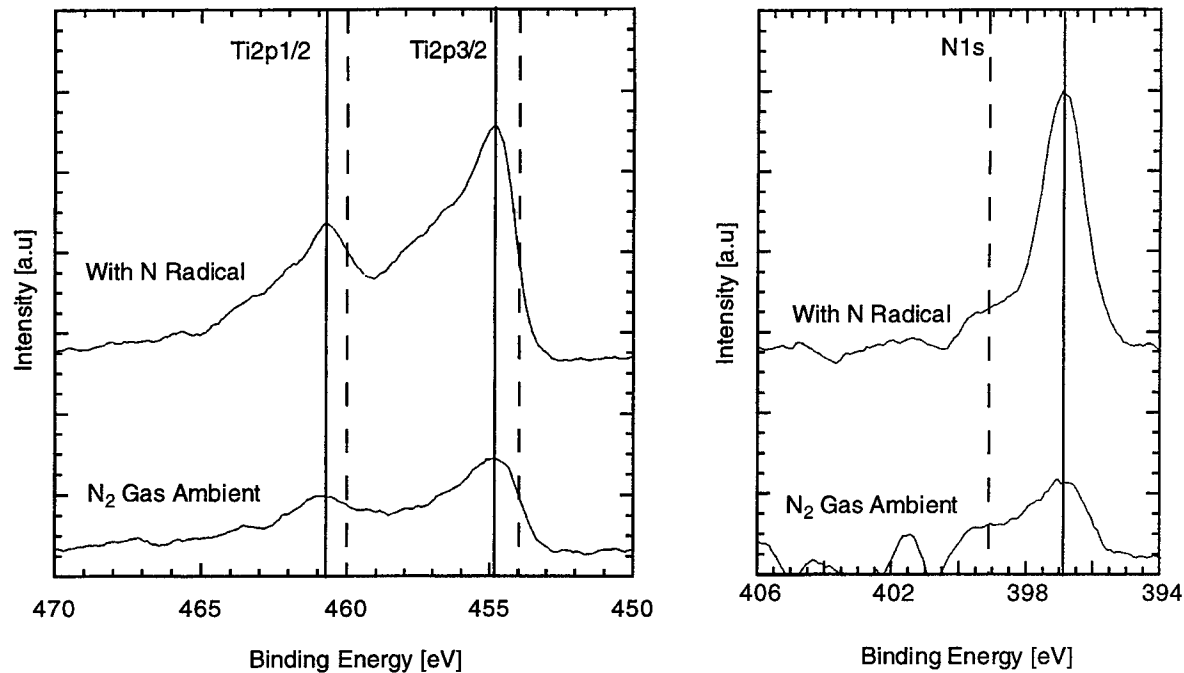


Figure 7. XPS spectra of Ti2p and N1s of TiN thin films grown in (a) nitrogen radical and (b) N₂ gas ambient at growth temperature of 900 °C.

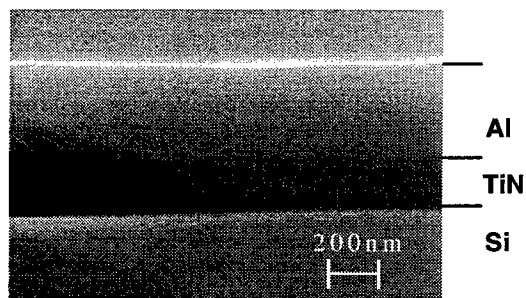


Figure 8. Cross-sectional image of SEM observation after thermal treatment at 500 °C for 30 min.

Excellent crystalline and stoichiometric TiN thin film can be applied for high-quality diffusion barrier metal in Si IC. Barrier characteristic of the grown film was examined by deposition of Al film of about 400 nm, followed by post-thermal treatment. Aluminum was deposited by RF sputtering at RT, then thermal treatment was carried out at 500 °C for 30 minutes in nitrogen gas ambient. Figure 8 shows cross-sectional SEM photograph of the film grown with nitrogen radical at the optimum condition. SEM photograph shows sharp contrasts at each interface. Therefore, little inter-diffusion induced by the thermal treatment occurs at each interface.

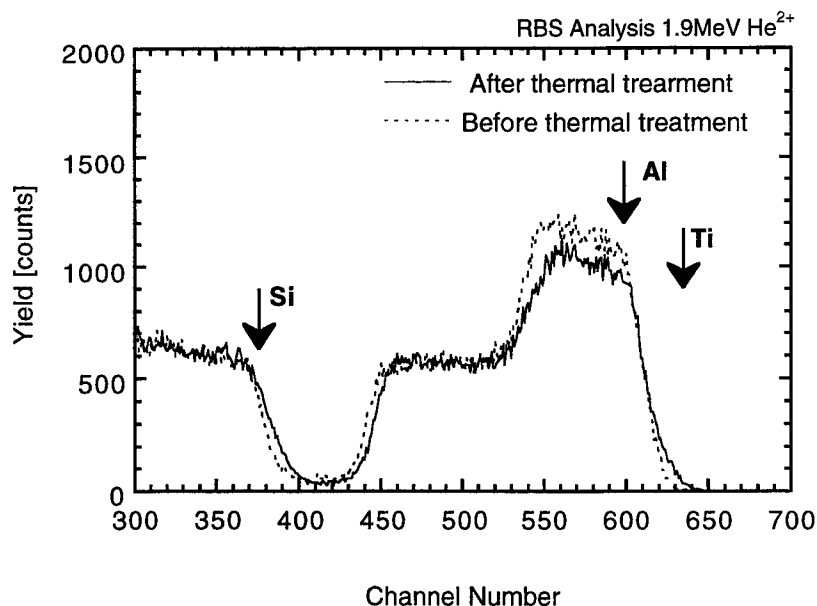


Figure 9. RBS spectra of TiN films grown with nitrogen radical before and after thermal treatment at 500 °C for 30 min.

The barrier metal characteristic was also evaluated by RBS. Figure 9 shows RBS random spectra before and after the thermal treatment. RBS spectrum of the sample after thermal treatment shifts to somewhat higher channel number compared with that of before thermal treatment. This is attributed to non-homogeneity of thickness of the TiN films and Al films. Spectra between 430 and 450 and between 370 and 400 correspond to Al signals from Al/TiN interface and to Si signals from TiN/Si interface, respectively. Gradients of both spectra after thermal treatment almost agree to those before thermal treatment, indicating that sharp interfaces between Al and TiN and between TiN and Si are maintained even after the thermal treatment. Thus, it is concluded that the grown TiN film has excellent property for Si barrier metal.

4. CONCLUSIONS

The high-quality TiN films were grown by PLD using a high purity titanium target with high reactive nitrogen radicals. XRD measurement revealed that the preferred growth of TiN(200) being parallel to the Si(100) substrate was obtained. The peak intensity of TiN(200) became stronger with increasing growth temperature. The FWHM of rocking curve of XRD was carried out as functions of growth temperature. The narrowest value of 0.998° was obtained at the optimum condition of 550 W, 2.5 J/cm², and 700 °C. Additionally, RBS spectra indicated that χ_{\min} was 19.6% which was compared to that published by other groups. RBS spectra also indicated that nitrogen radical suppressed silicidation at the interface between Si substrate and TiN film during the growth. Surface roughness of the grown films was less than 0.6 nm even at 700 °C of growth temperature. On the other hand, that of the film grown in N₂ gas ambient increased to more than 12 nm with increasing the growth temperature. The binding energy of Ti2p_{3/2} and N1s core level observed by XPS were 254.8 eV and 396.8 eV respectively, indicating formation of TiN compound. The grown films had almost stoichiometric composition of 0.97, while that by N₂ gas ambient showed Ti-rich. The film grown at the optimum condition kept sharp interface structures even after thermal treatment at 500 °C for 30min, indicating excellent property as barrier metal. Therefore, we conclude that the hybrid nitrogen radical beam-PLD is of great use for growth of high-quality TiN thin film for the barrier metal in Si IC.

ACKNOWLEDGMENT

The authors thank Y. Iimura, M. Otake, and M. Sakamoto for their helps in the measurement of XRD, AFM, and SEM respectively. One of the authors was supported by a grant from the Junior Research Associate (JRA) program of RIKEN.

REFERENCES

- [1] M. Wittmer, *J. Vac. Sci. Technol.*, **A2**, 273(1981).
- [2] N. Biunno, J. Narayan, S. K. Hofmeister, A. R. Srivatsa, and R. K. Singh, *Appl. Phys. Lett.*, **54**, 1519(1989).
- [3] M. Kottke, R. Gregory, F. Pintchovski, E. Travis, and P. J. Tobin, *J. Vac. Sci. Technol.*, **B9**, 74(1991).
- [4] S. Soube, T. Yamauchi, H. Suzuki, S. Mukainakano, O. Takenaka, and T. Hattori, *Appl. Surf. Sci.*, **117/118**, 308(1997).
- [5] B. O. Johansson, J. E. Sundgren, and J. E. Greene, *J. Vac. Sci. Technol.*, **A3**, 303(1985).
- [6] J. E. Greene, J. E. Sundgren, L. Hultman, I. Petrov, and D. B. Bergstrom, *Appl. Phys. Lett.*, **67**, 2928(1995).
- [7] P. M. Sumith and J. S. Custer, *Appl. Phys. Lett.*, **70**, 3116(1997).
- [8] J. Narayan, P. Tiwari, X. Chen, J. Singh, R. Chowdhurt, and T. Zheleva, *Appl. Phys. Lett.*, **61**, 1290(1992).
- [9] I. N. Mihailescu, E. Gyorgy, N. Chitica, V. S. Teodorescu, G. Mavin, A. Luches, A. Perrone, M. Martino, and J. Neamtu, *J. Mater. Sci.*, **31**, 2909(1996).
- [10] R. Timm, P. R. Willmott, and J. R. Huber, *Appl. Phys. Lett.*, **71**, 1996 (1997).
- [11] S. Xu, L. Du, K. Sugioka, and K. Toyoda, *J. Mater. Sci.*, **33**, 1777(1998).
- [12] K. Obata, K. Sugioka, H. Takai, and K. Midorikawa, *Appl. Surf. Sci.*, **138/139**, 335(1999).
- [13] K. Obata, K. Sugioka, K. Toyoda, H. Takai, and K. Midorikawa, *Appl. Phys.*, **A**, (in press).
- [14] D. Cracium and V. Cracium, *Appl. Surf. Sci.*, **54**, 75(1992).

Laser Ablation of Solid Films at a Cryogenic Temperature

Hiroyuki Niino*, Tadatake Sato, Akira Yabe
National Institute of Materials and Chemical Research (NIMC)
Higashi 1-1, Tsukuba, Ibaraki 305-8565 JAPAN

ABSTRACT

In order to create new possibilities of laser ablation technique, the laser ablation of nitrogen solid films deposited on a copper plate at 10 K was performed upon irradiation with a picosecond UV laser (FHG of Nd:YLF laser; $\lambda=263$ nm, $\tau=8$ ps, rep. rate=10 Hz) in vacuum. UV and visible emissions, which were ascribed to the transition from excited molecular and atomic nitrogen, were detected on the film during the laser irradiation at the fluence of 5 J/cm²/pulse. These excited species would be produced in a multi-photon absorption process of the nitrogen by the ps-laser irradiation. At the fluence of ca. 10 J/cm²/pulse, ablation of the film was observed. Plume of the ablation reacted with the surface of graphite (HOPG). XPS analysis indicated that nitrides formed on the graphite surface by the exposure to the plume. A novel technique for surface modification of materials is made possible by the ps-laser ablation of nitrogen solid film.

Keywords: laser ablation, nitrogen solid, picosecond UV laser, cryogenic temperature, plume reactivity, emission spectroscopy, surface reaction, X-ray photoelectron spectroscopy

1. INTRODUCTION

Ablative photodecomposition of materials with pulsed lasers has been shown to be useful for etching, surface modification, and thin film deposition.^{1,2} One aspect of the ablation process which has been studied extensively is the fact that the fragments emitted explosively from the surface of materials include large amounts of reactive intermediates such as radicals and ions.³⁻⁷ This suggests the possibility of utilizing the reactive intermediates in a novel method for the chemical modification of material surfaces, as this method can produce a pulsed beam of intermediates with a higher density compared to the pulsed super sonic method.⁸ In our previous reports,^{9,10} we investigated the chemical reactivity of the intermediates produced by the ablation of a solid film of a photoreactive organic molecule in an argon matrix at 10 K. In the present study to intend new possibilities of laser ablation technique, we have investigated the laser ablation of nitrogen solid films induced by UV picosecond (ps) laser irradiation at cryogenic temperature. Chemically activated nitrogen species is quite useful for fabricating a nitride material applied into electronics and optics. However, molecular nitrogen is an inert compound, and has no single-photon absorption band in UV, visible, and IR region^{11,12}. For such transparent molecule, multi-photon excitation by pulsed laser irradiation with high intensity would be an effective technique to form excited states of the molecules.^{13,14}

In this paper, we monitored precisely the photolysis of nitrogen solid film by UV-visible optical emission spectroscopy with an intensified CCD (ICCD) camera. Moreover, chemical modification of graphite surface was induced by exposure to a plume from ablated nitrogen solid, and detected by X-ray photoelectron spectroscopy (XPS). Electronic absorptions of molecular nitrogen were confirmed by a calculation according to time-dependent density functional theory (TD-DFT).¹⁵

*Correspondence: Email: niino@nimc.go.jp; Tel: +81-298-61-4562; Fax: +81-298-61-4474

2. EXPERIMENTAL

To prepare a solid film of nitrogen, nitrogen gas (>99.9995 %) was deposited on a copper plate at 8-10 K in a vacuum chamber (10^{-4} - 10^{-5} Pa). Thickness of the film on the plate was approximately 2 nm. The deposited film was irradiated with a UV ps-laser (Fourth harmonic wavelength (FHG) of Nd:YLF laser; $\lambda = 263$ nm (4.7 eV), $\tau = 8$ ps, intensity = $1.5 \text{ mJ} \cdot \text{pulse}^{-1}$, repetition rate = 10 Hz) in vacuum, as shown in Fig. 1. Four of dichroic mirror were employed to reduce the contamination of second harmonic wavelength (SHG) light in the FHG laser beam, because SHG wavelength is close to one of the atomic nitrogen emissions. The laser beam was focused with a plano-convex quartz lens.

Optical emission spectrum of photoproducts on the plate was measured with an ICCD camera system (Princeton Instruments, I-MAX) with a 105-mm Nikon telephoto lens (UV-Nikkor). The emission was detected on the ICCD through a monochromator (Acton Research Co., SP-150) having diffraction gratings of $1200 \text{ grooves} \cdot \text{mm}^{-1}$ (resolution: $< 0.5 \text{ nm}$) and $150 \text{ grooves} \cdot \text{mm}^{-1}$ (resolution: $< 2 \text{ nm}$). A glass filter (cut-off: 290 nm) was used to eliminate scattering of the excitation laser beam on the film. The emission was accumulated on a computer under the laser irradiation at 10 Hz for 5-100 s.

A plate of highly oriented pyrolytic graphite (HOPG) at room temperature (RT) was used as targets for exposure to the plume beam at a distance of ca. 2 cm from the cryogenic nitrogen solid. The surface of the modified HOPG plate was analyzed by XPS (Perkin Elmer Co., PHI-5600ci; X-ray: monochromatic Al-K α). The atomic ratio of the polymer surface was estimated from the peak areas of XPS spectra recorded by fine scanning.

Theoretical vacuum UV (VUV) absorption bands (singlet and triplet) of nitrogen were estimated by the TD-DFT method without scaling at the UB3LYP/6-311+G(3df) level¹⁵. Optimized structure of molecular nitrogen (symmetry: $D_{\infty h}$) calculated by DFT at the B3LYP/6-311+G(3df) level showed 0.109119 nm for the internuclear distance (experimental observation: 0.1098 nm), and 15.84 eV for the first ionization potential (exp. obs.¹⁸: 15.58 eV).

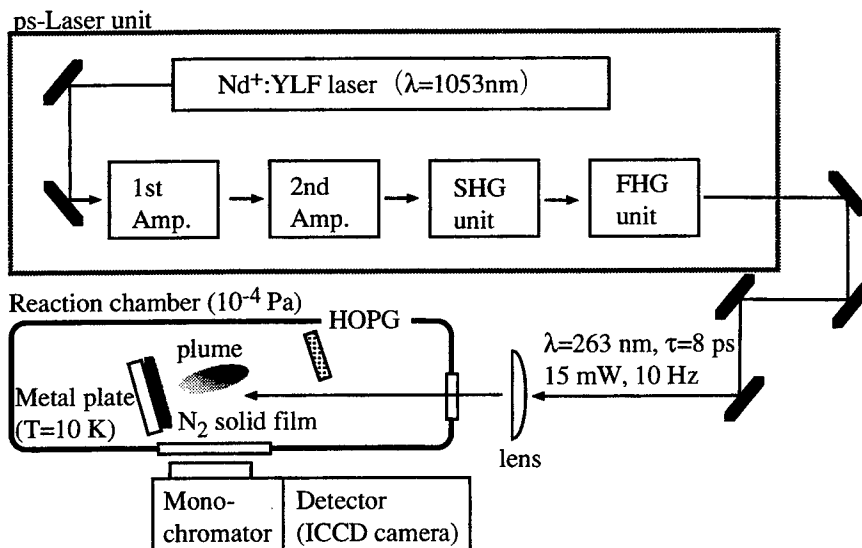


Fig. 1 Schematic drawing of experimental apparatus

3. RESULTS AND DISCUSSION

3.1 Photolysis of cryogenic nitrogen solid

When a cryogenic nitrogen solid film deposited on a copper plate at 10 K was irradiated with an ps-Nd:YLF laser at 263 nm with a fluence of $5 \text{ J} \cdot \text{cm}^{-2} \cdot \text{pulse}^{-1}$, new optical emission bands appeared in the UV and visible regions. Figure 2 shows emission spectrum in the range between 270 nm and 700 nm. The intense peak at 523.3 nm was ascribed to α emission (transition: $^2\text{D} \rightarrow ^4\text{S}$) of atomic nitrogen.¹⁶ The peak at 594.8 nm is a vibrational satellite (α' emission) line which corresponds to the simultaneous $0 \rightarrow 1$ transition in molecular nitrogen with the atomic $^2\text{D} \rightarrow ^4\text{S}$ emission. In the region between 280 nm and 400 nm, emissions from the electronically excited nitrogen molecule (Vegard-Kaplan system; $\text{A}^3\Sigma_u^+ (v'=0,1) \rightarrow \text{X}^1\Sigma_g^+ (v''=6-11)$) were observed. These phenomena indicated that excited molecular and atomic nitrogen were produced on the film by the laser irradiation. These excited species would be formed through a multi-photon absorption process of molecular nitrogen.

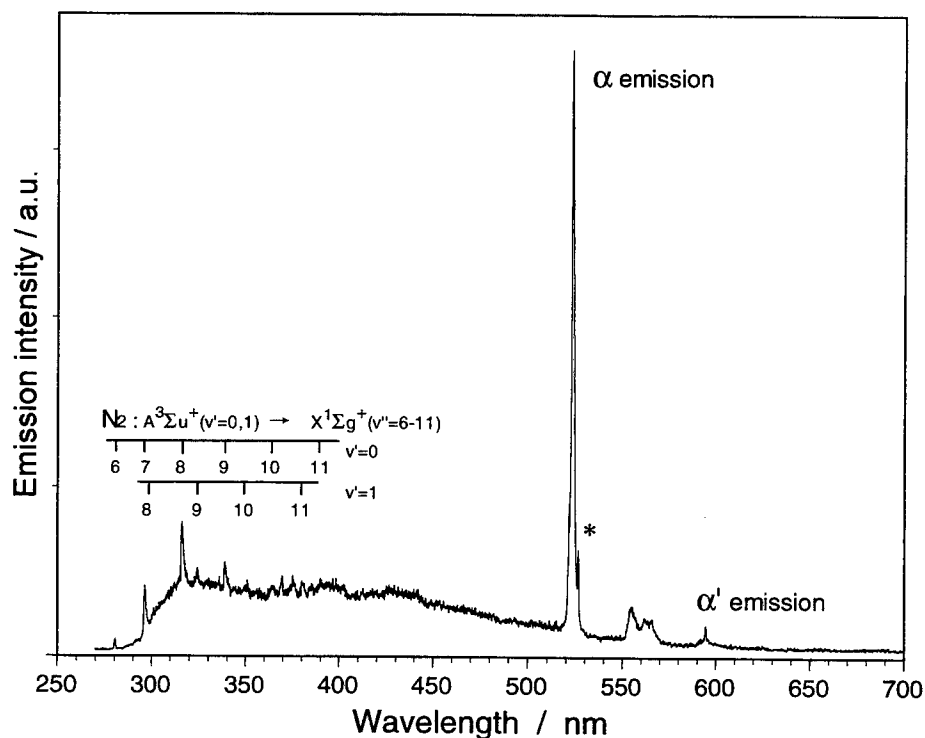


Fig. 2 Optical emission spectrum (high resolution) of a nitrogen solid film at 10 K. Excitation: ps-Nd:YLF laser at 263 nm with $5 \text{ J} \cdot \text{cm}^{-2} \cdot \text{pulse}^{-1}$. Asterisk in the Figure corresponds to scattering of the laser beam at the SHG wavelength of 526 nm.

Excitation states of the molecular nitrogen were estimated by TD-DFT calculation, as listed on Table 1. Due to some of the effects of electron correlation in modeling the excited state, TD-DFT method shows relatively good performance for estimation of high-lying bound electronic excitation energies of molecules.¹⁷ Tanaka and coworkers reported that the absorptions at the transitions of $X^1\Sigma_g^+(v'=0) \rightarrow B^3\Sigma_u^-(v''=0)$, $X^1\Sigma_g^+(v'=0) \rightarrow a^1\Pi_g(v''=0)$, $X^1\Sigma_g^+(v'=0) \rightarrow a'^1\Sigma_u^-(v''=0)$, $X^1\Sigma_g^+(v'=0) \rightarrow w^1\Delta_u(v''=0)$, and $X^1\Sigma_g^+(v'=0) \rightarrow C^3\Pi_u(v''=0)$ were experimentally observed at 151.9 nm, 145.0 nm, 147.6 nm, 139.4 nm, and 112.4 nm, respectively.¹² The ratio of observed and calculated energy (Calc./Obs.) on each transitions are 0.995, 1.096, 1.128, 1.109, and 0.968. Since these excitations are forbidden by the selection rule of orbital symmetry, absorption coefficient of the absorptions would be small. Koda and coworkers have reported that, at the irradiation of a nanosecond KrF excimer laser at 248 nm (5.0 eV), the increase rate of the a emission was experimentally dependent on the 2.8th power of the laser fluence.¹³ As shown in Table 1, a high oscillator strength of excitation states of $^1\Sigma_u^+$ and $^1\Pi_u$ at around 13 eV was theoretically predicted. These results suggested that molecular nitrogen would decompose to atomic nitrogen through a high-lying excited state having a sufficient oscillator strength.

Table 1 Electronic excited states of molecular nitrogen ($D_{\infty h}$ symmetry) from the ground state ($X^1\Sigma_g^+$), calculated by time-dependent density functional theory (TD-DFT)^{a)}.

Excited State	Multiplicity	Transition	Major transitions ^{b)}	Excitation energy / eV	Wavelength / nm (Experimental Obs.) ¹²	Oscillator strengths
1	Triplet	$^3\Sigma_u^+$	$5 \rightarrow 8, 6 \rightarrow 9$	7.2494	171.03	0.0000
2	Triplet	$^3\Pi_g$	$7 \rightarrow 8, 7 \rightarrow 9$	7.6831	161.37	0.0000
3	Triplet	$^3\Delta_u$	$5 \rightarrow 8, 6 \rightarrow 9$	8.1195	152.70	0.0000
4	Triplet	$^3\Sigma_u^-$	$5 \rightarrow 9, 6 \rightarrow 8$	8.1196	152.70 (151.9)	0.0000
5	Singlet	$^1\Pi_g$	$7 \rightarrow 8, 7 \rightarrow 9$	9.3680	132.35 (145.0)	0.0000
6	Singlet	$^1\Sigma_u^-$	$5 \rightarrow 9, 6 \rightarrow 8$	9.4740	130.87 (147.6)	0.0000
7	Singlet	$^1\Delta_u$	$5 \rightarrow 8, 6 \rightarrow 9$	9.8603	125.74 (139.4)	0.0000
8	Triplet	$^3\Pi_u$	$4 \rightarrow 8, 4 \rightarrow 9$	10.6821	116.07 (112.4)	0.0000
9	Triplet	$^3\Sigma_g^+$	$7 \rightarrow 10$	12.0733	102.69	0.0000
10	Singlet	$^1\Sigma_g^+$	$7 \rightarrow 10$	12.8103	96.78	0.0000
11	Triplet	$^3\Sigma_u^+$	$7 \rightarrow 11$	12.8575	96.43	0.0000
12	Singlet	$^1\Sigma_u^+$	$7 \rightarrow 11$	13.0227	95.21	0.3349
13	Triplet	$^3\Pi_u$	$7 \rightarrow 12, 7 \rightarrow 13$	13.0780	94.80	0.0000
14	Singlet	$^1\Pi_u$	$7 \rightarrow 12, 7 \rightarrow 13$	13.2091	93.86	0.0766
15	Triplet	$^3\Pi_u$	$5 \rightarrow 10, 6 \rightarrow 10$	13.2770	93.38	0.0000
16	Singlet	$^1\Pi_u$	$5 \rightarrow 10, 6 \rightarrow 10$	13.3663	92.76	0.2986
17	Singlet	$^1\Pi_u$	$4 \rightarrow 8, 4 \rightarrow 9$	13.7376	90.25	0.2302
18	Triplet	$^3\Sigma_g^+$	$5 \rightarrow 13, 6 \rightarrow 12$	13.9369	88.96	0.0000
19	Triplet	$^3\Pi_g$	$5 \rightarrow 11, 6 \rightarrow 11$	13.9588	88.82	0.0000
20	Singlet	$^1\Sigma_u^+$	$5 \rightarrow 8, 6 \rightarrow 9$	13.9729	88.73	0.3722
21	Triplet	$^3\Sigma_g^+$	$5 \rightarrow 12, 6 \rightarrow 13$	14.0232	88.41	0.0000
22	Singlet	$^1\Pi_g$	$5 \rightarrow 11, 6 \rightarrow 11$	14.0776	88.07	0.0000
23	Singlet	$^1\Sigma_g^+$	$5 \rightarrow 13, 6 \rightarrow 12$	14.1303	87.74	0.0000
24	Singlet	$^1\Sigma_g^+$	$5 \rightarrow 12, 6 \rightarrow 13$	14.1851	87.40	0.0000
25	Singlet	$^1\Sigma_g^+$	$7 \rightarrow 14$	14.4492	85.81	0.0000
26	Triplet	$^3\Sigma_g^+$	$7 \rightarrow 14$	14.4718	85.67	0.0000
27	Singlet	$^1\Sigma_g^+$	$7 \rightarrow 14, 6 \rightarrow 12$	15.0565	82.35	0.0000

^{a)} Calculation: UB3LYP/6-311+G(3df)//B3LYP/6-311+G(3df) on Gaussian 98

^{b)} Electronic configuration of the ground state of N_2 at the 6-311+G(3df) level:

$$(\sigma_g)^2 (\sigma_u)^2 (\sigma_g)^2 (\sigma_u)^2 (\pi_u)^2 (\pi_u)^2 (\sigma_g)^2 (\pi_g)^0 (\sigma_g)^0 (\sigma_u)^0 (\pi_u)^0 (\pi_u)^0 (\sigma_g)^0 \dots$$

The intensity of the α emission at 523 nm increased gradually with increases in the number of laser shots at the repetition rate of 10 Hz, as shown in Fig. 3. After the end of the laser irradiation, the emission intensity decayed single-exponentially with the rate constant of $k = 0.0272 \text{ s}^{-1}$ (mean life: $k^{-1} = 36.8 \text{ s}$). It is worth noting that, at the restart of the laser irradiation, the emission intensity was rapidly recovered to that at the final pulse before the last interruption. These observations indicate that atomic nitrogen formed by the photolysis was trapped in nitrogen solid. The trapped atoms were excited by the laser irradiation. Figure 4 shows the emission spectrum of the film after the end of the laser irradiation. The α and α' emissions were clearly observed.

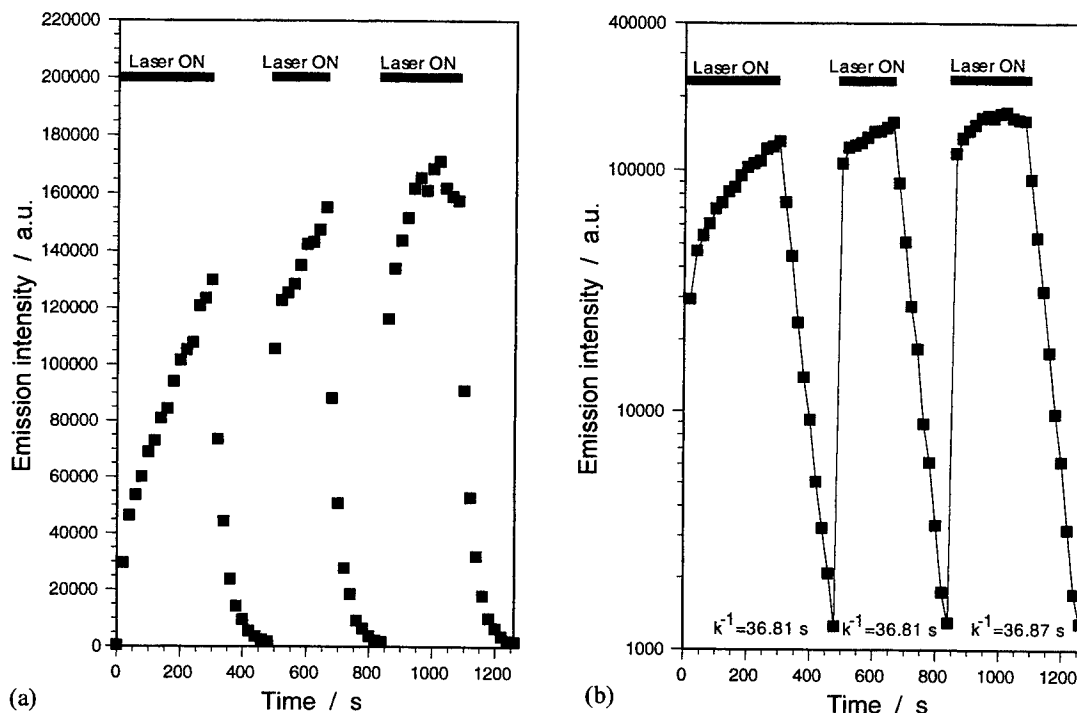


Fig. 3 The time course of intensity of atomic nitrogen emission ($^2\text{D} \rightarrow ^4\text{S}$); (a) normal scale, (b) logarithm scale. Bar means the period of the laser irradiation at 10 Hz.

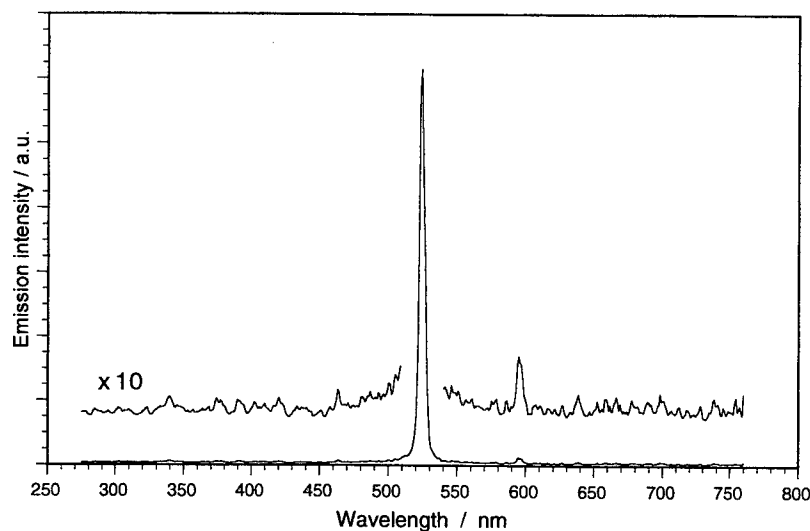


Fig. 4 Optical emission spectrum (low resolution) of a nitrogen solid film after the excitation of the ps-Nd:YLF laser.

3.2 Laser ablation of nitrogen solid film: surface modification of graphite using the plume of ablation

Upon the laser irradiation at fluence of $10 \text{ J} \cdot \text{cm}^{-2} \cdot \text{pulse}^{-1}$, the nitrogen film was ablated on the plate. An explosive plume emission of a considerable amount of the deposited material was observed. The chemical reactions of a HOPG surface with the reactive intermediates produced by the ablation of nitrogen solid film were studied in terms of surface modification of the plate. After treatment with a plume formed by the laser irradiation at $10 \text{ J} \cdot \text{cm}^{-2} \cdot \text{pulse}^{-1}$ for 30 s, a new N_{1s} peak was observed in an XPS spectrum for a HOPG plate (Fig. 5). This new peak indicates that the reactive intermediates produced by the ablation are immobilized through chemical bonds onto the HOPG surface, because the molecular nitrogen physically adsorbed on a substrate are easily desorbed from the surface at RT in a vacuum chamber. Figure 6 shows that the fine scan of C_{1s} and N_{1s} region on XPS. The C_{1s} spectrum of the laser-treated surface indicates new components as a shoulder at a high binding energy side of graphite peak of 285 eV. This shoulder would correspond to a nitride formation in the surface reactions. These XPS results suggest that the chemical reactivity of the plume can be mainly attributed to chemically activated nitrogen species.

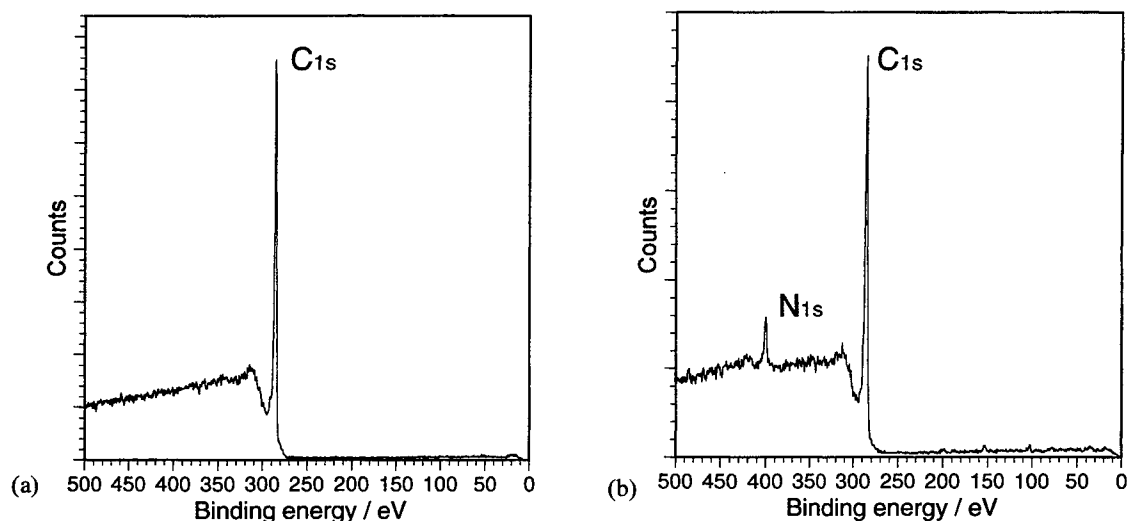


Fig. 5 XPS spectra recorded with a survey scan of the surface of HOPG; (a) before and (b) after plume treatment.

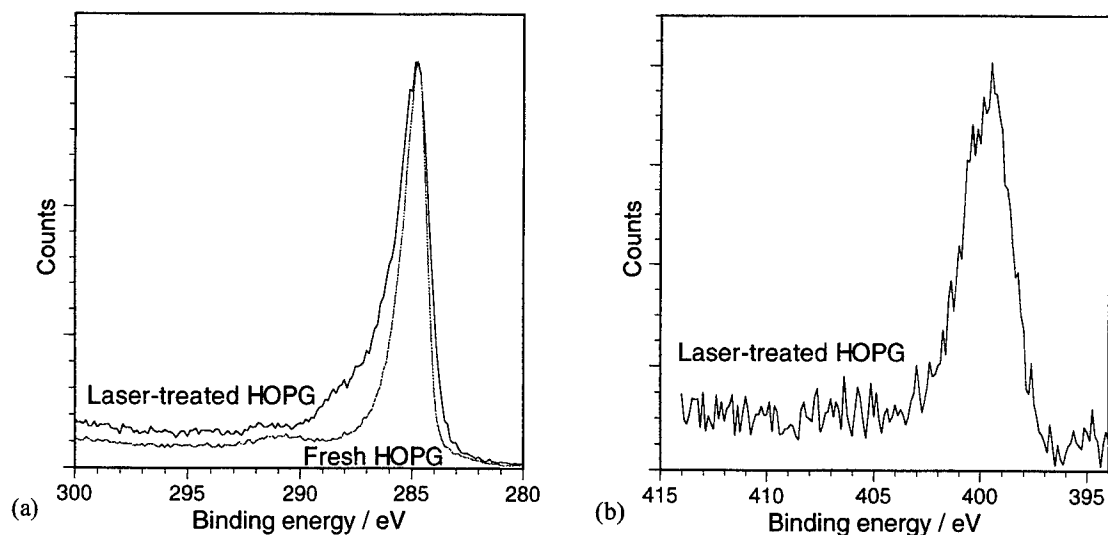


Fig. 6 XPS spectra recorded with a fine scan of the surface of HOPG; (a) C_{1s} region and (b) N_{1s} region.

4. CONCLUSION

We demonstrated that a new technique for the ablation of nitrogen induced by UV ps-laser irradiation. Multi-photon excitation of cryogenic nitrogen solid film would produce a plume including reactive species of nitrogen. By using the reactive nitrogen plume, chemical surface modification of a carbon material would be useful for fabricating nitrides for electronic and optical application.

REFERENCES

1. D. Bäuerle, *Laser Processing and Chemistry*, 2nd Edn., Springer-Verlag, Berlin, pp.191-228, 1996.
2. R. Srinivasan and B. Braren, "Ultraviolet laser ablation of organic polymers", *Chem. Rev.*, **89**, pp.1303-1316, 1989.
3. Y. Tsuboi, K. Hatanaka, H. Fukumura, and H. Masuhara, "The 248 nm Excimer Laser Ablation of Liquid Benzene Derivatives: A Relation between Ablation Threshold and Molecular Photochemical Reactivity", *J. Phys. Chem.*, **98**, pp.11238-11241, 1994.
4. M. Kobayashi, A. Sato, Y. Tanaka, H. Shinohara, and H. Sato, "Photodissociation of multilayered trimethylaluminum adsorbed on a cryogenic substrate: a time-of-flight mass-spectrometric study", *Appl. Organomet. Chem.*, **7**, pp.303-309, 1993.
5. H. Niino and A. Yabe, "Positively charged surface potential of polymer films after excimer laser ablation: application to selective-area electroless plating on the ablated films", *Appl. Phys. Lett.*, **60**, pp.2697-2699, 1992;
6. H. Niino and A. Yabe, "Excimer laser polymer ablation: formation of positively charged surfaces and its application into the metalization of polymer films", *Appl. Surf. Sci.*, **69**, pp.1-6, 1993.
7. H. Niino, T. Imura, T. Ohana, C. Nagai and A. Yabe, "ESR study and surface reaction of laser-ablated polymer films", *Chem. Lett.*, pp.1341-1344, 1994.
8. D. Weber, A. Baronavski, T. Heavner, and C. Gordon III, "Synthetic applications of molecular beams", *J. Chem. Soc., Chem. Commun.*, pp.912-913, 1987.
9. H. Niino and A. Yabe, "Laser ablation of phenylazide in an argon matrix: direct observation and chemical reactivity of ablated fragments", *Appl. Phys.*, **A69**, pp.605-610, 1996.
10. H. Niino, Y. Koga, and A. Yabe, "Surface reaction of organic materials by laser ablation of matrix-isolated photoreactive aromatic azido compound", *J. Photochem. Photobiol. A: Chem.*, **106**, pp.9-13, 1997.
11. R. W. B. Pearse and A. G. Gaydon, *The identification of molecular spectra*, 4th Edn., John Wiley & Sons, New York, pp.217-229, 1976.
12. Y. Tanaka, M. Ogawa, and A. S. Jursa, "Forbidden Absorption-band systems of N₂ in the vacuum-ultraviolet region", *J. Chem. Phys.*, **40**, pp.3690-3700, 1964.
13. H. Kajihara, F. Okada, and S. Koda, "Multi-photon induced atomic nitrogen production in a low-temperature nitrogen crystal", *Chem. Phys.*, **186**, pp.395-400, 1994.
14. Y. Hiroshima, T. Ishiguro, and K. Esaki, "Formation of a frozen nitrogen target and characterization for the application of pulsed laser deposition", *Jpn. J. Appl. Phys.*, **36**, pp.798-804, 1997.
15. Gaussian 98, Revision A.7, M. J. Frisch, G. W. Trucks, H. B. Schlegel, G. E. Scuseria, M. A. Robb, J. R. Cheeseman, V. G. Zakrzewski, J. A. Montgomery, Jr., R. E. Stratmann, J. C. Burant, S. Dapprich, J. M. Millam, A. D. Daniels, K. N. Kudin, M. C. Strain, O. Farkas, J. Tomasi, V. Barone, M. Cossi, R. Cammi, B. Mennucci, C. Pomelli, C. Adamo, S. Clifford, J. Ochterski, G. A. Petersson, P. Y. Ayala, Q. Cui, K. Morokuma, D. K. Malick, A. D. Rabuck, K. Raghavachari, J. B. Foresman, J. Cioslowski, J. V. Ortiz, A. G. Baboul, B. B. Stefanov, G. Liu, A. Liashenko, P. Piskorz, I. Komaromi, R. Gomperts, R. L. Martin, D. J. Fox, T. Keith, M. A. Al-Laham, C. Y. Peng, A. Nanayakkara, C. Gonzalez, M. Challacombe, P. M. W. Gill, B. Johnson, W. Chen, M. W. Wong, J. L. Andres, C. Gonzalez, M. Head-Gordon, E. S. Replogle, and J. A. Pople, Gaussian, Inc., Pittsburgh PA, 1998.
16. P. L. Kunsch and K. Dressler, "Calculation of dynamically induced electronic transitions of matrix-isolated atomic nitrogen", *J. Chem. Phys.*, **68**, pp.2550-2561, 1978.
17. M. E. Casida, C. Jamorski, K. C. Casida, and R. Salahub, "Molecular excitation energy to high-lying bound states from time-dependent density-functional response theory: Characterization and correction of the time-dependent local density approximation ionization threshold", *J. Chem. Phys.*, **108**, pp.4439-4449, 1998.
18. D. W. Turner, C. Backer, A. D. Baker, C. R. Brundle, *Molecular photoelectron spectroscopy: A Handbook of He 584A spectra*, John Wiley & Sons, London and New York, 1970.

Pulsed laser deposition of AlN thin films

Y. F. Lu*, Z. M. Ren, H. Q. Ni, Y. W. Goh, B. A. Cheong, S.

K. Chow, J. P. Wang, T. C. Chong

Laser Microprocessing Laboratory, Department of Electrical
Engineering and Data Storage Institute, National University of
Singapore, 10 Kent Ridge Crescent, Singapore 119260

ABSTRACT

Aluminium nitride (*c*-AlN) thin films were deposited at room temperature on silicon substrates by nitrogen-ion-assisted pulsed laser ablation of a hexagonal AlN target. A KrF excimer laser with pulse duration of 23 ns and wavelength of 248 nm was used as a laser source for the ablation. A nitrogen ion beam with energy in the range from 200 to 800 eV is used to co-process the deposition. With this technology, it's possible to independently control the energy of the AlN radicals in the ablated plasma and the nitrogen ions in the ion beam to improve the quality of the deposited thin films. Moreover, the nitrogen ion implantation can also compensate the loss of nitrogen species in the ablation process. X-ray diffraction (XRD), Raman spectrum and X-ray photoelectron spectroscopy (XPS) were used to characterize the deposited thin films. The deposited thin films exhibit good crystal properties with sharp XRD peaks. The influences of the nitrogen ion beam energy on the electronic and structural properties of the deposited thin films were studied. The nitrogen ions can effectively promote the formation of stable Al-N bonds and improve the crystal properties of the deposited thin films. A nitrogen ion energy of 400 eV is proposed.

Keywords: AlN, thin films, pulsed laser deposition, XRD, XPS, Raman spectrum

1. INTRODUCTION

Aluminium nitride is increasingly receiving high interests from materials research societies due to its wide band-gap, high thermal conductivity, high electrical resistivity (dielectric constant) and good acoustic properties¹⁻³. Many research groups are exploring the synthesis of high quality AlN materials. Some experimental methods have been used to deposit AlN thin films, including metalorganic chemical vapor deposition (MOCVD)⁴, plasma-assisted molecular beam epitaxy (PAMBE)⁵⁻⁷, RF reactive magnetron sputtering⁸⁻¹¹, ion-assisted chemical vapor deposition¹² and pulsed laser deposition (PLD)¹³⁻¹⁹. Most of the deposition methods require high substrate temperatures (normally above 800 °C) although the defects both in the thin films and at the interface between the substrate and the thin film cannot be avoided⁶. Such a high substrate temperature is always undesirable for semiconductor industries and therefore impeding the practical applications of the AlN materials. Up to date, most of the deposited AlN thin films have hexagonal structures with a highly textured orientation of (0001) on sapphire, silicon and glass substrates.

*Correspondence: Email: eleluyf@nus.edu.sg; WWW: <http://www.dsi.nus.edu.sg/tracks/laser>;
Telephone: 65 874 2118; Fax: 65 779 1103

In this study, PLD was used to deposit AlN thin films on silicon substrates at room temperature. PLD has been proven to be suitable to fabricate AlN thin films on silicon and sapphire substrates¹³⁻¹⁹. Compared with other methods, PLD has advantages mainly in two aspects. Firstly, it can faithfully transfer target material to substrate surface without obvious change of compositional ratios in compound materials. Secondly, the energetic radicals in the ablated plume are beneficial to the formation of ideal crystalline structures in the deposited thin films. In this studying, the ion-assisted PLD combines the advantages of both ion bombardment and pulsed laser ablation. With this technology, we can independently control the energy of the AlN radicals in the ablated plasma and the nitrogen ions in the ion beam to improve the quality of the deposited thin films. Moreover, the nitrogen ion implantation can also compensate the loss of nitrogen species in the ablation process.

2. EXPERIMENTAL

In the experimental set-up, as shown in Figure 1, a KrF excimer laser at a wavelength of 248 nm was used as a light source to ablate an AlN target. The deposition was carried out in a PLD system with a background vacuum of 1×10^{-6} Torr. An AlN target with hexagonal crystal structures and a purity of 99.995 % was mounted on a target holder that was rotated by an external motor. The target was placed 2 cm away from the substrate surface. The laser pulse duration was 23 ns. The laser fluence was around 2 Jcm^{-2} with a repetition rate of 10 Hz. A nitrogen ion beam which was produced by a 1-cm Kaufman-type ion source irradiated the substrate surface to assist the deposition. The ion flux was adjusted in a range of 1-2 mA/cm². The energetic nitrogen ions travel 10 cm distance before arriving on the substrate. The incident angle of the ion beam is 45°. By monitoring the microbalance mounted on the substrate, the deposition rate was set at $\leq 1 \text{ Å/sec}$ by adjusting the ion beam flux. Si(100) wafers were used as substrates.

X-ray diffraction (XRD), X-ray photoelectron spectroscopy (XPS) and Raman spectroscopy measurements were carried out to characterize the crystal, compositional and electronic properties of the deposited thin films. XRD measurements were performed on a Philips X'Pert-MRD system. Cu K α irradiation with average wavelength of 1.5418 Å was used as an X-ray source in the diffraction measurements. XPS measurements were carried out using a Mg K α 1253.6 eV X-ray source with power of 300 W. Raman spectroscopy measurements were done on a Renishaw Raman Scope.

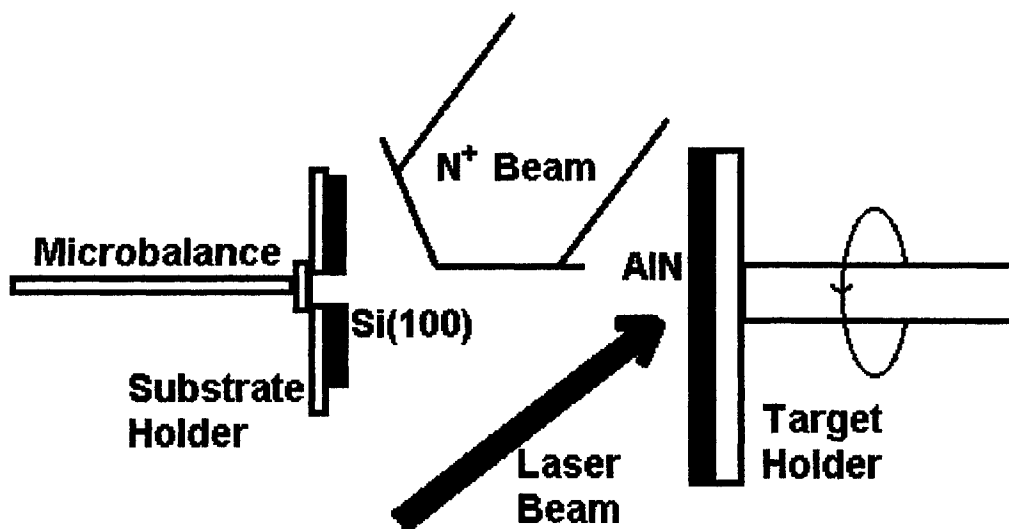


Figure 1 Experimental set-up.

3. RESULTS AND DISCUSSIONS

Figure 2 shows the XRD $\theta \sim 2\theta$ spectrum of a AlN thin film deposited by 400 eV nitrogen ion bombardment. In the spectrum, besides the Si(200) and Si(400) diffraction peaks, there are four obvious peaks at $2\theta = 38.5, 44.7, 65.3$ and 78.3 , corresponding to orientations of (111), (200), (220) and (311) of the cubic AlN crystal although the crystal structure of the target is hexagonal. The FWHM of the AlN(200) peak is about 0.27 degree, lower than those deposited by plasma source molecular beam epitaxy⁶. The formation of AlN cubic structures on Si(100) substrates is different from most other works where hexagonal AlN structures are formed^{15,18,19}. In the detailed studies^{6,7} of the microstructures and initial stages of thin film deposition, AlN films have an initial amorphous region at the interface between the substrate and the thin film, followed by c-axis oriented columnar grains. Substrate temperatures higher than 600°C can significantly reduce the amorphous regions at the interface and promote to grow AlN with hexagonal (0001) orientation. However, in our deposition, since substrate temperature is low, the c-axis-orientated growth of hexagonal AlN is not preferred. Instead, another metastable state of the crystal AlN with a cubic structure is obtained in our deposition, although the hexagonal AlN should be possibly a much stable state. The pulsed laser deposition at room-temperature with the assistance of ion-beam co-processing leads to mainly (111)-oriented c-AlN thin films.

We also deposited AlN thin films without nitrogen ion bombardment. The deposited thin films exhibit no XRD peaks, indicating only amorphous structures. The result reveals the important role of the nitrogen ions in the synthesis of AlN thin films with cubic crystal structures. Moreover, nitrogen ion energy lower than 400 eV leads to weaker and broader XRD peaks. Therefore, the nitrogen ions with an energy of 400 eV can effectively assist the formation of cubic crystalline structures in the deposited thin films. When nitrogen ion energy exceeds 400 eV, the deposition will be impeded due to the re-sputtering effect caused by the ion bombardment.

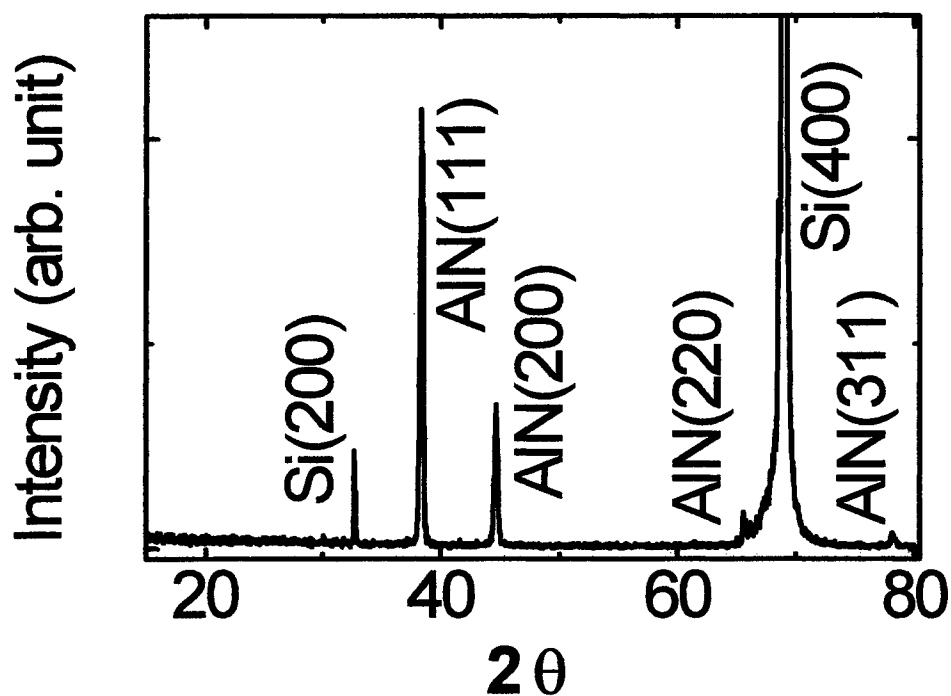


Figure 2 XRD $\theta \sim 2\theta$ spectrum of a AlN thin film deposited by KrF laser ablation with 400 eV N^+ bombardment at room temperature. The laser fluence is 2 J/cm^2 .

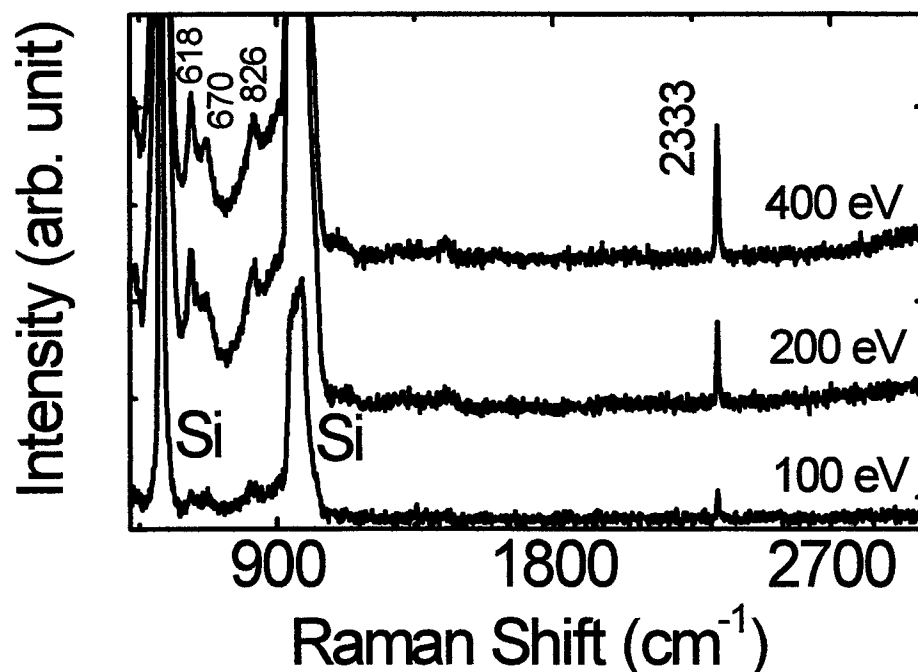


Figure 3 Raman spectra of AlN thin films deposited in N_2 atmosphere with a pressure of 100 mTorr and with the assistance of N^+ at different ion energies.

Figure 3 shows the Raman spectra of the AlN thin films deposited under different nitrogen ion energies of 100, 200, and 400 eV, respectively. Similar to most other publications, the Raman peaks of the AlN thin films are weak. The peaks at 618, 670 and 826 cm^{-1} reflect the phonon modes of $E_1(TO)$, $A_1(LO)$ and $E_1(LO)$, respectively, indicating the crystal structures of the deposited thin films. The intensities of these Raman peaks increase with the increasing nitrogen ion energy from 100 to 400 eV, implying that the nitrogen ion energy of 400 eV is optimal to the deposition of crystal AlN thin films, in coincidence with the XRD analysis. Besides these peaks, there is a sharp and strong peak at 2333 cm^{-1} which is observed for the first time. The intensity of this peak also increases with the nitrogen ion energy and reaches the maximum when ion energy increases to 400 eV. Therefore, this peak should be originated from the cubic structure of AlN.

For the thin films deposited without nitrogen ions, no obvious Raman peak can be observed, implying that the nitrogen ions can effectively improve the crystal property of the thin film. Although it induces defects, ion implantation can possibly benefit the growth of the crystal grains. The energetic nitrogen ions can enhance the chemical combinations between Al and N atoms and thus lead to more and large AlN crystal grains.

The deposition with the assistance of ion-beam bombardment is a nonequilibrium process. The low substrate temperature does not provide any energy for the equilibrium growth of AlN crystalline. The deposition is accomplished with energetic ions of hundreds eV. Therefore, the crystalline growth mechanism is quite different from other deposition methods where high substrate temperatures and low ion energies are employed. Hexagonal AlN thin films were deposited by PLD at substrate temperature higher than 675°C^{15,18} and by RF magnetic

sputtering and molecular beam epitaxy with substrate temperature higher than 400 °C^{6,9,10,19} on silicon^{6,9,18} and glass substrates¹⁰. However, in this study, the c-axis oriented growth which leads to hexagonal structures is not possible due to the lack of high substrate temperatures. On the contrary, the energetic ions promote the formation of another metastable state of crystal AlN with cubic structures. Therefore, the using of nitrogen ions of hundreds eV plays an important role in the formation of cubic AlN crystalline.

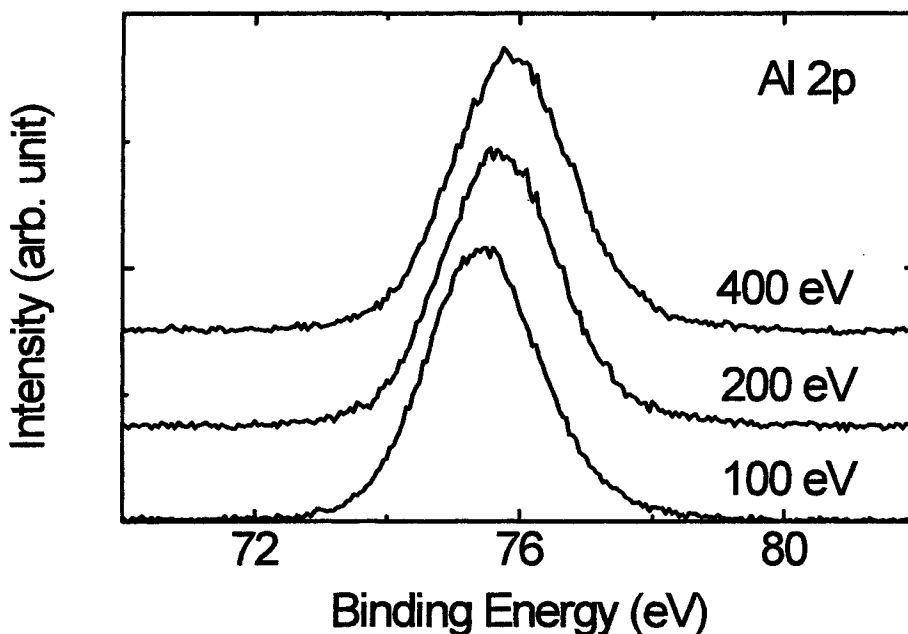


Figure 4 XPS Al 2p spectra of AlN thin films deposited with 100, 200 and 400 eV N^+ co-processing.

Figure 4 shows the XPS Al 2p spectra of three AlN thin films deposited with different ion energies of 100, 200 and 400 eV. It can be seen that the binding energy of Al 2p increases slightly with the increasing ion energy from 100 to 400 eV. This is due to the formation of more AlN compounds owing to the high energies supplied by the nitrogen ions. Generally, the binding energy of the Al 2p electron in the AlN compound is higher than that in atomic aluminium due to less shielding effect. The increase in N^+ energy causes formation of more Al-N bonds and thus increases the average binding energy of the Al 2p electrons. The FWHM of the Al 2p peak increases slightly when N^+ energy increases to 400 eV, possibly due to the bombardment-induced disorders in the deposited thin films.

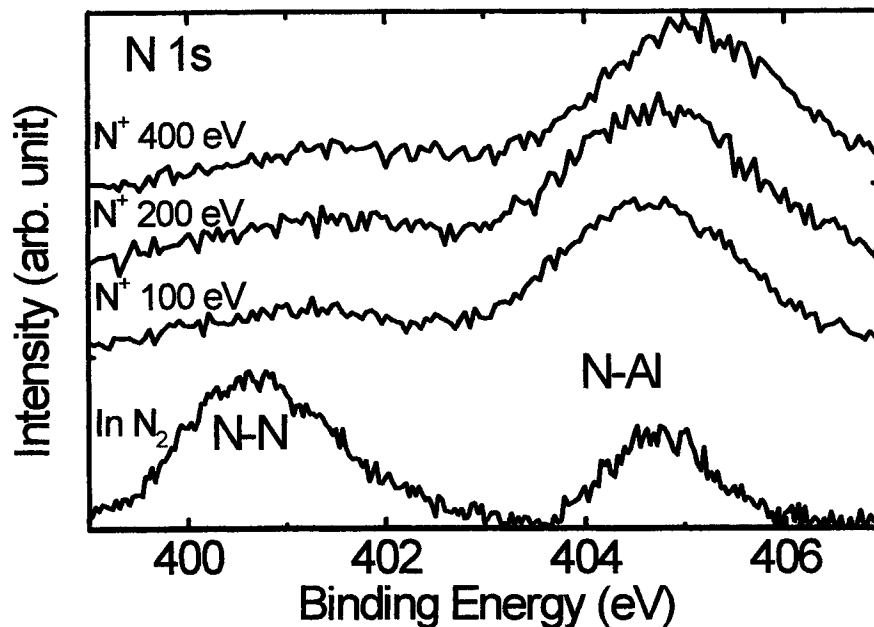


Figure 5. XPS N 1s spectra of AlN thin films deposited in N_2 atmosphere with a pressure of 100 mTorr and with the assistance of N^+ with energies of 100, 200 and 400 eV.

Figure 5 shows XPS N 1s spectra for AlN thin films deposited in N_2 atmosphere with a pressure of 100 mTorr and with the assistance of N^+ at different energies of 100, 200 and 400 eV. It can be seen that there are two nitrogen states, related to N-N and N-Al bonds. The difference between the thin films deposited with and without N^+ assistance is quite obvious. The thin film deposited in N_2 atmosphere has a very strong N-N peak whilst that deposited with N^+ assistance has a strong N-Al peak. The N^+ irradiation in the deposition promotes the formation of N-Al bonds and eliminates the formation of N-N bonds.

4. CONCLUSIONS

AlN thin films have been deposited at room temperature on Si(100) substrates by pulsed laser ablation of an AlN target with N^+ implantation. The low deposition temperature is beneficial for the practical applications of AlN thin films in semiconductor industries. The deposited thin films exhibit cubic crystal structures though the target is hexagonal. The N^+ beam can also compensate the loss of nitrogen in the thin films and promote the formation of Al-N bonds. The crystal property can be improved by the N^+ beam. A N^+ energy of 400 eV is optimal to produce AlN thin films with good crystal and electronic properties.

ACKNOWLEDGEMENTS

The authors would like to thank Miss. H. L. Koh for her technical assistance in this research work.

REFERENCES

1. W. R. L. Lambrecht, *Mater. Res. Symp. Proc.* **339**, 565(1994).
2. F.A. Ponce et al., "Nitride semiconductors: symposium held December 1-5, 1997, Boston, Massachusetts, U.S.A. " (Materials Research Society, 1998).
3. K. A. Jones, K. Xie, D. W. Eckart, M. C. Wood, V. Talyansky, R. D. Vispute, T. Venkatesan, K. Wongchotigul and M. Spencer, *J. Appl. Phys.* **83**, 8010(1998).
4. P. Kung, A. Saxler, X.Zhang, D. Walker, T. C. Wang, I. Furguson, and M. Razeghi, *Appl. Phys. Lett.* **66**, 2958(1995).
5. K. S. Stevens, A. Ohtani, M. Kinniburgh, and R. Beresford, *Appl. Phys. Lett.* **65**, 321(1994).
6. G. W. Auner, F.Jin, V. M. Naik, and R. Naik, *J. Appl. Phys.* **85**, 7879(1999).
7. J. R. Heffelfinger, D. L. Medlin, and K. F. Mccarty, *J. Appl. Phys.* **85**, 466(1999).
8. W. J. Meng, J. Heremans, and Y. T. Chang, *Appl. Phys. Lett.* **59**, 2097(1991).
9. E. Dogheche, D. Remiens, A. Boudrioua, and J. C. Loulergue, *Appl. Phys. Lett.* **74**, 1209(1999).
10. A. Rodriguez-Navarro, W. Otano-Rivera, L. J. Pilione, R. Messier, and J. M. Garcia-Ruiz, *J. Vac. Sci. Technol. A* **16**, 1244(1998).
11. H. Y. Joo, H. J. Kim, S. J. Kim, and S. Y. Kim, *J. Vac. Sci. Technol. A* **17**, 862(1999).
12. J. C. Sanchez-Lopez, L. Contreas, A. Fernandez, A. R. Gonzalez-Elipse, J. M. Martin, and B. Vacher, *Thin Solid Films* **317**, 100(1998).
13. T. F. Huang and J. S. Harris, Jr., *Appl. Phys. Lett.* **72**, 1158(1998).
14. V. Talyansky, R. D. Vispute, R. Ramesh, R. P. Sharma, T. Venkatesan, Y. X. Li, L. G. Salamanca-Riba, M. C. Wood, R. T. Lareau, K. A. Jones, and A. A. Iliadis, *Thin Solid Films* **323**, 37(1998).
15. G. S. Sudhir, H. Fujii, W. S. Wong, C. Kisielowski, N. Newman, C. Dieker, Z. Liliental-Weber, M. D. Rubin, and E. R. Weber, *Appl. Surf. Sci.* **127**, 471(1998).
16. R. D. Vispute, J. Narayan, and J. D. Budai, *Thin Solid Films* **299**, 94(1997).
17. M. He, N. Cheng, P. Zhou, H. Okabe, and J. B. Halpern, *J. Vac. Sci. Technol. A* **16**, 2372(1998).
18. A. Kumar, H. L. Chan, J. J. Weimer, and L. Sanderson, *Thin Solid Films* **308-309**, 406(1997).
19. K. Jagannadham, A. K. Sharma, Q. Wei, R. Kalyanraman, and J. Narayan, *J. Vac. Sci. Technol. A* **16**, 2804(1998).

SESSION 7

Pulsed Laser Deposition III

Production of photoluminescent Si-based nanostructures by laser ablation: effects of the ablation and post-deposition conditions

A. V. Kabashin^a, M. Charbonneau-Lefort^a, M. Meunier^a and R. Leonelli^b

^aEcole Polytechnique de Montreal, Departement de Genie Physique, Case Postale 6079, succ. Centre-ville, Montreal (Quebec), Canada, H3C 3A7

^bUniversite de Montreal, Departement de Physique, C.P. 6128, succ. Centre-Ville, Montreal (Quebec), Canada H3C 3J7

ABSTRACT

A method of Pulsed Laser Ablation (PLA) from a Si target in an inert He ambient has been applied in combination with different post-deposition oxidation procedures for the fabrication of Si/SiO_x nanocrystalline structures on Si substrates. After the growth of a thin natural oxide layer on the film surface, the structures exhibited a strong visible photoluminescence (PL), which remained stable even under a prolonged continuous irradiation of the sample by an excitation laser light. The peak energy of the PL spectra could be finely varied between 1.58 and 2.15 eV by a change in the residual gas pressure during the deposition process. An effect of thermal annealing on the PL properties of the Si/SiO_x films has been examined and compared with the results for Si-based films produced by thermal evaporation from a Si target in vacuum. For both deposition techniques, the thermal annealing led to a dramatic change of PL properties giving rise to a fixed PL peak around 2.2 eV. Photoluminescent properties of particles formed by PLA with natural oxidation were different than those of thermally oxidized amorphous Si films. A recombination through oxygen-related compounds in the upper film layer is considered as the most probable mechanism of PL.

Keywords: pulsed laser ablation, silicon nanoparticles, photoluminescence

INTRODUCTION

Because silicon is an indirect band gap material with a small band gap (1.11 eV at room temperature), it cannot emit visible light. This property significantly complicates the spreading of Si-based technologies to optoelectronics. However, recent observations of visible photoluminescence (PL) in porous silicon [1] and in other Si-based nanocrystalline structures (see, e.g., [2 - 4]) gave a promise for the development of some optical applications. The PL generation is usually attributed to a carrier recombination between quantum confined states in the nanoscale particles [1], but other mechanisms such as e.g., recombination states in surface-related structures such as siloxenes and polysilanes, or the recombination through SiO_x (0 < x ≤ 2) interfacial layer between the Si core and the SiO₂ surface layer [3] are also considered. Among the Si-based materials, porous silicon was found to exhibit the most intense PL in both the visible-infrared and the ultraviolet range [5]. However, porous silicon demonstrates poor electrical, thermal and mechanical properties [6], while its PL is very unstable. These factors complicate its application. In addition, a wet fabrication process of porous silicon is hardly compatible with modern silicon processing technology.

Continuous Si-based films such as Si/SiO_x complexes are considered as an alternative to porous silicon for optical applications. They are expected to provide more stable and reproducible characteristics, while some methods for their fabrication are well compatible with current microelectronics technologies. Among these methods, Pulsed Laser Ablation (PLA) manifests itself as one of the best candidates for the production of the Si-based nanocrystallites [7-11]. Due to the peculiarities of laser plasma formation and evolution, Si nanoscale clusters can be effectively produced by laser ablating a Si target into an inert gas ambient [12-15]. Using this technique, thin films containing nanocrystalline Si structures with dimensions of 0.5 - 10 nm have already been fabricated [7 - 11, 16]. Furthermore, the PL technique makes possible a control of the average size of the deposited structures by a variation of the residual gas pressure [9, 11, 16]. The PL properties of the films do not always correlate with the size distribution as predicted from a quantum confinement model. In most papers, the strong PL signals were detected only after a thermal annealing in air or oxygen of the deposited films, while the best results were obtained for the samples deposited in He. After annealing, fixed peaks around 1.5 - 1.7 eV and 2.1 - 2.2 eV were generally observed [9-11, 17, 18]. Nevertheless, the PL peak of about 1.6 eV was detected even without thermal annealing, though its intensity was relatively weak [9-11, 17, 18]. It was also shown in [19] that a variation in deposition parameters, mainly the laser fluence, could lead to a change of the PL peak position between 1.7 and 2.1 eV and a further jump to 3.5 eV without the annealing process. The blue shift of the peak position was accompanied by a certain decrease of the cluster average size. However, the existence of the strong peak jump from 2.1 to 3.5 eV was not confirmed by an adequate cluster size change,

which complicated a reasonable explanation of the experimental results by the quantum confinement model. Thus, in spite of the existence of the mentioned experimental data, many aspects of the phenomenon remain quite unclear, and the physical origin of the observed photoluminescence is still controversial. In particular, the role of natural and thermal oxidation of the films in the photoluminescent structures formation has not yet been studied.

In this paper, we studied in detail the properties of Si-based films produced by PLA and the effect of post-deposition oxidation on the formation of photoluminescent structures. In the PL measurements, the main attention has been given to the visible and near-infrared ranges of the spectrum (S-band), which are the most important for optoelectronics applications.

EXPERIMENTAL SETUP

The ablation of material from a rotating Si target ((1-0-0), N-type, resistivity 10 Ohm·cm) was produced by a pulsed KrF laser ($\lambda = 248$ nm, pulse length 15 ns FWHM). The radiation was focused on a focal spot 2×1 mm² on the target at the incident angle of 45°. The fluence was 7-10 J/cm² giving a radiation intensity of about $5 \cdot 10^8$ W/cm². The laser-induced plasma plume expanded perpendicularly to the target surface. The substrates, identical to the target, were placed on a rotating substrate holder at 2 cm from the target. Both the target and the substrate were kept at room temperature. The deposition was carried out in He at a constant ambient pressure. The pressure P of He was varied in different experiments between 50 mTorr and 10 Torr. For some comparative tests, the deposition was also performed in pure oxygen. In order to maintain a relatively intense plasma plume, the O₂ pressure did not exceed 200 mTorr. The chamber was pumped down to $P = 2 \cdot 10^{-7}$ Torr before filling with the gases. After several thousand laser shots, the thickness of the Si film on the substrate was 100 – 500 nm.

In addition, a technique of thermal evaporation from a Si target in vacuum has been used for comparative tests. In contrast to PLA, this technique is known to provide relatively large dimensions of deposited particles. A powder from a Si wafer with the same parameters was evaporated under the residual pressure of 10^{-7} Torr from a tantalum boat onto a Si substrate maintained at room temperature. The boat to substrate distance was about 15 cm, the deposition rate was 0.1-0.2 nm/s as measured by a quartz microbalance system. The thickness of deposited amorphous Si films on the substrate was 100-200 nm. To estimate the PL efficiency from the films fabricated by PLA, we also prepared samples of porous silicon by an anodization etching of a Si wafer with the same parameters in 1:1 mixture of 49% HF and ethanol. The anodizing current of 30 mA/cm² and the etching time of 5-20 min were selected to provide maximal PL intensity of the porous silicon samples. In some cases, the films deposited by PLA and thermal evaporation were annealed at 800° C in atmospheric air for 10 minutes. The increase and decrease rates of temperature were 10° C/min.

For the PL measurements, the samples were illuminated by the radiation of cw Ar⁺ laser (model INNOVA 100) with the wavelength 488 nm. The power was 10 mW and the power density was estimated to be 30 W/cm². The PL spectra were measured at room temperature using a double spectrometer (model U100, Instruments SA) and GaAs photomultiplier (Hamamatsu Photonics). The spectra were corrected to take into account the spectral response of the PL setup.

To determine the composition of the surface layer, we also analyzed the deposited films by X-ray photoemission spectroscopy (XPS) at a base pressure of $2 \cdot 10^{-8}$ Torr using a Perkin-Elmer 5500 system.

EXPERIMENTAL AND DISCUSSION

1. PL properties of as-deposited films.

In the first series of experiments, we studied the role of laser ablation and natural oxidation in a formation of photoluminescent Si-based structured. The Si-based films were fabricated by PLA in He ambient gas. To understand the PL origin, some spectral observations were carried out in situ, just after the deposition of the films in a vacuum chamber filled with He. The films were irradiated by a cw Ar⁺ laser with the intensity of 30 W/cm², while the integral visible PL from the samples was controlled both by eyes and by a Si photodetector after absorption of the main laser radiation by an optical filter. This method allowed us to control in the first approximation an appearance of relatively weak PL signals from the films. In addition, we were able to measure the PL spectra immediately after the exposition of the films to atmospheric air.

Our experiments revealed clear correlation between the growth of an oxide layer on the surface of deposited films and the appearance and enhancement of visible PL. No detectable PL from the as-deposited Si-based films has been observed in the wavelength range of 520 – 800 nm when He filled the vacuum chamber after the deposition process. However, an exposition of the films to 1 Atm of ambient air gave rise to visible PL. The PL signals were hardly observable by all methods at the first moments of the film exposition to ambient air, while an exposition for 30 – 180 minutes led to their dramatic enhancement. Typical spectra of the deposited films after different exposition times are presented in Fig. 1. One can see that the PL signals had a single distinct peak, while its intensity increased progressively with air exposition time. The exposition

was also followed by a slight red shift of the PL peak intensity. For example, the 4-week exposition to air led to the PL peak shift from 1.63 eV to 1.6 eV as shown in Fig. 1.

The increase rate of the PL signals with air exposition time can be seen in Fig. 1 (b). Under our conditions, the PL intensity increased by about an order of magnitude during the first 6 weeks after the deposition of the films. However, the PL intensity and PL peak position stabilized after 8-10 weeks. The maximal signals were very strong and easily visible by a naked eye. Nevertheless, they were weaker by a factor of 20-40 than the maximal PL signals from a porous silicon sample produced by anodization etching. A set of special tests showed that the evolution of the PL signals could be accelerated by an increase of the air relative humidity. This phenomenon is probably explained by a strong correlation between the formation of a photoluminescent structure and the thickness of the oxide layer. The growth rate of the oxide layer on Si surface is known to be accelerated by the increase of air relative humidity [20]. An XPS analysis of the upper film layer confirmed the presence of oxygen-related compounds in the film composition, namely the SiO_x complexes with x between 0 and 2. The value of x increased with time to air exposition, which was probably connected with an increase of relative contribution of the growing SiO_2 superficial layer in the XPS signal.

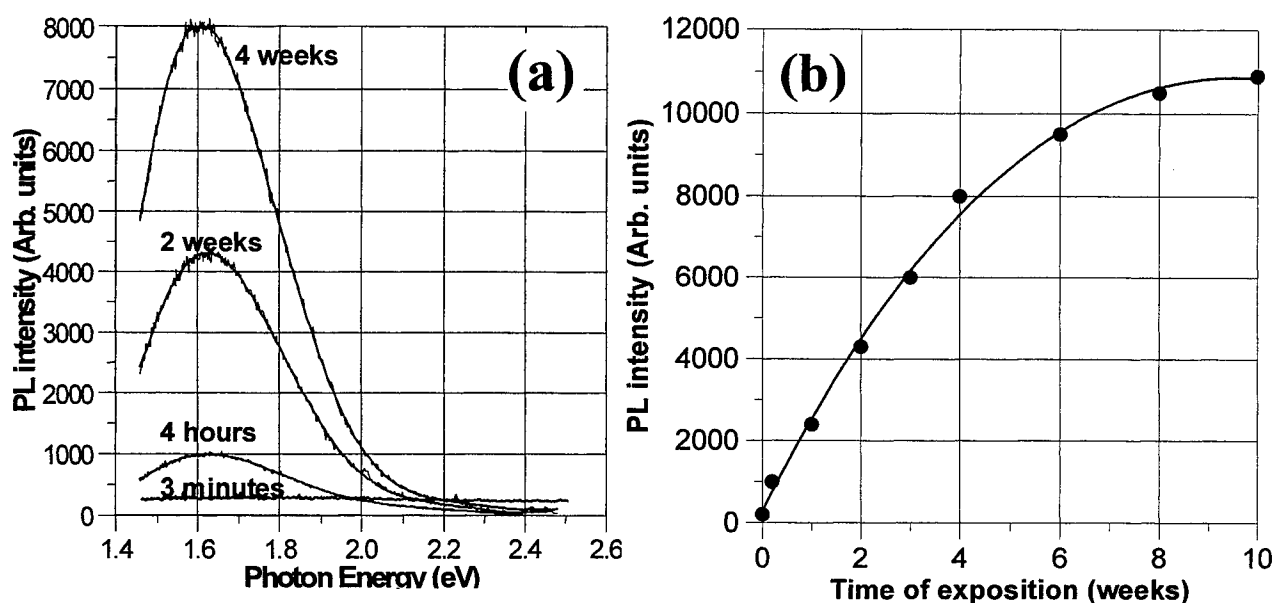


Fig. 1 (a) Photoluminescence spectra of a Si/SiO_x film deposited by pulsed laser ablation in He ($P = 2$ Torr) after different times of the film exposition to ambient air with a relative humidity 60%.
(b) Maximal amplitude of the PL spectra as a function of exposition time for the same film.

It was established that the position of the PL peak could significantly differ for the Si/SiO_x films deposited under different pressures of He in a vacuum chamber. A change of the He pressure from 3 Torr to 150 mTorr in different deposition experiments caused a progressive and fine shift of the PL peak position from 1.58 eV to 2.15 eV as shown in Fig. 2 (a). However, a wider displacement of the PL peak position by this method was found to be problematic. Under the pressures above 3 Torr, PL peaks remained always around 1.57 – 1.6 eV, while their intensity decreased significantly. On the other hand, the decrease of the pressure below 150 mTorr caused a dramatic decrease of plasma plume intensity, which led to too weak and hardly reproducible PL signals. Nevertheless, maximum PL intensities were found to be remarkably different for the peaks within the 1.58 – 2.15 eV range. As shows in Fig. 2 (b), the most intense PL signals were at about 1.60 – 1.63 eV, while PL intensities of other peaks could be weaker by orders of magnitude. Thus, in our experimental conditions there was a narrow optimum of pressures around 2 Torr for the production of Si-based films with strong visible PL.

Note that a correlation between the He pressure during the deposition and dimensions of deposited nanoparticles has been mentioned in some previous papers [9, 11, 16]. The decrease of the pressure always led to a reduction of the particles size as was found by AFM observation. However, in PL measurements in references [9, 11], one did not detect the blue shift of the spectra due to the size reduction as predicted from the quantum confinement model. Our experimental results clearly show such dependence. Nevertheless, a strong connection of the PL origin to the growth of oxide layer complicates an explanation

of experimental results by the quantum confinement mechanism, which is related to size effects in nanoscale particles. So, we can not exclude that the blue shift of the spectra in our experiments was caused by a change of some other film property such as e.g., surface roughness or amorphous extent. Along with the particle size, these film properties could also vary with He pressures.

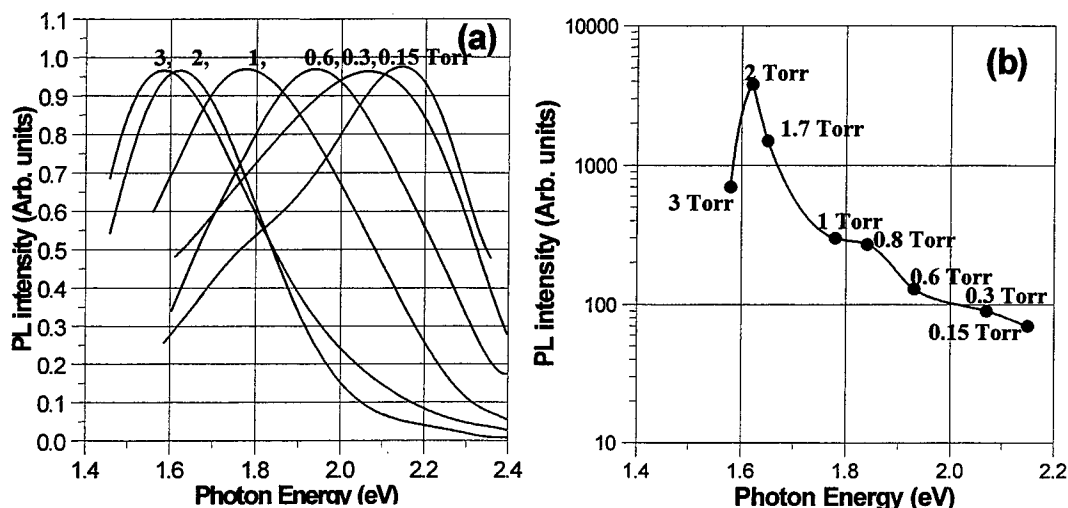


Fig. 2 (a) Photoluminescence spectra of Si/SiO_x films deposited at different He pressures. Spectra intensities are normalized to the peak value. The spectra were taken after exposition to air during two weeks. (b) Maximum PL intensities (in logarithmic scale) detected for different peaks.

Thus, the appearance of PL is strongly correlated with the formation of oxygen-related compounds in the upper surface layer, which arise due to the reaction between the Si and ambient air. The increase of the thickness of a natural SiO₂ layer is accompanied by a progressive improvement of the PL efficiency. In our opinion, it is not easy to explain these results by the quantum confinement model. It seems to be more probable that the PL mechanism is related to a recombination through SiO_x interfacial layer between the Si core and the SiO₂ surface layer. This mechanism was introduced in [3] for an explanation of visible PL from Si-based films produced by an optical breakdown in silane (SiH₄). In general, the PL properties of the films in [3] are similar to those from our experiments. Nevertheless, there are some differences. In particular, in contrast with our experiments, only a fixed PL peak of about 1.65 eV was observed in [3], whose position was independent of deposition conditions and dimensions of particles on the substrate. Such a difference of PL properties could be explained by the fact that PLA makes possible a variation of some other film parameter (e.g., the surface roughness), which finally leads e.g., to different x values in the interfacial SiO_x layer, as indicated by our XPS measurements.

2. PL properties of thermally oxidized films

In these series of experiments we considered in detail the influence of thermal annealing on the properties of PLA-fabricated Si/SiO_x films. All samples were annealed at 800° C in air during 10 minutes.

Fig. 3 presents the PL spectra of thermally annealed films, which were prepared by laser ablation at different He pressures. By comparing these spectra with those from Fig. 1 and Fig. 2 (a), one can conclude that thermal annealing resulted in dramatic changes in both PL peak positions and their relative intensities. In contrast to the case of natural oxidation, PL spectra with the same peak of about 2.2 eV were now observed for all films prepared under different pressures of He. The strongest PL signals (0.2 Torr) were detected for the films prepared under the relatively low pressures 0.2 – 0.3 Torr, which exhibited weak PL after the natural oxidation process [Fig. 2 (b)]. On the other hand, relatively weak PL signals (2 Torr) were detected for the films deposited at $P = 2$ Torr, while these films gave the strongest PL in the case of natural oxidation. This behavior is different with what was observed in previous studies [9-11, 17, 18] where annealing films generally increased PL signals. This discrepancy is probably explained by a difference of deposition conditions and optimal gas pressures for naturally oxidized and annealed films, or by a relatively short time of natural oxidation of the samples in these papers.

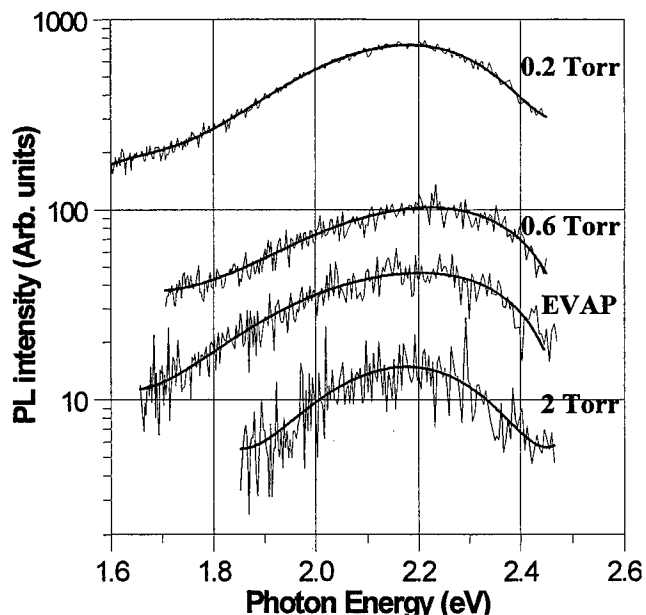


Fig. 3 Photoluminescence spectra (in logarithmic scale) of different Si/SiO_x films after a thermal annealing in air at 800 °C: Films are deposited by PLA in He at residual pressures 0.2 Torr, 0.6 Torr, and 2 Torr respectively, and by a thermal evaporation (EVAP) from a Si target in vacuum.

To clarify the mechanisms and conditions of formation of the PL structures, we carried out comparative experiment with Si-based amorphous films deposited by thermal evaporation from a Si target in vacuum, which is known to provide relatively large dimensions of deposited particles. Our experiments did not reveal visible PL from as-deposited films and the films did not exhibit PL even after a prolonged (for several months) air exposition. Nevertheless, the thermal annealing of the films led to a similar PL spectrum with a peak at 2.2 eV as shown in Fig. 3. Such a coincidence of PL peak positions gives a clear evidence for similar final microstructures of thermally annealed photoluminescent particles for the films deposited by different methods. This suggests that the laser ablation technique produces amorphous films with a certain morphology and mechanical properties, while the luminescent particles are produced during the thermal oxidation process of these amorphous films. The PL mechanism for thermally annealed films is probably related to a recombination through oxygen-related compounds such as the SiO_x interfacial layer or localized defects in SiO₂ [21]. A remarkable difference in PL properties for as-deposited and post-annealed films is probably due to peculiarities of photoluminescent structures formation by both methods, giving rise to different morphology or stoichiometry of oxygen-related compounds.

3. PL properties of Si-based films fabricated in O₂.

To clarify the role of oxygen-related compounds in the formation of the photoluminescent structures, we carried out the deposition of Si in an O₂ atmosphere. The pressure of oxygen (150 mTorr) was selected to provide maximum intensity of the plasma plume. However, the experiments in oxygen revealed much weaker PL signals, whose intensity decreased rapidly with Ar⁺ laser illumination time. Maximum PL signals from as-deposited films were less intense than in the case of He by about two orders of magnitude, while the PL peak position was independent of the deposition conditions and was always around 2.2 – 2.28 eV as shown in Fig. 4. In contrast to the PLA in helium, the PL signals could be observed immediately after the deposition process, while a prolonged exposition of the films to air did not result in any detectable increase of the PL intensity.

In contrast to PLA in He, thermal annealing of the deposited films at 800 °C did not give rise to a dramatic change of the PL properties. As shown in Fig. 4, the position of PL peak and spectral shape remained almost the same after the annealing. Nevertheless, the thermal annealing led to an increase of the PL intensity by a factor of 2–4.

Thus, the presence of oxygen during the deposition of Si leads to the formation of Si-based photoluminescent structures even without the post-oxidation process, though the PL intensity is weaker than in the case of He.

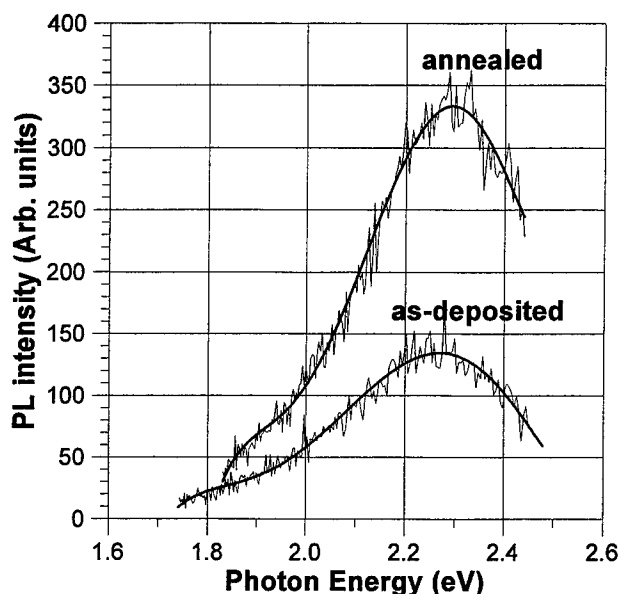


Fig. 4 Photoluminescence spectra of as-deposited and post-annealed Si/SiO_x film fabricated by PLA in O₂ ($P \approx 150$ mTorr).

4. Evolution of the PL spectra under continuous laser irradiation

To clarify the mechanisms and peculiarities of PL generation, we examined the time-dependent degradation of the PL spectra for the fabricated Si/SiO_x films. In these experiments, the evolution of the PL peak intensity was recorded while an Ar⁺ laser beam continuously illuminated the films prepared under different conditions. As shown in Fig. 5, the films deposited in O₂ suffered a dramatic degradation of the PL intensity after only few minutes of the continuous illumination. A similar phenomenon was observed for post-annealed films deposited in He or O₂ atmosphere. However, He-deposited and naturally post-oxidized films manifested quite different properties. After a small decrease during the first seconds of the experiment, the PL intensity remained stable for a prolonged continuous film illumination. Our experiments showed that even a 6-hours illumination did not result in any change in the PL peak position or intensity. Such a difference in PL properties gives an evidence for a distinct PL mechanism in the case of natural oxidation of He-deposited films. This mechanism gives an improvement of time-dependent PL properties, which are very important for optoelectronics applications. Further investigations are in progress to clarify the mechanism.

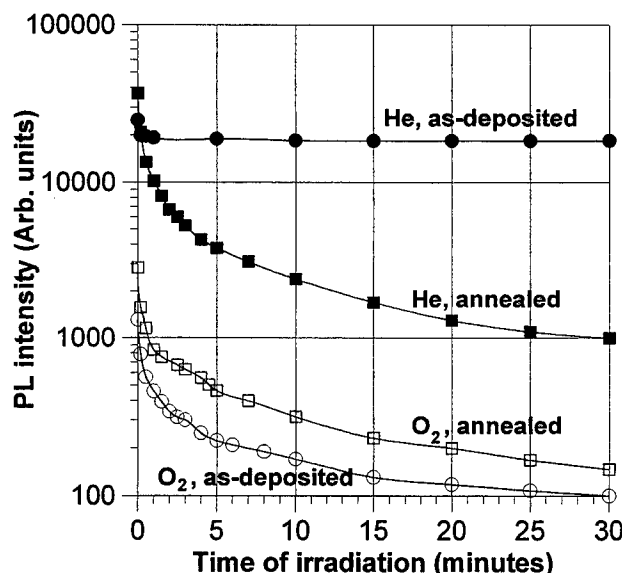


Fig. 5 Dependence of PL peak intensities on the excitation irradiation time in air. Filled and open symbols correspond to as-deposited and post-annealed films fabricated in helium ($P = 2$ Torr) and oxygen respectively.

CONCLUSIONS

Si/SiO_x nanocrystalline structures have been fabricated by PLA technique. The presence and enhancement of PL signals from the structures was found to be strongly connected with the presence of oxygen-related components in the film. These could be obtained directly by the deposition in oxygen atmosphere, or through a post-deposition growth of the oxide layer on the film surface. Nevertheless, the strongest PL signals were detected for the films deposited in inert He ambient after the growth of a natural oxide layer on their surface. The PL signals remained stable even after a prolonged continuous irradiation of these films by a laser beam, while the PL peak position could be varied by a change in He pressure during the deposition process. A clear identification of the PL mechanism requires further detailed study of mechanical, structural and PL properties of the deposited and annealed films. These investigations are in progress.

The authors are grateful to M. Cadotte and A. Essalik for an assistance during the preparation of the experiments, and to S. Poulin for the XPS measurements.

REFERENCES

- [1] L. T. Canham, "Silicon quantum wire array fabrication by electrochemical and chemical dissolution of wafers", *Appl. Phys. Lett.*, 57, pp. 1046-1048, 1990.
- [2] H. Takagi, H. Ogawa, Y. Yamazaki, A. Ishizaki, and T. Nakagiri, "Quantum size effects on photoluminescence in ultrafine Si particles", *Appl. Phys. Lett.*, 56, pp. 2379-2380, 1990.
- [3] Y. Kanemitsu, T. Ogawa, K. Shiraishi, and K. Takeda, Visible photoluminescence from oxidized Si nanometer-sized spheres: exciton confinement on a spherical shell", *Phys Rev. B*, 48, pp. 4883-4886, 1993.
- [4] H. Morisaki, H. Hashimoto, F. W. Ping, H. Nozawa, and H. Ono, "Strong blue light emission from an oxygen-containing Si fine structure", *J. Appl. Phys.*, 74, pp. 2977-2979, 1993.
- [5] A. G. Cullis, L. T. Canham, and P. D. J. Cadott, "The structural and luminescence properties of porous silicon", *J. Appl. Phys.*, 82, pp. 909-964, 1997.
- [6] S. P. Duttagupta, X. L. Chen, S. A. Jenekhe, and P. M. Fauchet, "Microhardness of porous silicon films and composites", *Solid State Commun.*, 101, pp. 33-37, 1997.
- [7] E. Werwa, A. A. Seraphin, L. A. Chiu, C. Zhou, and K. D. Kolenbrander, "Synthesis and processing of silicon nanocrystallites using a pulsed laser ablation supersonic expansion method", *Appl. Phys. Lett.*, 64, pp. 1821-1823, 1994.
- [8] I. A. Movtchan, R. W. Dreyfus, W. Marine, M. Sentis, M. Autric, G. Le Lay and N. Merk, "Luminescence from a Si-SiO_x nanocluster-like structure prepared by laser ablation", *Thin Solid Films*, 255, pp. 286-289, 1995.
- [9] Y. Yamada, T. Orii, I. Umezumi, Sh. Takeyama, and T. Yoshida, "Optical properties of silicon nanocrystallites prepared by excimer laser ablation in inert gas", *Jpn. J. Appl. Phys., Part 1*, 35, pp.1361-1365, 1996.

- [10] T. Makimura, Y. Kunii, and K. Murakami, "Light emission from nanometer-sized silicon particles fabricated by the laser ablation method", *Jpn. J. Appl. Phys., Part 1*, 35, pp.4780-4784, 1996.
- [11] T. Makimura, Y. Kunii, N. Ono, and K. Murakami, "Visible light emission from SiO_x films synthesized by laser ablation", *Jpn. J. Appl. Phys., Part 2*, 35, pp. L1703-L1705, 1996.
- [12] L. A. Chiu, A. A. Seraphin, and K. D. Kolenbrander, "Gas Phase Synthesis and Processing of Silicon Nanocrystallites: Characterization by Photoluminescence Emission Spectroscopy", *J. Electron. Matter*, 23, 347-352, 1994.
- [13] I. A. Movtchan, W. Marine, R. W. Dreyfus, U. C. Lee, M. Sentis, and M. Autric, "Optical spectroscopy of emission from Si-SiO_x nanoclusters formed by laser ablation", *Appl. Surf. Sci.*, 96-98, pp. 251-260, 1996.
- [14] J. Muramoto, Y. Nakata, T. Okada, and M. Maeda, "Observation of Nano-Particle Formation Process in a Laser-Ablated Plume Using Imaging Spectroscopy", *Jpn. J. Appl. Phys., Part 2*, 36, pp. L563-570, 1997.
- [15] D. B. Geohegan, A. A. Puretzky, G. Duscher, and S. J. Pennycook, "Time-resolved imaging of gas phase nanoparticle synthesis by laser ablation", *Appl. Phys. Lett.*, 72, pp. 2987-2989, 1998.
- [16] D. H. Lowndes, C. M. Rouleau, T. Thundat, G. Duscher, E. A. Kenik, S. J. Pennycook, "Silicon and zinc telluride nanoparticles synthesized by pulsed laser ablation: size distributions and nanoscale structure", *Appl. Surf. Sci.*, 127-129, pp. 355-361, 1998.
- [17] T. Makimura, Y. Kunii, N. Ono, and K. Murakami, "Silicon nanoparticles embedded in SiO₂ films with visible photoluminescence", *Appl. Surf. Sci.*, 127-129, pp. 388-392, 1998.
- [18] I. Umezu, K. Shibata, S. Yamaguchi, A. Sugimura, Y. Yamada and T. Yoshida, "Effects of thermal processes on photoluminescence of silicon nanocrystallites prepared by pulsed laser ablation", *J. Appl. Phys.*, 84, pp. 6448-6450, 1998.
- [19] L. Patrone, D. Nelson, V. Safarov, M. Sentis, W. Marine, "Size dependent photoluminescence from Si nanoclusters produced by laser ablation", *J. Luminescence*, 80, pp. 217-221, 1999.
- [20] M. Morita, T. Ohmi, E. Hasegawa, M. Kawakami, and M. Ohwada, "Growth of native oxide on a silicon surface", *J. Appl. Phys.*, 68, pp. 1272-1281, 1990.
- [21] S. M. Prokes, "Light emission in thermally oxidized porous silicon: Evidence for oxide-related luminescence", *Appl. Phys. Lett.*, 62, pp. 3244-3246, 1993.

Pulsed Laser Deposition growth of SBN and correlation study of structure and optical properties

Félix E. Fernández, Yelitza González, Huimin Liu,
Edgardo Rodríguez, Víctor Rodríguez, and Weiyi Jia

Department of Physics, University of Puerto Rico
Mayagüez, PR 00681-9016, USA

ABSTRACT

Strontium barium niobate ($\text{Sr}_x\text{Ba}_{1-x}\text{Nb}_2\text{O}_6$) thin films were grown by PLD and characterized as to their structure, composition, and both linear and nonlinear optical properties. Attempted composition of very nearly $x=0.61$ was achieved, as shown within experimental error of RBS and PIXE techniques. Films were deposited on MgO (001) and fused silica substrates at a range of growth rates, while keeping other factors constant. Films with excellent texture, and oriented with the c-axis normal to the substrate surface were obtained on the MgO substrates. Films grown on fused silica showed a range of structures, from essentially amorphous to well oriented, again with c-axis normal to the substrate surface. The absorption edge of the films was determined to be substantially blue-shifted in comparison with bulk material. This effect appears to correlate with film microstructure, with more disordered films grown on glass showing the largest shifts. Degenerate four-wave-mixing techniques were used to study the nonlinear optical response of the amorphous films. A considerable enhancement, by 2 orders of magnitude, of the third order nonlinear susceptibility $\chi^{(3)}$ in transverse alignment was found to occur with respect to bulk values.

Keywords: SBN; PLD; optical properties; microstructure

1. INTRODUCTION

Strontium barium niobate ($\text{Sr}_x\text{Ba}_{1-x}\text{Nb}_2\text{O}_6$ - SBN) with composition $0.25 \leq x \leq 0.75$ is the solid solution of the SrNb_2O_6 - BaNb_2O_6 binary system. SBN belongs to the tetragonal (4mm) tungsten-bronze family, and is a promising material for diverse optoelectronic applications such as E-O modulators, real-time holography, and information storage. It has very high pyroelectric, ferroelectric and photorefractive property coefficients. In the bulk, SBN exhibits an exceptionally large diagonal electro-optic (E-O) coefficient r_{33} compared to all known E-O crystals. For $0.6 \leq x \leq 0.75$ its E-O coefficient is in the range 400-1350 pm/V,^{1,2} much greater than that of LiNbO_3 (30 pm/V), the industry standard.

SBN with $x=0.61$ (SBN:61) is easier to grow in the bulk because this is the congruently melting composition of the SrNb_2O_6 - BaNb_2O_6 system.³ The Curie phase transition temperature for SBN:61 is $\sim 75^\circ\text{C}$, but spread over a region of width $\sim 5^\circ\text{C}$. SBN is described as a relaxor ferroelectric.² A recent investigation focused on identification of specific valence states of impurities in bulk SBN:61 through optical and magnetic resonance techniques.⁴ The information available for this particular composition makes it a good departure point for growth of SBN thin films, as it will be of interest to compare their properties with those of the bulk.

From the late 60's, studies on SBN have focused on improving bulk growth techniques, and on modification of the photorefractive and pyroelectric response of the material through the addition of dopants. Although these linear optical properties have been extensively studied, the third-order nonlinear optical (NLO) properties have not yet been well characterized. Moreover, optical properties in general of SBN thin films, which could depart from bulk properties, have not been much studied. Nevertheless, these are of interest for many of the possible applications of this material, which would require its use in thin film form. Pulsed Laser Deposition was recently proved very successful in growing thin films of this multicomponent material.⁵ For the work presented here, we prepared SBN thin films by PLD with a targeted composition with $x=0.61$ (SBN:61). Our main interest at this stage is to study the optical properties of the films in order to learn how these could vary from bulk values, and possibly how they could be controlled.

2. EXPERIMENTAL PROCEDURES AND RESULTS

2.1. Thin film preparation and characterization

SBN thin films were prepared for this work by reactive PLD. The stainless steel chamber used is evacuated by a turbomolecular pump. Pressures are measured with a capacitance gauge and an ionization gauge with a nude Bayard-Alpert tube. Substrates are heated by means of a PID-controlled substrate heater. A mass flow controller regulates gas admission for reactive PLD growth. A valve separating the TMP from the chamber permits pumping to be throttled, which allows for stable independent pressure control at a range of gas flow rates. The laser source is an excimer laser (Lambda Physik Compex 110) operating at 248 nm (KrF excimer) with a maximum repetition rate of 100 pulses per second. Beam incidence is $\sim 45^\circ$ onto rotating targets.

For this work, $\text{Sr}_x\text{Ba}_{1-x}\text{Nb}_2\text{O}_6$ targets with attempted composition $x = 0.61$ were fabricated in our laboratory. These were prepared by cold-pressing and subsequent sintering of SBN powders previously obtained from solid state reaction of high purity SrCO_3 , BaCO_3 , and Nb_2O_5 powders. Sintering was carried out at $1,300^\circ\text{C}$ for three days. The resulting targets were very hard, with a dark yellow appearance. Target density was 4.2 g/cm^3 , which is approximately 80 % of the bulk value for SBN:61. Stoichiometry of the target material was checked by XRD analysis, which showed that the peak pattern was consistent with the attempted composition, based on interpolation of standard ICDD diffraction patterns for $\text{Sr}_x\text{Ba}_{1-x}\text{Nb}_2\text{O}_6$ with $x = 0.5$ and with $x = 0.75$.

Film samples were grown on MgO (001) and fused silica substrates. These were cleaned in ultrasonic baths of trichloroethylene, acetone, and methanol, and dried in a flow of extra-dry nitrogen. The substrates were fixed to the heater surface with a silver emulsion paste. Chamber background pressure was $\sim 5 \times 10^{-7}$ Torr to 10^{-6} Torr, and targets were ablated *in vacuo*, while the substrate was covered by a shutter. For all films deposited for this study, attempted substrate temperature was 700°C , and target-substrate distance was 4 cm. O_2 was admitted to the chamber at a 4 sccm flow rate, and pressure was adjusted to 100 mTorr by throttling the pump. After deposition, substrates were cooled down in a static O_2 atmosphere of a few Torr.

Average fluence at the target surface for all depositions was approximately 2 J/cm^2 . Growth rate under these conditions was initially determined to be $\sim 0.325\text{ \AA/pulse}$ by interferometric measurement of a deposited step. Films were grown on both types of substrates with pulse repetition rates which were varied from 5 to 20 pulses/sec, equivalent to expected growth rates from 1.6 to 6.5 \AA/sec . Deposition times were adjusted in order to obtain films of nominally the same thickness ($6,000\text{ \AA}$). The measured film thicknesses, as determined from transmittance measurements, varied from as low as $4,800\text{ \AA}$ to as high as over $9,000\text{ \AA}$. The difference is attributed mainly to varying surface condition of the target used, but there is an uncertainty due to the thickness variation typical in PLD films grown without scanning.

2.2 Microscopic characterization

All films appeared smooth and clear, with optical interference fringes due to the thickness variation. For films grown at higher rate (20 pps), observation with an optical microscope up to 1,000X revealed no features for films grown on MgO except for some small needle-like crystals growing mainly along lines, possibly caused by substrate steps or polishing marks.

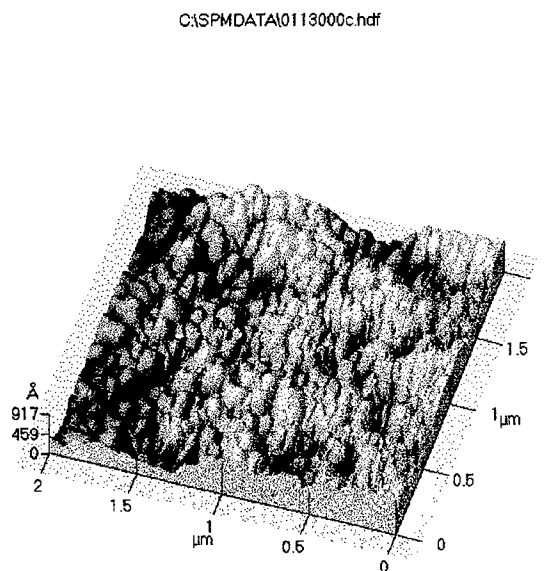


Figure 1 AFM image of SBN film on glass substrate at a 20 pps repetition rate. Surface roughness is $\sim 100\text{ \AA}$ rms.

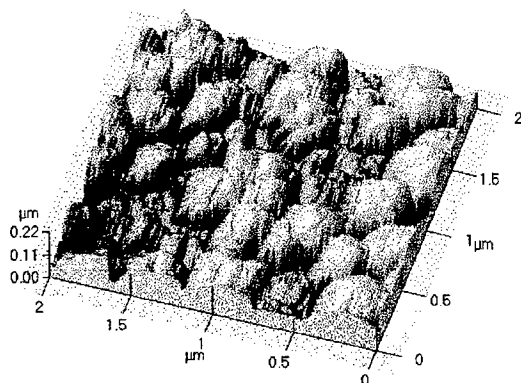


Figure 2 AFM image of SBN film on MgO substrate at a 5 pps repetition rate. Surface roughness is ~ 400 Å rms.

Figure 1), with sizes up to 0.1 to 0.2 μm , and low roughness (~ 100 Å rms). For films grown on MgO (001) substrates, there is increasing grain size with decreasing growth rate, with grains of ~ 0.5 μm observed, as shown in Figure 2, for the films grown at the lowest rate (5 pulses/second). Surface roughness also correlated with the growth rate, with smoother films (~ 100 Å rms) corresponding to the high growth rate, and rougher films (~ 400 Å) to the low growth rate.

2.3 Crystal structure characterization

Sample crystalline microstructure was studied with a standard powder diffractometer in Bragg-Brentano configuration (Siemens D-5000), and using $\text{Cu K}\alpha$ radiation. The $\text{Cu K}\alpha_2$ line was removed computationally. For all films, we were able to assign all observed diffraction peaks to the SBN:61 phase. All films grown on the MgO (001) substrates showed very strong texture, with the SBN c-axis normal to the substrate being the preferential orientation. This is the case even for films grown at the highest rate, as shown in Figure 3. In this case the film was $\sim 7,000$ Å thick, as determined from transmission measurements, and actual growth rate was ~ 2.7 $\mu\text{m/hr}$. Noting that the intensity axis is logarithmic in Figure 3, the (00 l) SBN reflections are shown to be extremely strong in comparison with others. The excellent crystal quality was confirmed

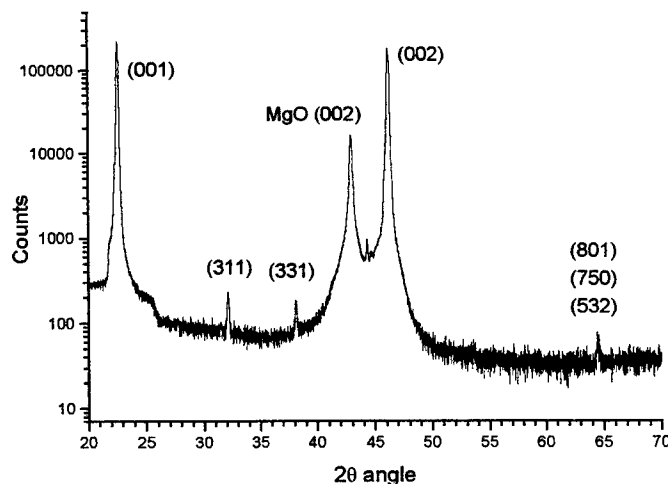


Figure 3 XRD scan of SBN sample grown at 20 pps on a MgO (001) crystal substrate. Note logarithmic intensity scale. Film is strongly textured.

For films grown on fused silica, the film surface appeared very smooth, except for cracking, likely due to the difference in expansion coefficients of substrate and film. There was little particulate inclusion.

Film surface morphology was further studied with an Atomic Force Microscope (Park Scientific Instruments, CP Autoprobe). For films grown under nominally identical conditions, but with two different substrate heaters, we have observed appreciable differences in microstructure, which are confirmed by X-ray diffraction studies. It is possible that the actual growth temperature of the two film batches were different, although calibrations were performed in both cases. The earlier films had a more disordered microstructure, and films grown on the glass substrates at the highest rate attempted (20 pulses/second, equivalent to over 2 $\mu\text{m/hr}$) were essentially amorphous, while films grown on MgO were polycrystalline, with poor orientation.⁶ These earlier results led us to prepare and study films deposited at a range of growth rates, with other conditions being held constant as much as possible. Unless otherwise noted, all subsequent characterization results presented pertain to the more recent batch of films, grown with the same substrate heater.

AFM images of the films show a microstructure which depends on the type of substrate and the growth rate. Films grown on glass present smaller grains (see

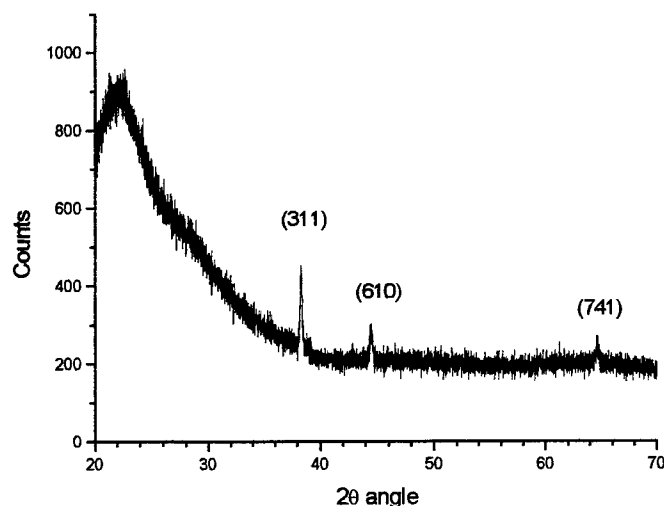


Figure 4 XRD scan for SBN film grown on fused silica at 15 pps. The film is essentially amorphous, but there is some crystal development.

this case we obtained some films which were very disordered, as shown in Figure 4, and others which are strongly textured, with preferred orientation along the c-axis, as shown in Figure 5. However, there is no clear correlation of microstructure with growth rate, except that, again, the film grown at the fastest rate showed the strongest texture. Additional study will be required in this respect.

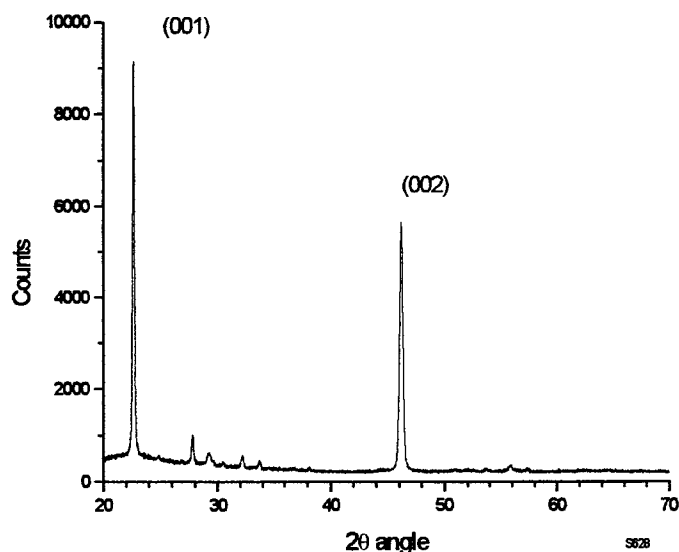


Figure 5 XRD scan for SBN film grown on fused silica at 20 pps. The film is polycrystalline, with strong orientation of the SBN c-axis normal to the substrate surface.

MgO (001) was analyzed with a high-resolution, triple axis x-ray diffractometer (Bede Instruments Model D-1). The FWHM for the Ω angle of the diffraction peak was 180 arc seconds. This is very narrow for a textured film, and resembles a moderately dislocated crystal. The quality of the MgO substrates used was rather poor, as found from a reciprocal space mapping performed in the same high-resolution diffractometer. Thus, film quality could be improved further if better substrates are used.

There is no clear correlation between growth rate and crystalline structure for films grown on MgO (001), at least as far as we can determine from the powder diffractometer scans, and for the limited range of growth rates used. We note, however, that the strongest orientation observed was for a film grown at the highest rate. This was also the film with the lowest surface roughness (~ 100 Å rms) and the lowest grain size, as seen by AFM.

There appears to be more microstructural variability for the films grown on glass substrates. In

2.4 Determination of composition

Metallic elements in SBN are not volatile at the substrate temperature we used during growth. Hence, film composition was not expected to vary significantly from that of the target. Nevertheless, we have verified this through Rutherford Backscattering Spectroscopy analysis of a sample previously grown on MgO. RBS was performed with 2.5 MeV $^4\text{He}^+$ ions. The Ba content measured was 11.8 ± 5 at. %, excluding the oxygen, which is masked by the substrate. This is very close to the expected value of 13 at. % (again excluding oxygen) for the attempted target composition. The Sr and Nb peaks could not be resolved in the RBS scans, as shown in Figure 2. In order to obtain the Nb and Sr areal concentrations, Particle Induced X-ray Emission (PIXE) analysis was performed. Combining the RBS and PIXE results, and taking into account experimental errors, which are larger (10 %) for PIXE results, we determined the metallic atomic fractions in the sample to be 0.19 ± 0.02 , 0.118 ± 0.006 , and 0.69 ± 0.07 for Sr, Ba, and Nb, respectively. This compares very well with the

attempted values of 0.20, 0.13, and 0.67, respectively. Thus, we are confident that PLD can indeed produce SBN thin films with stoichiometry very close to that of the target.

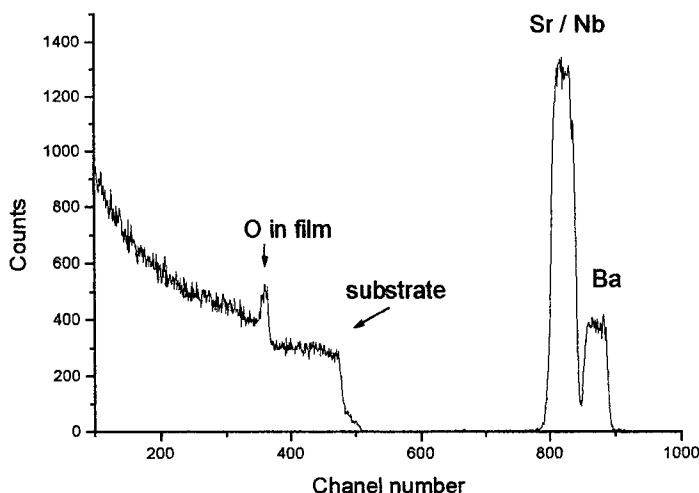


Figure 6 RBS spectrum of SBN film grown on MgO substrate. Sr and Nb peaks are not resolved.

2.5 Optical properties

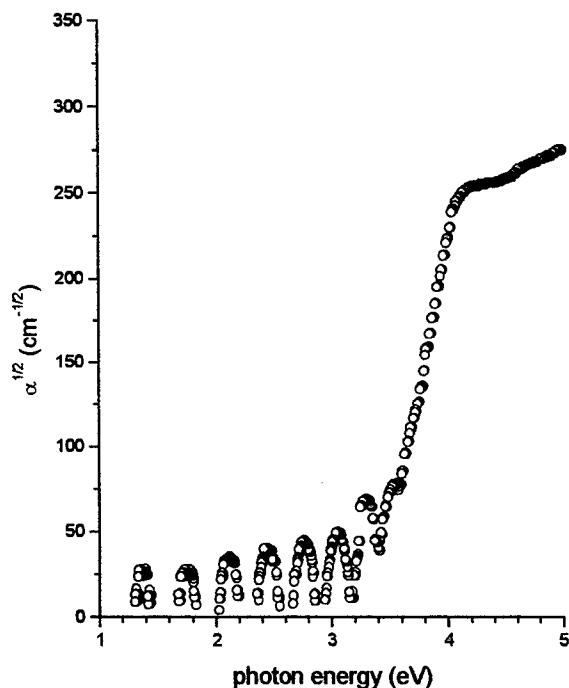


Figure 7 Square root of the estimated absorption coefficient vs. photon energy for an SBN film grown on MgO. The oscillations at low energy are interference fringes and do not represent material absorption.

All of the samples are relatively transparent throughout the visible and near IR, with an absorption edge in the near UV, as explained below. Transmission and absorbance spectra of samples grown on MgO and fused silica were obtained with a spectrophotometer. From the interference extrema in these spectra we determined the refractive index of the films in the transparent region and their thicknesses. In order to avoid wash-out of interference fringes due to film thickness variation, a 2 mm diameter central region of the sample was probed by using a mask. The index of the films grown on MgO can range from nearly the same as the bulk values ($n = 2.23$ at $\lambda = 633$ nm, for example) to substantially lower ($n = 2.0$ at $\lambda = 633$ nm). The index of the amorphous films is generally lower (ranging from 2.0 to 2.1 at $\lambda = 633$ nm, for example).

For both types of substrates used, absorption losses are negligible in the region of interest here. Reflection losses are fairly constant and were numerically compensated for. With this information, absorption measurements were corrected for reflection losses. From these corrected spectra, and using the determined thicknesses for the samples, we calculated the absorption coefficient (α) in units of cm^{-1} through the measured range. In the fundamental edge region the data for α can be approximately described as proportional to $(E_{\text{photon}} - E_{\text{gap}})^\gamma$, with $\gamma = 2$, which indicates an indirect transition between valence and conduction bands. However, the value for E_{gap} varies greatly, depending on sample microstructure. For samples

grown on MgO, the values are in general higher than those reported for bulk SBN:61. Absorption coefficient data for bulk SBN:61 crystals was given by Giles et al.⁴ The band edge was reported to occur near 3.26 eV. These authors measured the absorption spectra along an "a" axis of the crystal, i.e.: along a direction perpendicular to the optical axis for the tetragonal SBN:61. Since unpolarized light was used, the results are for a combination in equal parts of ordinary and extraordinary waves. In our case, for well-oriented samples, we are effectively measuring along the "c" axis, which is normal to the substrate. For such samples, as in the case shown in Figure 7, our estimates for E_{gap} indicate values from 3.3 to 3.4 eV. For samples with poor orientation, mainly those grown on glass, the values are much larger, ranging from 3.4 to 3.8 eV. The oscillations in the low-absorption region in Figures 7 and 8 are artifacts due to interference effects in the film causing reflection maxima and do not represent actual absorption. In this region, only the minima should approximate absorption coefficient values of the film material. Scattering losses are not considered in this simple treatment, so that estimated α values are expected to be higher than those for ideal bulk SBN:61. The α values for films grown on glass are always higher than those for films grown on MgO. This can be due to higher scattering losses in the former type of films, which is expected due to the more disordered microstructure.

While we can expect differences in the measured band edge for the films, with respect to the bulk value reported in Ref. 4, the shift towards the UV from bulk to disordered film appears to be significant. The absorption edge in SBN corresponds to the intrinsic interband transition between the valence band, which consists of $p\pi$ orbitals of the oxygen electrons, and the conduction band, which consists of $d\zeta$ orbitals of Nb electrons. The blue-shift observed appears to correlate with disorder. This may be due to narrowing of the energy bands in the disordered material, and resultant widening of the band gap.

2.6 Nonlinear optical properties

Degenerate four-wave mixing experiments were conducted on amorphous SBN:61 films grown on glass. A psec Nd:YAG laser was used as pump source. The experimental details have been described elsewhere.^{6,7} A significant enhancement of $\chi^{(3)}$ with respect to bulk values was found. The value of $\chi^{(3)}$ is estimated to increase by 2 orders of magnitude in transverse alignment. From the absolute diffraction efficiency measurements $\chi_{1111} = \chi_{2222} = \chi_{3333} = 2.6 \times 10^{-11}$ esu was obtained.^{6,7}

3. CONCLUSIONS

SBN:61 thin films were grown by reactive PLD on MgO (001) and fused silica glass substrates. A range of deposition rates was used, in order to study its effect on film structure and properties. Films had composition very close to the attempted one, as shown by RBS and PIXE analysis. SBN/MgO samples were very strongly textured, with the SBN c-axis normal to the substrate surface. Films grown at lower rates showed larger grains and higher roughness. SBN/glass films were much more disordered, as could be expected, but well oriented films were also obtained in some cases. Disorder in this case did not correlate well with growth rate within the range explored. Refractive index and absorption edge deviated from bulk values for disordered films. The absorption edge was substantially blue-shifted for very disordered films. NLO properties were measured for SBN/glass films, and $\chi^{(3)}$ was found to be much larger for the thin film material than has been reported for the bulk.

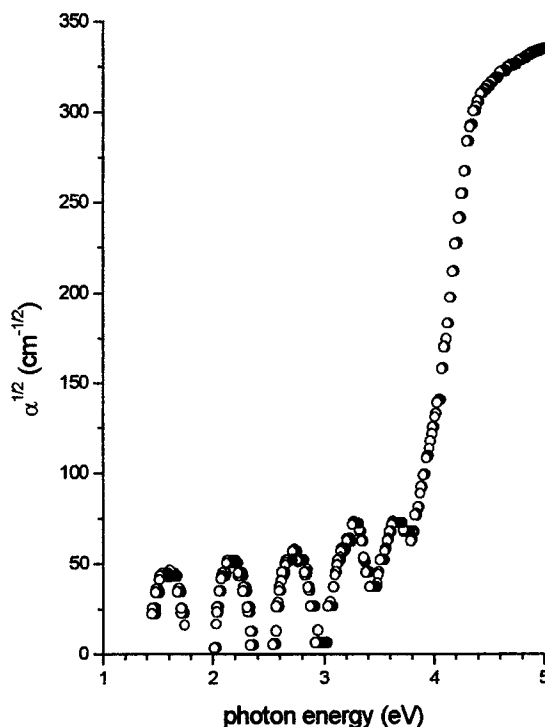


Figure 8 Square root of the estimated absorption coefficient vs. photon energy for an SBN film grown on fused silica. Again, oscillations at low energy do not represent material absorption. Note higher value of absorption edge.

ACKNOWLEDGMENTS

We are pleased to acknowledge the support for this work by US DoE (Grant DE-FRO2-94ER757640), US ARO (Grant DAAH04-96-10416), NASA-URC (Grant NCCW-0088) and NSF (Grant EHR-9108775). RBS and PLXE measurements were performed by L. McIntyre and his collaborators at the University of Arizona. We are grateful to Dr. Keith Bowen, of Bede Scientific, for the high-resolution XRD measurements on one of the samples.

REFERENCES

1. J.H. Weaver and P.R. Frederikse, *CRC Handbook of Chemistry and Physics*, D.R. Lide (ed.), CRC Press, Boca Raton, 76th edition (1995) p. 12-156.
2. R.A. Vasquez, M.D. Ewbank and P.R. Neurgaonkar, *Opt. Commun.*, **80** (1991) 235.
3. K.Megumi, N.Nagatsuma, Y.Kashiwada, and Y.Furuhata, *J.Mater.Sci.* **11**, 1583 (1986).
4. N.C. Giles, J.L. Wolford and G.J. Edwards, *J.Appl.Phys.*, **77** (1995) 976.
5. S.Schwyn Thöny, K.E.Youden, J.S.Harris, and L. Hesselink, *Appl. Phys. Lett.* **65**, (1994) 2018.
6. F.E. Fernández, H. Liu, C. Jin, and W. Jia, *Integrated Ferroelectrics* (1999) accepted.
7. H. Liu, S.T. Li, G.K. Liu, W. Jia, and F.E. Fernández, *Journal of Luminescence*, **83-84** (1999) 367.

Electric signal diagnostics of plasma dynamics at early stage of laser ablation

M. H. Hong, Y. F. Lu* and A. Foong

Laser Microprocessing Laboratory, Department of Electrical Engineering and
Data Storage Institute, National University of Singapore,
10 Kent Ridge Crescent, Singapore 119260

ABSTRACT

Plasma dynamics at early stage of laser ablation is investigated by a tiny metal probe. There are two negative peaks with different distributions in an electric signal. The first peak has a duration about 50 ns and delays 30 ns with respect to laser irradiation. The waveform and peak maximum position do not change with probe distance. It is attributed to plasma-induced electric field at the early stage. The second peak appears about 250 ns later with a profile duration higher than 1 μ s. The peak maximum position moves forward as probe distance reduces due to earlier charge particle arrival of the probe. Experimental results and theoretical modeling show that electric signal of plasma-induced electric field is resulted from an electric dipole with negative charge in front. It is constructed by electrons and positive ions emitted at early stage of laser ablation. Dependence of electric signal profile on probe distance, laser fluence and pulse number is studied. The electric signal detection can be used to monitor laser removal of metallic oxide layer in real time. Influence of substrate bias on the signal waveform is also analyzed. It may be applied to modify plasma dynamics and laser ablation.

Keywords: Laser ablation, plasma dynamics, electric signal, early stage

1. INTRODUCTION

High power short pulse laser irradiation has been extensively applied to ablate solid materials for thin film deposition and materials microprocessing.¹⁻³ Since there are many dynamic processes involved, pulsed laser ablation is a complicated process.⁴ A clear picture on the mechanisms of laser ablation and particle emission is still not available. To have a better understanding and control of laser processing, many efforts have been made to detect and analyze laser-ablation-induced signals. Such measurement includes audible acoustic wave detection for real-time monitoring of laser ablation and optical multi-channel analyses of emission spectra for laser-ablation-induced plasma.⁵⁻⁶ These detection techniques can provide the information on substrate vibration and electron transitions between different atomic levels. Electric signal diagnostic for charged particle emission is an alternative approach to study fundamental processes involved in the laser interaction with materials. There are three basic mechanisms attributed to charged particle emission during pulsed laser irradiation of solid substrate: surface photoeffect, thermionic emission and laser-ablation-induced plasma.⁷ Their contributions are closely related to materials properties and laser intensity. Surface photoeffect is a process in which electrons are emitted when UV light is irradiated on a metal surface. To measure photoelectron emission, a high vacuum and atomically clean substrate surface are generally required. When a laser beam irradiates on the substrate surface, electrons will absorb laser energy and cause the increase of surface temperature. A fraction of the electrons may obtain enough thermal energy and jump across a barrier defined by its work function. It is thermionic emission of electrons. High surface temperature can also result in positive ion emission. It has been reported that electron emission is dominant at low laser intensity. With laser fluence above melting threshold, ion emission increases tremendously.⁸ For laser fluence higher than ablation threshold for the solid substrate, the laser beam evaporates and ionizes the materials, creating a plasma plume above the substrate surface. There is explosive emission of electrons, ions and neutral atoms during the laser ablation. These fast ejected particles interact each other and also absorb incident laser energy, which greatly enhances electron and positive ion generation.⁷ Compared with laser-ablation-induced plasma, electric signals attributed to photoeffect and thermionic emission can be neglected.⁸ Therefore, plasma dynamics during laser ablation can be studied from the electric signal which reflects the emission of electrons and positive ions, especially at the early stage. To obtain more knowledge on the charged particle emission,

Correspondence: Email: eleluyf@nus.edu.sg; Telephone: 65-8742118; Fax: 65-7782968

appropriate electric signal detection is essential. Since charged particles emitted during laser ablation are moving outwards at high speeds, they induce electric fields in vicinities. With an electrode near the plasma, laser-ablation-induced electric signal can be detected. The signal could reflect properties and dynamics of charged particles emitted during laser ablation. Time-of-flight, Langmuir probe and Farady cup techniques have been widely applied to detect speed, distribution and generation of electrons and charged particles.⁹⁻¹¹ These techniques are based on direct interaction between the electrode and charged particles, which may induce emission of secondary charged particles from the electrode. It will affect electric signal detection accuracy.¹² Furthermore, signal measurement can only be carried out inside a high vacuum since the electrodes are normally placed several centimeters away from the substrates. Signals detected are microseconds delayed after the laser irradiation and therefore cannot reflect the early stage of laser ablation. It is also difficult for these techniques to detect charged particle emission during laser ablation in air since the plasma size is quite small. In this study, a tiny metal probe is used to detect electric signals generated during laser ablation. Variation of the electric signals is analyzed at different probe distances from the laser spot on the substrate surface. Dependence of peak amplitude and duration on laser fluence, substrate bias and pulse number is also investigated. Mechanisms on the electron and positive ion emission are discussed.

2. EXPERIMENTAL

Figure 1 shows experimental setup for the electric signal detection during pulsed laser ablation of solid substrates in air. A KrF excimer laser (Lambda Physik, LPX 100) was used as a light source. The laser beam has a wavelength of 248 nm and a pulse duration around 23 ns. After passing through a beam splitter, 5 % of the laser energy was irradiated into an ultrafast phototube (Hamamatsu R1328U-53, rise time: 60 ps and fall time: 55 ps) to capture the laser pulse profile. The other part of the laser energy was focussed onto the substrate surface by a quartz lens which has a diameter of 50 mm and a focal length of 150 mm. Laser fluence was changed by varying laser pulse energy. Laser light irradiates perpendicularly onto the substrate surface. The sample was placed on an X-Y stage which can change the laser irradiation position on the substrate surface after the electric signal detection and offer a fresh area for each laser pulse. The substrate was connected to the ground during the electric signal detection. A tiny metal probe (length: 0.5 cm and diameter: 0.2 mm) was used to detect the electric signal generated during the laser ablation. It was kept as 0.5 mm above the substrate surface. It was moved along the shorter axis of the laser-irradiated spot by a micrometer to change the probe position. The electric signal detected was then sent to a fast digital oscilloscope (Tektronix TDS 520, bandwidth: 500 MHz, sampling rate: 1 GS/s) with a time resolution of 1 ns. The synchronous output of the laser controller was also sent to the oscilloscope as a trigger signal for the electric signal and laser pulse detection. The digitized electric signals were then sent to a PC through an IEEE-488 interface for data storage and further processing. A power supply with the constant output from -110 to 110 V was used to apply an electric bias on the solid substrates and study bias modification of the electric signals.

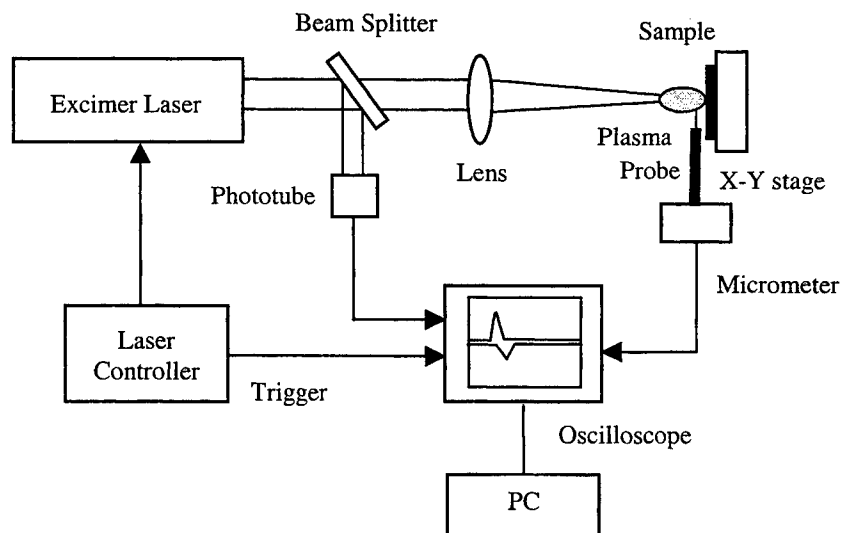


Fig. 1 Experimental setup for the electric signal detection during pulsed laser ablation of solid substrates in air.

3. RESULTS AND DISCUSSION

3.1 Electric signals:

Figure 2 shows electric signals detected during the excimer laser ablation of copper for a laser fluence of 9.2 J/cm^2 . Probe distances were 0.75 and 1.8 mm, respectively. For probe distance as 1.8 mm, there is only a negative peak in the signal. Peak duration is around 50 ns with its maximum position at a delay time of 30 ns after the laser irradiation. Since electrons and positive ions generated during the laser ablation are moving outwards at high speeds, they will reach the probe with a time delay and induce an electric signal on the probe. Meanwhile, electron and positive ion emission is in a fast dynamics during plasma formation. According to classical electrodynamics, the plasma will induce an electric field in its vicinity at once as the emission occurs. With a metal probe nearby, the electric signal can also be detected. To distinguish nature of the negative peak, electric signals at different probe distances up to 10 mm were detected. It is found that the signal waveform and peak maximum position do not change for different probe positions. It can be understood that this negative peak cannot be attributed to the electron and positive ion reaching the probe. Otherwise, the higher probe distance would delay the arrival of the electrons and positive ions. The peak maximum position would move to the right as probe distance increases. To confirm this conclusion, the metal probe was coated with one layer of wax. Electric signals detected with and without the wax layer were compared under the same experimental conditions. It was found that there is no difference for the signal waveforms and peak maximum positions. Wax is an electric insulator which can block electrons and positive ions reaching the probe. Therefore, it can be concluded that the negative peak signal is attributed to the plasma-induced electric field.

For probe distance of 0.75 mm, there are two negative peaks with different profiles in the signal. Compared with probe distance as 1.8 mm, the first negative peak has the same waveform and peak maximum position is at the same place. It is clear that the first peak is attributed to plasma-induced electric field. The second negative peak appears about 250 ns later. It moves to the left as probe distance reduces. By increasing time scale of the oscilloscope, it was observed that the second peak waveform is actually one part of a dual-peak structure. In this waveform structure, the negative peak appears first and follows by a positive one. Peak duration is in an order of microseconds. The experimental results imply that the second peak is attributed to the arrival of electrons and positive ions to the probe. Confined by high pressure of air molecules, plasma generated during the laser ablation in air is generally very small. It is very difficult for the charged particles to fly a long distance and reach the probe. This is why the second peak does not appear at a high probe distance.

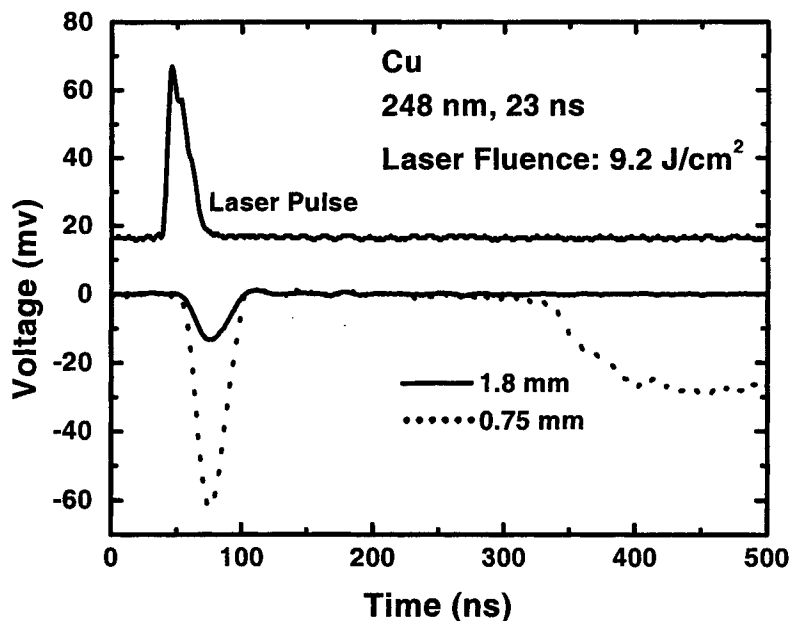


Fig. 2 Electric signals recorded during the excimer laser ablation of copper at a laser fluence of 9.2 J/cm^2 and probe distances of 0.75 and 1.8 mm.

To explain the experimental results, electron and positive ion emission at early stage of laser ablation was modeled as shown in Fig. 3. At the starting of laser ablation, there is only electron emission from the substrate surface. It induces a negative electric field nearby. Electric signal detected by the probe is negative. Signal amplitude increases as more and more electrons are emitted. However, subsequently emitted positive ions create a positive electric field nearby. Charge centres of the electrons and positive ions are different. Since charge centre displacement is much smaller than probe distance at the early stage, they behave like an electric dipole with the negative side in front. Negative peak amplitude of the signal corresponds to the electric dipole constructed by total electrons and ions emitted. Its value is proportional to total electric charges emitted during the laser ablation. As the dynamic process continues, the charge centre displacement increases up to a value comparable to the probe distance since the electrons are moving forward in a much higher speed than the positive ions. Their behaviors change back to two individual electric centres with the same electric charges but the opposite polarities. Total electric field induced by the charged particles reduces gradually to zero and the electric signal vanishes.

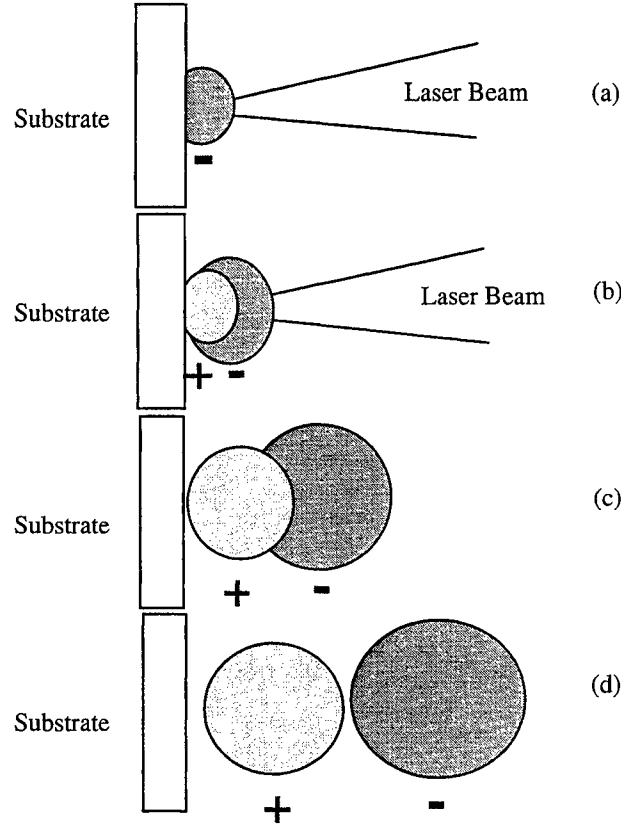


Fig. 3 Electron and positive ion emission at early stage of laser ablation.

3.2 Electric signal as a function of probe distance and laser fluence

It can be found in Fig. 2 that the first negative peak becomes sharper with a higher peak amplitude as probe distance reduces. In this study, full width at half maximum (FWHM) is applied to characterize peak width. Figures 4 (a) & (b) show FWHM and peak amplitude as a function of probe distance during the excimer laser ablation of silicon. Laser fluence applied was 3.7 J/cm^2 . It is clear that FWHM increases almost linearly with probe distance. While peak amplitude reduces greatly with probe distance. According to classical electrodynamics, electric potential induced by an electric dipole is inversely proportional to square of probe distance.¹³ Since the probe was kept 0.5 mm above the substrate surface, probe angle with respect to the laser spot on the substrate surface varies with probe distance. Considering probe angle contribution, the experimental results were fitted by the following equation:

$$V_p = \frac{ql}{4\pi\epsilon_0 r^2} \times \sin\alpha = \frac{qld}{4\pi\epsilon_0 r^3} \quad (1)$$

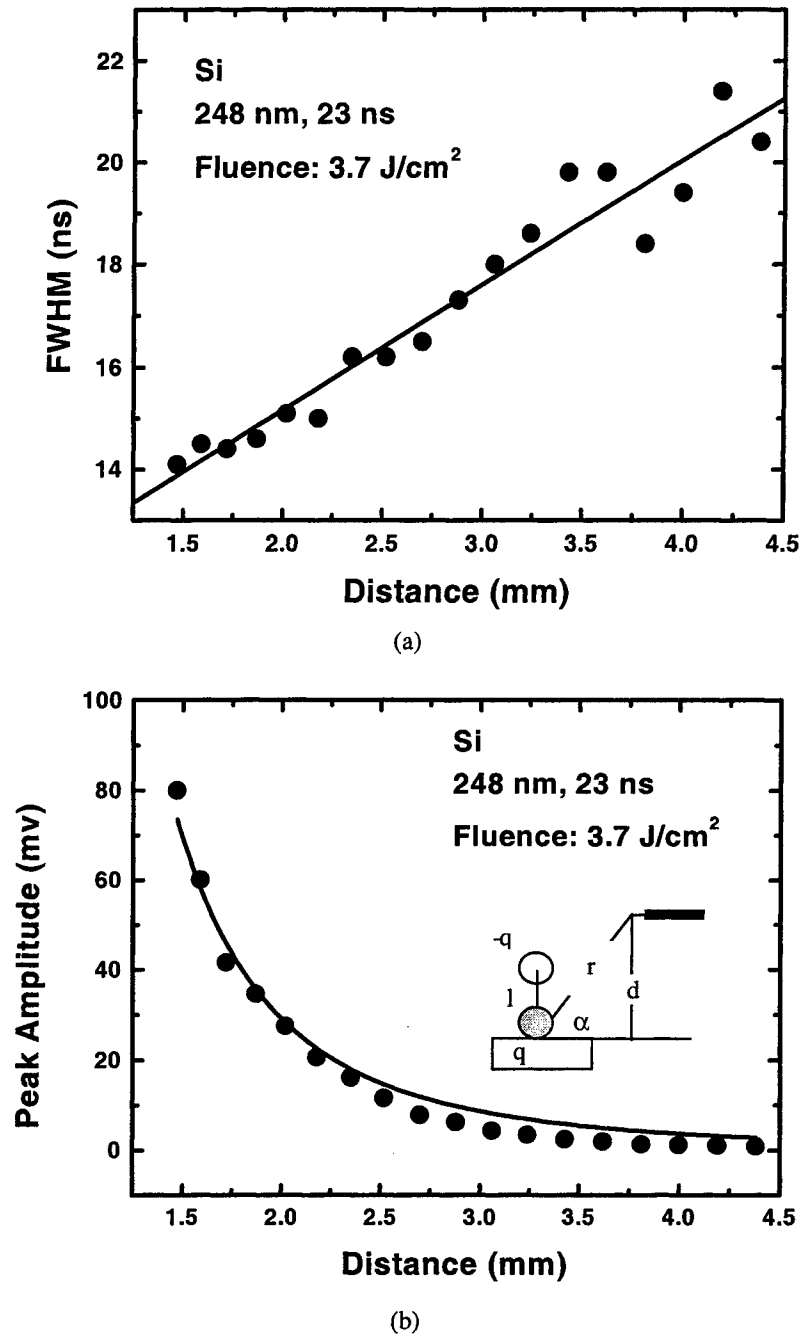


Fig. 4 Electric signal (a) FWHM and (b) peak amplitude as a function of probe distance during the excimer laser ablation of silicon for a laser fluence of 3.7 J/cm².

Where V_p is the peak amplitude, r the probe distance from the probe tip to the centre of the laser spot on the substrate surface, ϵ_0 the permittivity of vacuum, ql the electric dipole moment, d the distance between the probe and substrate surface and α the probe angle to the laser spot. It is clear from Fig. 4 (b) that equation (1) fits the experimental data very well. It confirms the conclusion that total electrons and positive ions emitted at early stage of laser ablation form an electric dipole, which induces a negative electric field in its vicinity.

Figure 5 presents dependence of peak amplitude and FWHM of the electric signal on laser fluence during the laser ablation of silicon. Probe distance was kept as 1.5 mm. It is clear that peak amplitude increases greatly while FWHM decreases slightly with laser fluence. At a higher laser fluence, the laser ablation is stronger which induces a higher density plasma. There are more electrons and positive ions emitted and the electric dipole moment is higher. Since pulsed laser ablation of solid substrates is mainly attributed to thermal mechanisms, the experimental results were fitted by thermal ablation model.¹⁴ According to this model, peak amplitude can be related to laser fluence as the following equation:

$$V_p = A_l \times \exp\left(-\frac{B_l}{\Phi}\right) \quad (2)$$

Where Φ is the laser fluence, A_l and B_l are two fitting parameters. It is clear that the experimental data can be fitted very well by the thermal ablation model.

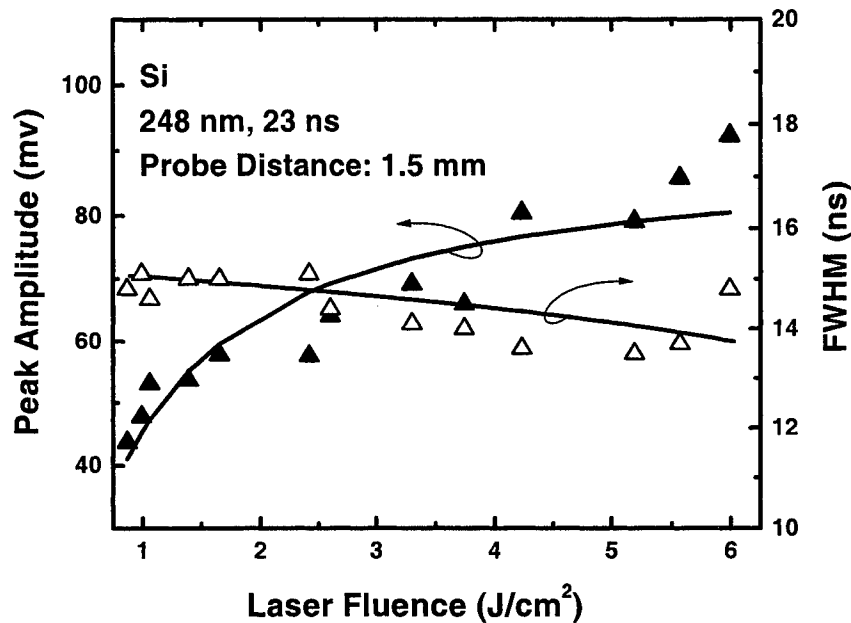


Fig. 5 Peak amplitude and FWHM versus laser fluence during the laser ablation of silicon at a probe distance of 1.5 mm.

3.3 Electric signal detected during pulsed laser removal of metallic oxide layer

Figure 6 shows electric signals detected at the 1st, 3rd, 5th, 10th, 20th and 50th pulses of the laser irradiation during the excimer laser removal of tungsten oxide layer at a probe distance of 6.9 mm. Laser fluences applied were 0.91 and 2.7 J/cm², respectively. It is clear that signal variation with pulse number is closely related to laser fluence. For laser fluence of 0.91 J/cm², peak amplitude reduces gradually to zero for pulse number higher than 10. It is attributed to laser removal of the oxide layer. Substrate surface morphology was compared under a microscopy before and after laser irradiation. It showed that the oxide layer was completely removed and there was no surface damage on tungsten substrate. By checking when peak amplitude reduces to zero, laser removal of metallic oxide layer can be monitored in real time. While for laser fluence of 2.7 J/cm², signal variation is more complicated. Peak amplitude increases at the first several pulse numbers. It is probably due to less electron and positive ion emission since concentration of tungsten atoms at the outside oxide layer is much lower. With a higher laser number, peak amplitude also decreases gradually but to a non-zero value. Surface morphology comparison showed that there was a crater on the substrate surface after the laser irradiation. It implies that the substrate was ablated, which also contributes to electron and charged particle emission. As pulse number increases, the oxide layer is removed gradually and peak amplitude decreases. For laser irradiation up to 10 pulses, the oxide layer was completely removed. There is only laser ablation of the substrate. Therefore, the electric signal is stabilized and peak amplitude equals to a constant. From the peak amplitude at a high pulse number, laser interaction with the substrate can be referred.

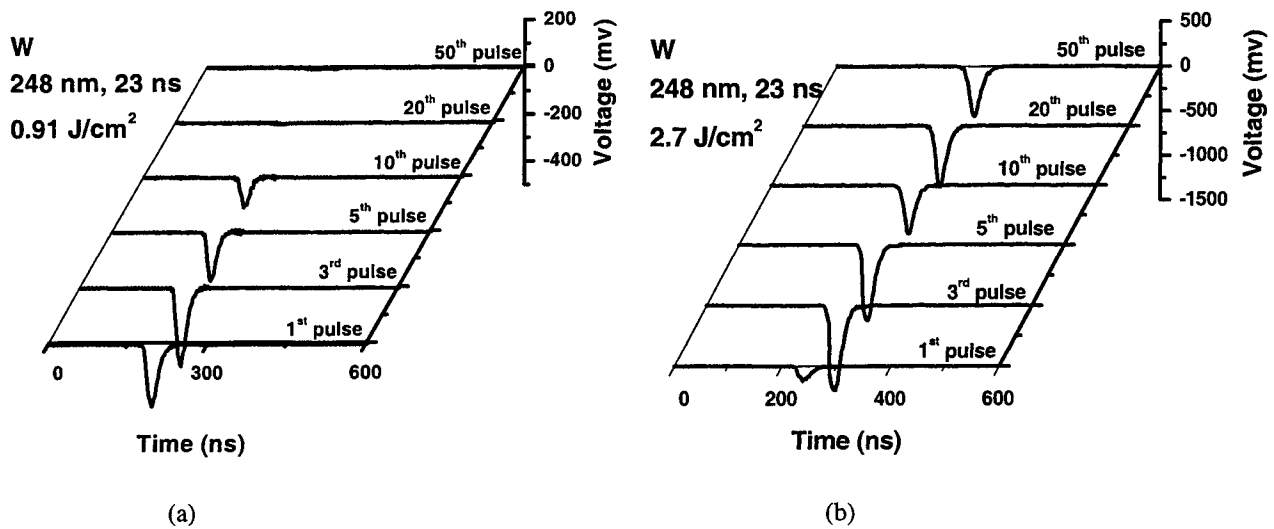


Fig. 6 Electric signals detected during the excimer laser removal of tungsten oxide layer for laser fluences of 0.91 and 2.7 J/cm² and pulse number of 1, 3, 5, 10, 20 and 50. Probe distance was 6.9 mm.

Figure 7 shows peak amplitude of the electric signal detected at the 50th pulse of laser irradiation versus laser fluence during the laser ablation. It can be found that peak amplitude increases with laser fluence due to more electrons and positive ions emitted during a stronger laser ablation. The amplitude is zero when there is no laser ablation of the substrate. By numerical fitting of the experimental results, threshold fluence for the excimer laser ablation of tungsten substrate can be estimated to be 1.3 J/cm².

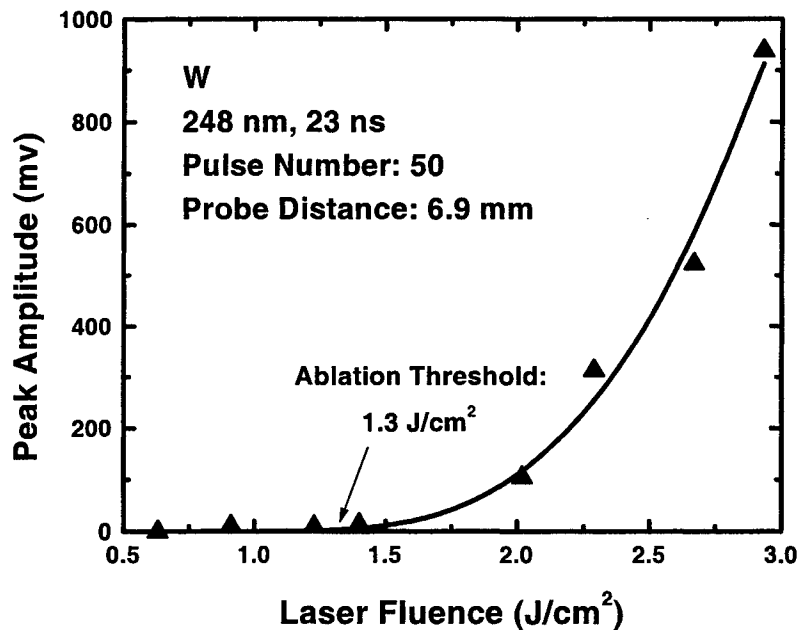


Fig. 7 Peak amplitude at a pulse number of 50 versus laser fluence during the laser removal of tungsten oxide layer for a probe distance of 6.9 mm.

3.4 Electric signal as a function of substrate bias

Electric signals in the previous discussion were detected for substrate bias as zero. Signal amplitude equals to electric potential difference between the probe and ground. Signal analyses show that there is a fast dynamic electric field generated at the early stage. If an external electric field is applied on the substrate, there are attracting or expelling forces acting on the electrons and positive ions. Plasma dynamics will be affected by the external field and the electric signal will be changed. It can influence collisions among plasma species and processing results after the laser ablation maybe modified.

Figure 8 shows electric signals detected during the excimer laser ablation of silicon at a laser fluence of 4.1 J/cm^2 and a probe distance of 1.4 mm. Substrate biases were -10, -5, -2, 0, 2, 5 and 10 v, respectively. Variation of electric signals is closely related to substrate bias. For a negative bias, negative peak profile does not change. Peak width and amplitude increase with the bias amplitude. From the previous discussion, the negative peak is attributed to an electric dipole with the electron centre in front. It is constructed by electrons and positive ions emitted at early stage of laser ablation. If the substrate is negatively biased, there is a negative field acting on the electrons and positive ions. It attracts the positive ions and expels the electrons at the same time, which weakens the plasma internal electric field. It delays completion of total positive ion emission, which increases the peak width. It also increases charge centre displacement between the electrons and positive ions, which results in a higher electric dipole moment and the higher peak amplitude. Electric signals are more complicated with a positive bias. For substrate bias lower than 2 v, signal profile does not change. Peak width and amplitude reduce with substrate bias. This is due to a positive field acting on the plasma. It attracts electrons and expels positive ions, which speeds up completion of total positive ion emission. It also reduces charge centre displacement between the electrons and positive ions. The less electric dipole moment results in the lower peak amplitude. For substrate bias in a range from 2 to 5 v, signal profile changes greatly. There is a positive peak following the negative one. As substrate bias increases, the negative peak shifts forward and the peak width and amplitude reduce gradually to zero. The positive peak also moves to the left but its peak width and amplitude increase gradually with the bias. At the starting of laser ablation, there is only electron emission. Fast moving electrons are slowed down due to the positive bias attraction. When positive ions are emitted, they are expelled and speeded up by the positive field. Charge centre displacement between the electrons and positive ions reduces, which results in a lower electric dipole moment and a smaller negative peak profile. If substrate bias is high enough, charge centre for the positive ions will catch up with that for the electrons as the time elapses. Negative peak amplitude will increase back to zero. As the time increases further, the charge centre for the positive ions will be in front of that for the electrons. The negative electric dipole will change to a positive one. It induces a positive peak in the electric signal. For substrate bias above 5 v, it can be observed that the negative peak is vanished. As substrate bias increases, the positive peak shifts forward and the peak width and amplitude also increase. It is because a higher positive field attracts the

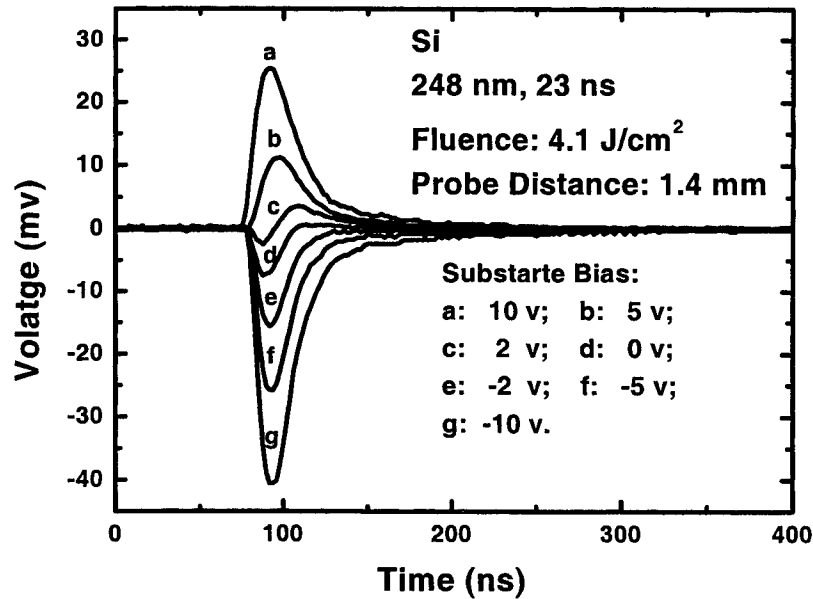


Fig. 8 Electric signals detected during the excimer laser ablation of silicon for a laser fluence of 4.1 J/cm^2 and a probe distance of 1.4 mm. Substrate biases are -10, -5, -2, 0, 2, 5, 10 v, respectively.

electrons and expels the positive ions stronger. It may cause earlier emission of the positive ions than the electrons. There is only the positive electric dipole existing during the laser ablation and the negative peak will disappear. Figure 9 shows the negative and positive peak amplitudes versus substrate bias during the laser ablation. It can be found that the peak amplitudes vary linearly with substrate bias. By numerical fitting of the experimental results, threshold fluences for negative peak disappearance and positive peak appearance are 2.67 and 0.98 J/cm², respectively.

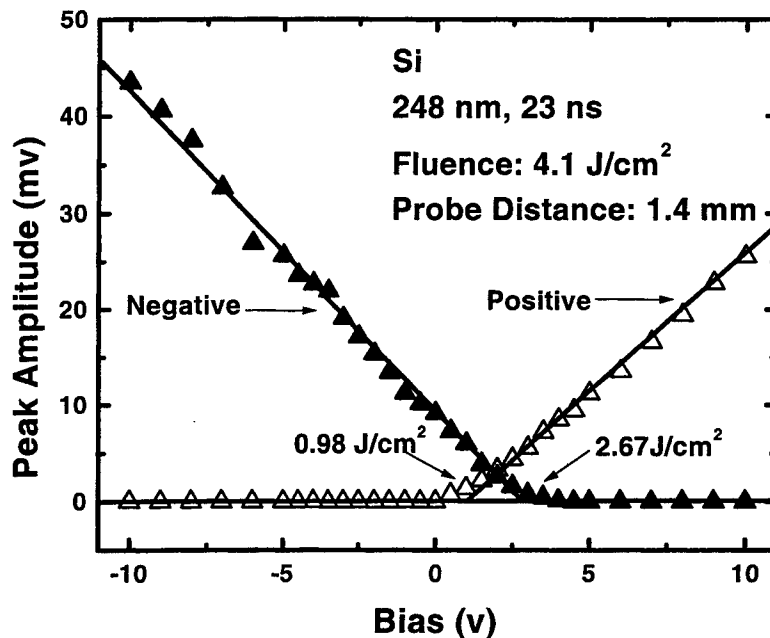


Fig. 9 Negative and positive peak amplitudes versus substrate bias for a laser fluence of 4.1 J/cm² and a probe distance of 1.4 mm

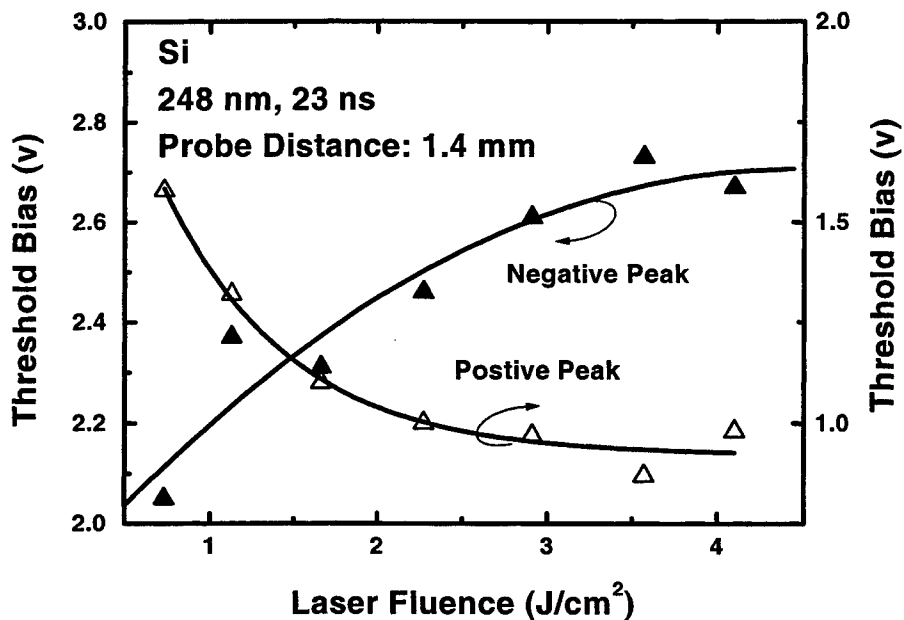


Fig. 10 Threshold biases for negative peak disappearance and positive peak appearance versus laser fluence during the excimer laser ablation of silicon at a probe distance of 1.4 mm.

Negative peak threshold bias characterizes an external bias which is strong enough to overcome plasma internal electric field during the laser ablation. While positive peak threshold bias is correlated with dynamics of electrons and positive ions at the early stage. Figure 10 shows threshold biases for negative peak disappearance and positive peak appearance versus laser fluence during the laser ablation at a probe distance of 1.4 mm. It can be found that threshold fluence for the negative peak increases with laser fluence. It is because there are more electrons emitted during the laser ablation for a higher laser fluence. It induces a stronger internal electric field for the plasma. A higher substrate bias is required to overcome this internal field. It can also be observed that threshold fluence for the positive peak reduces with laser fluence. It implies that the positive ions are in faster dynamics to catch up with the electrons for a positive bias applied on the substrate. It is closely related to plasma species interaction at early stage of laser ablation. Variation of the electron and positive ion dynamics with a substrate bias may result in modification of laser processing from the laser ablation.

CONCLUSIONS

Electric signal detection at early stage of laser ablation in air was studied. With different probe positions, electric signals detected are completely different. With the probe placed properly, the signal detected is a negative peak with a duration of around 50 ns. It is resulted from plasma-induced electric field in its vicinity. Experimental results and model explanation show that peak amplitude of the signal is inversely proportional to square of probe distance. It is attributed to an electric dipole constructed by electrons and positive ions emitted at the early stage. Peak amplitude increases while its FWHM reduces with laser fluence. Electric signals detected during the laser removal of tungsten oxide layer show that the signals reduce gradually to zero at a low laser fluence. It can be applied to monitor the laser removal of metallic oxide layer in real time. For laser fluence above substrate threshold fluence, peak amplitude also reduces but to a non-zero value due to the laser ablation of tungsten substrate. Peak amplitude at a high pulse number is applied to characterize laser interaction with the substrate. Threshold fluence for tungsten during the KrF excimer laser ablation is estimated about 1.3 J/cm^2 . Applied with a substrate bias, electric signals are modified. For a positive bias above a threshold value, a positive peak following the negative one appears. The negative peak vanishes at a higher substrate bias. Mechanisms of the electron and positive ion emission and their dynamics with the substrate bias are also discussed. It implies that substrate bias maybe applied to modify laser processing results from the laser ablation.

REFERENCES

1. R.K. Singh and J. Narayan, "Pulsed-laser evaporation technique for deposition of thin films: Physics and theoretical model", *Phys. Rev. B*, **41**, pp. 8843-8859, 1990.
2. Y.F. Lu, Y. Aoyagi, M. Takai and S. Namba, "Laser surface cleaning in air: mechanisms and applications", *Jpn. J. Appl. Phys.* **33**, pp. 7138-7143, 1994.
3. M.C. Gower, *Laser Processing in Manufacturing*, Chapman and Hall, London, 1993.
4. J.C. Miller, *Laser Ablation: Principles and Applications*, Springer-Verlag, New York, 1994.
5. Y.F. Lu, M.H. Hong, S.J. Chua, B.S. Teo and T.S. Low, "Audible acoustic wave emission in excimer laser interaction with materials", *J. Appl. Phys.* **79**, pp. 2186-2191, 1996.
6. S.S. Harilal, C.V. Bindhu, V.P.N. Nampoori and C.P.G. Vallabhan, "Time evolution of the electron density and temperature in laser-produced plasmas from $\text{YBa}_2\text{Cu}_3\text{O}_7$ ", *Appl. Phys. B*, **66**, pp. 633-638, 1998.
7. J.F. Ready, *Effects of High Power Laser Radiation*, Academic, New York, 1971.
8. A.M. Malvezzi, H. Kurz and N. Bloembergen, "Picosecond photoemission studies of the laser-induced phase transition in silicon", *Mat. Res. Soc. Symp. Proc.* **35**, pp. 75-80, 1984.
9. T.N. Hansen, J. Schou and J.G. Lunney, "Angle-resolved energy distributions of laser ablated silver ions in vacuum", *Appl. Phys. Lett.* **72**, pp. 1829-1831, 1998.
10. J.M. Hendron, C.M.O. Mahony, T. Morrow and W.G. Graham, "Langmuir probe measurements of plasma parameters in the late stages of a laser ablated plume", *J. Appl. Phys.* **81**, pp. 2131-2134, 1997.
11. T. Fujii, S. Inoue and F. Kannari, "Measurements of charged particles in the laser ablation plume of polymers", *J. Appl. Phys.* **78**, pp. 3401-3407, 1995.
12. J. Dieleman, E. Van De Riet and J.C.S. Kools, "Laser ablation deposition: mechanism and application", *Jpn. J. Appl. Phys.* **31**, pp. 1964-1971, 1992.
13. H.C. Ohanian, *Classical Electrodynamics*, Allyn & Bacon, London, 1988.
14. B. Luk'Yanchuk, N. Bityurin, S. Anisimov and D. Bäuerle, *Excimer Lasers*, Kluwer Academic Publishers, Boston, 1994.

SESSION 8

Lasers and Techniques III

KrF Excimer Laser Induced Ohmic Metallization of ZnO Substrate

T. Akane, K. Sugioka and K. Midorikawa

RIKEN (The Institute of Physical and Chemical Research),
Hirosawa 2-1, Wako, Saitama 351-0198, Japan

ABSTRACT

A non-alloy ohmic contact is fabricated on hydrothermally grown *n*-type ZnO substrate by KrF excimer laser pre-irradiation and metal deposition. The laser irradiation breaks Zn–O bonding, and turns ZnO surface layer to Zn-rich one which has lower sheet resistance than that of bulk, and has *n*-type conduction. The Zn-rich pre-metallized layer (ZnO_{*x*} layer, *x* = 0–1) enables current conducting into ZnO substrate with ohmic characteristics. Au/In/ZnO_{*x*} and In/ZnO_{*x*} contact fabricated by single pulse laser irradiation has specific contact resistivity of $\sim 7 \times 10^{-1} \Omega \text{ cm}^2$. Deterioration of contact resistance is confirmed after 5 min annealing at 300 °C in N₂, which is originated by re-bonding of Zn–O in laser irradiated area.

Keywords: ZnO, KrF excimer laser, Metallization, Non-alloy, Ohmic, X-ray photoelectron spectroscopy (XPS)

1. INTRODUCTION

Zinc oxide (ZnO) is the one of wide-gap II-VI semiconductor, expected to be a new material for blue or ultraviolet (UV) -emitting devices as well as III-nitride semiconductor such as GaN. Wurtzeit-ZnO has band-gap of 3.37 eV, and large exciton binding energy of 60 meV, hence, UV-photoemission associated with exciton recombination at room temperature (RT) is promising. Since the lattice parameters of Wurtzeit-ZnO are similar to those of Wurtzeit- GaN (ZnO: *a* = 0.325 nm, *c* = 0.521 nm, GaN: *a* = 0.319 nm, *c* = 0.519 nm) which has difficulty in bulk crystal growth, the use of Wurtzeit-ZnO as a substrate or buffer layer for GaN-based heteroepitaxial growth¹²³⁴ have been reported to show the importance of lattice-matching for obtaining high quality III-nitride epilayer. Large size ZnO bulk crystals can be grown by hydrothermal method,⁵ and they are provided in commercial base. In use of ZnO as a substrate for growing optical device structure consisted of either GaN- or ZnO-based lattice-matched heteroepitaxial layer, an *n*-type ohmic electrode fabrication at backside of the ZnO substrate with low contact resistance is important issue for device application. In this study, we demonstrate a non-alloy ohmic metallization technique for *n*-ZnO substrate using a KrF excimer laser irradiation.

2. EXPERIMENTAL

Substrates used were hydrothermally grown single crystalline undoped-ZnO (0001). Resistivity (ρ) was $\sim 2000 \Omega \text{ cm}$, and the conduction type was *n*. The substrate was transparent and colored light yellow. Crystal quality of received sample was examined by X-ray diffraction (XRD). Full-width at half maximum (FWHM) of the ZnO (0002) diffraction peak ranged from 64 to 72 arcsec.

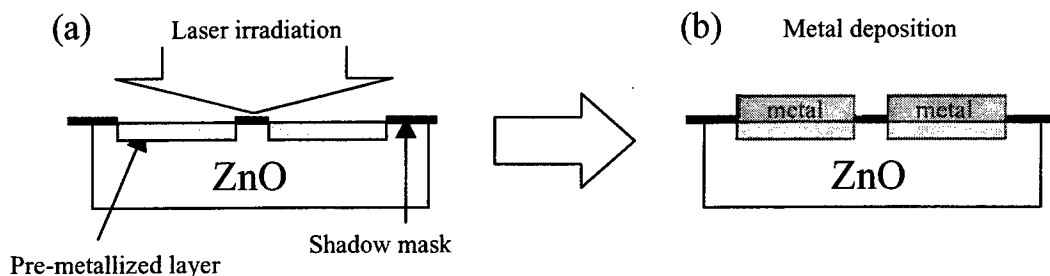


Figure 1. Schematic diagram of the sample preparation. (a) laser irradiation, (b) metal deposition.

The scheme of the metallization process is depicted in Fig. 1. The metallization process is consisted of laser irradiation (pre-metallization: Fig. 1(a)) and *ex-situ* metal deposition (Fig. 1(b)). A shadow mask made of stainless steel was set on the substrate throughout the metallization process. 50 nm-In, 50 nm-Au and 50 nm-In/50 nm-Au (Au on In) were deposited as a contact metal on the laser irradiated area by conventional vacuum evaporator. In order to examine the thermal stability of fabricated contact, post-annealing at 300 °C for 5 min was undertaken in N₂ flow.

The laser projection system are shown in Fig. 2. Base pressure of the process chamber was $\sim 1 \times 10^{-6}$ Torr.

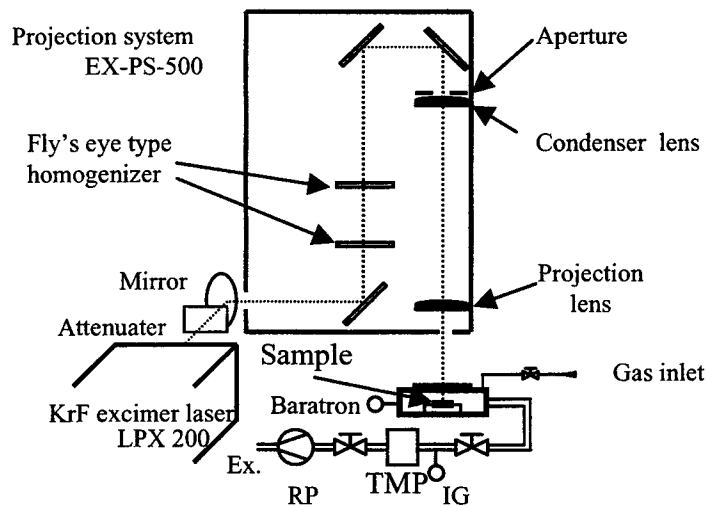


Figure 2. Laser projection system.

A KrF excimer laser ($\lambda=248$ nm, FWHM=34 ns, Lambda Physik: LPX205i) beam was homogenized and projected into 2×2 mm² area of the substrate set in the chamber. Ambient gas was 760 Torr N₂. The laser fluence (E_d) was ranged from 0.2 to 0.4 J/cm² and number of laser pulse (n) was set at 1.

Corresponding author: T. Akane, E-mail: akane@postman.riken.go.jp, Fax: +81 48 462 4682; Phone: +81 48 462 1111 ex. 4454

Surface morphology was observed by a conventional optical microscope. Hot probe checking was performed to determine conduction type (n or p) at laser irradiated area. Chemical bonding state of laser-irradiated area was evaluated by X-ray photoelectron spectroscopy (XPS). Sheet resistance (R_s) was measured by four-point probe method using geometry correction factor.⁶ I-V measurement was done for investigating ohmic characteristics of formed electrode. Contact resistance (ρ_c) was obtained from resistance-distance plot.⁷

3. RESULTS AND DISCUSSION

Figure 3 shows optical microscope images taken from sample irradiated with (a) $E_d = 0.3 \text{ J/cm}^2$ and (b) $E_d = 0.4 \text{ J/cm}^2$. Surface color change of as-irradiated samples was confirmed at $E_d = 0.3 \text{ J/cm}^2$ in naked eyes (Fig. 3

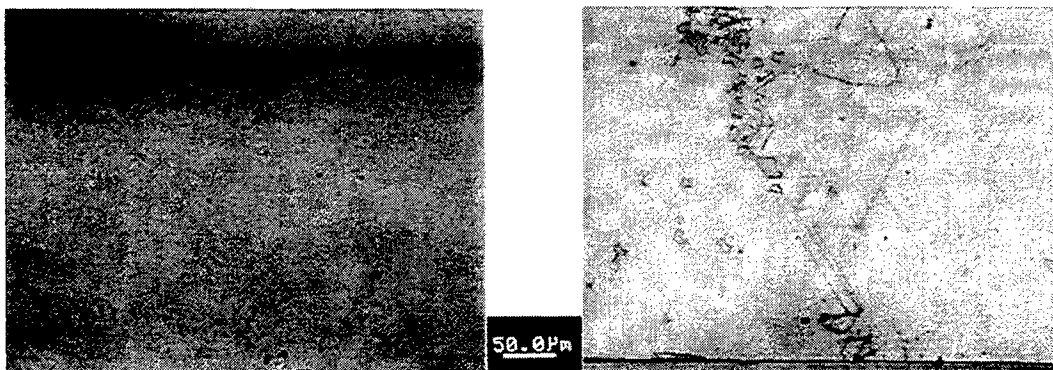


Figure 3. Optical microscope images of single-pulse irradiated area. (a) with $E_d = 0.3 \text{ J/cm}^2$ and (b) $E_d = 0.4 \text{ J/cm}^2$.

(a)), however, mirror like surface is maintained. Cracking and peeling-off at the surface were obvious in the sample irradiated with E_d of 0.4 J/cm^2 (Fig. 3 (b)). Almost no current was detected at $\pm 10 \text{ V}$ bias in I-V checking with $100 \mu\text{m}$ probe spacing at the laser-irradiated area for samples irradiated with E_d below 0.2 J/cm^2 . Therefore, in this experiment, we fixed the E_d at 0.3 J/cm^2 for pre-metallization.

Sheet resistance variation of as-irradiated samples with E_d is shown in Fig. 4. The sheet resistance decreases steeply beyond the E_d of 0.2 J/cm^2 . The conduction type of the irradiated area was confirmed to be n for all samples. At 0.3 J/cm^2 irradiation, sheet resistance was reduced by $\sim 4\%$ compared to that of the unirradiated sample. These n -layers formed by the laser irradiation are expected to improve contact resistance through the ohmic contact with the low-concentration n -type ZnO substrate.

Narrow-scan Auger spectra around the Zn *LMM* emission of unirradiated and irradiated samples are shown in Fig. 5. The shift of the main peak position in the obtained Zn *LMM* spectra was calibrated using the Cls core level photoemission peak position which was located at 285 eV . An off-stoichiometric Zn-rich phase (ZnO_x , $x=0-1$), whose peaks lies between the Zn *LMM* and ZnO levels, is detected even in the untreated sample (Fig. 5(a)), which indicated the existence of Zn interstitials in the as-received state.

The main peak shifts toward the Zn *LMM* position as E_d increases (Figs. 5(b) and (c)). Thus, the increase in E_d makes the laser-irradiated region more off-stoichiometric. In other words, the increase in E_d causes Zn-O bond dissociation, i.e., an increase in the number of oxygen vacancies, which can be donors,⁸ and this seems to be one origin of the resistivity lowering of the laser-irradiated area.

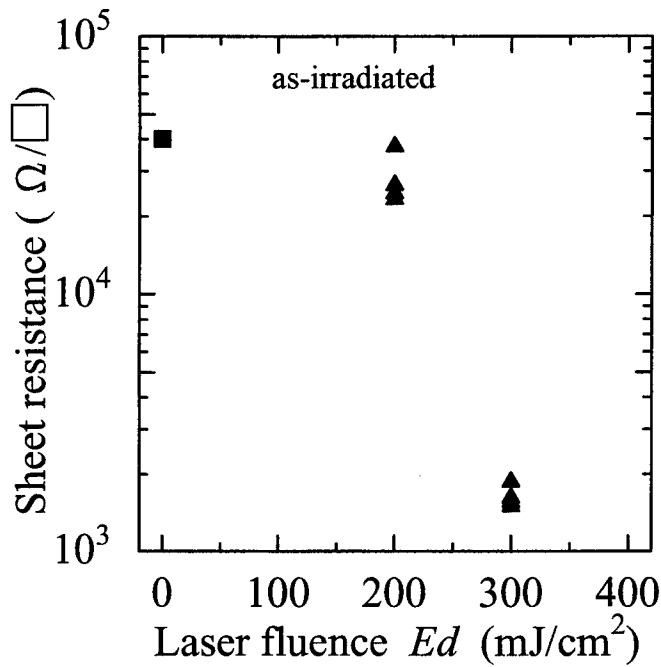


Figure 4. E_d dependence of R_s .

Figure 6 involves five I-V characteristics taken from: (i) the unirradiated samples with and without the contact metal, (ii) as-irradiated sample without contact metal, laser-irradiated sample with (iii) Au metallization, (iv) In metallization, and (v) In/Au metallization. The I-V measurements were performed between rectangular-shaped area with 100 μm spacing. The probe material was W. Generally, in ohmic contacts, current densities is strongly affected by a contact resistance R_c , which is given by the following equation⁹:

$$R_c \approx \exp \left[\frac{2\phi_B}{h/2\pi} \sqrt{\frac{\epsilon_s m^*}{N_d}} \right]. \quad (1)$$

Where, ϕ_B is the metal-semiconductor barrier height, ϵ_s is the dielectric constant, m^* is effective mass of electrons, h is the Planck's constant, and N_d is doping concentration. From Eq. 1, it is clear to see that increase of N_d and reduction of ϕ_B are effective for lowering R_c , i.e., increasing current density. I-V characteristics in Fig. 6 shows good ohmic features except that represented by line (i). Line (i) in Fig. 6 represents the I-V characteristic obtained from unirradiated samples, in which almost no current is detected at $\pm 10\text{V}$ bias regardless of whether there is contact metal deposition or not. The laser irradiation enables current conducting through the Zn-rich layer with good ohmic characteristics as shown by line (ii), however, the ϕ_B (barrier height between the probe and $n\text{-ZnO}$) seems to be high, and this may limits the current density in I-V measurement. The contact metal deposition improves current densities (line(iii) and (iv)). For these cases, since the work functions (ϕ) of Au ($\phi = 4.3\text{ eV}$) or In ($\phi = 3.8\text{ eV}$) are lower than the probe material (W: $\phi = 4.54\text{ eV}$), the ϕ_B may be lowered compared to the case of *direct contact*. In metallized sample showed better current density compared to Au metallized sample, however, In thin film exhibits less mechanical durability. In order to improve that, Au was deposited on In. The Au capping on In contact metal resulted almost same I-V characteristics compare to In metallization (line (v)).

5 min post-annealing at 300°C decreases current densities for all sample. The current decreasing is originated by increasing of contact resistance. The change of specific contact resistance (ρ_c) is summarized in Tbl.1.

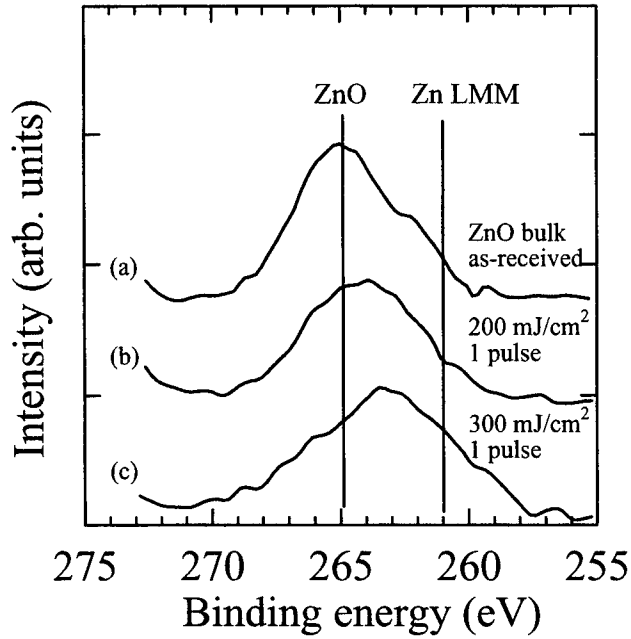


Figure 5. AES spectra obtained from as-laser irradiated area.

Fig.7 shows AES spectrum taken from the laser-irradiated sample after the annealing. No metal was deposited before the annealing. Main peak shift toward the ZnO position compared to the spectrum shown in Fig.5(c), which means that the off-stoichiometric laser-irradiated area becomes stoichiometric by the annealing, in other words, photo-decomposed Zn-O bonding is restored by the annealing. Thus, the deterioration of ρ_c is originated by re-bonding of Zn-O in the laser irradiated area.

4. CONCLUSION

In summary, laser-induced non-alloy ohmic metallization was performed on an undoped *n*-ZnO substrate in which ρ was as high as 2000 Ω cm. The non-alloy metallization process consisted of KrF excimer laser pre-irradiation and metal deposition. A Zn-rich layer was formed on the surface of the ZnO substrate by Zn-O bond dissociation

Table 1. ρ_c changes of fabricated ohmic contacts (in Ω cm²).

	As-deposited	After post-annealing in N ₂
In	$\sim 7 \times 10^{-1}$	$\sim 7.5 \times 10^{-1}$
In/Au	$\sim 7 \times 10^{-1}$	$\sim 7.5 \times 10^{-1}$
Au	$\sim 1.5 \times 10^0$	$\sim 2 \times 10^0$

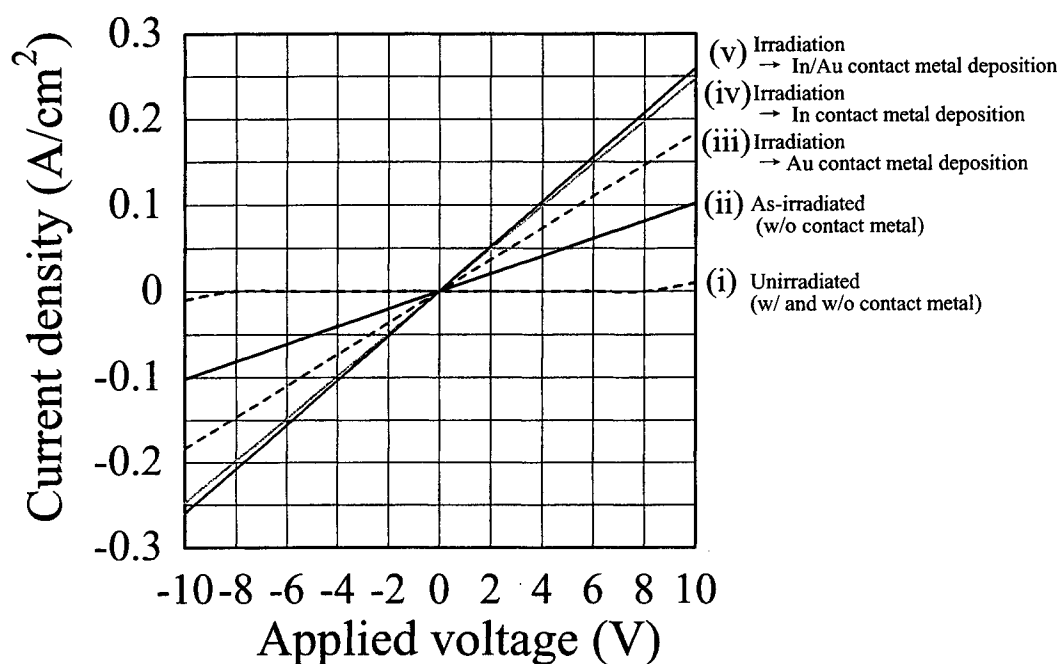


Figure 6. I-V characteristics of (i) unirradiated, (ii) as-irradiated, (iii) Au metallized, (iv) In metallized, and (v) In/Au metallized sample.

stimulated by KrF excimer laser irradiation. The Zn-rich layer, i.e., ZnO_x ($x = 0-1$) enables current conduction into the ZnO substrate. $\rho_c = 7 \times 10^{-1} \Omega \text{ cm}^2$ was measured in In/Zn-rich and Au/In/Zn-rich contact. 5 min annealing at 300 °C causes re-bonding of Zn-O which is once decomposed by the laser irradiation, and lead to deterioration of ρ_c . Laser pre-irradiation of the *n*-ZnO substrate was found to be an effective pre-treatment for fabricating an *n*-type non-alloy ohmic electrode.

ACKNOWLEDGMENTS

Acknowledgments: The authors would like to acknowledge T. Fuji-i of Keio University, Dr. J. S. Kim of Semiconductor Tech. Lab. of RIKEN, and N. Aoki of Science Univ. of Tokyo for experimental support. They also would like to thank to Professor Dr. S. Fujitsu of Shonan Inst. of Tech. for useful discussion.

REFERENCES

1. T. Matsuoka, N. Yoshimoto, T. Sasaki, and A. Katsui, *J. Electron. Mater.* **21**, 157 (1992).
2. T. Detchprohm, K. Hiramatsu, H. Amano, and I. Akasaki, *Appl. Phys. Lett.* **61**, 2688 (1992).
3. P. J. Molnar, P. Maki, R. Aggarwal, Z. L. Liao, E. R. Brown, I. Melngailis, W. Götz, L. T. Romano, and N. M. Johnson, *Mat. Res. Soc. Symp. Proc.* **423**, 221 (1996).
4. F. Hamdani, A. Botchkarev, W. Kim, H. Morkoç, M. Yeadon, J. M. Gibson, S. -C. Y. Tsen, D. J. Smith, D. C. Reynolds, D. C. Look, K. Evans, C. W. Litton, W. C. Mitchel, and P. Hemenger, *Appl. Phys. Lett.* **70**, 467 (1997).

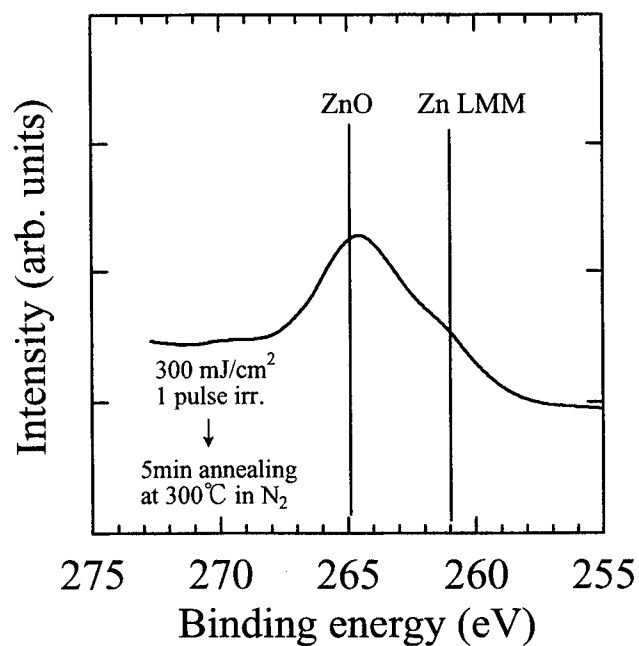


Figure 7. AES spectra obtained from annealed sample. No metal was deposited after the laser irradiation.

5. R. A. Laudise, E. D. Kolb, and A. J. Caporaso, *J. Am. Ceram. Soc.* **47**, 9 (1964).
6. W. E. Beadle, J. C. C. Tsai, and R. D. Plummer, *Quick Reference Manual* (Wiley, New York, 1985), pp. 2-37.
7. J. S. Foresi and T. D. Moustakas, *Appl. Phys. Lett.* **62**, 2859 (1993).
8. G. Neumann, *Current Topics in Materials Science* **7** Pt.1, Ed. E. Kaldis (North-Holland, Amsterdam, 1981) pp. 153-168.
9. S. M. Sze, *Physics of Semiconductor Devices*, 2nd ed. (Wiley, New York, 1981), p.304

Achievements in near-field investigations in Russia (IFMO SPb)

Vadim P. Veiko¹, Nikolay B. Voznesensky², Tatyana V. Ivanova

St.-Petersburg State Institute of Fine Mechanics and Optics (Technical University),
Sablinskaya ul., 14, St.-Petersburg, Russia, 197101

ABSTRACT

Nowadays near-field optics is one of the most attractive area for research, both for theoretical and experimental. Properly in the problem of near-field optics (not in applications) the most important things now are – the creation of more suitable and simpler approach to the description of near-field than MMP method and the creation of new generation of scanning near-field optical instruments (SNOI) such as microscopes, spectrometers, light generators for lithography, etc. The key of this SNOI generation is a variety of SNOM tips with the higher resolution and transparency and else one what may be even more important, the creation of method for SNOM tips certification. Both of these problems are being investigated in Russia. Short review of other directions for near-field investigation in Russia is also given, including important applications for quantum dots studying and investigation of optical strength of SNOM tips.

Keywords: nanoprobe, near-field optics theory and experiment, superresolution, SNOM tips fabrication.

1. INTRODUCTION.

As a significant member of scanning microscopy methods the scanning near-field optical microscopy (SNOM) which with the variety of its opportunities becomes more and more preferable for researchers and specialists in many fields. This microscopy may supply us an additional physical data about the nanosized matter. For example, the DVD disks demonstrate quite different topography in the STM and SNOM images what is very informative. The resolution of a SNOM device is fully dependent on the optical tip parameters – the sizes and shape of the tip aperture. However, the quality of the optical fiber tip is of decisive importance. There are two approaches to fabricate such tips – pulling and chemical etching the fiber. Both production processes are still highly empirical and full of defects in the first stage of pulling/etching and in the consequent metal coating stage as well.

Some time ago Chr. Obermüller and Kh. Karrai¹ had investigated the possibilities of far-field registration in order to define the aperture of a tip in submicron scale. This task leads to a generally formulated problem of investigating an arbitrary separate subwavelength sized optical object by its far-field diffracted light processing. The next problem is a rigorous concept of diffraction on mesoscopic elements at high angles. In this case the total electromagnetic energy is distributed between the radiating and evanescent modes or in other words far and near fields.

Recent experimental achievements in optical nanometer-scale science and technology require stable and effective computer aided concepts of light propagation through nanometer-sized structures². The methods of conventional diffraction theory which we know from the principles of optics³⁻⁵ are hardly suitable for computer application and, otherwise, not too universal to solve a variety of new tasks in optical technologies. Of great importance the problem is of near and far fields simultaneous treatment in computer simulation of scanning near-field optical microscopy (SNOM) because there is a variety of situations where far field itself is registered along with near field detection in order to obtain possibly full information. An approach to simulation of diffracted fields always must consider field components with different radiation properties, namely propagating and evanescent waves. One of important tasks for such simulation is the calculation of distribution of light field passing through a SNOM fiber-made probe. This process contains three stages which may be characterized as, the first – waveguide mode in the fiber, the second – light scattering and absorption in the media with nanosized features taking place in the tapered end, and, the third – propagation of light in the homogenous medium under high diffraction angles. Obviously the field structure of interest varies from micro- inside the tip end to macro-configuration in the open space. Commonly the light passing through small structures and diffraction phenomena have been considered separately. So the task of description of light propagation inside the tip up to the aperture is separated from the task of light diffraction description outside the tip.

This comes not only from conventional concepts but from great theoretical and calculational difficulties to characterize field features differing in value by several orders.

Therefore a taken simulation approach should be imposed by quite opposite requirements of detalization and generalization. To meet such requests a theory should be supplied by means of modeling the field components in two different spaces: the object space and frequency space, the latter being regarded as the space of angles of diffraction which are taken as basis functions parameters, basis functions being wave solutions of Helmgolz' equation. Such means cannot be obtained from the finite elements method (FEM or FDTD) which is intended for scattering tasks treatment. The FEM does not offer any analysis of a field structure and must be expanded by auxilliary technique to get out of its domain structure. Another approach implied in the multiple-multipole (MMP)² method is, in contrary to the FEM, based on the substitution of Maxwell's solutions into the field model. However this approach has the same disadvantage of describing the field inside domains with a hard possibility to get out of them. The MMP basis functions — multipoles are not represented in the space of parameters what makes it difficult to describe the field simultaneously as a micro- and macro structure. Thus one can see that there is a need of a theoretical approach to near scattered and far diffracted fields representation in one model. The most preferable way is the use of plane waves to represent fields distributions in all media of interest covered by a taken model. Here the well-known Debye's potentials and the angular plane waves spectrum technique take place of course, reminding the Huygense principle⁵. But a new approach must be free of a series of approximations and assumptions introduced into the Rayleigh-Sommerfeld diffraction theory according to Kirchhoff - Fresnel - Fraunhofer formulation. This approach should be rather rigorous to treat boundary effects of vector light field scattering and able to represent all the transformations of far-field as much as powerful scalar technique.

In the field of near-field optics regularly further experimental and scientific problems arise. As we know atom manipulation technique is closely related with creation of new microelectronics devices based on artificially induced properties of materials – metals, polymers, semiconductors, etc. So, one of such cases is investigation of quantum dots by means of scanning near-field optics. Such investigations are being successfully held in Nizhny Novgorod, Russia.⁶

A very interesting and having various theoretical and practical difficulties problem of optical strength of tapered fiber-made subwavelength probes has attracted attention of researchers with the State Vavilov Optical Center (SOI) in St.-Petersburg.⁷⁻⁹

2. DIFFRACTION THEORY AND NEAR-FIELD DISTRIBUTION MODELS

Most of modern simulation techniques being in use in near-field optics deal especially with near-field distributions either inside the tapered end of a tip or quite close to the exit aperture in the working nanosized space.^{2,10-12} Therefore the theory of near fields has been cut off from the general diffraction theory of light. But there are cases when the absence of relation between such important branches of modern optics is critical and having to be surely eliminated. We should point important tasks where the universal model of far and near fields can assist experiment in solving urgent practical problems. The tasks concern adequate treatment of near-field images in various modes of SNOM operation, e.g. photons tunneling and forbidden light observation modes, near-field photomask fabrication in photolithography and a new method of optical sertification of SNOM tips by far-field light measurements. All of these applications cannot be effectively realized without rigorous computer simulation of light transformations from near field to far field. And in addition the promote understanding light scattering processes may be of great use for new nanotechnologies including light control of epitaxial growing and p-n structures formation in optical communication devices.¹³

The light diffraction theory as a full concept of optics is mostly associated with linear systems scalar technique which is quite reasonable for such linear systems as conventional optical systems are. Meanwhile a great variety of optoelectronic instruments combine a long series of devices implying different physical laws and phenomena and not the last role belongs to photo processes when light interacts with various micro structures. In fact the linear systems theory which is based on scalar diffraction one fails to describe the facts where vector nature of light must be taken into account. The theories and approaches advanced in order to explain differences between scalar and vector predictions usually remained in frames of optical systems theory and hardly treated near-field phenomena that is why they could not be simply exceeded up to this area.^{3,15-18} Moreover their mathematical technique in principle was not intended for description of very small – subwavelength – details.

The situation which caused creation of a universal theory of light scattering on subwavelength features was the necessity of SNOM tip apertures certification by means of pure optical radiation treatment. As above mentioned alternate means especially SEM or other nano scanning techniques deliver insufficient information of aperture sizes and optical properties of tips. And also such techniques as always require rather complicated long measurements and image processing. So the theory formulation combining near and far field description in one concept has become an urgent task. In this paper a universal approach to vector treatment of light scattering phenomena based on Maxwell's equations harmonic solutions is presented. The difficulties of the use of harmonic solutions in inhomogeneous media are overcome with the help of especially elaborated iterative procedures intended for solution of integro-differential equations in rigorous electromagnetic initial conditions.

As a result of applying such technique to the tasks mentioned above we have obtained three solutions which are commonly based on the use of Fourier technique for calculations of spatial distributions of scattered light: 1) diffraction of light on a subwavelength hole in a metallic screen as a prototype task of light irradiation emerging from the tip aperture, 2) light propagation through a tapered part of a fiber-made metal coated SNOM tip, and 3) reconstruction of subwavelength aperture shape and sizes by mathematical inversion of far-field distribution of light emerging from the tip. The first difference between the proposed approach and earlier elaborated methods including the well-known MMP method is a surely supported relation of far and near fields in mathematical description. The second difference closely connected with the first one is the use of Fourier transform for diffraction modeling, transform of differential relationships into algebraic ones, and modeling light propagation through inhomogeneous media. Also a specific feature of the proposed approach is the opportunity to solve inverse tasks due to invariance of mathematical description of electromagnetic field with respect to direction of light radiation.

3. DIFFRACTION ON A SUBWAVELENGTH HOLE IN THE THIN SCREEN

The task of light diffraction on the hole in the infinitely conducting thin screen is a classic example demonstrating a fatal discrepancy between scalar and vector predictions. This paper deals with the use of the following representation of vector fields, which is taken from the reference² and was first introduced by Morse and Feshbach¹⁹:

$$\begin{aligned} \mathbf{E}(\mathbf{r}) &= -\nabla \times [f_e(\mathbf{r}), 0, 0] - \frac{1}{i\omega\epsilon} \nabla \times \nabla \times [f_m(\mathbf{r}), 0, 0] \\ \mathbf{H}(\mathbf{r}) &= \nabla \times [f_m(\mathbf{r}), 0, 0] - \frac{1}{i\omega\mu} \nabla \times \nabla \times [f_e(\mathbf{r}), 0, 0] \end{aligned} \quad (1)$$

The scalar functions $f_e(\mathbf{r})$ and $f_m(\mathbf{r})$ fulfill the homogeneous Helmgolz equation²:

$$(\nabla^2 + k^2)f_{e,m}(\mathbf{r}) = 0. \quad (2)$$

Our proposal is the use of $f_e(\mathbf{r})$ and $f_m(\mathbf{r})$ as independent scalar potentials being represented by a series of scalar plane waves with wide range of spatial frequencies. If we know distributions of scalar potentials $f_e(\mathbf{r})$ and $f_m(\mathbf{r})$ upon any structure we obtain the basis for determining vector values by applying the following formulae:

$$\mathbf{E} = \begin{pmatrix} E_x \\ E_y \\ E_z \end{pmatrix} = \begin{bmatrix} \frac{1}{i\omega\epsilon} \left(\frac{\partial^2 f_m}{\partial y^2} + \frac{\partial^2 f_m}{\partial z^2} \right) \\ -\frac{\partial f_e}{\partial z} - \frac{1}{i\omega\epsilon} \frac{\partial^2 f_m}{\partial x \partial y} \\ \frac{\partial f_e}{\partial y} - \frac{1}{i\omega\epsilon} \frac{\partial^2 f_m}{\partial x \partial z} \end{bmatrix}, \quad (3)$$

$$\mathbf{H} = \begin{pmatrix} H_x \\ H_y \\ H_z \end{pmatrix} = \begin{bmatrix} \frac{1}{i\omega\mu} \left(\frac{\partial^2 f_e}{\partial y^2} + \frac{\partial^2 f_e}{\partial z^2} \right) \\ \frac{\partial f_m}{\partial z} - \frac{1}{i\omega\mu} \frac{\partial^2 f_e}{\partial x \partial y} \\ -\frac{\partial f_m}{\partial y} - \frac{1}{i\omega\mu} \frac{\partial^2 f_e}{\partial x \partial z} \end{bmatrix}. \quad (4)$$

The $f_e(\mathbf{r})$ and $f_m(\mathbf{r})$ scalars in inhomogeneous structure are determined as continuous distributions and therefore the Maxwell's conditions on the boundaries of different media² will be surely fulfilled:

$$\begin{aligned} \mathbf{n}(\mathbf{r}_k) \times [\mathbf{E}_i(\mathbf{r}_k) - \mathbf{E}_j(\mathbf{r}_k)] &= 0 \\ \mathbf{n}(\mathbf{r}_k) \times [\mathbf{H}_i(\mathbf{r}_k) - \mathbf{H}_j(\mathbf{r}_k)] &= 0' \end{aligned} \quad (5)$$

where (\mathbf{r}_k) are the points of a boundary separating i and j media, $\mathbf{n}(\mathbf{r}_k)$ is the unit-normal vector to the boundary surface, $\mathbf{E}_i(\mathbf{r}_k)$, $\mathbf{H}_i(\mathbf{r}_k)$, $\mathbf{E}_j(\mathbf{r}_k)$, and $\mathbf{H}_j(\mathbf{r}_k)$ are field vectors on the boundary in two media correspondingly.

Other components undergo a "jump" proportionally to $\frac{\epsilon_j}{\epsilon_i}$ for electrical and $\frac{\mu_j}{\mu_i}$ magnetic fields correspondingly.

The use of Fourier transform lets us to make differential equations (1) and (3,4) be algebraic in the following way:

$$\tilde{\mathbf{E}} = \begin{pmatrix} \tilde{E}_x \\ \tilde{E}_y \\ \tilde{E}_z \end{pmatrix} = \begin{bmatrix} -\frac{4\pi^2}{i\omega\epsilon} (\mathbf{v}_y^2 \tilde{f}_m + C_{0z}^2 \tilde{f}_m) \\ 2\pi i C_{0z} \tilde{f}_e + \frac{4\pi^2 \mathbf{v}_x \mathbf{v}_y}{i\omega\epsilon} \tilde{f}_m \\ -2\pi i \mathbf{v}_y \tilde{f}_e + \frac{4\pi^2}{i\omega\epsilon} \mathbf{v}_x C_{0z} \tilde{f}_m \end{bmatrix}, \quad (6)$$

$$\tilde{\mathbf{H}} = \begin{pmatrix} \tilde{H}_x \\ \tilde{H}_y \\ \tilde{H}_z \end{pmatrix} = \begin{bmatrix} -\frac{4\pi^2}{i\omega\mu} (\mathbf{v}_y^2 \tilde{f}_e + C_{0z}^2 \tilde{f}_e) \\ -2\pi i C_{0z} \tilde{f}_m + \frac{4\pi^2}{i\omega\mu} \mathbf{v}_x \mathbf{v}_y \tilde{f}_e \\ 2\pi i \mathbf{v}_y \tilde{f}_m + \frac{4\pi^2}{i\omega\mu} \mathbf{v}_x C_{0z} \tilde{f}_e \end{bmatrix}, \quad (7)$$

where \sim means Fourier transforms which denote that components of electric and magnetic fields and scalars $f_e(\mathbf{r})$

and $f_m(\mathbf{r})$ are represented through scalar plane waves. Here we use spatial frequencies $\mathbf{v}_x = \frac{c_x}{\lambda_0}$ and $\mathbf{v}_y = \frac{c_y}{\lambda_0}$,

$$(c_x, c_y) - \text{direction cosines, and } C_{0z} = \sqrt{\left(\frac{I}{\lambda_0}\right)^2 - v_x^2 - v_y^2} \text{ for propagating plane waves satisfying } (v_x^2 + v_y^2) \leq \left(\frac{I}{\lambda_0}\right)^2 \text{ condition or } C_{0z} = i\sqrt{v_x^2 + v_y^2 - \left(\frac{I}{\lambda_0}\right)^2} \text{ for evanescent waves otherwise. Thus we obtain}$$

an approach which allows to construct universal sequence of operations suitable for treatment of any scattering structure and we may define the whole field distribution in any structure.¹⁴

In case of "s" linear polarization we may use only one scalar function $f_e(\mathbf{r})$. Our approach to the diffraction task differs from the solution by Bowkamp¹² by the use of a set of uniform operations intended to solve the following set of rigorous integro-differential equations:

$$\left\{ \begin{array}{l} \int_{-\infty-\infty}^{\infty} \int_{-\infty-\infty}^{\infty} f_e(\mathbf{r}) \exp[2\pi i(v_x x + v_y y)] dx dy = 0, \left(\frac{x}{a_x}\right)^2 + \left(\frac{y}{a_y}\right)^2 \geq 1 \\ \int_{-\infty-\infty}^{\infty} \int_{-\infty-\infty}^{\infty} \frac{\partial}{\partial z} f_e(\mathbf{r}) \exp[2\pi i(v_x x + v_y y)] dx dy = 0, \left(\frac{x}{a_x}\right)^2 + \left(\frac{y}{a_y}\right)^2 \geq 1 \end{array} \right., \quad (8)$$

where (a_x, a_y) – semi-dimensions of the hole. The task solution leads to an iterative procedure to determine a resultant scalar potential $f_e(\mathbf{r})$ by which near-field distributions of electric and magnetic fields should be calculated. After that the far-field distributions may be obtained by applying the Fourier transforms to near-field components in order to determine electric and magnetic far-field components and consequently to calculate the Poynting vector.

4. LIGHT PROPAGATION THROUGH THE TAPERED PART OF A SNOM TIP

The model of the fiber-made probe consists of the silicone core, glass cladding, and metal coating. This model corresponds to SNOM probes made by laser-heated drawing where the cladding and core last nearly up to the exit aperture — small hole in the metal coating. The very end of the tip is simulated as a conical shape with an arbitrary cone angle or parabolic. We let the axis z be vertical and the symmetry axis of the probe model and the axes x, y be horizontal. To perform calculations of propagating field amplitude we represent the probe and space around it as a sequence of layers formed by horizontal (x, y) planes separated by Δz . Thus the field on the first plane of a layer is regarded to be an input for calculations of the field on the second plane. The propagation of the field between two planes of a layer is represented by plane waves expansion and may be calculated with the use of exponent factors depending on Δz which are the parts of complex amplitude of plane waves⁵. In each plane the field is represented as a sum of plane waves by using forward and backward Fourier transforms in order to define approximation coefficients and construct the field propagating inside the layer. The reference¹⁴ deals in detail with the algorithm.

For example two probe models are presented – the first is similar to the reference² 2D model where the metal coating is thick and the light field is passing through narrow silicon end (fig. 1), and the second model represents the cross section of realistic probe end with tapered core, cladding and thin metal coating (fig. 2). Both tips end with the 50 nm aperture. Such structure is characteristic for fiber-made probes, for example, obtained in IFMO (St.-Petersburg, Russia) by drawing out process with laser heating²⁶. Our model offers to set an initial field within any region of the first layer of the probe. As in the reference we may let it be a plane wave or any field structure obtained by waveguide methods for those parts of the probe where the core width is greater than a wavelength. The height of the simulated part of the probe end may be about 1-2 wavelengths and some free space after the aperture (about 100 nanometers) is being treated as well.



Fig.1 Chemically etched end.

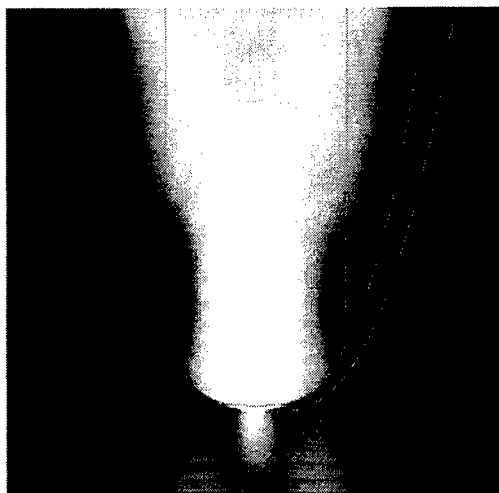


Fig.2 Laser assisted drawn end.

5. RECONSTRUCTION OF SUBWAVELENGTH APERTURE SHAPE AND SIZES FROM FAR-FIELD LIGHT DISTRIBUTION

The characterization technique to determine a tip quality before it is shipped to a user or mounted in the scanning head of a microscope is of great importance. The usual SEM approach is not too favorable because of low speed and troubles of the aperture sizes definition. Besides this an easy and fast method may be proposed by the use of far-field registration of light emitting from the tip. We regard that in this case something like the near-field optical transfer function of the tip may be recognized. However this result cannot be obtained directly and an additional mathematical procedure is required.

One of applicational extensions and an important advantage of the proposed model is its use in the task of optical measuring the subwavelength-sized apertures of SNOM probes. The principles of this task solution are based on analytical continuation of the registered part of the Fourier spectrum according to superresolution technique^{22,23}. The reference¹ deals with an experimental attempt of subwavelength-aperture SNOM tip investigation by measuring far-field intensity distribution. Here the idea of the aperture parameters restoration is formulated as an inverse task with the use of some empirical analytical relations between the aperture sizes and nonuniformities of the far-field light distribution. It is mentioned that the definition of exact relation requires the use of complicated electrodynamics methods which may solve only the direct task. Our proposal is the use of the Fourier based model not only for simulation of light passing through and out of the tip but for mathematical reversal of the process which is possible due to the use of reversible transformations. Of course, all the losses in the light energy and structure must be taken into account in order to maintain the model be adequate. Nevertheless such reversal may represent some information about the initial field before passing the simulated structure. This general approach may be applied to various situations provided that we know something a priori about the initial field. In case of SNOM tip apertures we know that they are less than a wavelength and have some simple shape – circular, elliptical, rectangular – with various azimuth angle.

The principles and results of applying Fourier based methods to solution of tip apertures restoration are discussed in detail in references^{24,25}. It is an example where far and near fields are considered simultaneously and the first attempt to demonstrate results of mathematical reversal of diffraction scattering. This case is considered with one linear polarization status of light emerging from the tip and the newly proposed technique has opportunities of considering general changes in polarization taking place while the light propagation through the tip. This is an additional advantage of applying Fourier based model to solution of SNOM tasks.

The figs. 3-8 show a result of computer reconstruction of some apertures.

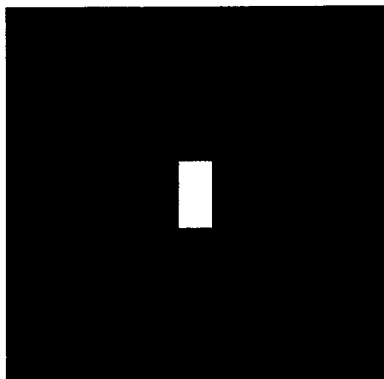


Fig. 3 Rectangle $90 \times 180 \text{ nm}^2$

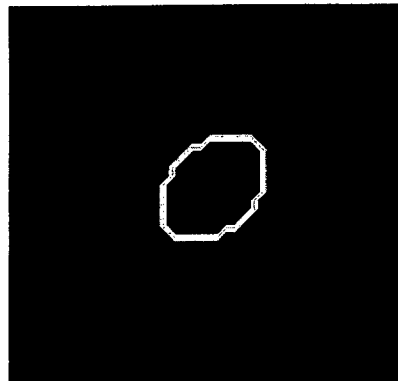


Fig. 6 Ellipse $180 \times 240 \text{ nm}^2$

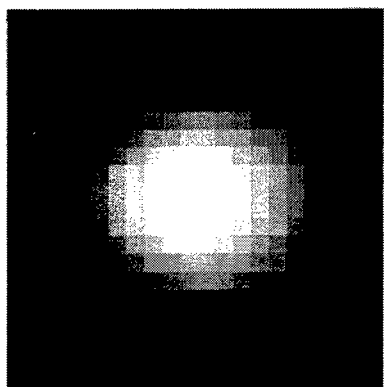


Fig. 4 Reconstruction without continuation

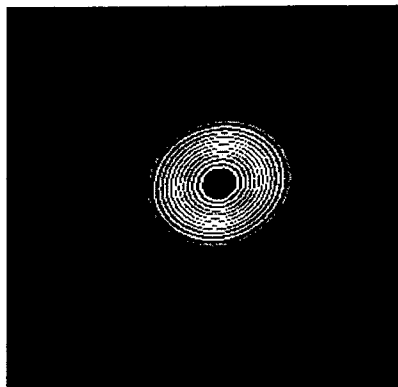


Fig. 7 Reconstruction without continuation

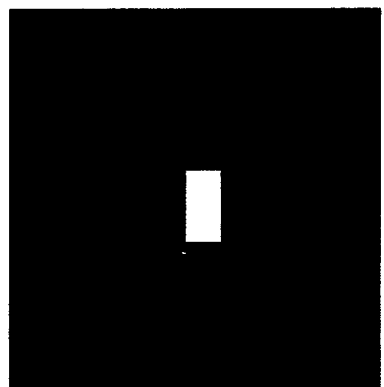


Fig. 5 Reconstruction after 12 iterations

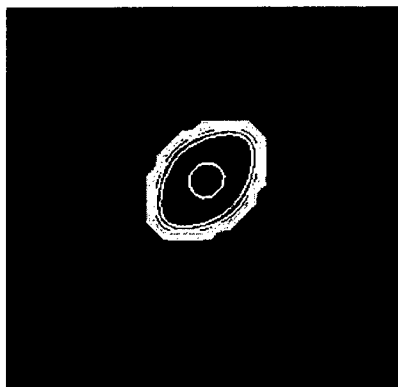


Fig. 8 Reconstruction after 10 iterations

6. LASER-ASSISTED DRAWING-OUT PROCESSING SNOM PROBES

Today the laser drawing-out set-ups contain optical schemes which do not allow to produce a uniform circular illumination of the heated surface (fig. 9). These schemes were checked by us and there was revealed the only positive consideration for their use in a set-up - the construction simplicity.

We propose a new optical scheme which can produce a uniform circular illumination of the heated fiber part. Also this scheme will make it possible to decrease greatly residual mechanical stresses in the tip due to smooth decline of its temperature. These properties of a new scheme are connected with an illumination mode realised by it which simulates a gas torch (is used in optical fiber manufacturing). This scheme was created and tested in our set-up with double-sided horizontal drawing-out mechanism. The basic set-up is presented in fig.10. The radiation of continuous CO₂ laser ($\lambda=10.6$ mcm) of 3W power inserts the lens ($f=75$ mm, KBr). After the lens the divergent beam by help of two plane mirrors falls on the spherical mirror ($f=45$ mm) which focuses the radiation on to the fiber. The optical axes of the fiber and spherical mirror coincide. As a result a uniform circular illumination is produced. Electro-mechanical shutter produces impulse lightning of 10 mcsec - 1 min. Therefore the drawing-out tips may be carried on in two modes - continuous and pulsed. In the continuous mode the fiber is heated by the CO₂ laser till the fiber breaks with a probe tip consequent forming. In the pulsed mode the fiber is heated under the effect of one impulse or a series of impulses produced by the shutter, energy of impulses being sufficient to heat the fiber and break it with consequent tip forming. The fiber is fit by two clips by which the drawing-out force ($F=1\div 2$ N) which is directly proportional to the certified load mass effects on the fiber. After reaching the temperature of softness of the heated part (reaching viscosity of the fiber material) the intensive drawing-out process starts (the tip forming) and ends by the break (the tapered tip forming). The whole process (heating + drawing-out) lasts during about 0.5 sec. The He-Ne laser and mirror system are used to place the fiber into the active zone accurately. On this set-up we have obtained probes (figs. 3) based on a unimodal quartz fiber (cladding = 125mcm, core = 9 mcm). The tips have the same shape (cone) but different dimensions. In the drawing-out process the longer tip (300-700 mcm long with the cone angle less than 20°) appeared from the spherical mirror side and the shorter one (150-200 mcm long with the cone angle less than 40°) appeared from the opposite side. This is connected with different conditions for tips forming (the shortest tip appears in the hotter zone).

To fabricate a subwavelength aperture and an opaque metallic coating covering the walls of the tapered fiber the drawn fiber probes have been metallized by means of convenient Al vacuum thermal deposition technique. The drawn fiber probes were fixed at the angle of 15...30° from the deposition direction and rotated at a rate of approximately 2...3 Hz. 100...150 nm thickness Al coating was fabricated. To definite the drawn fiber probes usefulness for scanning near-field optical investigation these fibers have been used as probes for self-made module type scanning probe microscope which operated at scanning near-field optical microscope mode. Shear-force and near-field optical reflection regimes were used. Some modifications of setup have been made against the version, which described previously^{20,21}. The experimental setup is shown schematically in fig.12. The laser diode module LDM115 from Imatronix Ltd. linearly polarized irradiation with wavelength 670nm was focused to the sample surface. Power density on the surface was about 500mW/mm². Part of the intensity of the reflected light field was coupled out with fiber probe which connected to photomultiplaying tube. Crystal quartz tuning fork scheme was used for the probe-surface distance control by means of shear-force registration. Drawn and metallized fiber probe have been glued onto the fork. Independent piezoceramic dither piezo served for the exciting of tuning fork-fiber probe system resonance oscillation.

Shear-force image of experimental Ni matrix is shown in fig.13a. Matrix is intended for the fluorescence compact disk production and the bumps are higher than the standard compact disk matrix bumps. Contact mode atomic force topographical image of the same sample is shown in fig. 13b for comparison. Atomic force image had been obtained by means of atomic force mode of module type scanning probe microscope. Contact ultra sharp Si cantilevers CSCI11/Si₃N₄ coated with Si₃N₄ from NT-MDT Co. had been used. These cantilevers have radius of tip curvature less than 20 nm and full tip cone angle less than 20°. Comparison the images in fig.13a and fig.13b demonstrate high quality of the manufactured fiber probes for shear-force mode and for aperture-sample distance stabilization, which is very important for scanning near-field optical microscopy.

Shear-force and near-field optical reflection images of the 400nm diffractive grating are shown in fig.14. The diffractive grating had been made by the laser induced photochemical etching of (001) n-InP surface. Direct correlation between fig.14a and fig.14b show subwavelength resolution, which obtained with laser-assisted drawn and Al metallized fiber probes.

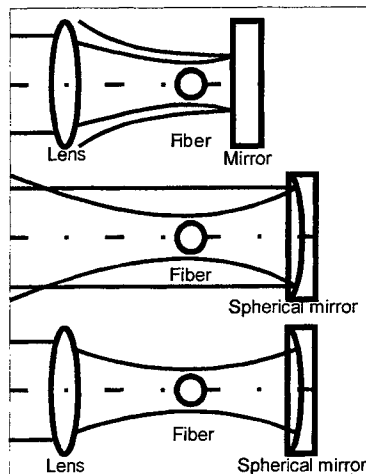


Fig. 9. The standard optical schemes of laser set-up

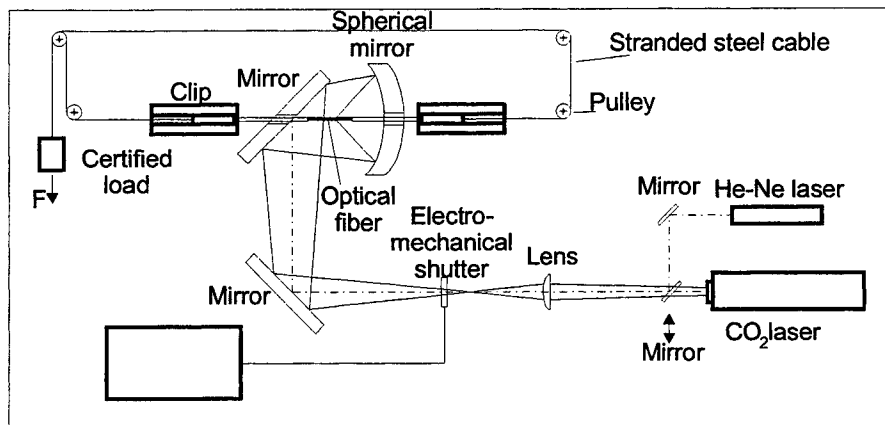


Fig. 10. Scheme of laser set-up

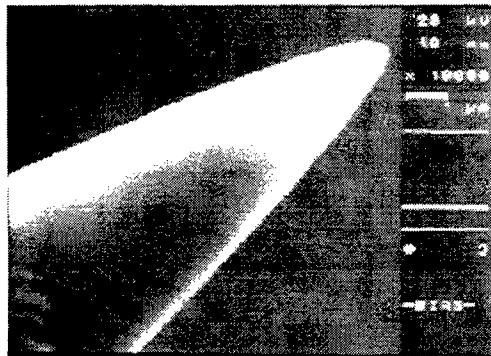


Fig. 11. Photograph of probe made by an electron microscope with magnification of 10000 \times

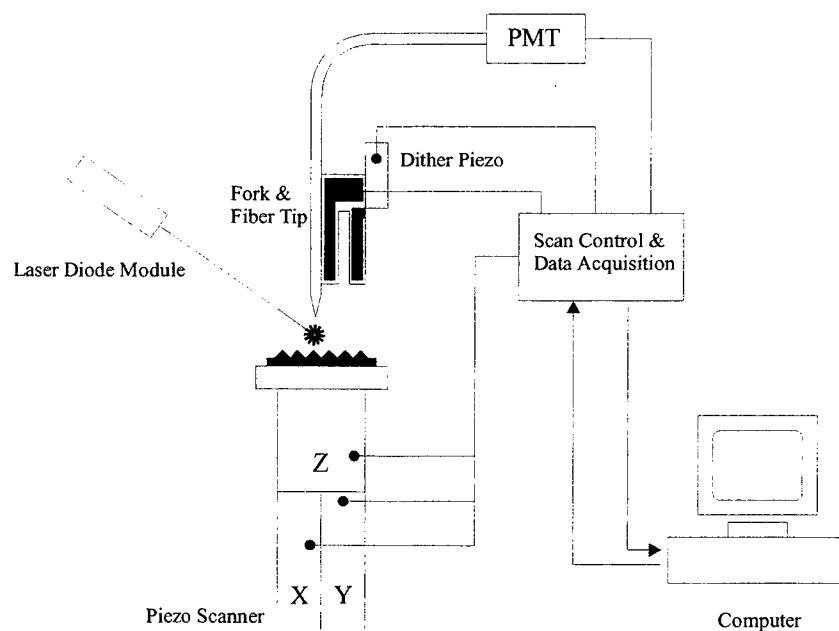


Fig. 12. Experimental set-up for scanning shear-force and near-field optical reflection investigation.

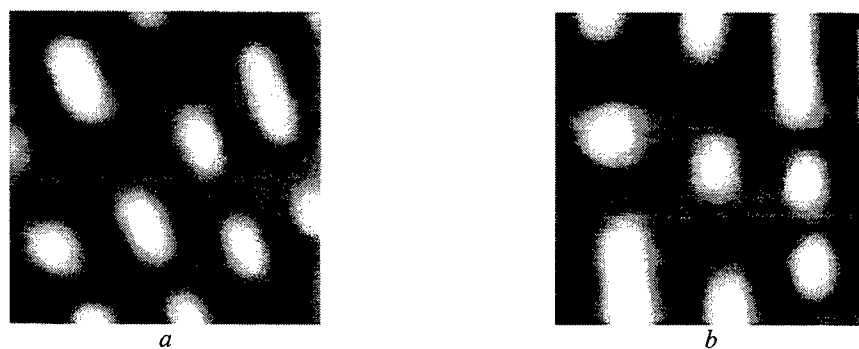


Fig. 13. $5.4\mu\text{m} \times 5.4\mu\text{m}$ shear-force (a) and atomic-force microscopy (b) images of the Ni matrix surface.

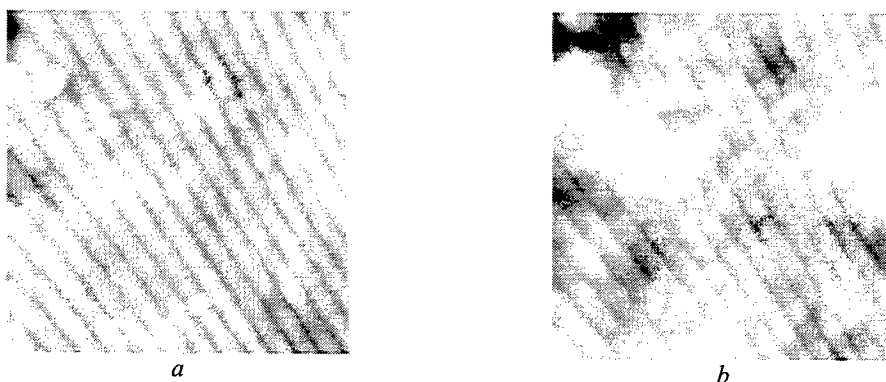


Fig. 14. $5.4\mu\text{m} \times 5.4\mu\text{m}$ shear-force (a) and near-field optical reflection (b) images of 400nm n-InP diffraction grating surface.

7. INVESTIGATIONS IN RUSSIAN ACADEMY INSTITUTIONS

The most attractive branches of today scanning microscopy in Russia have been occupied by various ATM-STM techniques what is the consequence of paying traditionally great attention to pure physics fundamental research. In this way the scientists had elaborated precise and stable instruments supplied with piezo ceramics and all the necessary means to detect extra weak signals sent by extra small objects. Now the well-known Russian company MDT-nanotechnologies provides scanning microscopes based mainly on ATM and shear-force principles. The reason of the lack of scanning near-field optical microscopes in Russian production and research is the lack of SNOM tips stable fabrication. The same problem is of importance in other parts of the World especially delivering certified tips.

Therefore the NFO investigations in Russia concern mainly modeling, design, fabrication²⁷, testing and certification of SNOM tips.

The most prominent scientific research in scanning probe microscopy (SPM) in Russia is being held in the RF Academia Institute of Physics of Nanostructures (IFN), Nizhny Novgorod. There is a series of projects with the use of near-field optical microscopy and spectroscopy to investigate properties of various opto-electronics matters and devices²⁸, electron resonances²⁹, and optical memory.³⁰ The Institute regularly collects specialists in scanning probe microscopy in annual meetings on SPM and due to its head Vice-Academician S.V.Gaponov takes significant part in international scientific cooperation.

ACKNOWLEDGEMENTS

The authors are very grateful to Prof. Sepold, Prof. Jüptner, Dr. Osten, Mr. Seebacher, Prof. Libenson, Prof. Rodionov, Dr. Jakovlev and Mr. Ezhov for useful discussions.

REFERENCES

1. Chr. Obermüller and Kh. Karrai, *Appl. Phys. Lett.*, **67**, No. 23, pp. 3408-3410, 1995.
2. L. Novotny, D. W. Pohl, and P. Regli, *J. Opt. Soc. Am. A.*, **11**, pp. 1768-1779, 1994.
3. C. J. Bouwkamp, "Diffraction theory", *Rep. Prog. Phys.* **17**, pp. 35-100 (1954).
4. A. Sommerfeld, *Optics* (Academic, New York, 1954).
5. M. Born and E. Wolf, *Principles of Optics*, 6th ed. (Pergamon, Oxford, 1970), p. 333.
6. V. J. Aleshkin, A. V. Biriukov, S.V. Gaponov, Z. F. Krasilnik and V. L. Mironov, *SPM-99* (IFN RAN RF, Nizhny Novgorod, 1999), pp. 44-49, in Russian.
7. V. Gurevitch and M. Libenson, *Ultramicroscopy*, **57**, pp. 277-282, 1995.
8. M. N. Libenson and G. A. Martsinovskiy, *SPM-99* (IFN RAN RF, Nizhny Novgorod, 1999), pp. 99-101, in Russian.
9. M. N. Libenson and G. A. Martsinovskiy, *Proceedings SPIE*, **3467**, 1998.
10. D. W. Pohl, L. Novotny, B. Hecht and H. Heinzelmann, *Thin Solid Films*, **273**, pp. 161-167, 1996.
11. O. J. Martin, *Proceedings SPIE*, **3791**, 1999.
12. Q. Zhou, H. Li, E. Chen, X. Zhu and Z. Gan, *Proceedings SPIE*, **3791**, 1999.
13. K. Okamoto, H. Inoue, Y. Inoue and S. Kawata, *Proceedings SPIE*, **3791**, 1999.
14. N. B. Voznessenski, *Proceedings SPIE*, **3791**, 1999.
15. C. J. R. Sheppard and M. Hrynevych, "Diffraction by a circular aperture: a generalization of Fresnel diffraction theory", *J. Opt. Soc. Am. A.*, **9**, pp. 274-281, 1992.
16. P. Hilion, "Relativistic theory of scalar and vector diffraction by planar apertures", *J. Opt. Soc. Am. A.*, **9**, pp. 1794-1800, 1992.
17. W. Hsu and R. Barakat, "Stratton-Chu vectorial diffraction of electromagnetic fields by apertures with application to small-Fresnel-number systems", *J. Opt. Soc. Am. A.*, **11**, pp. 623-629, 1994.
18. C. J. R. Sheppard and P. Török "Approximate forms of diffraction integrals in high numerical aperture focusing", *Optik*, **105**, pp. 77-82, 1997.
19. P. M. Morse and H. Feshbach, *Methods of Theoretical Physics* (McGraw-Hill, New York, 1953).
20. V. P. Veiko, V. A. Chuiko, M. P. Tokarev. "Laser-mechanical methods of optical fiber treatment for number of microoptical components fabrication", *Proceedings SPIE*, **2383**, Miniaturized Systems with Microoptics and Micromechanics, pp. 224-233, 1995.
21. V. P. Veiko, E. B. Jakovlev, A. K. Kromin. "Laser fabrication on MOC based on laser heating of glass and glass-like materials", *Proceedings SPIE*, **1992**, Miniature and Microoptics, pp.159-167, 1993.

22. J. L. Harris, "Diffraction and Resolving Power", *J. Opt. Soc. Am.*, **54**, pp. 931-936, 1964.
23. R. H. T. Bates and McDonnell, *Image Restoration and Recognition*, Chs. 2-3, Oxford: University Press, 1986.
24. N. B. Voznessenski, V. P. Veiko, V. M. Domnenko, A. E. Goussev, T. V. Ivanova and S. A. Rodionov "New approach to analysis of subwavelength sized secondary light sources", *SPIE: Far- and Near-Field Optics: Physics and Information Processing*, **3467**, pp. 313-321, 1998.
25. V. P. Veiko, N.B. Voznessenski, V. M. Domnenko, A. E. Goussev, T. V. Ivanova and S.A. Rodionov "New approach to optical measurements of small objects with superresolution", *Proc. SPIE*, **3736**, 452 pages, 1999.
26. V. P. Veiko, V. M. Voronin, N. B. Voznessenski, S. A. Rodionov, I. Smirnov and A. Kalachev "Optical nanoprobe for scanning near-field optical microscopy: functions, requirements, fabrication, and theoretical reconstruction from far-field investigation", *Proc SPIE*, **3688**, 1998.
27. V. F. Dryahlushin, A. Yu. Klimov, V. V. Rogov and D. O. Philatov, *SPM-99* (IFN RAN RF, Nizhny Novgorod, 1999), pp. 121-124, in Russian.
28. D. A. Lapshin, E. E. Kobylkin and V. S. Letokhov, *SPM-99* (IFN RAN RF, Nizhny Novgorod, 1999), pp. 113-120, in Russian.
29. A. M. Troyanovsky and V. S. Edelman,, *SPM-99* (IFN RAN RF, Nizhny Novgorod, 1999), pp. 74-84, in Russian.
30. A. A. Ezhov, S. A. Magnitsky, D. A. Muzychenko and V. I. Popov, *SPM-99* (IFN RAN RF, Nizhny Novgorod, 1999), pp. 125-131, in Russian.

¹ E-mail: veiko@lastech.ifmo.ru

² E-mail: vnb@aco.ifmo.ru

Scribing blue LED wafer using laser-induced plasma-assisted ablation with a q-switched Nd:YAG laser

Jong-Moo Lee^a, Jun-Ho Jang^b and Tae-Kyung Yoo^b

^aLGIS R&D Center, 533, Hoggae-dong, Anyang-shi, Kyongki-do, 431-080, Korea

^bLG CIT, 16, Woomyeon-dong, Seocho-gu, Seoul, 137-140, Korea

ABSTRACT

Transparent materials, such as sapphire, are found to be scribed and cut freely by sparks from metal surface on which q-switched Nd:YAG laser beam is focused through the transparent material. This method is successfully applied to split each device from a blue LED wafer including about ten thousands of blue LEDs grown on a sapphire wafer.

Keywords: Laser, blue LED, plasma, material processing, Nd:YAG

1. INTRODUCTION

Transparent and hard materials such as sapphire are used for many industrial applications as optical windows, hard materials on mechanical contact against abrasion, and substrate materials for opto-electronic semiconductor devices such as blue LED and blue LD etc. The materials should be cut along the proper shapes possible to be used for each application. In case of blue LED, the blue LED wafer should be cut to thousands of blue LED pieces, which are usually about 400 x 400 μm square plates with 100 μm thickness, at the final stage of manufacturing process. The process of cutting the wafer is usually divided into two steps. The wafer is scribed along the proper shapes at the first step. And then, it is broken and splitted at the next step, being inserted between transparent flexible sheet for easy handling. The harder materials such as diamond are usually used to scribe the wafer, while it has a problem of low depth of scribing and abrasion of the harder material itself. The low depth of scribing can induce failure in breaking the wafer along the scribed line. It was also known that the diamond tip, which is quite expensive, should be replaced frequently for the abrasion.

Many kinds of lasers which are absorbed well in materials are directly used in micro machining of the materials with the merits of fine accuracy and easy control of shape to cut. CO₂ laser beam is absorbed well in glass and it was used in cutting glass plate by melting the glass or by inducing thermal shock in glass.¹ It may be possible to use CO₂ laser in machining of sapphire material for some applications since it is absorbed well in sapphire, too. But it is hard to use CO₂ laser in scribing blue LED wafer since CO₂ laser machining accompanies a lot of heat by the absorption of laser in the material. The device can be easily damaged by the heat while scribed and it's very hard to be scribed so accurately and finely with CO₂ laser as with Nd:YAG laser because of the long wavelength of CO₂ laser. Ultra-Violet lasers such as KrF(248 nm) and ArF(193 nm) excimer laser was used in machining of some organic and inorganic materials by the combination of photothermal decomposition and photodissociative bond breaking mechanism.^{2,3} UV laser machining has a merit of low thermal problem due to the low heat generation compared with CO₂ laser. But the excimer lasers are hard to be applied in machining of sapphire since sapphire is almost transparent at UV region. Ultra-short laser pulses with very high intensity was used to ablate dielectric materials by multi-photon absorption with the instantaneous high electric field.⁴⁻⁶ Most of the dielectric materials are known to be ablated with ultra-short pulse laser regardless of the wavelength of it. But ultra-fast high power laser has many difficulties for practical use such as high photon cost, large size and short of reliability till now. So, it is hard to apply ultra-short pulse laser to the scribing of blue LED wafer in the manufacturing process, yet.

In this way, there's difficulty in using laser directly for the scribing of blue LED wafer in the manufacturing process. Another way of using laser in material processing is to use not only the laser but also the other assistant way together. An example is the laser-induced plasma-assisted ablation(LIPAA) method which was demonstrated by Jie Zhang et. al. at first.⁷⁻⁹ The method is an efficient way in machining of transparent hard materials. It can be applied to the machining of transparent material since the material is machined by plasma induced by laser not by the laser itself. They applied LIPAA for the fabrication of microgratings and hole drilling in fused quartz using KrF excimer laser,⁷

Correspondence : E-mail : optoman@chollian.net; phone : +82-343-450-7546; fax : +82-343-450-7599

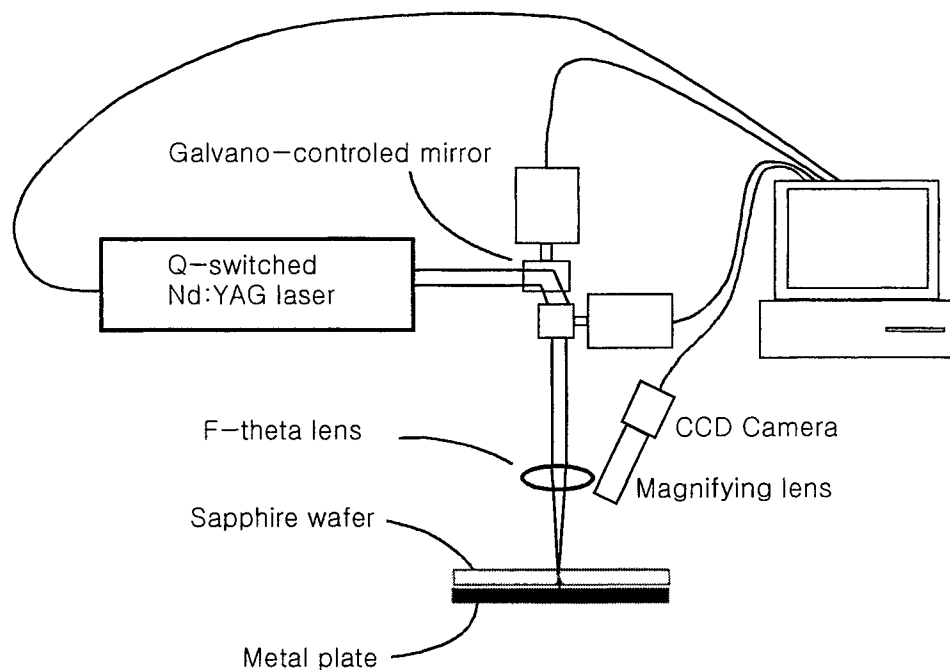


Figure 1. Experimental setup to scribe sapphire wafer using laser-induced plasma-assisted ablation(LIPAA) method.

second harmonic Nd:YAG laser⁸ and fifth harmonic Nd:YAG laser⁹ while the target is located in vacuum. Here, we demonstrated that sapphire wafer can be scribed and cut freely using the method, LIPAA, with q-switched fundamental Nd:YAG laser. The wafer is scribed by plasma generated from metal surface, on which q-switched Nd:YAG laser beam is focused through the wafer. It was experimented at atmospheric environment without vacuum chamber while the previous experiments were done in vacuum chamber.⁷⁻⁹ It is successfully applied to the manufacturing process of commercial blue LED by splitting each device from a blue LED wafer including about ten thousands of blue LED devices. It's the first application of LIPAA, in my knowledge, to the manufacturing process of commercial opto-electronic device and we cannot find any problems in operation of blue LED manufactured by this method.

2. EXPERIMENT

The experimental setup is as shown in Fig. 1. A diode-pumped solid-state Nd:YAG laser(Model DPY-S20IR) which is made by ourselves(LGIS), is used for the experiment. The wavelength of laser is $1.064 \mu\text{m}$ and it is q-switched with an acousto-optic q-switch within the oscillator. The maximum output power of the laser is 20 W at cw operation. To control the focal spot size, the laser beam is expanded through a beam expander and focused through a f-theta lens with the focal length of 163 mm. We can control the diameter of focal spot size from about 30 to $200 \mu\text{m}$ by adjusting the ratio of beam expanding. We used beam scanning method in scribing by composing an optical scanning system. It is composed with the f-theta lens and two sets of mirror mounted on galvanometer. The shape of scribing is controlled by adjusting the incident angle of laser beam using the optical scanner. Any shapes such as line, square, point and circle can be realized by controlling the angle of two mirrors while the q-switch is operated to generate output laser pulse only when it is needed. Optical distortion in f-theta lens is compensated by compensating the motion of galvanometer with a compensation table of 64×64 array in software controlling the scanning system. About $100 \times 100 \text{ mm}$ field at focal plane of f-theta lens can be scanned while the resolution is about $10 \mu\text{m}$. A metal plate is set on the focal plane while a sapphire wafer is set on the surface of it. And the laser beam is focused on the surface of metal plate passing through the wafer. A set of stage possible to adjust xyz position and rotation angle is used to align the position and the orientation of the wafer. A set of CCD camera and magnifying lens with a long working distance is mounted just beside the f-theta lens and used to observe the position and the orientation of the wafer accurately.

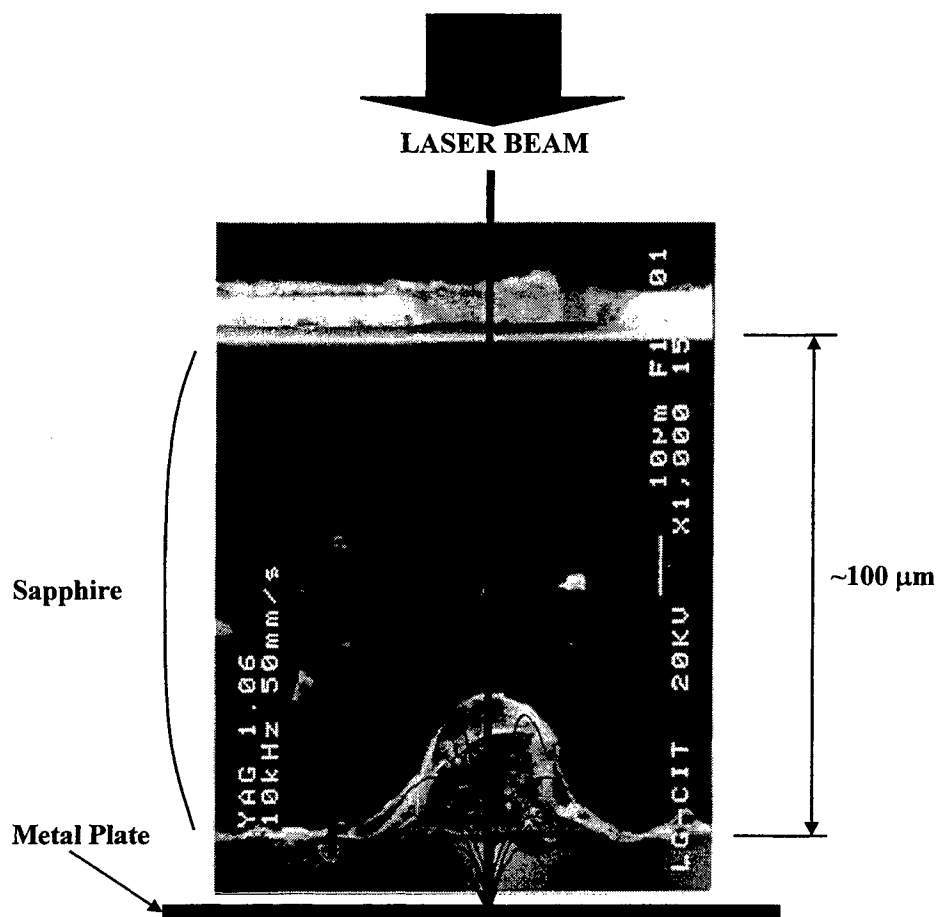


Figure 2. Photograph of cross section of sapphire wafer damaged by LIPAA.

The mechanism of scribing can be explained with Fig. 2 showing the cross section of sapphire wafer scribed by plasma induced by the laser. The photograph was taken by scanning electron microscopy (SEM). Plasma is generated from the metal plate by the absorption of laser beam and it induces damage into the bottom of the wafer. The faint region of upper part of the cross section is not a real image but a shadow of the sample in taking picture with SEM. The upper part was almost clean without damage by the laser. By scanning the laser beam, the wafer can be scribed in any shapes. We tried several types of metal plates, steel, steel coated by nickel, aluminium, and aluminium anodized in black. There are a little differences in efficiency of ablation with the plates. Ni-coated steel was found to be the best while the reason is not clear. The depth of scribing was found to depend on the output power, repetition rate of q-switch, spot size and scanning speed. The spot size was about $40\text{ }\mu\text{m}$ and the average output power of laser was about 5 W while q-switched at the repetition rate of 10 kHz . The pulse width of the q-switched pulse was about 150 ns . Over than $25\text{ }\mu\text{m}$ in depth was scribed while the speed of scanning is 20 mm/s . The depth can be increased as the scanning speed slow down, even though uncontrollable thermal cracks can be induced by excessively slow scanning speed. The peak power of the q-switched laser pulse grows as the repetition rate of q-switch is diminished. The upper part of sapphire was damaged a little when the higher intensity of laser pulse was used by focusing the laser more tightly and by decreasing the repetition rate with the higher average power. But the depth of the damage was very low and random spots of thermal crack was induced in the upper surface while the depth and shape of damage is not uniform even at the bottom in that case. So, the wafer is hardly to be scribed directly with the laser, and the proper conditions such as the proper power, repetition rate of q-switch, spot size should be provided for the application of LIPAA in scribing the wafer.

No vacuum chamber and any assistant gases are used in this process, while they are used in the previous experiments

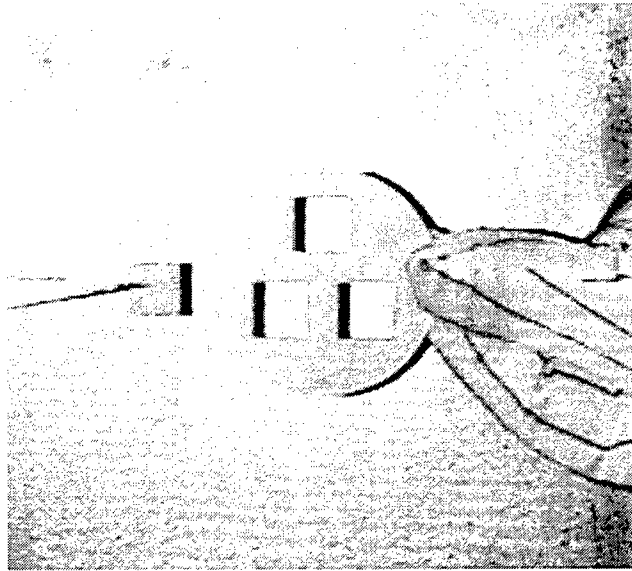


Figure 3. A 400 μm thick sapphire wafer with the diameter of 2 inch cut off by three 12 x 12 mm squares by LIPAA.

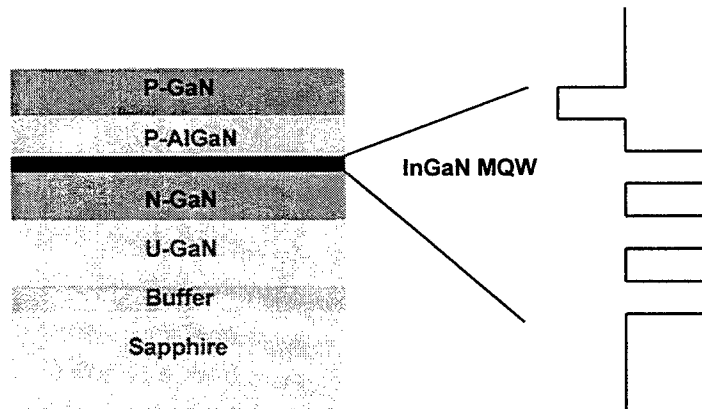


Figure 4. The structure of blue LED grown by us on sapphire substrate.

using LIPAA.⁷⁻⁹ We didn't tried the process in vacuum since it was enough to scribe and to cut the wafer successfully without vacuum chamber in our case, even though it was demonstrated in the previous experiments that the efficiency of LIPAA grows in vacuum.⁹ We set the wafer as close as possible and it may be the reason we can scribe the wafer without vacuum chamber. The wafer scribed more easily as we stick it to the metal plate but it has a problem in separating the wafer from the metal plate after the scribing especially with steel plate. So, we put the wafer about 100 μm above the plate when we apply it to the manufacturing process of blue LED.

Fig. 3 shows three 12 x 12 mm squares are cut off from 400 μm thick sapphire wafer by scanning the laser beam. It was done by scanning the square line more than ten times repeatedly. Commercial blue LED is usually composed of GaN layer on the substrate of sapphire and the structure of blue LED made by us is as shown in Fig 4. GaN buffer layer is grown on the substrate of sapphire and InGaIn-MQW/GaN/AlGaIn structure is grown to compose the device on the buffer layer. The color of emitting light of LED is known to be varied from violet to red according to

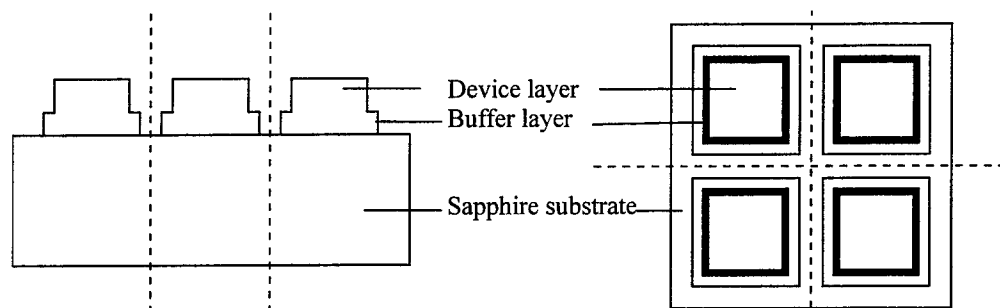


Figure 5. The structure of the blue LED wafer with narrow isolation region made by removing GaN layer to prevent the thermal damage of the device by the absorption of laser.

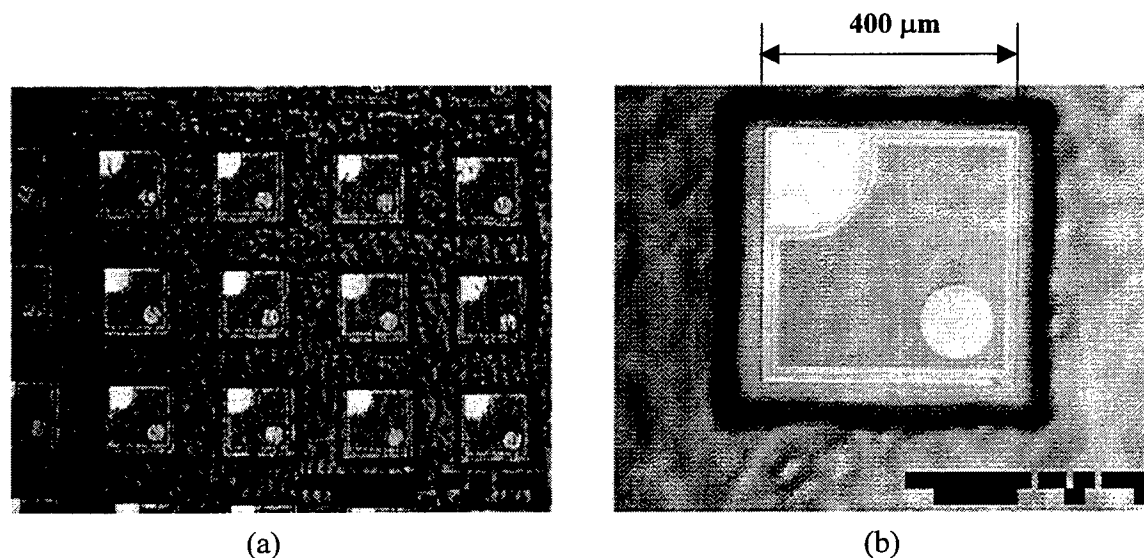


Figure 6. Photograph (a) of blue LED wafer and a detailed view (b) of it splitted after the scribing and breaking.

the indium composition of well layer.^{10,11} So, this scribing method can be applied to the LEDs with the color from violet to red. The device layer grown on sapphire substrate was found to be damaged more easily than the substrate layer when the laser passes through the wafer. And it was observed that only the GaN layer was ablated by the laser when we didn't use LIPAA i.e. when we didn't put the wafer on a metal plate. It seems to be because the laser beam is absorbed in GaN much better than in sapphire. Two disadvantages can be caused by the absorption of laser beam in GaN layer during the scribing process. One is that the devices in the wafer can be thermally damaged by the heat spreading from the spot where the laser beam is absorbed. The other is that the depth of scribing by LIPAA is decreased, since lots of laser power is wasted by the absorption in GaN layer. We solved the problems by making narrow isolated regions without GaN layer between each blue LED devices as shown in Fig 5. The laser beam passes through the isolated regions without absorption, and only the bottom of the wafer is scribed by LIPAA.

The blue LED wafer was scribed by LIPAA and splitted each other after it was broken as shown in Fig. 6. The photograph was taken while the wafer is inserted in couple of transparent flexible sheets for easy handling. About ten thousands of 400 x 400 μm blue LED devices grown on a sapphire wafer with the diameter of 2 inch are splitted

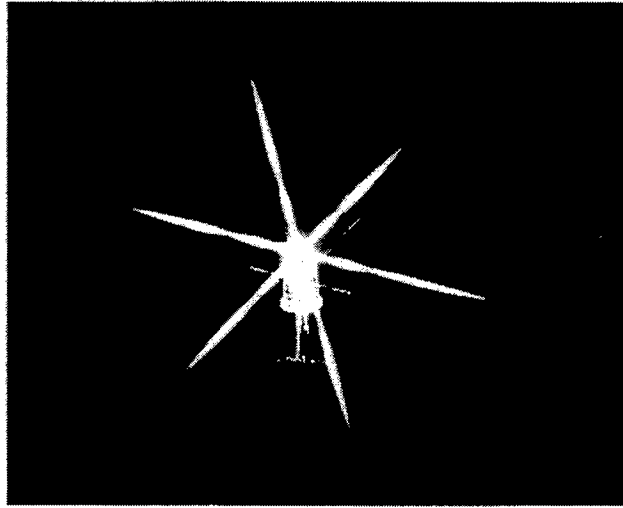


Figure 7. Photograph of a final product of blue LED emitting blue light.

finely as shown in the figure. The wafer was scribed after the thickness ground down into $100\ \mu\text{m}$ even though it is possible to scribe and cut the original wafer with the thickness of $400\ \mu\text{m}$. It's because that the wafer should be scribed as deeply as a quarter of the full thickness possible to be easily cut while heat is generated more to scribe more deeply. Heat generation can be a disadvantage of this method compared with the traditional method using diamond tip. So, we payed attention not to generate excessive heat in the manufacturing process by using the output power of laser as low as possible while maintaining the depth of scribing about a quarter of the thickness. The metal layer on the left upper corner is n-metal and the metal layer on the right lower corner is p-metal. N-metal is located on the bottom and p-metal is located on the top of the GaN device layer. The light is emitted from the surfaces of the device when electric current is turned on across the electrodes.

A section of narrow isolated region was damaged and the wafer was cut along the line of damage as shown in Fig. 6 (b), the detailed view of the sample. The width of isolation region was about $100\ \mu\text{m}$ and less than half of the width was damaged. The width of damage is expected to be decreased if the diameter of the beam spot is decreased by focusing the laser beam more tightly. We didn't decrease the diameter more since the accuracy of the scribing depends on the resolution and stability of the scanning system more than the spot size in this experiment. It is expected that the waste portion of the wafer can be diminished by using the smaller spot of beam and accurate linear stage instead of galvanometric scanning system in the future application. The ratio of failure in breaking the wafer was less than 10 %, which is quite nice compared with the result of traditional method using diamond tip. The main reason of the failure seems to be the mismatch in aligning the line of scribing with the blade to break the wafer. The line of scribing is a little far from a exact straight line due to the distortion through f-theta lens even though it is compensated through the compensation table in software controlling the motion of galvanometer. The machine used in breaking the wafer is not a special one for the sapphire wafer but a usual breaking machine used to break silicon or GaAs wafer. It was possible to use the machine in breaking the sapphire wafer since the depth of scribing is much more deep with this method than the traditional method using diamond tip. The failure in breaking the scribed wafer is expected to diminish by scribing the wafer even more deeply, but it was not applied in the manufacturing process because there is a possibility that the device can be damaged by excessive heat generated by the laser. Scribing the wafer in vacuum may be a way of improving the manufacturing process since it is expected that the wafer can be scribed deeply with the less output power of laser in vacuum.

For the exact estimation of this scribing method, it is necessary to compare the results using each method, LIPAA and the traditional method using diamond tip, with the same sample since the characteristics of blue LED depends on almost every processes including the scribing process. But we had no chance to compare the results directly between the method using LIPAA and the traditional method, since the main reason we tried LIPAA in the manufacturing process is to overcome the economical difficulty in providing the expensive machine using traditional method. Fig.

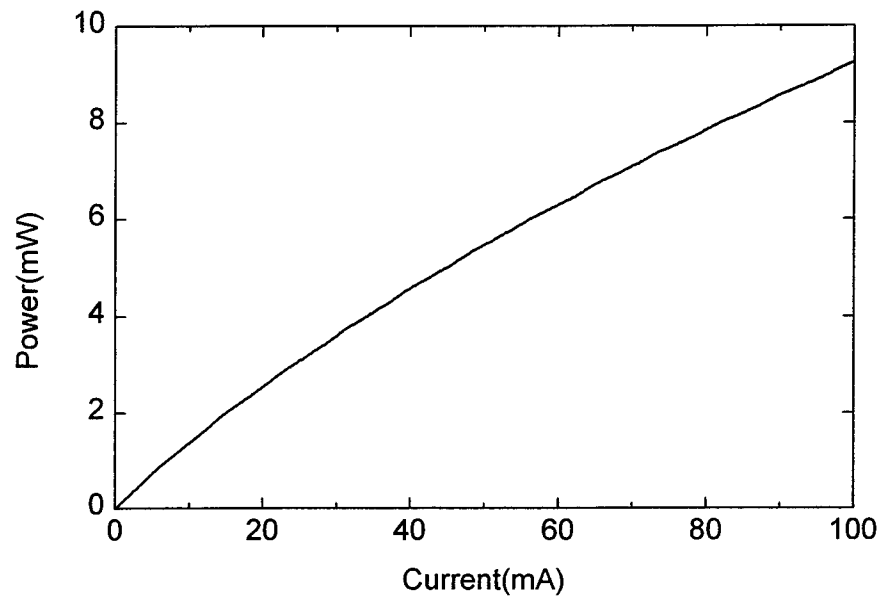


Figure 8. Output power of blue LED as a function of operation current.

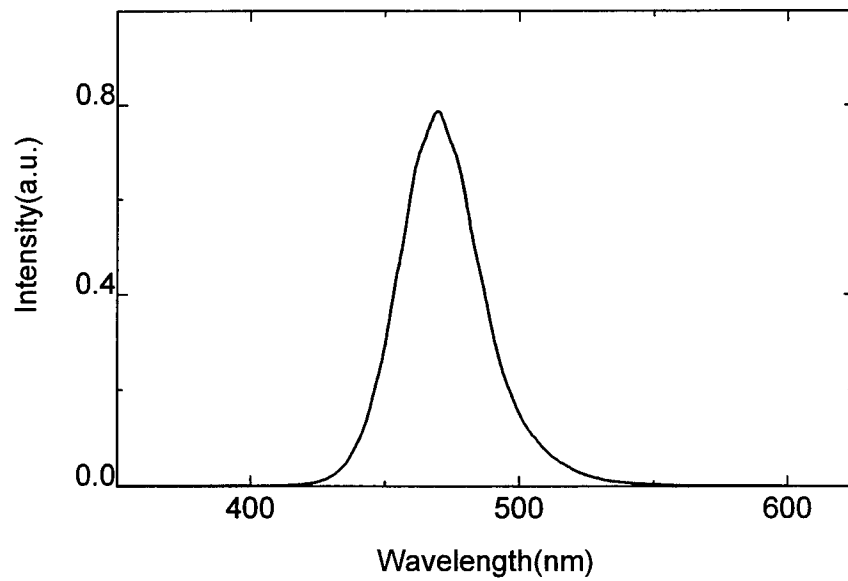


Figure 9. Emission spectrum of blue LED.

7 shows that light is emitted from the blue LED device finally produced as a commercial product using LIPAA, and Fig. 8 shows the output characteristics of it. The output power is about 2.5 mW at the usual operation current of 20 mA while the maximum output power is about 9.2 mW at 100 mA as shown in Fig. 8 (a). The color is blue as the peak wavelength of about 470 nm in Fig. 8 (b). These characteristics is comparable, in my knowledge, with the characteristics of other products manufactured using the traditional method in scribing the wafer. The blue LED devices manufactured using LIPAA have been on the market for more than one year and it is operated well without any problems. So, we can say that the method using LIPAA is successfully applied to the manufacturing process of blue LED by scribing the wafer.

3. CONCLUSION

It is demonstrated that sapphire wafer can be scribed and cut freely by the method, LIPAA, using a q-switched fundamental Nd:YAG laser. Blue LED wafer grown on sapphire substrate material is found to be scribed well using LIPAA and it is successfully applied to the manufacturing process of commercial blue LED device by splitting each device from the wafer including about ten thousands of blue LED devices. The wafer is scribed enough to be cut using a q-switched Nd:YAG laser with the average power of 5 W at atmospheric environment without vacuum chamber. From the result, we expect that the method to cut transparent materials by q-switched Nd:YAG laser can be used as an economical way, which is the main reason we applied it to the manufacturing process of blue LED, and accurate way to many applications using transparent and hard materials such as glass and sapphire.

ACKNOWLEDGEMENTS

The authors are grateful to Ki-Gwan Han, Ki-Young Um and Jae-Yong Jung for their assistance with the experiment. We also thank Koji Sugioka for helpful discussions during the preparation of this paper.

REFERENCES

1. H. Jones-Bey, "Glass cutting advances toward SID '99," *Laser Focus World*, **35**, pp. 86-88, 1999.
2. J. Ihlemann and B. Wolff-Rottke, "Excimer laser micro machining of inorganic dielectrics," *Appl. Surface Science* **106**, pp. 282-286, 1996.
3. H. Schmidt, J. Ihlemann, B. Wolff-Rottke, K. Luther, and J. Troe, "Ultraviolet laser ablation of polymers: spot size, pulse duration, and plume attenuation effects explained," *J. Appl. Phys.* **83**, pp. 5458-5468, 1998.
4. W. Kautek, J. Krüger, M. Lenzner, S. Sartania, Ch. Spielmann, and F. Krausz, "Laser ablation of dielectrics with pulse duration between 20 fs and 3 ps," *Appl. Phys. Lett.* **69**, pp. 3146-3148, 1996.
5. J. Krüger and W. Kautek, "Femtosecond-pulse visible laser processing of transparent materials," *Appl. Surface Science* **96-98**, pp. 430-438, 1996.
6. M. D. Perry, B. C. Stuart, P. S. Banks, M. D. Feit, V. Yanovsky, and A. M. Rubenchik, "Ultrashort-pulse laser machining of dielectric materials," *J. Appl. Phys.* **85**, pp. 6803-6810, 1999.
7. J. Zhang, K. Sugioka, and K. Midorikawa, "Direct fabrication of microgratings in fused quartz by laser-induced plasma-assisted ablation with a KrF excimer laser," *Opt. Lett.* **23**, pp. 1486-1488, 1998.
8. J. Zhang, K. Sugioka, and K. Midorikawa, "High-speed machining of glass materials by laser-induced plasma-assisted ablation using a 532-nm laser," *Appl. Phys. A* **67**, pp. 499-501, 1998.
9. J. Zhang, K. Sugioka, and K. Midorikawa, "Laser-induced plasma-assisted ablation of fused quartz using the fourth harmonic of a Nd⁺:YAG laser," *Appl. Phys. A* **67**, pp. 545-549, 1998.
10. S. Nakamura, "A Bright Future for Blue/Green LEDs," *IEEE Circuits & Devices Magazine* **11**, pp. 19-23, 1995.
11. T. Mukai, M. Yamada and S. Nakamura, "InGaN-based uv/blue/green/amber/red LEDs," *SPIE Proc.* **3621**, pp. 2-13, 1999.

SESSION 9

Laser Microengineering I

Microfabrication by femtosecond laser irradiation

Hiroaki Misawa^{*a}, Hong-Bo Sun^b, Saulius Juodkazis^b, Mitsuru Watanabe^a, Shigeki Matsuo^a

^a Department of Ecosystem Engineering, The University of Tokushima,
2-1 Minamijyosanjima, Tokushima 770-8506, Japan

^b Satellite Venture Business Laboratory, The University of Tokushima,
2-1 Minamijyosanjima, Tokushima 770-8506, Japan

ABSTRACT

Femtosecond (fs) laser microfabrication has been gathering more research interests due to its ability to create micro- and sub-micrometer three-dimensional (3D) structures. An extremely high light intensity ($\sim 10^{18}$ W/cm²) enables multiphoton absorption (MPA) in transparent materials, upon which the spatial resolution of fabricated elements is confined to the sizes even smaller than optical diffraction limit. Our report will formulate the principles of the laser microfabrication of such applications.

A direct application of single-shot pulse-induced optical damage is a 3D optical memory with a storage density of ca. 100 Gbits/cm² in silica. Photonic and optoelectronic applications such as optical gratings, 3D inlaid-"atom"-like and 2D cylinder-consisted photonic crystals have been fabricated in silica. Also, photopolymerization of photoresist by a scanning of focal point of laser irradiation solidifies submicrometer rods, which forms photonic lattices when packed into well-defined 3D pattern. Photonic bandgap effects (at 2–4 μ m) of above-mentioned structures were corroborated by infrared Fourier spectroscopy and numerical simulations, by which the success of laser microfabrication was evidenced.

Self-focusing of fs-pulses (optical Kerr effect) is another possibility of the microstructuring of transparent materials, which is demonstrated in the case of silica. This could find its application in sub-diffraction-limited recording.

Keywords: Laser microfabrication, Two-photon absorption, Multi-photon absorption, Self-focusing, 3-D optical memory, Photonic crystals, Silica, Resin

1. INTRODUCTION

The unique properties of focused femtosecond (fs) pulses are determined by their intensity of light, which can reach over 10^{18} W/cm², which in electrical field strength reaches 2.7×10^{10} V/cm. For example, standard setup of Ti:sapphire laser with regenerative amplifier can deliver up to 1 W at 1 kHz. When these pulses of 120 fs duration are focused into 1 μ m spot the intensity reaches 10^{18} W/cm². Such an electrical fields already exceeds the Coulomb field on the first electronic orbit of hydrogen atom (Bohr radius of which is r_B), given by $V_{AT} = \frac{e}{2r_B^2} \approx 3 \times 10^9$ V/cm or, in terms of intensity,

$I_{AT} \equiv \frac{1}{2} \epsilon_0 c |V_{AT}|^2 \approx 10^{16}$ W/cm², where ϵ_0 is the permittivity of free space and c is the velocity of light. This implies that discrete spectrum of atomic levels tends to change into continuum. Another characteristic intensity, when atom becomes unstable in respect to the tunneling ionization during the period of light wave, is even smaller: $I_T = (\hbar\omega/J)^2 I_{AT}$, where J is the ionization potential. Indeed, for Rydberg energy $J = 13.6$ eV and photon quantum of 1 eV we obtain $I_T \propto 10^{14}$ W/cm². As will be shown, the impact ionization has even lower threshold. If the intensity of 10^{19} W/cm² is reached for optical region of spectrum, the kinetic energy of electron oscillations in the field of light, E , becomes comparable with the rest energy of electron, $\frac{e^2 E^2}{4m\omega^2} = mc^2$, and relativistic approach is necessary (e , m are the charge and mass of electron, respectively).

As the ultimate limit of this intensity scale (not experimentally achievable) the optical breakdown of vacuum could be mentioned at $I = 10^{30}$ W/cm² when electron-positron pair is generated (the energy of the resting electron becomes equal to the energy of light field at the Compton wavelength of electron). This short overview of characteristic intensities shows that new phenomena and applications are expected when the femtosecond focused illumination is employed. Better understanding of the material response to the high intensity excitations is expected with the employment of sub-picosecond (ps) X-ray sources,¹ recently available, which will allow monitor non-thermal processes in relaxation of photo-excited materials.² The intensity profile of the fs-laser pulses can be significantly modified by the linear and non-linear (dependent

* Corresponding author. Email address: misawa@eco.tokushima-u.ac.jp.

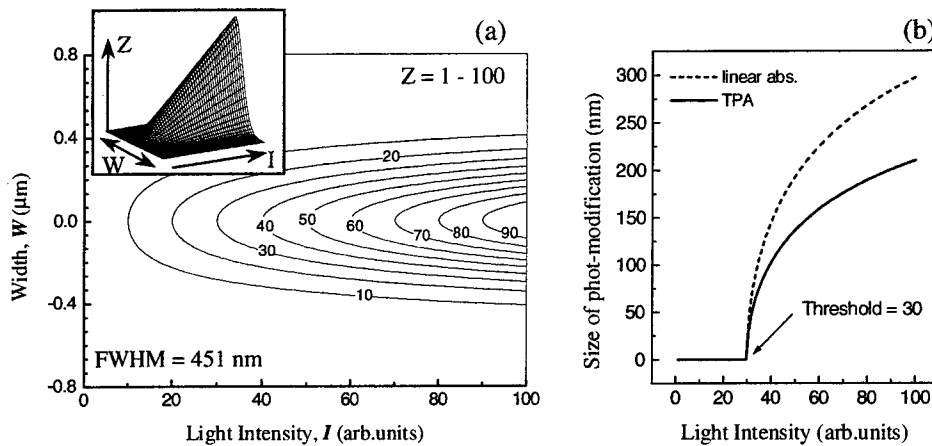


Fig. 2.1. (a) Contour plot of the 3D intensity profile (shown in the inset) of Gaussian beam of $FWHM = 451$ nm (the waist at $1/e$ level corresponds to the diffraction limited spot size $1.22\lambda/NA = 751$ nm, when $\lambda = 800$ nm and $NA = 1.3$). The entire intensity scale 1-100 is sectioned into 9 heights showing the size of the focal point at corresponding intensity. (b) The lateral size of the beam, where the intensity of the light is exceeding a photo-modification threshold, vs. light intensity (for the same Gaussian beam profile, which is plotted in (a)) for linear (----) and two-photon (—) absorption. Plotted by $Spot = \sqrt{\frac{FWHM^2}{-n \cdot 4 \ln 2} \ln \left(\frac{Threshold}{I_0} \right)}$, where I_0 is the intensity of the light and n is 1 or 2 for linear or TPA, respectively.

on the light intensity) interactions during their propagation in materials. For silica with normal dispersion the interplay of dispersion, self-focusing and self-phase modulation can lead to complex pulse splittings (single or multi-pulselets and their coalescence) and super-continuum generation.³ All the phenomena involved into the interaction of fs-pulses with materials at high-focusing (in microscope) conditions, such as multi-photon absorption, ionization, higher order dispersion are still not well understood nor modeled theoretically.

2. THE PRINCIPLES OF LASER MICROFABRICATION

2.1. Optical constraints on resolution

The term *laser microfabrication* inherently implies the usage of microscope as a tool in the fabrication process. Consequently, the axial and lateral resolutions are given, respectively, by:⁴

$$z = 2 \frac{n\lambda}{NA^2}, \quad (2.1)$$

$$r = 0.61 \frac{\lambda}{NA}, \quad (2.2)$$

where λ is the wavelength of irradiation light, n is the refractive index of material, and NA is the numerical aperture of objective lens. When the high spatial resolution is aimed, the oil-immersion objectives with $NA > 1$ are usually employed. Recently, the most widely used femtosecond light source is Ti:sapphire laser operating at around 800 nm. This gives the size of the focal spot (central Airy disk of Fraunhofer diffraction pattern) where 84% of light energy are contained $1.22\lambda/NA = 0.75 \mu m$ for $\lambda = 0.8 \mu m$ and $NA = 1.3$. One can expect more localized modification of material in the focal point (higher spatial resolution of fabrication) if the multi-photon absorption (MPA) is responsible for such an event, e.g., when Gaussian beams are considered $I = I_0 \exp(-4 \ln 2 (x/x_0)^2)$, the two-photon absorption (TPA) improves resolution by a factor $\sqrt{2}$. Here x_0 is the full width at half maximum (FWHM) of intensity, I , envelope, and absorbed energy in TPA process scales as $\propto I^2$. If the process of photo-modification can be considered having certain threshold (this is not rigidly correct for usually exponential phenomena) the dependence of lateral resolution on the intensity of irradiation can be presented by Fig. 2.1. Real dimensions of photo-modification are certainly dependent on the thermal conductivity, heat capacity, melting temperature, overheating of irradiation point, sound velocity of material, etc. The diffusion related processes scales as $\sqrt{t_p}$, where t_p is the pulse duration, and the photo-modification profile approaches that given by laser beam focusing optics.

2.2. Optical damage

3-D structuring of materials by light can be accomplished when the wavelength of irradiation is in the transparency region of these materials. This means that light-material interaction should be MPA in nature. Since the probability of MPA is exponentially dependent on the light intensity, the use of tightly focused ($NA > 0.6$) and short, sub-ps, pulses is desirable. The basics of light induced formation of a plasma state in gas, liquid or solid matter can be understood in frame of collisional-plasma formation, which correctly predicts the dependence of intensity threshold of material ionization on laser pulse duration $I_{th} \propto t_p^{-1}$. This classical description is valid for the electron-avalanche formation, which can start from a single free electron and in tens of generations by an impact ionization can transfer all the focal volume of material into a plasma state.

What energy can electron acquire in the field of intense laser irradiation? Let us compare the energy of electron obtained in the light field with the ionization potential of matter, $J \approx 10 - 15$ eV (the following derivation is based on ref. 5). The movement of electron in the field of light $E(t) = \frac{1}{2} E_0 \exp(-i\omega t) + c.c.$ can be expressed by:

$$\frac{\partial^2 r}{\partial t^2} = \frac{e}{m} E_0 \cos(\omega t) \quad (2.1)$$

in the frame of non-relativistic dipole approach ($v/c \ll 1$), when Lorentz interaction $[v, H]$ is not considered. Also, non-local effects are omitted $E(r, t) = E(t)$. Here, r , v , e , m are the coordinate, velocity, charge, and mass of electron; ω , c , E and H are the frequency, speed, electric and magnetic field strength of light, respectively; $c.c.$ stands for the complex conjugate and $i = \sqrt{-1}$.

Now, let's assume the electron moves, in average, time τ between two adjacent collisions. The solution for the velocity of electron at the time moment t (the collisions are taking place randomly at the time moments t_0) can be found from eq. 2.1

$$v(t, t_0) = \int_{t_0}^t \frac{eE}{m} \cos(\omega t') dt' + v' \quad (2.2)$$

The probability that an electron, which is accelerating at the moment t , was experiencing its last collision at the moment $t_0 < t$ is given by

$$f(t_0, t) dt_0 = \frac{1}{\tau} \exp\left(-\frac{t-t_0}{\tau}\right) dt_0 \quad (2.3)$$

Then, time average of velocity can be found directly by definition of an average:

$$v(t) \equiv \langle v(t) \rangle = \int_{-\infty}^t v(t_0, t) f(t_0, t) dt_0 \quad (2.4)$$

and solution is searched in the form $v(t) = \frac{1}{2} v_0 \exp(-i\omega t) + c.c.$ One can find ($\langle v' \rangle = 0$)

$$v_0 = i \frac{eE_0}{m\omega} + \frac{eE_0/(m\tau\omega)}{\omega + i/\tau} \quad (2.5)$$

The average work of the light field made over an electron can be found as $P_{av} = \langle eE(t)v(t) \rangle$. The first term of eq. 2.5 gives 0 due to $\pi/2$ phase shift between v and E . Second term of eq. 2.5 defines the energy gain per electron in the field of light due to absorption

$$\left(\frac{d\varphi}{dt}\right) = \frac{e^2 E_0^2}{2m} \frac{v}{\omega^2 + v^2} \quad (2.6)$$

, where $v = 1/\tau$ is the frequency of collisions. The energy change per electron due to collision with an ion of the mass M (the initial velocity of an ion is 0) can be found from the impulse conservation:

$$\Delta\varphi = \frac{\langle \Delta p^2 \rangle}{2M} = 2 \frac{m}{M} (1 - \langle \cos \theta \rangle) \varepsilon_0 \quad (2.7)$$

, where $\varepsilon_0 = p^2/2m$ is the kinetic energy of electron. An average value of cosines of the scattering angle of an electron can be considered $\langle \cos \theta \rangle \approx 0$ ('strong interaction'). Then, the final expression for the energy balance for electron reads

$$\left(\frac{d\varphi}{dt}\right) = \frac{e^2 E_0^2}{2m} \frac{v}{\omega^2 + v^2} - 2\varepsilon_0 \frac{m}{M} v \quad (2.8)$$

With the following solution found

$$\varphi(t) = \frac{M}{m} \frac{e^2 E_0^2}{4m(\omega^2 + \nu^2)} \left\{ 1 - \exp\left(-\frac{2m}{M} \nu t\right) \right\} \quad (2.9)$$

Then, the maximum value of energy obtained by an electron is

$$\varphi_{\max} \cong \frac{m}{M} I r_{el} \frac{\lambda^2}{2\pi c} \frac{1}{1 + (\nu/\omega)^2} \quad (2.10)$$

, where $r_{el} = e^2/mc^2 \cong 0.3 \times 10^{-12} \text{ cm}$ is the classical radius of electron, $I = cE_0^2/8\pi$ is the intensity of irradiation. By taking $I = 100 \text{ GW/cm}^2$, $\lambda = 1 \text{ }\mu\text{m}$, $M/m > 2 \times 10^3$ and low frequency of collisions as compared with that of light $\nu \ll \omega$, we will obtain $\varphi_{\max} > 20 \text{ eV}$.

The quantitative prediction of eq. 2.10 is not straight forward for solid matter (while correct for the gases at low pressure), because the mass of electron should be substituted by its effective mass, m^* , usually $m^* < m$. Also, the collision frequency can approach optical frequencies, $\nu \approx \omega$, because of high density of solid state media. Even though, the qualitative picture is correct, since the circumstances mentioned above tends to lower φ_{\max} , but the bandgap energy E_g ($E_g < J$) should be rather considered instead of ionization potential for the free-carriers generation. This shows that the energy of electron can reach the potential enough for impact ionization and interaction of heated electrons with the lattice is expected to be inelastic.

Avalanche and free-carrier-plasma formation. The mechanism described above has a potential to trigger an avalanche process of electron generation. If $\varphi_{\max} > E_g$ the number of free electrons and holes increases as the avalanche. Let assume, there is no diffusion of free-carriers from the excitation region and no recombination (it is an appropriate assumption for the short pulses of $t_p \leq 1 \text{ ps}$ duration). Then an avalanche can be defined as

$$N_e = N_{e0} \exp(\nu_{ion} t) \quad (2.11)$$

, where ν_{ion} is the ionization frequency. The time necessary for an electron to acquire the potential of ionization, $\tau_{ion} = 1/\nu_{ion}$, can be found from eq. 2.9

$$\tau_{ion} = \frac{\pi c E_g}{\nu I r_{el} \lambda^2} \left(1 + \nu^2/\omega^2 \right) \quad (2.12)$$

Let us suppose, the avalanche starts from one electron, $N_{e0} = 1$, and finishes when all molecules (atoms) in the volume of focal point are ionized and this requires certain time T . In case of quartz, the atomic density is $2.65 \times 10^{22} \text{ cm}^{-3}$ and T can be found from eq. 2.9 according to $2.65 \cdot 10^{22} = 1 \cdot \exp(T/\tau_i)$ (the volume density of quartz-SiO₂ is 2.648 g/cm^3 and molecular weight 60.084). This shows, that in 51 generations of electrons, $T \approx 51\tau_i$, all the volume of focal point is transferred into the ionized state (this means that all atoms contributed by one electron-hole pair to an electron-hole plasma). This exceeds the calculated lattice stability limit of 10^{22} cm^{-3} .⁶ Evidently the $t_p > T$ must hold, where t_p is the pulse duration for the avalanche to develop. From eq. 2.12 the threshold intensity in respect to impact ionization can be found

$$I_{th} \cong \frac{51 \pi c E_g}{t_p \nu r_{el} \lambda^2} \left(1 + \nu^2/\omega^2 \right) \quad (2.13)$$

The dependence $I_{th} \propto t_p^{-1}$ is valid. The collision frequency, ν , of electrons with the lattice atoms can be estimated from $\nu \cong n u_{rms} \sigma$, where $n [\text{cm}^{-3}]$ is the number density of atoms in material, u_{rms} is the root mean square velocity of electron given as

$$u_{rms} \equiv \sqrt{\langle u^2 \rangle} = \sqrt{3k_B T/m^*} = 1.18 \times 10^7 \sqrt{\frac{m}{m^*} \frac{T[K]}{300}} \text{ cm/s}$$

and σ is the cross-section of electron scattering over neutral atom. By taking former example of quartz with $n = 16 \times 2.65 \times 10^{22} \text{ cm}^{-3}$ (a factor 16 accounts for the number of valence electrons of SiO₂), $u_{rms} = 1.18 \times 10^7 \text{ cm/s}$ (supposing $m \approx m^*$ and $T \approx 300 \text{ K}$), and $\sigma = 10^{-15} \text{ cm}^2$, which is the "geometrical" cross-section of an atom, the estimate of collision frequency is $\nu = 5.0 \times 10^{15} \text{ s}^{-1}$. When applied to solid state, usually, the number of valence electrons is considered, as the maximum limit of possible ionization (excitation of deeper atomic shells is assumed not taking place). The optical frequency of 500 nm light is $c/\lambda \cong 6 \times 10^{14} \text{ s}^{-1}$, and the collision frequency approaches that of the light $\nu \approx 2\pi c/\lambda \approx \omega$. Now, we can make an estimate of the light induced damage threshold (LIDT) for impact ionization according to eq. 2.13. If quartz bandgap $E_g = 7 \text{ eV}$, $\lambda = 1 \text{ }\mu\text{m}$, and $1 + (\nu/\omega)^2 \cong 2$, are assumed, then the threshold defined by eq. 2.13 is $I_{th} = 38 \text{ GW/cm}^2$ for the pulse of $t_p = 1 \text{ ps}$. This threshold should be expected for the all bond ionization in the focal point (contributed by an electron-hole pair each to the free-carriers plasma), but this criteria is few times lower than the experimentally measured

LIDT, which is reached for silica at the fluence of 2 J/cm² in the case of 1 ps pulses (2 TW/cm²).⁷ This shows that the avalanche formation can't be accountable for the ablation of material, which experimentally observed for short (≤ 1 ps) pulses even at high light intensities.

Multi-photon excitation. Sub-picosecond pulses can create optical damage directly in MPA process without the development of avalanche, because basically $\tau_{ion} > \tau_p$ for sub-ps pulses.⁸ The probability of MPA transition of an electron from the initial state i to the final state f is given by the golden Fermi rule:

$$w_{i \rightarrow f}^{(n)} = \frac{2\pi}{\hbar} |H_{i \rightarrow f}^{(n)}|^2 \delta(E_f - E_i - n\hbar\omega) \quad (2.14)$$

, where $H_{i \rightarrow f}^{(n)}$ is the matrix element of the transition Hamiltonian, n is the number of quanta involved in transition, and $\delta(\cdot)$ stands for the delta function. The result of perturbation theory applied to eq. 2.14 yield in:⁵

$$w_{i \rightarrow f}^{(n)} = \frac{2\pi}{\hbar} \sum_{p=-\infty}^{\infty} |L_n(p)|^2 \delta(J + \frac{p^2}{2m} - \frac{e^2 E_0^2}{4m\omega^2} - n\hbar\omega) \quad (2.14a)$$

where re-normalized energy of ionization is $\tilde{J} = J + \frac{e^2 E_0^2}{4m\omega^2}$ and

$$|L_n(p)|^2 \propto \exp \left[-\frac{2\tilde{J}}{\hbar\omega} \left(\text{arsh} \gamma - \gamma \frac{\sqrt{1+\gamma^2}}{1+2\gamma^2} \right) \right] \quad (2.15)$$

$\gamma = \frac{\hbar\omega}{eE_0 r_B}$ with (Bohr radius $r_B = \frac{\hbar^2}{me^2}$). Further simplification can be obtained for two cases i) $\gamma \gg 1$ and ii) $\gamma \ll 1$.

i) this case corresponds to light intensity $I < 10^{12}$ W/cm² (at $\lambda = 1 \mu\text{m}$). By applying $\text{arsh}(\gamma) \approx \ln(2\gamma)$ eq. 2.14(a) reads

$$w_{i \rightarrow f}^{(n)} \propto |L_n(p)|^2 \propto \exp \left(-\frac{J}{\hbar\omega} \left(\frac{e^2 E_0^2}{4m\omega^2} \right)^n \right) \quad (2.16)$$

This predicts an expected relationship of MPA on the light intensity $\propto (E_0^2)^n \equiv I^n$.

ii) when $I > 10^{14}$ W/cm² intensity is reached eq. 2.14(a) can be presented as

$$w_{i \rightarrow f}^{(n)} \propto \exp \left(-\frac{4}{3} \frac{V_{AT}}{E_0} (1 - \text{Const} \cdot \gamma^2) \right) \quad (2.17)$$

with $\text{Const} \approx 1$ and $V_{AT} = \frac{e}{2r_B^2}$. The expression of eq. 2.17 resembles that for tunneling ionization of atoms in the static electrical field. For this reason the MPA at high light intensities such as $I > 10^{14}$ W/cm² can be considered as tunneling of an electron during the period of light oscillation.

The consideration presented above illustrates the phenomena of an avalanche development and MPA in free-carriers generation. To understand the dependence of optical damage on the pulse duration the time scales of the processes of free-carriers generation and their energy relaxation in material should be addressed. The light pulse energy delivered to the media is dissipated by different mechanisms sketched in Fig. 2.2. As far as sub-picosecond excitation of material is concerned the key features are: i) thermalization of free-carriers with the lattice is not finished during the pulse and the temperature of free carriers is higher than that of lattice, $T_{e,h} > T_l$, (it is the reason why processes induced by sub-ps pulses are considered as non-thermal) ii) free-carriers absorption (process 2 in Fig. 2.2) drives the energy towards impact ionization, and iii) multiphoton absorption (process 1 in Fig. 2.2) alone can yield in free carriers generation with the enough energy for impact ionization as well. Also, Auger recombination is expected to contribute to the overall carriers generation-recombination process, since sub-ps recombination times are, in general, expected at high free-carriers concentrations ($\tau_A \propto C/N^3$, where C is the Auger coefficient, which is, e.g., 7×10^{-31} cm⁶/s for wide-bandgap SiC⁹). The shorter the pulse the larger the share of excitation is on MPA.

3. EXPERIMENTAL. SETUP AND MATERIALS

Laser microfabrication system.^{10,11} Laser pulses used in fabrication were delivered by a setup consisting of a mode-locked Ti:Sapphire laser and a regenerative amplifier (*Tsunami & Spitfire*, *Spectra Physics*). The 400 nm second harmonic was obtained (e.g., when required for resin photo-polymerization) by frequency doubling of fundamental 800 nm wavelength in an angularly phase-matched BBO crystal. Pulse duration was measured by auto-correlation and was 120-150 fs (full width at half maximum (FWHM) value). The radiation power was up to 0.6 W measured at 1 kHz and 800 nm with the laser pulse energy stability of ca. 5%. The laser repetition rate was switchable from 1 Hz to 1 kHz. After a collimation the laser pulses

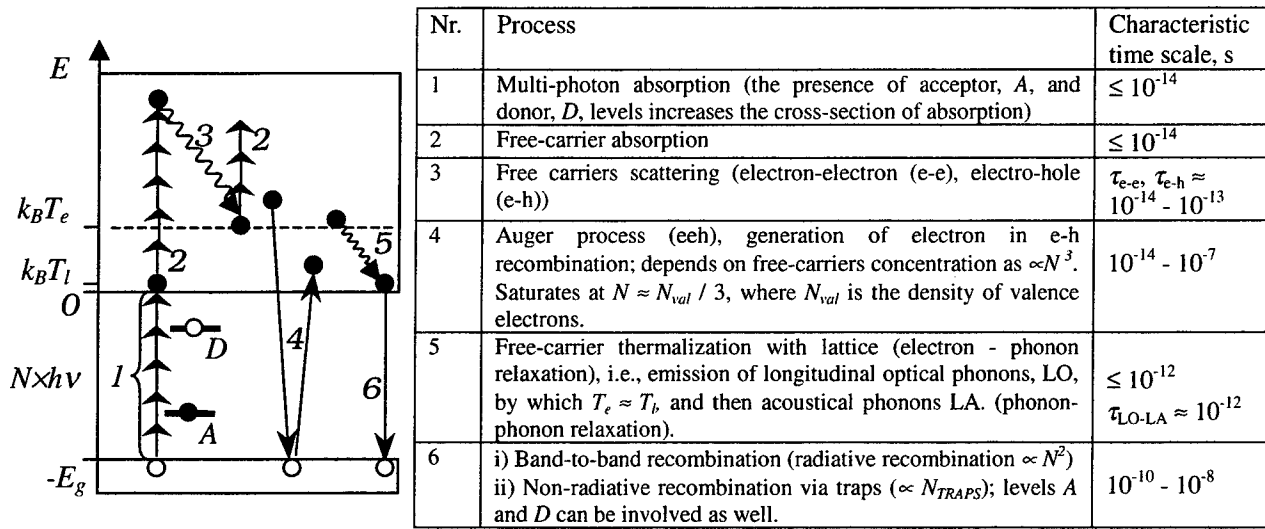


Fig. 2.2. Energy relaxation processes and their time scales in solid state materials.

were fed into inverted microscope (*Olympus IX70* with magnification $\times 100$ and numerical aperture $NA = 1.35$) or normal microscope (*Optiphot-2 Nikon*; $\times 100$, $NA = 0.8/1.3$) and tightly focused by an oil-immersion objective lens. The sample in which the fabrication to be made, was fixed onto a glass plate (standard scheme of operation of oil-immersion objectives), which, in turn, was affixed to a feedback-controlled piezoelectric translator (PZT) (*Physik Instrumente PZ48E*). This piezo-stage was scanned according to a preprogrammed computer-aided pattern with the accuracy of several-nm. A typical scanning speed of PZT was $16 \mu\text{m/s}$ and the spacing between the adjacent exposed sites was 16 nm at a 1 kHz of pulse repetition rate, much smaller than the laser wavelength and the size of focal spot given by diffraction laws (eqs.2.1-2). The entire fabrication process was *in situ* monitored with a CCD camera-monitor set (*Sony, DXC-930*, and *PVM-1442Q*) attached to the optical microscope.

Samples. We used dry (OH concentration $< 10 \text{ ppm}$) vitreous silica, v-SiO₂ (ED brand from *Nippon Silica Glass Co.*),¹² for the three-dimensional (3D) optical memory and photonic crystal (PhC) applications. The resins *Nopcure 800* (*San Nopco*) and *NOA 60* (*Norland Products, Inc.*) consisting of radical photo-initiator and acrylic acid ester were used as light-curing starting materials for PhC and 3D prototyping. The polymerized solid skeletons, the resin/air structures, were obtained after the unsolidified liquid resin was moved out by dipping the sample into a developer (acetone or methanol) for 15 minutes.

Definition of LIDT for 3D microstructuring. In our experiments the direct observation in microscope was used to justify the appearance of the optical damage in the focal point of irradiation. This was considered as a LIDT for microstructuring of material. Thus defined fluence of LIDT was about 8.7 times higher for silica, 17.3 J/cm^2 , as compared with the reported surface ablation experiments (ca. 2 J/cm^2),⁷ where determination was made by an observation in more accurate Nomarskii-type microscope over the mm-sized spots of ablation created by the optically collimated pulses. The definition we are using in this paper is applicable for the 3D microstructuring of transparent materials when focused laser beams are employed. The LIDT of the surface damage typically was found 1-1.5 times lower than that for the bulk irradiation (also depends on the surface quality). Pulse energy or intensity at the irradiation point was less than 25% of that at the entrance of the microscope (the losses comprise of the f-number mismatch at the entrance of microscope (transmission of ca. 32.8%) and the objective transmission itself, which was about 78% for the 400, 800 nm fabrication wavelengths). The pulse energy, fluence or intensity is given at the irradiation point unless specified.

4. RESULTS AND DISCUSSION

4.1. Three-dimensional laser fabrication in silica.

The bits of 3D memory or voxels (volume elements) were created by a single-shot microexplosion at the focal point of irradiation. By the focal point scanning these regions were arrayed into 3D patterns to form PhC. The primary issue aiming to achieve the high storage density of 3D optical memory or the distinct photonic bandgap out of 2D and 3D PhC is the size and shape of a photo-modified region.

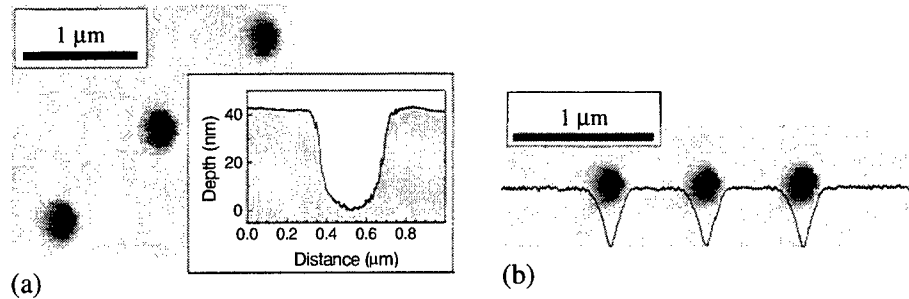


Fig. 4.1. Atomic force microscopy (AFM) images of the voxels made by micro-explosion in silica (a) and crystalline Al₂O₃ (b). The depth profiles are limited by the shape of AFM tip. The damage was induced by a single pulse at ca. $8LIDT$ of corresponding material at the depth of 40 μm (with $LIDT_{\text{sapphire}} = 1.24LIDT_{\text{silica}}$ at 800 nm) using $NA = 1.35$ objective lens. Samples were polished for the highest opening of the voxels.

4.1.1. Voxel's morphology. Microstructuring by self-focusing

Mechanical polishing of the sample after irradiation can evidence the void formation at the center of focal point, which was located tens-of-μm inside the bulk of material (amorphous or crystalline), as shown by atomic force microscopy (AFM) images in Fig. 4.1. The size and shape of the voxel can be characterized by optical transmission as well (Fig. 4.2.). The most spherical shape of the voxel is obtained when the pulse energy is 1–2 $LIDT$ ($LIDT = 76.8$ nJ or 17.3 J/cm² evaluated at the irradiation point in the case of fabrication in silica (Fig. 4.1.)) and the smallest sizes are attainable by the employment of high $NA = 1.3$ objective lens. Crack formation onset was found at the pulse energy of 0.64 μJ.

Rather different fabrication patterns were observed when the same objective lens was adjusted to $NA = 0.8$ (Fig. 4.2.), i.e., the longitudinal gradient of the light field was reduced about 1.5 times according to the light localization at a focus given by eqs. 2.1-2. The side view of an optical damage reveals the complex pattern of filament formation, which cannot be understood in terms of self-focusing alone. The axial position of a focal point must obey $z_f^{-1}(I) \sim I^{0.5}$ power dependence in the case of self-focusing.¹³ This has been proved to be correct for the 10 – 1 ps pulses in silica,¹⁴ but it was not observed experimentally for 120 fs pulses we employed (Fig. 4.2(a)). The steady-state paraxial wave equation analysis predicts a self-focusing towards a singularity when the light power exceeds the power of self-trapping, P_{cr} (beam spreading due to diffraction is compensated by self-focusing). $P_{cr} = (0.61\lambda)^2\pi/8n_0n_2$, where the refractive index is light intensity dependent $n(I) = n_0 + n_2I$. For silica at 800 nm $P_{cr} = 2.6$ MW ($n_2 = 2.5 \times 10^{-16}$ cm²/GW).¹⁵ The average light intensity we used for irradiation of silica was $2.0\text{--}6.8 \times 10^{15}$ W/cm² at the focus of 1.13×10^{-8} cm² area ($NA = 0.8$). This already exceeds the power of self-focusing in silica and a non-linear aspects of the light propagation must be addressed. Actual intensity can even

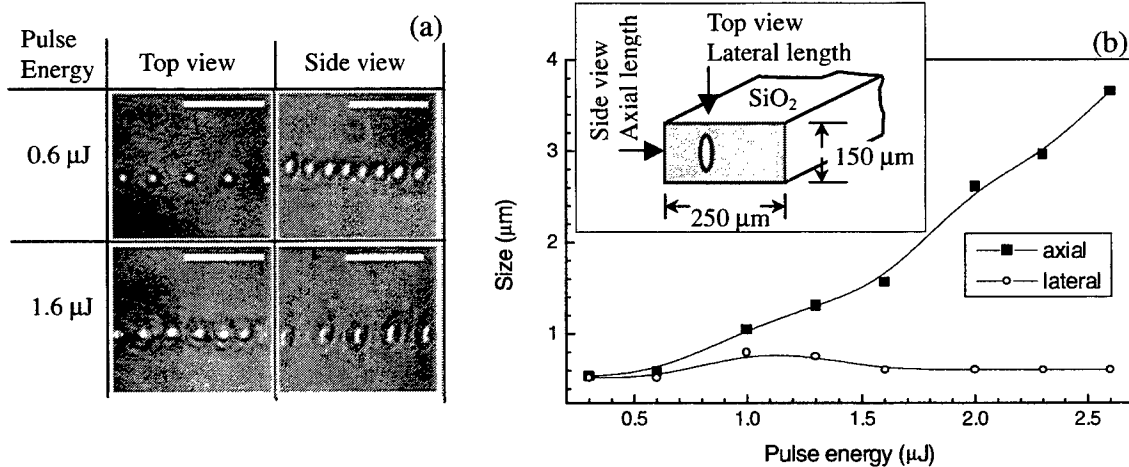


Fig. 4.2. (a) Top and side views of bits fabricated at two different pulse energies in silica. (b) Power dependence of the lateral and axial sizes of the bit. The damage was induced by 120 fs laser pulses (single shot per bit) at $\lambda = 800$ nm using $NA = 1.3$ objective lens. The size of the bright region in transmission image was taken as a measure of the bit's dimension. The pulse energy is given at the entrance of microscope; the transmission of microscope was 25%. Scale bars are 5 μm. Lines in (b) serves as eyeguides.

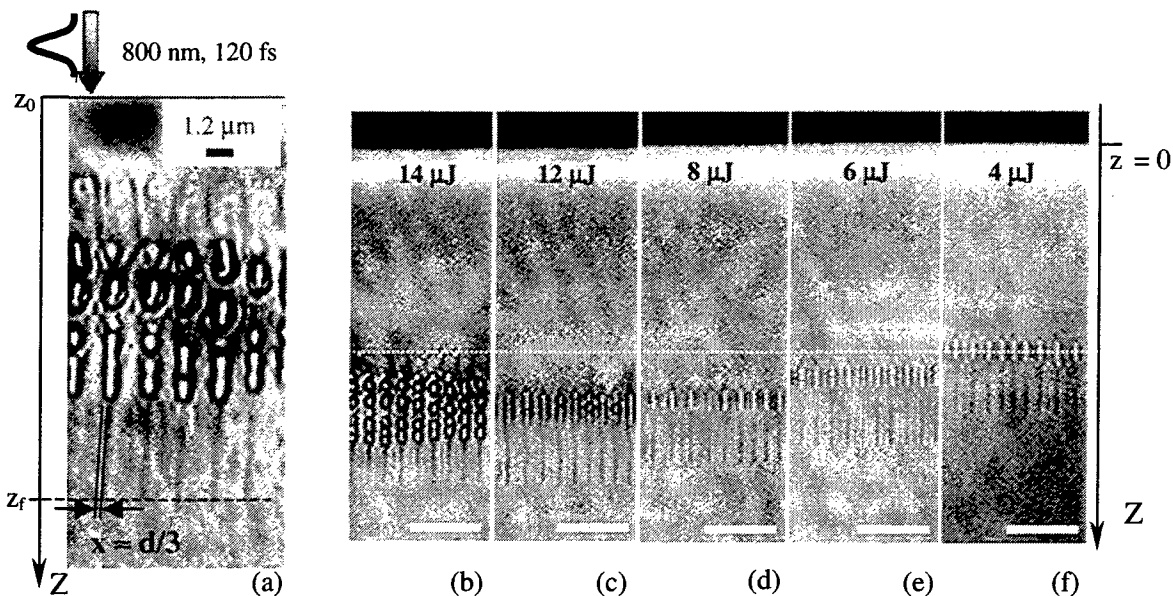


Fig. 4.3. Self-focusing traces in silica optically damaged by $\lambda = 800$ nm, 120 fs laser pulses in a single shot per trace. Diffraction-limited focal spot was $d = 1.2\lambda/NA = 1.2 \mu\text{m}$ (scale bar in (a)), where $NA = 0.8$ is the numerical aperture of the objective used for irradiation. The transmission image (side view of the trace) was recorded at higher resolution ($0.61\lambda/NA \approx 0.25 \mu\text{m}$) utilizing condensor illumination at 500-600 nm and $NA = 1.35$ objective lens. The focal spot of irradiation was positioned at $z_f = z_0 + 19 \mu\text{m}$ from the surface, where $z_0 \approx 30 \mu\text{m}$. Shot energy was 14 μJ (a). (b)-(f) side views of photo-modified regions aligned to the same height. Scale bars (b-f) are 10 μm . The length equivalent of 120 fs light pulse is 36 μm . The transmission of microscope with was 25%.

exceed few times the average at center of the pulse intensity envelope. The difference of the voxel shape in the case of $NA = 1.3$ (no filament formation) and $NA = 0.8$ (filament formation) fabrications we understand as originating from the different lateral light intensity gradient. In the case of more tightly focused irradiation, the dielectric breakdown is reached before the pulse is “shaped” by non-linear interaction. The free-carriers generated at the damage point defocus the pulse strongly enough that the secondary damage threshold is never reached.

The discussion in *Part II* deals with the light-material interaction in terms of free-carrier generation by an uniform illumination and subsequent their relaxation. The propagation of fs-pulses, which are spectrally broad (120 fs pulses at 800 nm we used for fabrication has spectral width of $FWHM = 10$ nm or in wavenumbers 150 cm^{-1}) in dispersive material is subjected to linear and nonlinear interaction with the mater and their spatial and time profiles (equally, the spectral pulse description can be considered) are changed. Group velocity dispersion (GVD), the linear interaction, which is independent on the light intensity, I , leads to the fs-pulse time/spectral spreading (here, we consider normal dispersion as in silica with $g = \frac{d^2k}{d\omega} \Big|_{\omega_0} < 0$). The main nonlinear interactions, which affect the pulse’s spatial and temporal shape are self-phase

modulation (SPM) and self-focusing, which can be considered as longitudinal and transverse Kerr effects (related to $\chi^{(3)}$ non-linearity), respectively. These effects are proved to be applicable for silica, the material, in which the propagation of fs-pulses is explored theoretically^{16,3,15} and experimentally.^{3,15} It was demonstrated that GVD can prevent from a collapse of fs-pulses into a singularity due to self-focusing below certain intensity threshold.¹⁷ With the increase of the pulse intensity, however, the non-linear effects leads to the pulse splitting. SPM and self-focusing alone or together with shock terms and Raman non-linearity causes splitting of the pulse into two¹⁵ or more pulselets.¹⁸ The pulse intensities for which the calculations were done are smaller than those obtainable under microscope focusing used in microfabrication. Fig 4.3 shows the patterns of microstructuring of silica by a single shots of $2.0\text{-}6.8 \times 10^{15} \text{ W/cm}^2$ intensity. The dotted filament seen in the transmission side-view, most probably, reflects the intensity profile of non-linearly modified, splitted, fs-pulse. This intensity profile is responsible for the free-carriers generation and their heating. In some locations, the intensity is higher than the threshold of damage. Eventually, after the pulse is passed, the light energy coupled into the electronic sub-system is released locally to the lattice creating the damage pattern. The side-views obtained this way can be considered as a snapshot of a fs-pulse. However, the multiple foci formation can be caused by other processes as saturation of non-linear refractive index,¹³ absorption, and free-carrier generation. Future theoretical and experimental work should answer these questions. The aberrations, if any, are adding spatial modulation of the intensity envelope, e.g. chromatic aberration acts as a

GVD increase (here we are not taking into account any aberrations since the objective lenses were aberration corrected and a nonlinear propagation of the light inside the objective can be excluded from a consideration as negligible due to the low intensity of the unfocused light).

Microstructuring of materials by the writing filament structures could be applied for 2D PhC formation. The photo-induced refractive index modulation can be written with superior spatial resolution (Fig. 4.3(a)) than that made by microexplosion. Fast and local (smaller than diffraction limit), Kerr's nonlinearity-driven response of materials is promising for high density data storage systems such as super-resolution near-field structures (super-RENS),¹⁹ where a thin, 10-20 nm photosensitive layer is optically "opened" (rendered transparent) for the writing into a deeper recording layer.

4.1.2. Three-dimensional optical memory

Rewritable 3D optical memory was first demonstrated in polymer matrix doped by photochromic spirobenzopyran dye.²⁰ Such a recording is an alternative way to extend a two-dimensional storage density without the usage of more sophisticated methods of near-field optics.²¹ Current technology of digital versatile disk (DVD standard of 1996) with the storage capacity of 4.7 Gbytes (60.7 Mbytes/cm²) can be increased up to 15 Gbytes per disk by the employment of GaN/InGaN based laser operating at 400 nm (this can be considered as a limit for such memory). By now, 3D patterns are fabricated in photochromic^{22,23,24}, photorefractive^{25,26} materials and photopolymers.^{27,28} The glass materials attracted attention as a matrix of read-only 3D memory due to the superior mechanical properties as compared with those of polymers and due to recording durability as it was shown in case of v-SiO₂.^{29,30,11} The high signal-to-noise ratio read-out, $S/N = 20 \log((T_{MAX} - T_{MIN}) / (T_{MAX} + T_{MIN})) > -3.5$ dB,¹¹ is possible in transmission, T , of a particular bit plane, which is in the focus (Fig. 4.4). An example of 0.1 Tbytes/cm³ memory fabricated by fs-irradiation is presented in Fig. 4.4(c). Such a high recording density can not be achieved with ps-pulses due to higher "frozen-in" stress, which eventually is released in a crack formation after (or during) the fabrication.

We found that 3D pattern of optical memory can be readout by its photoluminescence (PL) image as well, and that defect-related PL can be erased by an annealing for 30 min at comparably moderate 400°C temperature (the temperature of silica softening is about 1300 K).³¹ This makes possible two-bit data storage per single bit if PL and transmission readouts are employed. The PL of optically damaged regions of silica originates from the defects introduced by fabrication.³² The absorption band of oxygen vacancy, V_O, at 4.96 eV (250 nm) is apparent in the absorption spectra of photo-modified silica (Fig. 4.5(a)) and it was found responsible for PL at 280 nm, 470 nm, 650 nm and, in some silica, at 560 nm.¹² Weak absorption at 210-220 nm is due to E' center ($\equiv \text{Si}\bullet$, where \bullet and \bullet denotes bond and unpaired electron, respectively), which is non-radiative recombination center as the most of paramagnetic defects and gives no PL. Defect-related PL is usually too weak for practical applications due to low quantum efficiency $\eta_L = r_R / (r_R + r_{NR}) < 10^{-6}$, where $r_{R,NR}$ are the radiative and non-radiative transition rate, respectively. However, the concentration of the defects created locally near the focal point is very high (over 10^{18} cm⁻³), what, actually, allowed to succeed in PL readout of 3D memory. The concentration of the defects, N_{def} , can be evaluated from the absorption by Smakula's formula (supposed, the density is small enough to neglect their interaction):³³

$$N_{def} f \cong 1.3 \times 10^{17} \alpha_{def}^{MAX} \Delta E \quad (4.1)$$

, where α_{def}^{MAX} [cm⁻¹] is the absorption coefficient at its maximum and ΔE [eV] is the absorption line width. Oscillator strength of deep centers f is on the order 0.1-1 (for neutral oxygen vacancy in Ge-doped silica $f = 0.4$ is reported³⁴). The real optically damaged volume can be evaluated from the fabrication pattern and by the evaluation of bit size in microscope. In the case of data on Fig. 4.5(a), the diameter of photo-altered region was $d = 1$ μm and the in-plane separation of the bits was 5 by 3 μm . This allows to calculate the absorption coefficient of V_O defect (Fig. 4.5), which was induced by irradiation

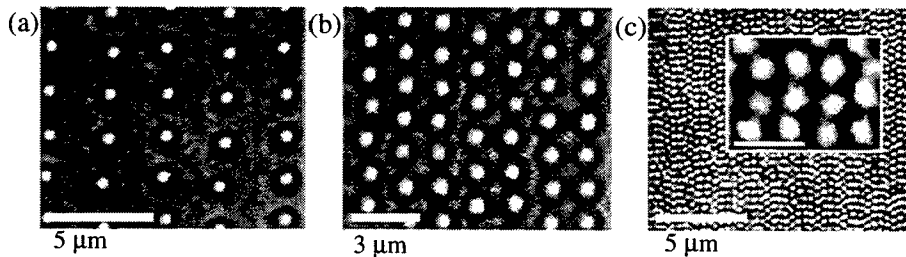


Fig. 4.4. The images of a single plane-XY from the 3D optical memory stacks. Voxel spacings XYZ are: 2.5, 2.5, 4.0 μm (a), 1.5, 1.5, 5.0 μm (b) with corresponding data storage densities 40 Gbit/cm³ and 88 Gbit/cm³, respectively. (c) An example of the 3D memory with density of ca. 0.8 Tbit/cm³ (volume occupied per bit $0.6 \times 0.6 \times 3.5$ μm^3). Scale bar of the zoomed-in area in the inset of (c) is 1 μm . Fabrication and memory read-out was made by the same $NA = 1.3$ objective. Fabrication wavelength was 800 nm.

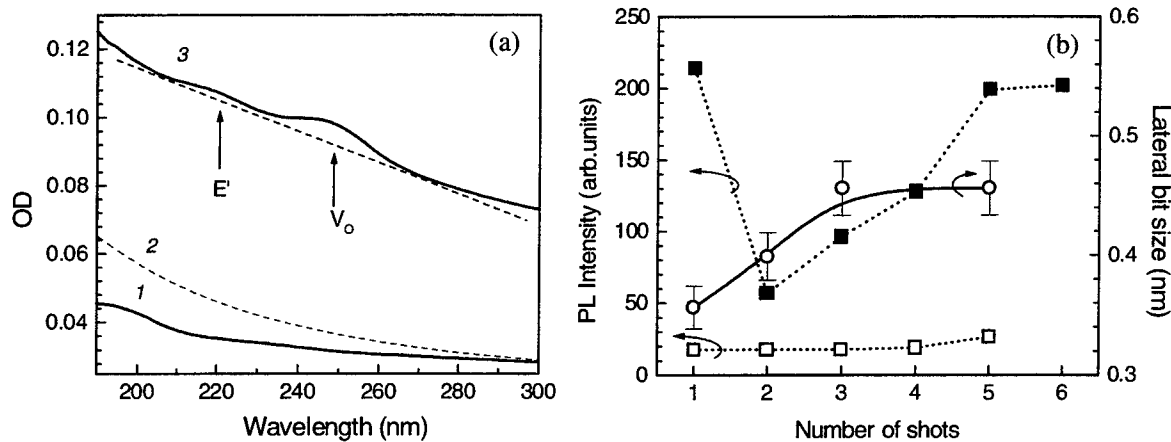


Fig. 4.5. Rewritable defect-related photoluminescence in silica. (a) The absorption spectra of silica before (1) and after (3) optical damaging by 800 nm irradiation (single-shot per bit). Line 2 shows functional dependence $(1/\lambda)^4$ of Rayleigh scattering. The absorption positions of E' center and oxygen vacancy, V_O, are marked. (b) PL intensity vs. the number of re-writing cycles. PL was excited by 120 fs pulses at 400 nm wavelength (82 MHz repetition rate) and registered in a 500 – 700 nm spectral window. PL intensity vs. the number of rewriting laser shots of 120 fs at 800 nm. PL was thermally erased by keeping the sample at 500°C for 1h. PL intensity is background corrected. The dependence of the bit's lateral size (right axis) vs. the number of shots of the energy 250 nJ (LIDT = 77 nJ).

$\alpha_{def}^{MAX} \cong 1.99 \times 10^3 \text{ cm}^{-1}$ ($\alpha_{def}^{MAX} d = A \times \ln(10) OD$, where the factor $A \approx 14.4$ accounts for the optically damaged volume and $OD = 6 \times 10^{-3}$ is the optical density at 250 nm corrected for Rayleigh scattering). Then the density of V_O can be evaluated from eq. 4.1 by substitution $\Delta E = 0.4 \text{ eV}$ and $f = 0.4$. We obtain $N_{def} = 2.59 \times 10^{20} \text{ cm}^{-3}$. This calculation was done without consideration of the void inside the bit, what even would increase already large value of N_{def} . The mechanism of the defect formation under fs-irradiation is expected to have new features, such as the excitation of the inner shell electrons. This mechanisms was recently demonstrated in proton irradiated silica, where the non-radiative decay of self-trapped bi-excitons by Auger recombination is creating Frenkel pairs of the defects by O 2s electron-shell ionization.³⁵ It is conceivable, that similar mechanism of the defect generation can be realized by fs-pulses. We have already demonstrated³² that the same defects as those induced by particle or X-, γ -ray irradiation can be created by fs-pulses in silica as well.

The experimental data on the writing-erasing cycles in silica are shown in Fig. 4.5(b). The PL measured out of a single bit was erased by an annealing at 500°C for 1 h, then once more irradiated at the same, high, fabrication intensity at 800 nm. PL was excited by irradiation of 400 nm, 120 fs pulses with the single pulse energy of ca. 10^6 times lower than that of fabrication.³¹ The bit already written acts as a scattering point for the every next writing cycle and the microexplosion conditions are much different. Thus, the subsequent writing-erasing cycles shows an increase of PL, which is, most probably, related to the bit's enlargement (Fig. 4.5(b)). Nevertheless, this principle hides a promise for the defect engineering by fs-irradiation and could find its way into the applications such as re-writable optical memory, especially in the glasses doped by the elements responsible for color centers formation.

4.1.3. Gratings and photonic crystals

When the voxels are 3D-ordered as single bits or lines (in-line overlapping bits) the formation of 3D and 2D PhC is expected. Quasi-1D PhC, a grating, most easily can be fabricated (Fig. 4.6). The grating allows to evaluate the refractive index change, which is one of the most important parameters for the full band-gap PhC formation. For the sinusoidal transmission modulation, the diffraction efficiency in the first diffraction order is $\eta_1 \propto |\Delta \tilde{n}|^2$, where the complex refractive index $\Delta \tilde{n} = \Delta n + i \Delta k$ is expressed in terms of the changes its real part, Δn , and extinction coefficient, Δk , which, in turn, is related to the modulation of the absorption coefficient, $\Delta \alpha$, by $\Delta k = \Delta \alpha \cdot c / (2\omega)$. Formally, the total light intensity losses due to the absorption and scattering can be combined by $\Delta \alpha = \Delta \alpha_{abs} + \Delta \alpha_{sc}$. The prediction of high refractive index modulation, $\Delta n > 10^{-2}$, from the diffraction patterns of fs-fabricated silica^{30,36} can be, however, incorrect provided the scattering and absorption are strong. This is usually the case for the fs-fabrication as can be seen in Fig. 4.5(a), where the Rayleigh scattering contributes considerably to the observed absorption (even at 800 nm the light losses due to scattering alone comprises 49% of the overall OD when fabrication was made by 3.5 LIDT at 800 nm). Thus, the pure refractive index changes measured by diffraction are expected to be smaller according to the separate contributions of the phase (refractive

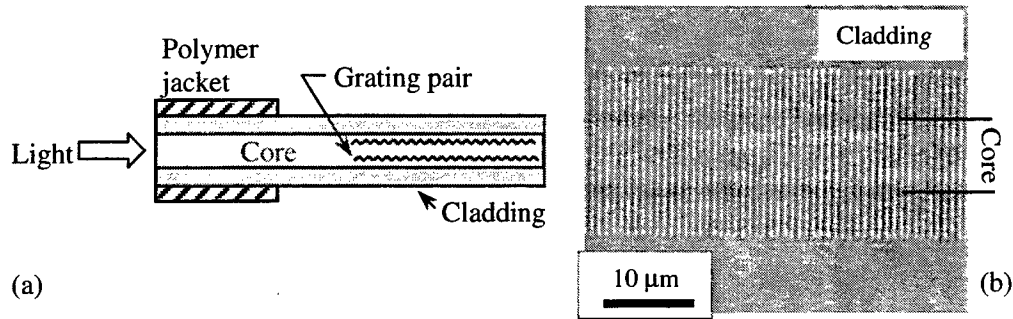


Fig. 4.6. Grating, a quasi-1D PhC structure, made in optical fiber. (a) Scheme of a device. (b) An image of the one of two gratings.

index) and the amplitude (absorption and scattering) gratings:³⁷

$$\eta_i = \left(\frac{\pi \Delta n d}{\lambda} \right)^2 + \left(\frac{\Delta k d}{4} \right)^2 \quad (4.2)$$

The light absorption and scattering can decrease transmission of PhC in the region of photonic bandgap as well. For this reason the fabrication and post-fabrication treatment of the sample needs to be optimized, e.g. annealing should be considered, to increase the performance of fs-fabricated gratings and PhC by reducing scattering and defect-related absorption. Indeed, the waveguides fabricated by scanning a focal point of fs-pulsed irradiation in glasses³⁸ showed $\Delta n \approx 10^{-2}$, but the fabrication procedure was multi-shot irradiation which acts as annealing. Also, the attenuation, which arises due to absorption and scattering has not been measured,³⁸ although the results were obtained on short, 15 mm, propagation length.

PhC can be constructed by packing the microexploded holes, “atoms,” into 3D lattice (Fig. 4.7(a)).³⁹ Intuitively the holes resembled the atoms in Thomson atom model, and therefore we call these structures inlaid-“atom”-like PhCs, which were made by positioning and translating the focal point of the laser irradiation inside silica. Each “atom” was written in a single laser shot. By using a $NA = 1.35$ objective lens near-spherical voids were obtained and the high reproducibility of their shape was favored by the stability of the laser pulse output. Since the microexplosion occurs only at the focal point where MPA is taking place, the voids can be spatially arranged freely. Different photonic lattices were realized just by varying computer-aided design program. As an example, one (111) plane of face centered cubic (fcc) lattice is shown in (Fig. 4.7(a)). The entire crystal was created through a layer-by-layer stacking of (111) planes.

To testify photonic bandgap effect, a transmission spectrum was measured with a Fourier transform infrared (FTIR) spectrometer (Fig. 4.7(b)). The minimum of transmittance occurred at 3490 cm^{-1} . The change of the lattice constant caused an according variation of the wavelength of the transmission dip as predicted by Bragg law, showing that the dip is indeed from the photonic band gap effect. A transmission spectrum was calculated by the full-vector analysis (transfer matrix technique)⁴⁰ to reproduce the experimental dip wavelength of 2.87 μm (3490 cm^{-1}), with the void radius r and the difference in the refractive index, Δn , as fitting parameters. As a result, $d = 250 \text{ nm}$ and $\Delta n = 0.45$ gave a good agreement between the measured and calculated dips. The value of d measured by AFM is larger than 250 nm used in calculations. The lateral size

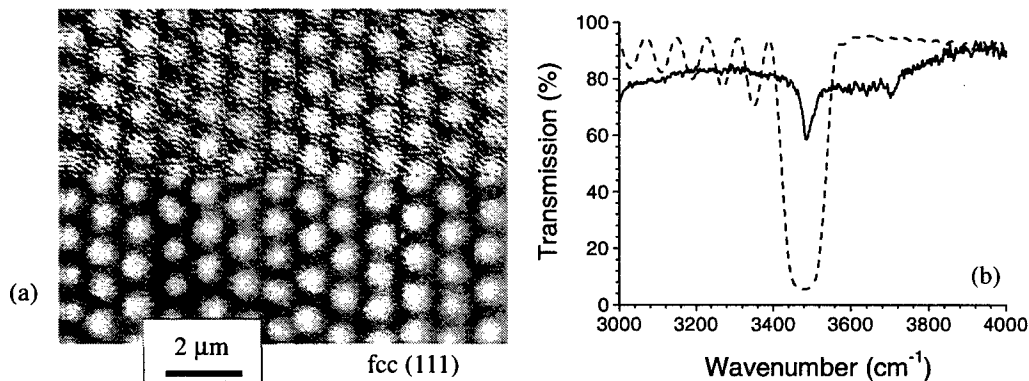


Fig. 4.7. fcc PhC structure. (a) optical microscopic image of a (111) PhC plane (upper half is shown using shadowing), and (b) simulated (dashed line) and measured by FTIR (solid) transmission spectra. Fabrication was made by irradiation with singles pulses of the energy 2.5JLDIT at 800 nm wavelength.

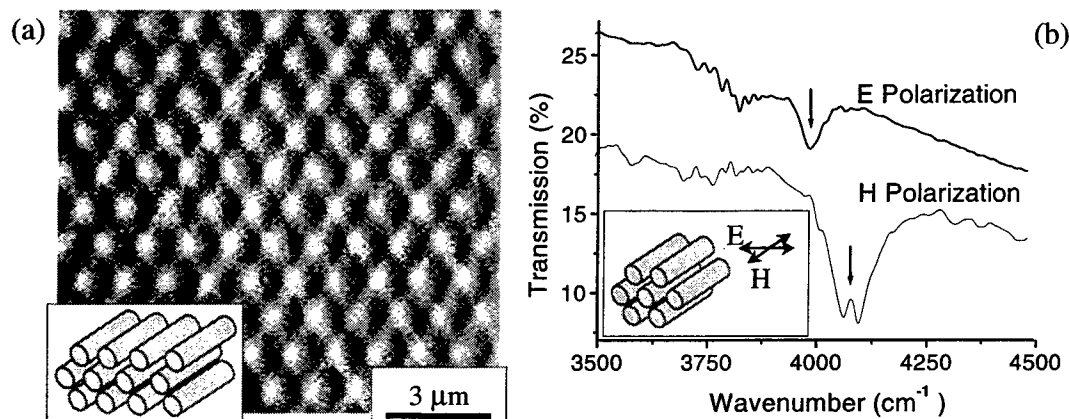


Fig.4.8. 2D triangular PhC lattice. (a) cross-sectional image with the rod alignment scheme in the inset and (b) FTIR transmission spectra. Fabrication was made by irradiation with singles pulses of the energy 2.5LIDT at 800 nm wavelength.

of the voxel might be altered by polishing and, also, the measurement by AFM must be de-convoluted from the tip's profile, which is not known; that is why we haven't fixed d in the simulation to the value measured by AFM.

By stacking the grating planes various 2D and 3D photonic lattices consisting of cylinders can be acquired. A direct application to 3D PhC is, layer-by-layer structure, in which adjacent layer is turned by a fixed angle, e.g. 90° , and the nearest layers with the same orientation are made with the half period offset. 2D triangular lattice (Fig. 4.8(a)) has the best geometry for achieving a full in-plane band gap for both E- (electric field parallel to the cylinder axis) and H-(magnetic field parallel to the cylinder axis) polarizations as have been shown theoretically⁴¹ and experimentally.⁴²

The cylinders were confirmed to be hollow by an AFM measurement. The fabricated structure was observed using optical microscope from the top and the side. For the side viewing, the glass plate was broken and end facet polished (Fig. 4.8(a)). The lattice constant was $1.2 \mu\text{m}$ and the lateral (XY) size of fabrication was $40 \times 40 \mu\text{m}^2$ (defined by PZT working distance). Typical transmission spectra of these PhC structures for both polarizations are shown in Fig. 4.8(b). The spectra were normalized to the transmission of randomly irradiated samples. Approximately 10% transmission dip for H-polarization occurred at a wavenumber of 4100 cm^{-1} , while that for E-polarization was less pronounced and located at 4000 cm^{-1} . A perfect air rod structure with refractive index difference of 1.45 (air-silica refractive index difference) should permit a full bandgap, i.e., light propagation is forbidden in all direction (in-plane for the 2D periodic lattice) if a sufficient filling ratio was offered. The filling ratio, f , is the percentage of the total volume which is occupied by a dielectric and, in the case of rigid dielectric rods LBL PhCs, is expressed as $f = \pi r^2 / a^2$, where r and a are the radius and in-plane pitch of the rods, respectively. However, the diameter of the cylinder was smaller than necessary, while reducing the line spacing or increasing the rod diameter (by increasing the laser power) would lead to a distortion of cylinders. What is noteworthy is that the band gap effects for H-polarization was always observed to be stronger than those for E-pol. This showed that H-pol. (or TE modes) was favored in a lattice of isolated low- n regions, consistent with the theoretical expectation.⁴³ The existence of an uncoupled mode,⁴⁴ which cannot be excited by an external plane in the cases of both 2D and 3D PhC should not be neglected. It means that the transmittance does not necessarily properly reflect the photonic state density. The

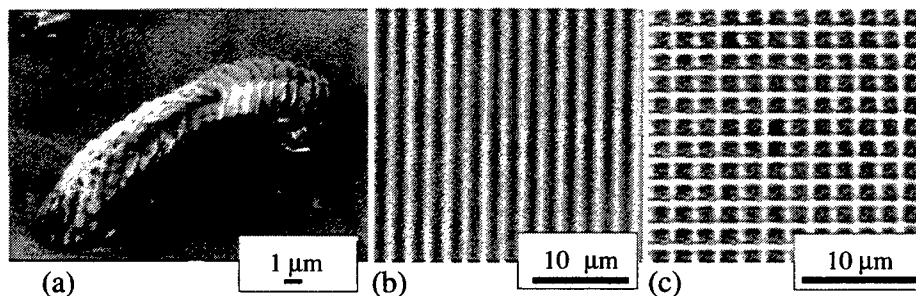


Fig. 4.9. Microfabrication in resins by fs-pulses. (a) SEM image of 3D fabrication by TPA at 400 nm in *Nopcore 800* (magnification $\times 5000$ at 5kV). (b) The grating fabricated by MPA in polymer (*NOA 60* resin), a quasi-1D photonic crystal structure, and (c) the planar mesh structure, a quasi-2D photonic crystal made in the same resin.

measured opaque region can be either from a band gap or an uncoupled mode. In both cases the transmission attenuation is closely relevant to the periodicity of the structures.

4.2. Laser fabrication in resin

In the current work, two 3.1 eV (400 nm) photons from the focused fs-laser were simultaneously absorbed by initiator molecules to start the photochemical reaction that is normally driven by one-photon absorption using the ultraviolet light. The two-photon absorption was enabled by an extremely high transient photon flux density, approximately at a level of $10^{32}/\text{cm}^2\text{s}$. Because of the quadratic dependence of photopolymerization rate on the photon flux density, solidification was confined to occur at a smaller region at the focal point comparing with the linear absorption, while the out-of-focus region was passed by the 400 nm laser light without absorption. The spatial resolution smaller than the laser diffraction limit can be achieved. This is one of the advantages of multiphoton excitation as was discussed in *Part II*.

4.2.1. 3-D structures and photonic crystals by photopolymerization

The examples of photopolymerization Figs. 4.9-10 demonstrate 3D structure and 1-2-3D PhC fabrication in resin.⁴⁵ Layer-by-layer (LBL) structure (Fig. 4.10(a)) has a symmetry of face centered tetragonal, fct (Fig. 4.10(b)). When $c/a = \sqrt{2}$, the lattice can be derived from fcc unit cell with a basis of two rods. For the laser fabrication, commonly, we have $c > a > 2r$. Scanning electron microscopy (SEM) image of the cross section of the orthogonal-plane LBL structure is shown in Fig. 4.10(c). The samples for SEM were fabricated by breaking the structures, at low temperature, and then coating with a-few-nm-thick Au film. The SEM image showed that a well defined 3D spatial structure had been achieved - the rods were

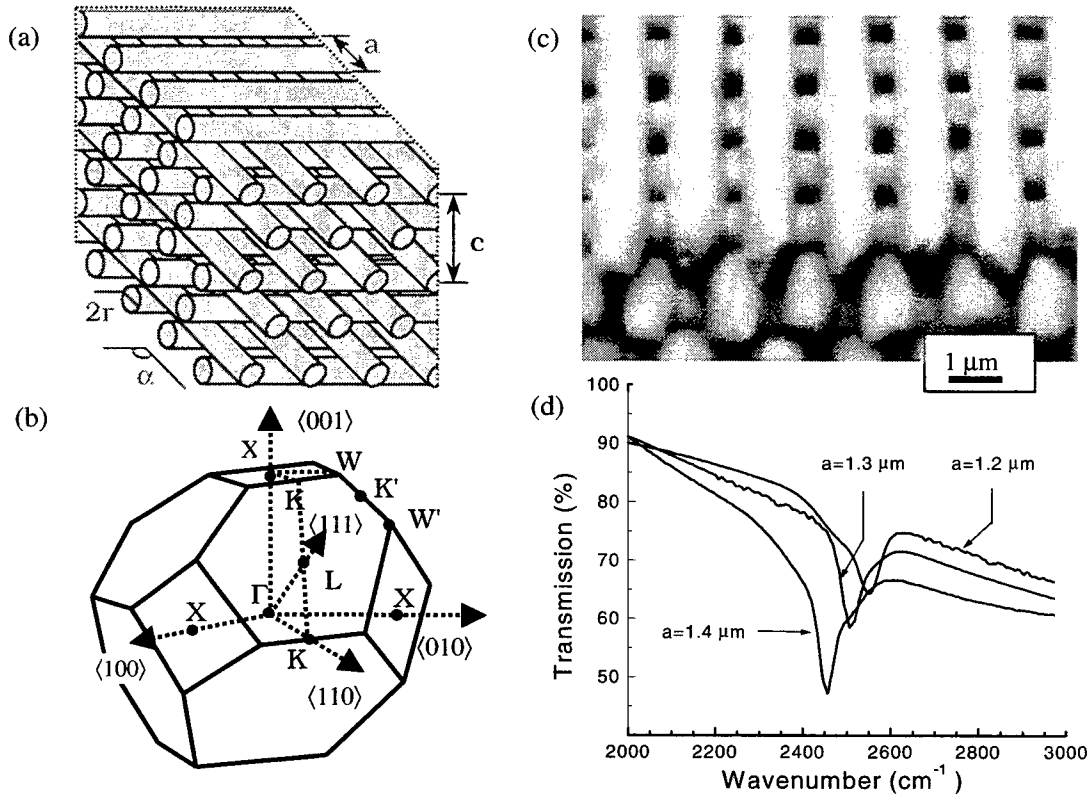


Fig. 4.10. Layer-by-layer PhC lattice. (a) schematic spatial structure, where a , c , r denote in-plane rod pitch, lattice constant, and rod diameter, respectively, and α is the angle between the neighboring planes. (b) first Brillouin zone of this lattice. The major symmetrical points and axis are specified. (c) SEM image of the cross section of PhC fabricated by TPA in resin and (d) its transmission spectra for different period a measured by FTIR. Fabrication laser pulse energy was 90 nJ/pulse. The rod diameter was approximately 1 μm .

arrayed regularly in the same plane half a period offset between the nearest layers of the same orientation. Plotted in Fig. 4.10(d) are the transmission spectra of 20-layer structures with different in-plane rod pitch: $a = 1.2, 1.3$, and $1.4 \mu\text{m}$ (N_2 was flowed through the entire light path to suppress the disturbance from the absorption by H_2O and CO_2 during FTIR measurements). The spectra had been normalized by the transmission of the uniformly solidified bulk resin. The transmittance dips under the normal incidence were at wavenumbers of 2550, 2510, and 2450 cm^{-1} for $a = 1.2, 1.3$, and $1.4 \mu\text{m}$, respectively. The corresponding wavelengths were located inside the transparency window of the resin. An increase in the wavelength of transmission dip versus lattice constant was interpreted by the fact that frequency scales as $1/n$ in a medium of refractive index, n . The mean dielectric constant increased with filling ratio of resin, which accordingly depends on the lattice constant. A depth of the dip increased with an increasing lattice constant, it was very possibly related with the completeness of developing, i.e., the larger the pitch between rods, the better the unsolidified resin was resolved.

5. CONCLUSIONS AND OUTLINE

The fs-laser microfabrication is a promising technique to apply where the high spatial resolution of photomodification are required and could find its way in the fields of optical memory (3D and super-RENS) and photonic crystals. This technique satisfies the requirements for an accomplishment of strong photonic bandgap effect, which is controlled by dielectric contrast, filling ratio and lattice type. A light-curling materials with a large index of refraction, $n > 2$, are necessary to maximize the dielectric contrast. Filling ratio of PhC can be continuously adjusted in the range of $0 < f < 1$. The unique merit of the laser microfabrication lies in the versatility of achievable spatial geometry. Only if the solidified structure can be self-supported, any lattices such as face-/body-centered cubic, simple cubic and diamond are obtainable. A natural and direct application of this technique is various layer-by-layer packings.

ACKNOWLEDGEMENTS

This work was supported in part by a Grant-in-Aid for Scientific Research (A)(2) from the Ministry of Education, Science Sports and Culture of Japan (No. 09355008), and by the Satellite Venture Business Laboratory of the University of Tokushima.

REFERENCES

1. R. W. Schoenlein, W. P. Leemans, A. H. Chin, P. Volfbeyn, T. E. Glover, P. Balling, M. Zolotarev, K.-J. Kim, S. Chattopadhyay, "Femtosecond X-ray pulses at 4\AA generated by 90° Thomson scattering: a tool for probing the structural dynamics of materials," *Science* **274**, pp.236-238, 1996.
2. C. W. Siders, A. Cavalleri, K. Sokolowski-Tinten, Cs. Toth, T. Guo, M. Kammler, M. Horn von Hoegen, K. R. Wilson, D. von der Linde and C. P. J. Barty, "Detection of nonthermal melting by ultrafast X-ray diffraction," *Science* **286**, pp.1340-1342, 1999.
3. A. A. Zozulia, S. A. Diddams, A. G. Van Engen, and T. S. Clement, "Propagation dynamics of intense femtosecond pulses: multiple splittings, coalescence and continuum generation," *Phys. Rev. Lett.* **82**, pp.1430-1433, 1999.
4. M. Bass ed., *Handbook of optics*. McGraw-Hill, Inc. New-York, 1995.
5. N. I. Koroteev, I. L. Shumai, *Physics of intense laser irradiation*. Nauka, Moscow, 1991. (In Russian).
6. P. Stampfli, K. H. Bennemann, "Time dependence of the laser-induced femtosecond lattice instability of Si and GaAs: role of longitudinal optical distortions," *Phys. Rev. B* **49**, pp.7299-7305 (1994).
7. B. C. Stuart, M. D. Feit, S. Herman, A. M. Rubenchik, B. W. Shore and M. D. Perry, "Nanosecond-to-femtosecond laser-induced breakdown in dielectrics," *Phys. Rev. B* **53**, pp.1749-1761, 1996.
8. B. C. Stuart, M. D. Feit, A. M. Rubenchik, B. W. Shore and M. D. Perry, "Laser-induced damage in dielectrics with nanosecond to subpicosecond pulses," *Phys. Rev. Lett.* **74**, pp.2248-2250, 1995.
9. A. Galeckas, J. Linnors, V. Grivickas, U. Lindelfelt, C. Hallin, "Auger recombination in 4H-SiC: unusual temperature behavior," *Appl. Phys. Lett.* **71**, pp.3269-3271, 1997.
10. M. Horiyama, H.-B. Sun, M. Miwa, S. Matsuo, and H. Misawa, "Three-dimensional microstructures created by laser microfabrication technology," *Jpn. J. Appl. Phys.* **38**, pp.L212-L215, 1999.
11. M. Watanabe, H.-B. Sun, S. Juodkazis, T. Takahashi, S. Matsuo, Y. Suzuki, J. Nishii, H. Misawa, "Three-dimensional optical data storage in vitreous silica," *Jpn. J. Appl. Phys.* **37**, pp.L1527-L1530, 1998.
12. S. Juodkazis, M. Watanabe, H.-B. Sun, S. Matsuo, J. Nishii and H. Misawa, "Optically induced defects in vitreous silica," *Appl. Surf. Sci.* **812**, 1999. In press.
13. J. H. Magdeburger, "Self-focusing: Theory," *Prog. Quant. Electron.* **4**, pp.35-110, 1975.
14. D. Ashkenasi, H. Varel, A. Rosenfeld, S. Henz, J. Herrmann, and E. E. B. Campbell, "Application of self-focusing of ps laser pulses for three-dimensional microstructuring of transparent materials," *Appl. Phys. Lett.* **72**, pp. 1442-1444, 1998.
15. A. A. Zozulya, S. A. Diddams, and T. S. Clement, "Investigations of nonlinear femtosecond pulse propagation with the inclusion of

- Raman shock, and third-order phase effects," *Phys. Rev. A* **58**, pp.3303-3310, 1998.
16. M. Trippenbach and Y. B. Band, "Dynamics of short-pulse splitting in dispersive nonlinear media," *Phys. Rev. A* **56**, pp. 4242-4253, 1997; "Effects of self-steepening and self-frequency shifting on short-pulse splitting in dispersive nonlinear media," *Phys. Rev. A* **57**, pp. 4791-4803, 1998.
 17. G. G. Luther, J. V. Moloney, A. C. Newell and E. M. Wright, "Self-focusing threshold in normally dispersive media," *Opt. Lett.* **19**, pp.862-864, 1994.
 18. J. K. Ranka, R. W. Schirmer, and A.L. Gaeta, "Observation of pulse splitting in nonlinear dispersive media," *Phys. Rev. Lett.* **77**, pp.3783-3786, 1996.
 19. J. Tominaga, T. Nakano, and N. Atoda, "An approach for recording and readout beyond the diffraction limit with an Sb thin film," *Appl. Phys. Lett.* **73**, pp.2078-2080, 1998.
 20. D. A. Parthenopoulos and P. M. Rentzepis, "Three-dimensional optical storage memory," *Science* **245**, pp.843-845, 1989.
 21. E. Betzig, J. K. Trautman, T. D. Harris, J. S. Weiner and R. L. Kostelak, "Breaking the diffraction barrier: optical microscopy on a nanometric scale," *Science* **251**, pp.1468-1470 (1991).
 22. M. Ishikawa, Y. Kawata, C. Egami, O. Sugihara, N. Okamoto, M. Tsuchimori and O. Watanabe, "Reflection-type confocal readout for multilayered optical memory," *Opt. Lett.* **23**, pp.1781-1783, 1998.
 23. A. Toriumi, S. Kawata and M. Gu, "Reflection confocal microscope readout system for three-dimensional photochromic optical data storage," *Opt. Lett.* **23**, pp.1924-1926, 1998.
 24. T. Tsujioka, M. Kume and M. Irie, "Super-low readout characteristics of photochromic memory," *Jpn. J. Appl. Phys.* **34**, pp.6439-6443, 1995.
 25. H. Ueki, Y. Kawata and S. Kawata, "Three-dimensional optical bit-memory recording and reading with a photorefractive crystal: analysis and experiment," *Appl. Opt.* **35**, pp.2457-2465, 1996.
 26. Y. Kawata, H. Ishitobi and S. Kawata, "Use of two-photon absorption in a photorefractive crystal for three-dimensional optical memory," *Opt. Lett.* **23**, pp.756-758, 1998.
 27. J. H. Strickler and W. W. Webb, "Three-dimensional optical data storage in refractive media by two-photon excitation," *Opt. Lett.* **16**, pp.1780-1782 (1991).
 28. H. E. Pudavar, M. P. Joshi, P. N. Prasad and B. A. Reinhardt, "High-density three-dimensional optical data storage in a stacked compact disk format with two-photon writing and single photon readout," *Appl. Phys. Lett.* **74**, pp.1338-1340 (1999).
 29. H. Misawa, Japanese patent application Nr.023614 (Feb. 1995); "3D storage technique," *Electronics Weekly* (UK), News page (May 31, 1995).
 30. E. N. Glezer and E. Mazur, "Ultrashot-laser driven microexplosions in transparent materials," *Appl. Phys. Lett.* **71**, pp.882-884, 1997.
 31. M. Watanabe, S. Juodkazis, H.-B. Sun, S. Matsuo, H. Misawa, M. Miwa, and R. Kaneko, "Transmission and photoluminescence images of three-dimensional memory in vitreous silica," *Appl. Phys. Lett.* **74**, pp.3957-3959, 1999.
 32. M. Watanabe, S. Juodkazis, H.-B. Sun, S. Matsuo and H. Misawa, "Luminescence and defect formation by visible and near-infrared irradiation of vitreous silica," *Phys. Rev. B* **60**, pp.9959-9964, 1999.
 33. Karl W. Böer, *Survey of Semiconductor physics*, Vol.1, Van Nostrand Reinhold, New York, 1990.
 34. H. Hosono, Y. Abe, D. L. Kinser, R. A. Weeks, K. Muta, and H. Kawazoe, "Nature and origin of the 5-eV band in SiO₂:GeO₂ glasses," *Phys. Rev. B* **46**, pp.11445-11451, 1992.
 35. N. Matsunami and H. Hosono, "Bi-self-trapped-exciton model for Frenkel defect formation in amorphous SiO₂ by proton irradiation," *Phys. Rev. B* **60**, pp.10616-10619, 1999.
 36. E. N. Glezer, M. Milosavljevic, L. Huang, R. J. Finalay, T.-H. Her, J. P. Calan, and E. Mazur, "Three-dimensional optical storage inside transparent materials," *Opt. Lett.* **21**, pp.2023-2025, 1996.
 37. H. J. Eichler, P. Gunter, and D. W. Pohl, *Laser induced gratings*, Springer, Berlin, 1986.
 38. K. Miura, J. Qiu, H. Inouye, and T. Mitsuyu, "Photowritten optical waveguides in various glasses with ultrashot pulse laser," *Appl. Phys. Lett.* **71**, pp. 3329-3331, 1997.
 39. H.-B. Sun, Y. Xu, S. Matsuo, and H. Misawa, "Micro-fabrication and characteristics of two-dimensional photonic crystal structures in vitreous silica," *Opt. Rev.* **6**, pp.396-398, 1999.
 40. J. B. Pendry, "Photonic band structures," *J. Mod. Opt.* **41**, pp.209-229, 1994.
 41. R. D. Meade, K. D. Brommer, A. M. Rappe, J. D. Joannopoulos, and O. L. Alerhand, "Photonic band states in periodic dielectrical materials," *Phys. Rev. B* **48**, pp.8434-8437, 1993.
 42. W. M. Robertson, G. Arjavalingam, R. D. Meade, K. D. Brommer, A. M. Rappe, and J. D. Joannopoulos, "Measurement of the photon dispersion relation in two-dimensional ordered dielectric arrays," *J. Opt. Soc. Am B* **10**, pp.322-327, 1993.
 43. E. Yablonovich, "Inhibited spontaneous emission in solid-state physics and electronics," *Phys. Rev. Lett.* **58**, pp.2059-2063, 1987.
 44. K. Sakoda, "Transmittance and Bragg reflectivity of two-dimensional photonic lattices," *Phys. Rev. B* **52**, pp. 8992-9002, 1995.
 45. H.-B. Sun, S. Matsuo, and H. Misawa, "Three-dimensional photonic crystal structures achieved with two-photon-absorption photopolymerization of resin," *Appl. Phys. Lett.* **74**, pp.786-788, 1998.

Laser Micromachining - New Developments and Applications

Nadeem Rizvi, David Milne, Phil Rumsby and Malcolm Gower

Exitech Limited
Hanborough Park, Long Hanborough, Oxford OX8 8LH, United Kingdom

ABSTRACT

Excimer laser micromachining has developed into a mature production method and many industrial applications such as the drilling of ink-jet printer nozzles, production of sensors and the manufacture of display panels now routinely use excimer laser microprocessing in production environments. The important concepts of excimer laser micromachining systems are described and the novel methods which have been developed in this area are presented. In particular, techniques for the production of complex, multi-level 3D microstructures are described and examples of such features are used to illustrate the relevant applications. Furthermore, some initial micromachining results from a sub-nanosecond, solid-state fibre laser are presented to highlight the rapidly-growing area of laser microprocessing using ultra-short pulse lasers.

Keywords: lasers, micromachining, excimer, ablation, MST devices, ultrashort pulses.

1. INTRODUCTION

Lasers have been in use in various industrial sectors such as the automotive and aerospace industries for many years performing cutting, welding and materials processing tasks [1]. More recently, there has been an upsurge in the micro-engineering applications of lasers where pulsed lasers, in particular, have played a major role in the development of numerous micro-systems technology (MST) areas. In some cases such as ink-jet printer nozzles, for example, the transfer of the production methods to laser-based systems has provided an improvement in the technical specification of the devices together with higher production yields as well [2]. In other fields (e.g. biomedical analysis "chips"), totally new forms of devices have been developed [3] as a result of the unique properties offered by laser micromachining techniques.

In general terms, the most important qualities provided by pulsed laser micromachining include:

- Good quality
- High resolution
- High precision
- High processing speeds
- Low thermal damage
- Excellent reproducibility
- Use with many materials
- High production yields
- Good tolerances
- Single-stage "dry" process
- High flexibility
- Economically attractive

Some or all of the above may be applicable at any one time but this is largely determined by the application, the choice of laser and the method of its use. One of the main attractions of laser microprocessing is that lasers offer great flexibility in the rapid prototyping and evaluation of different designs. Many different process routes can also be tried out with the same laser tool in a relatively short time so the developmental cycle is also much faster than with many conventional techniques.

Many different pulsed lasers have been used in micromachining trials world-wide and these have ranged in wavelength from the infra-red to the deep UV, in pulse duration from milliseconds to femtoseconds and in repetition rate from single pulses to many tens of kilohertz. The work described in this article concentrates on the use of UV excimer lasers since these have been at the forefront of many innovative developments in different applications areas. Some preliminary research on the use of a new type of solid-state laser is also presented since this may be of interest in some fields.

2. EXCIMER LASER MICROMACHINING

Excimer lasers are pulsed laser sources emitting in the ultra-violet (UV) region of the spectrum. They are relatively broadband sources and usually have a rectangular beam output of the order of $\sim 25\text{mm} \times \sim 10\text{mm}$. The beam divergence is usually $\sim 1\text{-}5\text{mrad}$ and it is different in the two orthogonal beam directions. Due to this relatively large and non-uniform beam divergence, and the fact that the beam has poor spatial coherence, the direct focussing of excimer lasers is generally unattractive. Hence, the technique of mask projection is commonly used in a large number of applications.

2.1 Mask Projection

The output beam from the excimer laser is not uniform and so usually some form of beam homogenisation is used to make a "flat-top" beam. This homogenisation is normally important since the ablated depth of the sample depends on the energy density of the beam at any point. A mask, which is used to define a shape or pattern which is required for the formation of the desired microstructures, is placed at the plane of optimum uniformity of the beam. It is then imaged onto the sample by appropriate high-resolution optics. The mask is typically either made from chrome-on-quartz or from a thin metal sheet.

In mask projection systems, the laser beam usually remains fixed and the mask and the workpiece can both be moved across it in a precisely controlled manner. The concept of mask projection is depicted in figure 1.

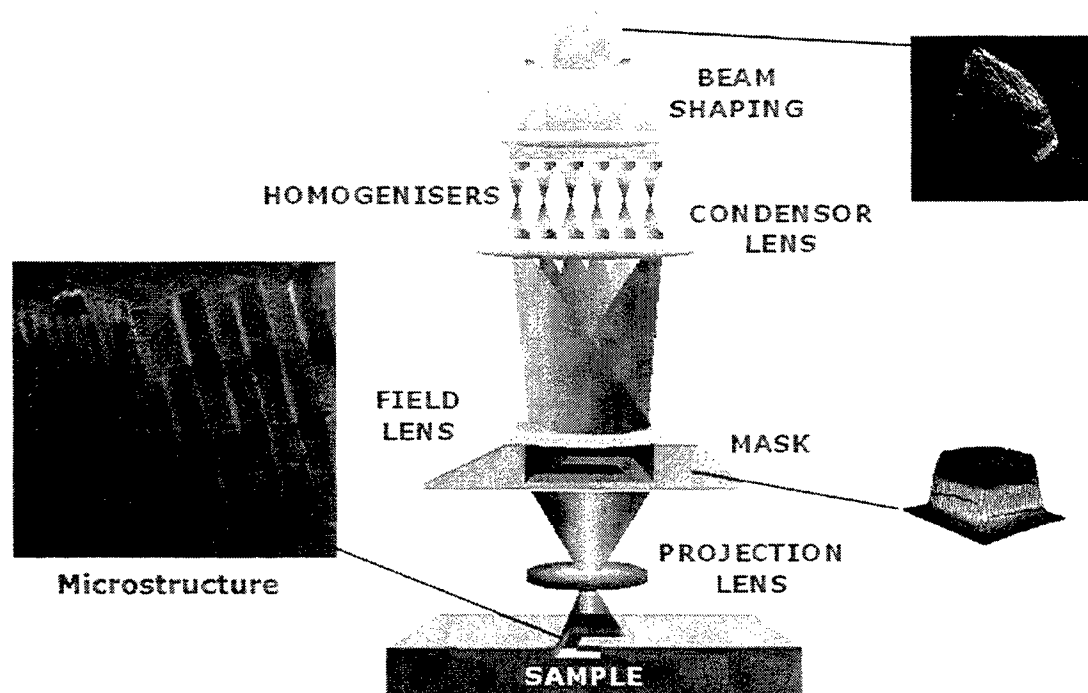


Figure 1. Representation of typical excimer laser mask projection system.

The mask projection method offers great flexibility and there are numerous features which can be utilised when considering micro-machining applications. These include:

- Mask dimensions

The projection lens usually de-magnifies the mask pattern onto the workpiece and so the features on the mask do not need to be as small as the micro-structures to be produced. Typically, de-magnifications of $\times 4$, $\times 10$ or $\times 30$ are used so the mask does not have to be made of ultra-high resolution features, thereby reducing its complexity and cost of manufacture.

- Mask Damage

Due to the de-magnification which is used, the energy density of the laser beam is much lower at the mask than at the sample. This reduces the risk of damage to the mask and increases the mask lifetime as well.

- Separation of Mask and Workpiece

Because the mask and workpiece are not in close proximity, the mask does not suffer from any debris or particulate damage from the sample ablation.

- Independent Control

Mask projection allows independent control of the motion of the mask and workpiece and this allows many different processing techniques to be used depending on the desired micro-engineering application.

- Resolution and Depth of Focus

The smallest feature resolution R which can be obtained is fundamentally governed by the projection lens being used and can be expressed as $R \propto k_1 \lambda / NA$, where λ is the laser wavelength and NA is the numerical aperture of the optical system and k_1 is a constant which depends on the sample material and processing conditions. The depth of focus (DoF) is similarly given by $DoF \propto k_2 \lambda / NA^2$ where k_2 is another optical/process-related constant.

Mask projection systems provide great flexibility in the range of micro-engineering tasks that can be performed with them - the same system can be used for the production of many diverse micro-structures for different applications.

2.2 Production of Microstructures

There are certain variables which can be adjusted in mask projection systems and the proper control of these parameters enables a variety of different effects to be accessed. The processing variables include the laser wavelength, the optical system design, the sample material, the laser energy density and repetition rate but the most important parameters in determining the *type* of micro-structure which can be produced are the positions and motion of the mask and sample during the firing of the laser. Therefore, the accurate control of the mask and the workpiece, together with precise synchronisation of these two elements to the laser pulses, is vital in the production of micro-machined structures.

2.2.1 Static Mask and Workpiece

Typical projection lenses have image field sizes which can range from hundreds of microns to many millimetres. Since the image is smaller than the mask by some factor (e.g. $\times 10$), the laser beam at the mask is usually up to tens of millimetres in size. If the structure to be produced is small and simple, or made-up of regular repeating patterns, then it is possible to use the technique of *static* mask projection, providing the basic "unit cell" of the pattern can be fully illuminated by the laser beam. This technique is most commonly applied in the production of holes - ink jet printer nozzles, for example - but any discrete feature can be produced. Figure 2 shows some 100 μ m diameter holes which have been drilled through a 50 μ m thick piece of ceramic.

There are two extensions of the basic process which can enhance the applicability of static projection. One involves the lateral motion of the sample in between the production of structures: the laser is fired with a static mask and workpiece to produce a structure; the laser is turned off; the sample is moved laterally in X or Y; the laser is fired again to produce the same structure again. By repeating this procedure, large areas can be covered with the same structure. This technique is called *step-and-repeat* processing.

The second extension of static projection involves the positioning of a new mask pattern in between production of the structures: the laser is fired with a static mask and workpiece to produce a structure; the laser is turned off; the mask is moved laterally to position another mask pattern under the laser beam; the laser is fired again over the same workpiece area to superimpose the new mask pattern over the previous one. This technique is called *indexed mask projection*.

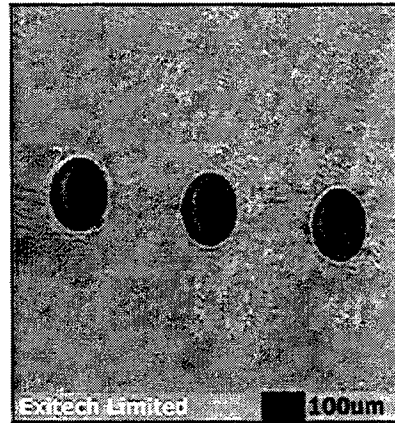


Figure 2. Holes drilled into a ceramic using an excimer laser.

These two methods can be considered extensions of the static projection technique since the mask and workpiece are stationary during the production of the micro-structures, even though the mask or workpiece are moved in between the processing steps. Examples of step-and-repeat and indexed mask projection are shown in figure 3.

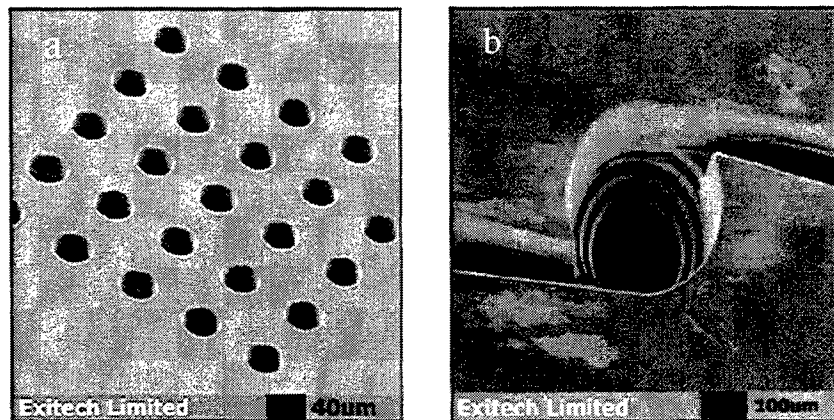


Figure 3. Micro-structures produced by (a) Step-and-repeat mask projection. (b) Indexed mask projection.

The holes shown in figure 3(a) were produced individually with the sample being moved in between each drilling step. Two points to note are the positioning accuracy of the holes (governed by the workpiece stages) and the reproducibility of the quality of the holes (determined mainly by the laser stability). Figure 3(b) shows a nozzle device where the central section contains a stepped structure leading down to a small hole. The steps inside the central well were produced by using different diameter apertures to define the different steps - a particular diameter circular section was machined to a specified depth, the mask changed for another one and the machining repeated for the new diameter and depth. In both cases, the sample material was polyester and a krypton fluoride (248nm) laser was used. Typical laser energy densities used for the structures in figure 3(a) and (b) were $\sim 300\text{mJ}/\text{cm}^2$.

Step-and repeat processing is now commonly used in applications such as the micro-drilling of ink-jet printer nozzle heads. In this case, the entire nozzle head (consisting of hundreds of holes) is drilled at the same time followed by the motion of the same to the next position for drilling. In industrial production of such nozzle plates, the sample is usually in the form of polyimide tape and the laser system automatically winds the tape, drills the holes and then winds the tape further. This tape handling has to be accomplished with high speed and precision to ensure that the tolerances in the nozzle diameters (typically $\pm 1\mu\text{m}$) are maintained and that the nozzles are also positioned correctly on the tape.

2.2.1 Moving Mask

If the mask is moved during the firing of the laser, then structures can be produced which have varying depth profiles, thereby introducing simple depth information into the features. This can be achieved by ensuring that an aperture moves across the laser beam in a precisely controlled manner during the laser firing – hence, the static workpiece is exposed to a continually-varying amount of energy across its exposed area which produces a depth gradient in the sample. This technique is also known as *mask dragging*.

Figure 4(a) shows an example of a simple linear ramp produced with this method in a polymer material. The relatively simple micro-structure shown in figure 4(a) can, of course, be elaborated upon for different applications, using the basic technique for the production of more complicated features. Examples of such features are shown in figures 4(b) and 4(c) where multiple ramped structures have been produced in a polymer – these have been produced by careful combination of mask aperture, mask motion, workpiece positioning and laser firing sequence.

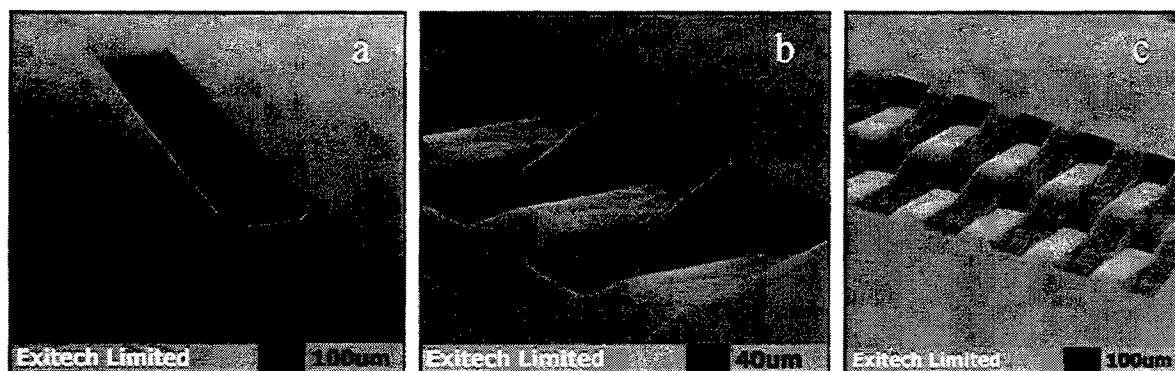


Figure 4. Linear ramps produced in PET at 248nm.

Some micro-optical- electro-mechanical-systems (MOEMS) applications require the referencing of two or more separate pieces with respect to each other and such positioning can be accomplished with the types of interlocking features shown in figure 4(b) and 4(c). Other areas, such as multi-functional sensor devices or multi-level micro-fluidic systems, often require the transfer of fluids from one area or plane to another. Such controlled guidance of fluids, for example, can also be achieved with these structures, particularly since other features such as nozzle holes can also be incorporated into these ramps or sloping channels.

2.2.2 Moving Workpiece

This is one of the most common extensions of the mask projection technique and involves the movement of only the sample during the laser firing. It is usually associated with the production of micro-channels or micro-grooves which may be used in various biomedical or optical applications. The concept of *workpiece dragging*, as this technique is also often called, involves using a static mask while moving the sample under the laser beam during firing. The laser processing conditions such as fluence and number of shots define the depth of the feature (as with all other mask projection methods) but the mask *shape* determines the depth profile of ablated structure. Therefore, the 2D layout of the channels can be defined by the motion of the workpiece and their cross-sectional profile by the mask shape – since these two aspects can be chosen independently, the technique allows a great deal of diversity in the details of the micro-structures which can be machined. Micro-channels of different cross-sections are shown in figure 5 where each of the cross-sections shown was produced using an appropriate mask (i.e. (a) triangle, (b) 'T' shape and (c) circle).

Figure 6 shows some micro-fins which have been produced using the workpiece dragging method for a gas pressure sensor application. These features were machined in a ceramic material as a demonstration for a prototype device using 248nm laser. All the fins were produced at the same time by using a mask with 5 rectangular slots in it.

The production of straight channels or grooves can be considered as workpiece dragging in one dimension (along the length of the channels). One of the reasons why workpiece dragging is an important technique is because it can be used for the production of controlled, multi-shaped 3D micro-structures. This is achieved by using workpiece dragging in two dimensions – making channels or shapes in two directions on the same sample. This can produce features such as pyramids, cones, pillars, lenses etc. and some typical pyramidal micro-structures produced with 2D workpiece dragging are shown in figure 7.

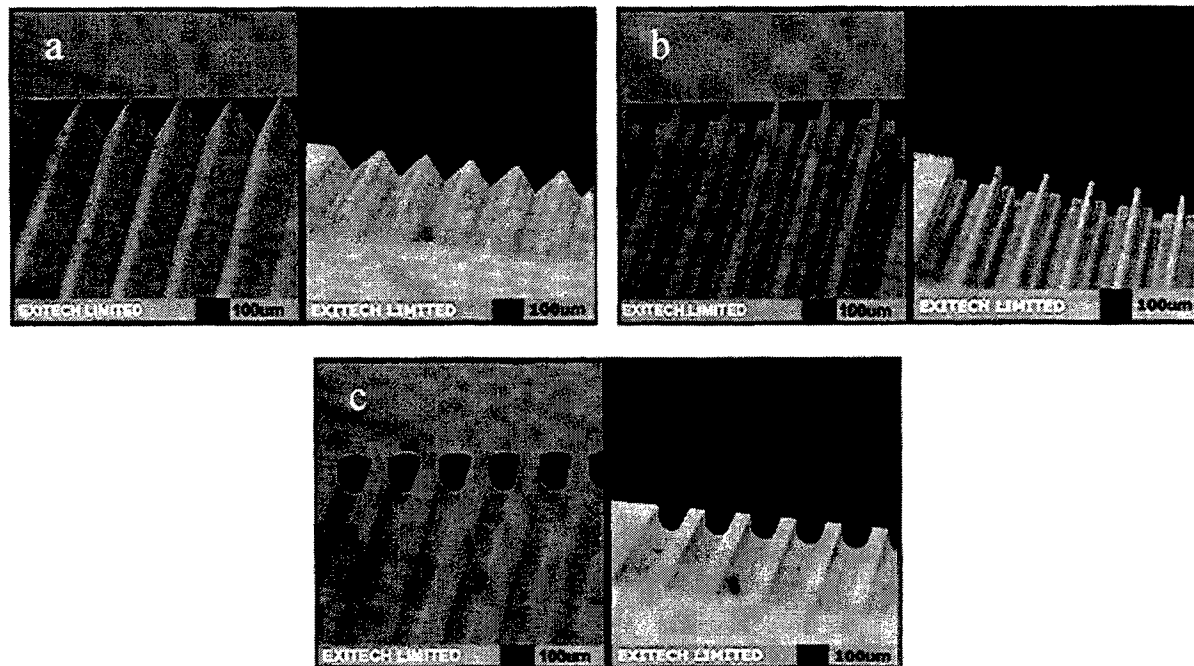


Figure 5. Shaped cross-section micro-channels produced using workpiece dragging technique.

Many applications require the types of structures shown in figure 7. These areas include optical technologies where light guidance or control is required for display panels and sources/detectors for micro-chip devices. The ability to micro-machine these structures directly onto the optical devices is a major factor in the development and viability of these systems. Such 3D pyramidal features can also act as anti-reflective (AR) structures for optical elements in the infra-red optical region where they mimic the response of multi-layer dielectric AR-coatings.

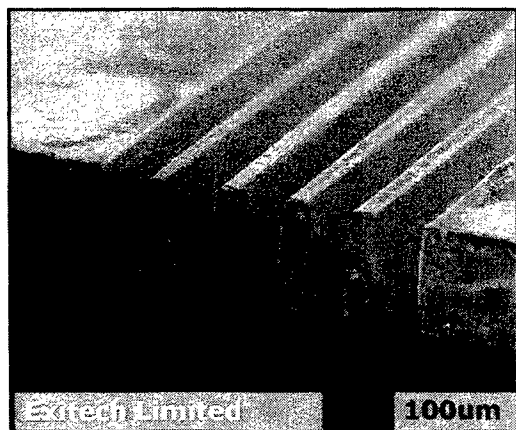


Figure 6. Micro-fins produced in ceramic at 248nm using workpiece dragging.

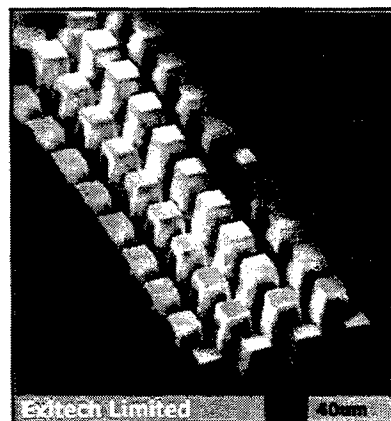


Figure 7. Microstructures produced in polymers using crossed workpiece dragging

The advantages of directly machining these AR structures on to the optics are that (i) they do not have any optical mismatch problems (since they are made of the same material), (ii) there is no issue of coating contamination or ageing and (iii) there is no damage constraint imposed by a coating. There are other interferometry-based methods by which these features can also be produced [4] but pulsed laser micro-machining can produce these structures directly in a single procedure.

2.2.3 Moving Mask and Workpiece

This technique is also referred to as *synchronised scanning* since both the mask and workpiece are moved in synchronism with each other during the machining process. Synchronised scanning is used where the pattern to be produced is large, non-repeating and cannot be produced by any of the three techniques detailed above. It has applications in printing (where the plates used to transfer the ink to the print medium can be laser-engraved), printed-circuit-board industries (for the definition of the electrode patterns) and display panels (for the electrodes), amongst other areas.

The motion of the mask and sample (which move at different speeds since there is a de-magnification involved) and the firing of the laser (taking the acceleration and deceleration of the stages into account) needs to be accomplished with high precision. If the pattern to be ablated requires a uniform depth, then care also has to be taken to fire the same number of laser shots over the entire sample.

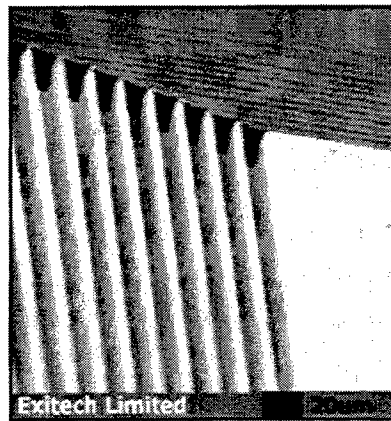


Figure 8. Pattern produced by synchronised scanning in polymer at 248nm.

Figure 8 shows an example of a micro-machined pattern produced in polyimide by synchronised scanning where the uniform depth of the ablation is apparent. The structure shown is part of a micro-coil device which is made from the polymer part produced by the laser system. Following the laser ablation, the sample can be metallised to form an inverse metal master from which multiple copies can be produced. This approach - known as *Laser LIGA* - is currently being pursued actively as it allows the mass reproduction of micro-products from a small number of high quality laser-produced masters.

The main disadvantage of synchronised scanning is that the entire pattern to be produced has to be contained on the mask. Otherwise, all the previously-listed benefits of laser micro-machining apply equally well to this method as well. It is usual with synchronised scanning to maintain the same depth in the micro-machined sample but another variation of this technique can also allow the depth to be varied across the sample. This is called *synchronised overlay scanning* and uses an element of workpiece dragging to add the depth information to the synchronised sample.

As was explained above, workpiece dragging uses the shape of the mask to define the cross-section of the micro-machined channels, i.e. the shape of the beam at the mask can be used to define the form of the machined depth. In synchronised overlay scanning, both the mask and the workpiece are scanned together as normal but, in addition, an aperture is introduced into the beam to shape the beam. The combination of the beam shaping and the scanning then gives the ability to pattern large, non-repeating patterns but with the added depth control offered by the beam shape. Figure 9 shows two

examples where micro-structures have been produced where the depth varies across the machined areas - (a) where one side of a set of triangles has a 45° slope and (b) where some micro-channels have been produced on a linear ramp.

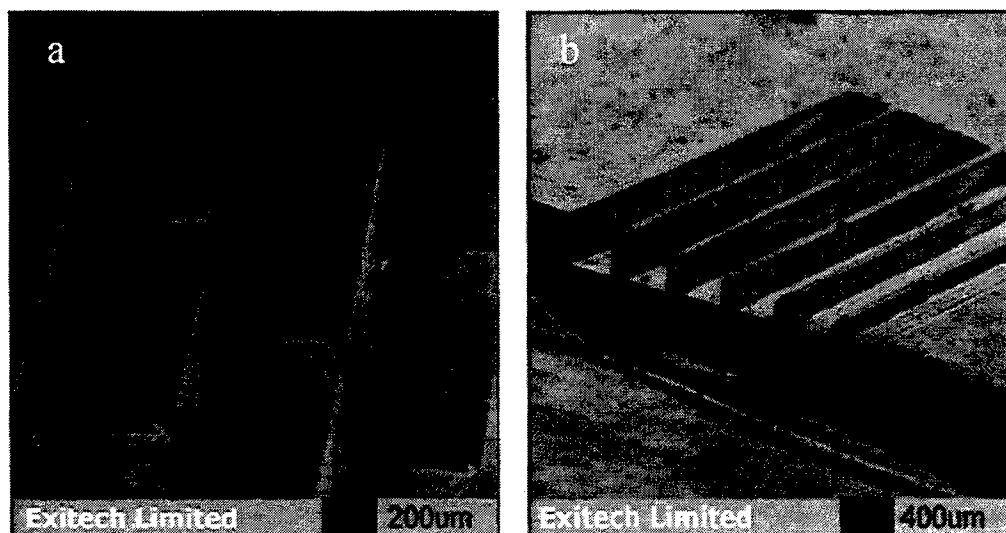


Figure 9. Microstructures produced by synchronised overlay scanning giving depth variation across the sample.

Synchronised overlay scanning also enlarges the areas where laser micro-machining techniques may be applied. Areas in fluid dynamical systems, for example, where parts in bearings and seals are required can be structured with special shapes for fluid flow requirements. Alternatively, various “chips” for bio-technology applications where multi-functional units need to be assembled on a single discrete package can incorporate different micro-features with varying depths.

2.3 Direct Writing using Mask Projection

Direct writing is a technique which is normally used with Nd:YAG or CO₂ lasers (which usually have good beam propagation characteristics) where the laser beam is focussed down to a small spot. The motion of either the laser beam or the sample (or sometimes both) is then used to produce the microstructures in the sample.

The two main advantages of direct writing are that:

- (i) it does not require a mask.
- (ii) the path to be machined can be fed directly into the control of the machining system (i.e. the laser system can be directly interfaced to the CAD generation of the pattern).

As was stated earlier, excimer lasers are generally not focussed directly but a mask projection system can be used in the manner of a direct writing tool if required. This is achieved by using a circular mask which defines a beam spot at the workpiece. By keeping this mask stationary, the system appears as a conventional direct write tool and design data can then be fed to the workpiece stages to control their motion across the laser beam. One big advantage that this method has over the conventional direct systems is that with the mask projection approach, changing the spot size of the beam is only a matter of changing the mask and does not involve changing lenses.

Figure 10 shows a demonstration of direct writing using a mask projection system where "Exitech" has been written in a polymer sample by moving it across a fixed excimer laser beam and figure 11 shows the use of this technique in a biomedical application where some micro-channels of different radii have been machine into a PET sample.

The use of direct writing using excimer laser mask projection systems is finding increasing use in the manufacture of complex structures in polymers for sensors and biomedical devices. This combines the benefits of excimer laser machining

of polymers with the advantages of direct writing of contoured paths where the use of masks to define the patterns is not attractive.



Figure 10. Direct writing using an excimer laser.

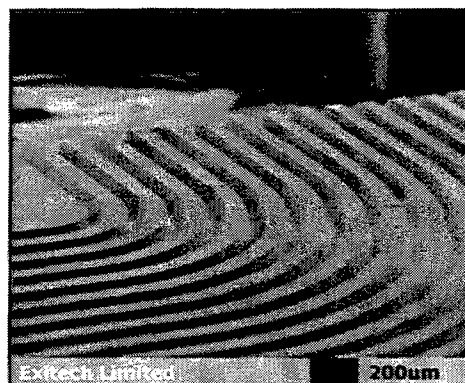


Figure 11. Production of micro-channels using excimer laser direct writing.

3. ULTRASHORT PULSE LASER MICROMACHINING

There has been intense interest recently in the use of ultrashort pulse lasers for various applications [5], especially in the use of femtosecond solid-state systems such as titanium sapphire lasers. Some of the areas which are already being researched include medical applications (e.g. eye surgery, medical imaging, cosmetic surgery), telecommunications, high-speed electronics and micromachining (e.g. printer nozzles, production of MEMS devices etc.) and the number of potential uses is growing rapidly [6]. Almost all of the work carried out so far in femtosecond micromachining has used amplified Ti:sapphire lasers where the pulse duration has been of the order of a few tens to a few hundreds of femtoseconds.

The main drawback of the titanium sapphire systems is that they are invariably bulky, relatively complex, expensive and often require some form of expert laser knowledge in obtaining optimum performance. Although major advances have been made in making these systems user-friendly, their uptake in industrial environments is still likely to be slow due to their perceived drawbacks, irrespective of whether these are real or not. There exists a real need for simple, compact lasers which can provide sufficient power to be useful in micro-processing applications and which can be integrated easily and reliably into industrial situations.

There exists a situation at present where laser micromachining is being performed with lasers with pulse durations in the nanosecond regime or longer (Nd:YAG or CO₂ lasers) and in the femtosecond regime (Ti:sapphire lasers). The former field is well-advanced and already at a mature level whereas the use of femtosecond pulses is gaining in importance. There has, however, been little work done on assessing the viability of lasers with pulse durations less than tens of nanoseconds but significantly above the femtosecond domain.

We have used a prototype Q-switched fibre laser which has been developed by IMRA America Inc. (Ann Arbor, Michigan, USA) to address some of the issues of laser micromachining. This laser - known as the *Picowatt laser* - operates at a wavelength of 1064nm and produces a linearly polarised output beam with a beam quality factor $M^2 < 1.2$. The laser produces an output pulse duration of 750ps and the maximum pulse repetition rate is 10kHz. Typical pulse energies are ~150µJ @ 1kHz and ~80µJ @ 10kHz which gives average powers of 150mW @ 1kHz and 800mW @ 10kHz. This laser, therefore, has peak powers of 200kW @ 1kHz and 106kW @ 10kHz. This peak power is, in fact, higher than most diode-pumped solid-state lasers available currently. The laser head is compact (approximately 21"x12"x4.5") and sealed with no external adjustments and the power supply (~21"x24"x12") plugs directly into a mains power point. The laser required no system warm-up and could be set-up ready for machining in a matter of minutes.

Using this IMRA prototype laser, we focussed the beam down to spot size of $\sim 15\mu\text{m}$ using a microscope objective ($\times 10$, 0.25NA) onto samples which were held on XY translation stages. The objective was mounted on an elevator stage to allow focal positioning to be accomplished and the stages were controlled via a CNC interface to allow programmed direct writing to be performed. A number of materials were machined to gain an overall qualitative picture of the effects of this *Picowatt* laser. These samples included borosilicate glass, stainless steel, silicon and CVD diamond.

The best results were obtained with the CVD diamond and the stainless steel samples. Figure 12 shows both sides of a CVD diamond wafer which was $\sim 100\mu\text{m}$ thick. The laser beam was trepanned over the sample in a square and circular fashion and the excellent quality of the cuts is clearly evident. Also, there appears to be no graphitisation of the surrounding areas as is often observed with the excimer laser or Nd:YAG laser cutting of diamond. The average cutting speed was $\sim 0.2\text{mm/sec}$ and so the holes shown in figure 12 only took a few seconds to cut out.

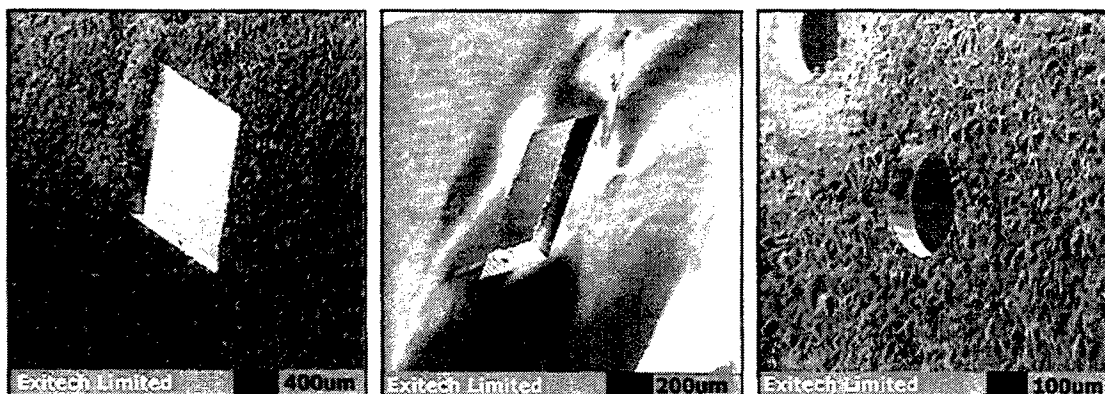


Figure 12. CVD diamond cut using a 750ps fibre laser.

As CVD diamond becomes available in larger sizes and with better quality, its unique set of properties is becoming more in demand for a range of uses such as optical components (laser optics, windows, lenses etc.) or thermal management devices for MEMS products. Laser microstructuring or smoothing can be achieved already with good results using excimer lasers but systems such as the Picowatt laser may offer an attractive alternative. These lasers appear to be effective in the machining of CVD diamond and this, combined with the small size, efficiency, running costs and ease of use, may make this type of laser extremely useful for these applications.

Similar cutting was tried with the stainless steel samples which were $50\text{--}75\mu\text{m}$ thick and a typical cut hole is shown in figure 13. The sample was trepanned under the laser using a stage speed of 10mm/sec and the total time taken to cut out the hole was ~ 12 seconds. The laser was used at 10kHz for both the diamond and the steel.

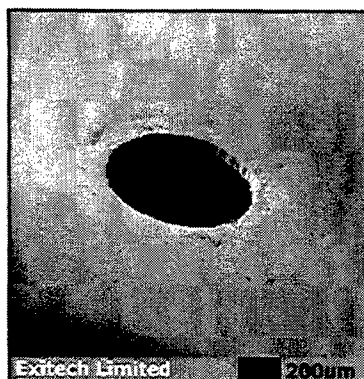


Figure 13. A thin sheet of stainless steel machined with a short pulse laser.

The results with the glass samples showed a lot of damage in the interaction sites and it seems clear that the peak intensity of the Picowatt laser is insufficient to machine glass cleanly. The silicon machined well for a certain depth but the ablation appeared to be self-limiting. This effect needs to be investigated further.

More quantitative work still needs to be done on different materials to measure the effects (e.g. etch rates, smoothness, debris issues) of these types of lasers and this work will continue in tandem with the development of the laser sources.

4. SUMMARY

The use of excimer lasers for the production of different multi-dimensional micro-structures has been described in detail with particular emphasis on the flexibility offered by mask projection systems. Some of the diverse applications where these features are used have been presented to highlight how technical advances in the laser techniques are helping in the development of some new MST fields.

Some initial trials using a sub-nanosecond fibre laser have also been detailed. It appears that ultrashort pulses in the femtosecond domain are not necessarily required for the micromachining of certain materials such as CVD diamond or stainless steel and that such lasers may find a niche in some areas as an alternative to excimer or Nd:YAG lasers.

5. ACKNOWLEDGEMENTS

The authors would like to thank their colleagues at Exitech Limited for technical assistance in the production of the microstructures described in this article, especially Dominic Ashworth, Tim Willford and Ben Simmons. We also gratefully acknowledge the loan of the Picowatt laser from IMRA America Inc. and thank Don Harter and Heinrich Endert for their helpful advice and co-operation.

6. REFERENCES

- [1] "Laser welding, cutting and surface treatment" R. C. Crafer (ed.), The Welding Institute, Cambridge, UK (1984)
- [2] "Excimer lasers drill precise holes with higher yields" C. Rowan, Laser Focus World (Aug 1995)
- [3] "Direct manufacture of miniature bioparticle electromanipulator devices using excimer laser mask projection techniques" Nadeem H. Rizvi, Phil T. Rumsby, Malcolm C. Gower, Julian P. H. Burt, Mark S. Talary, Jon A. Tame and Ron Pethig, Int. J. Japan Soc. of Prec. Eng. vol. 33, no. 2 100-104 (June 1999)
- [4] e.g. from Holographic Lithographic Systems Inc., Bedford, MA, USA.
- [5] "Ultrafast pulses promise better processing of fine structures" Bruce Craig, Laser Focus World (Sep. 1998)
- [6] "Commercial and Biomedical Applications of Ultrafast Lasers" SPIE Proceedings Vol. 3616, K Reed & J Neev (eds.) Jun 1999

Correspondence: e-mail: n.rizvi@exitech.co.uk; Tel: +44 1993 883324; Fax: +44 1993 883334

Excimer lamp stereolithography

Saburoh SATOH*, Takao TANAKA, Satoshi IHARA
and Chobei YAMABE

Department of Electrical and Electronic Engineering,
Faculty of Science and Engineering, Saga university

1 Honjyo-machi, Saga, 840-8502, Japan

ABSTRACT

For the laser stereo-lithography, a XeCl excimer lamp with cylindrical tube has been adopted to achieve a lower cost type UV light source. Because of excellent high output efficiency, it is possible to be down sizing of a power supplier and a lamp head and to be air-cooling. And moreover to extract the maximum output power and efficiency, we applied an optical fiber system for its lithography optics.

With this excimer lamp the maximum UV emission per pulse $25 \mu\text{J}$ at 100 Hz and the maximum average power 10 mW at 1000 Hz were obtained.

Keywords: Stereo-lithography, XeCl excimer lamp, cylindrical tube, and optical fiber system

1. INTRODUCTION

Although, a number of pulsed and/or continuous wave lasers were applied to the laser stereo-lithography¹⁻⁴, He-Cd laser and Ar ion laser which wave length are 325nm and 351/364nm respectively, have been used for an ultraviolet (UV) light source. These lasers weak point was not only output energy efficiency, which was less than 0.1%, but also the big machine size, and not so high output power, and very expensive. In near future, it is supposed that these laser performances are not high enough for a higher speed stereo-lithography system⁵, and more over, it will be demanded a lower cost type apparatus.

On the other hand, excimer laser, high peak pulsed power laser with UV light emission, is considered as an UV light source for a semiconductor and/or a photochemical process⁶. XeCl excimer laser (308nm) annealing for a liquid crystal display panel is now being a practical use⁷. This laser has a handy cap because it employ only pulse operation, but the output efficiency is over 1% which is the best record in UV-lasers and moreover it is easy to get the laser output power over 100W. To apply an excimer laser for a stereo-lithography, we proposed a new concept of mask type optical system⁸⁻⁹.

Because of excellent high output efficiency¹⁰, an excimer lamp will be achieved a lower cost type of stereo-lithography equipment. From this point, we are challenging to develop a special designed cylindrical excimer lamp as an UV light source. In this paper, we report about its fundamental characteristics.

2. TECHNOLOGY OF A STEREO-LITHOGRAPHY

The laser stereo-lithography is a kind of technology to create a 3 dimensional (3D) high precision model with photochemical reaction, which locally cure a liquid resin with UV-light. Figure 1 shows a schematic diagram of a principal of the stereo-lithography⁵. Beforehand, the 3D model is designed with a computer aided design (CAD) system, changes to counter data which indicate each cross section pattern, after that, UV-laser operates as a point pattern-maker on the surface of the liquid resin. In this resin, a photosensitive material (photoinitiator) is activated with the UV-light, polymerizes the surrounding molecules, and finally grows up to a huge molecule. With UV laser operating, only a thin layer of liquid resin surface is cured, which makes necessary the creation of one by one layer, successively.

* E-Mail:satoh@esp.ee.saga-u.ac.jp; TEL:+81-952-28-8655; FAX:+81-952-28-8651

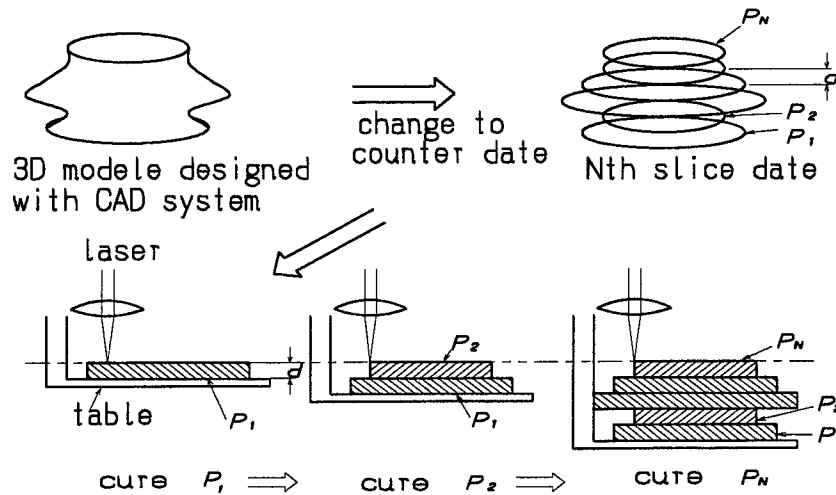


Fig. 1 Schematic diagram of a principal of the stereo-lithography

Table 1. Characteristics of several kinds of lasers and an excimer lamp

	Lasers			Lamp
	Ar	He-Cd	XeCl	XeCl
Continuous/pulse	Continuous	Continuous	Pulse 2kHz	Continuous
Wave length (nm)	364 351	325	308	308
Output power (mW)	100-500	20-40	1400	250
Input power (kW)	10-20	0.6-0.8	0.2	0.02
Cooling	Water	Air	Air	Air
Optical system	Galvanomirror	Galvanomirror	Mask	Fiber

Table 1 shows a comparison of the characteristics of several kind of lasers and an excimer lamp. Ar ion laser and He-Cd laser are conventional ones for stereo-lithography, XeCl excimer laser is a typical one for a industrial use which output power is low but repetition rate is high enough, and XeCl excimer lamp is one of our target that is now under development. It is expected for XeCl excimer lamp to be down sizing of a power supplier and a lamp head and to be air-cooling because of its excellent high output efficiency. More over, although its wavelength is shorter compare than that of Ar ion and He-Cd laser, it is possible to reduce the amount of photoinitiator and to be setting the absorption depth under 0.1 mm, and to be increasing the accuracy of a measure of length.

On the other hand, if a conventional optical system with galvanomirror of He-Cd laser were applied to its optics, it is impossible to extract the maximum power and efficiency from the excimer lamp. Because of the XeCl excimer lamp is easy to operation continuously but the output beam divergence is too high, we adopted an optical fiber system for its optics.

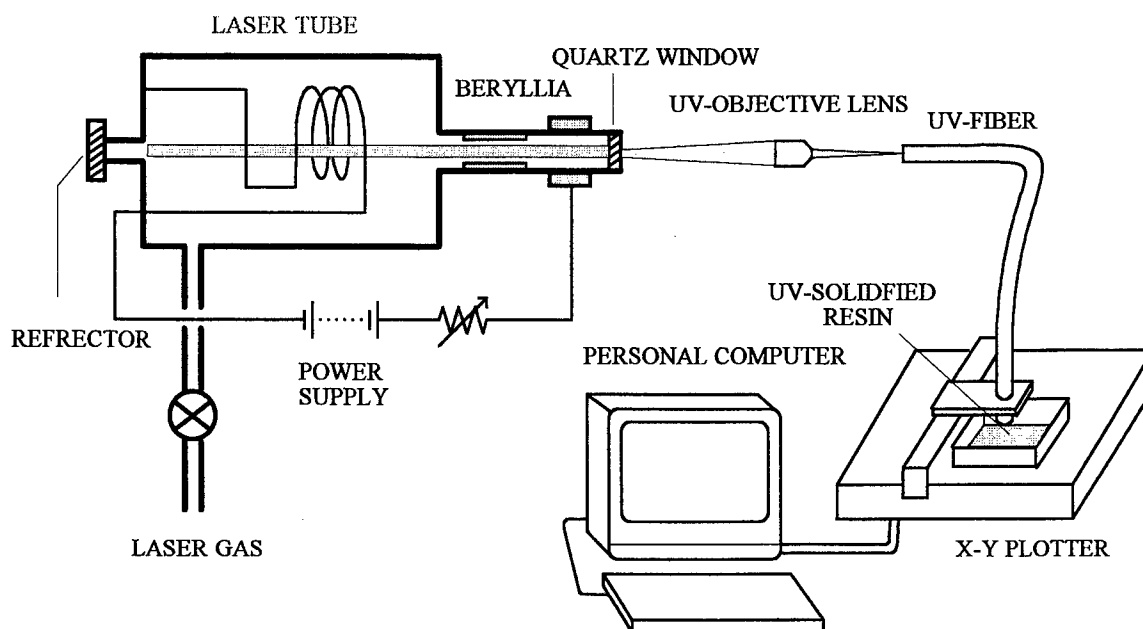


Fig. 2 Excimer lamp experimental setup

3. EXPERIMENT AND RESULT

Figure 2 shows an experimental setup with XeCl excimer lamp. A cylindrical type excimer lamp is a recycled tube used as an Ar ion laser LAI-2231 (TOSHIBA Corp.), whose two mirrors and inner gases were changed to a XeCl excimer laser specification. Figure 3 shows the excimer lamp configuration, its capillary tube made from beryllia (BeO) is 1mm in bore diameter and 50mm in length. The total reflector is fixed, but the output mirror quartz window is possible to alignment. The mixed gas, which composed HCl 0.2 %, Xe 2 % and Ne 97.8 %, is used 26.6 kPa in pressure. Figure 4 and 5 show a photograph of excimer lamp and a waveform of voltage, current and light emission, respectively.

An optical system is consisted with an UV achromatic objective lens LMU-10X-308nm (OFR Inc.), an optical UV-fiber SC200/250 (FUJIKURA Ltd.) of core/clad diameter 0.2/0.25 mm and length 2 m, and a X-Y plotter MP5300 (GRAPHTEC Inc.) controlled by a personal computer. A sample resin is "ADEKA LASCURE HS-660" produced by CMET Inc., which absorption depth is 0.1mm at He-Cd laser 325nm and is 0.04mm at XeCl excimer laser 308nm. The excimer lamp UV light is irradiated on the surface of the resin as a parameter of UV power density. After post curing the object with off-focused XeCl excimer laser EMG50E (Lambda Physik Inc.), the thickness and weight are measured with a micrometer and a chemical balance weight measure.

Finally, we tried to make a 3D article using the above fundamental results. It is set that the curing depth is 0.15 mm, and the UV light power density from the end of the fiber is less than $20\text{mJ}/\text{cm}^2$. After a layer is solidified, the object is sunk down of several mm into the liquid resin, immediately rising up, and setting the next position to which is added 0.15 mm from the previous setting with Z axis table controlled by a personal computer. Finally, the object is washed with alcohol in order to remove the non-cured resin and dried by off-focused excimer laser beam as a post curing.

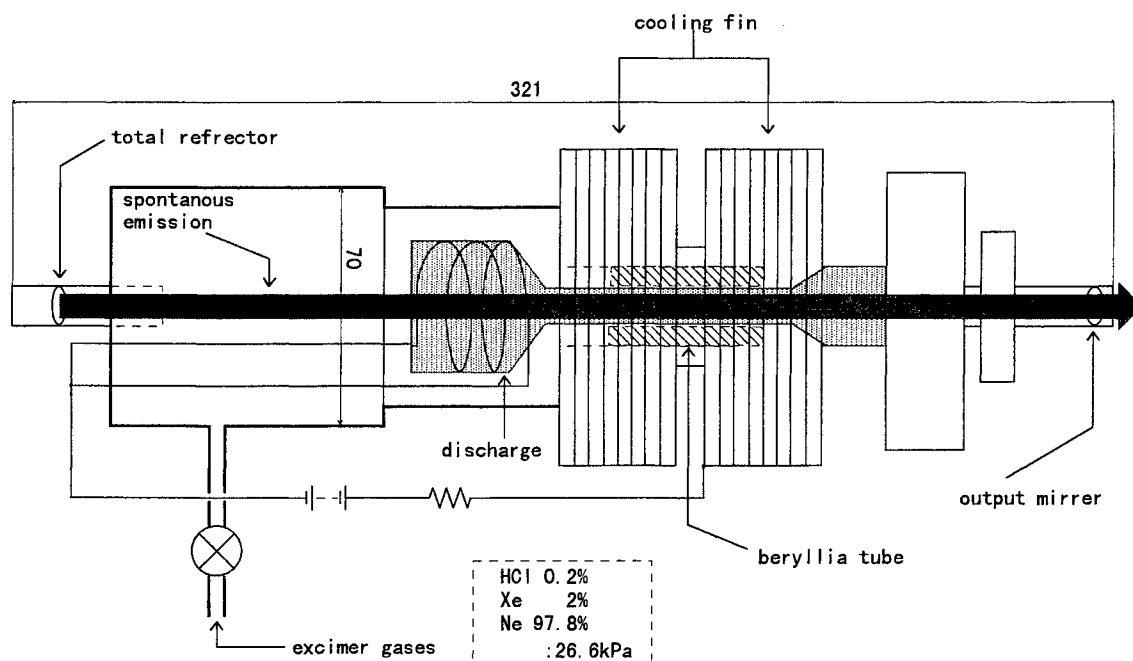


Fig. 3 Excimer lamp configuration.

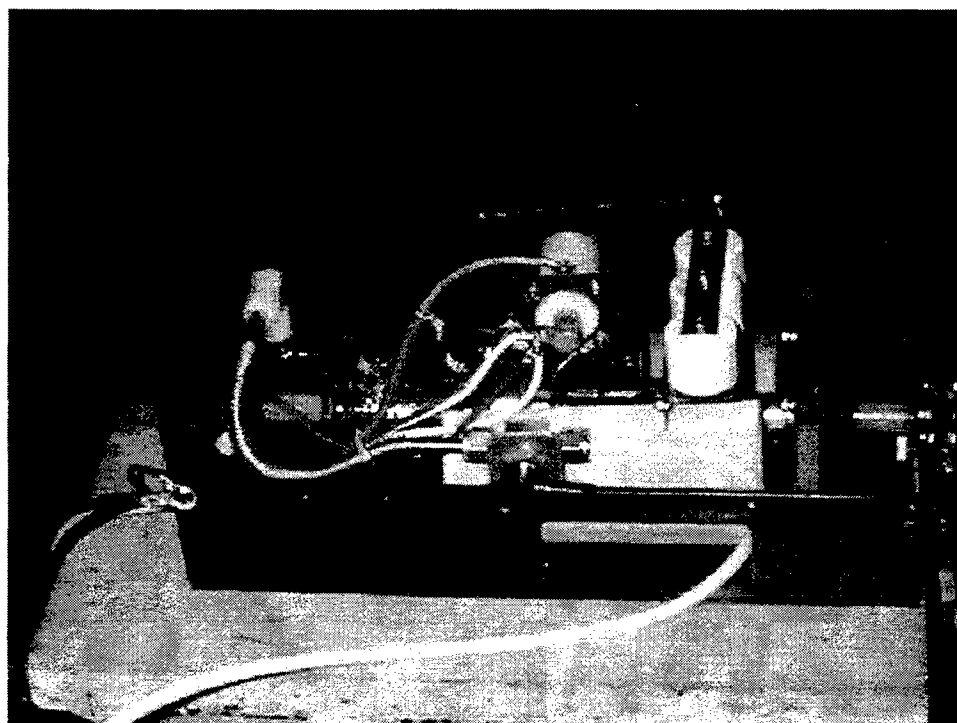


Fig. 4 Photograph of Excimer lamp

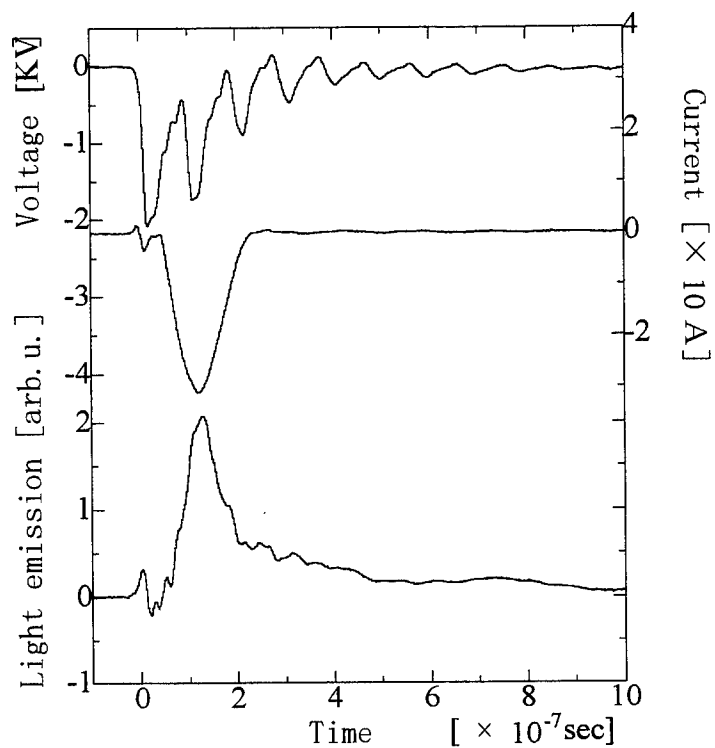


Fig. 5 Voltage, current and light emission wave forms of excimer lamp

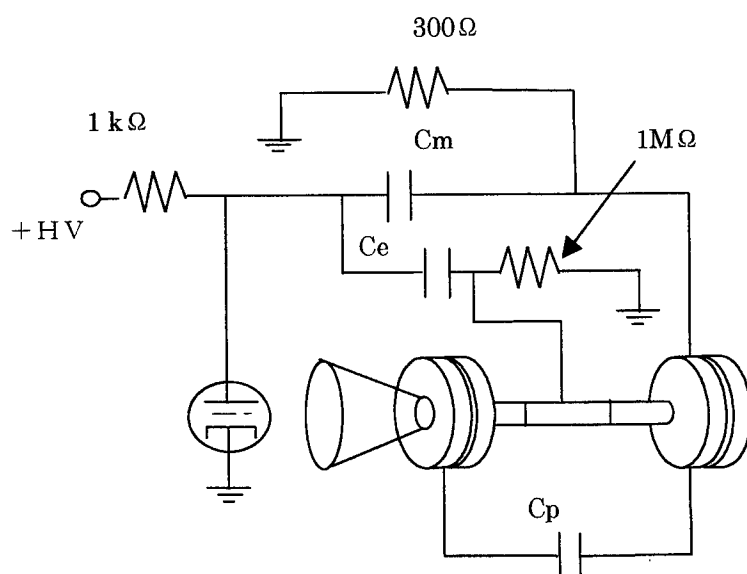


Fig. 6 Electric circuit for pulsed mode operation with a long excimer lamp.

Fig. 6 shows electric circuits for the pulsed mode operation with a long excimer lamp of capillary tube made from alumina ceramic (Al_2O_3) which is 3mm in bore diameter and 150mm in length, it will be achieved higher output power.

Figure 7 shows an output characteristic of pulsed mode operation at repetition rate 100 Hz. UV emissions increase with applied voltage and decrease with operating pressure. Comparing with the operating pressure of 13 kPa and 6.7 kPa, UV emission on 13 kPa is higher in turn at the applied voltage 26 kV. It is supposed that discharge uniformity is improved at higher applied voltage.

On the other hand, UV emission per pulse was slightly decreased with increase the repetition rate and gas pressure over 100 Hz and 8 kPa shown in Figure 8 and 9, respectively. The maximum UV emission per pulse 25 μJ at 100 Hz and 26 kV, and the maximum average power 10 mW at 1000 Hz were obtained.

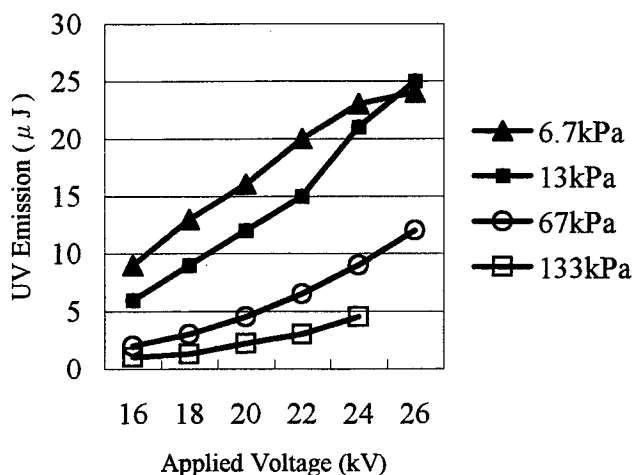


Fig. 7 Output characteristics of pulsed mode operation at 100 Hz.

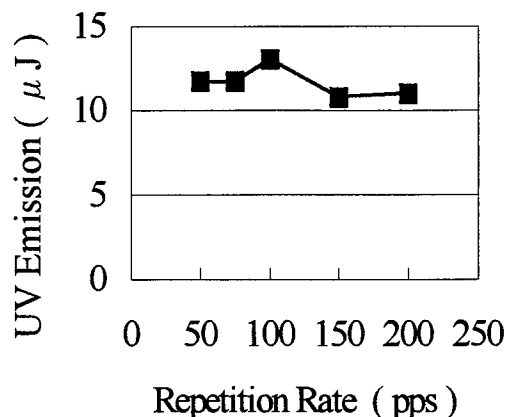


Fig.8 UV emission vs. repetition rate at applied voltage 20 kV and gas pressure 13 kPa.

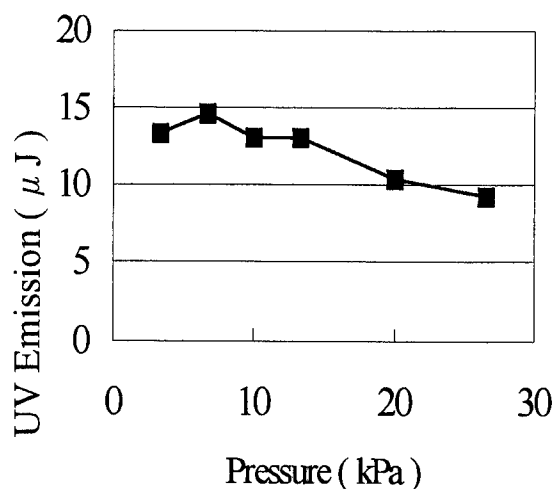


Fig. 9 UV emission vs. gas pressure at repetition rates 100 Hz and applied voltage 20 kV.

4. CONCLUSION

For the laser stereo-lithography, a XeCl excimer lamp has been adopted to achieve a lower cost type UV light source. Because of excellent high output efficiency of excimer lamp, it is possible to be down sizing of a power supplier and a lamp head and to be air-cooling. And moreover to extract the maximum output power and efficiency from the excimer lamp, we have adopted an optical fiber system for its scanning optics.

In this experiment, tow types of excimer lamp with cylindrical tube were examined. One was a recycled tube used as an Ar ion laser changed mirrors and inner gases for continuous operation, and the other one was a pulse operating tube of bore diameter 3mm and length 150mm. With pulsed operation, UV emissions increased with applied voltage and decreased with operating pressure. And emission per pulse was slightly decreased with increase the repetition rate and gas pressure over 100 Hz and 8 kPa. The maximum UV emission per pulse 25 μ J at 100 Hz and the maximum average power 10 mW at 1000 Hz were obtained.

In next study we will investigate the condition in which excimer lamp is the most useful for the stereo-lithography from the point of accuracy, a curl and a distortion to make 3D articles.

ACKNOWLEDGMENT

We would like to express our thanks to SMET Inc. for supplying "ADEKA LRASCURE HS-660" and Dr. T. Goto, who belonged in Toshiba now in BELL TECHNO Inc. and with who we held the discussions. This study was partially supported by a Grant-in-Aid for Scientific Research from Ministry of Education, Science, Culture and Sports.

REFERENCES

1. C.Decker : *J. Polym. Sci., Polym. Chem. Ed.*, **21**, pp.2451, 1983.
2. J.P.Fouassier, P.Jacques, D.J.Lougnot, and T.Pilot : *Polym. Photochem.*, **5**, pp.57, 1984.
3. M.A.Williamson, J.D.B.Smith, P.M.Castle, and R.N.Kauffman : *J. Polym. Sci., Polym. Chem. Ed.*, **20**, pp.1875, 1982.
4. C.E.Hoyle, M.Trapp, and C.H.Chang : "Laser initiated polymerization : The effect of pulse repetition rate," *Polym. Mater. Sci. Eng.*, **57**, pp.579-582, 1987.
5. P.F.Jacobs : *Rapid Prototyping & Manufacturing*, Nikkei BP (1993).
6. T.Goto, K.Kakizaki, S.Takagi, N.Okamoto, S.Satoh, S.Kosugi, and T.Ohishi : "5 kHz high repetition rate and high power XeCl excimer laser," *Rev. Sci. Instrum.*, **66**, pp.5162-5164, 1995.
7. T.Tanaka and N.Konishi : *OYO BUTURI*, **63**, pp.1034, 1994(in Japanese).
8. S.Satoh, K.Yokogawa, J.Shimada, S.Ihara, M.Ishimine, C.Yamabe, and T.Goto : "A fundamental study on stereo-lithography with KrF excimer laser," *KATAGIJYUTU*, **11(13)**, pp.62-62, 1996 (in Japanese).
9. S.Satoh, K.Yokogawa, M.Ishimine, S.Ihara, and C.Yamabe : "A study on mask type stereo-lithography with XeCl excimer laser," *Rev. Laser Engineering*, **26**, Special Supplement for APLS'98 , pp.121-124, 1998.
10. A.N.Panchenko, E.A.Sosnin, V.F.Tarasenko : "Improvement of output parameters of glow discharge UV excilamps," *Optics Communications*, **161**, pp249-252, 1999.

Femtosecond pulse laser machining of InP wafers

J. M. Wrobel^{a*}, J. Bonse^b, J. Krüger^b, and W. Kautek^b

^a Department of Physics
University of Missouri – Kansas City
Kansas City, MO 64110, USA

^b Laboratory for Thin Film Technology
Federal Institute for Materials Research and Testing
Unter den Eichen 87, D-12205 Berlin, Germany

ABSTRACT

Ablation of indium phosphide wafers in air was performed with 130 fs laser pulses at a wavelength of 800 nm at a low repetition rate of 10 Hz. In order to evaluate the role of the incubation effects, the relationship between the number of laser pulses used for the ablation and the threshold fluence was studied. Particular attention was paid to the chemical composition, surface morphology and structural variations of the ablated area.

Keywords: femtosecond laser ablation, indium phosphide, Auger electron spectroscopy

1. INTRODUCTION

Compared with longer pulses, sub-picosecond laser pulses significantly alter the ablation conditions for solids^{1,2,3}. Both the liquid phase and the heat affected zone, usually present during nanosecond laser ablation, are reduced by the rapid energy deposition⁴. As a consequence, the precision of the laser machining is often enhanced by the application of ultrashort pulses^{4,5,6,7,8}.

Indium phosphide (InP) is an attractive option because of its possible applications in electronics⁹ and photonics¹⁰. It has been suggested as a material for the fabrication of heterojunction bipolar transistors¹¹, high electron mobility transistors¹², microlenses¹³, optical gratings¹⁴, optical wave guides^{15,16} and semiconductor lasers^{17,18}.

In most cases, radiation from nanosecond lasers has been applied to process InP wafers. Ablation, chemical etching, quantum well intermixing, and several other technological treatments¹ have been performed. In this paper, investigations of the chemical and physical properties of a laser treated surface, as well as an analysis of the ablation process are presented.

2. EXPERIMENTAL DETAILS

A commercial Ti:sapphire laser system (Spectra Physics) was used for the ablation of (001) InP wafers in air. The system emitted linearly polarized near infrared pulses with a duration of 130 fs at a central wavelength of 800 nm. The beam was directed at normal incidence to the surface. A focusing plano-convex lens ($f = 60$ mm) formed an almost circular spot on the sample surface. A Gaussian intensity distribution with a $1/e^2$ -radius of $\omega_0 \approx 23$ μm was obtained.

A computer controlled xyz-stage allowed precise selection of the spot location on the wafer. For these studies, the energy of the light used for ablation was varied up to 50 μJ per pulse. With a repetition rate of 10 Hz, it is expected that heat dissipation is sufficient to prevent differences in the initial temperature of the ablated wafer during consecutive laser pulses.

* Correspondence e-mail: WrobelJ@umkc.edu

The characteristics of the ablated craters were investigated as a function of laser beam fluence and the number of laser pulses. An estimation of the chemical composition was carried out with Auger electron spectroscopy (AES). The morphology of the ablated surface was investigated using an optical microscope. In order to characterize the ablation process, the lateral and vertical dimensions of the craters were also determined with the microscope.

3. RESULTS AND DISCUSSION

Fig. 1 shows optical microscope images (Nomarski microscope) of several craters ablated at different fluence values and different numbers of laser pulses applied to the same spot. The craters were obtained with one, five and ten pulses at a constant fluence of 0.24 J/cm² (Fig. 1, 1.1 - 1.3), 0.39 J/cm² (Fig. 1, 2.1 - 2.3), 1.8 J/cm² (Fig. 1, 3.1 - 3.3) and 2.9 J/cm² (Fig. 1, 4.1 - 4.3), respectively.

Single-pulse ablation with the lowest fluence ($N = 1$, $\phi_0 = 0.24 \text{ J/cm}^2$) resulted in uniform craters (Fig. 1, 1.1). A ring of resolidified material near the edge of the craters is formed at intermediate fluences (Fig. 1, 2.1). At higher fluences, three distinct zones were observed (Fig. 1, 3.1 and 4.1).

The morphology of craters ablated with multiple pulses exhibits a characteristic ripple structure. Such features are commonly formed when linearly polarized light is used. The orientation of the ripples, resulting from the interference of the incident light with the light scattered on the surface inhomogeneities, favors the direction perpendicular to the polarization of the laser light.¹⁹ The average ripple period coincides with an incident laser wavelength of about $\lambda = 800 \text{ nm}$.

The chemical composition of the surface was examined by means of Auger electron spectroscopy. The spectra of the kinetic energy of the secondary Auger electrons, in the 30-1030 eV range, have been collected from several representative points in the crater as well as from the untreated surface for reference. The energy of the primary electrons was kept at 3.0 keV. The lateral resolution of the system used did not exceed 1 μm while the examined depth was in the order of a few nanometers. Fig. 2. shows normalized differentiated spectra, collected on a crater obtained with a single laser pulse at a fluence of 2.9 J/cm² (Fig. 1, 4.1).

In the top row of Fig. 2, the reference spectrum, collected at a location unaffected by laser radiation, is shown. The dominant MNN indium peak is split into a doublet (402 eV, 409 eV).²⁰ The LMM phosphorus line at 121 eV has about half the intensity of the indium line. The two less intense phosphorus lines, marked in the figure, indicate the presence of other chemical compounds of this element. The shape of the indium line is consistent with this statement. The untreated surface also exhibits the presence of carbon (KLL) and oxygen (KLL). The corresponding lines occur at 274 eV and 512 eV, respectively. This is in accordance with earlier results which showed that InP surfaces stored in air are covered with a thin layer of native oxides (above 30 Å), indium phosphates^{21,22} and carbon compounds.²³

The spectra in the bottom row of Fig. 2 were obtained at the central region of the crater. Despite the morphological differences in the ablated surface, compositional differences between various points within the crater were not observed in the AES experiments. However, a chemical difference is observed between the ablated surface and the untreated surface. As a result of the laser ablation, the relative concentration of the contaminants from the atmosphere, particularly oxygen, increases. The oxidation of the surface is manifested by the relative increase of the oxygen AES line intensity as well as by the shift of indium related lines (MNN) toward lower energy values ($\sim 3 \text{ eV}$).^{24,25} The absence of the 409 eV indium signal indicates that no metallic indium is present on the ablated surface.

For a Gaussian beam profile, the diameter of the ablated crater is related to the maximum beam fluence ϕ_0

$$D^2 = 2\omega_0^2 \ln \left(\frac{\phi_0}{\phi_{th}} \right) \quad (1)$$

where ϕ_{th} represents the ablation threshold fluence and ω_0 represents the $1/e^2$ -radius of the beam.²⁶ Fig. 3 represents data for a single-pulse ablation. The extrapolation of D^2 to zero yields the ablation threshold fluence. For single-pulse ablation, the process requires a minimum value of $\phi_{th} \approx 0.16 \text{ J/cm}^2$. The laser treated zone appears smooth and uniform (Fig. 1, 1.1). For increased laser fluences, three morphologically different zones can be observed (Fig. 1, 3.1). From the extrapolations of their squared diameters (Fig. 3), one can conclude that the additional two zones appear at $\phi'_{th} \approx 1.3 \text{ J/cm}^2$ and $\phi''_{th} \approx 1.7 \text{ J/cm}^2$, respectively.

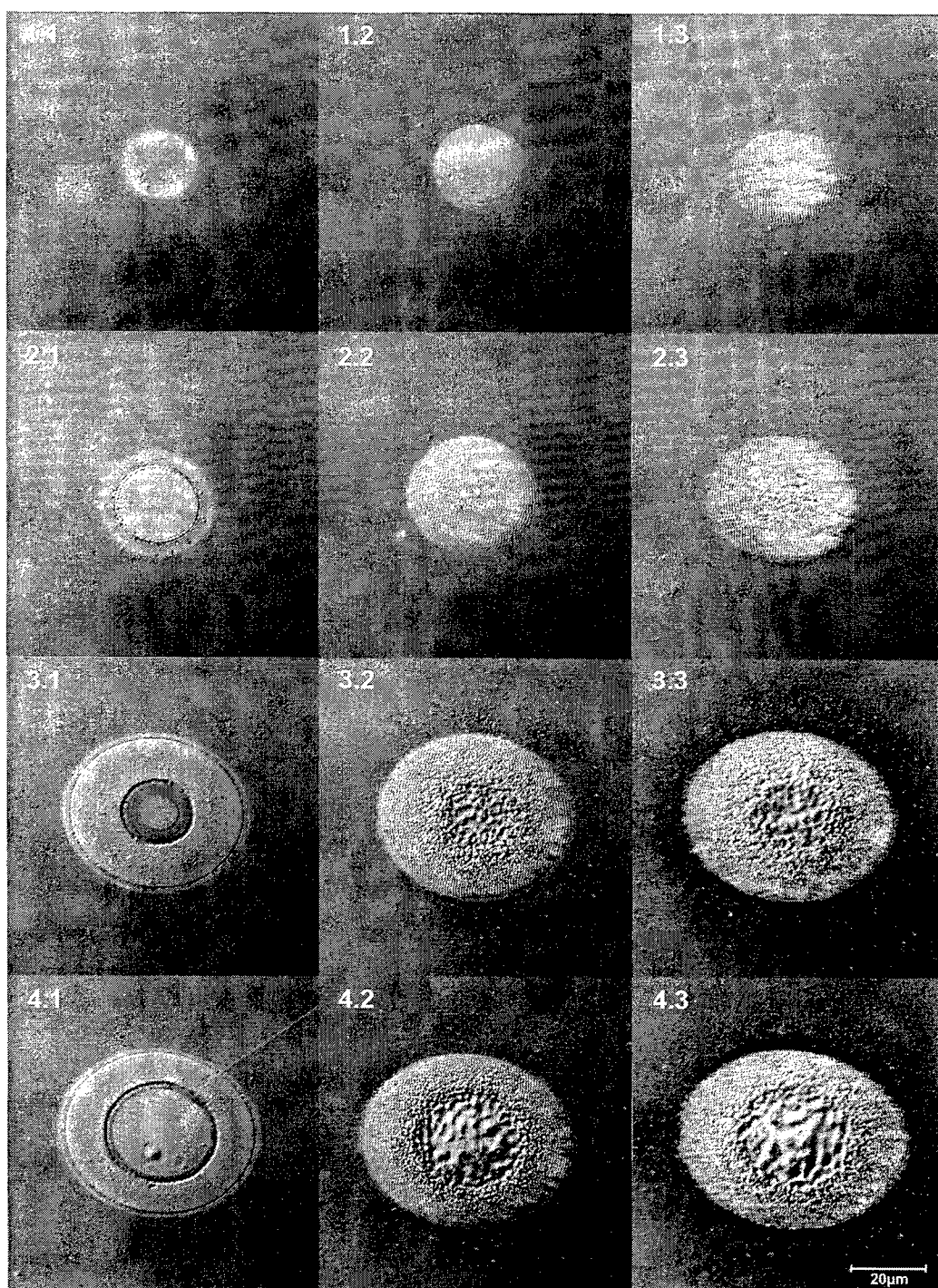


Figure 1. Optical microscope images of the craters ablated on the InP surface with a femtosecond laser ($\tau = 130$ fs, $\lambda = 800$ nm). The rows correlate to the fluence ($\phi_0 = 0.24$ J/cm², 0.39 J/cm², 1.8 J/cm², and 2.9 J/cm²) and the columns to the pulse number ($N = 1, 5, 10$).

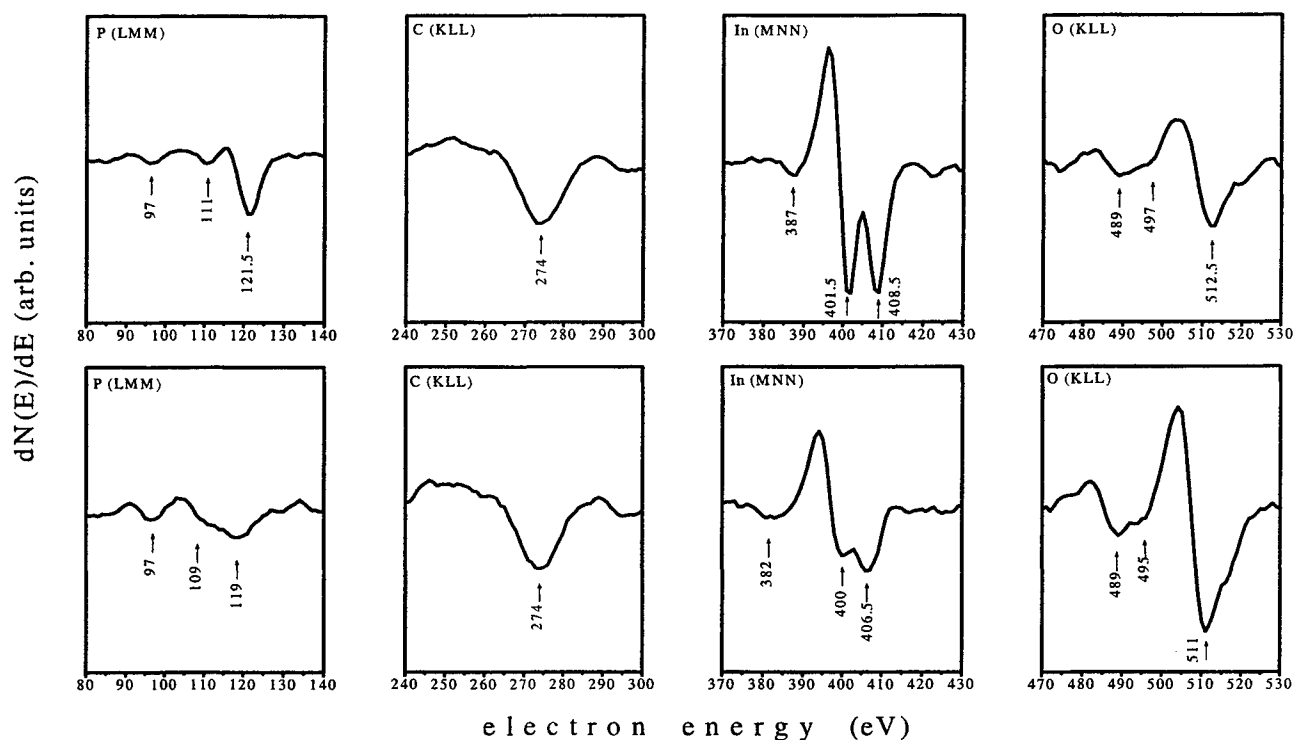


Figure 2. Auger electron spectra of an as received InP surface (top), and of a surface ablated with a femtosecond-pulse laser ($N = 1$, $\tau = 130$ fs, $\lambda = 800$ nm, $\phi_0 = 2.9$ J/cm²).

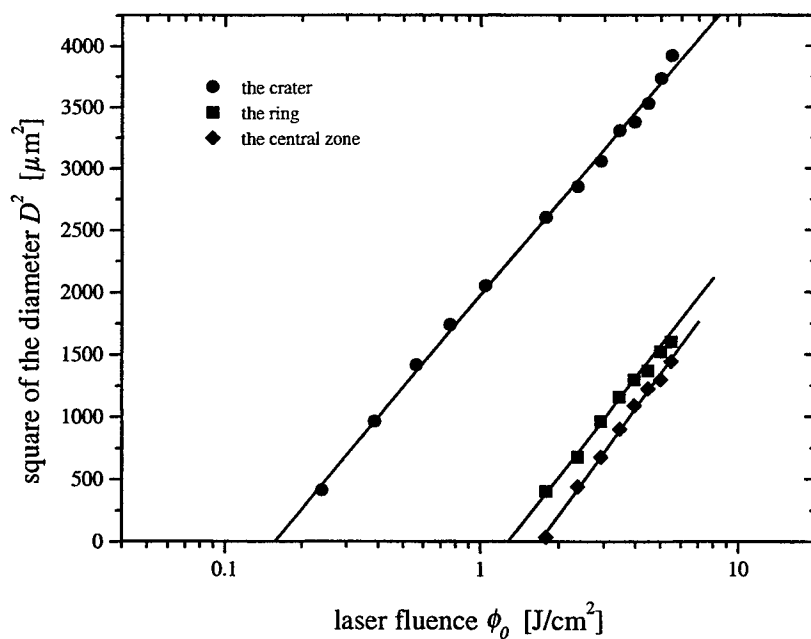


Figure 3. The squared diameters D^2 of the in-air laser modified surface of InP as a function of the laser fluence ϕ_0 ($N = 1$, $\tau = 130$ fs, $\lambda = 800$ nm).

An investigation of the effects of multiple-pulse ablation demonstrates that the ablation threshold fluence depends on the number of applied laser pulses. Beginning with a value of 0.16 J/cm^2 for a single pulse, the threshold fluence decreases to 0.06 J/cm^2 for one hundred pulses. Such behavior has been observed in dielectrics²⁷, metals²⁸, ceramics²⁹ and polymers³⁰, and has been explained in terms of an incubation process. In this model, the ablation threshold fluence $\phi_{th}(N)$ at N pulses is related to the single-pulse threshold fluence $\phi_{th}(1)$ by a power law³¹

$$\phi_{th}(N) = \phi_{th}(1) \cdot N^{\xi-1} \quad (2)$$

where the exponent ξ describes the degree of incubation. The slope of the accumulated threshold fluence $N \cdot \phi_{th}(N)$, plotted versus the number of laser pulses in a double logarithmic scale, is equal to the exponent ξ . The estimated value for the degree of incubation from Fig. 4 is $\xi = 0.78$.

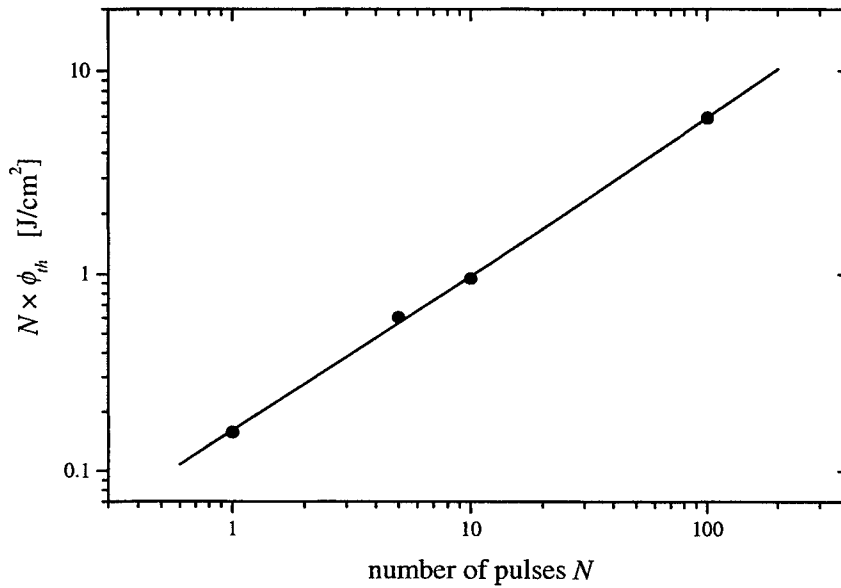


Figure 4. The accumulated laser fluence $N \cdot \phi_{th}(N)$ for the in-air ablation threshold of InP for different pulse numbers N ($\tau = 130 \text{ fs}$, $\lambda = 800 \text{ nm}$).

The ablation rate has also been studied in these experiments. Fig. 5 shows the relationship between the crater depth h and the number of applied laser pulses N for a fluence of $\phi_0 = 0.58 \text{ J/cm}^2$. This fluence is about three to four times greater than the threshold value for single-pulse ablation. A linear relationship between the depth and the number of laser pulses can be observed. The average ablation rate at this fluence, found from the slope of the plot in Fig. 5, is $d = 86 \text{ nm/pulse}$. This linear relationship between the depth h and the number of applied laser pulses N indicates that within the experimental limits a steady state regime of ablation was achieved.

It is apparent from a simple analysis of the radiation energy density within the material that the following relationship exists between the ablation rate d and the laser fluence ϕ_0

$$d(\phi_0) = \kappa \ln \left(\frac{\phi_0}{\phi_{th}} \right). \quad (3)$$

In a vacuum, the proportionality coefficient κ should be close to the penetration depth of the laser radiation⁵. Fig. 6 illustrates the dependency for $N = 100$ laser pulses. At $\phi_0 < 4 \text{ J/cm}^2$, a linear relationship between d and $\log(\phi_0)$ is observed. The estimated proportionality coefficient κ is 30 nm . At $\phi_0 > 4 \text{ J/cm}^2$, the rate of ablation d increases more than predicted by Eq. 3 suggesting involvement of mechanisms other than just those of simple absorption in the ablation process. Comparable behavior has been observed in silicon⁴ and metals³¹. The diffusion of laser induced hot electrons into the material has been suggested as the cause of the deviation from the above relationship³².

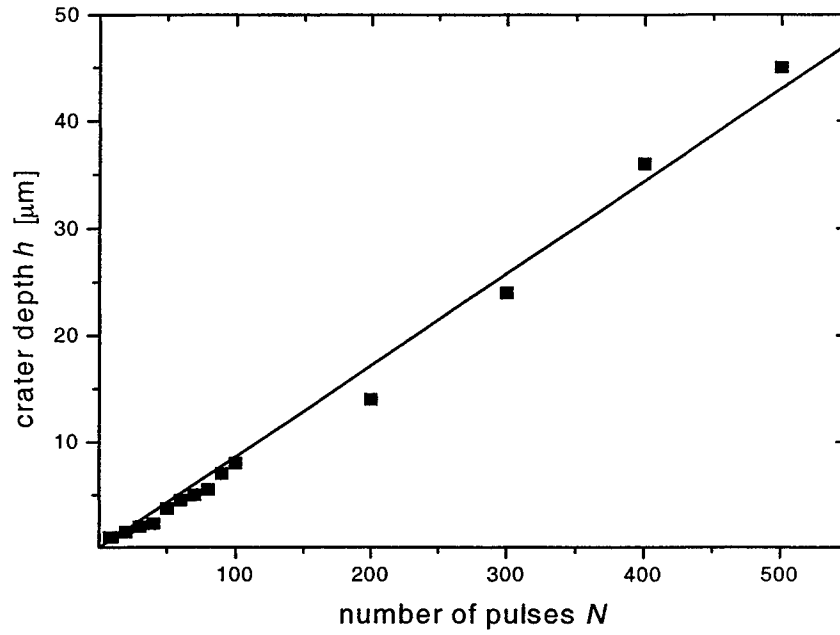


Figure 5. Dependency of the depth of the ablated crater h on the number of laser pulses N at $\phi_0 = 0.58 \text{ J/cm}^2$ for ablation of InP in air ($\tau = 130 \text{ fs}$, $\lambda = 800 \text{ nm}$).

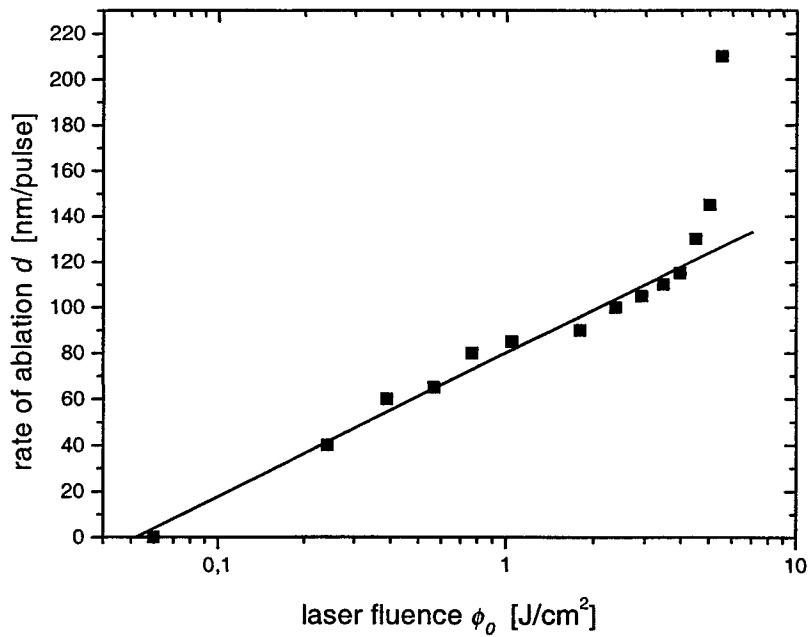


Figure 6. Average ablation rate d of InP in air for 100 pulses as a function of the laser fluence ϕ_0 ($\tau = 130 \text{ fs}$, $\lambda = 800 \text{ nm}$).

4. CONCLUSIONS

The threshold fluence for 130 fs single-pulse laser ablation of InP in air at a wavelength of 800 nm is $\phi_{th} \approx 0.16 \text{ J/cm}^2$. In addition, two other morphological regions of the surface are obtained for ablation fluences greater than $\phi'_{th} \approx 1.3 \text{ J/cm}^2$ and $\phi''_{th} \approx 1.7 \text{ J/cm}^2$, respectively. The ablated surface exhibits strong contamination with oxygen indicating a thermal oxidation process in the ambient air as a consequence of the laser treatment.

Increasing the number of pulses per spot, the ablation threshold fluence decreases. An incubation model, describing this effect in metals, ceramics and polymers, is also valid for the semiconducting InP. The exponent, characterizing the degree of incubation was estimated to be $\xi \approx 0.78$.

For fluences significantly greater than the single-pulse ablation threshold, the ablation rate is independent of the number of applied laser pulses. A logarithmic relationship of the ablation rate on the laser fluence has been verified for values lower than 4 J/cm^2 .

ACKNOWLEDGEMENTS

The authors wish to express their gratitude for financial support to the University of Missouri Research Board, the "Fonds der Chemischen Industrie im Verband der Chemischen Industrie e.V.", Frankfurt am Main, and the European Community, BRITE-EURAM III Project BRPR-CT96-0265. The technical assistance of B. Strauß, S. Benemann and D. Schmidt is gratefully acknowledged.

REFERENCES

1. D. Bäuerle, *Laser Processing and Chemistry*, 2nd Edition, Springer-Verlag, Berlin, 1996.
2. J. Krüger, W. Kautek, "The femtosecond pulse laser: a new tool for micromachining", *Laser Physics* **9**, pp. 30-40, 1999.
3. D. Ashkenasi, G. Herbst, A. Rosenfeld, H. Varel, M. Lorenz, R. Stoian, E.E.B. Campbell, "Laser ablation and structuring of transparent materials with ultrashort laser pulses", *SPIE Conf. Proc.* **3343**, pp. 400-410, 1998.
4. W. Kautek, J. Krüger, "Femtosecond pulse laser ablation of metallic, semiconducting, ceramic, and biological materials", *SPIE Conf. Proc.* **2207**, pp. 600-610, 1994.
5. S. Preuss, A. Demchuk, M. Stuke, "Sub-picosecond UV laser ablation of metals", *Appl. Phys. A* **61**, pp. 33-37, 1995.
6. J. Krüger, W. Kautek, "Femtosecond-pulse laser processing of metallic and semiconducting thin films", *SPIE Conf. Proc.* **2403**, pp. 436-447, 1995.
7. C. Momma, B.N. Chichkov, S. Nolte, F. von Alvensleben, A. Tünnermann, H. Welling, B. Wellegehausen, "Short-pulse laser ablation of solid targets", *Optics Comm.* **129**, pp. 134-142, 1996.
8. B.N. Chichkov, C. Momma, S. Nolte, F. von Alvensleben, A. Tünnermann, "Femtosecond, picosecond and nanosecond laser ablation of solids", *Appl. Phys. A* **63**, pp. 109-115, 1996.
9. A. Mesquida Küsters, K. Heime, "Al-free InP based high electron mobility transistors: design, fabrication and performance", *Solid-State Electronics* **41**, pp. 1159-1170, 1997.
10. S. Chandrasekhar, "Optoelectronic systems integration using InP-based HBTS lightwave communications", *Solid-State Electronics* **41**, pp. 1413-1417, 1997.
11. N. Shamir, D. Ritter, C. Cytermann, "Beryllium doped InP/InGaAsP heterojunctions bipolar transistors", *Solid-State Electronics* **42**, pp. 2039-2045, 1998.
12. T. Sonoda, Y. Yamamoto, N. Hayafuji, H. Yoshida, H. Sasaki, T. Kitano, S. Takamiya, M. Ostubo, "Manufacturability and reliability of InP HEMTs", *Solid-State Electronics* **41**, pp. 1621-1628, 1997.
13. R. Matz, H. Weber, G. Weimann, "Laser-induced dry etching of integrated InP microlenses", *Appl. Phys. A* **65**, pp. 349-353, 1997.
14. M. Ezaki, H. Kumagai, K. Toyoda, M. Obara, "Surface modification of III-V compound semiconductors using surface electromagnetic wave etching induced by ultraviolet lasers", *IEEE Journal of Selected Topics in Quantum Electronics* **1**, pp. 841-847, (1995).
15. C.A. Verschuren, P.J. Harmsma, Y.S. Oei, M.R. Leys, H. Vonk, J.H. Wolter, "Butt-coupling loss of 0.1 dB/interface in InP/InGaAs MQW waveguide-waveguide structures grown by selective area chemical epitaxy", *J. Crystal Growth* **188**, pp. 288-294, 1998.

16. H. Künzel, S. Ebert, R. Gibis, R. Kaiser, H. Kizuki, S. Malchow, G. Urmann, "Selective MOMBE growth of InP-based waveguide/laser butt-joints", *J. Crystal Growth* **192**, pp. 56-62, 1998.
17. A. Nutsch, B. Dahlheimer, R. Döhr, H. Kratzer, R. Lukas, B. Torabi, G. Tränkle, G. Abstreiter, G. Weimann, "Chemical beam epitaxy of integrated 1.55 μm lasers on exact and misoriented (100)-InP substrates", *J. Crystal Growth* **188**, pp. 275-280, 1998.
18. Y. Kashima, T. Nozawa, T. Munakata, "Metalorganic vapor-phase epitaxy (MOVPE) growth of InGaAsP multiple-quantum-well distributed feedback lasers on InP corrugated substrates", *J. Crystal Growth* **204**, pp. 429-433, 1999.
19. Z. Guosheng, P.M. Fauchet, A.E. Siegmann, "Growth of spontaneous periodic structures on solids during laser illumination", *Phys. Rev. B* **26**, pp. 5366-5380, 1982.
20. "Handbook of Auger Electron Spectroscopy", ed. C.L. Hedberg, third edition, Physical Electronics, Inc., Eden Prairie, Minnesota, USA, 1995.
21. S.J. Hoekje, G.B. Hoflund, "Surface characterization study of InP(100) substrates using ISS, AES and ESCA: comparison of substrates from two different commercial sources", *Appl. Surf. Sci.* **47**, pp. 43-48, 1991.
22. L.L. Kazmierski, P.J. Ireland, P. Sheldon, T.L. Chu, S.S. Chu, C.L. Lin, "Comparison of low-temperature oxides on polycrystalline InP by AES, SIMS and XPS", *J. Vac. Sci. Technol.* **17**, pp. 1061-1066, 1980.
23. J.B. Malherbe, "Sputtering of Compound Semiconductor Surfaces. I. Ion. Solid Interactions and Sputtering Yields" *CRC Crit. Rev. Solid State Mater. Sci.* **19**, pp. 55-127, 1994.
24. M.M. Sung, S.H. Lee, S.M. Lee, D. Marton, S.S. Perry, J.W. Rabalais, "Composition and morphology of InP{100} surfaces as a function of low energy Ar^+ bombardment and annealing", *Surf. Sci.* **382**, pp. 147-153, 1997.
25. V. Gorbenko, A. Gorban, J. Shvets, "Effects of H-atoms on basic processes in $\text{H}_2/\text{H}_2\text{O}/\text{InP}$ system", *Vacuum* **54**, pp. 179-182, 1999.
26. J.M. Liu, "Simple technique for measurements of pulsed Gaussian-beam spot sizes", *Opt. Lett.* **7**, pp. 196-198, 1982.
27. D. Askenasi, M. Lorenz, R. Stoian, A. Rosenfeld, "Surface damage threshold and structuring of dielectrics using femtosecond laser pulses: the role of incubation", *Appl. Surf. Sci.* **150**, pp. 101-106, 1999.
28. J. Bonse, P. Rudolph, J. Krüger, S. Baudach, W. Kautek, "Femtosecond pulse laser processing of TiN on silicon", *Appl. Surf. Sci.*, (in press).
29. J. Güdde, J. Holfeld, J.G. Müller, E. Matthias, "Damage threshold dependence on electron-phonon coupling in Au and Ni films", *Appl. Surf. Sci.* **127-129**, pp. 40-45, 1998.
30. S. Baudach, J. Bonse, J. Krüger, W. Kautek, "Ultrashort pulse laser ablation of Polycarbonate and Polymethylmethacrylate", *Appl. Surf. Sci.* (in press).
31. Y. Jee, M.F. Becker, R.M. Walser, "Laser-induced damage on single-crystal metal surface", *J. Opt. Soc. Am. B* **5**, pp. 648-659, 1988.
32. C. Suárez, W.E. Bron, T. Juhasz, "Dynamics and transport of electronic carriers in thin gold films", *Phys. Rev. Lett.* **75**, pp. 4536-4539, 1995.

SESSION 10

Laser Microengineering II

Custom Specific Fabrication of Integrated Optical Devices by Excimer Laser Ablation of Polymers

Thomas Klotzbücher, Martin Popp, Torsten Braune, Jens Haase, Anne Gaudron, Ingo Smaglinski,
Thomas Paatzsch, Hans-Dieter Bauer, Wolfgang Ehrfeld
Institut für Mikrotechnik Mainz GmbH, Carl-Zeiss-Str. 18-20, 55129 Mainz, Germany

ABSTRACT

Excimer laser ablation was used for direct writing of multimode waveguide structures with passive fiber alignment grooves in polymers. First, integrated optical multimode components were simulated by the method of beam propagation (BPM) to optimize the optical performance of the design. Then the CNC codes for laser machining were created directly from the corresponding CAD data. ArF Excimer laser radiation of wavelength $\lambda=193$ nm was used for ablation of adjacent grooves with a cross sectional area of $50 \times 50 \mu\text{m}^2$ and lengths in the order of several mm. The laser-written grooves were filled with a liquid pre-polymer which after UV-curing served as the waveguiding structures. The smoothest surfaces during laser ablation were achieved by applying several ablation scans with reduced material removal rates but higher feedrates. Debris formation, also influencing the surface roughness, was suppressed or minimized by making use of capable polymers. With the method of laser ablation linear waveguides of length $l=10$ mm with insertion losses L_i in the range of 1.3 to 1.9 dB have been realized for $\lambda=1310$ nm, depending on the polymer used. By means of 1x2-splitters, 4x4 as well as 4x16 starcouplers it was shown that laser ablation is a well suited tool for rapid prototyping of integrated optical multimode elements.

Keywords: integrated optical devices, passive fiber-to-chip coupling, polymers, rapid prototyping, Excimer laser ablation

1. INTRODUCTION

Optical data transmission become more and more important in fast processing and exchange of information. Recent examples, like 10 Gbit Ethernet (10GbE), home banking via internet or digital TV, which are widely known and used in everyday life, are rapidly growing. All of these applications require the transport of an increasing amount of data that can be achieved only by optical transmission techniques. The process of replacing copper wiring by optical fibers in data networks started out some years ago and took place mainly in the fields of wide area networks (WAN) and in the backbone of local area networks (LAN). For future it is expected that optical fibers will directly reach companies and private households (FTTH) carrying phone calls, TV channels and internet data. Moreover it is expected that optical data communication in multi-processor high speed computers will be realized through high bandwidth parallel optical links via optical backplanes for effective and fast data transport.

Therefore, the need of for example optical NxM couplers and 1xN splitters which distribute and route the signals for example in optical backplanes drastically increases. Usually these elements are demanded in large numbers therefore requiring low fabrication costs. The LIGA technique (German acronym for the main process techniques lithography, electroforming and replication) allows a cost effective mass production of plastic microparts by galvanofarming of microstructures, generated for example by X-ray lithography, electroplating and subsequent replication by injection molding or hot embossing^{1,2,3,4}. In the past it has been demonstrated that LIGA is a well suited technique for the mass production of optical^{4,5,6} as well as many other microsystems^{7,8}. It has also been used for fabrication of singlemode 1x2 optical splitters and multimode 4x4 optical starcouplers in a very precise manner on the basis of a LIGA mould insert, employing hot embossing in polymers^{9, 10}. With this technique a passive fiber-to-chip coupling was realized, strongly minimizing the fabrication costs of such elements.

However, often only small numbers for special custom specific applications like sensors, demonstrators or prototypes for verification of design functionality and fast design iteration are required. Therefore, a strong demand for techniques allowing cost effective production of small numbers or rapid prototyping exists which allows the fabrication of custom specified waveguide elements within shortest possible time. Excimer laser ablation of polymers has been demonstrated to be a potential technique for direct writing and rapid prototyping of fluidic microstructures^{11,12,13,14,15}. It was also shown that laser ablation in combination with galvanofarming and subsequent replication is well suited for cost effective mass production of microparts^{16,17}. However, for the fabrication of polymer waveguide structures by Excimer laser ablation certain requirements, like low surface roughness (optical quality), well defined cross section areas and ablation depths as

well as high ablation rates have to be met. Recently it was shown that laser ablation is well suited for the fabrication of optical elements on the basis of polymers, such as refractive and diffractive microlenses^{18,19}, diffraction gratings²⁰ and also waveguide structures²¹. The aim of this paper is to demonstrate that Excimer laser ablation has a large potential for rapid prototyping and small series production of multimode waveguide devices with passive fiber alignment grooves in polymers.

2. BASIC PROCESSES AND METHODS

1. Laser ablation

The ablation experiments were made with a commercial Excimer laser mask projection system (Exitech 7000 series) which already was described in detail elsewhere²² (Figure 1). An Excimer laser (LPX110i, Lambda Physik) which was operated with ArF gas fill at corresponding wavelength of $\lambda=193$ nm, served as the radiation source. The pre-shaped and homogenized laser radiation was focused onto a motorized mask aperture which was imaged onto workpieces' surface via a reflective objective, delivering a rectangular or square shaped radiation spot. Typical fluences on the sample surface were in the order of $\epsilon=1$ J/cm², being sufficient for micromachining of the investigated polymer materials. The radiation spot was moved on top of the sample surface by relative movement of the workpiece via an x-y-z-stage with an absolute positioning accuracy of ± 2 μ m. The movement of the x-y-z-stage was computer controlled using CNC codes that were directly generated from the corresponding CAD data.

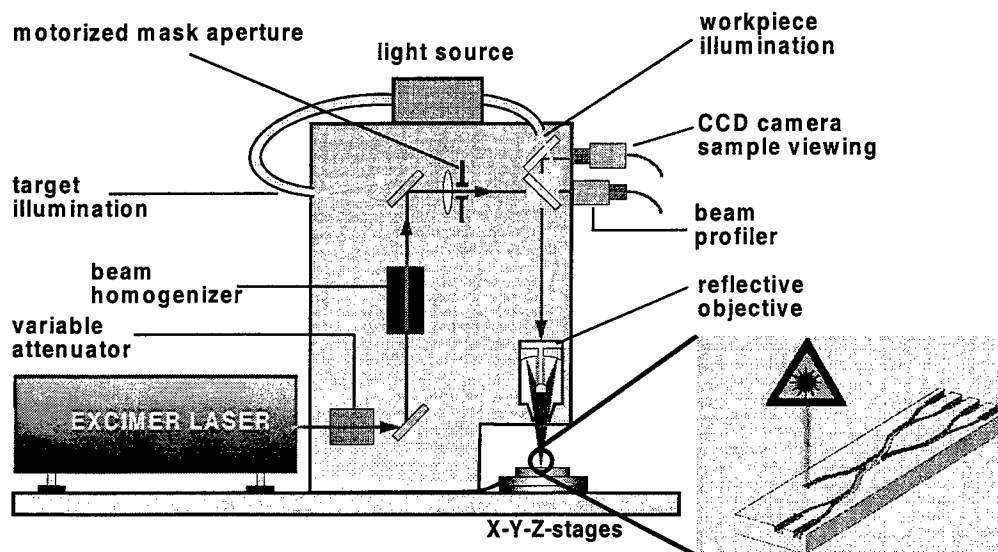


Figure 1: Excimer laser mask projection unit (Exitech 7000) with variable, motorized mask aperture²².

By movement of the workpiece during laser operation grooves with well defined geometry (width and depth) were generated, forming a system of cross linked grooves which, after filling with a liquid core material and subsequent UV-curing, serve as waveguide structures. The depths of the single grooves was controlled by the feedrate of the workpiece, determining the mean number of pulses per unit area, the laser pulse repetition rate, the mask aperture in the direction of propagation and the number of repeated scans along each groove. The width of the grooves was controlled by the mask aperture normal to the direction of propagation of the workpiece.

2. Design and assembly of waveguide components

The layout of optical multimode splitters and couplers was generally employed of cascaded Y-splitters²³ as shown in Figure 2. The waveguide cross sections were typically 50×50 μ m² and the refractive index difference between core and cladding was chosen to be 0.02. At each splitting / combining point the waveguides' lateral width was doubled or bisected, respectively. Besides low excess loss, a good uniformity value is desired. The uniformity is determined by the length of the straight mixing sections between the splitting regions and is expected to be best in the case of high length of the mixing section²³. The main advantages of such polymer waveguide components gain from a uniformity that is almost independent of the excited modes and the wavelength (in the band from 830 nm to 1310 nm). In the case of symmetrical $N \times M$ ($M \bmod N = 0$, for $M \geq N$) splitters / couplers the whole waveguide structure is established by laser ablation of M grooves with equal width of 50 μ m. The grooves are directly adjacent in the straight mixing regions, forming grooves with a total width of R

times $50\ \mu\text{m}$, R being the number of adjacent grooves of the corresponding mixing region. Asymmetrical splitters / couplers ($N \bmod M \neq 0$) were not realized yet.

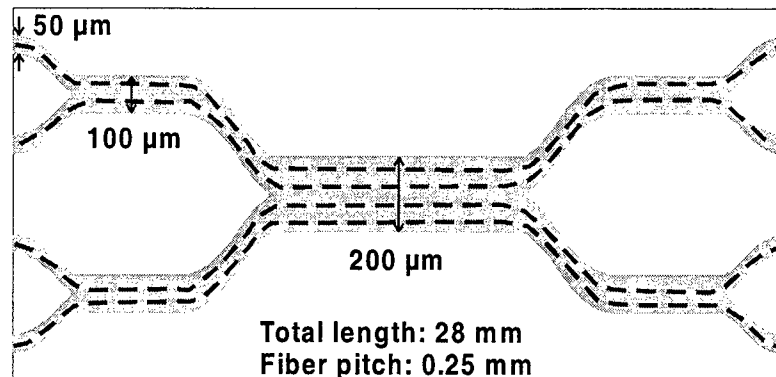


Figure 2: Schematic representation of the layout of a 4x4 starcoupler consisting of cascaded multimode Y-splitters. The dashed lines represent the four scan center lines of the projected mask aperture during laser ablation.

Designs were numerically simulated on the basis of the beam propagation method (BPM)^{24,25}. The BPM is based on numerical solutions of the classical wave equation for electromagnetic fields with the approximation of slow varying envelopes (SVE-approximation) of the propagating wave fronts, corresponding to small refractive index changes in the direction of propagation. Starting with a three-dimensional refractive index distribution $n(x,y,z)$ and an entrance field distribution $E(x,y,z_0)$, the field $E(x,y,z_0+\Delta z)$ at the position $z_0+\Delta z$ was calculated by methods of perturbation theory. By applying this method subsequently in the direction of propagation with the corresponding boundary conditions, the field distribution within the waveguide device was calculated. 4x4-multimode-starcouplers were modeled by applying this technique. The main requirement on 4x4 starcouplers was homogeneous distribution of an incoming field from one of the four inputs to the four outputs with uniform signal values.

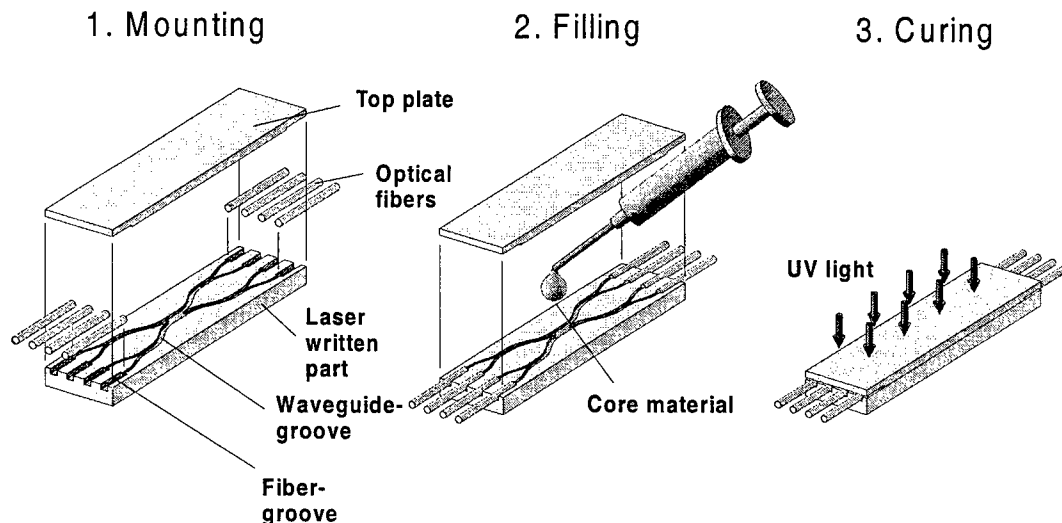


Figure 3: Sequential steps of assembly of optical waveguide structures.

The laser generated waveguide devices were assembled in three characteristic steps (Figure 3). In the first step the single fibers were mounted into the fiber alignment grooves of the laser-written part. Afterwards the waveguide grooves as well as the fiber alignment grooves were filled with a liquid core material (epoxy) the refractive index of which after UV-curing matches the required refractive index difference between core and cladding. The advantage of this assembly is the passive fiber-to-chip coupling, which circumvents totally any active alignment procedures, therefore reducing the cost of the assembly drastically. The filled device was covered with a top plate and afterwards cured by UV-radiation (third step). After curing a stable connection between the device and the top plate was obtained.

3. Optical loss measurements

Though polymer waveguide chips are appropriate for a wide wavelength band, beginning from 600 nm up to 1550 nm, optical loss measurements were carried out at 830 nm and 1310 nm using a singlemode (SM) laser diode. To reach conditions of light propagation in the connected 62.5 / 125 μm graded-index fibers (GI) comparable to those in an existing fiber network a so-called offset patch cord was used. This will produce a convenient optical field (70/70-excitation) while the centers of applied fibers (SM \Rightarrow MM) are laterally displaced.

Optical measurements shall obtain (all units in dB):

Insertion loss	$L_i = 10 \cdot \log \left(\frac{I_{ref}}{I_{out}} \right)$	Corresponds to signal reduction after inserting the device into an existing network.
Excess loss	$L_e = 10 \cdot \log \left(\frac{I_{ref}}{I_{out}} \right) + 10 \cdot \log \left(\frac{1}{M} \right)$	In case of an NxM multimode coupler / splitter. Corresponds to irretrievable power losses (scattered, absorbed or reflected shares of light). Excludes physical power-partition towards M outputs.
Uniformity	$U = \text{Max}(L_i) - \text{Min}(L_i)$	Represents the homogeneity of different outputs of a starcoupler.

The reference intensity without the waveguiding, distributing device (NxM coupler) and the different intensity signals of outputs (1 ... M) connecting the described incoming GI/MM fiber to inputs (1 ... N) were used as references.

3. FUNDAMENTAL INVESTIGATIONS

For the rapid prototyping of high performance multimode optical waveguide components with low optical losses by Excimer laser ablation the following requirements on the polymer material properties have to be made:

- low debris formation during ablation
- low surface roughness after ablation (no formation of bubbles or artifacts)
- refractive index in the range of 1,48 to 1,52
- high solubility resistance with respect to the liquid core material
- high heat and humidity resistance
- high mechanical strength
- high, well controllable ablation rate.

In a first step ablation experiments were concentrated on three different polymers, namely Polymethylmethacrylate (PMMA), a commercially Cycloolefin Copolymer (COC) and a newly designed polymer P1 that all have appropriate refractive indices. The polymers PMMA and COC have already been applied successfully for hot embossing of waveguide elements with mould inserts generated by the LIGA technique. The ablation rates of the investigated polymers at a fluence of $\epsilon=1 \text{ J/cm}^2$ were 0.45 $\mu\text{m/pulse}$ (PMMA), 0.19 $\mu\text{m/pulse}$ (COC) and 0.17 $\mu\text{m/pulse}$ (P1). For all polymers the fluence of $\epsilon=1 \text{ J/cm}^2$ corresponds to ablation rates that are independent of small fluence changes (saturation region of ablation), therefore representing the maximum ablation rate at wavelength $\lambda=193 \text{ nm}$. To investigate the debris formation and the development of surface roughness after laser ablation, well defined grooves of length $l=10 \text{ mm}$ were ablated in each of the three polymer types as a function of the number of ablation scans over each groove. The feedrate was set to a value so that the grooves had the desired depth of $d=50 \mu\text{m}$. The debris formation and hence the surface roughness of the grooves bottom and side walls strongly depends on the material used for ablation as well as from the number of scans which are used during ablation (Figure 4). PMMA and COC exhibited a strong debris formation in the case of small scan numbers. The debris sticks to the workpieces' surface but also to the side walls and the bottom of grooves, strongly enhancing the surface roughness. The polymer P1 showed almost no debris formation but in case of scan number $N=1$ some bubbles were formed on the bottom of the groove. The bubbles probably represent molten regions, generated by a higher mean temperature during ablation in the case of low feedrates because the mean number of pulses per unit area and time is higher compared to the higher feedrates used in the case of larger ablation scan numbers.

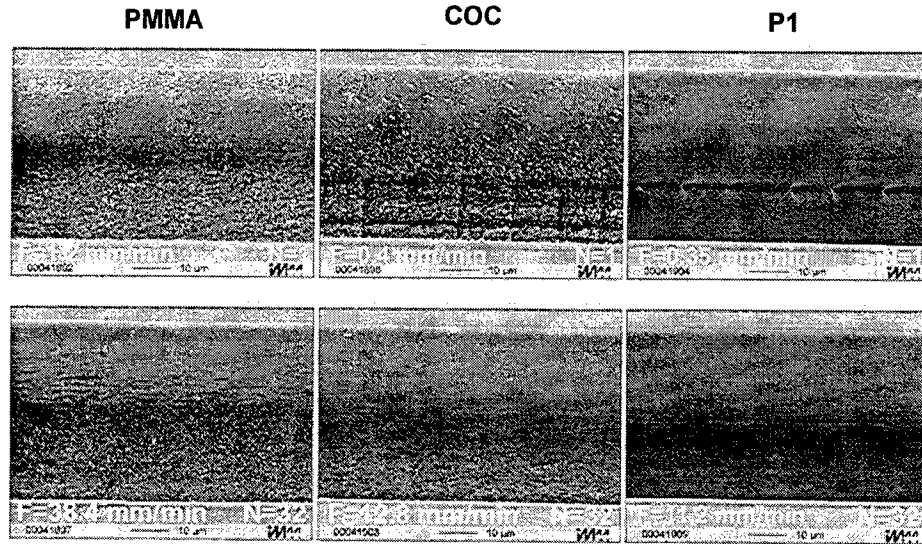


Figure 4: SEM analysis of grooves generated by Excimer laser ablation of PMMA, COC and P1. The grooves in the top row were ablated with $N=1$ scans and low feedrate and the grooves in the bottom row were ablated with $N=32$ scans and corresponding higher feedrates, respectively.

With increasing scan number the roughness decreases, especially on the sidewalls of grooves. The debris that has been formed during one ablation scan is almost totally removed by the next succeeding scan. Therefore the total roughness after finishing one groove is mainly determined by the debris, produced by the last ablation scan. In the case of P1 average roughness values of $R_a=0.19 \mu\text{m}$ ($N=2$) have been realized, as determined by optical profilometry. The corresponding maximum roughness values were higher, $R_z=1.22 \mu\text{m}$ ($N=2$), which is attributed to the discontinuous irradiation of the polymer by the pulsed laser radiation, forming a wavelike topography on the bottom of the grooves. Especially in the case of large feedrates (i.e. large scan numbers) when the lateral distance between two laser pulses becomes high, a long period wavelike topography was formed, increasing the surface roughness. This effect is predominant in the case of PMMA because it has the highest ablation rate of all the investigated polymers, therefore exhibiting the largest feedrates for a given depth of the grooves at constant scan number. Values of $R_z=7.18 \mu\text{m}$ ($N=32$) and $R_a=1.45 \mu\text{m}$ ($N=32$) compared to $R_z=3.37 \mu\text{m}$ ($N=2$) and $R_a=0.63 \mu\text{m}$ ($N=2$) have been observed for ablation of PMMA. Corresponding insertion loss values (best values), measured with a single mode laser of wavelength $\lambda=1310 \text{ nm}$, were $L_i=1.3 \text{ dB}$ for P1 ($N=2$), $L_i=1.5 \text{ dB}$ for COC ($N=2$) and $L_i=1.9 \text{ dB}$ for PMMA ($N=32$).

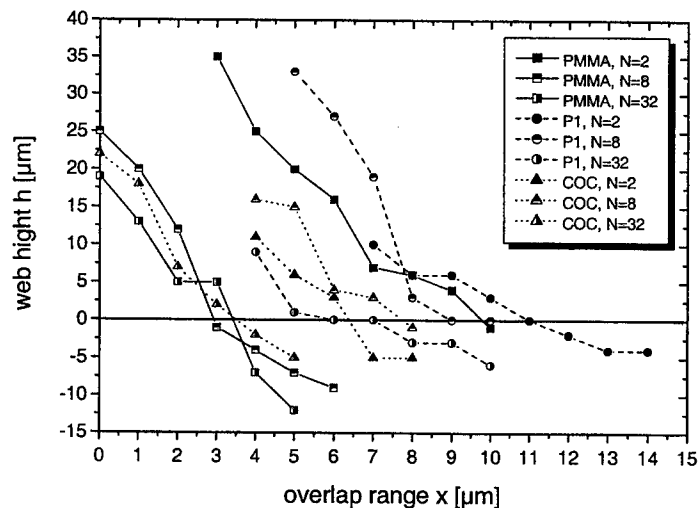


Figure 5: Web height between two adjacent grooves as a function of the overlap of the square mask image in the ablation region (the web height is measured relative to the bottom of the waveguide structure, positive values correspond to a web and negative values to a pit).

As mentioned above the optical splitters and couplers were realized by laser ablation of grooves that are directly adjacent in the mixing regions (Figure 2). For optimum functionality of the optical devices it is necessary to avoid the formation of webs or pits in the boundary region of two adjacent grooves. To control the web height between two adjacent grooves the overlap of the square shaped mask image was varied systematically for the polymers PMMA, COC and P1, respectively (Figure 5). The web height h as a function of lateral overlap strongly depends on the material used for ablation as well as on the number of scans N used for the ablation of grooves. Generally, the web height decreases with increasing lateral overlap x , independent from the polymer that was ablated. The overlap x , required for a desired web height of $h=0$, shifts to lower values with increasing number of scans N , except for the polymer COC that exhibits its maximum value for x at $N=8$. This behavior is expected, since in the case of multiple ablation scans the divergent radiation in the boundary region of the two grooves partially ablates material in the region of the adjacent groove. However, the geometry of the web which develops during laser ablation may also play a role, which can be an explanation for the somewhat different behavior of COC. Furthermore it is expected that the web formation strongly depends on the fluence used during ablation, therefore requiring further investigations.

4. RAPID PROTOTYPING OF OPTICAL DEVICES

With the insights grown from the fundamental investigations (Chapter 3), first experiments on rapid prototyping of 4x4 and 4x16 starcouplers by pulsed Excimer laser ablation of PMMA have been made. Figure 6 shows for example a 1x2 splitting region as well as the input region with the four fiber grooves of a 4x4 starcoupler that was realized in PMMA with $N=2$ ablation scans. The total writing time for the device was about 2.5 hours. For comparison, the same device would have been generated in P1 within 7.4 hours, a time that is about three times longer as in the case of PMMA.

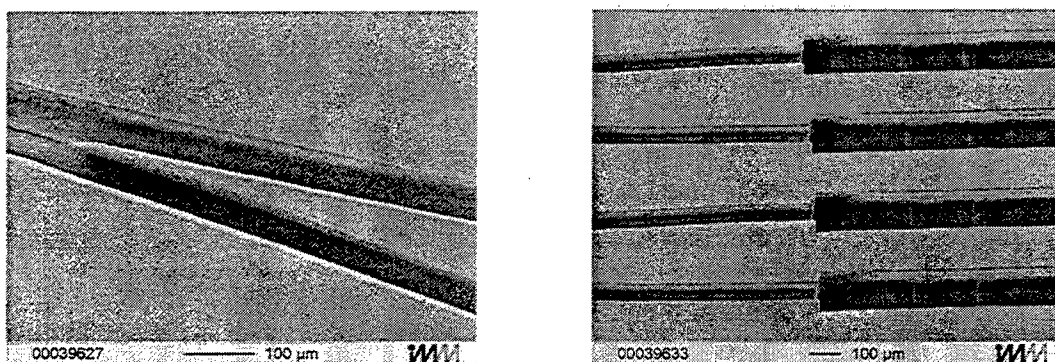


Figure 6: SEM pictures of a laser-written 4x4 starcoupler in PMMA. Left: 1x2 splitting region. Right: input region with fiber grooves as well as wave guide grooves.

From the SEM analysis (Figure 6) it became evident that the front part of the splitting section is formed extremely sharp during laser ablation, so that good uniformity may be expected. Optical loss measurements on laser-written 4x4 starcouplers showed that the uniformity of signal distribution of an input signal to the four outputs is indeed nearly constant and comparable to corresponding values of 4x4 starcouplers fabricated with LIGA tools (Figure 7). However, the insertion loss strongly depends on the input channel, resulting in larger uniformity values as in the case of LIGA devices. The best mean insertion loss values for laser-written 4x4 starcouplers, up to now, were about 13 dB. That is about 4 dB higher compared to the best devices fabricated with LIGA tools. The reason for the higher insertion loss is mainly based on the debris formation in the case of laser ablation of PMMA. For future investigations it is expected that similar devices fabricated in P1 will have smaller insertion loss values.

The relative difference in depth of fiber groove and waveguide groove also had an important influence on the insertion loss (Figure 7). In the case of too low feedrates during ablation of the fiber groove, the core of the assembled fiber did not match the center of the waveguide groove anymore, leading to an increased insertion loss because not all of the incoming light is delivered to the waveguiding device. To avoid optical losses due to misfits of fiber and waveguide grooves, an exact control of ablation depth during laser ablation is required. It has been observed that the ablation depth under identical conditions depends on the geometry of the groove to be ablated. Exact depth control was employed by ablation of test structures with identical width as the fiber or waveguide grooves and scaling up the measured depth values to the desired values.

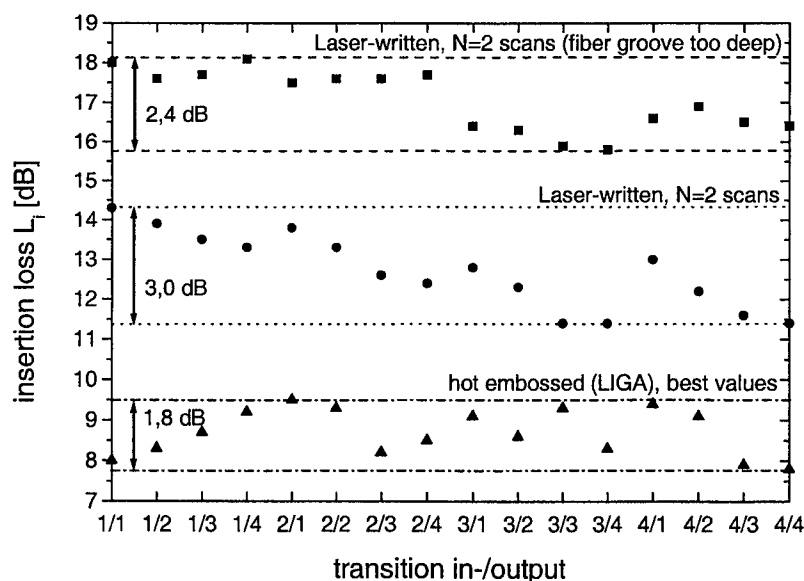


Figure 7: Insertion loss values for laser-written 4x4 starcouplers in PMMA compared to a similar device fabricated by hot embossing with a LIGA mould insert. The values beneath the double arrows indicate the uniformity values of the devices.

A prototype of a custom specified 4x16 multimode starcoupler has been realized by laser ablation of PMMA. In this case the waveguide grooves had a width of $w=100\text{ }\mu\text{m}$ and a depth of $d=200\text{ }\mu\text{m}$. The corresponding dimensions of the fiber grooves were $w=245\text{ }\mu\text{m}$ and $d=235\text{ }\mu\text{m}$, respectively. The design of the 4x16 starcoupler in this case was realized somewhat different compared to the outline given in chapter 2.2. Because it was impossible to realize 16 adjacent grooves with aspect ratio of 4:1 (ratio of depth to width) the device was build up from a 4x4 coupler with standard design and adapted T-junctions, which were designed in such a way that optical losses were minimized (Figure 8, left).

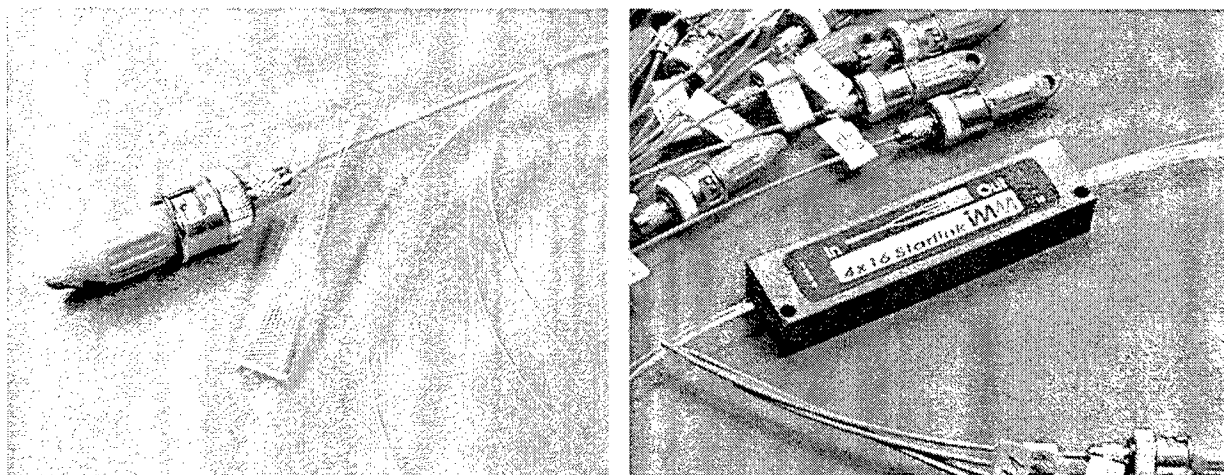


Figure 8: Prototype of a 4x16 starcoupler realized by the method of direct laser-writing in PMMA. Left: structured polymer chip. Right: assembled and packaged device.

Using PMMA as base material allowed the fabrication of the device within a total writing time of about 13 hours (scan number $N=8$). Including assembling, packaging and measuring it was therefore possible to fabricate the complete device within one week (Figure 8, right). The use of PMMA as the base material for rapid prototyping in this case also led to the above mentioned debris problem that together with the slightly modified design gave excess loss values of about 8 dB.

5. CONCLUSIONS

Direct writing of multimode waveguide structures ($50 \times 50 \mu\text{m}^2$) with passive fiber alignment grooves for the purpose of rapid prototyping was possible by Excimer laser ablation (ArF, $\lambda=193 \text{ nm}$) of PMMA, COC and P1. Symmetrical waveguide structures composed of adjacent grooves were generated directly from CNC codes for laser machining. The laser-written grooves were filled with a liquid pre-polymer which after UV-curing served as the waveguiding structures. Fundamental investigations showed that optical loss values strongly depend on the surface roughness which is affected by the material used for ablation and its debris formation properties. The smoothest surfaces during laser ablation were achieved by applying several ablation scans with reduced material removal rates but higher feedrates. Debris formation, also influencing the surface roughness, was suppressed or minimized by making use of capable polymers. With the method of laser ablation linear waveguides of length $l=10 \text{ mm}$ with insertion losses L_i of 1.3 dB for polymer P1 compared to 1.5 dB for COC and 1.9 dB for PMMA have been realized for $\lambda=1310 \text{ nm}$. By means of 4×4 as well as 4×16 starcouplers it was shown that laser ablation is a well suited tool for rapid prototyping of integrated optical multimode elements. However, during rapid prototyping always a conflict between fast processing and lower surface quality arose for the investigated polymers. Therefore, long processing times have to be accepted for prototypes with highest functionality, i.e. lowest optical loss values. Future experiments will concentrate on the search for other polymers, having the desired optical properties and exhibiting low debris formation, and on the reduction of debris formation for example by ablation in oxygen atmospheres.

REFERENCES

1. E. W. Becker, W. Ehrfeld, P. Hagmann, A. Maner, D. Münchmeyer, Fabrication of microstructures with high aspect ratios and great structural height by synchrotron radiation lithography, galvanofarming, and plastic moulding (LIGA process), *Microelectron. Eng.* 4 (1986) 35
2. W. Ehrfeld, D. Münchmeyer, *Three-dimensional microfabrication using synchrotron radiation*, *Nucl. Instrum. Methods A* 303 (1991) 523
3. W. Ehrfeld, H. Lehr, *Deep X-ray lithography for the production of threedimensional microstructures from metals polymers and ceramics*, *Radiat. Phys. and Chem.* 45 (1995) 394
4. W. Ehrfeld, H.-D. Bauer, *Application of micro- and nanotechnologies for the fabrication of optical devices*, *Proc. SPIE* 3276 (1998) 2
5. A. Picard, W. Ehrfeld, J. Reinhardt, D. Morlion, J. Vanderwege, J.P. Vetter, *High precision LIGA structures for optical fibre-in-board technology*, *Eur. Conf. on Electronic Packaging, Technol. & Int. Conf. on Interconn. Technol. In Electronics (EUPAC'96)*, Essen, 1996; *DVS-Berichte* 173 (1996) 77
6. K. Dunkel, H.-D. Bauer, W. Ehrfeld, L. Weber, G. Hörcher, G. Müller, *Injection-moulded fibre ribbon connectors for parallel optical links fabricated by LIGA technique*, *J. Microm. Microeng.* 8 (1998) 301
7. H. Lehr, W. Ehrfeld, M. Schmidt, E. Kallenbach, H. Tuan, *Application of the LIGA technique for the development of microactuators based on electromagnetical principles*, *J. Micromech. Microeng.* 2 (1992) 2
8. V. Hessel, W. Ehrfeld, H. Möbius, T. Richter, K. Russow, *Potentials and realization of microreactors*, *Proc. Int. Symp. on Microsystems, Intelligent Materials and Robots (MIMR)*, Sendai, Japan, 1995, p. 37
9. T. Paatzsch, I. Smagliniski, H.-D. Bauer, W. Ehrfeld, *Polymer waveguides for telecom, datacom and sensor applications*, *Miniaturized systems with microoptics and micromechanics III*, *Proc. SPIE* 3276 (1998) 16
10. T. Paatzsch, H.-D. Bauer, M. Popp, I. Smagliniski, W. Ehrfeld, *Polymer Star Couplers for Optical Backplane Interconnects Fabricated by LIGA Technique*, *Proc. of Seventh International Plastic Optical Fibre Conference*, pp. 324-331, Berlin 1998
11. M.A. Roberts, J.S. Rossier, P. Bercier, H. Girault, *UV laser machined polymer substrates for the development of microdiagnostic systems*, *Anal. Chem.* 69 (1997) 2035
12. M. Lapczynska, M. Stuke, *Rapid prototype fabrication of smooth microreactor channel systems in PMMA by VUV laser ablation at 157 nm for applications in genome analysis and biotechnology*, *Mat. Res. Soc. Symp. Proc.* 526 (1998) 143
13. N. Rizvi, *Micro-engineering applications of pulsed lasers*, *Proc. Conf. Micro-Engineering*, Stuttgart, Sep. 1999
14. H. Becker, T. Klotzbücher, *Polymer nanowells with variable slope angle*, *Proc. Int. Conf. on Microreact. Technol.*, Frankfurt, 19.-23. Apr., 1999

15. A. Krishnan, R. Nassar, *Rapid prototyping using Excimer laser microfabrication system*, Proc. SPIE 3512 (1998) 374
16. J. Arnold, U. Dasbach, W. Ehrfeld, K. Hesch, H. Löwe, *Combination of Excimer laser micromachining and replication processes suited for large scale production*, Appl. Surf. Sci. 86 (1995) 251
17. J. Arnold, W. Ehrfeld, K. Hesch, H. Möbius, *Kostengünstige Serienfertigung von Mikrobauteilen durch Laser-LIGA*, Feinwerktechnik, Mikrotechnik, Messtechnik (F&M) 103 (1995) 48
18. F.H.H. Lin, J.H. Huang, E.H.Y. Chou, C.R. Yang, B.C.S. Chou, R.K.S. Luo, W.K. Kuo, J.W. Chang, M.H. Lu, W.H. Huang, C.J. Chen, *Fabrication of binary microlens array by Excimer laser micromachining*, Proc. SPIE 3511 (1998) 67
19. S. Mihailov, S. Lazare, *Fabrication of refractive microlens arrays by Excimer laser ablation of amorphous teflon*, Appl. Optics 32 (1993) 6211
20. C.J. Newsome, M. O'Neill, R.J. Farley, G.P. Bryan-Brown, *Laser etched gratings on polymer layers for alignment of liquid crystals*, Appl. Phys. Lett. 72 (1998) 2078
21. S. Pelli, G.C. Righini, A. Scaglione, M. Guglielmi, A. Martucci, *Direct writing of ridge optical waveguides in silica-titania glass sol-gel films*, Optical Mater. 5 (1996) 119
22. M.C. Gower, P.T. Rumsby, *Excimer laser projector for material processing application*, Laser Ablation of Electronic Materials (Ed. E. Fogarassy, S. Lazare) EMRS Monographs, Vol. 4, North Holland, Amsterdam, 1992
23. D. Israel, R. Baets, M. Goodwin, N. Shaw, M. Salik, C. Groves-Kirby, *Comparison of Different Polymeric Multimode Star Couplers for Backplane Optical Interconnect*, J. Lightw. Technol. 13 (1995) 1057
24. M.D. Feit, J.A. Fleck, *Light propagation in graded-index optical fibres*, Appl. Opt. 17 (1978) 3990
25. R. März: *Integrated optics: design and modeling*, Artech House, Norwood, 1995

Laser-based microscale bending for microelectronics fabrication

Xianfan Xu
School of Mechanical Engineering
Purdue University
West Lafayette, IN 47907

ABSTRACT

This paper presents experimental and theoretical work on laser-based microscale bending. High precision bending of stainless steel and ceramic specimens is achieved with the use of a pulsed or a CW laser. Experiments are conducted to study the bending behavior of stainless steel and ceramics due to laser irradiation. The amount of bending is correlated with various laser and processing parameters. A theoretical model of the laser bending process is presented based on thermo-elasticity/plasticity. The laser bending process is explained as the result of the laser-induced non-uniform distribution of the residual strain. Numerical simulations are carried out to calculate the laser-induced temperature field, the residual stress field, and the amount of bending for both pulsed and CW laser irradiation. Applications of the laser bending technique in microelectronics fabrication are discussed.

Keywords: Laser forming, laser bending, thermal stress, thermomechanics, pulsed laser, CW laser, curvature modification

1. INTRODUCTION

Laser bending (also called laser forming or laser curvature adjustment) has attracted much attention recently. In general, laser bending has the advantages of non-contact, toolless, rapid, high precision, and causing a very small heat affected zone¹⁻⁴. When a pulsed laser is used, bending precision obtained is even higher, on the order of sub-microradian⁵. A schematic of the laser bending process is shown in Figure 1. A focused laser beam (or pulses) scans over the target, raising the temperature at the target surface rapidly. Heating and cooling cause plastic deformation in the laser heated area, thus change the curvature of the target permanently. The exact bending mechanism is determined by the transient temperature field that in turn is influenced by the thickness and thermophysical properties of the workpieces, the scanning velocity of the laser beam, the laser beam path, the laser power, etc. Three laser bending mechanisms have been discussed in the literature: the temperature gradient mechanism, the buckling mechanism, and the upsetting mechanism⁶. Detailed theoretical descriptions of the laser bending process was given by Chen *et al.*⁵.

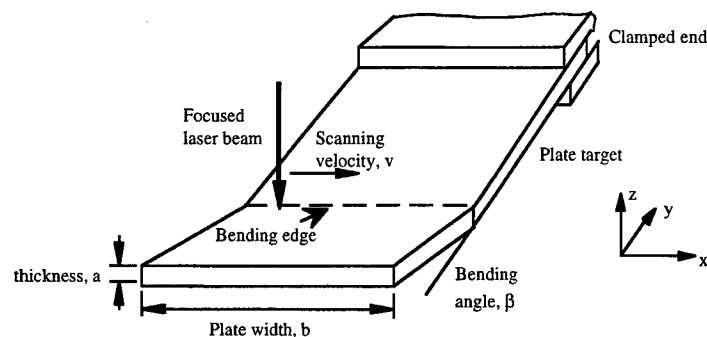


Figure 1: Illustration of the laser bending process

Previous applications of laser bending are mainly implemented using high power continuous wave (CW) lasers on large and thick workpieces for shaping ship bodies or straightening automobile body shells¹⁻⁴. On the other hand, less work has been performed on bending using a pulsed laser. Chen et al. were the first to use a pulsed laser to obtain bending with precision far exceeding any other methods⁵. In that study, sub-microradian curvature adjustment was achieved to correct distortions on magnetic disk heads. High precision was achieved owing to the extremely short heat affected depth (on the order of 1 μm) and the resulting short stressed/strained depth. Therefore, pulsed laser bending is ideal for applications in microelectronics fabrication where ultra high precision is needed

The focus of this paper is on microscale bending using a low power CW argon ion laser and a pulsed laser. The test specimens are stainless steels and ceramics. Results of experimental parametric studies of CW and pulsed laser bending are presented. A finite element model for computing CW and pulse laser bending is described, and calculation results are compared with experimental data.

2. EXPERIMENTAL

The experimental set-up for laser bending and for measuring the bending angle is shown in Fig. 2. The laser used in this work is a pulsed diode-pumped Nd:YLF laser with a pulsed width of about 10 nsec (FWHM) and a wavelength at 1047 nm, a pulsed lamp-pumped Nd:YAG laser with a pulse width of about 70 ns and a wavelength at 1064 nm, and a 4 W CW argon ion laser with multiple wavelengths at 488.0 nm (20% of total power), 514.5 nm (43% of total power), etc. The laser beam is expanded by a beam expander and then focused onto the target using a focusing lens. One end of the target is clamped. The mirror and the focusing lens are mounted together on a computer-controlled motion stage, so that the laser beam size on the target surface does not change when the laser beam is scanned over the target surface. The computer-controlled stage scans the laser beam over the specimen surface in the x-direction (the direction perpendicular to the paper) while bending is mainly achieved in the z-direction. The two-axis motion stage is controlled by two closed-loop precision linear actuators, each with a velocity accuracy better than 0.2%.

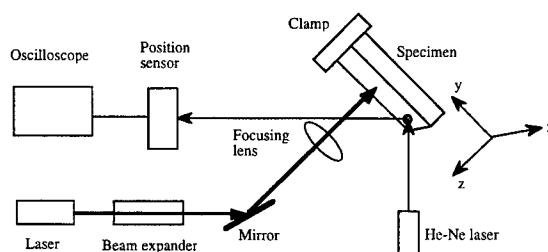


Figure 2: Experimental set-up

To measure out-of-plane bending angles in the z-direction, a HeNe laser beam is focused at the free end of the specimen. The reflected HeNe laser beam is received by a position sensitive detector whose position sensitivity is about 1 μm . When the distance between the sensor and the specimen is long enough, a small movement at the free end of the specimen produces a measurable displacement of the laser beam at the position sensor. The position change of the HeNe laser beam at the sensor is recorded by an oscilloscope, and is converted to the bending angle of the specimen using straightforward geometrical calculations. The whole experimental apparatus is set on a vibration-isolation table.

Full-hard 301 stainless steel and ceramic ($\text{Al}_2\text{O}_3/\text{TiC}$) targets are used as test materials. Before laser irradiation, stainless steel specimens are annealed at 400 $^\circ\text{C}$ for half an hour to relieve initial stresses caused in specimen preparation. Both steel specimens and ceramic specimens are used in pulsed laser experiments, while only steel specimens are used in CW laser experiments. The laser and specimen parameters are summarized in Table 1 and Table 2.

Table 1: Laser and specimen parameters used in CW laser bending

Laser power (W)	1.0 - 2.0
Laser scanning velocity (mm/sec)	8.0 - 33.5
Laser beam diameter (μm)	40.0 - 120.0
Specimen length (mm)	10.0
Specimen width (mm)	1.0
Specimen thickness (μm)	0.1

Table 2: Laser and specimen parameters used in pulsed laser bending

Specimen length (mm)	10.0	Specimen width (mm)	2.0
Thickness of ceramics (mm)	0.36	Thickness of steel (mm)	0.2
Laser pulse energy (μJ)	5 - 120	Pulse repetition rate (Hz)	1 - 2000
Laser beam diameter (μm)	20 - 55	Scanning velocity ($\mu\text{m/s}$)	0.15

3. THEORY AND NUMERICAL MODELLING OF LASER BENDING

The principle of laser bending based on the temperature gradient mechanism can be explained as follows. The laser beam (or the laser pulses) raises the temperature of the irradiated area rapidly, and a temperature gradient is established with the highest temperature at the center of the laser-heated area. During the heating period, compressive stresses arise because of thermal expansion of the heated area and bulk constraint of the materials surrounding the heated area. In high temperature regions, plastic deformation occurs. After laser heating, the surface cools and the material contracts. Due to the bulk constraint, tensile stresses arise in the plastically compressed area. The residual stress/strain at any location in the target is determined from its temperature history and temperature-dependent stress-strain relations of the specimen. At the center of the laser-irradiated area, compressive residual strains are generated, causing the target to bend in the direction toward the laser beam after cooling. Detailed theoretical descriptions of the laser bending process has been presented elsewhere⁵.

The transient temperature and stress fields in the laser bending process and the residual stress, strain, and deformation can only be obtained using numerical techniques. A number of numerical studies of CW laser bending⁷⁻⁹ and pulsed laser bending¹⁰ have been reported in the literature. In these studies, the de-coupled heat conduction equation and thermomechanics equations are calculated using the finite element method. The temperature of the target induced by laser irradiation is computed first. The calculated transient temperature field is then used to calculate the transient stress, strain, and displacement.

In this work, a non-linear finite element solver (ABAQUS*) is employed. The mathematical descriptions of the thermomechanical problem include the strain-displacement relation, force equilibrium, and constitutive relations between the stress and the strain. The total strain rate is assumed the summation of the elastic, plastic and thermal components. The von Mises yield criterion is used. Only bending of stainless steel is computed since the thermal and mechanical properties of ceramics are largely unknown. The steel target is modeled as a linearly elastic-plastic hardening material with temperature dependent properties. With rather simple boundary conditions of this problem, the displacement, strain (rate), stress, and residual strain and stress are calculated. The plastic deformation is computed using the standard incremental strain rate technique.

* HKS, Inc., Pawtucket, RI.

4. RESULTS AND DISCUSSIONS

4.1. Experimental Results

Bending angles are measured at various laser processing conditions. Figure 3a shows the measured bending angle of stainless steel specimens obtained by a single scan of the Nd:YLF laser pulses across the specimen surface in the x-direction. The laser energy per pulse is $80 \mu\text{J}$ and the laser beam diameter at the specimen surface is about $20 \mu\text{m}$. The scanning velocity of the laser beam is kept at a constant of 0.15 mm/sec , and the frequency of the laser pulse is varied between 1 and 2000 Hz . When the laser frequency increases, the distance between two adjacent laser spots decreases. Overlapping between laser spots occurs when the laser frequency is higher than 8 Hz . At a pulse frequency of 200 Hz , overlapping between laser pulses is about 96% , and at a pulse frequency of 2000 Hz , overlapping between laser pulses is over 99% . Figure 3a shows that the obtained bending angle increases with the laser pulse frequency up to 2000 Hz . When the frequency of the laser pulse is higher than 2000 Hz , the bending angle decreases due to the decrease of laser energy per pulse. At a laser frequency of 4000 Hz , the bending angle is about 0.047° , and at a laser frequency of 10000 Hz , the bending angle is only 0.015° .

By adjusting the pulse frequency, the bending angle achieved can be as small as the measurement sensitivity, $\sim 0.33 \mu\text{rad}$. Depending on the length of the specimen, this bending angle corresponds to a movement at the free end of about 10 to 50 nm . Therefore, very small amount of bending or deformation can be obtained with the use of laser pulses. The error bar in Fig.3a represents the repeatability of bending, which is better than 10% of the bending angle.

The bending angle as a function of multiple laser scans at the same location on the specimen is studied. The laser pulse energy and diameter are the same as those in the previous test. The pulse frequency is maintained at 2000 Hz . Figure 3b indicates that scanning over the target surface repetitively would increase bending, but the amount of additional bending achieved is less than what is obtained from a fresh surface. When the same location on the target surface is scanned more than 10 times, no bending or bending in the opposite direction could occur. These results show that the laser induced residual strains could be saturated after a number of laser pulses.

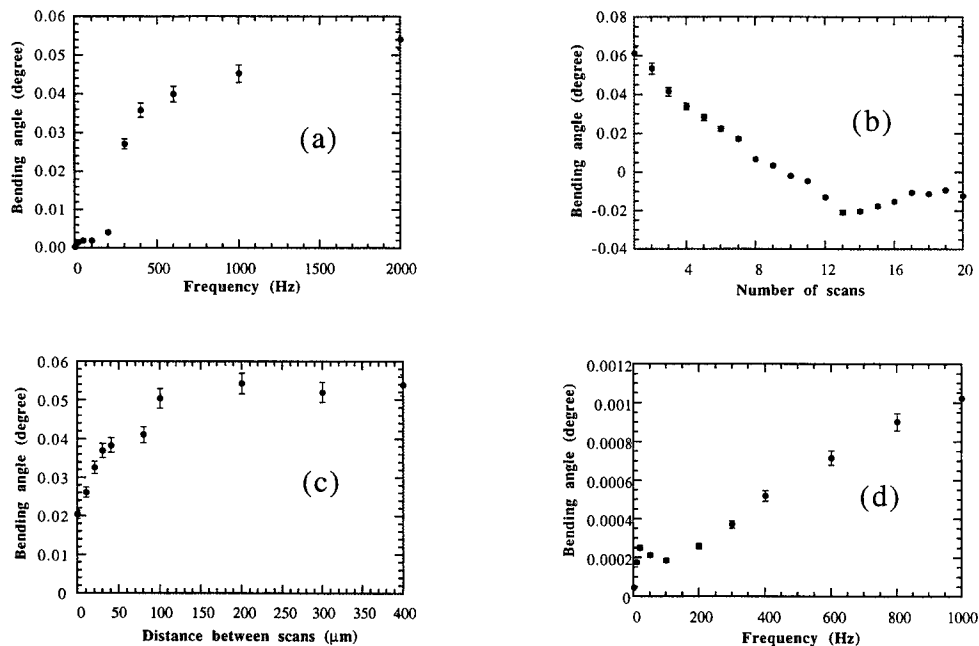


Figure 3: (a) Bending angle of stainless steel as a function of overlapping between laser pulses. (b) Bending angle of stainless steel as a function of number of repetitive laser scans. (c) Bending angle of stainless steel as a function of distances between laser scans. (d) Bending angle of ceramics as a function of overlapping between laser pulses.

If multiple laser scans are not applied to the same location on the specimen, but separated by a distance, then the obtained bending angle is a function of the separation distance. Variations of the bending angle with the distance between two adjacent scans are shown in Fig.3c. After the first scan, the second scan is located 400 μm apart, and then the third scan is 300 μm away to the second one, and so on. Figure 3c shows that the bending angle is almost a constant when the spacing between laser scans is greater than 100 μm . However, when the distance between laser scans is less than 100 μm , the additional bending angle achieved by the new laser scan decreases. This indicates the stress and strain affected zone (including the width of the laser beam) on each side of the laser path produced with the processing condition used in this work is about 50 μm wide.

Similar trends of variations of bending angle with processing parameters are obtained for ceramics. The result of the bending angle of the ceramic specimen as a function of pulse frequency, with laser energy of 80 μJ and a beam diameter of 20 μm , is shown in Fig.3d. The bending angle obtained for ceramics is more than one order of magnitude lower than that of the stainless steel because ceramic specimens are thicker and brittle with limited plastic deformation at elevated temperatures.

For CW laser bending of steel specimens, bending angles are measured at different laser powers, beam diameters and scanning velocities. Figure 4a shows the measured bending angle as a function of laser power at a scanning velocity of 8 mm/s and a beam diameter of 40 μm . The bending angle increases with the laser power because of the increase of the temperature. When the laser power is higher than 1.5 W, the surface is melted. Figure 4b shows the measured bending angle as a function of the beam diameter at a constant laser power of 2 W and a constant scanning velocity of 8 mm/s. The bending angle decreases with the increase of the beam diameter because of the decrease of the laser flux that leads to lower temperatures. At a beam diameter of 40 μm , the obtained bending angle is much higher. Melting occurs when the beam diameter is less than 50 μm .

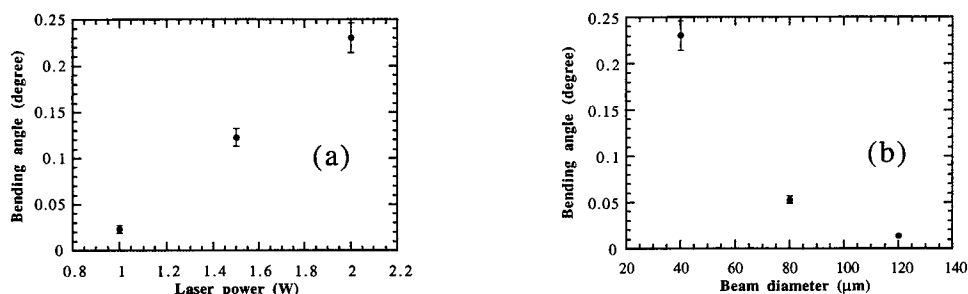


Figure 4: (a) Bending angle as a function of the laser power at a constant scanning velocity of 8 mm/s and a constant beam diameter of 40 μm . (b) Bending angle as a function of the laser beam diameter at a constant laser power of 2 W and a constant scanning velocity of 8 mm/s.

From Figs. 4a, b, it is seen that as long as the peak temperature is kept below the melting point, the repeatability of the obtained bending angle is better than 0.004 degree, indicating that the CW laser can also be used to achieve relatively high precision in bending.

With the laser parameters described above, bending is induced by the temperature gradient mechanism, i.e., bending is caused by the non-uniform residual strains in the direction normal to the specimen surface which in turn are caused by a temperature gradient in that direction. Bending angles are all developed toward the laser beam. If the scanning velocity is reduced, then the buckling mechanism could play a role. The buckling mechanism occurs when the laser scanning velocity is slow and the target is thin, and the heat diffusion length is much larger than the target thickness. Therefore, the region around the laser path is heated almost uniformly in the thickness direction. In this case, similar to a beam under compression, the nearly homogeneously heated section will buckle and the target may be bent either toward or away from the laser beam depending on the pre-curvature of the target and the initial residual stresses. In the experiment, it has been seen that if the scanning velocity is reduced to 0.15 mm/s, the bending direction depends on the pre-curvature of the target. The bending angle is as high as 10 degrees for the first laser scan for a specimen with thickness of 25 μm . Additional bending from subsequent laser scans decreases gradually. After about 40 scans, bending by 90 degrees is obtained.

4.2. Numerical Results and Comparison with Experimental Data

For pulsed laser bending, a two-dimension numerical simulation is conducted. Bending due to scanning of laser pulses is rather difficult to compute in terms of computational costs. The current analysis is based on solving the 2-D heat conduction equation in the cross section of the y-z plane, and solving the transient strain and stress using the plain strain model. To compare the numerical results with experimental data, experiments are modified by focusing the laser beam into a line-shape as shown in Fig. 5.

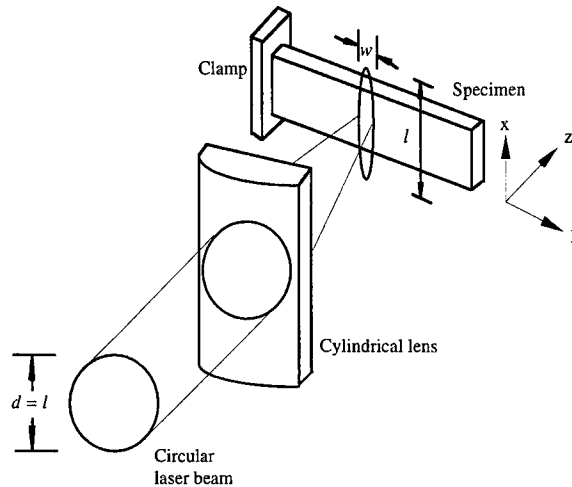


Figure 5: Formation of the line-shape laser beam

The numerical simulation is carried out first using a laser beam width of $29.2\text{ }\mu\text{m}$ and a pulse energy of $118.5\text{ }\mu\text{J}$. The surface temperature at the center of the laser irradiated area is shown in Fig. 6a. The temperature reaches its peak value within the laser pulse duration at $t = 13.7\text{ ns}$. With prescribed laser pulse energy, the maximum temperature obtained is below the melting temperature of steel.

Stress and plastic strain distributions are shown in Figs. 6b and 6c, respectively. The stresses vary from compressive in the region near the surface ($z < 0.7\text{ }\mu\text{m}$) to tensile in the region below $0.7\text{ }\mu\text{m}$ during the heating process. The residual stress near the surface is tensile, but the region below $0.7\text{ }\mu\text{m}$ has a compressive residual stresses in order to keep force equilibrium. Figure 6c shows that the plastically deformed depth increases with time when heat flows into the sub-layer. The final plastically deformed depth is $0.7\text{ }\mu\text{m}$. The residual plastic strain is compressive which explains the formation of the bending angle towards the laser beam.

The beam deflection history is shown in Fig. 6d. Bending is in the direction away from the laser beam during heating and toward the laser beam during cooling. Note that the bending angle resumes to zero from negative at $t = 0.5\text{ ms}$ which corresponds to temperature of 302 K at the center point of the surface, long after the laser pulse stops. The reason is that the laser pulse width is so short that the heat diffusion depth and correspondingly the plastically deformed depth are as thin as $0.7\text{ }\mu\text{m}$, as seen in Fig. 6c. The thicker, cooler neighboring material provides a strong constraint on the plastic zone. The target does not bend to the laser beam until the thermal strain is less than the summation of plastic and elastic strains.

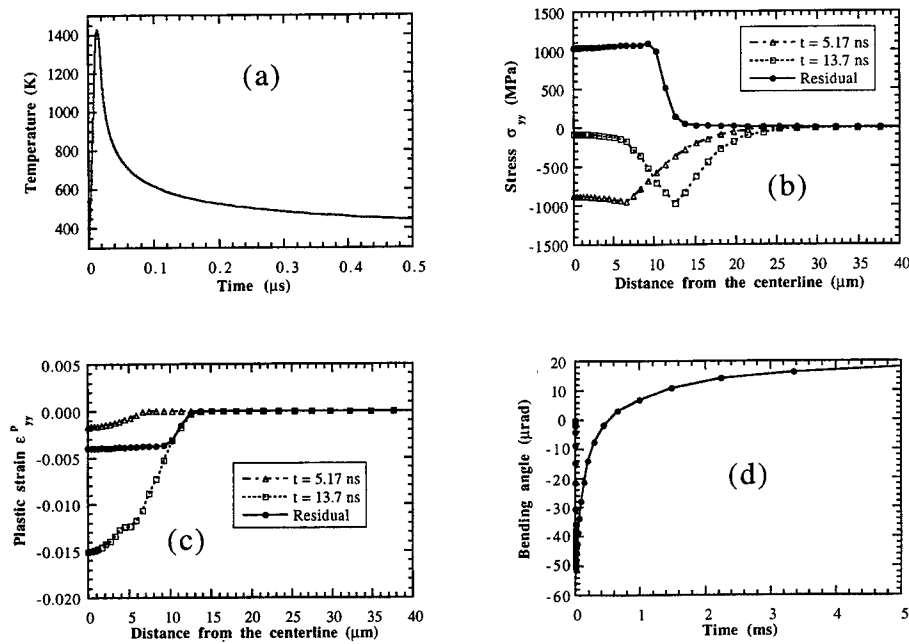


Figure 6: (a) Temperature history of the center point on the irradiated surface, (b) stress, (c) plastic strain distribution along the centerline, (d) the bending history

Figure 7a shows the comparison between the bending angles obtained numerically and experimentally as a function of laser beam width. The laser pulse energy is held at a constant of 118.5 μ J. The bending angle decreases with increasing laser beam width because of decreased laser intensity. It is seen that the calculated values agree with the experimental results within the experimental uncertainty. Figure 7b shows the bending angle as a function of laser pulse energy at a constant laser beam width of 29.2 μ m. Both the simulation and experiment show that the bending angle increases almost linearly with the pulse energy. Again, the calculated values agree with the experimental results within the experimental uncertainty. These agreements validate the theoretical model of laser bending.

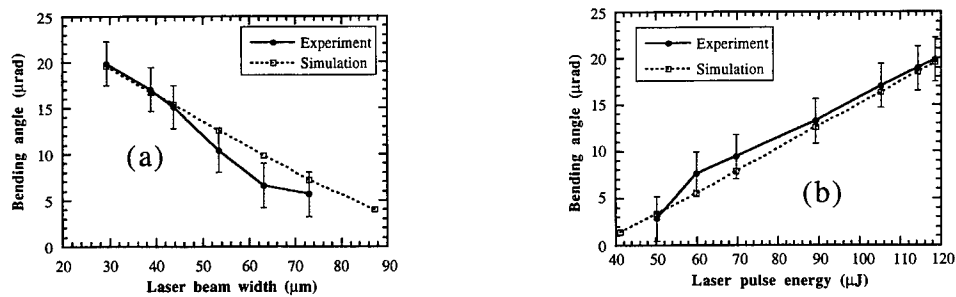


Figure 7: Bending angle as a function of (a) laser beam width at pulse energy of 118.5 μ J, and (b) laser pulse energy at a constant laser beam width of 29.2 μ m

Bending of steel with a CW Ar ion laser is simulated. A fully three-dimensional simulation is possible since the required computer resource is less demanding than that for pulsed laser bending. Results of bending with a laser power of 2 W, beam diameter of 80 μ m and scanning velocity of 8.0 mm/s are shown in Fig. 8. The temperature distributions on top and bottom surfaces along the line $x = 0$ are shown in Figs. 8a and 8b. When the laser beam starts to irradiate from one edge ($y =$

0) and moves forward, the temperature at the other edge ($y = 1$ mm) increases before the laser beam arrives because of heat diffusion. At the beginning of laser heating, the peak temperatures on the top and bottom surfaces increase gradually. When the laser beam moves closer to the other edge and just before the laser beam leaves the target at 0.128 s, the peak temperatures at both the top and the bottom surfaces rise quickly. This is because the boundary at $y = 1$ mm restricts the laser heat flux from being dissipated and thus accelerates the temperature increase in the target.

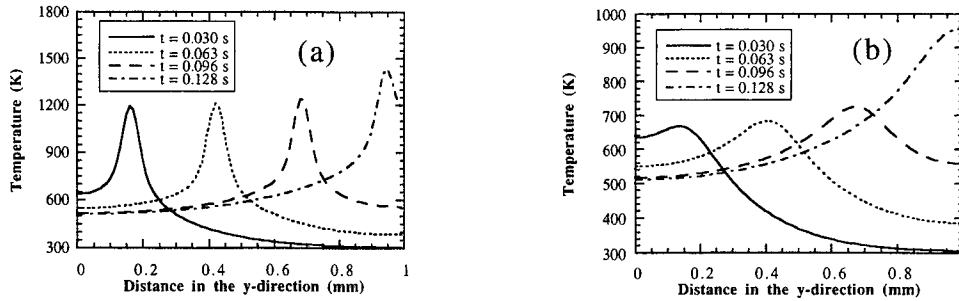


Figure 8: Temperature distributions along the y-direction at $x = 0$ at different times, (a) at the top surface, (b) at the bottom surface

Developments of stresses σ_{xx} and σ_{yy} at the surface along the beam path ($x = 0$) are shown in Figs. 9a and 9b, respectively. At time instants of 0.063 s and 0.096 s, compressive stresses are developed in the regions right ahead of the laser source, which are in the heating period; while tensile stresses are presented in the regions behind the laser source, which are in the cooling period. After the specimen cools down completely to the ambient temperature, the residual stresses along the entire laser path are tensile, while compressive residual plastic strains are distributed at the surface of the workpiece along the laser path at $x = 0$. The residual stress are also shown in Fig. 9. Very high tensile stresses are generated.

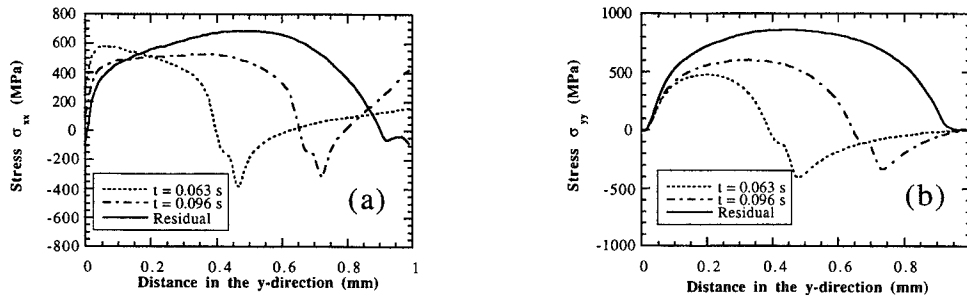


Figure 9: Stress distribution at the top surface along the line $x = 0$, (a) σ_{xx} , (b) σ_{yy}

Figure 10 compares the measured and calculated bending angles at a laser power of 2 W and a beam diameter of 80 μm , but at different scanning velocities. Increasing the scanning velocity decreases the bending angle because of the decrease of input energy. The calculated bending angle agrees with the trend of the measured results, but is about 20% lower.

4.3 Materials' Strength after Pulsed Laser Bending

One major concern of pulsed laser bending is the possible materials' degradation after laser irradiation. Materials strengths before and after pulsed laser bending are measured and compared. With the laser processing parameters used in the pulsed laser bending process, melting and evaporation always occur due to the high laser intensity of every pulse, and a V-shaped groove on the laser heated surface is created because of material removal. The V-shaped groove serves as a stress raiser, or notch, which causes stress to be locally elevated and consequently decreases the mechanical strength.

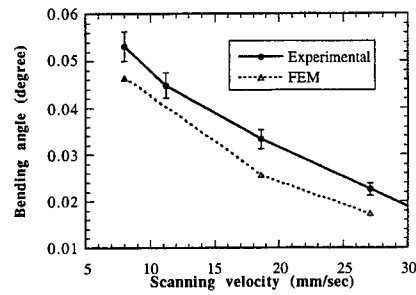


Figure 10: Comparison between the measured and calculated bending angles as a function of the scanning velocity at a laser power of 2 W and a beam diameter of 80 μm

The decrease of the materials mechanical strength due to material removal by pulsed laser ablation is investigated by conducting tension tests on steel specimens and three-point bending tests on ceramic specimens. For steel, a total of 18 pieces of specimens are arranged into six groups with three pieces in each group. One group is untreated and the other five groups are laser-treated at laser pulse energy of 40, 60, 80, 100, and 120 μJ , respectively. A total of 20 pieces of ceramic specimens are arranged into five groups with four pieces in each group. One group is untreated and the other four groups are laser-treated at laser pulse energy of 5, 10, 15, and 20 μJ , respectively. The laser scanning velocity is 1 mm/s and the beam diameters are 50 μm on steel specimens and 36 μm on ceramic specimens.

The measured breaking strength of steel specimens, defined as the ratio of the breaking load and the gross cross-sectional area, is shown in Fig. 11a. The bend strength of ceramics is shown in Fig. 11b. The laser used is the Nd:YAG laser. The breaking strength of steel decreases gradually due to the plastic deformation prior to breaking. At the pulse energy of 120 μJ , the breaking strength of steel decreases by only 16% compared with the untreated specimens. However, the bend strength of ceramics decreases drastically with the increase of laser pulse energy because of brittle fracture, in which the bend strength is determined by the crack length, or the groove depth. After laser treating at the pulse energy of 20 μJ , the bending strength is decreased by 53%, only 47% of that of the un-treated specimens. However, it is noted in the experiment that the Nd:YAG laser has a large energy fluctuation. If a stable pulsed laser (the Nd:YLF laser) is used, even with 20 μJ of laser energy, only surface roughening occurs, and the reduce of the bend strength, which is related to the surface defects or the groove depth, is much lower, less than 15%. Thus, using a stable laser is important for reducing the decrease of the bend strength of the ceramics.

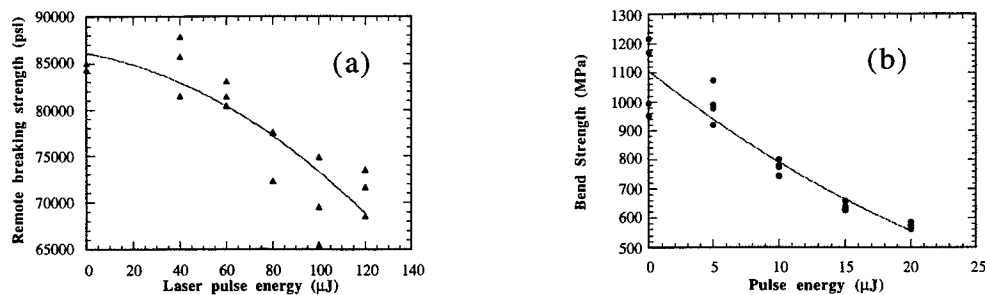


Figure 11: Materials strength tests: (a) breaking strength of steel specimens, (b) bend strength of ceramic specimens

5. CONCLUSIONS

This work demonstrated using pulsed and CW lasers for microscale bending of metal and ceramic components with high precision. Experimental studies were conducted to find out relations between bending angles and processing parameters. Results of numerical simulation agreed with the experimental data, indicating the validity of the bending theory as well as the predictability of the process. Material tests after the pulsed laser bending process revealed that the breaking strength of the steel specimen was not sensitive to the laser-ablated groove, while using a stable laser was necessary to minimize the decrease of the bend strength of ceramics.

ACKNOWLEDGMENTS

Supports to this work by the Purdue Research Foundation, the National Science Foundation, and IBM are gratefully acknowledged.

REFERENCES

1. K. Scully, "Laser Line Heating", *Journal of Ship Production*, **3**, pp. 237-246, 1987.
2. Y. Numba, "Laser Forming of Metals and Alloys", *Proc. of LAMP'87*, pp. 601-606, 1987.
3. M. Geiger, F. Vollertsen, and G. Deinzer, "Flexible Straightening of Car body Shells by Laser Forming", SAE paper 930279, pp. 37-44, 1993.
4. H. Frackiewicz, "Laser Forming Technology," *Fabtech International '93*, Rosemont (Chicago), Illinois, pp. 733-747, 1993.
5. G. Chen, X. Xu, C.C. Poon, and A.C. Tam, "Laser-Assisted Microscale Deformation of Stainless Steels and Ceramics," *Optical Engineering*, **37**, pp. 2837-2842, 1998.
6. M. Geiger and F. Vollertsen, "The Mechanisms of Laser Forming", *CIRP Annals*, **42**, pp. 301-304, 1993.
7. Y.-C. Hsiao, H. Shimizu, and K. Masubuchi, "Finite Element Modeling of Laser Forming," *Proc. of ICALEO'97*, Section A, pp. 31 - 40, 1997.
8. K. Tong, "A Numerical Study on Laser Forming of Titanium Plates," *Proc. of ICALEO'98*, Section E, pp. 131 - 140, 1998.
9. G. Chen and X. Xu, "Experimental and 3D Finite Element Analysis of the Laser Bending Process on Stainless Steel," submitted to *Journal of Manufacturing Science and Engineering*, 1999.
10. G. Chen, X. Xu, C.C. Poon, and A.C. Tam, "Experimental and 2D Numerical Studies on Micro-scale Bending of Stainless Steel with Pulsed Laser," *Journal of Applied Mechanics*, **66**, pp. 772 - 779, 1999.

Fabrication of Microgrooves with Excimer Laser Ablation Techniques for Plastic Optical Fibre Array Alignment Purposes.

Kris Naessens, An Van Hove, Thierry Coosemans, Steven Verstuyft, Heidi Ottevaere*, Luc Vanwassenhove, Peter Van Daele and Roel Baets.

Universiteit Gent / IMEC – Dept. of Information Technology (INTEC)

Sint-Pietersnieuwstraat 41, B-9000 Gent, Belgium.

Tel: +32-9-264-3316, fax: +32-9-264-3593, e-mail: kris.naessens@intec.rug.ac.be.

*Vrije Universiteit Brussel, Lab for Photonics, Dept. of Applied Physics and Photonics (TW-TONA)
Pleinlaan 2, B-1050 Brussel, Belgium.

ABSTRACT.

Laser ablation is extremely well suited for rapid prototyping and proves to be a versatile technique delivering high accuracy dimensioning and repeatability of features in a wide diversity of materials. In this paper, we present laser ablation as a fabrication method for micro machining of arrays consisting of precisely dimensioned U-grooves in dedicated polycarbonate and polymethylmetacrylate plates. The dependency of the performance on various parameters (wavelength, energy density and pulse frequency) is discussed. The fabricated plates are used to hold optical fibres by means of a UV-curable adhesive. Stacking and glueing of the plates allows the assembly of a 2D connector of plastic optical fibres for short distance optical interconnects.

Keywords: Excimer laser ablation, optical alignment, optical interconnect, plastic optical fibre.

1. INTRODUCTION.

A number of technologies are at our disposal for fabrication of microstructures: LIGA (German acronym for lithography, electroforming and molding), deep proton lithography and standard processes from the micro-electronic manufacturing technology. In general these fabrication methods suffer from low throughput, severe environmental requirements and high cost. Injection molding and embossing allow mass fabrication in a very fast way but due to expensive master tools (matrix), these technologies are unsuitable for fabrication of components in small or moderate amounts.

The last decade, excimer laser ablation has acquired the reputation of being a reliable technology for fabrication of microstructures. This non-resist technique does not require clean-room facilities, can be applied on a broad range of materials and is potentially fast since it allows parallel processing by means of mask patterns. It is therefore extremely suited for prototyping, proof-of-principle and fabrication of micro parts in small amounts. Typical applications for laser ablation are via-drilling in printed circuit boards, removal of short cuts in electronic circuitry, wire stripping, fabrication of waveguides, micro-lenses and alignment structures in polymers^{1,2,3,4,5}... In this paper we focus our attention on the latter and investigate the feasibility of the technique for optical interconnect applications. For short-distance purposes as e.g. chip to chip interconnect within racks, POF (Plastic Optical Fibre) can be a very valuable alternative for glass fibre based solutions. Due to its higher numerical aperture and core size in comparison to glass fibre, POF provides enhanced coupling efficiency, and relaxed alignment tolerances. In addition, the fibre is very flexible, allows easy end-facet preparation and is a basically low cost solution. However, at this moment only 1D connectors (MT-like ferrules) are commercially available while the ever-increasing need for higher bandwidth begs for 2D solutions. In this paper we demonstrate the fabrication of such a connector with laser ablation and report on our first results. FIG. 1 illustrates the concept of this 2D connector. It consists of

a number of stacked polymer plates (thickness slightly smaller than 250 micron) with U-grooves in which POFs are fixed at a pitch of 250 micron.

We chose a trench geometry as surface profile for plastic optical fibre alignment since the open upper side allows rather easy insertion of the fibre and the depth of the grooves, defined by the diameter of the fibres (125 micron), is within the limits of what one can achieve with excimer laser ablation by aperture or mask imaging.

The connector can be used for coupling light from a 2D array of RCLEDs into fibres by providing alignment features (e.g. pinholes) on the front side.

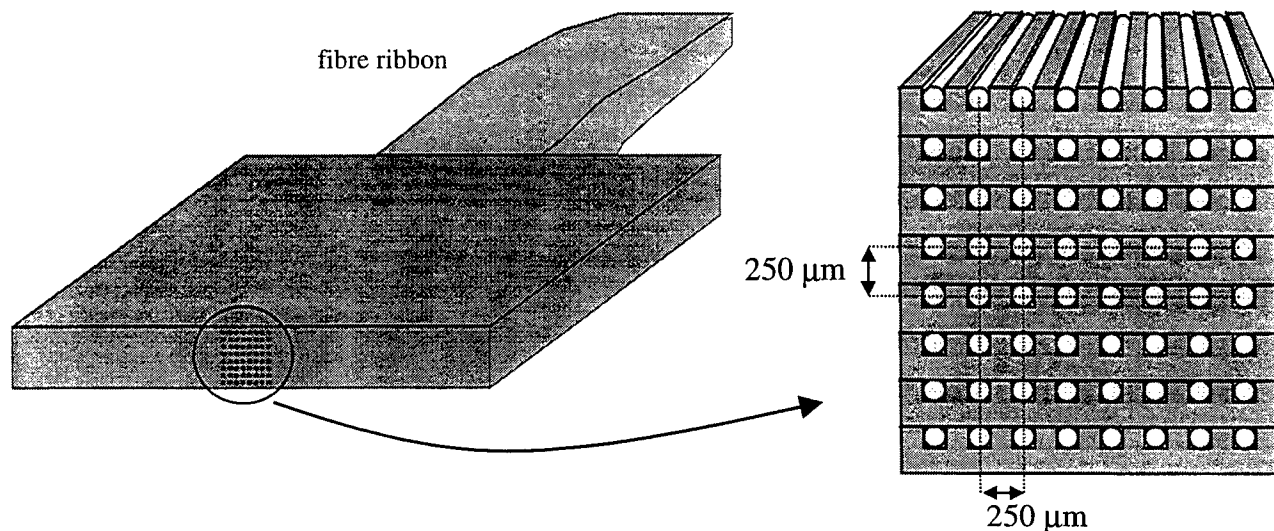


FIG. 1. The 2D connector concept for plastic optical fibres.

2. FABRICATION OF THE GROOVE ARRAY IN POLYMER PLATES.

For fabrication of grooves, we investigated two different kind of polymers, PMMA (PolyMethylMethAcrylate) and PC (Polycarbonate) as well as two excimer-laser source wavelengths: 248 nm (KrF) and 193 nm (ArF). PMMA has a rather low absorption coefficient (2000 cm^{-1} and 200 cm^{-1} at 193 and 248 nm⁷ respectively) which allows the pulse to penetrate deeper into the material (higher ablation rate) but which is also responsible for the higher threshold of the pulse intensity.

We applied two different methods (both common in micro machining) which we will call moving-aperture and mask method. The first implies the use of a suitable single aperture which is imaged onto a substrate that is translated slowly between two or more pulses. The latter involves the imaging of a more complex mask pattern. Depending on the pattern size, scanning might not be necessary anymore, although it may be beneficial to the resulting ablation quality of the trenches: by partially overlapping pulses (slow translation of the substrate), one averages depth variations of the ablated surface due to spatial inhomogeneity of the laser beam. This is only possible when the ablated geometry is translation invariant (e.g. a groove). We will call the combination of scanning and mask projection the hybrid mask method.

After ablation of the grooves, a cleaning step with water and pressurized air is necessary to remove debris (macroscopic particles which did not vaporize and remained in or close to the ablated region) on the polymer surface.

The experiments were carried out with a Lumonics Pulse Master 848 (suitable for both KrF and ArF gas mixtures) and by means of an optical set-up as in FIG. 2. A Molectron J3 pyroelectric joulemeter, put at far distance from the image plane, was used for the energy density measurements after the substrate was removed from the beam path.

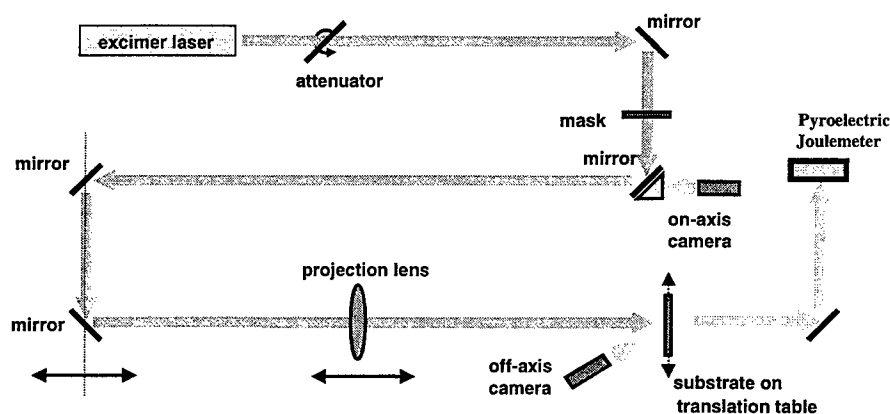


FIG. 2. Laser ablation set-up.

FIG. 3 and TABLE 1 illustrate the results. Both arrays consist of 8 grooves of 126 micron depth and 9 mm length with a pitch of 250 micron. The width has been optimized for carrying an optical plastic fibre taking the finite steepness of the trench into account. Fabrication time for the structure in polycarbonate with the moving aperture method (on the left) is approximately 11 hours while the one on the right (the same array in PMMA with the mask method) takes only 18 minutes. The mask pattern consists of 4 grooves of length 2.5 mm (500 micron on substrate level, taking an imaging from mask to sample with demagnification 5 into account) and is limited in size by the aperture of the projection lens. It consists of a quartz substrate (transparent for both excimer wavelengths) on which a metal pattern has been deposited. The maximum allowed energy density is about 100 mJ/cm^2 . Note that a mask with the full array geometry would result in a fabrication time of only a few minutes.

A number of parameters are at our disposal for ablating this structure: on-substrate energy density and pulse frequency. Both illustrated structures were fabricated at a low pulse frequency (10-15 Hz) and energy (lower than 200 mJ/cm^2). Although increasing each or both parameters speeds up the process, this is not very beneficial to the quality of the structure (roughness and morphology of the groove bottom): at high frequencies and energies we observed the creation of large macroscopic particles at the bottom (several microns to tens of microns) which cannot be removed anymore, and a brown-like colour shift of the polymer which suggests that the remaining material has been thermally damaged. Ablation at 248 nm seems more sensitive to this phenomenon in comparison to the ArF wavelength.

The ablated trench does not have vertical walls due to the imaging principle of an aperture or mask. However, the steepness of the latter can be controlled to a certain extent by the pulse energy density: we observed angles as low as 69 (low pulse intensity) up to almost 81 degrees (high energy densities).

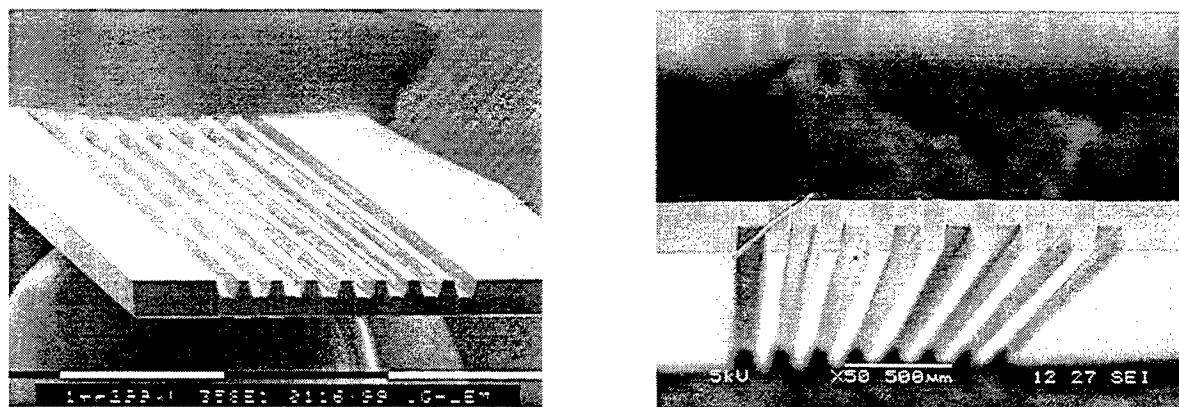


FIG. 3. Array fabricated with moving aperture method in PC at 248 nm (left), array with hybrid mask method in PMMA at 193 nm.

The grooves were not ablated to full depth at one go. Experiments pointed out that a process in two or more steps allows faster ablation and smoother structures than when ablated at once. This can be explained by the steepness of the exposed surface which undergoes ablation: in the first case this angle is much smaller than in the latter. Thus the energy density at this surface remains higher and ablation still takes place without much loss of speed.

Finally the experiments indicated that from an ablation speed and surface morphology point of view, PMMA ablates better at 193 nm (FIG. 4) while PC performs better at 248 nm.

	moving aperture method at 248 nm in PC	hybrid mask method at 193 nm in PMMA
on-substrate energy density	$\approx 178 \text{ mJ/cm}^2$	160 mJ/cm^2
pulse frequency	10 Hz	15 Hz
steepness	72 degrees	78 degrees
number of pulses per spot	282×3	224×2
ablation speed	$\approx 150 \text{ nm/pulse}$	$\approx 280 \text{ nm/pulse}$
RMS roughness	$0.40 \mu\text{m}$	$0.33 \mu\text{m}$
fabrication time	11 hours	18 minutes

TABLE 1. Ablation parameters and experimental results.

The final step in fabrication of the groove plate involves laser cutting of the plate end faces. Since vertical walls are required on the connector side, we used a contact mask in combination with a higher energy density and pulse frequency instead of a projection mask. It basically consists of a semiconductor plate (Si or GaAs) with a very flat facet on one side. A translation stage puts the mask at the desired position above the trenches and then brings it in direct contact with the grooved plate. A $500 \times 500 \mu\text{m}$ laser beam scans along the mask facet and fires higher energy pulses at 50 Hz, producing a rather smooth vertical cut in the polymer substrate (front side of the plate in FIG. 3 and 4, right).



FIG. 4. Surface scan (WYKO) of the groove bottom (left) and a close-up on the groove profile (SEM, right).

3. ALIGNMENT AND FIXING OF PLASTIC OPTICAL FIBRES.

Aligning the fibres in the grooves is performed by means of the ribbonisation set-up in FIG. 5: an array of POFs is tightened while the intermediate stage carrying the polymer plate(s), is translated upwards (Z direction). In this way the fibres are gradually introduced in the grooves by slightly adjusting the position of the substrate in the X, Y directions.

Fixation of the fibres is achieved with a UV-curable adhesive which is flown in the grooves and exposed to a UV-source afterwards. By cutting the fibres one by one along the front side of the plate with the hot knife technique (110°C), one achieves very smooth fibre facets due to a simultaneous cutting and melting process. The polymer plates are now ready to be stacked.

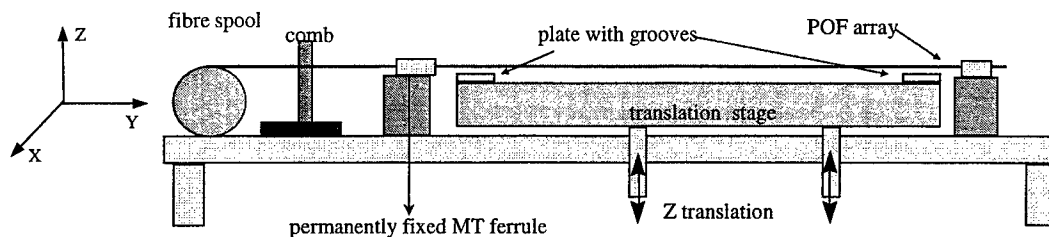


FIG. 5. The ribbonisation set-up.

4. ASSEMBLY OF A 2D CONNECTOR.

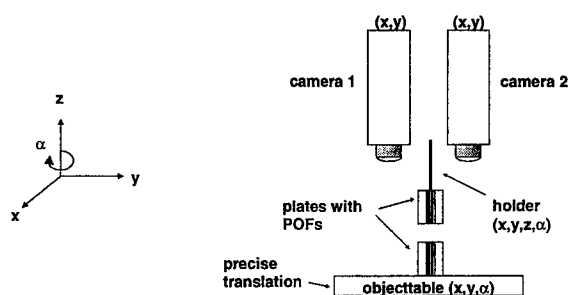


FIG. 6. The 'virtual alignment' set-up.

Accurate stacking of the POF carrying plates is performed with the set-up illustrated in FIG. 6 ('virtual alignment'). By means of two cameras (both with crosshairs alignment features on-screen) and a high precision translation and rotation table the first plate is aligned with the crosshairs (the exact procedure is explained schematically in FIG. 7). After this first substrate is moved over 250 micron the other plate is positioned and aligned along the crosshair pattern. The final step in the stacking process involves glueing the substrates together with an UV-curable adhesive. This procedure can be repeated for every other groove plate. The procedure does not require dedicated alignment features to be put on the plates themselves or fabrication of any mastertool. However it is only suitable at prototyping level since the method is rather time consuming.

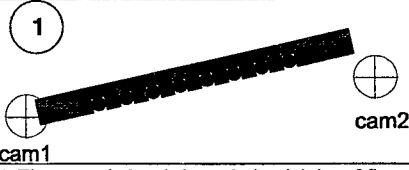
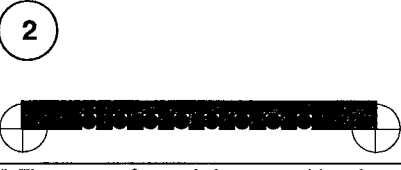
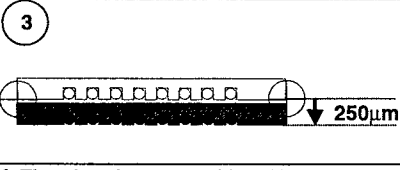
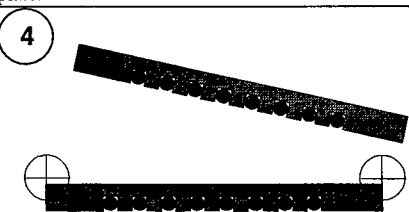
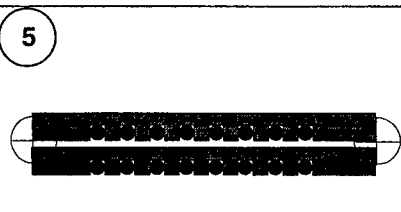
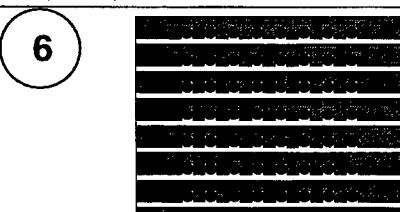
1. The first plate is looked at with two moveable cameras	2. The plate is rotated until its edges are parallel with the crosshairs. Cameras are positioned on the corners of the plate.	3. The plate is moved over an exact distance of 250mm. Lines of the crosshairs are parallel with movements of the translation tables.
		
4. The second plate is brought in vicinity of first plate.	5. The corners of second plate are positioned under crosshairs. Plates are glued together.	6. The other plates are positioned in an analogous way.
		

FIG. 7. The 'virtual alignment' procedure.

5. EXPERIMENTAL RESULTS.

We report here the results on a 2x8 POF ferrule. The exact position of the fibres was determined by coupling light into the loose ends and scan the connector facet with a suitable detector in proximity of the latter. The table underneath represents the accuracies we achieved with our first test plates. For both directions (X,Y) we measured the average value, and the standard deviation of the position of one fibre core towards the adjacent fibre cores. The values of x and y represent the spacing between two adjacent fibre cores in the horizontal and vertical direction respectively (ideal value is 250 micron); Δx and Δy indicate the deviation in position of fibre cores from their ideal position towards the neighbouring fibre in the vertical and horizontal direction respectively. α is the angle between the two plates. FIG. 8 illustrates the definition of the different parameters (left) and shows the facet of two stacked plates with fibre arrays (right). The average values of the upper mentioned parameters are put in TABLE 2.

x_{av}	σ_x	Δx_{ave}	$\sigma_{\Delta x}$	y_{ave}	σ_y	Δy_{ave}	$\sigma_{\Delta y}$	α
248 (250) μm	6 μm	4 (0) μm	7 μm	249.5 (250) μm	-	1.3 (0) μm	4.8 μm	0.15 (0) degrees

TABLE 2. Experimental results (ideal values are written between brackets). The meaning of the parameters is graphically represented in FIG. 8.

The depth of all the grooves was exactly $126 \mu\text{m} \pm 0.5$ micron to make sure each fibre can be buried in them. The measured vertical positions of the fibre cores are in agreement with this accuracy level, taking tolerances on the cladding diameter into account. However, concerning the lateral precision on fibre position in the horizontal direction, there is still room for improvement. The low average pitch (in comparison to the desired 250 micron spacing) between the cores is most probably caused by a slight error on the demagnification of the mask projection unit and can be adjusted rather easily. The deviation in the X direction can be improved as well by making the grooves smaller. This slightly complicates the introduction of the fibres in the grooves and most probably a compromise will have to be made. Another possible source of horizontal misalignment is the fibre cutting process: the hot knife tends to deteriorate the smoothness of the plate facet, and deform and loosen the fibre from the groove in the direction of knife movement (visible in FIG. 8). An alternative method is a second laser cutting procedure for the fibre termination instead of the hot knife technique, followed by a polishing step if required. Both possibilities will be investigated to enhance the accuracy of the core positions.

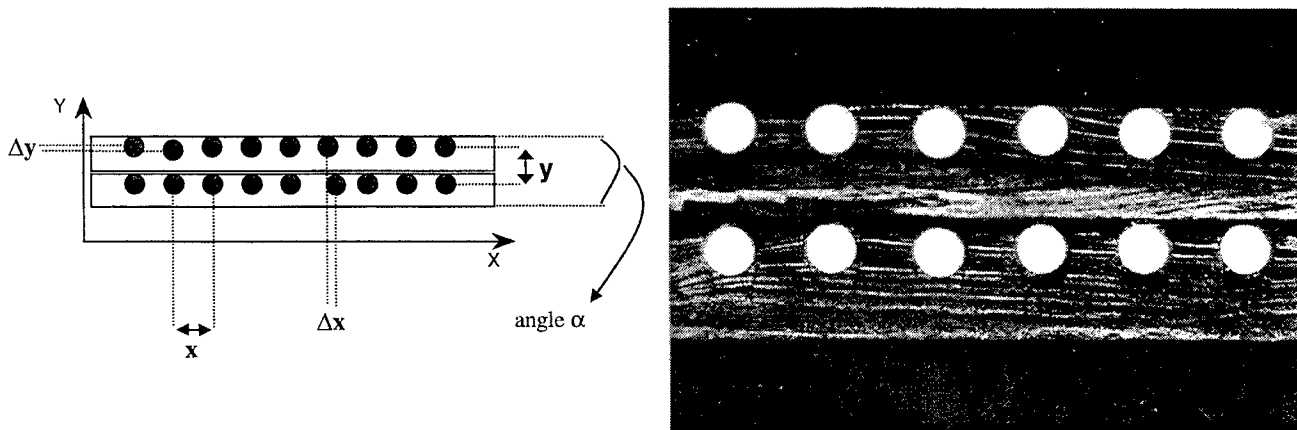


FIG. 8. Definition of the accuracy parameters (left), close-up on 2 stacked plates with fibre arrays (right).

6. CONCLUSION AND FUTURE WORK.

The experiment as explained above demonstrates that the required materials for 2D fibre-connector fabrication with laser ablation are readily available and generate fairly good accuracies. Based on the quality of the grooves, determined by the steepness of the trench profile, accurate control of the depth and the smoothness of the bottom, UV excimer laser ablation proves to be a very valuable technique for fabrication of optical alignment structures in polymer material.

The 2D connector we realised up till now is limited to 2 stacked plates each carrying 8 fibres, but can easily be extended to more stacked groove arrays. The achieved accuracy results are not limited by the ablation process of the grooves itself, and can still be improved by further optimisation of the assembly procedure.

In a next step we aim at the realisation of a 4x8 patchcord including alignment features (e.g. pinholes) which can be accomplished by excimer laser ablation.

7. ACKNOWLEDGEMENTS.

The authors would like to thank the Flemish IWT for equipment support as well as the Belgian DWTC project IUAP-13 and European ESPRIT project OIIC.

8. REFERENCES.

- ¹ Xiaomei Wang, James R. Leger and Robert H. Rediker, *Appl. Opt.* **36**, p. 4660-4663 (1997)
- ² N. A. Vainos, S. Mailis, S. Pissadakis, L. Boutsikaris, P. J. M. Parmiter, P. Dainty and T. J. Hall, *Appl. Opt.* **35**, p. 6304-6319 (1996)
- ³ S. Mihailov and S. Lazare, *App. Opt.* **32**, p. 6211-6218 (1993)
- ⁴ B. L. Booth, J. L. Hohman, K. B. Keating, J. E. Marchegiano and S. L. Witman, *SPIE 1377 Excimer Laser Materials Processing and Beam Delivery Systems*, p. 57-63 (1990)
- ⁵ M. Stiller, *SPIE 1377 Excimer Laser Materials Processing and Beam Delivery Systems*, p. 73-78 (1990)
- ⁶ J. Trehwella and M. M. Oprysko, *SPIE 1377 Excimer Laser Materials Processing and Beam Delivery Systems*, p. 64-72 (1990)
- ⁷ R. Srinivasan and B. Braren, *Appl. Phys. A* **45**, p. 289-292 (1988)

Spectroscopic Investigation of SiO₂ Surfaces of Optical Materials for High Power Lasers

S. G. Demos, L. Sheehan, M. R. Kozlowski
Lawrence Livermore National Laboratory, PO Box 808, Livermore, CA 94580.
Tel.: (925) 423 3388, Fax: (925) 423 2463

ABSTRACT

High quality surfaces of fused silica optical materials were studied using microscopic fluorescence imaging as well as Raman and emission micro-spectroscopy. For as-polished surfaces optically active defect formations were detected on the surface of the material which vary in geometry, relative intensity and concentration depending on the polishing process. A partial correlation of these defects with subsequent laser damage sites was indicated. Following laser-induced damage the Raman and photoluminescence spectra indicated extensive material modification within the damage site. Emission spectra show at least three characteristic luminescence bands centered at 1.9 eV (650 nm), 2.2 eV (560 nm) and ~4.7 eV (~440 nm). Raman scattering indicates that laser irradiation leads to compaction.

Key words: Fused silica, Surface quality, Spectroscopy, Raman scattering.

1. INTRODUCTION

The detection and characterization of surface defects in various materials in which high purity is critical for their performance has led to a great deal of research and development. Various analytical tools have been employed that have provided the means to characterize native and impurity defects leading to continuous improvements in quality and performance of the materials. In the fields of high-power laser development and applications, surface quality of the various optical components is of critical importance. The suitability of an optical material for high power laser applications is determined by its resistance to laser-induced ionization leading to plasma formation, energy deposition and irreversible chemical and mechanical modifications. Basic research studies in this field have been kindled by the desire to produce optical materials with reduced susceptibilities to laser-induced catastrophic breakdown. The performance, cost, and reliability of high-peak-power laser systems such as the National Ignition Facility [1] is significantly affected by laser induced damage issues. The surfaces of optical materials are more susceptible to laser induced damage because substances used during the polishing process lead to additional contamination and impurity or foreign substance incorporation.

Laser-induced damage can be discussed in terms of two key issues: damage initiation by a single pulse and damage growth due to subsequent laser pulses. In the first case, it is believed that damage at relatively low laser fluences is initiated by extrinsic factors. Point defects or defect clusters at which absorption of light can occur at wavelengths longer than the fundamental absorption edge can provide the initiation mechanism for the cascade processes leading to plasma formation and irreversible material modification. Nonabsorbing defects such as cracks and voids cause dielectric discontinuities that enhance the local electric field of an optical wave and/or serve as positive or negative lenses for the incident laser light, thus leading to damage at reduced average fluences [2,5]. The danger posed by absorbing particles has also been recognized and understood [6]. Such defects absorb energy, heat and expand, thereby thermally and mechanically stressing the surrounding material. As material quality has improved, interest has shifted to laser interaction with absorbing nanoparticles [7]. Such nanoparticles may be trapped in the bulk of the material during its production or induced into its surface during the polishing process. Simulations suggest that the buildup of stresses following exposure to laser irradiation can result in mechanical damage to the material. The simulations indicated that the peak temperature grows as the square of particle size for small particles resulting in the formation of micropits with size comparable to the thermal diffusion length [8]. The characteristic luminescence always present during damage indicates localized intense heating and plasma formation.

Material modifications resulting from the intense temperature rise and stresses associated with damage initiation likely play a critical role in growth of the damage site by subsequent illumination. The modified material may be responsible for absorption of energy during exposure to a subsequent laser pulses leading to "re-ignition" of the damage process and expansion of the damaged volume. For large aperture lasers, where some damage initiators will likely always be present, control of the damage growth process is of critical importance.

Fused silica (SiO₂) is one of the most commonly used optical materials for laser systems and the material of choice for near ultraviolet laser applications. SiO₂ is a highly studied material because it finds extensive use in various fields of technological importance such as the semiconductor and telecommunications industries. There is a number of native defects known to be thermodynamically stable in SiO₂ which, in sufficient concentrations, can change the macroscopic properties of the material and create sub-bandgap defect excited states. These changes may determine the laser-damage performance of the material.

In this work, microscopic fluorescence imaging and micro-spectroscopy are utilized to obtain information on defects located on the surface of fused silica optics both before and after laser induced damage to the surface.

2. EXPERIMENTAL SET-UP

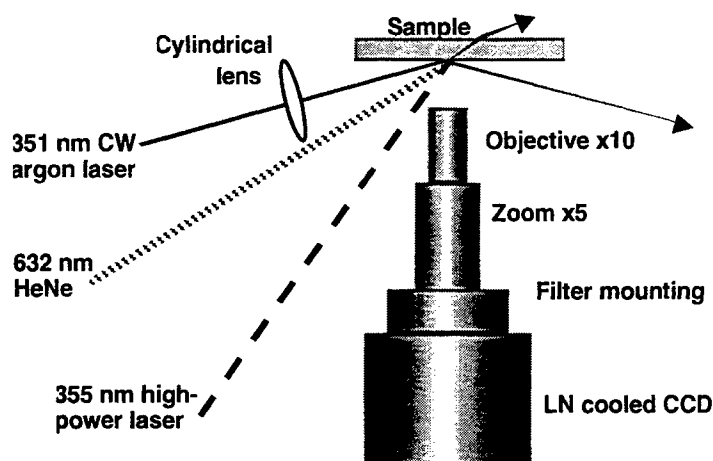


Figure 1. Schematic diagram of the experimental setup to study surface defect formations using microscopic fluorescence imaging and perform in-situ damage testing.

The experimental arrangement is shown in Fig. 1. The 351-nm output beam of an argon laser was used as the excitation source for the acquisition of microscopic fluorescence images of light absorbing defect formations located on the surface of the sample. The incidence angle on the surface of the sample is approximately 20 degrees and the beam is focused on the surface using a 15-cm focal length cylindrical lens. The illuminated area of the sample is imaged using a microscope system that is positioned perpendicular to the surface of the sample. This imaging system is composed of a X10 magnification, 30-mm working distance microscope objective followed by a X5 magnification zoom lens. The images were captured using a liquid nitrogen cooled CCD detector. The desired spectral region of the emitted light is selected using the appropriate optical filters positioned on the filter mounting assembly located between the CCD and the zoom lens. A 632,8-nm HeNe laser is used to illuminate the imaged area of the sample in order to obtain the light-scattering image of the same part of the sample for comparison with the fluorescence images. In addition, the 355-nm third harmonic of a 7-ns pulse-width, Q-switched, Nd:YAG laser is also used to irradiate the imaged part of the sample with high fluence pulses in order to perform in-situ damage testing experiments. All experiments were performed at room temperature using polished fused silica samples obtained from various vendors.

3. RESULTS

To evaluate the ability of the spectroscopic techniques to detect and image defect formations incorporated into the surface of the sample during the polishing process, samples obtained from different vendors were examined. Figure 2 shows

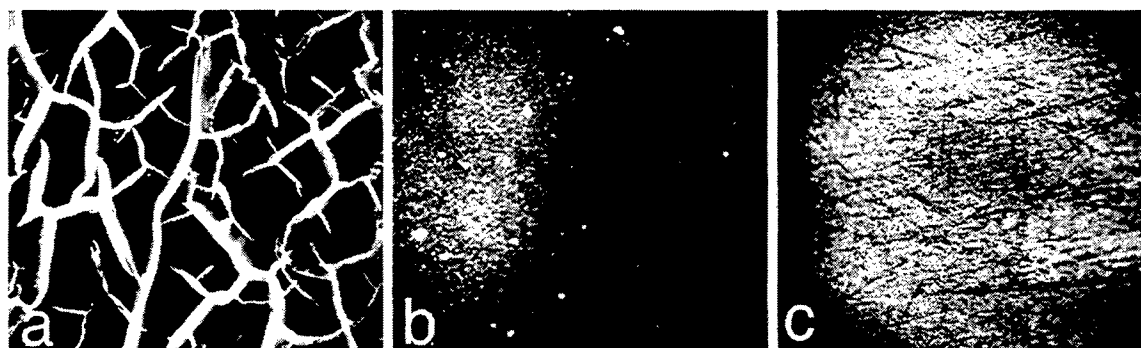


Figure 2: Microscopic fluorescence images of $720 \times 620 \mu\text{m}^2$ sections of the surface of three fused silica samples that were polished using different polishing processes.

microscopic fluorescence images of three samples that are representative of our experimental observations. These three images were obtained using a 540-nm, long-pass filter on the filter mounting. The first sample (see fig. 2a) exhibits strong emission from sub-surface cracks. The luminescence is due to either contamination deposited in the cracks during polishing or to electronic defects created at the crack surfaces. Laser induced damage in this material was predominantly initiated at the surface and the average damage threshold was measured to be 8 J/cm^2 . Fig. 2b shows a section of the surface of a sample that its damage threshold is $\approx 22 \text{ J/cm}^2$. This image contains a large number of defect structures having diameter of the order of $1 \mu\text{m}$ that appear as speckles and a smaller number of brighter features that are also very small in size. The overall emission intensity of the defect structures in the image of fig. 2b is much lower to those of the image shown in fig. 2a. The reduced defect population in the later image is consistent with its higher damage threshold indicating a correlation between the observed defect population and the damage threshold of the material. This correspondence was a common characteristic in all of our measurements. Fluorescence images of samples that exhibited a very high damage threshold contained very few if any highly emissive defect formations. This is demonstrated in fig. 2c where the image of a sample having damage threshold of $\approx 32 \text{ J/cm}^2$ is shown. In this image, the contrast was adjusted to highlight the most luminous features. Due to the absence of intense spots, the image is dominated by the nearly uniform surface emission. In this image, darker features that may be interpreted as scratches are visible.

A key question arising from the images shown in fig. 2 is whether the luminescing defect formations are responsible for damage initiation. To test this possibility, in-situ damage testing experiments were performed. Figure 3 shows the microscopic fluorescence image of the surface of a sample before exposure to high fluence laser irradiation and following

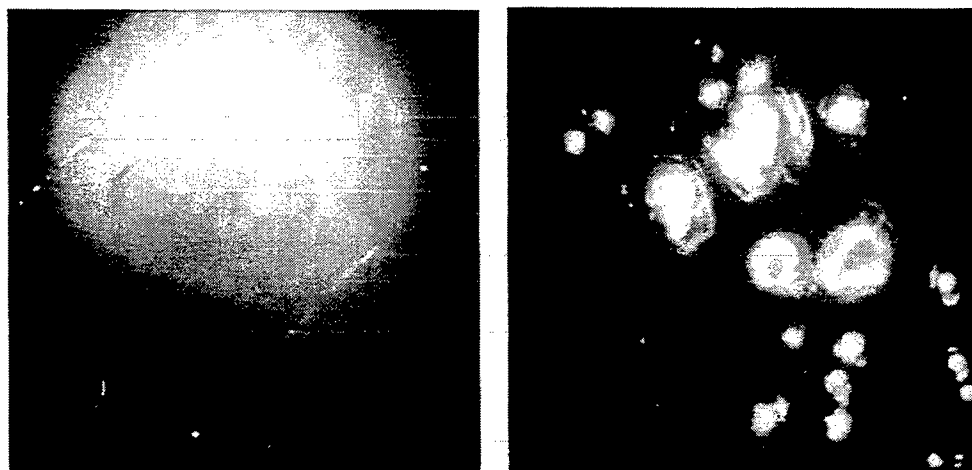


Figure 3: Fluorescence images of the exact area at the surface of an SiO_2 sample before (left) and after (right) laser induced damage.

irradiation with one pulse at $\approx 34 \text{ J/cm}^2$ that created multiple damage sites. From these two images, it appears that there is a good correlation between preexisting defect sites and laser induced damage sites. More specifically, most of the damage sites are at locations where a defect formation was present at the same location in the pre-irradiated image. However, there are damage sites that do not correlate to preexisting defects. This may be because some defects that can initiate damage are very small in size and their presence is hidden in the background emission of the surface. This image also reveals that the damage sites are highly emissive. This indicates the generation of a large population of defects at the damage sites.

The spectral characteristics of the emission from the damage sites were measured using the 351-nm laser beam of an argon laser to photoexcite the sample. A reflecting microscope objective was used to focus the laser beam into the sample and collect the emitted light. This configuration offers spatial resolution of $\approx 3 \mu\text{m}$. Spectra from three different points located in the same damage site are shown in fig. 4a. Figs. 4b and 4c show the light scattering and emission images, respectively, of the damage site. The spectra can be different from point to point. The spectral profiles appear to be composed of three spectra bands having peaks at $\approx 440\text{-nm}$, 560-nm and 650 nm . The difference in the spectral profiles appears to arise from a different contribution to the three main emission bands. The emission image of this damage site when compared to the light scattering image reveals that the emission is concentrated within the damage “crater” while areas where only mechanical damage was inflicted do not emit with equally high intensity (see for example cracked region on right side of damage site).

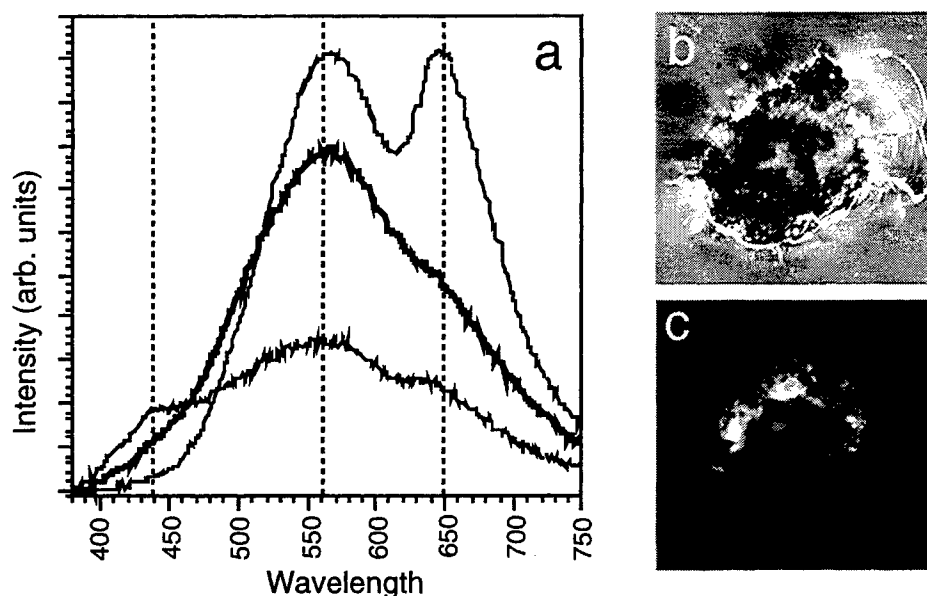


Figure 4: a) Emission spectra from three different points located in the same damage site under 351-nm excitation. b) Light scattering and c) emission images of the same damage site.

This behavior suggests that material modification due to plasma formation, accompanied by high temperature, melting and a shock wave, is different than that due only to mechanical failure.

To better understand the material modifications at the damage site and reveal information regarding structural changes, Raman scattering measurement at the damage sites were performed. The Raman spectrum of SiO_2 contains five spectral lines, three of which are broad and are centered at 436 , 800 and 1070 cm^{-1} (specified as ω_1 , ω_2 , and ω_3) and two sharper peaks at 490 and 604 cm^{-1} (specified as D_1 and D_2) [9]. The Raman lines ω_1 , ω_2 , and ω_3 are associated with the vibrational modes of the tetrahedral SiO_2 glass. The peaks D_1 and D_2 have been assigned to modes of regular rings of Si-O bonds of the SiO_2 tetrahedral that are vibrationally decoupled from the rest of the network [10].

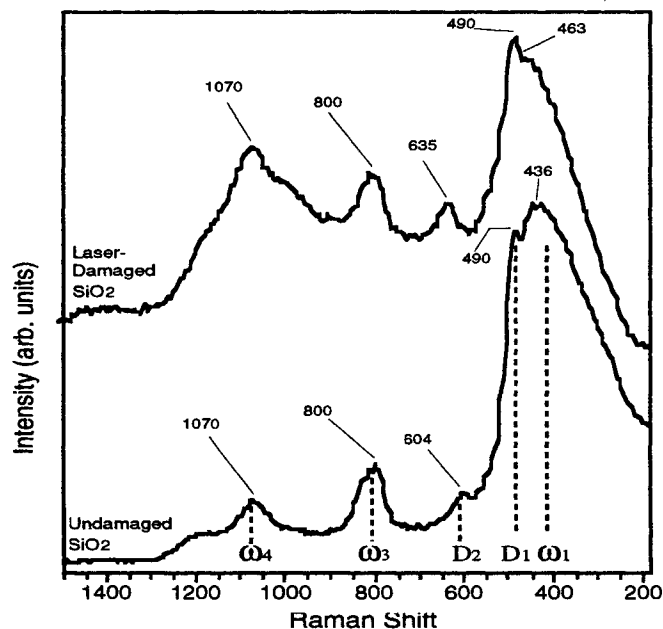


Figure 5: Raman scattering spectra of undamaged and laser damaged fused silica using a single 7-ns, 355-nm pulse. Raman spectra were obtained using 488 nm illumination.

More specifically, D_2 represent the breathing mode of 3- membered ring while D_2 that of a 4- membered ring. Raman spectra from undamaged and from 7-ns, 355-nm laser damaged fused silica are shown in fig. 5. The spectra are different indicating changes in the material structure. The differences in the Raman spectra involve enhancement of the relative intensities of D_2 and D_1 , shifting in frequency of D_2 , reduction of the intensity of ω_1 while ω_4 becomes broader and ω_1 narrower.

4. DISCUSSION

The correlation of a significant number of damage sites to pre-existing luminescent defects indicates that emission imaging may aid in locating and identifying some types of damage precursors. We will next measure the spectral characteristics of the luminescence in an effort to identify the nature of the defects. Once the defects are identified we can work with the optics manufacturers to minimize particular initiator sources.

Following laser-induced damage, the size of the damaged areas continues to grow with subsequent laser pulses likely as a result of increased absorption by generated defect species. The result is plasma "re-ignition" and expansion on subsequent high power laser pulses. The image of a damage site shown in fig. 3b demonstrates how this process leads to chipping and cracking along with removal of material. The scattering pictures defines more of the overall damage that has taken place where the emission image (fig. 3c) reveals the localized nature in the damage crater of the modified material. The strong emission from laser-induced damage sites at the surface of fused silica indicate the formation of excited state levels well below the band-gap of the host material. The spectra show at least three characteristic luminescence bands centered at 1.9 eV (650 nm), 2.2 eV (560 nm) and ~4.7 eV (~440 nm). The red and blue bands are likely associated with the non-bridging oxygen hole center (resulting from broken Si-O bonds) and the E' center (charged oxygen vacancies), respectively. [13,14] The interpretation of the green band is less clear, but it is likely associated with some type of oxygen deficiency in the silica. Potential explanations regarding the origin of this defect band, including silicon nanoparticles [15] and SiOx films [16] are discussed in reference 17.

The Raman scattering spectrum provides additional information on the nature of the laser-damage induced changes in the silica. The narrowing of the ω_1 peak in combination with the increase of the D_1 and D_2 peaks may indicate transformation of the material to a more dense state [11,12]. Such a change in the spectrum would be consistent with a collapse of open-ring configurations (i.e. six-membered rings or larger), common in the three-dimensional random network, in favor of small-ring configurations. 3-ring and 4-ring configurations are high density structures with the density of the D_2 component larger than that of the D_1 . The shift of the D_2 peak may be associated with compaction of the material that leads to partial coupling with the rest of the SiO₂ network. The reason for the increase of the intensity of the ω_4 peak is not clear but it may be associated with a new mode which appears as a shoulder located near 990 cm⁻¹ in the damage-site Raman spectrum. This new mode partially overlaps with the ω_4 which now appears broader and of increased intensity. These insights into the nature of the modified damage region are being used to develop strategies to slow or stop the growth of laser-damage.

ACKNOWLEDGMENTS

This work was performed at Lawrence Livermore National Laboratory under the auspices of the U.S. Department of Energy under Contract W-7405-Eng-48 through the Institute for Laser Science and Applications.

REFERENCES

1. E. M. Campbell, *Fusion Technology*, **26**, 755 (1994).
2. N. Bloembergen, *IEEE J. of Quantum Electr.*, **10**, 375, 1974
3. W. L. Smith, *Optic. Engin.* **17**, 489, 1978
4. S. C. Jones, P. Braunlich, R. T. Casper, X. A. Shen, *Optic. Engin.* **28**, 1039, 1989.
5. B. C. Stuart, M. D. Feit, A. M. Rubenchik, B. W. Shore and M. D. Perry, *Phys. Rev. B.*, **53**, 1749, 1996.
6. J. H. Pitts, *Laser-Induced Damage in Optical Materials: 1985*, NBS Special Publication **746**, 537(1986).
7. M. D. Feit, J. Campbell, D. Faux, F. Y. Genin, M. R. Kozlowski, A. M. Rubenchik, R. Riddle, A. Salleo, and J. Yoshiyama, *Laser-Induced Damage in Optical Materials: 1997*, A. H. Guenther, Ed., SPIE, **3244**, 350 (1998).
8. M. D. Feit, A. M. Rubenchik, D. Faux, R. Riddle, A. Shapiro, D. C. Eder, B. M. Penetrante, D. Milam, F. Y. Genin, M. R. Kozlowski, *Laser-Induced Damage in Optical Materials: 1996*, A. H. Guenther, Ed., SPIE, **2966**, 417 (1997).
9. F. L. Galeener, A. J. Leadbetter, M. W. Stringfellow, *Phys. Rev. B.*, **27**, 1052 (1983)
10. F. L. Galeener, R. A. Barrio, E. Martinez, R. J. Elliot, *Phys. Rev. Lett.*, **53**, 2429 (1984)
11. R. J. Hemley, H. K. Mao, P. M. Bell, B. O. Mysen, *Phys. Rev. Lett.*, **57**, 747 (1986)
12. B. Champagnon, G. Panczer, C. Chemarin, B. Humbert-Labeaumaz, *J. Non-Crystal Solids* **196**, 221, (1996)
13. Y. Hibino and H. Hanattusa, *J. Non-Crystal Solids* **107**, 23, (1988)
14. L. Skuja, *Solid State Comm.*, **84**, 613 (1992)
15. R. Carius, R. Fischer, E. Holzenkampfer, J. Stuke, *J. Appl. Phys.*, **52**, 4241 (1981)
16. S. Zhang, W. Zhang, J. Yuan, *Thin Solid Films*, 1998. **326**: p. 92-98.
17. M. R. Kozlowski, C. L. Battersby, S. G. Demos, *Laser-Induced Damage in Optical Materials: 1999*, SPIE 3902, to be published.

SESSION 11

Laser Microengineering III

Excimer laser micromachining for fabrication of diamond diffractive optical elements

V.I. Konov^a, V.V. Kononenko^{*a}, S.M. Pimenov^a, A.M. Prokhorov^a, V.S. Pavelyev^b, V.A. Soifer^b,
P.Muys^c, E. Vandamme^c

^aGeneral Physics Institute, 38 Vavilov str., 117942 Moscow, Russia

^bImage Processing Systems Institute, Molodogvardejskaya str. 151, 443001 Samara, Russia

^cLaser Power Europe N.V., Meersstraat 138E, B-9000 Gent, Belgium

ABSTRACT

Results of the development of multilevel diamond diffractive optical elements (DOEs) for high power CO₂ lasers are reported. For this purpose, the technique of selected-area laser ablation was applied to create a given phase microrelief on mechanically polished CVD polycrystalline diamond plates. High precision micromachining of the diamond plates was performed using a KrF excimer-laser-based system. The spherical (focal distances $f=50$ mm, $f=100$ mm) and cylindrical ($f=25$ mm) Fresnel lenses with an aperture up to 6×6 mm² were produced and tested with a cw CO₂ laser ($\lambda=10.6$ μ m). The diffraction efficiency of the developed DOE measured in the case of the cylindrical lens was found to be only 1-2% lower than the theoretical value. Also a diffractive shaper (with the aperture 6×6 mm² and the focal distance 100 mm) transforming a Gaussian beam of a CO₂ laser into a uniformly filled-in rectangle was designed and fabricated.

Key words: diamond films, laser ablation, patterning, diffractive optical elements

1. INTRODUCTION

Diffractive optical elements (DOEs) have a wide potential for beam shaping, spatial filtering and other applications.¹⁻⁴ They are based on the change of phase and spatial properties of light waves by diffraction. Our main interest in the fabrication of DOEs is to shape high power laser beams and, particularly, to obtain diffractive elements for operating with high power CO₂ lasers. High-quality CVD diamond films are advantageous for this application because of the unique combination of their optical properties (low optical absorption and weak temperature dependence of the refractive index) with high thermal conductivity.^{5,6} To form a required profile on the diamond surface is however a difficult task which certainly originates from the high hardness and chemical inertness of diamond and the problems related to the diamond processing. The solution that we propose is based on laser ablative etching of the diamond surfaces. This approach, allowing to remove diamond quite easily by local heating and graphitization, have also some additional advantages: no thermal damage to the surrounding areas following ablation (selective-area etching); and opportunity of the precise control of the etched depth and spatial pattern. Therefore, the main goal of the present study is to show that high quality planar optical elements can be constructed from CVD diamond plates using the laser ablation technique.

In Section 2, we describe the system components required for the fabrication and testing of diamond DOEs. In Section 3, we present the procedure of producing the one- and (two-) dimensional diffractive structures. At the first step, basics of the computer design of DOEs are discussed, which were applied for modelling of the diffractive microrelief of different Fresnel lenses and Gaussian beam shaper. Then, results of the laser ablation characteristics of diamond films are reported, and it is shown that the calculated phase microrelief is reproduced on the diamond surface by selected-area laser ablation. Views of the fabricated Fresnel lenses and the diffractive shaper of the Gaussian laser beam are presented. At the final step, the intensity distribution in the focal plane and the beam waist for the Fresnel lenses were measured with a cw CO₂ laser and the obtained results were compared with the data of computer simulations.

*Correspondence: Email: konvit@nsc.gpi.ru; Telephone: 095 132 8151

2. EXPERIMENTAL

Diamond films 300-400 μm thick were grown on polished Si substrates by a CVD technique using a microwave plasma chemical reactor (Model ASTeX-PDS19, 5 kW power, 2.45 GHz frequency).⁷ Upon separation from the substrates, the resulting free-standing diamond plates were cut with a laser into sections of about 1 cm^2 size, mechanically polished, and then were used for laser patterning experiments. One of the diamond samples (supplied by the Laser Power Europe N.V.) was a 800 μm thick diamond plate mechanically polished from both sides.

For selective-area material removal a KrF excimer laser (model EMG 1003i «Lambda Physik»), operating at 248 nm, was used as the laser source in a projection optical scheme (Fig. 1). The pulse duration is 15 ns, and the laser pulse energy is typically ~ 200 mJ, although only a small fraction of the output energy is utilized. The pulse repetition rate is 50 pps, and the pulse-to-pulse instability of the laser energy was 7%. The image of a mask (square) was projected onto the sample surface by a short-focal length objective with linear demagnification of 1:10. A diamond sample placed on a computer-driven X-Y stage was translated controllably (with a minimum translation step of 1 μm) so that a selected region of given coordinates (X,Y) on the diamond surface be irradiated by a certain number of laser shots to achieve the resulting surface profile close to the calculated one. The etching depth was controlled by the laser fluence (E) and the number of laser shots (N). Upon patterning, a laser-graphitized layer was removed from the diamond surface by annealing in air atmosphere at elevated temperatures (520-600°C). An atomic force microscope (AFM "UltraObjective", Carl Zeiss), a scanning electron microscope, and the Wyko surface profiler based on phase-shifting interferometry were used to characterize the depth and quality of the produced surface microstructures.

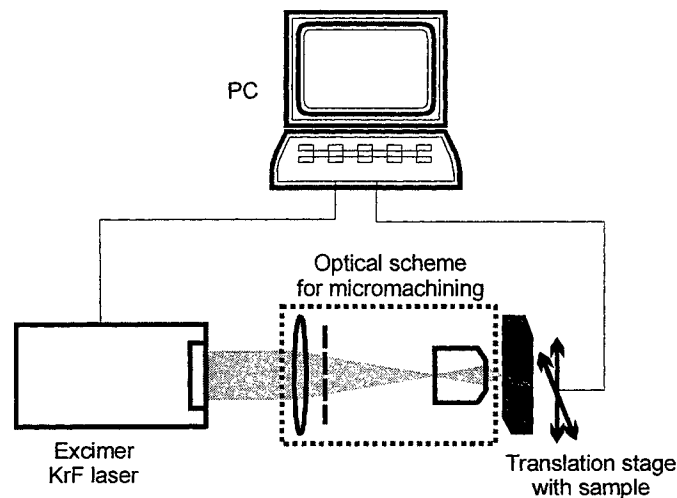


Fig. 1. Schematic view of the experimental setup for laser treatment of diamond films.

A multimode cw CO_2 -laser with an output power ~ 20 W and with quasi-Gaussian distribution of the intensity was used for tests of the produced optical elements. The radius of the beam was $w_1=1.55$ mm. The radiation from this laser, time-modulated by a chopper, was recorded by a pyroelectric detector. In some tests a single-mode cw CO_2 -laser ("Ultra Lasertech") with an output power of about 4 W was also used. The laser radiation with the beam radius $w_2=1.76$ mm was detected by the IR camera "Pyrocam" (Spiricon Co.) with matrix pixel size of 100 μm .

3. RESULTS

3.1. Basics of computer design of diamond Fresnel lenses

A traditional optical element is described by the smooth phase function $\varphi(\vec{u})$ (Fig. 2), where $\vec{u}=(u; v)$ are the coordinates of a point placed in the element plane.¹ The thickness of such an optical component may be as high as thousands of

wavelengths. Accordingly, the phase values φ are varied from 0 to thousands of 2π . A planar optical element can be constructed using the reduction of the phase function to the interval $[0, 2\pi)$ (Fig. 2).

The phase function of a Fresnel lens defined on the aperture D in paraxial approximation is described as follows:¹

$$\varphi(u, v) = \varphi(r) = -k \frac{u^2 + v^2}{2f}, \quad r \leq \frac{D}{2} \quad (1),$$

where $k=2\pi/\lambda$ is the wave number and f is the focal length.

The reduced phase function $\text{mod}_{2\pi} \varphi(u)$ to the interval $[0, 2\pi)$ divides the aperture into the Fresnel zones (Fig. 2). The width of a single zone Δ_j of the flat diffractive element is defined by the condition of the phase change by 2π :

$$\varphi(r_j) = -2\pi j, \quad \Rightarrow \quad \Delta_j = r_j - r_{j-1}, \quad j = \overline{1, J}, \quad r_j = \sqrt{2\lambda f j} \quad (2)$$

Thus, the zone width decreases towards the periphery of a lens. The height of a microrelief is determined by the following expression:

$$h(r) = \frac{\lambda}{n-1} \frac{1}{2\pi} \text{mod}_{2\pi} \varphi(r). \quad (3)$$

where n is the refraction index.

Two principal requirements, which would provide the performance of diffractive optical elements with the M -level microrelief approximation (Fig. 2), must be fulfilled in the course of laser surface structuring. First, the spatial (lateral) resolution of the surface structures should be better than Δ_{\min}/M , where Δ_{\min} is the minimum width of a Fresnel zone, i.e. of that placed at the periphery of a lens (see eq.(2)). Second, the deviation from the height h_{\max}/M should be less than 10%. For diamond ($n=2.4$) the maximum height of a DOE microrelief is $h_{\max}=7.57 \mu\text{m}$. The parameters of the designed diffractive optical elements (which were then fabricated by laser ablation) are shown in Table 1. Computer calculations of the phase profile were performed by solution of the inverse diffractive task using software "QUICK-DOE".⁸ The required spatial characteristics of the designed 1-D and 2-D DOEs (presented in Table 1) can be easily realized by the laser ablation technique, as the spatial selectivity of laser etching of diamond extends to micrometer range and the accuracy of material removal is controlled by a choice of the incident fluence and the number of shots.^{9,10}

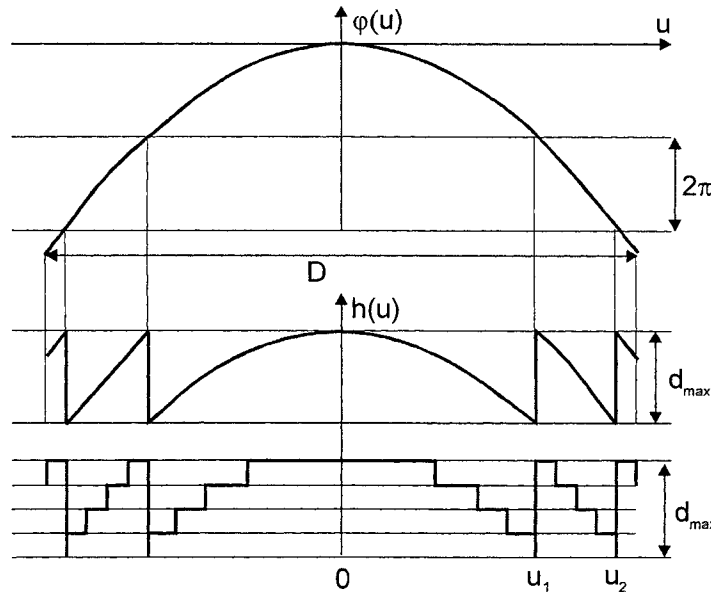


Fig. 2. The reduction of the smooth phase function (upper) to the interval $[0, 2\pi)$ (center) for a Fresnel lens and subsequent four-level approximation of the reduced phase function $\text{mod}_{2\pi} \varphi(u)$ (lower).

Table 1. Parameters of CVD diamond diffractive optical elements.

	cylindrical lens	spherical lenses		beam shaper
Focal length f , mm	25	100	50	100
Operating wavelength λ , μm	10.6			
Amount of levels of approximation M	4	8		
Aperture, mm^2	4×4	6×6		6.6×6.6
Required spatial resolution Δ_{min}/M , μm	36	49	35	
Required deviation of height, $0.1 \cdot (h_{\text{max}}/M)$, nm	200	100		

3.2. Laser microstructuring of diamond plates

One of the main tasks in the laser ablation study of diamond is to determine the ablation characteristics for a particular diamond plate to be further used in laser patterning experiments. The first reason is that the ablation character (value of the ablation threshold and the ablation rate-on-fluence behavior) depends strongly on the physical properties of a CVD diamond material.¹¹ And, secondly, since the ablation depth is determined as a product of the ablation rate and the number of laser shots, the exact data on the ablation rate-on-fluence dependence is needed to reach the resulting surface profile of a DOE with a high accuracy (see Table 1).

The ablation rate was measured as a function of the KrF laser fluence for the laser spot size of $40 \times 40 \mu\text{m}^2$. A set of the $40 \times 40 \mu\text{m}^2$ craters were etched at the diamond plate surface under variation in the incident fluence and number of shots, and then the depth of the craters was measured with an optical microscope (Carl Zeiss). Figure 3a shows the dependence of the ablation depth on the number of laser shots for the energy density varied from 10 to 60 J/cm^2 . It is seen that at a given fluence the depth increases linearly with the number of shots (at least, to the depth of 25–30 μm). These experimental plots are taken to determine the average ablation rate at a fixed laser fluence (Fig. 3b). It can be inferred from the ablation rate-on-fluence dependence that, if the ablation depth were regulated only by variation in the number of shots, the required accuracy of the microstructure height would be provided in the range of low fluences; e.g., for $E=10.7 \text{ J/cm}^2$ the etching rate is $v=95 \text{ nm/pulse}$. However, in this case the productivity of laser treatment is rather low, making it time consuming to fabricate a diamond DOE with the parameters shown in Table 1.

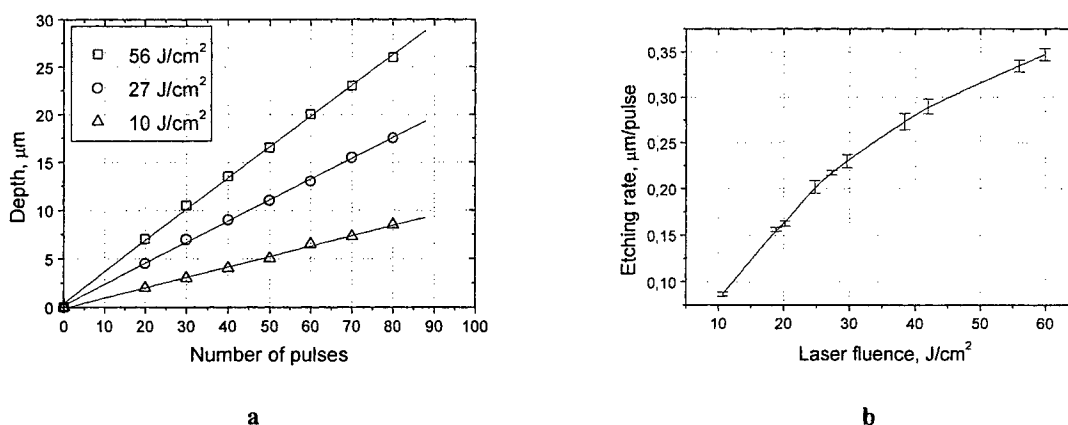


Fig.3. Characteristics of laser ablation of a diamond film by KrF excimer laser: (a) ablation depth vs number of pulses at different fluences, and (b) ablation rate vs laser fluence.

To increase the processing rate requires higher ablation rates (higher laser fluences) but, if $v > 0.1 \cdot h_{\max}/M$ (see Table 1), a proper optimization of irradiation condition is needed for a simple equality, $v \cdot N \cong h_{\max}/M$, be fulfilled. For manufacturing of the 2-D Fresnel lens, we selected the etching rate of 235 ± 5 nm/pulse obtained at $E = 30.5$ J/cm². The scatter in the ablation rate values is defined by the accuracy of the etching depth measurements and variations in the pulse energy. It should be noted that the ablation rate measurements (Fig. 3) were performed for the number of laser shots in the range $N = 30-100$, whereas the formation of the first-level relief structures requires only four laser shots. It is clear that the influence of the pulse-to-pulse instability (7%) of laser energy on fluctuations in the ablation depth increases when a small number of laser shots is applied, and this can cause some deviations of the depth of individual craters as compared with the average depth of the structures of the same approximation level. The degree of the influence of laser instability on the depth fluctuations of the M-level structures (particularly, for $M=1$) can be found from optical tests of a final element.

After optimization of the laser irradiation conditions, the designed diffractive microrelief of the lenses and beam shaper were reproduced on the surface of diamond plates. The surface profile of the laser-etched relief of the 1-D lens is shown in Fig. 4, and the resulting surface pattern etched over 4×4 mm² area consists of a set of parallel channels of various widths and depths. The patterning was done as follows: a rectangular laser spot of 40 μ m width was scanned in one direction (along X axis) with partial overlapping of successive spots to etch a 40- μ m-wide channel of a required depth, then after a given shift of the sample in the perpendicular direction (along Y axis) the scanning was repeated to form a new channel and so forth.

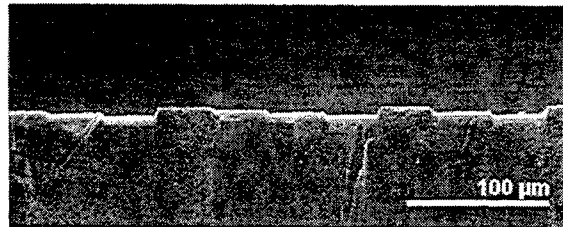


Fig. 4. A part of the surface profile of the diamond four-level cylindrical lens.

The 2-D micromachining of diamond plates was carried out in a different mode. The calculated surface relief for the eight-level DOEs is illustrated in Figs. 5a, 6a, and 8a. To reproduce it on the diamond surface, the diamond sample was discretely scanned back and forth, and the laser-induced relief consisted of a raster of square regions of 40×40 μ m² size and various depths as shown in Figs. 5b, 6b, 6c, and 7.

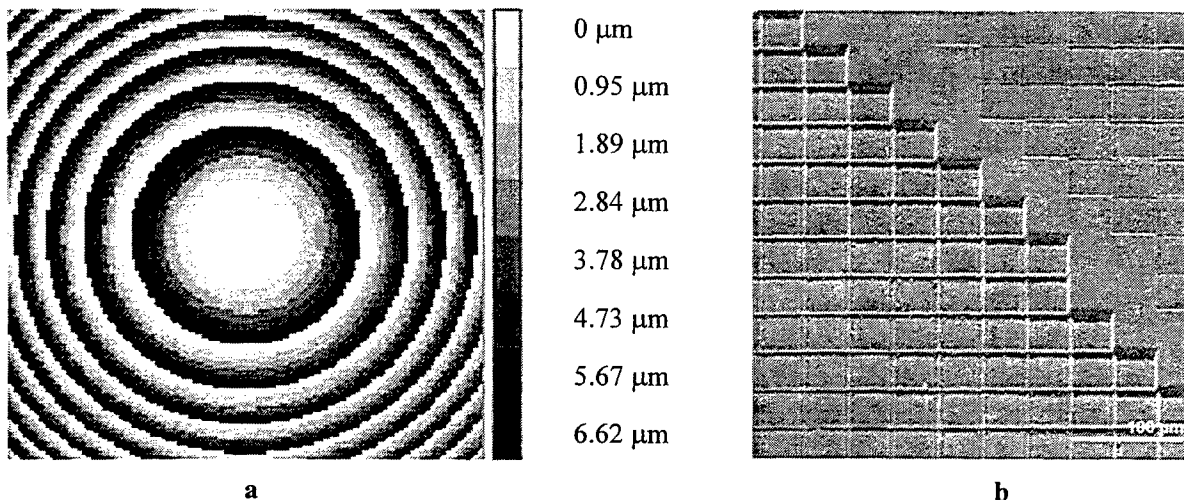


Fig. 5. The diamond eight-level spherical lens ($f=100$ mm): (a) a gray-tone picture of the designed phase relief and (b) SEM image of the laser-produced structures.

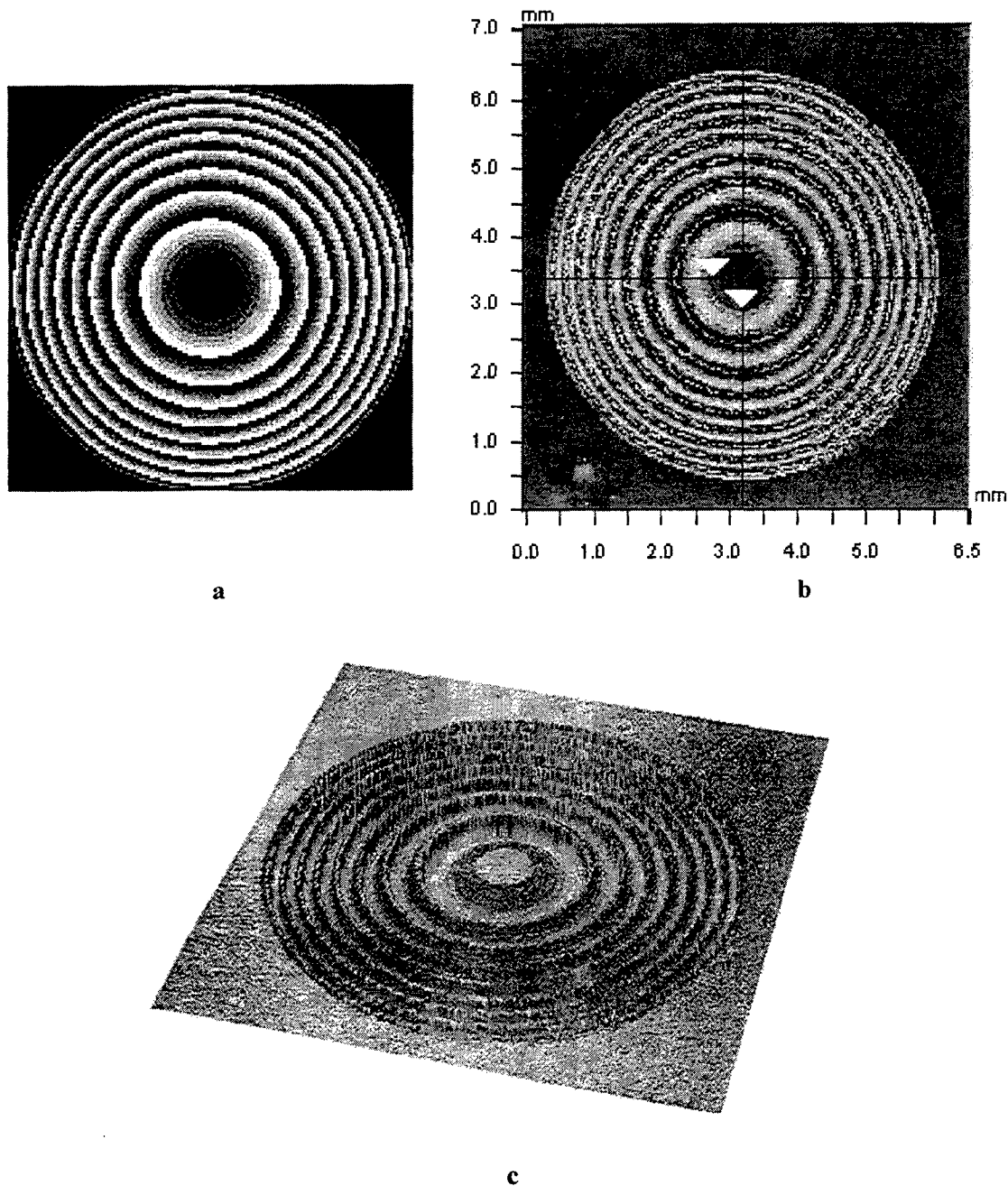


Fig. 6. The diamond eight-level spherical lens ($f=50$ mm): (a) a gray-tone picture of the designed phase relief, (b) 2D and (c) 3D interferometer microscope images of the laser-produced structures.

A more detailed view of the central part of the manufactured diamond eight-level spherical lens ($f=50$ mm) characterized by the interferometer microscope (IM) is shown in Fig. 7a. A surface profile corresponding to the central line across the IM image is plotted in Fig. 7b. The depth of the first-level ablated region is about $1.1\text{ }\mu\text{m}$ that is close to the required depth of $0.95\text{ }\mu\text{m}$. This difference is likely caused by oxidative removal of the graphitized surface layer (the IM examination was done after annealing), the thickness of which was estimated to be around 200 nm .¹²

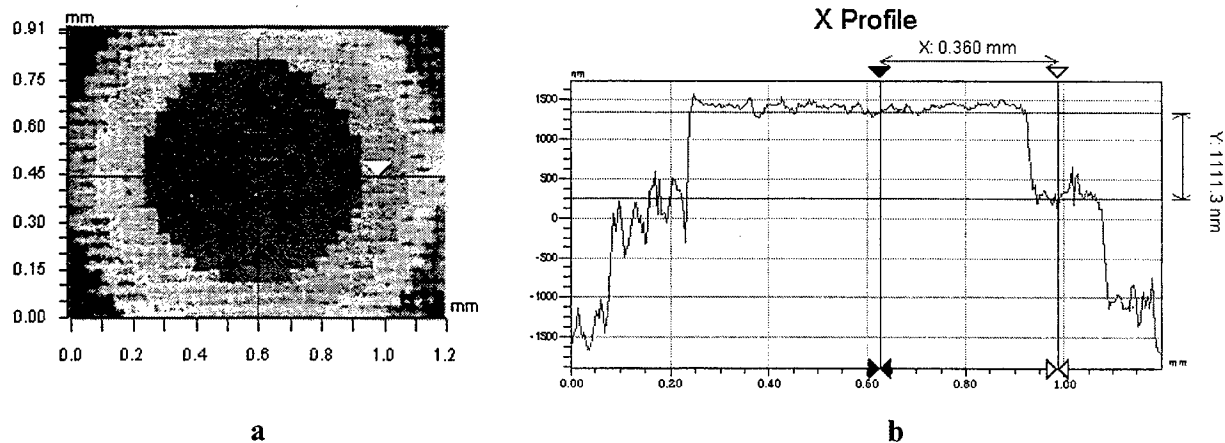


Fig. 7. The central part of the diamond eight-level spherical lens ($f=50$ mm): (a) 2D interferometer microscope image and (b) corresponding surface profile along the X direction.

In addition to the Fresnel lenses a diffractive optical element that converts a Gaussian beam with the radius of 1.85 mm into a uniformly filled-in rectangle was produced.⁴ The parameters of the shaper are presented in Table 1 and the size of the rectangle is 1.75×3.5 mm². The computer-designed phase relief is shown in Fig. 8.

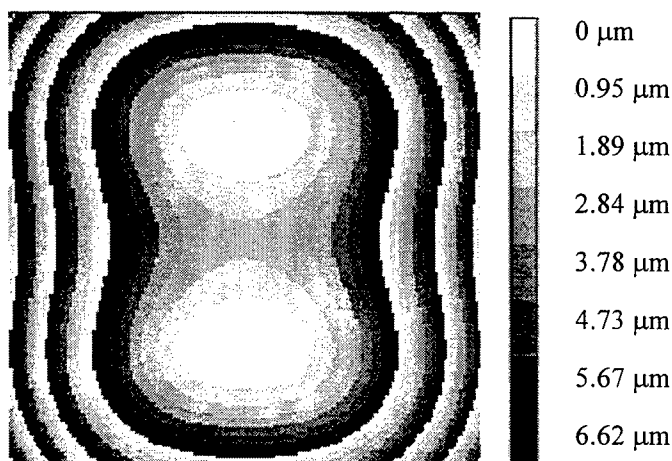


Fig. 8. The gray-tone picture of the designed phase relief of diamond eight-level diffractive shaper transforming a Gaussian beam into a uniformly filled-in rectangle.

The roughness analysis of the original and laser-etched diamond surfaces carried out with an AFM confirmed that the laser-ablated surface (inside 40×40 μm² squares) was very smooth. A typical AFM image of the boundary surface areas in the "second-level" 40×40 μm² squares is shown in Fig. 9. The initial roughness of the mechanically polished diamond surface was $\sigma_0=20$ nm. As a result of laser etching, the roughness increased to $\sigma=40 \div 50$ nm. Optical losses due to surface scattering can be evaluated by the expression:

$$T=T_0 \cdot \exp[-(4\pi\sigma/\lambda)^2] \quad (4)$$

where T_0 is the transmission of the polished plate, T is the transmission after laser surface processing, and λ is the wavelength. So, rough estimation of the increase in scattering losses after laser treatment is 0.3%. Note that formula (4) takes into account only incoherent light scattering. The presence of the periodical relief substructures between adjacent squares

(Figs. 5b and 7b) may be responsible for additional diffractive optical losses, which should be pronounced in an increased intensity of non-zero diffractive orders.

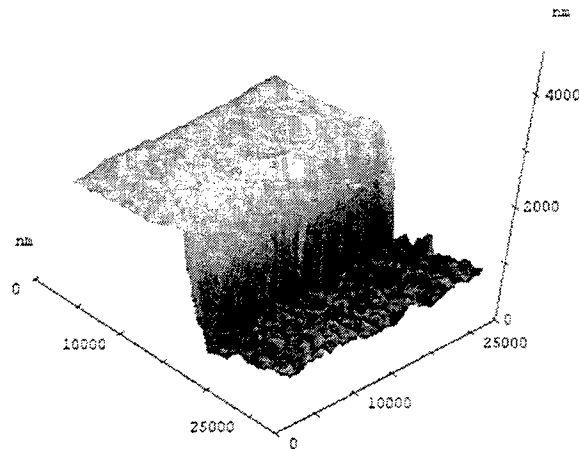


Fig. 9. AFM image of the second level of the 2D element profile.

During laser treatment, a thin graphite-like layer is formed at the ablated diamond surface. Evidently, this layer must be completely removed, as even a very thin layer of the absorbing graphitic material decreases both the optical transmission and damage threshold of the optical element by CO₂ radiation. In our previous papers^{13,14} it was reported that this absorbing surface layer can be effectively removed either by hydrogen plasma etching or by oxidation in air at elevated temperatures. In the present study, the laser-structured diamond plates were annealed in ambient air at 520-600°C for some time at each temperature. The transmission of the samples was measured at the CO₂ laser wavelength after each annealing step in 1 hour (Fig. 10). The obtained results showed that at the annealing temperatures ≤ 600°C the oxidative removal of the graphitized surface layer is a time-consuming process. Comparison of these data with those reported in Refs. [13,14] indicates that the oxidation stability of the laser-graphitized diamond surface is strongly affected by the laser irradiation parameters. It should be noted that further increase of the annealing temperatures is limited by oxygen-induced surface graphitization of diamond (which occurs above ≈900 K).¹⁵ This means that the laser-graphitized lasers formed at the diamond surface under high irradiation intensities and characterized by a high oxidation stability should be removed by plasma etching techniques.

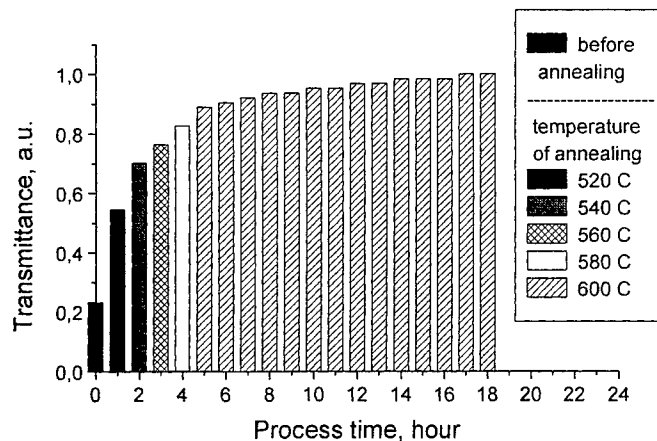


Fig. 10. Evolution of the optical transmission of a laser-structured diamond plate in the course of heat annealing in ambient air.

3.3. Testing of Fresnel lenses

Most of the optical tests of the cylindrical and spherical lenses were performed using a multimode CO₂ laser with the quasi-Gaussian distribution of the intensity ($w_1=1.55$ mm). In the focal region of the cylindrical lens the intensity distribution $I(u)$ retained the Gaussian form (Fig. 11a). The width w_u of the transformed beam was determined as half the distance between two points at which the radiation intensity decreased by the factor e^2 compared with the maximum value. A computer calculation of the intensities in various planes of the focal region of the lens was performed by numerical calculation of the Fresnel-Kirchhoff integral¹⁶ for the fundamental TEM₀₀ mode of laser beam illuminating an optical element. The increase of the beam width $w_u^{\text{exp}}=70.8$ μm , compared with the calculated value $w_u^{\text{theor}}=65.8$ μm , can be attributed, first, to deviations of the lens profile from the calculated one and, second, to the presence in the test laser beam of high-order modes with divergence larger than that of the fundamental mode. The experimental value of the diffractive efficiency of the cylindrical lens was 78% which is close to the theoretical estimation of 79-80%. The depth of focus was defined as the distance between points on the optic axis at which the radiation intensity fell by a factor of 2 compared with the maximum value: this depth was $\Delta f=5$ mm.

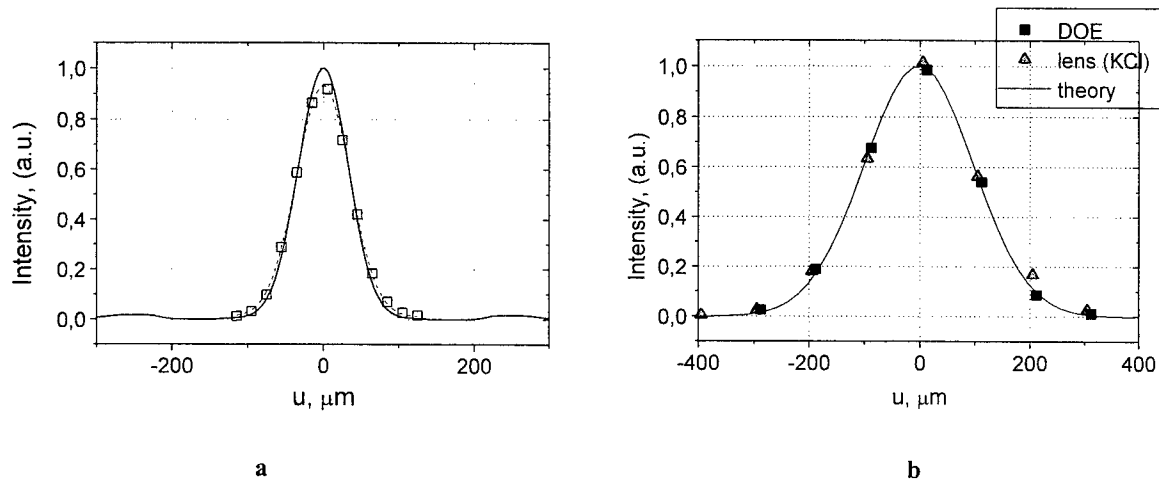


Fig. 11. The distribution of the CO₂ laser radiation intensity $I(u)$ in the focal plane of the (a) cylindrical lens and (b) spherical lens ($f=100$ mm): experimental characteristics of the investigated DOEs (squares), of a conventional KCl lens ($f=100$ mm) (triangles), and corresponding results of computer simulation for ideal diffractive elements (solid curve). A multimode CO₂ laser with the beam radius $w_1=1.55$ mm was used.

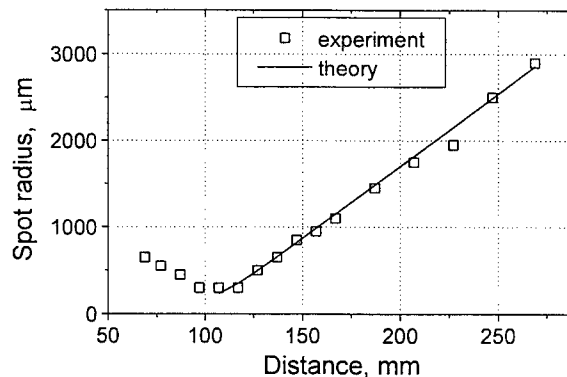


Fig. 12. The dependence of the Gaussian spot radius on the distance z from the plane of the spherical Fresnel lens (the focal length $f=100$ mm). A single-mode CO₂ laser with the beam radius $w_2=1.76$ mm was used.

The data of optical testing of the diamond spherical lens is also in good agreement with the results of computer simulations as well as with optical tests of a conventional spherical KCl lens with the same focal distance $f=100$ mm (Fig. 11b). Plotted in Fig. 12 is the waist profile of the laser beam in the focal region of the investigated 2-D DOE. The results obtained with a single-mode CO₂ laser are very close to those of theoretical simulations for an ideal lens with $f=100$ mm.

4. CONCLUSIONS

CVD diamond diffractive optical elements (Fresnel cylindrical and spherical lenses, beam shaper) have been fabricated by laser structuring of the diamond surface. The diffraction efficiency of the CVD diamond cylindrical lens was found to be only 1-2% lower than the theoretical prediction. The correlation between the experimental characteristics of the lenses and the results of numerical simulation suggests that the laser processing provides adequate accuracy for the formation of DOE microrelief. Thus, our investigations have shown that a laser ablation technique is a promising method for manufacturing of low loss multilevel diamond IR diffractive elements.

ACKNOWLEDGMENTS

The authors are thankful to S.V. Lavrishchev for electron microscopy study of diamond samples, and to B. Ludge and S.V. Karpeev for their assistance in optical testing of a diamond spherical lens. Parts of this work have been supported by Russian Ministry of Science and Technology and through the joint projects of General Physics Institute with Bremen Institute of Applied Beam Technologies.

REFERENCES

1. V.A. Soifer, *Introduction to Diffraction Micro-Optics*, Samara: Samara State Aerospace University, 1996 (in Russian).
2. D.H. Raguin, G.M. Morris, "Structured surfaces mimic coating performance", *Laser Focus World*, p.113, April 1997
3. M.A. Golub, I.N. Sisakyan, V.A. Soifer, "Iterative calculation, manufacture and investigation of DOE forming unimodal complex distribution", *Optics and Lasers in Engineering*, **15**, p. 297, 1991.
4. M. Duparre, M.A. Golub, B. Ludge, V.S. Pavelyev, V.A. Soifer, G.V. Uspleniev, S.G. Volotovskii, "Investigations of computer-generated diffractive beam shapers for flattening of single-modal CO₂ laser beams", *Applied Optics*, **34**, p. 2489, 1995.
5. D.C. Harris, "Diamond optics: status for infrared applications", Proc. 3rd Int. Conf. on Applications of Diamond Films and Related Materials, eds. A. Feldman, Y. Tzeng, W.A. Yarbrough, M. Yoshikawa, M. Murakawa, NIST Spec. Publ. 885, p. 539, Washington DC, 1995.
6. R.S. Sussmann, J.R. Brandon, S.E. Coe, C.S.J. Pickles, C.G. Sweeney, A. Wasenczuk, C.J.H. Wort, C.N. Dodge, *Finer Points*, **10** (2), p. 6, 1998.
7. V.G. Ralchenko, A.A. Smolin, V.I. Konov, K.F. Sergeichev, I.A. Sychov, I.I. Vlasov, V.V. Migulin, S.V. Voronina, A.V. Khomich, "Large-area diamond deposition by microwave plasma", *Diamond Relat. Mater.* **6**, pp. 417-421, 1997.
8. Doskolovich L.L., Golub M.A., Kazanskiy N.L., Khramov A.G., Pavelyev V.S., Seraphimovich P.G., Soifer V.A., Volotovskiy S.G. *Proceedings SPIE*, **2363**, pp. 278-284, 1995.
9. T.V. Kononenko, V.V. Kononenko, V.I. Konov, S.M. Pimenov, S.V. Garnov, A.V. Tishchenko, A.M. Prokhorov, A.V. Khomich, "Formation of antireflective surface structures on diamond films by laser patterning", *Appl. Phys. A*, **68**(1), pp. 99-102, 1999.
10. V.V. Kononenko, V.I. Konov, S.M. Pimenov, A.M. Prokhorov, V.S. Pavelyev, V.A. Soifer, "Diamond diffraction optics for CO₂ lasers", *Quantum Electronics*, **29**, pp. 9-10, 1999.
11. V.G. Ralchenko and S.M. Pimenov, "Laser processing of diamond films", *Diamond Films Technol.* **7**, pp. 15-40, 1997.
12. U. Bögli, A. Blatter, S. M. Pimenov, A. A. Smolin and V. I. Konov, "Smoothing of diamond films with an ArF laser", *Diamond and Related Materials*, **7**, pp. 782-788, 1992.
13. S.M. Pimenov, A.A. Smolin, V.G. Ralchenko, V.I. Konov, G.A. Sokolina, S.V. Bantsekov, and B.V. Spitsyn, "UV laser processing of diamond films: effects of irradiation conditions on the properties of laser-treated diamond film surface", *Diamond and Related Materials*, **2**, pp. 291-297, 1993.
14. S.M. Pimenov, V.V. Kononenko, V.G. Ralchenko, V.I. Konov, S. Gloor, W. Lüthy, H.P. Weber, A.V. Khomich, "Laser polishing of diamond plates", *Applied Physics A*, **69** (1), pp. 81-88, 1999.
15. S. Evans, "Surface properties of diamond", in *The Properties of Natural and Synthetic Diamond*, ed. J.E. Field (Academic Press, London, 1992), p.181.
16. M. Born and E. Wolf, *Principles of Optics*, 3rd edition (Oxford, Pergamon Press, 1965).

Study of Micro-processing of Glass Materials by Laser-induced Plasma Assisted-ablation Using Nanosecond Pulsed Lasers

Jie Zhang*, Koji Sugioka and Katsumi Midorikawa

RIKEN (The Institute of Physical and Chemical Research), Wako, Saitama, 351-0198, Japan.

(*Present address, Uni. Of Toronto, Toronto, ON M5S 3G4, Canada)

ABSTRACT

In this paper, we demonstrate formation of micro-grating in fused silica by laser-induced plasma assisted-ablation (LIPAA) using different wavelength lasers projected through a metallic mask. With becoming longer wavelengths from 266, 532 to 1060nm, the ablation rate of fused silica at $1.5\text{J}/\text{cm}^2$ decreases from 21, 2 to 0nm/pulse. While the ablation threshold of laser fluence increases from 0.7, 1.5 to $3.75\text{J}/\text{cm}^2$. The 2.0mm deep through holes in Pyrex glass are drilled by single-beam 532nm-laser ablation. While the same deep through holes in fused quartz are only drilled by double-pulse-train of 532nm-laser ablation with a time-delay of 3.3ns. Finally, the ablation process was analyzed by an in-situ observation of laser-produced plasma, revealing different natures for surface patterning and channel-drilling.

Key words: Micro-processing, Laser ablation, glass and channel-drilling

1. INTRODUCTION

Laser micro-machining of glass materials is becoming quite attractive due to the fact that micro-structure inscription in glass materials is important for fabricating the photonic devices, such as fiber grating, etc¹. In addition, compact laser systems offer a wide assortment of wavelengths (vacuum-ultraviolet to infrared), pulse durations (femtosecond to continuous), and power levels to precisely control laser-interaction interactions and provide the special capabilities needed for exploiting a much broader base of industrial application. Short-wavelength excimer lasers (248, 193 and 157nm) and solid-state lasers (355, 266 and 213nm) define the small features on the wafers. Reliable ultrafast lasers afford another power tool for a high-resolution micro-machining of materials. Thus, we now have more options of choosing photon in driving physical and chemical processes on material surface, based on the properties of material. However, due to the wide-band-gap (9.0 eV) and the large bond-strength (9.3 eV) only "big photon" from 157nm-laser (7.9 eV) or "multi-photon" from fs-laser (100-200 fs) is qualified to realize the high-quality and high-efficiency micro-machining of fused silica. A quite few papers are already published about this²⁻⁴. Since ns-lasers with the wavelengths from infrared (IR) to ultraviolet (UV) provide high pulse energy and are commercial available we need to expand our option to the micro-machining of fused silica by use of IR, visible or UV ns-laser. Therefore, a novel ablation technique of hybrid-laser-ablation was recently developed. That is, a third medium is introduced into the interaction system of laser and glass. The main role of the medium, be it high-energy photons, high energetic species (ions, radical or electrons), thin metal film or chemical solutions, is to generate a high-absorption of glass to laser beam. One of features of this method is that the laser beam must be transparent to the substrate. The ablation occurs at the interface between glass and medium. Thus, ns-lasers with the wavelengths from IR (1060nm), visible (532nm) to UV (266 or 248nm) can be utilized for a high-quality and high-efficiency ablation of transparent materials, as reported previously⁵⁻⁸. In our group, a new method of hybrid-laser ablation, that is, laser-induced plasma-assisted ablation (LIPAA) has been presented. The plasma from metal target can provide either high energetic species or thin film. In this paper, we mainly demonstrate the influence of laser wavelength on ablation of glass material for either micro-grating formation or channel-drilling, and the analysis of dynamic process of ablation as well.

2. EXPERIMENTAL

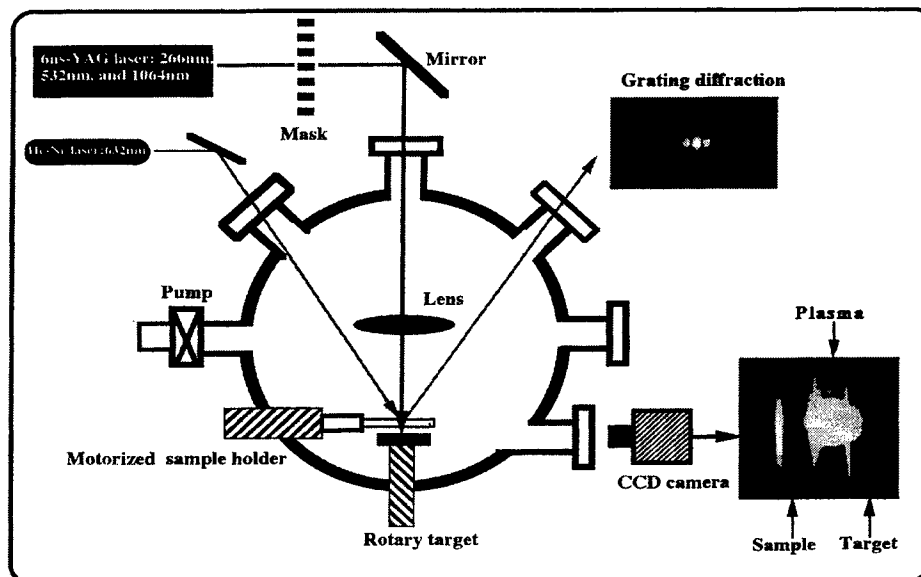


Fig.1. Schematic diagram of the experimental set-up

Optical grade fused quartz substrates (Viosil 600 μ m thick, Shinetsu Quartz Co., Ltd) and normal Pyrex glasses were employed in our experiments. Before irradiation, the substrates were ultrasonically cleaned with trichloroethylene, acetone and ethanol, followed by rinsing with DI water. The experimental principle is reported elsewhere⁶. That is, a single laser beam passes through the sample from front side (laser entrance) and is absorbed on Ag target for plasma generation. The distance between sample and target is variable from 1.5 to 2.0mm. The ablation takes place on the rear side of sample (laser exit), where plasma touched. The experimental set-up is shown in Fig.1. A commercial Q-switched Nd³⁺: YAG laser (Spectra-Physics, GCR-100, 266nm, 532nm or 1064nm, 6ns) was used as light source for both the generation of metal plasma and ablation of fused quartz. The repetition rate of laser irradiation is 1 and 10Hz. The stencil mask possessing a period of 130 μ m is used for projection printing. The ablation was performed in a vacuum chamber (10^{-2} - 10^{-4} Torr). A He-Ne laser beam is used to probe the formation of the surface grating (diffraction pattern). A CCD camera is used to observe the laser-induced metal plasma. The ablated samples were cleaned by use of acidic solution, such as HNO₃ to remove metallic residues.

3. RESULTS and DISCUSSION

3.1. Influence of laser wavelength on the micro-grating formation



Fig.2. The SPM images of micrograting in fused quartz using 266nm (a), 532nm (b) and 1060nm (c) laser, respectively.

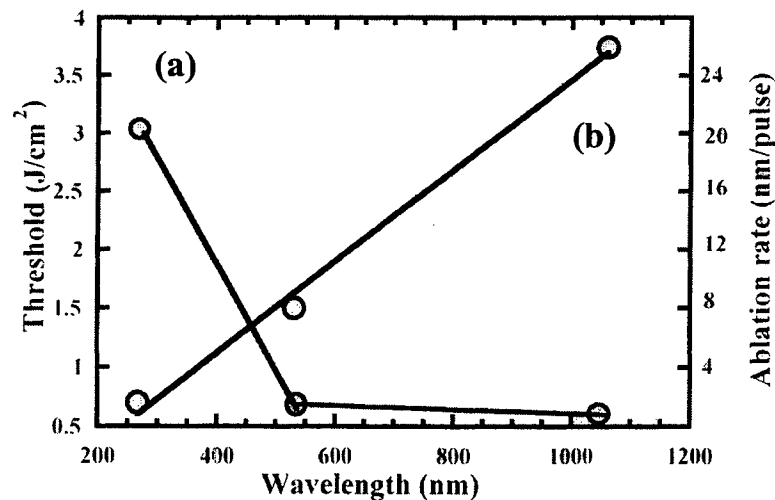


Fig. 3. The dependence of ablation rate (a) and ablation threshold of laser fluence (b) on the laser wavelength

Though the damage-free micro-grating in fused silica is produced by use of either IR, visible or UV laser the ablation difference is observed from both surface morphology and ablation rate (or ablation threshold of laser fluence), as we shall describe below. Figure 2 shows a three-dimensional scanning probe microscope (SPM) image of the grating fabricated in fused quartz by use of (a) 266nm (2.5J/cm² and 5pulses) (b) 532nm (4.0J/cm² and 60pulses), and (c) 1064nm (5.8J/cm² and 20pulses) lasers, respectively. The distance (d) between metal target and sample is 1.5mm. The grating appears to be clean and well-defined, having a period of 14μm at 266nm, 20μm at 532nm and 30μm at 1064nm. Therefore, the wavelength is longer, the grating period is larger due to the limitation of optical system. Moreover, the ablation rate and the ablation threshold of laser fluence are much more dependent on the laser wavelengths, as shown Fig. 3. When laser wavelength becomes longer the ablation rate at 2J/cm² is 20nm/pulse at 266nm, 1nm/pulse at 532nm and 0 at 1064nm, respectively. The threshold of fluence is 0.7J/cm² at 266nm, 1.5J/cm² at 532nm and 3.7J/cm² at 1064nm laser, respectively. The main reason is that the shorter laser wavelength has a smaller penetration depth in deposited metal film, and a lower fluence threshold for producing the plasma as well.

3.2. Channel-drilling in fused silica and Pyrex glass

We also investigate a deep channel-drilling of glass materials by LIPAA technique using different wavelength lasers. 266nm-laser cannot be used for deep channel-drilling, but only produce the channel damage. The reason is not clear yet. Figure 4 shows the optical microscope images of the cross-section of through channels drilled in 2.0mm thick Pyrex glass using 532nm-laser and 1060nm-laser, respectively, indicating that the 532nm-laser drilled channel appears to be much less destructive than 1060nm-laser drilled. Thus, 532nm laser is more suitable for the channel-drilling comparing with 1064nm-laser. The single-beam of 532nm-laser cannot, however, achieve a less destructive deep through channel in 2.0mm thick fused silica (in Fig.5a). It was already reported that multi-pulse train of picosecond (ps) could be effectively used for the channel-drilling of glass materials⁹. One of the main reasons is that the first pulse could change the glass from brittleness to ductility within several ns, and then the second bursts the ductile. We adopt this idea into the ns-laser induced channel-drilling. We use a beam-splitter to separate 532nm-laser beam to form a double-pulse-train with time delay of 3.3ns. The energy of each pulse is 1.4J/cm², slightly lower than the ablation threshold of 532nm-laser fluence. The through channel was drilled after 21600 pulses although the damage appears on the wall (in Fig.5b). While for the case of channel-drilling by use of single beam 532nm-laser at 2.8J/cm² the channel totally cracks after 21600 pulses.

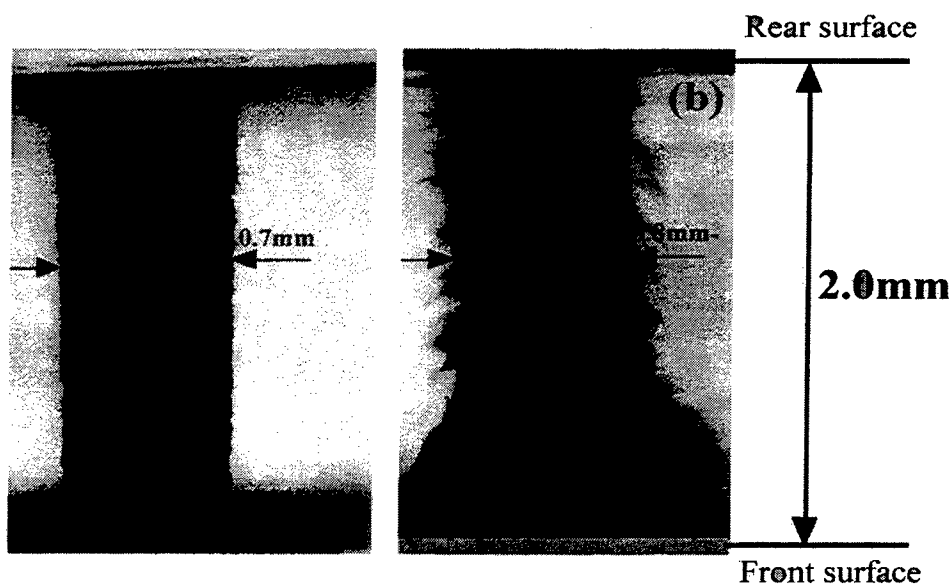


Fig.4. The optical microscopy images of cross-section of the through channel drilled in 2.0mm thick Pyrex glass substrate by use of (a) 532nm ($7.7\text{J}/\text{cm}^2$ and 9000pulses) and (b) 1064nm ($15.1\text{J}/\text{cm}^2$ and 12000pulses)

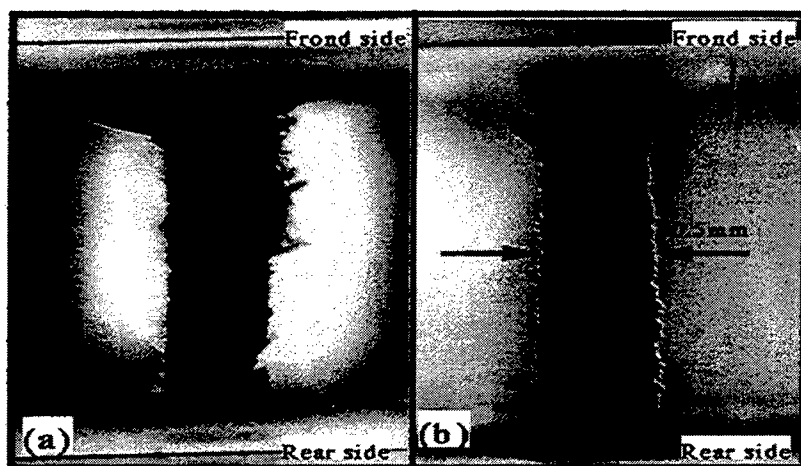


Fig.5. The optical microscopy images of cross-section of the channels drilled by (a) single beam of 532nm laser ablation ($2.8\text{J}/\text{cm}^2$, 2Hz and 21600pulses) and (b) double-pulse-train of 532nm laser with time-delay of 3.3ns ($1.4\text{J}/\text{cm}^2$ for each pulse, 2Hz and 21600pulses)

3.3. Analysis of the ablation process

Our experimental results about the wavelength dependence of the ablation of glass materials indicate that surface structuring appears a different ablation mechanism from deep channel-drilling of glass materials. For the surface structuring, that is, at the initial stage of ablation process, either IR, visible or UV IR laser beam can pass through the

substrate and generate the metallic plasma to assist the ablation. The ablated area appears to be regular and less destructive (see Fig. 6a).

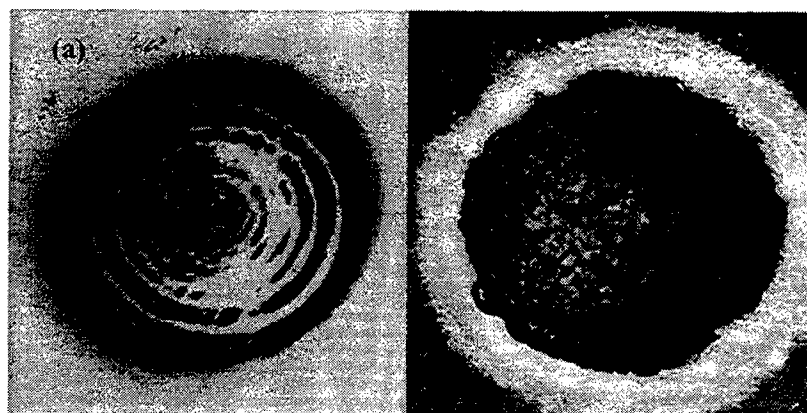


Fig.6. The optical microscopy images of single beam of 532nm-laser ablated bottoms at the depths of (a) 20μm (5.9J/cm² and 300pulses) and (b) 80μm (5.9J/cm² and 1800pulses)

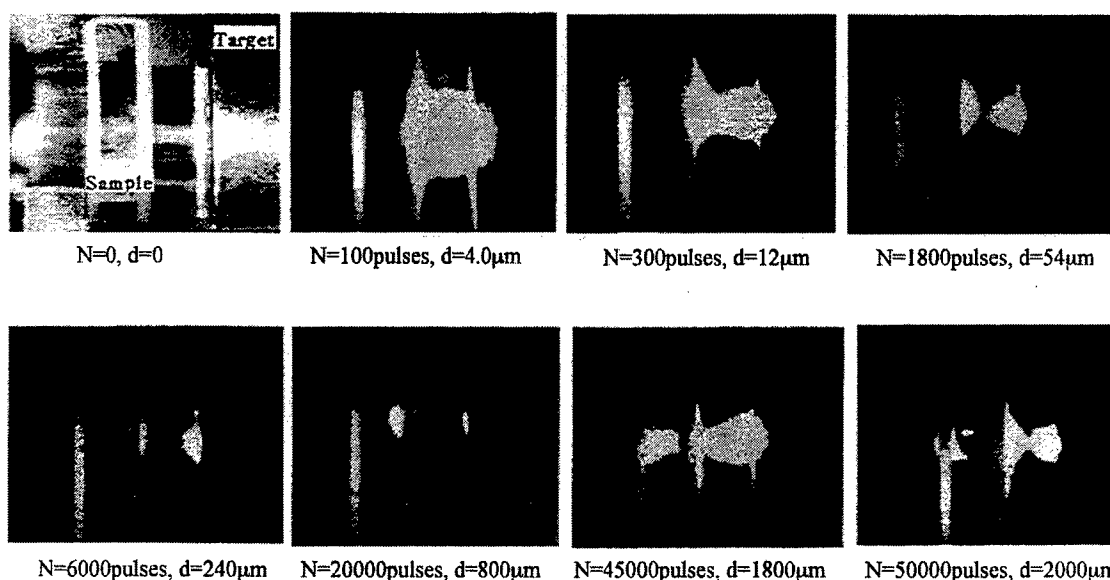


Fig.7. The change of single-beam of 532nm-laser-induced metal plasma between target and glass substrate (5.9J/cm²)

The mechanism is considered to be either contribution of energetic species in the plasma or absorption of laser beam by thin metal film deposited at the rear surface of the sample⁸. While for the channel drilling, the ablated area becomes rough, destructive and opaque (see Fig. 6b). The subsequent laser pulses are shielded by the roughened channel-bottom and thus cannot reach to the metallic target for the generation of metal plasma. Therefore, in the channel-drilling process, contribution of the metal plasma for ablation cannot be expected. In order to understand the ablation process well, we use a

CCD-camera to observe the shape of laser-induced plasma between glass substrate and metallic target related to the ablated depth during the channel-drilling of 2.0mm thick Pyrex glass by use of single-beam of 532nm-laser ($5.9\text{J}/\text{cm}^2$). We can see from Fig. 7 that at the depths of 4 and $12\mu\text{m}$ (surface structuring), laser-induced-plasma appears to be a full shape due to little influence of ablated area. At the depths of larger than $54\mu\text{m}$ laser-induced plasma divides, however, into two parts, since a part of laser energy is deposited on the roughen surface of channel bottom. When channel is through, the full shape of plasma recovers. The significant change of laser-induced-plasma indeed reflects a different ablation mechanism between the surface structuring and the channel-drilling.

4. CONCLUSION

We demonstrate that the wavelength dependence of the surface structuring and the channel-drilling of both fused quartz and Pyrex glass. Either shorter wavelength (266nm) laser or longer (532 and 1060nm) is suitable for the surface structuring. While, the longer wavelength lasers (532 and 1064nm) are suitable for the channel-drilling. The surface structuring and the channel-drilling appears to be a different ablation mechanism.

ACKNOWLEDGMENTS

J. Zhang would like to acknowledge the Japan Science and Technology Agency (STA) Fellowship for his support. The support from Professor Peter R. Herman is gratefully acknowledged.

REFERENCES

1. D. Bauerle: *Laser Processing and Chemistry* (Springer-Verlag, Berlin Heidelberg), pp.191-207, 1996.
2. P. R. Herman, K. Beckley, B. Jackson, D. Moore, T. Yamanishi, and J. Yang, "Processing application with the 157-nm fluorine excimer laser", *SPIE Proc.* 2992, pp. 86-94, 1997.
3. H. Varel, D. Ashkenasi, A. Rosenfeld, M. Wahmer, and E. E. B. Campbell, "Micromachining of quartz with ultrashort laser pulses", *Appl. Phys. A* 65, pp. 367-373, 1997.
4. K. Sugioka, S. Wada, A. Tsunemi, T. Sakai, H. Takai, H. Moriwaki, A. Nakamura, H. Tashiro, and K. Toyoda, "Micropatterning of quartz substrates by multi-wavelength vacuum-ultraviolet laser ablation," *Jpn. J. Appl. Phys.* 32, pp 6185-6189, 1993.
5. J. Wang, H. Niino, and A. Yabe, "One-step microfabrication of fused quartz by laser ablation of an organic solution", *Appl. Phys. A* 68, pp. 111-113, 1999.
6. J. Zhang, K. Sugioka, and K. Midorikawa, "Laser-induced plasma-assisted ablation of fused quartz using the fourth harmonic of a YAG: laser," *Appl. Phys. A* 67, pp. 545-549, 1998.
7. J. Zhang, K. Sugioka, and K. Midorikawa, "High-speed machining of glass materials by laser-induced plasma-assisted ablation using a 532-nm laser ", *Appl. Phys. A* 67, pp. 499-501, 1998.
8. J. Zhang, K. Sugioka, and K. Midorikawa, " Micromachining of glass materials by laser-induced plasma-assisted ablation (LIPAA) using a conventional nanosecond laser," *SPIE Proc.* 3618, pp. 363-368, 1999.
9. P. R. Herman, A. Oettl, K. P. Chen, P. Herman, and R. Marjoribanks, "Laser micromachining of transparent fused silica with 1-ps pulses and pulse trains", *SPIE Proc.* 3616, pp. 148-155, 1999.

Novel technique for high-quality microstructuring with excimer lasers

Stephan Roth*, Prof. Manfred Geiger

Chair of Manufacturing Technology, Univ. of Erlangen-Nuremberg, 91058 Erlangen, Germany

ABSTRACT

Laser micromachining has become increasingly established in many microsystems applications during the past years. These new fields occasion higher demands on the quality of micromachined devices combined with high resolution and working velocity. Due to the disadvantages of conventional excimer laser processing, a novel technique is required to meet these demands. The main problems of conventional excimer laser machining are the redeposition of ablated material on the irradiated work piece and the formation of a strong melting phase especially for metals. These difficulties greatly reduce the applicability of excimer laser material processing for manufacturing microsystems technology components. By applying a thin water film to the substrate surface, the redeposition of ablated material can be completely avoided, which results in a better quality of the microstructures. Usage of a water film, however, has proved to lead to a marked reduction of the ablation rate for the examined materials - ceramics and stainless steel. Therefore, one of the objectives of future research will be to raise the ablation rate in order to render excimer laser processing more interesting economically. Adding alcoholic additives, among others, has improved the wetting of the liquid films on the surface. The effect of the modified chemical composition of the liquid on ablation rate and structure quality for various materials is presented here.

Keywords: Production process, excimer laser, microstructuring, structure quality

1. INTRODUCTION

The miniaturization of parts for diverse areas of technical applications increasingly determines the design of new products. This trend also makes new demands on the respective manufacturing methods. A consequence of the increasing demand for miniaturized work pieces is that the required processing quality has to be improved further. In many cases, laser irradiation is a suitable tool for material processing. It can be used to machine a great variety of materials.¹ Its importance keeps increasingly especially in the area of microsystems technology. Here, ceramic materials are used more and more for parts under stress from heat. Because of their special properties, ceramic materials are machined mainly with excimer lasers. Since the absorption length of UV light is very short for most materials, the energy is deposited in a very thin surface layer. The high pulse energy and the extremely short pulse duration of excimer lasers, typically a few 10 ns, lead to a sudden melting, evaporation and plasma formation of the irradiated material. A large portion of the laser energy is immediately removed with the ablated material so that the total heat transfer into the bulk material is relatively small. Therefore, this method is very well suited for machining materials with high thermal shock and stress sensitivity, such as ceramics and glass. In the case of metals, the material is mainly removed as molten metal. Sub-micron particles or melt droplets deposit on or close to the already produced structures. Avoiding this redeposition is a requirement for improving the processing quality of excimer laser microstructuring. The subsequent deposition removal – if at all possible – is very costly and rarely economical.

Several approaches to avoid these material redepositions have been examined.^{2,3} A main focus of this research is the application of an additional layer onto the surface to be treated. This can be a thin water film, which is sprayed onto the surface, or a coat of lacquer, which has to be removed after processing. In the past, a thin water film was used, for example, to remove impurities from waver surfaces with a laser beam.⁴ This method was then transferred to the processing of mostly ceramic materials: a redeposition of material is to be avoided through the creation of a thin water film at the point of processing.⁵ Because of the successes made so far in improving the structural quality, this approach is the subject of further recent research.

* Correspondence: Email: S.Roth@lft.uni-erlangen.de; WWW: <http://www.lft.uni-erlangen.de>; Telephone: +49 9131 852-7953; Fax: +49 9131 36403

2. EXCIMER LASER MICROSTRUCTURING

There are some significant differences between excimer laser irradiation and the systems used mainly in the automobile industry and mechanical engineering, such as CO₂ and solid state lasers. The short pulse duration, high pulse energy and extremely small penetration depth of the radiation into the irradiated surfaces facilitate the machining of ceramics and glass. Another special characteristic is the large beam profile of this kind of laser. This makes it possible to create many differently shaped structures at the same time. The so-called mask projection technique projects a mask containing the geometrical information onto the surface of the work piece; the mask is either made of cut stainless sheet steel or chrome-coated and structured silica glass substrate. In order to achieve on the work piece an energy density sufficient for the processing, the area of the laser beam must be decreased with optical elements. Only high-quality mirror and lens systems are used to avoid optical errors that could negatively influence the processing quality.

The length of the process is mainly determined by the number of pulses needed for structuring. Here, the ablation rates of the different materials are important. For ceramics and steels they are between 0.1 and 0.2 μm per pulse. For polymers, however, they can be up to 1 μm per pulse. Because of the low ablation rates, deep structures take a lot of time and are therefore often uneconomic. This is especially true for ceramic and metallic materials.

Figure 1 shows the different processing areas that are distinguished in the excimer laser machining of ceramics. Here, the ablation threshold is of fundamental importance. It marks the energy density value where ablation of the material begins. Below this threshold, the substrate material remains virtually unaffected, only organic residues (grease, oil) left in surface indentations are removed. Additionally, the irradiation is reflected from the walls of existing cavities, which can lead to a sufficient energy density at the bottom of these indentations. Both phenomena evidently increase the roughness of the substrate. When the ablation threshold is exceeded slightly, the roughness peaks of the work piece surface melt. This material flows into the existing indentations, which decreases the roughness. Thus, excimer laser irradiation can be used to selectively modify the roughness.

When the ablation threshold of the processed material is exceeded distinctly, extensive ablation results. Because of reduced projection achieved through mask projection, excimer laser machining can realize structures measuring only a few micrometers. Especially high-quality lenses make it possible to create even structures measuring within the dimensions of the utilized laser wavelength. This technique is used above all in the production of semiconductors.

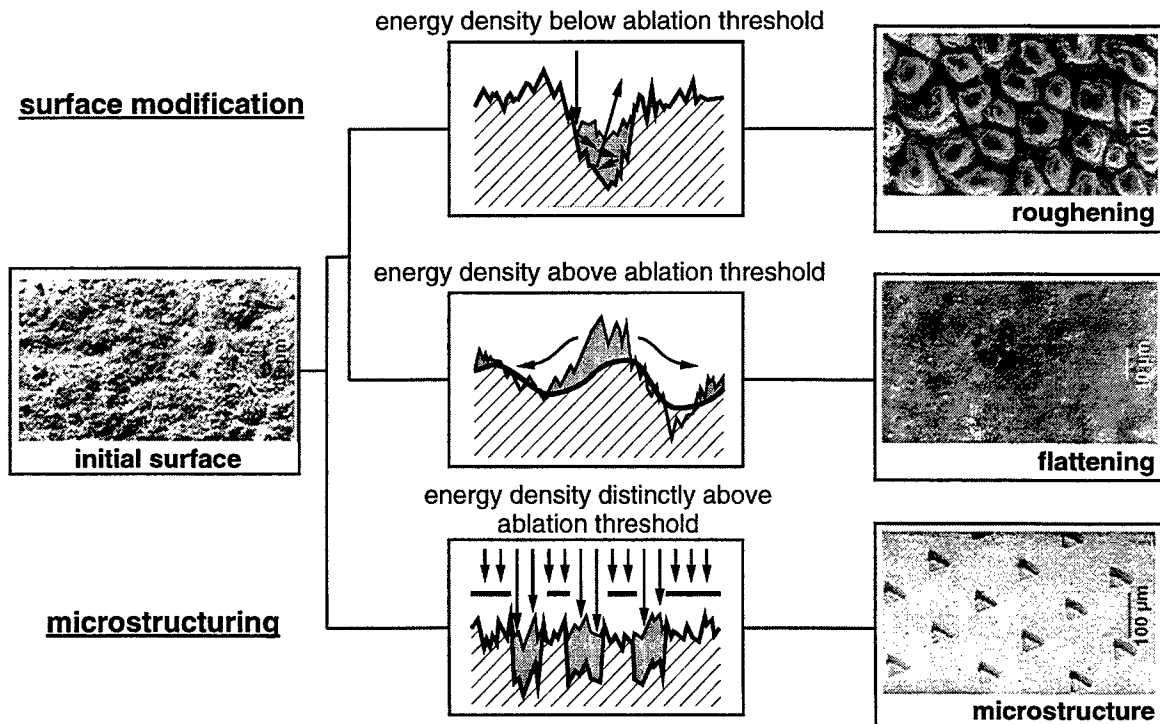


Fig. 1: Processing of ceramics by excimer laser radiation¹.

3. MACHINING UNDER THIN WATER FILM

The findings on the removal of impurities on silicon wafers were used as a basis for experiments on the improved ablation of ceramic materials. Here, though, the water film is continuously sprayed onto the vertical work piece; moreover, spraying on the water film and machining coincide. This makes sure that drained and evaporated fluid is continually replaced. A disadvantage of this method is that atomizing of the water causes a thick fog to develop at the machining point. This fog weakens and disperses the excimer laser beam, which in turn reduces the quality of the machined structure.

3.1. Materials

The experiments regarding the qualification of excimer laser ablation under a sprayed-on liquid film on one the hand use materials that can be structured very well with excimer laser radiation, such as different ceramics. On the other hand, they concentrate on materials whose structurization with an excimer laser has so far been problematic, but which play an important part in many industrial applications. This is especially true for steels: a distinct melting phase often occurs during their processing.

The following ceramics were chosen for the experiments: aluminum oxide (Al_2O_3 , FRIALIT-DEGUSSIT F 99,7, FRIATEC AG), silicon carbide (SiC , Ekasic D) and silicon nitride (Si_3N_4 , Ekasin S, both Elektroschmelzwerk Kempton GmbH). As so-called high-performance ceramics, they are used in many areas of vehicle construction, mechanical engineering and machine-making. A high-speed steel 1.3343 (S 6-5-2) was used as steel material. It is utilized mainly for cutting and forming tools.

3.2. Experimental setup

The laser treatment was carried out with KrF ($\lambda = 248 \text{ nm}$) and XeCl ($\lambda = 308 \text{ nm}$) excimer laser radiation. Here, the KrF laser stands out due to its higher pulse frequency of 150 Hz at a pulse energy of 800 mJ. The XeCl laser in contrast has a pulse energy of 2 J at a maximum pulse frequency of 20 Hz. High quality beam controls with beam homogenizers are available for both laser systems. They work according to the mask projection method. This makes it possible to create structures measuring only micrometers.

A working chamber with a closed liquid cycle was constructed for the experiments. From a reservoir, the liquid mixture, in a pre-defined chemical composition, is pumped into the working chamber and there atomized using an atomizer pistol. The lance of the atomizer pistol can be exchanged to produce differently sized droplets. The liquid is sprayed onto the vertical work piece, collected in the chamber and piped back to the reservoir through a filter unit. The strong atomization creates a fog in the working chamber, which fouls the optical element such as the imaging lens. Therefore, the chamber is closed up with a UV permeable silica glass top at the point of entry of the light beam. This avoids liquid droplets on the lens. The silica glass top can be cleaned easily after the processing. In this way, a negative influence on the beam properties is reduced. In order to keep the spray from overly dispersing the laser light over the work piece, the focus of the spray jet is placed over the actual point of processing. Thus, the laser beam hits the surface of the work piece within the draining water jet. The thickness of the film is determined by the amount of water being sprayed on.

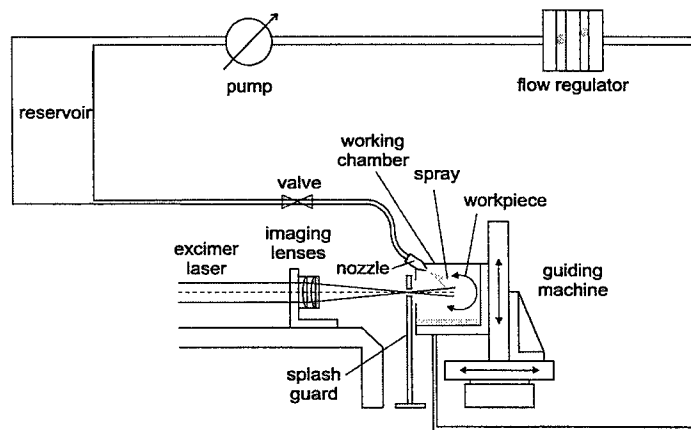


Fig. 2: Working chamber for applying liquid film during laser irradiation

3.3. Ablation behavior

The experiments with a water film sprayed on during excimer laser ablation showed that the reposition of ablated work piece particles can be avoided nearly completely. There are no melt particles or warps either around or in the structures. Figure 3 shows SiC structures produced both in the conventional, dry way (left) and with a sprayed-on liquid film (right). The dry-processed structure shows strong impurities. The original surface of the work piece is completely covered with material deposits around the structures. After processing under the water film, however, the surface remains practically unchanged.

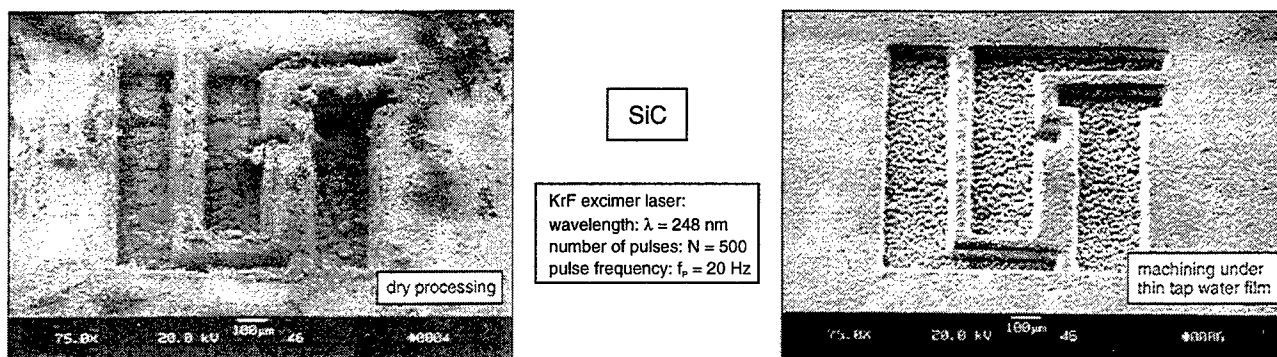


Fig. 3: Conventional dry processing of SiC (left); machining of SiC under thin tap water film (right)

The ablation rate is an important variable in excimer laser processing. Figure 4 shows a comparison of the ablation rates of different ceramics for dry processing and when using a water film (tap water). As the energy density grows, the ablation rates steadily increases once the ablation threshold has been exceeded. Then, a saturation value is reached at about 0.2 to 0.3 μm per pulse. Further raising the energy density increases the ablation rate only negligibly. For most ceramics, this behavior does not change much when a water film is used, though the ablation rate level is pushed toward lower values. Al_2O_3 is an exception to this rule, here, the ablation rate increases considerably. The quality of the structure, however, decreases distinctly for this material.⁵ There is no projection of the structures on the mask. The structures created are characterized by a cratered bed. Evidently, larger chunks of the material broke away during lasering.

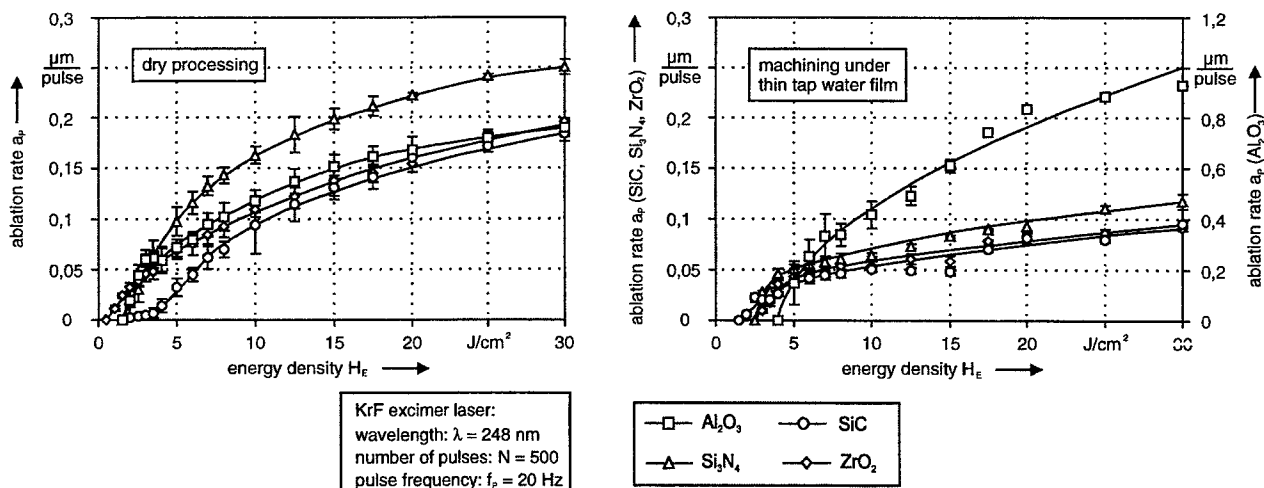


Fig. 4: Ablation rates for structuring under thin tap water film

During observation of the ablation process it is observed that both acoustic and light emissions decrease drastically during microstructuring under a water film in contrast to conventional processing. Around the irradiated surface area, the water is vaporized explosively, and accelerated away from the surface of the work piece. The sequence of events can be made visible by short-time recordings (Figure 5). For the experiments, the samples were irradiated with an excimer laser from straight above after a thin water film had been deposited on the horizontal samples. The recordings show that fog and ablated material do not break the water film until 5 to 10 μs after the laser pulse has ended. At a high speed, they are catapulted out of the processing area vertically. This process is finished after about 500 μs . If you compare this temporal sequence with that of conventional excimer laser processing (start of ablation already during the excimer laser pulse, after about 5 to 10 ns, and fading of the plasma light after about 2.5 μs)⁶, a considerable delay of ablation phenomena becomes clear. An explanation for this behavior could be that super heated water with a temperature of noticeably more than 100°C can exist in an instable state for a certain time before it finally vaporizes explosively (“defervescence”).

At the water-work piece interface, the water is heated and superheated suddenly. Defervescence does not occur until after a temporal delay of a few μs – long after the laser pulse has finished –, and the superheated water vaporizes explosively. The higher the energy density of the laser pulse, the higher the superheating of the water, and the higher the blast pressure that has to be expected. Because of the water film’s cooling, the steam bubbles implode after a certain period of time. The implosion shock waves can cause cavity erosions.

Absorption, reflection and dispersion losses caused by the water film and water droplets as well as changed ablation mechanisms are possible explanations for the usually lower ablation rates. Additionally, the cooling of the irradiated surface by the water film could cause a slightly lower ablation rate. On the other hand, the absence of processing plasma allows more laser energy to reach the work piece surface than conventional irradiation. Up 30% of laser energy are absorbed in the plasma in excimer laser processing.⁷

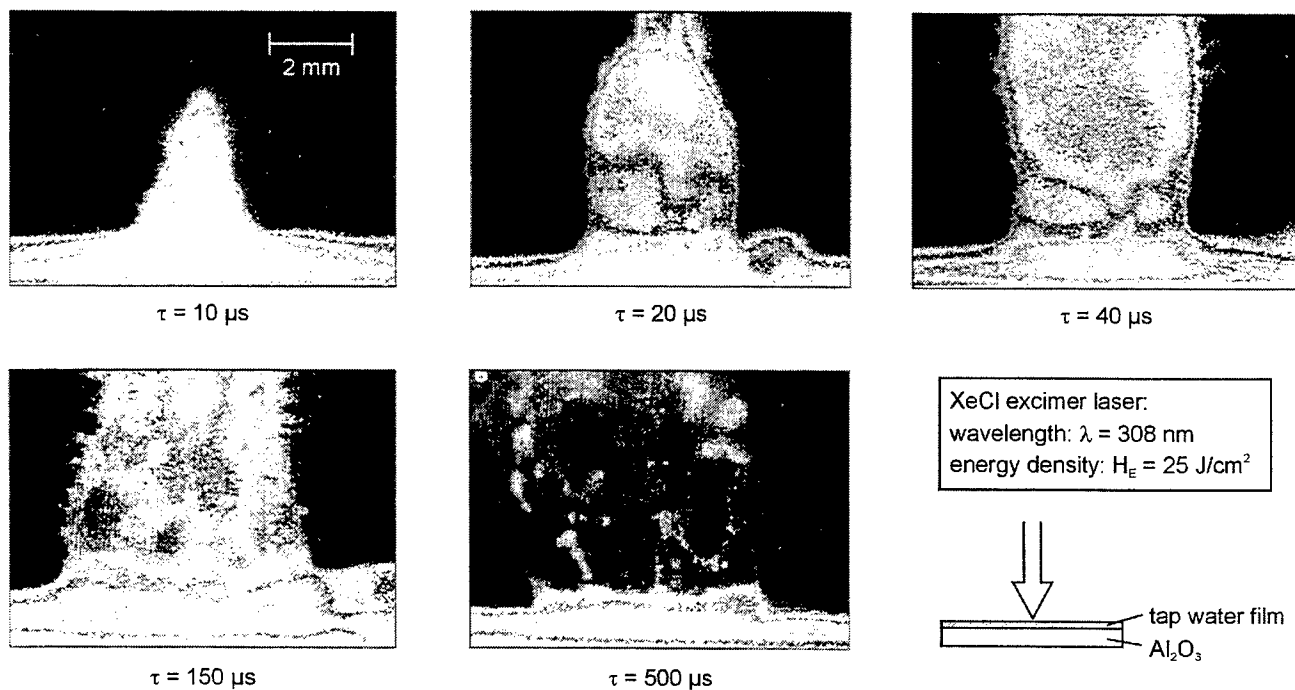


Fig. 5: Behavior of the water film during laser irradiation (short-time shutter camera; exposure time 5 ns)

While during conventional excimer laser machining, melting and vaporization of the material and finally appearance of a plasma occur immediately after the beginning of the laser pulse, contact with a water film evidently suppress these events. Enclosing the interaction zone in a water film, or the latter’s cooling effect possibly make the vaporization and sublimation of the material much more difficult. This could explain the absence of processing plasma. But since some laser processed work piece surfaces show structures that suggest a solidified melting phase, is it safe to assume that at least some of the irradiated material melts and finally evaporates.

3.4. Mechanical Stability

During excimer laser processing with a water film the explosive evaporation of the water causes strong blast waves – at least according to today's understanding of ablation mechanisms. This can possibly damage the marginal zone of the processing area, which might negatively influence the stability of ceramic work pieces. Therefore, transverse rupture tests are conducted with Al_2O_3 and Si_3N_4 ceramics. Both materials were chosen because of their totally different ablation behaviors which suggest different ablation mechanisms. With Al_2O_3 ablation rate increases greatly when processed under water. At the same time, many break outs can be seen at the edges of the machined microstructures, which suggest a greater mechanical stress caused by the processing. This makes it safe to assume that the marginal zone is damaged as well. Si_3N_4 , however, does not show these effects which gives reason to hope that the stability of the work piece is not influenced negatively. The results show that excimer laser processing decreases the stability of the materials when compared to their unprocessed initial state. With Si_3N_4 , however, processing under water results in a slightly higher stability than conventional excimer laser processing. The blast waves caused by the water's evaporation therefore do not necessarily lead to a weakening of the work piece. The Al_2O_3 ceramic shows contrary results. Here, processing under water drastically decreases the stability.

4. LIQUID MIXTURES WITH ALCOHOLIC ADDITIVES

An even liquid film is also necessary for a good processing result. In order to achieve this, the surface of the work piece must be wetted evenly. Optimizing the wetting behavior of the utilized liquid mixtures is another important goal of the experiments. The angle of contact between the liquid and the substrate is to be reduced by adding appropriate additives. This is possible, for example, with alcoholic (methanol or ethanol) or non-alcoholic additives.

4.1. Wetting behavior

In order to attain a thinner and more even liquid film, additives are to improve the wettability of the liquid on the substrate surface. The formation of droplets can locally change the thickness of the film, which can directly influence the processing result by leading to a decreased quality of the structure. In order to avoid this formation of liquid droplets on the substrate surface, the surface tension of the water is reduced with alcoholic additives. It is well-known that low amounts of methanol or ethanol can significantly reduce the surface tension of water. The tests were done with a contact angle measuring system, which optically analyses the angle between the lateral face of a liquid droplet and the substrate surface. Figure 6 shows that as the wetting angle decreases significantly the concentrations of both the ethanol ($\text{C}_2\text{H}_5\text{O}$) and the methanol (CH_3O) additive increase. Aluminum oxide and silicon carbide were chosen as substrate materials, since both materials show very different surface properties. Reservations that the irradiation could lead to heavy combustion reactions as the share of alcohol in the liquid was too high led to the decision that the water-alcohol mixture should contain a maximum of 5 % alcohol. For both investigated materials (Al_2O_3 and SiC), the wetting angle is a maximum of 75° with this percentage of alcohol.

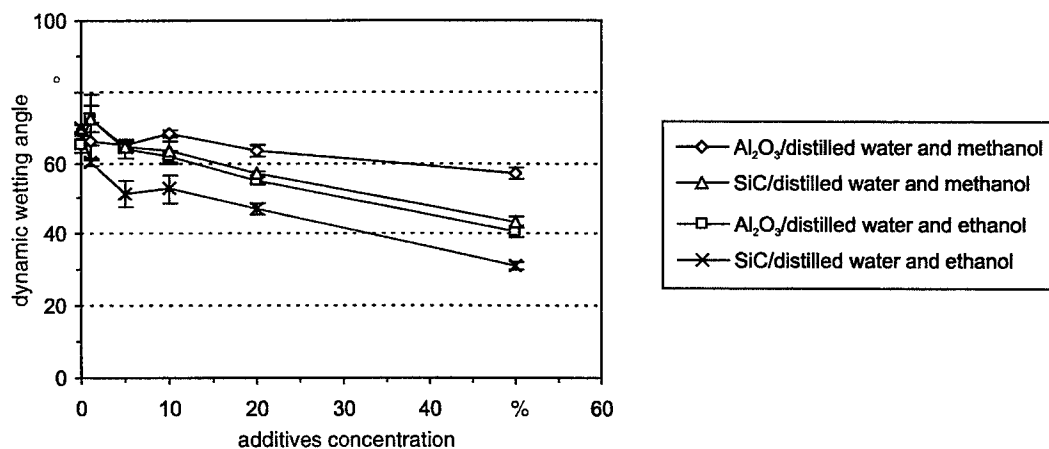


Fig. 6: Influence of methanol and ethanol on wetting angle

What must not be forgotten, however, is that is not only the wetting of the liquid that is change but possibly the transmission behavior as well. The addition of additives may not impair the transmission for the wavelengths in use. Otherwise, it would lead to a partly irregular absorption of the irradiation both in the water fog and in the liquid film on the surface. In order to avoid this unwanted influence, the mixtures were examined with regard to their transmission. It turns out that the transmission does not decrease continually as the share of alcohol in the mixture increases. It is also established, however, that there are only minimal differences in transmission between the different mixtures. At the KrF excimer laser's wavelength ($\lambda = 248 \text{ nm}$) transmission is between 80 % and 85 %. At this wavelength, the differences in transmissions for methanol are even smaller than for ethanol.

4.2. Ablation rate

As has been discussed extensively in the previous chapter, the spraying-on of water can significantly increase the quality of the structure in excimer laser microstructuring. Problems that have so far occurred in ablation processing (material redeposition; formation of melting) are avoided for almost all examined materials. However, the ablation rates of most ceramic and metal materials are greatly reduced. Therefore, the essential goals of further tests are to increase the ablation rates and the quality of the structure for the processing of aluminum oxide.

The results presented so far were attained with simple tap water. Therefore, distilled water is used in the following experiment. In order to improve wetting, 5 % of methanol and ethanol, respectively, are added. The low amount of additives can be explained by the fact the pre-tests showed that a higher amount of alcohol can lead to heavy combustion reactions during irradiation. The resulting flame has a similar effect as the plasma that is produced during conventional processing. The irradiation is greatly absorbed and dispersed, the processing results are distinctly worse and inhomogeneous.

The results for distilled water are similar to those attained with tap water. The ablation threshold is pushed towards higher energy density values. The reposition of material is avoided completely with the use both of methanol and ethanol. Figure 7 shows, however, that the ablation rates are similar to those of tap water. This is true for Al_2O_3 as well. The structure qualities of the examined materials are comparable as well.

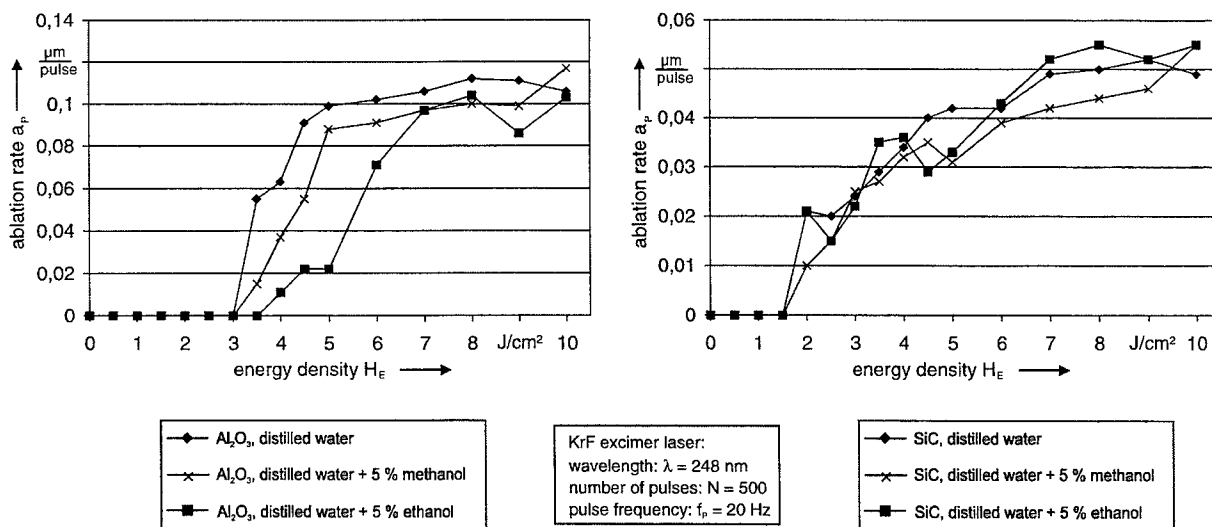


Fig. 7: Ablation rates for structuring under distilled water with additions of ethanol and methanol

4.3. Roughness

When structuring under a liquid film, the structure ground is roughened strongly, as Figure 8 shows on silicon nitride. Some of the resulting micro-cavities show a distinct orientation. Depending on the application, this increased roughness of the structures can lead to an unwanted limitation of work piece properties. On the other hand, the formation of oriented cavities offers the possibility of using this orientation to optimize bearing work pieces, for example. Therefore, it is a possible approach to avoid or purposely create the phenomena for the respective application. This is not only true for the roughness

within the structures but also and especially for modification of the roughness of the entire work piece surface. The roughness values R_a measured within the structures and as presented in Figure 9 do not show a significant dependency on the used liquid. Moreover, the results are similar for all examined materials. All roughness values are slightly higher than those of conventionally machined structures.

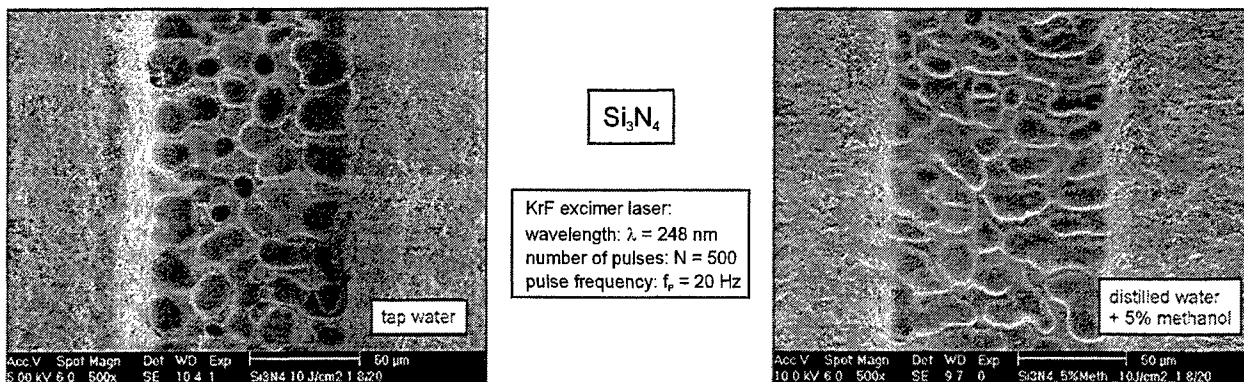


Fig. 8: Surface formation at the structure ground of a Si_3N_4 sample

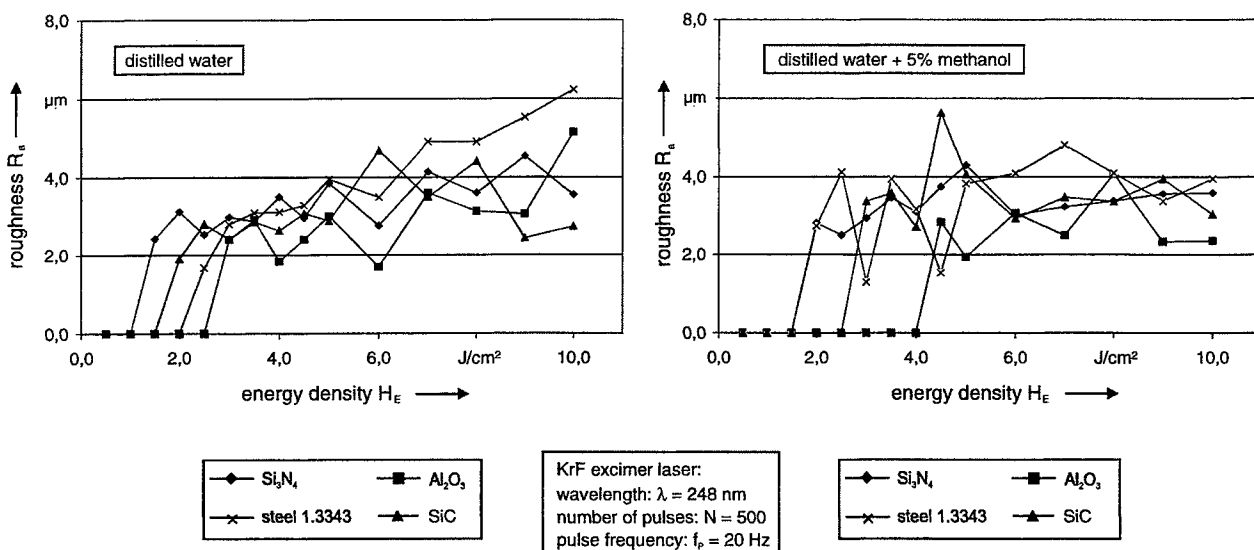


Fig. 9: Roughness value R_a for different materials

5. CONCLUSION

The influences of the energy density of the utilized laser irradiation and the composition of the liquid on the processing under a sprayed-on water film were examined for different ceramics (SiC , Si_3N_4 , Al_2O_3) and steel. Besides ablation rate and structure quality, the focus was on the attainable degree of surface roughness. Similar to "dry" excimer laser processing, the energy density of the laser irradiation considerably influences the processing result. It is decisive for the ablation rates of the different materials. It is, however, reduced distinctly when a liquid film is used during irradiation. This was proven for both tap water and the examined ethanol and methanol mixtures, whose goal was to improve wetting. It became clear that the original approach to achieve an increased processing quality and higher ablation rates by improving the wetting of water on the substrate surface did evidently not have the desired effect. However, so far only alcoholic additives (ethanol and methanol) were used, which can cause heavy combustion reactions during irradiation when their concentration is too high. In first tests, the use of soapy additives, which can also decrease the surface tension, showed that a strong foam builds

during atomization, which disqualifies this possibility. Because of the inadequate results for an improved wetting, another approach is going to be the use of liquids that show a reduced wetting on the substrate. This prevents a premature draining of the liquid film before the next laser pulse, which can occur at high spray pressures.

ACKNOWLEDGEMENTS

Financial support for this research was given by the Deutsche Forschungsgemeinschaft (DFG) within the Schwerpunktprogramm „Mikromechanische Produktionstechnik 1998“ under reference number Ge 530/29-3. The authors wish to thank Mrs. A. Töpperwien for her extensive and helpful work within this research project.

REFERENCES

1. W. Becker, *Oberflächenausbildung und tribologische Eigenschaften excimerlaserstrahlbearbeiteter Hochleistungskeramiken*, Reihe Fertigungstechnik, Band 95, Hanser, München, 1999.
2. P. Burck, W. Reitzenstein, H.K. Tönshoff, and H. Kappel, "Mikrostrukturierung von Keramiken in reaktiven Gasatmosphären mit UV-Lasern", ECLAT'96, F. Dausinger, H.W. Bergmann, and J. Sigel, pp. 699-706, AWT e.V., Wiesbaden, 1996.
3. H. Kappel, *Oberflächenmodifikation technischer Keramik mit Excimer-Laserstrahlung*, Fortschr.-Ber. VDI Reihe 2 Nr. 469, Düsseldorf, 1998.
4. W. Zapka, W. Ziemlich, and A.C. Tam, "Efficient pulsed laser removal of 0.2 μm sized particles from a surface", *Appl. Phys. Lett.* **58**, pp. 2217-2219, 1991.
5. M. Geiger, S. Roth, and W. Becker, "Microstructuring and surface modification by excimer laser machining under thin liquid films", *Laser Surface Processing*, V.I. Pustovoy, SPIE Vol. 3404, pp. 200-208, Limoges, 1997.
6. N. Lutz, *Oberflächenfeinbearbeitung keramischer Werkstoffe mit XeCl-Excimerlaserstrahlung*, Reihe Fertigungstechnik, Band 39, Hanser, München, 1994.
7. O. Gedrat, *Strukturierung technischer Keramik mit Excimer-Laserstrahlung*, Fortschr.-Ber. VDI Reihe 2, Nr. 276, Düsseldorf, 1992.

Micromachining by Laser Ablation of Liquid: Superheated Liquid and Phase Explosion

J. Wang, H. Niino, and A. Yabe*

National Institute of Materials and Chemical Research,
Higashi 1-1, Tsukuba, Ibaraki 305-8565, Japan

ABSTRACT

Transparent materials such as quartz, calcium fluoride and fluoropolymer, are difficult to fabricate by conventional laser processing. We fabricated them successfully with a micron-size by laser ablation of liquid layer attached on the backside of the target. The threshold fluence for etching depends on absorption coefficient of liquid, and thermal properties of target materials. In the further study, we observed the dependency of the etch rate on etch size. The results suggest that the thermal energy diffuses more efficiently when the irradiation area is too small. However, when increase the etch depth to high aspect ratio, in the strong laser fluence, the etch rate becomes faster than that with large irradiation area and low aspect ratio. We discussed that the mechanism is due to the combination of two processes in the interface of a target material and a liquid: one is a heating process (phase explosion, explosive boiling) by the superheated liquid and the other is an attacking process by high temperature and pressure. We suggested that the temperature of the superheated liquid can exceed the thermodynamic critical temperature T_c upon irradiation at a high laser fluence, and the liquid corresponded to "transient supercritical fluid". The generation of super-heated liquid is based on a enormous heat release from organic molecule by a cyclic multiphoton absorption mechanism.

Keywords: laser ablation, micro-machining, fused silica, calcium fluoride, quartz crystals, phase explosion, pyrene

1. INTRODUCTION

Laser ablation continues to grow as an important technique for film deposition, micromachining and surface modification for various materials.¹ However, laser ablation is limited to photon-absorbing materials and has difficulties in the processing of the materials which are transparent at the wavelength of the laser.² Recently our group has developed a method to fabricate fused silica,³ fluoropolymer film,⁴ and calcium fluoride⁵ using excimer lasers. We refer to our method as *laser-induced backside wet etching* (LIBWE). Our method makes it possible to fabricate UV-transparent materials using conventional excimer lasers.

In order to reveal the mechanism of LIBWE, we investigated the dependency of threshold fluence for etching on absorption coefficient of liquid, thermal properties of target materials. In the further study, we observed the dependency of the etch rate on etch size.

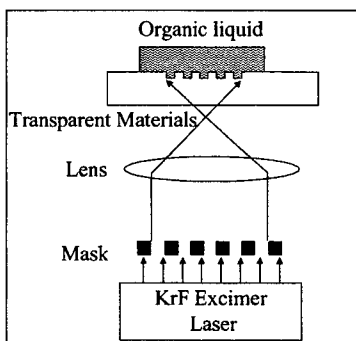


Fig. 1 Diagram of LIBWE apparatus used for etching a fused silica plate with irradiation of a KrF laser.

Further author information:

J.W.: Taiyo Yuden R&D Center, Nakamuroda 5607-2, Haruna, Gunma 370-3347 Japan; E-mail: wangjun@jty.yuden.co.jp

H.N.: E-mail: niino@nimc.go.jp, A.Y.: E-mail: yabe@nimc.go.jp, Fax: +81-298-61-4474

2. EXPERIMENTAL

The four kinds of materials, a transparent fused silica (a-SiO₂) plate (Suprasil II, Heraeus) with a thickness of about 0.5 mm, a transparent quartz crystal plate (c-SiO₂; X-cut, 1120) with a thickness of 2.0 mm, a calcium fluoride (CaF₂, random cut) plate with a thickness of 1 mm, a lithium fluoride (LiF, random cut) plate with a thickness of 1 mm and an UV-transparent fluoro-polymer film (FEP (fluorinated ethylene-propylene copolymer); Nitto Denko Co.) with a thickness of about 50 μm, were used as the samples. KrF excimer laser (248 nm, FWHM 30 ns, Lambda Physik, EMG201MSC) and XeCl excimer laser (308 nm, FWHM 20 ns, Lambda Physik, EMG102MSC) were used as a light source. The intensity of the laser beam was attenuated with a dielectric mirror positioned in front of the laser output. One side of the plate was in contact with acetone (Ac) and tetrahydrofuran (THF) solution containing pyrene (Py) and the other side was irradiated with the laser at room temperature, as shown in Fig. 1. A mask with a square aperture was used to investigate the etching rate. The etched size was about 0.65 x 0.65 mm². Etching was carried out with 100-pulses irradiation with a repetition rate of 2 Hz, unless otherwise noted. Depth profiles were determined with a Stylus instrument (Talystep, Taylor-Hobson). A metal stencil mask was used to etch a pattern of 10 μm lines and spaces. The etched pattern was measured by scanning electron microscopy (SEM: DS-720, Topcon).

3. RESULTS AND DISCUSSION

3.1 Micromachining of transparent materials by laser ablation of liquid

Irradiation with a KrF excimer laser was carried out under conditions using an organic solution containing pyrene at a concentration of 1.0 or 0.4 mol/dm³. SEM photographs of the lines pattern on a-SiO₂ plate are shown in Fig. 2. The lines, whose width was 10 μm and depth was 8 μm, had well-defined sharp edges. Also, there was neither debris nor cracks on the surface around the etched area compared to conventional laser ablation² and ultra-short pulse laser ablation.⁶ The etched surface was also smooth and debris-free. We also obtained very smooth wall and bottom surface on a-SiO₂ after 1000 shots laser irradiation, as shown in Fig. 3.

Figure 4 shows a cross SEM photograph of a lines pattern in the c-SiO₂ using a KrF laser at 2.0 J/cm². Although a c-SiO₂ plate was more brittle than a a-SiO₂ plate, we obtained the same etch quality in c-SiO₂ as that in a-SiO₂.³ The line pattern, whose width was 10 μm and depth was 30 μm, was obtained at high aspect ratio of 3. Interestingly, the etched surface and walls show solidification. The results would be explained that melting occurred on the surface induced by the irradiation with much higher laser intensity.

Figure 5 shows a SEM photograph of a lines pattern in the case of calcium fluoride plate. Compared with the result of fused silica and quartz crystals, the etched surface has micro-roughness and the pattern edge is not sharp. Differences in the etched surfaces would be explained by the crystallinity of $\alpha\text{-SiO}_2$, c-SiO_2 , and CaF_2 .

SEM photographs of the square and line patterns on the FEP film are shown in Fig. 6. After irradiation with 400 pulses at 230 mJ/cm^2 , the etched lines, whose width was $10 \text{ }\mu\text{m}$ and depth was $3.0 \text{ }\mu\text{m}$, had well-defined sharp edges without debris and cracks around the etched area. The etched surface also shows smooth without any debris.

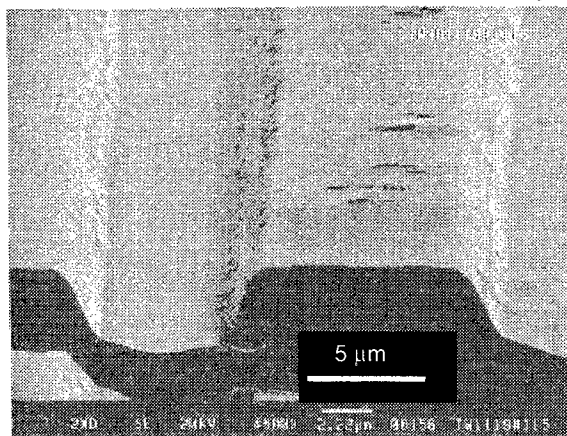


Fig. 2 Scanning electron micrographs of fused silica (a-SiO₂) radiated with 400 pulses of KrF laser at 0.65 J/cm², using an THF solution containing pyrene at a concentration of 1.0 mol/dm³.

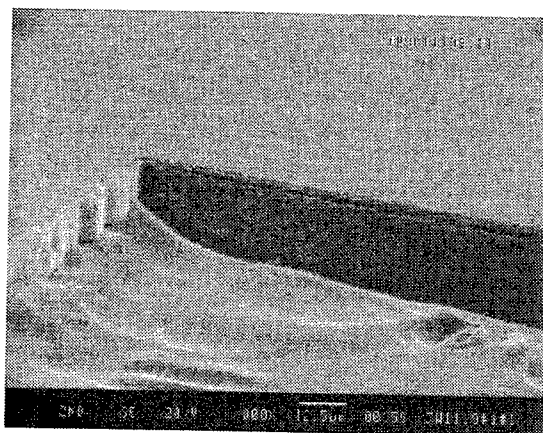


Fig. 3 Scanning electron micrographs of fused silica (a-SiO₂) irradiated with 1000 pulses of KrF laser at 0.65 J/cm², using an acetone solution containing pyrene at a concentration of 1.0 mol/dm³. (Bar = 12.5 μm)

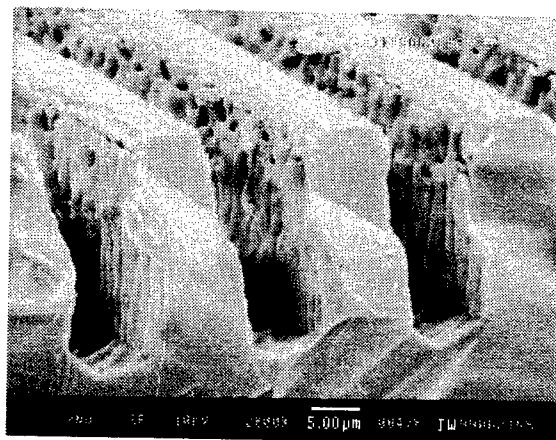


Fig. 4 Scanning electron micrographs of the quartz crystals (c-SiO₂) irradiated with 200 pulses of KrF laser at 2.0 J/cm², using an acetone solution containing pyrene at a concentration of 0.4 mol/dm³. (Bar = 5 μm)

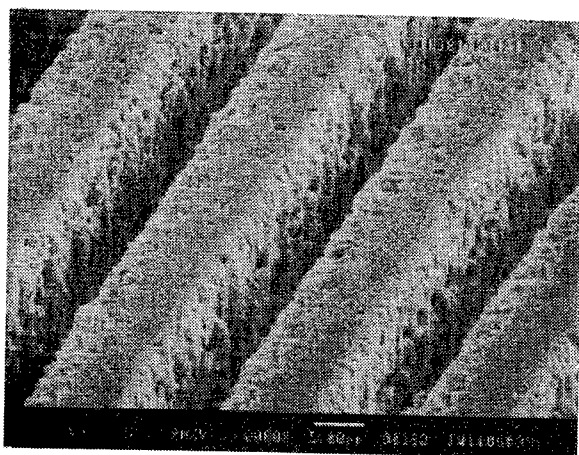


Fig. 5 Scanning electron micrographs of the calcium fluoride (CaF₂) plate irradiated with 500 pulses of KrF laser at 900 mJ/cm², using an acetone solution containing pyrene at a concentration of 0.4 mol/dm³. (Bar = 5 μm)

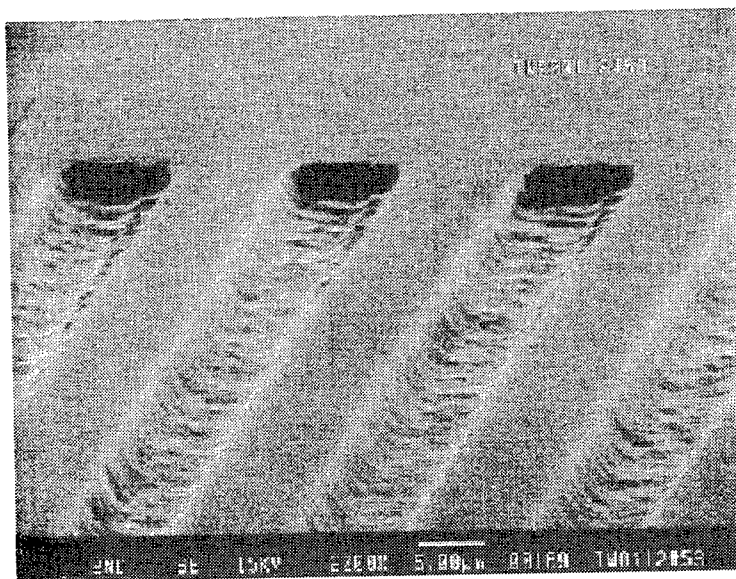


Fig. 6 Scanning electron micrographs of the FEP irradiated with the XeCl excimer laser with 400 pulses at 230 mJ/cm^2 using a THF solution containing pyrene at a concentration of 1.0 mol/dm^3 . (Bar = $5 \mu\text{m}$)

3.2 Dependency of the etch rates on different materials

Figure 7 is the plot of the etch rates as a function of laser fluence used for irradiation of a-SiO₂, c-SiO₂, CaF₂, and FEP. In these samples the relationship between etch rate and laser fluence was almost linear. In the case of fused silica using pyrene-acetone solution, the etch rate increased from 5 to 25 nm/pulse as the laser fluence increased from 0.4 to 1.3 J/cm^2 . However, when a laser fluence of more than 1.5 J/cm^2 was applied, cracks were generated in the silica plate. The extrapolate thresholds for the etching of the materials were summarized in Table 1, as well as the their thermal properties. The threshold fluence for the etching of a-SiO₂ is about 0.24 J/cm^2 , which is 1/40 lower than that of conventional KrF laser ablation. The extrapolate thresholds for etching of c-SiO₂ was about 0.33 J/cm^2 . On the other hand, in the case of CaF₂, higher fluences are required compared with those of silica. The threshold fluence for the etching of CaF₂ is about 740 mJ/cm^2 , which is also higher than that of fused silica. In the case of FEP using pyrene-THF solution, the threshold fluence for the etching was about 0.045 J/cm^2 , which lower than that for the etching of a-SiO₂ using the same solution (0.17 J/cm^2). The lowest etching threshold of FEP among the materials was due to a low melting point and poor thermal conductivity. The higher etch threshold of c-SiO₂, compared with that in the glass state, suggested that SiO₂ in the crystal state needed additional energy to be etched.

In a higher laser fluence region, the difference in etch rates between a-SiO₂ and c-SiO₂ was negligibly small. The melting point of a-SiO₂ is about 1900 K while that of c-SiO₂ is about 2000 K.⁷ The melting points of a-SiO₂ and c-SiO₂ only affected the etch rates in a lower laser fluence region, especially the extrapolate threshold for etching.

In the case of CaF₂, the fused enthalpy is higher than that of fused silica. The threshold of CaF₂ etching was higher than that of fused silica, although the melt point of CaF₂ is lower than fused silica. In the case of LiF and Al₂O₃, we did not observe the etching on the surface, even if we used the laser fluence of 1.5 J/cm^2 . LiF has a higher specific heat than that of CaF₂. Al₂O₃ has the highest melting point and thermal conductivity among the materials.

Table 1 The different threshold fluences (F_{th}) of the etching of six kinds of materials.

Matial	Liquid type ^{a)}	F_{th} (J/cm ²)	m.p. ^{b)} (C)	ΔH ^{c)} (kJ/mol)	C_p ^{d)} (J/g K)	κ ^{e)} (W/cm K)
FEP	THF / Py	0.05	273		0.9	0.004
a-SiO ₂	THF / Py	0.17	1883	8.535	0.72	0.014
a-SiO ₂	Ac / Py	0.24	1883	8.535	0.72	0.014
c-SiO ₂	Ac / Py	0.33	1953	8.535	0.72	0.014
CaF ₂	Ac / Py	0.74	1691	29.7	0.85	
Al ₂ O ₃	Ac / Py	> 1.5	2323		0.75	0.30
LiF	Ac / Py	> 1.5	1121	27.087	1.9	

^{a)} THF / Py = tetrahydrofuran/pyrene, Ac / Py = acetone/pyrene

^{b)} Melting point

^{c)} Fused enthalpy

^{d)} Specific heat

^{e)} Thermal conductivity

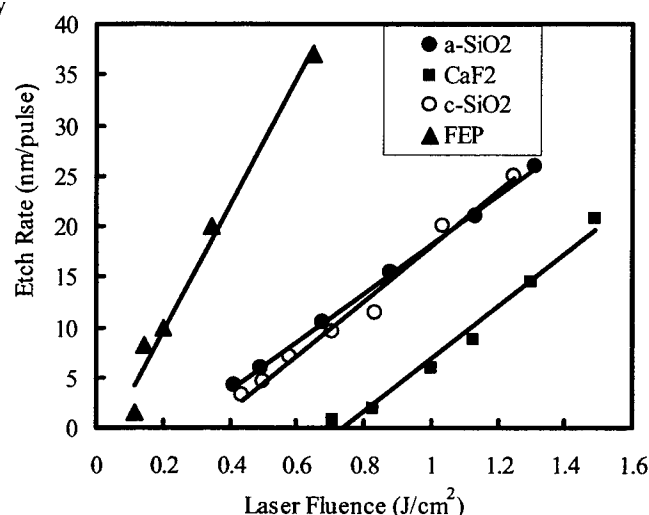


Fig. 7 Plots of etch rate as a function of laser fluence in the irradiation by a KrF laser using an acetone solution containing pyrene at concentrations of 0.4 M in the case of fused silica (a-SiO₂, ●), CaF₂ (■), quartz crystal (c-SiO₂, ○), and FEP (▲).

3.3 Dependency of etch rate on different liquids

When the concentration of pyrene in the acetone decreased, the etching rate became slower and the threshold fluence increased, as shown in Table 2. Although a higher concentration of pyrene gives a higher etching rate, the concentration of 0.4 mol/dm³ is almost the maximum solubility in acetone solvent. In order to increase the concentration of pyrene, we used THF as solvent instead of acetone. The threshold fluence of a-SiO₂ using THF-pyrene solution at 1.0 M was about 0.17 J/cm². Using acetone-benzil solution and pure methyl benzoate, as shown in Table 2 and Fig. 8, we measured the etching rate of fused silica. These solutions have the property that is high absorption coefficient at the wavelength of 248 nm. The efficient etching of LIBWE is due to the deposition of laser energy in these liquid near the rear surface of a-SiO₂ plate. The absorption coefficient (α) of the solution can be calculated from the molar absorption coefficient (ϵ) of pyrene and benzil in dilute solutions, as shown in Table 2. It is well known that the transmission of laser is a function of laser fluence in the laser ablation of polymer.^{8,9} Recently, we developed a method to analyze the nonlinear absorption behavior in the laser ablation of polymer doped with pyrene by introducing an absorption coefficient dependent on laser intensity ($\alpha(I)$). Similar to the laser ablation of the polymer, the absorption coefficients for the solution would depend on the laser fluence when the solution was irradiated at a high fluence. We estimated a corrected absorption coefficient at the threshold fluence (α_{th}) using our previous results.¹⁰

On the basis of these estimation, we obtained the optical penetration depth $1/\alpha_{th} = 0.7 \mu\text{m}$ for the acetone solution containing pyrene at 0.4 mol/dm³. It means that most of the laser energy was deposited in the solution layer in the thickness

of less than 1 μm away from the surface of silica. We calculated the maximum temperature of the solution layer at threshold fluence based on the assumption that the absorbed laser energy was converted entirely into heat and that the heat diffusion was much slower than the laser pulse duration:¹¹

$$T_{\text{th}}^{\text{max}} = T_0 + \alpha_{\text{th}} F_{\text{th}} / \rho C$$

where $T_{\text{th}}^{\text{max}}$ is the maximum temperature at threshold, T_0 is room temperature. ρ and C are the density and the heat capacity of solvents,¹² respectively. The results are summarized in Table 2. $T_{\text{th}}^{\text{max}}$ is the maximum possible temperature if the liquid is heated to a superheat state without evaporation. The temperature of the fused silica surface in contact with the superheat liquid will rise up to about 2000 K, which is higher than the softening temperature of fused silica (1900 K)¹³. In fact, the thermodynamic critical temperature (T_c) of the liquid of acetone is about 500 K. In laser ablation of liquid, Kim and Grigoropoulos¹⁴, reported that irradiation of a laser on absorbing-liquid surface could heat liquid to a higher temperature than spinodal limit ($T_{\text{sp}}=0.84 T_c$) and close to T_c if a high fluence was applied by a short pulse laser irradiation. When the liquid was in this metastable state, the volumetric evaporation effect (homogeneous-bubble nucleation) dominates the evaporation process since the random-fluctuation energy of the liquid molecule is comparable with the activation energy for vaporization. In our SEM photograph of quartz crystals in Fig. 4., the etched surface and walls show solidification, although the quartz have no absorption to KrF laser. The interesting fact is that the temperature of the absorbing-liquid can reach more than 2000 K after irradiation of laser on liquid through quartz at 2 J/cm². This temperature of 2000 K is much more than the T_c of acetone. It means that the super-heated liquid corresponded to "transient supercritical fluid" with the same density as normal liquid of acetone.¹⁵

Table 2 Absorption coefficient (α_0), revised absorption coefficient (α_{th}) at etching threshold (F_{th}) of a-SiO₂, and estimated maximum temperature at threshold ($T_{\text{th}}^{\text{max}}$) in an acetone containing pyrene at different concentrations.

Liquid type ^{a)}	Concentration (mol/dm ³)	α_0 (μm^{-1})	α_{th} (μm^{-1})	F_{th} (mJ/cm ²)	$T_{\text{th}}^{\text{max}}$ (K)
Ac / Py	0.10	0.20	0.48	580	1900
Ac / Py	0.20	0.39	0.90	350	2100
Ac / Py	0.40	0.78	1.40	240	2300
THF / Py	1.0	2.0	2.9	170	3600
Ac / Bz	0.8	0.65	1.8	390	4410
c	neat			200	

^{a)} Ac / Py = acetone/pyrene, THF / Py = tetrahydrofuran/pyrene, Ac / Bz = acetone/benzil, Benzoate = methyl benzoate

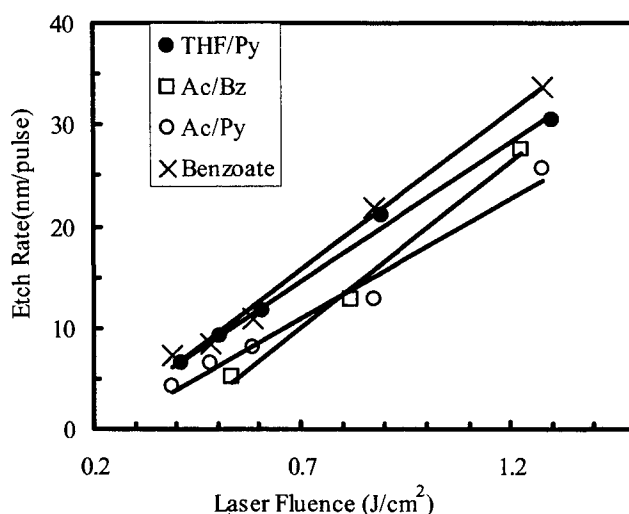


Fig. 8 Plots of etch rate as a function of laser fluence in the irradiation by a KrF laser in case of fused silica (a-SiO₂) using THF-pyrene (●), acetone-benzil (□), acetone-pyrene (○), and pure methyl benzoate (X).

3.4 Dependency of etch rates upon etch sizes

In the further study, we observed the dependency of the etching rate on the size of irradiated area. Figure 9 shows the plot of the etching rates as a function of etch sizes using acetone-pyrene solution at 0.4 mol/dm^3 for irradiation of fused silica. In the small irradiate area, the thermal energy of the liquid layer lost the energy to surround liquid in comparison with the case of larger area. Also, in the process of heating transparent materials, smaller area made it difficult that transfer thermal energy to a deep level of substrate because of the loss of energy by surround materials. The third reason may be due to explore process of liquid. The force of attracting transparent material by the exploring phase transition increase with the increase of the volume of the super-heated liquid.

However, when increase the etching depth at the strong laser fluence of 2 J/cm^2 , the etch rate becomes faster than that with large irradiation area and low aspect ratio. As shown in Fig. 4, the etch depth of $30 \mu\text{m}$ is much higher than the predicted etch depth from the linear relation between etching rate and laser fluence in Fig. 7. In this case, the loss of thermal energy due to surrounded liquid was decreased. Also, the force of the attracting was emphasized in close space, which is similar as the emphasize effect of explosion in a house than outside.

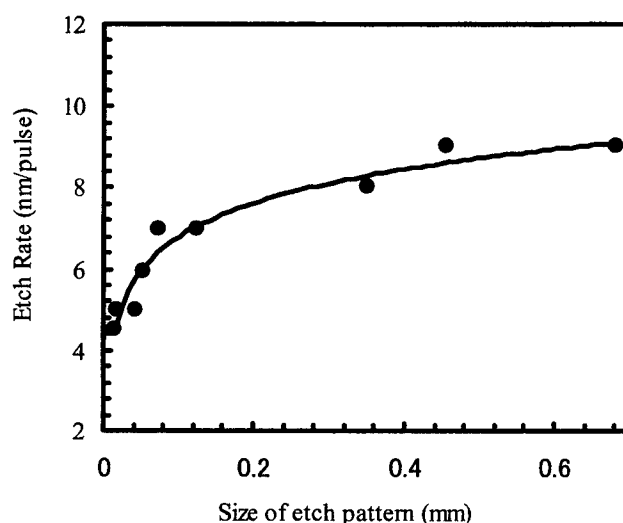


Fig. 9 Plots of etch rate as a function of irradiate size in the irradiation by a KrF laser (0.65 mJ/cm^2) in case of fused silica (a-SiO_2) using acetone-pyrene at 0.4 mol/dm^3 .

3.5 Mechanism of etching

On the basis of our results, we suggest the mechanism for LIBWE to be as follows. The solution absorbs the laser energy and reaches high temperatures, which can exceed T_c of the liquid. The superheated liquid, corresponding to "transient super-critical fluid", shows the volumetric evaporation effect and generated homogeneous-bubble nucleation, where the process dominates the evaporation process since the random-fluctuation energy of the liquid molecule is comparable with the activation energy for vaporization. The vapor with high temperature and high pressure attacks the softened surface of the materials. A debris of the material is removed from the bulk substrate into a liquid phase. After the laser pulse is over, the irradiated area is cooled immediately. This rapid cooling behavior prevents the bulk of transparent material from being thermally damaged.

4. CONCLUSION

We suggest the mechanism is due to the combination of two processes in the interface of a target material and a liquid: one is a heating process (phase explosion, explosive boiling) by the superheated liquid and the other is an attacking process by high temperature and pressure. We also indicated that the temperature of the super-heated liquid can exceed the thermodynamic critical temperature T_c when using high laser fluence, and the liquid corresponded to the "transient super-critical fluid". The generation of super-heated liquid is based on a enormous heat release from organic molecule by a cyclic multiphoton absorption mechanism.

ACKNOWLEDGMENTS

J.W. expresses his gratitude to Japan Science and Technology Corporation for Domestic Research Fellowship and to the Science Technology Agency (STA) of Japan for partial financial support of this work.

REFERENCES

1. D. Baeuerle, "Laser Processing and Chemistry", Springer, Berlin, 1996.
2. J. Ihlemann, B. Wolff-Rottke, "Excimer laser micromachining of inorganic dielectrics", *Appl. Surf. Sci.* **106**, pp.282-286, (1996).
3. J. Wang, H. Niino, A. Yabe, "One-step microfabrication of fused silica by laser ablation of an organic solution", *Appl. Phys. A* **68**, pp.111-113 (1999).
4. J. Wang, H. Niino, A. Yabe, "Microfabrication of a fluoropolymer film using conventional XeCl excimer laser by laser-induced backside wet etching", *Jpn. J. Appl. Phys.*, **38**, pp.L761-L763 (1999).
5. J. Wang, H. Niino, A. Yabe, "Micromachining of transparent materials with super-heated liquid generated by multiphotonic absorption of organic molecule" *Appl. Surf. Sci.*, in press.
6. H. Varel, D. Ashkenasi, A. Rosenfeld, M. Waechmer, E. E. B Campbell, "Micromachining of quartz with ultrashort laser pulses", *Appl. Phys. A*, **65**, pp.367-373 (1997).
7. W. G. Driscoll, "Handbook of Optics", McGraw-Hill, New York, pp 7-130 (1978).
8. G. H. Pettit, M. N. Ediger, D. W. Hahn, and R. Sauerbrey, "Transmission of polyimide during pulsed ultraviolet laser irradiation", *Appl. Phys. A*, **58**, pp.573-579 (1994).
9. H. Fujiwara, T. Hayashi, H. Fukumura, and H. Masuhara, "Each dopant can absorb more than ten photons: transient absorbance measurement at excitation laser wavelength in polymer ablation," *Appl. Phys. Lett.*, **64**, pp.2451-2453, (1994).
10. J. Wang, H. Niino, A. Yabe, "Laser ablation of poly(methyl methacrylate) doped with aromatic compounds: laser intensity dependence of absorption coefficient", *Jpn. J. Appl. Phys.*, **38**, pp.871-876 (1999).
11. H. Fukumura, N. Mibuka, S. Eura, H. Masuhara, "Porphyrin-sensitized laser swelling and ablation of polymer films", *Appl. Phys. A*, **53**, pp.255-259 (1991).
12. CRC Handbook of Chemistry and Physics, 78th ed. Chemical Rubber, Boca Raton, FL, pp. 5-33 (1997).
13. Kirk-Othmer John edn., "Encyclopedia of Chemical Technology", Wiley & Sons. Inc., New York, p.807 (1980).
14. D. Kim, M. Ye, C. P. Grigoropoulos, "Pulsed laser-induced ablation of absorbing liquids and acoustic-transient generation", *Appl. Physics A*, **67**, pp.169-181 (1998).
15. "Supercritical Fluid Engineering Science", ed. by E. Kiran and J. F. Brennecke, American Chemical Society (1992).

SESSION 12

Laser Microengineering IV

Analysis of Excimer Laser Patterning Process of Cu Thin Film

Tomokazu Sano*, Isamu Miyamoto, Hideaki Hayashi and Humihiro Ochi

Department of Manufacturing Science, Graduate School of Engineering, Osaka University
2-1 Yamada-Oka, Suita, Osaka 565-0871, Japan

ABSTRACT

The front and rear patterning process of metal thin film irradiated by the KrF excimer laser is analyzed in this study. In the front patterning of Cu thin film with a thickness of 0.1-0.6 μm on polymer substrate, high speed shadowgraphs were taken by irradiating a SHG YAG laser beam coaxially with the excimer laser beam. At the optimal fluences, the molten film separated along the outer edge of the laser-irradiated region was driven toward the center of the irradiated region by the surface tension force, and the was detached from the substrate as small droplets. No explosive removal was observed in our laser patterning experiment contrary to the case reported in the literature. Under this condition, little change in the reflectivity, approximately 25%, was observed during laser irradiation. At the excess fluences, the recoil force of evaporation provided the outward radial flow to extend the patterning zone into the unirradiated zone so that the edge of the unirradiated region was peeled off by the momentum of the metal driven by the recoil force. As a result, the reflectivity decreased drastically in the latter half of laser pulse. In the rear patterning, the feature of the deposited metal on opposite substrate removed from the thin film was observed by an optical microscope. Intensities of incident and transmitted beam were measured simultaneously using PIN-Photodiodes. Film removal started after approximately 20 ns of laser incidence during laser pulse. The peak intensity of the transmitted beam is approximately 1/100 of that of the incident beam. In the rear patterning process it was found that the recoil force of the evaporation and plasma expansion generated between the film and the substrate pressed the film subsequently, the molten part at the edge of the unirradiated part was peeled and flied away by the momentum from the recoil force.

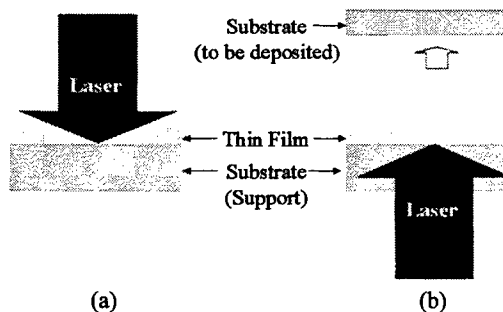
Key Words: KrF excimer laser, front/rear patterning, removal mechanism, patterning preciseness, behavior of edge

1. INTRODUCTION

Patterning of metal thin film has been one of the most important applications and many papers have been reported¹⁻⁴⁾, which include dotted-picture¹⁾ and circuit patterning²⁾.

Clarifying the removal mechanism of metal thin film is important in order to understand the main factors which are critical to the patterning preciseness. Several removal mechanisms of metal thin film have been reported so far. These mechanisms include complete evaporation⁵⁾, explosive removal owing to high gas pressure evolved instantaneously at the film-substrate interface⁶⁾, and removal by liquid metal flow driven outward by the evaporation pressure⁷⁾. We have found that, however, these mechanisms can not explain our experimental results completely.

The purpose of this study is to investigate the patterning mechanisms, particularly the behavior of the patterned edge which are critical to the patterning preciseness. In this study, two patterning methods, laser irradiation from front side and rear side



(a) (b)
Fig. 1 Schematic illustration of (a) front and (b) rear patterning.

* Email: sano@mapse.eng.osaka-u.ac.jp, Telephone: +81-6-6879-7535, Fax: +81-6-6879-7534

of thin film, are investigated. Here, the former is defined as "front patterning," and the latter as "rear patterning" as shown in Fig. 1. In the rear patterning, thin film deposited on transparent support is irradiated by a laser through the support different from the usual front patterning. The rear patterning experiment was conducted to better understand the patterning phenomena.

In the front patterning, the removal process was analyzed based on thermal conduction theory, reflectivity measurements from thin film, and high speed photographing techniques. In the rear patterning, a new removal mechanism was proposed based on the relationship of the start of incident and transmitted beam.

2. EXPERIMENTAL PROCEDURES

2.1 Front patterning

In the front patterning, a KrF excimer laser ($\lambda = 248$ nm) which has pulse duration of 37 ns was used to remove metal thin film. The specimen used in this experiments were Cu thin film with thickness of 0.15, 0.3 and 0.6 μm deposited on visibly transparent polymethylmethacrylate (PMMA) substrates using the ion sputter deposition method. The specimen was uniformly irradiated by a KrF excimer laser with a circular or a rectangular cross section area using a mask projection optics. Laser fluence was adjusted ranging from 0.5 to 2.6 J/cm^2 .

Intensities of the incident and the reflected beams were measured using a high sensitive PIN-Photodiode as shown in Fig. 2. Reflectivity during pulse duration was estimated from these intensity measurements.

An image intensifier with a minimum gate time of 3 ns was used to photograph the dynamic behavior of the film removal illuminated by a SHG YAG laser ($\lambda = 532$ nm) as shown in Fig. 3. The removal process was observed by a series of photographs taken at different time delays after excimer laser irradiation.

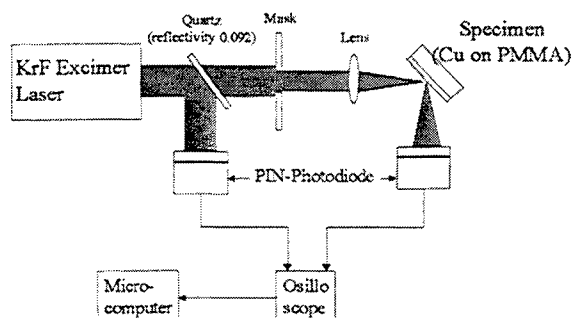


Fig. 2 Experimental setup for reflectivity measurement.

2.2 Rear patterning

KrF excimer laser with a pulse duration of 25 ns was irradiated from the rear side to remove the metal thin film. Cu thin film was deposited on a quartz glass using the ion sputter deposition method. The film thicknesses were 160 and 750 nm. Laser fluence was changed from 0.2 to 1.0 J/cm^2 , and film-substrate distance was changed from 10 to 1000 μm . Si wafer was used as the substrates to be deposited.

Intensity of incident and transmitted beams were measured using highly sensitive PIN-Photodiodes as shown in Fig. 4.

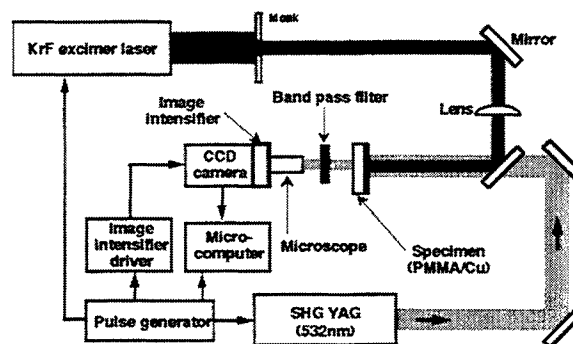


Fig. 3 Experimental setup for high speed photographing of thin film removal.

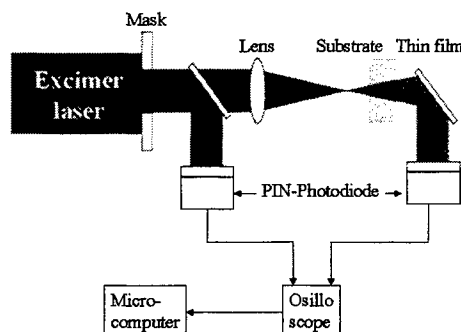


Fig. 4 Experimental setup for transmitted intensity measurement in the rear patterning.

3. RESULTS AND DISCUSSION

3.1 Front patterning

3.1.1 Removal characteristic of Cu film

Figure 5 shows the appearance of the film removed by the irradiation of a single shot KrF excimer laser. At the optimal laser fluence, the film at the irradiated zone was removed with clearly defined edges. At the excess fluences, the edge of the film was peeled from the substrate around the irradiated zone. Droplets of the molten metal deposited near the irradiated zone indicate that the film was removed in the liquid state. It should be noted, however, that no droplets were observed within the irradiated zone. The film at the unirradiated region was melted by the droplets when the thickness is 0.3 μm .

The quality of the film removal was evaluated from the definition of the removed edge because the deposition of the droplets can be prevented by directing the film face downward and by irradiating the excimer laser upward. The dimensional preciseness of the removed zone was also acceptable when the clearly defined edge with no peeling was obtained. The quality of the film removal is shown in Fig. 6. The laser fluence of the acceptable quality increases linearly as the film thickness increases. The laser fluence required per unit volume of thin film removal is about 10-14 kJ/cm^3 in order to provide acceptable film removal.

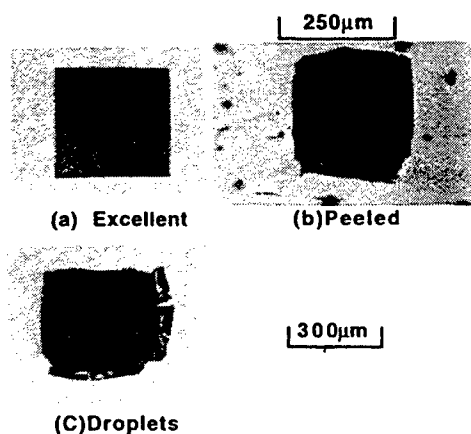


Fig. 5 Quality of laser machining.

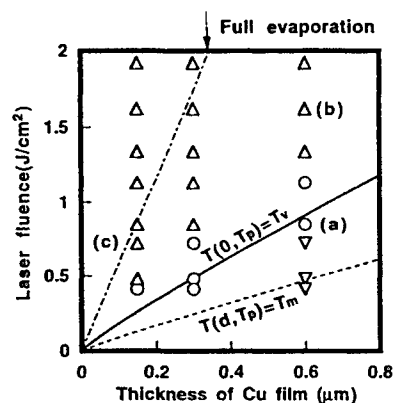


Fig. 6 Quality of laser removal. Solid and dotted lines indicate calculated laser fluence to heat the film up to T_v and T_m respectively.

(Δ : peeled, \circ : excellent, ∇ : partially removed)

3.1.2 Calculation of film temperature

The temperature of the Cu thin film irradiated by the excimer laser was estimated based on the thermal conduction theory. In this analysis, one-dimensional heat conduction is assumed owing to extremely thin thickness of the Cu film in comparison with the laser irradiated size. It is further assumed that changes in the thermophysical properties of the metal film and the substrate, radiation losses and latent heat of fusion and evaporation were negligible. Therefore, the temperature rise of the film can be described by the follows thermal conduction equations,

$$\frac{\partial^2 T_1}{\partial x^2} - \frac{1}{k_1} \frac{\partial T_1}{\partial t} = \frac{1}{k_1} \frac{W}{\delta} \exp\left(-\frac{x}{d}\right) \quad (1)$$

$$\frac{\partial^2 T_2}{\partial x^2} - \frac{1}{k_2} \frac{\partial T_2}{\partial t} = 0 \quad (2)$$

In Eq. (1) and Eq. (2) the subscript 1 refers to the thin film and 2 to the substrate, and $T_{1,2}$ is temperature, $K_{1,2}$ thermal conductivity, $k_{1,2}$ thermal diffusivity, d thickness of the film, W the laser power, δ penetration depth at which the laser intensity is diminished to 1/e of the value of the surface of metal, A absorptivity of laser beam at the metal film and t time. When A and W are constants, the solution of Eq. (1) and Eq. (2) solved under the initial conditions of $t = 0$, $T_1 = T_2 = 0$ and the boundary conditions of $x = d$, $T_1 = T_2$ and

$$K_1 \frac{\partial T_1}{\partial x_1} = K_2 \frac{\partial T_2}{\partial x_2} \quad (3)$$

is given by the following equation¹⁾.

$$T_h(x, t) \cong \frac{W}{K_1} \sum_n \left[2\sqrt{k_1 t} \alpha^{n+1} \operatorname{ierfc} \left\{ \frac{2(n+1)d \pm x}{2\sqrt{k_1 t}} \right\} - 2\sqrt{k_1 t} e^{-\frac{d}{\delta}} \frac{\Lambda \alpha^n}{1+\Lambda} \operatorname{ierfc} \left\{ \frac{2(n+1)d \pm x}{2\sqrt{k_1 t}} \right\} \right. \\ \left. + 2\sqrt{k_1 t} e^{-\frac{d}{\delta}} \frac{\alpha^n}{1+\Lambda} \operatorname{erfc} \left\{ \frac{2(n+1)d \pm x}{2\sqrt{k_1 t}} \right\} - \delta e^{-\frac{x}{\delta}} + 2\sqrt{k_1 t} \operatorname{ierfc} \left\{ \frac{x}{2\sqrt{k_1 t}} \right\} \right] \quad (4)$$

where

$$\alpha \equiv \frac{\Lambda - 1}{\Lambda + 1}$$

$$\Lambda = \frac{K_1}{K_2} \sqrt{\frac{k_1}{k_2}}$$

The thermophysical constants of Cu and PMMA used in this calculation are shown in Table 1.

Table 1 Thermophysical properties of Cu and PMMA

	Cu	PMMA
Specific heat (cal/g deg) c	0.0914	0.8
Mass density (g/cm ³) ρ	8.94	1.19
Thermal conductivity (cal/s cm deg) K	0.93	0.0004
Thermal diffusivity (cm ² /s) k	1.14	0.00112
Melting point (K) T_m	1358	-
Boiling point (K) T_v	2566	-
Latent heat of fusion (J/g) L_m	207	-
Latent heat of evaporation (J/g) L_v	4721	-

The temperature rise at the film surface is plotted in a solid line in Fig. 7(a); the film temperature increases almost linearly during the pulse duration. A dotted line indicates temperature rise calculated under the assumption that the film is heated adiabatically. It is seen that approximately 1/4 of the absorbed laser energy is conducted to the PMMA substrate despite that the thermal conductivity of PMMA is much smaller than that of Cu. Fig. 7(b) shows the temperature distribution in the film calculated at the end of laser pulse, $t = 37$ ns; the temperature is seen to be almost uniform throughout the Cu film.

The solid and dotted lines in Fig. 6 represent the calculated fluences required to heat the film up to the boiling and melting points of Cu, respectively. The laser fluence for evaporating the

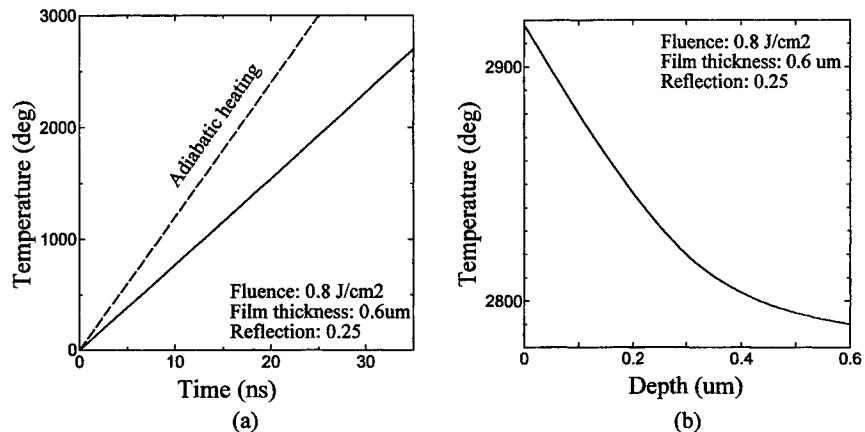


Fig. 7 Temperature rise of Cu thin film calculated using Eq. (4).
(a) Time change in the surface temperature of the film.
(b) Temperature distribution in the film at the end of laser pulse.

metal film in the entire laser irradiated zone is plotted in a chain line. By relating these calculated values with the observed quality of the removal film, it is found that the film removal with acceptable removal quality can be obtained when the molten film of the boiling point of Cu is produced. The removal by the complete evaporation is seen to require laser fluences 4 - 5 times larger than the values for high quality removal. These results indicate that the optimal conditions of laser irradiation can be approximately estimated by the thermal conduction calculation.

3.1.3 Measurement of reflectivity of Cu film

Reflectivity measurement at low fluences when the film is not melted and not completely removed are shown in Fig. 8. The reflectivity keeps approximately 25 % except in the netlike zone where the signal varies widely owing to the weak incident beam. The measured value is in good agreement with the value in the literature⁸⁾. This result means the film surface keeps flat during laser pulse. The same result was obtained under the optimal condition when the film is completely removed and patterned edge is sharp. This means that the film remains on the substrate during laser pulse and that the film removal starts after the laser pulse exists. The reflectivity measurements at the excess fluences when the edge is peeled from the substrate around the irradiated zone are shown in Fig. 9. In the first half of laser pulse the reflectivity is constant. In the latter half its value decreases drastically to 2-3 %, which is in agreement with the measured value of PMMA. This means that the film starts to be removed from the substrate and that the substrate is exposed during the laser pulse.

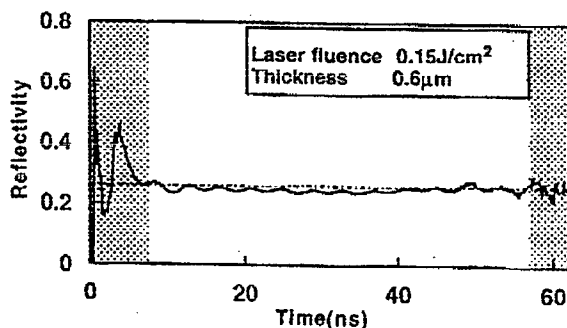


Fig. 8 Reflectivity from Cu thin film at low fluences.

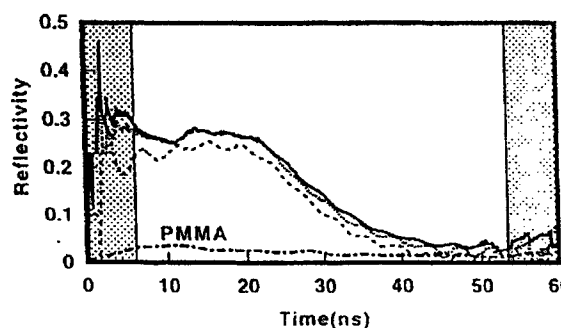


Fig. 9 Reflectivity at excess fluences.

3.1.4 Observation of removal process by high speed photography

Figure 10 shows a series of photographs taken at different delay time for the film thickness of 0.6 μm at the optimal laser fluence (0.8 J/cm^2). In this experiment, the laser beam was irradiated with a circular area of 330 μm in diameter. Although the motion of the molten metal appears discontinuous, the temporal and spatial resolutions of these photographs are high enough to analyze the removal process. No change is seen in several hundreds of nanoseconds from the excimer laser irradiation, indicating that the laser irradiated region was entirely covered with the Cu thin film. The laser - heated Cu thin film circle is separated from the unirradiated region at approximately 500 ns, and then the molten metal edge begins to move toward the center of the irradiated circle. At 5 - 10 μs , the molten metal gathers at the center of the circle and then break into small droplets, spreading outward radially by their inertia.

Figure 11 shows the photographs taken at an excess laser fluence (1.3 J/cm^2) when calculated temperature of the metal film becomes higher than the boiling point of Cu. In this case, no gathering of the molten metal in the irradiated circle was observed unlike the case of the optimal condition, 0.8 J/cm^2 .

3.1.5 Removal mechanism of thin metal film

Figure 12 illustrates the removal mechanism at the optimal laser fluence. By neglecting the latent heat of evaporation, the thermal conduction analysis indicates that the metal film is heated up to the boiling point of Cu by the laser irradiation. The metal film is separated at the irradiated/unirradiated boundary by the local high power density produced by diffraction. The molten metal edge is then forced to move toward the center of the irradiated circle radius of the curvature is as small as the metal film thickness. The accelerated molten metal is broken into small droplets at the center, which then fly away.

The removal mechanism at the excess fluences is shown in Fig. 13. The calculated temperature is much higher than the boiling point of Cu, and the excess laser energy is used for the latent heat of evaporation. Thus the strong recoil force of vaporization presses down the molten metal to produce outward radial flow of the molten metal. The preciseness of the film

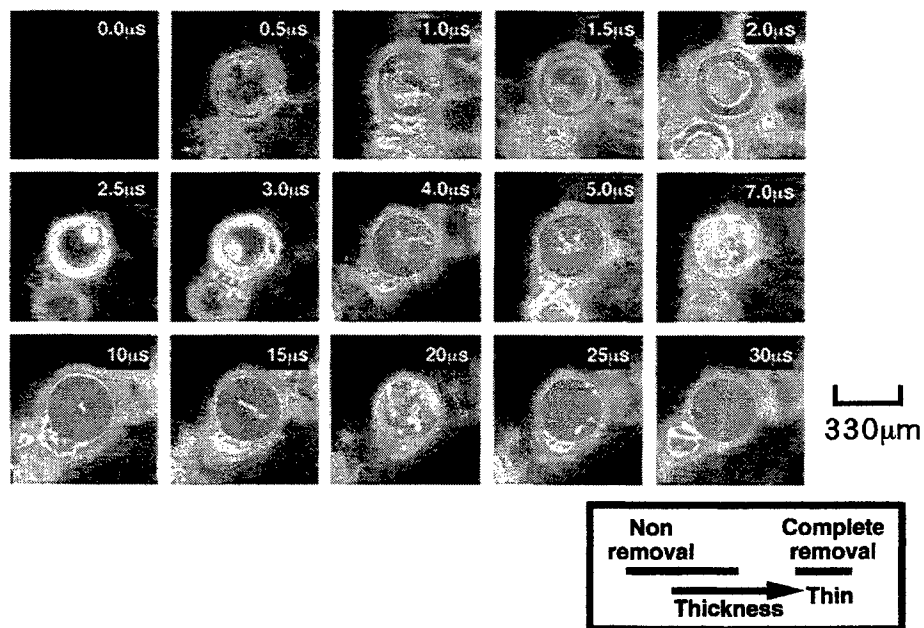


Fig. 10 Dynamic behavior of Cu thin film at optimized fluences.

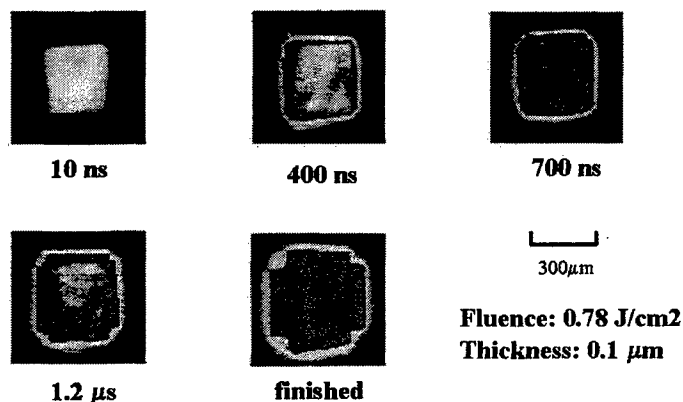


Fig. 11 Dynamic behavior of Cu thin film taken by high speed camera at excess fluences.

removal is considered to depend on the outward velocity of the molten metal flow, since the hot metal secondarily melts the film in the unirradiated region. The removal area is expanded as the laser fluence increases, since the increased recoil force accelerate the outward flow. The molten metal flow not only remelts the surrounding film, but also peels the outer film by its momentum as schematically shown in Fig. 13. At excess fluences, no molten metal flow toward the center of the irradiated region was observed.

3.1.6 Preciseness of metal film removal

The size of the removed zone of the thin metal film, d , was compared with the size removed in polyimide, d_0 , where no liquid flow is produced. An optical microscope with the resolution of 2-3 μm was used for the size measurement. The size error, $\Delta = d - d_0$, measured at different film thickness and fluences is shown in Fig. 14. The value of d decreases with decreasing laser fluence on the conditions of the complete film removal. Thin is because the outward molten metal flow decreases as the laser energy decreases.

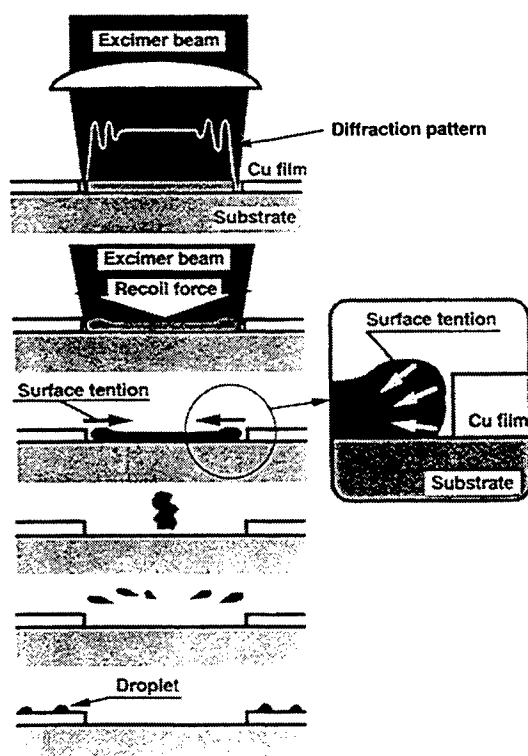


Fig. 12 Schematic illustration of metal thin film removal process at optimized fluences.

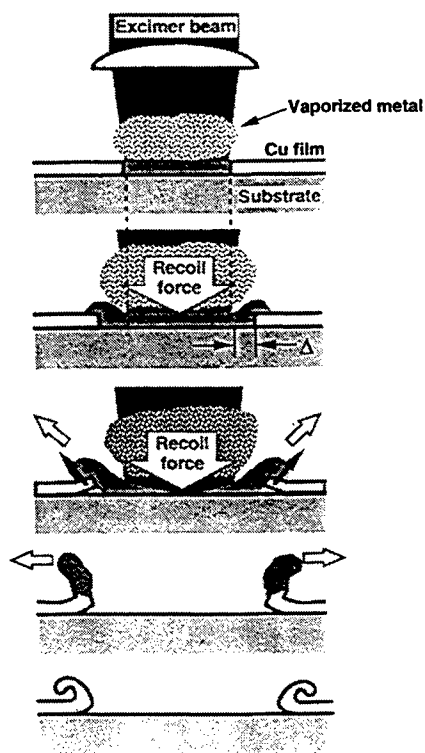


Fig. 13 Schematic illustration of metal thin film removal process at excess fluences.

3.2 Rear patterning

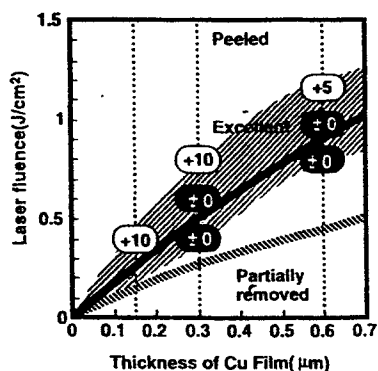


Fig. 14 Removal preciseness in front patterning at different laser fluences and film thickness.

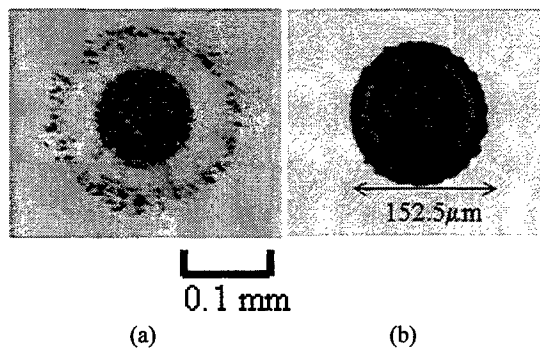


Fig. 15 Typical optical microscope images of (a) deposited Au on Si target and (b) removed region of thin film.

3.2.1 Deposited metal

Figure 15 shows the appearance of Au deposited on the opposite Si substrates and the removed region of the film with a spot size of 140 μm . A splattered ring is observed around the deposited circle, which consists of droplets of a size of several μm . The diameter of the ring becomes larger as the fluence increases. Figure. 16 shows that the diameter of the splattered

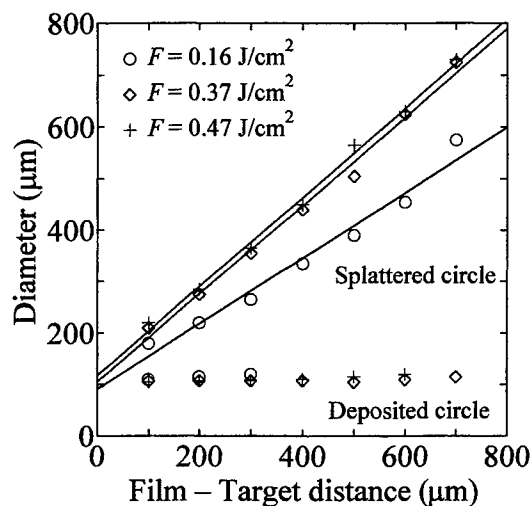


Fig. 16 Diameter of splattered circle and deposited circle.

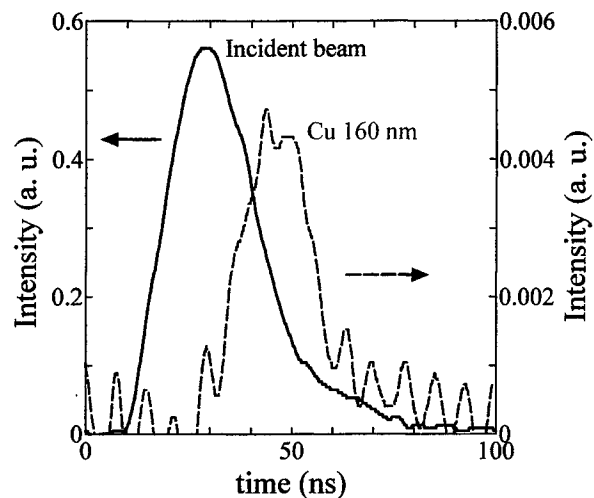


Fig. 17 Transmitted intensity through Cu thin film.

ring increases linearly in proportion to film - target distance at each fluence. On the other hand, the diameter of deposited circle was constant independent of the laser fluences. This means that the molten part detached at the edge of the unirradiated part flew away at an angle, which is dependent on the laser fluence.

3.2.2 Measurement of intensity of incident and transmitted beam

Figure 17 shows the waveform of the incident and transmitted beam intensity for Cu thin film with 160 μm in thickness at the laser fluence of 1.0 J/cm². Transmitted laser began to be detected at 20 ns from the irradiation of the laser. The peak intensity of the transmitted laser power was as small as approximately 1/100 of that of incident beam. This means film removal starts during laser pulse. This indicates that a clearance was generated in the film after laser irradiation.

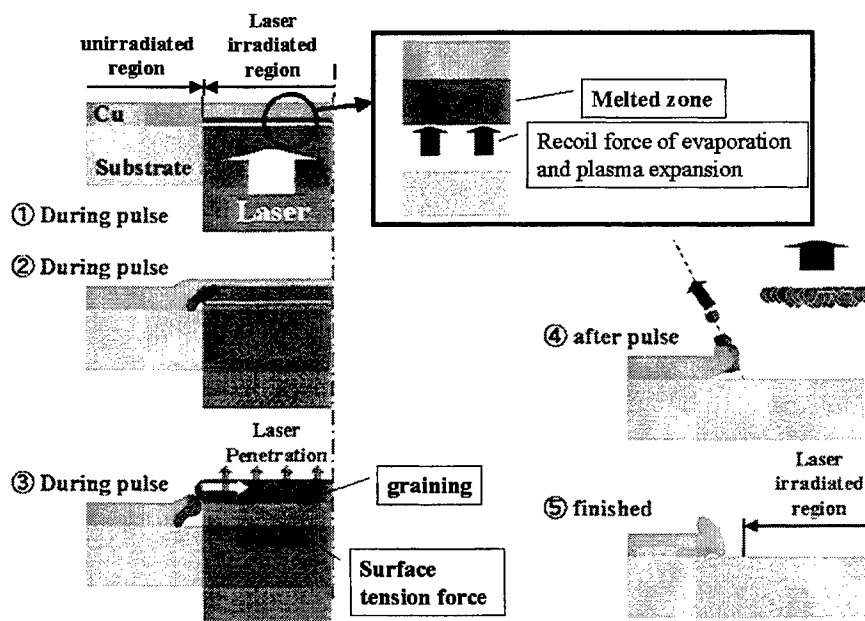


Fig. 18 Schematic illustration of removal process in the rear patterning.

3.2.3 Removal mechanism of rear patterning

Based on the above-mentioned results in the rear patterning, removal mechanism of the rear patterning is shown in Fig. 18. During the laser pulse, the irradiated region is melted and evaporated, and then detached from the substrate by the recoil force owing to evaporation and plasma expansion. The temperature attained in the rear patterning is higher than the case of the front patterning, because the film partially detached from the substrate is heated with less thermal conduction loss. A part of melted region flows into the edge of the unirradiated region. Although the edge of the detached circle is driven toward the center by surface tension force owing to thin film, the film is broken into small clusters immediately after removal to make its surface energy minimum. The outer diameter of the circular disk consisting of molten clusters keeps constant as no external force exerts any more. The molten part at the edge of the unirradiated part flies away by the momentum at a given angle to produce. Eventually the diameter of the removed region in the film becomes larger than that of the laser irradiated region.

4. CONCLUSION

The removal mechanism of metal thin film was analyzed in both front and rear patterning with KrF excimer lasers. The edge quality of the removed zone which is critical to patterning preciseness is also considered. The obtained results are summarized as follows:

- (1) In the front patterning at optimal fluences, the film is removed in the liquid state. The melted film inside the irradiated zone is accelerated towards the center of the irradiated region by the surface tension force, and is eventually broken into small droplets which fly away radially.
- (2) In the front patterning at excess fluences, a strong recoil force presses the molten film to produce a radial molten metal flow. Consequently, the radial flow expands the removed region, and eventually peels the surrounding film.
- (3) In the rear patterning, the recoil force owing to evaporation and plasma expansion generated between the film and the substrate presses the film. The detached part changes to the clusters which have a constant diameter as no external force acts on the clusters. The molten part at the edge of the unirradiated part is peeled and then flies away by the momentum.

ACKNOWLEDGMENT

The authors wish to thank Mr. K. Ohara and Mr. S. Asada, Osaka University, for their assistance in performing the experiment, and Mr. Y. Tsukuda, Sanwa Kenma Co. Ltd., for his cooperation for preparing the thin film targets.

REFERENCES

- 1) D. Maydan, The Bell System Technical Journal, 50 (6) (1971) 1761.
- 2) M. I. Cohen, B. A. Unger and J. F. Milkosky, The Bell System Technical Journal, (1968) 385.
- 3) J. E. Andrew, P. E. Dyer, R. D. Greenough and P. H. Key, Appl. Phys. Lett., 43 (11) (1983) 1076.
- 4) K. J. Schmoatiko, H. Durchholz and G. Endres, Proc. SPIE, 1023 (1988) 194.
- 5) U.C. Peak and A. Kestenbaum, J. Appl. Phys. 44 (5) (1973) 2260.
- 6) V.Z. Zaleckas, Appl. Phys. Lett., 31 (9) (1977) 615.
- 7) V.P. Veiko, S.M. Metev, A.I. Kaidanov, M.N. Libenson and E.B. Jakovlev, J. Phys. D, 13 (1980) 1565.
- 8) J.F. Ready, Industrial Applications of Lasers, Academic Press (1978) 341.

High Accuracy Microdrilling of Steel with Solid-State UV Laser at 10 mm/sec Rate.

Sergei V. Govorkov, Evgueni V. Slobodtchikov, Alexander O. Wiessner, Dirk Basting

Lambda Physik USA, Ft. Lauderdale, FL 33309

ABSTRACT

We investigated wavelength- and intensity-dependence of ablation rate achievable with a diode-pumped Q-switched Nd:YAG laser with frequency doubling and tripling. The laser produced 15 ns-long pulses at a repetition rate of 10 kHz and output power of 28 W in the fundamental beam, and 15 W and 10 W in the second and third harmonics, respectively. We found that in thin stainless and carbon steel foils, fast ablation starts at the laser fluence level of 10 J/cm^2 . The ablation rate remains close to $1 \mu\text{m}$ per pulse with very little change as the laser fluence increases by more than order of magnitude above this threshold. In thicker samples, average ablation rate decreases, due to attenuation of the beam in the vapor and plasma toward exit of the hole. This attenuation is strongly dependent on the laser wavelength. Particularly, using third harmonic output, we were able to sustain average drilling speed of more than $1 \mu\text{m}$ per pulse in samples up to 1 mm thick. At the same time, removal rate at fundamental wavelength decreased by almost an order of magnitude.

Keywords: Solid-state UV laser, micromachining, microdrilling, steel

1. INTRODUCTION

Multi-kiloHerz lasers with high brightness and pulse length of 10 to 30 nanoseconds allow high accuracy, high throughput micro-machining of steel and ceramics¹⁻³. This is primarily due to the fact that most of material is removed in a vapor state, as opposed to melt ejection dominating long-pulse drilling. In order to maintain high accuracy and minimize heat affected zone, the laser fluence has to be limited to few 10 J/cm^2 , so as to reduce plasma shielding and post-pulse plasma heating effects¹. This level of intensity produces material removal rate of about $1 \mu\text{m}$ per pulse. Thus, high repetition rate is essential in increasing micromachining speed.

Metal vapor and plasma shielding becomes a major limiting factor in drilling of high aspect ratio holes in thicker, on the order of 1 mm thick, steel. In order to reach the bottom of the deep and narrow hole, laser beam has to penetrate 1 mm-thick layer of dense vapor and plasma, whereas the thickness of plasma layer at the surface is limited to roughly $100 \mu\text{m}$ during the length of the pulse. Thus, it is desirable to employ all possible means, such as using shorter wavelength, in order to reduce plasma formation.

In this paper, we investigated wavelength- and intensity-dependence of ablation rate achievable with a diode-pumped Q-switched Nd:YAG laser with frequency doubling and tripling. The results indicate that for drilling thick metal samples, using UV output of the laser gives significant advantage due to higher average drilling speed and accuracy, and minimal recast layer.

2. EXPERIMENTAL

The laser source consisted of side-pumped, q-switched Nd:YAG oscillator (Lambda Physik's Gator2000) followed by three-stage diode-pumped amplifier. The oscillator produced 15-nsec pulses in TEM₀₀ beam with an average power of 10 W at 1064 nm and nominal repetition rate of 10 kHz. Amplifier output was 28 W at the fundamental wavelength, and 15 W and 10 W at the second and third harmonic wavelength correspondingly. Divergency of the amplified beam was within 1.2 times of diffraction limit.

In experiments with all three wavelengths we focused beam with the “best form” lens with nominal focal length of 50 mm. Beam diameter on the lens was varied in experiments which required variable focal spot diameters. Polarizer mounted onto rotational stage served as an adjustable attenuator. Quarter wave plate in the beam path ensured circular polarization of the beam incident on the sample. Two kinds of microdrilling techniques were employed: percussion drilling and trepanning. In trepanning, rotating wedge was inserted into the beam path before the lens, so that the focal spot on the sample draw a circle. Rotational frequency of the wedge was adjustable, in order to optimize quality of the holes. In percussion drilling, wedge was removed and beam was held at a fixed position. A pair of photodetectors monitored incident and transmitted through the sample beams. This allowed us to measure time required for percussion drilling and subsequently calculate average removal rate per pulse. Incident beam was switched on and off by means of fast electro-mechanical shutter. Focal distance was optimized for each wavelength by minimizing drilling time necessary for thin foil (50 μm). All experiments were completed in ambient air. For removing recast layer in some samples, we utilized electro-chemical etching.

3. RESULTS AND DISCUSSION

3.1. Intensity dependence of ablation rate in stainless steel

For 15 nsec-long laser pulses, the laser fluence threshold for fast material removal is on the order of 10 J/cm^2 ¹⁻³. As opposed to photo-chemical reaction in UV laser ablation of organic materials, the material removal mechanism in metals is basically thermal, via fast melting and evaporation. However, term “ablation” is commonly used to distinguish from melt ejection mechanism in long pulse drilling. Fig.1 a-c shows laser fluence dependence of average ablation rate for three different thicknesses of stainless steel samples. In 50 μm -thick foil, ablation can be considered a surface ablation, since the beam diameter at the surface (20 to 30 μm) is comparable to the sample thickness. Fast material removal begins at approximately 10 J/cm^2 , with ablation rate reaching roughly $1 \mu\text{m}$ per pulse. Consistently with the previous works^{2,3}, ablation rate increases only slightly as the laser fluence is increased by more than order of magnitude above this threshold. Similar tendency is clear in case of 370 μm -thick sample (Fig.1 b). Several mechanisms that limit ablation rates at higher fluences, involving laser beam absorption and scattering in plasma and metal vapor and droplets have been discussed extensively in the past⁴. Notably, vapor expansion rates reach several km/sec, thus approaching thermodynamic limit of gas expansion⁴. Therefore, increasing laser fluence causes increase in plasma density due to photoionization and inverse bremsstrahlung effect, instead of faster vapor removal. In effect, increased portion of laser energy is transferred to the plasma, rather than to the sample.

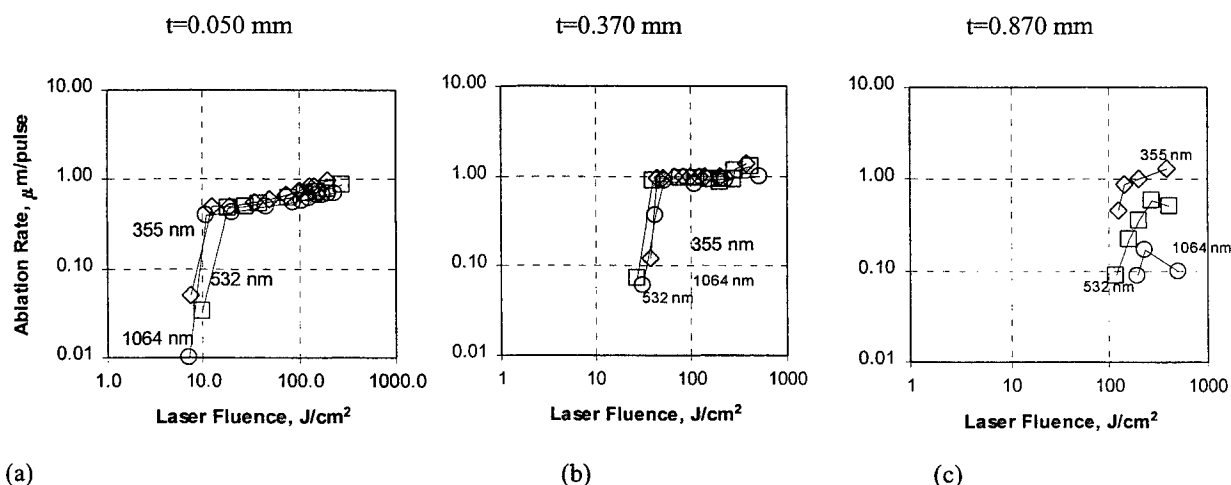


Fig.1. Ablation rate per pulse in stainless steel as a function of laser fluence at different wavelengths and thickness of the sample a) 50 μm , b) 370 μm and c) 870 μm .

As the thickness t of the sample increases (Fig.1 b,c), the minimum laser fluence required to penetrate entire sample increases from 10 J/cm^2 to 30 J/cm^2 for $t=370 \mu\text{m}$, and 100 J/cm^2 for $t=870 \mu\text{m}$. Apparently, at lower laser fluence, ablation terminates at a certain depth, due to attenuation of the beam in the column of vapor and plasma that fill the hole. Since vapor expansion rate at the surface was measured⁴ to be less than 10 km/sec , the characteristic depth at which the beam path length in plasma

at least doubles compared to surface condition is roughly 100 to 200 μm . Another factor leading to increased attenuation inside the hole is that the vapor flows in single dimension, as opposed to three-dimensional expansion at the surface. This creates higher density of vapor and plasma thus leading to stronger attenuation.

3.2. Effect of the wavelength on drilling speed of thicker samples

As the sample thickness approaches 1 mm, ablation rate becomes strongly wavelength-dependent (see Fig.1 c). At similar laser fluence, UV laser beam provides almost an order of magnitude faster drilling than IR beam. This trend is summarized in Fig.2.

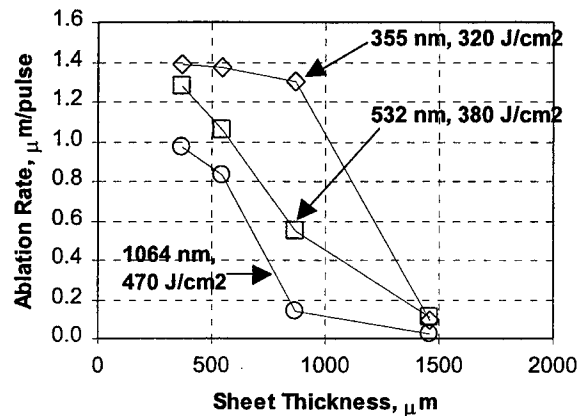


Fig.2. Ablation rate as a function of sample thickness at three different wavelengths.

The characteristic sample thickness at which average ablation rate starts decreasing, is greater for shorter wavelength. Apparently, in the thicker samples, beams of different wavelength are attenuated to different degree inside the hole. Although ablation rates at the surface are similar for all three wavelengths (Fig.1 a), attenuation of the beam towards the exit of the hole and subsequent reduction in material removal in thick samples lead to reduction of average ablation rate, as plotted in Fig.2.

One possible mechanism responsible for such drastic wavelength dependence is inverse bremsstrahlung effect. Simple estimate of the plasma absorption using formula⁴:

$$\alpha(\text{cm}^{-1}) = 1.37 \lambda^3 n_e^2 T_e^{-1/2} \quad (1)$$

and assuming plasma density $n_e = 1.4 \cdot 10^{19} \text{ cm}^{-3}$, plasma temperature $T_e = 20,000\text{K}$, leads to extinction length $L(1064) = 0.5 \text{ mm}$ at 1064 nm, $L(532) = 4 \text{ mm}$ at 532 nm and $L(355) = 13 \text{ mm}$ at 355 nm. Additionally, one has to account for avalanche-like increase of n_e, T_e for longer wavelength due to radiation heating of plasma.

3.3. High aspect ratio drilling

Due to nearly diffraction-limited beam quality of the solid-state laser, it is possible to achieve intensity levels above ablation threshold even with relatively small pulse energy. However, the high aspect ratio of the hole for the thicker samples becomes the limiting factor. In Fig.3, we illustrate this trend by comparing average ablation rate in 1.46 mm-thick stainless steel sheet at different wavelength and laser spot diameter. We tried to maintain roughly constant laser fluence at the surface. Obviously, this required increasing average power of the beam proportionally to its cross-section area, as the aspect ratio decreased. As was expected, for each given wavelength, higher aspect ratios led to significantly lower ablation rates, even though the laser fluence remained nearly constant. Besides factors associated with the flow of melt and vapor in high aspect ratio holes, there may be influence of local temperature build-up from pulse to pulse. Assuming simple cylindrical symmetry, heat transfer rate dQ/dt from the hole walls into the bulk of the sample is independent on the hole diameter d :

$$dQ/dt = \text{const}(d). \quad (2)$$

At the same time, heat input rate scales as a cross-section area of the beam:

$$dQ/dt \sim d^2. \quad (3)$$

Therefore, for larger diameter and lower aspect ratio holes, each subsequent pulse is incident onto material with higher temperature and thus, smaller portion of its energy is required to bring material temperature to melting and boiling point.

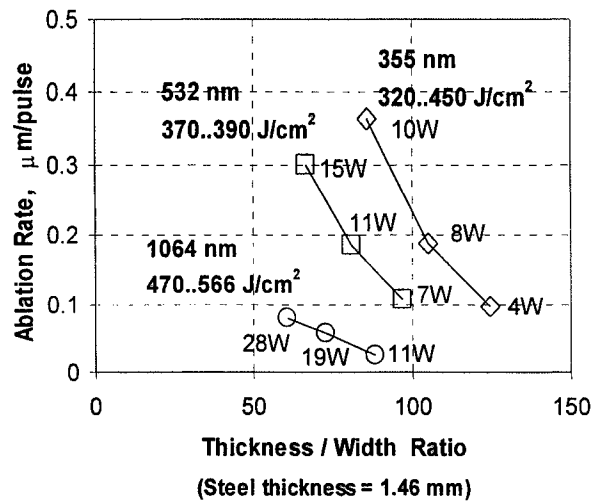


Fig.3. Average ablation rate in 1.46 mm-thick stainless steel sample as a function of aspect ratio. Laser fluence was maintained at roughly constant level as the beam diameter was varied. This required adjusting laser average power proportionally to the beam cross-section area, as labeled next to each experimental point.

Besides aspect-ratio dependence, even more pronounced is the dependence of ablation rate on wavelength. Basically, our finding is that shorter wavelength allows drilling higher aspect ratio holes at a higher speed for the sample thickness exceeding 1 mm. Again, this dependence is so strong because the beam has to penetrate thick layer of dense plasma and vapor, which is not present in drilling thin foils.

3.4. Practical drilling examples

In practical applications, one is concerned not only with drilling speed but also with quality of holes. For thick metal sheet, it is generally difficult to minimize taper of the holes and maintain smooth and round exit. The reason for this is that as the beam is attenuated towards the exit, intensity in peripheral areas of the hole fall below ablation threshold, thus leading to reduced exit diameter and irregular, rough edge. Therefore, using shorter wavelength is beneficial for improving quality of the holes drilled in thick metal samples.

We were able to drill holes with aspect ratio as high as 50 in 1.46 mm-thick stainless steel using percussion method with 10W UV beam. Taper did not exceed 15% and total drilling time was less than 0.4 sec. Using trepanning with relatively low UV power of 4 W, we produced low taper holes with good roundness in 0.55 mm-thick stainless steel and 0.75 mm-thick carbon steel. Figures 4,5 show SEM images of these trepanned holes.

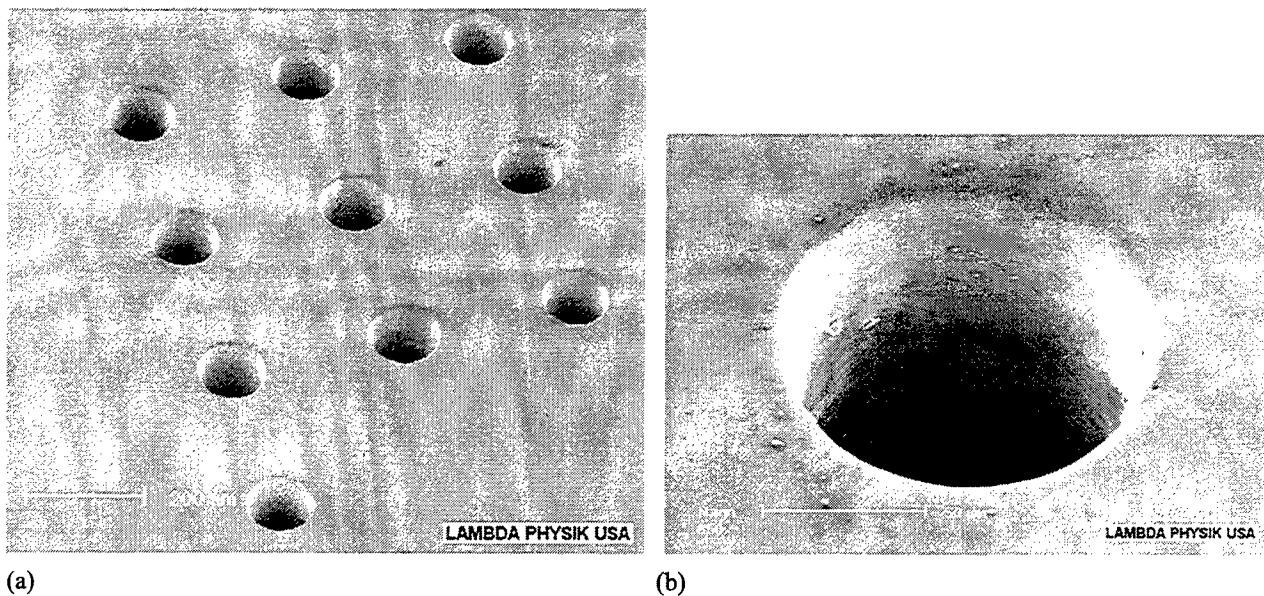


Fig.4. Holes trepanned in 0.55 mm-thick stainless steel with 4W UV beam: a) overview; b) close-up of entrance side. Hole diameter is 110 μm .

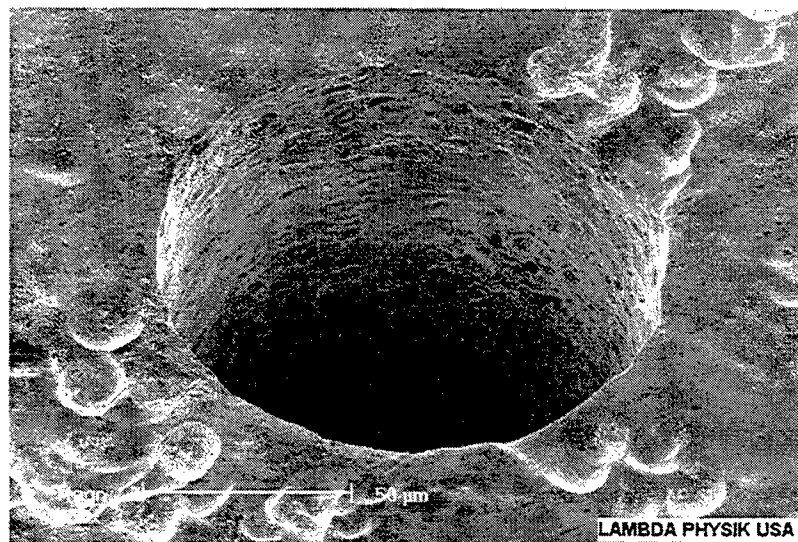


Fig.5. Close-up view of hole trepanned in 0.75 mm-thick carbon steel with 4W UV beam

CONCLUSION

In conclusion, we showed that using UV output of high repetition rate diode-pumped, q-switched solid state laser is beneficial in high speed, high accuracy micromachining of steel. The main difference from IR output arises from significantly reduced plasma formation which tends to be a limiting factor for drilling speed and quality in thicker, on the order of 1 mm, steel samples.

We presented practical examples of trepanning of 100 μm -diameter holes in steel sheet with roundness and taper errors within few micrometers, as well as percussion drilling of 30 μm -diameter holes in 1.5 mm steel with aspect ratio of 50.

ACKNOWLEDGMENTS

We would like to thank Dr.M.Lynn of University of Miami for producing SEM images of micro-machined samples.

REFERENCES

1. J. J. Chang, B.E. Warner, E.P. Dragon and M.W. Martinez, "Precision micromachining with pulsed green lasers", *Journal of Laser Applications*, **10**, pp.285-291, 1998.
2. M.A. Norton, J.E. Murray, C.D. Boley, K.H. Sinz, "Laser ablation of stainless steel from 1 J/cm² to 10 kJ/cm²", *OSA Technical Digest*, CLEO'98, paper CWS2 (Optical Society of America, Washington, D.C., 1998).
3. T.V. Kononenko, S.V. Garnov, S.M. Klimentov, V.I. Konov, E.N. Loubnin, F. Dausinger, A. Raiber, C. Taut, "Laser ablation of metals and ceramics in picosecond-nanosecond pulsewidth in the presence of different ambient atmospheres", *Applied Surface Science*, **109/110**, pp.48-51, 1996.
4. J. J. Chang, B.E. Warner, "Laser-plasma interaction during visible-laser ablation of metals", *Appl.Phys.Lett.*, **69**, pp.473-475, 1996.

Laser beam joining of optical fibers in silicon-V-grooves

Stefan Kaufmann^{*a}, Andreas Otto^b, Gerhard Luz^c

^aBavarian Laser Center, Erlangen, Germany

^bChair of Manufacturing Technology, Univ. of Erlangen-Nuremberg, Germany

^cAlcatel Corporate Research Centre, Stuttgart, Germany

ABSTRACT

The increasing use of optical data transmission systems and the development of new optical components require adjustment-insensitive and reliable joining and assembling techniques. The state of the art includes the utilization of silicon submounts with anisotropically etched V-grooves. Several glass fibers are fixed in these V-grooves with adhesive. Adhesive bonds tend towards degradation under the influence of temperature and moisture. For this reason, the alternative joining processes laser beam welding and laser beam soldering are relevant. The goal is a reliable joining of optical fibers in V-grooves without damage to the fibers or the silicon submount. Because of the anomaly of silicon during phase transformation, a positive joining can be realized by laser beam welding. A melt pool is created through the energy of a Nd:YAG-laser pulse. During solidification, the volume of silicon increases and a bump is formed in the center. Experiments have shown that this phenomenon can be used for joining optical fibers in silicon-V-grooves. With suitable parameters the silicon flows half around the fiber during solidification. For each fiber, several welding points are necessary. Another promising joining method is laser beam soldering. In this case, a second silicon sheet with a solder deposit is placed on the fibers which lie in the V-grooves of the metalized silicon submount. The laser heats the upper silicon until the solder melts by heat conduction.

Keywords: laser beam joining, laser beam welding, laser beam soldering, silicon, optical fibers, optical components

1. INTRODUCTION

Both, active and passive optical components are necessary for an optical communication network. **Figure 1** shows a power splitter. This passive optical component splits the light of one fiber into eight or even more fibers and is used for example in television distribution devices. Power splitter, wavelength division multiplexer and attenuators consist of an integrated optical chip with optical waveguides. An example for an active component is shown in **figure 2**. The laser submount consists of the electro-optical chip and an optical glass fiber which lies in the V-groove. The coupling of fibers to the optical or electro-optical chip is a technological difficult and expensive production step. As mono mode fibers are used in communication networks, the fiber-chip-coupling must suffice tolerances smaller than one micron. The state of the art includes the utilization of silicon submounts with anisotropically etched V-grooves. Optical glass fibers are passively adjusted in these V-grooves and fixed with adhesive. Adhesive bonds tend towards degradation under the influence of temperature and moisture. This can lead to premature component failure¹.

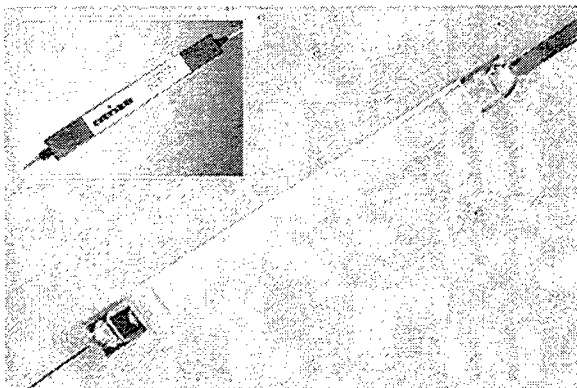


Fig. 1: Unhoused 1x8 power splitter

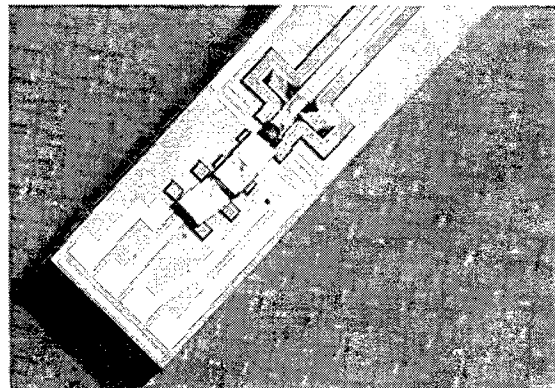


Fig. 2: Laser submount

^{*}Correspondence: Email: s.kaufmann@blz.org; WWW: <http://www.blz.org>; Phone: +49 9131 85-28315; Fax: +49 9131 36403

For the coupling of fibers to optical chips or electro-optical components, laser assisted methods of joining might replace gluing. The main objective is an increase in reliability under high temperatures and moisture. The basis of the experiments are silicon submounts with V-grooves for optical mono mode fibers. In comparison with glass or polymers, silicon has an important advantage. Both, electrical and optical conduction can be realized on one substrate. This is one of the fundamentals for optical hybrids with integrated optical and electrical functions².

2. FUNDAMENTALS OF LASER BEAM TREATMENT OF SILICON

2.1. Properties of silicon

The properties of silicon are important for evaluation of experimental data and process simulation. The most interesting data of pure mono crystalline silicon are summarized in **table 1**³. Basis for the presented joining process are the different densities in liquid and solid condition. During melting, the density rises, that means the volume decreases during phase transformation by about 9 %.

The absorption coefficient of the semiconductor silicon depends on the wavelength and the temperature. Silicon has a low absorption for CO₂-laser radiation ($\lambda=10600$ nm), but absorbs the radiation from an excimer laser ($\lambda=308$ nm) within an absorption length of 7 nm. The Nd:YAG-laser, which was used in the experiments delivers infrared light (1064 nm). The energy of this wavelength is nearly as high as the band gap of silicon at 300 K. Basis of the optical absorption is the electron transfer from the valence band to the conduction band. The temperature dependence of the absorption coefficient α is caused by the band gap, which declines with rising temperature. **Figure 3** shows the temperature dependence of the absorption coefficient α and the optical absorption length $1/\alpha$ ⁴. The optical absorption length is higher than 500 μm under room temperature. It decreases to some microns at a temperature of 500 °C. Liquid silicon absorbs the Nd:YAG-laser beam radiation within some nanometers.

2.2. Experimental setup

For the following experiments, concerning laser beam treatment of silicon and laser assisted clamping of optical fibers, a pulsed Nd:YAG-laser is used (**figure 4**). The pulse power available on the sample varies between 0.1 kW and 2 kW. A pulse duration from 0.1 ms to 20 ms is possible. The laser light is guided by an optical cable with a core diameter of 200 μm . With various focusing optics, focus diameter from less than 100 μm to several 100 μm are possible. The system is realized as an "aim and shoot system", so the process is easy to handle. The sample can be positioned with a three axis positioning system, which has a bidirectional accuracy of 5 μm . A xy-scanner is used for high speed positioning. For laser beam soldering with additional aluminum and laser beam soldering, a continuous wave Nd:YAG-laser is integrated. The laser

Melting point	$T_M = 1687 \text{ K}$
Boiling point	$T_B = 3504 \text{ K}$
Density (300 K)	$\rho = 2,329 \text{ g/cm}^3$
Density (1687 K, solid)	$\rho_{\text{solid}} = 2,30 \text{ g/cm}^3$
Density (1687 K, liquid)	$\rho_{\text{liquid}} = 2,51 \text{ g/cm}^3$
Thermal expansion (300 K)	$\alpha_{\text{th}} = 2,6 \times 10^{-6} / \text{K}$
Band gap (300 K)	$E_G = 1,126 \text{ eV}$

Table 1: Material properties of silicon³

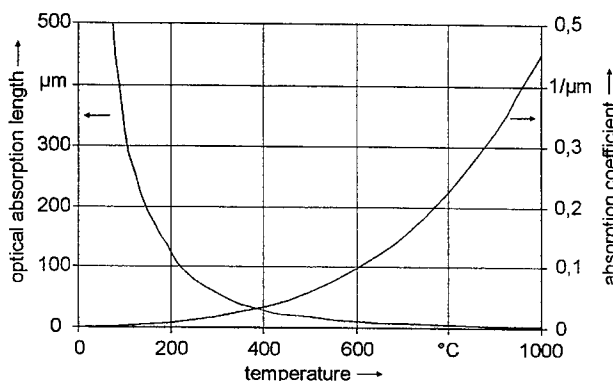


Fig. 3: Temperature dependence of the absorption coefficient and the optical absorption depth⁴

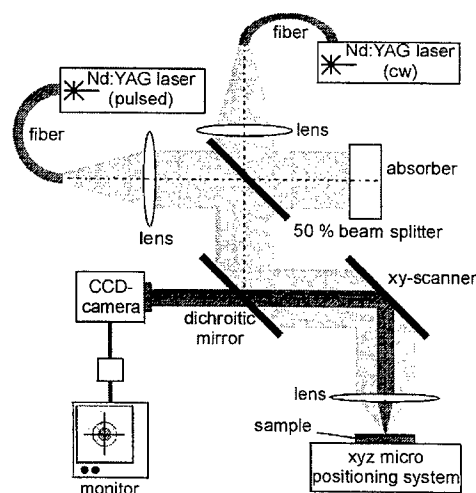


Fig. 4: Experimental setup

power is tuneable between 30 W and 300 W. With a vacuum chamber ($p_{\min}=0,01$ mbar) experiments under vacuum are possible.

2.3. Melting of silicon with the Nd:YAG-laser

First of all, the effects of a laser pulse on planar mono-crystalline silicon must be analyzed. A single laser pulse heats, melts and evaporates a small part of silicon. After the pulse, the liquid silicon solidifies. Depending on the laser parameters, cracks and porosities can occur. **Figure 5** shows the principle appearance of solidified silicon. The reason for the appearance of bumps are the different densities of silicon in solid and liquid phase at the melting point.

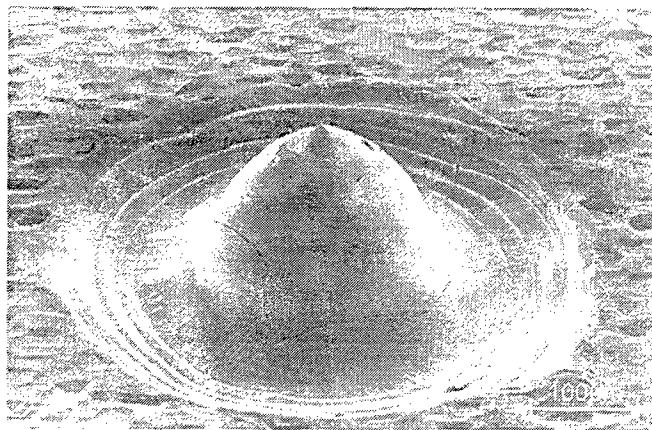


Fig. 5: Laser beam treatment of silicon ($\tau=1$ ms, $P=380$ W)

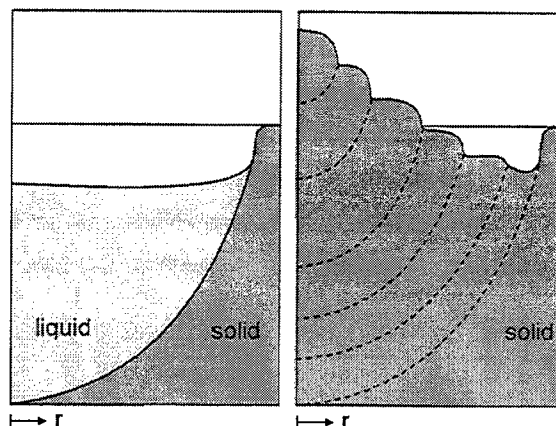


Fig. 6: Scheme of phase transformation

Figure 6 illustrates the growing bump. Due to the volume contraction during phase transformation solid-liquid a radially symmetrical depression is formed. Pictures of a high speed camera show this melt pool at the end of a laser pulse. During solidification, the volume expands by about 9 % and forms the bump in the center of the solidified melt pool. Microscopical pictures from grinded samples in **figure 7** confirm this model. Porosities occur primarily under air. Experiments under vacuum lead to samples without porosities and with a smaller bump. The laser beam treatment of silicon causes cracks. High laser power leads to cracks in the center of the melted and solidified zone. A laser pulse with less power causes marginal cracks. For the reduction of cracks, there are several promising approaches like pre- and postheating. Further investigations on this topic are necessary.

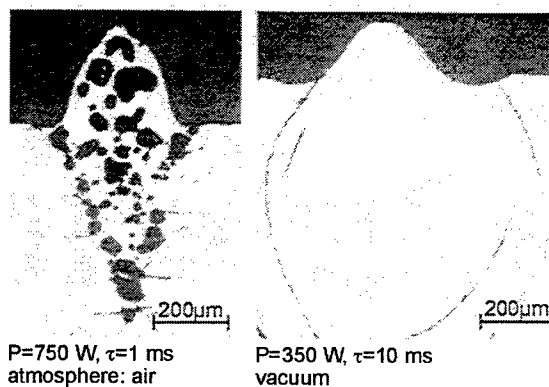


Fig. 7: Pictures from grinded samples

3. LASER BEAM JOINING OF OPTICAL FIBERS IN SILICON-V-GROOVES

Silicon substrates with V-grooves are qualified for precise passive alignment of fibers. Anisotropical etching of V-grooves in $\langle 100 \rangle$ -silicon is a well-known and trouble-free production step. The angle of the V-groove is very precise, because it depends on the crystal lattice. The width (depth) of the groove is determined by the previous lithography. At the moment, optical fibers are industrially fixed in V-grooves with adhesives. The geometry of a mono mode fiber and a silicon submount with V-grooves, fibers and plate is shown in **figure 8**. After stripping the coating, eight fibers are positioned in the V-grooves. A silica plate on the fibers presses them into the V-grooves during the joining process. The SEM-picture gives an example of a glued fiber array (**figure 9**). The fiber arrays are used for connecting optical fibers and optical chips. There are several possibilities of laser beam joining optical fibers in silicon-V-grooves. In the following chapters, laser

assisted clamping (welding), laser beam welding with additional aluminum and laser beam soldering are presented. The advantages and disadvantages of each method are briefly discussed.

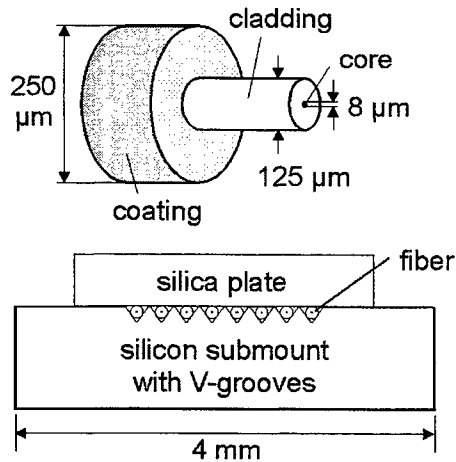


Fig. 8: Geometry of a mono mode fiber and a silicon submount with V-grooves, fibers and cover plate

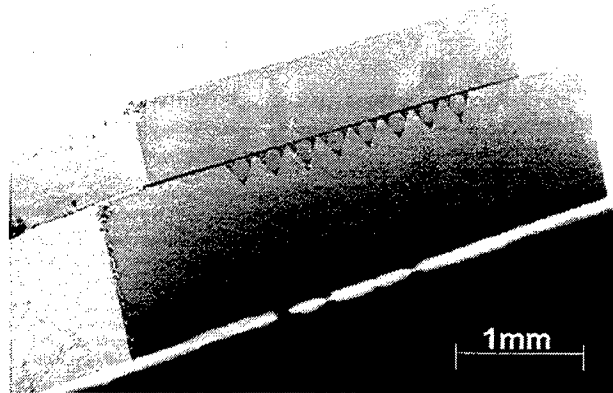


Fig. 9: SEM-picture of a glued fiber array

3.1. Laser assisted clamping (welding)

In former publications, a method for joining optical fibers in silicon-U-grooves was presented⁵. The silicon on both sides of the fiber is melted by a Nd:YAG-laser. The solidified silicon fixes the fibers in their position. The usage of anisotropical etched V-grooves instead of U-grooves makes it more difficult to create a melt pool which is big enough to clamp the fibers during solidification. But as mentioned before, V-grooves are easy to manufacture and have a high precision. In contrast to this, fibers in U-grooves can have a little slackness due to manufacturing tolerances, which can lead to a higher insertion loss. It will be analyzed in this chapter, whether the described bumps are usable for the fixation of optical fibers in silicon-V-grooves⁶.

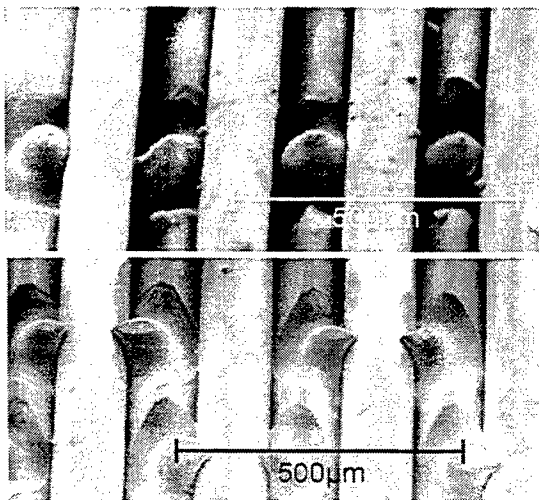


Fig. 10: Joined optical fibers

hand, the silicon submount and the fibers must not be damaged. The decision whether a sample is damaged or not, is possible with the help of SEM-pictures and grindings. Additionally, it is necessary to verify optical attenuation and mechanical stability.

The fiber array, shown in **figure 8**, is used for laser beam joining. Both, the fibers and the silica plate do not absorb Nd:YAG-laser radiation. Thermal stress in fibers can only appear by thermal conduction. The beam diameter is an important parameter as it determines the size of the melt pool. Silicon on both sides of the fiber must be melted. The beam diameter should be at least the distance between two fiber axes (250 μm). The laser beam is directed to the fiber axis and not to the gap between two fibers. Melting the silicon between the fibers does not fix the fibers (**figure 10 top**). A laser pulse, directed to the middle of a fiber, melts the silicon on both sides of the fiber and below the fiber. After solidification, the fiber is clamped (**figure 10 bottom**). There is a partially adhesive bond between silicon and silica. The shaping of the bumps is positively influenced by the plate above the fibers. The plate disables the free growth of the bumps and improves the clamping.

The choice of suitable laser parameters is important. On the one hand, the volume of a bump must have a certain size. On the other

Figure 11 shows the specified process window. The dotted line represents the pulse energy $E_p = 1$ J. The diagram can be split into three areas, which have no clear borders. The energy of laser pulses located in zone 1 is too small to create a bump, which is big enough for clamping the fiber (**figure 12a**). Zone 2 is similar to the process window. These laser parameters are suitable for fixing optical fibers in silicon V-grooves (**figure 12b**). The experimental results show, that the laser energy required depends on the pulse duration. Because of heat conduction, during long pulses energy is also flowing into the substrate which leads to a higher energy demand. Too high pulse power or too long pulse duration can damage the substrate and fibers. **Figure 12c** shows a sample where the joining partners are damaged (zone 3). It has to be noticed that the beam diameter has an influence on the classification into the three zones. A reduced beam diameter will raise the energy density. The process window will move to a lower energy level. Another condition is the exactly lateral positioning of laser beam and fiber. The sample in **figure 12d** demonstrates a bad clamp. The laser beam should be directed to the middle of the fiber in order to create two similar bumps on both sides of the fiber.

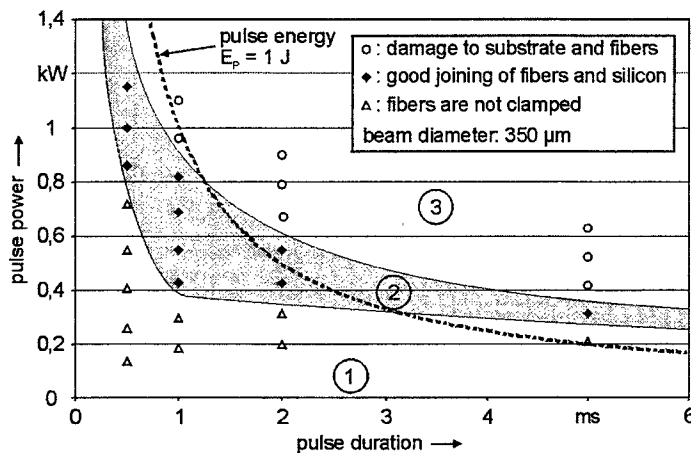


Fig. 11: Process window for the laser beam joining

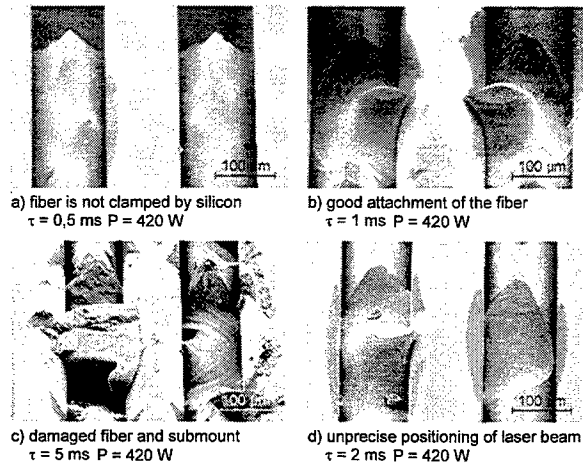


Fig. 12: Influence of the laser parameters

Because of the experimental results of laser beam treatment of silicon under air atmosphere, porosities are expected. **Figure 13a** affirms this supposition. Further on, fine cracks in silicon are visible. The laser pulses, one per fiber, have a width of 1,1 ms and a power of 420 W. Porosities appear lateral and under the fibers. The space between two fibers is filled with silicon. On the one hand, porosities weaken the mechanical properties, but on the other hand, the space between the fibers is filled. An example for a connection without porosities is shown in **13b**. The process was realized with the same laser parameters under vacuum. Only 50 % of a fiber are surrounded by silicon.

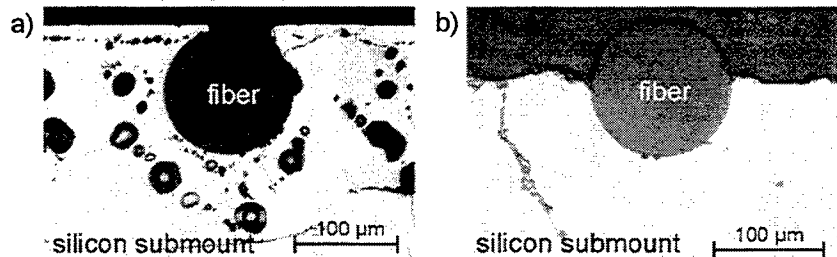


Fig. 13: Joined optical fibers (a: air; b: vacuum)

Figure 14 shows the top side of an optical fiber array. Eight fibers are clamped in silicon-V-grooves. On a length of 3 mm up to five welding points fix each fiber.

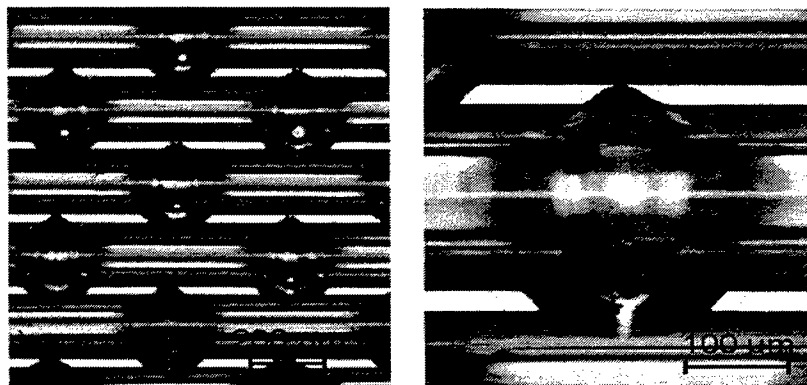


Fig. 14: Part of an optical fiber array (view on top side without cover plate)

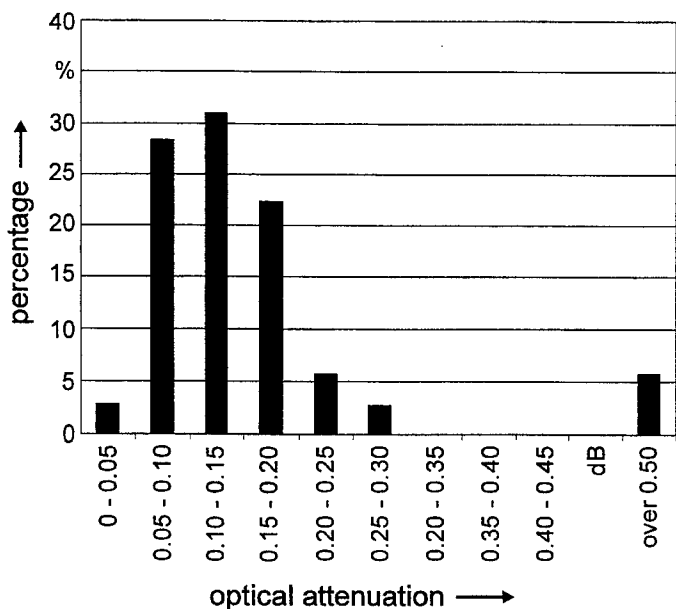


Fig. 15: Optical attenuation of joined fibers

In this section, the optical attenuation of laser beam joined fibers is analyzed. Therefore, a single mode fiber is positioned in front of the fiber array. This fiber inserts light with a wavelength of 1550 nm into each fiber of the array. The detector at the end of the fibers measures the light intensity. The attenuation can be calculated from the measured light intensity and a reference measure without fiber array. The unit of attenuation is dB. Measuring errors may occur due to an angular misalignment of fibers. This can lead to an attenuation of 0.2 dB. Five out of 40 fibers fixed were damaged by manipulation. **Figure 15** shows the histogram of the optical attenuation. 85 % of the fibers have an optical attenuation between 0 dB and 0.20 dB. It can be assumed that the two fibers with higher loss were damaged after and not during the joining process. The measured average insertion loss of 0.13 dB indicates that the joining process has no or only a small influence to the optical attenuation. This result is also valid for the polarization dependent loss.

For the qualification of fiber arrays, their mechanical properties are relevant too. Bare fibers are sensitive to bending stress. Manipulation of fiber arrays can lead to movements of the free fiber endings. Due to the resulting bending stress, the fiber may break next to the fiber clamp. The drawing in **figure 16** shows the appearance of a fiber break. The SEM-picture shows a sample with a broken bare fiber. For this reason, an additionally fixation of the coated fiber is necessary. An adhesive bond between the coated fiber and the silicon substrate avoids movements of the fiber and absorbs pulling forces. According to the present knowledge, the existing cracks in silicon do not weaken the mechanical stability. The optical fiber is the weak point. Reliability tests under various climatic conditions are carried out at the moment.

3.2. Laser beam welding with additional aluminum

Laser beam welding with additional aluminum is another method of joining optical fibers and silicon-V-grooves. **Figure 17** shows the phase diagram of silicon and aluminum. The materials form an eutectic alloy. For the following experiments, a silicon cover plate instead of a silica cover plate is used. The direct treatment of aluminum is difficult because of the high reflection of the laser beam at the surface of aluminum. A high laser power is necessary for coupling the laser beam into the material. After the absorption in aluminum, the high laser power damages the silicon. The silicon cover plate has a good absorption of Nd:YAG-laser radiation. Due to the heat transfer through the silicon cover plate, the aluminum

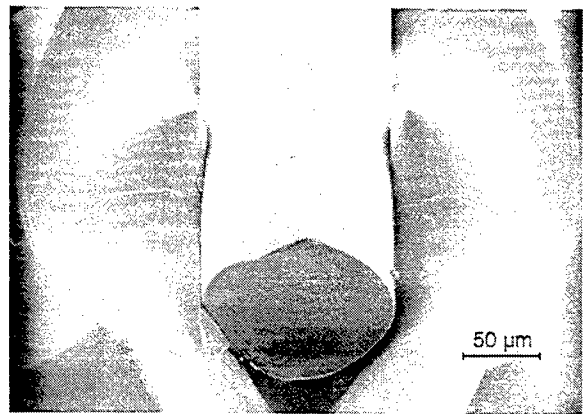
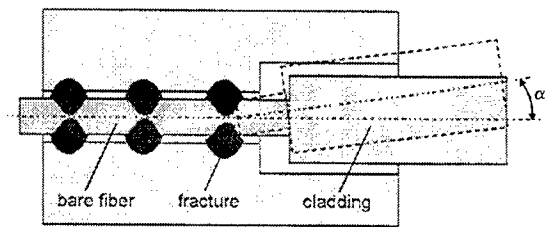


Fig. 16: Fracture of a bare fiber in consequence of fiber move

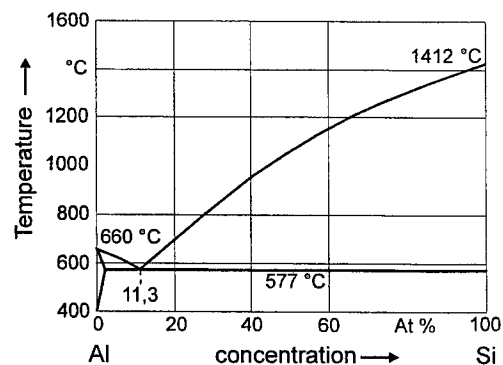


Fig. 17: Phase diagram of silicon and aluminum

foil between the silicon substrate with fibers and the cover plate melts. By using sufficient energy and pressure a tight connection can be obtained. **Figure 18** shows the joining area between two silicon plates. The thickness of the aluminum foil decreased from 100 μm to approximately 20 μm . The bright matrix between the silicon substrates is the eutectic alloy of aluminum and silicon. The dark and oblong structures in this matrix picture crystalline silicon.

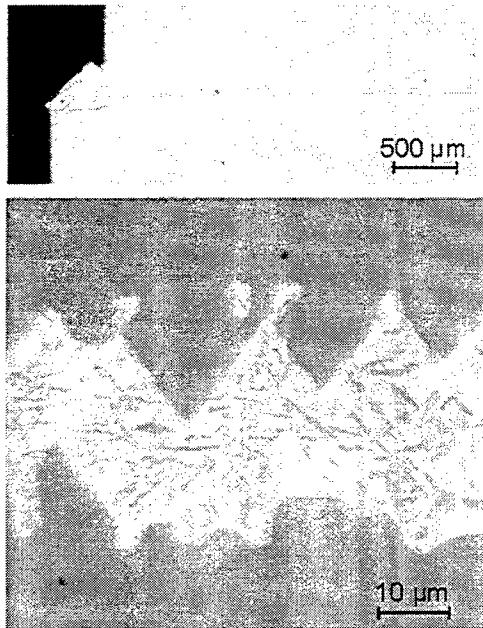


Fig.18: Laser welded silicon substrates with additional aluminum

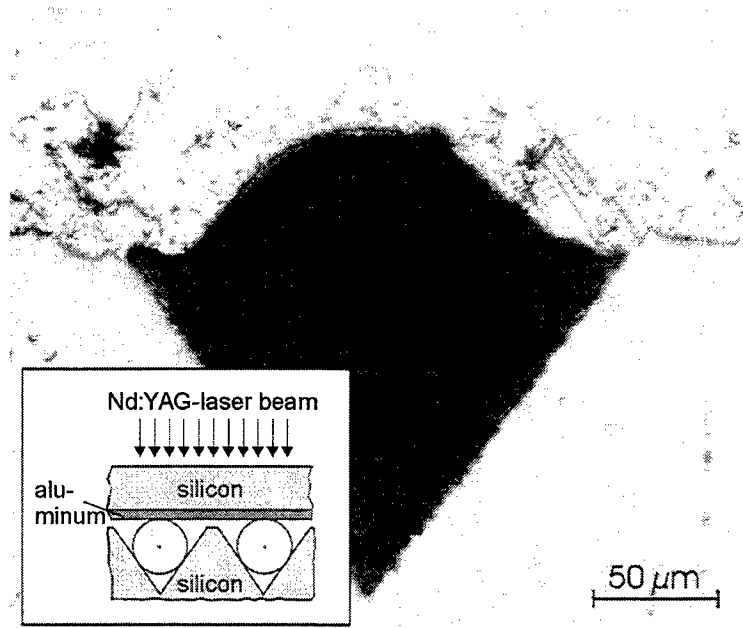


Fig. 19: Joined optical fiber

Experiments have shown, that laser beam welding of silicon with additional aluminum could be used for the fixation of optical fibers in silicon-V-grooves. An aluminum foil between the silicon substrate with the fibers and the silicon cover plate is melted by heat conduction. **Figure 19** shows the scheme of the joining process and a part of a welded fiber array. The fibers partially supplant the aluminum foil. An improved construction of the mounting device should ensure the exact position of the fibers in the V-grooves. Therefore, it is important to respect the essential pressure to the cover plate during the joining process. A disadvantage is the high temperature (over 900 K) in the joining gap for some seconds. Further investigations are necessary to optimize the mechanical stability of the joined fibers.

3.3. Laser beam soldering

Laser beam soldering is similar to the joining method previously mentioned. AuSn-solder is utilized instead of aluminum. Before soldering the parts, the V-grooved silicon substrate and the silicon cover plate have to be metallized. The first layer is the bonding layer (CrNi). After that, the metallizing layer (Ni) and protecting layer (Au) are deposited. The solder deposit is on the bottom side of the cover plate. The continuous wave Nd:YAG-laser heats the silicon cover plate. The solder is melted by means of heat conduction. The resulting temperatures are considerable lower than those during laser welding. No damage to the joining partners occurs. Current experiments should indicate, whether a metallization of the fibers is

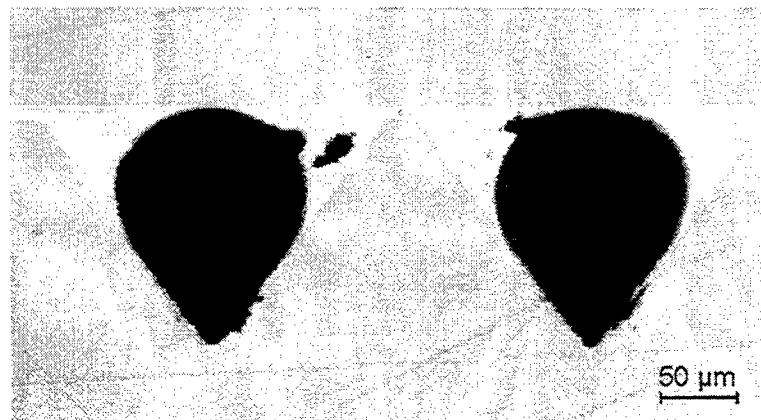


Fig. 20: Laser beam soldered fibers

necessary. **Figure 20** shows part of a soldered fiber array. This sample was joined with a laser pulse of approximately 200 W and pulse length of four seconds. The results of mechanical qualification tests of soldered fiber arrays are promising. Some of the joined fibers passed the fiber pulling test. To pass this test, an optical fiber must transmit a pulling force of 5 N to the array. Pictures of grinded samples taken by the use of a light microscope show no cracks or porosities in silicon. There are only some porosities in the solder. The reliability of fiber arrays will be detected with qualification tests under various climatic conditions. In comparison to glued arrays, a high reliability is expected.

4. CONCLUSION AND OUTLOOK

By means of laser beam melting and the subsequent solidification, bumps are formed. Their size and internal structure depend on the laser parameters and environmental conditions. The bumps are suitable for the coupling of optical fibers and optical components. The fibers are clamped and there is an adhesive bond between silicon and the optical fiber, too. There is no significant rise in optical attenuation. In case of optical fiber arrays, an additional fixation of the coated fibers should secure the fibers. No metallization of the joining partners is needed. The influence of the fine cracks must be analyzed in further experiments.

Because of the lower joining temperature, laser beam soldering is more advantageous than laser beam welding with additional aluminum. The experiments performed so far show good mechanical properties. Further investigations are necessary to determine the reliability of both, laser beam soldered and welded fiber arrays.

ACKNOWLEDGEMENT

The results presented were gathered within the project "laser assisted assembly of micro optical components". This project is supported by the Bavarian Research Foundation.

REFERENCES

1. T. W. Draycott, D. C. Levitt, A. P. Skeats, "An Assessment of the Reliability Status of Passive Optical Splitters", *Photonic Networks, Optical Technology and Infrastructure*, D. W. Faulkner, A. L. Harmer, IOS Press, 1997.
2. A. Ambrosy, "Anforderungen an die optische Hybridtechnik", *Grundlagen für eine optische Hybridtechnik*, VDI/VDI Technologiezentrum Informationstechnik, Berlin, 1996.
3. B. Elvers, *Ullmann's Encyclopedia of Industrial Chemistry*, Vol. A 23., VCH Verlagsgesellschaft, Weinheim, 1993.
4. G. E. Jellison Jr., "Optical and Electrical Properties of Pulsed Laser-Annealed Silicon", *Semiconductors and Semimetals*, R. F. Wood, C. W. White, R. T. Young, Vol. 23, Academic Press, Orlando, 1984.
5. M. Becker, R. Güther, R. Staske, "Laserschweißen als Präzisionsfügeverfahren für optische Mikrosysteme", *Jahrbuch für Optik und Feinmechanik 1996*, W. D. Prenzel, Schiele & Schön, Berlin, 1996.
6. S. Kaufmann, A. Otto, "Lasergestützte Fügeverfahren für die Lichtwellenleitertechnik", *Laser in der Elektronikproduktion & Feinwerktechnik*, M. Geiger, A. Otto, pp. 65-76, Meisenbach, Bamberg, 1999.

Study on CO₂ Laser Drilling of Printed Wiring Boards and Development of In-process Monitoring System

T.Nakayama^{*a}, T.Sano^a, I.Miyamoto^a, K.Tanaka^b, Y.Uchida^b

^aDepartment of Manufacturing Science, Graduate School of Engineering, Osaka University
2-1, Yamada-Oka, Suita, Osaka 565-0871, Japan

^bMaterial Processing R&D Group, Production Engineering R&D Center,
Matsushita Electric Works, Ltd.
1048 Kadoma, Osaka 571-8686, Japan

Abstract

In this paper, CO₂ laser drilling process for printed wiring board and the application to the in-process monitoring of the via hole quality are described. The process of CO₂ laser drilling was investigated on the basis of high speed photograph, the light emission and thermal conduction. It was found that the temperature of the decomposed epoxy resin suddenly increased when the smear thickness become less than 2 μ m. Based on this analysis, a simple in-process monitoring technique was developed to estimate the smear feature by detecting the light emission using a photo sensor. The removing process of the smear by KrF excimer laser was also investigated on the basis of the spectrum of the light emission and the reflected excimer laser. The electric contact was accomplished by excimer laser removal the smear.

Keyword: Laser drilling, Printed wiring board, CO₂ laser, In-process monitoring, smear, KrF excimer laser, Excimer laser removal

1. Introduction

Recently, the mounting density of electronic devices has been increasing rapidly due to downsizing of electronic machines such as personal computer and portable telephone with increasing performance. CO₂ laser drilling of via hole of printed wiring boards (PWB) is a matter of concern¹⁾⁻⁵⁾. This method is able to drill via hole smaller than the conventional mechanical method at drilling speed faster than 1000 holes per seconds. However, one of the problems of this technique is the thin layer of resin called smear is left on the inner copper foil. And it is necessary to remove to achieve the electric contact.

There are two ways to remove the smear; one is an exiting method of chemical process, this requires the thickness of the smear in CO₂ laser drilling process less than 2 μ m to remove successfully. In-process monitoring to

^{*}Correspondence: Email: nakayama@mapse.eng.osaka-u.ac.jp; Telephone+81-6-6879-7535; Fax:+81-6-6879-7534

estimate the thickness of smear in CO₂ laser drilling process is desirable. An in-process monitoring technique has been developed to detect CO₂ laser reflection from the inner copper layer by using HgCdTe sensor⁶). Simpler detecting technique is required to be developed for assuring the quality of the drilled hole. In this study, a novel monitoring technique to detect light emission from the laser irradiated zone to monitor the thickness of the smear. The another possibility is to remove the smear by UV laser irradiation. This can be called dry desmear. In this study, dry desmear by means of KrF excimer laser is also described.

2. Experimental procedures

In this study, we used the epoxy substrate, which contains a 80 μ m-thick epoxy layer and a 15 μ m-thick inner copper foil. The surface of the inner copper foil was of oxidation treatment to increase the attaching strength to epoxy layer. Specific heat of epoxy resin is 1.05J/gK and density is 1.2g/cm³.

Experimental setup used in this study for CO₂ laser drilling is schematically shown in Fig.1. RF discharged pulse-CO₂ laser beam was irradiated to the PWB (Printed wiring board) with mask projection optics. The average output power of CO₂ laser beam was measured by a power meter (Ophir 10A) and the waveform was detected by a HgCdTe sensor operating at liquid nitrogen temperature. Figure 2 shows an example of the pulse waveform of nominal pulse width of $T_p=100\mu$ s.

Most laser drilling experiment was carried out with a laser spot diameter of about 100 μ m. The image of the ejecting plume magnified by a microscope lens was photographed by CCD camera with an image intensifier having a minimum gate time of 3ns during laser irradiation. Scattering images of the plume were also taken with illuminating He-Ne laser. The

plume images were taken at different delay times from the onset of the CO₂ laser pulse. The light emission from the laser irradiate zone was detected by a photo diode off-axially with CO₂ laser beam as shown in Fig.1 where a quartz lens was used to collect the light emission to the photo diode. Emitted light signal were acquired at a sampling interval of 0.4 μ s, and stored in a personal computer after A/D conversion.

Figure 3 shows the experimental setup for dry desmear. KrF excimer laser with uniform intensity was irradiated to the PWB with

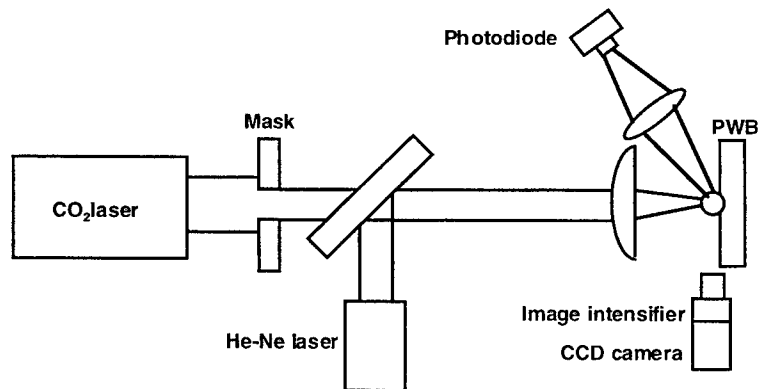


Fig.1 Experimental setup for CO₂ laser drilling.

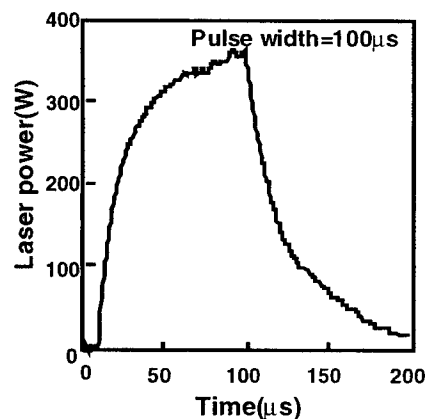


Fig.2 Waveform of CO₂ laser output.

mask projection optics. The light emission from CO₂ laser drilled portion during excimer laser irradiation was measured by a streak camera. The light emission was collected to the optical fiber by using a quartz lens. The reflected excimer laser was also detected by the Si photodiode off-axially with excimer laser beam. The appearance of the bottom of hole was observed by electron microscope.

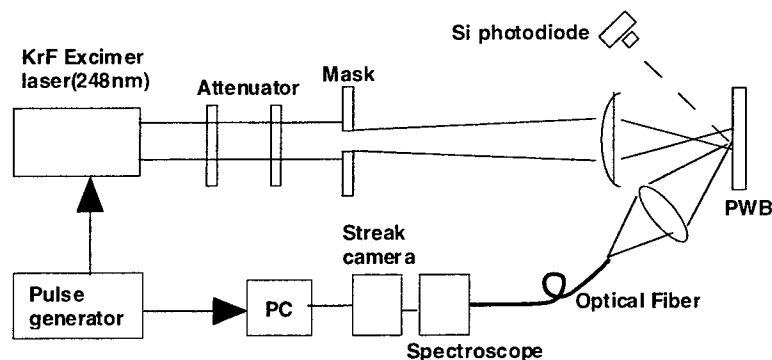


Fig.3 Experimental setup for dry desmear by KrF excimer laser.

3. Via hole drilling by CO₂ laser

3.1 Drilling process

The depth of the drilled hole was measured with different laser pulse width. In this measurement, the laser fluence was decreased down to estimate the drilling speed exactly. Figure 4 shows the relationship between laser fluence and the hole depth measured at its center. The hole depth is seen to increase in proportion to laser fluence until the bottom is nearly reached at the inner copper foil. Since the thermal conduction of the epoxy resin is very small, the hole depth h is given by Eq(1)

$$h = K \cdot F + G \quad (1)$$

where F is laser fluence, K laser energy for ablating unit volume of the epoxy resin and G threshold energy for decomposition. The value of K was determined be $2.15 \times 10^{-4} \text{ cm}^3/\text{J}$.

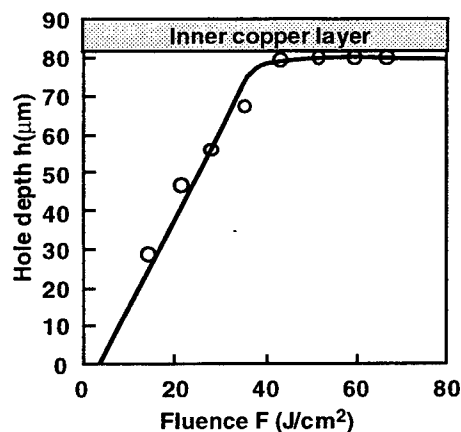


Fig.4 Laser fluence vs hole depth.

3.2 The measurement of light intensity

The photographs of ejecting plume image were taken by using the image intensifier during laser drilling. Figure 5 shows the photographs of the ejection plume image taken at a gate time of $1 \mu\text{s}$ with and without He-Ne laser illumination co-axially with CO₂ laser beam. With He-Ne laser illumination, the image of the ejecting epoxy resin particles was taken by light scattering. Without He-Ne laser illumination, no visible plume was taken until

approximately 50μs corresponding to the drilling time of the bulk of the epoxy resin. Bright plume began to be observed without He-Ne laser illumination around 53μs and the ejecting velocity of the plume was about 500m/s. These results indicate that the resin with the high temperature ejected when the bottom of the hole reached the inner copper foil.

Figure 6 shows the light intensity curve detected by photo diode. The hole depth estimated by Eq(1) is also plotted in Fig.6. The light emission was suddenly increased around 55μs corresponding to the time when bright plume was observed. At this time, the thickness of residual resin is estimated to be less than approximately 2μm.

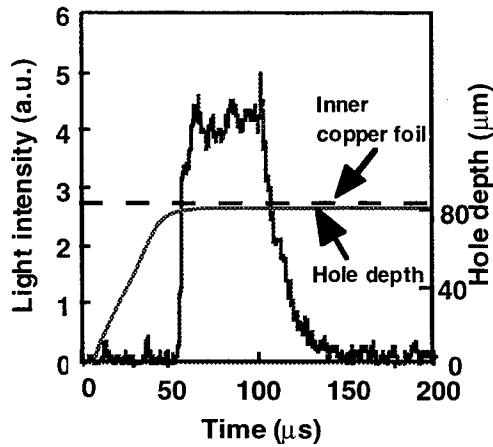


Fig.6 Light intensity and hole depth.

3.3 Discussion of light emission

The surface temperature of the inner copper foil was calculated assuming the simple thermal conduction model. The laser beam of Gaussian distribution of a radius of 50μm was irradiated for pulse width of 50μs to the copper foil with infinitive thickness. The light emission intensity q was assumed to be the forth power of the temperature, and is given by Eq(2)

$$q = \varepsilon \cdot \sigma \theta^4 \quad (2)$$

$$\left\{ \begin{array}{l} \theta = A \frac{W_0 a}{K} \tan^{-1} \frac{2}{a} \sqrt{k(\tau - \tau_1)} \\ \theta = A \frac{W_0 a}{K} \left\{ \tan^{-1} \frac{2}{a} \sqrt{k(\tau - \tau_1)} + \tan^{-1} \frac{2}{a} \sqrt{k(\tau - \tau_2)} \right\} \end{array} \right. \quad \begin{array}{l} (50 \leq \tau \leq 100 \mu s ; \tau_1 = 50 \mu s) \\ (100 \leq \tau \leq 200 \mu s ; \tau_2 = 100 \mu s) \end{array}$$

where A is absorption of copper foil at 10.6μm, W_0 laser power, k thermal diffusivity and K thermal conductivity.

Figure 7 shows the calculated light intensity. The detected light intensity shown in Fig.6 is seen to be more

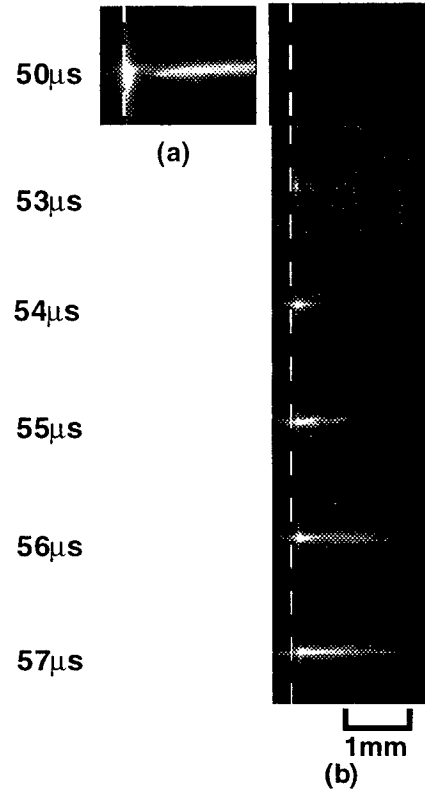


Fig.5 Plume image.(a)with and (b)without He-Ne irradiation.

rapidly increased than calculated one. The reason this difference is accounted for as follow; **Figure 8** shows the appearance and cross-section of the drilled via hole. A lot of convex portions like babbles with diameter of approximately $5\mu m$ are observed, and the oxide layer is seen to be separated from the inner copper foil. The oxide layer shows needle like branches at the surface as shown **Fig.9**. The tips of the branches can be rapidly heated and the oxide layer is separated from the inner copper foil. Therefore the thermal conduction to the inner copper foil is prevented and the epoxy resin is heated up quickly to temperature high enough to irradiate the visible light emission.

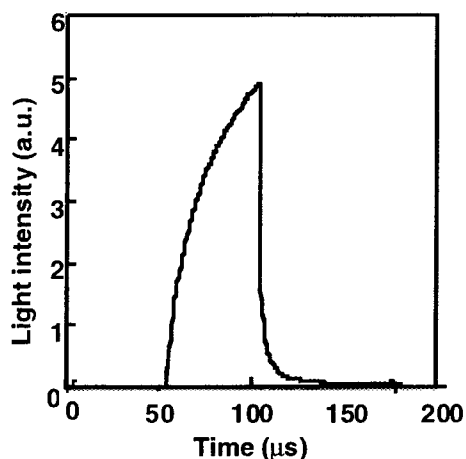


Fig.7 Calculated radiation intensity.

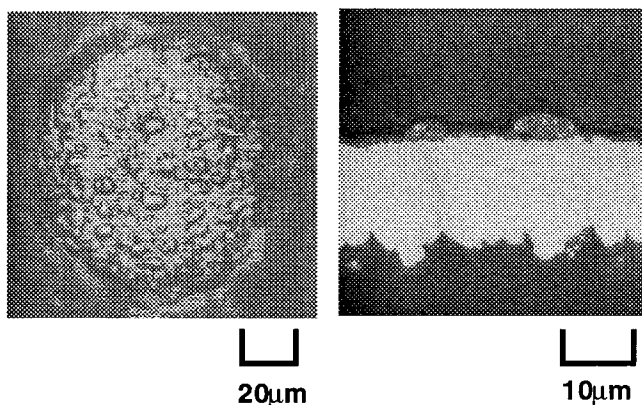


Fig.8 Appearance and cross section of via hole.

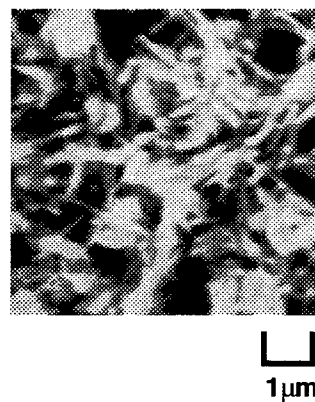


Fig.9 Surface of oxide layer.

3.4 In-process monitoring of via hole quality

Figure 10 shows the relationship between the integrated light intensity and bottom area where the thickness of the smear was less than $2\mu m$, when the laser beam was irradiated to the difference pulse width and the number of shot. It is seen that the bottom area is in proportion to the integrated light intensity. Thus a simple the in-process monitoring technique has been developed to estimate the bottom area with the smear thickness less than $2\mu m$ by detecting the light intensity.

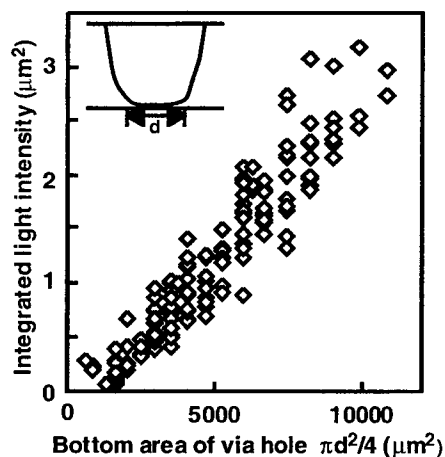


Fig.10 Bottom area of via hole and integrated light intensity.

4. Dry desmar by KrF excimer laser

4.1 Spectral intensity

KrF excimer laser was irradiated to a square region of $500\mu\text{m} \times 500\mu\text{m}$ where CO_2 laser drilled hole was includes as shoen in **Fig.11**. The spectral intensity of the light emission was measured by a streak camera to investigate the drilling process during the excimer laser irradiation to the bulk epoxy resin, the inner copper foil and CO_2 laser-drilled portion with the smear thickness of 1 or $2\mu\text{m}$. The fluence of the KrF excimer laser was $1.68\text{J}/\text{cm}^2$. **Figure 12** shows the spectrum region 516nm to 524nm. In these cases of the inner copper

foil and CO_2 laser drilled portion, the copper spectrum of 521.8nm was observed. In the case of CO_2 laser-drilled hole, the inner copper foil with the thin epoxy resin was ablated by the excimer laser passing through the epoxy resin. **Figure 13** shows the reflection of the excimer laser. The reflected intensity from the CO_2 laser-drilled portion was lower than the case of the inner copper foil. This is because the intensity of excimer laser decreased during passing through the epoxy resin.

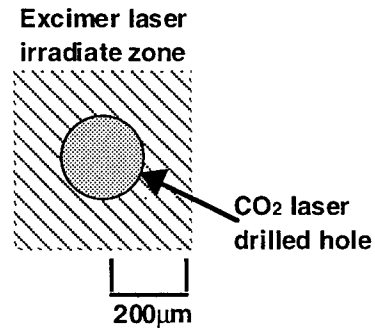


Fig.11 Excimer laser irradiatte zone.

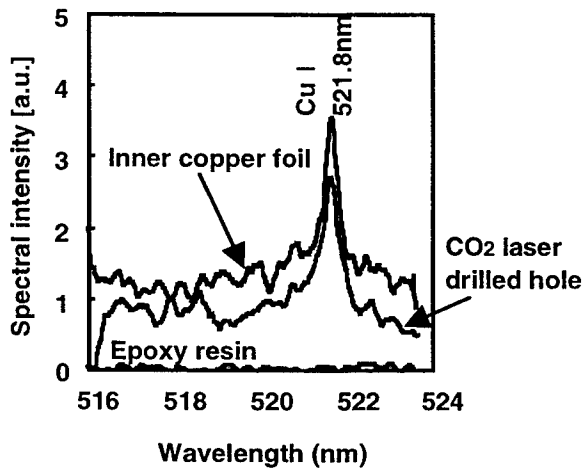


Fig.12 Spectral intensity in excimer laser irradiation.

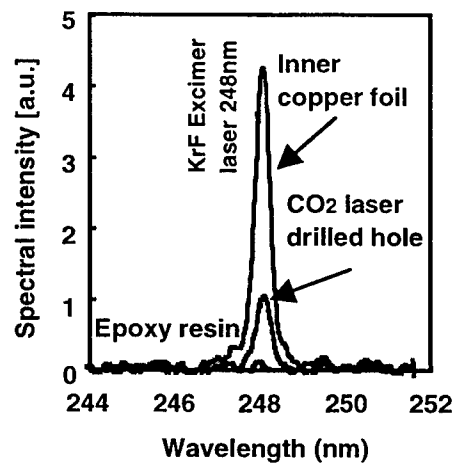


Fig.13 Reflection of excimer laser.

4.2 The intensity of excimer laser reflection

The intensity of excimer laser reflection from the CO_2 laser drilled portion was detected by a Si photodiode.

Figure 14 shows the relationship between the number of excimer laser shot and the peak intensity of the reflected excimer laser. The reflected intensity increased with increasing the number of the laser shot until the fourth shot. However the reflected intensity decreased after the fourth laser shot. The reason for this change of the reflection intensity is accounted for as follows.

Figure 15 shows the SEM image of the appearance of the hole bottom. At second shot, the inner copper foil is still covered with the epoxy resin. At the fourth shot corresponding to the maximum reflection intensity, the epoxy resin is removed and the inner copper foil is exposed. The reflection intensity of the excimer laser increases because residual thickness of the resin was reduced by excimer laser irradiation. At more laser shots, the exposed surface of the inner copper foil became roughened. Therefore the less intensity of the reflection was detected due to the diffused reflection at the roughened copper surface.

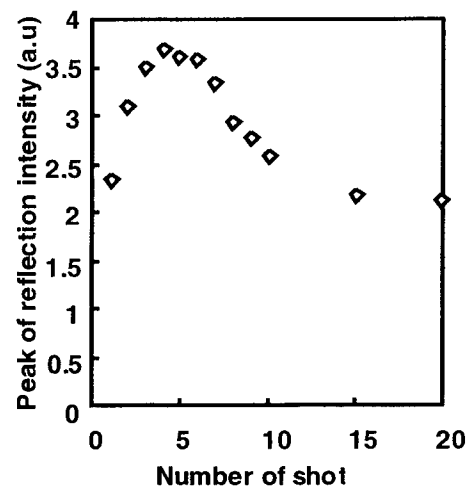


Fig.14 Peak of reflection intensity vs. number of shot.

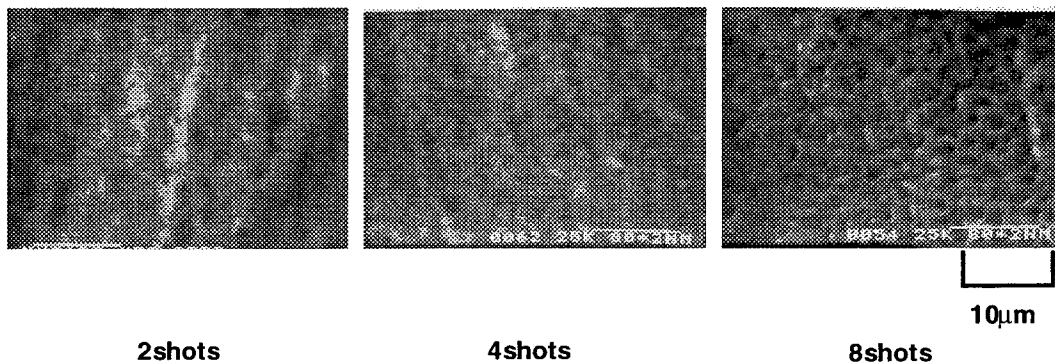


Fig.15 Bottom surface of via hole.

4.3 Dry desmear by KrF excimer laser.

The KrF excimer laser was irradiated to the CO₂ laser-drilled portion to remove the smear adjacent to the inner copper foil. **Figure 16** shows the cross-section of the plated via hole. In these cases, the CO₂ laser drilled hole was determined by 0, two and four shots of excimer laser irradiation. Electric contact was not achieved at 0 and two shots. At four shots, the smear was removed and the electric contact was accomplished. This indicates that it is possible to remove the smear by irradiating the excimer laser.

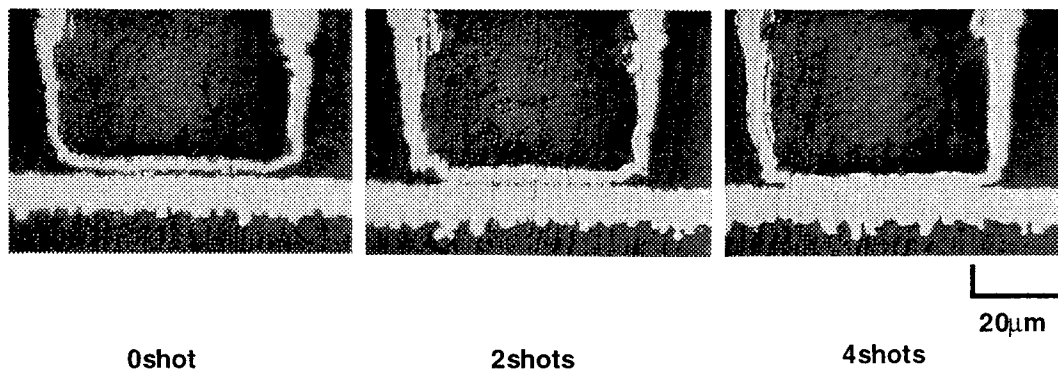


Fig.16 Cross-section of plated via hole.

5. Conclusions

The via hole drilling process by CO₂ laser was investigated on basis of high speed photograph, detecting the light emission and thermal conduction calculation. Dry desmear by KrF excimer laser was also investigated by measuring the spectrum of the light emission and detecting the reflection of the excimer laser. The results obtains are summarized as follows:

- (1) The light emission was detected at smear thickness less than approximately 2 μ m during CO₂ laser irradiation, and the bottom area with the smear thickness less than 2 μ m can be evaluated in-process by detecting the light intensity.
- (2) The light emission from the PWB with inner copper foil of black oxide treatment during the CO₂ laser irradiation is caused by heating needle like branches of the oxide layer thermally isolated from the inner copper foil.
- (3) Dry desmear was successfully accomplished by KrF excimer laser where the desmear process can be monitored by detecting the laser reflection.

Reference

- (1) T.karasaki, et al. Journal of Japan Laser Processing Society, Vol.5,No.2, (1998) pp.5-11
- (2) S.Takeno, M.Moriyasu,S.Hiramoto, Proc. Laser materials Processing Conference, ICALEO'92.LIA Vol.78 (1992) pp.459-468
- (3) T.Kadya, Journal of Japan Laser Processing Society,Vol.5,No.2, (1998) pp32-33
- (4) S.Takeno, Proceeding of 42th Laser Material Processing Conference, (1997) pp.71-81
- (5) S.Takeno, Journal of Japan Laser Processing Society, Vol.6,No.2, (1999) pp.26-29
- (6) H.Karasaki,K.Isaji,H.Kinosita, Proc. Laser Material Processing Conference, ICALEO'98. LIA, Vol.85, (1998) ppG50-57

Poster Session

Laser-induced temperature-rise measurement by infrared imaging

Jianhui Gu^{*a}, Siu-Chung Tam^a, Yee-Loy Lam^a, Qiguang Zheng^b, and Xueqin Wei^b

^a Photonics Lab, School of EEE, Nanyang Technological University, Singapore 639798

^b State Key Laboratory of Laser Technology, Huazhong University of Science & Technology,

Wuhan, Hubei 430074, P R China

ABSTRACT

The characteristics of laser-induced temperature-rise are important information in laser material processing. In our experiment, several kinds of metals such as mild carbon steel, stainless steel, aluminum alloy and copper, and non-metals namely epoxy and polymethyl methacrylate were irradiated by using a high-power CW CO₂ laser beam, while the temperature distribution and variation on their surfaces were measured by using a fast scanning infrared camera to image the laser irradiated area. The CO₂ laser beam power was varied from several tens of Watts to several hundreds of Watts for the irradiating of different materials. 2-D and 3-D temperature distributions and the temperature variations against the time of laser irradiation on certain points within the laser-irradiated area were recorded and measured. It is found that the temperature distribution on the surfaces of the irradiated materials was tightly related to the laser beam mode, and the temperature fluctuations corresponded to the laser beam power fluctuations. The results of this research could be applied to laser material processing.

Keywords: Laser material processing, infrared imaging, temperature measurement.

1. INTRODUCTION

The technology of infrared thermal imaging has always been used to measure the temperature of an object surface. In this way, object temperature is not measured directly, but in directly through the infrared radiation incident on the detector in the imager. In the infrared region, the detector is often mercury cadmium telluride (TeCdHg) in two separate spectral bands, i.e., 3~5 μm and 8~12 μm , which are sensitive and accurate for temperature measurement at low and high temperature region respectively.¹

Infrared thermal imaging, an old and established optical technology, has found many applications in different areas with different aspects because it is able to provide useful and accurate information such as temperature distribution and variation on the surface of imaged target. It can provide useful and accurate information like temperature distribution and variation on the target surface when used in the application of interaction between high-power laser beam and material. In these kinds of applications, especially for laser material processing, direct and online measuring of target surface temperature, in some cases, is essential for the controlling of the quality of processed materials. It is always needed to measure the temperature directly because there is no exact and direct relation between the temperature distribution and variation and the parameters of the incident laser beam. Under other circumstances, when the processing results are very sensitive to the temperature distribution in material, or the variation of laser beam parameters (beam power, beam mode, and focusing condition, etc.) may cause evident temperature fluctuation in the material, the investigation and measurement of target temperature is very important for the application of laser material processing.

The information about temperature and temperature variation are always very important in the application of high-power lasers, such as the investigation of the interaction between laser beam and material²⁻⁴. In this paper, the traditional infrared thermal imaging technique was employed to investigate and finally measure the temperature of object surface when different materials were irradiated using a high-power CW CO₂ laser beam with different interaction parameters. Followed

* Correspondence: E-mail: ejhgu@ntu.edu.sg; Tel: + 65 790 5461; Fax: + 65 790 4161

the introduction we described in detail about the experimental layout. Then we reported the experimental results from the measurement of the temporal and spatial distribution the temperature on object surface.

2. EXPERIMENT LAYOUT

The experiment layout is illustrated in Fig.1. A CW multimode laser beam with the wavelength of $10.6\text{ }\mu\text{m}$ was output from a traverse flowing cooled and DC discharge excited carbon dioxide laser. The laser beam power and its fluctuation were monitored and then recorded by using a power meter. In order to achieve a relatively larger beam spot size on the target surface, and thereby a relatively larger infrared image through the infrared thermal imager, the output laser beam was projected directly onto the target surface. Therefore, unlike the optical delivery and focusing systems used in most of laser material processing system, no focusing lens was used in the experiment. The overall interaction time between the laser beam and the target was controlled and adjusted by using an optical shutter.

In the experiment, an HWRX-3 type fast scanning infrared thermal imager (North China Optic-Electronic Inc) was employed to record the thermal images of laser irradiated and heat affected zone on the target surface. The angle θ in Fig.1 was approximately 30 degrees. The noise equivalent temperature difference (NEAT) of the imager is 0.138 degree centigrade. Its spatial resolution is 0.91micro-radian. Temperature higher than 3000 K could be measured using this IR imager. The distance from the imager to the object surface was about 50 cm. A filter was used to completely eliminate the $10.6\text{ }\mu\text{m}$ radiation reflected and scattered back from the target surface since the imager's responding wavelength is in the range of $8\sim 12\text{ }\mu\text{m}$. A little fraction of the reflected or scattered laser beam at $10.6\text{ }\mu\text{m}$ could saturate the TeCdHg detector. The sampling time for one image was 40 ms. This was the temporal resolution of the IR imager. The minimum sampling time interval between two images could be adjusted to as short as zero, i.e., CW sampling available. In order to ensure that we could sample the very beginning of the interaction of the laser beam with the target material, we started the sampling of the IR imager about 2 seconds before the opening of the optical shutter.

In order to investigate the temperature response of different materials to different laser beam powers and their fluctuations, metals such as mild carbon steel (MCS) and stainless steel (ST) with relatively lower thermal conductivity, aluminum alloy (Al) and copper (Cu) with very high thermal conductivity, and non-metals such as epoxy plate (EP) and polymethyl methacrylate (PM) were tested. The tested targets were all plates and located about 1.5 meters away from the output window of the CO_2 laser. The laser beam was projected normally onto the object surface. The laser energy was absorbed by a water-cooled heatsink before the optical shutter was opened.

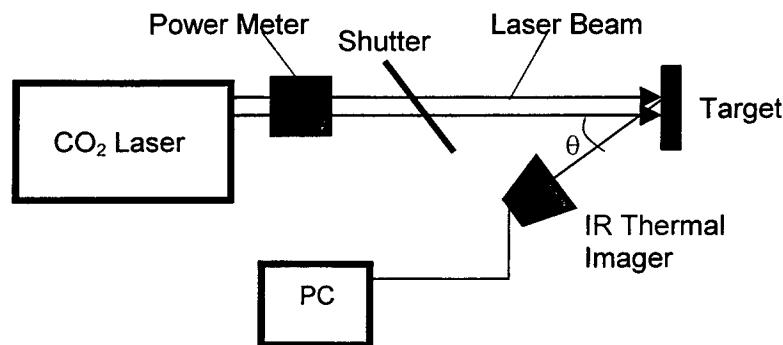


Fig.1 The layout of the experiment

3. EXPERIMENTAL RESULTS

3.1. Experimental parameters

The research work reported in this paper was mainly focused on investigating the temperature rise and variation on target surface from the very beginning when laser beam was projected onto a target. Therefore, temperature measuring and thermal image recording was restricted in a relatively lower temperature region. Thus, for different materials, laser beam

power was adjusted to avoid evident melting or burning on target surface in most cases so that we can get more detailed information on the characteristics of the temperature rise and temperature fluctuations. Some typical experiment parameters and thermal properties of the tested materials are listed in Table 1.⁵

The laser beam powers shown in Table 1 indicate the range of the laser beam power fluctuation while irradiating on the target. In the experiment, for each sampling we adjusted the output laser beam power to a desired value, let the laser operate for about 3 to 5 minutes to achieve a relatively stabilized output, and then opened the optical shutter and imaged the irradiated object surface. The large fluctuation in laser beam power was caused by the laser system itself. The laser beam spot size was about 20 mm × 40 mm at the output power of about 800 watts, and about 15 mm × 30 mm at the low output power. This laser device output a laser beam with a multimode which varied within a large scale with the variation in output laser beam power. The laser beam changed to nearly round with a beam size of about 40 mm in diameter when the output power laser beam was increased to about 2000 watts.

Table 1. Experimental parameters and properties for different materials

Material	Laser beam power / W	Sampling interval time / s	Emissivity	Thermal conductivity / Wcm ⁻¹ °C ⁻¹
MCS	387 ~ 480	0.1	0.80	0.835
ST	780 ~ 825	0.1	0.50	0.168
Al	805 ~ 820	0.0	0.09	2.36
Cu	801 ~ 815	0.0	0.61	4.01
EP	230 ~ 285	0.0	0.84	0.00158
PM	43 ~ 48	0.0	0.95	0.00154

All the infrared thermal images sampled by the IR imager were recorded and saved in a PC simultaneously. A maximum of 888 images could be sampled and stored for each sampling operation. By employing some particular image processing methods, the temperature distribution and its variation could be obtained from the stored thermal images after the experiment. The sampling interval time of 0.0 s means that we sampled one image every 40 ms according to the temporal resolution of the IR imager.

3.2. Temporal temperature distribution

Fig. 2 to Fig. 4 show the temperature variation in the center point and the edge point in the vertical direction of the laser beam irradiated area, respectively. The shapes of the laser irradiated and heat affected area for each material recorded by the

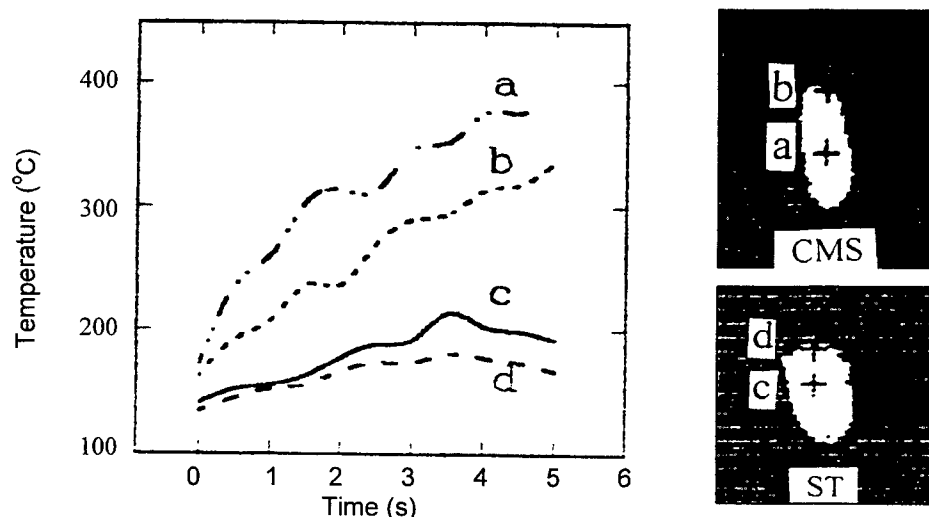


Fig. 2 Measured temperature variation in laser irradiated region for materials CMS (curves a and b) and ST (curves c and d). (a and c: at the center points; b and d: at the edge points)

IR imager and the location of the temperature measuring points were also indicated in the figures on the right hand side of each figure.

The results of the irradiating of MCS and ST were shown in Fig. 2. The laser beam power for irradiating of MCS fluctuated within 387 ~ 480 watts, and for ST was 780 ~ 825 watts. MCS has higher emissivity and thermal conductivity than ST. So it has a higher temperature and temperature rises on the object surface although irradiated with a lower laser beam power, and the temperature rise for MCS was fast than that of ST. It was found that the fluctuation in laser beam power could cause the fluctuation in temperature on the surface of the irradiated target. Another characteristic was that the temperature at the center of the irradiated area was higher than that at the edge because of thermal conduction.

Fig. 3 shows the results on the irradiation of Al and Cu plates. The irradiating laser beam powers were within the fluctuation range of 805 ~ 820 watts and 801 ~ 815 watts for Al and Cu, respectively. Because Al and Cu have high thermal conductivity, the temperature and temperature rise on the surfaces of these two materials were lower, less than 60 °C. It was interesting to find that, for Cu, the temperature on its surface increased very fast initially under the irradiating of the laser beam, then came down at the edge of the irradiated area and tended to be stabilized at about 48 °C at the center, although the laser irradiation was continuing to input into the object. This might be contributed by the very high thermal conductivity of Cu and implied that it would be very difficult for the laser material processing of Cu, especially for using CW laser beam.

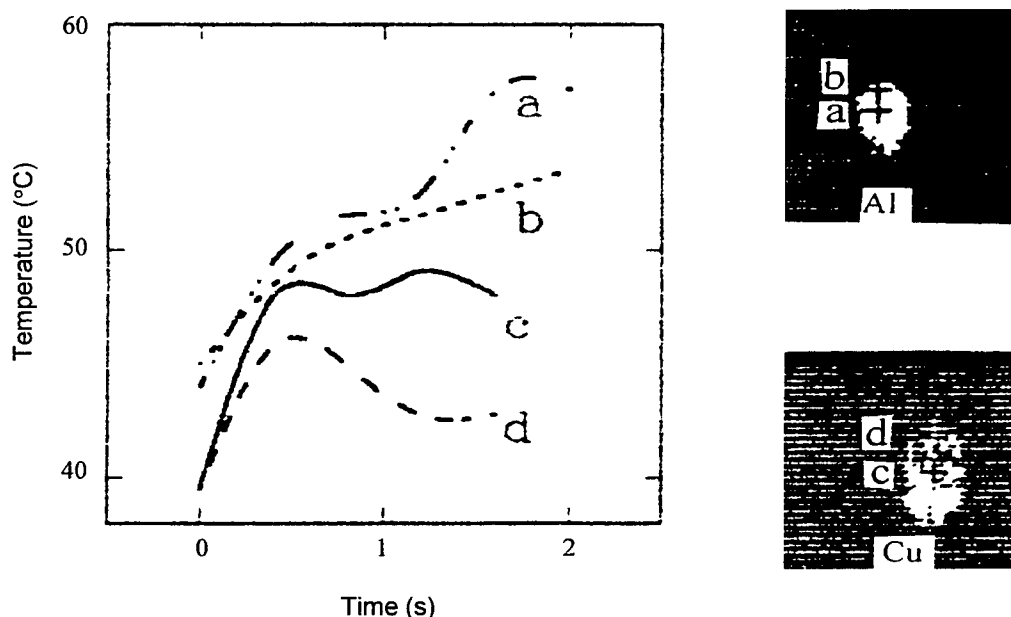


Fig.3 Measured temperature variation in laser beam irradiated region for materials Al (curves a and b) and Cu (curves c and d). (a and c: at the center points; b and d: at the edge points)

For non-metals, their burning points are much lower than those of metals. So a relatively low laser beam power was employed for non-metals to avoid melting and burning of the material. For EP, the irradiating laser beam power fluctuated within the range of 230 ~ 285 watts, and for PM it was in the range of 43 ~ 48 watts. The curves in figure 4 indicated that the temperatures on the surfaces of the non-metals were much high even with a rather low irradiating laser beam power. This was because of their very low thermal conductivities which tended to keep the input laser beam energy within the irradiated area. The low thermal conductivities also made the large difference between the center point and the edge of the irradiated area. It was also found that the larger the fluctuation in laser beam power, the larger the fluctuation in temperature of the object surface.

Temperature rise in laser beam irradiated region for both Al and Cu was very little, not more than 20 degree, because of their much higher thermal conductivity and much higher reflectivity to 10.6 μm CO_2 laser beam than those of other materials (Fig.3). Therefore, it needs much high power intensity to meet the needs of laser processing of Al and Cu. Fig.3

also shows that the temperature of Cu even decreases when laser beam was still continuing irradiating on it with a laser beam power of about 800 watts. This was also caused by its high thermal conductivity.

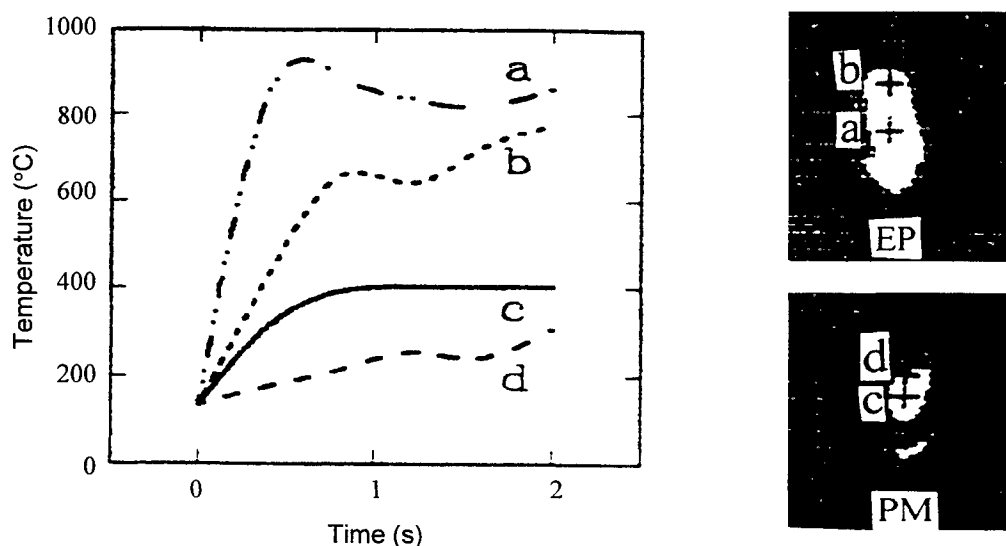


Fig.4 Measured temperature variation in laser beam irradiated region for materials EP (curves a and b) and PM (curves c and d). (a and c: at the center points; b and d: at the edge points)

Also from Fig.2 to Fig.4, it was found that the temperature difference between the center point and the edge point in the irradiated region for lower thermal conductivity materials CMS and ST was several tens degrees, which was apparently higher than that for relatively high thermal conductivity materials Al and Cu which was less than ten degrees. This kind of difference for non-metals EP and PM was nearly two hundred degrees, which was much higher than that of metals because of their very much lower thermal conductivities and emissivity. The emissivity of a material is related to its surface reflectivity. The larger the reflectivity, the lower the emissivity. Al has the lowest emissivity because of its high reflectivity ($> 95\%$) at the wavelength of $10.6\ \mu\text{m}$.

3.3 Spatial temperature distribution

This IR imager could also provide the information about the spatial temperature distributions on the irradiated object surfaces. The three dimensional (3-D) temperature distribution and the corresponding linear temperature distribution (2-D) along the center vertical line of laser beam irradiated region for CMS, ST, Al, Cu, EP and PM are showed in Fig. 5, Fig. 6,

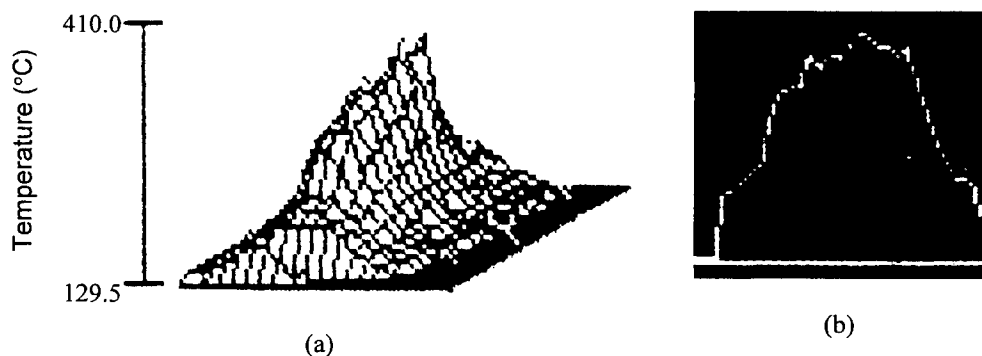


Fig.5 The 3-D temperature distribution (a) and the corresponding 2-D temperature distribution (b) of CMS

Figures 7-10, respectively. The laser parameters and the image sampling parameters are the same as those of listed in Table 1. The pictures and curves in these figures are selected from the stored images which were corresponded to the highest temperature appeared on the object surface.

From Fig.5 to Fig.10, it is evident that the temperature distributions, both in 3-D and in 2-D, for all materials tested are non-homogeneous mainly because of the non-homogeneous distribution of laser intensity and partly the thermal conducting in the materials. The highest temperature point corresponded to the highest laser beam intensity point in the irradiated regions. From the figures it was found that for MCS and ST the temperature rise and the temperature difference were larger than those of Al and Cu which was because that both Al and Cu had higher reflection to the wavelength of $10.6\text{ }\mu\text{m}$ and much high thermal conductivity. Non-metals EP and PM might absorb nearly 100 percent of laser beam power irradiated on their surfaces, and their thermal conductivities were very low. Therefore, their surface temperatures rose sharply to a very high level, even burning within a very short time (See Fig.9 and Fig.10).

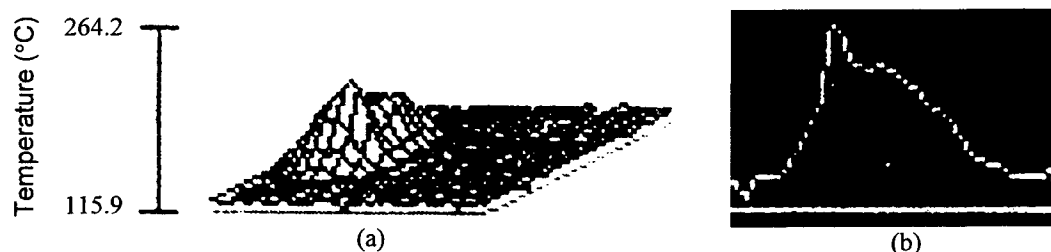


Fig.6 The 3-D temperature distribution (a) and the corresponding linear temperature distribution (b) of ST



Fig.7 The 3-D temperature distribution (a) and the corresponding 2-D temperature distribution (b) of Al

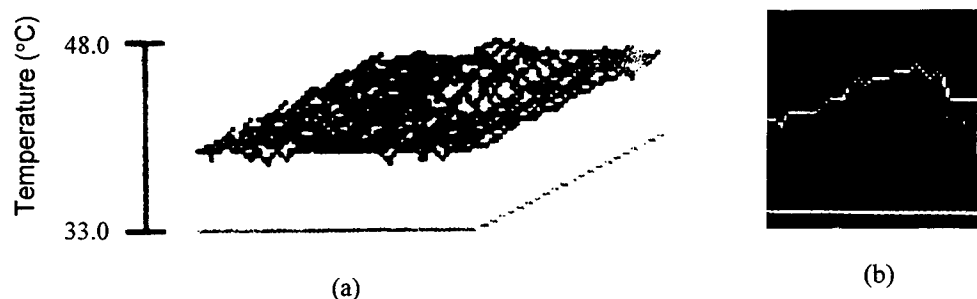


Fig.8 The 3-D temperature distribution (a) and the corresponding 2-D temperature distribution (b) of Cu

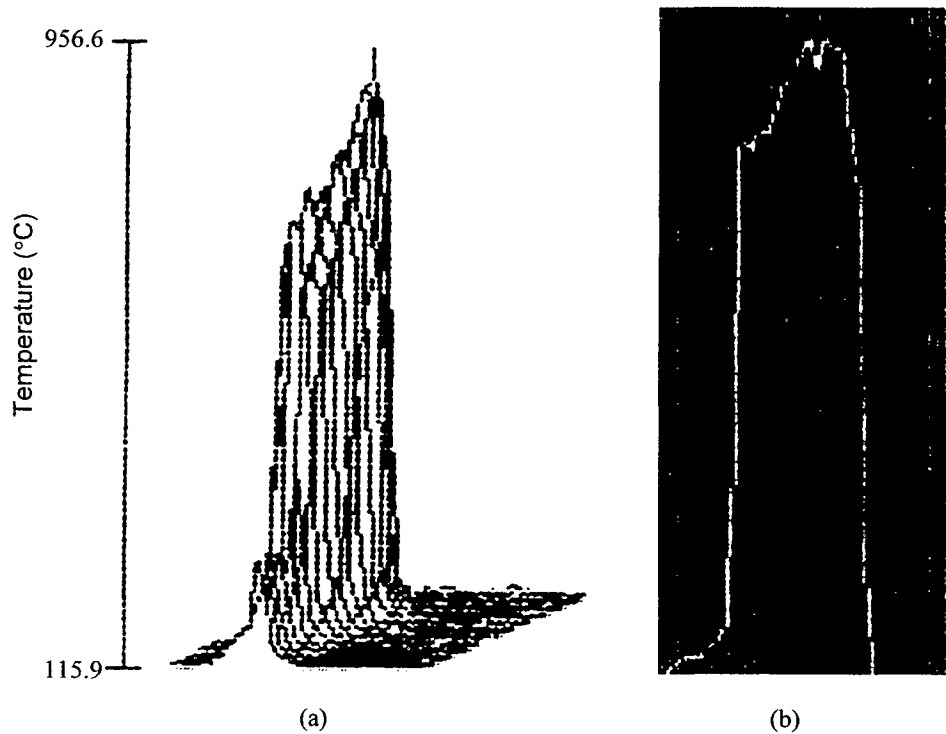


Fig.9 The 3-D temperature distribution (a) and the corresponding 2-D temperature distribution (b) of EP

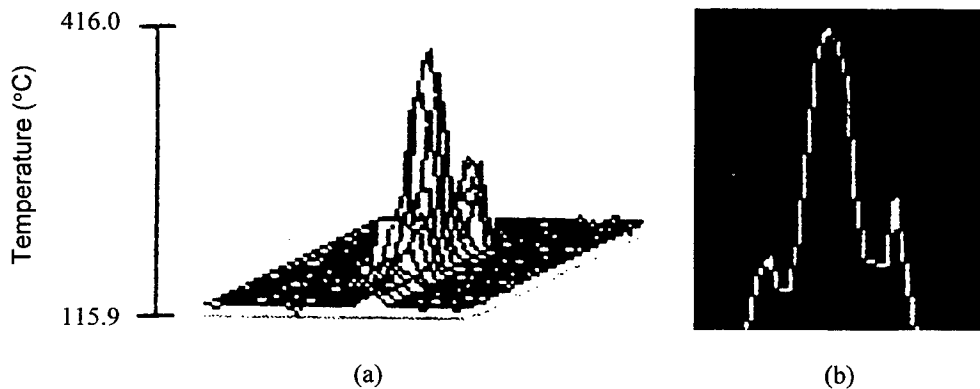


Fig.10 The 3-D temperature distribution (a) and the corresponding 2-D temperature distribution (b) of PM

4. CONCLUSION AND DISCUSSION

From the experiment and the analysis of the above, it is found that by using infrared thermal imaging technology, the laser beam shape and even laser beam mode distribution could easily be recognized and measured. For the carbon dioxide laser used in the experiment, the laser beam shape, or laser mode, varied with its output beam power. The beam shape might be totally different between low power laser beam and high power laser beam. It could be seen from the six laser beam spots imaged in the figures that the laser beam shape is several separate points when its output power is very lower (<100 watts). When the laser beam power is increased from several hundred watts to nearly one kilowatt, the laser beam shape changes

from rectangle to nearly circular. This kind of variation in laser beam shape is caused by the variation in laser beam power is certainly harmful and should be avoided in the industrial applications by improving laser beam quality.⁶

The measured point temperatures rise when irradiating time of laser beam increases. Almost all of the temperature curves, however, were not smooth. This was mainly caused by the fluctuating of the irradiating laser beam power. A more detailed theoretical study on the relation between laser beam power fluctuation and temperature fluctuation is being undergone, and the results will be published elsewhere. This is an interesting research project, which might be applied to analyze and control processing quality in laser material processing by studying the fluctuation of laser beam parameters.⁷

Through the experiment, point temperature, lineal 2-D temperature distribution and 3-D temperature distribution were all been successfully attained by infrared thermal imaging. It has found that infrared thermal imaging is a very useful tool for temperature measurement in such kind of applications like interaction between laser beam and material, especially for the application of high-power lasers since the temperature rise maybe much high which is difficult to be measured by using traditional temperature measuring techniques.

In the experiment, the biggest unknown parameter affecting infrared thermal imaging measurements was the surface emissivity of the object being imaged. Generally, the emissivity should be determined in each measurement, and input and stored in the imager computer. In practice, actually, to exactly determine the emissivity of an object being irradiated by the laser beam is very difficult and nearly impossible, especially for the situation when phase change occurs on the object surface. Therefore, a large measurement error might result from non-accurate emissivity measuring or setting in infrared thermal imaging measurement. However, this technology has a great advantage to measure relative temperature distribution and variation by non-contact online measuring.

REFERENCES

1. B. Linnander, "Thermal imaging answers the question: How hot is hot?," *Laser Focus World*, **29**, No.6, pp. 95-99, 1993.
2. Z. Guo, Z. Xia, J. Gu, D. Xu, Q. Cai, and L. Wang, "Aligning focusing system for high-power laser beam," *Government Report of American*, **AD-A256907**, USA
3. J. Gu, Q. Zheng, T. Wang, X. Tao, and Z. Li, "Non-equilibrium sintering of ZrO₂ solid electrolyte using high power CO₂ laser beam," *SPIE 2207 / Laser Materials Processing*, pp. 525-531, 1994.
4. J. Gu, Q. Xu, Z. Li, and S. Chen, "Fundamental theory and technology of laser propulsion," *Propulsion Technology*, **16**, no.2, pp. 80-84, 1995.
5. L. Li, *Modern Laser Material Processing and Its Systems*, **Chapter 6**, Beijing University of Science and Technology Press, Beijing, 1993.
6. G. Herzigr, "Physics of laser materials processing," *SPIE 650 / High Power Lasers and Their Industrial Application*, pp. 188-194, 1986.
7. E. Beyer, G. Herzigr, and A. Gasser, "Plasma fluctuations during laser machining with CW CO₂ laser," *SPIE 801 / High power Lasers*, pp. 178-184, 1987.

NEW INFRARED STEREOLITHOGRAPHY: CONTROL OF THE PARAMETERS OF THE LOCALIZED CURING THERMOSENSITIVE MATERIALS.

Marco A. F. Scarparo ^a, André L. J. Munhoz ^b, Gilson Marinho ^b,
Djalma S. Salles ^b and Susan D. Allen ^c

State University of Campinas - Brazil

^a Institute of Physics – Laboratory of Laser Application in Stereolithography

^b Mechanical Engineering Faculty

^c Florida State University – USA

Abstract

In normal practice, stereolithography has been used for photosensitive resins where ultraviolet light (HeCd laser $\lambda=0.352\mu\text{m}$) initiates the curing process for prototypes construction. In this work we developed a new aspect of stereolithography, using CO₂ laser ($\lambda=10.6\mu\text{m}$) in thermosensitive materials where no shrinkage and post-cure treatment was observed. The bulk curing process in resins, epoxy unlike, has been proved useful in a new technique for fabrication of prototypes. Control of the laser parameters appears as an important tool for localized cure in the material. Our resin basic sample is composed by the thermosensitive epoxy resin proved to be (in weight) 10 parts, 1,4 parts diethylene triamine (the curing agent) and 0.7 parts silica powder. Silica play an important hole in the curing process Tests with fumed silica and non treated fumed silica showed considerable difference in the obtained final product We also developed a physical and chemical models of the setting process determine the time delay for onset of curing as a function of temperature and the profiles of the isotherms in the sample. In order to model the flow of the heat in laser-induced curing we used theoretical approach to solve the time dependent heat equation in cylindrical coordinator. The data show the curing rate as function of temperature. Activation energy results were derived from differential scanning calorimetry (d.s.c.).

Key Words - laser, polymer, local curing, stereolithography, prototype, infrared radiation.

1. Introduction

Stereolithography is a powerful means to producing two and three dimensional models of prototypes [1,2]. Conventional stereolithography uses ultraviolet (uv) light, to cure photosensitive polymer [3] (Fig 1). Several papers [4,5] have been studied the thermal curing of thermosensitive resins. The application of infrared laser (CO₂) to cure thermosensitive materials (epoxy resin) may provide a novel and cost-effective means to manufacturing industrial prototypes [6]. This paper is intended to provide a more profound physical basis for this new technique of the Rapid Prototyping. The use of Rapid Prototyping for fabrication of models and prototypes can reduce 75% of the development time, improving not only the speed but also the cost of the products developed. In conventional stereolithography, ultraviolet (uv) light, typically a HeCd laser at $0.352\mu\text{m}$ is used to photocuring a photosensitive polymer in a carefully designed pattern. Generally, using computer control of the optical and mechanical elements as well as the thermal and chemical conditions, it has proved to be possible to fabricate complex structures. The important parameters are by now well understand as are the mechanism of uv photocuring.

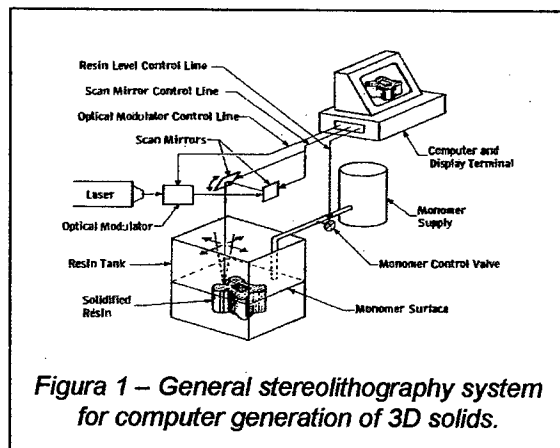


Figure 1 – General stereolithography system for computer generation of 3D solids.

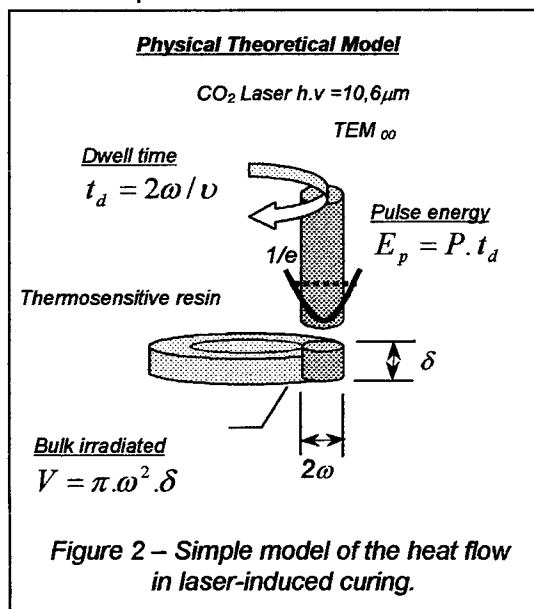
This particular work presents a study of an new technique of application of infrared radiation CO₂ laser working $\lambda=10.6\ \mu\text{m}$ on thermosensitive resins by means of stereolithography. The aim of the infrared stereolithography application is because this technique showing no significant shrinkage and requiring almost no post-cure treatment. Our results showed we can confine the CO₂ laser heating in the epoxy resin based material and, therefore, it's curing in all three dimensions.

A simple physical description of the localized cure process has been presented along with the time-dependent heat equation using Crank-Nicholson finite difference method. We also discussed the differential scanning calorimetry (d.s.c.) to obtain the activation energy of the curing reaction as a function of temperature and study the rate sample behavior as temperature change.

Importants tests has been carried to ascertain the performance of the laser scan head along with effective implementation of the operating parameters. Results showed up that the laser parameters and the stoichiometric combination of the sample compounds play an important hole in the final results of the curing process as well as the type of silica powder involved. Our basic resin sample is composed by the thermosensitive resin proved to be (in weight) 10 parts, 1.4 parts diethylenetriamina (the curing agent) and 0,7 parts of silica powder.

2. Theoretical considerations and temperature calculation in the laser processing

The experimental analysis was carried out taking in account the thermal characterization of the sample, the stoichiometric characterization of the sample combined along with the lasers parameters, and the application of the differential scanning calorimetry to the sample. A physical theoretical model (Fig. 2) has been worked out aiming at the exact characterization of every physical phenomenon occurred in the process of local curing. The model describes the energy flow deposited by the laser in terms of the control of the operational parameters and the behavior of the resin, aiming at the local curing. Initially, in order to obtain the power associated to the laser beam, the dwell time of the beam in the sample was determined. The local curing in the beginning of our experiment was achieved by scanning a continuous wave (cw) CO₂ laser repeatedly over a circular trajectory on the sample's surface with a scan speed v . By dividing the beam diameter 2ω by the scan speed, one obtains the dwell time: $t_d = 2\omega / v$ (1), concerning the time of interaction laser/resin at a surface point. As the resin is highly absorptive at the CO₂ laser wavelength ($10.6\mu\text{m}$), it is assumed that, during the dwell time, nearly all the beam energy has go into the inner part of the sample at a distance from the surface equivalent to the absorption depth δ . The absorption depth was determined by measuring the transmittance of a non-cured sample, having a thickness of $80\mu\text{m}$ at the band of the CO₂ ($\lambda=10.6\mu\text{m}$) laser emission spectrum. It was found to be $\delta = 22,4\mu\text{m}$. It is assumed that energy E has been absorbed in the small cylindrical volume V during the dwell time, the volume being defined as: $V = \pi\omega^2\delta$ (2). The energy released in V is the product of the laser power by dwell time: $E = P t_d$ (3). The approach of (2) is reasonable in the experiment because the sample absorbs at very small depths. Energy absorption in materials is quite critical concerning the depths they reach. In materials which do not absorb the energy strongly, the absorption depth may exceed the focus depth of the beam. As a consequence the confinement of energy at the surface of the model is not maintained. By the mean energy E it is possible to



determine the variation of temperature, which is proportional to the deposited energy concerning the thermal capacity C_p and mass m of the material contained in volume V , according to the following equation: $E_p = C_p \cdot m \cdot \Delta T$ (4), the mass of the heated volume may be calculated by using the mass

density of the sample $\rho = 1,16 \text{ g/cm}^{-3}$. If it is assumed that nearly all the flow of energy deposited by the laser beam is absorbed every moment the laser passes at a point on the surface of the sample, it follows that the irradiated volume will undergo a temperature increase which is determined by the expression:

$$\Delta T = \frac{E_p}{m \cdot C_p} = \frac{P \cdot t_d}{\pi \cdot \omega^2 \cdot \delta \cdot \rho \cdot C_p} \quad (5).$$

As the laser induces a linear heating rate, the general equation for conduction of heat dependent on time [7] is applied as follows:

$$\nabla^2 T = \frac{1}{D} \cdot \frac{\partial T}{\partial t} - \frac{G}{K} \quad (6)$$

where D stands for the thermal diffusivity of the sample, K is the thermal conductivity, and G describes the rate of energy generated by the laser source.

In Gaussian profile [8] of intensity of the laser beam, the term of source G generated by the CO_2 laser may be expressed by:

$$G = \left(\frac{P}{\pi \cdot \omega^2 \cdot \delta} \right) \exp \left(-\frac{r^2}{\omega^2} - \frac{|z|}{\delta} \right) \cdot S(t_d) \quad (7)$$

for $0 \leq t \leq t_d$, $S(t_d) = 1$; $t > t_d$, $S(t_d) = 0$ where $S(t_d)$ is the function which considers the term of source in the general equation, r is the distance from the beam center, z is depth of sample surface, δ is the absorption depth, P is the output power of the laser. The displacement scan speed over the trajectory way resulted in repetition rate of the laser equal to 35 ms , and the dwell time of $625 \mu\text{s}$ for a beam focused to $1/e$ of the 0.5 mm radius. These parameters can be used in the numerical

simulation, the constant of radial thermal transient τ being defined as follows: $\tau = d^2/D$ (8),

where $D = 22 \times 10^{-5} \text{ cm}^2 \cdot \text{s}^{-1}$ and d is the appropriate characteristic length. Thus τ is about 10 s for the radial transient ($d = \omega = 500 \mu\text{m}$) and about 60 ms for the axial transient ($d = \delta = 37 \mu\text{m}$). The Crank-Nickolson method of infinite differences can be used to solve the equation for the conduction heat dependent on time in the cylindrical co-ordinates. The thermal conductivity of the epoxy sample is $K = 0.359 \times 10^{-3} \text{ mW/cmK}$, which is near the conductivity of air $K = 0.24 \times 10^{-3} \text{ mW/cmK}$. As a concern to the theoretical model, it was assumed that thermal properties K and D , as well as the optical properties δ and reflectivity are all of them independent of temperature. The influence of silica in the process of local curing was disregarded.

3. Experimental procedure and analysis

As mentioned above the experimental analysis were carried out in three stages:

Stage I – Initially, for the thermal characterization of the thermosensitive resin, it was essential the study of the sample behavior under the influence of the heat action. For that purpose, it was decided to simulate experimentally how the sample reacts when submitted to an external source of heat. In order to carry out the experimental analysis, a small semi-liquid volume of the sample was heated at different external temperatures. Although the result of the local curing may also be obtained with polyester resin, the decision to use the epoxy resin (DGEBA - diglicidil eter of bisfenol A) was

taken because of its low coefficient of thermal diffusivity $D = 22 \times 10^{-5} \text{ cm}^2 \cdot \text{s}^{-1}$, as well as its appropriate viscosity, thermosensitive and stability in the course of the curing process. Though the epoxy resin presents a shorter handling time (pot-life) than the polyester resin, it offers less risk concerning toxicity, and presents greater rigidity as a final product.

The localized cure was obtained with the use of the CO_2 laser operating continuously within the infrared spectral absorption band at a wavelength of $10.6 \mu\text{m}$. The initial aim was to detail the experimental results of the localized cure with the use of laser, since they are essential to the understanding of this process. However, in order that the explanations might be coherent, we were firstly decided to characterize the curing process occurring in the bulk of the sample. For that purpose, a small volume of liquid sample was heated in a beaker wrapped in heat tape, which enabled to control the parameters which could bring information concerning the curing process. Initially, the temperature of the sample volume in terms of time was monitored by means of a thermocouple by applying different surrounding temperatures (external). The thermocouple signal recorded by the thermometer was sent to a digital oscilloscope connected to a data acquiring modulus where the data concerning the evolution of the sample temperature were stored. Simultaneously, in the apparatus the transmittance of the sample for the HeNe laser was measuring by means of a detector. Transmittance, which allows the obtainment of the depth absorption of the material, is a simple method to identify the beginning of the curing in the sample, provided the liquid resin is relatively transmissible to the visible light of the HeNe laser, becoming opaque while it cures. Through the correlation between the evolution of the sample internal temperature and the transmittance record, it is possible to determine the rate of curing in function of the sample temperature. Temperatures of 37°C , 44°C , 57°C , and 80°C were selected for the analysis of the curing behavior of the sample. At temperatures higher than 80°C , the curing took place quite rapidly, reaching a very high speed in a period of time which was faster then the time response of the apparatus, which risked the accuracy of the experiment. The evolution of the curing is shown terms of temperatures and time of curing in Fig 3. The results obtained in the graphics initially indicate a similar behavior in the evolution process of the curing at the different temperatures applied; however, it is clearly observed a much faster answer to the curing as the temperature increases. It is also noticed that the beginning of the curing process occurs in a very narrow temperature band of the sample (onset the curing). Such a variation arises out of the difficulty in controlling stoichiometry when preparing the sample.

Stage II - In order to predict more accurately the rate at which the reaction occurs as a function of temperature, we used the standard differential scanning calorimetry (d.s.c.) method. A typical plot is shown in Fig 4. Using the performed tests at different temperatures (within $\pm 0.5^\circ\text{C}$) we obtained the linearly scanned temperature where we monitored the flow of the heat to the sample. The average value obtained for the enthalpy of the reaction over several differential temperature scans was about $\Delta H = (65.5 \pm 1) \text{ KJ/mol}$. By using the isothermal scans, where a small amount of the sample is heated quickly to a prescribed temperature (as showed in Fig 4), and maintained at that temperature for the duration of the reaction. In Figure 4 the initial increase in power flow represent the energy required to heat the sample to the desired temperature. Integrating the difference of the non-reactive sample curve and the reaction sample curve from $t=0\text{s}$ to t gives the amount of energy released by the reaction prior to t . As $t \rightarrow \infty$ the energy released in the isothermal scan approach ΔH .

Stage III - The diagnostic tests of the laser scanning parameters^[9] to obtain the localized cure in thermosensitive process has been performed using the apparatus showed in Fig 1, by extracting the resin tank and applying the laser direct to the sample over a convenient substrate. We achieved localized cure by scanning laser over several different paths on the sample surface, varying the laser speed and the laser revolution time. Several stoichiometric composition of the sample were taking in account, as well as the laser parameters, involved in the curing process (Table I).

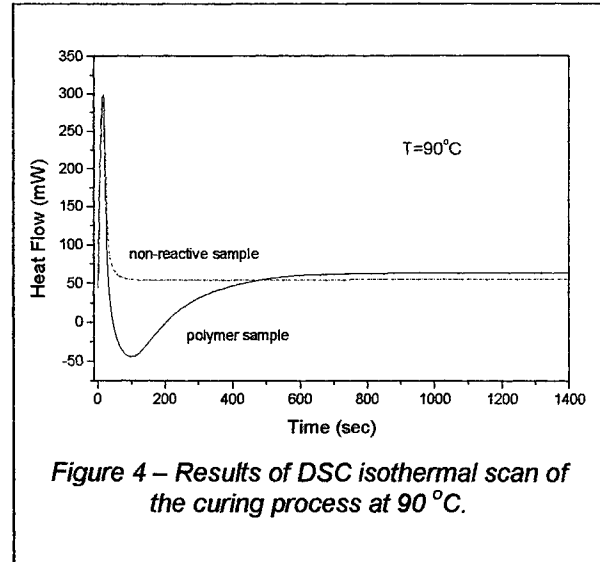
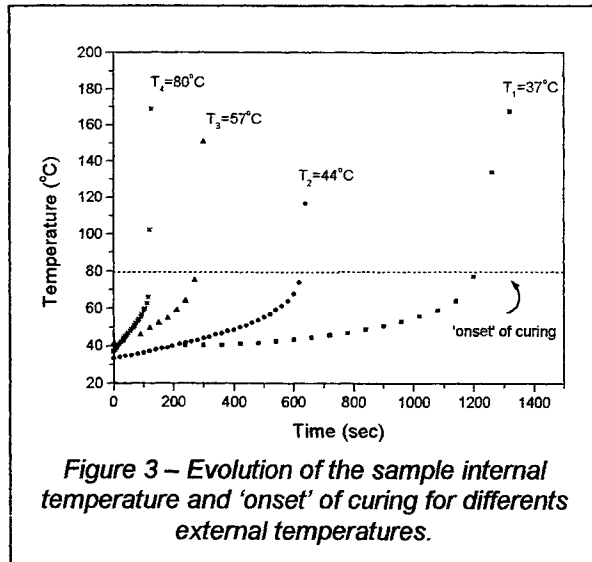


Table I – Diagnostic test involving: stoichiometric compositions, laser parameters and spatial resolution.

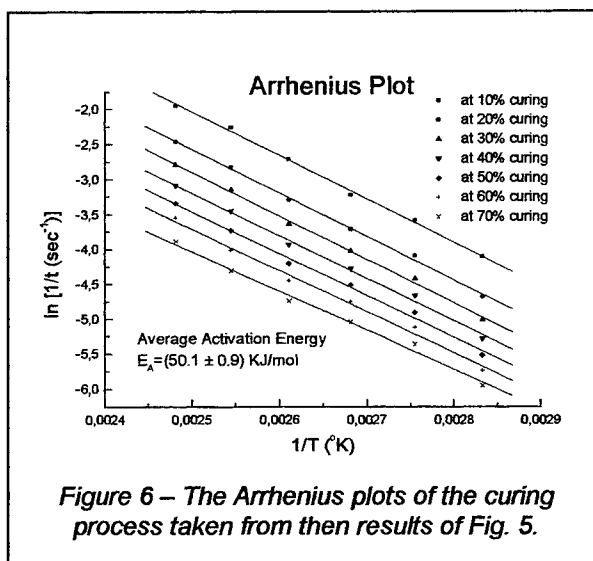
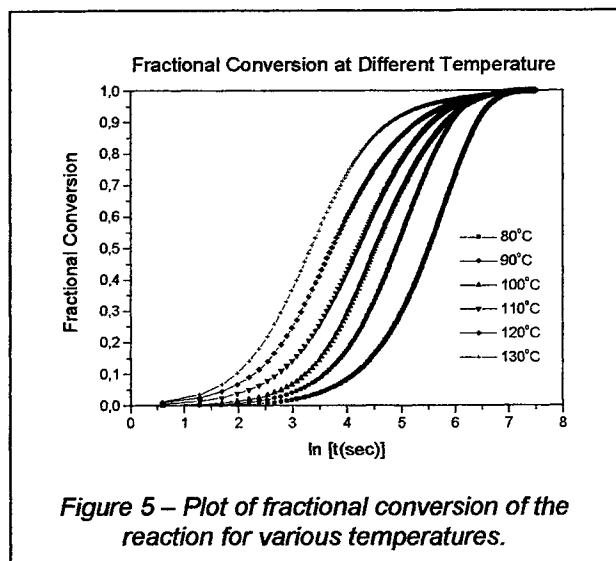
Variables	Parameters	Value	
		Prototype A	Prototype B
CO ₂ Laser ($\lambda=10.6\mu\text{m}$)	energy $E_p = P \cdot t_d$ [mJ]	9.52	8.66
	power P [W]	20	20
	laser beam size 2ω [mm]	0.76	0.76
Scan Head (Stereolithography system)	scan speed $v = \frac{\text{step size}}{\text{step period}} \times \frac{\text{field size}}{65535} \times 10^6$ [mm/s]	1595.4	1755.0
	dwell time $t_d = \frac{2\omega}{v}$ [μs]	476	433
	laser revolution time [x pass]	12	15
Composition (Thermosensitive resin)	DGEBA (diglicidil eter of bisfenol A) [parts]	10	10
	DETA (diethylenetriamine) [parts]	1.4	1.4
	Silica powder [parts]	0.70	0.54
	Type of silica	L 90 (hydrophilic)	TS – 720 (hydrofobic)
	absorption depth δ [μm]	61.1	70.9
Spatial resolution (final product)	cured volume $V = \pi \cdot \omega^2 \cdot \delta$ [mm ³]	110×10^{-3}	129×10^{-3}
	layer by layer width [μm]	300	140
	lateral layer width [mm]	0.90	1.20
	sample height [mm]	5.5	5.8
	sample length [mm]	16.0	13.5

4. Results and Discussions

A standard procedure^[10,11] to obtain E_A (activation energy) is by using:

$$\ln(t_{1\beta}) - \ln(t_{2\beta}) = \frac{E_A}{R} \left[\frac{1}{T_1} - \frac{1}{T_2} \right] \quad (9)$$

where $t_{1\beta}$ and $t_{2\beta}$ are the times required to reach a given fractional conversion at two different temperature T_1 and T_2 , and R is the molar gas constant ($R = 8.314 \text{ J/K.mol}$). We are performed several isothermal scans of the epoxy sample and the semi-log plots of β versus $\ln(t)$ are shown together in Fig. 5. The standard Arrhenius plot correspondent to the Fig 5 is shown in Fig 6, where each of the lines represents one specific fractional conversion β . The results show that the activation energy for the curing process is $E_A = (50.1 \pm 0.9) \text{ KJ/mol}$.



The stoichiometric tests performed with several samples compositions and laser parameters determined among others that silica plays an important part in controlling the local curing as it hinders heat diffusion to zones which are outside of the irradiated area. The amount of silica is understood to be important in the process of the local curing, since of the silica occurs excessively in the composition, its restricts the curing of the reagents and absorbs most of the laser energy, thus the curing is not complete, even if it occurs. On the other hand, if the silica occurs in small amount, heat may diffuse to undesirable areas. As important factor to be considered in this local curing process is the type of silica to be used. For example, considerable difference in the curing process has been showed when you choose treated fumed silica and non treated fumed silica^[12]. Treated fumed silica is high-purity silica which has been treated with a dimethyl silicone fluid. Both acts differently in the prototype process construction, probably because of the silicone fluid interference. The layer by layer prototype construction results in differents spatial resolution in final product as showed in the picture of the Fig 7.

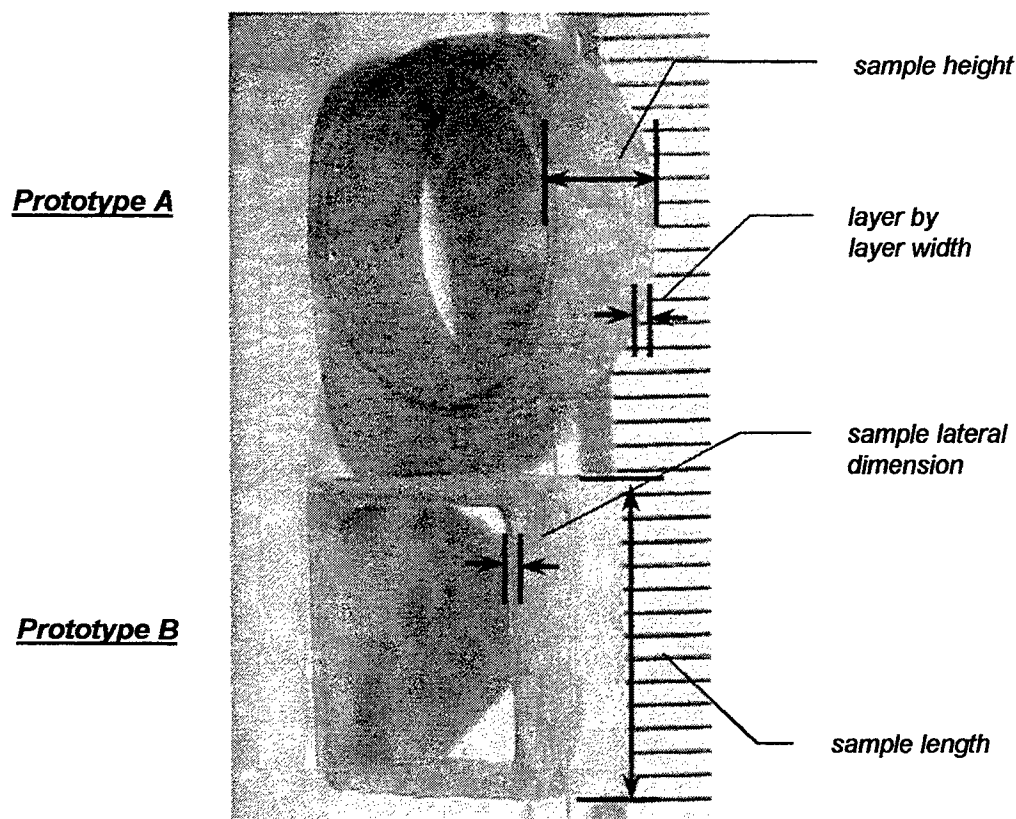


Figure 7 – Layer by layer construction: prototype A (with hidrofílic silica) and prototype B (hidrofóbica silica).

Others parameters such as energy delivered by laser, speed scan, dwell time, laser revolution time, resin pot life and cured layer, are important in curing process as well as in spatially selective cure. Also those mentioned parameters play an important role in the spatial resolution as well as in lateral resolution of the obtained prototype. As showed in table I, prototype A (circular) and prototype B (square) has been constructed along with same parameters but at different values. Prototype A shows much better spatial resolution than prototype B. In prototype A the lateral dimensions curing confinement is 18% larger than the diameter of the laser versus 58% larger than the diameter of the laser for the prototype B.

5. Conclusion

We showed a new use of infrared laser as a localized heat source in a polymer material system. We have found that localized cure occurs only for optimized processing, involving laser parameters and stoichiometric sample composition. Another series of experiments performed with d.s.c. made use of a fixed temperature as a function of time, where the flow of power to the sample was monitored. A small sample is quickly heated to a present temperature for the duration of the

reaction. A typical comparison is shown in the Fig 4, where the initial increase in the power flow represents the energy required to heat the sample to the desired temperature. The power flow to the non-reactive alumina sample quickly equilibrates, whereas the flow to the reactive epoxy sample shows the variations induced by heat released in its curing process. Using the standard means of extracting the activation energy E_A (Arrhenius plot) we obtained from d.s.c. data, $E_A = (50.1 \pm 0.9) \text{ KJ/mol}$ which is expected for this kind of curing process. Unfortunately this value could not be obtained by using the external temperature data processed in Fig 3. The localized cure occurs as we mentioned before only for optimized processing and that final product obtained with CO₂ laser curing is hard and stable, showing no significant shrinkage and requiring no post-cure treatment. Depth resolution is determined by the thickness of the uncured liquid layer. With applied smaller CO₂ laser beam sizes, the technique should be capable of producing structures with lateral resolution of tens of microns. According table I several experimental parameters has been taking in account to construct the prototypes. As mentioned the stoichiometric tests with several samples (we choose samples A and B) compositions has been carried where silica play an important hole.

Tests with fumed silica and non treated fumed silica showed considerable difference in obtained final product. During the manufacture, the surface of the silica non treated is completed coated with silicone fluid treating agent. The silicone fluid is reacted onto the silica via the surface hydroxyl groups, resulting surface chemistry TS-720 fumed silica (treated). The silicone fluid react with both the isolated and adjacent hydroxyl groups on the fumed silica surface. However, they are very effectively shielded from interactions due to the presence of the silicone polymer. This changes the nature of the silica surface from hydrophilic (L90) to extremely hydrophobic (TS-720). As far as we can go at moment seems that the silicone fluid difficult the sample components reaction and restrict the successive layer adhesion, since our sample has a relatively low thermal conductivity and it strongly absorbs the CO₂ laser irradiation. In the case of construction of multilayers prototypes using CO₂ laser in sample composed (in weight) by 10 parts epoxy, 1.4 parts diethylenetriamine and 0.7 parts silica powder. The fumed silica can be considered as better heat sink than treated silica.

Acknowledgment

The authors wish to thank the financial support of the FAPESP, and Mario A. Solari from Cabot Brazil and Cristina Latrucci Alziati from and Dow Chemistry S.A. Brazil, for helpful discussions and products provision.

References

- [1]. Kaplan, R., *Photonics Spectra*, 74, June, 1990.
- [2]. Belfore, D.A., *Laser Focus World*, 126, June, 1993.
- [3]. Fouassier, J.P., Rabek, J.F., *Lasers in Polymer Science and Technology: Applications*, v. III, 1990.
- [4]. Scarparo, M.A.F., Chen, Q.J., Miller, A.S., Zhang, J.H. and Allen S.D., *J. of Applied Polymer Science*, vol.62, 1996.
- [5]. Munhoz, A.L.J., Wagner, P.R.S., Ierardi, M.C.F., Kiel, A., Scarparo, M.A.F., *J. Braz. Soc. of Mech. Sci.*, vol. XX, 1998.
- [6]. Scarparo, M.A.F., Munhoz, A.L.J., Wagner, P.R.S., Ierardi, M.C.F., Allen, S.D., *SPIE*, vol. 3272, pp. 110-119, 1998.
- [7]. Carslaw, H.S. and Jaeger, J.C. *Conduction of Heat in Solids*, 2nd ed, Oxford University, NY, 1959.
- [8]. Sanders, D.J., *Applied Optics*, vol.23, no.1, pp.30-35, 1984.
- [9]. General Scanning Inc, PC-Mark MT – Programmer's Manual, pp. 86, 1996.
- [10]. Wisanrakkit G. and Gilham J.K., *Polymer Characterazation, Advances in Chemistry Series*, vol. 227, 1990.
- [11]. Willard P.E., *Polymer Eng. Sci.*, 1972.
- [12]. Cabot Brazil CAB-O-SIL Division.

Correspondence: Email: scarparo@ifi.unicamp.br, Fax: (055) 019 869 3304

Pulsed X-ray emission by laser plasma triggered electron beam

Yuzo Nagumo^a, Shigeki Hayashi^a, Takashi Yagi^b, Takeshi Matsumura^b, Susumu Yamazaki^b,
Kazumasa Honda^c and Isao Kojima^c

^aTechnology Research Laboratory, Shimadzu Corporation, Hadano 239-1304, Japan

^bDept. of Physics, Tokai University, Hiratsuka 239-1292, Japan

^cNational Institute of Materials and Chemical Research, Tsukuba 305-8565, Japan

ABSTRACT

Pulsed hard X-ray was radiated from the electrode at positive high electric potential, when a laser plasma was created on the grounded electrode positioned a few cm apart from the positively charged electrode. We considered the possibility that electrons extracted from the laser plasma were accelerated and collided with positively charged electrode, radiating the pulsed X-ray. The dependence of dosage and pulse width of the X-ray on laser pulse energy and on electrode spacing was investigated, and some evidence to describe the X-ray radiation mechanism was obtained.

Keywords: X-ray emission, pulsed laser, laser plasma

1. INTRODUCTION

The non-destructive inspection by X-ray radiography has become an indispensable technique in the field of electronics and machine industry. However, the laser plasma X-ray technology, which has recently made remarkable progress, is not suitable for the transmission image measurement, since the laser plasma created by a moderate size laser can only radiate the soft X-ray¹. Some researchers have reported on hard X-ray emission from the laser plasma created by an ultra-high intensity femtosecond laser^{2,3,4}. However, the femtosecond laser for this applications is usually very large and expensive to be utilized for the industrial application. It was reported that pulse hard X-ray was radiated from the positively charged electrode, while a laser plasma was created on it^{5,6,7,8}. This phenomenon could be due to the fast pulse electron beam triggered from the grounded electrode by the laser plasma. The electrons are accelerated in the electric field, colliding to the positive electrode to radiate the hard X-ray. However, the detail mechanism of X-ray emission is still unclear. We have found that the hard X-ray emission is occurred when a laser plasma is generated not only on the positive electrode but also on the grounded electrode. In the present work, the property of dosage and pulse width of the X-ray radiated from positive electrode, when the laser plasma is created on the grounded electrode; and their dependence on the laser pulse energy and on the electrode spacing, are presented and possible mechanism is proposed.

2. EXPERIMENTAL SETUP

The schematic of the experimental setup used for this study is shown in Figure 1. The positive electrode, made of a rod in 4 mm diameter with a rounded tip face, and a disk with diameter of 5 cm as a grounded electrode are placed in the vacuum chamber. The positive and negative electrodes are made from copper. High voltage power supply (20 kV) charges ceramic capacitors (6 nF) through the resistance of 20 M Ω . The FHG (266 nm) and SHG (532 nm) of the Q-switched YAG laser beam is irradiated to the grounded electrodes in the vacuum chamber through the fused silica window. The laser beam is focused with a lens of 800 mm in focal length. The 532 nm radiation is produced from Spectra Physics GCR-230-10, and the 266 nm radiation is produced from Lotis LS-2131. Emitted X-ray is observed through the 30 μ m beryllium window with a scintillation probe. Two kinds of scintillation materials are used. One is thallium doped NaI crystal, which possesses a few microsecond decay time. The fluorescence is measured with a photomultiplier. Another is lead-doped plastics with a decay time of 2 nanosecond, which provides fast enough response together with a fast photomultiplier (Hamamatsu H3177). The dosage and the pulse waveforms of X-ray are measured with a NaI scintillator and plastic scintillator, respectively. Electric current flowing through the grounded electrode is measured with a current transformer (Pearson Electronics Model 410).

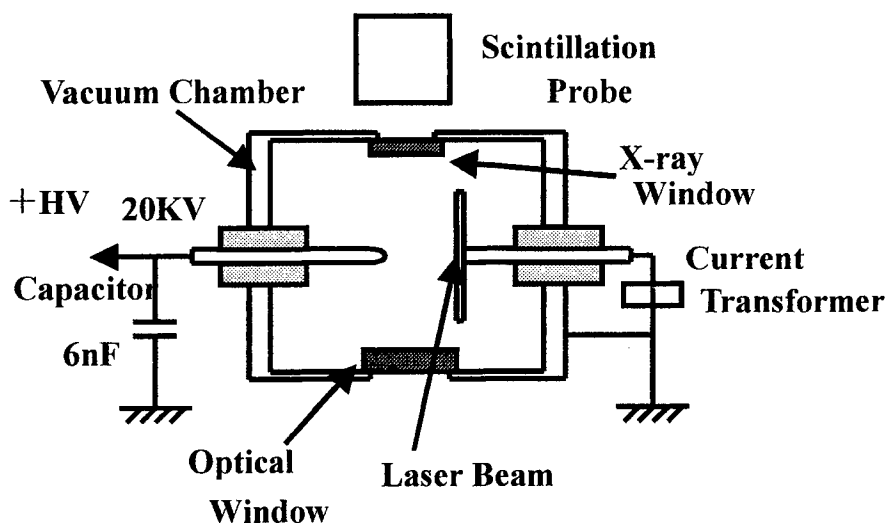


Fig. 1 Schematic of experimental setup

3. RESULTS AND DISCUSSION

First, we examined the effect of the plasma created at grounded electrode on the X-ray emission from the positive electrode. A 266 nm laser beam with a pulse energy of 20 mJ, and pulse duration of 10 ns was irradiated to the grounded electrode while applying positive static potential of 20 kV to the positive electrode. The electrode spacing

was 10 mm. A dosage of the X-ray was recorded with the NaI scintillator at each laser shot. There was no X-ray emission when a laser pulse was not applied. Hence, the electric field intensity was below the level of inducing a field emission. Figure 2 shows the X-ray dosage with respect to the laser pulse energy with 266 nm laser beam being focused or without being focused to the grounded electrode. When the laser beam is not focused, the X-ray dosage shows almost linear increase with respect to the laser energy. Since the photon energy is above the work function of copper, photoelectron current, which should be in proportional to the laser pulse energy, produces the X-ray and explains the increasing X-ray dosage with respect to the pulse laser energy. While, the X-ray dosage, as the laser beam is focused, shows a similar gradual increase with the laser pulse energy until sudden increase takes place at the pulse energy of 13 mJ. The two orders of magnitude increase in X-ray dosage is essentially different feature from the photoelectric current. The existence of the threshold suggests an effect of a plasma created on the grounded electrode by the laser beam.

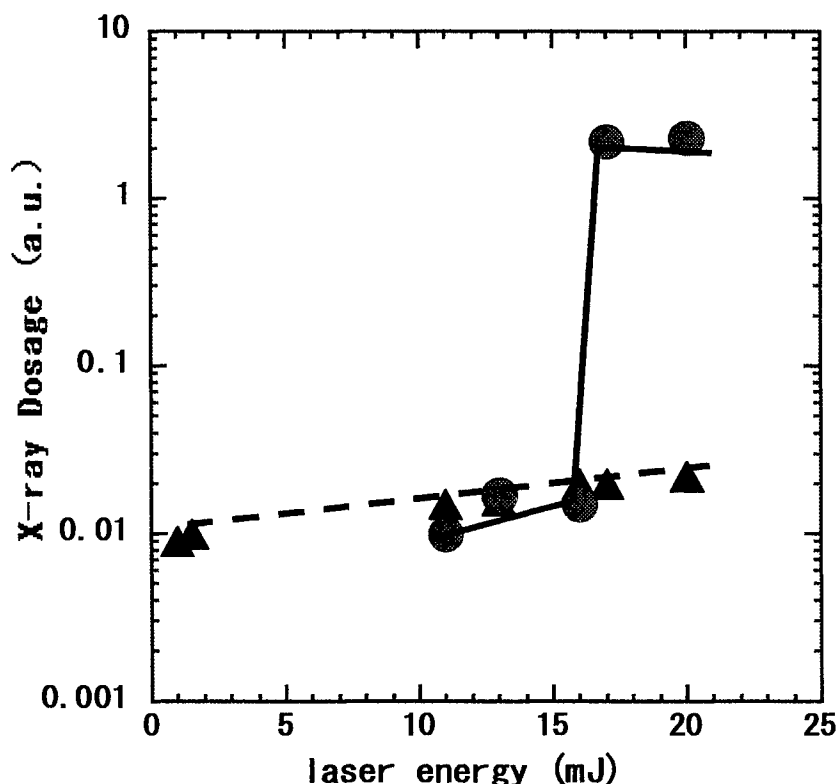


Fig. 2 X-ray dosage as a function of laser pulse energy

Laser: 266 nm Q-switched Nd:YAG laser.

Laser beam is focused with a lens, generating laser plasma (circle). Laser beam is irradiated directly (triangle).

Next, the effect of the plasma formed on the grounded electrode on the formation of the electron beam was examined by focusing a laser beam with pulse energy of 60 mJ at 532 nm to the grounded electrode. The electrode spacing was 10 mm as the previous experiment. Figure 3 shows the pulse form of the X-ray formed on the positive electrode and the electric current flowing through the grounded electrode when a laser shot is applied to it. The result shows the X-ray emission starts 30 nanosecond after the laser pulse irradiation. This delay is due to the transit time of the photomultiplier. The X-ray emission peaks in 100 nanosecond and falls to nearly zero. The duration of X-ray is about 200 nanosecond. The current flowing through the grounded electrode shows a gradual increase until the X-ray intensity reaches a maximum. Then the current shows rapid increase and reaches its maximum value followed by a periodical oscillation due to the LCR resonance in the electrode circuit. Early part of the current before the peak value is considered to be responsible to the X-ray production. The maximum value of the current is always observed at the time when the X-ray intensity falls to zero. The rapid falling of the X-ray intensity coincidentally observed with the current peak is considered to be due to the reduced electric field intensity by the impedance reduction between the electrodes associated with the plasma diffusion. Similar phenomenon of the falling off the X-ray emission followed by the peaking of the cathode current is common to the conventional pulse X-ray tube⁵.

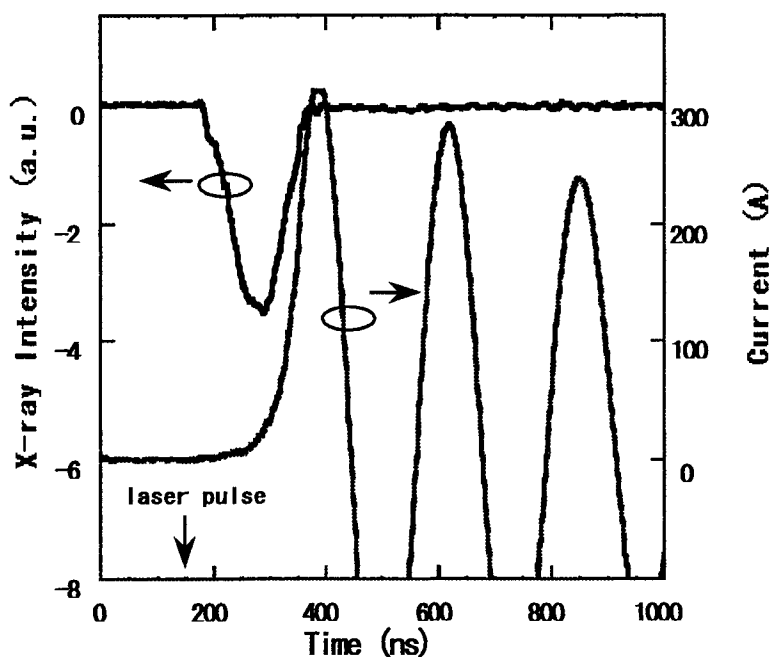


Fig. 3 Waveforms of X-ray intensity (upper trace, inverted output) and of current transformer output (lower trace).

Laser: a Q-switched 532 nm Nd:YAG.

Laser pulse is irradiated at 150 ns.

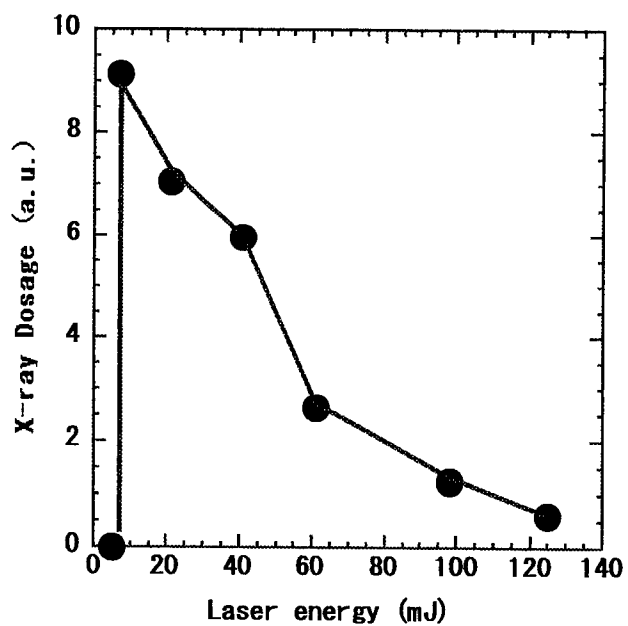


Fig. 4 X-ray dosage as a function of laser pulse energy.

Laser: a 532 nm Q-switched Nd:YAG. Electrode spacing: 10 mm.

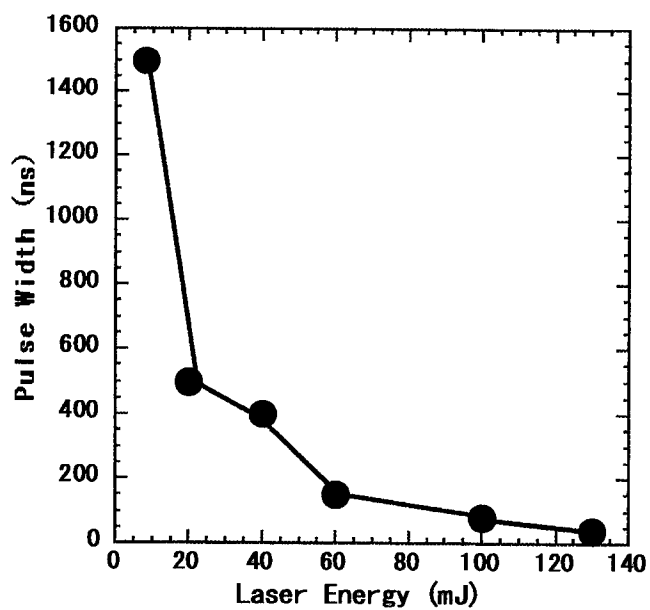


Fig. 5 X-ray pulse width as a function of laser pulse energy.

laser: a 532 nm Q-switched Nd:YAG. Electrode spacing: 10 mm.

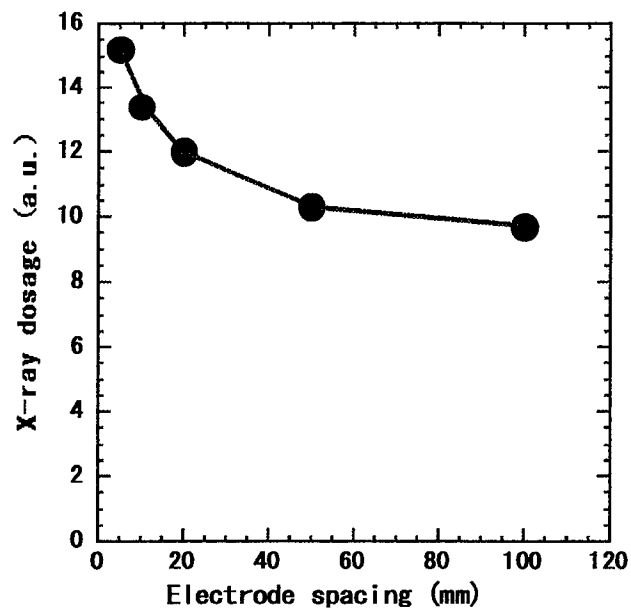


Fig. 6 X-ray Dosage as a function of electrode spacing., when laser beam (20 mJat 532 nm) is focused.to the grounded electrode.

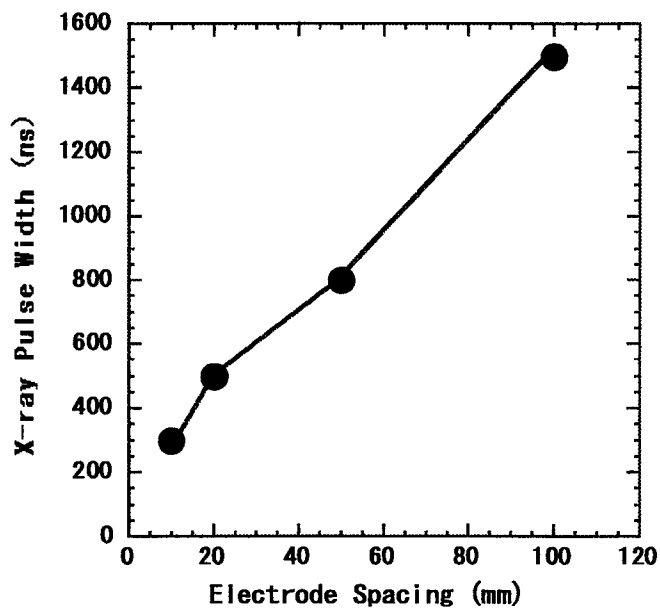


Fig. 7 X-ray pulse width as a function of electrode spacing, when laser beam (20 mJ at 532 nm) is focused to the grounded electrode.

The dependence of the emitted X-ray dose on the laser pulse energy at 532 nm with 10 mm electrode spacing is shown in Figure 4. As the result shows there is a clear threshold at about 10 mJ in the laser pulse energy to produce X-ray dose. The X-ray dosage reduces as the laser pulse energy increases from the threshold value. The X-ray pulse width dependence on the laser pulse energy is presented in Figure 5. The X-ray pulse width decrease suddenly as the laser pulse energy increases. Compared with the X-ray dosage, the pulse width shows quite similar dependence on the laser pulse energy. From these results, the reducing X-ray dose with increasing laser pulse energy is primarily due to the reduction of the X-ray pulse width. The reducing X-ray pulse width is considered to be due to the larger electron density created by the larger laser pulse energy, resulting in earlier commencement of the impedance reduction between the electrode.

The dependence of the emitted X-ray dose on electrode spacing, when the laser pulse energy is 60 mJ at the wavelength of 532 nm, is shown in Figure 6, and electrode spacing dependence of the X-ray pulse width is shown in Figure 7. The X-ray dosage reduces as the electrode spacing is increased, and the X-ray pulse width increases with the increase of electrode spacing. The time of flight of the plasma diffusion increases as the electrode spacing is increased, and hence, the duration of the electron current should proportionally increase with the electrode spacing. The pulse width of the X-ray emission then increases. The electric field intensity in the diffusing plasma; plasma plume, is reduced compared with the electric field outside the plume, and the electrons flowing through the plasma plume reach to the positive electrode with reduced velocity. And the effect of the plasma plume on the electron energy will be prominent, as the electrode spacing is larger than the Debye length, which is a few cm in the present case. Hence, the X-ray dosage shows the sharp reduction followed by the gradual decrease approaching to some constant value as the electrode spacing is increased. The detailed mechanism of the electron extraction and acceleration needs further study.

4. CONCLUSION

Pulsed X-ray emission from positive electrode was observed, when laser pulse was focused to the grounded electrode to generate laser plasma. The dependence of the X-ray dosage on laser pulse energy shows the existence of emission threshold. This suggests that electrons are extracted from a laser plasma formed at the grounded electrode, and accelerated in high electric field to collide with the positive electrode and radiate the X-ray. The X-ray pulse width reduces as the laser pulse energy increases, as the electrode spacing is reduced. The X-ray dosage diminishes with increasing laser pulse energy and with increasing electrode spacing.

The X-ray can be easily synchronized with a laser pulse or with a trigger signal that starts laser pulse, so that the timing jitter of the X-ray emission is fairly low. When the electric field is supplied with a low-jitter Marx generator¹⁰, the X-ray source will emit harder component of X-ray with orders of magnitude larger dosage, and would be very useful for ultra-fast radiography such as transmission image measurement of fast rotating wheel: e.g. engine, motor.

ACKNOWLEDGMENTS

This work was conducted in the program "Advanced Photon Processing and Measurement Technologies", consigned to the R&D Institute for Photonics Engineering from New Energy and Industrial Technology Development Organization (NEDO) of Japan.

REFERENCES

1. M. Fraenkel, A. Zigler, Y. Horowitz, A. Ludmirsky, S. Maman, E. Moshe, Z. Henis, and S. Eliezer, "Optimal X-ray source development in the spectral range 4-14 Å using a Nd:YAG high power laser" J. Appl. Phys. Vol. 80, pp5596-5603, (1996)
2. J. D. Kmetec, "Ultrafast Laser Generation of Hard X-rays" IEEE J. Quantum Electron. , vol. 28, pp2382-2387, (1992)
3. C. L. Gordon III, G. Y. Yin, B. E. Lemoff, Perry M. Bell, and C. P. J. Barty, "Time-gated imaging with an ultrashort-pulse, laser-produced-plasma x-ray source" Opt. Lett., vol. 20, pp1056-1058, (1995)
4. C. Tillman, I. Mercer, S. Svanberg and K. Herrlin, "Elemental biological imaging by differential absorption with a laser-produced x-ray source" J. Opt. Soc. Am. B, vol. 13, pp209-215, (1996)
5. Gy. Farkas and Z. Gy. Horvath, "Picosecond laser plasma creation in the presence of high electrostatic field on the surface of metals" Optics Comm. vol. 21, pp408-410, (1977)
6. S. G. Dinev, Ch. I. Radev, K. V. Stannov and K. A. Stankov, "X-ray emission from a laser irradiated target in the presence of high electric field", Optics Comm. vol. 30, pp219-223, (1979)
7. E. Hontzopoulos, D. Charalambidis, C. Fotakis, Gy. Farkas, Z. Gy. Horvath and Cs. Toth, "Enhancement of ultraviolet laser plasma emission produced in a strong static electric field", Optics Comm. vol. 67, pp124-128, (1987)
8. T. Yagi and H. Kusama, "Enhanced vacuum ultraviolet and X-ray radiation from electrically controlled KrF laser plasma", Advanced Materials '93, Trans. Mat. Res. Soc. Jpn. vol. 17, pp241-244, (1994)
9. A. Jamet and G. Thomer, "Flash Radiography", Elsevier, Amsterdam, pp35 (1975)
10. T. Yagi and H. Kusama, "Laser plasma X-ray for non-destructive inspection", Proceedings of the 6th International Symposium on Advanced Nuclear Energy, pp817-821, (1992)

Light scattering by rough dielectric surface

Vitali E.Gruzdev*, Anastasia S.Gruzdeva*

State Research Center "S.I.Vavilov State Optical Institute"
Birzhevaya Liniya 12, St.Petersburg, 199034, Russia

ABSTRACT

Numerical modelling is applied to investigation of scattering of plane linearly polarized monochromatic wave by sine variations of dielectric surface relief. The modelling is based on finite-difference time-domain technique. Results of modelling include 1) space distribution of scattered light, 2) dependence of field amplification on ratio of roughness amplitude to laser wavelength, and 3) dependence of field amplification on ratio of roughness period to laser wavelength. Obtained results show that for TE polarization a) transmitted signal is more sensitive to roughness parameters than reflected one, b) there is narrow resonance in dependence of amplitude of scattered field on laser wavelength and roughness period, c) dependence of amplitude of scattered field on roughness amplitude is described by parabolic function for small values of relief amplitude. Depending on relief amplitude and period, scattering by sine roughness can result in formation of inhomogeneous space field distribution consisting of periodic field maxima inside dielectric or formation of homogeneous distribution such that both transmitted and reflected signals are close to plane wave. We consider the following applications of obtained results: 1) possibility to develop a new technique for in-situ surface roughness characterisation, 2) possible mechanisms of feedbacks during laser-induced formation of surface ripples, and 3) anti-reflection effect.

Keywords: surface roughness, light scattering, computational modelling, antireflection effect, surface characterisation, laser-induced surface ripples

1. INTRODUCTION

Development of modern laser technologies for surface treatment is tightly connected with problem of light scattering by surface roughness. It plays important role in developing of techniques for optical characterisation of the roughness, determining of optimal laser-beam parameters for surface treatment, and in other areas of surface science and technology.

Light scattering by rough surface is one of old "classical" problems which has not got complete solution so far in spite of being under investigation since the beginning of 1900s [1] and its great applied and fundamental meaning. Mainly that is connected with complexity of the problem due to what only several particular cases have been considered in details. Practically in all cases analytical studies are based on asymptotical expansions (Rayleigh-Rice perturbation method [1, 2]), Ewald-Oseen extinction theorem [3, 4] or Kirchhoff's integral approximation [5]. General drawbacks of those methods are the following assumptions about roughness geometry restricting their validity range [6]:

- 1) the mean height deviations h from ideally smooth surface are much smaller than wavelength λ , i.e., $h/\lambda \ll 1/2\pi$,
- 2) roughness slopes are much smaller than 1;
- 3) maximum linear size of irradiating beam is much larger than correlation length of the roughness structure.

Thus, all mentioned above analytical methods can be applied to investigation of scattering by slightly rough surface only. Interesting point is also that general rigorous approaches to surface scattering problem based on integral equations [7 and references herein] are usually applied to metal surfaces while the cases of dielectric and semiconductor surfaces stay slightly treated. On the other hand, general feature of many works on light scattering is that integral characteristics of scattered light are usually obtained as final results while surface roughness is treated as random and characterized by distribution function, correlation length and other statistical parameters [2 - 9]. Thus, only amplitude (or intensity) distribution of scattered light can be obtained while phase characteristics are usually lost due to deriving mean values [10]. That excludes exact calculation of field distribution near the surface what can be important in many problems. For example, the latter problems include study of high-power laser-surface interaction resulting in appearing of laser-induced surface ripples. Initial stages of that process are well known to be managed by surface roughness which parameters can be critical

* Tel. 7-81272-246-22, fax 7-81272-246-22, e-mail: gru@mailbox.alkor.ru

for dynamics of all later laser-induced processes.

Thus, there is a variety of problems connected with light scattering at rough surface, which has not been studied well. The problems are mainly concerned with *rigorous calculation of electromagnetic-field distribution near dielectric surface appearing due to light scattering by arbitrary (not only slightly) rough surface*. Obviously, the only suitable approach to this problem is numerical calculation that can be based on Maxwell's equations (for example, finite-difference time-domain technique [11, 12]), on wave equation [13, 14] or on integral equations [7]. We gave preference to finite-difference time-domain technique (FDTD) based on wave equation because it allows both calculation of scattering and straight study of dynamics of field variations near the surface. The latter can be especially important for study of dynamical problems such as growth of laser-induced ripples when field distribution and surface relief vary in self-consistent manner.

2. MODELLING TECHNIQUE

This section is devoted to modelling technique utilized for simulation of light scattering by rough surface. There are considered geometry of the problem, basic equations and difference relations, influence of resolution on calculation error, stability of calculations, "transparent" boundary conditions at boundaries of calculation space and other involved points.

1. Geometry of the problem under consideration is depicted in Fig. 1. 2D geometry with sine roughness is considered, and partial derivatives with respect to z-coordinate are zero. Spatial period of surface relief was varied from a quarter to one and a half of radiation wavelength in vacuum. Amplitude of roughness was varied from zero to one radiation wavelength. Incident light is represented by linearly polarized plane monochromatic wave of two orthogonal linear polarizations (TE or TM). Angle of incidence is zero for the most presented below results while it can be varied slightly near zero if required. All considered materials are homogeneous and isotropic dielectrics characterised by constant refractive index and (in several particular cases) absorption. Symmetry and periodicity of the surface relief and radiation allow calculations to be carried out for one period of surface relief what reduces simulation time and requirements for computational resources (e.g., memory).

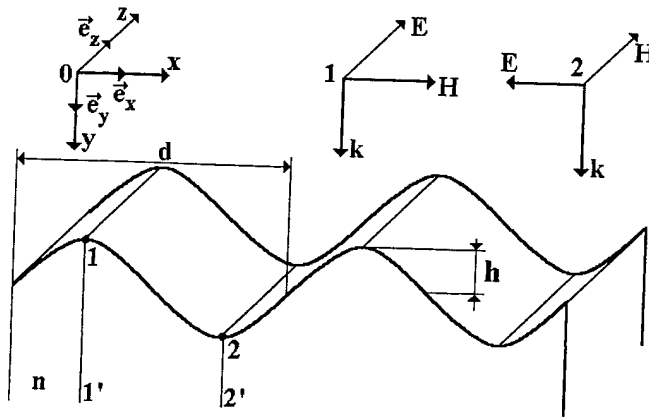


Fig. 1. Geometry of the problem for modelling of light scattering by dielectric or semiconductor surface with refractive index n with sine variations of surface relief (sine roughness) of period d and amplitude h . Two linear polarizations (1 - TE; 2 - TM) of incident monochromatic plane wave are considered. The surface ripples are assumed to be infinitely long in z-direction (so called 1D surface). It is considered normal incidence of light.

2. To study field distribution and its dynamics near rough dielectric surface we modified FDTD technique [11 - 14]: in contrary to classical FDTD approach based on Maxwell's equations [11, 12], we take wave equation as basic one for calculations [13, 14]. It has the following form for linear propagation in dielectric without absorption:

$$\frac{\partial^2 \vec{E}}{\partial t^2} - \frac{c_0^2}{\epsilon_0} \cdot \Delta \vec{E} = 0. \quad (1)$$

Light propagation in absorbing materials is described by the following wave equation:

$$\frac{\partial^2 \vec{E}}{\partial t^2} + \omega_0 \sqrt{1 - \left(\frac{0.5 \cdot \epsilon_0 + (\alpha(T_0)/k_0)^2}{0.5 \cdot \epsilon_0} \right)^2} \frac{\partial \vec{E}}{\partial t} - \frac{c_0^2}{\epsilon_0} \cdot \Delta \vec{E} = 0, \quad (2)$$

where c_0 - is light speed in vacuum, $\epsilon_0 = n_0^2$ - is dielectric constant, n_0 - linear part of refractive index, $k_0 = 2\pi/\lambda_0$ - is wave number in vacuum, α - absorption, $\Delta = \partial^2/\partial x^2 + \partial^2/\partial y^2$ - differentiating operator.

Basic idea of simulation method used by the authors is similar to FDTD technique [11, 12]: calculations are performed for updating difference relation describing dependence of field magnitude at fixed time-space point on field magnitudes at previous moments at neighbouring points. That difference dependence is derived from wave equations (1) or (2) by reducing them to a finite-difference equation in traditional way [15]. For example, in the simplest case of central differences the following updating finite-difference equation is obtained for linear equation (1):

$$(E'_{x,y})_L = 2E'_{x,y} - E'_{x,y} + \frac{(c_0 \cdot \Delta t)^2}{(n_0 \cdot \Delta x)^2} (E'_{x+\Delta x,y} - 2E'_{x,y} + E'_{x-\Delta x,y} + E'_{x,y+\Delta y} - 2E'_{x,y} + E'_{x,y-\Delta y}) \quad (3)$$

where $\Delta x = \Delta y$ is period of regular spatial mesh, and Δt is corresponding time increment. Scattering of TE-polarized light is described by one relation (3) (for z-projection of electric field only) while scattering of TM-polarized light is described by two relations similar to (3) for x- and y-projections of electric field. Required simulation time and computer memory are 2 times more for TM polarization than for TE polarization because of that reason. Relation (3) involves field magnitudes at four neighbouring points and at two previous time moments (points A', A'', B, C, D, E in Fig. 2) for both polarizations. Such geometry is characteristic of FDTD technique based on Maxwell's equations while using of wave equation allows to increase stability of calculation code through involving of 8 neighbouring space points (Fig. 2). Using of wave equation allows also decreasing value of computer memory required for simulation.

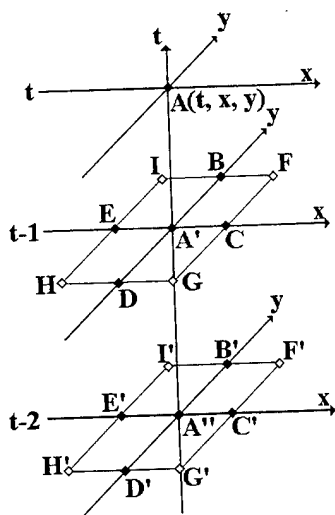


Fig. 2. Geometry of points involved into calculations. According to traditional FDTD technique 6 points (A, A', B, C, D, E) are involved. The simplest version of modified FDTD technique involves 7 time-space points (A, A', A'', B, C, D, E) corresponding to involving of only 4 neighbouring space points in relation (3). Code with improved stability can involve 11 points (A, A', A'', B, C, D, E, F, G, H, I), 15 points (A, A', A'', B, C, D, E, F, G, H, I, B', C', D', E') or 19 points (A, A', A'', B, C, D, E, F, G, H, I, B', C', D', E', F', G', H', I') and corresponds to involving of 8 neighbouring space points. The more points are involved, the better stability and accuracy are achieved. On the other hand, the more points involved at each step of calculation, the slower field distribution is calculated. To our experience, involving of 11 points gives good stability, nice accuracy and appropriate speed of calculations.

Solid points correspond to the following time-space points: $A=(t, x, y)$, $A'=(t-\Delta t, x, y)$, $A''=(t-2\Delta t, x, y)$, $B=(t-\Delta t, x, y+\Delta y)$, $C=(t-\Delta t, x+\Delta x, y)$, $D=(t-\Delta t, x, y-\Delta y)$, $E=(t-\Delta t, x-\Delta x, y)$, $B'=(t-2\Delta t, x, y+\Delta y)$, $C'=(t-2\Delta t, x+\Delta x, y)$, $D'=(t-2\Delta t, x, y-\Delta y)$, $E'=(t-2\Delta t, x-\Delta x, y)$. Hollow points correspond to the following time-space points: $F=(t-\Delta t, x+\Delta x, y+\Delta y)$, $G=(t-\Delta t, x+\Delta x, y-\Delta y)$, $H=(t-\Delta t, x-\Delta x, y-\Delta y)$, $I=(t-\Delta t, x-\Delta x, y+\Delta y)$, $F'=(t-2\Delta t, x+\Delta x, y+\Delta y)$, $G'=(t-2\Delta t, x+\Delta x, y-\Delta y)$, $H'=(t-2\Delta t, x-\Delta x, y-\Delta y)$, $I'=(t-2\Delta t, x-\Delta x, y+\Delta y)$.

The obtained updating dependence describes linear field evolution in medium with given parameters if field source is given. In case of plane wave, the source is described as $E_S(t, x, y=0) = E_0 \sin(\omega t)$. Field evolution is observed in the form of animation that can be stopped at any appropriate time. One can observe field distribution along a line crossing calculation area in arbitrary direction and have look at 3D plot of instantaneous space field distribution (both total and only scattered without incident plane wave) at the time step.

Wave equation (1) or (2) allows calculating electric field strength without calculating space distribution of magnetic field. If desired, the latter can be obtained from one of Maxwell's equations

$$\frac{\partial \vec{H}}{\partial t} = -\frac{c_0}{\mu_0} \cdot \vec{\nabla} \times \vec{E}. \quad (4)$$

Calculated values are instant space distribution of electric-field strength $E(x, y, t)$, its squared value E^2 determining space concentration of electric-field energy, amplification of electric field $A = \max E(x, y, t)/E_0$ in selected area of calculation mesh (E_0 is amplitude of incident-wave electric field), varied values are time, space coordinates, and parameters: amplitude h and period d of surface roughness, refractive index and absorption. Relation (4) allows calculating both vector of magnetic field and vector of electromagnetic energy flux what can be important, for example, for control of energy balance.

3. Artificial reflection of scattered waves at boundaries of calculation area is one of the most serious problems of FDTD

modelling of electrodynamical processes. Influence of wrong conditions at calculation-mesh boundary can result in large distortion of modelling results due to reflection of tangential waves [12-14, 17]. One of possible approaches to the problem is to separate scattered and incident waves at all the four boundaries of rectangular calculation mesh and to make scattered field satisfying asymptotical conditions well known from scattering theory [16]:

$$\frac{\partial E_i}{\partial r} + \sigma \cdot \frac{n_0}{c_0} \cdot \frac{\partial E_i}{\partial t} = 0. \quad (5)$$

Matching parameter σ is introduced to make condition (5) true both for near field and for far field at distances $r \gg \lambda_0$. Condition (5) assumes that all scattering objects are inside calculation area. The only exception is the case of periodic structures (e.g., periodic surface relief) when one can apply periodic boundary conditions at two opposite sides together with condition (5) at two other opposite sides of calculation mesh. Appearing of the mentioned above distortions due to artificial reflection at mesh boundary are usually detected through tests including propagation of plane waves and scattering by dielectric sphere or cylinder [12, 17]. The tests are not effective if there is no possibility to look at 3D graph of instant space field distribution. For this reason we have tested our code using graphs of 3D space field distribution.

4. Stability of calculations is one more important problem. In the most cases the stability is improved by making space Δx and time Δt steps to satisfy the following condition

$$c \cdot \Delta t < n_{min} \cdot \Delta x. \quad (6)$$

Together with using (6) we introduced stability parameter γ into (3) to make calculations more stable and precise. This well known method [18] allows to exclude exponentially growing error in the solution for arbitrary ratio of $c \cdot \Delta t$ to Δx . Appearing of growing errors can also be controlled through energy conservation law for electromagnetic field. For that reason we calculated vector of electromagnetic energy flux and density of both electric and magnetic field energy at each point of calculation mesh. After integrating over all calculation area we obtained required relation for energy balance which was under control at each time step. Obtained numerical solution to wave equation can be numerically differentiated twice with respect to space coordinates. The derivatives are smooth even if they have discontinuities what allows to obtain smooth distribution of electric field of TM mode near boundaries between different dielectrics where it has discontinuity.

5. Influence of poor spatial resolution on calculations is very important too. Poor space discreteness can result in large calculation error coming through slow modulation of field amplitude which can be detected only in 3D graph of space distribution of electric field (see for example Fig. 4). It can be illustrated by results of simulation of plane-wave scattering by dielectric cylinder (Fig. 3) - two times decreasing of space resolution results in calculation error growing with increasing of size parameter x and sufficient perturbation of amplification spectrum. This effect can give large errors in modelling of light scattering by resonant particles like a sphere or cylinder. Resolution of 200-400 space mesh cells per laser wavelength was used to catch resonances in light scattering by sine roughness and to make the obtained results more precise. According to tests calculation error is about 0.05% both in bulk and at boundary of calculation mesh.

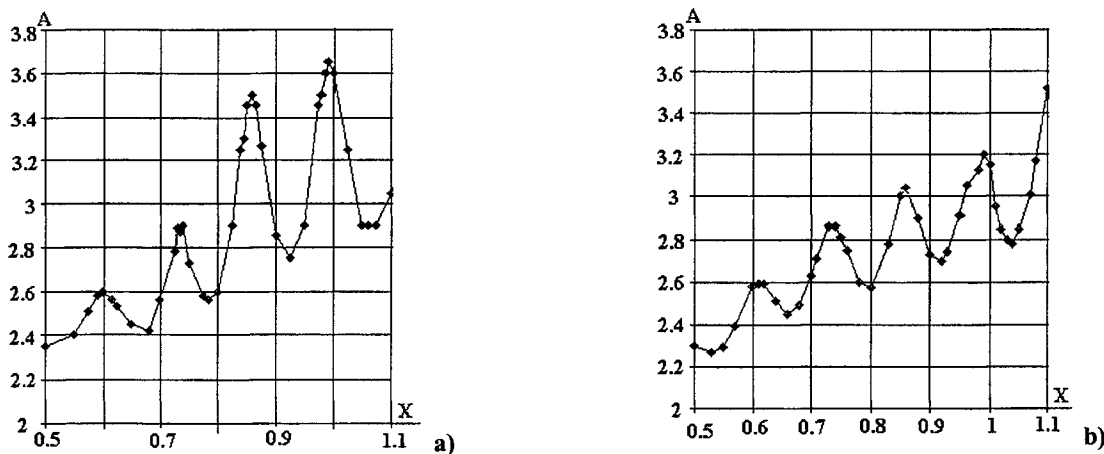


Fig. 3. Dependence of maximum field amplification $A = \max |E_{in} / E_0|$ inside dielectric cylinder with refractive index $n=1.50$ on size parameter $x=2\pi a/\lambda_0$. for resolution a) 200 cells per wavelength; b) 100 cells per wavelength.

6. Several benchmark problems were used to evaluate the validity of solutions produced by developed code. First, propagation of cylindrical waves excited by point source in vacuum in the centre of the mesh was simulated (Fig. 4a). No artificial reflection at mesh boundary was observed after more than 150 waves had left the mesh through the boundary. Obtained field distribution was compared with exact 2D solution to equation (1) for point source that is given by Bessel's functions of the 1-st order of the second type. Calculated field profile coincides with the exact solution within 0.05% error.

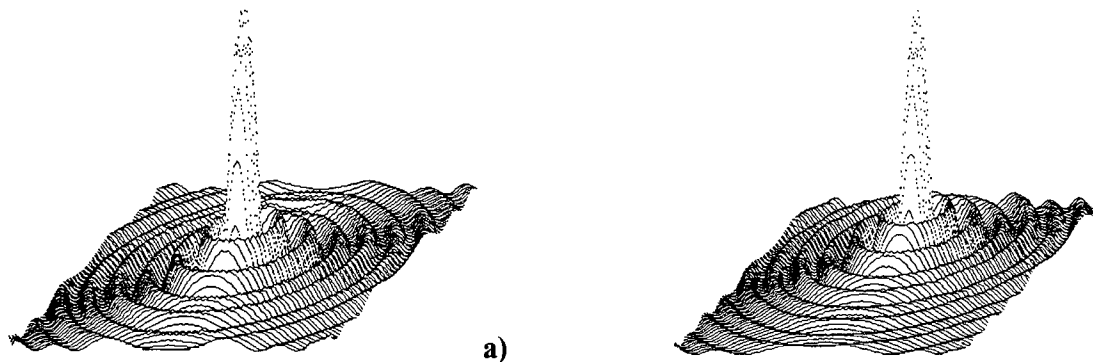


Fig. 4. Instantaneous distribution of electric field within a plane perpendicular to axis of point source in vacuum. The source is placed in the center of spatial mesh (a) and 1 wavelength away from the center (b). Space resolution 20 cells per wavelength

The point field source was moved from mesh centre to test functioning of the developed code for non-symmetrical outgoing waves (Fig. 4b). No reflection at mesh boundaries was observed in that case too. This shows that scattered waves of any complicated structure can pass through mesh boundary without artificial reflection because any outgoing 2D wave can be expanded into series with respect to cylindrical waves, and the latter leave calculation mesh without reflection. One more interesting feature is obvious from Fig. 4: one can see low-frequency modulation of cylindrical wave front together with high-frequency noise. The first effect appears due to poor discretization that was 20 cells per wavelength in the case depicted in Fig. 4. The second effect appears due to low-resolution imaging of calculation results on computer display.

The functioning of developed program was also tested for outgoing waves of complicated form, which were obtained from interference of two synchronous point sources placed at various distances. Obtained field patterns agreed perfectly with those calculated from exact analytical solution to linear wave equation.

3. RESULTS OF MODELLING

Results of computational modelling of plane-wave scattering by sine roughness of dielectric surface include: dependence of field amplification $A = \max E(x, y, z)/E_0$ on roughness period d (spectral dependence, Fig. 5) and roughness amplitude h (amplitude dependence Fig. 6), and space distribution of scattered light (Fig. 7, 8). Most of presented results were obtained for TE polarization. Several reasons for that are discussed in this section.

One of the most interesting features of light scattering by dielectric surface is narrow resonance in spectral dependence for TE incident polarization (Fig. 5) which is accompanied by smaller and wider peak. Calculations for several materials show that position of the resonant peak corresponds exactly to roughness period $d = \lambda/n$. For example, in case of glass sample $d/\lambda = 0.67$ for glass with $n = 1.50$ (Fig. 5). Thus, position of the peak depends on refractive index and laser wavelength while its height depends also on roughness amplitude (Fig. 6). Other interesting feature is plateau in spectral dependence at small values of roughness periods (Fig. 5). It corresponds to constant amplification of electric field which value depends on roughness amplitude and refractive index. Characteristic feature of the plateau is that amplitude of reflected wave (corresponds to $A_R = 1.096$ in Fig. 5) is smaller than that for case of ideally smooth surface (the latter is shown in Fig. 5 by thin solid line corresponding to $A_R' = 1.20$). At the same time, amplitude of transmitted wave (corresponds to $A_T = 0.9955$) is larger than that for the case of smooth surface (corresponding to $A_T' = 0.80$). That feature is discussed in section 4.1 in connection with anti-reflection effect.

One of general conclusions from investigated spectral dependence for different materials is that transmitted signal (corresponds to amplification is glass in Fig. 5) is more sensitive to roughness parameters than reflected wave (corresponding to amplification in vacuum) especially at resonance. Amplitude of reflected signal becomes sufficiently

larger than transmitted one only for roughness period larger than 0.85 – 0.90 of laser wavelength (Fig. 5). Important feature is also structure of space field distribution at various values of roughness period what is discussed below in this section. Other important feature is absence of sharp resonance in spectral dependence for TM incident polarization. In general, spectral dependence of field amplification for TM polarization is smoother and weaker than that for TE polarization for roughness period smaller than 0.75 of laser wavelength. $d=0.75\lambda$ is the point at what calculation of spectral dependence for TM polarization case was stopped because of sufficient increase of simulation time.

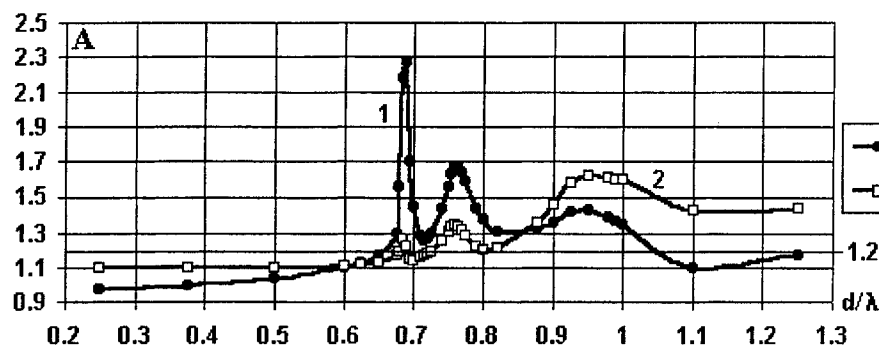


Fig. 5. Dependence of amplification A on ratio of roughness period to laser wavelength d/λ for TE polarization of incident plane wave (electric field vector is parallel to surface ripples) scattered by glass sample (dielectric constant $\epsilon_0=2.25$) with roughness of amplitude $h = 0.1\lambda$. 1 – Amplification of electric field in glass (transmitted radiation), 2 – amplification of electric field in vacuum (reflected radiation).

Example of dependence of field amplification on roughness amplitude for incident TE polarization is depicted in Fig. 6 for glass sample. Maximum amplification as well as shape of the dependence is determined by refractive index and roughness period. Clear maximum of field amplification is always observed in material with higher refractive index while amplitude of reflected wave shows smoother and weaker dependence on roughness amplitude. Important point is that amplification of transmitted field is higher for rather small roughness amplitude (not more than 0.4 of laser wavelength for considered glass) what confirms observed in Fig. 5 stronger sensitivity of transmitted field to roughness parameters. Amplitude of transmitted wave reaches absolute maximum only in case of resonant period (field amplification is $A=2.723$ for $h/\lambda=0.175$). After reaching the maximum, it decays fast tending to the limit close to 1. Amplitude of reflected wave approaches the same limit at resonant roughness period (Fig. 6). General trend in considered dependence is that amplitudes of both reflected and transmitted waves tend to certain constant limits which are different for reflected and transmitted waves except the resonance case.

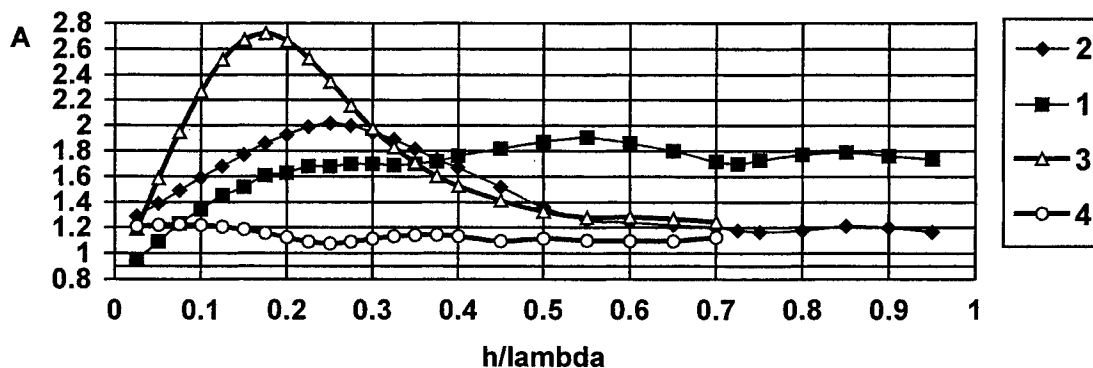


Fig. 6. Dependence of field amplification A for TE polarization on roughness amplitude h/λ for sine surface roughness of glass sample with off-resonance period $d=\lambda$ (curves 1 and 2) and resonant period $d=0.69\lambda$ (curves 3 and 4). 1, 3 – Amplification of field amplitude in glass (transmitted radiation); 2, 4 – field amplification in vacuum (reflected radiation)

Calculation of dependence of field amplification on roughness amplitude for TM incident polarization has not been finished yet by the authors because of limited available computational resources (PC with CPU Intel Pentium II, 266 MHz, 32 Mb RAM). First calculations for small roughness amplitudes show much weaker roughness-amplitude dependence than that for TE polarization.

Space field structure was also investigated for various values of roughness amplitude and period (Fig. 7, 8). It depends

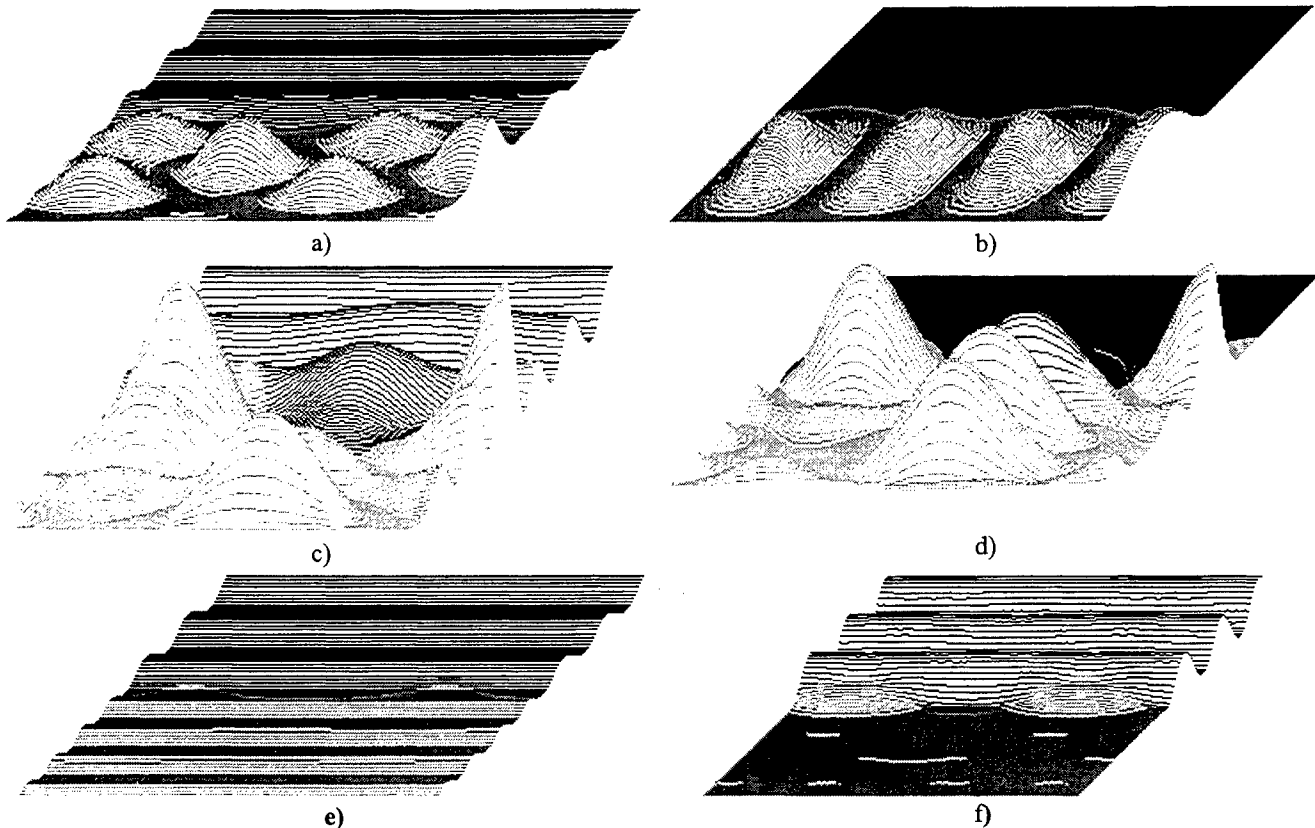


Fig. 7. Instant space distribution of scattered TE polarization near glass surface with sine roughness corresponding to time moment when field reaches amplitude values at characteristic points. **a), b)** - space period $d=0.69\lambda$, roughness amplitude $h=0.1\lambda$ (resonant peak in Fig. 5); **c), d)** - space period $d=\lambda$ and amplitude $h=0.55\lambda$; **e), f)** - period $d=0.375\lambda$, roughness amplitude $h=0.1\lambda$, λ - radiation wavelength in vacuum. There are depicted space distributions of total squared electric field E^2 (**a, c, e**) and pure scattered squared electric field $E_s^2=(E-E_{inc})^2$ (**b, d, f**) Grey - field distribution in glass with $n=1.50$, black - field distribution in vacuum ($n=1.0$). Fig. **c), d)** are 5 times scaled as compared to **a), b)** to show more detailed structure of field, Fig. **f)** is 100 times scaled because scattered field is about 1% of total field in that case.

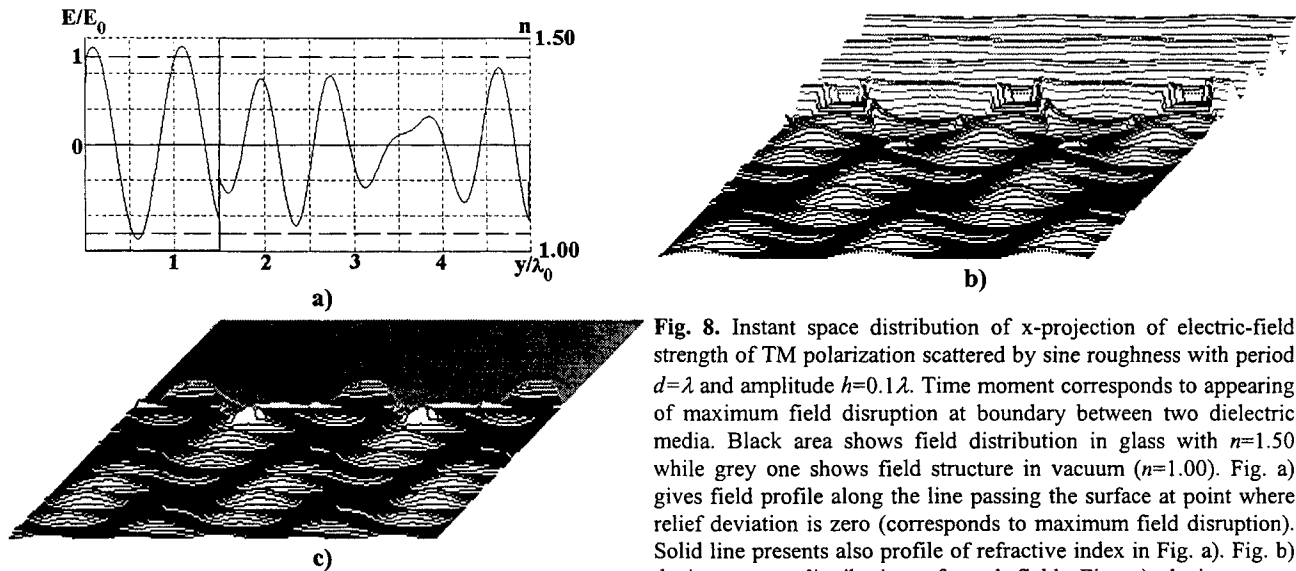


Fig. 8. Instant space distribution of x-projection of electric-field strength of TM polarization scattered by sine roughness with period $d=\lambda$ and amplitude $h=0.1\lambda$. Time moment corresponds to appearing of maximum field disruption at boundary between two dielectric media. Black area shows field distribution in glass with $n=1.50$ while grey one shows field structure in vacuum ($n=1.00$). Fig. **a)** gives field profile along the line passing the surface at point where relief deviation is zero (corresponds to maximum field disruption). Solid line presents also profile of refractive index in Fig. **a)**. Fig. **b)** depicts space distribution of total field, Fig. **c)** depicts space distribution of pure scattered field.

critically on roughness period. For TE polarization scattering by sine roughness with period less than $0.9\lambda/n$ results in formation of both plane reflected wave and plane transmitted wave with small perturbations disappearing fast with going away from the surface (Fig. 7 e, f). Scattering by sine surface roughness with resonant period results in formation of periodic field structure that is practically exact standing wave in dielectric with higher refractive index (Fig. 7 a, b). Reflected wave is of very small amplitude (about 0.1% of incident-field amplitude in Fig. 7 b). Scattering by sine roughness with period larger than $0.9\lambda/n$ results in periodic field structure both in dielectric and in vacuum (Fig. 7 c, d) which results from superposition of travelling E_{TR} and standing E_{ST} waves. Roughness amplitude and period determine energy transfer from incident wave to those two waves. Perturbations of the form of plane reflected wave disappear with going away from the surface. Period of field structure of the standing wave is exactly the same as roughness period in all considered cases while field amplitude varies depending on roughness parameters (Fig. 7).

Space distribution of x - and y -projections of electric-field strength for TM incident polarization can also be represented as superposition of travelling and standing waves in dielectric material with higher refractive index (Fig. 8). Period of standing-wave field is similar to roughness period as it is observed for the case of TE polarization. Reflected wave is close to plane one with small perturbations disappearing far from the surface. Some kind of resonance field structure was observed for TM polarization too when practically all incident wave turns into standing wave. Y -projection of electric field is more sensitive to roughness parameters than x -projection and can be associated with some kind of surface wave travelling along rough surface. For both projections, field disruptions were observed at vacuum-to-solid boundary (Fig. 8), and they satisfy traditional boundary conditions $\varepsilon_1 E_{1j} = \varepsilon_2 E_{2j}$ [16] for $j=x, y$.

Thus, in general, field structure near sine rough surface inside transparent dielectric can be represented as follows:

$$E(x, y, t) = E_{TR} + E_{ST}. \quad (7)$$

Energy transfer to travelling or standing wave depends on roughness parameters. In case of resonance practically all power of incident wave goes to power of standing wave.

4. APPLICATIONS OF RESULTS

Among applications of obtained results we concentrate on the following: 1) anti-reflection effect due to scattering at tiny surface roughness; 2) possible technique for real-time in-situ roughness control; 3) insight into mechanisms of feedbacks appearing during laser-induced surface modification.

4.1. Anti-reflection effect

This effect is clear from obtained results (Figs. 5, 6, 7). The following key points are important for anti-reflection:

- 1) coefficient of reflection must be less than that of ideally smooth surface (Fig. 5, curve 2);
- 2) coefficient of transmission must be higher than that of smooth surface (Fig. 5, curve 1);
- 3) structure of reflected and transmitted waves must be close to plane wave (Fig. 7).

As one can see from Figs. 5, 6, 7, there is a range of roughness parameters for which all these points are true: practically ideal plane waves of reflection and transmission are obtained for roughness period less than $0.5 \lambda/n$ and roughness amplitude less than 0.15λ (for considered glass sample). Reflection R and transmission T coefficients can be calculated from field amplitudes or amplification for transmitted A_T and reflected A_R waves:

$$R = (A_R - 1)^2, \quad (8)$$

$$T = A_T^2. \quad (9)$$

Using data from Fig. 5 for plateau area in spectral dependence ($A_R = 1.0960$, $A_T = 0.9955$) one obtains the following values: $R = 0.009$, $T = 0.991$. Thus, sine roughness can give no worse anti-reflection than multilayer coatings while producing of sine variations of surface relief can be more suitable for some applications. For example, such roughness anti-reflection can be more suitable for high-power laser optics because it does not give local field maximum near the surface that can initiate laser-induced damage. Multilayer coatings usually result in field one or more maximum inside the layers.

4.2. Possible technique for real-time *is-situ* surface roughness characterisation

The key point for the second application is obtained relation between roughness parameters and those of space distribution

of scattered radiation. This allows to propose the following technique for measuring of surface roughness (Fig. 9). Surface relief with rather arbitrary roughness can be represented as Fourier series of sine surface harmonics. Among them only resonant harmonic of period d_1 will play dominant role in scattering of incident monochromatic light with fixed wavelength λ_1 corresponding to resonance condition $d/\lambda=1/n$ (in case of considered glass surface it is $d_1=0.69\lambda_1$). Then space period of standing wave of scattered radiation inside sample corresponds to space period of resonant spatial harmonic of surface relief while amplitude of the resonant roughness harmonic determines standing-wave amplitude. Laser radiation of other wavelength λ_2 excites other surface resonant harmonic (with period of $d_2=0.69\lambda_2$ for considered glass surface). Thus, varying wavelength of incident light to excite other harmonics of surface roughness, one can scan harmonics of surface relief within laser spot, and then reconstruct and calculate roughness profile as Fourier series. The only problem is to fix space distribution of scattered light inside irradiated sample and then to measure its space period and amplitude.

To measure radiation distribution inside the sample the following method can be used (Fig. 9). Standing wave appears beneath the surface due to scattering of high-power wide-waist laser beam referred to as pump beam. Power of the beam must high enough to induce local variations of refractive index due to its non-linearity described by $n=n_0+n_2E^2$. Then radiation scattering by resonant harmonic of surface roughness results in periodic laser-induced modulation of refraction which spatial structure follows that of squared electric field (Fig. 7 a). Low-power probe beam can be scattered by that periodic structure, and scattered light is deflected in a manner similar to diffraction grating [16] resulting in appearing of diffraction maxima at certain angles. Deflection angle and amplitude of diffraction maxima are unambiguously connected with period and amplitude of laser-induced space variations of refraction. One can measure amplitude and deflection angle of probe beam with high accuracy and extract information about amplitude and space period of laser-induced variations of refraction and, then, about amplitude and period of resonant harmonic of surface roughness. That technique can be especially effective for photo-refractive materials.

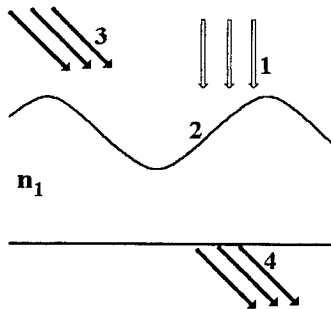


Fig. 9. Illustration for proposed idea of measurements of surface roughness. 1 – high-power pump laser beam to induce periodic modulations of refraction in bulk (3D diffraction grating) through scattering at resonant sine-shaped surface roughness (2). 3 – low-power probe laser beam which is scattered by both surface roughness and laser-induced diffraction grating. 4 – deflected laser beam corresponding to diffraction maximum obtained from probe beam after it has been scattered.

Other methods to fix space distribution of scattered light inside investigated sample are also possible to realize presented idea, for example, intensity-dependent laser-induced variation of absorption which is suitable for semiconductors. Main requirements to the methods are using of intensity-dependent material properties and reversibility of their laser-induced changes.

Qualitative consideration suggests existence of optimal parameters for both pump and probe laser beams. Pulse duration determines operation rate of the method: the shorter the pulse, the faster the measurement but pulse duration should be large enough for setting stationary distribution of scattered radiation of both pump and probe beams (about 30 - 100 fs, according to our simulation). Thus, response time can be decreased by using of picosecond or femtosecond laser pulses. Using of short pulses allows also to avoid heating of irradiated samples. Femtosecond pulses are also the most suitable for methods based on laser-induced absorption variations because in that case light-generated electrons do not have time to diffuse and their space distribution and, therefore, space distribution of absorption follow that of radiation. Amplitude of probe laser beam should be high enough to induce variations of refractive index or absorption but less than damage threshold of investigated material. At last, wavelength of pump and probe beams is the most critical for both vertical and horizontal resolutions. As it is seen from Fig. 6, the best vertical resolution corresponds to roughness harmonics which amplitude varies from zero to a half of radiation wavelength while decreasing of wavelength allows to detect small-period surface roughness and make reconstruction of surface relief more detailed. Thus, the less pump wavelength, the higher resolution. On the other hand, short-wavelength radiation is absorbed too much, and space grating cannot be formed.

A brief review of methods for surface-relief measuring shows real need for developing of one more optical technique.

Those methods can be divided into four groups which are as follows: interference difference-contrast microscopy (e.g. Nomarski microscope), electron microscopy, microscopy with scanning probe (scanning tunnelling microscopes (STM), atomic-force microscopy (AFM), scanning near-field optical microscopy (NFOM)), profilers (contact and optical) and scattering-based techniques (total integral scattering (TIS), angle-resolved scattering (ARS)). All of those techniques have their own advantages and disadvantages. Some characteristics of enumerated groups are shown in table I as they are described in [10].

Table I. Comparison of main techniques for surface characterisation. IDCM – interference difference-contrast microscopy, EM – electron microscopy, SM – microscopy with scanning probe, CP – contact profilers, OP – optical profilers, SBM – scattering-based methods

<i>IDCM</i>	<i>EM</i>	<i>SM</i>	<i>CP</i>	<i>OP</i>	<i>SBM</i>
Sample dimensions					
unlimited	< 5 mm	several mm	10 µm-10 mm	100mm	unlimited
Measured surface characteristics					
relief	relief	relief	profile	profile	statistical parameters
Horizontal resolution					
10 Å	10-150 Å	1-2 Å	0.2 mkm	1 mkm	-
Vertical resolution					
<1 Å	2-5 Å	1-2 Å	1 Å	1 Å	-
Characterised materials					
high – reflecting materials	conductive materials	conductive materials – for STM; any – for AFM, NFOM	any	any	any
Additional surface processing (preparing of replica, metal-layer deposition)					
needed for low-reflect. materials	needed for non-conductive materials	needed for non-conductive materials	no	no	no
Possible destroying of sample					
no	no	yes	yes	no	no
In-situ measurement					
yes	no	no	no	yes	yes

As one can see from this table, characteristics of each type of the devices depend on operation conditions. High-resolution microscopes (such as electron and scanning probe microscopes) provides characterisation of surface only for comparatively small samples and are not able to perform on-line diagnostics due to low measurement rate and complicated arrangement. Moreover, those methods require additional processing of surface [10], which can change surface relief and damage the sample. This problem limits using of electron and scanning microscopy and contact profilers. Optical profilers are non-destructive method allowing to perform in-situ measurement but they yield low spatial resolution which is not enough for characterisation of optical and microelectronics elements. Methods based on light scattering are rather simple and can be used for on-line diagnostics but they have serious drawback: they give no information about surface relief but only about statistical characteristics, such as rms roughness (TIS, ARS), auto covariance function (ARS), power spectral density (ARS). Besides that, most of described techniques are suitable only for investigation of surfaces of high-reflecting materials, e.g., metal films deposited on dielectric or semiconductor samples. Thus, there is no method that could provide non-destructive in-situ real-time characterisation of dielectric or semiconductor surface with rather high resolution. Proposed idea of two-beam technique can be the method combining high resolution with advantages of optical methods.

4.3. Influence of surface scattering on laser-induced surface modification

In this section we discuss briefly several aspects of laser-surface interaction connected with influence of space field distribution near the surface on laser-induced processes.

1. Dependence of field amplification on roughness amplitude (Fig. 6) shows possibility of both positive and negative feedbacks between laser field and roughness amplitude. Nearly linear increasing of scattered-field amplitude inside dielectric material with increasing of roughness amplitude shows possibility of formation of *positive feedback* at initial stage of laser-induced ripple growth when the ripples are tiny. Really, *increasing of field amplitude near surface hillocks* results in *increasing of laser-induced refraction gradient*. In turn, that leads to *increasing of local field-induced force* described by (11), and results in *increasing of surface roughness due to surface deformation* leading, in turn, to *increasing of scattering and growth of field amplitude beneath the surface*. This process corresponds to increasing of efficiency of energy transfer from incident radiation to roughness-excited standing wave with increasing of roughness amplitude that stops as soon as the latter reaches certain value (0.6λ for particular sample depicted in Fig. 6) corresponding to stopping of field-amplification increasing with increasing of roughness amplitude. Further increasing of roughness amplitude leads to decreasing of field amplification and results in *negative feedback* between laser field and roughness amplitude. Such mechanisms of feedbacks result from the following dependence of field amplification A on roughness amplitude h

$$A = \mu_1 h - \mu_2 h^2, \quad (10)$$

which approximates very well initial part of dependence shown in Fig. 6. Relation (10) confirms amplitude dependence of field amplification used by other authors [20]. Feedbacks appearing due to light scattering can work simultaneously with other feedbacks of thermal or hydrodynamical nature [20] playing important role in laser-induced surface modification.

2. As it follows from Fig. 5, period of laser-induced surface ripples depends on presence of "resonant" space harmonic in spectrum of surface relief. If such harmonic is in the spectrum, then period of surface ripples is λ/n (resonant peak in Fig. 5). If "resonant" harmonic is weak or absent, then period of laser-induced ripples can be a bit more than λ/n (corresponds to broader maximum just after resonant peak in Fig. 5) or it can be about λ what corresponds to the broadest maximum of field amplification. Those values of laser-induced surface-ripple period have been observed by different authors [21, 22] and can originate from electrodynamical mechanisms connected with light scattering by initial and growing roughness. Variation of laser-induced ripples period during their growth is possible and can originate from fluctuations of roughness.

3. Next important point is appearing of laser-induced force acting beneath the surface during high-power laser action. Scattered field can induce inhomogeneous distribution of refraction just below dielectric surface (see Fig. 7, 8). This results in appearing of light-induced forces in bulk and at surface leading to medium deformation [23]:

$$\vec{f} = -\frac{E^2}{8\pi} \cdot \nabla \varepsilon + \nabla \left(\rho \frac{E^2}{8\pi} \left[\frac{\partial \varepsilon}{\partial \rho} \right]_{T=\text{const}} \right) + \frac{\varepsilon \mu - 1}{4\pi c} \frac{\partial}{\partial t} [\vec{E} \times \vec{H}] \quad (11)$$

where $\varepsilon = n^2 = n_0^2 + 2n_0 \Delta n$ and $\Delta n = n_2 E^2$, ρ is medium density, $\mu = \text{const}$ is magnetic permeability. In case of femtosecond pulses this force can dominate in processes of laser-induced modification of surface relief because thermo-mechanical, hydrodynamical and other forces have response time much larger than pulse duration. Presented FDTD modelling technique is very effective for calculation of the force given by (11).

5. CONCLUSIONS

Thus, there is presented a new approach to investigation of surface scattering by means of FDTD modelling. In contrary to most traditional approaches [1-9], it is based on modelling of time variations of space field distribution. Described technique is especially effective for calculation of space field distribution near scattering surface and simulation of laser-induced dynamical processes (heating, surface modification) when surface relief is varied during laser action. Obtained results (spectral and amplitude dependence of field amplification) for sine roughness shows several interesting features among which rather sharp resonant peak in spectral dependence is the most attractive and interesting. Dielectric surface with random roughness can be modelled by the surface with several sine components of Fourier series with random amplitudes representing the roughness. If amplitudes of the components do not differ much, then the closest to resonant period component is expected to give the most contribution to formation of space field structure resulting from scattering while others are expected to give smaller contributions. Scattering by random roughness is under investigation by authors.

Being based on correct high-resolution calculation of space distribution of light scattered by sine surface roughness, new two-beam method for surface characterisation has been suggested. It can be used for real-time in-situ diagnostic of low-

reflecting surfaces of dielectric or low-absorbing semiconductor. For example one can use the technique for in-situ real-time monitoring of surface evolution during film growth. Existence of optimal parameters of pump and probe beams is shown. They can be determined by modelling for real materials. Modifications of described method can include using of several probe beams of different wavelengths at different incident angles what can help to improve spatial resolution. More detailed modelling of two-beam interactions will be done by authors in the nearest future.

Discussed AR effect from scattering by sine roughness can be one of promising applications. It is no less effective than action of anti-reflecting coatings while roughness anti-reflection is not accompanied by appearing of intensity maximum in transparent material. That can be important for increasing of laser-induced damage threshold of AR surfaces in lasers. AR effect has already been touched upon in literature [19] but it was done for other polarization (TM) and other roughness parameters. We also believe the technique proposed in [19] gives large perturbations to reflected and transmitted waves.

Other discussed points connected with obtained results are dependence of laser-induced surface ripple period on initial surface roughness and mechanisms of feedback acting during laser-induced modification of surface relief.

6. REFERENCES

1. Lord Rayleigh, *Theory of Sound*, vol. 2, MacMillan, London, 1929, pp. 89-96.
2. S.O.Rice, "Reflection of Electromagnetic Waves from Slightly Rough Surface", *Commun. on Pure and Appl. Math.*, v. 4, p. 351, 1951.
3. F.Toigo, A.Marvin, and N.R.Hill, "Optical Properties of Rough Surfaces: General Theory and the Small Roughness Limit", *Phys. Rev.*, v. 15, p. 5618, 1977.
4. D.Maystre, O.Mata Mendez, and A.Roger, "A New Electromagnetic Theory for Scattering from Shallow Rough Surfaces", *Opt. Acta*, v. 30, p. 1707, 1983.
5. P.Beckmann, A.Spizzichino, *The Scattering of Electromagnetic Waves from Rough Surfaces*, Pergamon Press, New York, 1963, 492 p.
6. R.Schiffer, "Reflectivity of slightly rough surface", *Appl. Opt.*, v. 26, N 4, pp. 704-712, 1987.
7. A.V.Kostin, Ph.D. theses, St.Petersburg IFMO (Technical University), 1998.
8. O.Carlo-Perez, A.Sentenac, J.-J.Greffet, "Light scattering by a two-dimentional, rough penetrable medium: A mean-field theory", *Radio Science*, v. 34, N 2, pp. 311-335, 1999.
9. A.Sentenac, and J.-J.Greffet, "Mean-field theory of light scattering by one-dimensional rough surface", *Journal of the OSA A*, v. 15, N 2, pp. 528-532, 1998.
10. J.M.Bennett, L.Mattson, *Introduction to Surface Roughness and Scattering*, OSA, Washington, D.C., 1999.
11. K.S.Yee, "Numerical solution of initial boundary value problems in isotropic media", *IEEE Transactions on Antennas and Propagation*, AP-14, p.302, 1966.
12. A.Dunn, C.Smithpeter, A.J.Welch, and R.Richards-Kortum, "Finite-Difference Time-Domain Simulation of Light Scattering from Single Cells", *Journal of Biomed. Optics*, v. 2, N 3, pp. 262-266, 1997; A.Dunn, and R.Richards-Kortum, "Three-Dimensional Computation of Light Scattering From Cells", *IEEE Journal of Selected Topics in Quantum Electronics*, v. 2 (4), pp. 898-905, 1996.
13. V.E.Gruzdev, A.S.Gruzdeva, "Computer simulation of light propagation through optical coatings with inhomogeneous microstructure", in *High-Power Laser Ablation*, Proc. SPIE, v. 3343, pp. 305-316 1998.
14. V.E.Gruzdev, A.S.Gruzdeva, M.N.Libenson, "Evolution of rough dielectric surface in high-power laser field", *High-Power Laser Ablation*, Proc. SPIE, v. 3343, part 1, pp. 465-476, 1998.
15. W.E.Milne, *Numerical Solution of Differential Equations*, New York, 1953, Ch. VIII.
16. M.Born, E.Wolf, *Principles of Optics*, 4-th ed. Pergamon Press, New York, 1968, Ch.1.6
17. J.F.DeFord, and M.R.Kozlowski, "Modeling of Electric-Field Enhancement at Nodular Defects in Dielectric Mirror Coatings", *Laser-Induced Damage in Optical Materials: 1992*, Proc. of SPIE, v. 1848, pp.455-469, 1992.
18. N.N.Kalitkin, *Numerical Methods*, Nauka Publ., Moscow, 1978, Ch. XIII (in Russian).
19. M.Auslender, D.Levy, S.Hava, "One-dimensional anti-reflection gratings in (100) silicon: a numerical study", *Appl. Opt.*, v.37, N 2, pp. 369-373, 1998.
20. S.A.Akhmanov, V.I.Emel'yanov, N.I.Koroteev, V.N.Seminogov, "The Action of Powerful Laser Radiation on Surfaces of Semiconductors and Metals: Nonlinear Optical Effects and Nonlinear Optical Diagnostics", *Uspekhi Fizicheskikh Nauk* (Russian), v. 147 (4), pp. 675-745, 1985 and references therein.

21. E.E.B.Campbell, D.Ashkenasi, and A.Rosenfeld, "Ultra-short-Pulse Laser Irradiation and Ablation of Dielectrics", in *Lasers in Materials*, edited by R.P.Agarwal (Trans Tech Publ., 1998), Ch. 5.
22. L.D.Landau, E.M.Lifshits, "*Electrodynamics of Continuos Media*", Moscow, Nauka, 1992.

Capacitive Discharge Excilamps

Edward A. Sosnin, Mikhail V. Erofeev, Alexei N. Panchenko, Mikhail I. Lomaev,
Victor S. Skakun, Dmitrii V. Shitz, Victor F. Tarasenko*

High Current Electronics Institute, Akademicheskii ave., 4, Tomsk, Russia, 634055
Phone: (3822) 258-686, Fax: (3822) 259-410, email: badik@loi.hcei.tsc.ru

ABSTRACT

Investigation was made of the characteristics of XeCl ($\lambda \sim 308$ nm), KrCl ($\lambda \sim 222$ nm) and XeI ($\lambda \sim 253$ nm) capacitive discharge excilamps. High efficiency of exciplex molecules and simple design have been obtained under capacitive HF discharge excitation. Cylindrical excilamps with radiation output through side surface of the cylinder and through one or two windows placed on the tube ends have been developed. High UV radiation power and electrical power deposition to fluorescence conversion resulted in efficiencies of up to 12%.

The study of XeCl, KrCl and XeI excilamps have shown, that it is possible to create sealed-off samples with lifetime more than 1000 hours. The stability of output parameters of the capacitive discharge excilamps is studied and the mechanism of chlorine losses in low pressure halogencontaining excilamps made of quartz was determined.

The possibility of creation of capacitive discharge excilamps with short pulse duration was studied. In capacitive discharge cylindrical KrCl-excilamp, at $\lambda \sim 222$ nm the radiation pulse power up to 2.5 kW was obtained. Powerful radiation pulses 50 ns in duration were obtained at pulse repetition rate of 1 kHz.

Key words: capacitive discharge, ultraviolet, excilamp, lifetime

1. INTRODUCTION

In recent decade, interest in design and development of new types of UV and VUV spontaneous radiation sources, in particular excilamps, has considerably grown¹⁻¹⁰. The highest emission efficiencies of XeCl ($\lambda \sim 308$ nm) and KrCl ($\lambda \sim 222$ nm) excilamps in glow discharge^{3,6} and dielectric barrier discharge^{4,7,8} were obtained. The life-time of glow discharge sealed-off excilamps is limited by the fact of Cl-contained operating mixture contact with electrodes which have high temperature in the course of operation. For example, in XeCl-excilamp with a binary mixture Xe/Cl₂ = 5/1 (total pressure of 4.5 mmHg) and output power per cm³ from 0.29 up to 1.1 W/cm³ in case of stainless electrodes the lifetime t_l did not exceed one hour and to regain the started output emission parameters it was necessary to refresh the mixture at regular intervals. At decreasing of average radiation power more than on the order and with use of ballast volume nickel-based electrodes the life-time more than 100 hours has been gained¹⁰. Obviously it is insufficient for many practical applications. Alternatively, it is known, that in barrier discharge excilamp the mixture has a contact only with lamp quartz bulb (the electrodes are set outside). Because of this, the operational life-time here exceeds 1000 hours^{4,9}. It is pertinent to note that the barrier discharge is a version of capacitive discharge¹¹; the latter can be realized not only in planar and coaxial excilamp bulb geometry, but also in cylindrical ones. For example, the cylindrical geometry was earlier used at CO₂-lasers pumping by low pressure capacitive discharge¹².

In the present paper an efficient low-pressure sealed-off cylindrical excilamp with capacitive discharge excitation is under discussion. For the purpose of finding out conditions where the radiation power density and radiation pulse power maximal values can be reached, the research of amplitude-temporal characteristics of structurally simple KrCl and XeCl-excilamps at unipolar short pulse excitation (0.04–3 μ s) and at sine wave operation has been carried out.

* Correspondence: E-mail: VFT@loi.hcei.tsc.ru; Telephone: (3822) 258-686; Fax: (3822) 259-410

2. EXPERIMENTAL RESULTS AND DISCUSSION

2.1. Experimental setup and measurement procedure

The main excilamp characteristics, circuit elements parameters of exciting generators and gas filling components are listed in table 1. Figure 1 presents the schematic of the typical excilamp (1.1, 1.2). The cylindrical electrodes were made of the intimate mated to outer quartz tube surface Al-foil. The distance between electrodes and the length of each other were from 2 to 38 cm and from 1 to 19 cm, correspondingly. We also tested lamps the radiation of which was injected through a flat quartz window located at an end face of tube. All the lamps were filled in with binary mixtures of Kr (or Xe) with molecular chlorine Cl_2 or vaporized I.

In experiments excitation of the operating mixtures were realized by pulse generators of two types. In the first place, sine wave generators with output power up to 20, 35 and 55 W at frequency of 22 kHz were used. It was possible to regulate the voltage amplitude on discharge load at similar operating mixture compositions. In the second place, unipolar wave thyristor-magnetic generator similar to described in¹² was used. The generator provided voltage pulses with amplitude up to 36 kV and duration from 120 to 5 μs . The voltage pulse risetime differed and, in particular, in our experiments made of 3; 0.6; 0.19 and 0.04 μs . Besides, in the unipolar excitation case for change of matching of generator impedance and the lamp were used additional resistance R_v or inductance L_v (Fig. 2).

Average output UV power was measured by FEK-22SPU photocathode. The photocathode has peak sensitivity at wavelengths near 300 nm and is insensitive to the radiation at wavelengths over 600 nm. Besides, calibrated light filters transparent only for UV placed in front of the photocathode were used to separate UV radiation in the excilamp output. Spontaneous radiation spectra in a range from 190 to 600 nm were recorded by MUM-monochromator or by monochromator MDR-23 with a photomultiplier FEU-100 and a register.

2.2. Cylindrical Capacitive Discharge Excilamps

High-frequency volume discharge radiating with high efficiency on B-X transitions of exciplex molecules can readily be obtained at low pressure inert gas / halogen (the chlorine or iodine at the present work) mixtures. The main results obtained in these conditions are shown on Figs. 3 – 7. The optimal pressure value depends on mixture composition, distance between electrodes, tube diameter and fall in the range from shares of mmHg to several mmHg that is in close agreement with operating pressure values of glow discharge excilamps^{2,3}. Operating mixture components ratio also closely match the chlorine-contained mixtures of the glow discharge.

Figure 3 gives average power and efficiency of the XeCl^* and KrCl^* molecules radiation at fixed pressure as a function of product of pressure on distance between electrodes (pd -value).

As it is seen from Fig. 3 at the fixed pressure the radiation efficiency grows with increasing of interelectrode distance. The maximal radiation efficiency values are close to the values obtained under glow discharge excitation. The duration of a separate radiation pulse at high-frequency excitation depends on composition and pressure of operating gas mixture, distance between electrodes and operation voltage, electrodes square and excilamp bulb diameter. For example, for XeI -excilamp with diameter of 4 cm and distance between electrodes 9 cm, at operating pressure of 10 mmHg, the duration of separate radiation pulses conformed to each discharge current half-cycle and made up approximately 20 μs (Fig. 4). With mixture pressure increasing and electrodes square decreasing, the duration of separate radiation pulses reduced. As a rule, increasing of the voltage values on electrodes tended to radiation pulse duration reduction.

The radiation spectrums of XeCl and KrCl excilamps are similar to spectrums obtained at glow discharge excitation conditions^{2,3,6}. Radiation band-width of XeI^* ($\lambda \sim 253$ nm) molecule has made of 2 nm and also corresponded to our glow discharge excitation case (Fig. 5). However, radiation efficiency of XeI^* molecules was approximately in 5–10 times below either at capacitive discharge excitation case or the glow discharge in comparison with radiation intensities of XeCl^* and KrCl^* molecules.

The average radiation power of KrCl excilamp versus average discharge current is shown on Fig. 6(a). In conditions of excilamp overheating absence the linear growth of average radiation power was observed with the discharge current increasing.

The main advantages of capacitive discharge excitation in comparison with glow discharge case are the simple design excilamp bulb, absence of a contact between operating mixture and electrodes and, as a consequence, essential sealed-off excilamps life-time increase. Fig. 6(b) gives the XeCl-molecules average radiation power as a function of lamp operating time. Similar results were obtained for XeI-excilamp. The tests have shown, that the sealed-off excilamps mixture resource exceeds 1000 hours. In comparison with barrier discharge excitation the capacitive discharge allows to realize more homogeneous excitation (there are no separate filaments), to form narrower radiation spectrum bands, to get effective energy output into operating mixture at low pressure and, accordingly, to have higher UV radiation source efficiency values.

2.3. Capacitive discharge excilamps with short pulse duration

For investigations in this case the binary mixtures at total pressure up to 2 mmHg and excilamps 2.1, 2.2 were used. The radiation pulse shape of capacitive discharge excilamp strongly depends on established in parallel to an excilamp resistance R_v and inductance L_v values (Fig. 2). For example, we varied resistance R_v value in the range from 100 k Ω to 100 Ω . In experiment the radiation pulse shape transforms from conventional for capacitive discharge lamps multi-peak shape to single-peak shape (Fig. 7). At the same time the radiation pulse power falls off. In particular, this result derives from the fact that at large R_v values there are voltage oscillations on a lamp because of capacitive character of the load.

In optimal mixtures from the point of view of maximal UV-radiation output ($Kr/Cl_2 = 25/1$) at total pressure $p \sim 0.2$ mmHg the pulse power through end face of a lamp (the end face square makes approximately 10 cm²) was 2.5 kW. Total pulse output power value in solid angle 4π was about 15 kW, when taken into account that output light flow was terminated by excilamp elements (electrodes, dispersion on places of a junction quartz tube with flat window).

The distinctive feature of capacitive discharge excilamps is a long life-time in quasi-sealed-off mode in comparison with longitudinal discharge excilamps. For example, in¹⁴ after approximately 10^4 number of pulses the intensity of inner metal electrodes contained cylindrical glow discharge XeCl-excilamp has fallen on third by value. Whereas in our experiments radiation intensities in about 10^6 number of pulses has not changed essentially.

3. CONCLUSION

In the present paper the investigations of low pressure high-frequency capacitive discharge spontaneous radiation sources are presented. For the first time the sealed-off cylindrical XeCl ($\lambda \sim 308$ nm), KrCl ($\lambda \sim 222$ nm) and XeI ($\lambda \sim 281$ nm) excilamps with high efficiency have been developed. Excilamps are characterized by a simple design. On XeCl* and KrCl* molecules at sine wave operation are obtained UV-radiation efficiency of about 12 % and average radiation power of about 3 W at operating volume 250 cm³. Under unipolar short pulse excitation (0.04-3 μ s) in cylindrical KrCl-excilamp ($\lambda \sim 222$ nm) the radiation pulse power up to 2.5 kW was obtained. Use of capacitive discharge allows to increase excilamp life-time. So, the life-time of sealed-off XeCl and XeI excilamps exceeds 1000 hours.

REFERENCES

1. B.A. Koval, V.S. Skakun, V.F. Tarasenko, Fomin E.A., E.B. Yankelevitch, "," *Prib. i Tech Exp.*, No.4, pp. 244-245, 1992.
2. M.I. Lomaev, A.N. Panchenko, V.S. Skakun, E.A. Sosnin, V.F. Tarasenko, M.G. Adamson, B.R. Myers, F.T. Wang, "Excilamp producing up to 130 W of output power and possibility of its application," *Laser and Particle Beams*. 15(2), pp. 241- 246, 1997.

3. A.N. Panchenko, E.A. Sosnin, V.F. Tarasenko "Improvement of output parameters of glow discharge UV excilamps," *Opt. Comm.* 166, pp. 249-252, 1999.
4. E. Arnold, R. Dreiskemper, S. Reber, "High-Power Excimer Sources," *Proc. of the 8th Int. Symp. on Science and Technol. of Light Sources (LS-8)*, Graifswald, Germany, pp. 90-98, 1998.
5. B. Gellert and V. Kogelschatz, "Generation of Excimer Emission in Dielectric Barrier Discharges", *Appl. Phys. B.* 52, pp. 14-21, 1991.
6. A.N. Panchenko, V.F. Tarasenko, "," *Optica i Spectroskopia.* 84(3) pp. 389-392, 1998
7. F. Vollkommer, L. Hitzschke, "Dielectric Barrier Discharge," *Proc. of the 8th Int. Symp. on Science & Technology of Light Sources*, Greifswald, Germany, pp. 51-60, 1998.
8. E.A. Sosnin, V.S. Skakun, V.F. Tarasenko, "Coaxial and Planar Excilamps pumped by Barrier Discharge," *Proc. of the 8th Int. Symp. on Science & Technology of Light Sources*, Greifswald, Germany, pp. 240-241, 1998.
9. E.A. Sosnin, M.I. Lomaev, A.N. Panchenko, V.S. Skakun, V.F. Tarasenko, "," *Proc. SPIE*, 3403, pp. 308-311, 1999.
10. A.P. Golovitskii, S.N. Kan, "UV radiation excimer continua in low pressure glow discharge," *Optica i Spectroskopia.* 75(3), pp. 604-609, 1993.
11. Y.I. Raizer, M.N. Sneider, and N.A. Yatsenko, *Radio-frequency Capacitive Discharges*, N.Y., CRC Press, 1995.
12. Yu. I. Raizer, "Radio-frequency capacitive discharge and its applications," *Soros Educational Journal*. No.8, pp. 90-96, 1999.
13. N.G. Shybkii, S.P. Sichev, V.A. Vizi'r, "Resistor-magnetic pulse generator," *Prib. i Tech Exp.* No.3, pp. 96-97, 1990.
14. Bollanti S., Clementi G., Di Lazzaro P., Flora F., Giordano G., Letardi T., Muzzi F., Schina G., and Zheng C.E. "," *IEEE Transactions and Plasma Science.* 27(1), pp. 211-218, 1999.

FIGURES AND TABLES

Table 1. Excilamps' and power supplies' parameters

Lamp №	Discharge space dimensions: diameter / length (cm)	Operating mixture	PRR (Hz) / Voltage pulse amplitude U_g (kV)	C_g (nF) / R_v (k Ω) / L_v (μ H)
1.1	2-4 / up to 40	Xe(Kr) + Cl ₂	22000 / up to 4	- / - / -
1.2	2-4 / up to 40	Xe + I ₂	22000 / up to 4	- / - / -
2.1	3.8 / 3.6	Kr + Cl ₂	250-1000 / up to 36	0.25 / 0.1 - 100 /
2.2		Xe + Cl ₂		0.25 - 40

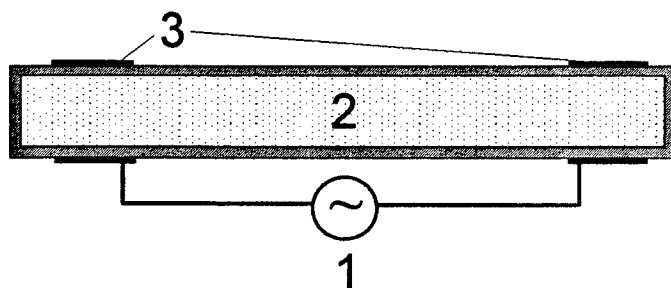


Fig. 1. Schematic of capacitive discharge excilamps. 1 – power supply, 2 - discharge volume, 3 - electrodes.

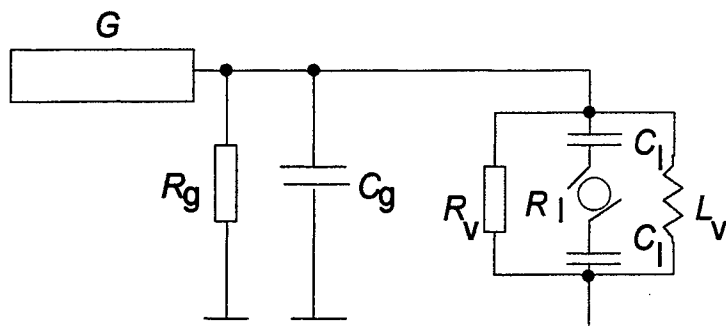


Fig. 2. Schematic diagram of capacitive discharge excilamp pumping circuit: G - external pulse generator; C_g - capacitor bank (2-5 nF); C_1 - excilamp dielectric wall capacity (we have estimated it as $9 \cdot 10^{-6}$ F); R_1 - resistance of excilamp gap; R_v and L_v - circuit elements for current outflow.

Fig. 3. Output power and efficiency of KrCl (a) and XeCl (b) excilamps versus product of pressure on distance between electrodes pd . Kr:Cl₂ = 8:1 mixture at total pressure 4.2 mmHg. Xe:Cl₂ = 8:1 mixture at total pressure 1.8 mmHg.

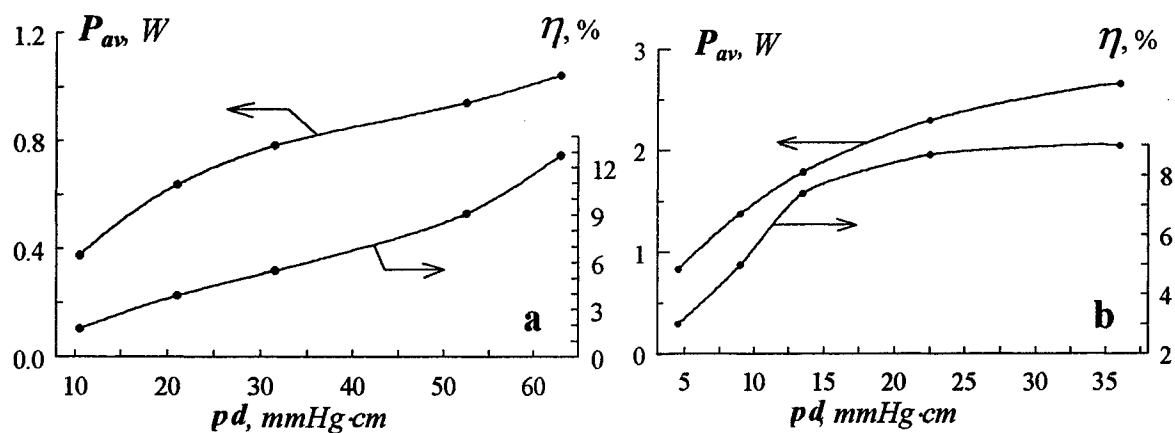


Fig. 4. Oscilloscope traces of voltage (a), discharge current (b) and UV radiation (c) obtained for XeI-excilamp at total pressure of about 10 mmHg. Tube diameter is 4 cm and $d = 9$ cm.

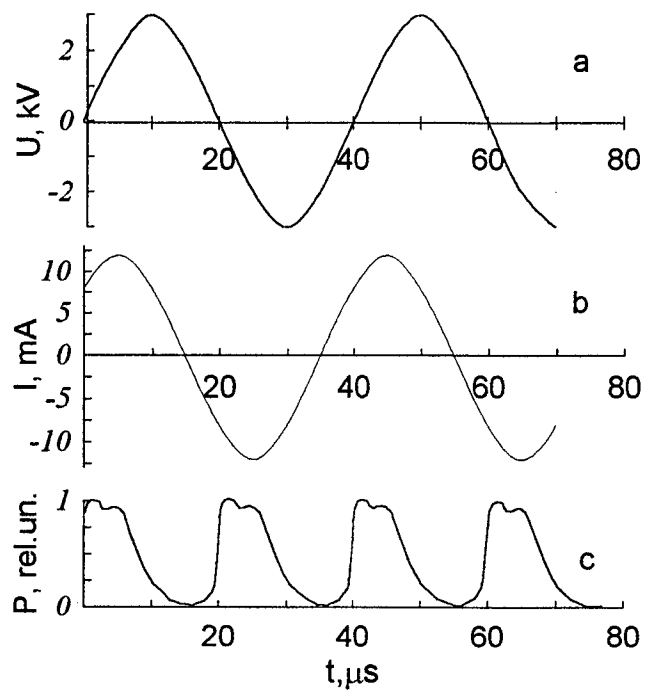


Fig. 5. XeI-excilamp spectrum at total pressure about 10 mmHg.

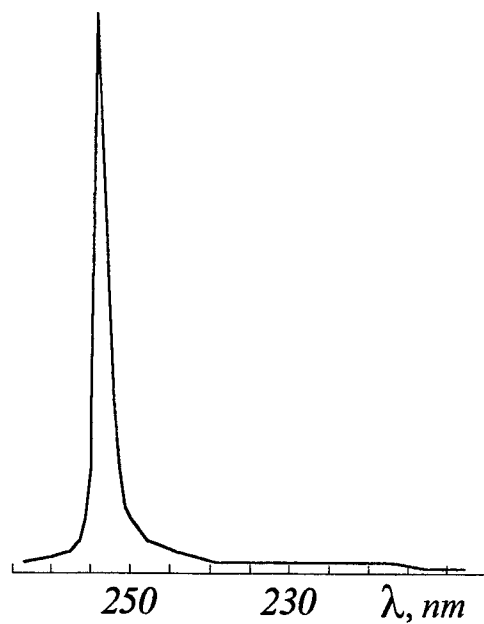


Fig. 6. The UV output and efficiency of KrCl excilamp versus the discharge current (a) and the operation time (b). a - gas mixture Kr/Cl₂=8/1, total pressure 2.1 mmHg. b - sealed-off XeCl excilamp, gas mixture Xe/Cl₂=8/1, total pressure 3.3 mmHg.

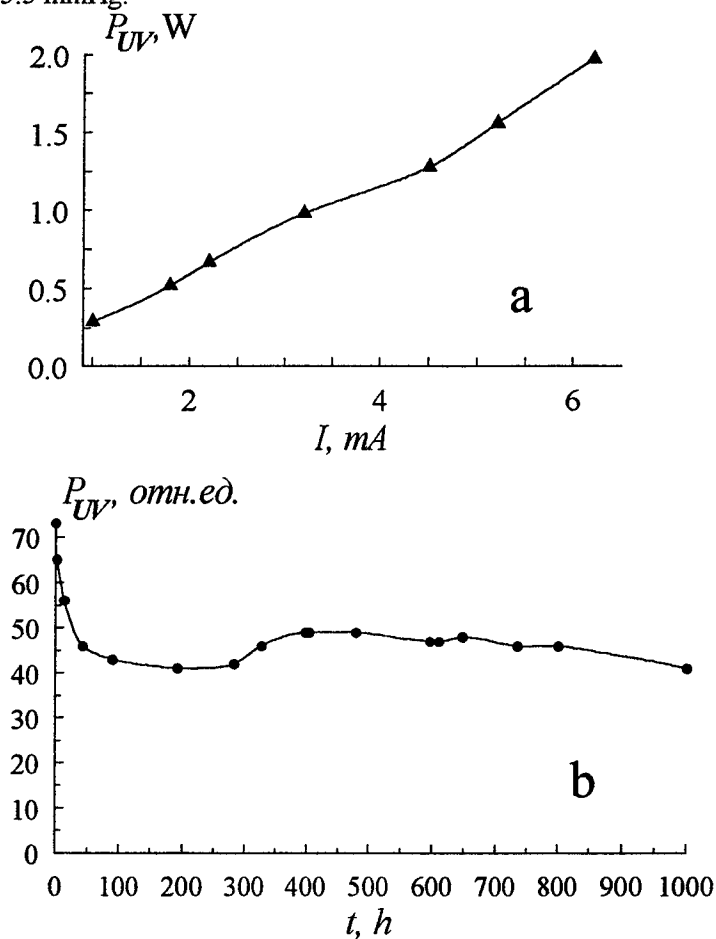
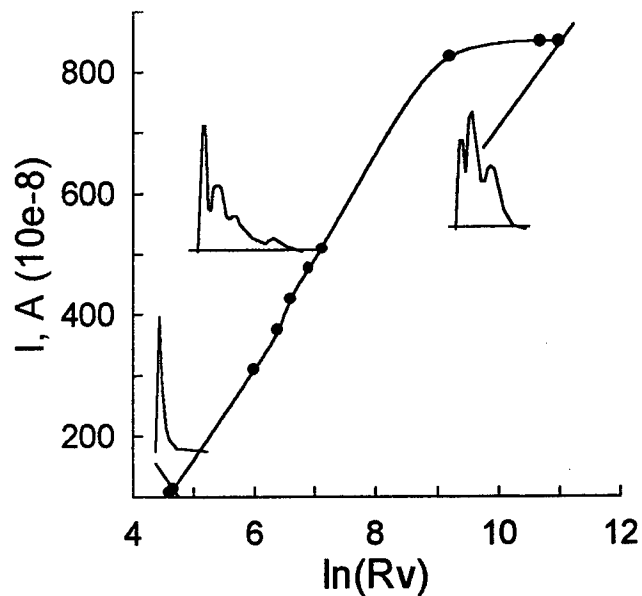


Fig. 7. Intensity of output radiation and typical waveforms of lamp intensity of capacitive discharge excilamp versus current outflow elements R_v varying. $L_v = 0$. PRR = 1 kHz.



Optimization of nanosecond UV laser illumination for semiconductor materials (Si, HgCdTe, InSb)

A. R. Novoselov(Novosselov)¹¹, A. G. Klimenko, E. V. Fedosenko, A. E. Plotnikov,

Institute of Semiconductor Physics (Russia)

ABSTRACT.

We studied stages of formation of laser craters for the purpose of decreasing a defeat zone of a semiconductor material close to laser craters. The researches were carried out using SEM and optical microscopy. This paper is devoted to results of optimization of the laser radiation for applications in microelectronics. The principles of optimization of a wavelength, pulse duration and repetition frequency of laser radiation are determined. The effect of the diameter of a laser spot onto the process of formation of a laser crater is shown. It is opinion of the authors, that the main criteria that necessarily should be taken into account when doing the laser scribing of semiconductor wafers, are as follows:

Selection of a laser source wavelength with maximum coefficient of absorption in a target.

The energy density in a laser spot on target must be less than threshold for the material;

The time gap between pulses is determined by time of the ending of processes in the material of the target.

The decrease in diameter of a laser beam allows maximum depth to diameter relation to be achieved.

Keywords: Laser ablation, laser-material processing, semiconductor.

1. INTRODUCTION.

For optimization of a laser radiation, we used the following principles:

1. The energy of laser radiation in semiconductor is swallowed by an electronic subsystem of a material, generating a large number of non-equilibrium carriers in it, for example, a concentration of non-equilibrium carriers in silicon amounted to 10^{21} cm^{-3} by ps - laser. The velocity (g) of generation of electron - hole pairs depends on an energy density of laser radiation (I) and factors of absorption (α)¹. The velocity of generation attains its maximum at the surface. The expression for the velocity of generation of electron - hole pairs can be described as:

$$g = I\alpha / h\nu \quad , (1)$$

Where $h\nu$ - energy of a photon, for energy of a photon higher than the bandgap.

2. The movement of an electron in an ideal periodic lattice is limited by the boundaries of crystal. The hot electrons disperse on the deviations of an ideal period of a crystalline lattice².

3. The motion of hot electrons in a bulk of the semiconductor brings changes in physical properties of the material³.

4. The hot electrons have characteristic time of formation $\tau_{e-ph} \approx 10^{-12}$ seconds⁴. In case of high concentration of hot electrons and holes the carrier lifetime can be calculated as:

$$\tau_r \approx (B_r \cdot \Delta n)^{-1} \quad , (2)$$

Where $B_r \approx 7,2 \times 10^{-10} \text{ cm}^3/\text{s}$ ⁵.

¹ Correspondence: Email: novoselov@thermo.isp.nsc.ru

5. The standard time – of – flight techniques had shown, that the important factor was merely the number of photons and not the pulse duration ⁶.

This paper article is devoted to the results of optimization of a laser radiation for applications in microelectronics. The principles of optimization of a wavelength, pulse duration and repetition frequency of laser pulses are determined. The effect of a of a laser spot diameter onto the process of formation of the laser crater is shown.

2. OPTIMIZATION OF LASER RADIATION.

When analyzing points 1, 3 and 5, described in introduction, it is possible to make a conclusion that the laser source should provide minimum of energy density of laser radiation in a target. The optimal wavelength for semiconductor materials is that in UV range. It has the maximum absorption coefficient of laser radiation by the material of the semiconductor and, therefore, the process of interaction between laser radiation and material of the semiconductor takes place in a smaller volume. It decreases the influence of a laser radiation down to values, which do not change physicochemical properties of material of target around the spot of interaction.

In Fig. 1 the SEM - image is shown of a surface segment of a MCT film on GaAs substrate near the laser cut, after etching in etch ⁷ which gives triangular pits of dislocation. Chemical etching of MCT film has shown unchanged quantity of pits near the laser cut. The dislocation density was about $6 \times 10^6 \text{ cm}^{-2}$.

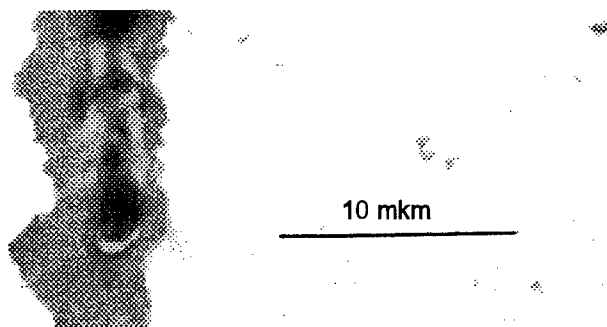


Fig. 1. The SEM - image of a surface segment of a MCT film on GaAs substrate near the laser cut, after etching in etch which gives triangular pits of dislocation.

We used ⁸ $\text{Hg}_{1-x}\text{Cd}_x\text{Te}$ heteroepitaxial structures grown on GaAs(130) substrates with a CdTe buffer layer. The films had composition varying through the depth with high CdTe content toward the boundary with the buffer and the outer boundary ($x_{\text{CdTe}} = 0.35$). In the bulk of p-type MCT film the composition was equal to $x_{\text{CdTe}} = 0.225$, which corresponded to the threshold wavelength of sensitivity at $T = 78 \text{ K}$ (about $10 \text{ }\mu\text{m}$).

The MCT - dielectric interface was formed by CVD of a low-temperature silicon dioxide 70 nm thick at low pressure in the process of monosilane oxidation by oxygen in argon flow at $T = 100^\circ \text{C}$ without additional activation. The interface was further passivated by plasmochemical deposition of silicon nitride 50 nm thick in the process of chemical reaction between monosilane and ammonia in a glow-discharge plasma at $T = 50^\circ \text{C}$.

The laser source was a pulse UV laser of $0.34 \text{ }\mu\text{m}$ wavelength with 7 ns pulses at 100 Hz repetition rate focused at a spot of $6 \text{ }\mu\text{m}$, the cutting depth $25 \text{ }\mu\text{m}$, and speed of sample movement with respect to the immobile laser beam $2 \text{ }\mu\text{m/s}$. The energy density at the spot on HgCdTe surface was 1.5 J/cm^2 .

The natural limiter of the pulse duration was the moment of laser ablation, which swallows the radiation.

The plasma by a laser ablation swallows photons and, in view of items 3 and 4, described in introduction, the principal advantage ⁹ of femto - pulses becomes unacceptable for interaction of laser radiation with semiconductor wafers.

Next problem is the repetition frequency of laser pulses. All processes in the semiconductors, after beginning of laser irradiation, only take place for a definite time. If the repetition frequency of laser pulses is less than the relaxation time of all

processes in the target, this allows lowering of the energy density. In Fig.2 the SEM - images of laser kerfs for different repetition frequencies are shown.

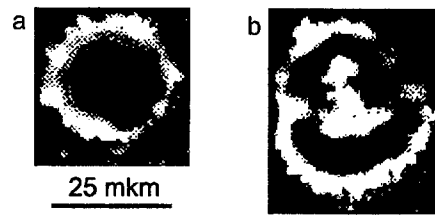


Fig.2. The SEM - images of laser kerfs for different repetition frequency: a.) the repetition frequency of laser radiation 100 Hz; b.) repetition frequency 10 Hz

Image a). The repetition frequency of laser radiation was equal to 100 Hz. On the photo one can see the presence of the recrystallized materials (Si) around the crater. If the processes of relaxation in the material have not ended before next pulse, the part of a liquid phase will be derivated. The liquid phase augments area of the heated material around the laser crater and creates conditions for self-focusing of laser radiation, that results in deepening of the laser crater. The experimental data will be discussed below.

Image b). A repetition frequency was equal to 10 Hz. The time gap between pulses of laser radiation was long enough to terminate all processes in silicon. This results in almost total absence of area with the thrown out material around the laser crater. The profile of a laser crater repeats the distribution of radiation density in the beam zone.

All above we illustrate in a graphic form.

In Fig.3 the curves of changes in diameters of throats of laser craters in silicon versus number of pulses are shown for repetition frequencies 100 Hz and 10 Hz.

The following experiment was carried out for a visual definition of area of temperature distribution around the laser crater. For the experiment, we have taken different semiconductor targets with different melting points. Dynamics of changes in throats of laser craters in different semiconductor materials as a function of number of pulses has shown good comparability of experimental results.

In Fig.4 the curves of changes in diameters of throats of laser craters for two semiconductors with different melting points ($T_{Si} = 1420^{\circ}\text{C}$ and $T_{InSb} = 525^{\circ}\text{C}$) are shown.

The curve shape analysis allows us to discriminate between three characteristic stages during formation of a laser crater.

First stage. The processes arising in the target results in distribution of thermal area around the point of interaction. The power of each incoming pulse (repetition frequency 100 Hz) is high enough to increase the temperature of heated area up to melting point. The dynamics of melting (diameters of throat of laser craters) of target material in different semiconductors is not the same. More fusible materials give faster increase of diameter of a laser crater.

The process of increase of diameter of a crater ceases, when the laser beam is not in contact with walls of a laser crater. It is where the second stage of formation of a crater begins. All material is thrown out of an interaction range in a liquid phase and in ionized state. This can be judged from the comparability of diameters of laser craters.

The third stage. When the pressure of evaporation of the material is not enough for full depletion of liquid phase (having a reflection coefficient close to 1) from the laser crater, we observe the reduction of diameter of the laser crater.

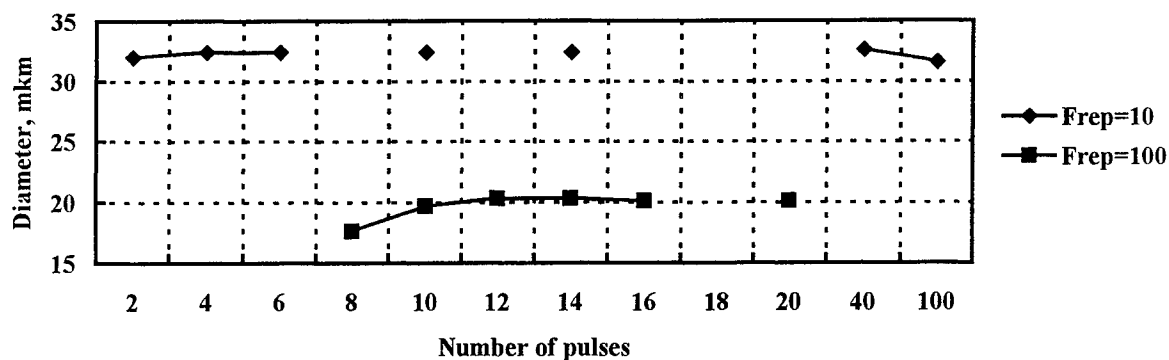


Figure 3. Diameters of throats of laser craters in silicon versus number of pulses at repetition frequencies 100 Hz and 10 Hz.

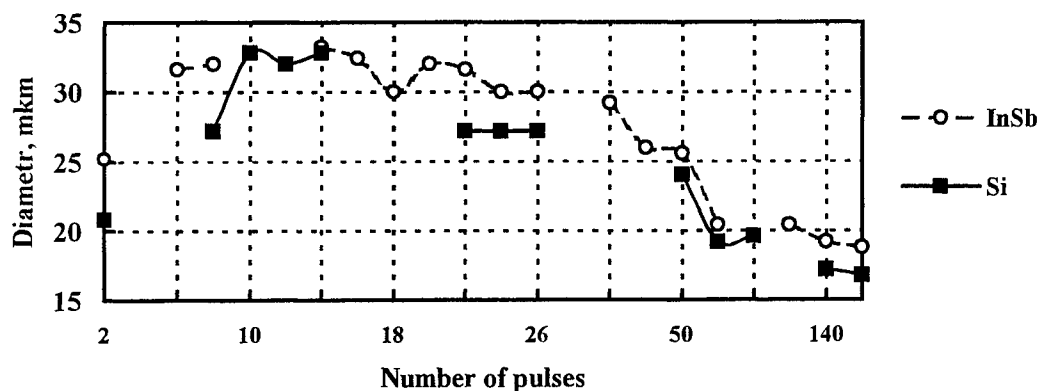


Figure 4. Diameters of throats of laser craters versus number of pulses for two semiconductors with different melting points ($T_{Si} = 1420^{\circ}\text{C}$ and $T_{InSb} = 525^{\circ}\text{C}$).

To check the above explanation of the first stage, we have carried out an experiment on measurement of changes in diameter of the laser crater from number of pulses for two semiconductor materials (InSb and HgCdTe). We used an N_2 laser with 7 ns pulse at $0.34\text{ }\mu\text{m}$. The initial laser beam had effective diameter of 2mm. From its central part we separated an area by a diaphragm $226\text{ }\mu\text{m}$ in diameter and focused it further into a spot of $3.6\text{ }\mu\text{m}$. The energy density of pulse in the target was about 1.1 J/cm^2 . The experimental data are shown in Table 1.

Table 1.

Diameter of laser kerf	$T_{\text{melting}}^{\circ} \text{C}$	Number of pulses	Number of pulses
DInSb	525	2	5
DHgCdTe	800	3,4	3,8
DinSb/DhgCdTe		3,0	3,2
		1,13	1,18

As one can see, the diameter of a laser crater in the material with lower melting point temperature grows faster.

The analysis of conditions of optimization of laser radiation for applications in semiconductors would be incomplete without considering process of derivation of depth of laser crater as a function of laser beam diameter and number of pulses.

In Fig.5 the changes of depth of a laser crater from number of pulses are shown. The laser source was an UV pulse laser at $0,34 \mu\text{m}$ wavelength with 7 ns pulses at 100 Hz repetition.

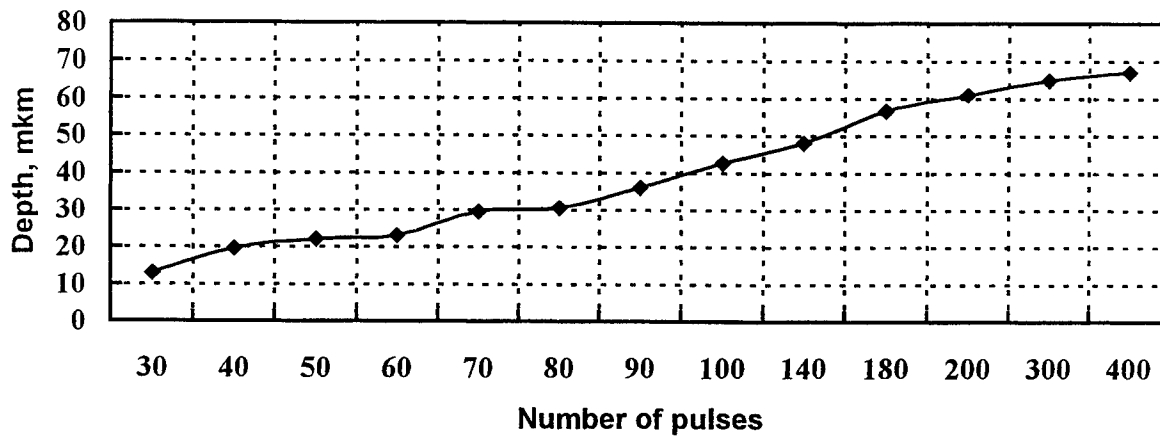


Fig.5. Changes of depth of a laser crater versus number of pulses.

To minimize the area of interaction between laser radiation and surface of semiconductor, we have carried out an experiment for studying the effect of laser beam diameter onto a value of depth to diameter ratio of a laser crater.

In Fig.6 the measured diameter and depth of the laser crater are shown as a function of number of pulses for different laser beam diameter. The analysis of the obtained data has shown that despite the reduction of depth of the laser crater, the depth to diameter ratio considerably increased. For a wide beam it attains maximum depth / maximum diameter - 3,475, for a narrow beam - 8,82. At the same time, we observed the dependence of number of pulses required for maximum of laser crater, from diameter of a laser beam.

The data in Fig.5 and 6 were calculated from SEM - images.

3. CONCLUSIONS.

It is opinion of the authors, that the main criteria that necessarily should be taken into account when doing the laser scribing of semiconductor wafers, are as follows:

Selection of a laser source wavelength with maximum coefficient of absorption in a target.

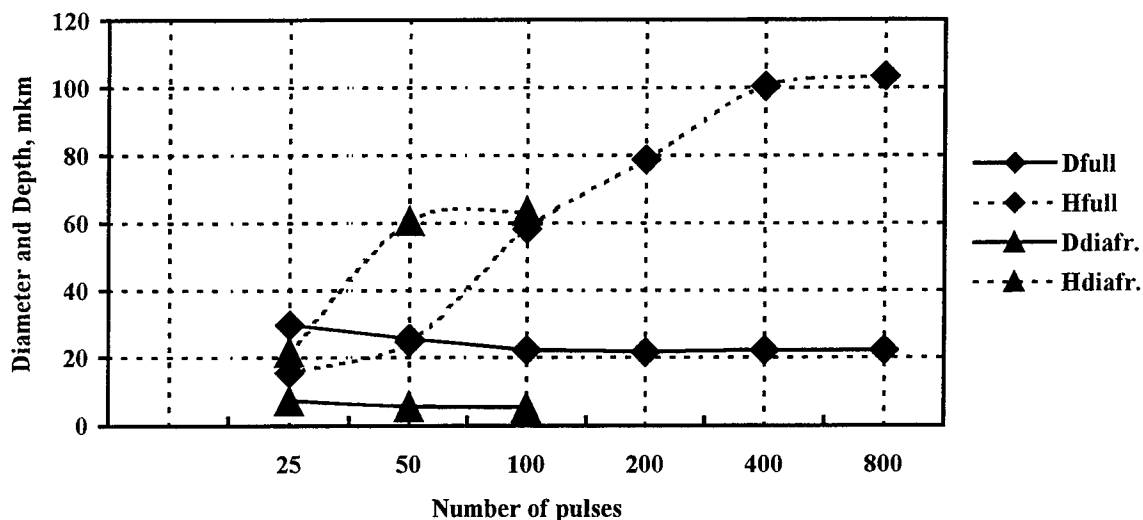


Figure 6. The experimental outcomes of diameter and depth of a laser crater via quantity of pulses, for a laser beam having different diameter.

The energy density in a laser spot on target must be less than threshold for the material;

The time gap between pulses is determined by time of the ending of processes in the material of the target.

The decrease in diameter of a laser beam allows maximum depth to diameter relation to be achieved.

The described principles of optimization of laser radiation allow minimization of areas required for laser scribing of semiconductor materials.

REFERENCES.

1. B.G. Garcia, J. Martinez, and J. Piqueras, Laser melting of GaAs covered with metal layers, J. Applied Physics A 51, pp. 437-445, 1990.
2. F. Bloch, Zs. Physics, 52, p.555, 1928.
3. A.R. Novoselov, and A.G. Klimenko, Degradation zones of semiconductor target(Si) formed as a result of nanosecond UV laser material processing, Proc. SPIE, vol. 3884, p. 269-276, 1999.
4. K. Seeger, Semiconductor Physics, Springer, Berlin, Heidelberg, 1989.
5. M.H. Pikuhn, handbook on Semiconductors, ed. By T.S. Moss, C.H. Hilsum, North - Holland, Amsterdam, v.4, p. 539, 1981.
6. R.M. Williams, K.M. Beck, A.G. Joly, J.Th. Dickinson, and W.P. Hess, Pulse-width influence on laser-induced desorption of positive ions from ionic solids, Proc. SPIE, vol. 3618, p. 37-44, 1999.
7. I. Höhnert, and M. Schink, New defect atchant for CdTe and Hg_{1-x}Cd_xTe, J. Of Crist. Growth, 101, 1990, pp. 251-255
8. A.R. Novoselov, A.G. Klimenko, D.G. Esaev, and V.V. Vasilyev, Laser scribing of HgCdTe narrow-bandgap semiconductor substrates, Avtometriya, 5, 1998, pp. 86-91.
9. X. Liu, D. Du, and G. Mourou, Laser ablation and micromachining with ultrashort laser pulses, IEEE J. Of Quantum Electronics, vol. 33(10), 1997, pp.1706-1716.

Reprography method for nondestructiveness testing micro-cracks inside wall of a pinhole micromanufactured by laser

Chenbo Zhou^{*a} Wenying Yu^a Jinzuo Sun^a Hengfu Chen^b

^aPhysics Department of Yantai University, Shangdong, China, Yantai, 264005

^bXi'an medicine University, Shanxi, China, Xi'an, 710000

ABSTRACT

A new method of reprography and detection employing scan electron microscope (SEM) for the non-destructiveness testing the micro-cracks with width about 1 μm on the inner surface of the pinhole has been presented in this paper. The results show that the new method is a feasible approach to test the micro-cracks of the inner surface of the pinhole with sub-millimeter aperture.

Keywords: Laser perforate, pinhole inner surface, micro-cracks, reprography, non-destructiveness, scan electron microscope, acetic acid hollocellulose.

1. INTRODUCTION

It's well known that high power laser, for example Nd YAG, can perforate the pinhole with sub-millimeter aperture in industry. A re-melt layer at the pinhole inner surface with many micro-cracks is born of thermal fusion effect during the perforation process by laser. The micro-crack is a serious hide danger for the work-piece and may be extend to make it rend when work-piece works in thermal environment at high speed rotation especially.

Many different technologies to test defects of the work-piece have been studied up to now, such as acoustic scan electron-microscope method^{1,2}, electromagnetism testing technogloy³, optical testing method⁴, microwave nondestructive testing⁵ and laser ultrasounics techniques^{6,7} and so on. These methods or techniques to test the work-piece were in view of the different physics aspects. Among them, acoustic scan election-microscope method was only inspected in the surface defects outside the pinhole but can't test the micro-cracks in the inner surface of the pinhole. Laser ultrasound testing method can test some bigger micro-cracks (width bigger than 100 μm) of the work-piece but can't test the micro-cracks because pulse laser was limited by the parameters of width and the diffraction effect of the laser ultrasound. None of the method or technique above can test the micro-cracks (width about 1 μm) in the pinhole inner surface with sub-millimeter aperture nondestructively. As far as we know, the method of non-destructiveness testing the micro-cracks of the pinhole inner surface with sub-millimeter aperture has not reported.

Our method of the non-destructiveness testing the micro-cracks, with a micro-cracks width about 1 μm , on the pinhole inner surface is major to fill the pinhole with acetic acid hollocellulose and solidify them at room temperature. A small cylinder is taken out from the pinhole. Its surface has a copy image of the pinhole inner surface. We can observe and take

* Correspondence: Email: rxj@sea.ytu.edu.cn; Telephone: 86 0535 6902064;

Fax: 86 0535 6903201

photo of the surface of the reprography cylinder using SEM. The inner surface of the pinhole needs polishing process if you want to obtain clearer micro-cracks images. The reprography images will be clearer where the pinhole inner surface is smooth and clean.

2. PRINCIPLE

The reprography SEM method for the non-destructively testing the micro-cracks of the pinhole inner surface perforated by laser is base on the follow principle. First, fill the pinhole with material of the acetic acid hollocellulose, then, melt the acetic acid hollocellulose using a little of acetone solvent. It will be formed a small solid cylinder after solidifying 1 to 2 hours at room temperature. The reprography material soaks into the micro-cracks of the pinhole inner surface in liquid with some viscosity. It will be shrunk and solidify gradually during solidifying process. The surface of the reprography on a cylinder which is taken out from the pinhole will be one copy pattern of the pinhole inner surface. Since the acetic acid hollocellulose has the infiltration capacity, fine particles, better tenacity, better intensity and no deformation after solidified, it is widely used to analyze the fine structure of the body surface, so can copy the actual pattern of the pinhole inner surface. In order to further improve the contrast of the reprography pattern, the small cylinder should be adhered to the small active working platform of the SEM and the ion gold-plating was plated on the surface of the reprography cylinder at 45° direction. We use the gold that is used in industry as the plating material because of its fine particles, its small atomic radius and its stronger reflectivity. Finally, the experiment results are gained to be observed and taken photo by SEM.

Since it is like a mirror image relationship between the copy pattern of the reprography object and the actual pattern of the pinhole inner surface and the opposite phase each other for the images, it has some difficulty to observe and identify image taken from the reprography object. In order to distinguish the protrusive image that is the micro-cracks image after reprography from other patterns, we choose a sample to cut one of the pinhole along lengthwise direction (axial direction of pinhole) and polish the groove of the pinhole cross section. Then we do reprography experiment on the groove of the pinhole cross section and get different reprography experiment results.

Through comparing the reprography experiment results of the groove of pinhole cross section with the non-reprography results observed by SEM, we can identify the pattern of the micro-cracks of the pinhole inner surface.

By the method mentioned above, we can observe and record the situation of the space distribution, width and continuity or interruption of the micro-cracks of the pinhole inner surface employing SEM.

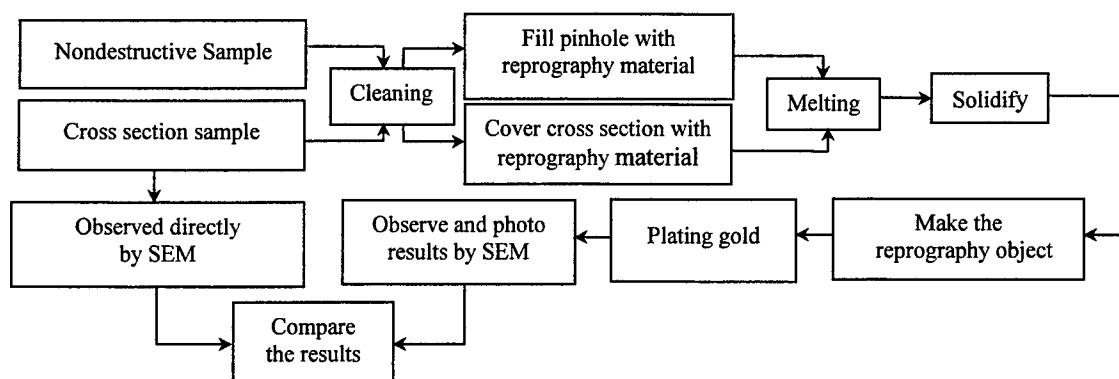


Fig. 1 Block diagram for the experiment principle of the reprography SEM method

The key process of this method is the make of the small reprography cylinder in the non-destructiveness experiment. It's a careful work and a procedure with skilled craft if you want to gain better pattern of the inner surface of the pinhole. On the other hand, it should be an experiment process to identify this kind of copy image.

Figure 1 shows the block diagram for the experiment principle of the reprography SEM method. The model of the SEM in this experiment is KYKY-2000 that is made by Factory of Apparatus, Chinese Academic of Science.

3. RESULTS

Table 1 shows the parameters of the experiment samples perforated by Nd YAG laser. Table 2 shows data of the width of the groove on the lengthwise (axial direction of pinhole) of the pinhole cross section measured actually. Table 3 shows the aperture data of the non-destructiveness pinhole measured actually. Shape of the pinhole sample with cross section is shown as Fig. 2a. Figure 2b shows the shape of the pinhole sample without cross section.

Table 1 Data of the experiment sample perforated by Nd YAG laser

Measurement data					
No.	Sample radial (mm)	Sample thickness (mm)	Pinhole number	Pinhole Radial (mm)	Material
1	13	4	3	0.8	DZ22
2	13	4	3	0.8	DZ22
3	13	4	3	0.8	DZ22
4	13	4	3	0.8	DZ22
5	13	4	3	0.8	DZ22

Table 2 Groove width on the lengthwise (axial direction of the pinhole) of the pinhole cross section

Groove width			
No.	Polished (mm)	No.	No polished (mm)
1	0.375	6	0.400
2	0.409	7	0.430
3	0.333	8	0.392
4	0.405	9	0.390
5	0.360	10	0.412
average	0.376	average	0.405

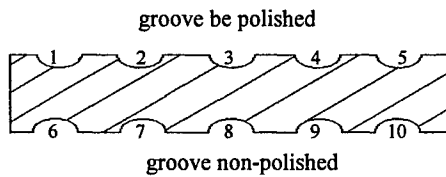
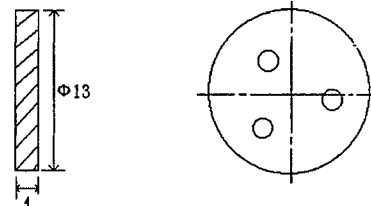
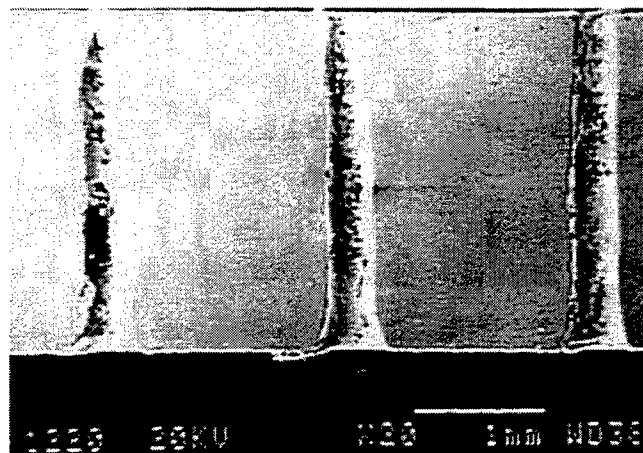
As above, in order to understand the pattern of micro-cracks on the reprography object, the cross section of the pinhole is directly observed by SEM. Figure 3 shows one micrograph of the pinhole cross section (magnification is 200). Figure 4 shows the micrograph of micro-cracks at groove of the cross section (magnification is 200). In order to observe these micro-cracks clearly, enlarged micrograph with magnification times 800 is shown in Fig. 5. Those images show that micro-cracks like cracks on the withered land.

From above experimental images, we can observe the detail of the micro-cracks with space distribution, continuity or interruption and width. We would have possessed a preliminary knowledge to the reprography method so that we will do

Table 3 Measured data of the pinhole aperture on the experiment sample

Pinhole aperture			
No.	Direction X(mm)	Direction Y(mm)	Average Radial(mm)
1	1.185	1.350	1.268
2	1.240	2.075	1.658
3	1.440	1.200	1.320
4	1.315	1.210	1.263
5	0.860	0.813	0.837
6	0.820	0.791	0.806

next step. Then we observe the micro-cracks and take photo them as follow two methods. The one is to observe them via SEM directly. The another is to copy them through reprography object. These two methods work on a fixed part of one pinhole and to compare the results between the two. Figure 6 shows the enlarged micrograph of the micro-cracks on the re-melt layer of the cross section of pinhole inner surface in lengthwise direction (axial direction) photo via SEM directly (magnification is 203). Figure 7 shows the enlarged micrograph reprography image corresponding part with Fig. 6. Through analyzing and compression, we do further study on reprography about non-destructiveness pinhole. Figure 8 shows the enlargement image observed by SEM on the reprography object of the inner surface of the pinhole after polishing process. This result shows that the pattern of the micro-cracks of the pinhole inner surface with sub-millimeter aperture can be obtained by reprography method although it has some difficult to make the reprography cylinder.

**Fig. 2a** Shape of the pinhole sample with cross section**Fig. 2b** Shape of the pinhole sample without cross section**Fig. 3** Micrograph of the pinhole cross section (magnification 20)

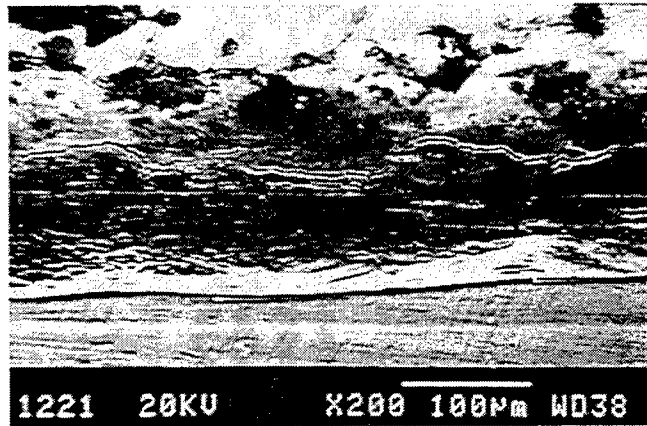


Fig. 4 Micrograph of micro-cracks at groove of the cross section (magnification 200)

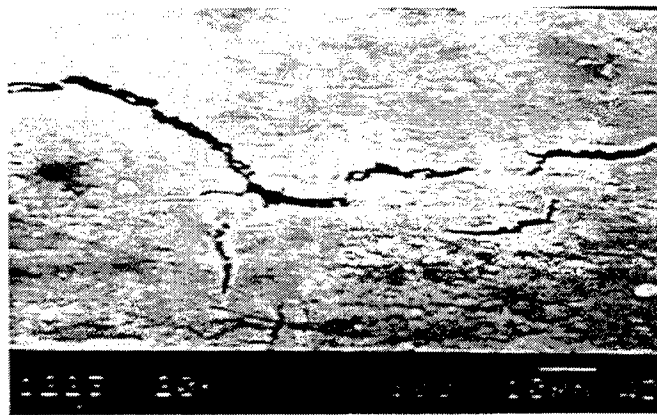


Fig. 5 Enlarged micrograph corresponding with Fig.4 (magnification 800)

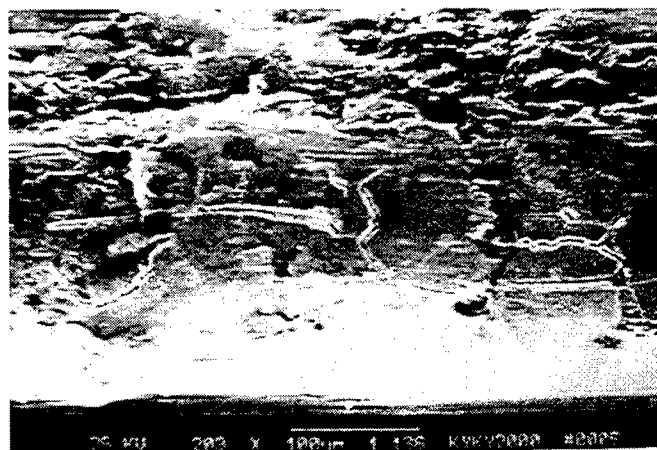


Fig. 6 Enlarged micrograph of the micro-cracks on the re-melt layer of the pinhole cross section (axial direction)

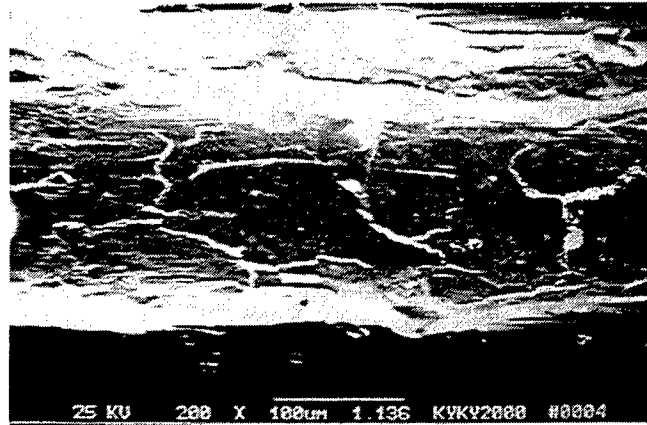


Fig. 7 Enlarged micrograph reprography image corresponding part with Fig. 6

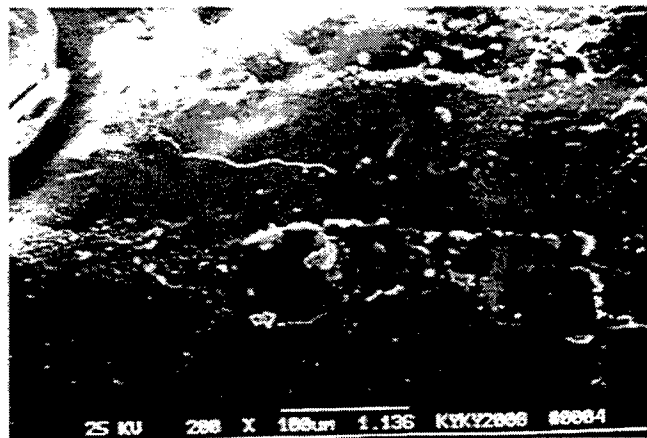


Fig. 8 Enlargement image on the reprography object of the pinhole inner surface after polishing process

4. DISCUSSION AND CONCLUSION

The study on the experiments and results show the feasibility of the reprography SEM method for the micro-cracks of the pinhole inner surface with sub-millimeter aperture perforated by laser. From the experiment results, the image taken by SEM directly and the image taken from reprography object is phase reversal image each other and the micro-cracks are black in the image taken by SEM directly. The reason is the electron-beam is stray reflected by the inner surface of the micro-cracks and its energy fades out when the electron-beam enter the micro-cracks. The residual weak reflected random beam couldn't be reflected into the collection system of the electron microscope. In the other words, the scatter electron-beam is reflected out of the collection aperture of the electron microscope so that fringes are black. The micro-cracks on the reprography object look like bellied because they are plated by total-reflection material so that electron number being reflected from part of micro-cracks is different from that of other parts. That is why the shape of the micro-cracks is light-white in the image.

The key of the testing work is to make micro reprography cylinder with sub-millimeter aperture during the research process. It should be fill the pinhole with acetic acid hollocellulose completely and appressed to the pinhole inner surface

tightly after melting and solidification. This will ensure that the reprography object will reflect the pattern of pinhole inner surface actually. In addition, it's necessary to polish and clean the pinhole inner surface because the inner surface of the pinhole perforated by the laser is not smooth. This will effect the distinguishability of the reprography. Smoothing and cleaning the inner surface will make the reprography work better.

It's easy to distinguish whether there are micro-cracks and the shape of the micro-cracks by comparing the reprography results of the pinhole being crossed and non-destructived.

In conclusion, the reprography method for the non-destructiveness test to the micro-cracks of the pinhole inner surface perforated by laser is a feasible technology approach. No special request is required for the work-piece material in this method.

ACKNOWLEDGMENTS

The authors would like to express their appreciation to Jian Wang and Xianbing Zhang from Beijing Aviation Technology Institute and to Rongxi Jiang from Physics Department of Yantai University for their useful discussions on our research work.

REFERENCES

1. Quate C F, "Acoustic Microcopy with Mechanical Scanning", *A Review Proceeding IEEE*, **67**, 1979.
2. Er Guan, Siping He, *et al*, "Test of Art Defects for Laser Perforation", *Journal of Experimental Mechanics (China)*, **12**(1), 1997.
3. John H Floract, *et al*, "Deep Penetration Eddy Current Applications", 11th, WCNDT, 1990.
4. Guanchang Jin, "Optical Nondestructive Testing and It's Industry Applications", *Applied Laser (China)*, **10**(1), 1990.
5. Zaiqi Zhou, "Development of Microwave Nondestructive Testing in Aerospace Industry ", *NDT (China)*, **17**(10), 1995.
6. Andrew D M, Robert C A Jr, "Practical Considerations for The Rapid Inspection of Composite Materials Using Laser-Based Ultrasound", *Ultrasonics*, **32**(5), pp.333-345, 1994.
7. Xingeng Zhou, Cunfu He, "Laser Ultrasonics Techniques for Nondestructive Testing", *Journal Of Experimental Mechanics (China)*, **11**(4), 1996.

A MODEL PREDICTING THE MICROHOLE PROFILES OF LASER DRILLING PROCESSES IN CARBON FIBER COMPOSITES

Fushun Wu*, Richard D. Pilkington
Department of Physics, Salford University, Salford M5 4WT, UK

ABSTRACT: Laser induced ablation of materials has become an extremely important area of research and application. The laser sources for ablation cover the wavelengths from ultraviolet (most are excimer lasers), visible (copper vapor lasers, argon ion lasers) to the infrared (Nd:YAG lasers, CO₂ lasers). The laser material processing technique is intensely used in both the electronic and aerospace industries. In this paper, a new theoretical model describing laser microhole drilling processes in carbon fiber composites (CFC) has been developed, which can predict the profiles of the microholes for certain incident beam profiles. The calculated results for several specific incident beams will be presented in this paper. We show how the peak fluence, the beam diameter, and the material parameters (absorption coefficient, threshold ablation fluence) affect the hole shapes. Although the model is specific to CFC, it can be applied to any other laser micromachining process for materials such as polyimide, polymethylmethacrylate (PMMA), polyethylene terephthalate (PET) *etc.*

We not only present a new method to model the drilling hole profiles but also explain why hole drilling will stop under certain circumstances in the low fluence regime for polymers and fiber reinforced composites. The model explains tapered wall formation and stabilized drilling, from which, high efficient laser drilling and cutting can be predicted in low fluence regimes. This new model is suitable for most well defined beams and materials such as polymers, fiber CFC, glass fiber composites and some ceramics.

Key Words: laser microhole drilling, hole profile, modeling.

1. INTRODUCTION

A new theoretical model describing excimer laser hole drilling processes for polymers and fiber reinforced composites (FRC) has been developed. The model not only explains the tapered wall formation and stabilized hole formation but also can predict the hole shapes for certain incident beam profiles such as Gaussian incident beams, diffraction beams, triangle beams and isosceles trapezoid beams, which was confirmed with experimental data.

Laser induced ablation of materials has become an extremely important area of research and application. The laser sources for ablation cover the wavelengths from ultraviolet (most are excimer lasers), visible (copper vapour lasers, argon ion lasers) to the infrared (Nd:YAG lasers, CO₂ lasers). The laser material processing technique is intensely used in both the electronic and aerospace industries.

The first report using pulsed UV-laser radiation for organic material was published in 1982 [1]. Since then, intense research activities have been carried out in this area [2-6] due to the many applications in electronic and other manufacturing processes. At present, the processing materials are mainly polyimide (Dupont KaptonTM) [6-8] (used in electronic packing industry), polymethylmethacrylate (PMMA) [9-11], polyethylene-terephthalate (PET) [12-13], ceramics (with organic polymer binding) [14], and polyphenylquinoxaline (PPQ) (a thermostable polymer used in microelectronics) [15]. Carbon fiber composites (CFCs) are also studied intensely because of their applications as acoustic damping panels in the aerospace industry [16-17].

Most of the theoretical models published are based on thermal diffusion equations [18-20] and because of its complication most models do not give a directly obvious relationship of how the laser parameters affect the related ablation rate, drilling depth and drilling shape. Most experimental works [2-15] confirm that the laser ablation for polymers and fiber reinforced composites obeys the simple Beer's law. There are several publications to establish simple models for the ablation rate with modified Beer's law [15, 21-43]. Although occasionally there are conical [44], domelike [7, 45-46], trapezoidal or V [6] shaped holes reported, only Olson and Swope [14] calculated the Gaussian beam drilling hole profiles, however their model is restricted to only one pulse and can not explain the stabilized hole formation in the low fluence regime. In this paper, we not only present a new simple method to model the drilling hole profiles but also explain why hole drilling will stop under

* Current address: ALFT, Inc., 189 Deveau St., #7, Hull, P.Q. Canada J8Z 1S7

certain circumstances in the low fluence regime for polymers and fiber reinforced composites. This model is not suitable for high fluence regimes and for materials like metals. For laser ablation in the high fluence regime, it is believed that there are other mechanisms involved, which will be discussed in the future.

2. BASIC THEORY

The model is presented for pulsed laser ablation or etching; however, the final results can be extended to continuous wave (cw) laser ablation. It is believed that hole drilling is more efficient with multiple laser pulses of low fluence than with a single high fluence pulse [47]. This model addresses the multiple pulse hole drilling case. In the calculations, the laser pulse width is not considered due to the narrow range of pulse widths (15~35 ns) of excimer lasers, and because of this, fluences instead of power intensities are normally used in descriptions of excimer lasers and their ablation processes. The ablation process is generally regarded as a photo-decomposition or cool ablation process instead of photothermal process [48-50]; therefore, the threshold fluence and the absorption coefficient are used, rather than the other material parameters such as: specific heat, vapor temperature and thermal diffusivity, *etc.*

At present, an excimer laser pulse can remove one micrometer to several micrometers of organic or FRC materials. The fluences involved range from tenths of a joule to several joules per square centimeter. In the low fluence regime, there are two general points which are accepted:

- (1). A threshold fluence exists, below which the ablation is greatly reduced or nearly zero. If the input fluence is higher than the threshold, there is significant material removal. Thresholds depend on the materials and laser wavelengths.
- (2). The etch depth per pulse for all the organic material ablations follow Beer's law, that is:

$$\Delta H = \frac{1}{\alpha} \ln \left(\frac{F}{F_T} \right) \quad (2.1)$$

where ΔH is the ablation depth per pulse, F is the incident fluence (J/cm^2), F_T is the threshold fluence which is decided by experiments and α is the effective absorption coefficient of the material.

If the laser beam has a Gaussian profile, from equation (2.1), it can be found that the ablation rate is different in space because of fluence variations and a hole with sloping walls will be built up under this beam action. Even for a uniform beam profile, there may exist two sloping wings (Figure 9). Therefore, for a uniform beam, an oblique wall can be formed in the sloping wing corresponding region. Once the oblique wall is formed in the drilling process, the effect of a laser acting on a oblique surface is different from it perpendicularly acting on a surface.

2.1 Theoretical ideas

When a laser beam with fluence F is propagated at angle θ incident to the ablation surface, the effect of the fluence acting on the oblique surface must be considered. The idea is shown in Figure 1, which represents a very small finite element. From the diagram, the energy incident to the normal area ΔS is $E = F \times \Delta S$, where F is the measured incident fluence (J/cm^2). From the law of conservation of energy, the same energy will act on the oblique surface with area $\Delta S'$, therefore the fluence acting on the oblique surface can be written as:

$$F' = \frac{E}{\Delta S'} = \frac{F \times \Delta S}{\Delta S'} = \frac{F \times (a \times b)}{(b \times c)} = \frac{F \times a}{a / \cos(\beta)} = F \cos(\beta) = F \sin(\theta) \quad (2.2)$$

The fluence F' obeys the threshold condition, that is, if $F' \leq F_T$, ablation stops for the incident beam with incident fluence F . Therefore, the incident fluence threshold condition becomes $F \sin(\theta) = F_T$. When the beam is vertically incident to the surface, $F' = F$ and ablation only exists if $F \geq F_T$. If the beam is parallel to the surface, $F' = 0 < F_T$, there is no ablation. In this paper, these conditions are used to model the hole drilling profiles and to analyze calculated results.

In the low fluence regime, the threshold fluence keeps constant. In the modeling process, we assume that the light intensity along the light transmission direction is uniform, that is, the light intensity is not changing along the hole drilling direction during the drilling process.

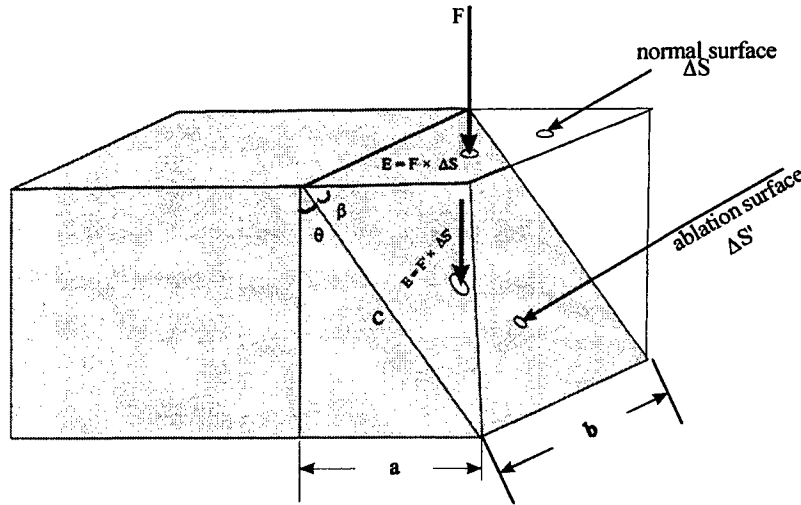


Figure 1. The schematic diagram of an incident beam acting on an oblique wall, θ is the wall angle.

Using equation (2.1) and condition $F \sin(\theta) = F_T$, the model for the hole drilling process was established. If the etch depth at the N th shot is ΔH_N , after N shots, the total etch depth at point x is $H = \Delta H_1 + \Delta H_2 + \Delta H_3 + \dots + \Delta H_N$. With more shots, the wall angle θ will decrease. At some points, the angle θ will satisfy $F' = F \sin(\theta) = F_T$ and there is no further ablation. At some other points, more than N shots may be needed to satisfy the condition. Therefore, after a certain number of shots, there exist some points where etching stops. This is called a stabilized hole.

3 CALCULATIONS AND CONCLUSIONS FOR GAUSSIAN INCIDENT BEAMS

3.1 Calculated hole drilling shapes with Gaussian incident beams

The expression for the incident laser Gaussian beam shape is described as:

$$F(x) = F_0 \exp \left\{ -\left(\frac{x}{r} \right)^2 \right\} \quad (3.1)$$

Where $F(x)$ is the fluence at the point x . F_0 is the peak fluence of the laser beam at $x = 0$. x is described as the beam intensity distribution and r is the Gaussian beam waist radius (fluence reduces from maximum to e^{-1} point). The beam shape is shown in Figure 2a.

The hole drilling process shown in Figure 2b utilizes a Gaussian beam with a peak fluence of 2.5 J/cm^2 , beam radius of $100 \mu\text{m}$, threshold fluence of 0.5 J/cm^2 and effective absorption coefficient of $5 \mu\text{m}^{-1}$. From Figure 2b, it is clear that for certain incident beam parameters and processing materials, there exists a stabilized hole with a maximum hole drilling depth. Also, the ablation rate will reduce at the bottom of the hole and the high-speed ablation regime is at the upper part of the hole drilling. For Gaussian beams, to get efficient drilling, the material thickness should be less than 80% of the maximum drilling depth. The number of shots corresponding to the 80% of the maximum drilling depth was called as efficient shots. Here, the ablation rate for the efficient shots is higher than that of non-efficient shots. According to the example shown in Figure 2b, the maximum number of shots corresponding to the maximum depth is about 2000. If 5000 shots are used for the hole drilling, about 3000 of these will not contribute to the ablation process and their energy will partially transfer to heat which may cause heat damage or a bigger heat affected zone (HAZ), especially with high repetition rate laser processing [51] or for low thermal conductivity materials.

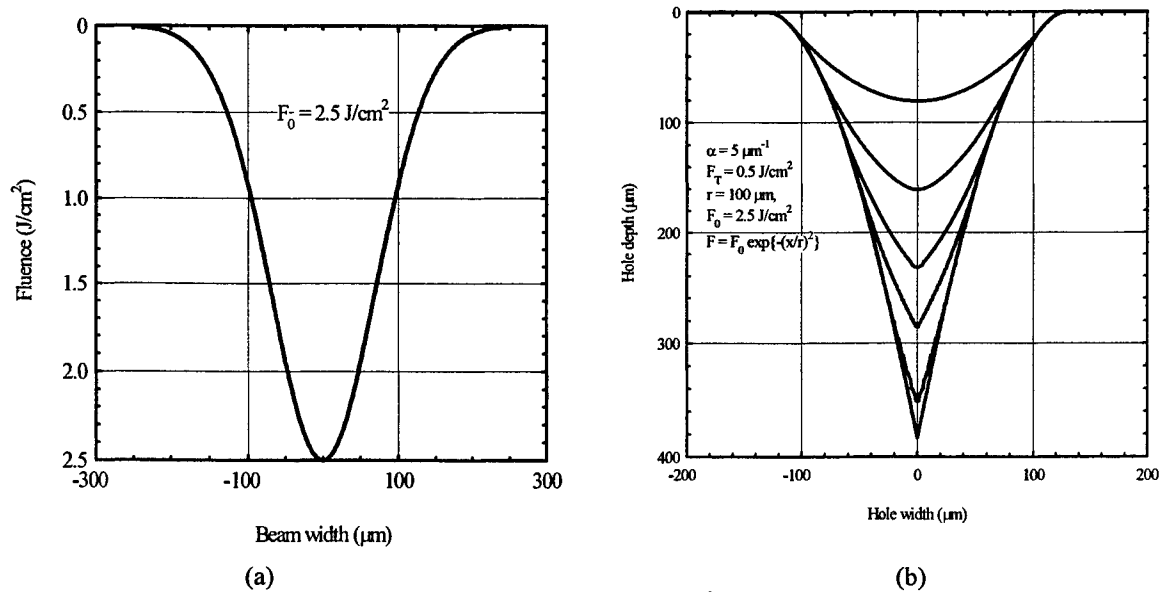


Figure 2. (a). The incident Gaussian beam, peak fluence $F_0 = 2.5 \text{ J/cm}^2$, beam radius $r = 100 \mu\text{m}$. (b). Hole drilling process, $F_T = 0.5 \text{ J/cm}^2$, $F_0 = 2.5 \text{ J/cm}^2$, curves from top to bottom corresponding to 250, 500, 750, 1000, 1500, 2000 shots.

In the modeling process, it was found that the effective absorption coefficient has no direct effect on the final hole shape although there may exist a connection between the threshold fluence and the absorption coefficient [25]. This conclusion was also made by Olson and Swope [14]. However, the effective absorption coefficient affects the drilling speed and the maximum number of effective shots. In further calculations, the effective absorption coefficient was not considered and only the parameters such as threshold fluence, incident fluence and beam width were included.

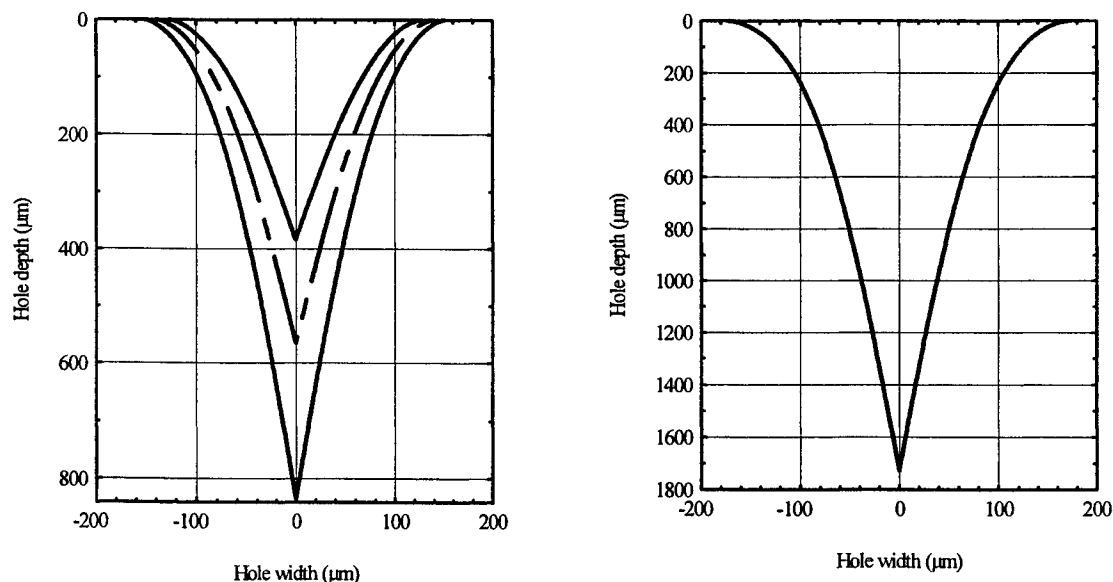


Figure 3. The final hole shapes for different incident fluences. (left). Curves from top to bottom corresponding to peak fluence 2.5, 3.3, 5 J/cm². (right). Peak fluence of 10 J/cm²; threshold fluence 0.5 J/cm², beam radius 100 μm. If the ratio of the peak fluence to the threshold fluence (F_0/F_T) is constant, the hole shapes are same. The graphs are not drawn to ratio.

Figure 3 shows how the incident fluence theoretically affects the hole drilling depths and shapes. In the calculations, it was

found that the ratio of incident fluence to threshold fluence is a key factor affecting the drilling process. From Figure 3, it can be seen that under the same Gaussian beam radius using a same material, the final hole depth and the entrance hole width will increase with the increasing incident fluence. It is also inferred that for different materials, the final hole depth and the entrance width are bigger for the low threshold fluence materials than for the high threshold fluence materials. Figure 3 shows a blind hole drilling case, in which the material thickness is assumed to be unlimited or the material is too thick to drill through. If the processing material has a certain thickness such as 500 μm , a beam with specific parameters may drill through while another may not. For a drilling through hole, it was found that the exit hole width is decided by the material thickness, the threshold fluence, the incident peak fluence, the beam width, shot number and effective absorption coefficient, which is shown in Table 1.. In general, the exit hole width increases with the increment of peak fluence.

Table 1 The relationships of the hole shapes and the incident beam parameters

Incident beam parameters	Hole shape parameters
Peak fluence \uparrow or threshold fluence \downarrow	Hole width and depth \uparrow
Peak fluence \uparrow	Hole slope \uparrow
Peak fluence \uparrow	Exit hole width \uparrow
F_0/F_T constant	Hole shape does not change
Beam width \uparrow	Hole depth, hole entrance width \uparrow

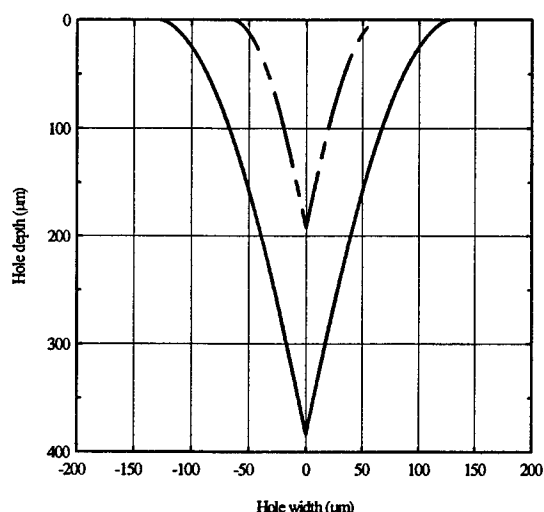


Figure 4. Calculated results under same incident peak fluence 5 J/cm² and threshold fluence 0.5 J/cm², but with two different beam widths. Upper curve: beam width 2r = 100 μm ; Lower curve: beam width 2r = 200 μm .

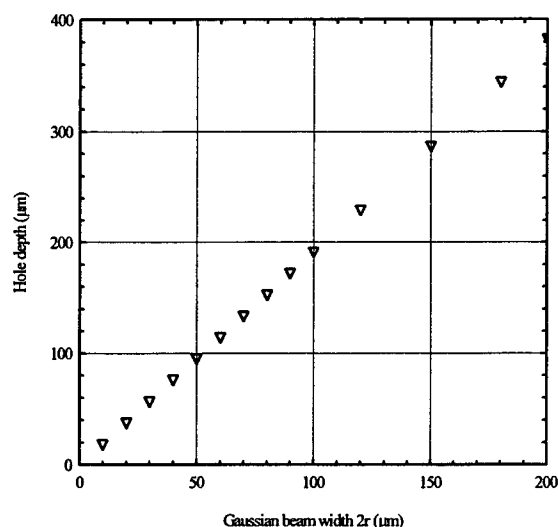


Figure 5. The relationship of the calculated hole width and depth under same incident fluence.

Figure 4 shows the calculated results for the same incident peak fluence of 5 J/cm² with two different beam widths (upper curve: 2r = 100 μm ; lower curve: 2r = 200 μm). It can be seen that, with a Gaussian incident beam, the bigger the beam width, the deeper the hole drilling depth and the wider the entrance hole width. The relationship of the calculated hole width and depth is shown in Figure 5 for a Gaussian incident beam with the peak fluence of 5 J/cm² and threshold fluence of 0.5 J/cm². The hole drilling depth and the entrance hole width are linearly proportional to the beam width. For the Gaussian beam, the ratio of depth to width of the hole is not affected by the beam width under the same peak fluence.

3.2 Conclusions from the theoretical calculations

From the above calculations, in the low fluence regime the following conclusions were made:

- (1). A stabilized hole profile exists. Under the same incident beam width $2r$, the entrance hole width (W_{in}) and drilling depth (H_{max}) increase with the increment of the incident laser peak fluence F_0 or the decrease of the material threshold fluence F_T , that is, if $F_0 \uparrow$ (or $F_T \downarrow$), $W_{in} \uparrow$ and $H_{max} \uparrow$. For a drilling through hole, the exit hole width increases with the increment of peak fluence, that is, if $F_0 \uparrow$, $W_{exit} \uparrow$.
- (2). Under the same incident beam width, a higher peak fluence (or lower threshold fluence) produces a steeper hole, i.e., if $F_0 \uparrow$, $\theta \downarrow$.
- (3). Under the same incident laser beam width, if the ratio (F_0/F_T) of the peak fluence to the threshold fluence is constant, the final results are constant. This is only true in a low incident fluence regime.
- (4). Under the same peak fluence F_0 and the material threshold F_T , the hole entrance width and the hole depth increase proportionally with incident beam width, i.e., H_{max} and $W_{in} \propto r$. The hole shape (the ratio of depth to width) will be constant. Therefore, a deep hole can be drilled with a big beam width, however the entrance hole width will be large. If the peak fluence for a Gaussian beam is fixed, the drilling hole depth is decided by the beam width.
- (5). There exists a maximum drilling depth for a certain incident beam. The corresponding shot number is called the maximum shot N_c which is decided by the maximum hole depth, the effective absorption coefficient, the peak fluence and the threshold fluence. Beyond the maximum number of effective shots N_c , there is no more etching even if more shots are used. Therefore, the final hole has no relationship with the total shots N , if N is bigger than N_c . In fact, the shots beyond the number of high efficient shots should be avoided, as their energy transfers into heat which may cause heat damage or unnecessary big HAZ.

The final hole shape is decided by the beam width parameter r , the incident beam peak fluence F_0 and the material ablation threshold fluence F_T .

- (6). The final hole shape has no direct relationship with the material's effective absorption coefficient. However, the absorption coefficient affects the hole drilling speed and the maximum number of effective shot N_c .

4. CALCULATED HOLE DRILLING PROFILES FOR DIFFRACTION INCIDENT BEAMS

One of the important applications for many industries is the manufacture of porous panels and acoustic damping panels [16-17], *etc.* The processing surface can be several square meters while the typical hole diameter is only about 100 μm with hole intensities of around $4 \times 10^6 \text{ J/m}^2$. To maximize the laser drilling speed, a highly efficient beam delivery system is required, including diffractive optical elements (DOEs). It is therefore important to calculate the required parameters before carrying out the ablation process.

The diffraction beam for a rectangular aperture can be expressed by [51]:

$$I(x) = I_0 \left(\frac{\sin(\psi)}{\psi} \right)^2, \quad \psi = \frac{\pi x}{D} \quad (4.1)$$

where $x = 0$ is the center of the aperture, the half length of aperture along one direction D is very small, and x is a position along the D direction.

For a circular aperture, $I(x) = I_0 \left(\frac{2J_1(x)}{x} \right)^2$, $x = \frac{1.22 \pi r}{R}$, where $J_1(x)$ is the first order of Bessel function. Here, we only discuss the diffraction for a rectangular aperture.

Figure 6 shows the final hole shapes for different incident fluences, curves from top to bottom corresponding to peak fluence 2.5, 3.5, 5 and 10 J/cm^2 , threshold fluence 0.5 J/cm^2 , aperture half width 100 μm . The diffraction beam profile is defined by equation (4.1).

Comparing the calculated results of the Gaussian beams (shown in Figure 3) and the diffracted beams, it was found that under the same peak fluence, the final hole depth using a diffracted beam is much less than that using a Gaussian beam. This is because there is substantial fluence beyond the beam waist for a Gaussian beam but not for a diffracted beam.

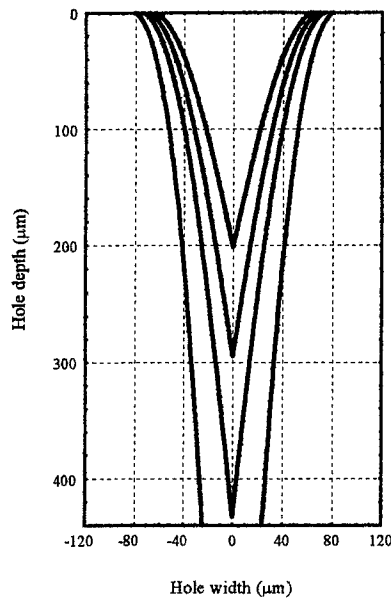


Figure 6. The final hole shapes for different incident fluences, curves from top to bottom corresponding to peak fluence 2.5, 3.5, 5 and 10 J/cm^2 , threshold fluence 0.5 J/cm^2 , aperture half width 100 μm .

5. CALCULATIONS FOR TRIANGLE SHAPE BEAMS

A similar approach is used as that for the Gaussian incident beams and the diffraction beams.

Figure 7(b) shows the calculated hole drilling shape corresponding to the incident beam shown in Figure 7(a). The incident peak fluence was 10 J/cm^2 and the threshold fluence was 1 J/cm^2 . The incident beam width was 20 length units as shown in Figure 7(b).

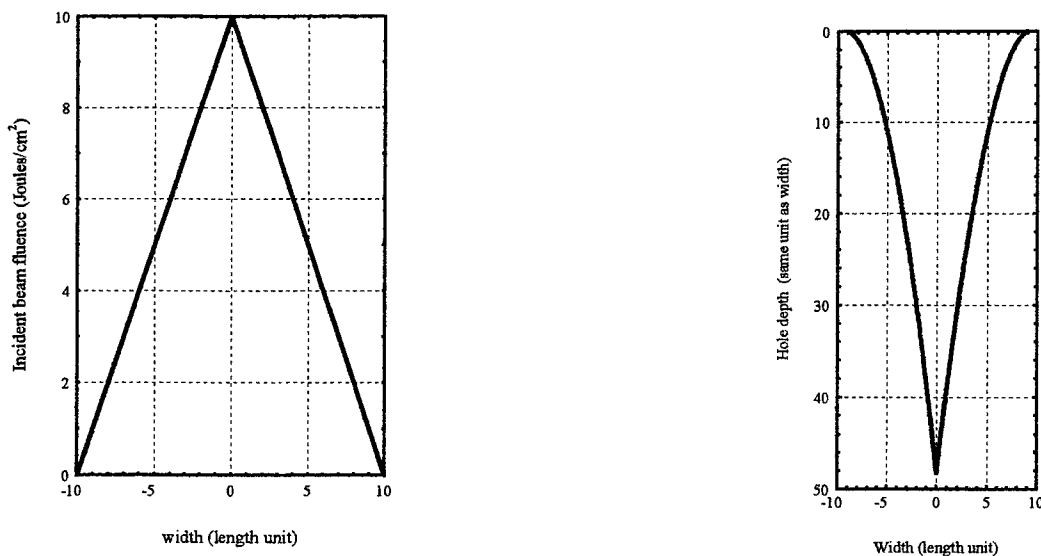


Figure 7. (a). left, the triangular incident beam, peak fluence 10 J/cm^2 , beam width 20 length unit.
(b). right, the calculated hole drilling shape, threshold fluence 1 J/cm^2 .

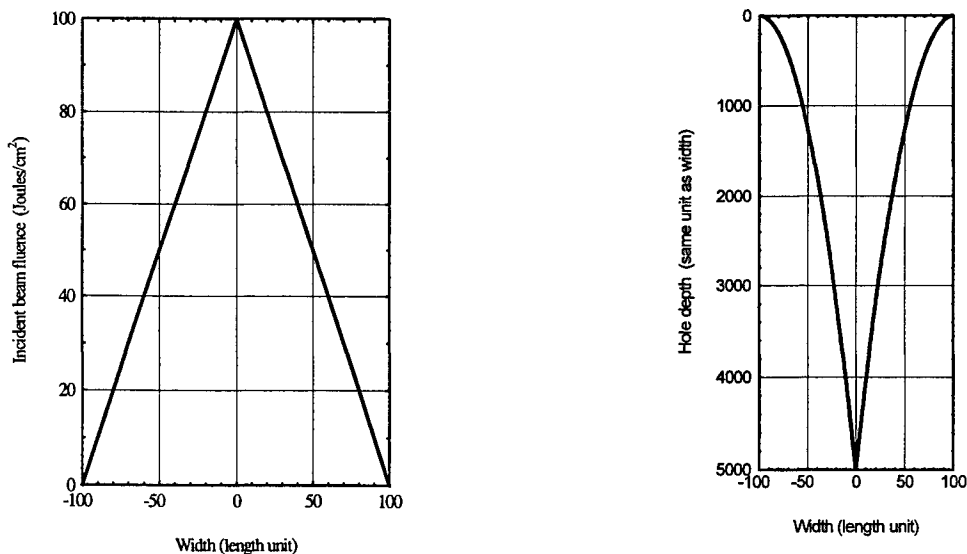


Figure 8. (a). left, the triangular incident beam, peak fluence 100 J/cm², beam width 200 length unit.
(b). right, the calculated hole drilling shape, threshold fluence 1 J/cm².

Similarly, Figure 8(b) shows the calculated hole drilling shape corresponding to the incident beam shown in Figure 8(a). The incident peak fluence was 100 J/cm² and the threshold fluence was 1 J/cm². The incident beam width was 200 length units as was in Figure 8(b). Note, Figure 8(b) is not drawn to scale due to the large ratio of hole depth to the hole width.

Conclusions:

Most of the conclusions for Gaussian incident beams are valid for the triangle incident beams, such as: the hole width and the hole depth increase with the incident fluence, the entrance hole and exit hole widths increase with the incident fluence, the hole depth increases with beam width, *etc.* However, the drilling depth, the degree of the sloping wall and the entrance width are different to the Gaussian beam even for the same incident fluence.

6 CALCULATIONS FOR FLAT SHAPE BEAMS

6.1 Calculations for the isosceles trapezoid shape beams

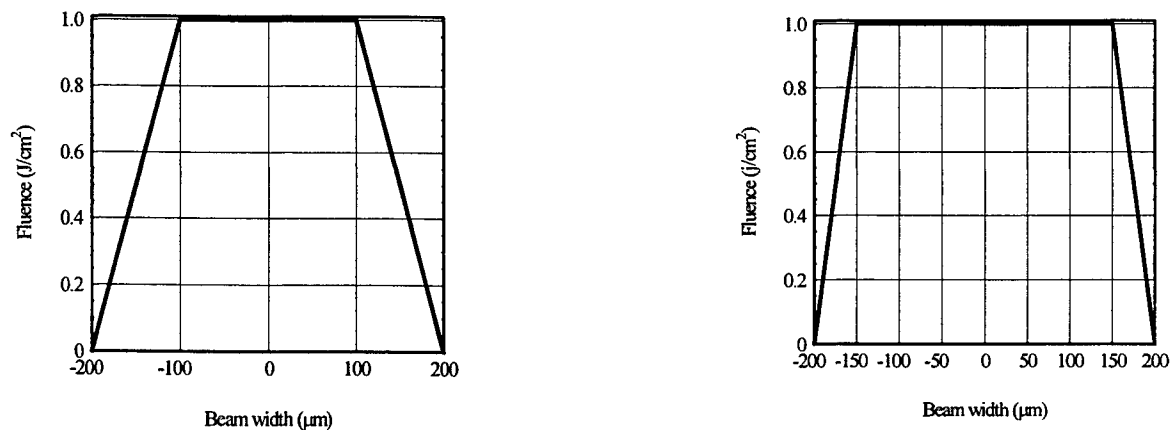


Figure 9. The trapezoidal incident beam shapes.

For most excimer lasers, the incident beam has a flat top with two sloping wings. Therefore, modeling for this beam shape is important. The two side wings can be of various shapes such as Gaussian, linear or some other shapes which can not be easily described by a simple function. The model can cover all of these beam shapes, however, we only present results for linear side wings for simplification. Figure 9 shows the incident beam shapes.

Comparing with the Gaussian incident beam, the trapezoidal shape beam is more complicated. For the drilling wall corresponding to the two side wings, it is easy to understand that a tapered wall is formed. For the plane wave part, there are two possible proposals:

(1). *High fluence vertically drill through*; the hole shape will have a flared entrance with vertical bottom. It is believed this could happen when a certain width and certain high fluence beam drills through a certain thickness of material.

(2). *Low fluence keeps the same angle corresponding to the top point of the side wings, i.e. a tapered hole*; initially the hole shape has oblique walls and a flat bottom. As more ablation takes place, the hole width narrows reducing the flat base to a zero width i.e. a point. The following two possible mechanisms may explain this phenomenon:

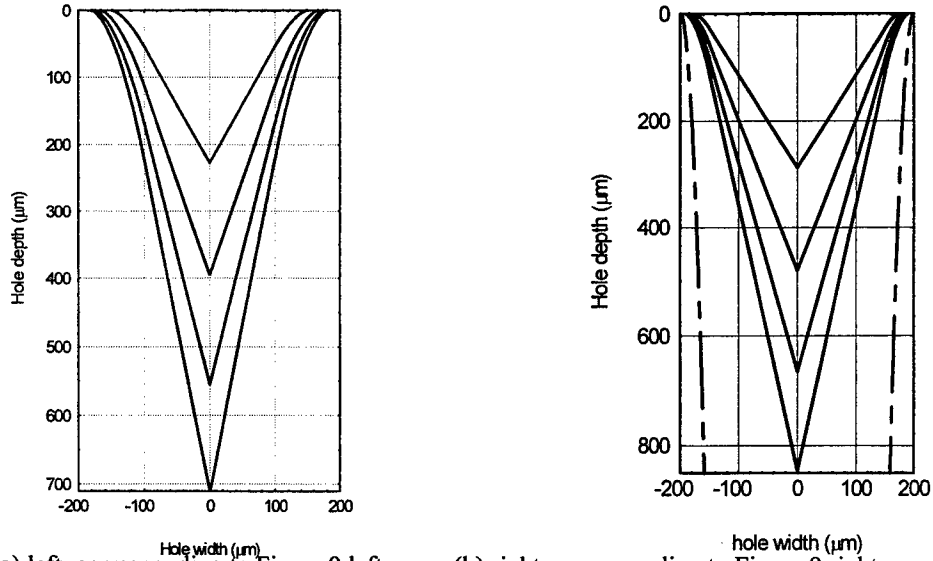
- A. Referring to Figure 2 for the Gaussian beam, the flat point corresponding to the peak fluence disappears at the bottom of the hole.
- B. The second possible mechanism may be due to the reflected beam. At the beginning of the ablation process, because the wall is shallow and the reflection is very small, the reflected beam has little or no contribution to the reduction of the flat bottom. After a certain number of shots, the sidewall corresponding to the side wings will stabilize and a minimum wall angle corresponding to the maximum side wing fluence is established which satisfies:

$$\theta = \arcsin\left(\frac{F_T}{F_0}\right) \quad (6.1)$$

Once this condition is satisfied, a shallow "pedal trenching" may exist at the joint of the flat bottom and the sloping wall due to the reflected beam. The pedal trenching will assist the erosion of the flat base until its width is zero. Because the incident fluence is constant, the wall angle will also be constant until the hole width is nearly zero. The wall angle corresponding to the flat top fluence also satisfies $\theta = \arcsin(F_T / F_0)$, where F_0 is the flat top fluence. This model coincides with an empirical conclusion from Dyer and Sidhu [44].

If the beam width is large and the material is very thin, using proposal (1) produces an acceptable result. As an example, the dashed line in Figure 10(b) shows a result for 20 J/cm² incident fluence. For this high fluence, it is believed that there are other mechanisms involved as well as the mechanism described in proposal (1). However, in most circumstances, proposal (1) does not provide an overall explanation to model the high fluence regime.

From Figure 10, it can be seen that there exists a final stabilized hole shape for a trapezoidal shape incident beam. The hole shape has a flared entrance and conical bottom. The flared entrance is also decided by the sloping wings. From these figures, it can be ascertained that the higher the fluence, the smaller the flared entrance and steeper the hole walls. If pass through drilling is considered, the exit hole diameter increases with fluence increment. This is not suitable for the high fluence case, where, the exit hole is decided by the beam diameter. From Figure 11, it can be seen that the longer (or smaller sloping value) the sloping wings, the shallower the entrance hole; the steeper the beam edge, the steeper the drilling entrance hole. Most of the conclusions for the Gaussian beam are suitable for the trapezoid incident beam except conclusions (3) and (4), however, it is still true that the hole depth increases with the increment of beam width for conclusion (4). If the side wings are very steep, the drilling depth increases approximately linearly with the beam width. Unlike the Gaussian beam, a flat top always exists until its width becomes zero.



(a) left, corresponding to Figure 9 left. (b) right, corresponding to Figure 9 right.
Figure 10. The hole drilling shape for a trapezoid beam, curves from top to bottom corresponding to flat top fluence 0.8, 1.2, 1.6, 2 J/cm² for threshold 0.4 J/cm²; the dash line in Figure 10(b) corresponding to incident fluence 20 J/cm².

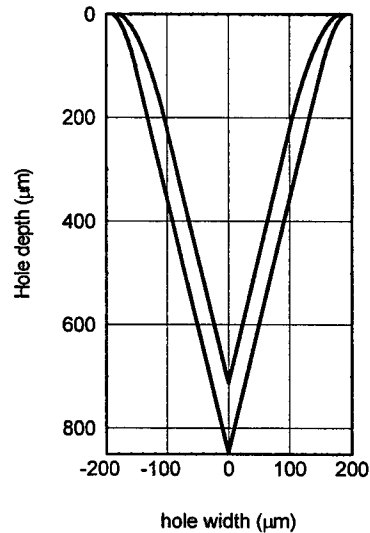


Figure 11. Comparison of two incident beam profiles. The incident beam peak fluence is 2 J/cm², and the threshold fluence is 0.4 J/cm². Incident beam profile for upper curve was shown in Figure 9(a); for lower curve in Figure 9(b).

6.2 Possible further Applications

According to the model, if a flat top beam with fluence F_0 is incident to a material with threshold fluence F_T , a tapered wall with angle θ is formed and the angle satisfies $\sin(\theta) = F_T / F_0$. From this theory, two points can be predicted:

- For a specified material of a certain thickness, a minimum fluence is required to drill or cut through the material. In reverse, for a specified fluence, there is a maximum thickness of a material which can be drilled or cut.
- The beam dimension will also influence the maximum thickness of drilling materials.

From the above two points, if the rectangular incident beam in space with width W and length L (here, $W < L$ is assumed), the drilling material thickness can be expressed by: $H = \frac{1}{2}W / \tan(\theta)$, thus: $H = \frac{1}{2}W \sqrt{\left(\frac{F_0}{F_T}\right)^2 - 1}$. If $F_0 \gg F_T$, then $H \approx \frac{1}{2}W \frac{F_0}{F_T}$.

Hole drilling and cutting speed

If f is the laser frequency, τ is the time for drilling a hole and ΔH is the ablation depth per shot, a hole drilling speed for a thickness H of material is:

$$v = \frac{1}{\tau} = \frac{\Delta H f}{H} \quad (\text{holes/s}) \quad (6.2)$$

The hole drilling speed is proportional to the laser operating frequency and ablation depth per shot, while it is inversely proportional to the material thickness.

This formula can be further inferred to a laser cutting speed:

$$v = \frac{\Delta H f}{H} l \quad (\text{mm/s}) \quad (6.3)$$

The laser cutting speed is proportional to the laser beam length l , the laser operating frequency f and the ablation depth per shot ΔH ; while the cutting speed is also inversely proportional to the material thickness.

7 SUMMARY AND DISCUSSION

From the above calculations and analyses, for low fluence incident beams, the hole wall was shown to be tapered and there exists a maximum drilling depth for a certain fluence. The corresponding maximum number of shots is called the maximum effective shot. Beyond it, the shot energy partially transfers to heat that may cause heat damage or bigger HAZ. The hole shape is decided by the incident fluence, beam shape and the material threshold fluence. For most incident beams, the entrance holes have flared entrances and the bottoms of the holes are conical. The hole entrance shape is decided by the shape of the beam wings. From the model, the hole shape can be predicted if the threshold fluence in the laser drilling process is constant. The ablation rate is not constant and the average ablation rate is not accurate enough to describe laser drilling process under certain circumstances, such as under a Gaussian beam, the ablation rate reduces with more shots after a certain number of shots.

In the laser drilling of CFC materials, the entrance holes for Nd:YAG laser are elliptical instead of circular. The long axis of the ellipse is parallel to the fiber direction while the short axis is perpendicular to the fiber direction. When using a square excimer laser beam profile for the drilling, a wedged shape with flared entrance was obtained. The wedge length is parallel to the fiber direction while the wedge width is perpendicular to the fiber direction. It is believed that the threshold fluence to cut the fiber is higher than that to ablate the resin (parallel to the fiber direction). This is easy to be explained using the model. According to our model, the drilling shape is different for different threshold fluences. It predicts that for isotropic materials the entrance hole dimensions will be different to those for inhomogeneous materials.

This new model is suitable for most well defined beams and materials such as polymers, fiber CFC, glass fiber composites and some ceramics. The model explains tapered wall formation and stabilized drilling, from which, high efficient laser drilling and cutting can be predicted in the low fluence regime.

Experimental results match, almost exactly, those predicted by this new model. The further comparison of the model and experimental results will publish in near future.

ACKNOWLEDGEMENTS

Fushun Wu would like to thanks British Aerospace and British CVCP for offering funding.

REFERENCES

1. R. Srinivasan, V. Mayne-Banton, *Applied Physics Letters* **41**, 576 (1982).
2. P. E. Dyer, J. Sidhu, *J. Appl. Phys.* **57** (4), 1420 (1985).
3. P. E. Dyer, R. Srinivasan, *J. Appl. Phys.* **66** (6), 2608 (1989).
4. R. Srinivasan, *J. Appl. Phys.* **73** (6), 2743 (1993).
5. M. Bertolotti, A. Ferrari, G. L. Liakhou, R. Li Voti, A. Marras, T. A. Ezquerro, F. J. Balta-Calleja, *J. Appl. Phys.* **78** (9), 5706 (1995).
6. R. Srinivasan, R. R. Hall, W. D. Loehle, W. D. Wilson, D. C. Allbee, *J. Appl. Phys.* **78** (8), 4881 (1995).
7. Belgacem Haba, Yukio Morishige, *Applied Physics Letters* **66** (26), 3591 (1995).
8. M. N. Ediger, G. H. Pettit, *J. Appl. Phys.* **71** (7), 3510 (1992).
9. G. M. Davis, M. C. Gower, C. Fotakis, T. E. Epthimiopoulos, P. Argurakis, *Appl. Phys. A* **36**, 27 (1985).
10. R. Srinivasan, *J. Appl. Phys.* **70** (12), 7588 (1991).
11. S. Huper, S. Modaresi, M. Stuke, *J. Phys. Chem.* **94**, 7514 (1990).
12. J. E. Andrew, P. E. Dyer, D. Forster, P. H. Key, *Appl. Phys. Lett.* **43** (8), 717 (1983).
13. P. E. Dyer, G. A. Oldershaw, J. Sidhu, *J. Phys. Chem.* **95**, 10004 (1991).
14. R. W. Olson, W. C. Swope, *J. Appl. Phys.* **72** (8), 3686 (1992).
15. Sylvain Lazare, Vincent Granier, *Appl. Phys. Lett.* **54** (9), 862 (1989).
16. S. W. Williams, P. J. Marsden, *Proc. 2nd European Laminar Flow Conference*, Bordeaux, June, 1996.
17. S. W. Williams, P. J. Marsden, N. C. Roberts, J. Sidhu, M. A. Venables, *XI International symposium on gas flow and chemical lasers and high power laser conference*, August, 1996, Edinburgh, UK.
18. R. J. Harrach, *J. Appl. Phys.* **48** (6), 2370 (1977).
19. A. Matsunawa, V. Semak, *J. Phys. D* **30**, 798 (1997).
20. B. Yilbas, A. Z. Sahin, R. Davies, *Int. J. Mach. Tools Manufact.* **35** (7), 1047 (1995).
21. G. D. Mahan, H. S. Cole, Y. S. Liu, H. R. Philipp, *Appl. Phys. Lett.* **53** (24), 2377 (1988).
22. N. P. Furzikov, *Appl. Phys. Lett.* **56** (17), 1638 (1990).
23. A. Matsunawa, V. Semak, *J. Phys. D* **30**, 798 (1997).
24. G. Scott, K. Henry, *SPIE* **1835**, 119 (1992).
25. E. Sutcliffe, R. Srinivasan, *J. Appl. Phys.* **60** (9), 3315 (1986).
26. H. H. G. Jellinek, R. Srinivasan, *J. Phys. Chem.* **88**, 3048 (1984).
27. J. H. Brannon, J. R. Lankard, A. I. Baise, F. Burns, J. Kaufman, *J. Appl. Phys.* **58**, 2036 (1985).
28. T. Keys, R. H. Clarke, J. M. Isner, *J. Phys. Chem.* **89**, 4191 (1985).
29. V. Srinivasan, M. A. Smrtic, S. V. Babu, *J. Appl. Phys.* **59** (11), 3861 (1986).
30. L. B. Kiss, P. Simon, *Solid State Communications* **65**, 1253 (1988).
31. G. D. Mahan, H. S. Cole, Y. S. Liu, H. R. Philipp, *Appl. Phys. Lett.* **53** (24), 2377 (1988).
32. Sylvain Lazare, Vincent Granier, *Appl. Phys. Lett.* **54** (9), 862 (1989).
33. R. Sauerbrey, G. H. Pettit, *Appl. Phys. Lett.* **55**, 421 (1989).
34. D. L. Singleton, G. Paraskevopoulos, R. S. Taylor, *Chem. Phys.* **144**, 415 (1990).
35. J. Singh, N. Itoh, *Chem. Phys.* **148**, 209 (1990).
36. M. S. Kitai, V. L. Popkov, V. A. Semchishen, *SPIE* **1352**, 210 (1990).
37. S. Kuper, S. Modaresi, M. Stuke, *J. Phys. Chem.* **94**, 7514 (1990).
38. N. P. Furzikov, *Appl. Phys. Lett.* **56** (17), 1638 (1990).
39. G. A. Oldershaw, *Chem. Phys. Lett.* **186**, 23 (1991).
40. S. Etienne, J. Perez, R. Vassoile, P. Bourgin, P. Bourgin, *J. Phys. III* **1**, 1587 (1991).
41. N. P. Furzikov, *SPIE* **1503**, 231 (1991).
42. H. Gai, Gregory A. Voth, *J. Appl. Phys.* **71** (3), 1415 (1992).
43. S. R. Cain, F. C. Burns, C. E. Otis, *J. Appl. Phys.* **71** (3), 4107 (1992).
44. P. E. Dyer, S. D. Jenkins, J. Sidhu, *Appl. Phys. Lett.* **49** (8), 453 (1986).
45. Belgacem Haba, Yukio Morishige, *Jpn. J. Appl. Phys.* **33**, L1499 (1994).
46. Belgacem Haba, Yukio Morishige, S. Kishida, *Applied Physics A* **60**, 27 (1995).
47. C. Y. Yeo, S. C. Tam, S. Jana, Michael W. S. Lau, *J. Material Processing Technology*, **42**, 15-49 (1994).
48. R. Srinivasan, V. Mayne-Banton, *Chem. Rev.* **89**, 1303 (1989).
49. P. E. Dyer, *Laser ablation of polymers*, in *Photochemical processing of Electronic Materials*, 359 (Academic, London 1992).
50. R. Srinivasan, *Interaction of laser radiation with organic polymers*, in *Springer Series in Materials Science*, Vol. 28 *Laser ablation*, 107 (Springer-Verlag Berlin 1994).
51. K. Ito, M. Moriyasu, *Microelectronic Engineering* **25**, 305 (1994).

Microscopic observation of laser-induced forward transfer process by two-dimensional laser induced fluorescence technique

Yoshiki Nakata^{*a}, Tatuo Okada^a, Mitsuo Maeda^a

^aDepartment of Electrical and Electronic Systems,
Graduate School of Information Science and Electrical Engineering, Kyushu University,
6-10-1 Hakozaki, Fukuoka, 812-8581 Japan

ABSTRACT

The behaviors of atomic particles and droplets in laser-induced forward transfer (LIFT) process were observed by two-dimensional laser-induced fluorescence (2D-LIF) technique and by thermal emission detection. The behavior of the ejected particles in gas phase was observed with different parameters such as ablation laser energy, film thickness, gas pressure. The interaction of the particles with substrate was also observed.

Keywords: laser-induced forward transfer, thin films, two-dimensional laser-induced fluorescence

1. INTRODUCTION

Laser-induced forward transfer (LIFT) is a very promising technique for the fabrication of micron-sized thin films. Recently, this method was applied to fabricate a micron-sized capacitance¹ or correct the oscillation frequency of a quartz oscillator. Many investigations have been reported on the surface morphology of deposited films,²⁻⁴ and to understand the LIFT process, the behavior of ejected film in gas phase has been investigated by shadowgraph technique.^{5,6} These approaches allowed to observe the behavior of particles, which are thought to be liquid or solid. On the other hand, the behavior of atoms in LIFT process has not been observed.

In this study we have introduced a long working distance microscope with the two-dimensional laser induced fluorescence (2D-LIF) technique to observe the behavior of atoms in micron-sized LIFT process of gold thin film. The behavior of droplets, which can be observed with thermal radiation, was also imaged. In the study, the ablation parameters such as laser energy, gas pressure, and film thickness were changed. The reflection of ablated particles in front of a substrate was observed.

2. EXPERIMENTAL SETUP

The experimental setup is shown in Fig.1. The chamber was evacuated by a rotary pump. A gold thin film on a SiO₂ substrate was placed inside the chamber, and the film was irradiated from the backside by a dye laser through a pin hole (1 mm in diameter) and a lens. The thin film was positioned at the focus point of the dye laser. The wavelength of the dye laser was around 440 nm, and the pulse width was approximately 9 ns. The gold atoms in the gas phase were excited by a probe laser, which was the second harmonic wave of an optical parametric oscillator (MPO-730, Quanta Ray). The wavelength of the probe laser was 267.6 nm, and it irradiated the whole volume of LIFT process. The resultant fluorescence at 627.8 nm was observed by an image-intensified CCD camera (Hamamatsu C2925, C5895) through a bandpass filter and a long working distance microscope (Edmund KV microscope). The droplets, which have been observed by the shadow graph technique,^{6,5} was observed by the thermal radiation. The observation of thermal radiation was done without the bandpass filter and the probe laser.

Correspondence: Email: nakata@ees.kyushu-u.ac.jp; WWW: <http://photon.ees.kyushu-u.ac.jp>; Telephone: +81-92-642-3895; Fax: +81-92-642-3965

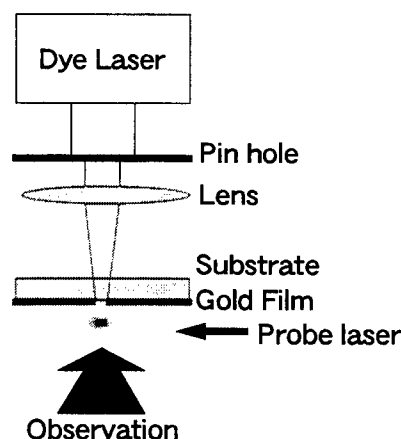


Figure 1. Experimental setup

3. RESULTS

3.1. BEHAVIOR OF PARTICLES IN GAS PHASE

Fig. 2 shows the spatial distributions of the ablated gold atoms and droplets in vacuum with different ablation laser energy. The film thickness was 100 nm. The ablation laser energy is shown on the lefthand side, and the delay time after ablation is shown on the bottom. The distance from the film surface is shown on the righthand side, and the position of the film surface is shown by dotted lines. The images above the dotted lines are the mirror images of the real images reflected from the Au film surface or noise. The temporal resolution in the observation of atoms can be estimated by the lifetime of atom the pulse width of the probe, and the resolution is thought to be about 10 ns. On the other hand, in the case of the observation of droplets, it was limited to 100 ns decided by the gate width of the image intensifier.

In all images, the brightness was normalized corresponding to the peak signal intensity in each image. From Fig. 2, it is very clear that the plume of atoms was expanded with the delay time, and the density was reduced with decrease in laser energy. Atoms were hardly observable with the ablation laser energy of 13 μJ . In the case of droplets also, the signals were weak with decrease in the ablation laser energy. The speeds of the atoms and droplets with different ablation conditions are summarized later.

Fig. 3 shows the behavior of atoms and droplets in a vacuum with different film thicknesses. The ablation laser energy was maintained at 45 μJ . Compared with the film thickness of 100 nm (Fig. 3 (e)), the droplets were not confined in the smaller volume in the case of the film thickness with 500 nm (Fig. 3 (f)). On the other hand, the droplets could hardly be seen with the film thickness of 20 nm, and this is thought to be due to the atomization of whole ejected film. Further, at the ablation laser energy of 13 μJ , almost no atom was observed for all film thicknesses.

Fig. 4 shows the difference in the behaviors of gold atoms and droplets in vacuum and atmospheric air. The ablation laser energy was 45 μJ . The distribution of atoms was shrunk in the atmospheric air as shown in Fig. 4 (c). At this pressure, the ablated atoms can condense to particles in gas phase.⁷⁻⁹ Therefore, the atoms disappeared earlier compared to the case in vacuum. On the other hand, the behavior of droplets in vacuum did not differ much from that in the atmospheric condition, as shown in Fig. 4 (b) and (d).

From the observed images shown above, the position of the front edge of the atoms and the densest region of the droplets at a delay time of 0.3 μs can be derived as shown in Fig. 5. Solid lines show the data of atoms, and dotted lines show those of droplets. The film thickness and atmospheric condition is written in the figure. It is apparent that the speed of atoms is faster than that of droplets. In the case of atoms, the speed becomes faster as the ablation laser energy increases. With 500 nm of film thickness, the speed is slow compared with the case of another film thicknesses. In an atmospheric air, the speed is about one third of that in vacuum. In the case of droplets, the speed does not differ depending on the laser energy, film thickness and the background gas pressure.

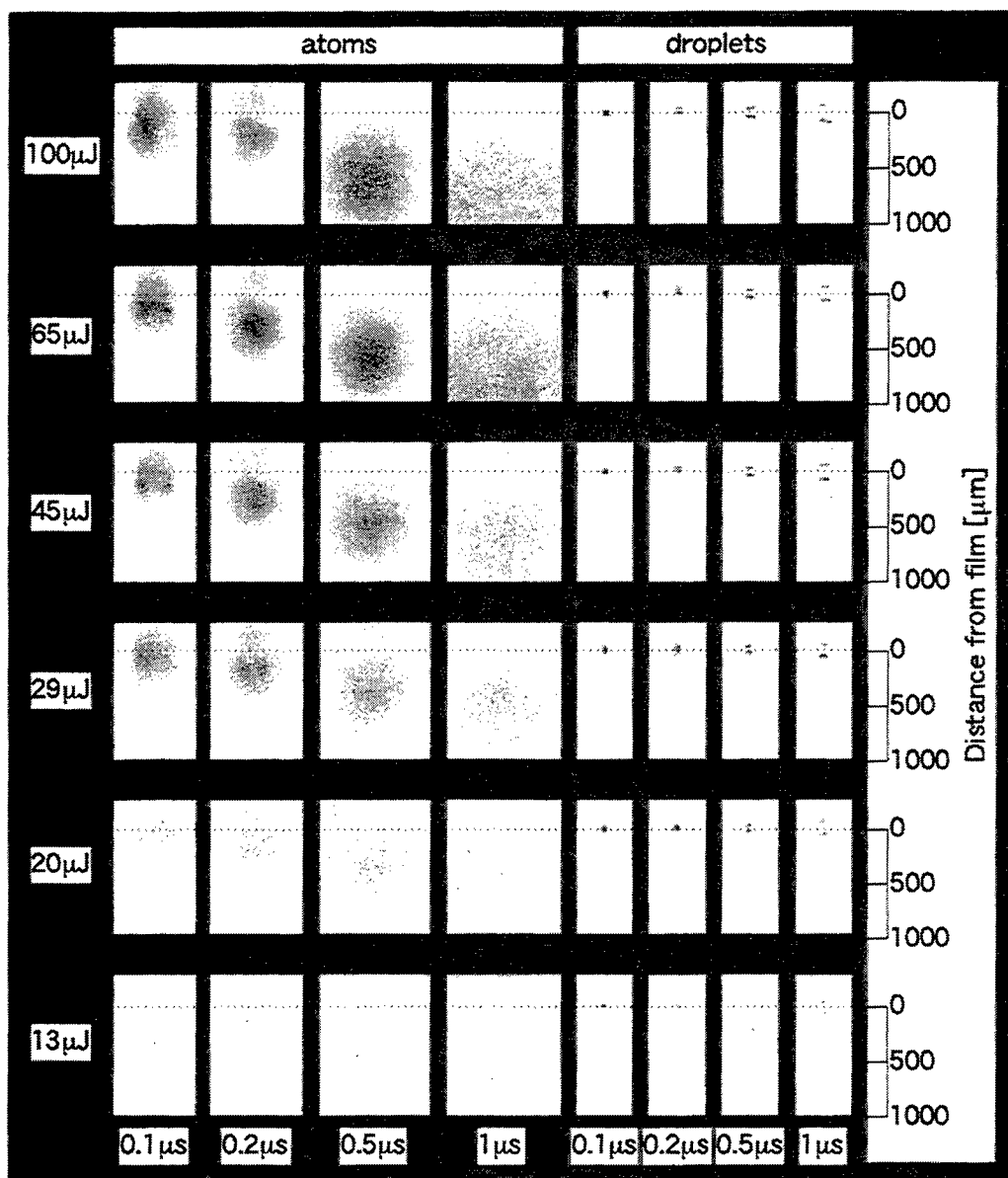


Figure 2. Spatial distributions of ablated gold atoms and droplets in vacuum with different ablation laser energy.

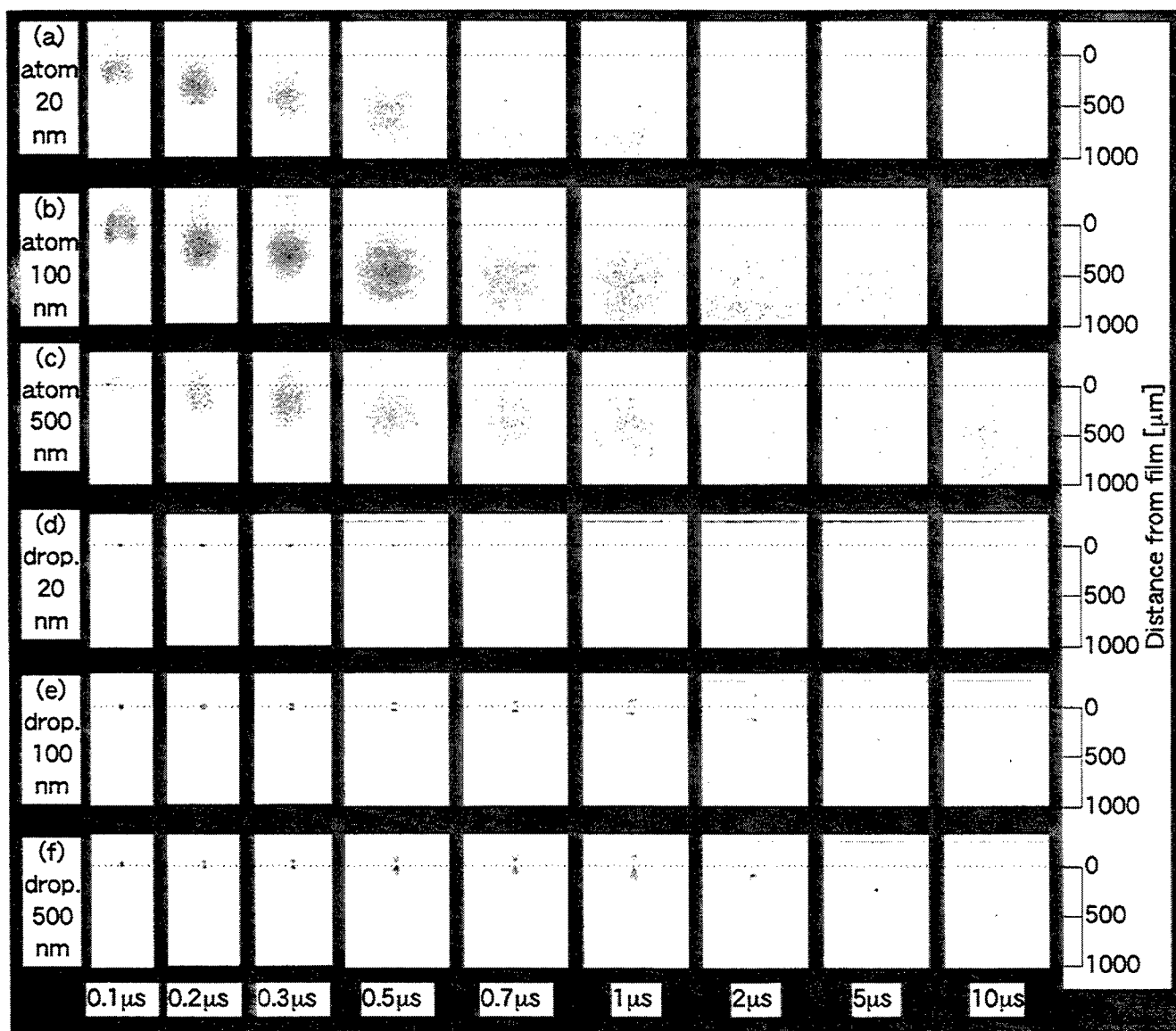


Figure 3. Spatial distributions of ablated gold atoms and droplets for different film thickness.

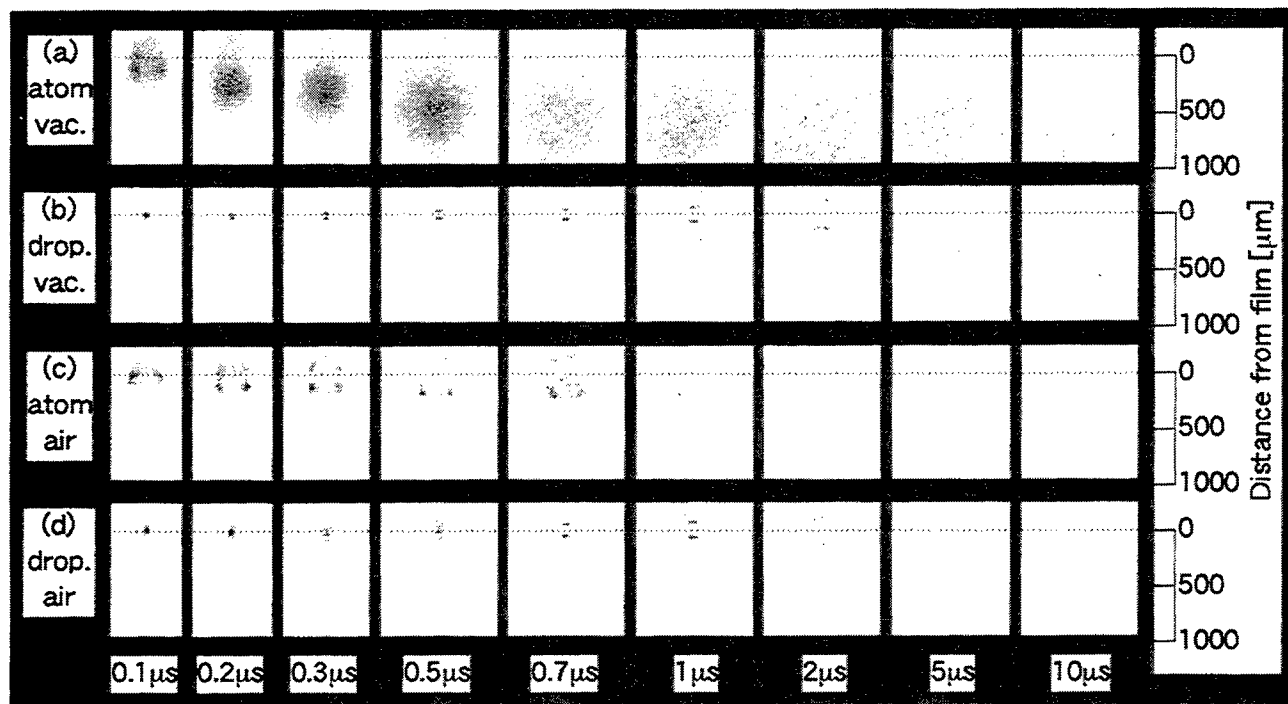


Figure 4. Spatial distributions of ablated gold atoms and droplets in vacuum and air.

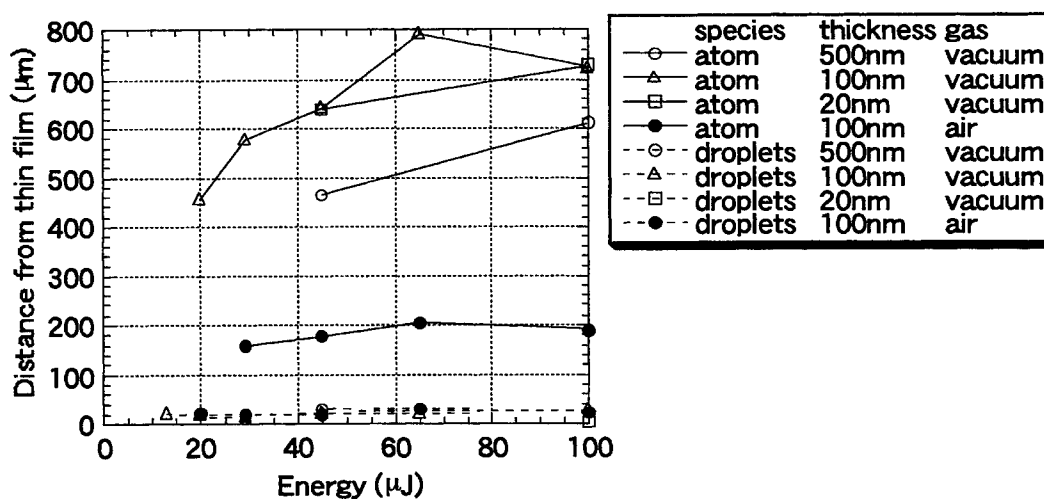


Figure 5. Position of the front edge of the atoms and densest region of droplets as a function of ablation laser energy and with different film thickness.

In the investigations by another groups, deposited film spreaded in some case.³ By using the long gate width in the observation of droplets, the diverging behavior in gas phase was observed. Fig. 6 shows the droplets observed with the gate width of 20 μ s. The gate was opened at the delay time of 1.0 μ s. In all ablation conditions, the droplets fly with some divergence angles. In vacuum condition in Fig. 6 (a), the divergence angle decreased with the decrease in the ablation laser energy. Similar observation were made in atmospheric air condition as shown in Fig. 6 (b). In vacuum condition, the droplets flew over 1 mm, but in the atmospheric air they flew about 0.3 mm with all the ablation laser energies. This is due to the cooling of the particles by air. With the film thickness of 20 nm, the emission was hardly observed as shown in Fig. 6 (c). On the other hand, the particles flew forward with 500 nm film thickness compared to 100 nm, as shown in Fig. 6 (a) and (d), respectively.

The divergence angle derived from the images observed with a long gate width is plotted in Fig. 7. It is clear that the angle increased and saturated with the ablation laser energy both in the vacuum and the atmospheric air, but the divergence angles were smaller in the air. The saturated values was 50 and 33 degree, in vacuum and air respectively. This spreading angle is very important if we want to make a smaller size of deposited film. For the smaller size of deposited film requirements, the deposition should be in air with the smaller ablation energy and thicker film thickness. In the case of 500 nm in film thickness and with the ablation laser energy of 100 μ J in vacuum, the largest divergence angle of 77 degree was observed.

In a conventional laser ablation process, a laser irradiates a target, and the surface is photo-dissociated or thermally dissociated. The behavior of ejected atoms and droplets in a laser ablation has been observed by 2D-LIF¹⁰⁻¹² and the observation of thermal radiation,¹³ which are also used in this study. It is interesting to compare the behaviors of ablated particles in conventional laser ablation and LIFT process. Fig. 8 shows the behaviors of atoms and droplets in LIFT and conventional laser ablation process. The behavior of Ba atoms in the laser ablation process of YBa₂Cu₃O_{7-x} superconducting material in vacuum is shown in Fig. 8 (c), and which was observed also by 2D-LIF.¹⁰ The ablation conditions are shown in the image. The distribution of atoms is similar with the LIFT process as shown in Fig. 8 (a) and (c). The speed of atoms in the process exceeded 1 km/s, and which is the same as in LIFT. Fig. 8 (d) shows the behavior of droplets in the laser ablation process of silicon. The observation was done with the gate width of 300 μ s and the gate was opened at 200 μ s. The droplets fly as the spraying droplets, and each particles fly straight. The speed of the droplets was spreaded over a wide range from 10 m/s to 90 m/s. On the other hand, the speed of the droplets in LIFT process is almost unique, as shown in (b). The speed of droplets in both processes is slower compared to the atoms in both processes.

The images of the donor films after LIFT process observed by an optical microscope are shown in Fig. 9. Images are observed for different ablation laser energies and film thicknesses. The diameters of the holes are also shown with the images. The images on top 3 rows were observed from the front side as explained in Fig. 9 (a). The bottom images were observed from the back side as shown in Fig. 9 (b). It is clear that the diameter decreased with the decrease of the ablation laser energy. On the other hand, it seems that the size was not so different respect to the film thickness. The diameter was almost of the same size that of the droplets at earlier delay time as shown in Fig. 3. It seems that the edge of the film is melting with 500 nm film thickness.

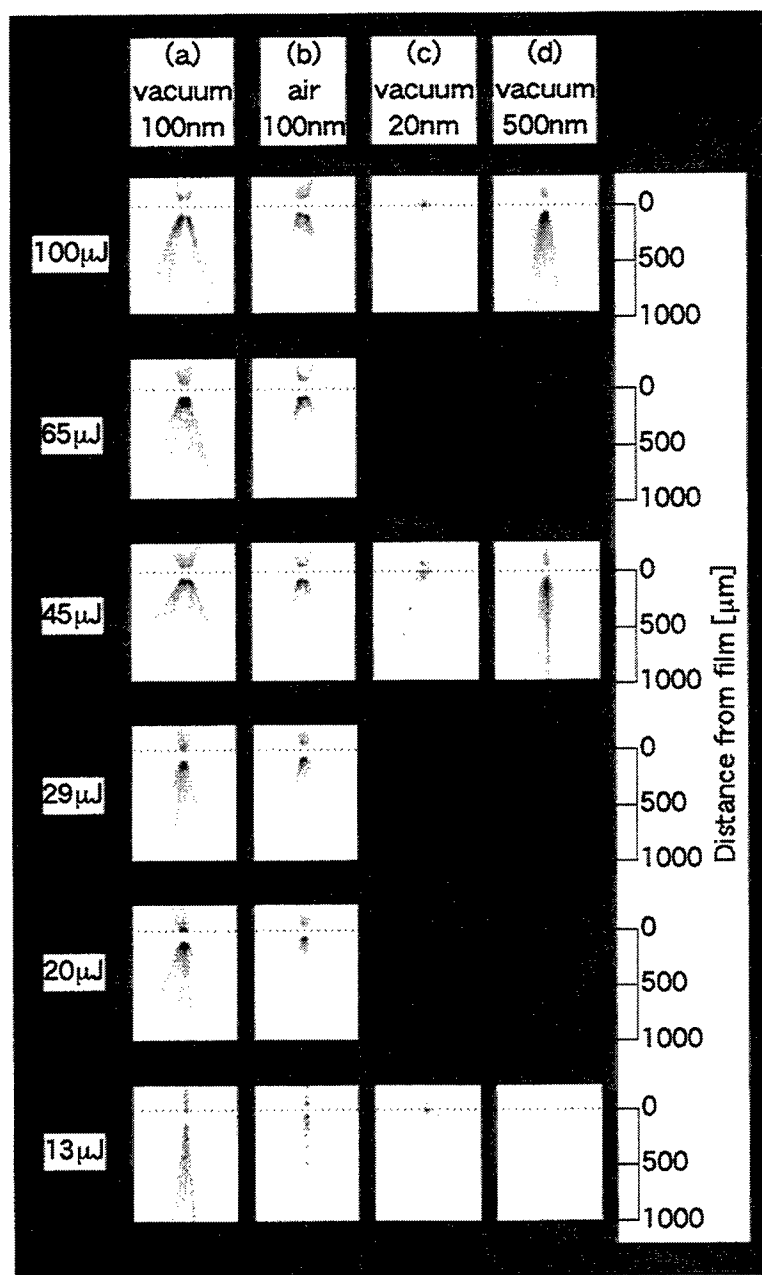


Figure 6. Behavior of droplets observed with the long gate width of 20 μs .

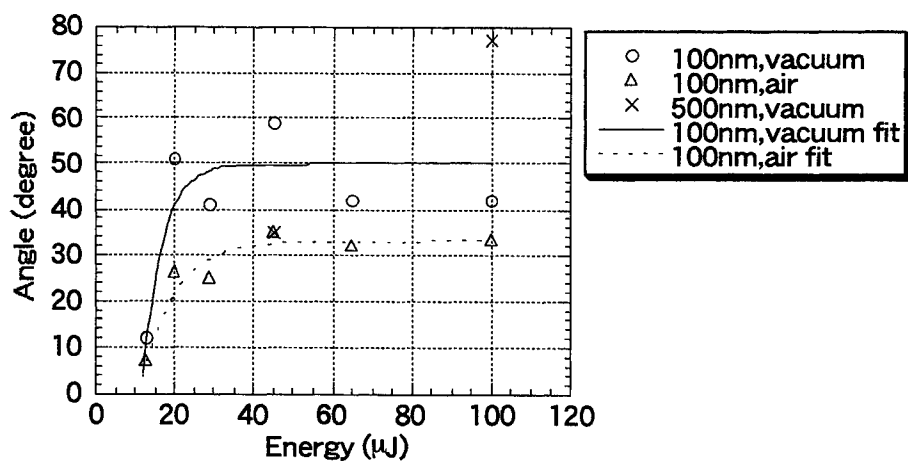


Figure 7. Spreading angle as a function of ablation laser energy.

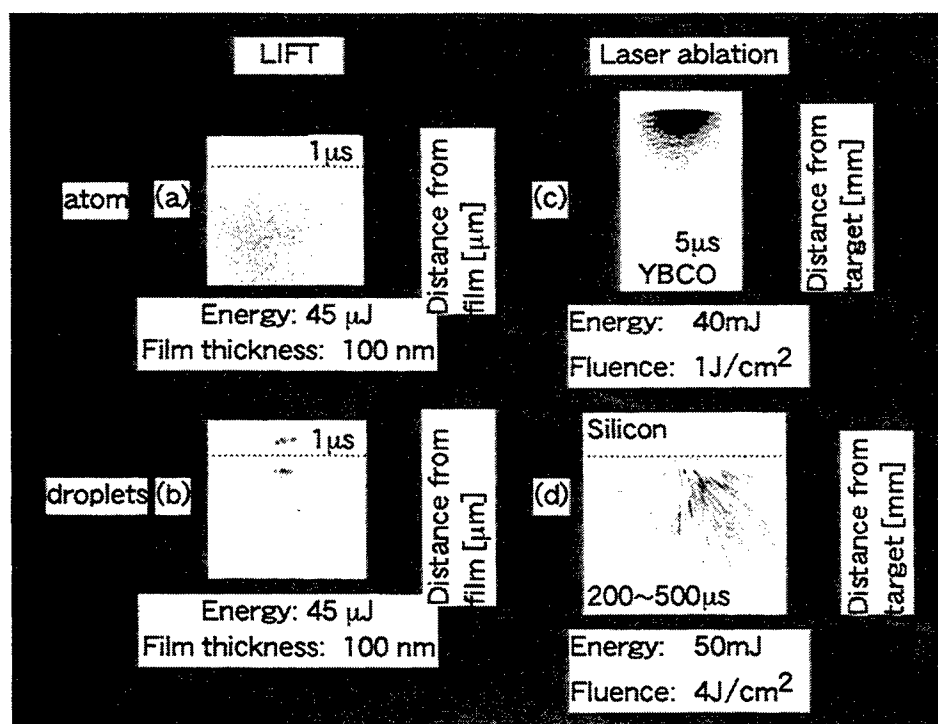


Figure 8. Behaviors of atoms and droplets in LIFT and conventional laser ablation process.

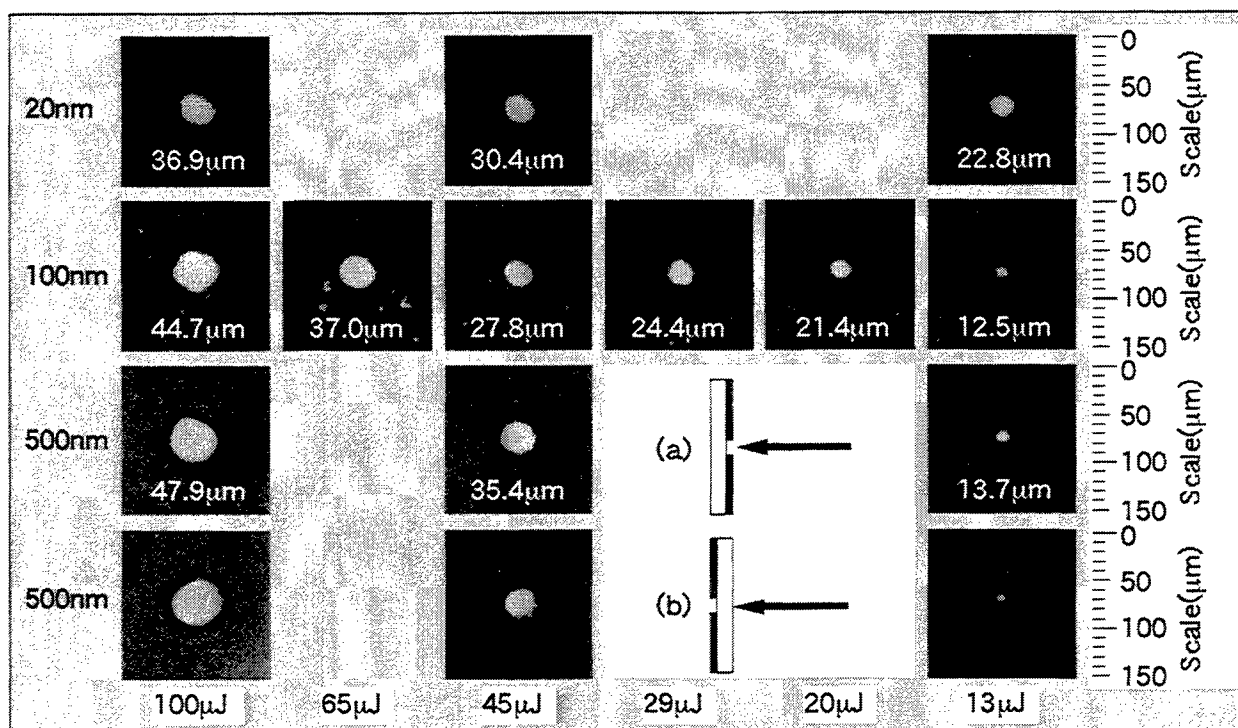


Figure 9. Surface of donor films after LIFT process.

3.2. BEHAVIOR OF PARTICLES WITH SUBSTRATE

In the actual LIFT process, a substrate as an acceptor is placed in front of the film. Figure 10 shows the behavior of the ablated species between a film and a substrate. The observation was done in vacuum. The position of the substrate is shown with the dotted lines. In Fig. 10 (b) the substrate was placed 200 μm from the film. It seems that the atoms are confined in a smaller volume compared to those without the acceptor substrate as shown in Fig. 10 (a). The atoms disappeared faster in (b), and this can be due to the sticking of the atoms on the substrate. When the distance was 70 μm as shown in Fig. 10 (c), the atoms were protruded from the interstice between the donor and acceptor substrate.

Fig. 11 shows the behaviors of droplets with a substrate observed with a gate width of 20 μs . The delay times at the bottom of images show the delay time of opening gate of the image intensifier. The observation was done in vacuum. Fig. 11 (a), (b) and (c) shows the change of the distance between film and substrate. When the distance was 500 μm which is shown in Fig. 11 (b), the reflection in front of the substrate was clearly observed. It is more clear with smaller distance of 70 μm as shown in Fig. 11 (c). The magnification is 3.8 times large of Fig. 11 (a), (b) and (c) in (d) and (e). With the distance of 70 μm , the signal intensity from droplets decreased as the delay time. Fig. 11 (f), (g) and (h) shows the behavior with the change in the laser energy. With larger ablation laser energy, the reflection was more intense, and we can see the mirror like reflection. This reflection shows the low sticking coefficient of the particles in this condition. In a real deposition process, the reflection and scattering of the particles worsen the film quality, because they can spread the film size. To obtain an ideal film quality, the energy and the distance should be optimized.

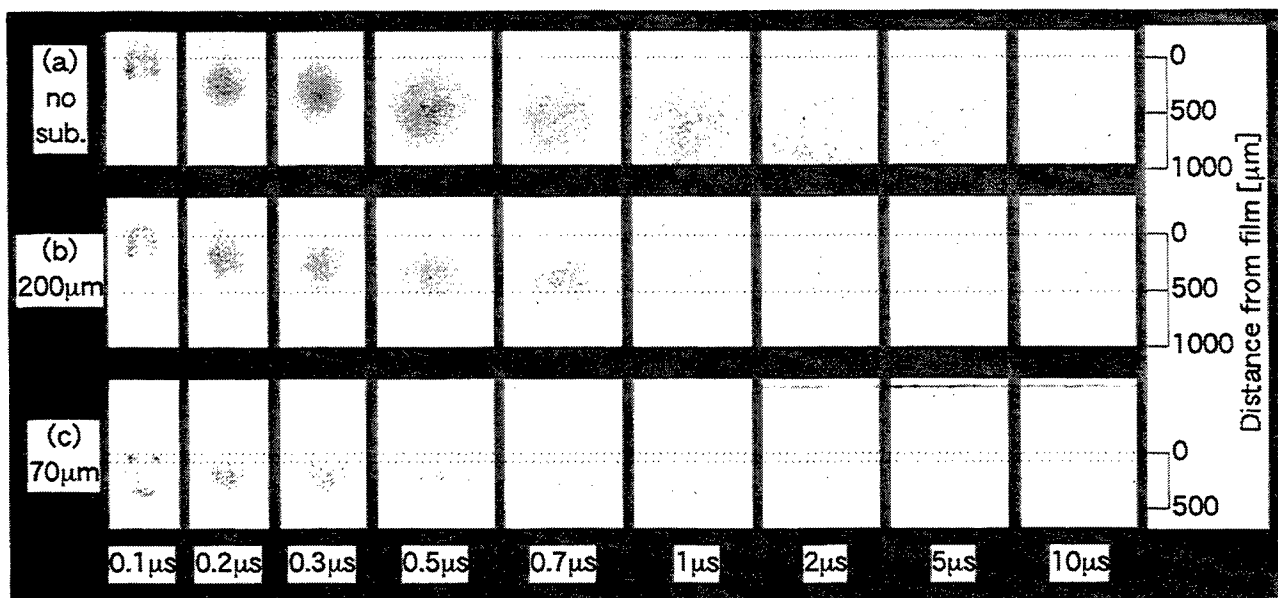


Figure 10. Behavior of atoms with acceptor substrate.

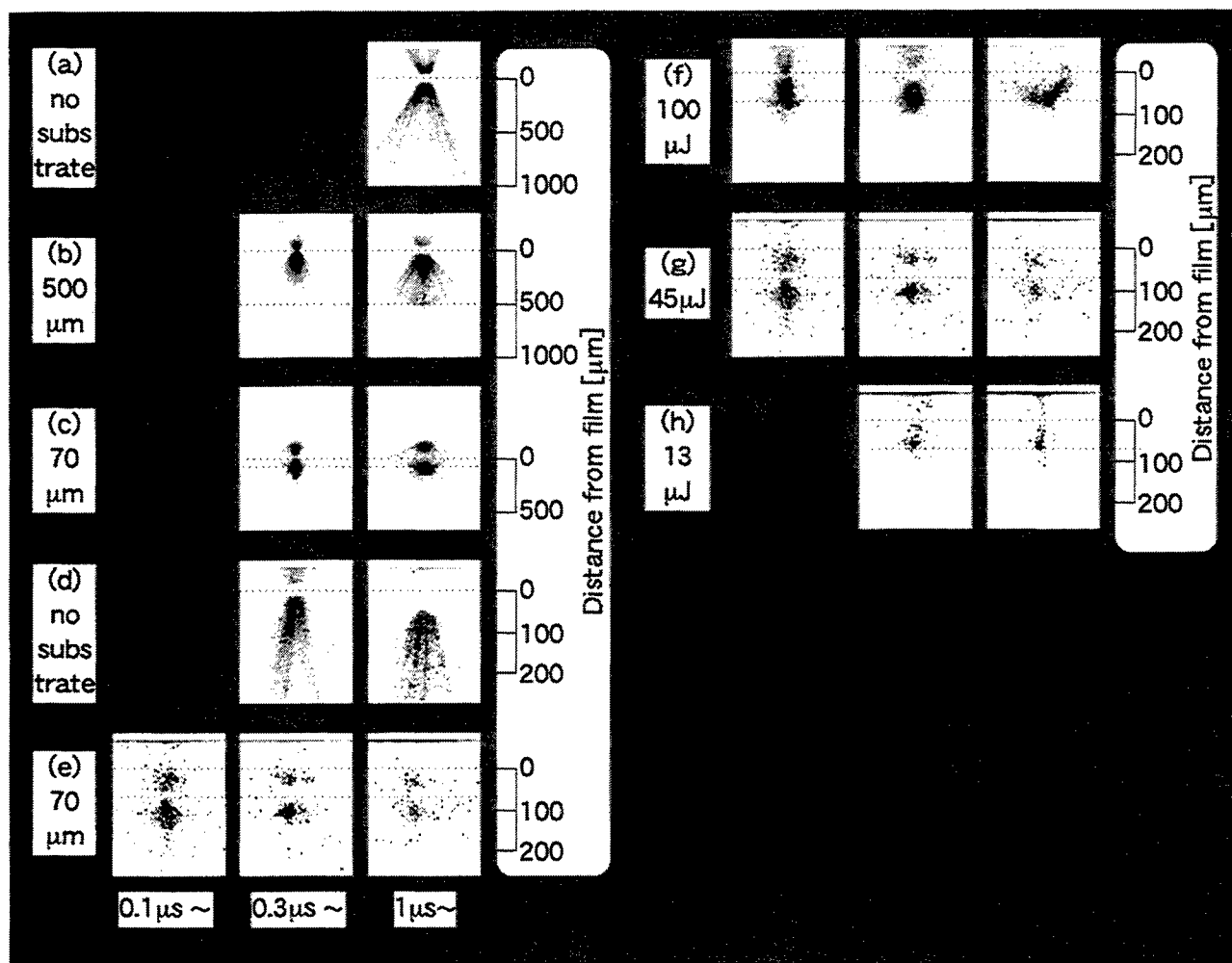


Figure 11. Behavior of droplets with acceptor substrate.

4. CONCLUSION

In this study we observed the behavior of atoms and droplets in LIFT process of gold thin film for the first time. Observations were done for different ablation conditions. Results are as follows:

1. The atoms propagated as a delay time, and the speed of the fastest component exceeded 2 km/s. The density was increased with the increase in the laser ablation energy. The droplets were hardly seen with the film thickness of 20 nm. In the atmospheric air, the distribution was confined in a smaller volume, compared to that in vacuum.
2. The behavior of droplets was observed with thermal radiation. It was spreading in the propagation in gas phase. The speed was slow compared with that of atoms, and did not change with the ablation conditions.
3. The behavior of atoms and droplets in LIFT and conventional laser ablation process was compared. The speed of atoms in both process was in the same range. The speed of droplets in LIFT was almost unique, on the other hand it spreaded over a wide range from 10 m/s to 90 m/s in the conventional laser ablation process of silicon.
4. The interaction of atoms and droplets with a substrate was observed. Atoms were confined in a interstice region, and they disappeared faster compared to the case without an acceptor substrate. A mirror like reflection of droplets in front of a substrate was observed, and the reflection was distinct with increasing the ablation laser energy.

REFERENCES

1. A. Pique, D. B. Chrisey, R. Y. Auyeung, S. Lakeou, R. Chung, R. A. McGill, P. K. Wu, M. T. Duignan, W. Warren, "Laser direct writing of circuit elements and sensors," *Proc. SPIE* **3618**, pp. 330-339, 1999.
2. J. Bohandy, B. F. Kim and F. J. Adrian, "Metal deposition from a supported metal film using an excimer laser," *J. Appl. Phys.* **60**, pp. 1538-1539, 1986.
3. J. Bohand, B. F. Kim, F. J. Adrian and A. N. Jette, "Metal deposition at 532 nm using a laser transfer technique," *J. Appl. Phys.* **63**, pp. 1158-1162, 1987.
4. I. Zergioti, S. Mailis, N. A. Vainos, P. Papakonstantinou, C. Kalpouzos, C. P. Grigoropoulos, C. Fotakis, "Microdeposition of metal and oxide structures using ultrashort laser pulses," *Appl. Phys. A* **66**, pp. 579-582, 1998.
5. Z. Tóth, B. Hopp, Z. Kántor, F. Ignácz, T. Szörényi, Z. Bor, "Dynamics of excimer laser ablation of thin tungsten films monitored by ultrafast photography," *Appl. Phys. A* **60**, pp. 431-436, 1995.
6. A. B. Bullock and P. R. Bolton, "Laser-induced back ablation of aluminum thin films using picosecond laser pulses," *J. Appl. Phys.* **85**, pp. 460-465, 1999.
7. T. Okada, Y. Nakata, J. Muramoto and M. Maeda, "New developments of pulsed-laser deposition process," *Proc. SPIE* **3274**, pp. 246-254, 1998.
8. J. Muramoto, Y. Nakata, T. Okada and M. Maeda, "Influences of preparation conditions on laser-ablated Si nano-particle formation processes observed by imaging laser spectroscopy," *Appl. Surf. Sci.* **127-129**, pp. 373-377, 1998.
9. J. Muramoto, I. Sakamoto, Y. Nakata, T. Okada and M. Maeda, "Influences of electric field on the behavior of Si nanoparticles generated by laser ablation,"
10. Y. Nakata, H. Kaibara, T. Okada and M. Maeda, "Two-dimensional laser-induced fluorescence imaging of a pulsed-laser deposition process of $\text{YBa}_2\text{Cu}_3\text{O}_{7-x}$," *J. Appl. Phys.* **80**, pp. 2458-2466, 1996.
11. Y. Nakata, G. Soumagne, T. Okada and M. Maeda, "Pulsed-laser deposition of barium titanate films and plume dynamics," *Appl. Surf. Sci.* **127-129**, pp. 650-654, 1998.
12. Y. Nakata, W. K. A. Kumuduni, T. Okada and M. Maeda, "Two-dimensional laser-induced fluorescence imaging of non-emissive species in pulsed-laser deposition process of $\text{YBa}_2\text{Cu}_3\text{O}_{7-x}$," *J. Appl. Phys.* **80**, pp. 2458-2466, 1996.
13. Y. Nakata, H. Uetsuhara, S. Goto, N. Vasa, T. Okada and M. Maeda, "Pulsed-laser deposition of Ti:sapphire thin films using high-speed rotating target," *Proc. SPIE* **3618**, pp. 504-511, 1999.

Ion-Source-Assisted Pulsed Laser Deposition of Carbon Nitride Thin Films

Z. F. He, Y. F. Lu¹, Z. H. Mai and Z. M. Ren

Laser Microprocessing Laboratory
Department of Electrical Engineering and Data Storage Institute
National University of Singapore, 10 Kent Ridge Crescent, Singapore 119260

ABSTRACT

Ion source assisted pulsed laser deposition has been used to synthesize carbon nitride thin films. This synthesis method has both advantages of pulsed laser deposition (PLD) and ion implantation. The average ion beam current, the beam voltage, the laser pulse energy, and substrate temperature can be controlled systematically. Scanning tunneling microscopy (STM) has been used to study the surface properties. The $(dI/dV)/(I/V)$ values have been calculated to study the local density of states (LDOS) on the film surface. Experiment results have been analyzed by Raman spectra to see the influence of the substrate temperature. Thin films CN_x with nitrogen content of 32% have been investigated by X-ray photoelectron spectroscopy (XPS). The results can reveal the formation of different bonds. Fourier transform infrared spectra (FTIR) was also used to study the bonding of films. The hardness of the synthesized thin film was analyzed by a nanoindenter. The result shows that the carbon nitride films have high hardness.

Keywords: Carbon Nitride, Pulsed Laser Deposition, Raman Spectra, X-ray Photoelectron Spectroscopy

1. INTRODUCTION

Carbon nitride is widely believed to be a possible superhard material since the prediction of Liu and Cohen^{1,2}. It is assumed that β - C_3N_4 would adopt the known structure of Si_3N_4 . Calculation shows that the cohesive energy of β - C_3N_4 would be sufficiently large to yield a metastable solid. This result attracted many researchers to synthesize the hypothesized material to obtain superior properties such as high compressional strength, thermal conductivity and spectral transmittance³. These properties may make the novel material serve well as protective coatings of the mechanical tools and protective anti-reflection coatings for IR optics⁴. It seems that β - C_3N_4 can be a good alternative to diamond especially in applications at high temperature, where diamond is unstable⁵. Niu and Lieber first reported strong electron diffraction from crystallites found in their carbon nitride thin films⁶. Their method is laser ablation of graphite assisted with nitrogen atom source. Different synthesis methods are also possible and widely tried by other researchers, such as classical chemical vapor deposition (CVD)⁷, plasma enhanced chemical vapor deposition (PEVCD)⁸, reactive d.c. magnetron sputtering⁹, laser deposition¹⁰, r.f. sputtering¹¹, electron cyclotron resonance (ECR) plasma¹², nitrogen ion implantation to carbon¹³, and pyrolysis of organic C-N compounds¹⁴. Films prepared with these methods have a big range of N/C ratios. The ratio can be as high as 1.5¹⁵. These films are usually amorphous. Some researchers claim to have produced nanometer size crystallites embedded in an amorphous matrix with the expected crystal structure of β - C_3N_4 . However, further effort is still required to obtain crystal β - C_3N_4 . Nevertheless, even the synthesized amorphous carbon nitride has shown good properties¹⁶.

Our previous work studied pulsed laser deposition (PLD) of a graphite target to synthesize carbon nitride thin films¹⁰. The purpose of this study is to investigate the role of nitrogen implantation in the PLD of carbon nitride thin film. Samples prepared under different substrate temperature were studied. STM, Raman, XPS, FTIR, Ellipsometer and Nanoindenter were used to study the properties of the thin film. The surface structure was obtained by STM. The electronic structure was studied by Raman and FTIR. Ellipsometer and STM show the band structures of the thin film. The mechanical property of the thin film was studied with nanoindenter.

2. EXPERIMENTS

Carbon nitride films were prepared in a PLD system, as shown in Fig.1. A KrF excimer laser beam was focused on a graphite target through a quartz lens. The laser operated at a wavelength of 248 nm, a pulse width of 30 ns, and a repetition

¹Correspondence: Email:leluyf@nus.edu.sg; www: <http://www.dsi.nus.edu.sg/trackslaser/>; Tel:65-8742118; Fax:65-7791103

rate of 10 Hz. The graphite target was mounted on a rotating holder, which can avoid over-ablation of the same location on the target. Silicon (100) wafer was chosen as the substrate, which was cleaned in acetone before deposition. The substrate was mounted on a substrate holder. The distance between the substrate and the target was 5 cm. The temperature of the holder can be controlled in a range from room temperature to 900°C. A 1 cm diameter Kaufman source was used as assisting ion source. The PLD system was evacuated to a background vacuum of 2.0×10^{-5} Torr. Nitrogen gas was filled into Kaufman source to a nitrogen pressure of 1.0×10^{-4} Torr.

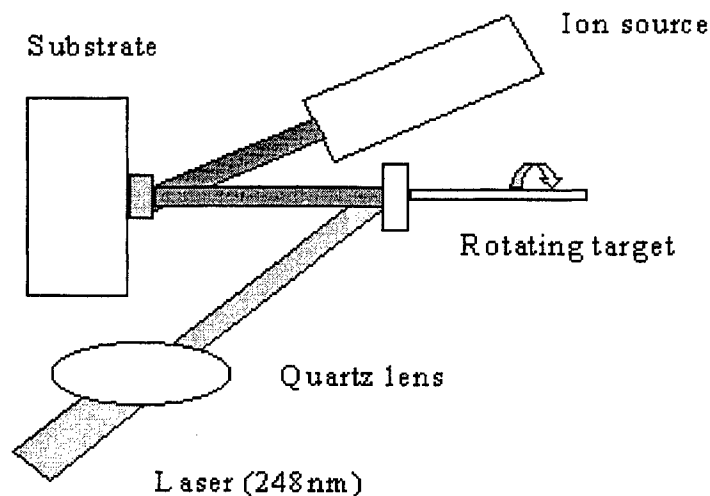


Fig. 1. System setup of pulsed laser deposition assisted with ion source

STM was used to obtain the 3-D images of the carbon nitride surface. The sample had a bias of -2 volts with respect to the tip. The tunneling current was set at 0.5 nA. An I-V curve was measured with the same tip immediately after scanning. Raman spectroscopy measurement was carried out on a Renishaw Raman scope with a polarized line of 514.5 nm from an Ar^+ laser. The FTIR measurement was performed on a Nicolet MAGNA-IR 850 spectrometer. The film thickness and hardness were characterized by a surface profiler and a nanoindenter, respectively.

3. RESULTS AND DISCUSSIONS

Deposition of the samples were carried out with a laser fluence of 4.0 J cm^{-2} for 10 minutes at a repetition rate of 10 Hz. Ion beam works at a beam energy of 100 eV. The beam current was maintained at 1 mA to see the influence of different energy for the ion bombardment. The deposition time was 20 minutes. The samples were prepared from room temperature to 800°C. When the ion beam was present, the nitrogen atoms were ionized and accelerated by the ion source. The effects of ion bombardment are twofold. High ion energy may help to form strong CN bonds, which can make the thin films with good properties. However, nitrogen ion with high energy may also remove the carbon atoms from the thin film surface.

A typical STM image of carbon nitride thin film is shown in Fig. 2. STM image was obtained with constant tunneling current. In the constant-current mode, a feedback mechanism was enabled to maintain a constant current while a constant bias was applied between the sample and the tip. STM image of this mode can provide information of both the surface morphology and the surface electronic properties. It is noticed that the surface of the thin film is rather smooth and the peak-to-valley roughness is around 30 Å, which is the size of only several ten atoms. For the samples prepared with ion implantation, the ions can transfer energy to the carbon atoms on the surface. This helps the carbon atoms to move laterally to form a smooth surface. Energetic nitrogen ions can also remove some carbon atoms on the surface of the thin film and flatten the surface.

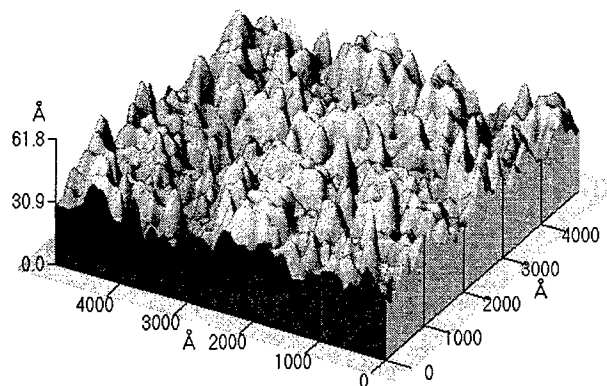


Fig. 2. Typical STM image of carbon nitride thin film

The relation between tunneling current and the bias voltage was measured for the samples prepared by ion assisted PLD of graphite target. The I-V relation can reveal the electronic structure of the surface. A typical I-V curve is shown in Fig. 3. The tunneling current was measured at a fixed point above the sample while the bias voltage varied in a certain range. The current direction from the tip to the sample was defined as positive. The current varied from +50 to -40 nA, when the sample bias varied from -1 to 1 V. From the I-V relation, the information of local density of the state (LDOS) can be obtained. The ratio of differential conductance (dI/dV) to the total conductance (I/V) has been demonstrated to provide a convenient way to measure surface state density for metallic and small-band-gap surfaces¹⁷. The $(dI/dV)/(I/V)$ curve has been shown in Fig. 4. For large-band-gap surfaces, the ratio diverges at the band edge. This divergence is undesirable for obtaining an experimental approximation of the surface state density. Some researchers have avoided the divergence problem either by adding a small constant to I/V , or by applying certain amount of broadening to the I/V values¹⁸. A different approach was used in this study. The tunneling current was first fitted into a polynomial. We simply deleted the data, which correspond to the zero-current point. That is why the $(dI/dV)/(I/V)$ curve breaks around Fermi-level in Fig. 5. It is noticed that there are two band edges at -0.5 and +0.5V respectively. One explanation is that the two bands correspond to the conduction band and valence band with a band gap of 1 eV. Another explanation is that the two bands are only dopant-like bands, because carbon nitride should be a large-band-gap material like diamond. Both explanations cannot be confirmed currently due to the amorphous property of the carbon nitride thin film. Further investigation is needed to understand the band structure of the carbon nitride.

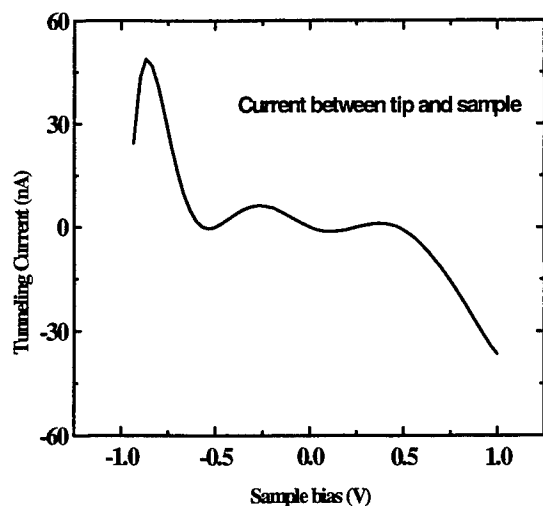


Fig. 3. I-V relation of carbon nitride surface

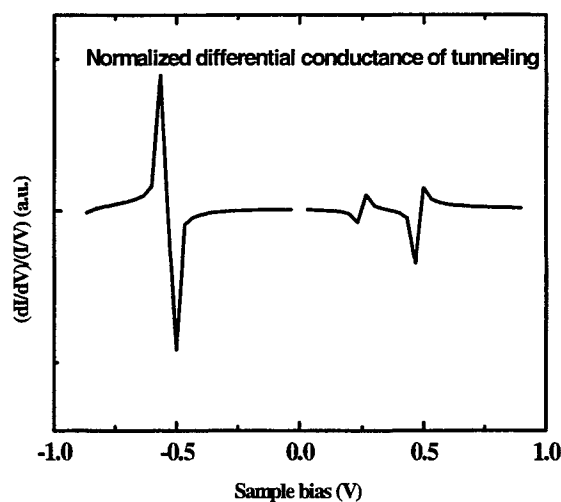


Fig. 4. $(dI/dV)/(I/V)$ curve of carbon nitride surface

Figure 5(a) illustrates Raman spectra of carbon nitride thin films prepared under different temperature. D and G bands can be identified in the figure. The D band centers around 1370 cm^{-1} , which is due to a zone edge A_{1g} mode activated by disorders associated with finite crystal size¹⁹. The G band of the film centers around 1580 cm^{-1} , which originates from an in-plane vibration of E_{2g} symmetry. The I_D/I_G ratio of the samples are shown in Fig. 5(b). It is noticed that a temperature of 400°C results in the highest I_D/I_G ratio. The ratio decreases while the deposition temperature increases or decreases. According to a conventional analogy with graphite²⁰, the I_D/I_G ratio increases with decreasing sp^2 cluster size. The large I_D/I_G ratio of the sample suggests a small sp^2 cluster size. It is known that the width of the band gap varies inversely with the sp^2 cluster size. Therefore, the small size of sp^2 clusters may result in a wide band gap in the bulk. The I_D/I_G ratio of different deposition temperature suggests that 400°C is suitable for the synthesis of the carbon nitride thin film. The full width at half maximum (FWHM) value of both D and G bands are calculated in Fig. 3(c). It is noticed that D bands have large FWHM values than G bands for all the samples. The large FWHM suggests that the sp^3 -bonded CN crystallites embedded in the amorphous sp^2 bonded C_xN_y have a small grain size¹⁹. It is also noticed that all D band centers have a shift from the standard diamond band center of 1332 cm^{-1} in Fig. 5 (d). The shifts are not influenced by the deposition temperature.

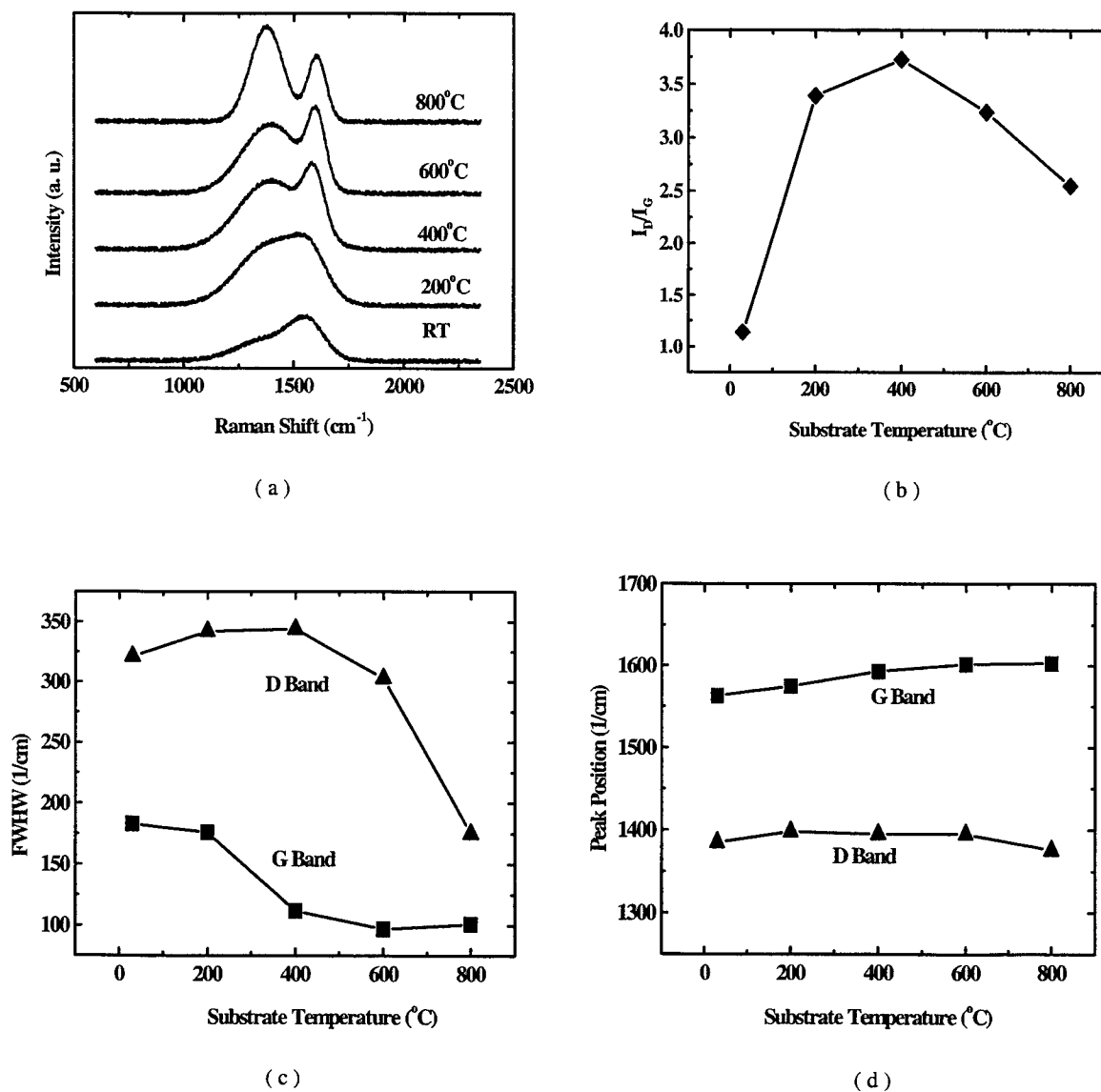


Fig. 5 (a) Raman spectra of carbon nitride thin films under different deposition temperature (b) I_D/I_G ratio of the thin films (c) Full width at half maximum value of the spectra (d) Peak positions of D bands and G bands

Figure 6 illustrates XPS spectrum for N 1s peak of the sample prepared with 100 V ion bombardment. Its C 1s peak spectrum is shown in Fig. 7. The Shirley method was used to subtract the background²¹. The atomic concentration of nitrogen in the film is evaluated by

$$\text{Concentration} = \frac{A_N / 0.5}{A_N / 0.5 + A_C / 0.31} \quad (1)$$

Here A_N and A_C are the areas under the N 1s and C 1s curve respectively. The constants 0.5 and 0.31 are the nitrogen and carbon sensitivity factors of the equipment. For above sample, the concentration is 32%. It is still lower than 57% of β - C_3N_4 . The spectrum show carbon and nitrogen peaks are at about 286 and 400 eV. Unfortunately, the spectrum achieved from XPS is a combination of several carbon and nitrogen configurations. Those configurations of atoms, differing only in a few eV, cannot be identified directly from the spectra. The usual approach is to separate single peaks into three or four lines. According to Marton et al²² by analogies with organic compounds, our spectra are fitted into three Gaussians. This can give some quantitative analysis of the synthesized thin film. In Fig. 6, the N 1s spectrum show a low content of β - C_3N_4 , centered at 398.3 eV, since the total nitrogen concentration is low. It is observed that most nitrogen tends to form structures between C_5N and C_2N , which centers at 400.0 eV. Only a small fraction of nitrogen forms N-N bond at 402.0 eV. In Fig. 7, amorphous carbon occupied the major fraction of the spectrum. This result agrees well with the Raman spectra results. The expected configuration of β - C_3N_4 , centered at 287.7 eV, shows only a small peak. Another part is a Gaussian centered at 285.9 eV, which belongs to configurations between C_5N and C_2N . From the analysis, it is found that most significant work of synthesizing β - C_3N_4 is to increase the nitrogen concentration. Otherwise other structures of carbon and nitrogen will take its place.

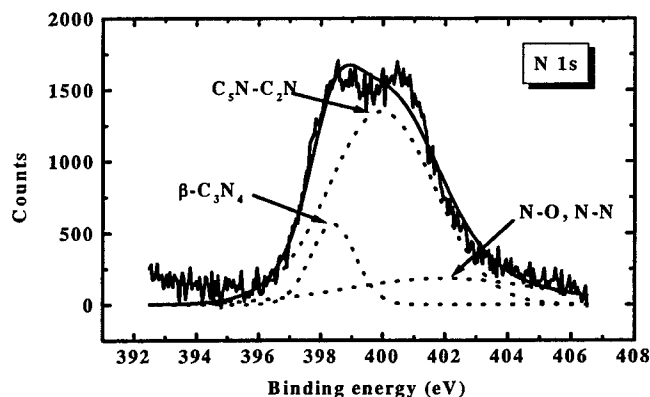


Fig. 6. X-ray photoelectron spectrum of N 1s peak of a typical carbon nitride thin film

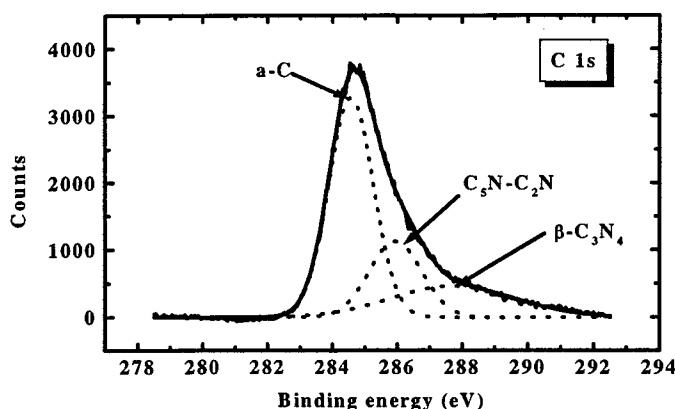


Fig. 7. X-ray photoelectron spectrum of C 1s peak of a typical carbon nitride thin film

FTIR spectra of carbon nitride thin films prepared under different temperatures are shown in Fig. 8. It is known that G band is normally IR forbidden, the incorporation of nitrogen into the structure can break the sp^2 symmetry and make the sp^2 bond IR active²³. That is why both D and G bands can be observed in Fig. 8. The peak positions of D and G band are at 1370 and 1580 cm^{-1} , respectively. The D band center position agrees the measurement of Raman spectra. The peaks at approximately 2350 cm^{-1} are due to the presence of CO_2 . It is noticed that the absorption band at 1200 cm^{-1} exists in the sample prepared at room temperature. The peak corresponds to the bond between nitrogen and sp^3 carbon atom²⁴. When the deposition temperature is 800°C, the peak does not exist. This suggests that high deposition temperature may prohibit the formation of N-(sp^3)C bond, which is predicted to be a strong bond by theory. Besides the N-(sp^3)C bond, the peak at 980 cm^{-1} may also be attributed to C-N vibration²⁵. The broad absorption band between 3500 and 4000 cm^{-1} may correspond to N-H bonds and C-O bonds, which formed after the samples were exposed in the air. Other researchers believe that C=N and C≡N bonds absorb near 1650 and 2250 cm^{-1} , respectively²⁶. They are not found in the spectra. It may suggest that most CN bonds are single bonds in the samples.

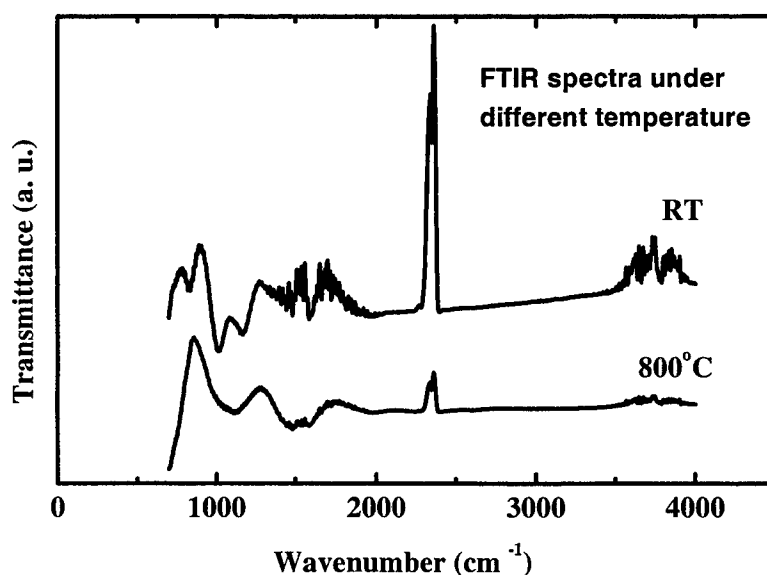


Fig. 8. Fourier transform infrared spectra of thin films prepared under different temperature

The optical band gap was measured for the samples deposited under different temperature. The temperature were room temperature, 400, and 800°C, respectively. The absorption coefficient and photon energy were measured by the ellipsometer. The measurement was made from a photon energy range between 1.5 and 4.2 eV. The optical band gap can be estimated from a plot following the Tauc equation²⁷, which expresses the absorption coefficient α of an amorphous-semiconductor thin film as

$$\alpha(E) = \text{const} \frac{(E - E_{\text{opt}})^2}{E} \quad (2)$$

where E_{opt} is defined as the optical band gap of the amorphous semiconductor. Figure 9 illustrates the relation between photon energy $(\alpha h\nu)^{1/2}$ and $h\nu$. Extrapolation of the straight line to the photon energy axis yields the optical band gap E_{opt} . The E_{opt} is a useful parameter to identify the performance of the deposited amorphous semiconductor thin film, although the value may not represent the true value of the band gap. A high quality amorphous thin film with a low level of disorder will have an E_{opt} close to that of its crystal phase²⁷. In Fig. 9, the E_{opt} values are 0.3, 0.5, and 0.65 eV for different temperatures. It is known that the crystalline carbon nitride is theoretically predicted to be a large band gap material. The expected band gap is around 6 eV, which is much higher than the measured E_{opt} . This suggests that the deposited thin film contains a high level of disorder.

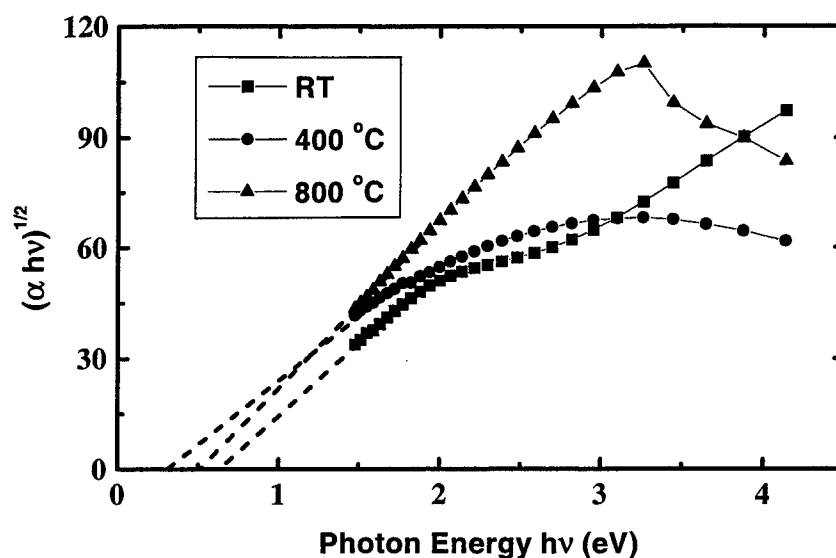


Fig. 9. The relation of $(\alpha hv)^{1/2}$ and hv used to determine the optical gap

Figure 10 shows the results of nanoindentation hardness measurement of a carbon nitride sample. It is found that thin films prepared under different substrate temperature differs not very much in hardness. Figure 10 illustrates a typical measurement result. In general, the published data show that the carbon nitride films are very elastic and the friction coefficient is in a range from 0.12 to 0.14²⁸. Measurements in this study concentrated on the mechanical properties of the thin films. Both the hardness and the bulk modulus were measured. In Fig. 10, the measurement results were given at different indentation displacement. The maximum bulk modulus and hardness are 250 and 19 GPa, respectively. The bulk modulus and the hardness reach their maximum values at different indentation displacement. This is because the bulk modulus measures only the ability of resisting compression while hardness can measure the material's ability of resisting shear and tension. The carbon nitride film shows different ability in resisting different deformations. The obtained hardness suggests that the thin film may serve well as a protective coating in applications.

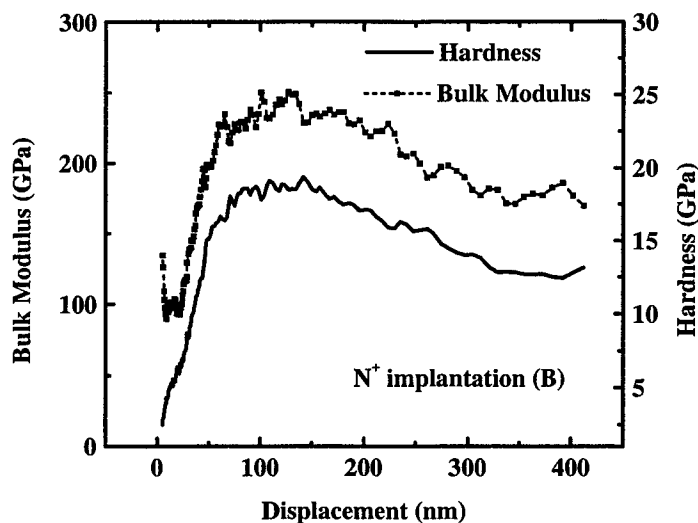


Fig. 10. Nanoindentation measurement of the thin film

4. CONCLUSIONS

Carbon nitride thin films were prepared by laser ablation of a graphite target assisted with nitrogen ion bombardment. The local density of the states was studied by STM. Two band edges were found, which gives a band gap of 1 eV. XPS has found several CN bonding in the thin films. In the results of FTIR measurement, it is found that higher ion energy is not good for the formation of N-(sp³)C bond. The band gap of the thin film were measured by ellipsometer. The mechanical properties are also studied. The hardness of the thin films is found around 19 GPa.

ACKNOWLEDGEMENTS

The authors would like to thank Dr. W. D. Song and Mr. H. Q. Ni for their suggestions on thin film preparation. Many other members in Data Storage Institute provided assistance in equipment operation. The National University of Singapore provided the scholarship for the authors to carry out the research.

REFERENCES

1. A. Y. Liu and M. L. Cohen, "Prediction of new low compressibility solids", *Science* **245** 841(1989)
2. A. Y. Liu and M. L. Cohen, "Structural properties and electronic structure of low compressibility material β -Si₃N₄ and hypothetical β -C₃N₄", *Phys. Rev. B* **41** 10727(1990)
3. C. M. Sung and M. Sung, "Carbon nitride and other speculative superhard materials", *Mater. Sci. and Phys.* **43** 1(1996)
4. J. Bulir, M. Jelinek, V. Vorlicek, J. Zemek and V. Perina, "Study of nitrogen pressure effect on the laser deposited carbon films", *Thin Solid Films* **292** 318(1997)
5. J. Yacaman, J. M. Gil, F. J. M. Gil, M. Sarikaya and M. X. Qian, "New carbon-nitrogen materials: a likely alternative to diamond", *Mater. Sci. and Phys.* **47** 109(1997)
6. C. Niu, Y. Z. Lu, C. M. Lieber, "Experimental realization of the covalent solid carbon nitride", *Science* **261** 334(1993)
7. H. X. Han and B. J. Feldman, "Iron doped amorphous hydrogenated carbon nitride" *Solid State Commun.* **65**, 921 (1988)
8. J. H. Kaufman, S. Metin and D. D. Saperstein, "Symmetry breaking in nitrogen doped amorphous carbon infrared observation of the raman-active G-bands and D-bands", *Phys. Rev. B* **39** 13053(1989)
9. M. Y. Chen, X. Lin, V. P. Dravid, Y. W. Chung, M. S. Wong and W. D. Sproul, "Synthesis and tribological properties of carbon nitride as a superhard coating and solid lubricant", *J. Vac. Sci. Technol. A* **11** 521(1993)
10. Z. M. Ren, Y. Du, Y. Qiu, J. D. Wu, Z. Ying and F. Li, "Carbon nitride films synthesized by combined ion-beam and laser ablation processing", *Phys. Rev. B* **51** 2211(1995)
11. C. J. Torng, J. M. Sivertsen, J. H. Judy and C. Chang, "Structure and bonding studies of the C-N thin films produced by RF-sputtering method", *J. Mater. Res.* **5** 2490(1990)
12. M. Diani, A. Mansour, L. Kubler, J. L. Bischoff and D. Bolmont, "Search for carbon nitride CN_x compounds with a high nitrogen content by electron-cyclotron-resonance plasma deposition", *Diamond Relat. Mater.* **3**(3) 264 (1994)
13. A. Hoffman, I. Gouzman and R. Brener, "Possibility of carbon nitride formation by low-energy nitrogen implantation into graphite in-situ electron-spectroscopy studies", *Appl. Phys. Lett.* **64** 845(1994)
14. T. Sekine, H. Kanda, Y. Bando, M. Yokoyama and K. Hojou, "A graphitic carbon nitride", *J. Mater. Sci. Lett.* **9** 1376(1990)
15. J. P. Riviere, D. Texier, J. Delafond, M. Jaouen, E. L. Mathe and J. Chaumont, "Formation of the crystalline β -C₃N₄ phase by dual-ion beam sputtering deposition", *Mater. Lett.* **22** 115(1995)
16. H. Deng, T. W. Scharf and A. Barnard, "Adhesion assessment of silicon carbide, carbon and carbon nitride ultra-thin overcoats by nanoscratch techniques", *J. Appl. Phys.* **81**(8) 5396(1997)
17. M. A. Lutz, R. M. Feenstra, and P. M. Mooney, "Facet formation in strained Si_{1-x}Ge_x films" *Surf. Sci.* **316**, 1075 (1994)
18. R. M. Feenstra, "Tunneling spectroscopy of the (110) surface of direct-gap III-V semiconductors", *Phys. Rev. B* **50**, 4561(1994)
19. R. J. Nemanich, L. Bergman, and K. F. Turner "Properties of interface of diamond" *Physica B* **185**, 528(1993)
20. L. C. Chen, T. R. Lu, and C. T. Kuo, "The use of a biomolecular target for crystalline carbon nitride film deposition by Ar ion-beam sputtering without any other source of nitrogen" *Appl. Phys. Lett.* **72** 3449(1998)
21. G. C. Smith, *Surface Analysis by Electron Spectroscopy*, Plenum Press, NY, 1994
22. D. Marton, K. J. Boyd, A. H. Al-Bayati, S. S. Todorov and J. W. Rabalais, "Carbon nitride deposited using energetic

- species a 2-phase system", *Phys. Rev. Lett.* **73** 118(1994)
23. J. H. Kaufman, S. Metin and D. D. Saperstein, "Symmetry breaking in nitrogen doped amorphous carbon infrared observation of the raman-active G-bands and D-bands", *Phys. Rev. B* **39** 13053(1989)
24. D. Dolphin and A. Wick, *Tabulation of Infrared Spectral Data*, Wiley, New York, 1977.
25. A. Bubbenzer, "Fundamental plasma reactions and phenomena related to thin-film technology", *Vacuum* **38**, 945(1988)
26. N. B. Colthup, L. H. Daly, S. E. Wiberley, *Introduction to Infrared and Raman Spectroscopy*, Academic Press, 1964
27. N. F. Mott and E. A. Davis, *Electronic Processes in Non-Crystalline Materials*, 2nd ed. Clarendon, Oxford, 1979
28. I. H. Murzin, G. S. Tompa and E. W. Forsythe, "Use of sputtering and negative carbon ion sources to prepare carbon nitride films" *J. Vac. Sci. Technol A* **15** 1179 (1997)

Pulsed laser deposition of hydrogenated amorphous carbon films from a polymeric target

S. M. Huang ^a, Y. F. Lu ^a, Z. Sun ^b

^aLaser Microprocessing Laboratory, Department of Electrical Engineering and Data Storage Institute, National University of Singapore, 10 Kent Ridge Crescent, Singapore 119260

^bSchool of Electrical and Electronic Engineering, Nanyang Technological University, Nanyang, Singapore 639798

ABSTRACT

The phenylcarbyne polymer possesses a diamond-like structure. Because of its special structure, this polymer can be converted into diamond-like carbon phases at atmospheric pressure by thermal decomposition. In this article, we report on the growth of hydrogenated amorphous carbon films (a-C:H) films by pulsed laser (KrF excimer, $\lambda = 248$ nm) ablation of a phenylcarbyne polymer target under vacuum. a-C:H films were deposited with various laser fluences and at different substrate temperatures. Chemical and structural characteristics of these films were analysed using X-ray-excited Auger electron spectroscopy (XAES), photoelectron loss spectroscopy (PELS), and Raman spectroscopy. It was found that the fourfold-coordinated component increases with laser fluence at 80 °C or increases with temperature increasing from 25 °C to 60 °C at a fluence of 1×10^9 W/cm². When the deposition temperature is increased from 60 °C to 200 °C at a fluence of 1×10^9 W/cm², the graphitic component increases. The variation in chemical structures of these films is explained in terms of the changes in the fraction of sp²-bonded clusters and changes in the termination of the graphitic clusters and sp³-bonded networks by hydrogen in the a-C:H films.

Keywords: Hydrogenated amorphous carbon (a-C:H) films, Phenylcarbyne polymer, Pulsed laser deposition

1. INTRODUCTION

In recent years, hydrogenated amorphous carbon (a-C:H) films have attracted great attention because of their interesting combination of optical, electrical and mechanical properties. These properties include transparency in visible and near infrared regions, optical absorption in the ultraviolet spectral region, hardness, controllable electrical resistance and good substrate adhesion for protective coatings [1, 2]. Depending on preparation conditions, a-C:H films also indicate soft (graphite-like or polymer-like) and hard (diamond-like) characters, which are intermediate between diamond, graphite, and hydrocarbon polymers. It has been reported that a-C:H films can be prepared using deposition techniques such as radio-frequency (RF) plasma-enhanced chemical vapour deposition (PECVD) [3,4], ion-beam deposition [5], sputtering [6], cathodic arc and direct ion beam deposition [7], and pulsed laser deposition (PLD) [8]. The source materials are carbon-containing gases, pure solid graphite targets, and occasionally polymeric targets [9]. Among these techniques, PLD is becoming an effective method for the preparation of a-C:H films owing to its extremely high power ($>10^8$ W) delivered in a nanosecond order pulse interval. The technique can be utilized not only to deposit materials which reproduce the stoichiometry and properties of the target, but also to produce films with desired properties quite different from those of the target material. In the case of PLD techniques, several studies aimed at deposition and investigation of the properties of hard a-C:H films have been reported. The properties of soft a-C:H films have not been extensively studied yet. Very recently, we have succeeded in growing diamond clusters and diamond-like films from poly(phenylcarbyne) polymer by a pulsed Nd:YAG laser ($\lambda = 532$ nm) irradiation [10,11]. Also, this polymer was found to be one of the most effective target materials for studying the properties of both soft and hard a-C:H films by PLD technique.

In present work, we report our recent experimental work on the preparation of a-C:H films by pulsed laser ablation of a poly(phenylcarbyne) polymer target. The main purpose of this work is to investigate the changes in chemical structure and nano-hardness of a-C:H films versus laser fluence and deposition temperature in the PLD system.

2. EXPERIMENTAL DETAILS

The poly(phenylcarbyne) polymer was synthesized by reductive condensation of 1,1,1-trichlorotoluene monomer with an ultrasonically generated NaK alloy emulsion in tetrahydrofuran (THF) in an inert atmosphere [12]. The product $[\text{C}_6\text{H}_5\text{C}]_n$ was obtained from the reaction as tan powders. Measurements from nuclear magnetic resonance (NMR), IR spectra, UV-VIS spectrometry and photoluminescence spectra show that the polymer consists of a randomly constructed rigid network of tetrahedral phenylcarbyne units in which each carbyne carbon forms three C-C bonds to the network and one to the phenyl substituent [12]. The polymer powder was pressed into pellets.

a-C:H films were prepared in a PLD system shown in Fig. 1. The distance between the polymeric pellet target and substrate surface was about 3 cm. The 248 nm KrF excimer laser (Lambda Physik LPX 100) was used to produce a laser beam with a pulse duration of 23 ns. The output power of the laser can be changed to provide fluence from 1×10^7 to 1×10^9 W/cm² (or from 230 to 23000 mJ/cm²) on the target surface. A repetition rate of 10 Hz is used through this experiment. The chamber was evacuated to a base pressure of 10^{-6} Torr prior to deposition. For a fixed substrate temperature, the deposition rates varied from about 7 to 360 nm/min as the laser fluence changed from 1×10^7 to 1×10^9 W/cm².

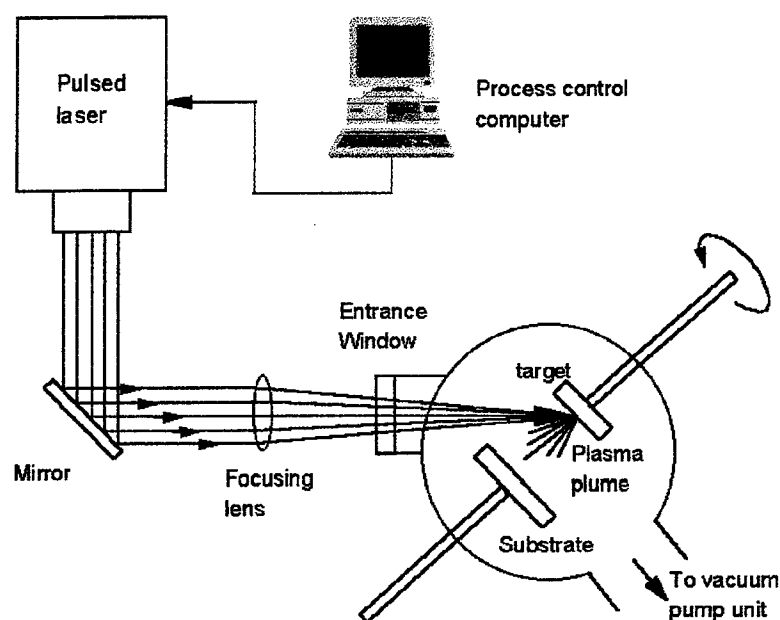


Fig.1 A schematic diagram of the experimental setup

Two groups of samples were prepared. One group (B) of samples was produced under laser fluences of 1×10^7 (B1), 1×10^8 (B2), 2.5×10^8 (B3), 3.5×10^8 (B4), and 1×10^9 (B5) W/cm² at the temperature of 80° C, respectively. The other group (H) of samples were prepared at various substrate temperatures of 25 (H1), 60 (H2), 80 (B5), 100 (H4), 150 (H5), and 200 (H6) °C at a laser fluence of 1×10^9 W/cm². Quartz and Si (100) wafers were used as substrates. All the substrates were cleaned by acetone and deionized water in an ultrasonic bath. The cleaned wafer was placed into the vacuum chamber soon after.

X-ray-excited Auger electron spectroscopy (XAES) and photoelectron loss spectroscopy (PELS) were examined. XAES and PELS were performed by an ESCALAB 220I-XL instrument. The X-ray source monochromator Al K α (1385.6 eV) was used. The spectrometer worked at constant pass energy. The XAES and energy loss measurements were carried out with a pass energy of 50 eV and a step of 0.5 eV. Highly oriented pyrolytic graphite (HOPG), a polycrystalline diamond film and DLC film were used as reference samples. The polycrystalline diamond sample was prepared in a conventional hot-filament

(HF) CVD system at the substrate temperature of 800° C with the CH₄/H₂ ratio being 0.5 %. The DLC sample was deposited at room temperature with a fluence of 1×10^9 W/cm² from a graphite target in the same PLD system. The micro-Raman measurements were made with Renishaw Ramanscope using an argon-ion laser operating at 514.5 nm, which has a resolution of 1 cm⁻¹.

3. RESULTS AND DISCUSSION

3.1 Chemical bonding structure from XAES and PELS

All the samples were analyzed using XAES and PELS. Figure 2 shows the measured integral $N(E)$ and derivative form dN/dE CKLL Auger spectra from freshly cleaved HOPG, polycrystalline diamond, DLC and a-C:H films deposited at 80° C with laser fluence 3.5×10^8 (B4) W/cm².

The major difference between the graphite, diamond, DLC and a-C:H spectra of Fig. 2 (a) is the main Auger transition energy. The main transition energy in all $N(E)$ spectra ranges from 260 to 280 eV, being 268.4 eV for graphite, 262.5 eV for diamond, 263.4 eV for DLC and ~262 eV for a-C:H. It is clear from Fig. 2 that the CKLL Auger spectrum of a-C:H film are quite similar to that of diamond sample or DLC sample rather than that of graphite.

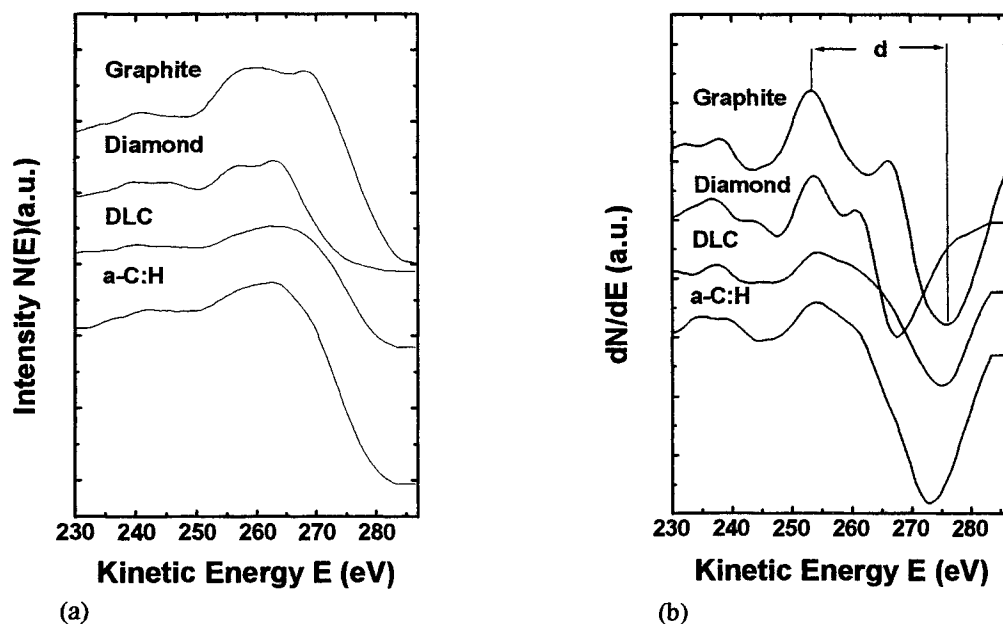


Fig. 2 XAES CKLL spectra from various sample: (a) the XAES $N(E)$ spectra, (b) the first derivative of the XAES $N(E)$ spectra

Analysis of the fine structure of the carbon Auger signal can yield information concerning the average degree of hybridization of the carbon atoms in the film. The distance d , as displayed in Fig. 2(b), between the positive and negative maxima in the first-derivative carbon Auger spectrum, is sensitive to hybridization, and can be used as a finger-print of the type of carbon presented [13, 14]. X-ray-excited Auger data have shown previously that the value of d is approximately 14 eV in the case of diamond and 23 eV in the case of graphite, indicating typical values for films composed entirely of sp^3 and sp^2 carbon atoms [13]. An important caveat is that carbon films are very sensitive to electron-beam damage from electron

beams in the energy range (3-10 KV) typically used to obtain Auger spectra [13]. This makes it essential, when using electron-excited Auger spectroscopy, to employ brief exposure times and electron-beam energies that are as low as possible.

In the derivative spectra in Fig. 2 (b), the maximum (at ~ 253 eV) is quite fixed for all the samples, whereas the variation of the minimum, and thus the variation of the distance d , can be seen clearly. This variation could be attributed to the different arrangement carbon atoms. From Fig. 2 (b), The value of the d is 14.3 eV for CVD diamond, 22.5 eV for graphite, and 20.1 eV for DLC. Figure. 2 (b) show that the d value for a-C:H film is intermediate between those of diamond and DLC. In our work, we found the d value increases a little with decreasing laser fluence. The increase in d could be associated with the increasing number of sp^2 sites in the film with decreasing laser fluence.

The energy loss of photoelectrons leaving the sample due to the interactions with plasmon oscillations was revealed by some structures that appear in the kinetic energy region lower than ~ 1202 eV which is, in our samples, the value corresponding to photoemission of 1s transition of the carbon. Figure 3 shows energy loss spectra obtained by the photoelectrons from freshly cleaved HOPG, polycrystalline diamond, DLC and a-C:H films deposited at 80°C with laser fluence 3.5×10^8 (B4) W/cm^2 . In the layered structure of graphite, the collective excitation of the π -electrons gives rise to the loss at 6.5 eV, whereas the plasmon of σ - and π -electrons together is responsible for the loss maximum at 29.5 eV below the C 1s line. The spectrum of polycrystalline CVD-diamond consists of a broad peak centered at 33 eV with a prominent shoulder at 24 eV, matching the spectra of natural or synthetic diamond crystals. The spectrum of the DLC sample is distinct from that of graphite, consisting of a single broad plasmon peak centered at 31.4 eV. The spectra of a-C:H films are similar in characteristics to that of the DLC sample, but the energies of the peaks are slightly lower (about 27 eV). For these two kinds of samples, a weak shoulder of $\pi - \pi^*$ antibonding transition peak at 6.5 eV implies its disordered structure and a low fraction of sp^2 bonding in the films. The shift to lower energies of the plasmon peak from crystalline diamond may be a result of reduction of the density of the films due to their amorphous structure. But, for the DLC sample, the energy is high than that of graphite, and so is the density. For the a-C:H film, the energy are lower than that of graphite, and so are their densities. Other a-C:H films show the similar results.

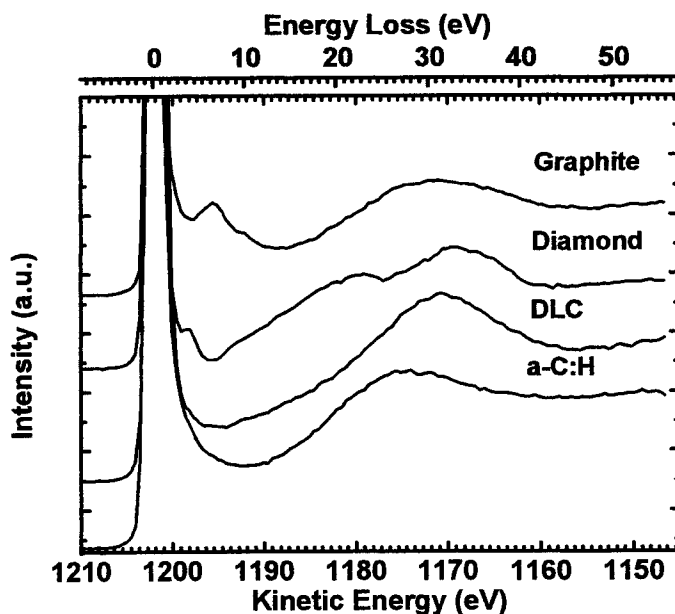


Fig. 3 Photoelectron energy loss spectra of various samples.

3.2 Chemical bonding and microstructure of a-C:H films from Raman shift

Raman spectroscopy is powerful to analyse carbon films owing to its ability to distinguish between different bonding types and domain sizes. Generally, single crystalline diamond shows a single sharp peak at 1332 cm^{-1} . Large single crystal graphite and highly oriented pyrolytic graphite (HOPG) display a single sharp peak at about 1580 cm^{-1} (G band). Disorder or fine

graphite crystallites (below 30 nm) show an additional disorder at about 1355 cm^{-1} (D band), and the G band may shift to higher frequency (up to about 1600 cm^{-1}) [15]. The peak at 1580 cm^{-1} in graphite is due to the Raman allowed E_{2g} mode [16]. The peak at about 1355 cm^{-1} in disorder graphite results from a relaxation of the $k = 0$ selection rule for Raman scattering in crystals [16]. The Raman spectrum of a-C:H film consists of a broad peak at about 1550 cm^{-1} (G band) and a shoulder around 1360 cm^{-1} (D band). The Raman peak maximum at 1560 cm^{-1} is characteristic of DLC films [17].

Figure 4 shows the details of the Raman spectra between 800 cm^{-1} and 2000 cm^{-1} obtained from B-group samples. It is seen that the shapes of the experimental curves vary as a function of laser fluence. For sample B1, the Raman spectrum is fit by two peaks with Lorentzian line shapes and a background centered at 2030 cm^{-1} . This background is very strong and broad. It can be attributed to the fluorescence in the sample. For the rest samples in group-B, the experimental data are fit best by two peaks with Lorentzian line shapes and a background around 1960 cm^{-1} . The background around 1960 cm^{-1} is broad and weak, attributing to the second-order combination scattering of two main structures at 550 and 1550 cm^{-1} [18]. Each plot consists of the experimental data and the fitted curves. From the fitting parameters the peak position, peak width, and integrated intensity ratio of the two peaks are obtained.

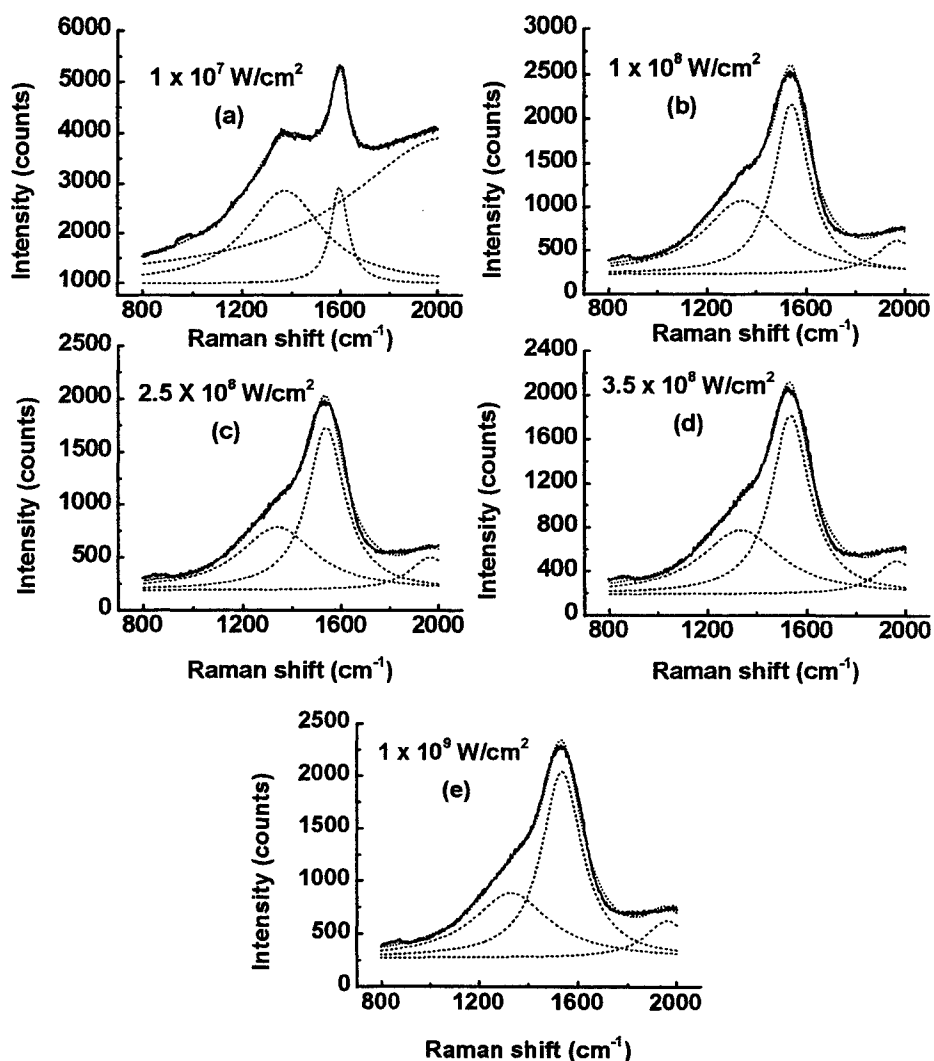


Fig.4 Raman spectra of a-C:H films (B-group) deposited with different laser fluences at a deposition temperature of 80°C .

Table I shows all the fitting parameters for spectra from B-group samples. Three important features can be noticed: as the laser fluence increases from 1×10^7 to 1×10^9 W/cm², (1) both the D and G band positions shift to lower frequencies; (2) the intensity ratio I_D/I_G also decreases from 4.17 to 0.67; (3) the G band width increases from 87 cm⁻¹ to 193 cm⁻¹.

Table I. Experiment results from Raman spectra for films (B-group) deposited with various fluences at 80 ° C.

Sample	Raman peak position		Raman FWHM		I_D/I_G
	G-band (cm ⁻¹)	D-band (cm ⁻¹)	G-band (cm ⁻¹)	D-band (cm ⁻¹)	
B1	1597	1372	87	376	4.17
B2	1543	1346	174	381	0.96
B3	1540	1341	186	370	0.77
B4	1537	1337	187	388	0.74
B5	1537	1331	193	375	0.67

The Raman spectra of the carbon samples are analysed in terms of band position, width, and integrated intensity ratio of the G and D bands [16, 19-22]. In a theoretical study, Beeman et al. modeled bulk amorphous carbon using increasing amounts of bond angle disorder and fourfold coordination. It was found that increasing the percentage of four fold coordination bonds leads to a decrease in both the G and D peak frequencies instead of a mixture of the Raman peaks associated with diamond and graphite [20]. Richter et al. calculated the frequency of the G band using a simple valence force model weighted by the fraction of sp³ and sp² bonds. They found that frequency shifts in the G band are caused only by changes in the force constants and correspond to a certain sp³ bonding fraction [21]. The Raman shift of D band towards lower wave number, in carbon films prepared with rf sputtering [22], has been attributed to carbon atoms in sp³ sites.

Consequently, the simultaneous downshift in both the G and D peaks with increasing laser fluence over the entire range for B-group samples indicates an increase of sp³-bonded atomic sites. In particular, this result shows that the sp³/sp² ratio increases significantly for fluence below 2.5×10^8 W/cm². The range of the observed frequency shift for the G band corresponds to a sp³-bonding fraction of 4 to 20% in the model of Richter et al [21]. This change in the Raman spectrum suggests that the film becomes more diamond-like (higher sp³/sp²) when laser fluence is increased from 1×10^7 to 1×10^9 W/cm² for W-group samples. The film hardness for B-group samples was measured and found to increase from 1.5 to 8.5 GPa as laser fluence increases from 1×10^7 to 1×10^9 W/cm². This result provides direct evidence for the above Raman analysis and its conclusion. In addition, the conclusion from Raman results is consistent with that of XAES results in section 3.1.

Robertson and O'Reilly [23] have reported that amorphous carbon films consist of clusters of threefold-coordinated sp² carbon embedded in an sp³-bonded matrix, while the sp² clusters are responsible for properties such as the optical gap, the sp³ clusters are mainly responsible for the mechanical properties such as hardness [23]. Yoshikawa et al. [24] have previously reported that the ratio of sp² to sp³ bonds in amorphous carbon films increases with the intensity ratio I_D/I_G in Raman spectrum. Therefore, the decrease in the intensity ratio I_D/I_G is consistent with the simultaneous shifting of both the G and D peak positions towards lower frequencies and the tendency for the films to be more diamond-like (hence lower sp²/sp³ ratio) at higher fluences.

We also measured Raman spectra from H-group samples deposited with a fluence of 1×10^9 W/cm² at various substrate temperatures. Figure 5 shows the Raman spectra between 800 and 2000 cm⁻¹. It is shown that the shapes of the experimental curves vary as a function of substrate temperature. Using the same fitting method for the spectra from B-group samples in Fig. 4, the peak position, peak width, and integrated intensity ratio of the two peaks are obtained from the spectra in Fig. 5. Table II shows all the fitting parameters for the spectra of H-group samples. From Fig. 5 and Table II, when the temperature increases from 25 °C to 60 °C, the spectrum shows a similar trend occurred in B-group samples with increasing laser fluence previously mentioned. Both the D and G band positions show large downshifts, from 1583 to 1534 cm⁻¹ and from

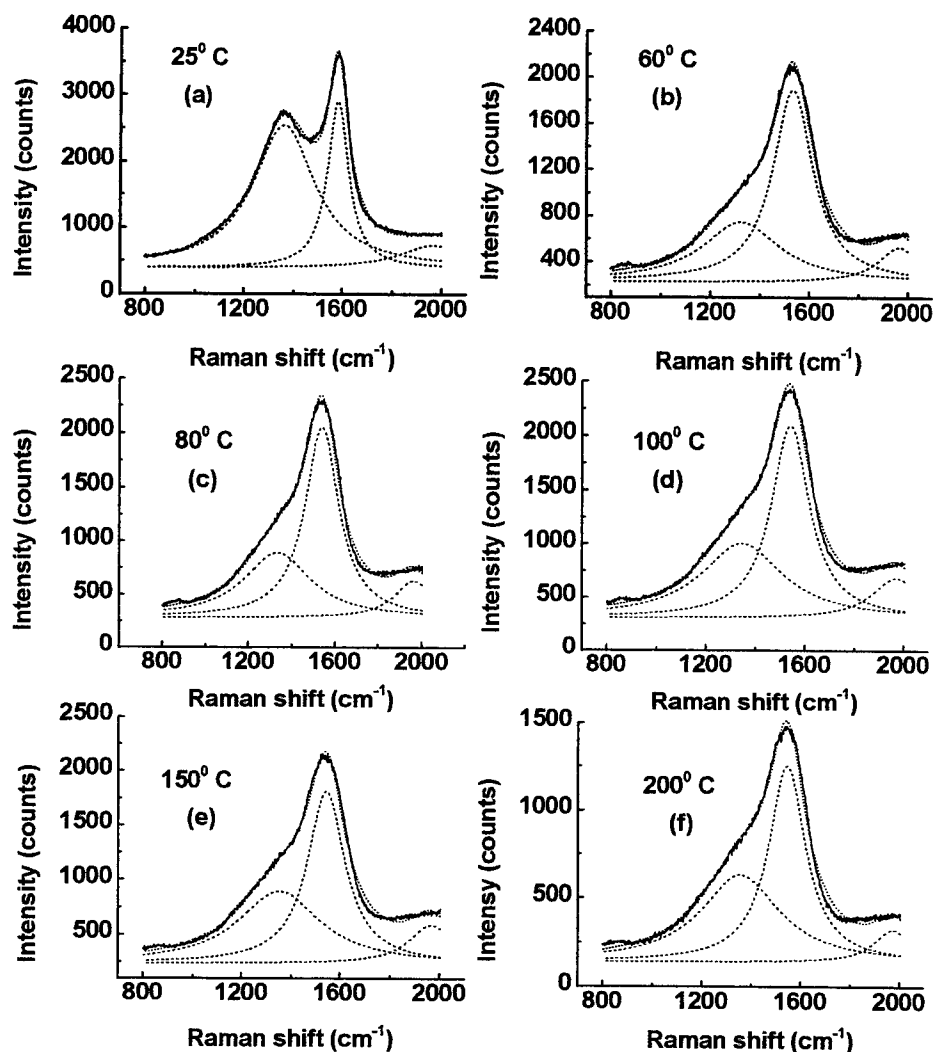


Fig. 5 Raman spectra of a-C:H films (H-group) deposited at different deposition temperatures with a fluence of $1 \times 10^9 \text{ W/cm}^2$.

1363 to 1324 cm^{-1} , respectively. The intensity ratio also shows a large decrease from 2.51 to 0.58. These changes indicate an increase of sp^3/sp^2 ratio and the film being more diamond-like as the temperature increases from 25 to 60°C . The spectra of the films deposited above 25°C are similar. They are dominated by the peak at about 1540 cm^{-1} and show a weak shoulder at about 1355 cm^{-1} . Their G peak is broad, indicating large stress, disorder and high sp^3 content. When the temperature increases from 60 to 200°C , the G band shows a weak frequency increase from 1534 cm^{-1} to 1544 cm^{-1} , the D band shifts from 1324 to 1355 cm^{-1} , and the intensity ratio I_D/I_G also shows a weak increase from 0.58 to 0.93. These changes suggest a weak increase of sp^2/sp^3 ratio [20-22, 24] with temperature. The D band shifting to higher wave number can also be related to the decrease of hydrogen content and internal stress in the films [25-27].

For the H-group samples, the film hardness increases from 5.5 to 12 GPa as the temperature increases from 25 to 150°C , and shows no change with further temperature increase. The hardest films are deposited around 150°C . In contrast, the a-C:H films that appear to contain a higher sp^2 -bonding fraction have higher hardness. The high hardness of H-group samples deposited around 150°C may result from changes in microscopic morphology of the films due to hydrogen. At low temperature of 60°C , the sp^3 and hydrogen contents are high [25-27], so the film is less hard. At higher temperature around

Table II Experiment results from Raman spectra for films (H-group) deposited at various temperatures with a fluence of 1×10^9 (W/cm²).

Sample	Raman peak position		Raman FWHM		
	G-band (cm ⁻¹)	D-band (cm ⁻¹)	G-band (cm ⁻¹)	D-band (cm ⁻¹)	I _D /I _G
H1	1583	1363	104	305	2.51
W7	1534	1324	197	375	0.58
H3	1537	1331	193	375	0.67
H4	1540	1344	189	398	0.82
H5	1542	1352	187	400	0.89
H6	1544	1355	182	382	0.93

150 °C, the hydrogen content is lower, and sp³ content is still quite high. It is controversial whether hydrogen preferentially bonds to specific atomic sites (sp²- or sp³-bonded) or not [28, 29]. However, incorporation of hydrogen in the amorphous carbon should result in termination (C-C) sp³-bonded network as well as reducing the bonding between graphitic clusters and surrounding sp³-bonded networks. Removing hydrogen and transformation of hydrogenated sp³ to sp² bonds allows more cross-linking and results in the decrease of disconnected sp²-bonded clusters and terminated C-C sp³-bonded networks. Then, increase in hardness of the film is expected. Further improvement of the film quality can be obtained by creation of more dehydrogenated sp³ carbon. Jansen et al [30] reported similar variation in the hardness, density, and chemical bonding configurations (sp²/sp³) with hydrogen for hydrogenated carbon.

4. CONCLUSION

Two groups of amorphous hydrogenated carbon films prepared by laser ablation of a poly(phenylacetylene) target were investigated. Changes in laser fluence and the deposition temperature resulted in systematic changes in XAES, PELS, hardness, and Raman spectroscopy measurements of these films. We interpret these results as a systematic variation in the chemical structure of the amorphous hydrogenated carbon films as a function of the deposition parameters.

The a-C:H films were studied as a function of laser fluence at 80° C. Results from Raman spectroscopy suggest that the sp³-bonding fraction increases with increasing laser fluence. The hardness of the a-C:H films increases with fluence. The a-C:H films were also studied as a function of the deposition temperature at a fluence of 1×10^9 W/cm². When the temperature is increased from 25° C to 60° C, results from Raman spectroscopy indicate that the sp³-bonding fraction increases with the temperature. When the temperature increases from 60° C to 200° C, results from Raman suggest that the sp²-bonding fraction increases. XAES and PELS results also support the conclusion from Raman analysis. The variation in chemical structures of these films can be explained in terms of the changes in the fraction of sp²-bonded clusters and changes in the termination of the graphitic clusters and sp³-bonded networks by hydrogen in the a-C:H films.

References

1. J. C. Angus, P. Koidl, and S. Domitz, in *Plasma Deposition Thin Films*, edited by J. Mort and F. Jansen, CRC, Boca Baton, FL, 1986, pp.530.
2. J. Robertson, "Hard amorphous (diamond-like) carbons," *Prog. Solid State Chem.* **21**, pp.199-333, 1991.
3. H. Vora and T. J. Moravec, "Structural investigation of thin films of diamondlike carbon," *J. Appl. Phys.* **52**, pp. 6151-6157, 1981.
4. G. J. Varentop, M. Kawasaki, R. M. Nix, I. G. Brown, M. Salmeron, and G. A. Somorjai, "Formation of hydrogenated amorphous carbon films of controlled hardness from a methane plasma," *Phys. Rev. B* **41**, pp. 3200-3210, 1990.

5. S. Aisenberg and R. Chabot, "Ion-beam deposition of thin films of diamondlike carbon," *J. Appl. Phys.* **42**, pp. 2953-2958, 1971.
6. N. Savvides, "Optical constants and associated functions of metastable diamondlike amorphous carbon films in the energy range 0.5-7.3 eV," *J. Appl. Phys.* **59**, pp. 4133-4145, 1986.
7. P. J. Fallon, V. S. Veerasamy, C. A. Davis, J. Robertson, G. A. J. Amaratunga, W. I. Milne, and J. Koskinen, "Properties of filtered-ion-beam-deposited diamondlike carbon as a function of ion energy," *Phys. Rev. B* **48**, pp. 4777-4782, 1993.
8. C. B. Collins, F. Davanloo, E. M. Juengerman, W. R. Osborn, and D. R. Jander, "Laser plasma source of amorphous diamond," *Appl. Phys. Lett.* **54**, pp. 216-218, 1989.
9. I. S. Athwal, A. Mele, and E. A. Ogryzlo, "Techniques for depositing DLC films by pulsed laser ablation of organic solids", *Diam. Relat. Mater.* **1**, pp. 731, 1992.
10. S. M. Huang, Y. F. Lu, and Z. Sun, "Conversion of diamond clusters from a polymer by Nd:YAG pulsed laser (532nm) irradiation," *Appl. Surf. Sci.* **151**, pp. 244-250, 1999.
11. Y. F. Lu, S. M. Huang, Z. Sun, *J. Appl. Phys.*, in press
12. T. Visscher, D. C. Nesting, J. V. Badding and P. A. Bianconi, "Poly(phenylcarbyne): A polymer precursor to diamond-like carbon," *Science* **260**, pp. 1496, 1993.
13. Y. Mizokawa, T. Miyasato, S. Nakamura, K. M. Geib, and C. W. Wilmsen, "Comparison of the C KLL first-derivative Auger spectra from XPS and AES using diamond, graphite, SiC and diamond-like-carbon films" *Surf. Sci.* **182**, pp. 431, 1987.
14. Y. Mizokawa, T. Miyasato, S. Nakamura, K. M. Geib, C. W. Wilmsen, "The C KLL first-derivative x-ray photoelectron spectroscopy spectra as a fingerprint of the carbon state and the characterization of diamondlike carbon films," *J. Vac. Sci. Technol. A* **5**, pp. 2809, 1987.
15. R. J. Nemanich, J. T. Glass, G. Lucovsky and R. E. Shroder, "Raman scattering characterization of carbon bonding in diamond and diamondlike thin films," *J. Vac. Sci. Technol. A* **6**, pp. 1783, 1988.
16. F. Tuinstra, J. L. Koenig, "Raman spectrum of graphite," *J. Chem. Phys.* **53**, pp. 1126, 1970.
17. M. Yoshikawa, "Raman spectra of diamondlike amorphous carbon films," *Mater. Sci. Forum* **52 & 53**, pp. 365-385, 1989.
18. W. S. Bacsa, J. S. Lannin, D. L. Pappas, and J. J. Cuomo, "Raman scattering of laser-deposited amorphous carbon," *Phys. Rev. B* **47**, pp. 10931, 1993.
19. P. Lespade, R. Al-Jishi, and M. S. Dresselhaus, "Model for Raman scattering from incompletely graphitized carbons," *Carbon* **20**, pp. 427, 1982.
20. D. Beeman, J. Silverman, R. Lynds, and M. R. Anderson, "Modeling studies of amorphous carbon," *Phys. Rev. B* **30**, pp. 870, 1984.
21. A. Richter, H.-J. Scheibe, W. Pompe, K.-W. Brzezinka, and I. Muhling, "About the structure and bonding of laser generated carbon films by Raman and electron energy loss spectroscopy," *J. Non-Cryst. Solids* **88**, pp. 131, 1986.
22. R. O. Dillon, J. A. Woollam, and V. Katkanant, "Use of Raman scattering to investigate disorder and crystallite formation in as-deposited and annealed carbon films," *Phys. Rev. B* **29**, pp. 3482, 1984.
23. J. Robertson, and E. P. O'Reilly, "Electronic and atomic structure of amorphous carbon," *Phys. Rev. B* **35**, pp. 2946, 1987.
24. M. Yoshikawa, G. Katagiri, H. Ishida, and A. Ishitani, "Raman spectra of diamondlike amorphous carbon films," *J. Appl. Phys.* **64**, pp. 6464, 1988.
25. R. E. Shroder, R. J. Nemanich, and J. T. Glass, "Analysis of the composite structures in diamond thin films by Raman spectroscopy," *Phys. Rev. B* **41**, pp. 3738, 1990.
26. K. Kobashi, K. Nishimura, V. Kawate, and T. Horiuchi, "Synthesis of diamonds by use of microwave plasma chemical-vapor deposition: morphology and growth of diamond," *Phys. Rev. B* **38**, pp. 4067, 1988.
27. J. A. Woollam, B. N. De, Orzeszko, N. J. Lanno, P. G. Snyder, S. A. Alterovitz, J. J. Pouch, R. L. C. Wu, and D. C. Ingram, "Diamondlike carbon applications in infrared optics and microelectronics," *Mater. Sci. Forum* **52 & 53**, pp. 577-608, 1989.
28. B. Dischler, A. Bubenzer, and P. Koidl, "Bonding in hydrogenated hard carbon studied by optical spectroscopy", *Solid State Commun.* **48**, pp. 105, 1983.
29. M. P. Nadler, T. N. Donovan, and A. K. Greene, "Structure of carbon films formed by the plasma decomposition of hydrocarbons", *Appl. Surf. Sci.* **18**, pp. 10, 1984.
30. F. Jansen, M. Machonkin, S. Kaplan, and S. Hark, "The effects of hydrogenation on the properties of ion beam sputter deposited amorphous carbon" *J. Vac. Sci. Technol. A* **3**, pp. 605, 1985.

Preparation of polyperinaphthalenic organic semiconductor thin films by excimer laser ablation and application to anode electrodes for ultra thin rechargeable lithium ion batteries

Satoru Nishio^{*a}, Sigenori Kuriki^a, Yukari Tsujine^a, Akiyoshi Matsuzaki^a, Hiroyasu Sato^a,

Nobuo Ando^b, Yukinori Hato^b, Kazuyoshi Tanaka^c

^aDepartment of Chemistry for Materials, Faculty of Engineering, Mie University, 1515,

Kamihama-cho, Tsu 514-8507, Japan

^bKanebo, LTD., 3-1, Kanebo-cho, Hofu, Yamaguchi, 747-0823, Japan

^cDepartment of Molecular Engineering, Kyoto University, Sakyo-ku, Kyoto, 606-8501, Japan

ABSTRACT

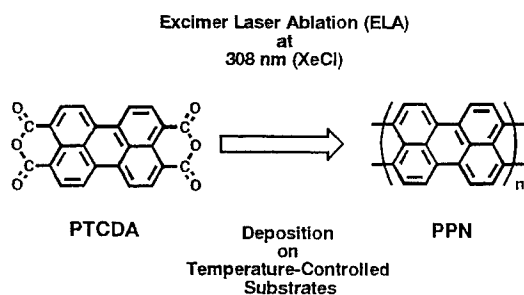
Amorphous organic semiconductor thin films are prepared on temperature-controlled substrates by excimer laser ablation (ELA) of 3, 4, 9, 10-perylenetetracarboxylic dianhydride (PTCDA) or PTCDA/Co mixture target with a 308(XeCl) pulsed excimer laser beam. Drastic increase in conductivity was observed along with decrease in the IR peak intensities related to the side groups of PTCDA monomers for films prepared on substrates above 200°C. Electric conductivity of a film prepared on a substrate at 300°C comes up to 10⁻¹Scm⁻¹. Although carbon radicals are detected to some extent, indicating incomplete polymerization, Raman spectroscopic measurement reveals that this film basically consists of polyperinaphthalene (PPN) structure. This material is named polyperinaphthalenic organic semiconductor (PPNOS). ELA of mixture target of PTCDA and Co enables us to obtain PPNOS at room temperature. Electrochemical doping of PPNOS films with lithium ion suggests the passable performance of this film as anode electrodes of ultra thin rechargeable lithium ion batteries.

Keywords: Amorphous organic semiconductor, excimer laser ablation, polyperinaphthalene, anode electrodes, ultra thin rechargeable lithium ion batteries

1. INTRODUCTION

Recently, amorphous carbon materials as the anode electrodes of ultra thin rechargeable lithium ion batteries have attracted a great deal of attention because of their higher capacities and potentials against the positive electrode than current anode materials such as polymers, metal oxides and chalcogenides as well as better cycling performance^{1,2}. Various models for lithium accommodation are proposed. Dahn et al.³ have pointed out that in carbons that contain substantial amounts of hydrogen, the maximum amount of lithium that can be inserted is proportional to the hydrogen content, which suggests that the lithium binds somehow in the vicinity of the H atoms. Ago et al.⁴ reported that lithium adsorbed at the periphery of condensed aromatic rings with trans-polyacetylene-type structure (acene-edge) contributes to high capacity by ab initio calculations. In contrast, an opinion that high capacities and hysteresis are due to lithium bonded covalently with carbon atoms at the periphery with cis-polyacetylene-type structure (phenanthrene-edge) is proposed by Zheng et al.⁵ A result by semiempirical calculations with AM1 supporting this is also reported by Papanek et al.⁶ However, structural intricateness of carbonaceous materials themselves makes it difficult to understand the lithium doping mechanism.

* Correspondence: E-mail: nishio@chem.mie-u.ac.jp; Telephone: +81-59 231 9424; Fax: +81-59 231 9471



Scheme I

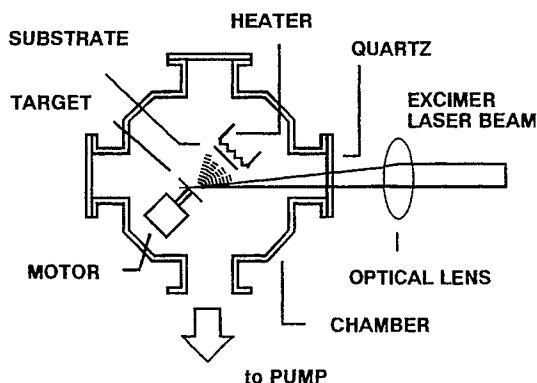


Fig. 1. Experimental setup.

Apart from these fundamental subjects, studies on thin lithium ion batteries with film anode and cathode electrodes are abruptly made for the purpose of application to a backup or main power supply for microelectronic devices.⁷ Therefore, it is desirable to develop the method to prepare carbonaceous material films for anode thin electrodes of ultra thin rechargeable lithium ion batteries.

In recent years, laser ablation has been regarded as one of the promising techniques for preparation of deposited films without structural defects from various polymers as well as from several organic monomeric compounds.⁸⁻¹⁰ Furthermore, positive control of chemical reactions by selection of wavelength and fluence of the laser beams allows us to prepare novel functional organic films such as semiconducting organic films with unique structures different from target materials.^{11,12} Few attempts have so far been, however, made at preparation of amorphous carbon films for anode thin electrodes for ultra thin rechargeable lithium ion batteries.

In this study, amorphous thin films consisting basically of polyperinaphthalene (PPN)^{13, 14}, one of the quasi-one-dimensional conducting polymers, were prepared by excimer laser ablation (ELA) of 3,4,9,10-perylenetetracarboxylic dianhydride (PTCDA)¹⁵⁻¹⁷ or PTCDA/Co mixture target under careful selection of the ablation conditions. (See scheme I) Electrochemical doping of lithium ion into the films obtained by ELA were performed to appraise performance of the films as anode thin electrodes for ultra thin rechargeable lithium ion batteries and to verify the lithium doping mechanism.

2. EXPERIMENTAL

2.1. Film preparation by ELA and their characterization

The experimental setup is shown in Fig. 1. PTCDA or mixture of PTCDA and Co powder (PTCDA/Co), the mixture ratio by mole ([PTCDA]/[Co]) of which was 0.25, was compressed into pellet to use as a target. Laser ablation of PTCDA or PTCDA/Co target was performed for 2-3 hours in a reaction chamber evacuated below 10^{-3} Torr with a 308 nm (XeCl) pulsed beam of an excimer laser at a repetition rate of 5 Hz. Deposited films were prepared on quartz or KBr substrates located at a distance of 3-4 cm from the target. The substrate temperature (T_s) was controlled with a heater between 20°C and 400°C. The laser beam was focused on the PTCDA target with a quartz lens. The fluence of the laser beam was varied ranging from 0.25 to 2 Jcm⁻²pulse⁻¹. The target was spun with a motor, preventing a laser beam from concentrating on a fixed spot.

Structure and electric properties of the deposited films were investigated by scanning electron micrography (SEM), FT-IR, Raman, X-ray photoelectron spectroscopy (XPS), electron spin resonance (ESR), electron diffraction, and electric conductivity measurements at room temperature.

2.2. Electrochemical doping the films prepared by ELA with lithium ion

For the films prepared by ELA of PTCDA on Cu substrates at $T_s = 300^\circ\text{C}$ (1 μm in thickness and 1 cm x 1 cm in area),

electrochemical doping with lithium ions was performed. Lithium metal foils were used as both counter and reference electrodes. 1M LiPF₆ in propylene carbonate (PC) was applied for electrolyte. Each electrode was separated with glass filters. The cells were fabricated in a dry box filled with Ar.

Electrochemical properties of the film was investigated by charge-discharge cycling tests. The electrochemical measurements were carried out at 25°C. After the films were rinsed with tetrahydrofuran (THF) and dried in Ar atmosphere, Raman spectra were measured for the films doped with lithium ions at several doping levels in the initial charge and discharge cycle.

3. RESULTS AND DISCUSSION

3.1. Preparation of films with PPN structure

In order to prepare films possessing PPN structure with high quality, ablation conditions such as substrate temperature, laser fluence, target material were optimized. For the film prepared under optimized conditions, structure and electric /electronic properties were investigated.

3.1.1 Optimization of substrate temperature and laser fluence for ablation of PTCDA target

Films prepared on substrates at T_s below and above 200°C were reddish and black with somewhat metallic luster, respectively. Deposition rate decreases gradually with increasing T_s . While deposition rate of the film prepared by ELA on a substrate at T_s of 20°C was approximately 250nm hour⁻¹, that at T_s of 300°C was 100nm hour⁻¹.

FT-IR spectra for the films prepared on KBr substrates at T_s of 20°C, 100°C, 200°C, 300°C and 400°C together with that for a PTCDA film by vacuum evaporation are shown in Fig. 2. In the spectra, peaks at 1750cm⁻¹, 1780cm⁻¹, 1300cm⁻¹ and 1020cm⁻¹ related to the side groups of the PTCDA monomer and a peak at 1600cm⁻¹ related to condensed aromatic ring of perylene skeleton in the monomer are also observed in the films prepared by ELA at T_s below 200 °C, showing that the films keep the original structure of the PTCDA monomer. For the films prepared at T_s of 300 and 400°C, in contrast, extraordinary decrease of peak intensities at 1750cm⁻¹ and 1780cm⁻¹ is observed, indicating the elimination of the

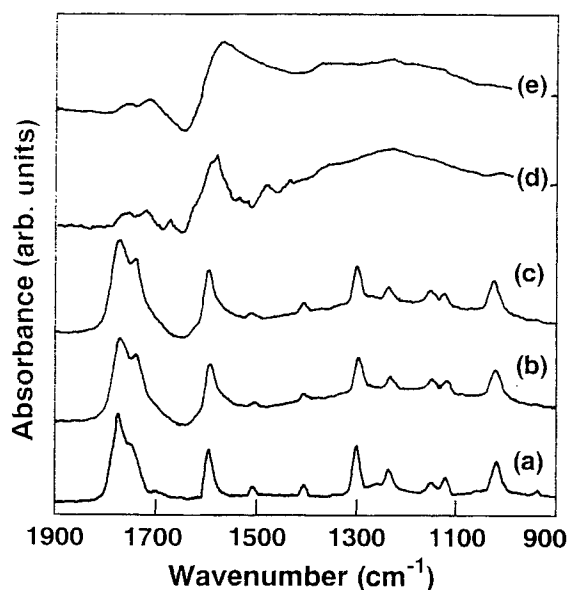


Fig. 2. FT-IR spectra for the films prepared on KBr substrates at T_s of 20(b), 200(c), 300(d) and 400°C(e) together with that for a PTCDA film by vacuum evaporation (a).

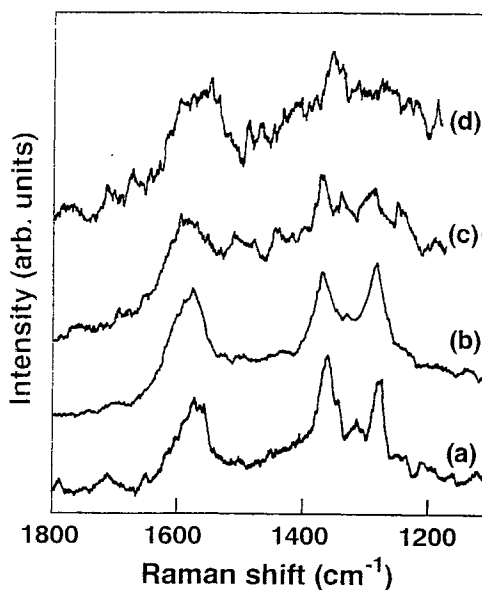


Fig. 3. Raman spectra of the films prepared on substrates at 300°C by ELA at 0.1(a), 0.5(b), 1.0(c) and 2.8 Jcm⁻² pulse⁻¹ (d).

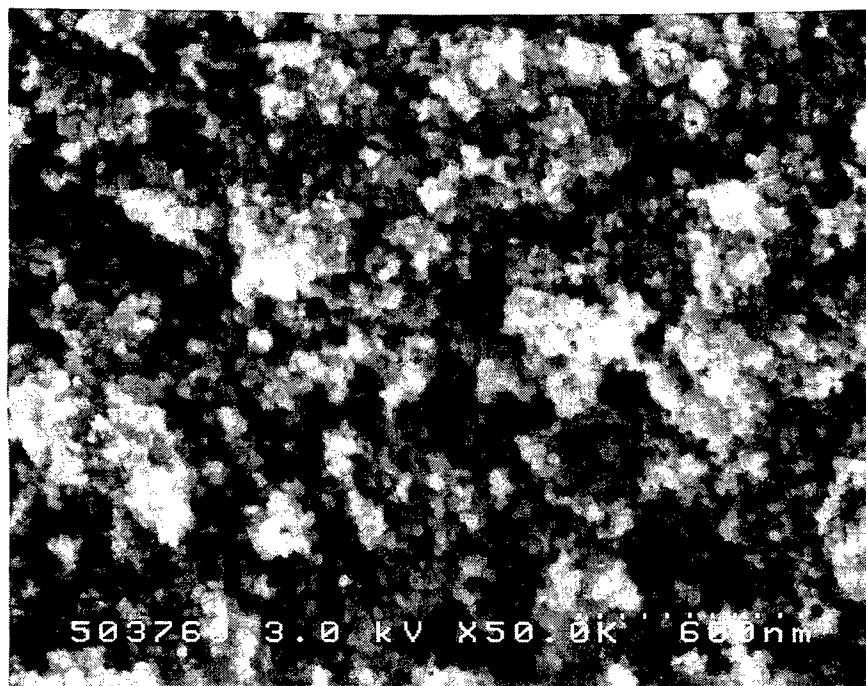


Fig. 4. Surface morphology of the film prepared at T_s of 300°C.

side groups of PTCDA monomers.

In FT-IR spectra for the films on substrates at 300°C, peaks related to the side groups of PTCDA vanished regardless of the fluence used. Figure 3 shows Raman spectra of the films prepared on substrates at 300°C by ELA at various fluence. Structure of films prepared on substrates at 300°C depends strongly on fluence. While the peak at 1280 cm^{-1} remains in each film prepared at less than 0.5 $\text{Jcm}^{-2}\text{pulse}^{-1}$, it disappears and the spectrum turns into that of common amorphous carbon with a peak at 1600 cm^{-1} and broad band around 1380 cm^{-1} for each film prepared at more than 1.0 $\text{Jcm}^{-2}\text{pulse}^{-1}$. This means decomposition of perylene skeleton in the PTCDA.

3.1.2. Characterization of the films prepared by ELA

These results allow us to conclude that it is necessary to select fluence and substrate temperature to be less than 1.0 $\text{Jcm}^{-2}\text{pulse}^{-1}$ and more than 200°C, respectively, in order to prepare films without damaging perylene skeleton. For the film prepared under these condition, structure and electric/electronic properties were investigated. Surface morphology of the film prepared at T_s of 300°C is shown in Fig. 4. It is observed that the film consists of fine particles of less than 100nm in diameter. The electron diffraction pattern obtained previously ¹⁶, showed that this film was neither single crystal nor polycrystal, but stripes consisting of several meander lines with space of ca. 5 Å was distinctly observed in some places in a high resolution TEM image. ¹⁷

According to the ESR measurement for films prepared at T_s of 20°C, 200°C and 300°C, g -value of every film was between 2.0025 and 2.0033, ¹⁶ characteristic of carbon radical. Spin density of each film prepared by ELA was more than 3 orders higher than that of PTCDA film by vacuum deposition, suggesting incomplete polymerization of deposited materials by ELA. However, more than 70% of spins were extinguished for the film at T_s of 300°C compared with those for the film at T_s of 200°C. This indicates the effective recombination of radicals by increasing T_s , resulting in development of π -conjugated systems. XPS results ¹⁶ show shift of C_{1s} peak position to lower energy direction and decrease of [O] / [C] with increasing T_s , also supporting the development of π -conjugated systems by recombination of radicals.

Raman spectra for the films prepared on quartz substrates at T_s of 20°C, 100°C, 200°C and 300°C are shown in Fig.

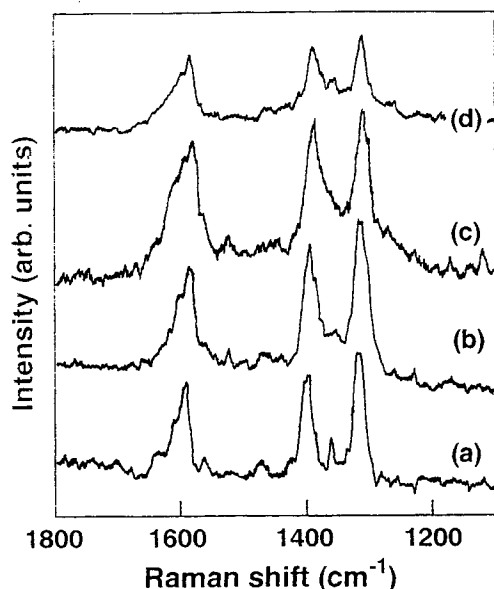


Fig. 5. Raman spectra for the films prepared on quartz substrates at T_s of 20(a), 100(b), 200(c) and 300°C(d).

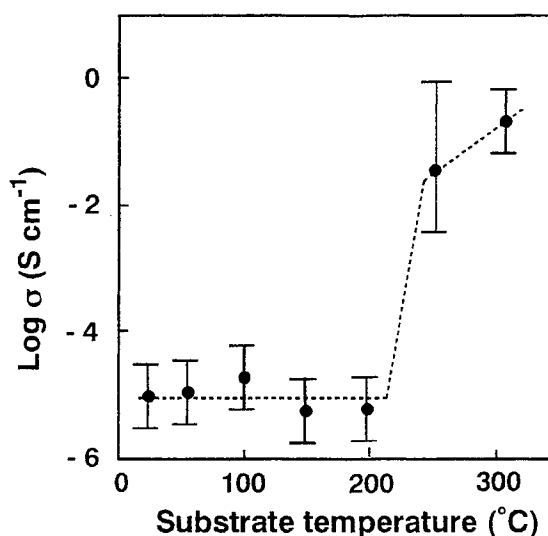


Fig. 6. Dependence of electric conductivity on T_s .

5. Sharp peaks at 1400 cm^{-1} and 1280 cm^{-1} due to in-plane C-H bending as well as peak at 1600 cm^{-1} due to aromatic rings are observed for the film at T_s of 20°C. The peaks at 1600 cm^{-1} , 1400 cm^{-1} and 1280 cm^{-1} are also observed in the spectra of films at T_s of 100°C, 200°C and 300°C, meaning that the perylene structure is basically preserved in these films. The Raman spectrum of a film prepared on a substrate at 400°C showed disappearance of a peak at 1280 cm^{-1} , suggesting that elimination of hydrogen atoms in PTCDA were induced to form amorphous carbon with two-dimensionally developed π -conjugation system.¹⁵

Although every film by ELA at T_s below 200°C possesses the electric conductivity around $10^{-5} \text{ S cm}^{-1}$ at room temperature, drastic increase in conductivity at T_s around 200°C can be observed as shown in Fig. 6. These suggest that π -conjugated system develops for the film at T_s above 200°C owing to polymerization with elimination of side groups of PTCDA, resulting in increase of electric conductivity. The conductivity comes up to $10^{-1} \text{ S cm}^{-1}$ for the film prepared at T_s of 300°C.

These results together with that from FT-IR measurement as described above, convince us of partial formation of PPN structure in the film prepared at T_s of 300°C. Actually, the Raman spectrum for this film is nearly similar to that for PPN prepared with vapor polymerization method by Murakami et al.¹³ except for the intensity ratio of the peak at 1280 cm^{-1} against that at 1380 cm^{-1} . Considering from these results, although structural defects such as carbon radicals are detected to some extent, it is safely be said that this film basically consists of polyperinaphthalene (PPN) structure. Hereafter we call this material polyperinaphthalenic organic semiconductor (PPNOS). The temperature dependence of the electric conductivity of the PPNOS film prepared by ELA on a substrate at 300°C can be explained in terms of the three dimensional variable range hopping (3D-VRH) mechanism¹⁸, meaning that electric conductivity results from carrier hopping between localized states near the Fermi level.

As for the PPNOS formation mechanism, it should be noted, here, that the elimination of the side groups of PTCDA monomers does not occur at T_s between 200°C and 300°C, considering the decomposition temperature of the PTCDA more than 400°C. Except for vapor molecules such as CO and CO₂, almost all fragments including PTCDA monomers are deposited on substrates at T_s below 200°C. On the other hand, "naked" perylene skeletons without side groups, which probably have high reactivity, can be deposited selectively on substrates at T_s above 200°C since monomers and small fragments are sparingly deposited on such a high-temperature surface. Furthermore, high temperature (300°C) assists

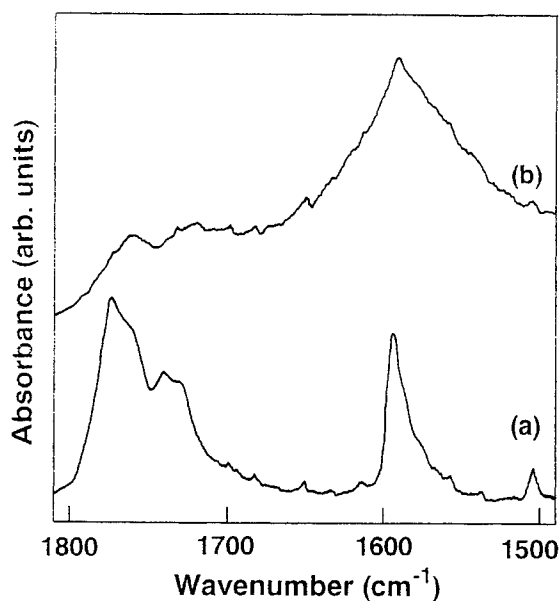


Fig. 7. FT-IR spectrum ranging between 1500 and 1800 cm^{-1} for the film prepared on a substrate at 20°C by ELA of a PTCDA/Co target (a) together with that for the film prepared by ELA of PTCDA on substrate at 20°C (b).

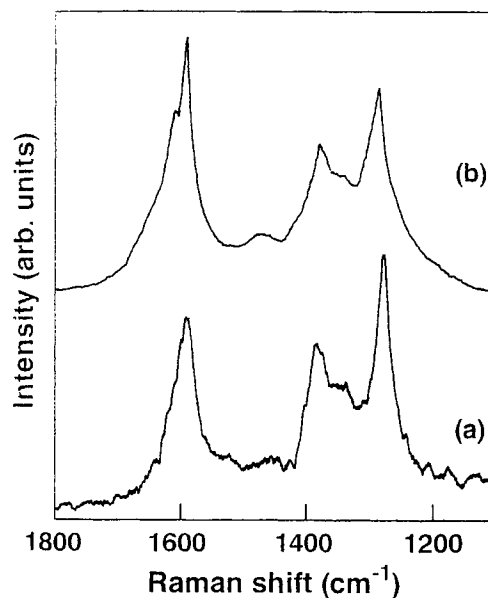


Fig. 8. The Raman spectrum for the film prepared on a substrate at 20°C by ELA of a PTCDA/Co target (a) together with that for PPN prepared by Murakami et al.¹³ (b).

recombination of radicals to form PPN structure. Hence, an increase of T_s contributes to selective deposition of the fragments containing perylene skeleton without side groups as well as development of polymerization.

3.1.3. Ablation of PTCDA/Co target

In this study, addition to PTCDA target, PTCDA/Co target was ablated for the purpose of preparation of PPNOS films at lower substrate temperature. Films were deposited on substrates at 20°C. Quite different results from that with PTCDA target were obtained. The FT-IR spectrum of the film ranging between 1500 cm^{-1} and 1800 cm^{-1} is shown in Fig. 7 together with that for the film prepared by ELA of PTCDA on substrate at 20°C. Although peaks at 1750 cm^{-1} and 1780 cm^{-1} related to the side groups of PTCDA monomers are detected, their intensity is quite low compared with those for the film prepared by ELA of PTCDA. This suggests that fragments without carboxylic dianhydride groups are effectively produced. The Raman spectrum of the film is virtually the same as that for PPN prepared by Murakami et al. as shown in Fig. 8. This result involves an unexplored and intriguing subject concerning to physics of interaction of high intense photons with condensed phase under participation of catalytic reaction, although much still remains to be done for clarification of this reaction mechanism.

3.2. Electrochemical doping of lithium ion into PPNOS thin films

Electrochemical doping of lithium ion into the PPNOS thin film prepared by ELA of a PTCDA target on a substrate at T_s of 300°C was performed to appraise performance of this film as anode thin electrodes for ultra thin rechargeable lithium ion batteries as well as to verify the lithium doping mechanism.

3.2.1. Cyclic voltammetry

According to cyclic voltammograms after 20 cycles, doping [D] or undoping [UD] amount depends on the sweep ratio. At the sweep rate of 10mVsec⁻¹, [D] and [UD] were 365mAhg⁻¹ and 337mAhg⁻¹, respectively. [D] and [UD] increased with

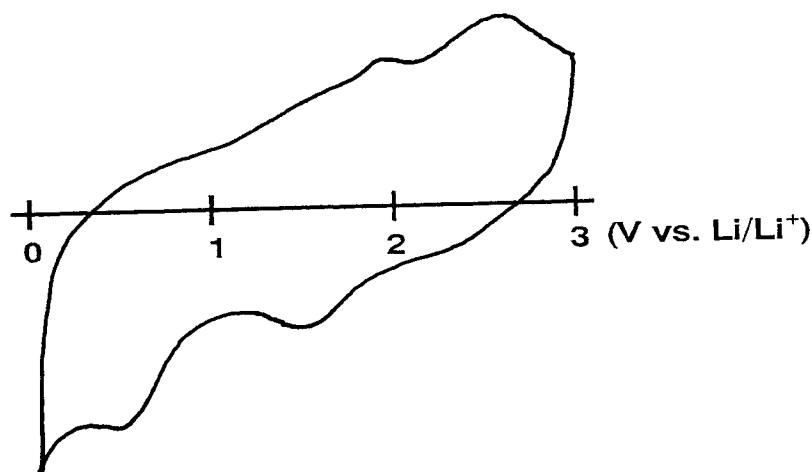


Fig. 9. Cyclic voltammogram at a sweep rate of 10mVsec^{-1} for the PPNOS electrode after 20 cycles.

decreasing the sweep rate up to 683mAhg^{-1} and 500mAhg^{-1} , respectively, though $[\text{UD}]/[\text{D}]$ was 0.64, considerably lower than that at the sweep rate of 1mVsec^{-1} (0.92). These values are superior to that for graphite electrode (372mAhg^{-1})², meaning that PPNOS films are promising as anode thin electrodes for ultra thin rechargeable lithium ion batteries. The cyclic voltammogram at a sweep rate of 10mVsec^{-1} for the PPNOS electrode after 20 cycles is shown in Fig. 9. Redox peaks are detected at ca. 1.2V and 2.0V clearly, different from various carbonaceous material electrodes.²

3.2.2. Charge-discharge profile

In order to clarify doping/undoping behavior of lithium ion at the first cycle, charge (lithium doping)-discharge (lithium undoping) profile was investigated. Figure 10(a) and (b) show surface morphologies of PPNOS film after immersing in the electrolyte and that doped with lithium ions up to 0V, respectively. The morphology of the former is not so different from that without immersing in the electrolyte (see Fig. 4) where each particles can be clearly detected. For the latter, in contrast, particles adhere to each other to form lump. Charge-discharge curves for the PPNOS film electrode at the first cycle is shown in Fig. 11. When the film electrode is discharged up to 3V after full charge up to 0V, 40% of lithium ions are trapped in the PPNOS electrode as irreversible capacities.

Raman spectra were measured for the PPNOS films doped with lithium ion at various doping levels. Figure 12 shows the spectra for the films doped at 0.5V and the film undoped at 3V after doped at 0.5V at the first cycle together with that without doping. In the spectrum for the film doped at 0.5V, it is observed that the peak at 1280cm^{-1} assigned to C-H in-

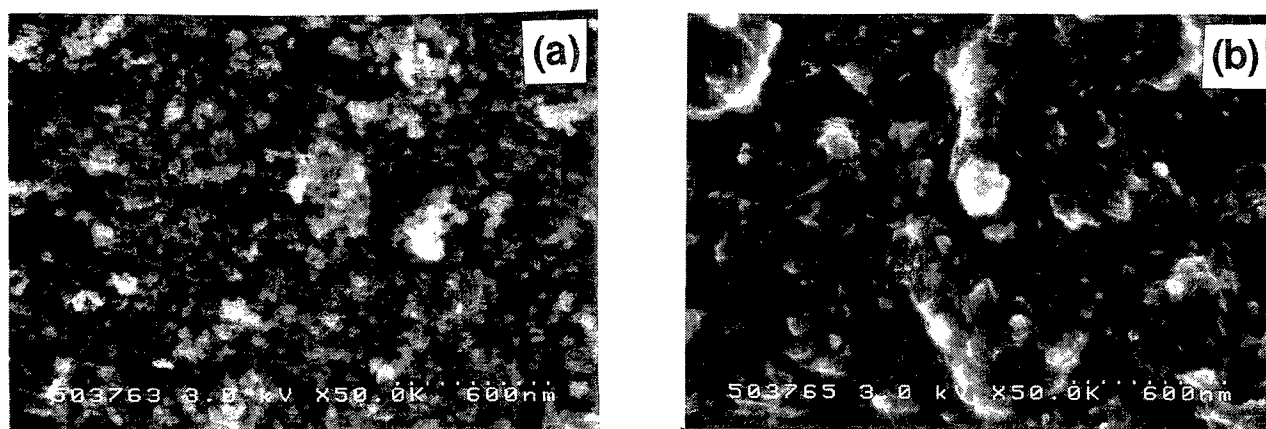


Fig. 10. Surface morphology of a PPNOS film after immersing in the electrolyte (a) and that doped with lithium ions up to 0V (b).

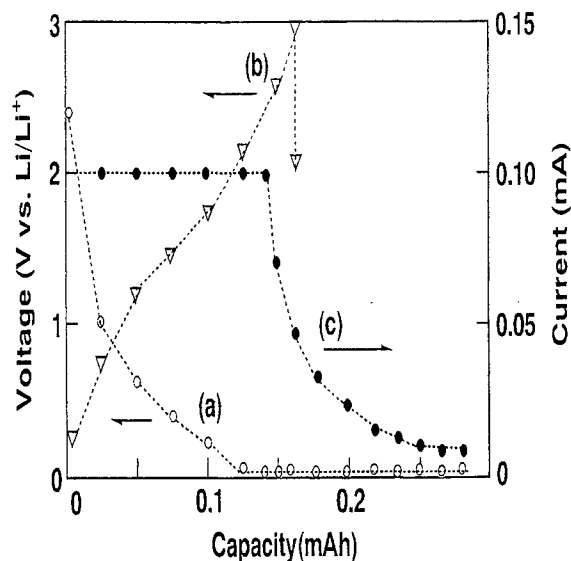


Fig. 11. Charge-discharge curves for the PPNOS film electrode at the first cycle.

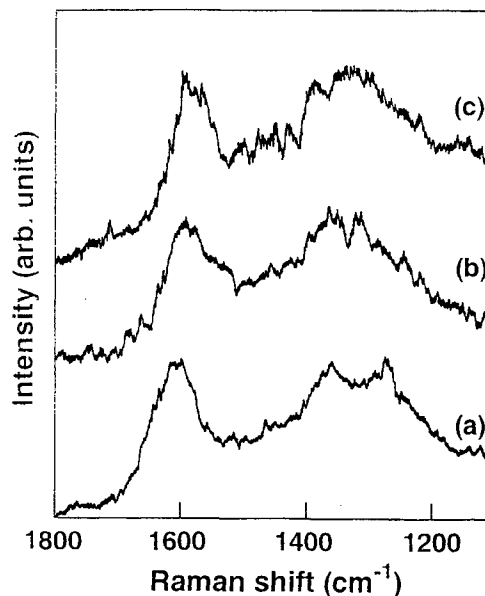


Fig. 12. Raman spectra for the films doped at 0.5V (b) and undoped at 3V after doped at 0.5V (c) at the first cycle together with that without doping (only immersed in the electrolyte) (a).

plane bending mode slightly shifts to higher wavenumber direction with decrease of its intensities as well as broadening of the peak at 1600cm^{-1} , the full width at half maximum (FWHM) of which is 125cm^{-1} . These results suggest that lithium ions interact not only with condensed aromatic rings of perylene skeleton but with carbon atoms at the edge of perylene structure. Although the value of FWHM for the peak at 1600cm^{-1} returns to that for the film without doping (100cm^{-1}) by undoping up to the level at 3V, behavior of the peak at 1280cm^{-1} is irreversible: that is, lithium ions are deeply trapped at the phenanthrene edge of the polyperinaphthalene skeleton, supporting results obtained by Zheng et al. ⁵

4. CONCLUSION

Amorphous organic semiconductor thin films were prepared on temperature-controlled substrates by excimer laser ablation (ELA) of 3, 4, 9, 10-perylenetetracarboxylic dianhydride (PTCDA) or PTCDA/Co mixture target with a 308nm (XeCl) pulsed excimer laser beam. Drastic increase in conductivity and decrease in the IR peak intensities related to the side groups of PTCDA monomers were observed for films prepared on substrates above 200°C . Electric conductivity of a film prepared on a substrate at 300°C came up to 10^{-1}Scm^{-1} . Although carbon radicals were detected to some extent, indicating incomplete polymerization, Raman spectroscopic measurement revealed that this film basically consisted of polyperinaphthalene (PPN) structure. This material is named polyperinaphthalenic organic semiconductor (PPNOS). It revealed that ELA of mixture target of PTCDA and Co enabled us to obtain PPNOS at room temperature, meaning that fragments without carboxylic dianhydride groups were effectively produced when PTCDA/Co mixture target was ablated with a 308nm beam.

Electrochemical doping of lithium ion into the PPNOS thin films obtained by ELA were performed to appraise the performance of PPNOS films as anode thin electrodes for ultra thin rechargeable lithium ion batteries and to verify the lithium doping mechanism. According to cyclic voltammetry measurements, doping and undoping amount increased with decreasing the sweep rate up to 683mAhg^{-1} and 500mAhg^{-1} , respectively, at the sweep rate of 1mVsec^{-1} . These values are superior to that for graphite electrode (372mAhg^{-1}) as anode thin electrodes for ultra thin rechargeable lithium ion batteries. Our Raman spectroscopic results suggested that lithium ions interacted not only with condensed aromatic rings of perylene skeleton but also with carbon atoms at the phenanthrene-edge of PPNOS and that lithium ions at the phenanthrene edge were deeply trapped, supporting results obtained by Zheng et al.

ACKNOWLEDGEMENTS

The authors are grateful to Miss. Sachiko Umeda and Mr. Koji Tanimoto for assistance. This work is a part of the project of Institute for Fundamental Chemistry, supported by Japan Society for the Promotion of Science - Research for the Future Program (JSPS-RFTF96P00206).

REFERENCES

1. P. Novak, K. Muller, K. S. V. Santhanam, and O. Hass, "Electrochemically Active Polymers for Rechargeable Batteries," *Chem. Rev.*, **97**, pp. 207-281, 1997.
2. M. Wakihara, and O. Yamamoto (Eds.), *Lithium Ion Batteries-Fundamentals and Performance*, Kodansha, Tokyo, 1998.
3. J. R. Dahn, T. Zheng, Y. Liu, and J. S. Xue, "Mechanism for Lithium Insertion in Carbonaceous Materials," *Science*, **270**, pp. 590-593, 1995.
4. H. Ago, M. Kato, K. Yahara, K. Yoshizawa, K. Tanaka, and T. Yamabe, "Ab Initio Study on Interaction and Stability of Lithium-Doped Amorphous Carbons," *J. Electrochem. Soc.*, **146**, pp. 1262-1269, 1999.
5. T. Zheng, W. R. McKinnon, and J. R. Dahn, "Hysteresis during Lithium Insertion in Hydrogen-Containing Carbons," *J. Electrochem. Soc.*, **143**, pp. 2137-2145, 1996.
6. P. Papanek, M. Radosavljevic, and J. E. Fischer, "Lithium Insertion in Disordered Carbon-Hydrogen Alloys: Intercalation vs Covalent Binding," *Chem. Mater.*, **8**, pp. 1519-1526, 1996.
7. B. Wang, J. B. Bates, F. X. Hart, B. C. Sales, R. A. Zuhr, and J. D. Robertson, "Characterization of Thin-Film Rechargeable Lithium Batteries with Lithium Cobalt Oxide Cathodes," *J. Electrochem. Soc.*, **143**, pp. 3203-3213, 1996.
8. D. Dijkkamp, T. Venkatesan, X. D. Wu, S. A. Shaheen, N. Jisrawi, Y. H. Min-Lee, W. L. McLean, and M. Croft, "Preparation of Y-Ba-Cu oxide superconductor thin films using pulsed laser evaporation from high Tc bulk material," *Appl. Phys. Lett.*, **51**, pp. 619-621, 1987.
9. G. B. Blanchet, C. R. Fincher Jr., C. L. Jackson, S. I. Shah, and K. H. Gardner, "Laser Ablation and the Production of Polymer Films," *Science*, **262**, pp. 719-721, 1993.
10. E. Ina, N. Matsumoto, E. Shikada, and F. Kannari, "Laser ablation deposition of crystalline copper-phthalocyanine thin films," *Appl. Surf. Sci.*, **127-129**, pp. 574-578, 1998.
11. S. Nishio, T. Chiba, A. Matsuzaki, and H. Sato, "Control of structures of deposited polymer films by ablation Laser wavelength: polyacrylonitrile at 308, 248 and 193 nm," *J. Appl. Phys.*, **79**, pp. 7198-7204, 1996.
12. S. Nishio, S. Kato, A. Matsuzaki, H. Sato, H. Kinoshita, S. Yata, K. Tanaka, and T. Yamabe, "Preparation of Polyacenic Semiconductive Thin Films by Excimer Laser Ablation," *Synth. Met.*, **83**, pp. 67-71, 1996.
13. M. Murakami, S. Iijima, and S. Yoshimura, "Morphology and structure of a one-dimensional graphite polymer, Poly-peri-naphthalene," *J. Appl. Phys.*, **60**, pp. 3856-3863, 1986.
14. M. Yudasaka, Y. Tasaka, M. Tanaka, H. Kamo, Y. Ohki, S. Usami, and S. Yoshimura, "Polyperi-naphthalene film formation by pulsed laser deposition with a target of perylenetetracarboxylic dianhydride," *Appl. Phys. Lett.*, **64**, pp. 3237-3239, 1994.
15. S. Nishio, and H. Sato, "Preparation of Organic Semiconductive Thin Films by Laser Ablation: Control of Structure and Electric Properties by Selecting Wavelength, Fluence, and Substrate Temperature," *Electrical Engineering in Japan*, **125**, pp. 19-26, 1998.
16. S. Nishio, R. Mase, T. Oba, A. Matsuzaki, and H. Sato, "Preparation of Amorphous Organic Semiconductor Thin Films with Polyperinaphthalene Structure on Temperature-Controlled Substrates by Excimer Laser Ablation of 3,4,9,10-Perylenetetracarboxylic Dianhydride," *Appl. Surf. Sci.*, **127-129**, pp. 589-594, 1998.
17. S. Nishio, H. Sato, and T. Yamabe, "Control of Structure and Electric Properties of Amorphous Organic Semiconductive Thin Films Prepared by Excimer Laser Ablation," *Appl. Phys.*, **A**, in press.
18. N. F. Mott, and E. A. Davis, *ELECTRONIC PROCESSES IN NON-CRYSTALLINE MATERIALS*, 2nd ed., Clarendon Press, Oxford, 1979.

Novel thin-film deposition method and system with IR-FEL

Masato Yasumoto^{*a}, Norimasa Umesaki^a

^aOsaka National Research Institute, AIST 1-8-31 Midorigaoka Ikeda Osaka 563-8577, Japan

Takio Tomimatsu^b, Akira Ishizu^b, Kunio Awazu^b

^bFree Electron Laser Research Institute, 1-8-9 Tuda-yamate Hirakata Osaka 573-0128, Japan

ABSTRACT

We propose a novel method for a thin film deposition with an IR-FEL using the IR-FEL wavelength tunability in infrared region. This is an unique method in which only the vapor deposition molecule is activated by applying laser of vibrational excitation wavelength of the vapor deposition molecule on the substrate surface, when the thin film intends to deposit on the substrate. We developed two equipments in order to realize and evaluate the new method. One is IR-FEL assisted RF sputter deposition chamber system, the other is IR-FEL assisted laser ablation chamber system. Moreover using the former equipment, we carry out the preliminary experiment on the preparation of ITO (In-Sn-O) thin film.

Keywords: Free electron laser (FEL), thin film fabrication, laser ablation

1. INTRODUCTION

Free electron laser (FEL) is a different lasing-system from ordinary lasers. The FEL in principle has continuous wavelength-tunability in infrared (IR) through X-ray wavelength region. Especially the only FEL has continuous tunability in the IR wavelength region, while ordinary lasers can discretely be tuned in the region. The IR-FEL can induce the specific vibration mode of various molecules, when the energy of IR-FEL is corresponding to the one of the vibration mode. Therefore the IR-FEL can be applied in many applications^{1,2}. Due to the applying the feature in material processing we have been made many attempts. In this paper we propose the IR-FEL assisted thin film deposition method and introduce two fabrication equipment.

2. FEL FACILITIES AND USER STATIONS AT THE FELI

There are four FEL facilities, FEL-1~FEL-4 opened for users since 1996 at Free Electron Laser Research Institute (FELI). Table 1 shows tunable wavelength regions for the four FEL facilities¹. The FEL-1 & the FEL-4 are uniquely tunable in mid-IR and far-IR region comparing with other conventional lasers³. The mid-IR & far-IR FEL have a possibility to induce the specific vibration and rotation mode of molecules. The research using this property was numerously carried out. The 6 and 9 μ m FELs are especially used well for bio-medical applications and solid-state applications, respectively. The FEL-3 has been keeping the world record for the shortest wavelength oscillation of linac-based FELs with a thermionic gun up to 278nm^{4,5}.

*Correspondence E-mail: yasumoto@onri.go.jp, Telephone: +81-727-51-9537, Fax: +81-727-51-9631

Table 1 Tunable wavelength regions

FEL facilities	Wavelength (μm)
FEL-1	4.6~20
FEL-2	1.8~3.3
FEL-3	0.27~0.7
FEL-4	18~40

The FELI has four user rooms and fourteen user stations described in Figure 1. The user stations are in series located along evacuated optical pipes (beam lines) in which the IR-FEL beam is transported from the FEL machine. The beam line is penetrated at the upper part of each laboratory. Therefore, only in the allocated time the mirror is inserted in the beam line, it leads to the IR-FEL beam on the optical bench. The window application for taking out the IR-FEL from the beam line is dependent on the wavelength of the IR-FEL. Figure 1 shows the arrangement of the outlet window materials and the applicants. FEL manipulator is conveniently used for temporary user and microscopic irradiation device can be used to investigate structure modification of irradiated cell⁶. Present thin film production experiment is used at user station in the upstream of laboratory 4. The laboratory is the clean room specification.

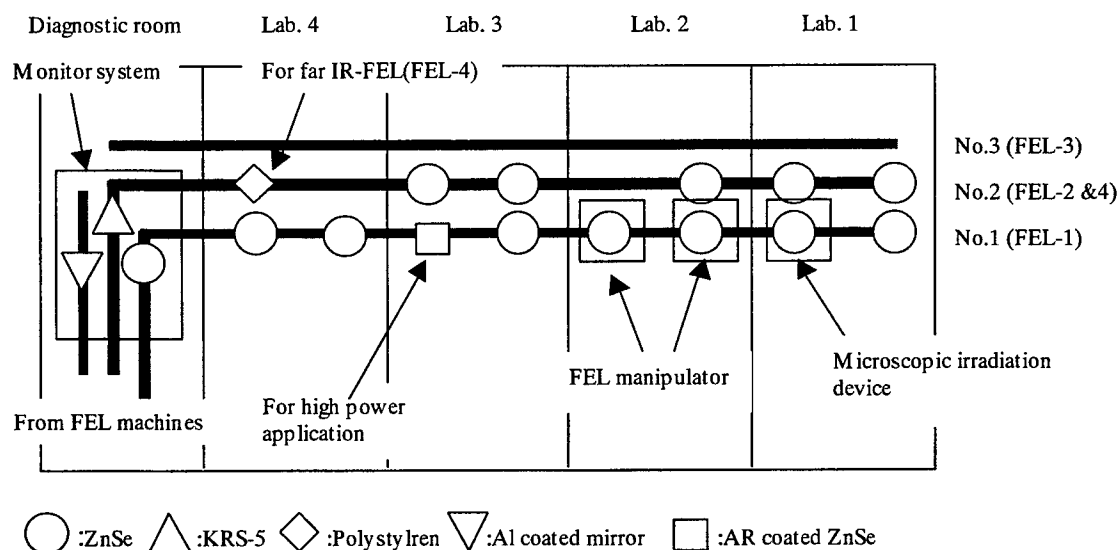


Figure 1 Arrangement of the windows for the FEL outlet.

3. THIN FILM PREPARATION METHODS ASSISTED WITH THE IR-FEL

It is possible to easily apply the IR-FEL to thin film preparation process. The method realizes an in-situ irradiation for the substrate with both preparation beam and IR-FEL beam. By giving vibrational energy of the film production molecule in a thin film production process, it becomes possible that high-quality film production is carried out in approach low temperature for this method. The method is applicable to various thin film preparation processes. We have therefore made many attempts on the improvement of thin film preparation method with the IR-FEL assistance⁷.

The method is more advantageous of three than a thin film forming method by other beams. Firstly, The IR-FEL beam can introduce into the thin film preparation equipment simply, while other beams such as ions; electrons require necessary condition for actions such as degree of vacuum. By installing the IR-FEL introduction window in the chamber side, it is possible to irradiate the substrate in the chamber. In addition, it is also easy to make film by causing ablation phenomenon by projecting the target after collecting of the IR-FEL or other laser. In chapter 4 the equipment of this method is described in detail.

Secondly, the power of the IR-FEL is enough to reduce the moderate intensity. If it is high intensity, the IR-FEL can easily make an ablation phenomena of the deposited film on the substrate. Especially the FELI IR-FEL is a pico-second order bunched laser and the peak power reaches GW/cm^2 class, if it is focused⁸. There is no reducer to change the power linearly in the IR wavelength region, thus the beam is enough to be defocused on the substrate at the irradiation. When the IR-FEL is defocused to reduce the sufficient intensity, it is difficult to measure the intensity at the irradiation.

Thirdly, the wavelength of the IR-FEL in the irradiation perfectly agrees with a vibrational excitation wavelength of the film production molecule. In the general laser, wavelength variable range is a visible range and the laser energy is not matched with the excitation energy, therefore, the laser beam is usually reflected or transmitted. The matched IR-FEL gives the energy to the objective molecule efficiently^{9,10,11,12}.

4. FEL ASSISTED DEPOSITION SYSTEMS

The FEL assisted thin film preparation method described in the above is easily carried out in ordinary preparation chamber. We have developed two systems used with the method. One is applied in an RF sputter preparation system, the other is a laser ablation deposition system.

4.1. IR-FEL ASSISTED RF SPUTTER DEPOSITION CHAMBER SYSTEM

Table 2 shows the parameters of the RF sputter deposition chamber assisted with the IR-FEL beam. This system has an RF sputter source and an inlet window of the IR-FEL. The IR-FEL beam and the sputter source are constituted in order to irradiate for the substrate shown in Figure 2. In Figure 3 the positional relation of the IR-FEL and the sputter target was shown in the illustration.

Table 2 Parameters of the RF sputter deposition chamber assisted with the IR-FEL beam.

Ultimate vacuum pressure	$\sim 1 \times 10^{-5} \text{Pa}$
Substrate	Glass, Si(111) etc.
Variable range of substrate temperature	R.T. $\sim 800^\circ\text{C}$
Deposition source	Magnetron RF sputter gun
RF power	500W (max)
Sputter gas	Ar or Ar mixed gas
FEL inlet window	ZnSe for $5\sim 15\mu\text{m}$
Distance from the target to the substrate	80mm

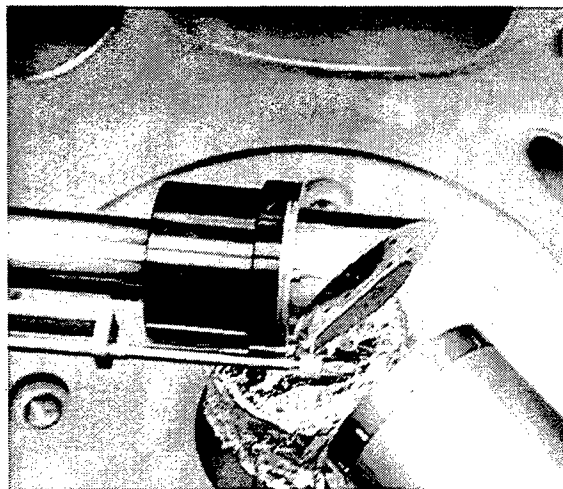


Figure 2 Photograph of the substrate and the target in the chamber system.

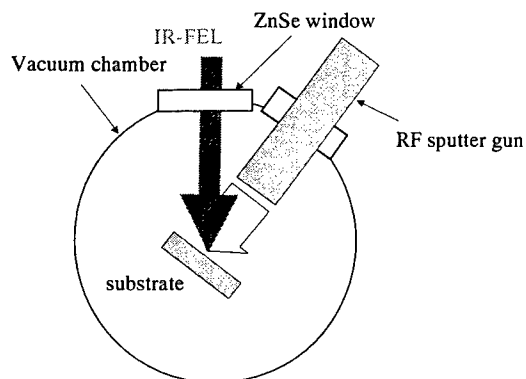


Figure 3 Illustration of the RF sputter deposition chamber assisted with the IR-FEL beam.

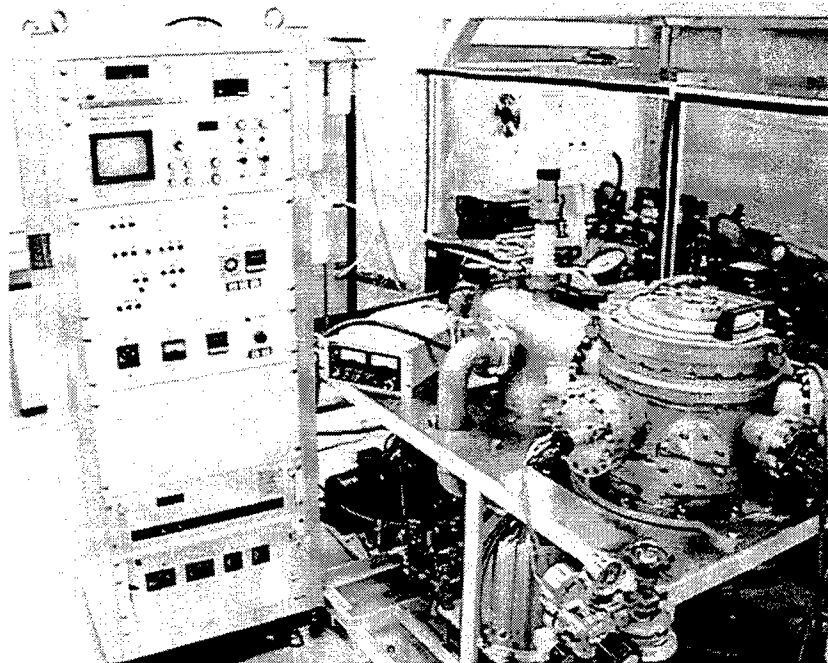


Figure 4 Photograph of the RF sputter deposition chamber assisted with IR-FEL

In Figures 4, the complete view photograph of the equipment is shown. The equipment has been equipped with quadruple mass spectrometer in order to analyze residual gas after irradiation. The equipment has been installed in the laboratory 4 of the FELI.

4.2. IR-FEL ASSISTED LASER ABLATION CHAMBER SYSTEM

Thin film preparation method by laser ablation is high selectivity reaction in low-temperature state in comparison with the thin film preparation by ordinary thermal equilibrium process, because it is non-thermal equilibrium process. Therefore, this method is effective for the thin film preparation of multi-element material and metal oxide¹³. We developed the equipment which is combined the assist by the IR-FEL with this method. This time laser for ablation must be a pulsed laser with the high intensity which cause the ablation phenomena. Instead of the general pulsed laser, it is also possible to use the IR-FEL in the ablation. Since it is a pulsed laser of the pico-second order, it is possible to cause the ablation phenomenon, if the IR-FEL is sufficiently converged on the target. The method realizes a fabrication of the thin film with two different processes (physical process and chemical process) simultaneously. One is an ablation deposition by intense pulses (up to $1\text{TW}/\text{cm}^2$) of the IR-FEL, and the other is photochemical reaction by the wavelength tunability ($5\sim 40\mu\text{m}$) of the IR-FEL. These processes are two major characteristics of the IR FEL. In addition, novel materials which have passed through the reaction unlike ordinary laser may be done are ablated with IR-FEL irradiating which wavelength agrees with vibrational excitation energy of the target material.

Figure 5 indicates the photograph of the laser ablation deposition chamber assisted with the IR-FEL. The chamber has two inlet windows for the target and for the substrate. It is possible that the window application of installation port for the target is freely exchanged by adjusting to the wavelength of introducing laser. The window applications must be the quartz, when Nd:YAG lasers is used. When the ablation laser is chosen with the IR-FEL, the window applications must be the ZnSe. At that time the transported IR FEL can be divided two directions with a beam splitter. One is for the target and one is for the substrate. In this case the high power of the IR-FEL is more important than the wavelength tunability. The IR-FEL has double pulse format, macropulse and micropulse. One macropulse has thousands micropulses. The pulse duration of the macropulse and the micropulse are $\sim 25\mu\text{s}$ and $\sim 3\text{ps}$, respectively. The repetition rate of the macropulse and micropulse are 10Hz and 11.2MHz, respectively. The focused FEL intensity reaches over $5\text{GW}/\text{cm}^2$ for the micropulse or over

1.3MW/cm² for the macropulse. Thus normal target materials for the ablation can be ablated with the focused IR FEL beam.

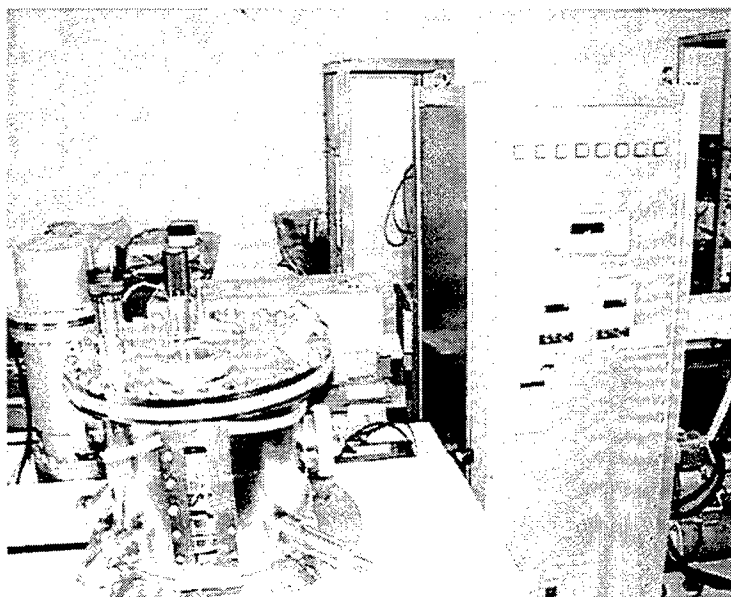


Figure 5 Photograph of the laser ablation deposition chamber assisted with the IR-FEL.

Table 3 indicates parameters of the laser deposition chamber. This equipment was developed in order to use for research of the ablation phenomenon by the IR-FEL and research of the thin film preparation. Therefore temperature of not only the substrate but also the target can be changed.

Table 3 Parameters of the laser deposition chamber assisted with the IR-FEL beam.

Ultimate vacuum pressure	1×10^{-7} Pa
Substrate	Glass, Si(111) etc.
Variable range of substrate temperature	R.T. ~ 800°C
Variable range of target temperature	R.T. ~ 500°C
Inert gas	O ₂ or O ₂ mixed gas
Inlet window for ablation	Quartz or ZnSe
FEL inlet window	ZnSe for 5~15μm
Distance from the target to the substrate	Variable (~100mm)

5. ITO THIN FILM PREPARATION

Using the equipment of the superscription, we carry out the preliminary experiment on the preparation of ITO (In-Sn-O) thin film. The ITO film is usually used in a liquid-crystal display panel and a solar-battery panel. In addition, the technology which makes film in plastic substrates has been required in order to use for screens of the touch panel, etc.. However, in the film production in low-temperature state, the crystallization of a thin film does not advance, and it is difficult that the sufficient electrical conduction property is obtained. Therefore, the method for making a high-quality thin film the oversensitive substrate for the temperature like the plastic film has been required. Various trials are carried out in order to realize the manufacture at the low temperature. The goal temperature is under 100°C in case of the ITO film. The method is expected to be very effective, because it is possible to irradiate the energy for the ITO thin film, while the low-temperature state was maintained as a whole system.

The ITO film fabrication assisted with IR-FEL beam is fabricated using with the RF sputter thin film deposition machine assisted with the IR-FEL. The fabrication conditions are shown in Table 4. Vibrational excitation wavelengths of In - O and Sn - O which constitutes ITO film are 14.2 μ m and 12.1 μ m, respectively. Deposition rate is 50 Å/s.

Table 4. Parameters of the fabrication condition about the ITO thin film.

Target material	In ₂ O ₃ -SnO ₂ (90wt%-10wt%)
Substrate material	Glass (Corning #7059)
Substrate temperature	100°C
RF Power	20W
Sputter gas	Ar+5%O ₂
Vacuum pressure	6×10 ⁻² Pa
FEL wavelength	12 μ m
FEL average power	~20mW

6. CONCLUSIONS

We proposed the new method for making a thin film using infrared region FEL. By increasing the vibration of the film production molecule under thin film production more, it is possible that only the film production molecule is activated for this method. We developed two kinds of equipment in order to realize this method. One is the IR-FEL assist RF sputtered thin film production equipment, and the other is the FEL assist laser ablation equipment. The former is an introduction to the sputtering equipment in which the film production speed is slow, and the latter is an introduction to the equipment in which the film production speed is rapid. The film production experiment of the ITO thin film is at present carried out as the preliminary experiment in order to verify the effect of this method.

ACKNOWLEDGEMENTS

We would like to thank Dr. Shigeharu Tamura of ONRI for his valuable discussion on preparation of the ITO thin film.

REFERENCES

1. T. Tomimasu et al., *Nucl. Inst. and Meth.* B 144 (1998) 1.
2. T. Tomimasu et al., *Proc. of the ECOMAP-98 (Kyoto Japan, 1998)*.
3. A. Zako et al., *Nucl. Inst. and Meth.* A 429 (1999) 136.
4. T. Tomimasu et al., *Nucl. Inst. and Meth.* A 393 (1997) 188.
5. T. Tomimasu et al., *Nucl. Inst. and Meth.* A429 (1999)141.
6. M. Yasumoto et al., *Nucl. Inst. and Meth.* A 387 (1997) 459.
7. M. Yasumoto et al., *Proc. of the 4th Asian Free Electron Laser Symposium (Taejon Korea, 1999)*.
8. M. Yasumoto et al., *Nucl. Inst. and Meth.* B144 (1998) 176.
9. M. Yasumoto et al., *SPIE 3614 (1999)* 182.
10. T. Ohyama et al., *Appl. Phys. Lett.* 71 (1997) 823.
11. S. Ogino et al., *Nucl. Inst. and Meth.* B144 (1998) 236.
12. M. Okoshi et al., *Nucl. Inst. and Meth.* B144 (1998) 147.
13. T. Kawai et al., *Nature* 349 (1991) 200.

Structure and Properties of Porous PZT Ceramics, Synthesized by Selective Laser Sintering Method.

Ekatherina Yu. Tarasova, Galina V. Kryukova, Alexey L. Petrov, Igor V. Shyshkovsky.

P. N. Lebedev Physics Institute Samara Branch, 221 Novo-Sadovaya st. Samara, 443011, Russia

ABSTRACT

A method of layer by layer selective laser sintering is proposed to synthesize structural piezoelectric elements out of PZT ceramics. The dependence of density of sintered elements on the regimes of sintering was investigated. X-ray diffraction and X-ray phase analysis were performed. It is shown that phase content and lattice structure had changed as a result of laser treatment.

1. INTRODUCTION

Traditionally, the ceramic materials based on a lead zirconate titanate $\text{Pb}(\text{Zr}_x\text{Ti}_{1-x})\text{O}_3$ (PZT family) solid solution are manufactured as monolithic composites. In particular, sintered, formed and polarized powder found widespread use in engineering, because of its piezoelectric effect ^[1]. However, there are applications that require better hydrostatic properties (hydrology, medical ultrasonics) and acoustic match between the ceramics and the researched media, through which acoustic signal is transmitted or received, even at the expense of other properties. The development of such piezoelectric ceramics and composites requires new technological approaches.

Rapid prototyping - a novel layer by layer fabrication technique, gained a significant interest in recent years, due to its inherent flexibility for manufacturing of simple and complex shaped parts without any specific tooling from a computer aid design (CAD) file ^[3]. In particular, in the paper ^[4] a manufacturing of functional piezoelectric ceramics prototypes was described using direct fused deposition ceramics (FDC) process. Green ceramics parts are created from the beforehand prepared PZT powder by a method of selective fused deposition (piston extrusion) of thermoplastic polymer binder. Then, a green ceramics part follows a conventional post processing techniques (anneal), which removes a binder from green parts and sinters them to full density.

In this paper work, layer by layer selective laser sintering (SLS) process is proposed to produce porous PZT parts. The dependencies of density, phase content and lattice structure on conditions of SLS process were investigated.

2. EXPERIMENT

As a raw material for laser sintering the mixture of powdered PbO , ZrO_2 and TiO_2 at molar proportion of 2.05:1.12:1 was used. However, direct laser synthesis of PZT out of these oxides was unsuccessful. The sintered layers turned out to be fragile and it was impossible to produce a three-dimensional part.

Therefore, two-stage process was used to produce piezoceramics. First, the mixture was annealed as follows: temperature rise up to 850°C and 1.5 hours exposure, then rise up to 950°C and 1.5 hours exposure, then 10 hours of slow cooling. After annealing the mixture contained the following oxides: PbTiO_3 , PbZrO_3 and PbO and was used for laser sintering at the second stage.

SLS was performed using cw Nd-YAG laser with maximum power 20 Wt. Focal spot diameter was ~50 microns. Powder layer thickness was determined by vertical step movement of the platform that served as a base for the sintered model. The sintering was performed in air.

Additional annealing of three-dimensional parts after laser sintering was performed in a vacuum furnace as follows: 30 min temperature rise up to 1000°C, 10 min exposure, further rise up to 1240°C, 3 hours exposure, 10 hours cooling. The aim of the additional annealing was to increase density and PZT phase content in the specimens.

The phase content of PZT ceramics was determined by X-ray phase analysis.

3. RESULTS AND DISCUSSION

In experiment, laser power P, scanning velocity V and powder layer thickness H were varied. The key technological parameter for sintering is powder layer thickness. In our experiments H varied in the region of 0.2 – 0.6 mm. During sintering of PZT ceramics strong shrinkage of the sample takes place. An additional advantage of laser sintering method is its ability to compensate in part the shrinkage applying additional layers.

To modes of applying the layers were used in experiment: 1 – the base moved down when one layer of powder was sintered; 2 – the base moved down when two layers of powder were sintered. In the 1-st mode powder layer thickness was a little larger than base movement step to compensate shrinkage, in the 2-nd – every second layer compensated shrinkage of the first one. The resulting density of the specimens are shown in the table 1.

Table 1. Density of the specimens depending on parameters of sintering .

#	Laser power, W	Scan velocity V, mm/s	Base step, microns	Mode of layer application	Density g/sm ³
1	9,7	65	400	1	3,4
2	9,7	33	400	1	3,4
3	9,7	22	600	1	2,1
4	10,6	44	200	2	4,1
5	12,9	65	400	1	3,2
6	12,9	65	400	2	3,9
7	12,9	47	400	1	3,6
8	12,9	47	400	2	3,9
9	12,9	33	400	1	3,0
10	13,0	213	200	2	2,8
11	13,0	129	200	2	2,9
12	13,0	93	200	2	3,9
13	13,2	72	200	2	3,9
14	20,7	161	400	2	3,4
15	20,7	161	400	1	3,5
16	20,7	108	200	1	3,9
17	20,7	108	400	1	3,5

As it is seen from table 1 the density of the synthesized porous PZT ceramics lies in the region from 3 to 4 g/cm³ (the density of monolithic PZT ceramics PZT 501A is ~7.9 g/cm³), which is similar to that of PZT-polymer composites, produced by extrusion method.

Four samples # 4,5,6,17 from table 1 were chosen for X-ray phase analysis. The analysis was performed in monochromator chamber FR-553 (Cu K α radiation). Ge was used for the inner standard. Phase analysis had shown that in all specimens ZrO₂ and PbTiO₃ phases are present. Besides in the specimens # 4 and 5 a few weak lines of an unidentified phase were present. In all the samples, the lines arising from the phase PbTiO₃ were shifted from reference Ge lines that indicates changes of the unit cell parameters. The lines of the roentgenogram were identified and the results are represented in the table 2.

Table 2. Results of identification of roentgenogram lines.

#	Specimen #4			Specimen #6			Specimen #17			Specimen #5			hkl
	d, Å	Qe	Qc	d	Qe	Qc	d	Qe	Qc	d	Qe	Qc	
1	4,164	577	586	4,15	581	581	4,155	579	583	4,155	579	579	001
2	3,9434	643	646	3,9499	641	947	3,9697	645	645	3,9499	641	648	100
3	2,8474	1233	1232	2,8512	1230	1228	2,8602	1222	1222	2,8564	1226	1227	101
4	2,783	1291	1292	2,7792	1294	1295	2,798	1227	1275	2,7868	1288	1290	110
5	2,3089	1875	1879	2,3099	1874	1876	2,3205	1857	1857	2,3093	1875	1875	111

6	1,9666	2586	2584	1,9653	2589	2590	1,977	2559	2559	1,9638	2593	2593	200
7	1,7753	3172	3171										201
8	1,6152	3833	3817	1,6179	3820	3819							211

where d – interplanar distance, $Q_e = 10^4/d^2$ – experimental values, $Q_c = 10^4/d^2$ – calculated values.

Table 3. PbTiO₃ unit cell parameters.

Specimen #	a, Å	b, Å	c, Å	cell volume, Å ³
4	3.934(1)	3.934(1)	4.130(6)	63.91(11)
6	3.930(1)	3.930(1)	4.146(1)	64.04(2)
17	3.956(2)	3.956(2)	4.143(3)	64.84(6)
5	3.936(2)	3.936(2)	4.134(3)	64.06(7)
Standard PbTiO ₃	3,899	3,899	4,1532	

The increase of a and b and decrease of c in comparison to standard values indicates that Zr atoms edge their way into PbTiO₃ lattice.

4. CONCLUSIONS

In this paper the possibility to implement SLS for porous ZTS ceramics piezoelements fabrication is shown. The density of sintered specimens was measured and its dependence on sintering parameters shown. X-ray diffraction analysis had shown changes in phase content of the sintered specimens. The unit cell parameters of the PbTiO₃ phase produced by laser sintering differ from that obtained by furnace annealing.

5. REFERENCES.

1. Glosman I. A. *Piezoelectric ceramics*. Moscow: 'Energy' Published, 1972. 288 P.
2. Gururaja T. R. "Piezoelectrics for Medical Ultrasonic Imaging". *American Ceramic Society Bulletin*. 1994. V. 73. N 5. P. 50-55.
3. Ivanova A. M. et al. "Physical characteristics of selective laser sintering of metal-polymer powder compositions". *Journal of Russian Quantum Electronic*. 1998, V.25. N 5. P.433-438.
4. Bandyopadhyay A., Panda R. K. et al. "Processing of Piezocomposites by Fused Deposition Technique". *Journal of the American Ceramic Society*. 1997. V. 80. N 6. P. 1366-1372.
5. Bagrov V. V. et al. "Selective laser sintering basis's development for metal-polymer powder compositions". *Pre-print FIAN* N 14, 1996. Moscow. P.19.

Selectively Deposit Copper on Laser-treated Polyimide Using Electroless Plating

Gang Zhao^{a,b,c}, H.M. Phillips^b, Hongyu Zheng^b, Siuchung Tam^a, Wenqing Liu^c,
Gongling Wen^c, Zhiben Gong^c, Yeeloy Lam^a

^aSchool of E.E.E., Nanyang Technology University, Nanyang Ave. , Singapore 639798

^bGintic Institute of Manufacture Technology, 71 Nanyang Drive, Singapore 638075

^cAnhui Institute of Optics and Fine Mechanics, Hefei, China, 230032

ABSTRACT

Many reviews about the interconnection line fabrication by laser processing method were reported recently. UV laser process polyimide has been studied thoroughly during the past decade. In this report, we discussed the utilization of surface potential changing on polyimide film irradiated by excimer KrF laser and metallized the UV laser treated polyimide surface by electroless copper deposition. A new negatively charged polymer stabilized Pd solution (Pd-sols) was applied as catalyst in this experiment. We also produced pattern-wised fine line on KrF laser induced PI surface using this method.

Keywords: KrF laser, Laser induced, Polyimide film, electroless plating, Pd-sols

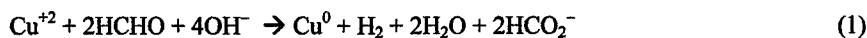
1. INTRODUCTION

With the growing trend of miniaturization in the electronics industry, many reviews about the interconnection line fabrication by laser processing method were reported^{1,2,3}. UV laser processing polyimide has been studied thoroughly during the past decade because of its potential application in electrical package and PCB manufacture. The physical and chemical characteristics of the laser irradiation area were investigated. According to recent report¹¹, some organic polymer material such as PI can change its surface potential to positive when irradiated by UV laser. Electroless, or autocatalytic, plating is a non-electrolytic method of deposition metal from solution. It is a traditional and popular method for metallization non-conductive and semiconductor materials in microelectronics industry. Catalyst play an important role during eletroless deposition because metal ions inside the plating bath can only be reduced on catalyst because of lower chemical reaction potential during electroless plating. However, because of the adherent properties of common Pd colloid catalyst, it is hard to get selective deposition during electroless plating. Some assistant technique and manufacture process must be applied in order to get required pattern such as masking.

In this report, we discussed the effect of the surface potential changing in polyimide film irradiated by excimer KrF laser and selectively metallized the UV laser treated polyimide surface using negative charged catalyst by electroless copper deposition. A kind of negatively charged polymer (PVP) stabilized Pd solution was discussed and was applied as catalyst. By changing the concentration of the PVP-sols, we produced pattern-wise electroless deposition copper on KrF laser induced PI surface.

2. BACKGROUND

The overall electroless copper plating reaction is theoretically given as:



From a physicist point of view, electroless copper deposition is a heterogeneous electron-transfer reaction in which electrons are transferred, across interface, from a reducing agent to copper ions. The overall electron-transfer reaction can be re-written as:



* Correspondence: Email: zhaogang98@hotmail.com

Where Red is the reducing agent and Ox is the oxidation product of Red. Various common reducing agents have been suggested for the electroless copper baths, namely formaldehyde, dimethylamine borane, borohydride, hydrazine, sugars (sucrose, glucose), etc.⁶. Because the oxidation-reduction reaction proceeds only on a catalytic surface, initial grain structure is largely determined by the randomly distributed catalyst particles on the substrate. The intent of our experiment is to selective deposit copper on non-conductive substrate like polyimide. As stated above, the electroless metallization of semiconductors and non-conducting materials requires a catalytically active surface, the distribution of catalyst particles on substrate surface may cause the possibilities of pattern-wise electroless metallization. When we back to chemistry once again, we can find any of a wide range of metals, including copper, nickel, gold, silver and all the other precious metals (Group VIII B) may be used as catalyst. In practice, however, because of cost consideration and preferential adsorption of the catalyst to certain surface, only a few metals and physical/chemical forms of these have found acceptance in the electroless copper industry. Palladium-tin colloid is by far the most commonly used catalyst^{8,9}. It is a stable reaction product of palladium and tin chlorides in acidic solution. The colloid size is about 10–50 Å, consisting of a palladium-rich inner core and bearing hydrous Sn(IV) chlorides in the outer sphere. Because Sn(IV) is inherently a strong adherent material, the resultant film over the entire substrate surface is tenaciously retained even when rinsing. A major disadvantage, however, is the marked lack of selectivity; all exposed surface are heavily catalyzed and the resultant electroless copper deposit exhibited poor selective.

Recently, another polymer stabilized Pd solution was reported¹⁰. These negatively charged colloidal Pd particles were prepared in aqueous solution by the reduction of Pd²⁺ ions with hypophosphate in the presence of polyvinylpyrrolidone (PVP). The schematic of the Pd particles in this sol is shown as Figure 1. The extraordinary merit of this type catalyst is that the size of Pd particle can be changed by increasing or decreasing the concentration of the amount of PVP. Meanwhile, as state above, some organic polymer material such as PI can change its surface potential to positive when irradiated by UV laser. By all these means, we can selective adhere negatively charged Pd-sols on positively charged PI surface after treated by KrF excimer laser and adjust the coverage percentage of Pd on the PI substrate surface as well.

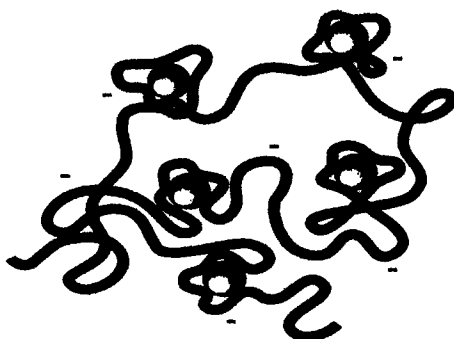


Figure 1. The schematic of the Pd particles inside the PVP sols

3. EXPERIMENT

3.1 Substrate preparation:

KrF(248nm) excimer laser and 3rd harmonic wavelength (266nm) pulse Nd:YAG laser were utilized to modify the surface of PI film (amorphous; 60 μm thickness; DuPont (KAPTON)). In order to investigate the role of excimer laser during the particle-substrate and polymer-substrate absorption process, we choose some typical fluence based on the property of the interaction between UV laser and polyimide. They are include 50 mJ/cm² and 65 mJ/cm², which around the conductivity threshold^{1,2}, 80mJ/cm², the ablation threshold² and much higher fluence as 170mJ/cm² and 250mJ/cm². Laser shots is another main factor during the experiment. Under threshold fluence like 50mJ/cm², 65mJ/cm² and 80mJ/cm², we treated the polyimide by 100, 300, 500, 1000 and 1500 shots. When using as high as 170mJ/cm² and 250mJ/cm², we treated the polyimide by 50, 100, 200, 300 and 400 shots. The other work we did was to produce some fine line pattern on the polyimide surface. The laser fluence we used to make fine line were 50mJ/cm² and 170mJ/cm². The line width was about 50 μm and line spaces are from 15 μm to 90 μm by the optical lens system with the magnificent of 4 times.

3.2 Sols preparation:

All chemical used were of analytical grade, and the solutions were prepared with deionized water. The detail process can be found in W. Hoogsteen and L.G. J. Fokkink's paper¹⁰. A 0.056M palladium chloride solution and 0.48M sodium hypophosphate solution were prepared first. Sodium hypophosphate was used as the reducing agent. In order to get the palladium sols containing Pd, PVP, and hypophosphate in varying concentration ratios, we prepared PVP solution by adding 1 g PVP into 1 liter water. By changing the amount of the PVP solution, we can get difference concentration ratios. The whole process like this: First, a solution containing the required amount of Pd and PVP was prepared. While the solution was stirred, a given volume of the hypophosphate solution was added. After an "induction period" of 3 to 5 min, the color of the solution turned from yellow to transparent brown due to the formation of metallic Pd.

3.3 Pre-treatment before plating

During the experiment, pretreatment is very important. The first rinse step of pre-treatment procedure is to remove the debris touched on the other areas than laser treated area and the foreign matters on the substrate surface during laser irradiation. Ultra-sonic instrument was specially implied in this step. We immersed the specimen into DI water and methanol alcohol separately in order to find the suitable solution. The rinsing procedure to clean the surface by ultra-sonic will take about 10 min. Methanol was chosen because it is the less harmful to PI film than other alcohol solutions. The results show that the DI water cannot clean the surface effectively. After the catalyst absorption process, the specimen must be rinsed carefully once again. The purpose of this step is to get rid of the catalyst, which stuck to the unwanted area during the adsorption period. Since the Pd-sols are no solvable and on intimate terms with laser treated PI surface, running water was shown to be the best way in this step. As stated above, there are some kinds of charge attraction between Pd particles in the Pd-sols and the changed surface potential on PI film irradiated by UV laser. So the Pd particles will remain on the laser treated area of the PI surface and the Pd particles will be get rid of on the un-treated areas. According to the reports, the average size of Pd particles may be around some nano-level¹⁰.

4. RESULTS AND DISCUSSION

4.1 Laser Irradiation

The surface potential of some polymer film can be changed with the irradiation of excimer laser with a fluence near the threshold for APD(Ablative Photodecomposition) in air¹¹. Table 1 shows surface potential before and after APD¹¹.

Table 1. Surface potential of PEI, PI and PES films irradiated by excimer laser with 100 shots in ambient air and successively rinsed by DI(deionized) water

Surface Potential	PET	PI	PES
Before Irradiation	-0.5 ~ 0.5 V	0.2 ~ 0.4 V	0.0 ~ 0.2 V
After Irradiation	2.5 ~ 3.0 V	1.6 ~ 1.8 V	3.0 ~ 3.8 V
After Rinsed by DI water	16 ~ 25 V	3.5 ~ 4.5 V	12 ~ 14 V

We investigated the surface potential of PI film irradiated by ArF excimer laser with the fluence of 50 mJ/cm² in air by the method of contact angle. The data was shown in Figure 2.

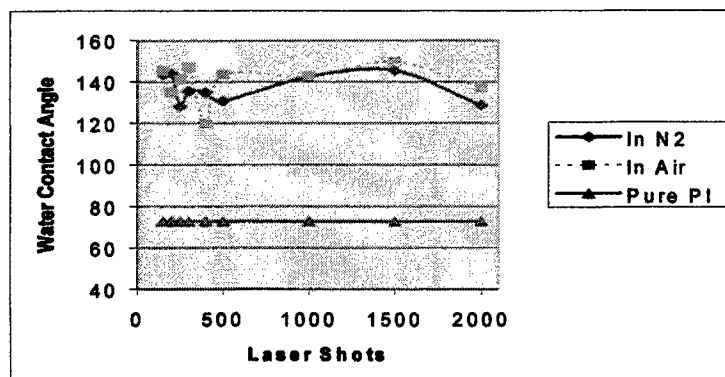


Figure 2. Water Contact Angle Data Under Different Circumstance

As showed in Figure 2, the surface of pure PI was hydrophobic (water contact angle $\sim 73^\circ$) originally. UV laser shots changed the properties of the surface so much that the water contact angle is changed to as high as around 140° . It is clear that the Pd-sols in the solution would like to contact the laser treated area other than pure PI. However, the fluence result exhibit little difference between high and low fluence. With the increasing the shots of laser, the roughness of the surface increased and the water contact angle decreased a little probably due to the surface roughness. The most reasonable cause of positive charged of the surface potential may be explained in terms of the preferential deposition of cationic species compared with anionic fragment during laser irradiation. Hiroyuki gave the evidence that when irradiated by KrF laser in vacuum, the surface potential of PET changed a little from $0.0 \sim 0.5V$ to $1.0 \sim 1.5V$ ¹¹. With the nitrogen blowing the surface of PI, there is a little decrease of the water contact angle compared to in ambient air. That means nitrogen only dedicated to the increasing of the conductivity during laser irradiation.

On the basis of the results mentioned above, we intended to apply the surface potential behavior into an electroless plating process in order to get selective deposition. The plating process was divided into two parts. One is catalyst absorption and the other is plating process. According to the previous discussed, we know that the location and coverage percentage of catalyst particles on substrate film are very important during autocatalytic deposition for pattern wised plating. During the experiment, we found that moderate concentration of Pd-sols is significant. No metal can be reduced when less concentration. No selective results can be getting when with much more concentration. It is turned out to be very necessary to pre-treat the specimen accordingly before dip it into catalyst bath and plating bath. Unfortunately, the exact data of the percentage of the Pd particle on the laser treated area can not be get because of some reasons.

4.2 Plating Results and Discussion

After plating the specimen in the electroless plating bath of High Build type for 10 min, we used SEM to observe the surface morphs of the plating results. Some SEM pictures with difference laser treating specimen were shown as Figure 3. We can find that a thin copper layer covered the grain "rock" on the substrate, which was produced by laser ablation polyimide surface. Because of the short plating time, the copper layer cannot fill the "gap" between the rocks. Figure 4 gives the cross section of the grain "rocks". Because the plating bath was High Build type, which will deposit two or three μm in about 20 minute^{8,9}. The thickness of the copper layer can be estimated around $1 \mu m$. The conductivity of the surface is not necessary for the initial formation of copper growth in electroless process unlike electrolytic process. So this method can overcome the shortcoming of direct electrolytic method on non-metal substrate such as low plating speed and limited plating area. Also because electroless process was used to pre-nucleation in industrial application, the following electrolytic process is necessary. Undoubtedly, this copper layer will give great help to the following electroplating process. More laser shots and higher laser fluence will improve the adhesion between the plated Cu layer and the substrate by the way of enlarging the contact area. Since copper ions can be reduced only on the Pd surface, the size of catalyst particles become important for the origin formation of copper. We cannot control the deposition rate once the oxidation-reduction happened. However, these SEM graphs can indicate the fine grain crystal formed. Amorphous or polycrystalline Cu is likely formed according to plating theory. Fine line with the line width of $50 \mu m$ can be get as well using such method as shown in Figure 5. That means we can get very high space resolution in the laser-ablated trench.

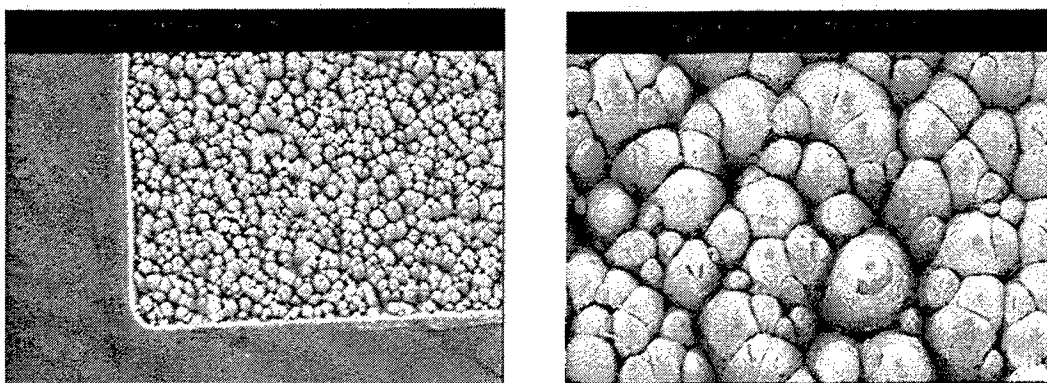


Figure 3a. SEM graph of High Build plating 10 minutes on the Polyimide film treated by KrF excimer laser with the fluence of 250 mJ/cm², 400 shots. (200 ×), Figure 3b. SEM graph of High Build plating 10 minutes on the Polyimide film treated by KrF excimer laser with the fluence of 250 mJ/cm², 400 shots. (1,000 ×)

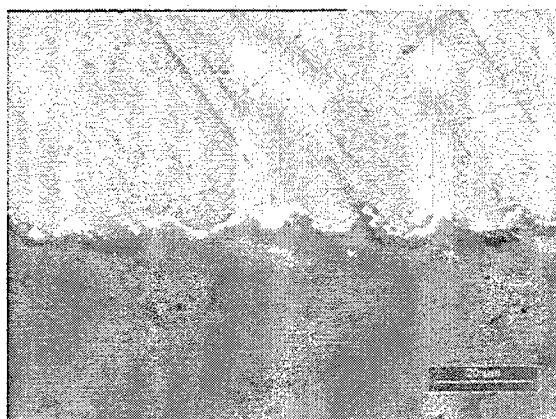


Figure 4. Cross-section of High Build plating 10 minutes on the Polyimide film treated by KrF excimer laser with the fluence of 80 mJ/cm² 1000 shots. (500 ×).

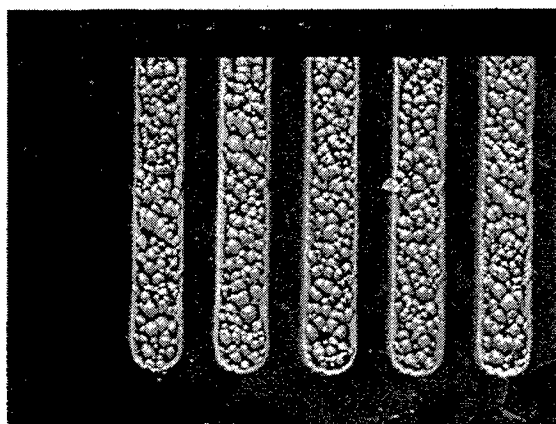


Figure 5. SEM of plating Cu on KrF laser with the fluence of 250 mJ/cm² 100 shots

5. CONCLUSION

Under very short period of plating time, the fine crystal copper grain can be selectively deposited on the laser treated area after some pretreatment. Very thin copper layer followed the shape of the surface modified by UV laser. Longer plating time and some other kind of plating solution can get thicker layer. Unlike electrolytic plating process, ablation fluence looks better for electroless process. The pretreatment is very important during electroless process. Catalyst adsorption process will definitely affect the quality of selectivity. More work should be done to improve such process. Measurements of adhesion between copper and PI substrate need be done as well to verify the reliability for industry application.

6. ACKNOWLEDGEMENTS

The authors specially thank Dr. Fokkink for many discussions and advices on the preparation of the PVP-sols. Many colleagues in GINTIC such as Dr. G.C Lim and Mr. Liu Fengming and Dr. Yihong Chen were also very appreciated for their kind help and assistant on the measurements of SEM and microscope.

REFERENCE

1. J. C. Miller, R. F. Hagland, Jr (eds): Laser ablation-Mechanics and Applications, Let. Notes Phys., Vol.389 (Springer, Berlin, Heidelberg 1991)
2. M. Von Allmen: Laser-beam Interaction with Materials, Springer Ser. Mater. Sci. Vol 2 (Springer, Berlin, Heidelberg 1987)
3. W. Boyd, E. Fogarassy, M. Stuke (eds): Proc 1990 Spring Meeting of E-MRS, Appl. Surf. Sci. 46 (1990)
4. F. Pearlstein, in Modern Electroplating, 3rd Edition, F. A. Lowenheim, Ed., John Wiley & Sons, New York, NY, 1974; Ch31.
5. Cheryl A. Deckert: Plating & Surface Finishing, Feb 1995, Vol 82, No. 2, P48 ~ 55
6. F. E. Stone in electroless Plating: Fundamentals and Applications, G. O. Mallory & J. B. Hajdu, Eds. , AESF, Orlando, FL, 1990
7. Specification IPC-AM-372, Institute for Interconnecting and Packaging Electronic Circuits, Lincolnwood, IL
8. C. R. Shipley, U. S. Paten 3,011,920(1961)
9. E. D.'Ottavio, U. S. Paten 3,532,518(1970)
10. Williem Hoogsteen, Lambertus G. J. Fokkink: Journal of Colloid and Interface Science 175, 12 - 26 (1995), P12 ~ 26
11. Hiroyuki Niino and Akia Yabe, Applied Surface Science 69 (1993) 1-6

Addendum

The following papers were announced for publication in this proceedings but have been withdrawn or are unavailable.

- [3933-02] **Tailoring metallic nanostructures and their optical properties through irradiation with short laser pulses**
F. Stietz, J. Bosbach, D. Martin, T. Wenzel, F. Traeger, Univ. of Kassel (Germany)
- [3933-03] **Micromachining of fused silica in the mid-infrared**
R. F. Haglund, Jr., D. R. Ermer, M. R. Papantonakis, Vanderbilt Univ. (USA)
- [3933-07] **Low-fluence pulsed UV laser induced effects in metal samples**
D. P. Taylor, H. Helvajian, The Aerospace Corp. (USA)
- [3933-16] **Surface topography and laser texturing process**
J. Jiang, W. Zhao, Harbin Institute of Technology (China)
- [3933-20] **Effect of stress on the microwave dielectric properties of $\text{Ba}_{0.5}\text{Sr}_{0.5}\text{TiO}_3$ thin films**
J. S. Horwitz, W. Chang, W. J. Kim, S. B. Qadri, J. M. Pond, S. W. Kirchoefer, D. B. Chrisey, Naval Research Lab. (USA)
- [3933-26] **Fabrication of nanostructured thin films by PLA**
V. I. Marine, Univ. Aix-Marseille I & II (France)
- [3933-30] **Characteristics of laser ablation for environmental and other chemical analysis applications**
R. E. Russo, Lawrence Berkeley National Lab. (USA); S. Amimoto, D. J. Chang, The Aerospace Corp. (USA)
- [3933-51] **Recent developments in lasers for stereolithography**
J. P. Partanen, 3D Systems, Inc. (USA)
- [3933-66] **Excimer laser decontamination of an industrial surface**
V. I. Marine, Univ. Aix-Marseille I & II (France)

Author Index

- Akane, Toshimitsu, 218
 Allen, Susan D., 396
 Amimoto, Sherwin, Addendum, 113
 Ando, Nobuo, 487
 Andrews, J. Thomas, 14
 Auyeung, Raymond C. Y., 105
 Awazu, Kunio, 496
 Bachmann, Friedrich G., 90
 Baets, Roel G., 309
 Bandis, C., 2
 Barzilay, Izhak, 77
 Basting, Dirk, 365
 Bauer, Hans-Dieter, 290
 Birkitt, Andra D., 113
 Bonse, Jörn, 280
 Bosbach, Johannes, Addendum
 Braune, Torsten, 290
 Budai, J. D., 124
 Chang, Dick J., Addendum, 113
 Chang, Wontae, Addendum
 Charbonneau-Lefort, M., 192
 Chen, Hengfu, 438
 Cheong, B. A., 182
 Chisholm, M. F., 124
 Chong, Tow Chong, 182
 Chow, S. K., 182
 Chrisey, Douglas B., Addendum, 105, 140
 Christen, D. K., 124
 Coosemans, Thierry, 309
 Dawes, M. L., 2
 Demos, Stavros G., 316
 Dickinson, J. Thomas, 2
 Dubowski, Jan J., 58
 Ehrfeld, Wolfgang, 290
 Engel, Michael Y., 77
 Ermer, David R., Addendum
 Erofeev, Michail V., 425
 Fedosenko, E. V., 432
 Fernández, Félix E., 200
 Fitz-Gerald, J., 105
 Foong, A., 207
 Gaudron, Anne, 290
 Geiger, Manfred, 338
 Gilmore, C. M., 140
 Goh, Y. W., 182
 Gong, Zhiben, 505
 González, Yelitza, 200
 Govorkov, Sergei V., 365
 Gower, Malcolm C., 261
 Gruzdev, Vitali E., 34, 412
 Gruzdeva, Anastasia S., 34, 412
 Gu, Jianhui, 388
 Haase, Jens, 290
 Haglund, Richard F., Jr., Addendum
 Hato, Yukinori, 487
 Hayashi, Hideaki, 356
 Hayashi, Shigeki, 404
 He, Z. F., 469
 Helvajian, Henry, Addendum
 Henyk, Matthias, 26
 Honda, Kazumasa, 404
 Hong, Ming Hui, 207
 Horwitz, James S., Addendum, 140
 Huang, Su Mei, 478
 Ihara, Satoshi, 272
 Ishizaka, Yuri, 46
 Ishizu, A., 496
 Ivanova, Tatyana V., 225
 Jang, Jun-Ho, 237
 Jia, Weiyi, 200
 Jiang, Jianfeng, Addendum
 Juodkasis, Saulius, 246
 Kabashin, Andrei V., 192
 Kafafi, Zakya H., 140
 Kaufmann, Stefan, 371
 Kautek, Wolfgang, 280
 Kawaguchi, Y., 2
 Kim, Heungsoo, 140
 Kim, W. J., Addendum
 Kirchoefer, Steven W., Addendum
 Klimenko, Anatoly G., 432
 Klotzbücher, Thomas, 290
 Kojima, Isao, 404
 Kononenko, V. V., 322
 Konov, Vitali I., 322
 Kozłowski, Mark R., 316
 Kroeger, D. M., 124
 Krüger, Joerg, 280
 Kryukova, Galina V., 502
 Kuriki, Sigenori, 487
 Kushto, Gary P., 140
 Lakeou, Samuel, 105
 Lam, Yee-Loy, 388, 505
 Langford, Steve C., 2
 Lee, Jong-Moo, 237
 Lee, Y. E., 124
 Leonelli, Richard, 192
 Liu, Huimin, 200
 Liu, Wenqing, 505
 Livshits, Boris, 77
 Lomaev, Mikhail I., 425
 Lu, Yong Feng, 131, 182, 207, 469, 478
 Luz, Gerhard, 371
 Maeda, Mitsuo, 457

- Mai, Zhi Hong, 469
 Marine, Vladimir I., Addendum
 Marinho, Gilson, 396
 Martin, Dietrich, Addendum
 Matsumura, Takeshi, 404
 Matsuno, Ken-ichi, 152
 Matsuo, Shigeki, 246
 Matsuzaki, Akiyoshi, 487
 McGill, Robert A., 105
 Meunier, Michel, 192
 Midorikawa, Katsumi, 166, 218, 332
 Milne, David K., 261
 Misawa, Hiroaki, 246
 Miyamoto, Isamu, 46, 356, 379
 Munhoz, André L. J., 396
 Muys, Peter F., 322
 Naessens, Kris, 309
 Nagumo, Yuzo, 404
 Nakata, Yoshiki, 457
 Nakayama, Takayuki, 379
 Ni, H. Q., 182
 Niino, Hiroyuki, 174, 347
 Nishio, Satoru, 487
 Norton, David P., 124
 Novoselov, Andrew R., 432
 Obata, Kataro, 166
 Ochi, Humihiro, 356
 Ogata, Kiyoshi, 69
 Ohmura, Etsuji, 46
 Okada, Tatsuo, 457
 Ottevaere, Heidi, 309
 Otto, Andreas, 371
 Paatzsch, Thomas, 290
 Panchenko, Alexei N., 425
 Papantonakis, Michael R., Addendum
 Park, Chan, 124
 Partanen, Jouni P., Addendum
 Pavelyev, Vladimir S., 322
 Petrov, Alexey L., 502
 Phillips, Harvey M., 505
 Pilkington, Richard D., 445
 Pimenov, Sergej M., 322
 Piqué, Alberto, 105, 140
 Plotnikov, A. E., 432
 Pond, Jeffrey M., Addendum
 Popp, Martin, 290
 Prokhorov, Alexander M., 322
 Qadri, Syen B., Addendum
 Qiu, H., 131
 Reif, Juergen, 26, 62
 Ren, Zhong Min, 182, 469
 Rizvi, Nadeem H., 261
 Rodríguez, Edgardo, 200
 Rodríguez, Victor, 200
 Roth, Stephan, 338
 Rumsby, Phil T., 261
 Russo, Richard E., Addendum
 Saitoh, Masakazu, 69
 Salles, Djalma S., 396
 Sano, Tomokazu, 356, 379
 Sato, Hiroyasu, 487
 Sato, Tadake, 174
 Sato, Toshio, 152
 Satoh, Saburoh, 272
 Scarparo, Marco A. F., 396
 Schmid, Rainer, 62
 Schneider, Thomas, 62
 Sen, Pratima, 14
 Sheehan, Lynn M., 316
 Shitz, Dmitrii V., 425
 Shyshkovsky, Igor V., 502
 Skakun, Victor S., 425
 Slobodtchikov, Evgueni V., 365
 Smaglini, Ingo, 290
 Soifer, Victor A., 322
 Sosnin, Edward A., 425
 Stietz, Frank, Addendum
 Sugioka, Koji, 166, 218, 332
 Sun, Hong-Bo, 246
 Sun, Jinzuo, 438
 Sun, Z., 478
 Suzuki, Kenkichi, 69
 Takahashi, Michiko, 69
 Takai, Hiroshi, 166
 Tam, Siu-Chung, 388, 505
 Tanaka, Kazuyoshi, 487
 Tanaka, Kenichiro, 379
 Tanaka, Takao, 272
 Tarasenko, Victor F., 425
 Tarasova, Ekatherina Yu., 502
 Taylor, David P., Addendum
 Tomimasu, Takio, 496
 Toyoda, Koichi, 166
 Traeger, Frank, Addendum
 Tsujine, Yukari, 487
 Uchida, Yuichi, 379
 Umesaki, Norimasa, 496
 Van Daele, Peter, 309
 Van Hove, An, 309
 Vandamme, E., 322
 Vanwassenhove, Luc, 309
 Veiko, Vadim P., 225
 Verebelyi, D. T., 124
 Verstuyft, Steven, 309
 Voznesensky, Nikolay B., 225
 Wang, J. P., 182
 Wang, Jun, 347
 Watanabe, Koji, 46
 Watanabe, Mitsura, 246
 Wei, Xueqin, 388
 Wen, Gongling, 505
 Wenzel, Thomas, Addendum
 Wiessner, Alexander O., 365
 Wolfram, Dirk, 26, 62
 Wrobel, Jerzy M., 280
 Wu, F. Fushun, 445

Wu, H. D., 105
Xu, Xianfan, 299
Yabe, Akira, 174, 347
Yagi, Takashi, 404
Yamabe, Chobei, 272
Yamazaki, Susumu, 404
Yasumoto, Masato, 496
Yogev, David, 77
Yoo, Tae-Kyung, 237
Yoshida, Takehito, 152
Yoshida, Yoshiaki, 152
Yu, Wenying, 438
Zeid, Shaik, 77
Zhang, Jie, 332
Zhao, Gang, 505
Zhao, Wansheng, Addendum
Zheng, Hongyu, 505
Zheng, Qiguang, 388
Zhou, Chenbo, 438

ISSN 0277-786X
ISBN 0-8194-3550-3